FIBROBLAST GROWTH FACTORS AND STEM CELLS IN REGENERATIVE PHARMACOLOGY AND ANTI-AGING INTERVENTION

EDITED BY: Zhouguang Wang, Xiaokun Li, Q. Adam Ye, Saverio Bellusci and Yidong Wang

PUBLISHED IN: Frontiers in Cell and Developmental Biology, Frontiers in Pharmacology and Frontiers in Genetics

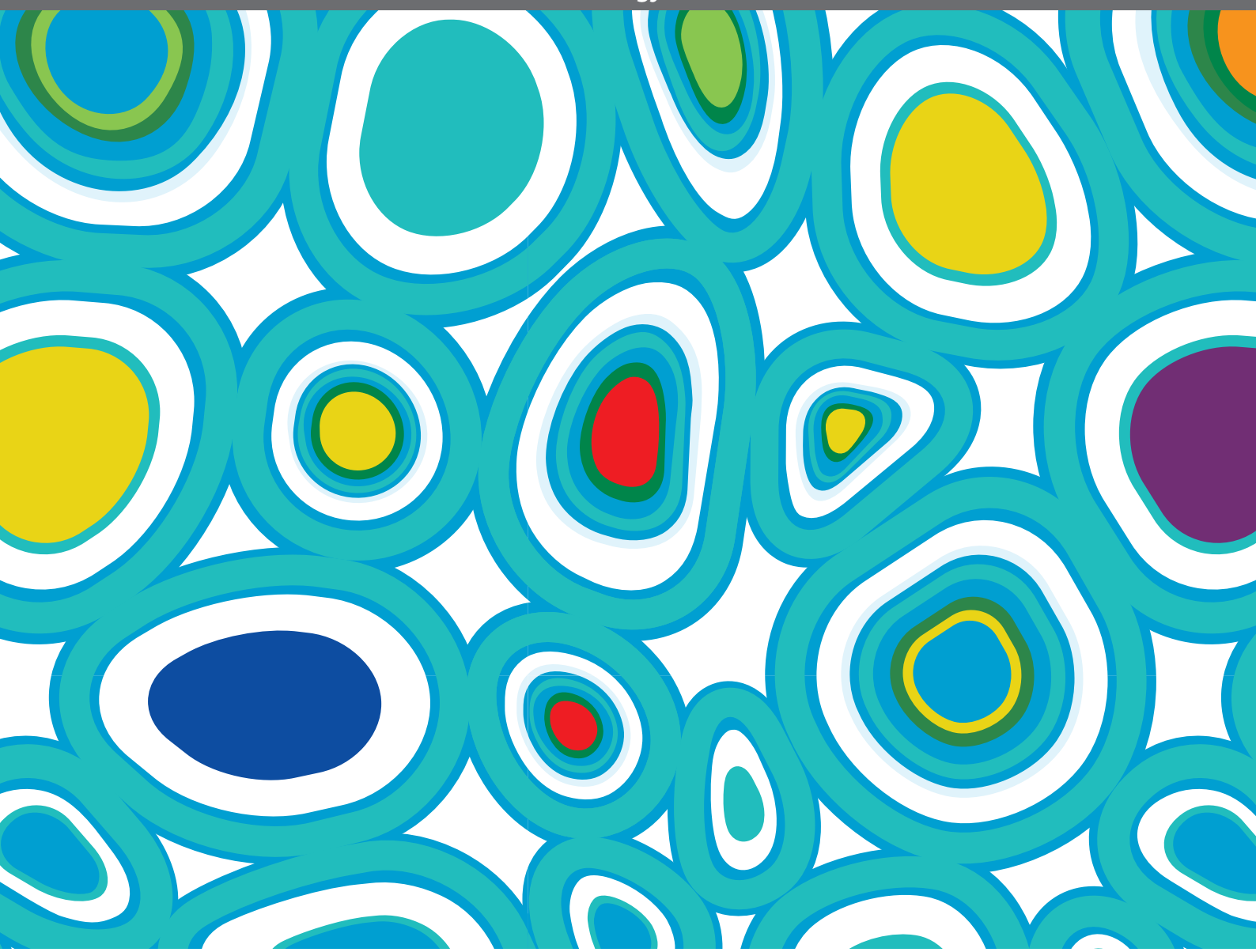

frontiers Research Topics

frontiers

ISSN 1664-8714
ISBN 978-2-88976-288-0
DOI 10.3389/978-2-88976-288-0

About Frontiers

Frontiers is more than just an open-access publisher of scholarly articles: it is a pioneering approach to the world of academia, radically improving the way scholarly research is managed. The grand vision of Frontiers is a world where all people have an equal opportunity to seek, share and generate knowledge. Frontiers provides immediate and permanent online open access to all its publications, but this alone is not enough to realize our grand goals.

Frontiers Journal Series

The Frontiers Journal Series is a multi-tier and interdisciplinary set of open-access, online journals, promising a paradigm shift from the current review, selection and dissemination processes in academic publishing. All Frontiers journals are driven by researchers for researchers; therefore, they constitute a service to the scholarly community. At the same time, the Frontiers Journal Series operates on a revolutionary invention, the tiered publishing system, initially addressing specific communities of scholars, and gradually climbing up to broader public understanding, thus serving the interests of the lay society, too.

Dedication to Quality

Each Frontiers article is a landmark of the highest quality, thanks to genuinely collaborative interactions between authors and review editors, who include some of the world's best academicians. Research must be certified by peers before entering a stream of knowledge that may eventually reach the public - and shape society; therefore, Frontiers only applies the most rigorous and unbiased reviews.
Frontiers revolutionizes research publishing by freely delivering the most outstanding research, evaluated with no bias from both the academic and social point of view. By applying the most advanced information technologies, Frontiers is catapulting scholarly publishing into a new generation.

What are Frontiers Research Topics?

Frontiers Research Topics are very popular trademarks of the Frontiers Journals Series: they are collections of at least ten articles, all centered on a particular subject. With their unique mix of varied contributions from Original Research to Review Articles, Frontiers Research Topics unify the most influential researchers, the latest key findings and historical advances in a hot research area! Find out more on how to host your own Frontiers Research Topic or contribute to one as an author by contacting the Frontiers Editorial Office: frontiersin.org/about/contact

FIBROBLAST GROWTH FACTORS AND STEM CELLS IN REGENERATIVE PHARMACOLOGY AND ANTI-AGING INTERVENTION

Topic Editors:
Zhouguang Wang, Albert Einstein College of Medicine, United States
Xiaokun Li, Wenzhou Medical University, China
Q. Adam Ye, Massachusetts General Hospital, Harvard Medical School, United States
Saverio Bellusci, University of Giessen, Germany
Yidong Wang, Xian Jiaotong University, China

Citation: Wang, Z., Li, X., Ye, Q. A., Bellusci, S., Wang, Y., eds. (2022). Fibroblast Growth Factors and Stem Cells in Regenerative Pharmacology and Anti-Aging Intervention. Lausanne: Frontiers Media SA. doi: 10.3389/978-2-88976-288-0

Table of Contents

frontiers in Cell and Developmental Biology

ORIGINAL RESEARCH
published: 03 December 2020
doi: 10.3389/fcell.2020.625151

Biological Behavioral Alterations of the Post-neural Differentiated Dental Pulp Stem Cells Through an *in situ* Microenvironment

Lihua Luo[1†], Xiaoyan Wang[1†], Yanni Zhang[1†], Yuwei Wu[1†], Fengting Hu[1], Zhenjie Xing[1], Lei Wang[2], Jian Xiao[3], Fernando Guastaldi[4], Yan He[4,5] and Qingsong Ye[1,4,6*]*

[1] School and Hospital of Stomatology, Wenzhou Medical University, Wenzhou, China, [2] Wenzhou Institute of Biomaterials and Engineering, Wenzhou Medical University, Wenzhou, China, [3] School of Pharmaceutical Sciences, Wenzhou Medical University, Wenzhou, China, [4] Skeletal Biology Research Center, Massachusetts General Hospital, Harvard University, Boston, MA, United States, [5] Tianyou Hospital, Wuhan University of Science and Technology, Wuhan, China, [6] Center of Regenerative Medicine, Renmin Hospital of Wuhan University, Wuhan, China

OPEN ACCESS

Edited by:
Zhouguang Wang, Albert Einstein College of Medicine, United States

Reviewed by:
Xiaogang Xu, Zhejiang University, China
Junchao Wei, Nanchang University, China

***Correspondence:**
Yan He
helen-1101@hotmail.com; yhe9@mgh.harvard.edu
Qingsong Ye
qingsongye@foxmail.com

† These authors have contributed equally to this work

Specialty section:
This article was submitted to Stem Cell Research, a section of the journal Frontiers in Cell and Developmental Biology

Received: *02 November 2020*
Accepted: *16 November 2020*
Published: *03 December 2020*

Citation:
Luo L, Wang X, Zhang Y, Wu Y, Hu F, Xing Z, Wang L, Xiao J, Guastaldi F, He Y and Ye Q (2020) Biological Behavioral Alterations of the Post-neural Differentiated Dental Pulp Stem Cells Through an in situ Microenvironment. Front. Cell Dev. Biol. 8:625151. doi: 10.3389/fcell.2020.625151

Transplantation of undifferentiated dental pulp stem cells (DPSCs) may suffer from tumorigenesis. Neuronal differentiated DPSCs (d-DPSCs) have emerged as an ideal source to treat central nervous system (CNS) disorders. Moreover, different components of culture medium functioned on the characteristics of d-DPSCs *in vitro*. In this study, d-DPSCs were cultured in three types of medium: Neurobasal®®-A medium supplemented with 2% B27 (the 2% B27 NM group), Neurobasal® -A medium supplemented with 2% B27 and 5% FBS (the 2% B27 + 5% FBS NM group), and α-MEM containing 10% FBS (the 10% FBS α-MEM group). We found that d-DPSCs in the 2% B27 + 5% FBS NM group had lower proliferation and reduced expression of transient receptor potential canonical 1 (TRPC1) and CD146, whereas up-regulated Nestin and microtubule-associated protein-2 (MAP-2). Notably, d-DPSCs in the 10% FBS α-MEM group possessed high proliferative capacity, decreased expression of neuron-like markers and partially restored stemness. It was demonstrated that d-DPSCs cultured in the 2% B27 + 5% FBS NM could maintain their neuron-like characteristics. Besides, d-DPSCs cultivated in the 10% FBS α-MEM could partially recover their stem cells properties, indicating that neural differentiation of DPSCs was reversible and could open novel avenues for exploring the pluripotency of DPSCs.

Keywords: central nervous system, dental pulp stem cells, post-neural differentiation, regenerative medicine, culture microenvironment

INTRODUCTION

The central nervous system (CNS) is the center of all motor output and sensory perception. Neuroinflammation, traumatic events, neurodegenerative disorders, and so on, can cause CNS tissue destruction along with function disablement, severely impacting patients and their families (Hong et al., 2016; Kahveci et al., 2017; Baumard et al., 2018). In the lesion site, apart from the lack of neuronal precursors, activated astrocytes and microglia cells would induce apoptosis of neurons and inhibit regeneration of axons (de Amorim et al., 2020). Recently, stem cells-based therapy has

provided a promising treatment option for neuronal injury and disease due to the capacity of stem cells to differentiate into multiple neurogenic lineages (Bianco et al., 2016; Caseiro et al., 2016).

Dental pulp stem cells (DPSCs), which are a type of mesenchymal stem cells (MSCs), have MSCs-like properties such as the ability to undergo self-renewal and multi-differentiation (Gronthos et al., 2000, 2002). DPSCs express MSCs-like phenotypic markers, including CD73, CD90, CD105, CD146, and STRO-1, and do not express hematopoietic lineage surface molecules, such as CD14, CD34, CD45, and HLA-DR (Gronthos et al., 2002; Kawashima, 2012). DPSCs, which originate from embryonic neural crest ecto-MSCs and oral-derived epithelial stem cells, can be readily isolated from extracted human teeth such as impacted third molars and orthodontically extracted premolars (Karaoz et al., 2011; Pisciotta et al., 2020). Therefore, DPSCs can be collected without the need for invasive surgical procedures and without ethical concerns (Geng et al., 2017; Xiao et al., 2017). Moreover, DPSCs have the ability to express neural stem cell-like markers such as Nestin, glial fibrillary acidic protein (GFAP), β-III tubulin, and microtubule-associated protein-2 (MAP-2) without the pre-induction of neuronal differentiation (Sakai et al., 2012; Feng et al., 2013). Additionally, upon induction, DPSCs can differentiate into mature neurons, dopaminergic-like cells, Schwann cells, oligodendrocyte progenitors, neuroglial cells, and retinal ganglion-like cells using neurogenic supplements (Heng et al., 2016; Mead et al., 2017; Sanen et al., 2017). Recent reports have shown that DPSCs have a much better neurogenic differentiation capability than MSCs, which are derived from other tissues such as bone marrow and adipose tissue (Luo et al., 2018b). Thus, DPSCs have been applied widely in stem cell therapy to treat CNS diseases such as spinal cord injury, stroke, Parkinson's disease, Alzheimer's disease, and retinal degeneration (Martens et al., 2013; Chalisserry et al., 2017; Mead et al., 2017).

Although most previous studies have demonstrated that the transplantation of undifferentiated DPSCs has neuro-regenerative potential for neural lesions in animal models *in vivo*, there are some disadvantages in utilizing undifferentiated DPSCs for neural regeneration (Heng et al., 2016). Firstly, undifferentiated DPSCs have a tendency to undergo spontaneous differentiation into multiple lineages upon grafting, which may attenuate their clinical efficacy because only a small proportion of the transplanted DPSCs differentiate into neural lineages *in vivo*. Secondly, there is a risk that undifferentiated DPSCs can generate undesired lineages at the transplantation site, such as fibrotic scar tissue, which may hinder neural regeneration. Moreover, the injured site of neurological tissue presents an obviously different environment compared with the carefully controlled environment *in vitro*. There are also limitations in that the migration of transplanted DPSCs to the injured site may be limited *in vivo* (Mead et al., 2017). Additionally, as dental pulp derived-MSCs, DPSCs have the potential to undergo tumorigenesis or tumor growth and progression at the transplantation site (Ohkoshi et al., 2017; Ridge et al., 2017). Accordingly, pre-neuronal differentiated DPSCs (d-DPSCs) can express neuron-associated surface molecules before grafting *in vivo*, which may enhance their integration into the host's nervous system. Meanwhile, the transplantation of pre-neuronal d-DPSCs can also reduce tumorigenesis and promote neurogenesis.

Recently, it has been confirmed that DPSCs can be induced to form neurospheres or differentiate into mature neurons by endogenous signaling cues (Heng et al., 2016). Many factors, for instance, the extracellular matrix, mechanical force, growth factors, culture systems, oxygen stress, and microfluidic systems, have been reported as critical factors for the induction of neuronal differentiation (Heng et al., 2016; Thompson and Chan, 2016; Yamazaki et al., 2016; Kim et al., 2018; Liu et al., 2020). However, few in-depth studies have examined the effects of the surrounding microenvironment on the survival, proliferation, and expression of markers of DPSC post-neuronal differentiation. In this study, we aimed to evaluate the characteristics of post-neuronal d-DPSCs using different *in vitro* culture medium protocols in order to explore the possible development of transplanted neuronal d-DPSCs *in vivo* during stem cell therapy for CNS diseases.

MATERIALS AND METHODS

Primary Isolation and Culture

The isolation and culture procedures for DPSCs were described previously (Luo et al., 2018a), and ethic approval was obtained from the Ethics Committee of Wenzhou Medical University (Project No. 2018008). Briefly, impacted third molars were collected from the Department of Oral and Maxillofacial Surgery, Stomatological Hospital of Wenzhou Medical University, Wenzhou, China. Dental pulp tissues were extracted, rinsed three times in phosphate-buffered saline (PBS), and cut into small pieces. The tissue pieces were treated with 3 mg/mL collagenase type I (Gibco, Gaithersburg, MD) and 4 mg/mL dispase (Sigma-Aldrich, Steinheim, Germany) in a shaker (150–180 rpm) for 10 min at 37°C. Digestion was terminated with 1 mL fetal bovine serum (FBS; Gibco) followed by centrifugation at room temperature for 10 min at 1,500 rpm. The collected cells and pulp tissue were resuspended in α-modified Eagle's medium (α-MEM; Gibco) supplemented with 20% FBS, 100 U/mL penicillin, and 100 μg/mL streptomycin (Gibco). The cell suspension was plated in cell culture flasks and incubated at 37°C in a 5% CO_2 humidified atmosphere. The culture medium was initially replaced at day 5, and then replaced every other day. The morphology of DPSCs was observed by light microscopy (TS100; Nikon, Tokyo, Japan), and the proliferation rate of DPSCs was evaluated by a Cell Counting Kit-8 (CCK-8) assay (Dojindo Molecular Technologies, Kumamoto, Japan) as described previously (Luo et al., 2018a).

Immunophenotype and Multi-Differentiation of DPSCs

The immunophenotype of DPSCs were characterized by immunofluorescence analysis. Briefly, DPSCs were seeded onto

glass slides that were placed in 6-well plates, fixed with 4% paraformaldehyde for 30 min, washed three times with PBS, and blocked with 5% bovine serum albumin (BSA; Amresco, Solon, OH, United States) containing 0.1% Triton X-100 (Solarbio, Beijing, China) for 30 min. DPSCs were incubated with primary antibodies against CD146 (1:200; Abcam, Cambridge, United Kingdom) and STRO-1 (1:50; Santa Cruz Biotechnology, Santa Cruz, CA, United States) at 4°C overnight, washed 3 times with Tween-20, and stained with secondary antibodies to donkey anti-rabbit IgG H&L (1:500; Abcam) and donkey anti-mouse IgG H&L (1:500; Abcam) for 1 h at room temperature in the dark. Cell nuclei were stained with 4′,6-diamidino-2-phenylindole (DAPI; Beyotime, Shanghai, China) for 5 min. The glass slides were treated with Antifade Mounting Medium (Beyotime) and observed by fluorescence microscopy (Eclipse 80i; Nikon, Japan).

As for multi-differentiation, DPSCs were cultured to be confluent for osteogenic and adipogenic differentiation. The culture medium was replaced by the OriCell^{TM} osteogenic differentiation medium and adipogenic differentiation medium (all from Cyagen Biosciences, CA, United States), respectively. After being induced for 21 days, cells were fixed in 4% formaldehyde, mineralized nodules and lipid droplets were stained by Alizarin Red solution and Oil Red O solution (all from Sigma-Aldrich), respectively. Concerning chondrogenic differentiation, 2.5×10^5 cells were centrifuged at 1,000 rpm for 5 min at room temperature in a 15 mL conical tube. Afterward, the cell pellets were cultivated in the OriCell^{TM} chondrogenic differentiation medium for 30 days, then this spheroid-like structure was fixed with 4% formaldehyde and embedded in paraffin for Alcian blue staining. Images were taken and analyzed by light microscopy (TS100; Nikon).

Neurogenic Differentiation of DPSCs and Culture of d-DPSCs

The neurogenic differentiation of DPSCs was described previously (Heng et al., 2016). Briefly, DPSCs were plated in 6-well plates at a density of 1.0×10^5 cells/well in complete α-MEM containing 10% FBS and incubated at 37°C in a 5% CO_2 humidified atmosphere. After 24 h, the cell culture medium was changed to neuron-inducing Neurobasal®-A medium (Thermo Fisher Scientific, Waltham, MA, United States) supplemented with 2% B27 (Thermo Fisher Scientific), 20 ng/mL basic fibroblast growth factor (bFGF; Thermo Fisher Scientific), and 20 ng/mL epidermal growth factor (EGF; Thermo Fisher Scientific) for 12 days. The neuron-inducing medium was replaced every 3 days. On day 12, the cells were determined and verified by immunofluorescence staining with an anti-GFAP antibody (1:200; Sigma-Aldrich).

After 12 days, d-DPSCs were digested, collected, and re-suspended in complete α-MEM with 10% FBS. d-DPSCs were plated in 6-well plates at a density of 1.5×10^5 cells/well. After 24 h, d-DPSCs were divided into 3 different medium groups: Neurobasal®-A medium supplemented with 2% B27 (the 2% B27 NM group), Neurobasal®-A medium supplemented with 2% B27 and 5% FBS (the 2% B27 + 5% FBS NM group), and complete α-MEM containing 10% FBS (the 10% FBS α-MEM group). Undifferentiated DPSCs that were cultured with complete α-MEM containing 10% FBS were used as the control group. The morphology of the cells was observed by light microscopy (TS100; Nikon).

CCK-8 Assay

The proliferation of d-DPSCs cultured in the different media was evaluated by a CCK-8 assay (Dojindo Molecular Technologies) as described previously (Luo et al., 2018a). Briefly, d-DPSCs were plated in 96-well plates at a density of 2.0×10^3 cells/well. After 24 h, the cell culture medium was changed to 2% B27 NM, 2% B27 + 5% FBS NM, or 10% FBS α-MEM. Undifferentiated DPSCs treated with complete α-MEM containing 10% FBS, 100 U/mL penicillin, and 100 μg/mL streptomycin were used as the control group. The cell culture medium was changed every other day. After incubation for 1, 3, 6, and 9 days, 10 μL CCK-8 solution was added to 100 μL culture medium of each well and incubated for 1 h at 37°C in a 5% CO_2 humidified atmosphere. Optical density (OD) was measured photometrically at 450 nm using an absorbance microplate reader (Varioskan LUX; Thermo Fisher Scientific).

Immunofluorescence Staining

The expression of proliferation (e.g., transient receptor potential canonical 1, TRPC1), stemness (e.g., CD146), and neuronal differentiation (e.g., Nestin and MAP-2) markers was determined in d-DPSCs cultured in the different media by immunofluorescence staining as described previously (Luo et al., 2018a). At the designated time points after culture, the cells were fixed in 4% paraformaldehyde for 30 min and incubated for 30 min in a blocking solution containing 5% BSA (Amresco) and 0.1% Triton X-100 (Solarbio) at room temperature. The cells were incubated with the following primary antibodies at 4°C overnight: anti-TRPC1 (1:50; Santa Cruz Biotechnology), anti-CD146 (1:200; Abcam), anti-Nestin (1:1000; Sigma-Aldrich), and anti-MAP-2 (1:500, Sigma-Aldrich). The secondary antibodies were donkey anti-rabbit IgG H&L and donkey anti-mouse IgG H&L (1:500; Abcam). Cell nuclei were stained with DAPI (Beyotime), and images were taken by fluorescence microscopy (Eclipse 80i; Nikon, Japan). Both the culture of undifferentiated DPSCs in complete α-MEM containing 10% FBS for 6 days and the culture of DPSCs in continuous neuronal differentiation medium for 12 days (the neural-induction group) served as control groups.

Western Blot Analysis

The protein expression of d-DPSCs cultured in the different media was analyzed by western blotting (Luo et al., 2018a). d-DPSCs were plated in 6-well plates and incubated with 2% B27 NM, 2% B27 + 5% FBS NM, or 10% FBS α-MEM for 6 days. The cells were lysed in sodium dodecyl

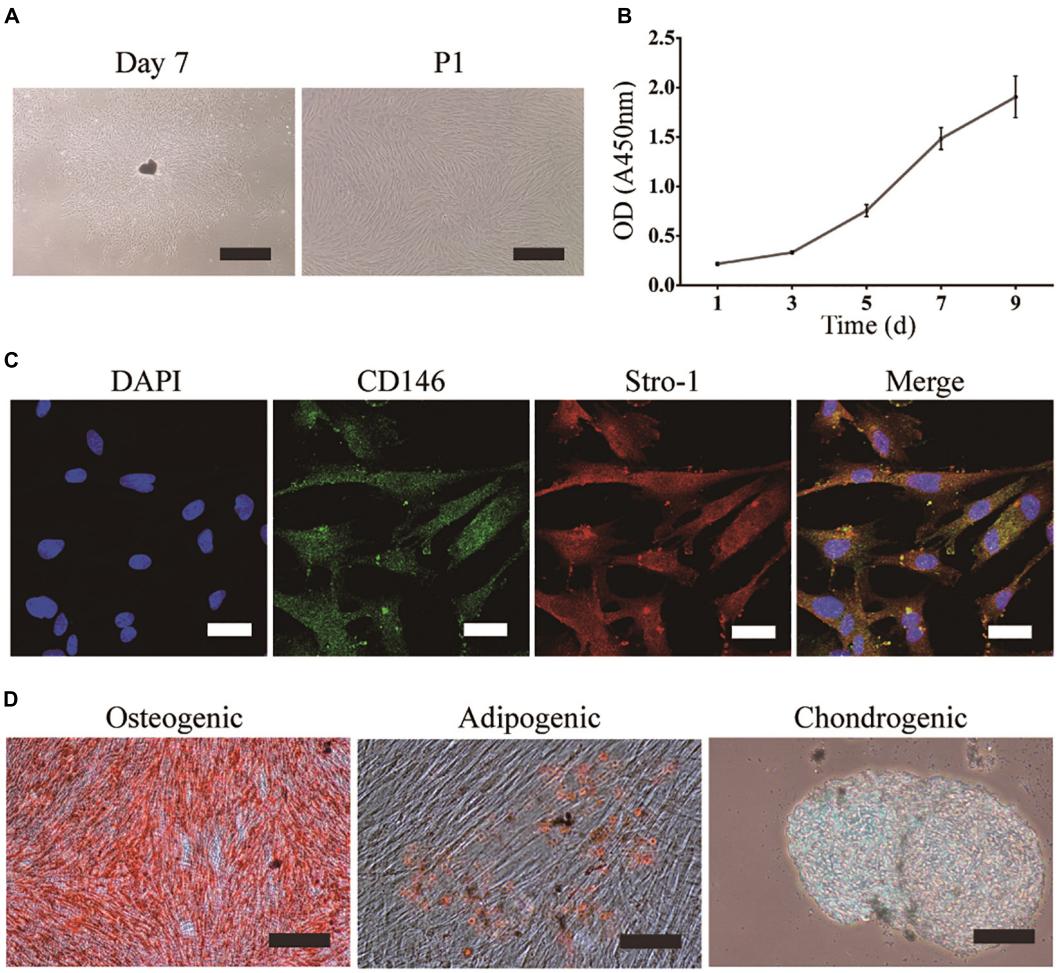

FIGURE 1 | Isolation, culture, and identification of DPSCs. **(A)** DPSC culture at day 7 (scale bar: 500 μm), and the first passage (P1) (scale bar: 200 μm). **(B)** Proliferation of DPSCs at days 1, 3, 5, 7, and 9. **(C)** Expression of CD146 and STRO-1 (scale bar: 33.3 μm). **(D)** Osteogenic, adipogenic, and chondrogenic differentiation of DPSCs (scale bar: 100 μm).

sulfate (SDS) lysis buffer, and the proteins were collected for western blot analysis. Culture of undifferentiated DPSCs for 6 days and the 12-day neural-induction group were used as control groups. Proteins (20 μg) were separated by 10% SDS-polyacrylamide gel electrophoresis, followed by transfer to a polyvinylidene fluoride membrane (Millipore, Darmstadt, Germany) in transfer buffer. The membranes were blocked with 5% (w/v) milk (BD Bioscience, Franklin Lakes, NJ, United States) in Tris-buffered saline with Tween-20 for 90 min and incubated with the following primary antibodies at 4°C for 16 h: anti-CD146 (1:1000; Abcam), anti-TRPC1 (1:300; Santa Cruz Biotechnology), anti-Nestin (1:1000; Sigma-Aldrich), and anti-MAP-2 (1:300; Santa Cruz Biotechnology). The secondary antibodies were horseradish peroxidase-conjugated and were added to the membranes for 1 h at room temperature. Detection of the target proteins were performed using the ChemiDoc XRS + Imaging System (Bio-Rad Laboratories, Hercules, CA, United States). All experiments were repeated three times.

Flow Cytometry

The MSCs-like characteristics of d-DPSCs cultured in 10% FBS α-MEM were identified by flow cytometry as described previously (Luo et al., 2018a). Undifferentiated DPSCs cultured in complete α-MEM containing 10% FBS were used as the control group. Briefly, after the cells reached 90% confluence, they were identified by flow cytometry using primary antibodies against human CD90, CD73, CD146, CD105, CD14, CD34, CD45, and HLA-DR (all from BioLegend, San Diego, CA, United States) according to standard protocols. The data were analyzed with a CytoFLEX flow cytometer (Beckman Coulter, Brea, CA, United States).

STATISTICAL ANALYSIS

Statistical analyses were performed using SPSS 19.0 software (SPSS Inc., Chicago, IL). All data were presented as mean ± standard deviation (SD). One-way ANOVA was used for

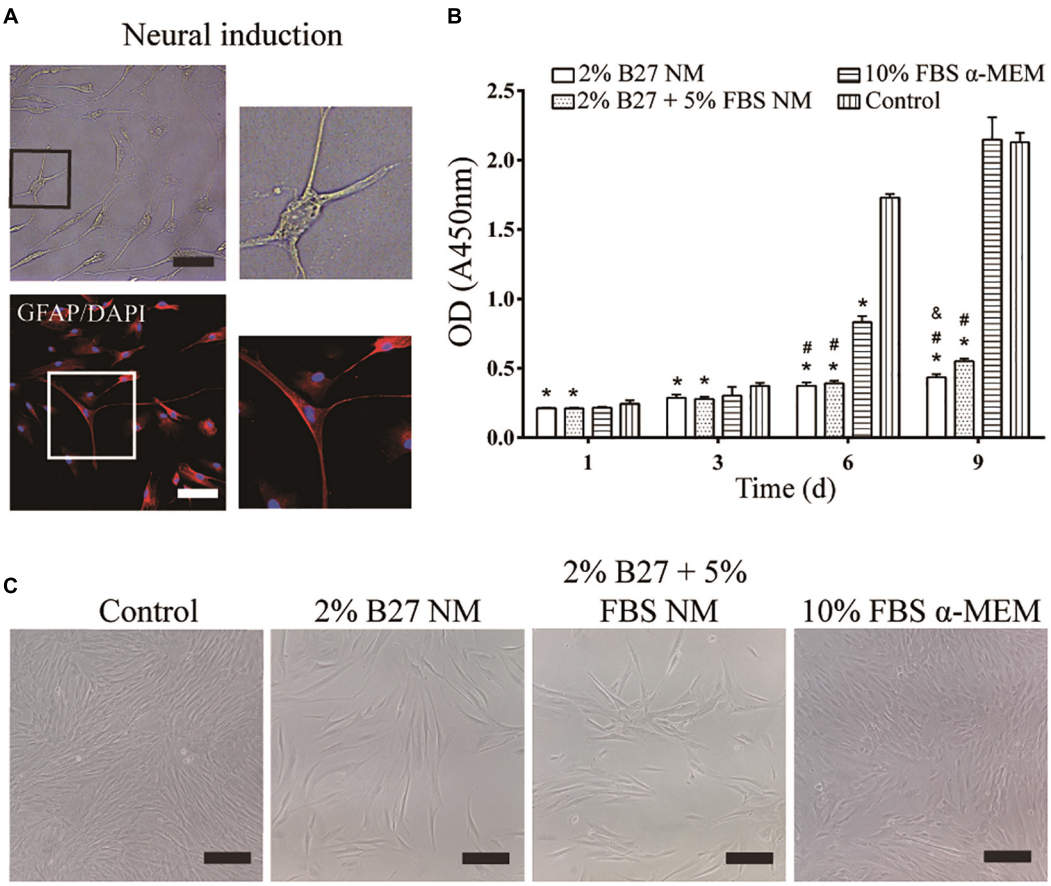

FIGURE 2 | Neurogenic differentiation of DPSCs and their proliferation in the different media. **(A)** d-DPSCs showed a typical neuron-like cell morphology (scale bar: 100 μm). **(B)** Proliferation of d-DPSCs after culture in the different media. **(C)** Morphology of d-DPSCs cultured in the different media at day 6 (scale bar: 200 μm). $^{*}P < 0.05$ vs. Control group; $^{\#}P < 0.05$ vs. 10% FBS α-MEM group; $^{\&}P < 0.05$ vs. 2% B27 + 5% FBS NM group.

multiple comparisons. Tukey's test or Dunnett's test was used as *post hoc* test. $P < 0.05$ was considered statistically significant.

RESULTS

Characterization and Analysis of the Multipotency of DPSCs

DPSCs were grown in a homogeneous layer of plate-adherent cells and presented with typical fibroblastic and spindle-shaped morphology. DPSCs had a high proliferation rate as OD values (450 nm) increased from 0.2 on day 1 to 1.9 on day 9 (**Figures 1A,B**). To evaluate the MSCs-like properties of DPSCs, immunocytochemistry and multilineage differentiation were performed. Immunofluorescence staining indicated that DPSCs expressed MSCs-like markers such as CD146 and STRO-1 (**Figure 1C**). The multipotency of DPSCs was examined by osteogenic, adipogenic, and chondrogenic differentiation. Alizarin Red and Oil Red O staining displayed the deposition of mineralized nodules and formation of lipid droplets, respectively. Moreover, Alcian blue staining indicated that proteoglycans were synthesized during chondrogenic induction (**Figure 1D**).

Morphology of Neuronal d-DPSCs and the Effect of Different Culture Media on Their Proliferation

After neurogenic-induced differentiation with Neurobasal®-A medium (Thermo Fisher Scientific) containing 2% B27 (Thermo Fisher Scientific), 20 ng/mL bFGF, and 20 ng/mL EGF (Thermo Fisher Scientific) for 12 days, DPSCs showed neuron-like cellular morphology with a large perikaryon and peripheral cytoplasmic extensions, and expressed the neuronal marker GFAP (**Figure 2A**). The effect of the different culture media on the proliferation of d-DPSCs was evaluated by a CCK-8 assay (**Figure 2B**). The results indicated that d-DPSCs grew slowly in the 2% B27 NM and 2% B27 + 5% FBS NM groups, and their viability in these groups was significantly different compared to the control group until day 9 and with the 10% FBS α-MEM group at days 6 and 9. The proliferation of d-DPSCs in the 10% FBS α-MEM group was significantly different compared with the control group at day 6, but was similar to that of the

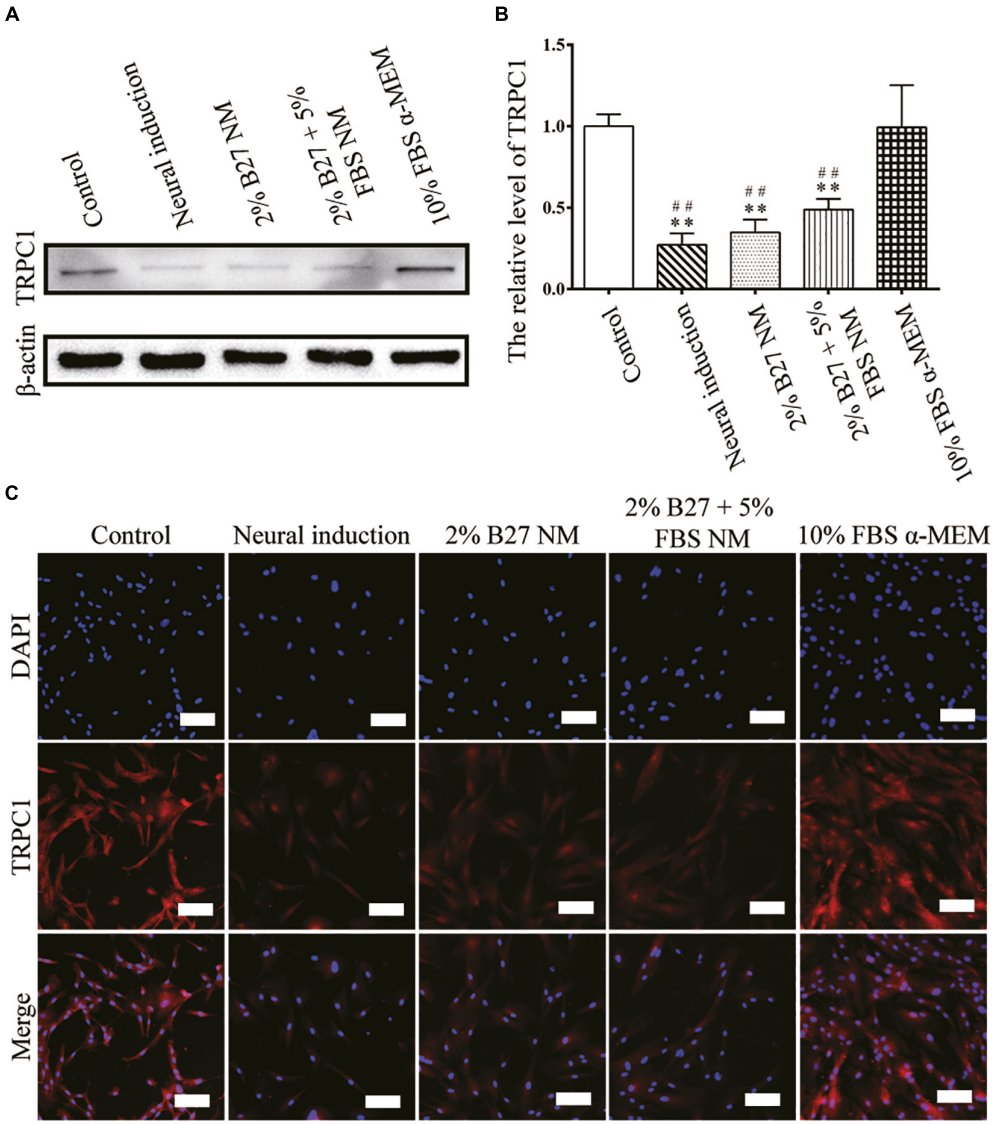

FIGURE 3 | Expression of the proliferation marker TRPC1 in d-DPSCs cultured in the different media. **(A)** Expression of TRPC1 protein. **(B)** Quantification of TRPC1 expression. **(C)** Immunofluorescence staining of TRPC1 (scale bar: 100 μm). $^{**}P < 0.01$ vs. Control group; $^{\#\#}P < 0.01$ vs. 10% FBS α-MEM group.

control group at day 9. The morphology of d-DPSCs varied in the different culture media; for example, the cells tended to display a fibroblast-like shape in the 10% FBS α-MEM group at day 6 (**Figure 2C**). Moreover, cell density in the 10% FBS α-MEM group was similar to that in the control group, but much higher than that of the 2% B27 NM and 2% B27 + 5% FBS NM groups.

Protein Expression and Immunofluorescence Staining of Proliferation and Stemness Markers of d-DPSCs After Culture in the Different Media

The proliferation and stemness characteristics of d-DPSCs in the 2% B27 NM, 2% B27 + 5% FBS NM, and 10% FBS α-MEM groups were verified by western blot and immunofluorescence staining analyses. The results indicated that TRPC1 protein expression was much higher in the 10% FBS α-MEM group than in the other experimental groups and in the neural-induction group, but similar to that of the control group (**Figure 3**). TRPC1 expression was not significantly different between the 10% FBS α-MEM and control groups (**Figure 3B**). According to immunofluorescence staining analysis, TRPC1 expression was maintained at a higher level in the 10% FBS α-MEM and control groups compared to the other groups, which was consistent with the data from western blot analysis (**Figure 3C**).

CD146 protein expression was examined to evaluate the stemness properties of d-DPSCs cultured in the different media. In the experimental groups, CD146 expression was the highest

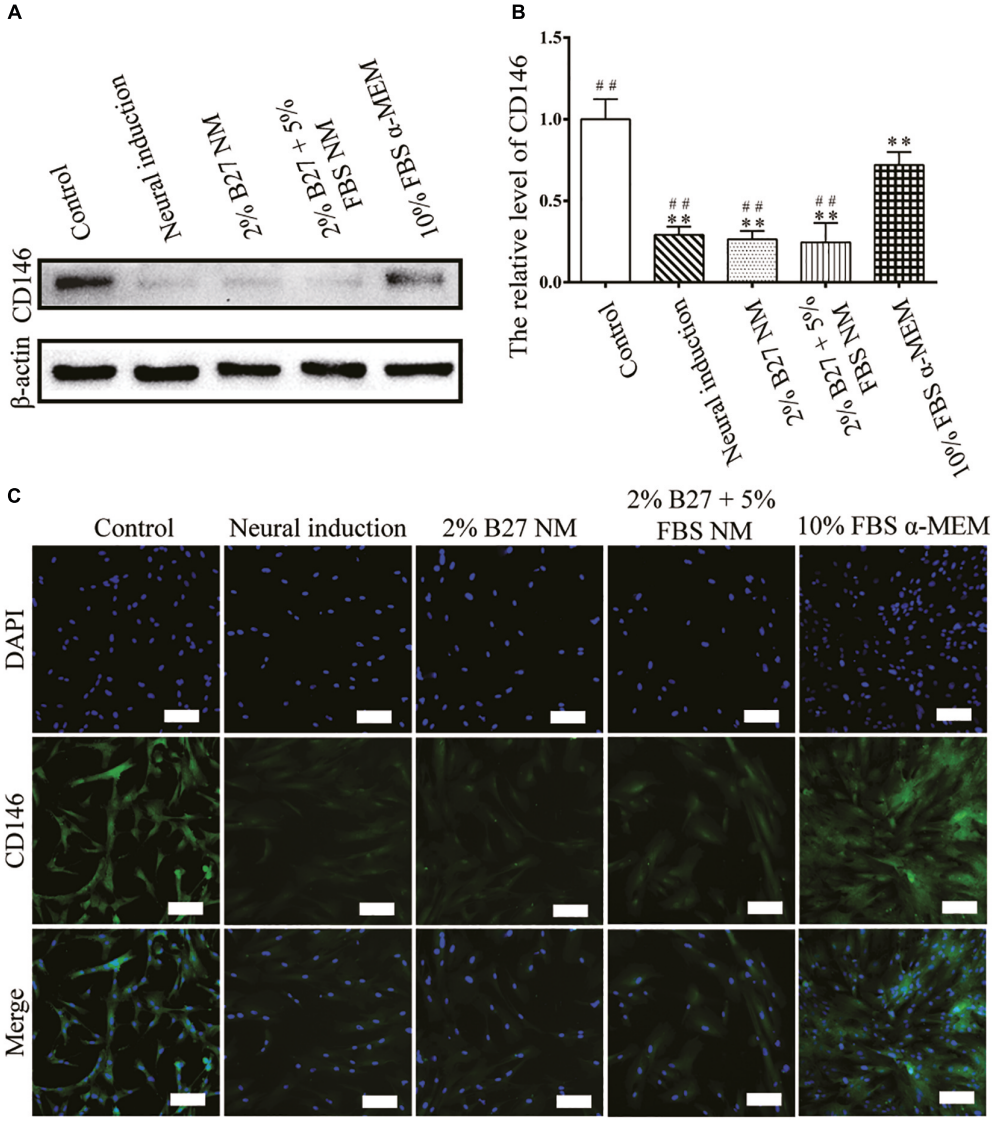

FIGURE 4 | Expression of the stemness marker CD146 in d-DPSCs cultured in the different media. **(A)** Expression of CD146 protein. **(B)** Quantification of CD146 expression. **(C)** Immunofluorescence staining of CD146 (scale bar: 100 μm). $^{**}P < 0.01$ vs. Control group;$^{\#\#}P < 0.01$ vs. 10% FBS α-MEM group.

in the 10% FBS α-MEM group; however, it was lower than that of the control group. Moreover, CD146 expression was barely detected in the neural-induction group (**Figures 4A,B**). CD146 was expressed at a high level in the 10% FBS α-MEM and control groups, which was similar to the results from western blot analysis (**Figure 4C**).

Protein Expression and Immunofluorescence Staining of Neuronal Markers of d-DPSCs After Culture in the Different Media

The expression of neuronal markers (e.g., Nestin and MAP-2) was examined in d-DPSCs in the 2% B27 NM, 2% B27 + 5% FBS NM, and 10% FBS α-MEM groups. Nestin and MAP-2 expression was higher in the 2% B27 + 5% FBS NM and neural-induction groups. Whereas, Nestin and MAP-2 expression was decreased in the 10% FBS α-MEM and control groups. MAP-2 was expressed at a high level in the 2% B27 NM group, but Nestin was expression at a low level (**Figures 5A,B**, **6A,B**). Immunofluorescence staining indicated that Nestin and MAP-2 were expressed in all experimental and control groups, with significantly increased expression in the 2% B27 NM, 2% B27 + 5% FBS NM, and neural-induction groups (**Figures 5C**, **6C**).

Expression of MSCs-Like Markers by d-DPSCs in the 10% FBS α-MEM Group

According to the results of CCK-8, western blot, and immunofluorescence staining analyses, the characteristics

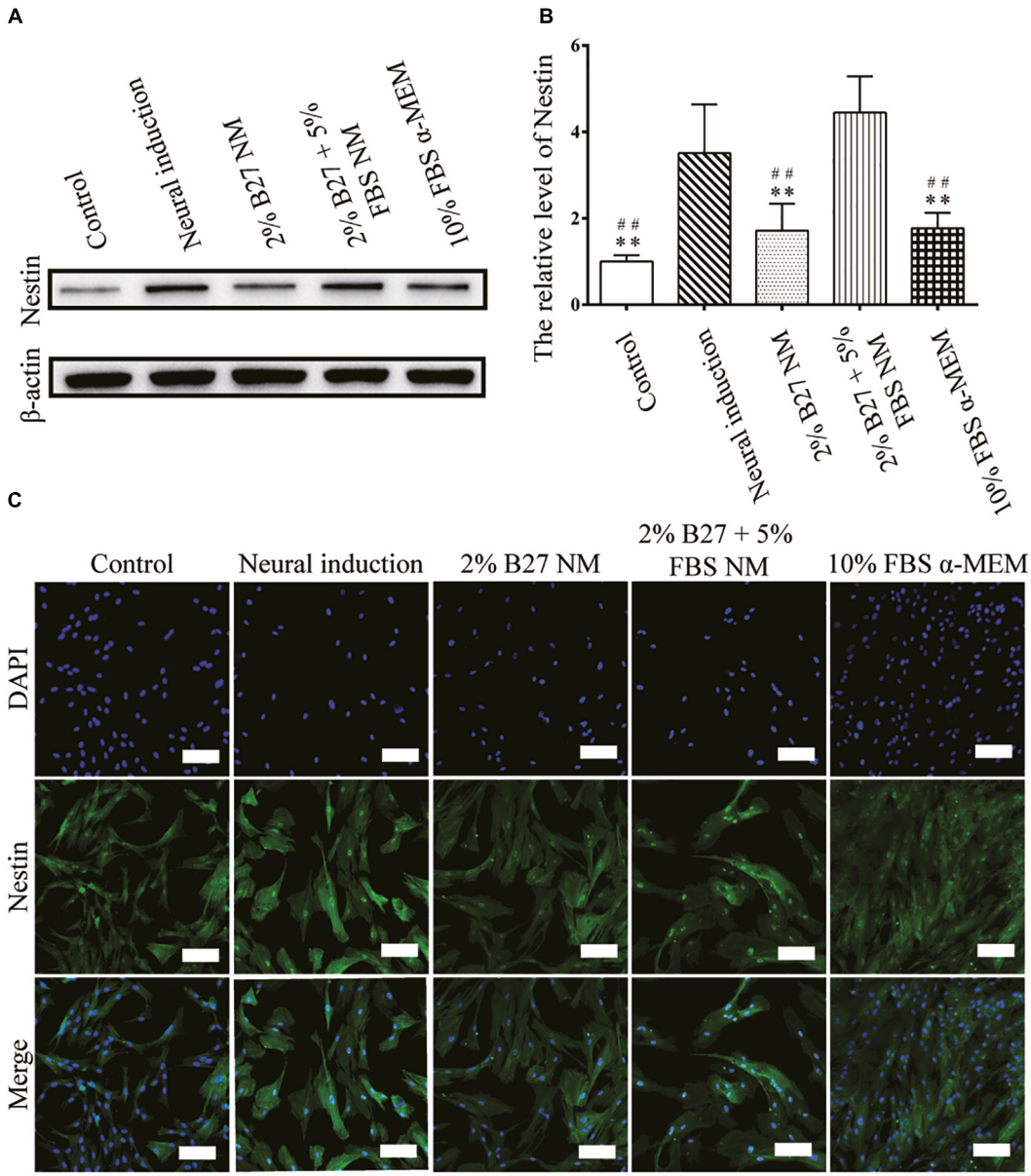

FIGURE 5 | Expression of the neuron-like marker Nestin in d-DPSCs cultured in the different media. **(A)** Expression of Nestin protein. **(B)** Quantification of Nestin expression. **(C)** Immunofluorescence staining of Nestin (scale bar: 100 μm). $^{**}P < 0.01$ vs. Neural-induction group; $^{\#\#}P < 0.01$ vs. 2% B27 + 5% FBS NM group.

of d-DPSCs in the 10% FBS α-MEM group were similar to those of the control group. Therefore, the MSCs-like properties of d-DPSCs in the 10% FBS α-MEM group were evaluated by flow cytometry using the MSCs markers CD73, CD90, CD105, CD146, CD34, CD14, CD45, and HLA-DR. Flow cytometry demonstrated that d-DPSCs were positive for CD73, CD90, CD105, and CD146 in the 10% FBS α-MEM group, where the expression of CD105 and CD146 was reduced compared to the control group; CD105 and CD146 expression was decreased from 99.37 to 58.41% and from 97.60 to 69.75%, respectively (**Figure 7A**). d-DPSCs did not express CD34, CD14, CD45, and HLA-DR in the 10% FBS α-MEM group, which was in line with the properties of MSCs in the control group (**Figure 7B**).

DISCUSSION

DPSCs, which are derived from the cranial neural crest, have MSCs-like biological properties and possess the capacity to differentiate into neuron-like cells and secrete neuron-related trophic factors (Heng et al., 2016; Kumar et al., 2017). Recently, it has been reported that non-differentiated and d-DPSCs are emerging as new cell sources for the treatment of CNS diseases,

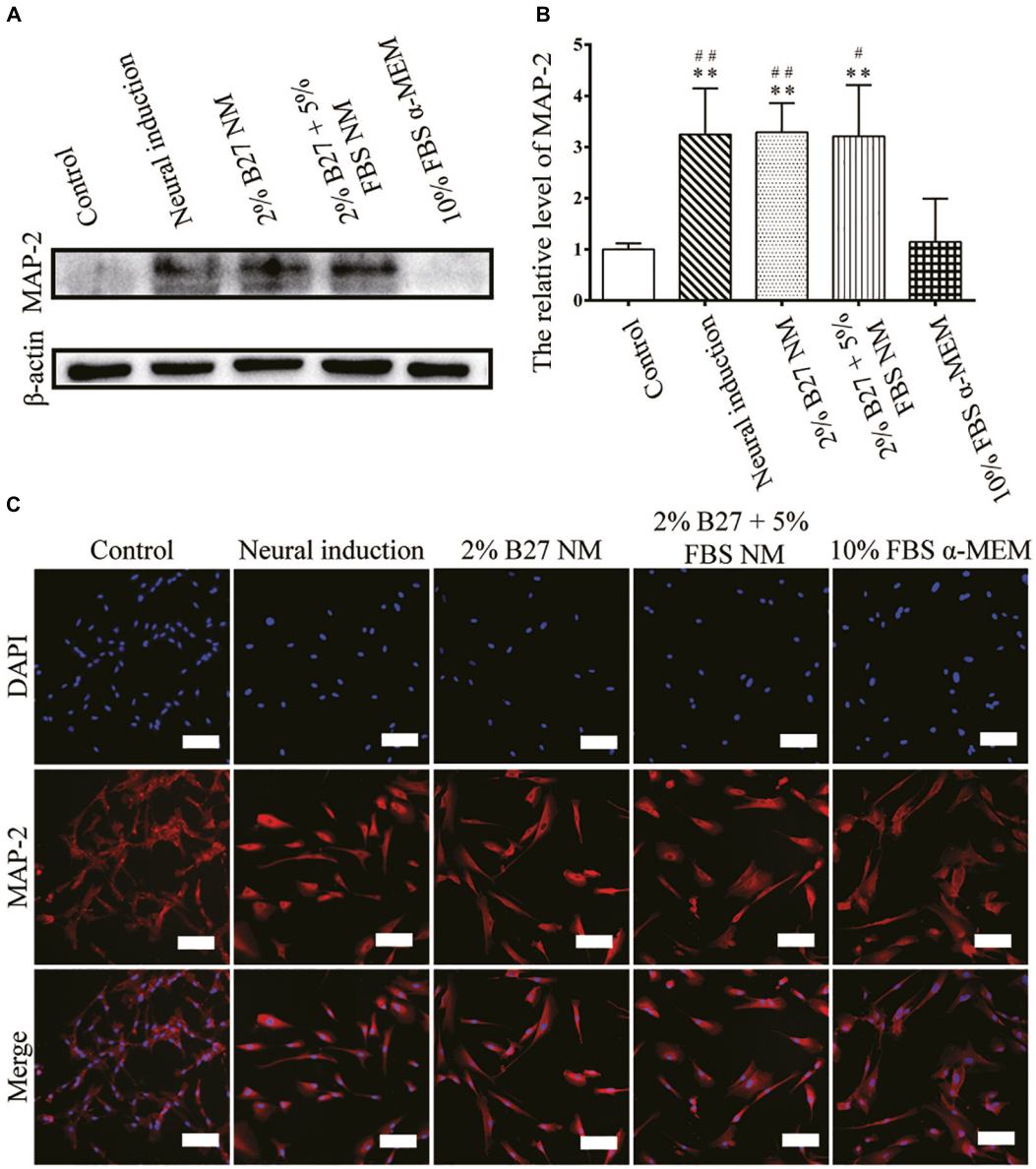

FIGURE 6 | Expression of the neuron-like marker MAP-2 in d-DPSCs cultured in the different media. **(A)** Expression of MAP-2 protein. **(B)** Quantification of MAP-2 expression. **(C)** Immunofluorescence staining of MAP-2 (scale bar: 100 μm). $^{**}P < 0.01$ vs. Control group; $^{\#\#}P < 0.01$ vs. 10% FBS α-MEM group; $^{\#}P < 0.05$ vs. 10% FBS α-MEM group.

such as spinal cord injury, stroke, Parkinson's disease, and Alzheimer's disease (Mead et al., 2017). DPSCs have huge advantages over other tissue-derived stem cells for CNS therapy due to their ease of harvesting without invasive surgery, low immunogenicity, and high expression of neuron-like markers (e.g., GFAP, β-III tubulin, MAP-2, and Nestin) without pre-induced differentiation (Sakai et al., 2012; Özdemir et al., 2016). Moreover, DPSCs have vascularization and immunomodulatory properties, which can directly or indirectly stimulate the formation of new blood vessels and enhance blood supply to sites of injury (Nakashima et al., 2009; Gorin et al., 2016; Piva et al., 2017). Thus, DPSCs have been used widely in the field of CNS treatment either by the transplantation of a DPSC suspension alone or in combination with biomaterial scaffolds (Zhang et al., 2016; Mead et al., 2017). However, the microenvironment of transplanted DPSCs in injured neurological tissue is vastly different from that of the induction environment *in vitro* (Mead et al., 2017). Moreover, there is a possible risk of tumorigenesis with DPSCs due to their MSCs biological properties such as multi-differentiation (Ohkoshi et al., 2017; Ridge et al., 2017). Taken together, *in vitro* neuronal d-DPSCs are emerging as a more appropriate cell source for the future treatment of CNS diseases. Therefore, it is important to understand how the neuron-like characteristics of DPSCs can be maintained

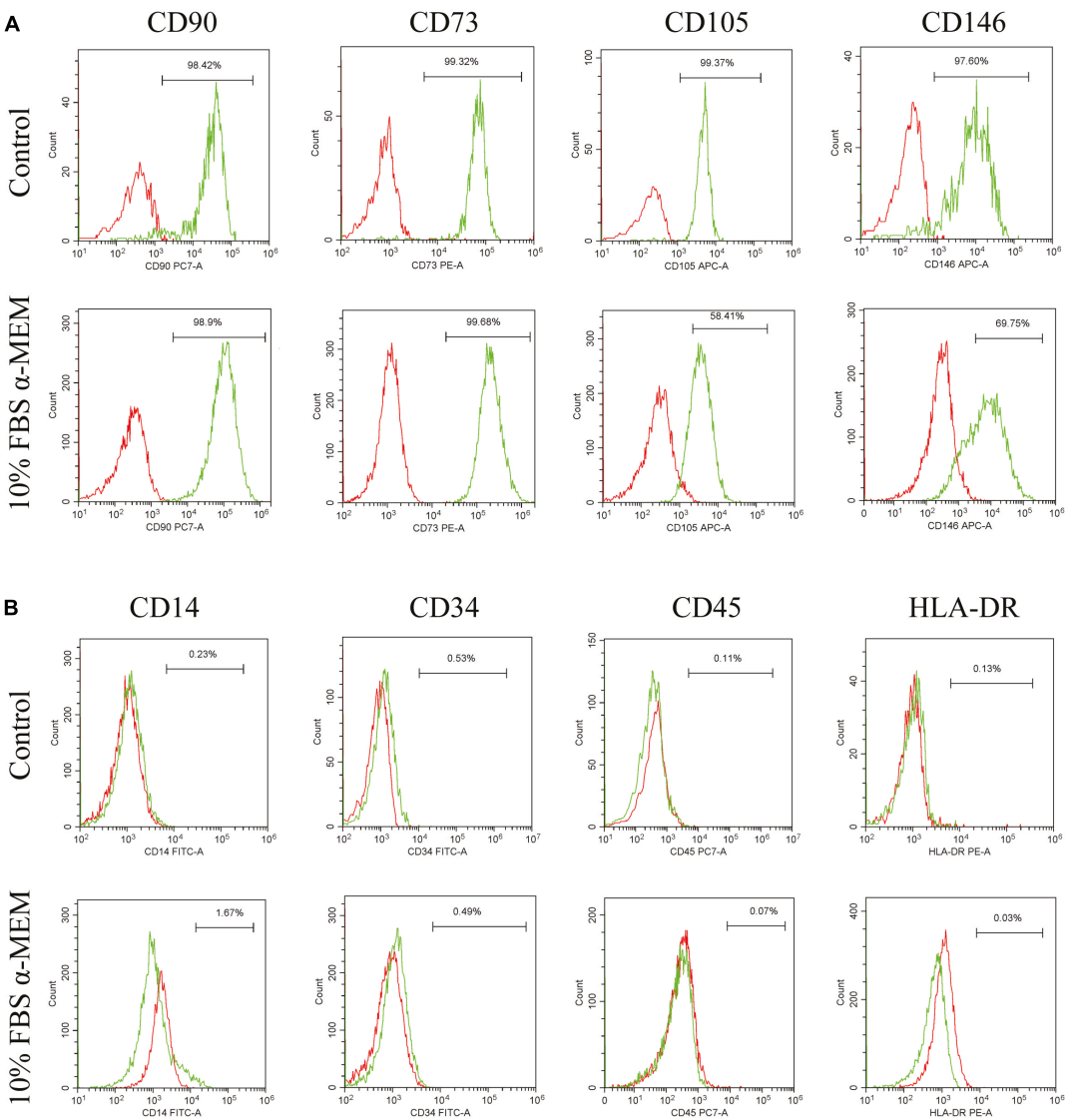

FIGURE 7 | Expression of MSCs-like markers by d-DPSCs in the 10% FBS α-MEM group. **(A)** Positive expression of d-DPSC surface markers. **(B)** Negative expression of d-DPSC surface markers.

after differentiation. In this study, we used various types of culture medium to simulate different *in vivo* microenvironments for neuronal d-DPSCs over an extended period of time. We characterized these d-DPSCs using CCK-8, western blot, immunofluorescence staining, and flow cytometry analyses in comparison to undifferentiated DPSCs.

DPSCs are adult stem cells that possess enormous proliferative capacity, whereas neuron-like cells act as terminally differentiated cells with weak proliferative ability (Heng et al., 2016). We hypothesized that the microenvironment of d-DPSCs not only has an impact on their neuron-like characteristics but also restores their stemness. A CCK-8 assay showed that d-DPSCs in the 2% B27 NM and 2% B27 + 5% FBS NM groups grew slowly from days 1 to 9. Whereas, the survival and proliferation of d-DPSCs in the 10% FBS α-MEM group showed a sharp increase from days 6 to 9. The proliferation of d-DPSCs was not significantly different between the 10% FBS α-MEM and control groups at day 9. Moreover, the morphology of d-DPSCs also subsequently changed into a typical MSCs-like phenotype in which fibroblast-like elongation was observed. Further, the effects of the microenvironment on proliferation (e.g., TRPC1), stemness (e.g., CD146), and neuron-like (e.g., Nestin and MAP-2) markers of d-DPSCs supported our hypothesis.

Multiples studies have reported that the biological functions of MSCs, including differentiation, proliferation, and apoptosis, are mediated by intracellular calcium (Ca^{2+}) concentration (Deng et al., 2015; Peng et al., 2016). TRPC1 is a voltage-independent membrane channel that mobilizes the extracellular calcium pool to induce Ca^{2+} influx (Clapham, 2003). Torossian et al. (2010) reported that TRPC1 is expressed by MSCs and plays

an important role in their proliferation. According to our study, TRPC1 was expressed at the highest level in the 10% FBS α-MEM group, at a similar level to that of the control group. Whereas, TRPC1 was barely expressed in the other experimental groups and the neural-induction group. These results were consistent with those of the CCK-8 assay, which indicated that d-DPSCs cultured in 10% FBS α-MEM had a greater proliferative capacity.

CD146 is an integral membrane glycoprotein that mediates vascular endothelial cell activity and angiogenesis. Notably, CD146 is recognized as an appropriate marker of the stemness of MSCs (Lv et al., 2014). CD146 expression indicates that MSCs possess high clonogenicity and multipotency as well as hematopoiesis capacity (Russell et al., 2010; Lv et al., 2014). As shown in **Figure 4**, CD146 expression was significantly higher in d-DPSCs of the 10% FBS α-MEM group than in the other experimental groups, but this was not significantly lower than that of the control group, in which undifferentiated DPSCs were cultured. These results indicated that d-DPSCs did lose their stemness during the induction of neural differentiation, while their stemness could be partially preserved using normal MSCs culture medium.

Nestin expression indicates endothelial progenitors and/or newly formed endothelium. Under normal conditions, human dental pulp does not contain true lymphatic vessels, as the lymph drainage system of human dental pulp is poorly developed, and this system consists of interstitial tissue channels devoid of endothelium. In stressed pulp, lymphangiogenesis is characterized by vessel formation. $Nesin^{+}$ cells reportedly participate in angiogenesis as MSCs or endothelial progenitor cells in several tissues and have been found in lymph nodes (Koning et al., 2016). The literature indicates that Nestin expression characterizes a subset of bone marrow perivascular MSCs (Xie et al., 2015). Nestin is a neuronal stem cell marker and its expression is considered a prerequisite for stem cells to differentiate into a neural lineage (Kanao et al., 2017). One study reported that murine DPSCs expressing Nestin at a high level have a considerable capacity to differentiate into a neuron-like phenotype and increase the expression of MAP-2, a marker of mature neurons (Young et al., 2016). MAP-2 associates with actin during early axonal development (Tatiana et al., 2010; Kanao et al., 2017). Our previous studies demonstrated that Nestin expression is significantly increased in DPSCs upon neural-induced differentiation (Luo et al., 2018a). In the present study, Nestin and MAP-2 were highly expressed in d-DPSCs cultured in 2% B27 + 5% FBS NM, similar to the levels observed in the neural-induction group. Therefore, the 2% B27 + 5% FBS NM culture medium could provide an appropriate microenvironment for d-DPSCs to maintain their neuron-like characteristics *in vitro*. Nestin and MAP-2 were expressed at very low levels in d-DPSCs of the 10% FBS α-MEM and control groups, suggesting that the biological features of d-DPSCs in the 10% FBS α-MEM group were very similar to those of undifferentiated DPSCs.

DPSCs maintain the properties of MSCs and express MSCs-like markers, including CD73, CD90, CD105, and CD146, but do not express hematopoietic cell markers, such as CD34, CD14, CD45, and HLA-DR (Gronthos et al., 2002; Kawashima, 2012). In our study, flow cytometric analysis demonstrated that d-DPSCs in the 10% FBS α-MEM group were positive for CD73, CD90, CD105, and CD146, and negative for CD34, CD14, CD45, and HLA-DR. However, CD105 and CD146 expression was lower than that observed in the control group; CD105 and CD146 expression was decreased from 99.37 to 58.41% and from 97.60 to 69.75%, respectively. CD146 and CD105 are both primarily endothelial cell markers associated with vascular endothelial cell activity and angiogenesis (Nakashima et al., 2009; Gao et al., 2020). These results again suggested that d-DPSCs cultured in 10% FBS α-MEM had the ability to restore partly their stemness but had less capacity for angiogenesis.

Recently, stem cells-based therapy has provided a fascinating new approach for the repair of CNS diseases. d-DPSCs have become an attractive source over than the other types of MSCs because of their optimal neurogenic and neurotrophic properties. However, cellular therapy usually requires amplification of cell population. And repetitive passage will ultimately lead d-DPSCs to enter an irreversible proliferation-arrested state and pluripotency-lost position. Therefore, it is very important to provide a suitable method to maintain the biological characteristics of d-DPSCs. Our findings provide clues and cues in modulating the de-differentiation of DPSCs, and it also proves DPSCs as an ideal source for stem cell-based nerve tissue engineering.

CONCLUSION

Our study is the first to evaluate the effects of the surrounding microenvironment on the properties of neural d-DPSCs. Our results clearly demonstrated that the basic Neurobasal®-A medium supplemented with 2% B27 and 5% FBS could provide a suitable culture microenvironment for d-DPSCs to maintain their neuron-like characteristics *in vitro*. Moreover, d-DPSCs cultured in complete α-MEM containing 10% FBS could partially recover their stem cell properties, indicating that the neural differentiation of DPSCs has a reversible characteristic, which might provide a novel strategy for future research into the multi-differentiation of DPSCs. Furthermore, DPSCs seem to be a promising source of stem cells for nerve regeneration.

DATA AVAILABILITY STATEMENT

The raw data supporting the conclusions of this article will be made available by the authors, without undue reservation.

AUTHOR CONTRIBUTIONS

QY and YH: conceptualization and supervision. LL, XW, YZ, YW, FH, ZX, and LW: methodology and validation. XW, YZ, and LL: data curation and analysis. LL and XW: writing-original draft preparation. JX, FG, and YH: writing-review and editing. YH and QY: funding acquisition. All authors have read and agreed to the published version of the manuscript.

FUNDING

This work was supported by the National Natural Science Funding of China (81701032 and 81871503), the Wenzhou Science and Technology Association Project, the Wenzhou Major Scientific and Technological Innovation Key Medical and Health Project (ZY2019010), the Wenzhou Medical University grant (QTJ16026), Wenzhou Basic Research Project (Y20180131), Zhejiang Province Program of the Medical and Health Science and Technology (2018KY537), Zhejiang Natural Science Foundation (LGF18C100002), and Zhejiang Xinmiao Talents Program (2018R413186 and 2019R413020).

REFERENCES

Baumard, J., Lesourd, M., Remigereau, C., Jarry, C., Etcharry-Bouyx, F., Chauvire, V., et al. (2018). Tool use in neurodegenerative diseases: Planning or technical reasoning? *J. Neuropsychol.* 12, 409–426. doi: 10.1111/jnp.12121

Bianco, J., De Berdt, P., Deumens, R., and des Rieux, A. (2016). Taking a bite out of spinal cord injury: do dental stem cells have the teeth for it? *Cell. Mol. Life Sci.* 73, 1413–1437. doi: 10.1007/s00018-015-2126-5

Caseiro, A. R., Pereira, T., Ivanova, G., Luis, A. L., and Mauricio, A. C. (2016). Neuromuscular Regeneration: Perspective on the Application of Mesenchymal Stem Cells and Their Secretion Products. *Stem Cells Int.* 2016:973. doi: 10.1155/2016/9756973

Chalisserry, E. P., Nam, S. Y., Park, S. H., and Anil, S. (2017). Therapeutic potential of dental stem cells. *J. Tissue Eng.* 8:2531. doi: 10.1177/2041731417702531

Clapham, D. E. (2003). TRP channels as cellular sensors. *Nature* 426, 517–524. doi: 10.1038/nature02196

de Amorim, V. C. M., Oliveira, M. S., da Silva, A. B., David, J. M., David, J. P. L., Costa, M. D. D., et al. (2020). Agathisflavone modulates astrocytic responses and increases the population of neurons in an in vitro model of traumatic brain injury. *Naunyn Schmiedebergs Arch. Pharmacol.* 393, 1921–1930. doi: 10.1007/s00210-020-01905-2

Deng, H., Gerencser, A. A., and Jasper, H. (2015). Signal integration by Ca(2+) regulates intestinal stem-cell activity. *Nature* 528, 212–217. doi: 10.1038/nature16170

Feng, X., Xing, J., Feng, G., Sang, A., Shen, B., Xu, Y., et al. (2013). Age-dependent impaired neurogenic differentiation capacity of dental stem cell is associated with Wnt/β-catenin signaling. *Cell Mol. Neurobiol.* 33, 1023–1031. doi: 10.1007/s10571-013-9965-0

Gao, K. W., He, S. Q., Kumar, P., Farmer, D., Zhou, J. D., and Wang, A. J. (2020). Clonal isolation of endothelial colony-forming cells from early gestation chorionic villi of human placenta for fetal tissue regeneration. *World J. Stem Cells* 12, 123–138. doi: 10.4252/wjsc.v12.i2.123

Geng, Y. W., Zhang, Z., Liu, M. Y., and Hu, W. P. (2017). Differentiation of human dental pulp stem cells into neuronal by resveratrol. *Cell Biol. Int.* 41, 1391–1398. doi: 10.1002/cbin.10835

Gorin, C., Rochefort, G. Y., Bascetin, R., Ying, H., Lesieur, J., Sadoine, J., et al. (2016). Priming Dental Pulp Stem Cells With Fibroblast Growth Factor-2 Increases Angiogenesis of Implanted Tissue-Engineered Constructs Through Hepatocyte Growth Factor and Vascular Endothelial Growth Factor Secretion. *Stem Cells Transl. Med.* 5, 392–404. doi: 10.5966/sctm.2015-0166

Gronthos, S., Brahim, J., Li, W., Fisher, L. W., Cherman, N., Boyde, A., et al. (2002). Stem cell properties of human dental pulp stem cells. *J. Dental Res.* 81, 531–535. doi: 10.1177/154405910208100806

Gronthos, S., Mankani, M., Brahim, J., Robey, P. G., and Shi, S. (2000). Postnatal human dental pulp stem cells (DPSCs) in vitro and in vivo. *Proc. Natl. Acad. Sci. U S A.* 97, 13625–13630. doi: 10.1073/pnas.240309797

Heng, B. C., Lim, L. W., Wu, W. T., and Zhang, C. F. (2016). An Overview of Protocols for the Neural Induction of Dental and Oral Stem Cells In Vitro. *Tissue Eng. Part B Rev.* 22, 220–250. doi: 10.1089/ten.teb.2015.0488

Hong, H., Kim, B. S., and Im, H. I. (2016). Pathophysiological Role of Neuroinflammation in Neurodegenerative Diseases and Psychiatric Disorders. *Int. Neurourol. J.* 20, S2–S7. doi: 10.5213/inj.1632604.302

Kahveci, K., Dincer, M., Doger, C., and Yarici, A. K. (2017). Traumatic brain injury and palliative care: a retrospective analysis of 49 patients receiving palliative care during 2013-2016 in Turkey. *Neural Regen. Res.* 12, 77–83. doi: 10.4103/1673-5374.198987

Kanao, S., Ogura, N., Takahashi, K., Ito, K., Suemitsu, M., Kuyama, K., et al. (2017). Capacity of Human Dental Follicle Cells to Differentiate into Neural Cells In Vitro. *Stem Cells Int.* 2017, 1–10. doi: 10.1155/2017/8371326

Karaoz, E., Demircan, P. C., Saglam, O., Aksoy, A., Kaymaz, F., and Duruksu, G. (2011). Human dental pulp stem cells demonstrate better neural and epithelial stem cell properties than bone marrow-derived mesenchymal stem cells. *Histochem. Cell Biol.* 136, 455–473. doi: 10.1007/s00418-011-0858-3

Kawashima, N. (2012). Characterisation of dental pulp stem cells: A new horizon for tissue regeneration? *Arch. Oral Biol.* 57, 1439–1458. doi: 10.1016/j.archoralbio.2012.08.010

Kim, J. H., Sim, J., and Kim, H. J. (2018). Neural Stem Cell Differentiation Using Microfluidic Device-Generated Growth Factor Gradient. *Biomol. Ther.* 26, 380–388. doi: 10.4062/biomolther.2018.001

Koning, J. J., Konijn, T., Lakeman, K. A., O'Toole, T., Kenswil, K. J., Raaijmakers, M. H., et al. (2016). Nestin-Expressing Precursors Give Rise to Both Endothelial as well as Nonendothelial Lymph Node Stromal Cells. *J. Immunol.* 197, 2686–2694. doi: 10.4049/jimmunol.1501162

Kumar, A., Kumar, V., Rattan, V., Jha, V., and Bhattacharyya, S. (2017). Secretome Cues Modulate the Neurogenic Potential of Bone Marrow and Dental Stem Cells. *Mol. Neurobiol.* 54, 4672–4682. doi: 10.1007/s12035-016-0011-3

Liu, H. Q., Xu, X. T., Tu, Y. J., Chen, K. X., Song, L., Zhai, J. Y., et al. (2020). Engineering Microenvironment for Endogenous Neural Regeneration after Spinal Cord Injury by Reassembling Extracellular Matrix. *Acs Appl. Mater. Interf.* 12, 17207–17219. doi: 10.1021/acsami.9b19638

Luo, L. H., Albashari, A. A., Wang, X. Y., Jin, L., Zhang, Y. N., Zheng, L. N., et al. (2018a). Effects of Transplanted Heparin-Poloxamer Hydrogel Combining Dental Pulp Stem Cells and bFGF on Spinal Cord Injury Repair. *Stem Cells Int.* 2018:2398521. doi: 10.1155/2018/2398521

Luo, L. H., He, Y., Wang, X. Y., Key, B., Lee, B. H., Li, H. Q., et al. (2018b). Potential Roles of Dental Pulp Stem Cells in Neural Regeneration and Repair. *Stem Cells Int.* 2018:1731289. doi: 10.1155/2018/1731289

Lv, F. J., Tuan, R. S., Cheung, K. M., and Leung, V. Y. (2014). Concise review: the surface markers and identity of human mesenchymal stem cells. *Stem Cells* 32, 1408–1419. doi: 10.1002/stem.1681

Martens, W., Bronckaers, A., Politis, C., Jacobs, R., and Lambrichts, I. (2013). Dental stem cells and their promising role in neural regeneration: an update. *Clinic. Oral Investigat.* 17, 1969–1983. doi: 10.1007/s00784-013-1030-3

Mead, B., Logan, A., Berry, M., Leadbeater, W., and Scheven, B. A. (2017). Concise Review: Dental Pulp Stem Cells: A Novel Cell Therapy for Retinal and Central Nervous System Repair. *Stem Cells* 35, 61–67. doi: 10.1002/stem.2398

Nakashima, M., Iohara, K., and Sugiyama, M. (2009). Human dental pulp stem cells with highly angiogenic and neurogenic potential for possible use in pulp regeneration. *Cytokine Growth Fact. Rev.* 20, 435–440. doi: 10.1016/j.cytogfr.2009.10.012

Ohkoshi, S., Hara, H., Hirono, H., Watanabe, K., and Hasegawa, K. (2017). Regenerative medicine using dental pulp stem cells for liver diseases. *World J. Gastr. Pharmacol. Ther.* 8, 1–6. doi: 10.4292/wjgpt.v8.i1.1

Özdemir, A. T., Özdemir, R. B. Ö, Kırmaz, C., Sarıboyacı, A. E., Halbutoğları, Z. S. Ü, Özel, C., et al. (2016). The paracrine immunomodulatory interactions between the human dental pulp derived mesenchymal stem cells and CD4 T cell subsets. *Cell. Immunol.* 310:S0008874916300818. doi: 10.1016/j.cellimm.2016.08.008

Peng, H., Hao, Y., Mousawi, F., Roger, S., Li, J., Sim, J. A., et al. (2016). Purinergic and Store-Operated Ca2+ Signalling Mechanisms in Mesenchymal Stem Cells and Their roles in ATP-Induced Stimulation of Cell Migration. *Stem Cells* 34:2102. doi: 10.1002/stem.2370

Pisciotta, A., Bertoni, L., Vallarola, A., Bertani, G., Mecugni, D., and Carnevale, G. (2020). Neural crest derived stem cells from dental pulp and tooth-associated stem cells for peripheral nerve regeneration. *Neural Regen. Res.* 15, 373–381. doi: 10.4103/1673-5374.266043

Piva, E., Tarle, S. A., Nor, J. E., Zou, D. H., Hatfield, E., Guinn, T., et al. (2017). Dental Pulp Tissue Regeneration Using Dental Pulp Stem Cells Isolated and

Expanded in Human Serum. *J. Endodont.* 43, 568–574. doi: 10.1016/j.joen.2016.11.018

Ridge, S. M., Sullivan, F. J., and Glynn, S. A. (2017). Mesenchymal stem cells: key players in cancer progression. *Mol. Cancer* 16:31. doi: 10.1186/s12943-017-0597-8

Russell, K. C., Phinney, DGLacey, M. R., Barrilleaux, B. L., Meyertholen, K. E., and O'Connor, K. C. (2010). In Vitro High-Capacity Assay to Quantify the Clonal Heterogeneity in Trilineage Potential of Mesenchymal Stem Cells Reveals a Complex Hierarchy of Lineage Commitment. *Stem Cells* 28, 788–798. doi: 10.1002/stem.312

Sakai, K., Yamamoto, A., Matsubara, K., Nakamura, S., Naruse, M., Yamagata, M., et al. (2012). Human dental pulp-derived stem cells promote locomotor recovery after complete transection of the rat spinal cord by multiple neuro-regenerative mechanisms. *J. Clin. Invest.* 122, 80–90. doi: 10.1172/jci59251

Sanen, K., Martens, W., Georgiou, M., Ameloot, M., Lambrichts, I., and Phillips, J. (2017). Engineered neural tissue with Schwann cell differentiated human dental pulp stem cells: potential for peripheral nerve repair? *J. Tissue Eng. Regen. Med.* 11, 3362–3372. doi: 10.1002/term.2249

Tatiana, T., Laurence, L., Marielle, D., Martine, M., Christine, M., Alain, D., et al. (2010). Bone marrow-derived mesenchymal stem cells already express specific neural proteins before any differentiation. *Differentiation* 72, 319–326. doi: 10.1111/j.1432-0436.2004.07207003.x

Thompson, R., and Chan, C. (2016). Signal transduction of the physical environment in the neural differentiation of stem cells. *Technology* 4, 1–8. doi: 10.1142/s2339547816400070

Torossian, F., Bisson, A., Vannier, J. P., Boyer, O., and Lamacz, M. (2010). TRPC expression in mesenchymal stem cells. *Cell Mol. Biol. Lett.* 15, 600–610. doi: 10.2478/s11658-010-0031-3

Xiao, L., Ide, R., Saiki, C., Kumazawa, Y., and Okamura, H. (2017). Human Dental Pulp Cells Differentiate toward Neuronal Cells and Promote Neuroregeneration in Adult Organotypic Hippocampal Slices In Vitro. *Int. J. Mol. Sci.* 18:18081745. doi: 10.3390/ijms18081745

Xie, L., Zeng, X., Hu, J., and Chen, Q. (2015). Characterization of Nestin, a Selective Marker for Bone Marrow Derived Mesenchymal Stem Cells. *Stem Cells Int.* 2015:762098. doi: 10.1155/2015/762098

Yamazaki, K., Fukushima, K., Sugawara, M., Tabata, Y., Imaizumi, Y., Ishihara, Y., et al. (2016). Functional Comparison of Neuronal Cells Differentiated from Human Induced Pluripotent Stem Cell-Derived Neural Stem Cells under Different Oxygen and Medium Conditions. *J. Biomol. Screen* 21, 1054–1064. doi: 10.1177/1087057116661291

Young, F. I., Telezhkin, V., Youde, S. J., Langley, M. S., Stack, M., Kemp, P. J., et al. (2016). Clonal Heterogeneity in the Neuronal and Glial Differentiation of Dental Pulp Stem/Progenitor Cells. *Stem Cells Int.* 2016:1290561. doi: 10.1155/2016/1290561

Zhang, J., Lu, X., Feng, G., Gu, Z., Sun, Y., Bao, G., et al. (2016). Chitosan scaffolds induce human dental pulp stem cells to neural differentiation: potential roles for spinal cord injury therapy. *Cell Tissue Res.* 366, 1–14. doi: 10.1007/s00441-016-2402-1

Conflict of Interest: The authors declare that the research was conducted in the absence of any commercial or financial relationships that could be construed as a potential conflict of interest.

frontiers in Pharmacology

ORIGINAL RESEARCH
published: 27 January 2021
doi: 10.3389/fphar.2020.628369

Systemic Administration of Fibroblast Growth Factor 21 Improves the Recovery of Spinal Cord Injury (SCI) in Rats and Attenuates SCI-Induced Autophagy

Sipin Zhu[1,2,3†], Yibo Ying[1,3†], Lin Ye[1,3†], Weiyang Ying[1,3††], Jiahui Ye[1,3], Qiuji Wu[1,3], Min Chen[1,3], Hui Zhu[4], Xiaoyang Li[1], Haicheng Dou[1], Huazi Xu[1], Zhouguang Wang[1,5*] and Jiake Xu[1,2*]*

[1]Department of Orthopaedics, The Second Affiliated Hospital and Yuying Children's Hospital of Wenzhou Medical University, Wenzhou, China, [2]School of Biomedical Sciences, The University of Western Australia, Perth, WA, Australia, [3]The Second School of Medicine, Wenzhou Medical University, Wenzhou, China, [4]Spinal Cord Injury Treatment Center, Kunming Tongren Hospital, Kunming, China, [5]Department of Molecular Pharmacology, Albert Einstein College of Medicine, Bronx, NY, United States

Protecting the death of nerve cells is an essential tactic for spinal cord injury (SCI) repair. Recent studies show that nerve growth factors can reduce the death of nerve cells and promote the healing of nerve injury. To investigate the conducive effect of fibroblast growth factor 21 (FGF21) on SCI repair. FGF21 proteins were systemically delivered into rat model of SCI via tail vein injection. We found that administration of FGF21 significantly promoted the functional recovery of SCI as assessed by BBB scale and inclined plane test, and attenuated cell death in the injured area by histopathological examination with Nissl staining. This was accompanied with increased expression of NeuN, GAP43 and NF200, and deceased expression of GFAP. Interestingly, FGF21 was found to attenuate the elevated expression level of the autophagy marker LC3-II (microtubules associated protein 1 light chain 3-II) induced by SCI in a dose-dependent manner. These data show that FGF21 promotes the functional recovery of SCI via restraining injury-induced cell autophagy, suggesting that systemic administration of FGF21 could have a therapeutic potential for SCI repair.

Keywords: spinal cord injury, fibroblast growth factor 21, autophagy, nerve regeneration, fibrotic scar

OPEN ACCESS

Edited by:
Yidong Wang,
Xian Jiaotong University, China

Reviewed by:
Chen Li,
Charité – Universitätsmedizin Berlin, Germany
Huacheng He,
Wenzhou University, China

****Correspondence:***
Sipin Zhu
sipinzhu@163.com
Jiake Xu
jiake.xu@uwa.edu.au
Zhouguang Wang
wzhouguang@gmail.com

†These authors have contributed equally to this work
††The author share co-first authorship

Specialty section:
This article was submitted to Integrative and Regenerative Pharmacology, a section of the journal Frontiers in Pharmacology

Received: *11 November 2020*
Accepted: *30 December 2020*
Published: *27 January 2021*

Citation:
Zhu S, Ying Y, Ye L, Ying W, Ye J, Wu Q, Chen M, Zhu H, Li X, Dou H, Xu H, Wang Z and Xu J (2021) Systemic Administration of Fibroblast Growth Factor 21 Improves the Recovery of Spinal Cord Injury (SCI) in Rats and Attenuates SCI-Induced Autophagy. Front. Pharmacol. 11:628369. doi: 10.3389/fphar.2020.628369

INTRODUCTION

Spinal cord injury (SCI) is a devastating neurological disorder resulting in the loss of motor and sensory function (Taccola et al., 2018; Li et al., 2019). Due to the non-reproducibility of neurons, the natural self-repair from SCI is very limited (Zholudeva et al., 2018). SCI can be operationally divided into primary injury initiated by mechanical impact, and secondary injury caused by autophagy, inflammation, apoptosis, oxidative stress and other factors (Kim et al., 2018; Ko et al., 2020; Vismara et al., 2020). In SCI, following the primary injury, a large number of nerve cells are damaged by subsequent secondary injury, resulting in severe functional loss (Qian et al., 2020; Zhang et al., 2020). The damaged nerve fiber degeneration, local edema, ischemia and hypoxia caused by SCI will lead to a series of secondary injury reactions such as anaerobic metabolism, tissue acidosis and free radical reaction, which could promote the apoptosis and autophagy of spinal cord neurons due to the

hypoxia microenvironment, resulting in continuous impairment of spinal cord function (Lipinski et al., 2015; Gonzalez Porras et al., 2018; Abbaszadeh et al., 2020). Therefore, the suppression of secondary SCI to reduce the death of neurons has become a key step for SCI repair therapy.

Autophagy is an important process of secondary SCI and has become a hotspot in SCI repair research (Li et al., 2019; Wu and Lipinski, 2019). Under physiological condition, autophagy is characterized by "cellular self-digestion" of autophagosomes with bilayer membrane structures in the cytoplasm (Schutter and Graef, 2020), and is beneficial to maintaining cell activity. However, in the pathogenesis of SCI, lysosomal injury and dysfunction could cause defects in autophagy flux, accumulation of autophagosomes and initiation of long-term and excessive-scale autophagic activity, which results in the damage of nerve cells (Rong et al., 2019). Microtubules associated protein 1 light chain 3-II (LC3-II), located on autophagy vesicles of mammalian cells is a specific marker of autophagy, and has been used to indicate the level of autophagy in cell (Malla et al., 2019). In the early stages of SCI, oxidative stress and apoptotic pathways are activated rapidly, mediating the death of spinal cord cells. In the chronic recovery period, autophagy is dominant. Although autophagy can clear damaged organelles in cells, overactivation of autophagy can also induce cell death. Therefore, inhibition of overactivative autophagy has become a key strategy for SCI recovery (Tang et al., 2015; Rong et al., 2019; Gu et al., 2020; Ko et al., 2020).

FGF21 is a member of FGF superfamily, which plays a role in regulating lipid and glucose balance and preventing metabolic disorders (Li, 2019; Keipert et al., 2020). In addition, FGF21 has been shown to promote nerve cell repair and regulate nerve development, survival and plasticity (Owen et al., 2014; von Holstein-Rathlou et al., 2016; Xiao et al., 2019). Interestingly, pancreas-derived FGF21 was found to promote the proliferation of oligodendrocyte precursor cells (OPC) and drive remyelination in the central nervous system (Kuroda et al., 2017). It was identified that OPCs expressed FGF21 coreceptor β-klotho, and knockdown of β-klotho expression in OPCs prevented the increase in OPC proliferation and remyelination (Kuroda et al., 2017). More recently, it has been reported that FGF21 can inhibit autophagy and promote the recovery of peripheral nerves (Lu et al., 2019), but the therapeutic effect of systemic administration of FGF21 on SCI and the role of FGF21 in SCI-induced autophagy remain unclear. In this study, FGF21 was administrated to SCI rats via tail vein injection to observe its therapeutic effect on the recovery of the damaged spinal cord. Here, we demonstrated for the first time that FGF21 promotes functional recovery from SCI, protects neurons and axons, and inhibits SCI-induced autophagy, and thus might serve as a promising molecule for the therapy of SCI repair.

MATERIALS AND METHODS

Materials

Primary antibodies including neurofilament 200 (NF200, ab4680), glial fibrillary acidic protein (GFAP, ab7260), NeuN (ab104224), growth associated protein 43 (GAP43, ab75810), and LC3-II (ab192890), and secondary antibodies including goat anti-mouse 488 (ab150113), goat anti-rabbit 488 (ab150077), goat anti-chicken 488 (ab150169) and goat anti-rabbit tritc (ab6718) were purchased from Abcam (MC, United Kingdom). The DAPI was also under the supply of Abcam (MC, United Kingdom). Recombinant human FGF21 (rhFGF21) was obtained from Prof. Xiaokun Li, Zhejiang Provincial Key Laboratory of Biopharmaceuticals, Wenzhou Medical College, Wenzhou, Zhejiang, China. It was previously reported that rhFGF21 was produced using *Escherichia coli* and purified to be endotoxin free (Wang et al., 2010), and its biological effect further tested in nerve cells (Lu et al., 2019).

Animal Model of SCI

Forty adult female SD rats were provided by the Animal Center of Chinese Academy of Sciences (Shanghai, China). The average weight of the rats is from 220 to 250 g at the time of surgery. Animal experiments were ethically approved by the Animal Care and Use Committee of Wenzhou Medical College (wydw2014-0074). The experiment was conducted according to the national institutes of health's guidelines for the care and use of laboratory animals. For experimental purposes, these rats were divided into four groups at random, including Sham group, SCI group, treatment group with 100 μg/ml FGF21, and treatment group with 500 μg/ml FGF21 (Lu et al., 2019). After 10% chloral hydrate (3.5 ml/kg, i. p.) anesthesia, SD rats were made an incision along the middle of the back skin to expose the eighth to 10th thoracic spinal vertebrae. By striking T9 segment of the spinal cord using a 10 g hammer and a 25-mm-height free fall, the acute injury of SCI model was generated. Animals in sham group underwent the same operation procedures except the collision damage. Animal care and treatment included bladder massage twice a day, in the morning and evening, to help SD rats expel urine.

FGF21 Injection Through the Tail Vein to Treat SCI

Half an hour after the SCI model was established, 200 μl of 100 μg/ml FGF21 and 500 μg/ml FGF21 were injected into rats in different treatment groups through the tail vein, and then repeated every other 2 days. The Sham group was injected with saline alone at the same time. Tail vein injection was chosen to more readily deliver the drug into the site of SCI via blood circulation than intramuscular injection in this study. All the animals stayed at cage to recover. Same moderate diet was given to each group at fixed times.

Locomotion Recovery Assessment

The Basso, Beattie and Bresnahan (BBB) locomotor rating scale scoring was conducted based on the natural process of exercise recovery of SCI rats, which ranges from 0 (responding to paralysis of the lower limbs) to 21 (reacting to normal motor function). The slanted test refers to a test device that was used to test and record the max angle at which rats could not fall and at least keep their position for 5 s. After wetting the rats' hind feet with red dye,

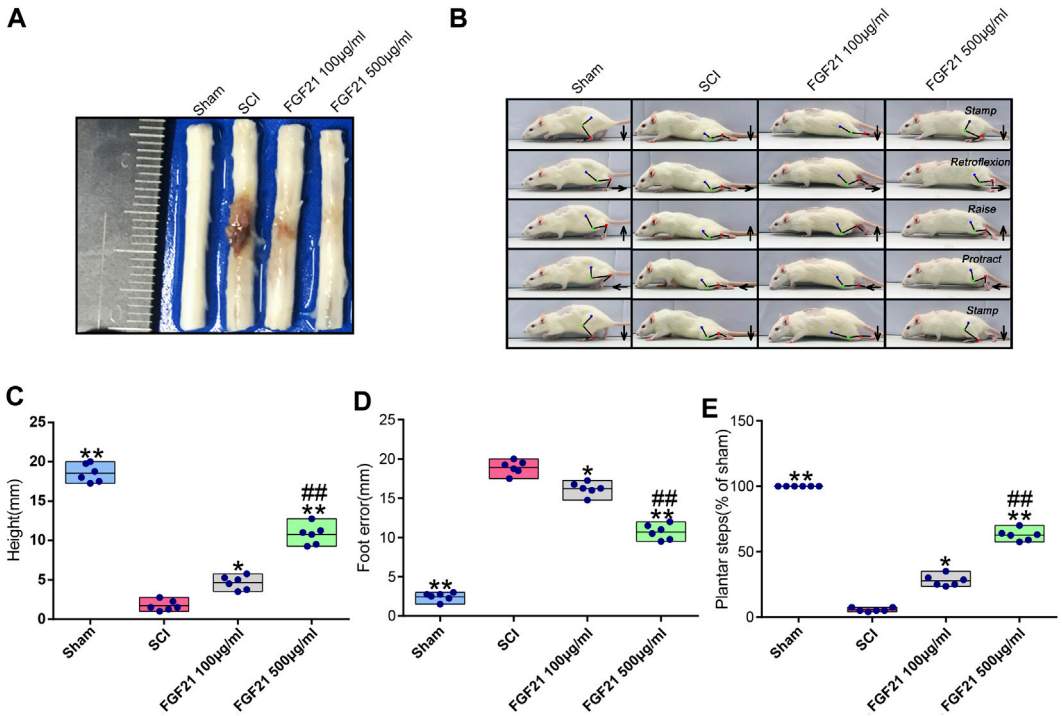

FIGURE 1 | FGF21 treatment improves the recovery of spinal cord appearance and hindlimb function **(A)** Image to show different appearance of spinal cords in every group **(B)** Motional sequence of rats in every group. The blue, green and red dot marks represent Hip (iliac crest), knee and ankle joints; respectively. And they are connected by lines. Arrow displays the directions in which feet movement **(C–E)** Statistical graphs of height of trunk above the ground, foot-placement error and number of successful plantar steps. Representation of data is mean values ±SEM, $n = 6$, "*" and "**" represent $p < 0.05$ or $p < 0.01$ vs the SCI group, "##" represent $p < 0.01$ vs the 100 μg/ml FGF21 group.

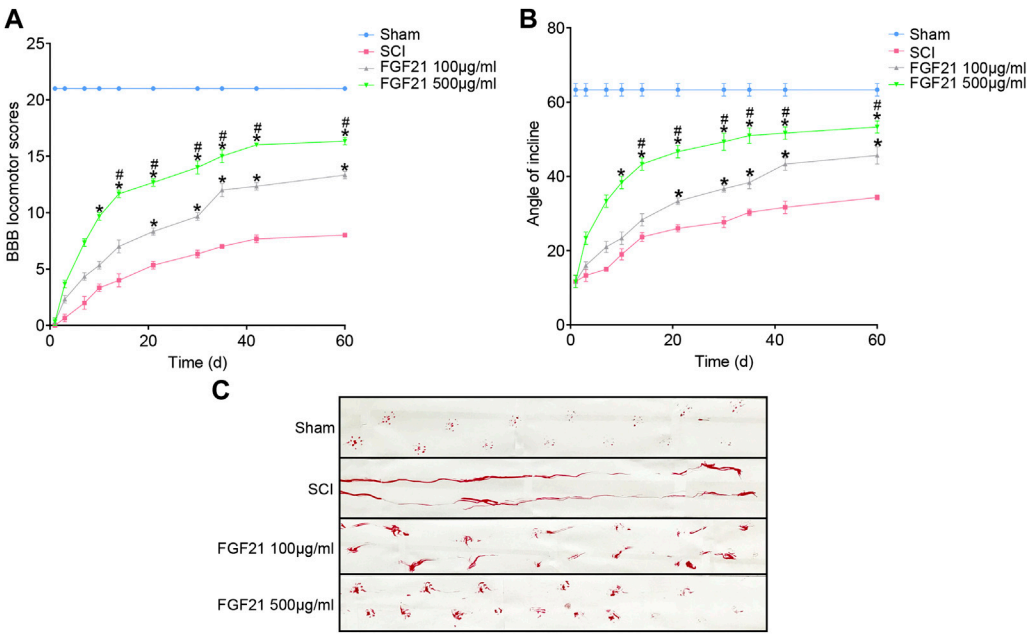

FIGURE 2 | FGF21 treatment facilitates locomotor function after SCI **(A,B)** Assessment of BBB scale and inclined plane test for each group. BBB score of 21 represented by the sham group is regarded as full score. Representation of data is mean values ±SEM, $n = 6$, "*" and "**" represent $p < 0.05$ or $p < 0.01$ vs the SCI group, "#" represent $p < 0.05$ vs the 100 μg/ml FGF21 group **(C)** Image of footprint analyses of sham, SCI group, 100 μg/ml FGF21 group and 500 μg/ml FGF21 group.

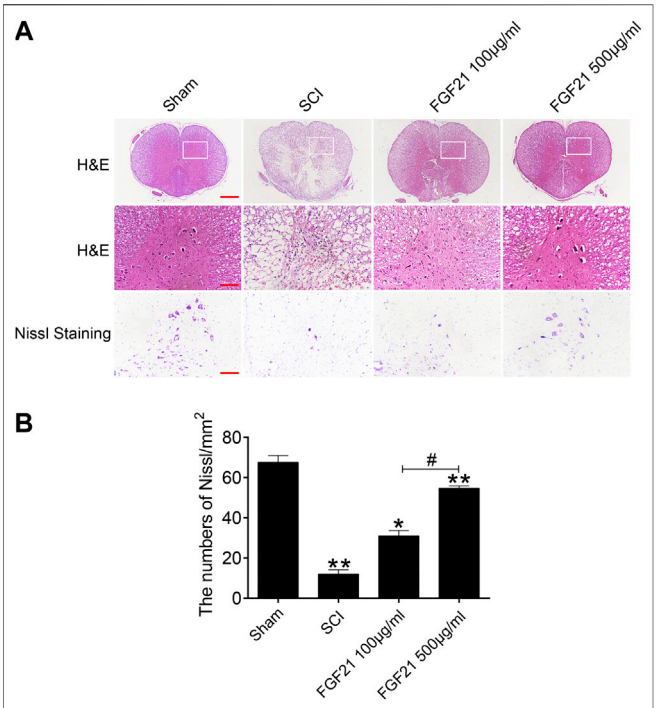

FIGURE 3 | FGF21 treatment improves the tissue structure and number of Nissl bodies **(A)** Images captured after H&E staining and Nissl staining. The images showed the whole cross section of spinal cord, scale bar = 100 μm. The part restricted by a rectangle represents region with high power images, scale bar = 100 μm. The scale bar of Nissl staining images are 100 μm **(B)** Statistical graph of quantification of Nissl staining data from **(A)**. Representation of data is mean values ±SEM, $n = 6$, "*" and "**" represent $p < 0.05$ or $p < 0.01$ vs the SCI or Sham group, "#" represent $p < 0.05$ vs the 100 μg/ml FGF21 group.

they were allowed to crawl through the suitable size box, then performing footprint scanning and digital image analysis.

H & E Staining and Nissl Staining

To prepare samples for H & E staining, 10% chloral hydrate (3.5 ml/kg, i.p.) was applied to anesthetize the SD rats, and then thoracotomy was performed on the 60th day after injection. Rats were perfused with 0.9% NaCl, subsequently 500 ml paraformaldehyde phosphate buffer was injected into the heart to harden the tissue of rats. The spinal cord was removed at the eighth to 10th thoracic spinal vertebral level around the injury. The spinal cord was fixed overnight in 4% paraformaldehyde, and paraffin embedding was then performed. Hematoxylin and eosin (H & E) and Nissl staining was then performed to paraffin sections (5 μm thick) for histopathological examination.

Video Imaging of Locomotor Function

Six female SD rats were randomly selected from each group for video imaging of locomotor function, including sham group, SCI group, 100 μg/ml FGF21 group and 500 μg/ml FGF21 group. Using a camera (Leica), rats of each group walked on a 1-m-long glass runway with marker on the hind limbs to take photos of the position of hips, knees, ankles and feet. Parameters to evaluate locomotion were listed as follows. Firstly, weight support, including height, hip height minus trunk width, equal to the torso gap on the ground. Secondly, leg extensor spasms (Quantifying the extent of extensor spasm by the time the foot is overstretched and dragged and by the relative duration of the legs on the back). Thirdly, the number of footsteps was recorded (Previous steps counted as reference). Fourthly, the posture of the foot (Measuring foot offset behind the hip at the beginning of the ankle) was also recorded. The front legs were used to determine the pace of walking steps (front leg steps/second) (Li et al., 2017).

Immunofluorescence Staining

After pretreatment with xylene, and sodium citrate etc., the sections were incubated in PBS with 10% normal bovine serum and 0.1% Triton X-100 at 37°C for 1 h, and then with an appropriate primary antibody at 4°C overnight. The following primary antibodies against GFAP43 (1:500), NeuN (1:1000), NF200 (1:1000), GFAP (1:1000), LC3-II (1:500) were used. Next, the sections were washed with PBS for three times at room temperature. After that, the corresponding secondary antibodies (1: 500) were applied and incubated at 37°C avoiding light for 1 h. Sections were then washed 3 times with PBS, 5 min each time. Then DAPI (0.25 mg/ml) dye was applied for 7 min to allow nuclei staining. A Nikon ECLIPSE Ti microscope (Nikon, Tokyo, Japan) was used to take images. Fluorescent images were taken at the boundary between the normal area and the damaged area in comparable matching anatomical regions. Imagine J software was used to count the region of interest of at least three images and then SPSS13 software to process the obtained data to produce the statistical graph.

Statistical Analysis

Statistical package for the social sciences (SPSS) analysis was used to evaluate the data which were expressed as mean ± SEM. When the experimental group was conducted in two groups, the student t test was applied to confirm the statistical significance. One-way analysis of variance (ANOVA) and Dunnett's post-mortem test were employed to evaluate the data when the comparison was conducted more than two groups. $p < 0.05$ was considered statistically significant.

RESULTS

Systemic Administration of FGF21 Improves the Recovery of Spinal Cord Appearance and Hindlimb Function

To evaluate the treatment effect of FGF21 systemic injection on SCI, the visual images of morphology of spinal cords were taken. The spinal cord in the SCI group showed blackened and shrinked appearance, whereas in the group with systemic administration of FGF21, the spinal cord showed decreased color change and less atrophy (**Figure 1A**). In addition, video recording sequences revealed that the hind legs of SCI rats were stiff with no evident joint movement, whereas FGF21 treated groups showed varying degrees of improvement in hind leg movement as measured by height and plantar steps (**Figure 1B**). Further, when compared with

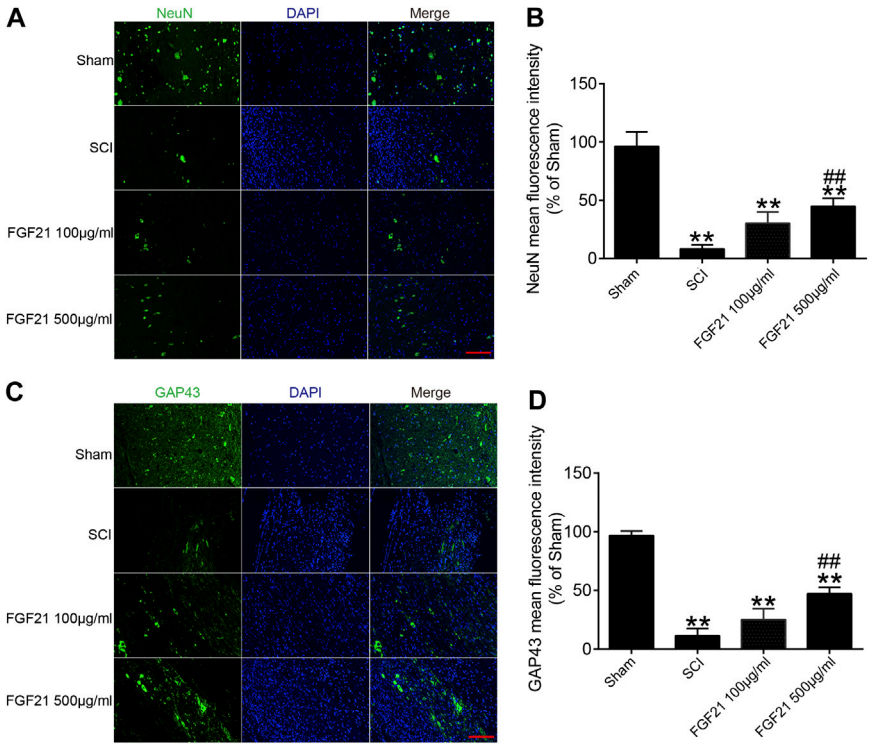

FIGURE 4 | FGF21 treatment increases the expression of NeuN and GAP43 **(A,C)** Image of Immunofluorescence staining of NeuN and GAP43 in spinal cord lesions for each group. The bright green dots are positively stained neurons marked with obvious NeuN and GAP43; respectively. DAPI (blue) is applied to mark nuclei. scale bar = 100 μm **(B,D)** Analysis of mean fluorescence intensity. Representation of data is mean values ±SEM, $n = 6$, "**" represent $p < 0.01$ vs the SCI or Sham group, "##" represent $p < 0.01$ vs the 100 μg/ml FGF21 group.

SCI group, the footstep errors of the FGF21 treated groups were decreased as measured by the heights of trunk above the ground, foot-placement errors and number of successful plantar steps (**Figures 1C–E**).

Further, using BBB scale and inclined plane test, we found that FGF21 treated groups exhibited improved locomotor function, when compared with SCI group ($F = 4.229$ in BBB scale, $F = 4.158$ in inclined plane test. **Figures 2A,B**). Consistently, by footprint analysis, FGF21 treated groups showed improved functional recovery of SCI when compared with SCI group (**Figure 2C**). Collectively, these results demonstrate a therapeutic effect of FGF21 systemic administration on SCI repair.

FGF21 Treatment Promotes the Survival of Neurons and the Improvement of Tissue Density

H & E staining and Nissl staining were performed to examine the structure of the spinal cord tissues. The staining of sham group showed a complete organizational appearance with quite a few large and medium-sized neurons. SCI group showed that the some tissues at SCI sites were damaged, accompanied with a massive reduction in the number of neurons. In FGF21 treated groups, small and sporadic voids were detected with no apparent necrosis. Noticeably, FGF21 treated group with administration of 500 μg/ml FGF21 group displayed a more complete organizational structure with significantly more neurons and Nissl bodies than 100 μg/ml FGF21 group and SCI group, indicative of a dose dependent effect (**Figure 3**).

FGF21 Treatment Increases the Expression of NeuN, GAP43 and NF200, and Deceases the Expression of GFAP

Next, the protein expressions of NeuN and GAP43 were used to evaluate neural regeneration. The immunofluorescence staining of NeuN showed that more green fluorescence signals in FGF21 treated groups, when compared with the SCI group (**Figures 4A,B**). Similarly, the immunofluorescence staining of GAP43 showed that more green fluorescence signals in FGF21 treated groups, when compared with the SCI group (**Figures 4C,D**). These results indicated that FGF21 had a positive effect on the survival and regeneration of axon.

Further, the immunofluorescence staining of NF200 showed that the expression of NF200 was higher in FGF21 treated groups, when compared with SCI group (**Figure 5**). These results suggest that the systemic administration of FGF21 has the potential to promote or maintain the regeneration of axon expanded over the scar boundary after SCI.

In addition, protein GFAP is used to determine the formation of the glial scar after SCI. Consistently, the immunofluorescence staining of GFAP revealed that the GFAP expression were lower

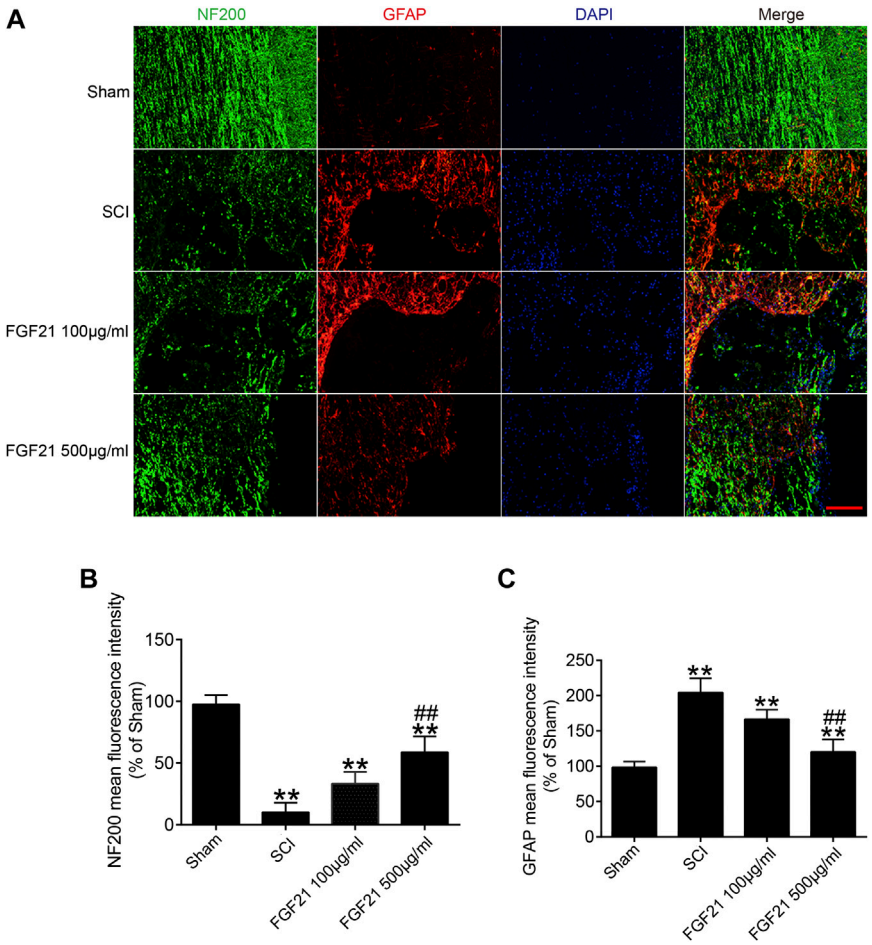

FIGURE 5 | FGF21 treatment increases the expression of NF200, and deceases the expression of GFAP **(A)** NF200 and GFAP staining in the sham, SCI group, and FGF21 treated groups. The positive bright green dots represent NF200 staining, while the bright red dots represent GFAP staining. DAPI (blue) is in application to mark nuclei, Scale bar = 100 μm **(B,C)** Quantification of the NF200 and GFAP positive staining is reflected by mean fluorescence intensity. Representation of data is mean values ±SEM, $n = 6$, "**" represent $p < 0.01$ vs the SCI or Sham group, "##" represent $p < 0.01$ vs the 100 μg/ml FGF21 group.

in FGF21 treated groups when compared with SCI group. These data suggest that FGF21 systemic injection could inhibit glial scar formation of SCI (**Figure 5**). Taken together, these results indicate that FGF21 treatment inhibits formation of glial scar and promotes axon regeneration expanded over the scar boundary.

FGF21 Administration Attenuates Autophagy Induced by SCI

To further explore whether the mechanism of FGF21's *in vivo* effect may involve regulating autophagy. We applied immunofluorescence staining to detect the protein expression of LC3-II, an autophagy marker, and found that LC3-II protein expression was upregulated in SCI (**Figure 6**). Interestingly, the expression level LC3-II protein was decreased in FGF21 treated groups in a dose dependent manner, when compared with SCI group. Collectively, our results indicate that FGF21 is able to attenuate the SCI-induced autophagy, consistently with its *in vivo* therapeutic effect on the functional recovery of SCI (**Figure 6**).

DISCUSSION

In this study, using systemic administration of FGF21 to rat model of SCI, we have shown that FGF21 promotes the functional recovery of SCI and inhibits SCI-induced autophagy, suggesting a promising potential of FGF21 systemic administration in the therapy of SCI repair for the first time.

FGF21 is generally considered to be an effective metabolic regulator (Keipert et al., 2020; Zarei et al., 2020). There are few reports on the role of FGF21 in mediating neuroprotection and nerve regeneration. For instance, decreased FGF21 signal has been shown not only to reduce the number of new axons formed in the damaged loci, but also to alter the molecular structure of axons(Douris et al., 2017; Lovadi et al., 2017; Xiao et al., 2019). However, the role of FGF21 systemic administration in SCI repair remains hitherto unknown. In this study, we showed the effect and underlying molecular mechanism of FGF21 in mediating neuroprotection and nerve regeneration after SCI. Interestingly, we have found that FGF21 has a potent neuroprotective effect on

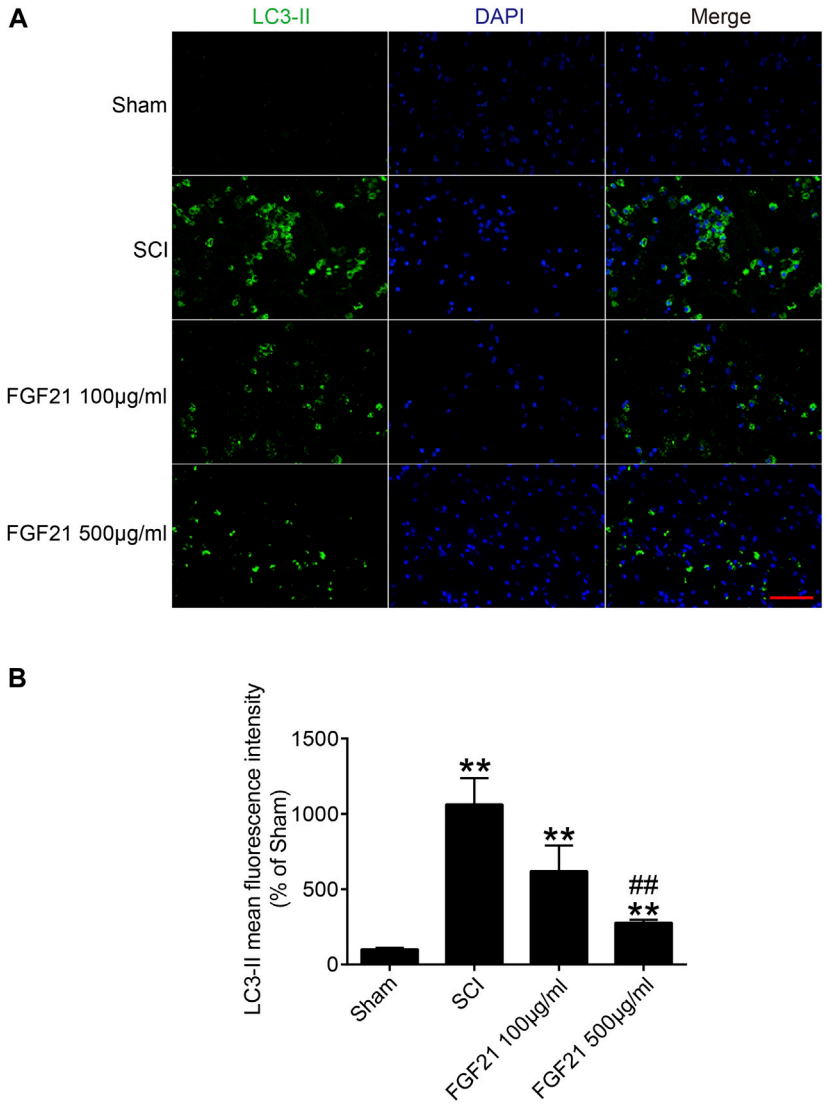

FIGURE 6 | FGF21 administration results in attenuation of SCI-induced autophagy **(A)** The immunofluorescence staining for LC3-II in Sham, SCI group, and FGF21 treated groups. Green fluorescence represents LC3-II. DAPI (blue) is applied to stain nuclei. Scale bar = 50 μm **(B)** Quantitation of the Immunofluorescence staining results of LC3-II by mean fluorescence intensity. Representation of data is mean values ±SEM, $n = 6$, "**" represent $p < 0.01$ vs the SCI or Sham group, "##" represent $p < 0.01$ vs the 100 μg/ml FGF21 group.

SCI, manifested in the recovery of motor function, inhibition of neuronal death, and promotion of axonal elongation. In order to further explore the protective mechanism of FGF21 on neurons, we have investigated the effect of FGF21 on the autophagy.

After SCI, a microenvironment of ischemia, hypoxia and inflammatory infiltration is formed at the injury site (Fan et al., 2020; Kumar et al., 2020; Qian et al., 2020). Subsequently, lysosomal damage and dysfunction can occur within affected cells, leading to autophagy flux defects, accumulation of autophagosomes, initiation of long-term large-scale autophagy, and active cell death, which is not conducive to the survival of neurons (Bae et al., 2019; Rehorova et al., 2019). Inhibition of excessive autophagy activation by pharmacological intervention has been suggested to be a new tactic to reduce neuronal death (Lee et al., 2020). Compared with the short-term stress responsees such as oxidative stress and apoptosis, autophagy exists in the whole process of SCI (Cortes et al., 2014; He et al., 2016; Vahsen et al., 2020). Consistently, we found that autophagy-related protein level LC3 II was significantly induced in SCI, and whereas FGF21 attenuated SCI-induced autophagy and improves the functional recovery of SCI.

Previous studies have shown that SCI can lead to the death of a large number of neurons, the rupture of axons, and the formation of dense glial scar to block axon growth and elongation (Wang et al., 2019; Ma et al., 2020; Tran et al., 2020). These pathological changes could result in severe motor sensory dysfunction (Su et al., 2019). There is increasing evidence that autophagy is critically involved in the death of nerve cells in the central nervous system injury conditions (Pivtoraiko et al., 2009; Chen et al., 2017; Yan et al., 2019). Since it is

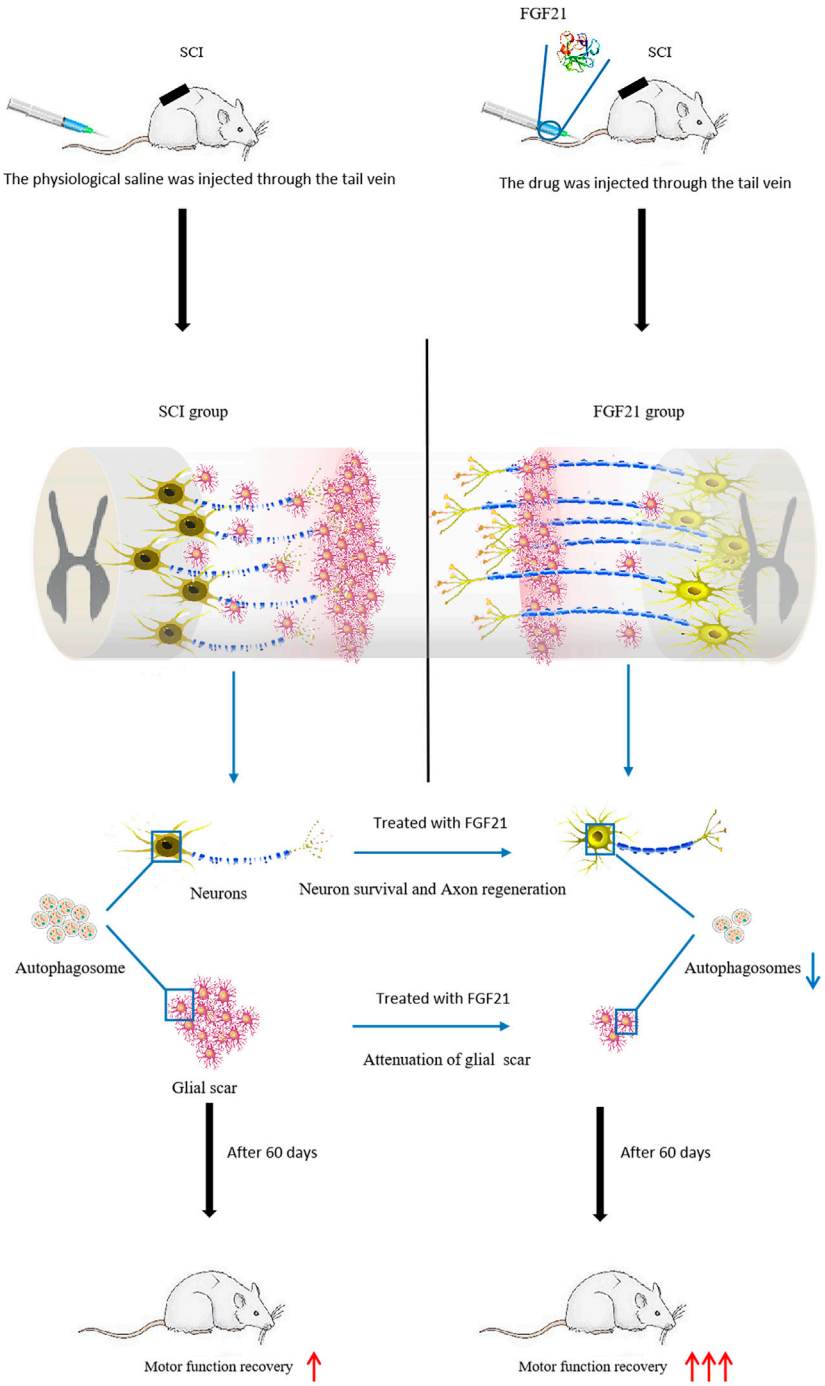

FIGURE 7 | Injection of FGF21 inhibits autophagy and promotes motor function recovery.

difficult for neurons to regenerate, the best solution for neuron injury is to protect neurons and reduce excessive autophagy in neurons (Tsumuraya et al., 2015). Therefore, blocking autophagy cell death by FGF21 may represent an effective strategy to inhibit neuron death and promote axonal elongation after SCI.

Taken together, our data indicate that systemic administration of FGF21 can effectively improve the functional recovery after SCI, reduce neuron death, and inhibit autophagy, and thus imply that FGF21 may serve as a potential therapeutic molecule for SCI repair (**Figure 7**).

DATA AVAILABILITY STATEMENT

The raw data supporting the conclusions of this article will be made available by the authors, without undue reservation.

ETHICS STATEMENT

The animal study was reviewed and approved by Animal Care and Use Committee of Wenzhou Medical College (wydw2014-0074).

AUTHOR CONTRIBUTIONS

SZ coordinated and carried out most of the experiments and data analysis, and participated in drafting the manuscript. YY and LY provided technical assistance. WY, JY, QW, and MC provided assistance on data analysis and manuscript preparation. SZ, HZ, XL, HD, HX, JX, and ZW supervised the project and experimental designs and data analysis. JX and ZW revised the manuscript. All authors approved the final manuscript.

FUNDING

This study was partly funded by a grant the National Natural Science Funding of China (81802235), Zhejiang Medical and Health Science and Technology Plan Project (2021KY212), and Wenzhou Basic Science Research Plan Project (Y2020050, Y2020388, Y20190265).

ACKNOWLEDGMENTS

SZ was a visiting scholar to UWA. SZ and JX made mutual collaborative visits.

REFERENCES

Abbaszadeh, F., Fakhri, S., and Khan, H. (2020). Targeting apoptosis and autophagy following spinal cord injury: therapeutic approaches to polyphenols and candidate phytochemicals. *Pharmacol. Res.* 160, 105069. doi:10.1016/j.phrs.2020.105069

Bae, J. E., Kang, G. M., Min, S. H., Jo, D. S., Jung, Y. K., Kim, K., et al. (2019). Primary cilia mediate mitochondrial stress responses to promote dopamine neuron survival in a Parkinson's disease model. *Cell Death Dis.* 10, 952. doi:10.1038/s41419-019-2184-y

Chen, K., Yuan, R., Geng, S., Zhang, Y., Ran, T., Kowalski, E., et al. (2017). Toll-interacting protein deficiency promotes neurodegeneration via impeding autophagy completion in high-fat diet-fed ApoE. *Brain Behav. Immun.* 59, 200–210. doi:10.1016/j.bbi.2016.10.002

Cortes, Cj., Miranda, Hc., Frankowski, H., Batlevi, Y., Young, Je., Le, A., et al. (2014). Polyglutamine-expanded androgen receptor interferes with TFEB to elicit autophagy defects in SBMA. *Nat. Neurosci.* 17, 1180–1189. doi:10.1038/nn.3787

Douris, N., Desai, Bn., Fisher, Fm., Cisu, T., Fowler, Aj., Zarebidaki, E., et al. (2017). Beta-adrenergic receptors are critical for weight loss but not for other metabolic adaptations to the consumption of a ketogenic diet in male mice. *Mol. Metab.* 6, 854–862. doi:10.1016/j.molmet.2017.05.017

Fan, Z., Liao, X., Tian, Y., Xuzhuzi, X., and Nie, Y. (2020). A prevascularized nerve conduit based on a stem cell sheet effectively promotes the repair of transected spinal cord injury. *Acta Biomater.* 101, 304–313. doi:10.1016/j.actbio.2019.10.042

Gonzalez Porras, Ma., Sieck, Gc., and Mantilla, Cb. (2018). Impaired autophagy in motor neurons: a final common mechanism of injury and death. *Physiology (Bethesda, Md.* 33, 211–224. doi:10.1152/physiol.00008.2018

Gu, C., Li, L., Huang, Y., Qian, D., Liu, W., Zhang, C., et al. (2020). Salidroside ameliorates mitochondria-dependent neuronal apoptosis after spinal cord ischemia-reperfusion injury partially through inhibiting oxidative stress and promoting mitophagy. *Oxid. Med. Cell Longev.* 2020, 3549704. doi:10.1155/2020/3549704

He, M., Ding, Y., Chu, C., Tang, J., Xiao, Q., and Luo, Zg. (2016). Autophagy induction stabilizes microtubules and promotes axon regeneration after spinal cord injury. *Proc. Natl. Acad. Sci. U.S.A.* 113, 11324–11329. doi:10.1073/pnas.1611282113

Keipert, S., Lutter, D., Schroeder, B. O., Brandt, D., Ståhlman, M., Schwarzmayr, T., et al. (2020). Endogenous FGF21-signaling controls paradoxical obesity resistance of UCP1-deficient mice. *Nat. Commun.* 11, 624. doi:10.1038/s41467-019-14069-2

Kim, H. Y., Kumar, H., Jo, M. J., Kim, J., Yoon, J. K., Lee, J. R., et al. (2018). Therapeutic efficacy-potentiated and diseased organ-targeting nanovesicles derived from mesenchymal stem cells for spinal cord injury treatment. *Nano Lett.* 18, 4965–4975. doi:10.1021/acs.nanolett.8b01816

Ko, S. H., Apple, E. C., Liu, Z., and Chen, L. (2020). Age-dependent autophagy induction after injury promotes axon regeneration by limiting NOTCH. *Autophagy*, 16, 2052–2068. doi:10.1080/15548627.2020.1713645

Kumar, H., Su Lim, C., Choi, H., Prashad Joshi, H., Kim, K. T., Ho Kim, Y., et al. (2020). Elevated TRPV4 levels contribute to endothelial damage and scarring in experimental spinal cord injury. *J. Neurosci.* 40, 1943–1955. doi:10.1523/JNEUROSCI.2035-19.2020

Kuroda, M., Muramatsu, R., Maedera, N., Koyama, Y., Hamaguchi, M., Fujimura, H., et al. (2017). Peripherally derived FGF21 promotes remyelination in the central nervous system. *J. Clin. Invest.* 127, 3496–3509. doi:10.1172/JCI94337

Lee, D. E., Yoo, J. E., Kim, J., Kim, S., Kim, S., Lee, H., et al. (2020). NEDD4L downregulates autophagy and cell growth by modulating ULK1 and a glutamine transporter. *Cell Death Dis.* 11, 38. doi:10.1038/s41419-020-2242-5

Li, X., Liu, D., Xiao, Z., Zhao, Y., Han, S., Chen, B., et al. (2019). Scaffold-facilitated locomotor improvement post complete spinal cord injury: motor axon regeneration versus endogenous neuronal relay formation. *Biomaterials* 197, 20–31. doi:10.1016/j.biomaterials.2019.01.012

Li, X. (2019). The FGF metabolic axis. *Front. Med.* 13, 511–530. doi:10.1007/s11684-019-0711-y

Li, Y., Jones, J. W., M C Choi, H., Sarkar, C., Kane, M. A., Koh, E. Y., et al. (2019). cPLA2 activation contributes to lysosomal defects leading to impairment of autophagy after spinal cord injury. *Cell Death Dis.* 10, 531. doi:10.1038/s41419-019-1764-1

Li, Y., Lucas-Osma, Am., Black, S., Bandet, Mv., Stephens, Mj., Vavrek, R., et al. (2017). Pericytes impair capillary blood flow and motor function after chronic spinal cord injury. *Nat. Med.* 23, 733–741. doi:10.1038/nm.4331

Lipinski, M., Wu, J., Faden, Ai., and Sarkar, C. (2015). Function and mechanisms of autophagy in brain and spinal cord trauma. *Antioxidants Redox Signal.* 23, 565–577. doi:10.1089/ars.2015.6306

Lovadi, E., Csereklyei, M., Merkli, H., FüLöp, K., Sebők, Á., Karcagi, V., et al. (2017). Elevated FGF 21 in myotonic dystrophy type 1 and mitochondrial diseases. *Muscle Nerve* 55, 564–569. doi:10.1002/mus.25364

Lu, Y., Li, R., Zhu, J., Wu, Y., Li, D., Dong, L., et al. (2019). Fibroblast growth factor 21 facilitates peripheral nerve regeneration through suppressing oxidative damage and autophagic cell death. *J. Cell Mol. Med.* 23, 497–511. doi:10.1111/jcmm.13952

Ma, W., Zhan, Y., Zhang, Y., Xie, X., Mao, C., and Lin, Y. (2020). Enhanced neural regeneration with a concomitant treatment of framework nucleic acid and stem cells in spinal cord injury. *ACS Appl. Mater. Interfaces* 12, 2095–2106. doi:10.1021/acsami.9b19079

Malla, S. R., Krueger, B., Wartmann, T., Sendler, M., Mahajan, U. M., Weiss, F. U., et al. (2019). Early trypsin activation develops independently of autophagy in

caerulein-induced pancreatitis in mice. *Cell. Mol. Life Sci.* 77, 1811–1825. doi:10.1007/s00018-019-03254-7

Owen, B. M., Ding, X., Morgan, D. A., Coate, K. C., Bookout, A. L., Rahmouni, K., et al. (2014). FGF21 acts centrally to induce sympathetic nerve activity, energy expenditure, and weight loss. *Cell Metabol.* 20, 670–677. doi:10.1016/j.cmet.2014.07.012

Pivtoraiko, V. N., Stone, S. L., Roth, K. A., and Shacka, J. J. (2009). Oxidative stress and autophagy in the regulation of lysosome-dependent neuron death. *Antioxidants Redox Signal.* 11, 481–496. doi:10.1089/ARS.2008.2263

Qian, Z., Chang, J., Jiang, F., Ge, D., Yang, L., Li, Y., et al. (2020). Excess administration of miR-340-5p ameliorates spinal cord injury-induced neuroinflammation and apoptosis by modulating the P38-MAPK signaling pathway. *Brain Behav. Immun.* 87, 531–542. doi:10.1016/j.bbi.2020.01.025

Rehorova, M., Vargova, I., Forostyak, S., Vackova, I., Turnovcova, K., Kupcova Skalnikova, H., et al. (2019). A combination of intrathecal and intramuscular application of human mesenchymal stem cells partly reduces the activation of necroptosis in the spinal cord of SOD1(G93A) rats. *Stem Cells Transl. Med.* 8, 535–547. doi:10.1002/sctm.18-0223

Rong, Y., Liu, W., Wang, J., Fan, J., Luo, Y., Li, L., et al. (2019). Neural stem cell-derived small extracellular vesicles attenuate apoptosis and neuroinflammation after traumatic spinal cord injury by activating autophagy. *Cell Death & Disease* 10, 340. doi:10.1038/s41419-019-1571-8

Schutter, M., and Graef, M. (2020). Localized de novo phospholipid synthesis drives autophagosome biogenesis. *Autophagy* 16, 770–771. doi:10.1080/15548627.2020.1725379

Su, Y., Chen, Z., Du, H., Liu, R., Wang, W., Li, H., et al. (2019). Silencing miR-21 induces polarization of astrocytes to the A2 phenotype and improves the formation of synapses by targeting glypican 6 via the signal transducer and activator of transcription-3 pathway after acute ischemic spinal cord injury. *Faseb. J.* 33, 10859–10871. doi:10.1096/fj.201900743R

Taccola, G., Sayenko, D., Gad, P., Gerasimenko, Y., and Edgerton, V. R. (2018). And yet it moves: recovery of volitional control after spinal cord injury. *Prog. Neurobiol.* 160, 64–81. doi:10.1016/j.pneurobio.2017.10.004

Tang, Y., Jacobi, A., Vater, C., Zou, L., Zou, X., and Stiehler, M. (2015). Icariin promotes angiogenic differentiation and prevents oxidative stress-induced autophagy in endothelial progenitor cells. *Stem Cell.* 33, 1863–1877. doi:10.1002/stem.2005

Tran, K. A., Partyka, P. P., Jin, Y., Bouyer, J., Fischer, I., and Galie, P. A. (2020). Vascularization of self-assembled peptide scaffolds for spinal cord injury repair. *Acta Biomater.* 104, 76–84. doi:10.1016/j.actbio.2019.12.033

Tsumuraya, T., Ohtaki, H., Song, D., Sato, A., Watanabe, J., Hiraizumi, Y., et al. (2015). Human mesenchymal stem/stromal cells suppress spinal inflammation in mice with contribution of pituitary adenylate cyclase-activating polypeptide (PACAP). *J. Neuroinflammation* 12, 35. doi:10.1186/s12974-015-0252-5

Vahsen, Bf., Ribas, Vt., Sundermeyer, J., Boecker, A., Dambeck, V., Lenz, C., et al. (2020). Inhibition of the autophagic protein ULK1 attenuates axonal degeneration *in vitro* and *in vivo*, enhances translation, and modulates splicing. *Cell Death Differ.* 27, 2810–2827. doi:10.1038/s41418-020-0543-y

Vismara, I., Papa, S., Veneruso, V., Mauri, E., Mariani, A., De Paola, M., et al. (2020). Selective modulation of A1 astrocytes by drug-loaded nano-structured gel in spinal cord injury. *ACS Nano*. 14, 360–371. doi:10.1021/acsnano.9b05579

Von Holstein-Rathlou, S., Bondurant, L. D., Peltekian, L., Naber, M. C., Yin, T. C., Claflin, K. E., et al. (2016). FGF21 mediates endocrine control of simple sugar intake and sweet taste preference by the liver. *Cell Metabol.* 23, 335–343. doi:10.1016/j.cmet.2015.12.003

Wang, H., Xiao, Y., Fu, L., Zhao, H., Zhang, Y., Wan, X., et al. (2010). High-level expression and purification of soluble recombinant FGF21 protein by SUMO fusion in Escherichia coli. *BMC Biotechnol.* 10, 14. doi:10.1186/1472-6750-10-14

Wang, J. L., Luo, X., and Liu, L. (2019). Targeting CARD6 attenuates spinal cord injury (SCI) in mice through inhibiting apoptosis, inflammation and oxidative stress associated ROS production. *Aging (Albany NY).* 11, 12213–12235. doi:10.18632/aging.102561

Wu, J., and Lipinski, M. M. (2019). Autophagy in neurotrauma: good, bad, or dysregulated. *Cells* 8, 693. doi:10.3390/cells8070693

Xiao, F., Guo, Y., Deng, J., Yuan, F., Xiao, Y., Hui, L., et al. (2019). Hepatic c-Jun regulates glucose metabolism via FGF21 and modulates body temperature through the neural signals. *Mol. Metab.* 20, 138–148. doi:10.1016/j.molmet.2018.12.003

Xiao, F., Guo, Y., Deng, J., Yuan, F., Xiao, Y., Hui, L., et al. (2019). Hepatic c-Jun regulates glucose metabolism via FGF21 and modulates body temperature through the neural signals. *Mol. Metab*. 20, 138–148. doi:10.1016/j.molmet.2018.12.003

Yan, C., Liu, J., Gao, J., Sun, Y., Zhang, L., Song, H., et al. (2019). IRE1 promotes neurodegeneration through autophagy-dependent neuron death in the Drosophila model of Parkinson's disease. *Cell Death Dis.* 10, 800. doi:10.1038/s41419-019-2039-6

Zarei, M., Pizarro-Delgado, J., Barroso, E., Palomer, X., and Vazquez-Carrera, M. (2020). Targeting FGF21 for the treatment of nonalcoholic steatohepatitis. *Trends Pharmacol. Sci.* 41, 199–208. doi:10.1016/j.tips.2019.12.005

Zhang, Y., Li, L., Mu, J., Chen, J., Feng, S., and Gao, J. (2020). Implantation of a functional TEMPO-hydrogel induces recovery from rat spinal cord transection through promoting nerve regeneration and protecting bladder tissue. *Biomater Sci.* 8, 1695–1701. doi:10.1039/c9bm01530b

Zholudeva, L. V., Qiang, L., Marchenko, V., Dougherty, K. J., Sakiyama-Elbert, S. E., and Lane, M. A. (2018). The neuroplastic and therapeutic potential of spinal interneurons in the injured spinal cord. *Trends Neurosci.* 41, 625–639. doi:10.1016/j.tins.2018.06.004

Conflict of Interest: The authors declare that the research was conducted in the absence of any commercial or financial relationships that could be construed as a potential conflict of interest.

frontiers in Pharmacology

ORIGINAL RESEARCH
published: 29 January 2021
doi: 10.3389/fphar.2020.632809

Loss of FGFR3 Delays Acute Myeloid Leukemogenesis by Programming Weakly Pathogenic CD117-Positive Leukemia Stem-Like Cells

Chen Guo[1,2†], Qiuju Ran[2†], Chun Sun[2†], Tingting Zhou[2], Xi Yang[2], Jizhou Zhang[2], Shifeng Pang[1] and Yechen Xiao[1,2]**

[1]Department of Biotechnology, Guangdong Medical University, Dongguan, China, [2]Department of Biochemistry and Molecular Biology, College of Basic Medical Science, Jilin University, Changchun, China

OPEN ACCESS

Edited by:
Zhouguang Wang,
Albert Einstein College of Medicine,
United States

Reviewed by:
Xiaoping Wu,
Jinan University, China
Huiyan Wang,
Jilin Medical University, China
Zhichao Ni,
Zhejiang University, China

***Correspondence:**
Shifeng Pang
psf1975@126.com
Yechen Xiao
yechenxiao2400@126.com

†These authors have contributed equally to this work

Specialty section:
This article was submitted to Integrative and Regenerative Pharmacology, a section of the journal Frontiers in Pharmacology

Received: 24 November 2020
Accepted: 21 December 2020
Published: 29 January 2021

Citation:
Guo C, Ran Q, Sun C, Zhou T, Yang X, Zhang J, Pang S and Xiao Y (2021) Loss of FGFR3 Delays Acute Myeloid Leukemogenesis by Programming Weakly Pathogenic CD117-Positive Leukemia Stem-Like Cells. Front. Pharmacol. 11:632809. doi: 10.3389/fphar.2020.632809

Chemotherapeutic patients with leukemia often relapse and produce drug resistance due to the existence of leukemia stem cells (LSCs). Fibroblast growth factor receptor 3 (FGFR3) signaling mediates the drug resistance of LSCs in chronic myeloid leukemia (CML). However, the function of FGFR3 in acute myeloid leukemia (AML) is less understood. Here, we identified that the loss of FGFR3 reprograms MLL-AF9 (MA)-driven murine AML cells into weakly pathogenic CD117-positive leukemia stem-like cells by activating the FGFR1-ERG signaling pathway. FGFR3 deletion significantly inhibits AML cells engraftment *in vivo* and extends the survival time of leukemic mice. FGFR3 deletion sharply decreased the expression of chemokines and the prolonged survival time in mice receiving FGFR3-deficient MA cells could be neutralized by overexpression of CCL3. Here we firstly found that FGFR3 had a novel regulatory mechanism for the stemness of LSCs in AML, and provided a promising anti-leukemia approach by interrupting FGFR3.

Keywords: leukemia (acute myeloid), stem-like cancer cells, fibroblast growth factor receptor 3, FGFR1, erg, CCL3 chemokine

INTRODUCTION

Acute myeloid leukemia (AML) is a malignant disease with a heterogeneous molecular panel of mutations participating in the blockade of differentiation and the uncontrolled clonal proliferation of myeloid hematopoietic stem and progenitor cells (Ferrara and Schiffer, 2013). Chemotherapeutic patients with AML often relapse and produce drug resistance due to the existence of leukemia stem cells (LSCs) (Fernandez et al., 2019). LSCs in AML represent a minor fraction at the apex of a cellular hierarchy which initiates and maintains the disease, exhibiting properties of self-renewal, cell cycle quiescence, and drug resistance (Siveen et al., 2017). It is urgent to find the regulatory mechanism of LSCs so that AML could be cured by eliminating LSCs.

Fibroblast growth factors (FGFs) play important roles in regulating cell proliferation, differentiation, and survival during embryo development and the adult stage by the FGF receptor (FGFR1-4)-mediated signaling pathway (Wesche et al., 2011). Previous studies showed that FGF signaling is very essential for promoting hematopoietic stem cell (HSC) expansion *in vitro* and *in vivo* (de Haan et al., 2003). FGF1 was also used for the *in vitro* culture of LSCs (Peng et al., 2010). Nevertheless, how FGFs affect biological functions remains unclear. FGFR3, an important member of the FGFR family, is highly expressed in HSCs (Dvorak and Hampl, 2005), and increased in LSCs ($CD34^+BCR\text{-}ABL^+$) from chronic myeloid leukemia (CML) (Dvorak et al., 2003). FGF2

induces imatinib resistance in patients' $CD34^+$ CML cells via reactivation of FGFR3-RAS-MAPK signaling (Traer et al., 2014). A previous study showed that the FGFR3 fusion protein (TEL-FGFR3) induced T-lymphoma and subsequently progressed to AML (Maeda et al., 2005). Up to date, there have been few reports on the relationship between FGFR3 and AML as well as AML-LSCs.

In this study, an MLL-AF9 (MA)-transduced AML cell model was constructed to study the functions of FGFR3 signaling in AML. We found that FGFR3 deletion reprogrammed MA-AML cells into $CD117^+$ leukemia stem-like cells by activating the FGFR1-ERG-CD117 signaling pathway. We also found that FGFR3-deficient leukemia cells were weakly pathogenic due to the downregulation of chemokines genes. Collectively, we firstly identified a novel regulatory mechanism of FGFR3 in AML and provided evidence supporting its clinical significance in AML.

METHODS

Mice

FGFR3$^{-/-}$ mice on a C57BL/6 background were constructed via CRISPR/Cas9-mediated genome engineering and provided by Cyagen Biosciences Inc (Suzhou, China). The C57BL/6 mice were purchased from Changsheng Inc. (Benxi, China). All mice used in this study were housed in the animal facility at the College of Basic Medical Sciences of Jilin University and handled according to the guidelines of Animal Care and Use Committee of Jilin University.

Genotyping

Genomic DNA was extracted from mice tails as described previously (Xiao et al., 2011), and the FGFR3 gene fragment was amplified by PCR. The PCR product was detected by 1.5% agarose electrophoresis, and confirmed for DNA sequencing (Sangon, Shanghai, China). To identify the FGFR3 knockout (KO) mouse model, three primers were designed as follows: FGFR3-F (5′-CTGTGTCCGCCTAGTGGAGG AGC-3′), FGFR3-R (5′-GAACGGAGGAGGCGGGGGTT-3′), and FGFR3-Wt/He-R (5′-AGTGCCAAG AAGGGTTTCAGACAA C-3′), respectively.

Expression Plasmid Construction, Virus Packing, and Infection

The genes used in this study, including ERG (mouse), CCL3 (mouse), and constitutively active FGFR1 (CA-FGFR1, human) (Petiot et al., 2002) were synthesized and cloned into retrovirus vector MSCV-GFP by ZooNBio Biotechnology (Nanjing, China).

For retrovirus construction, the MSCV-GFP or MSCV-MLL-AF9 plasmid and Gag-pol plasmid were both transfected into 293T cells by liposome (Jinchuan, Changchun, China), and the supernatant was collected at 36 h and 72 h, respectively. The virus was concentrated by a centrifugal filter (Millipore, USA). $CD117^+$ cells from murine BM were selected by magnetic beads according to the method of the EasySep mouse CD117-positive screening kit (STEMCELL Technologies Inc., Canada), then they were infected with the retrovirus containing different genes at 32°C centrifugation for 4 h, and the GFP^+ cells were sorted by flow cytometry. For lentivirus construction, lentivirus containing a short hairpin RNA (shRNA) plasmid against mouse ERG (LV-U6 > mERG [shRNA]-mPGK > mCherry/T2A/Puro), was provided by Cyagen Biosciences Inc (Guangzhou, China). The target sequence of mouse ERG (CGACATTCTTCTCTCACAT) was simply adapted from the human ERG gene as described previously (Sun et al., 2008; Tsuzuki et al., 2011).

Cell Culture

For primary BM $CD117^+$ cells, the cells were cultured in DMEM medium containing 15% bovine fetus serum, 100 ng/ml of SCF, 10 ng/ml of IL3, and 10 ng/ml of IL6. For primary MLL-AF9-transduced cells, the cells were cultured in DMEM medium containing 10% bovine fetus serum, 20 ng/ml of SCF, 10 ng/ml of IL3, and 10 ng/ml of IL6.

Mouse AML Cell Transplantation

For the primary transplantation assays, MA-transduced cells were injected by the tail vein into lethally irradiated (8.5 Gy) 8 to 10-week-old C57BL/6 recipient mice with 2×10^5 donor cells per mouse plus a radioprotective dose of 5×10^5 whole BM cells. For the secondary transplantation assays, 2×10^4 leukemic cells isolated from the bone marrow or spleen of primary recipient mice were further transplanted into lethally irradiated C57BL/6 secondary recipient mice. The survival of recipient mice was monitored over time and analyzed by Kaplan-Meier survival graphing.

Flow Cytometry and Antibodies

BM, SP, and PB were collected from the different types or different treatments of the mice. MNCs were isolated from these tissues after red blood cell lysis. Cells were suspended in fluorescence-activated cell sorting buffer (PBS supplemented with 2% FBS) at a concentration of 1×10^7 cells/ml and aliquoted into flow cytometry tubes (100–200 μL per tube) for antibody staining. The analysis was performed with flow cytometry (BD LSRFortessa ™ or BD Accuri ™ C6) as described previously (Xiao et al., 2011). Antibodies used in this study were purchased from eBioscience, including Gr1-FITC (RB6-8C5), B220-FITC (RA3-6B2), Ter119-FITC (TER-119), CD11b-FITC (M1/70), CD3e-FITC (145-2C11), Gr1-PE (RB6-8C5), CD3e-PE (145-2C11), Ter119-PE (TER-119), ISO Control-PE (Ebr2a), CD11b-PE (M1/70), CD117-PE (2B8), B220-PE (RA3-6B2), CD11b-APC (M1/70), CD117-APC (ACK2), Gr1-APC (RB6-8C5), CD11b-PECy5.5 (M1/70), CD4-PECy5.5 (RM4-5), B220-PECy5.5 (RA3-6B2), CD4-PECy5 (GK1.5), CD11b-PECy5 (M1/70), B220-PECy5 (RA3-6B2), and CD8a-PECy5 (53–6.7). The secondary antibody (Goat pAb to Rb IgG/PE, ab72465) was purchased from Abcam.

RNA Sequencing Analysis

For RNA sequencing (RNA-seq) analysis of the leukemia cells, 2×10^6 MA-WT cells or MA-KO cells were stored in TRIzol solution and delivered to Sangon Biotech (Shanghai, China) for

RNA-seq analysis using the Illumina Hiseq2000 Genome Analyzer instrument (Illumina, San Diego, CA). The analysis was performed as described previously (Yao et al., 2019).

RNA Isolation, cDNA Synthesis, and Quantitative Real-Time PCR

Total RNA from different types of cells was extracted using TRIzol reagent (Thermo) according to the manufacturer's instruction, and cDNA was prepared using a reverse transcription (RT) kit (TransGen Biotech, Beijing, China). Quantitative real-time PCR analysis was performed by a SYBR Green kit (TransGen Biotech) using a MX3000 P system. The expression level of each gene was quantified and normalized to the β-actin expression using the following primer pairs (all mouse):

CXCL10 forward: 5′-GTCATTTTCTGCCTCATCCT-3'; CXCL10 reverse: 5′-GCCCTTTTAGACCTTTTTTG-3'; CCL2 forward: 5′-GATCAGAACCTACAACTTTATT-3'; CCL2 reverse: 5′-TCACTGTCACACTGGTCACTCC-3'; CCL3 forward: 5′-GCCCTTGCTGTTCTTCTCTGTA-3'; CCL3 reverse: 5′-CGATGAATTGGCGTGGAATCTT-3'; CCL4 forward: 5′-TCTCTCTCCTCTTGCTCGTG-3'; CCL4 reverse: 5′-TGCTGGTCTCATAGTAATCC-3'; CCL5 forward: 5′-CTG CTTTGCCTACCTCTCCCTC-3'; CCL5 reverse: 5′-TCTTGA ACCCACTTCTTCTCTG-3'; CCR2 forward: 5′-GAATCTTTT TCATTATCCTCCT-3'; CCR2 reverse: 5′-GACTACACTTGT TATCACCCCA-3'; CCR5 forward: 5′-GTAGGAATGAGA AGAAGAGGCA-3'; CCR5 reverse: 5′-TCGGAACTGACCCTT GAAAATCCAT-3'; MESIS1 forward: 5′-ATTATGGGGGTA TGGATGGAGT-3'; MESIS1 reverse: 5′-TGCTAAGAGAGG GAAGAGGGGG-3'; FGFBP3 forward: 5′-AAGCTCCCAGCC GGAAAAGAAG-3'; FGFBP3 reverse: 5′-GTTGACAAAGAA GTTGCAAAGG-3'; STAT5a forward: 5′-TGGGGGAAGATG GGTTTTTGC-3'; STAT5a reverse: 5′-CGTTCTCCGTGTCCT GTGTGA-3'; STAT5b forward: 5′-TGAACAAGCAACAGG CCCACGA-3'; STAT5b reverse: 5′-AAAAGGCATCAGATT CCAAAAC-3'; HOXA9 forward: 5′-CCCTGACTGACTATG CTTGTGG-3'; HOXA9 reverse: 5′-ACCTGCCTTTCGGTG AGGTTGA-3'; HOXA10 forward: 5′-CCCTTCGCCAAATTA TCCCACA-3'; HOXA10 reverse: 5′-CACCAACACCAGCCT CGCCTCT-3'; HOXA11 forward: 5′-CGTGGTCCCTGCTCC TCTAACA-3'; HOXA11 reverse: 5′-GGGCTCAATGGCGTA CTCTCTG-3'; FGFR1 forward: 5′-AGACGGACAACACCA AACCAAA-3'; FGFR1 reverse: 5′-TCCCATACTCATTCTCCA CGAT-3'; FGF10 forward: 5′-TGTTGCTCTTTTTGGTGTCTT-3'; FGF10 reverse: 5′-CTCCGATTTCCACTGATGTTA-3'; PBX3 forward: 5′-CTCCGAGAACAGAGTAGAA-3'; PBX3 reverse: 5′-GCTGAGGTGTGAGTAAAAA-3'; ERG forward: 5′-AGTGTGAACAAAGGTGGGAAGA-3'; ERG reverse: 5′-AGT CAGATGTGGAAGGGGAGTC-3'; c-Kit forward: 5′-ACAAAA GCAACATCAGATAT-3'; c-Kit reverse: 5′-TGAGACAGGAGT GGTACACC-3'; Cyclin D1 forward: 5′-TCTCCTGCTACCGCA CAACGC-3'; Cyclin D1 reverse: 5′-TCCACTTCCCCCTCCTCC TCA-3'; β-actin forward: 5′-GGAGATTACTGCCCTGGCTCC TA-3'; β-actin reverse: 5′-GACTCATCGTACTCCTGCTTG CTG-3'.

ChIP–PCR Assay

The plasmid MSCV-puro-ERG or MSCV-puro was transformed into HEK293 T cells, and the cells were cultured for 48 h. The subsequent Chromatin Immunoprecipitation (ChIP) assay was performed according to previously described methods (Jiao et al., 2017). The cells were crosslinked with 0.1% formaldehyde. Chromatin was broken down into 200–500 bp fragments using an ultrasonicator (Xinzhi, Ningbo, China). The HA antibody was added into the lysate and incubated overnight at 4°C, then ChIP–grade Protein A Dynabeads were added into each IP tube and incubated for 2 h. DNA was purified with the general method and eluted DNA was subjected to quantitative PCR (qPCR) to measure the enrichment according to the previous method. Primers against CD117 promoter region used for ChIP-PCR were designed as follows:

CD117-P1 forward: 5′-TTACACTTTTAAGCATTCTG-3'; reverse: 5′-TGTGTTCTTTCTCTCCACTG-3'. CD117-P2 forward: 5′-ATCTTCTCTACTTCATAACG3'; reverse: 5′-TCTACCTAGGGACATTTCAC-3'; CD117-P3 forward: 5′-AGTAAAACACTCATACACAT-3'; reverse: 5′-TTTTAATCT CACCCTCAACA-3'. CD117-P4 forward: 5′-AGCCAGCCG CCTGGACTGAA-3'; reverse: 5′-CCTAGTGCCCGGGGCTCT CG-3'.

Luciferase Reporter Assay

Using genomic DNA from mouse BM as a template, a 2000 bp DNA fragment, CD117p containing the CD117 promoter region was amplified by the PCR method as described previously (Li et al., 2017) and cloned into a pGL3-Basic plasmid, then three plasmids, including control plasmid pRL-TK, recombinant plasmid pGL3-CD117p or pGL3-Basic as well as MSCV-puro-ERG or MSCV-puro, were transfected into HEK293T cells, and the cells were cultured for 48 h. A luciferase reporter assay was performed as described previously (Jiang et al., 2019). The activity of firefly luciferase and Renilla luciferase was assayed using a Trans Detect Double-Luciferase Reporter Assay Kit (TransGen) in a multifunctional chemiluminometer. The relative luciferase activity was normalized by the ratio of firefly luciferase to Renilla luciferase for each transfected well. Each experiment was performed in quadruplicate and repeated three times.

Colony-Forming/Replating Assays

A total of 1,500 different types of MA cells were seeded in the methylcellulose (MethoCult™ M3434, StemCell Technologies) and colonies were counted on day 7 of culture using an inverted microscope (Olympus). For the replating assay, the colonies were washed twice with PBS and centrifuged at 1,000 rpm for 5 min. The cells were resuspended with DEME medium and then 1,500 live cells were used for the colony-forming assay according to the previous description.

Analysis of Chemokine Production in BM Supernatant by ELISA

BM cells from the femur and tibia of one mouse leg were washed with 1 ml of PBS, then the cells were removed by

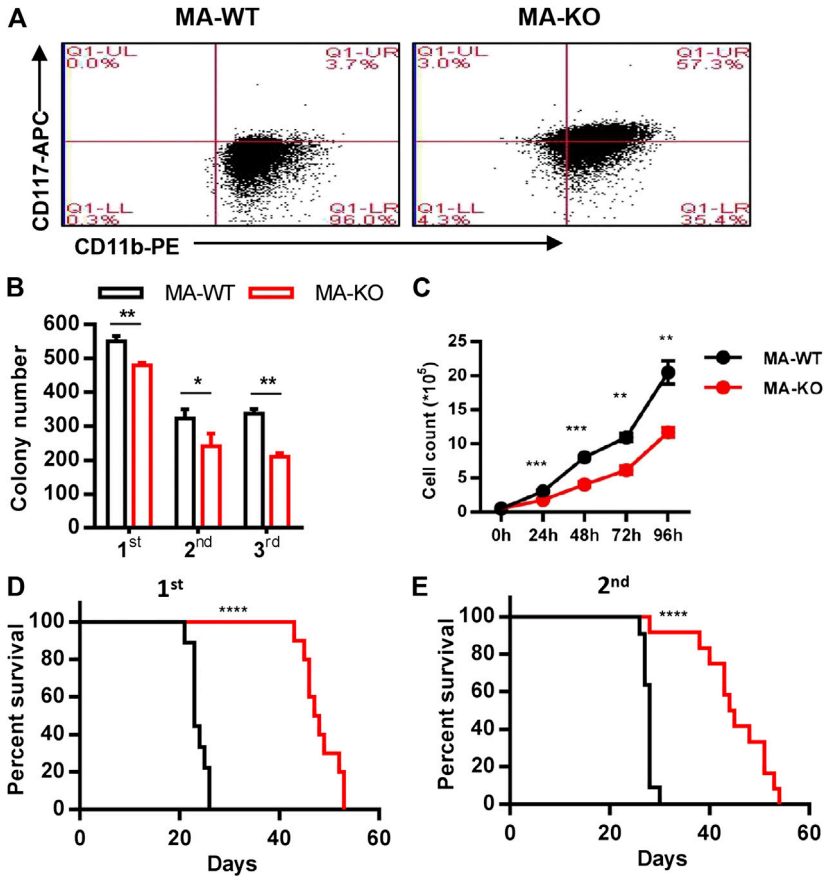

FIGURE 1 | Loss of FGFR3 promotes the generation of weakly pathogenic CD117$^+$ MLL-AF9-driven leukemia cells. **(A)** Representative flow cytometric analysis of MA-WT and MA-KO cells with CD117 and CD11b staining **(B)** *In vitro* colony-forming assay of MA-WT and MA-KO cells (n = 3). **(C)** Growth curve at indicated time from MA-WT and MA-KO cells (n = 5). **(D,E)** Effects of FGFR3 deletion in MLL-AF9-mediated *in vivo* leukemogenesis. Kaplan-Meier curves are shown for two groups of transplanted mice including MA-WT (n = 9), and MA-KO (n = 10) in a primary BMT assay **(D)**, and for two groups of transplanted mice including MA-WT (n = 11), and MA-KO (n = 12) in the secondary BMT assay **(E)**.*$p < 0.05$, **$p < 0.01$, ***$p < 0.001$, ****$p < 0.0001$.

centrifugation and the BM supernatant was collected. For CCL3 and CCL4 detection, the standard working solution was diluted by gradient for the preparation of the standard curve (Elabscience ELISA kit). All experimental procedures were performed according to the kit instructions. When the reaction was terminated, the absorbance at a wavelength of 450 nm was immediately measured using a microplate reader.

Western Blot and Antibodies

In vitro cultured cells or murine tissue samples were harvested and lysed with NP-40 (Thermo). Proteins from the lysate were fractionated by electrophoresis through 12% polyacrylamide gels and transferred onto PVDF membranes (Thermo) using Tris-Glycine Transfer buffer. The membrane was incubated overnight to block nonspecific binding with 5% nonfat milk powder, and incubated with the relative primary antibody (1: 1,000) for 1 h, then washed and incubated with a 1:10,000 dilution of secondary HRP-conjugated antibody. Immunoreactive bands were visualized using an ECL kit (Thermo Scientific). For Western blotting and ChIP assays, the following antibodies were used: p-ERK (CST; #4370S; 1: 1,000), ERK (Bioworld; BS1112; 1:1,000), AKT (CST; #9272S; 1:1,000), p-AKT (CST; 4060S; 1:1,000), FGFR1 (CST; 9740S; 1: 1,000), p-FGFR1 (Affinity; AF3157; 1:1,000), ACTIN (CMCTAG; AT0001; 1:1,000), Goat Anti-Rabbit IgG (Bioworld; BS13278; 1:10,000), FGFR3 (NOVUS Biologicals; JM110–33; 1:1,000), ERG (abcam; ab92513; 1:1,000), HA Tag (Life Science; AB10004; 1:1,000).

Statistical Analysis

Normally distributed experimental data were performed using the *Student's t* test for single comparison and one-way or two-way ANOVA for multiple comparisons from GraphPad Prism Version 6 (GraphPad Software, La Jolla, CA, United States). The data were demonstrated using means ± SD and $p < 0.05$ was considered as statistically significant. *$p < 0.05$, **$p < 0.01$, ***$p < 0.001$, and ****$p < 0.0001$.

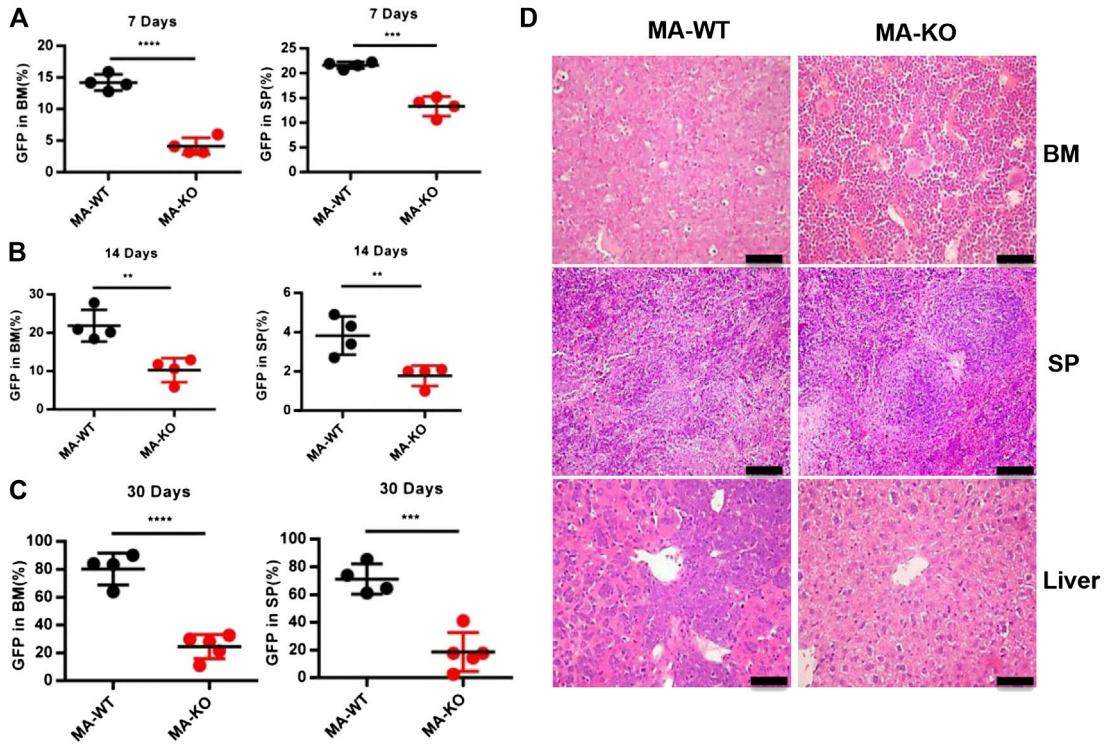

FIGURE 2 | FGFR3 deletion significantly inhibits *in vivo* engraftment of leukemic mice. **(A–C)** The engraftment ability of GFP$^+$ MA-WT and MA-KO cells from BM and SP at day 7 **(A)**, day 14 **(B)**, and day 30 **(C)** after transplantation. **(D)** Representative image of hematoxylin and eosin-stained sections at day 30 after transplantation of MA-WT and MA-KO cells. $^{**}p < 0.01$, $^{***}p < 0.001$, $^{****}p < 0.0001$.

RESULTS

Loss of FGFR3 in MA-Driven AML Cells Promotes the Generation of Weakly Pathogenic CD117-Positive Leukemia Stem-like Cells

To study whether FGFR3 is a potential target gene for AML therapy, MA-transduced pre-leukemia cells were constructed with CD117$^+$ BM cells from *FGFR3*$^{-/-}$ and wild-type (WT) mice via infection of retrovirus (**Supplementary Figures S1A,B**). Leukemia cells were acquired from the BM or SP of leukemic mice which were transplanted with pre-leukemia cells according to the strategy (**Supplementary Figure S1C**). Firstly, we surprisingly found that CD117-positive leukemia stem-like cells (GFP$^+$CD117$^+$CD11b$^{+/low}$) have a 20-fold higher percentage in MA-induced FGFR3-knockout leukemia cells (MA-KO) than in MA-induced WT leukemia cells (MA-WT) (**Figure 1A**). The colony forming assays of three continuous generations showed that MA-KO cells had lower growth rates than that of MA-WT cells (**Figure 1B**), which was also consistent with the *in vitro* cell growth curve at the indicated time (**Figure 1C**). Significantly delayed leukemia development and reduced leukemia-related mortality were observed in mice receiving MA-KO cells upon primary transplantation (**Figure 1D**) and secondary transplantation (**Figure 1E**) compared with the mice receiving MA-WT cells. These results showed that FGFR3 deletion in MA-driven AML cells inhibits cell proliferation and promotes the generation of weakly pathogenic CD117-positive leukemia stem-like cells.

FGFR3 Deletion Does Not Affect the Homing Ability of MA-Leukemia Cells but Significantly Inhibits *In Vivo* Engraftment

In order to define which stage affects mice survival, the homing ability of leukemia cells was analyzed at 24 h after transplantation, and the results showed that there was no significant difference in BM, SP, and PB in leukemic mice transplanted with MA-WT or MA-KO cells (**Supplementary Figures S2A–C**). However, the *in vivo* engraftment ability of MA-KO cells was remarkably lower than that of MA-WT cells at day 7, day 14, and day 30 (**Figures 2A–C**). Hematoxylin and eosin staining results confirmed that there were less infiltrative leukemia cells in BM, SP, and the liver of MA-KO transplanted mice than MA-WT transplanted mice at day 30 after transplantation (**Figure 2D**). These observations indicated that FGFR3 deletion attenuates the *in vivo* engraftment ability of MA-leukemia cells.

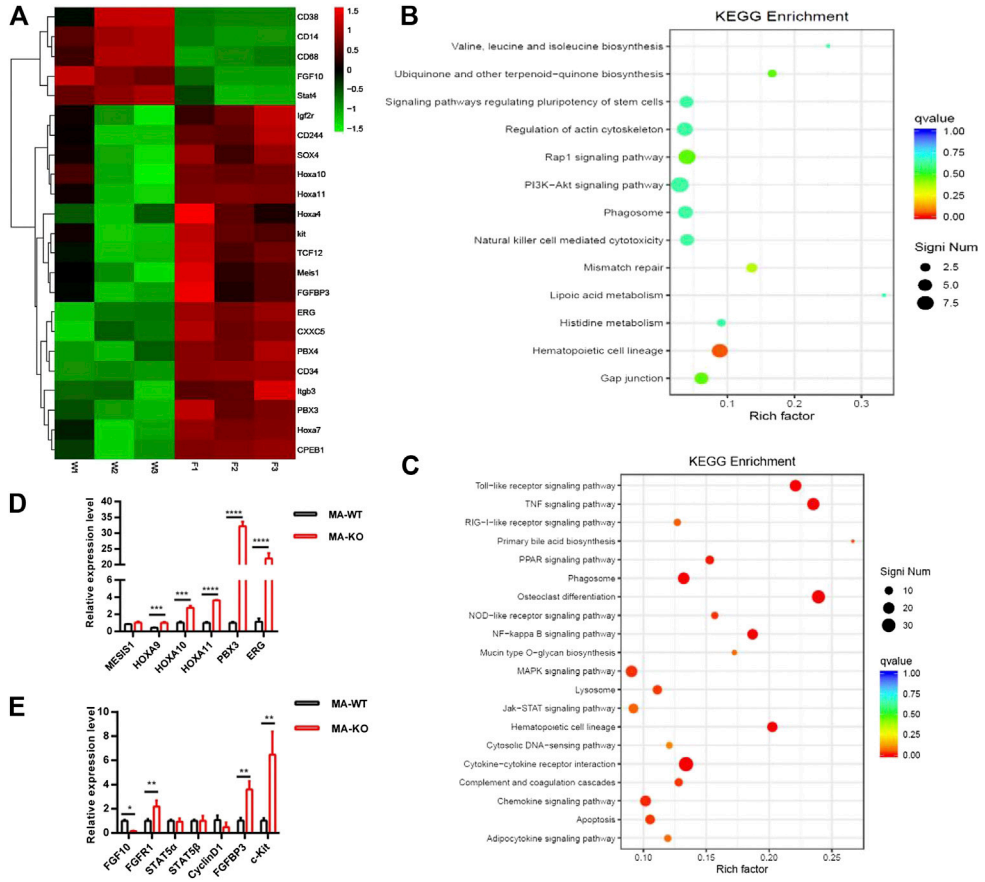

FIGURE 3 | RNA-seq and differential gene analysis of MA-WT and MA-KO cells. **(A)** Heat maps showing gene expression kinetics from RNA-seq results of MA-WT samples (W1, W2, and W3) and MA-KO samples (F1, F2, and F3). **(B,C)** KEGG enrichment of pathway in MA-KO cells compared to MA-WT cells. **(D,E)** qRT-PCR assay of differential genes from **(A)** (n = 4). *$p < 0.05$, **$p < 0.01$, ***$p < 0.001$, ****$p < 0.0001$.

FGFR3 Deletion Reprograms Leukemia Cells Into CD117-Positive Leukemia Stem-like Cell by Activating the FGFR1-AKT-ERG Signaling Pathway

To elucidate the molecular mechanism of how FGFR3 deletion promotes the generation of CD117-positive leukemia stem-like cells, RNA-seq analysis and accompanying quantitative reverse transcription-PCR (qRT-PCR) of MA-WT and MA-KO cells were performed. The results showed that some stemness-related genes (such as Hoxa9, Hoxa10, PBX3, etc.) and receptor genes (such as FGFR1 and c-Kit, etc.) were notably upregulated in MA-KO cells compared with MA-WT cells (**Figures 3A–E**). FGFR1 has been reported in promoting the proliferation of HSCs (de Haan et al., 2003; Magnusson et al., 2005; Zhao et al., 2012) and FGFR1 or its fusion protein drives AML development (Karajannis et al., 2006; Lee et al., 2013; Wang et al., 2016). In order to study whether FGFR1 signaling promotes the generation of CD117-positive leukemia cells, MA-WT and MA-KO cells were treated with FGFR1 inhibitor (PD173074, PD17), AKT inhibitor (LY294002, LY), and MEK inhibitor (PD98059, PD98), respectively. The results showed that PD17 and LY treatment, not PD98 treatment, significantly reduced the percentage of CD117-positive leukemia cells in MA-KO cells compared to MA-WT cells (**Figure 4A**), suggesting FGFR1 may promote CD117-positive leukemia cells by AKT signaling.

ERG, which is a member of the ETS family, was significantly upregulated in MA-KO cells compared to MA-WT cells (**Figures 3A,D**). ERG is a key transcriptional factor in the reprogramming of non-blood cells into hematopoietic stem and progenitor cells (Batta et al., 2014; Sugimura et al., 2017). Our results showed that FGFR1 activation upregulated ERG expression in 293T cells (**Figure 4B**), suggesting that ERG is a downstream target gene of FGFR1 signaling. To further identify whether ERG directly regulates the CD117-positive leukemia stem-like cell pool, we constructed MA-WT-ERG cells which overexpressed ERG in MA-WT cells (**Supplementary Figure S3A**) and MA-KO-shERG cells which downregulated ERG in MA-KO (**Supplementary Figure S3B**). The results showed that overexpression of ERG significantly increases the 3-fold percentage of total CD117-positive leukemia cells (**Figure 4C**). In contrast, knockdown of ERG in MA-KO cells decreases 30 percent of the total CD117-positive leukemia cells (**Figure 4D**).

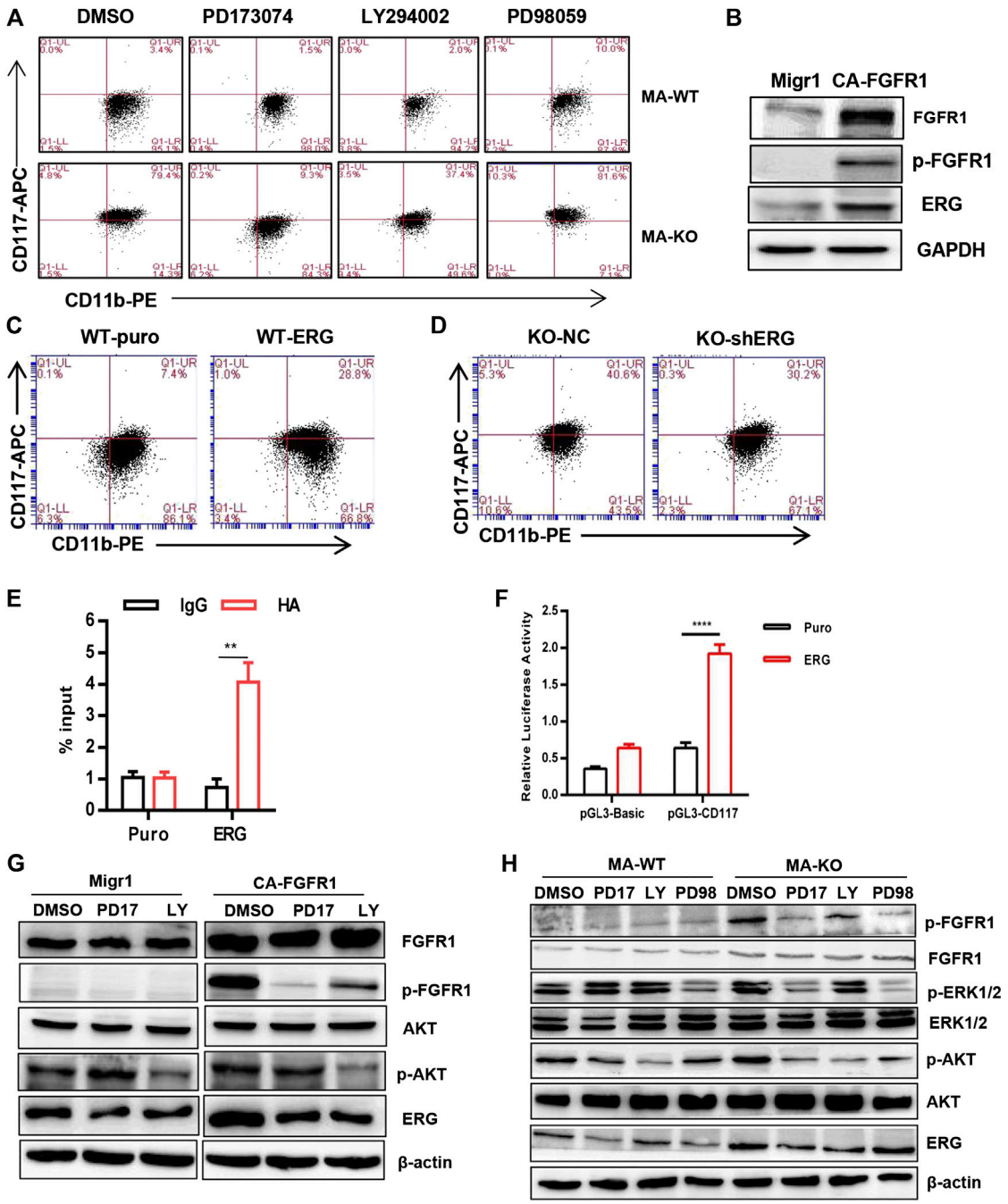

FIGURE 4 | FGFR3 deletion programs CD117^{+} leukemia cells by activating the FGFR1-ERG-CD117 signaling pathway. **(A)** Representative flow cytometric analysis of CD117^{+}CD11b$^{+/low}$ in MA-WT and MA-KO cells with FGFR inhibitor (PD173074, 4 μM), AKT inhibitor (LY294002, 50 μM), and MEK inhibitor (PD98059, 50 μM). **(B)** Western blot analysis of ERG expression in 293T cells expressing CA-FGFR1. **(C,D)** Flow cytometric analysis of CD117^{+}CD11b$^{+/low}$ in WT-ERG cells **(C)** and KO-shERG cells. **(D,E)** ChIP-qPCR assay of potential binding of ERG at the promoter region of CD117 (n = 4) **(F)** luciferase report assay of transcriptional regulation function of ERG (n = 4). **(G)** Western blot analysis of ERG expression in 293T cells expressing CA-FGFR1 in the presence of signaling inhibitor. **(H)** The expression of *p*-FGFR1, *p*-ERK1/2, *p*-AKT, and ERG in MA-WT and MA-KO cells treated with PD173074 (5 μM), LY294002 (50 μM), and PD98059 (50 μM) for 16 h $^{**}p < 0.01$, $^{****}p < 0.0001$.

These findings indicated that the dosage of ERG controls the frequency of CD117-positive leukemia cells.

To further study how ERG promotes the generation of CD117-positive leukemia cells, we analyzed the promoter region of CD117, and found several ERG binding sites (CGGA (A/T). The ChIP-qPCR result from the second pair of primers showed that ERG highly binds to the promoter region of the CD117 gene (**Figure 4E**). Further, the double luciferase reporter assay proved

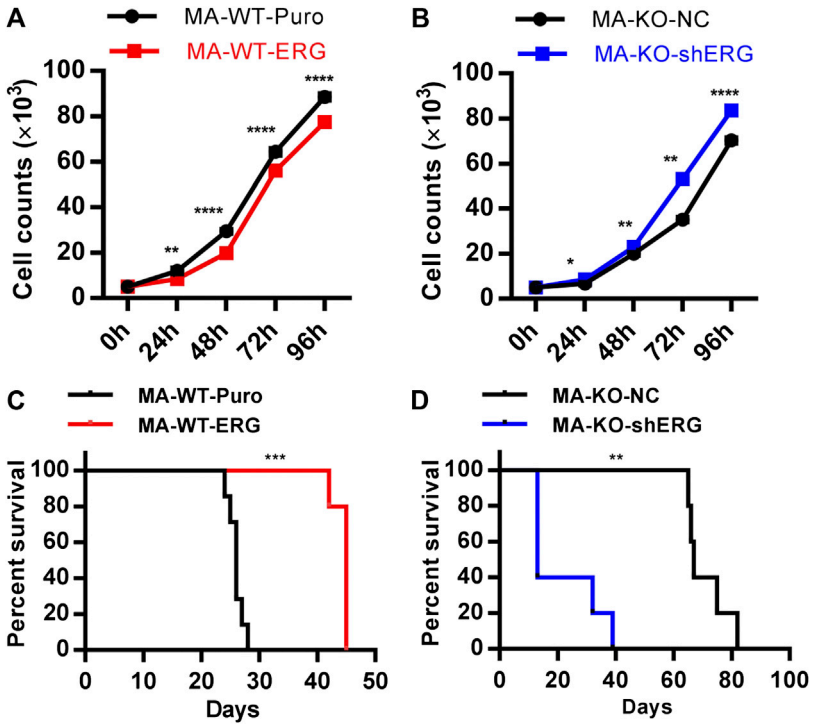

FIGURE 5 | ERG dosage is essential for the pathogenicity of leukemia cells. **(A)** The growth curve of MA-WT-ERG cells compared to the corresponding control cells. **(B)** The growth curve of MA-KO-shERG cells compared to the corresponding control cells. **(C)** Kaplan-Meier curves are shown for leukemogenesis in two groups of mice transplanted with MA-WT-puro cells (n = 7), and MA-WT-ERG cells (n = 5). **(D)** Kaplan-Meier curves are shown for leukemogenesis in two groups of mice transplanted with MA-KO-NC cells (n = 5), and MA-KO-shERG cells (n = 5). *$p < 0.05$, **$p < 0.01$, ***$p < 0.001$, ****$p < 0.0001$.

that ERG transcriptionally upregulates CD117 gene expression (**Figure 4F**). These results indicated that FGFR3 deletion reprograms leukemia cells into CD117-positive leukemia cells by activating the FGFR1-ERG-CD117 signaling pathway, suggesting that FGFR1 signaling is essential for maintaining the pool of LSCs.

ERG is often regulated by the MAPK/ERK (Huang et al., 2016) or AKT signal (Metzger et al., 2007; Shah et al., 2017). To elucidate how ERG expression was regulated by FGFR1 signaling in MA-KO cells, the inhibitors, including PD17, LY, and PD98, were used to treat FGFR1-active 293T cells and leukemia cells, respectively. The results showed that the inhibition of FGFR1 and AKT, not ERK1/2, significantly reduced FGFR1 activation-induced ERG expression in 293T cells (**Figure 4G**) and leukemia cells (**Figure 4H**), suggesting that FGFR1 upregulates ERG expression by activating PI3K/AKT signaling.

ERG Dosage Is Essential for the Pathogenicity of Leukemia Cells

The previous study showed that ERG reprograms leukemia cells into CD117-positive leukemia stem-like cells. The further studies indicated that overexpression of ERG in MA-WT cells inhibited cell growth at the indicated time (**Figure 5A**). In contrast, ERG knockdown in MA-KO-shERG cells promoted cell growth at the indicated time (**Figure 5B**). *In vivo* transplantation further confirmed that the survival time was significantly extended in MA-WT-ERG-transplanted mice (**Figure 5C**) and significantly reduced in MA-KO-shERG-transplanted mice compared with respective control mice (**Figure 5D**). All the above results indicated that the upregulation of ERG increases the frequency of CD117-positive leukemia cells and its dosage is essential for the pathogenesis of MA-driven leukemia cells.

FGFR3 Deletion Decreased the Expression of the Inflammation Factors and the Extended Survival Time of MA-KO-Transplanted Mice Could Be Neutralized by the Overexpression of CCL3

Why are MA-KO cells weakly pathogenic? We found that many enriched inflammatory response genes, such as CCL2, CCL3, CCL4, CCL5, were sharply downregulated in MA-KO cells compared to MA-WT cells (**Figures 6A–C**). *The in vivo* concentration of CCL3 and CCL4 in the BM supernatant of MA-KO-transplanted mice also significantly decreased compared to that of MA-WT-transplanted mice at day 30 after transplantation (**Figures 6D,E**), suggesting that FGFR3 signaling promotes the expression of these chemokines genes. This regulatory mechanism was also found in hepatocellular carcinoma cells (Liu et al., 2016) and multiple myeloma (Masih-Khan et al., 2006). CCL3 is an important

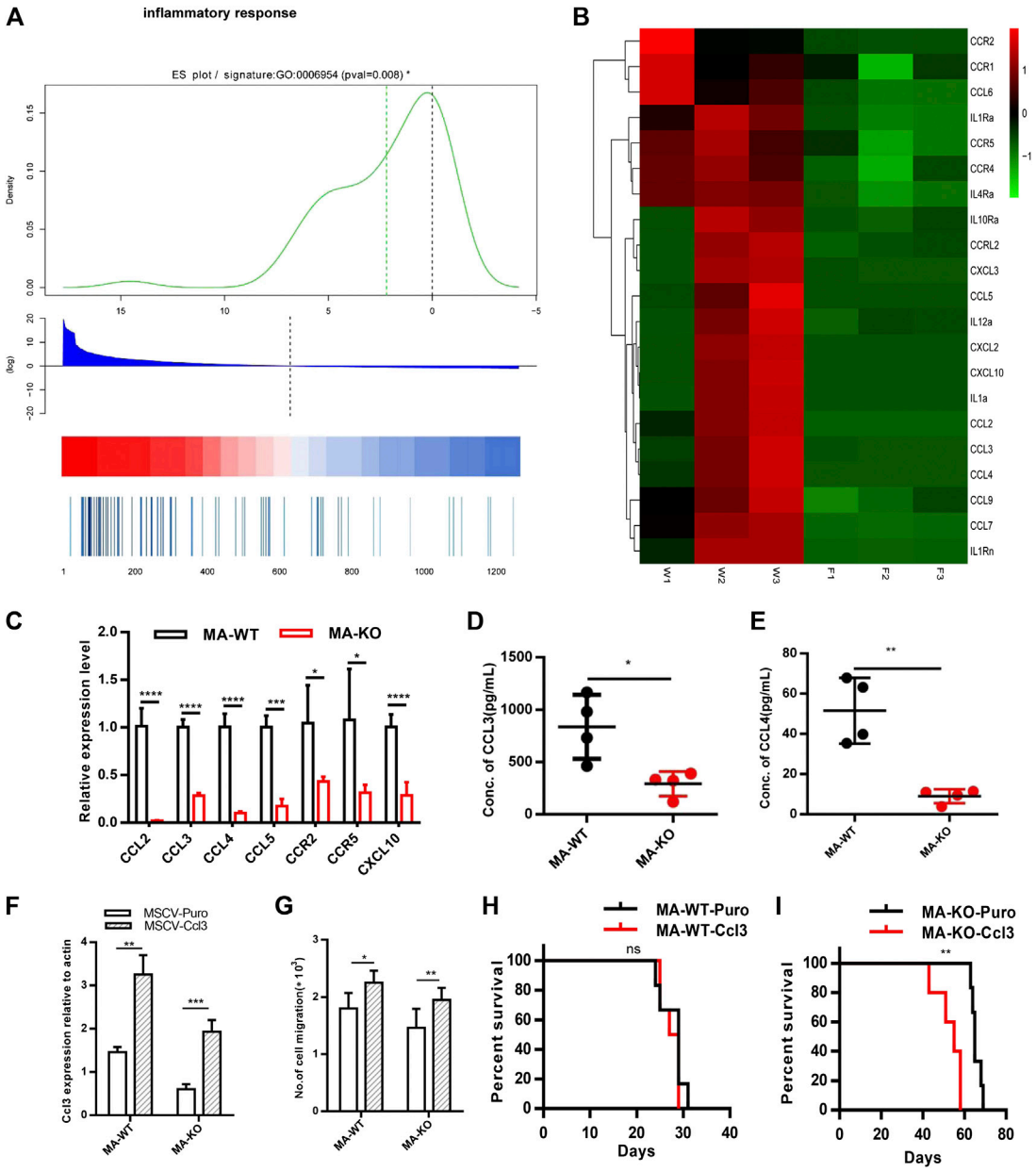

FIGURE 6 | FGFR3 deletion decreases the expression of the inflammation factors and the extended survival time of MA-KO cell-transplanted mice could be neutralized by overexpression of CCL3. **(A)** Gene list rank about inflammatory response genes from RNA-seq data. **(B)** Heat map on the expression level of inflammatory response genes in MA-WT samples (W1, W2, and W3) and MA-KO samples (F1, F2, and F3). **(C)** Differential expression genes from **(B)** by qRT-PCR analysis (n = 4). **(D,E)** The concentration of CCL3 **(D)** and CCL4 **(E)** in BM supernatant of leukemic mice at day 30 after transplantation by ELISA (n = 4). **(F)** Overexpression of CCL3 in MA-WT and MA-KO cells (n = 4). **(G)** Number of cell migration from 100,000MA-WT-CCL3 or MA-KO-CCL3 cells compared with respective control cells (n = 3). **(H,I)** Kaplan-Meier curves are shown for *in vivo* leukemogenesis in two groups of mice transplanted with leukemia cells, including MA-WT-puro cells (n = 6), and MA-WT-CCL3 cells (n = 5) **(H)** as well as MA-KO-puro cells (n = 6), and MA-KO-CCL3 cells (n = 5) **(I)**. $^{*}p < 0.05$, $^{**}p < 0.01$, $^{***}p < 0.001$, $^{****}p < 0.0001$.

regulator to maintain CML cells by inhibiting normal hematopoiesis (Baba et al., 2013; Baba et al., 2016), and its expression was regulated by FGFR3 signaling (Masih-Khan et al., 2006). To assess whether CCL downregulation is essential for the weak pathogenesis of MA-KO cells, MA-WT-CCL3 cells and MA-KO-CCL3 cells which overexpressed CCL3 were constructed by retrovirus infection (**Figure 6F**), and the two cell lines both exhibited a higher migration ability compared to their respective control cells (**Figure 6G**), suggesting that overexpression of CCL3 performs a better biological function. *In vivo* transplantation demonstrated that the survival time had no notable difference in MA-WT-CCL3-transplanted mice (**Figure 6H**) and was significantly reduced in MA-KO-CCL3-transplanted mice (**Figure 6I**) compared with respective control mice, suggesting that the extension of survival

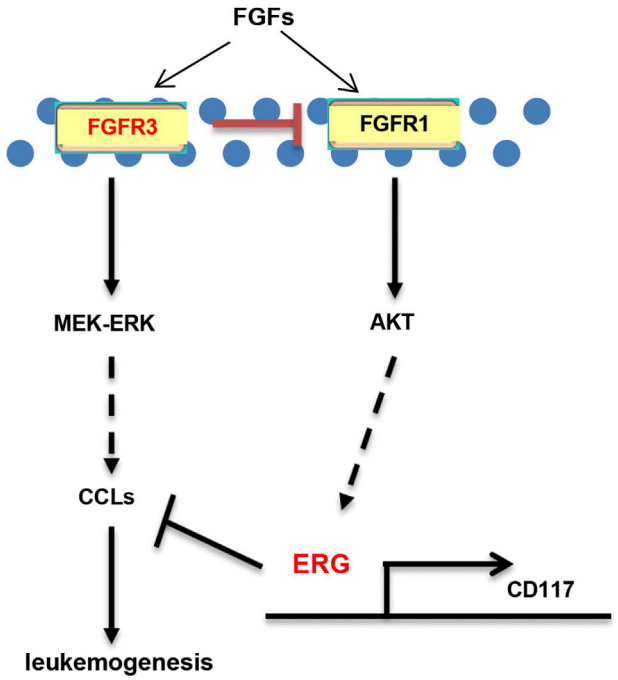

FIGURE 7 | Schematic model of FGFR3 signaling in AML. Schematic model showed that FGFR3 might upregulate CCL expression by activating MEK-ERK1/2 to maintain leukemogenesis. In addition, FGFR3 deletion programs weakly pathogenic CD117$^+$ leukemia stem-like cells by activating FGFR1-AKT-ERG-CD117 signaling. Furthermore, ERG does not only promote the stemness of LSCs by upregulating the expression of CD117, but also suppresses *in vivo* leukemogenesis by inhibiting the expression of chemokines genes.

time in MA-KO-transplanted leukemic mice is at least partially due to reduced chemokines production. Excitingly, the expression of these chemokines genes (such as CCL2, CCL3, CCL4, and CCL5) was regulated by ERG (**Supplementary Figures S4A,B**). ERG not only promotes the generation of CD117-positive leukemia cells by transcriptionally upregulating CD117, but is also an important regulator for the weak pathogenesis of CD117-positive leukemia cells by inhibiting the expression of chemokines genes. Collectively, our results indicated that FGFR3 might have dual functions in AML cells. The one is that it upregulates CCL expression by activating MEK-ERK1/2 to maintain leukemogenesis as described previously (Masih-Khan et al., 2006). The other is that it might inhibit the stemness of LSCs by antagonizing FGFR1-AKT-ERG-CD117 signaling (**Figure 7**).

DISCUSSION

FGFR3 was identified as a key oncogene in many types of tumors, especially multiple myeloma (Katoh and NaKagama, 2014) and bladder cancer (Wang et al., 2015). FGFR3 overexpression or active mutation promotes tumor cell proliferation, survival, and drug resistance (L'Hote and Knowles, 2005; Iyer and Milowsky, 2013; Javidi-Sharifi et al., 2015). FGFR3 signaling mediated FGF2-induced imatinib resistance in CML (Traer et al., 2014). However, FGFR3 functions in AML as well as AML-LSCs are rarely reported. In our studies, FGFR3-KO mice which were constructed by CRISPR-Cas9 technology display typical bone abnormity as described previously (Deng et al., 1996). Hematopoietic analysis results showed that FGFR3 is dispensable for the functions of HSCs in steady-state hematopoiesis (Ran et al., 2020). To study the functions of FGFR3 in AML, FGFR3-deficient MA-transduced cells were constructed by an infection of retrovirus. Extraordinarily, we found that FGFR3 mediates a novel reprogramming mechanism by which leukemia cells (non-LSCs) could be converted into CD117$^+$ leukemia stem-like cells.

In this study, we found that ERG, at the downstream of FGFR1 signaling, is required for FGFR3 deletion-induced reprogramming. ERG highly binds to the promoter region of the CD117 gene and transcriptionally upregulates CD117 gene expression (**Figures 4E,F**). This is consistent with the previous study which showed that ERG promotes the stem cell signature of leukemia cells (Tsuzuki et al., 2011). Although ERG was always identified as an oncogene in leukemogenesis (Martens, 2011), a study by Mandoli et al. showed that ERG inhibits oncogene expression to protect leukemia cells from apoptosis (Mandoli et al., 2016). Our results indicated that overexpression of ERG in MA-WT cells inhibited cell growth and reduced *in vivo* leukemogenesis. In contrast, downregulation of ERG in MA-KO cells promoted cell growth and enhanced *in vivo* leukemogenesis, suggesting that ERG functions might depend on the expression level of ERG and leukemic type.

Our findings showed that FGFR3 deletion programs leukemia cells (non-LSCs) into CD117$^+$ leukemia stem-like cells. It could be a novel regulatory mechanism involving the origin and maintenance of MA-driven LSCs. However, CD117$^+$ FGFR3-deficient leukemia cells are not real LSCs because of a defect of FGFR3 downstream signaling and gene expression. Our results indicated that FGFR3 deletion significantly decreased the expression of chemokines and chemokines receptors, suggesting that these genes might be regulated directly by FGFR3 like those in a previous report (Masih-Khan et al., 2006). Further studies showed that the extended survival time of MA-KO cell-transplanted mice could be neutralized by overexpression of CCL3. However, the survival time of MA-WT cell-transplanted mice had no significant difference compared with that of control. One possible reason is that the concentration of CCL3 had attained the threshold because MA-WT cells themselves secret abundant chemokines to bind CCRs on the cell membrane of hematopoietic cells in BM.

In summary, our studies showed that FGFR3 negatively regulates the generation of CD117$^+$ leukemia stem-like cells by activating FGFR1-ERG-CD117 signaling. FGFR3-deficient leukemia cells are weakly pathogenic because of downregulation of chemokines genes. Inhibition of FGFR3 will be a promising approach for clinical leukemia therapy.

DATA AVAILABILITY STATEMENT

The datasets presented in this study can be found in online repositories. The name of the repository and accession numbers can be found below: National Center for Biotechnology Information (NCBI) Sequence Read Archive (SRA), https://

www.ncbi.nlm.nih.gov/sra/, SRR13234569, SRR13234570, SRR13234571, SRR13234572, SRR13234573, and SRR13234574.

ETHICS STATEMENT

Animal experiments were approved by the Animal Experiment Ethics Committee of the Basic Medical College of Jilin University.

AUTHOR CONTRIBUTIONS

CG, QR, and CS performed experiments and analyzed figures. TZ performed partial experiments. XY, JZ, and SP provided materials and revised the manuscript. YX conceived the project, supervised experiments, analyzed data, and wrote the manuscript. All authors read and approved the final manuscript.

FUNDING

This work was supported by National Natural Science Foundation of China (81370640 and 81570149) and funding from Jilin Provincial Science and Technology Department (20180201030YY).

SUPPLEMENTARY MATERIAL

The Supplementary Material for this article can be found online at: https://www.frontiersin.org/articles/10.3389/fphar.2020.632809/full#supplementary-material.

REFERENCES

Baba, T., Naka, K., Morishita, S., Komatsu, N., Hirao, A., and Mukaida, N. (2013). MIP-1α/CCL3-mediated maintenance of leukemia-initiating cells in the initiation process of chronic myeloid leukemia. *J. Exp. Med.* 210 (12), 2661–2673. doi:10.1084/jem.20130112

Baba, T., Tanabe, Y., Yoshikawa, S., Yamanishi, Y., Morishita, S., Komatsu, N., et al. (2016). MIP-1α/CCL3-expressing basophil-lineage cells drive the leukemic hematopoiesis of chronic myeloid leukemia in mice. *Blood* 127 (21), 2607–2617. doi:10.1182/blood-2015-10-673087

Batta, K., Florkowska, M., Kouskoff, V., and Lacaud, G. (2014). Direct reprogramming of murine fibroblasts to hematopoietic progenitor cells. *Cell Rep.* 9 (5), 1871–1884. doi:10.1016/j.celrep.2014.11.002

de Haan, G., Weersing, E., Dontje, B., van Os, R., Bystrykh, L. V., Vellenga, E., et al. (2003). *In vitro* generation of long-term repopulating hematopoietic stem cells by fibroblast growth factor-1. *Dev. Cell* 4 (2), 241–251. doi:10.1016/s1534-5807(03)00018-2

Deng, C., Wynshaw-Boris, A., Zhou, F., Kuo, A., and Leder, P. (1996). Fibroblast growth factor receptor 3 is a negative regulator of bone growth. *Cell* 84 (6), 911–921. doi:10.1016/s0092-8674(00)81069-7

Dvorak, P., Dvorakova, D., Doubek, M., Faitova, J., Pacholikova, J., Hampl, A., et al. (2003). Increased expression of fibroblast growth factor receptor 3 in cd34+ bcr-abl+ cells from patients with chronic myeloid leukemia. *Leukemia* 17 (12), 2418–2425. doi:10.1038/sj.leu.2403152

Dvorak, P., and Hampl, A. (2005). Basic fibroblast growth factor and its receptors in human embryonic stem cells. *Folia Histochem. Cytobiol.* 43 (4), 203–208.

Fernandez, S., Desplat, V., Villacreces, A., Guitart, A. V., Milpied, N., Pigneux, A., et al. (2019). Targeting tyrosine kinases in acute myeloid leukemia: why, who and how? *Int. J. Mol. Sci.* 20 (14), 3429. doi:10.3390/ijms20143429

Ferrara, F., and Schiffer, C. A. (2013). Acute myeloid leukaemia in adults. *Lancet* 381 (9865), 484–495. doi:10.1016/S0140-6736(12)61727-9

Huang, Y., Thoms, J. A., Tursky, M. L., Knezevic, K., Beck, D., Chandrakanthan, V., et al. (2016). Mapk/erk2 phosphorylates erg at serine 283 in leukemic cells and promotes stem cell signatures and cell proliferation. *Leukemia* 30 (7), 1552–1561. doi:10.1038/leu.2016.55

Iyer, G., and Milowsky, M. I. (2013). Fibroblast growth factor receptor-3 in urothelial tumorigenesis. *Urol. Oncol.* 31 (3), 303–311. doi:10.1016/j.urolonc.2011.12.001

Javidi-Sharifi, N., Traer, E., Martinez, J., Gupta, A., Taguchi, T., Dunlap, J., et al. (2015). Crosstalk between kit and fgfr3 promotes gastrointestinal stromal tumor cell growth and drug resistance. *Cancer Res.* 75 (5), 880–891. doi:10.1158/0008-5472.CAN-14-0573

Jiang, Y., Liu, F., Zou, F., Zhang, Y., Wang, B., Zhang, Y., et al. (2019). Pbx homeobox 1 enhances hair follicle mesenchymal stem cell proliferation and reprogramming through activation of the akt/glycogen synthase kinase signaling pathway and suppression of apoptosis. *Stem Cell Res. Ther.* 10 (1), 268. doi:10.1186/s13287-019-1382-y

Jiao, H. L., Ye, Y. P., Yang, R. W., Sun, H. Y., Wang, S. Y., Wang, Y. X., et al. (2017). Downregulation of safe sustains the nf-kappab pathway by targeting tak1 during the progression of colorectal cancer. *Clin. Canc. Res.* 23 (22), 7108–7118. doi:10.1158/1078-0432.CCR-17-0747

Karajannis, M. A., Vincent, L., Direnzo, R., Shmelkov, S. V., Zhang, F., Feldman, E. J., et al. (2006). Activation of fgfr1beta signaling pathway promotes survival, migration and resistance to chemotherapy in acute myeloid leukemia cells. *Leukemia* 20 (6), 979–986. doi:10.1038/sj.leu.2404203

Katoh, M., and Nakagama, H. (2014). Fgf receptors: cancer biology and therapeutics. *Med. Res. Rev.* 34 (2), 280–300. doi:10.1002/med.21288

L'Hôte, C. G., and Knowles, M. A. (2005). Cell responses to fgfr3 signalling: growth, differentiation and apoptosis. *Exp. Cell Res.* 304 (2), 417–431. doi:10.1016/j.yexcr.2004.11.012

Lee, H., Kim, M., Lim, J., Kim, Y., Han, K., Cho, B. S., et al. (2013). Acute myeloid leukemia associated with fgfr1 abnormalities. *Int. J. Hematol.* 97 (6), 808–812. doi:10.1007/s12185-013-1337-5

Li, T., Hu, J., Gao, F., Du, X., Chen, Y., and Wu, Q. (2017). Transcription factors regulate gpr91-mediated expression of vegf in hypoxia-induced retinopathy. *Sci. Rep.* 7, 45807. doi:10.1038/srep45807

Liu, X., Jing, X., Cheng, X., Ma, D., Jin, Z., Yang, W., et al. (2016). Fgfr3 promotes angiogenesis-dependent metastasis of hepatocellular carcinoma via facilitating mcp-1-mediated vascular formation. *Med. Oncol.* 33 (5), 46. doi:10.1007/s12032-016-0761-9

Maeda, T., Yagasaki, F., Ishikawa, M., Takahashi, N., and Bessho, M. (2005). Transforming property of tel-fgfr3 mediated through pi3-k in a t-cell lymphoma that subsequently progressed to aml. *Blood* 105 (5), 2115–2123. doi:10.1182/blood-2003-12-4290

Magnusson, P. U., Ronca, R., Dell'Era, P., Carlstedt, P., Jakobsson, L., Partanen, J., et al. (2005). Fibroblast growth factor receptor-1 expression is required for hematopoietic but not endothelial cell development. *Arterioscler. Thromb. Vasc. Biol.* 25 (5), 944–949. doi:10.1161/01.ATV.0000163182.73190.f9

Mandoli, A., Singh, A. A., Prange, K. H. M., Tijchon, E., Oerlemans, M., Dirks, R., et al. (2016). The hematopoietic transcription factors runx1 and erg prevent aml1-eto oncogene overexpression and onset of the apoptosis program in t(8;21) amls. *Cell Rep.* 17 (8), 2087–2100. doi:10.1016/j.celrep.2016.08.082

Martens, J. H. (2011). Acute myeloid leukemia: a central role for the ets factor erg. *Int. J. Biochem. Cell Biol.* 43 (10), 1413–1416. doi:10.1016/j.biocel.2011.05.014

Masih-Khan, E., Trudel, S., Heise, C., Li, Z., Paterson, J., Nadeem, V., et al. (2006). Mip-1alpha (ccl3) is a downstream target of fgfr3 and ras-mapk signaling in multiple myeloma. *Blood* 108 (10), 3465–3471. doi:10.1182/blood-2006-04-017087

Metzger, D. E., Xu, Y., and Shannon, J. M. (2007). Elf5 is an epithelium-specific, fibroblast growth factor-sensitive transcription factor in the embryonic lung. *Dev. Dynam.* 236 (5), 1175–1192. doi:10.1002/dvdy.21133

Peng, C., Chen, Y., Yang, Z., Zhang, H., Osterby, L., Rosmarin, A. G., et al. (2010). Pten is a tumor suppressor in cml stem cells and bcr-abl-induced leukemias in mice. *Blood* 115 (3), 626–635. doi:10.1182/blood-2009-06-228130

Petiot, A., Ferretti, P., Copp, A. J., and Chan, C. T. (2002). Induction of chondrogenesis in neural crest cells by mutant fibroblast growth factor receptors. *Dev. Dynam.* 224 (2), 210–221. doi:10.1002/dvdy.10102

Ran, Q., Guo, C., Sun, C., Liu, Q., He, H., Zhao, W., et al. (2020). Loss of fgfr3 accelerates bone marrow suppression-induced hematopoietic stem and progenitor cell expansion by activating fgfr1-elk1-cyclin d1 signaling. *Biol. Blood Marrow Transplant.* S1083-8791 (20) 30571-1. doi:10.1016/j.bbmt.2020.09.019

Shah, A. V., Birdsey, G. M., Peghaire, C., Pitulescu, M. E., Dufton, N. P., Yang, Y., et al. (2017). The endothelial transcription factor erg mediates angiopoietin-1-dependent control of notch signalling and vascular stability. *Nat. Commun.* 8, 16002. doi:10.1038/ncomms16002

Siveen, K. S., Uddin, S., and Mohammad, R. M. (2017). Targeting acute myeloid leukemia stem cell signaling by natural products. *Mol. Canc.* 16 (1), 13. doi:10.1186/s12943-016-0571-x

Sugimura, R., Jha, D. K., Han, A., Soria-Valles, C., da Rocha, E. L., Lu, Y. F., et al. (2017). Haematopoietic stem and progenitor cells from human pluripotent stem cells. *Nature* 545 (7655), 432–438. doi:10.1038/nature22370

Sun, C., Dobi, A., Mohamed, A., Li, H., Thangapazham, R. L., Furusato, B., et al. (2008). Tmprss2-erg fusion, a common genomic alteration in prostate cancer activates c-myc and abrogates prostate epithelial differentiation. *Oncogene* 27 (40), 5348–5353. doi:10.1038/onc.2008.183

Traer, E., Javidi-Sharifi, N., Agarwal, A., Dunlap, J., English, I., Martinez, J., et al. (2014). Ponatinib overcomes fgf2-mediated resistance in cml patients without kinase domain mutations. *Blood* 123 (10), 1516–1524. doi:10.1182/blood-2013-07-518381

Tsuzuki, S., Taguchi, O., and Seto, M. (2011). Promotion and maintenance of leukemia by erg. *Blood* 117 (14), 3858–3868. doi:10.1182/blood-2010-11-320515

Wang, Q. Y., Zhao, Y., and Zhang, R. (2015). The role of mutations and overexpression of the fibroblast growth factor receptor-3 in bladder cancer. *Minerva Med.* 106 (6), 333–337.

Wang, Y., Gao, A., Zhao, H., Lu, P., Cheng, H., Dong, F., et al. (2016). Leukemia cell infiltration causes defective erythropoiesis partially through MIP-1α/CCL3. *Leukemia* 30 (9), 1897–1908. doi:10.1038/leu.2016.81

Wesche, J., Haglund, K., and Haugsten, E. M. (2011). Fibroblast growth factors and their receptors in cancer. *Biochem. J.* 437 (2), 199–213. doi:10.1042/BJ20101603

Xiao, Y., Li, H., Zhang, J., Volk, A., Zhang, S., Wei, W., et al. (2011). TNF-α/Fas-RIP-1-induced cell death signaling separates murine hematopoietic stem cells/progenitors into 2 distinct populations. *Blood* 118 (23), 6057–6067. doi:10.1182/blood-2011-06-359448

Yao, S., Zhou, R., Jin, Y., Huang, J., and Wu, C. (2019). Effect of co-culture with tetragenococcus halophilus on the physiological characterization and transcription profiling of zygosaccharomyces rouxii. *Food Res. Int.* 121, 348–358. doi:10.1016/j.foodres.2019.03.053

Zhao, M., Ross, J. T., Itkin, T., Perry, J. M., Venkatraman, A., Haug, J. S., et al. (2012). Fgf signaling facilitates postinjury recovery of mouse hematopoietic system. *Blood* 120 (9), 1831–1842. doi:10.1182/blood-2011-11-393991

Conflict of Interest: The authors declare that the research was conducted in the absence of any commercial or financial relationships that could be construed as a potential conflict of interest.

frontiers in Cell and Developmental Biology

ORIGINAL RESEARCH
published: 04 March 2021
doi: 10.3389/fcell.2021.648201

Cartilage Endplate Stem Cells Transdifferentiate Into Nucleus Pulposus Cells via Autocrine Exosomes

Liwen Luo[1,2†], Junfeng Gong[1†], Hongyu Zhang[3], Jinghao Qin[1], Changqing Li[1], Junfeng Zhang[4], Yu Tang[1], Yang Zhang[1], Jian Chen[2], Yue Zhou[1], Zhiqiang Tian[2,5*], Yao Liu[6*] and MingHan Liu[1*]*

[1] Department of Orthopaedics, Xinqiao Hospital, Army Medical University, Third Military Medical University, Chongqing, China, [2] Institute of Immunology, PLA, Army Medical University, Third Military Medical University, Chongqing, China, [3] Department of Emergency, Second Affiliated Hospital of Chongqing Medical University, Chongqing, China, [4] Institute of Hepatopancreatobiliary Surgery, Chongqing General Hospital, University of Chinese Academy of Sciences, Chongqing, China, [5] State Key Laboratory of Silkworm Genome Biology, Biological Science Research Center, Southwest University, Chongqing, China, [6] Department of Pharmacy, Daping Hospital, Army Medical University, Third Military Medical University, Chongqing, China

OPEN ACCESS

Edited by:
Zhouguang Wang,
Albert Einstein College of Medicine,
United States

Reviewed by:
Xiang Cui,
First Affiliated Hospital of the General Hospital of PLA, China
Guangzhi Ning,
Tianjin Medical University General Hospital, China

***Correspondence:**
MingHan Liu
liuminghan2008@hotmail.com
Yue Zhou
happyzhou@vip.163.com
Zhiqiang Tian
tzhiq009@163.com
Yao Liu
swhliuyao@163.com

[†] These authors have contributed equally to this work

Specialty section:
This article was submitted to Stem Cell Research, a section of the journal Frontiers in Cell and Developmental Biology

Received: 31 December 2020
Accepted: 16 February 2021
Published: 04 March 2021

Citation:
Luo L, Gong J, Zhang H, Qin J, Li C, Zhang J, Tang Y, Zhang Y, Chen J, Zhou Y, Tian Z, Liu Y and Liu M (2021) Cartilage Endplate Stem Cells Transdifferentiate Into Nucleus Pulposus Cells via Autocrine Exosomes. Front. Cell Dev. Biol. 9:648201. doi: 10.3389/fcell.2021.648201

Stem cells derived from cartilage endplate (CEP) cells (CESCs) repair intervertebral disc (IVD) injury; however, the mechanism remains unclear. Here, we evaluated whether CESCs could transdifferentiate into nucleus pulposus cells (NPCs) via autocrine exosomes and subsequently inhibit IVD degeneration. Exosomes derived from CESCs (CESC-Exos) were extracted and identified by ultra-high-speed centrifugation and transmission electron microscopy. The effects of exosomes on the invasion, migration, and differentiation of CESCs were assessed. The exosome-activating hypoxia-inducible factor (HIF)-1α/Wnt pathway was investigated using lenti-HIF-1α and Wnt agonists/inhibitors in cells and gene ontology and Kyoto Encyclopedia of Genes and Genomes enrichment analysis in normal and degenerated human CEP tissue. The effects of GATA binding protein 4 (GATA4) on transforming growth factor (TGF)-β expression and on the invasion, migration, and transdifferentiation of CESCs were investigated using lenti-GATA4, TGF-β agonists, and inhibitors. Additionally, IVD repair was investigated by injecting CESCs overexpressing GATA4 into rats. The results indicated that CESC-Exos promoted the invasion, migration, and differentiation of CESCs by autocrine exosomes via the HIF-1α/Wnt pathway. Additionally, increased HIF-1α enhanced the activation of Wnt signaling and activated GATA4 expression. GATA4 effectively promoted TGF-β secretion and enhanced the invasion, migration, and transdifferentiation of CESCs into NPCs, resulting in promotion of rat IVD repair. CESCs were also converted into NPCs as endplate degeneration progressed in human samples. Overall, we found that CESC-Exos activated HIF-1α/Wnt signaling via autocrine mechanisms to increase the expression of GATA4 and TGF-β1, thereby promoting the migration of CESCs into the IVD and the transformation of CESCs into NPCs and inhibiting IVDD.

Keywords: cartilage endplate stem cells, differentiation, exosome, GATA binding protein 4, transforming growth factor-β1, intervertebral disk degeneration

INTRODUCTION

Low back pain (LBP) is a pathology that can cause disability, leading to increased social burden among the expanding and aging population (GBD 2016 Disease and Injury Incidence and Prevalence Collaborators, 2017), and intervertebral disc (IVD) degeneration (IVDD) is the most common cause of LBP (Freemont, 2009; Schol and Sakai, 2019). IVDD is an age-related disease associated with multiple factors (Stokes and Iatridis, 2004; Risbud and Shapiro, 2014; Vo et al., 2016) and characterized by the degradation of extracellular matrix components, such as collagens, proteoglycans, and fibronectin/laminins, as well as upregulation of matrix-degrading enzymes (Le Maitre et al., 2004; Roughley, 2004). Nucleus pulposus (NP) and annulus fibrosus (AF) are the main structural elements of IVDs. NP cells (NPCs) secrete extracellular matrix components to maintain the biomechanical functions of the IVD, and hypocellularity of functional NP cells leads to IVDD (Vo et al., 2016). Thus, regenerating NPCs could be a potential therapeutic strategy for IVDD (Li et al., 2017; Zhang et al., 2020). In clinical trials, autologous or allogeneic mesenchymal stem cell (MSC) transplantation has been performed in IVD repair and LBP release (Orozco et al., 2011; Noriega et al., 2017). In our previous study, we identified cartilage endplate (CEP) stem cells (CESCs) in the CEP (Liu et al., 2011). These CESCs were found to be similar to MSCs in terms of stem cell characteristics; however, they showed better capacity in osteogenesis and chondrogenesis. Additionally, CESCs with the characteristics of stem cells in CEP tissues have been shown to migrate to the NP and differentiate into NPCs, thereby promoting the repair of the IVD and inhibiting IVDD (Wang et al., 2014). However, the specific mechanisms remain unclear.

Exosomes are extracellular vesicles of endosomal origin that are secreted by prokaryotes and eukaryotes (Kalluri and Lebleu, 2020) and exhibit a diameter of 40–160 nm (Kourembanas, 2015). These vesicles are present in a variety of body fluids, including plasma, semen, saliva, urine, amniotic fluid, synovial fluid, and breast milk (Simpson et al., 2008; Properzi et al., 2013). Exosomes have been shown to encapsulate many different components, including mRNAs, microRNAs, ribosomal RNAs, non-coding RNAs, cytokines, proteins, and lipids (Simons and Raposo, 2009). Additionally, exosomes play important roles in altering signaling transduction related to proliferation, differentiation, autophagy, and other cellular activities (Barile and Vassalli, 2017; Chang et al., 2018). Notably, MSC-derived exosomes can ameliorate IVDD via various mechanisms after injection into the IVD (Liao et al., 2019; Xia et al., 2019). Moreover, previous studies have shown that CESCs can inhibit the apoptosis of NPCs by secreting exosomes and thus slow down or reverse the IVDD process (Luo et al., 2021). However, we do not know whether the migration and differentiation of CESCs into NPCs can be regulated by CESC-Exos in an autocrine manner, thereby slowing down IVDD; this mechanism could provide an innovative approach to the treatment of IVDD by regulating CESC migration and differentiation.

GATA-binding protein 4 (GATA4), a DNA-binding zinc finger transcription factor, has been shown to regulate various biological processes, including proliferation, differentiation, and angiogenesis (Molkentin, 2000; Patient and Mcghee, 2002). During bone formation and development, GATA4 plays important roles in promoting osteogenic differentiation and function by regulating Runt-related transcription factor 2, bone morphogenic protein, transforming growth factor (TGF)-β, Fas ligand, and other key proteins (Miranda-Carboni et al., 2011; Güemes et al., 2014; Khalid et al., 2018). Recent studies have shown that GATA4, a key transcription factor, regulates MSC differentiation (Li et al., 2015; Xu et al., 2016). However, to date, no researchers have evaluated the roles of GATA4 in the migration and differentiation of CESCs into NPCs.

Accordingly, in this study, we assessed whether autocrine exosomes could promote CESC migration and transdifferentiation into NPCs by activating the hypoxia-inducible factor (HIF)-1α/Wnt pathway and increasing GATA4/TGF-β expression, thereby blocking IVDD. Our findings provide important insights into the mechanisms through which CESCs ameliorate IVDD and the application of CESCs as a therapy for IVDD.

MATERIALS AND METHODS

Reagents and Antibodies

The Wnt pathway inhibitors MSAB and Wnt agonist 1, the TGF-β agonist SRI-011381, and the TGF-β1 inhibitor pirfenidone (PFD) were obtained from Selleck (Shanghai, China). Antibodies against collagen I, CD9, and CD63 were obtained from Beyotime (Shanghai, China). Antibodies against glyceraldehyde 3-phosphate dehydrogenase (GAPDH), collagen II, GATA4, aggrecan (Acan), tumor susceptibility gene 101 (TSG101), and TGF-β1 were purchased from Proteintech (Wuhan, China). Collagenase II was purchased from Sangon Biotech (Shanghai, China). Antibodies against a disintegrin and metalloproteinase with thrombospondin motifs 5 (ADAMTS5), sirtuin 9 (SOX9), transcription factor 4, and β-catenin were purchased from Bioss (Beijing, China). Antibodies against HIF-1α were obtained from Santa Cruz Biotechnology (Dallas, TX, United States). PKH26 was obtained from Sigma (St. Louis, MO, United States). MSC osteogenic differentiation medium, chondrogenic differentiation medium, and adipogenic differentiation medium were provided by Cyagen (Guangzhou, China).

Isolation and Identification of CESCs

Cartilage endplate stem cells were isolated from CEPs of 4-week-old male Sprague-Dawley rats. We cleaned and washed CEPs with 0.1 M sterile phosphate-buffered saline (PBS). Then, the CEP tissues were mechanically sliced into pieces and digested with 0.2% type II collagenase for 3 h at 37°C. The suspension was filtered, washed in PBS, and centrifuged at 1,000 rpm for 5 min. Finally, cells were cultured in Dulbecco's modified Eagle medium (DMEM; cat. no. SH30023.01; HyClone) containing 10% fetal bovine serum (cat. no. A6903FBS-500; Invitrogen, Carlsbad, CA, United States) and 1% penicillin-streptomycin at 5% CO_2 and 37°C. The culture medium was replaced twice a week, and CESCs from passage 2 or 3 were used in our experiments.

To induce CESC chondrogenic differentiation, the cells were cultured in 6-well plates in chondrogenic differentiation medium (cat. no. MUCMX-9004; Cyagen Biosciences, Guangzhou, China) for up to 21 days. The culture medium was changed every 3 days. For inducing CESC osteogenic differentiation, the CESCs were cultured in 6-well plates in osteogenic differentiation medium (cat. no. MUBMX-90021; Cyagen Biosciences) for up to 21 days, with replacement of the culture medium every 3 days. To induce CESC adipogenic differentiation, CESCs were cultured in 6-well plates in adipogenic differentiation medium for up to 21 days with changes in the culture medium to medium A or medium B (cat. no. MUBMX-90031; Cyagen Biosciences) for 3 days. After culturing in elective induction medium according to the above protocols, Alcian blue, Alizarin red, and Oil red O staining were performed to confirm the differentiation of each type. To detect cell surface markers, a flow cytometer (BD Biosciences, CA, United States) was used to identify CESCs by positive expression of CD90 and CD44 and negative expression of CD45 according to the manufacturer's instructions.

Exosome Extraction

Exosomes were extracted by differential ultracentrifugation as previously described (Théry et al., 2006). CESCs were cultured in serum-free DMEM (cat. no. SH30023.01; HyClone) for 2 days at 37°C in 5% CO_2. The culture supernatants were collected and centrifuged at 300 × *g* for 10 min, 2000 × *g* for 10 min, and 10,000 × *g* for 30 min to remove cells, dead cells, and cellular debris. The supernatant was transferred to clean tubes and centrifuged at 100,000 × *g* for 70 min at 4°C. The supernatant was then removed completely, and the pellet was resuspended in PBS. Next, the sample was filtered through a 0.22-μm filter and centrifuged at 100,000 × *g* for 70 min at 4°C. After removing the supernatant as completely as possible, the exosomes were resuspended in 200 μL PBS.

Identification of Exosomes and Analysis of Exosome Internalization by CESCs

Exosome morphology was observed using transmission electron microscopy (TEM; Philips, Amsterdam, Netherlands), identified according to the expression of characteristic markers, including TSG101, CD63, and CD9, using western blotting. The purified CESC-exosomes (CESC-Exos) were incubated with PKH26 for 5 min at room temperature. Then, 5% bovine serum albumin (BSA) was added to stop the reaction, and exosomes labeled with membrane dyes were obtained. Next, the PKH26-labeled exosomes were resuspended in DMEM and incubated with CESCs at 37°C for 10 h. CESCs stained with 4-6-diamidino-2-phenylindole (DAPI) were placed under a fluorescence microscope (Olympus, Tokyo, Japan) for observation.

Wound Scratch Assay and Transwell Migration Assay

For wound scratch assays, CESCs treated with different concentrations of exosomes were seeded onto 6-well plates. After the cells reached 80–90% confluence, a pipette tip was used to inflict a wound. The cells were then washed with PBS to remove debris and floating cells. The wound areas were photographed at 0 and 48 h after scratching using a microscope. For transwell migration assays, transwell chambers were placed in 24-well plates, and treated cell suspensions were then seeded onto the interior chambers. The chambers were removed 24 h after seeding, and cells that had migrated through the membranes were enumerated using a microscope.

Lentiviral Transfection

Lentivirus overexpressing HIF-1α was purchased from GENECHEM (Shanghai, China), and lentivirus overexpressing GATA4 was purchased from Taitool Bioscience (Shanghai, China). CESCs were seeded into 6-well plates at a density of 1.0×10^5 cells/well, and the next day, cells were infected with the lentivirus (multiplicity of infection: 40) in culture medium containing 6 μg/mL polybrene. The medium was replaced with normal medium 24 h after transfection. We used fluorescence microscopy (Olympus, Tokyo, Japan) to measure the efficiency of transfection 3 days later. Western blotting and polymerase chain reaction (PCR) were also performed to analyze the expression of HIF-1α and GATA4 in transfected cells.

Quantitative PCR Analysis

Total RNA was isolated with TRIzol reagent according to the manufacturer's protocol (Aioub et al., 2007). cDNA was synthesized from RNA using an RT reagent kit (Takara, Japan). Then, Quantitative PCR (qPCR) was performed in triplicate to analyze gene expression levels using a Bio-Rad CFX96 qPCR machine (Bio-Rad Laboratories, Hercules, CA, United States) with β-*actin* as a normalization control. The primer sequences are listed in **Table 1**.

Western Blotting

Cells were harvested, and proteins were extracted using RIPA lysis buffer containing the protease inhibitor phenylmethylsulfonyl fluoride. Protein concentrations were measured using a spectrophotometer (Beckman, Fullerton, CA, United States). Equivalent amounts of protein were separated by sodium dodecyl sulfate polyacrylamide gel electrophoresis and transferred to polyvinylidene fluoride membranes by electroblotting. The membranes were blocked in 5% (w/v) skimmed milk for 1 h at room temperature. After blocking, the membranes were incubated with appropriate primary antibodies overnight at 4°C. Subsequently, the membranes were washed three times with PBS and incubated with the corresponding horseradish peroxidase-conjugated secondary antibodies at room temperature for 1 h. Then, the ECL working solution (Millipore, MO, United States) was added to the membranes. Finally, proteins were visualized and detected using a chemiluminescence system (Bio-Rad Laboratories).

Immunofluorescence

Cartilage endplate stem cells were fixed with 4% paraformaldehyde for 20 min at room temperature and permeabilized using Triton X-100 solution. The cells were then blocked with goat serum for 40 min and incubated with

the appropriate primary antibodies overnight at 4°C. After washing three times with PBS, cells were incubated with the fluorescently labeled secondary antibody for 1 h and then stained with DAPI for 5 min at room temperature. Finally, a fluorescence microscope (Olympus, Tokyo, Japan) was used to capture images of stained CESCs.

Animal Experiments and Micro-Magnetic Resonance Imaging Analysis

All animal experiments were conducted with the approval of the Medical Ethics Committee of Army Medical University. Twenty 2-month-old Sprague-Dawley rats were obtained from the Model Animal Research Center of the Army Medical University and used for *in vivo* experiments. Rats were randomly divided into four groups: control group (n = 5), IVDD group (n = 5), IVDD + CESC group (n = 5), and IVDD + GATA4-overexpressing CESC group (n = 5). The IVDD model was established as described previously (Han et al., 2008). Briefly, after the rats (weighing approximately 250 g each) were anesthetized with 2 mL of 5% (w/v) chloral hydrate, the AF of the rats was punctured using a 21-G needle through the tail skin. The length of the needle into the IVD was approximately 5 mm. Then, we rotated the needles 360° and maintained the needle in the disk for 60 s. In the IVDD + CESC group and IVDD + GATA4-overexpressing CESC group, rats were subjected to intradiscal injection of a CESC suspension (20 μL, 10^5/mL) or GATA4-overexpressing CESC suspension (20 μL, 10^5/mL). 4 weeks after injection, Micro-magnetic resonance imaging (MRI) was performed using a 7.0-T animal magnet (Bruker Pharmascan, Germany) to evaluate the signal and structural changes of IVD. Rats were sacrificed after micro-MRI scanning, and the disk and CEP tissues were isolated for immunofluorescence analysis.

TABLE 1 | Primers used for qPCR in this study.

Gene	Primer sequence (5′ to 3′)
GATA4(homo)-F	CGACACCCCAATCTCGATATG
GATA4(homo)-R	GTTGCACAGATAGTGACCCGT
GATA4(rat)-F	AGGGGATTCAAACCAGAAAACG
GATA4(rat)-R	GCTGCTGTGCCCATAGTGAGAT
HIF1α-F	ACCTTCATCGGAAACTCCAAAG
HIF1α-R	CTGTTAGGCTGGGAAAAGTTAGG
SOX9(homo)-F	CTCTGGAGACTTCTGAACGA
SOX9(homo)-R	ACTTGTAATCCGGGTGGTC
SOX9(rat)-F	CATGAACGCCTTCATGGTG
SOX9(rat)-R	CTCTCGTTCAGCAGTCTCC
CCR1-F	CTCATGCAGCATAGGAGGCTT
CCR1-R	ACATGGCATCACCAAAAATCCA
CCR3-F	TCAACTTGGCAATTTCTGACCT
CCR3-R	CAGCATGGACGATAGCCAGG
CCR9-F	CTTCAGCTATGACTCCACTGC
CCR9-R	CAAGGTGCCCACAATGAACA
CXCR3-F	TACCTTGAGGTTAGTGAACGTCA
CXCR3-R	CGCTCTCGTTTTCCCCATAATC
CXCR6-F	GAGTCAGCTCTGTACGATGGG
CXCR6-R	TCCTTGAACTTTAGGAAGCGTTT
TGFbeta -F	CTAAGGCTCGCCAGTCCCC
TGFbeta -R	ATTGCGTTGTTGCGGTCCA
EGF-F	TCCAAACGCCGCAGACTTA
EGF-R	CCTCTTGTTCACCCTTATTACCG
FGF2-F	GCGACCCACACGTCAAACTA
FGF2-R	TCCCTTGATAGACACAACTCCTC
CSF1-F	ATGAGCAGGAGTATTGCCAAGG
CSF1-R	TCCATTCCCAATCATGTGGCTA
PDGFa-F	GAGGAAGCCGAGATACCCC
PDGFa-R	TGCTGTGGATCTGACTTCGAG
Actin-F	GGCTGTATTCCCCTCCATCG
Actin-R	CCAGTTGGTAACAATGCCATGT

Patient Tissues and Histologic Analysis

Cartilage endplate tissues were obtained from patients who underwent spinal fusion at Xinqiao Hospital of Army Medical University for qPCR, western blot, and immunohistochemical staining. This study was approved by the Medical Ethics Committee of Army Medical University, and all patients signed informed consent for tissue collection. Changes in the CEP on MRI were evaluated by two blinded orthopedic doctors using the Modic Classification of degenerative lumbar endplate (type I, II, III; (Modic et al., 1988)). The patient detail information was shown in **Table 2**. The tissues were fixed with 4% neutral-buffered formalin and decalcified with 10% ethylenediaminetetraacetic acid. The specimens were then dehydrated and embedded in paraffin for serial sectioning. For immunohistochemical analysis, the sections were autoclaved in 0.01 M citrate buffer at 110°C for 15 min to achieve antigen retrieval. Then, 3% H_2O_2 was used to block endogenous peroxidase activity for 10 min, and sections were treated with 5% BSA at 37°C for 30 min to block non-specific binding sites. The sections were incubated with primary antibodies overnight at 4°C. Finally, the sections were incubated with the corresponding horseradish peroxidase-conjugated secondary antibodies for 30 min at room temperature and visualized with 3,30-diaminobenzidine-tetrahydrochloride. For immunofluorescence analysis, the sections were incubated in 10% hydrogen peroxide/formaldehyde solution at room temperature for 30 min, permeabilized in 0.2% Triton for 5 min, blocked with 5% (w/v) BSA, and incubated with corresponding primary antibodies overnight at 4°C. Then, the sections were incubated with the corresponding fluorescent secondary antibodies and stained with DAPI (Beyotime).

TABLE 2 | Patient information in this study.

CEP tissue no.	Age, year	Gender	Modic classification
1	45	Female	I
2	52	Female	I
3	40	Male	I
4	55	Female	II
5	58	Male	II
6	43	Male	II
7	62	Male	III
8	49	Female	III
9	56	Female	III

Finally, the stained sections were observed using a fluorescence microscope (Olympus).

Statistical Analysis

Quantitative results are described as means ± standard deviations. Statistical data were analyzed by Student's *t* tests and one-way analysis of variance using GraphPad Prism 7.0 (GraphPad Software Inc., CA, United States). Results with *P* values less than 0.05 were considered statistically significant.

RESULTS

Exosomes Promoted the Migration, Invasion, and Transdifferentiation of CESCs Into NPCs via an Autocrine Mechanism

Cartilage endplate stem cells were isolated and purified from the CEP of rat tail vertebrae and showed a fibroblast-like morphology with a spindle-like appearance (**Supplementary Figure 1A**). Low-passage CESCs were induced to differentiate into osteocytes, chondrocytes, and adipocytes in special medium (**Supplementary Figure 1B**). Flow cytometry showed that stem cell-positive markers (CD90 and CD44) were detected in more than 80% of CESCs, whereas less than 3% of cells expressed the negative marker (CD45; **Supplementary Figure 1C**). CESC-Exos were collected and purified from CESC culture medium, and the morphology and protein markers of CESC-Exos were identified by TEM and western blotting, respectively. The morphology of CESC is shown in **Figure 1A**. Western blotting showed that CESC-Exos expressed higher levels of exosomal marker proteins (CD9, CD63, and TSG101) than CESCs (**Figure 1B**). These results suggested that CESCs could secrete exosomes, similar to other types of stem cells. Exosomes labeled with PKH26 were incubated with CESCs to examine the uptake of exosomes by CESCs. The immunofluorescence results showed that exosomes were dispersed throughout the cytoplasm of CESCs (**Figure 1C**), indicating that exosomes affected CESCs in an autocrine manner.

Exosomes derived from stem cells promote the differentiation of other cells and may have potential therapeutic applications in some diseases (Zhang et al., 2018; Biswas et al., 2019). To explore the effects of CESC-Exos on CESCs themselves, CESCs were treated with CESC-Exos (20 or 40 μg/mL) at 37°C for 24 h. As shown in **Figures 1D,E**, treated CESCs exhibited enhanced migratory ability, as demonstrated by increased cell penetration and quicker scratch closure. The qPCR results showed that the activation level of chemokines related to cell migration increased significantly after exosome treatment (**Figure 1F**). Taken together, autocrine exosomes increase the migration capacity of CESCs. Next, we examined whether CESC-Exos induced CESC differentiation into NPCs. Immunofluorescence showed that the levels of collagen II (an NPC marker protein) were increased following exosome treatment (**Figure 1G**). Collagen II, SOX9, collagen I, and Acan levels were then measured by western blotting. As expected, the expression of the NPC marker proteins collagen II and SOX9 increased, and that of the negative proteins collagen I and Acan decreased in the treatment group (**Figure 1H**). Additionally, we found that CESC-Exos could promote the proliferation of NPCs demonstrated by immunofluorescence analysis (**Supplementary Figure 2**).

CESC-Exos Facilitated CESC Invasion, Migration, and Differentiation by Activating HIF-1α

The expression level of HIF-1α in NPCs is higher than that in surrounding AF and chondrocytes (Rajpurohit et al., 2002; Risbud et al., 2006). In this study, the protein levels of HIF-1α in cells treated with CESC-Exos were higher than those in CESCs (**Figure 2A**). Therefore, the effects of HIF-1α in CESCs were tested using lentivirus to overexpress HIF-1α. HIF-1α mRNA and protein levels in the Lenti-HIF-1α group were increased (**Figure 2B**). As shown in **Figures 2C,D**, the migration and invasion capacities of CESCs were increased in the HIF-1α group compared with those in the Exo group (40 μg/mL), and these improvements in migration and invasion were even more apparent in the HIF-1α group cotreated with CESCs-Exos (40 μg/mL). Consequently, these data showed that CESC-Exos promoted CESC invasion and migration by increasing HIF-1α expression. Moreover, collagen II increased and collagen I decreased in the HIF-1α group, as demonstrated by immunofluorescence analysis (**Figure 2E**). Furthermore, treatment of the HIF-1α group with CESC-Exos (40 μg/mL), resulted in a greater increase in collagen II. Compared with exosome treatment, protein expression levels of collagen II and SOX9 increased in HIF-1α-overexpressing cells, whereas the protein expression of collagen I and ADAMTS5 decreased (**Figure 2F**). These results revealed that CESC-Exos facilitated CESC differentiation by activating HIF-1α signaling.

HIF-1α Promoted CESC Differentiation Into NPCs by Activating the Wnt/GATA4 Pathway

Hypoxia-inducible factor-1α has been shown to be correlated with the Wnt signaling pathway (Chen et al., 2018; Vallée et al., 2018; Boso et al., 2019), an important pathway modulated by hypoxia (Mazumdar et al., 2010). The GATA4 transcription factor plays key roles in Wnt signaling-regulated processes (Watt et al., 2004; Holtzinger and Evans, 2005), such as differentiation, growth, and survival (Molkentin, 2000; Patient and Mcghee, 2002), in various cell types. In this study, Kyoto Encyclopedia of Genes and Genomes (KEGG) enrichment analyses showed that Wnt signaling was related to CEP degeneration (**Figure 3A**). Moreover, western blotting showed that the expression of GATA4 increased in the Lenti-HIF-1α group and decreased in the Lenti-HIF-1α + MSAB group (**Figure 3B**). When CESCs were treated with different concentrations of Wnt agonist 1 (0, 10, or 20 μg/ml), the protein expression levels of β-catenin, TCF-4, SOX9, and GATA4 gradually increased (**Figure 3C**). Additionally, the protein levels of GATA4 and SOX9 in cells treated with Wnt agonist 1 increased, as demonstrated using immunofluorescence analysis (**Figure 3D**). These results show that increased HIF-1α enhanced the activation of Wnt

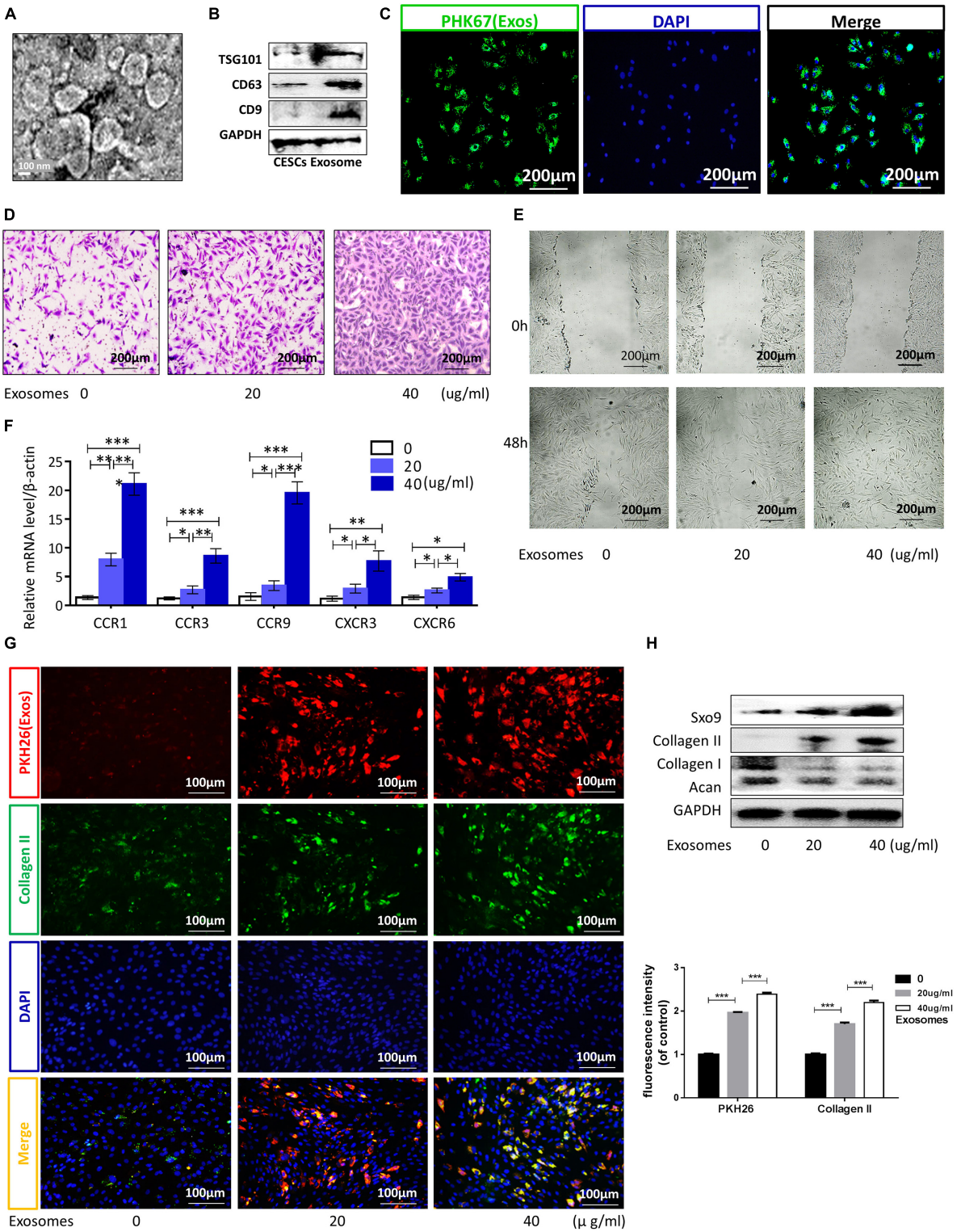

FIGURE 1 | Exosomes promoted CESC migration, invasion, and differentiation into nucleus pulposus cells via autocrine signaling. **(A,B)** TEM images and western blot analyses for identification of exosomes. **(C)** Immunofluorescence of exosomes (green) in CESCs. **(D,E)** Migration and invasion of CESCs treated with 0, 20, or 40 μg/mL exosomes. **(F)** Expression levels of chemokines related to cell migration and invasion in CESCs treated with 0, 20, or 40 μg/mL exosomes. **(G)** Double immunofluorescence of exosomes (red) and collagen II in CESCs. **(H)** Representative western blots and quantification of data for SOX9, collagen II, collagen I, and Acan in CESCs treated with 0, 20, or 40 μg/mL exosomes. All data represent means ± standard deviations. $P < 0.05$ was considered statistically significant. ns: $P > 0.05$; $^{*}P < 0.05$; $^{**}P < 0.01$; and $^{***}P < 0.001$.

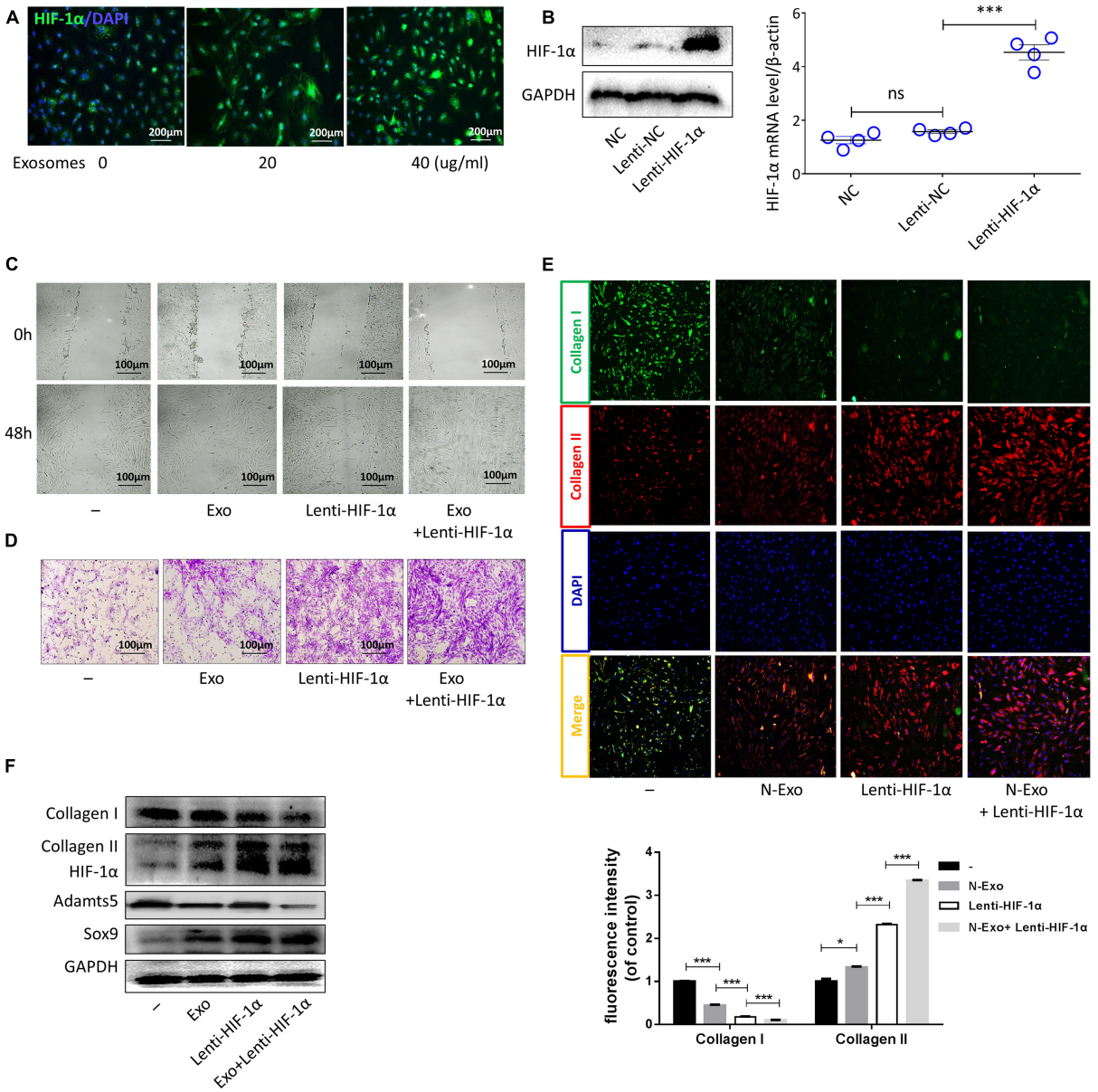

FIGURE 2 | Exosomes promoted CESC invasion, migration, and differentiation by increasing HIF-1α expression. **(A)** HIF-1α expression in CESCs treated with 0, 20, or 40 μg/mL exosomes. **(B)** Representative western blots of HIF-1α and RT-qPCR assays in CESCs treated with NC, Lenti-NC, or Lenti-HIF-1α. **(C,D)** Migration and invasion in CESCs treated with NC, exosomes (40 μg/mL), Lenti-HIF-1α, Lenti-HIF-1α + exosomes (40 μg/mL). **(E)** Double immunofluorescence of collagen I (green) and collagen II (red) in CESCs treated with NC, exosomes (40 μg/mL), Lenti-HIF-1α, or Lenti-HIF-1α + exosomes (40 μg/mL). **(F)** Western blots of collagen I, collagen II, HIF-1α, ADAMTS5, and SOX9 in CESCs treated as described above. All data represent means ± standard deviations. $P < 0.05$ is considered statistically significant. NC: normal control; ns: $P > 0.05$; $^{*}P < 0.05$ and $^{***}P < 0.001$.

signaling, thereby stimulating GATA4 expression to promote CESC differentiation.

GATA4 Promoted CESC Activation in a TGF-β1-Dependent Manner

Gene ontology (GO) and protein correlation analyses were performed to investigate the mechanisms underlying the roles of GATA4 in CESC invasion, migration, and differentiation. GO analysis showed that the Wnt signaling pathway and TGF-β were related to the process of CEP differentiation and degeneration (**Figure 4A**). As shown in **Figure 4B**, the protein expression levels of TGF-β1, COL2A, SOX9, and epidermal growth factor (EGF) were closely related to GATA4, as demonstrated using correlation analysis of important proteins. Therefore, we hypothesized that GATA4 may promote CESC activation via the TGF-β1 signaling pathway. To confirm this hypothesis, CESCs were infected with lentiviruses to overexpress GATA4. After transfection,

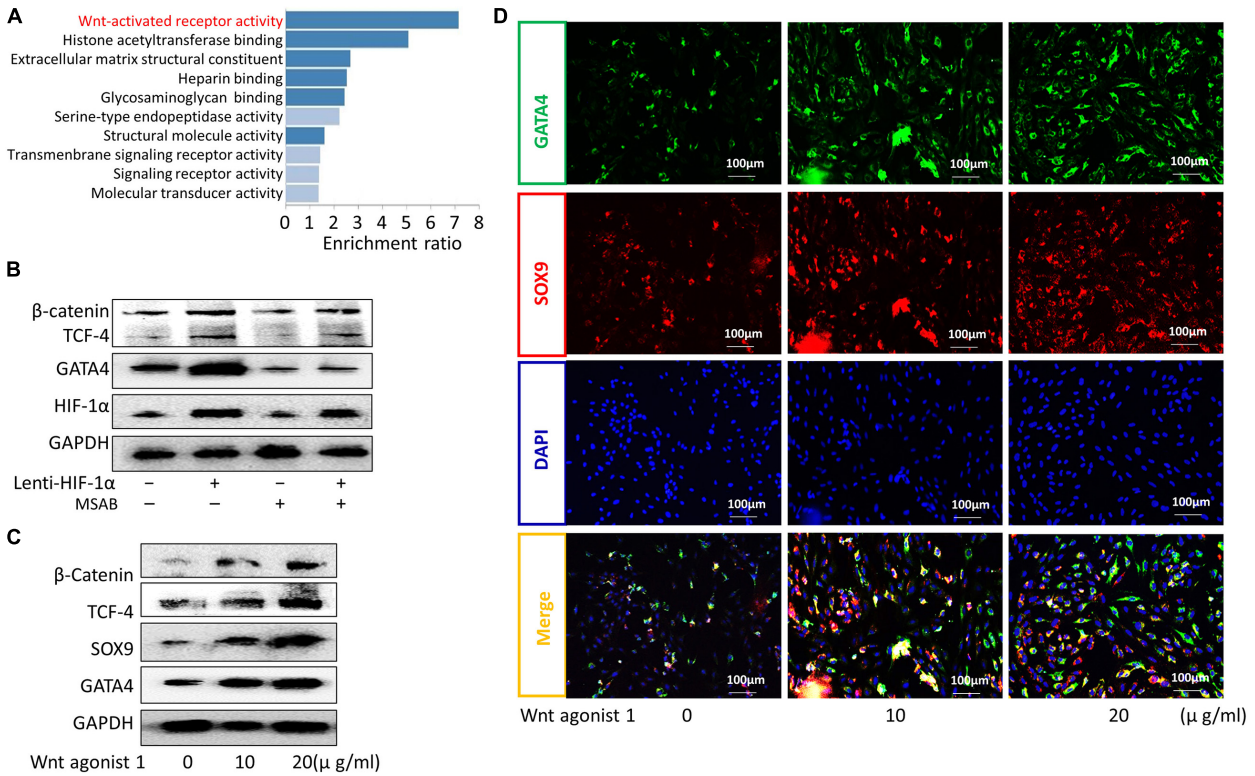

FIGURE 3 | HIF-1α promoted the differentiation of CESCs into NPCs via activation of the Wnt/GATA4 pathway. **(A)** KEGG enrichment analysis of normal and degenerated human cartilage endplate tissue. **(B)** Representative western blots of β-catenin, TCF-4, GATA4, and HIF-1α in CESCs treated with NC, Lenti-HIF-1α, MSAB (inhibitor of the Wnt pathway), or Lenti-HIF-1α + MSAB. **(C)** Western blots of β-catenin, TCF-4, SOX9, and GATA4 in CESCs treated with different concentrations of Wnt agonist 1 (0, 10, or 20 μg/ml). **(D)** Double immunofluorescence of GATA4 (green) and SOX9 (red) in CESCs treated with different concentrations of Wnt agonist 1 (0, 10, or 20 μg/ml).

the mRNA and protein levels of GATA4 were increased, as demonstrated by qPCR and western blotting (**Figure 4C**). qPCR showed that the expression levels of TGF-β1 and EGF increased and that the expression levels of colony stimulating factor-1 (CSF-1) and platelet-derived growth factor (PDGF) decreased in Lenti-GATA4 CESCs (**Figure 4D**). In addition, the protein level of TGF-β1 was increased in Lenti-GATA4 CESCs, as demonstrated by western blotting (**Figure 4E**). These results indicated that GATA4 increased the expression of TGF-β1. Moreover, the protein expression of SOX9 and TGF-β1 increased in the Lenti-GATA4 group and decreased in the Lenti-GATA4 group cotreated with the TGF-β inhibitor PFD, indicating that the effects of GATA4 on promotion of CESC differentiation into NPCs was blocked by the TGF-β inhibitor (**Figure 5A**). Immunofluorescence analysis also indicated that the effects of GATA4 on promoting CESC differentiation into NPCs were blocked by the TGF-β inhibitor (**Figure 5B**). As shown in **Figures 5C–E**, the invasion and migration capacities of cells with or without GATA4-expressing lentivirus were blocked by PFD, whereas the TGF-β agonist SRI-011381 improved the invasion and migration capacities of CESCs without treatment. The protein levels of collagen II and SOX9 were increased in CESCs treated with SRI-011381 but decreased in CESCs treated with PFD, as demonstrated by immunofluorescence analysis, indicating that TGF-β promoted CESC differentiation (**Figure 5F**). The western blotting results were consistent with the observations under fluoroscopy (**Figure 5G**). Based on the above results, we concluded that GATA4 promoted CESC invasion, migration, and differentiation via TGF-β1 signaling.

CESCs Overexpressing GATA4 Ameliorated IVDD *in vivo*

To further explore the therapeutic effects of CESCs overexpressing GATA4 in IVDD, an IVDD animal model was used in our experiment. Two groups of IVDD rats (n = 5 rats/group) were injected with CESCs (20 μL, 10^5/mL) and CESCs overexpressing GATA4 (20 μL, 10^5/mL; **Figure 6A**). IVDD model rats were assessed by micro-MRI at 4 weeks after operation. The MRI results showed that the IVDD of rats in CESCs and CESCs overexpressing GATA4 was less severe and that IVDD was more effectively ameliorated in GAT4-overexpressing CESCs than in CESCs (**Figure 6B**). Histological immunofluorescence analysis showed that SOX9 and GATA4 were upregulated in CESCs and CESCs overexpressing GATA4 and decreased in the IVDD group without injection; however, the degeneration of the IVD was minimal in CESCs overexpressing GATA4, indicating that CESCs differentiated into NPCs to repair

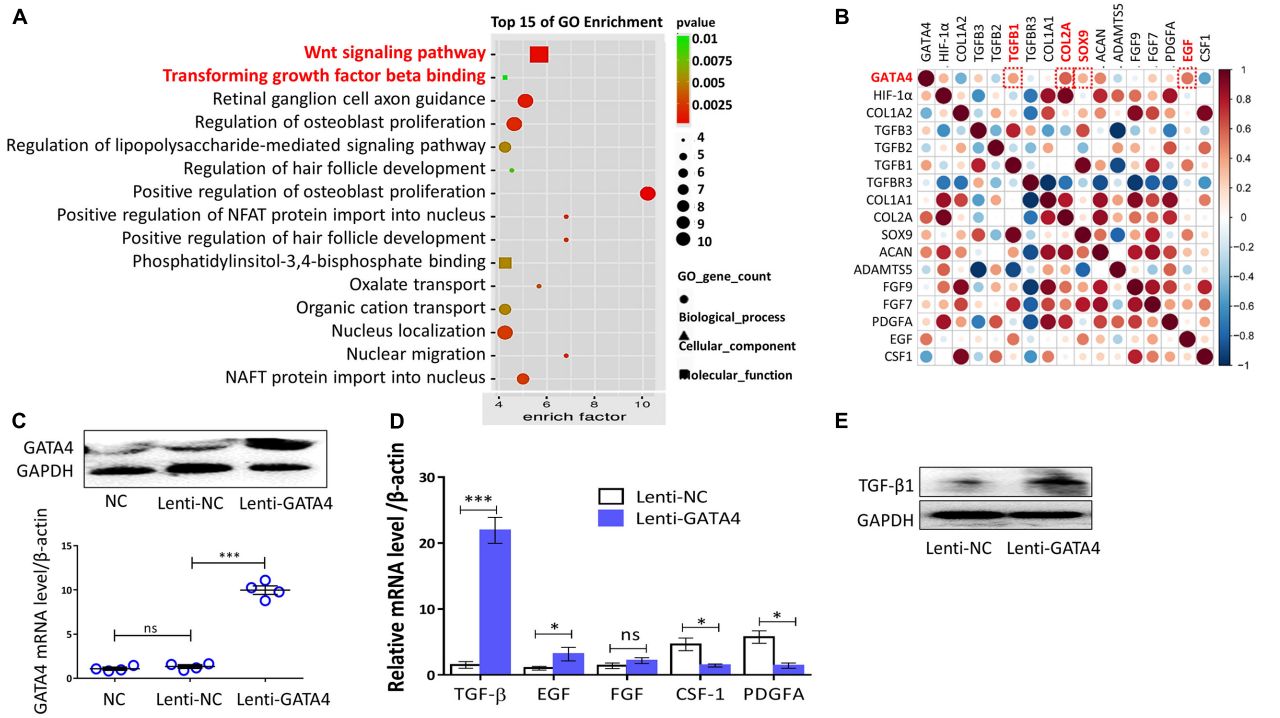

FIGURE 4 | GATA4 significantly increased TGF-β1 expression. **(A)** Gene Ontology (GO) analysis of all differential proteins in normal and degenerated or differentiated human cartilage endplate tissue. **(B)** Correlation analysis of important proteins expressed in human cartilage endplate tissue (GSE153761, https://www.ncbi.nlm.nih.gov/). **(C)** Representative western blots of HIF-1α and RT-qPCR assays in CESCs treated with NC, Lenti-NC, or Lenti-GATA4. **(D)** Expression of *TGF-β*, *EGF*, *FGF*, *CSF-1*, and *PDGFA* in CESCs treated with Lenti-NC or Lenti-GATA4. **(E)** Western blots of TGF-β in CESCs treated with Lenti-NC or Lenti-GATA4. All data represent means ± standard deviations. $P < 0.05$ is considered statistically significant. NC: normal control; ns: $P > 0.05$; $^{*}P < 0.05$ and $^{***}P < 0.001$.

IVDs via GATA4 signaling (**Figure 6C**). Consequently, CESCs enhanced IVD repair and ameliorated IVDD deterioration *in vivo*.

CESCs Were Converted Into NPCs in Degenerated and Differentiated CEPs

Cartilage endplates were isolated from the patients. As shown in **Figure 7A**, there was a clear linear positive correlation between the mRNA levels of *SOX9* and *GATA4* in CEP differentiation and degeneration. The protein levels of SOX9 and GATA4 increased with the development of CEP degeneration, as demonstrated by western blotting (**Figure 7B**). The results of immunofluorescence and immunohistochemical analyses for SOX9 and GATA4 were similar to those of western blotting (**Figures 7C,D**). These results suggested that CESCs could be converted into NPCs through the progression of endplate differentiation and degeneration.

DISCUSSION

Physiotherapy and medicine treatments can relieve the symptoms of LBP in most patients with IVDD, but do not reverse disk degeneration (Lindbäck et al., 2018). Lumbar fusion is the most common choice for severe IVDD; however, adjacent segment degeneration may cause adjacent segment symptoms (Kim et al., 2016; Okuda et al., 2018). Other alternative therapeutic treatments that can repair and regenerate IVD are needed. MSC transplantation has been performed successfully in human degenerated IVD (Noriega et al., 2017). In our study, we found that CESCs could migrate and transdifferentiate into NPCs via autocrine mechanisms. After activation of the HIF-1α/Wnt pathway and increasing GATA4/TGF-β expression, we observed inhibition of IVDD by CESC-Exos.

Exosomes are small vesicles secreted by various types of cells and can establish a potent mode of intercellular communication (Luga et al., 2012). Following their secretion, exosomes can work on their original cells in an autocrine manner, on vicinal cells in a paracrine manner, or on distant cells in an endocrine manner (Milman et al., 2019). After being taken up by cells, exosomes play roles in various cellular activities, including proliferation and differentiation (Barile and Vassalli, 2017; Chang et al., 2018). After treatment with exosomes, we found that CESC migration capacity was significantly improved and that the expression of NPC markers (SOX9 and collagen II) increased. This suggested that CESC-Exos could promote CESC migration and transdifferentiate the CESCs into NPCs in an autocrine manner.

Nucleus pulposus cells live in an avascular and hypoxic niche of the IVD, and the level of HIF-1α in NPCs is increased compared with that in the surrounding cells

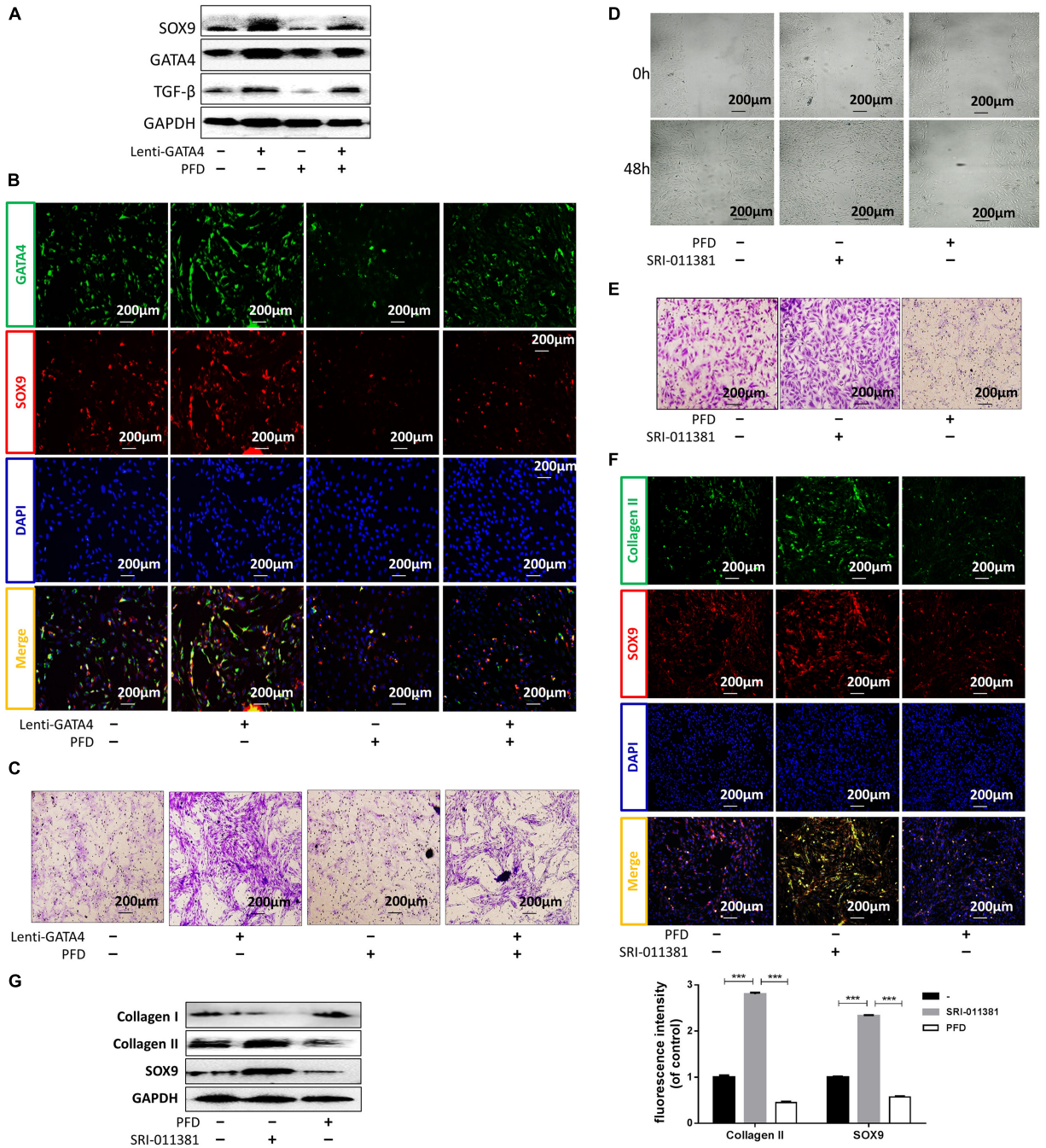

FIGURE 5 | GATA4 promoted CESC invasion, migration, and differentiation via the TGF-β1 signaling pathway. **(A)** Western blots of SOX9, GATA4, and TGF-β in CESCs treated with Lenti-NC or Lenti-GATA4. **(B,C)** Double immunofluorescence of GATA4 (green) and SOX9 (red) and transwell analysis in CESCs treated as described above. **(D,E)** Ability of CESCs to invade and migrate after addition of the TGF-β agonist SRI-011381 or inhibitor pirfenidone (PFD). **(F)** Double immunofluorescence of collagen II (green) and SOX9 (red) in CESCs treated with SRI-011381 or PFD. **(G)** Western blots of collagen I, collagen II, and SOX9 in CESCs treated with NC, SRI-011381, or PFD. All data represent means ± standard deviations. $P < 0.05$ was considered statistically significant. ***$P < 0.001$.

(Rajpurohit et al., 2002; Risbud et al., 2006). HIF-1α is a transcription factor that is important for maintaining NPC matrix synthesis and regulating glycolytic metabolism (Risbud et al., 2006; Agrawal et al., 2007, 2008). Additionally, HIF-1α is necessary for postnatal NPC survival and to maintain intracellular pH homeostasis by regulating carbonic anhydrases 9 and 12 (Merceron et al., 2014; Silagi et al., 2018). Some growth factors, such as insulin-like growth factor-2 and transforming growth factor-α, are HIF-1α target genes (Feldser et al., 1999; Krishnamachary et al., 2003). These factors activate signal

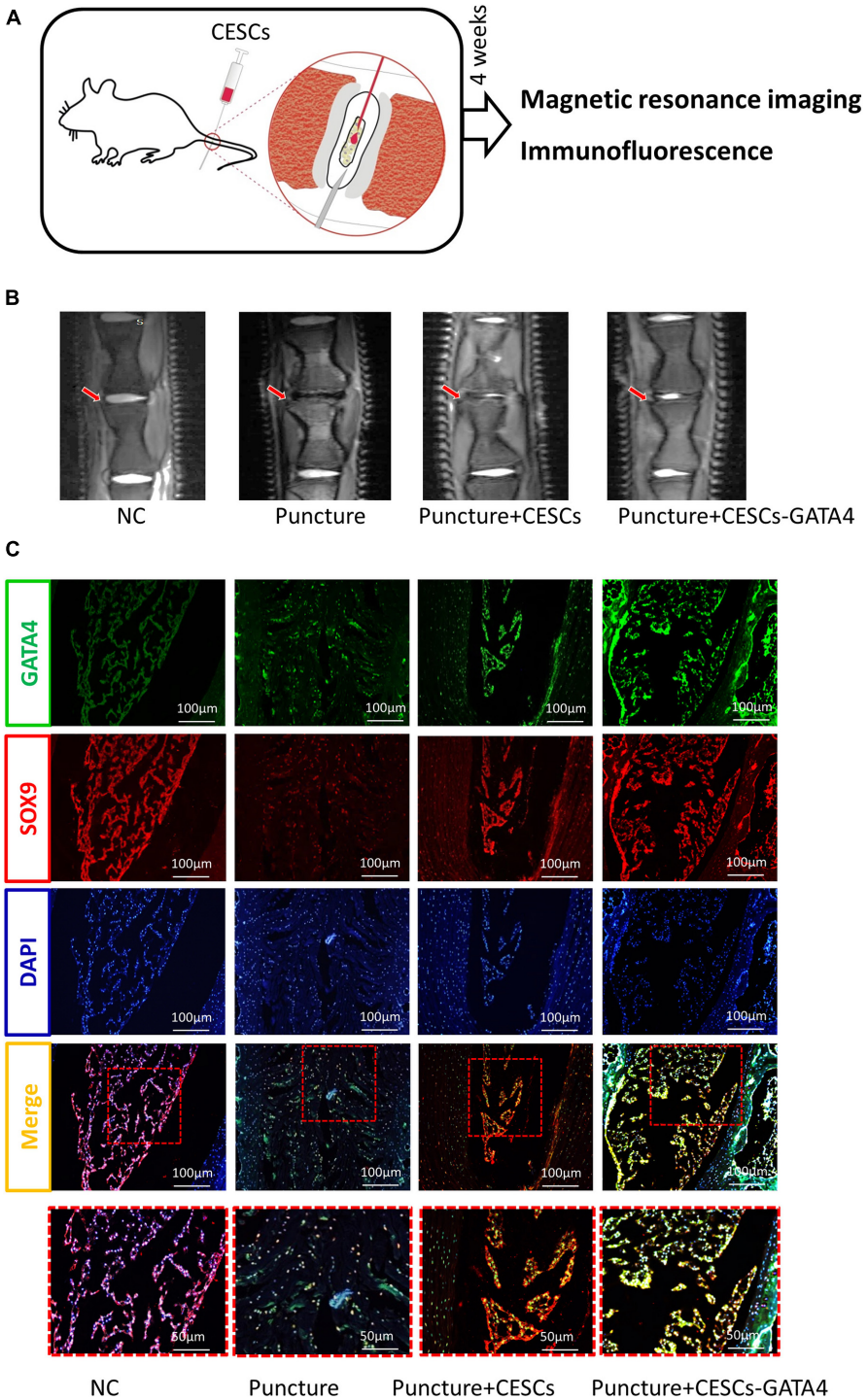

FIGURE 6 | CESCs overexpressing GATA4 enhanced intervertebral disk repair and inhibited intervertebral disk degeneration. **(A)** Experimental steps for CESC treatment via microsyringe in the IVDD model. **(B)** Representative MRI results for rat intervertebral disks treated with NC, puncture, puncture + CESCs (20 μL, 10^5/mL), or puncture + CESCs overexpressing GATA4 (20 μL, 10^5/mL). **(C)** Representative double immunofluorescence of SOX9 (red) and cleaved GATA4 (green) images for rat disks in each group (n = 5 rats/group).

transduction pathways that lead to cell proliferation by binding to their cognate receptors (Semenza, 2003). Furthermore, previous studies suggested that HIF-1α was associated with tumor metastasis, promoting cell migration and invasion (Liu et al., 2016; Hu et al., 2020). Our immunofluorescence results revealed that the expression level of HIF-1α increased

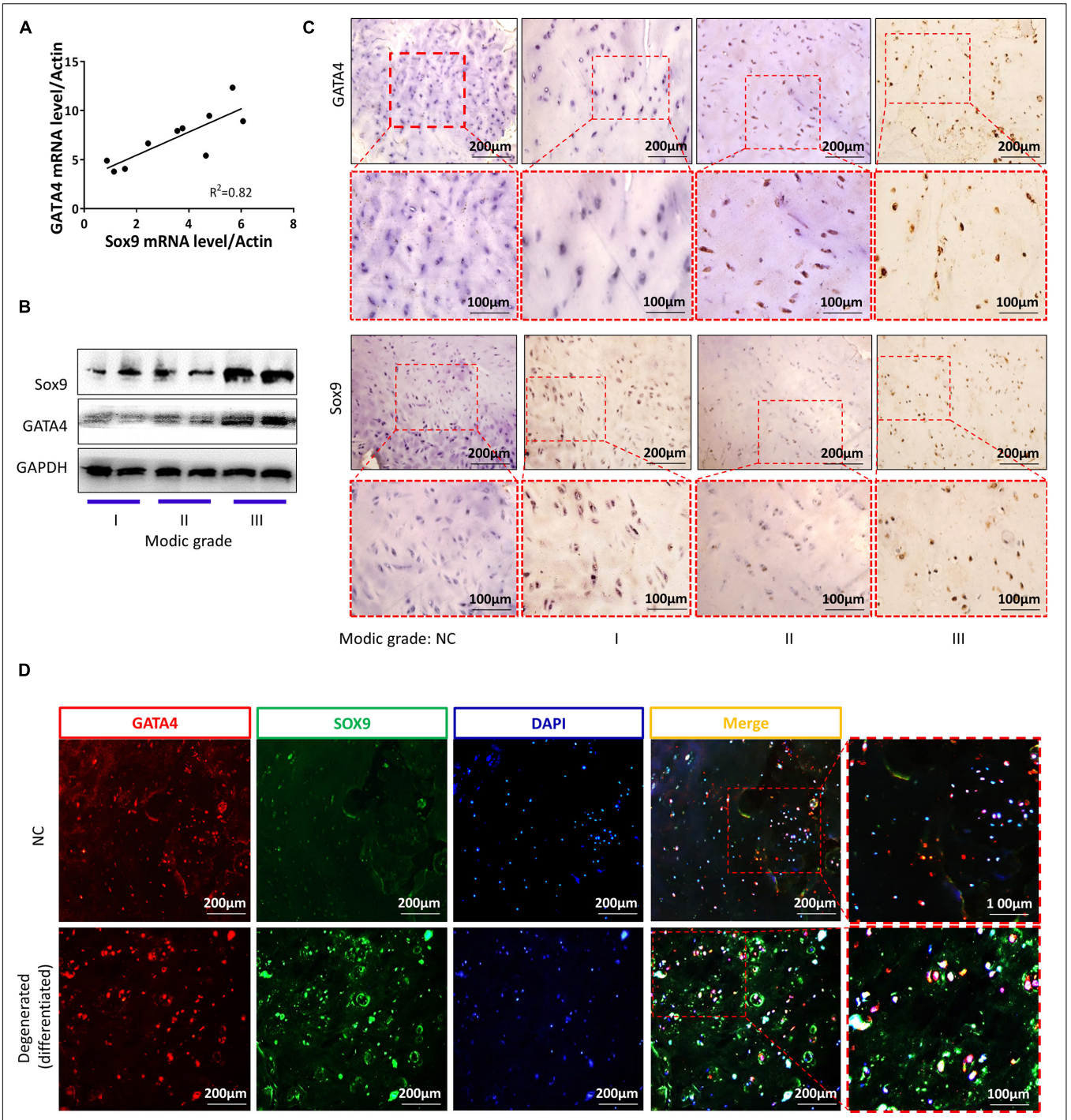

FIGURE 7 | GATA4 and SOX9 levels were increased in degenerated and differentiated cartilage endplates. **(A)** mRNA expression levels of *GATA4* and *SOX9* in cartilage endplates. **(B)** Representative western blots of GATA4 and SOX9 in cartilage endplate inflammation based on Modic grading. **(C)** Immunohistochemical staining of GATA4 and SOX9 in stages 1–3 of cartilage degeneration and differentiation. **(D)** Double immunofluorescence of GATA4 (red) and SOX9 (green) in normal or degenerated and differentiated cartilage endplates.

in CESCs after treatment with exosomes, indicating that HIF-1α played important roles in CESC transdifferentiation. Subsequently, overexpression of HIF-1α CESCs was used in our experiments to explore the underlying mechanisms of CESC transdifferentiation. Immunofluorescent staining, western blotting, wound scratch assays, and transwell migration assays showed that exosomes promoted CESC migration and differentiation by increasing HIF-1α expression. The

Wnt/β-catenin pathway is an important pathway modulated by hypoxia (Giles et al., 2006; Mazumdar et al., 2010). Based on our KEGG enrichment analysis, we suspected that the increase in HIF-1α activated the Wnt/β-catenin pathway to react with CESCs. Therefore, MSAB and Wnt agonist 1 were used to treat HIF-1α-overexpressing CESCs and CESCs, respectively. As expected, we verified that increasing HIF-1α expression activated the Wnt pathway to promote the migration and differentiation of CESCs into NPCs.

GATA-binding protein 4 was first discovered in cardiac tissue and was shown to regulate heart development (Kelley et al., 1993). GATA4 is a member of the highly conserved zinc-finger transcription factor family and plays key roles in regulating cell differentiation, growth, and survival in addition to cardiac cells (Molkentin, 2000; Patient and Mcghee, 2002). Some studies have demonstrated that Wnt/β-catenin signaling regulates the expression of GATA4 at the transcriptional level (Watt et al., 2004; Holtzinger and Evans, 2005). Consistent with previous studies, our western blotting and immunofluorescence analyses showed that GATA4 was regulated by the Wnt signaling pathway. We concluded that increased HIF-1α enhanced the activation of Wnt signaling and upregulated GATA4 expression to promote CESC differentiation. According to GO and protein correlation analyses, we found that GATA4 may be related to the TGF-β1 signaling pathways. To confirm the relationship between GATA4 and TGF-β1, CESCs overexpressing GATA4 as well as PFD and SRI-011381 were used in our experiments. Although TGF-β1 and EGF are both related to GATA4 signaling, qPCR indicated that the expression of TGF-β1 increased more significantly compared with the expression of EGF. Finally, our results demonstrated that GATA4 promoted CESC migration and differentiation by increasing TGF-β1 expression.

We further examined the roles of CESCs in a rat model of IVDD. Consistent with our previous *in vitro* study, our current findings showed that CESCs could ameliorate IVDD deterioration *in vivo* and that the degree of IVDD was minimal in CESCs overexpressing GATA4. This suggested that CESCs may promote transdifferentiation and effectively ameliorate IVDD via GATA4 signaling. IVDD is accompanied by CEP degeneration, and CEP inflammation is a characteristic of IVDD. Our results suggested that the CESCs were gradually converted into NPCs with the development of CEP degeneration in humans.

In conclusion, we demonstrated that the HIF-1α/Wnt signaling pathway in CESCs was activated by autocrine exosomes to increase the expression of GATA4 and TGF-β1, thereby promoting the migration of CESCs into the IVD and the transformation of CESCs into NPCs and inhibiting IVDD. Our findings provide insights into the potential applications of CESCs in the treatment of IVDD.

DATA AVAILABILITY STATEMENT

The original contributions presented in the study are included in the article/**Supplementary Material**, further inquiries can be directed to the corresponding author/s.

ETHICS STATEMENT

The Ethics Committee of the Xinqiao Hospital of Army Medical University approved the present study (AF/SC-08/1.0). The patients/participants provided their written informed consent to participate in this study. The animal study was reviewed and approved by The Animal Ethics Committee Army Medical University approved all studies [No. SYXK(yu)2017-0002].

AUTHOR CONTRIBUTIONS

LL and JG: conception and design, conducting experiments, collection and/or assembly of data, data analysis, and interpretation manuscript writing. HZ, YT, JQ, and JZ: provision of study material and data analysis. YaZ, JC, and CL: conducting experiments and animal modeling assistance. YuZ, ZT, YL, and ML: revising the manuscript, administrative support, and financial support. All authors contributed to the article and approved the submitted version.

FUNDING

This work was supported by the National Natural Science Foundation of China (Grant Numbers: 81874028 and 81702182); Innovation ability enhancement project of Army Medical University (Grant Number: 2019ZLX007); the Research Program of Foundation Science and Application Technology of Chongqing (Grant Number: cstc2018jcyjA1826); and Basic Medical College Foundation of Army Medical University (2019JCZX10).

ACKNOWLEDGMENTS

We thank all authors involved in the study and are grateful to the Animal Center of Army Military Medical University (Third Military Medical University) for providing the rats.

SUPPLEMENTARY MATERIAL

The Supplementary Material for this article can be found online at: https://www.frontiersin.org/articles/10.3389/fcell.2021.648201/full#supplementary-material

Supplementary Figure 1 | Extraction and identification of CESCs derived from rat CEP. **(A)** Morphology of P1 and P3 CESCs at 80% confluence and P5 CESCs at 100% confluence. **(B)** Oil red O, Alcian blue, and Alizarin red S staining analysis of stem cell characteristics after adipogenic, chondrogenic, and osteogenic induction. **(C)** Flow cytometry analysis of stem cell-positive and -negative markers CD90, CD44, and CD45 in CESCs. The blue curves represent the fluorescence intensity of unstained cells, and the red curves indicate the fluorescence intensity of CESCs stained with the corresponding antibodies.

Supplementary Figure 2 | Exosomes promote the proliferation of NPCs. Double immunofluorescence of EdU (green) and PKH26 (red) in NPCs treated with different concentrations of exosomes (0, 20, or 40 μg/ml).

REFERENCES

Agrawal, A., Gajghate, S., Smith, H., Anderson, D. G., Albert, T. J., Shapiro, I. M., et al. (2008). Cited2 modulates hypoxia-inducible factor-dependent expression of vascular endothelial growth factor in nucleus pulposus cells of the rat intervertebral disc. *Arthrit. Rheum* 58, 3798–3808. doi: 10.1002/art.24073

Agrawal, A., Guttapalli, A., Narayan, S., Albert, T. J., Shapiro, I. M., and Risbud, M. V. (2007). Normoxic stabilization of HIF-1alpha drives glycolytic metabolism and regulates aggrecan gene expression in nucleus pulposus cells of the rat intervertebral disk. *Am. J. Physiol. Cell Physiol.* 293, C621–C631. doi: 10.1152/ajpcell.00538.2006

Aioub, M., Lezot, F., Molla, M., Castaneda, B., Robert, B., Goubin, G., et al. (2007). Msx2 -/- transgenic mice develop compound amelogenesis imperfecta, dentinogenesis imperfecta and periodental osteopetrosis. *Bone* 41, 851–859. doi: 10.1016/j.bone.2007.07.023

Barile, L., and Vassalli, G. (2017). Exosomes: Therapy delivery tools and biomarkers of diseases. *Pharmacol. Ther.* 174, 63–78. doi: 10.1016/j.pharmthera.2017.02.020

Biswas, S., Mandal, G., Roy Chowdhury, S., Purohit, S., Payne, K. K., Anadon, C., et al. (2019). Exosomes Produced by Mesenchymal Stem Cells Drive Differentiation of Myeloid Cells into Immunosuppressive M2-Polarized Macrophages in Breast Cancer. *J. Immunol.* 203, 3447–3460. doi: 10.4049/jimmunol.1900692

Boso, D., Rampazzo, E., Zanon, C., Bresolin, S., Maule, F., Porcù, E., et al. (2019). HIF-1α/Wnt signaling-dependent control of gene transcription regulates neuronal differentiation of glioblastoma stem cells. *Theranostics* 9, 4860–4877. doi: 10.7150/thno.35882

Chang, Y. H., Wu, K. C., Harn, H. J., Lin, S. Z., and Ding, D. C. (2018). Exosomes and Stem Cells in Degenerative Disease Diagnosis and Therapy. *Cell Transplant.* 27, 349–363. doi: 10.1177/0963689717723636

Chen, X., Zhou, B., Yan, T., Wu, H., Feng, J., Chen, H., et al. (2018). Peroxynitrite enhances self-renewal, proliferation and neuronal differentiation of neural stem/progenitor cells through activating HIF-1α and Wnt/β-catenin signaling pathway. *Free Radic. Biol. Med.* 117, 158–167. doi: 10.1016/j.freeradbiomed.2018.02.011

Feldser, D., Agani, F., Iyer, N. V., Pak, B., Ferreira, G., and Semenza, G. L. (1999). Reciprocal positive regulation of hypoxia-inducible factor 1alpha and insulin-like growth factor 2. *Cancer Res.* 59, 3915–3918.

Freemont, A. J. (2009). The cellular pathobiology of the degenerate intervertebral disc and discogenic back pain. *Rheumatology* 48, 5–10. doi: 10.1093/rheumatology/ken396

GBD 2016 Disease and Injury Incidence and Prevalence Collaborators (2017). Global, regional, and national incidence, prevalence, and years lived with disability for 328 diseases and injuries for 195 countries, 1990-2016: a systematic analysis for the Global Burden of Disease Study 2016. *Lancet* 390, 1211–1259.

Giles, R. H., Lolkema, M. P., Snijckers, C. M., Belderbos, M., Van Der Groep, P., Mans, D. A., et al. (2006). Interplay between VHL/HIF1alpha and Wnt/beta-catenin pathways during colorectal tumorigenesis. *Oncogene* 25, 3065–3070. doi: 10.1038/sj.onc.1209330

Güemes, M., Garcia, A. J., Rigueur, D., Runke, S., Wang, W., Zhao, G., et al. (2014). GATA4 is essential for bone mineralization via ERα and TGFβ/BMP pathways. *J. Bone Miner Res.* 29, 2676–2687. doi: 10.1002/jbmr.2296

Han, B., Zhu, K., Li, F. C., Xiao, Y. X., Feng, J., Shi, Z. L., et al. (2008). A simple disc degeneration model induced by percutaneous needle puncture in the rat tail. *Spine* 33, 1925–1934. doi: 10.1097/BRS.0b013e31817c64a9

Holtzinger, A., and Evans, T. (2005). Gata4 regulates the formation of multiple organs. *Development* 132, 4005–4014. doi: 10.1242/dev.01978

Hu, X., Lin, J., Jiang, M., He, X., Wang, K., Wang, W., et al. (2020). HIF-1α Promotes the Metastasis of Esophageal Squamous Cell Carcinoma by Targeting SP1. *J. Cancer* 11, 229–240. doi: 10.7150/jca.35537

Kalluri, R., and Lebleu, V. S. (2020). The biology, function, and biomedical applications of exosomes. *Science* 2020:367. doi: 10.1126/science.aau6977

Kelley, C., Blumberg, H., Zon, L. I., and Evans, T. (1993). GATA-4 is a novel transcription factor expressed in endocardium of the developing heart. *Development* 118, 817–827.

Khalid, A. B., Slayden, A. V., Kumpati, J., Perry, C. D., Osuna, M. A. L., Arroyo, S. R., et al. (2018). GATA4 Directly Regulates Runx2 Expression and Osteoblast Differentiation. *JBMR Plus* 2, 81–91. doi: 10.1002/jbm4.10027

Kim, J. Y., Ryu, D. S., Paik, H. K., Ahn, S. S., Kang, M. S., Kim, K. H., et al. (2016). Paraspinal muscle, facet joint, and disc problems: risk factors for adjacent segment degeneration after lumbar fusion. *Spine J.* 16, 867–875. doi: 10.1016/j.spinee.2016.03.010

Kourembanas, S. (2015). Exosomes: vehicles of intercellular signaling, biomarkers, and vectors of cell therapy. *Annu. Rev. Physiol.* 77, 13–27. doi: 10.1146/annurev-physiol-021014-071641

Krishnamachary, B., Berg-Dixon, S., Kelly, B., Agani, F., Feldser, D., Ferreira, G., et al. (2003). Regulation of colon carcinoma cell invasion by hypoxia-inducible factor 1. *Cancer Res.* 63, 1138–1143.

Le Maitre, C. L., Freemont, A. J., and Hoyland, J. A. (2004). Localization of degradative enzymes and their inhibitors in the degenerate human intervertebral disc. *J. Pathol.* 204, 47–54. doi: 10.1002/path.1608

Li, Q., Guo, Z. K., Chang, Y. Q., Yu, X., Li, C. X., and Li, H. (2015). Gata4, Tbx5 and Baf60c induce differentiation of adipose tissue-derived mesenchymal stem cells into beating cardiomyocytes. *Int. J. Biochem. Cell Biol.* 66, 30–36. doi: 10.1016/j.biocel.2015.06.008

Li, X. C., Tang, Y., Wu, J. H., Yang, P. S., Wang, D. L., and Ruan, D. K. (2017). Characteristics and potentials of stem cells derived from human degenerated nucleus pulposus: potential for regeneration of the intervertebral disc. *BMC Musculoskelet Disord* 18:242. doi: 10.1186/s12891-017-1567-4

Liao, Z., Luo, R., Li, G., Song, Y., Zhan, S., Zhao, K., et al. (2019). Exosomes from mesenchymal stem cells modulate endoplasmic reticulum stress to protect against nucleus pulposus cell death and ameliorate intervertebral disc degeneration in vivo. *Theranostics* 9, 4084–4100. doi: 10.7150/thno.33638

Lindbäck, Y., Tropp, H., Enthoven, P., Abbott, A., and Öberg, B. (2018). PREPARE: presurgery physiotherapy for patients with degenerative lumbar spine disorder: a randomized controlled trial. *Spine J.* 18, 1347–1355. doi: 10.1016/j.spinee.2017.12.009

Liu, L. T., Huang, B., Li, C. Q., Zhuang, Y., Wang, J., and Zhou, Y. (2011). Characteristics of stem cells derived from the degenerated human intervertebral disc cartilage endplate. *PLoS One* 6:e26285. doi: 10.1371/journal.pone.0026285

Liu, M., Wang, D., and Li, N. (2016). MicroRNA-20b Downregulates HIF-1α and Inhibits the Proliferation and Invasion of Osteosarcoma Cells. *Oncol Res.* 23, 257–266. doi: 10.3727/096504016X14562725373752

Luga, V., Zhang, L., Viloria-Petit, A. M., Ogunjimi, A. A., Inanlou, M. R., Chiu, E., et al. (2012). Exosomes mediate stromal mobilization of autocrine Wnt-PCP signaling in breast cancer cell migration. *Cell* 151, 1542–1556. doi: 10.1016/j.cell.2012.11.024

Luo, L., Jian, X., Sun, H., Qin, J., Wang, Y., Zhang, J., et al. (2021). Cartilage endplate stem cells inhibit intervertebral disc degeneration by releasing exosomes to nucleus pulposus cells to activate Akt/autophagy. *Stem Cells* 2021:3322. doi: 10.1002/stem.3322

Mazumdar, J., O'brien, W. T., Johnson, R. S., Lamanna, J. C., Chavez, J. C., Klein, P. S., et al. (2010). O2 regulates stem cells through Wnt/β-catenin signalling. *Nat. Cell Biol.* 12, 1007–1013. doi: 10.1038/ncb2102

Merceron, C., Mangiavini, L., Robling, A., Wilson, T. L., Giaccia, A. J., Shapiro, I. M., et al. (2014). Loss of HIF-1α in the notochord results in cell death and complete disappearance of the nucleus pulposus. *PLoS One* 9:e110768. doi: 10.1371/journal.pone.0110768

Milman, N., Ginini, L., and Gil, Z. (2019). Exosomes and their role in tumorigenesis and anticancer drug resistance. *Drug Resist. Updat.* 45, 1–12. doi: 10.1016/j.drup.2019.07.003

Miranda-Carboni, G. A., Guemes, M., Bailey, S., Anaya, E., Corselli, M., Peault, B., et al. (2011). GATA4 regulates estrogen receptor-alpha-mediated osteoblast transcription. *Mol. Endocrinol.* 25, 1126–1136. doi: 10.1210/me.2010-0463

Modic, M. T., Masaryk, T. J., Ross, J. S., and Carter, J. R. (1988). Imaging of degenerative disk disease. *Radiology* 168, 177–186. doi: 10.1148/radiology.168.1.3289089

Molkentin, J. D. (2000). The zinc finger-containing transcription factors GATA-4, -5, and -6. Ubiquitously expressed regulators of tissue-specific gene expression. *J. Biol. Chem.* 275, 38949–38952. doi: 10.1074/jbc.R000029200

Noriega, D. C., Ardura, F., Hernández-Ramajo, R., Martín-Ferrero, M., Sánchez-Lite, I., Toribio, B., et al. (2017). Intervertebral Disc Repair by Allogeneic Mesenchymal Bone Marrow Cells: A Randomized Controlled Trial. *Transplantation* 101, 1945–1951. doi: 10.1097/TP.0000000000001484

Okuda, S., Nagamoto, Y., Matsumoto, T., Sugiura, T., Takahashi, Y., and Iwasaki, M. (2018). Adjacent Segment Disease After Single Segment Posterior Lumbar Interbody Fusion for Degenerative Spondylolisthesis: Minimum 10 Years Follow-up. *Spine* 43, E1384–E1388. doi: 10.1097/BRS.0000000000002710

Orozco, L., Soler, R., Morera, C., Alberca, M., Sánchez, A., and García-Sancho, J. (2011). Intervertebral disc repair by autologous mesenchymal bone marrow cells: a pilot study. *Transplantation* 92, 822–828. doi: 10.1097/TP.0b013e3182298a15

Patient, R. K., and Mcghee, J. D. (2002). The GATA family (vertebrates and invertebrates). *Curr. Opin. Genet. Dev.* 12, 416–422. doi: 10.1016/S0959-437X(02)00319-2

Properzi, F., Logozzi, M., and Fais, S. (2013). Exosomes: the future of biomarkers in medicine. *Biomark Med.* 7, 769–778. doi: 10.2217/bmm.13.63

Rajpurohit, R., Risbud, M. V., Ducheyne, P., Vresilovic, E. J., and Shapiro, I. M. (2002). Phenotypic characteristics of the nucleus pulposus: expression of hypoxia inducing factor-1, glucose transporter-1 and MMP-2. *Cell Tissue Res.* 308, 401–407. doi: 10.1007/s00441-002-0563-6

Risbud, M. V., and Shapiro, I. M. (2014). Role of cytokines in intervertebral disc degeneration: pain and disc content. *Nat. Rev. Rheumatol.* 10, 44–56. doi: 10.1038/nrrheum.2013.160

Risbud, M. V., Guttapalli, A., Stokes, D. G., Hawkins, D., Danielson, K. G., Schaer, T. P., et al. (2006). Nucleus pulposus cells express HIF-1 alpha under normoxic culture conditions: a metabolic adaptation to the intervertebral disc microenvironment. *J. Cell Biochem.* 98, 152–159. doi: 10.1002/jcb.20765

Roughley, P. J. (2004). Biology of intervertebral disc aging and degeneration: involvement of the extracellular matrix. *Spine* 29, 2691–2699. doi: 10.1097/01.brs.0000146101.53784.b1

Schol, J., and Sakai, D. (2019). Cell therapy for intervertebral disc herniation and degenerative disc disease: clinical trials. *Int. Orthop.* 43, 1011–1025. doi: 10.1007/s00264-018-4223-1

Semenza, G. L. (2003). Targeting HIF-1 for cancer therapy. *Nat. Rev. Cancer* 3, 721–732. doi: TargetingHIF-1forcancertherapy

Silagi, E. S., Schoepflin, Z. R., Seifert, E. L., Merceron, C., Schipani, E., Shapiro, I. M., et al. (2018). Bicarbonate Recycling by HIF-1-Dependent Carbonic Anhydrase Isoforms 9 and 12 Is Critical in Maintaining Intracellular pH and Viability of Nucleus Pulposus Cells. *J. Bone Miner. Res.* 33, 338–355. doi: 10.1002/jbmr.3293

Simons, M., and Raposo, G. (2009). Exosomes–vesicular carriers for intercellular communication. *Curr. Opin. Cell Biol.* 21, 575–581. doi: 10.1016/j.ceb.2009.03.007

Simpson, R. J., Jensen, S. S., and Lim, J. W. (2008). Proteomic profiling of exosomes: current perspectives. *Proteomics* 8, 4083–4099. doi: 10.1002/pmic.200800109

Stokes, I. A., and Iatridis, J. C. (2004). Mechanical conditions that accelerate intervertebral disc degeneration: overload versus immobilization. *Spine* 29, 2724–2732. doi: 10.1097/01.brs.0000146049.52152.da

Théry, C., Amigorena, S., Raposo, G., and Clayton, A. (2006). Isolation and characterization of exosomes from cell culture supernatants and biological fluids. *Curr. Protoc. Cell. Biol.* 2006:3.22. doi: 10.1002/0471143030.cb0322s30

Vallée, A., Guillevin, R., and Vallée, J. N. (2018). Vasculogenesis and angiogenesis initiation under normoxic conditions through Wnt/β-catenin pathway in gliomas. *Rev. Neurosci.* 29, 71–91. doi: 10.1515/revneuro-2017-0032

Vo, N. V., Hartman, R. A., Patil, P. R., Risbud, M. V., Kletsas, D., Iatridis, J. C., et al. (2016). Molecular mechanisms of biological aging in intervertebral discs. *J. Orthop. Res.* 34, 1289–1306. doi: 10.1002/jor.23195

Wang, H., Zhou, Y., Huang, B., Liu, L. T., Liu, M. H., Wang, J., et al. (2014). Utilization of stem cells in alginate for nucleus pulposus tissue engineering. *Tissue Eng. Part A* 20, 908–920. doi: 10.1089/ten.tea.2012.0703

Watt, A. J., Battle, M. A., Li, J., and Duncan, S. A. (2004). GATA4 is essential for formation of the proepicardium and regulates cardiogenesis. *Proc. Natl. Acad. Sci. U S A* 101, 12573–12578. doi: 10.1073/pnas.0400752101

Xia, C., Zeng, Z., Fang, B., Tao, M., Gu, C., Zheng, L., et al. (2019). Mesenchymal stem cell-derived exosomes ameliorate intervertebral disc degeneration via anti-oxidant and anti-inflammatory effects. *Free Radic. Biol. Med.* 143, 1–15. doi: 10.1016/j.freeradbiomed.2019.07.026

Xu, H., Yi, Q., Yang, C., Wang, Y., Tian, J., and Zhu, J. (2016). Histone modifications interact with DNA methylation at the GATA4 promoter during differentiation of mesenchymal stem cells into cardiomyocyte-like cells. *Cell Prolif.* 49, 315–329. doi: 10.1111/cpr.12253

Zhang, Q., Fu, L., Liang, Y., Guo, Z., Wang, L., Ma, C., et al. (2018). Exosomes originating from MSCs stimulated with TGF-β and IFN-γ promote Treg differentiation. *J. Cell Physiol.* 233, 6832–6840. doi: 10.1002/jcp.26436

Zhang, Y., Zhang, Z., Chen, P., Ma, C. Y., Li, C., Au, T. Y. K., et al. (2020). Directed Differentiation of Notochord-like and Nucleus Pulposus-like Cells Using Human Pluripotent Stem Cells. *Cell Rep.* 30, 2791.e–2806.e. doi: 10.1016/j.celrep.2020.01.100

Conflict of Interest: The authors declare that the research was conducted in the absence of any commercial or financial relationships that could be construed as a potential conflict of interest.

frontiers in Cell and Developmental Biology

ORIGINAL RESEARCH
published: 18 March 2021
doi: 10.3389/fcell.2021.648866

Napabucasin Induces Mouse Bone Loss by Impairing Bone Formation via STAT3

Xiangru Huang[1†], Anting Jin[1†], Xijun Wang[1†], Xin Gao[1], Hongyuan Xu[1], Miri Chung[1], Qinggang Dai[2], Yiling Yang[1]* and Lingyong Jiang[1]**

[1] Shanghai Key Laboratory of Stomatology & Shanghai Research Institute of Stomatology, Department of Oral and Cranio-maxillofacial Surgery, National Clinical Research Center of Stomatology, Center of Craniofacial Orthodontics, Ninth People's Hospital, Shanghai Jiao Tong University School of Medicine, Shanghai, China, [2] Shanghai Key Laboratory of Stomatology & Shanghai Research Institute of Stomatology, National Clinical Research Center of Stomatology, The 2nd Dental Center, Ninth People's Hospital, Shanghai Jiao Tong University School of Medicine, Shanghai, China

OPEN ACCESS

Edited by:
Q. Adam Ye,
Massachusetts General Hospital and Harvard Medical School, United States

Reviewed by:
Xia Lin,
Baylor College of Medicine, United States
Juan Li,
Sichuan University, China

***Correspondence:**
Qinggang Dai
daiqinggang@126.com
Yiling Yang
yangyiling_2017@alumni.sjtu.edu.cn
Lingyong Jiang
jianglingyong@sjtu.edu.cn;
247416218@qq.com

[†] These authors have contributed equally to this work and share first authorship

Specialty section:
This article was submitted to Stem Cell Research, a section of the journal Frontiers in Cell and Developmental Biology

Received: 02 January 2021
Accepted: 22 February 2021
Published: 18 March 2021

Citation:
Huang X, Jin A, Wang X, Gao X, Xu H, Chung M, Dai Q, Yang Y and Jiang L (2021) Napabucasin Induces Mouse Bone Loss by Impairing Bone Formation via STAT3. Front. Cell Dev. Biol. 9:648866. doi: 10.3389/fcell.2021.648866

The novel small molecule Napabucasin (also known as BBI608) was shown to inhibit gene transcription driven by Signal Transducer and Activator of Transcription 3 (STAT3), which is considered a promising anticancer target. Many preclinical studies have been conducted in cancer patients examining the selective targeting of cancer stem cells by Napabucasin, but few studies have examined side effects of Napabucasin in the skeleton system. In the present study, we found treating bone marrow mesenchymal stem cells (BMSCs) with Napabucasin *in vitro* impaired their osteogenic differentiation. In terms of mechanisms, Napabucasin disrupted differentiation of BMSCs by inhibiting the transcription of osteogenic gene osteocalcin (Ocn) through STAT3. Moreover, through micro-CT analysis we found 4 weeks of Napabucasin injections induced mouse bone loss. Histological analysis revealed that Napabucasin-induced bone loss in mice was the result of impaired osteogenesis. In conclusion, this study provided evidence for the effect of Napabucasin on mouse bone homeostasis and revealed its underlying mechanisms *in vivo* and *in vitro*.

Keywords: napabucasin, STAT3, BMSCs, osteopenia, osteogenesis

INTRODUCTION

Signal Transducer and Activator of Transcription 3 (STAT3), which plays a role in cell proliferation and other significant functional activities, is a key regulator of many oncogenic pathways and is therefore considered a promising anticancer target (Hubbard and Grothey, 2017; Aigner et al., 2019). In recent years, scientists have paid more attention to the crosstalk between immune and skeletal systems transmitted via critical signals, including STAT3, which is a key oncogenic transcription factor and is also reported to be a significant signal for bone homeostasis (Li, 2013). Several STAT3 inhibitors have been shown to affect the survival and differentiation of osteoblasts and osteoclasts (Li et al., 2013, 2018; Cheng et al., 2017; Cong et al., 2017). Furthermore, it was reported that Icariin prevented estrogen deficiency–induced bone loss through the activation of STAT3 (Xu et al., 2020).

Napabucasin (also known as BBI608), the focus of this investigation, is a novel small molecule shown to inhibit gene transcription driven by STAT3 (Hubbard and Grothey, 2017). Based on the promising effects observed in animal xenograft models (Li et al., 2015; Zhang et al., 2016), several preclinical studies were conducted in patients with advanced or metastatic cancers (Li et al., 2015, 2020; Bekaii-Saab et al., 2017; Grothey et al., 2017; Nagaraju et al., 2020). In fact, when this manuscript was written, there were 27 preclinical studies listed in the ClinicalTrials.gov database. Encouragingly, BBI608 blocked survival and self-renewal of stemness-high cancer cells. A multicenter phase I/II trial assessed that Napabucasin with pembrolizumab treatment showed antitumor activity for patients with metastatic colorectal cancer (Kawazoe et al., 2020). Li et al. (2015) also found that Napabucasin selectively targets cancer stem cells without affecting normal hematopoietic stem cells.

Bone marrow mesenchymal stem cells (BMSCs) are the major stem cell for osteogenesis. According to our previous studies, STAT3 significantly regulated rodent bone anabolism and was an alternative molecular target for the treatment of bone diseases (Xu et al., 2020). Similarly, researchers reported that inactivation of STAT3 in osteoblasts disrupted bone formation (Itoh et al., 2006; Zhou et al., 2011). Nevertheless, in the reported pre-clinical studies about Napabucasin, the most frequently reported adverse events were grade 1–2 gastrointestinal toxicities, diarrhea, nausea, vomiting, abdominal cramps, and fatigue (Langleben et al., 2013; Bekaii-Saab et al., 2017; Bendell et al., 2017). Currently, to the best of our knowledge, no study has ever mentioned any effects in the skeletal system, and there is little evidence *in vitro* or *in vivo* on the effects of napabucasin in bone metabolism.

As the number of preclinical studies about Napabucasin in cancer treatment has increased, the latent side effects on bone metabolism should not be ignored. The present study examined the effects of Napabucasin on mouse bone homeostasis and determined its underlying mechanisms *in vivo* and *in vitro*. Our results suggest that monitoring bone mass may help improve the quality of life and lengthen the life spans of cancer patients treated by Napabucasin.

MATERIALS AND METHODS

Cell Culture and Osteoblastic Differentiation

BMSCs were washed out from the femurs and tibias of 4-week-old wild-type (WT) C57BL/6 mice as previously described (Yang et al., 2019). The bone marrow was flushed with a 10-ml injection of α-MEM (Corning, Cat#: 10-022-CV). BMSCs were cultured in α-MEM with 10% fetal bovine serum (Gibco, Cat#: 10099-141) and 1% penicillin-streptomycin (Gibco, Cat#: 15140122) at 37°C in 5% CO_2. The medium was refreshed every 3 days until BMSCs reached 70–80% confluence. The cells were passaged and seeded into six-well plates at a density of 1.0×10^5 cells per well and treated with 0.01, 0.1, 1, or 2 μM Napabucasin (Selleck, Cat#: S7977), with 1 μL/mL DMSO (Cyagen, Cat#: MUBMX-90021) as control in osteogenic induction medium according to our previous study (Xu et al., 2020).

CCK8 Assay

After BMSCs reached 80–90% confluence, they were treated with Napabucasin at the dose of 0.01, 0.1, 1, or 2 μM, while 1 μL/mL DMSO was used for control cells. A CCK8 kit (Beyotime, Cat#: C0037) was used to measure cell proliferation and survival of treated BMSCs on days 1, 3, 5, and 7 following the manufacturer's protocol.

Annexin V FITC Apoptosis Assay

An Annexin V FITC Apoptosis Detection Kit (Beyotime, Cat#: C1062S) was used to assess the effect of Napabucasin on apoptosis in BMSCs. After BMSCs reached 80–90% confluence, they were treated with Napabucasin at the dose of 0.01, 0.1, 1, or 2 μM for 2 days according to previous study (Xu et al., 2020), while DMSO was used as a control. Cells were collected and analyzed using the FACSCalibur system (BD Biosciences).

Western Blot Assay

Cells were lysed with SDS lysis buffer (Beyotime, Cat#: P0013G) and mixed with protease and phosphatase inhibitors (Thermo Fisher Scientific). Western blot assays were performed using a previously described protocol (Yang et al., 2019). The primary antibodies used were as follows: β-actin (Cell Signaling Technology, Cat#: 3700), STAT3 (Cell Signaling Technology, Cat#: 9139), and pSTAT3 (Cell Signaling Technology, Cat#: 9145). After incubation, the membranes were washed and incubated in HRP-linked IgG secondary antibody (Beyotime, Cat#: A0239, A0258). An enhanced chemiluminescence detection system was used to visualize the protein.

Alkaline Phosphatase and Alizarin Red Staining

BMSCs were fixed in 4% paraformaldehyde at room temperature for 10 min and stained with alkaline phosphatase (ALP) working solution (Beyotime) at 37°C in the dark for 2 h or with 40 mmol/L Alizarin Red (Cyagen, Cat#: MUBMX-90021) for 15 min following the manufacturer's protocol.

RT-PCR Assay

RNA was extracted using TRIzol reagent (Takara, Cat#: 9109) and reverse-transcribed into cDNA using a Prime Script RT master kit (Takara, Cat#: RR036A). The primers used were as follows. β-Actin sense: 5′-CCCATACCCACCATCACACC-3′, β-Actin antisense: 5′-CACCCGCGAGTACAACCTTC-3′; Runx2 sense: 5′-CCTCCAGCATCCCTTTCTT-3′, Runx2 antisense: 5′-CCTCCAGCATCCCTTTCTT-3′; Col1a1 sense: 5′-GCTCCTCTTAGGGGCCACT-3′, Col1a1 antisense: 5′-CCACGTCTCACCATTGGGG-3′; osteocalcin (Ocn) sense: 5′-GAATAGACTCCGGCGCTACC-3′, Ocn antisense: 5′-AG CTCGTCACAATTGGGGTT-3′; Alp sense: 5′-CGGGACTGG TACTCGGATAA-3′, Alp antisense: 5′-ATTCCACGTCGGTT CTGTTC-3′.

Luciferase Assay

HEK 293T cells were seeded into 24-well plates. Plasmids containing an Ocn promoter-driven pGL3-based luciferase

reporter gene, along with plasmids encoding Stat3 and Renilla luciferase, were transfected into cells with Lipofectamine 2000 (Thermo Fisher Scientific, Cat#: 11668019) according to a previously reported protocol (Xu et al., 2020). Cells were treated with different concentrations of Napabucasin (0.1, 1, or 10 nM). At 36–48 h after transfection, cells were collected and lysed and the supernatants were used for dual-luciferase reporter assays according to the manufacturer's instructions (Promega, Cat#: E1960).

Cleavage Under Targets and Tagmentation (CUT&Tag) and Quantitative RT-PCR Analysis

The CUT&Tag assay was performed with the Hyperactive *In Situ* ChIP Library Prep Kit for Illumina (Vazyme, Cat#: TD901-01) as previously described according to the manufacturer's instructions (Kaya-Okur et al., 2019; Dan et al., 2020). Briefly, C3H10 T1/2 cells treated with 0.1 μM Napabucasin or vehicle control were washed with wash buffer containing 1× protease inhibitor cocktail (Sigma-Aldrich, Cat#: 5056489001). Cell pellets were resuspended in wash buffer and Concanavalin A-coated magnetic beads were added and incubated at room temperature. Bead-bound cells were resuspended in antibody buffer (20 mM HEPES pH 7.5, 150 mM NaCl, 0.5 mM spermidine, 0.05% digitonin, 2 mM EDTA, 0.1% BSA and 1× protease inhibitor cocktail). Then, 1 μg of STAT3 antibody (Cell Signaling Technology, Cat#: D3Z2G) or normal IgG (Cell Signaling Technology, Cat#: 2729) was added and incubated overnight at 4°C. After removing the primary antibody, 1 μg of secondary antibody (Vazyme, Cat#: ab206) diluted in Dig-wash buffer (20 mM HEPES pH 7.5, 150 mM NaCl, 0.5 mM spermidine, 0.05% digitonin and 1× protease inhibitor cocktail) was added and incubated at room temperature. The cells were then incubated with Hyperactive pG-Tn5 Transposase diluted in Dig-300 buffer (20 mM HEPES pH 7.5, 300 mM NaCl, 0.5 mM spermidine, 0.01% digitonin and 1× protease inhibitor cocktail) at room temperature for 1.5 h. Finally, the cells were resuspended in tagmentation buffer (10 mM $MgCl_2$ in Dig-300 buffer) and incubated at 37°C for 1.5 h. DNA was purified using phenol-chloroform-isoamyl alcohol extraction and ethanol precipitation after RNase A treatment. Precipitated DNA was detected by quantitative RT-PCR with specific primers. The primers for the STAT3 binding site in the Ocn promoter were 5′GGATACCCCATGTTCCCAGC3′ and 5′TGCAGCCCGTCTACTGGAGC3′.

Animals and Treatment

Non-pregnant female C57BL/6 mice (4 weeks old, $n = 22$) were purchased from Charles River Laboratories (Shanghai, China). All mice were bred and maintained under specific pathogen-free conditions in a temperature-controlled room (21°C) with a 12 h light/12 h dark cycle and were provided food and water *ad libitum*. Mice were randomly divided into two groups as follows: Control group received injections of 5% DMSO + 40% PEG 300 + 5% Tween 80 + ddH2O (i.p.) every 2 days for 1 month; Napabucasin group received injection of Napabucasin (Selleck, Cat#: S7977; 10 mg/kg, i.p.) every 2 days for 1 month according to previous studies (Guha et al., 2019).

Ten mice were used for micro-CT analysis and were randomly divided into two groups: Control group ($n = 5$) and Napabucasin group ($n = 5$). Six mice were used for histological investigation and Alizarin red and calcein double labeling, and were divided into two groups: Control group ($n = 3$) and Napabucasin group ($n = 3$). Six mice were used for cell culture, $n = 3$ each for the control and Napabucasin groups.

All animal experiments were performed according to protocols approved by the animal care committee guidelines of the Shanghai Jiao Tong University biomedical ethics committee for laboratory animal welfare ethics.

Micro-CT

Mice (8 weeks old) were euthanized with carbon dioxide, and the femora were dissected and stored in ethanol, then scanned with a micro-CT scanner (Scanco Medical AG, Cat#: vivaCT 80). A 1-mm width of trabecular bone close to the distal growth plate of the femur and a 1-mm-wide section of cortical bone from the middle of the femur were reconstructed three-dimensionally and analyzed according to a previously described protocol (Yang et al., 2020). The microarchitectural parameters included in this experiment were bone mineral density (BMD), bone volume fraction (BV/TV), trabecular thickness (Tb.Th.), trabecular number (Tb.N.), trabecular separation (Tb.Sp.), and cortical thickness (Ct.Th.).

Histological Analysis

Femurs from 8-week-old mice were fixed with 4% paraformaldehyde for 48 h. Specimens were then decalcified in 15% EDTA with an ultrasonic decalcifier for 3 weeks. Specimens were embedded in paraffin and cut into consecutive 4-μm sections. Paraffin sections were stained with hematoxylin and eosin according to a previously described protocol (Yang et al., 2020). Tartrate-resistant acid phosphatase (TRAP) staining was performed using a TRAP staining kit (MultiSciences, Cat#: 70-CK20203) according to the manufacturer's protocol.

Immunofluorescence Staining

Immunofluorescence staining was performed as described in a previous protocol (Zou et al., 2013). Sections were de-waxed and rehydrated, followed by antigen retrieval with proteinase K at 37°C for 20 min. Sections were blocked in PBS with 10% horse serum for 1 h and then incubated overnight at 4°C with antibodies against pSTAT3 (Cell Signaling Technology, Cat#: 9145), OCN (Santa Cruz Biotechnology, Cat#: sc-390877) and cathepsin K (CTSK; Santa Cruz Biotechnology, Cat#: sc-48353). Goat anti-mouse cy3 (Molecular Probes, Cat#: M30010) and goat anti-rabbit cy3 (Molecular Probes, Cat#: A10520) were used as secondary antibodies for 1 h at room temperature. DAPI (Sigma, Cat#: D8417) was used for counterstaining. Sections were mounted on slides with anti-fluorescence mounting medium (Dako, Cat#: S3023), and images were acquired with a confocal microscope (Leica, Cat#: Leica TCS SP8). The number of positively stained cells was counted in the whole femur

subchondral bone area in each specimen according to previous study (Cui et al., 2016).

Alizarin Red and Calcein Double Labeling

Mice received injections of calcein (Sigma, Cat#: C0875) and Alizarin Red (Sigma, Cat#: A5533) 7 and 3 days before euthanasia, respectively. Isolated femurs and tibias were dehydrated and embedded in polymethylmethacrylate. Specimens then were cut into continuous 5-μm thick sections with a rotary microtome. Images were captured as previously described (Yang et al., 2020).

Statistical Analysis

All quantitative data were expressed as means ± S.D. Two groups were compared using independent-samples *t*-tests. One-way analysis of variance was performed for multiple comparisons. $P < 0.05$ was considered a significant difference. Data analysis was performed with SPSS 16.0 analysis software.

RESULTS

Effects of Napabucasin on Proliferation and Apoptosis of BMSCs

To investigate the effects of Napabucasin on BMSCs, we first isolated BMSCs from 4-week-old WT mice and cultured them with osteoblast differentiation medium, then treated them with different concentrations of Napabucasin to test their rates of proliferation and apoptosis. The growth curve of BMSCs was determined by CCK8 assay. As shown in **Figure 1A**, high doses of Napabucasin (1 or 2 μM) slowed BMSC proliferation in a dose-dependent manner. Furthermore, apoptosis assays of BMSCs after 2 days of Napabucasin treatment showed a concentration-dependent increase in the rate of apoptosis, especially at doses of 1 or 2 μM (**Figure 1B**). Therefore, lower concentrations of Napabucasin (0.01 or 0.1 μM) were used in the following experiments to explore the effects of Napabucasin on osteogenesis of BMSCs.

Napabucasin Impaired Osteogenic Differentiation of BMSCs

Subsequently, we probed the protein expression of STAT3 and pSTAT3 in BMSCs treated with Napabucasin at the concentrations of 0.01 or 0.1 μM. Western blotting assay (**Figure 2A**) and immunofluorescence staining (**Figures 2B,C**) showed that Napabucasin inhibited pSTAT3 expression but not STAT3 in BMSCs after 12 h. We then examined the effects on osteogenic differentiation of BMSCs caused by Napabucasin treatment. ALP staining on day 7 of BMSC treatment with Napabucasin showed diminished ALP activity at Napabucasin concentrations of 0.01 or 0.1 μM compared with the control group (**Figure 2D**). Moreover, Alizarin Red staining on day 14 demonstrated fewer calcified nodules with Napabucasin at concentrations of 0.01 or 0.1 μM compared with the control group (**Figure 2E**). Quantitative RT-PCR showed downregulated expression of the osteogenic marker genes *Runx2*, *Col I*, *Alp*, and *osteocalcin (Ocn)* (**Figures 2F–I**). All these data indicated that Napabucasin impaired osteogenic differentiation of BMSCs, but the mechanism underlying Napabucasin regulation of osteogenic differentiation of BMSCs was still not clear.

Napabucasin Modulated *Ocn* Transcription Through STAT3

As Xu et al. reported previously, STAT3 regulated osteoblast differentiation of BMSCs by activating transcription of osteogenic gene *Ocn* (Xu et al., 2020). In this experiment, as shown in **Figure 2I**, the mRNA expression of *Ocn* was greatly downregulated after Napabucasin treatment. Immunofluorescence investigation of Napabucasin-treated BMSCs also showed decreased expression of OCN (**Figures 3A,B**). Therefore, in this experiment, we intended to test if STAT3-induced Ocn activation was the reason of impaired osteogenic differentiation under Napabucasin treatment. We then analyzed the promoter of *Ocn* and found one potential STAT3 binding site (**Figure 3C**). Next, we transfected promoter-driven luciferase reporters encoding *Ocn* and STAT3 into HEK 293T cells. Luciferase assays confirmed that STAT3 promoted *Ocn* transcription. Meanwhile, when we added Napabucasin to HEK 293T cells to block the function of STAT3, the enhancement of *Ocn* transcription was strongly inhibited (**Figure 3D**). The reduced binding of STAT3 to the *Ocn* promoter was validated by CUT & Tag-qPCR in C3H10 T1/2 cells treated with 0.1 μM Napabucasin (**Figure 3E**). Therefore, we assumed that Napabucasin modulated *Ocn* transcription through STAT3, eventually affecting osteogenic differentiation of BMSCs.

Napabucasin Injection Caused Osteopenia in Mice

To directly investigate the *in vivo* effect of Napabucasin on bone metabolism, we injected Napabucasin into 4-week-old female mice. In our experiment, after injecting Napabucasin (10 mg/kg) for 1 month, the terminal mouse body weights were greatly reduced in the Napabucasin group compared with mice in the control group (**Figure 4A**). As shown in **Figures 4B,C**, the phosphorylation of STAT3 was obviously blocked after one-month of Napabucasin injections in our immunofluorescence investigation. H&E staining shown that Napabucasin injection-induced bone loss in the femora (**Figure 4D**). Then we assessed the bone mass of femora from mice injected with vehicle or Napabucasin by micro-CT. The bone loss of trabecular bone in the Napabucasin-injected group was shown by reconstructed micro-CT-scanned images (**Figure 4E**), but the bone mass of cortical bone did not appear to be different (**Figure 4F**). Quantitative microarchitectural parameters were measured to analyze the quantity and quality of bone in mice receiving Napabucasin injection or vehicle. Parameters such as BMD (**Figure 4G**), BV/TV (**Figure 4H**), Tb.Th. (**Figure 4I**), and Tb.N. (**Figure 4J**) were apparently reduced after 1-month injections of Napabucasin, while Tb.Sp. (**Figure 4K**) increased. However, Ct.Th. (**Figure 4L**) did not differ in this experiment. These results

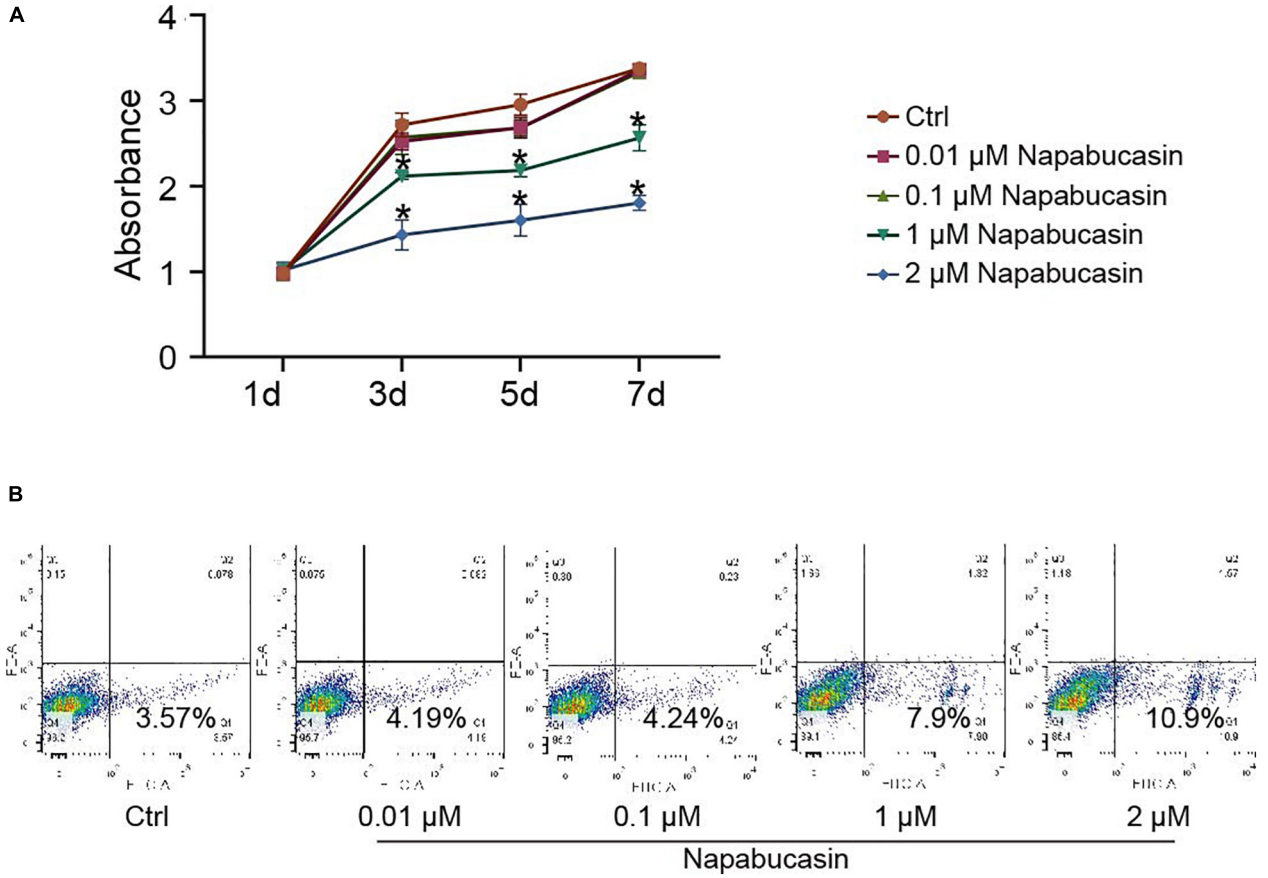

FIGURE 1 | Effects of Napabucasin on proliferation and apoptosis of BMSCs. **(A)** CCK8 assay of BMSCs after treatment with DMSO or with different concentrations of Napabucasin for 1, 3, 5, and 7 days. $N = 5$. Data are represented as means ± S.D. $^*P < 0.05$. **(B)** Apoptosis assay of BMSCs treated with DMSO or with different concentrations of Napabucasin for 2 days.

implied that the STAT3 inhibitor Napabucasin decreased the bone mass of WT mice.

Napabucasin Impaired Bone Formation Without Influencing Bone Resorption

To explore the reason for bone loss caused by STAT3 inactivation *in vivo*, we inspected the bone metabolism of mice. Unbalanced bone metabolism is usually the result of abnormal bone formation and/or bone resorption. The mineral apposition rate (MAR) was measured by calcein and Alizarin Red double labeling (**Figure 5A**), which represented the new bone formation rate. As shown, after 1 month of Napabucasin injections, the MAR of trabecular bone from tibiae apparently decreased, indicating that Napabucasin impaired bone mineralization in the mice (**Figure 5B**). The downregulated expression of osteogenic marker OCN in immunofluorescence staining also implied impaired osteogenesis (**Figures 5C,D**). TRAP staining was performed to detect the change in osteoclastogenesis in femora from Napabucasin-injected mice (**Figure 5E**). The number of $TRAP^+$ multi-nucleated osteoclasts from femora was not significantly influenced by Napabucasin injections (**Figure 5F**). Moreover, the immunofluorescence investigation of CTSK expression was fully consistent with that of TRAP staining (**Figures 5G,H**). In conclusion, Napabucasin-induced bone loss after 1 month of injections was the result of impaired bone formation.

DISCUSSION

The promising novel STAT3 inhibitor Napabucasin has undergone several preclinical studies (Hubbard and Grothey, 2017; Li et al., 2020; Nagaraju et al., 2020). Considering that the classic STAT3 trigger point of the immune system was also a significant signal in bone homeostasis (Li, 2013; Yang et al., 2019), we had good reason to be concerned that long-time anti-tumor treatment with Napabucasin would also affect the skeletal system of patients, which has never been reported to our knowledge.

Considering that Napabucasin can selectively target cancer stem cells (Li et al., 2015), we first tested the effect of Napabucasin on BMSCs as the major stem cell responsible for osteogenesis. Through CCK−8 and apoptosis assays, we determined that the optimal concentration for the effect of Napabucasin on BMSCs was 0.01–0.1 μM. Downregulated osteogenic differentiation of BMSCs treated with Napabucasin was determined by ALP

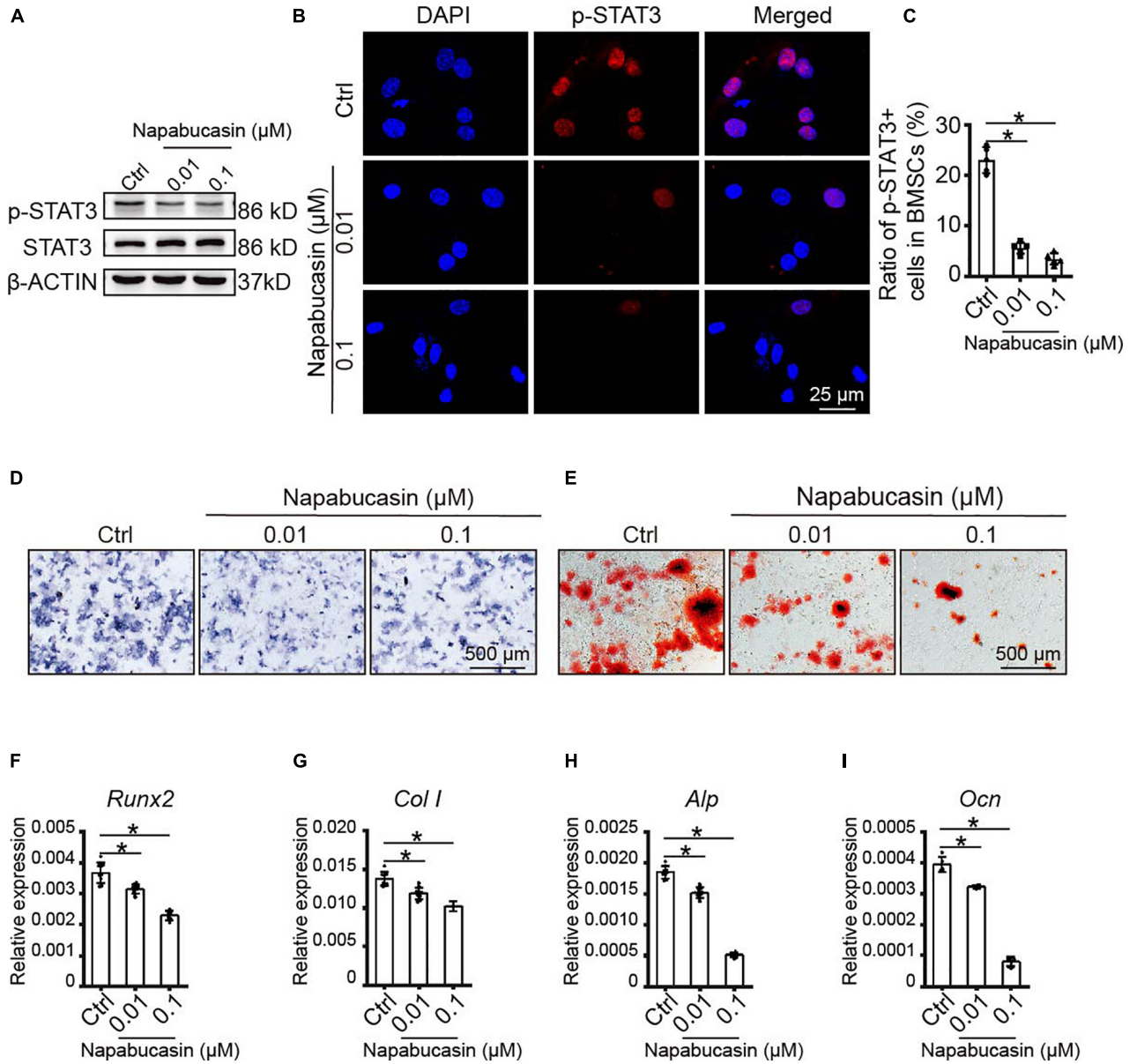

FIGURE 2 | Napabucasin impaired osteoblast differentiation of WT BMSCs. **(A)** Western blotting assay of STAT3 and pSTAT3 expression in BMSCs treated with DMSO or with different concentrations of Napabucasin for 12 h. **(B)** Representative immunofluorescence image of pSTAT3 expression in BMSCs after exposure to Napabucasin. **(C)** Number of pSTAT3^{+} cells were counted. $N = 5$. **(D)** ALP staining of BMSCs after osteoblast differentiation for 7 days following treatment with DMSO or with different concentrations of Napabucasin. **(E)** Alizarin Red staining of BMSCs after osteoblast differentiation 14 days following treatment with DMSO or with different concentrations of Napabucasin. **(F–I)** Osteoblast-specific expression of genes *Runx2*, *Col I*, *Alp*, *and Ocn* in BMSCs during osteoblast differentiation after treatment with DMSO or with different concentrations of Napabucasin for 7 days. $N = 9$. Data are represented as means ± S.D. $^{*}P < 0.05$.

staining and Alizarin Red staining, complemented by qPCR analysis of osteogenic marker genes. All of these data indicated that Napabucasin impaired the differentiation of BMSCs, but the underlying mechanism remained unknown.

It is known that activated STAT3 is phosphorylated and translocates to the nucleus to bind target-gene promoter sequences (Bromberg, 2002). Numerous key molecular markers and genes responsible for cancer stem cell proliferation were found to be downregulated by Napabucasin treatment (Li et al., 2015). As for BMSCs, according to our previous study, STAT3 directly bound to the Ocn promoter and subsequently activated its transcription (Xu et al., 2020). Importantly, the STAT3-activated transcription of *Ocn* could be obstructed by pharmaceuticals. Immunofluorescence investigation and qPCR showed an obvious decrease of OCN expression in Napabucasin-treated BMSCs. Therefore, in this experiment, we analyzed the role of Napabucasin on *Ocn* promoter activity using a luciferase reporter system and our data showed that Napabucasin affected

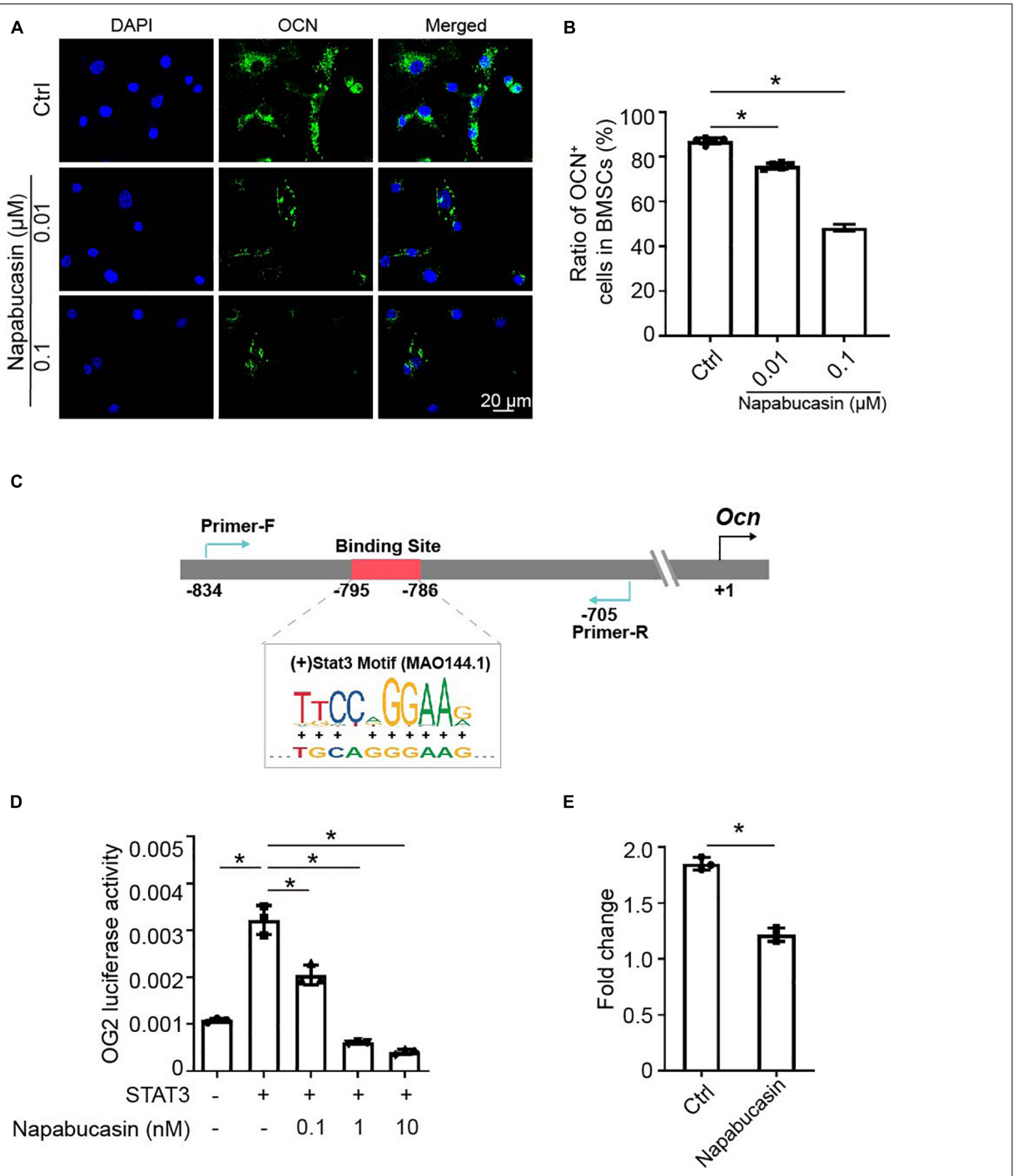

FIGURE 3 | Napabucasin impaired *Ocn* transcription through STAT3. **(A)** Representative immunofluorescence image of OCN expression in BMSCs after exposure to Napabucasin. **(B)** Number of OCN^+ cells were counted. $N = 5$. Data are represented as means ± S.D. **(C)** Illustration of predicted STAT3 binding sites in the *Ocn* promoter. **(D)** 293T cells were transfected with STAT3 and *Ocn* luciferase constructs and treated with DMSO or with different concentrations of Napabucasin. After 48 h, luminescent signals were detected to represent reporter activity. $N = 5$. Data are represented as means ± S.D. **(E)** CUT & Tag and subsequent quantitative PCR analysis of STAT3 showing decreased occupancy of the OCN promoter in C3H10 T1/2 cells treated with Napabucasin. Data are shown as fold enrichments to the IgG control. Data are represented as means ± S.D. $^*P < 0.05$.

Ocn transcriptional activity through STAT3 signaling. Moreover, the reduced binding of STAT3 to the *Ocn* promoter was validated by CUT & Tag-qPCR in BMSCs treated with Napabucasin. Therefore, we assumed that Napabucasin modulated *Ocn* transcription through STAT3, eventually affecting osteogenic differentiation of BMSCs.

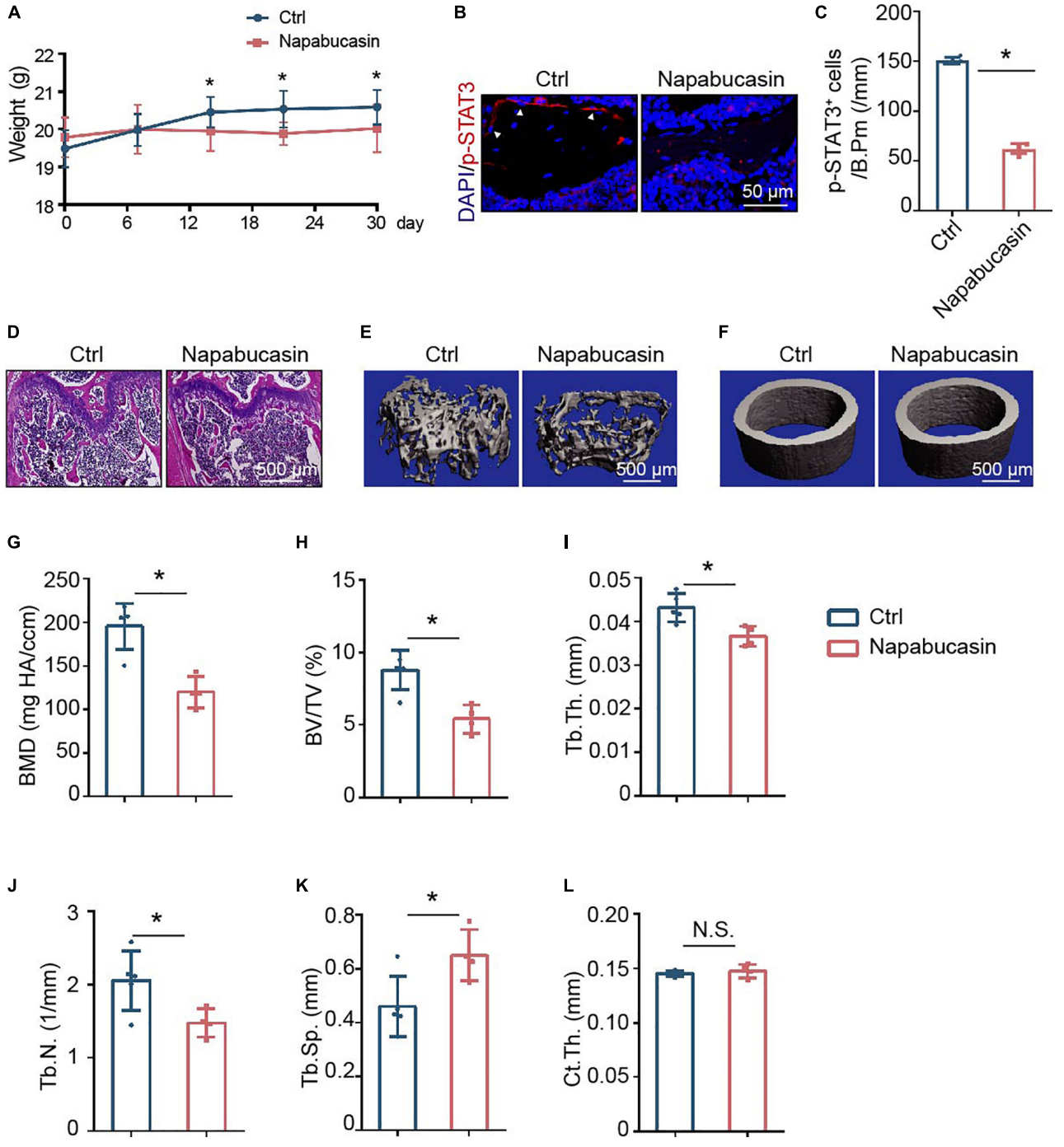

FIGURE 4 | Napabucasin injection caused osteoporosis in mice. **(A)** Representative immunofluorescence image of pSTAT3 staining in the femurs of mice injected with vehicle or Napabucasin (10 mg/kg). **(B)** Number of pSTAT3^{+} cells were counted. $N = 5$. Data are represented as means ± S.D. $^{*}P < 0.05$. **(C)** Body weights of mice injected with vehicle or Napabucasin (10 mg/kg) were recorded on different days. **(D,E)** Three-dimensional micro-CT reconstruction images of trabecular bone **(D)** and cortical bone **(E)** of femora from the above mice. **(F–K)** Quantitative microarchitectural parameters from micro-CT. $N = 5$. Data are represented as means ± S.D. $^{*}P < 0.05$. **(L)** HE staining of femora from the above mice.

In the present study, we found that 4-week Napabucasin injections induced mouse bone loss as a result of impaired osteogenesis. Initially, micro-CT analysis confirmed the bone loss of Napabucasin-injected mice, but the change in bone metabolism required further investigation. Interleukin-6 (IL-6)/Janus kinase (JAK)-2/STAT3 signaling has been

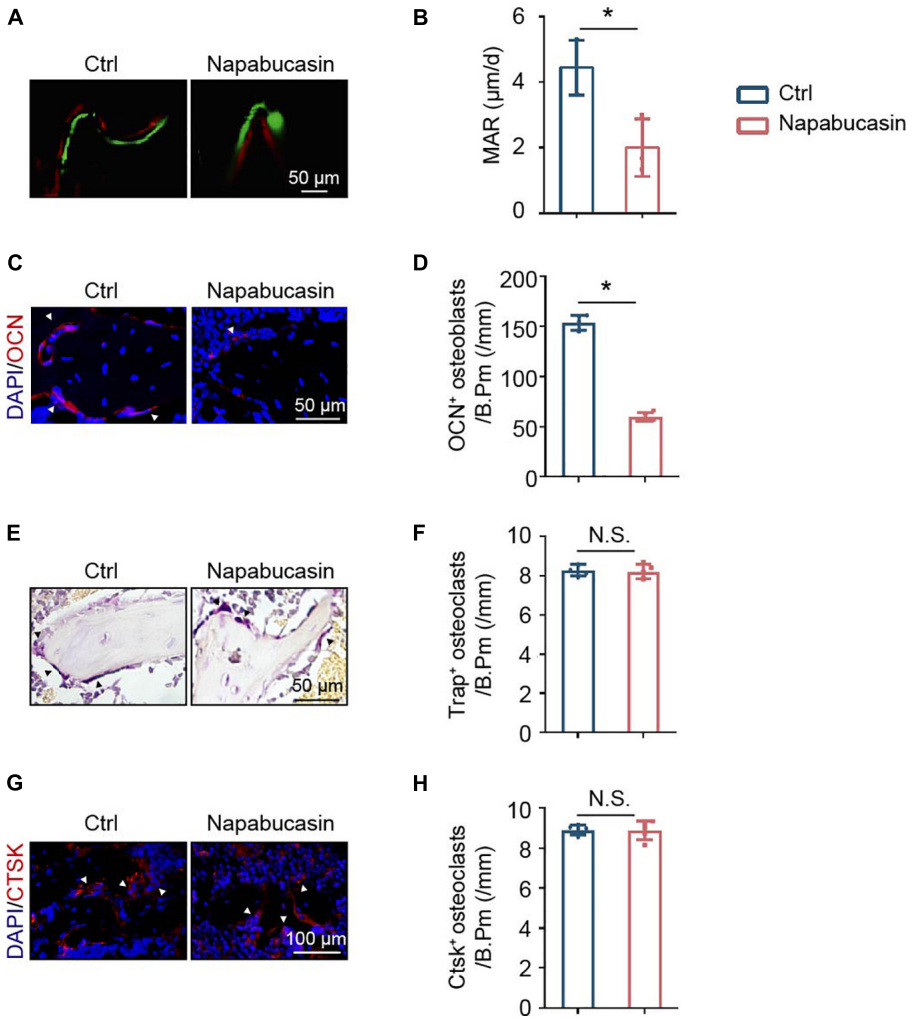

FIGURE 5 | Napabucasin impaired bone formation but did not change bone resorption. **(A)** Osteogenic activity in femora of mice determined by calcein and Alizarin Red double staining. **(B)** Mineral apposition rate (MAR) detected by histomorphometric analysis. $N = 3$. **(C)** Representative immunofluorescence image of OCN staining in femurs from the above mice. **(D)** Number of OCN^+ cells were counted. $N = 5$. **(E)** TRAP staining of femora from the above mice. **(F)** Number of $TRAP^+$ multi-nucleated osteoclasts were counted. $N = 5$. **(G)** Representative immunofluorescence image of CTSK staining in the femurs from the above mice. **(H)** Number of $CTSK^+$ cells were counted. $N = 5$. Data are represented as means ± S.D. $^*P < 0.05$.

widely studied in anti-tumor therapy and participates in the differentiation of osteoblasts. STAT3 is the downstream gene of multiple drugs inhibiting IL-6 and JAK-2 (Duplomb et al., 2008; Jo et al., 2018). In addition, the chemical inhibition of STAT3 phosphorylation abolished Icaritin-induced increases in osteoblast proliferation and function (Lim et al., 2017). In the present experiment, decreased bone formation, which was detected by calcein and Alizarin Red double labeling, was also considered to be the main reason for the aforementioned bone loss. Regarding bone catabolism, the increase of Tyrosine (705) phosphorylation of STAT3 upon IL-6 stimulation was reported to lead to the formation of macrophages instead of osteoclasts (Cheng et al., 2017; Li et al., 2018). According to our previous studies, STAT3 participates in osteoclast differentiation and ablation of Stat3 in osteoclasts resulted in decreased bone resorption *in vivo* (Yang et al., 2019), but in the present experiment, bone resorption was obviously not influenced by Napabucasin injection.

Clinical data shows that osteopenia is often a long-term complication of anti-neoplastic treatment (Aisenberg et al., 1998). As a first-in-class cancer stemness inhibitor, the side effects of Napabucasin should not be underestimated. Our research focused on the side effects of Napabucasin on the skeletal system, which may be helpful for monitoring bone mass over time. Napabucasin is an oral drug, and further research should be undertaken using oral administration to provide results with greater clinical value.

In conclusion, our data has provided evidence of an effect of Napabucasin on mouse bone homeostasis and determined its underlying mechanisms *in vivo* and *in vitro* involve modulation of STAT3. The latent side effects on bone metabolism after long-time anti-tumor therapy with

Napabucasin should therefore be considered before patient treatment decisions.

DATA AVAILABILITY STATEMENT

The datasets generated for this study can be found in the online repositories. The names of the repository/repositories and accession number(s) can be found in the article/supplementary material.

ETHICS STATEMENT

The animal study was reviewed and approved by the Animal Experimental Ethical Inspection Shanghai Ninth People's Hospital affiliated to Shanghai Jiao Tong University, School of Medicine.

AUTHOR CONTRIBUTIONS

XH, AJ, and XW designed the experiment. XH, AJ, XW, HX, MC, and XG collected and analyzed the data. LJ, YY, and QD contributed to the interpretation of the results and critical revision of the manuscript and approved the final version of the manuscript. All authors agreed to be accountable for the content of this work.

FUNDING

This work was supported in part by grants from the National Natural Science Foundation of China (NSFC) (82071083, 81870740, 81570950, and 81800949), Program of Shanghai Academic/Technology Research Leader (20XD1422300), Shanghai Summit and Plateau Disciplines, the SHIPM-mu fund from the Shanghai Institute of Precision Medicine, Shanghai Ninth People's Hospital, Shanghai Jiao Tong University School of Medicine (JC201809), the Incentive Project of High-Level Innovation Team for Shanghai Jiao Tong University School of Medicine, the Crossdisciplinary Research Fund of Shanghai Ninth People's Hospital, Shanghai Jiao Tong university School of Medicine (JYJC201902), Innovative Research Team of High-Level Local Universities in Shanghai (SSMU-ZLCX20180501), and the Students Innovation Training Program (1420Y504 and 1420Y507). And LJ is a scholar of the Outstanding Youth Medical Talents, Shanghai "Rising Stars of Medical Talent" Youth Development Program, and the "Chen Xing" project from Shanghai Jiaotong University.

REFERENCES

Aigner, P., Just, V., and Stoiber, D. (2019). STAT3 isoforms: alternative fates in cancer? *Cytokine* 118, 27–34. doi: 10.1016/j.cyto.2018.07.014

Aisenberg, J., Hsieh, K., Kalaitzoglou, G., Whittam, E., Heller, G., Schneider, R., et al. (1998). Bone mineral density in young adult survivors of childhood cancer. *J. Pediatr. Hematol. Oncol.* 20, 241–245.

Bekaii-Saab, T. S., Li, C.-P., Okusaka, T., O'Neil, B. H., Reni, M., Tabernero, J., et al. (2017). CanStem111P trial: a phase III study of napabucasin (BBI-608) plus nab-paclitaxel (nab-PTX) with gemcitabine (gem) in adult patients with metastatic pancreatic adenocarcinoma (mPDAC). *J. Clin. Oncol.* 35:TS4148. doi: 10.1200/JCO.2017.35.15_suppl.TPS4148

Bendell, J. C., O'Neil, B. H., Starodub, A., Jonker, D. J., Halfdanarson, T. R., Edenfield, W. J., et al. (2017). Cancer stemness inhibition and chemosensitization: phase 1b/II study of cancer stemness inhibitor napabucasin (BBI-608) with FOLFIRI +/- bevacizumab (Bev) administered to colorectal cancer (CRC) patients (pts). *J. Clin. Oncol.* 35:593. doi: 10.1200/JCO.2017.35.4_suppl.593

Bromberg, J. (2002). Stat proteins and oncogenesis. *J. Clin. Invest.* 109, 1139–1142. doi: 10.1172/jci15617

Cheng, X., Wan, Q. L., and Li, Z. B. (2017). AG490 suppresses interleukin-34-mediated osteoclastogenesis in mice bone marrow macrophages. *Cell Biol. Int.* 41, 659–668. doi: 10.1002/cbin.10771

Cong, F., Liu, J., Wang, C., Yuan, Z., Bi, L., Liang, J., et al. (2017). Ginsenoside Rb2 inhibits osteoclast differentiation through nuclear factor-kappaB and signal transducer and activator of transcription protein 3 signaling pathway. *Biomed. Pharmacother.* 92, 927–934. doi: 10.1016/j.biopha.2017.05.115

Cui, Z., Crane, J., Xie, H., Jin, X., Zhen, G., Li, C., et al. (2016). Halofuginone attenuates osteoarthritis by inhibition of TGF-β activity and H-type vessel formation in subchondral bone. *Ann. Rheum. Dis.* 75, 1714–1721. doi: 10.1136/annrheumdis-2015-207923

Dan, L., Liu, L., Sun, Y., Song, J., Yin, Q., Zhang, G., et al. (2020). The phosphatase PAC1 acts as a T cell suppressor and attenuates host antitumor immunity. *Nat. Immunol.* 21, 287–297. doi: 10.1038/s41590-019-0577-9

Duplomb, L., Baud'huin, M., Charrier, C., Berreur, M., Trichet, V., Blanchard, F., et al. (2008). Interleukin-6 inhibits receptor activator of nuclear factor kappaB ligand-induced osteoclastogenesis by diverting cells into the macrophage lineage: key role of Serine727 phosphorylation of signal transducer and activator of transcription 3. *Endocrinology* 149, 3688–3697. doi: 10.1210/en.2007-1719

Grothey, A., Shah, M. A., Yoshino, T., Van Cutsem, E., Taieb, J., Xu, R., et al. (2017). CanStem303C trial: a phase III study of napabucasin (BBI-608) in combination with 5-fluorouracil (5-FU), leucovorin, irinotecan (FOLFIRI) in adult patients with previously treated metastatic colorectal cancer (mCRC). *J. Clin. Oncol.* 35:TS3619. doi: 10.1200/JCO.2017.35.15_suppl.TPS3619

Guha, P., Gardell, J., Darpolor, J., Cunetta, M., Lima, M., Miller, G., et al. (2019). STAT3 inhibition induces Bax-dependent apoptosis in liver tumor myeloid-derived suppressor cells. *Oncogene* 38, 533–548. doi: 10.1038/s41388-018-0449-z

Hubbard, J. M., and Grothey, A. (2017). Napabucasin: an update on the first-in-class cancer stemness inhibitor. *Drugs* 77, 1091–1103. doi: 10.1007/s40265-017-0759-4

Itoh, S., Udagawa, N., Takahashi, N., Yoshitake, F., Narita, H., Ebisu, S., et al. (2006). A critical role for interleukin-6 family-mediated Stat3 activation in osteoblast differentiation and bone formation. *Bone* 39, 505–512. doi: 10.1016/j.bone.2006.02.074

Jo, S., Wang, S. E., Lee, Y. L., Kang, S., Lee, B., Han, J., et al. (2018). IL-17A induces osteoblast differentiation by activating JAK2/STAT3 in ankylosing spondylitis. *Arthritis Res. Ther.* 20:115. doi: 10.1186/s13075-018-1582-3

Kawazoe, A., Kuboki, Y., Shinozaki, E., Hara, H., Nishina, T., Komatsu, Y., et al. (2020). Multicenter phase I/II trial of napabucasin and pembrolizumab in patients with metastatic colorectal cancer (EPOC1503/SCOOP trial). *Clin. Cancer Res.* 26, 5887–5894. doi: 10.1158/1078-0432.ccr-20-1803

Kaya-Okur, H. S., Wu, S. J., Codomo, C. A., Pledger, E. S., Bryson, T. D., Henikoff, J. G., et al. (2019). CUT&Tag for efficient epigenomic profiling of small samples and single cells. *Nat. Commun.* 10:1930. doi: 10.1038/s41467-019-09982-5

Langleben, A., Supko, J. G., Hotte, S. J., Batist, G., Hirte, H. W., Rogoff, H., et al. (2013). A dose-escalation phase I study of a first-in-class cancer stemness inhibitor in patients with advanced malignancies. *J. Clin. Oncol.* 31:2542. doi: 10.1200/jco.2013.31.15_suppl.2542

Li, C. H., Xu, L. L., Jian, L. L., Yu, R. H., Zhao, J. X., Sun, L., et al. (2018). Stattic inhibits RANKL-mediated osteoclastogenesis by suppressing activation

of STAT3 and NF-kappaB pathways. *Int. Immunopharmacol.* 58, 136–144. doi: 10.1016/j.intimp.2018.03.021

Li, C. H., Zhao, J. X., Sun, L., Yao, Z. Q., Deng, X. L., Liu, R., et al. (2013). AG490 inhibits NFATc1 expression and STAT3 activation during RANKL induced osteoclastogenesis. *Biochem. Biophys. Res. Commun.* 435, 533–539. doi: 10.1016/j.bbrc.2013.04.084

Li, J. (2013). JAK-STAT and bone metabolism. *JAKSTAT* 2:e23930. doi: 10.4161/jkst.23930

Li, X., Wei, Y., and Wei, X. (2020). Napabucasin, a novel inhibitor of STAT3, inhibits growth and synergises with doxorubicin in diffuse large B-cell lymphoma. *Cancer Lett.* 491, 146–161. doi: 10.1016/j.canlet.2020.07.032

Li, Y., Rogoff, H. A., Keates, S., Gao, Y., Murikipudi, S., Mikule, K., et al. (2015). Suppression of cancer relapse and metastasis by inhibiting cancer stemness. *Proc. Natl. Acad. Sci. U.S.A.* 112, 1839–1844. doi: 10.1073/pnas.1424171112

Lim, R., Li, L., Chew, N., and Yong, E. L. (2017). The prenylflavonoid Icaritin enhances osteoblast proliferation and function by signal transducer and activator of transcription factor 3 (STAT-3) regulation of C-X-C chemokine receptor type 4 (CXCR4) expression. *Bone* 105, 122–133. doi: 10.1016/j.bone.2017.08.028

Nagaraju, G. P., Farran, B., Farren, M., Chalikonda, G., Wu, C., Lesinski, G. B., et al. (2020). Napabucasin (BBI 608), a potent chemoradiosensitizer in rectal cancer. *Cancer* 126, 3360–3371. doi: 10.1002/cncr.32954

Xu, H., Zhou, S., Qu, R., Yang, Y., Gong, X., Hong, Y., et al. (2020). Icariin prevents oestrogen deficiency-induced alveolar bone loss through promoting osteogenesis via STAT3. *Cell Prolif.* 53:e12743. doi: 10.1111/cpr.12743

Yang, Y., Chen, Q., Zhou, S., Gong, X., Xu, H., Hong, Y., et al. (2020). Skeletal phenotype analysis of a conditional stat3 deletion mouse model. *J. Vis. Exp.* e61390, doi: 10.3791/61390

Yang, Y., Chung, M. R., Zhou, S., Gong, X., Xu, H., Hong, Y., et al. (2019). STAT3 controls osteoclast differentiation and bone homeostasis by regulating NFATc1 transcription. *J. Biol. Chem.* 294, 15395–15407. doi: 10.1074/jbc.RA119.010139

Zhang, Y., Jin, Z., Zhou, H., Ou, X., Xu, Y., Li, H., et al. (2016). Suppression of prostate cancer progression by cancer cell stemness inhibitor napabucasin. *Cancer Med.* 5, 1251–1258. doi: 10.1002/cam4.675

Zhou, H., Newnum, A. B., Martin, J. R., Li, P., Nelson, M. T., Moh, A., et al. (2011). Osteoblast/osteocyte-specific inactivation of Stat3 decreases load-driven bone formation and accumulates reactive oxygen species. *Bone* 49, 404–411. doi: 10.1016/j.bone.2011.04.020

Zou, W., Greenblatt, M. B., Brady, N., Lotinun, S., Zhai, B., de Rivera, H., et al. (2013). The microtubule-associated protein DCAMKL1 regulates osteoblast function via repression of Runx2. *J. Exp. Med.* 210, 1793–1806. doi: 10.1084/jem.20111790

Conflict of Interest: The authors declare that the research was conducted in the absence of any commercial or financial relationships that could be construed as a potential conflict of interest.

frontiers in Cell and Developmental Biology

REVIEW
published: 25 March 2021
doi: 10.3389/fcell.2021.640388

Biophysical and Biochemical Cues of Biomaterials Guide Mesenchymal Stem Cell Behaviors

Jianjun Li[1,2,3†], Yufan Liu[1,2†], Yijie Zhang[1,2], Bin Yao[1,2,4], Enhejirigala[1,2,5,6], Zhao Li[1], Wei Song[1,2], Yuzhen Wang[1,2,7], Xianlan Duan[1,2,8], Xingyu Yuan[1,2,8], Xiaobing Fu[1,2,9] and Sha Huang[1]**

[1] Research Center for Tissue Repair and Regeneration, Medical Innovation Research Department and the Fourth Medical Center, Chinese PLA General Hospital, PLA Medical College, Beijing, China, [2] PLA Key Laboratory of Tissue Repair and Regenerative Medicine and Beijing Key Research Laboratory of Skin Injury, Repair and Regeneration, Chinese PLA General Hospital, PLA Medical College, Beijing, China, [3] Department of General Surgery, The Sixth Medical Center, Chinese PLA General Hospital, Beijing, China, [4] The Shenzhen Key Laboratory of Health Sciences and Technology, Graduate School at Shenzhen, Tsinghua University, Shenzhen, China, [5] College of Graduate, Tianjin Medical University, Tianjin, China, [6] Institute of Basic Medical Research, Inner Mongolia Medical University, Hohhot, China, [7] Department of Burn and Plastic Surgery, Air Force Hospital of Chinese PLA Central Theater Command, Datong, China, [8] School of Medicine, Nankai University, Tianjin, China, [9] Research Unit of Trauma Care, Tissue Repair and Regeneration, Chinese Academy of Medical Sciences, Beijing, China

OPEN ACCESS

Edited by:
Q. Adam Ye,
Harvard Medical School,
United States

Reviewed by:
Jianxun Ding,
Chinese Academy of Sciences, China
Xingang Wang,
Zhejiang University, China

***Correspondence:**
Xiaobing Fu
fuxiaobing@vip.sina.com
Sha Huang
stellarahuang@sina.com

† These authors have contributed equally to this work and share first authorship

Specialty section:
This article was submitted to Stem Cell Research, a section of the journal Frontiers in Cell and Developmental Biology

Received: *11 December 2020*
Accepted: *09 February 2021*
Published: *25 March 2021*

Citation:
Li J, Liu Y, Zhang Y, Yao B, Enhejirigala, Li Z, Song W, Wang Y, Duan X, Yuan X, Fu X and Huang S (2021) Biophysical and Biochemical Cues of Biomaterials Guide Mesenchymal Stem Cell Behaviors. Front. Cell Dev. Biol. 9:640388. doi: 10.3389/fcell.2021.640388

Mesenchymal stem cells (MSCs) have been widely used in the fields of tissue engineering and regenerative medicine due to their self-renewal capabilities and multipotential differentiation assurance. However, capitalizing on specific factors to precisely guide MSC behaviors is the cornerstone of biomedical applications. Fortunately, several key biophysical and biochemical cues of biomaterials that can synergistically regulate cell behavior have paved the way for the development of cell-instructive biomaterials that serve as delivery vehicles for promoting MSC application prospects. Therefore, the identification of these cues in guiding MSC behavior, including cell migration, proliferation, and differentiation, may be of particular importance for better clinical performance. This review focuses on providing a comprehensive and systematic understanding of biophysical and biochemical cues, as well as the strategic engineering of these signals in current scaffold designs, and we believe that integrating biophysical and biochemical cues in next-generation biomaterials would potentially help functionally regulate MSCs for diverse applications in regenerative medicine and cell therapy in the future.

Keywords: microenvironment, biomaterial, stem cell therapies, cell behavior, tissue engineering

INTRODUCTION

Mesenchymal stem cells (MSCs) have received increasing attention in the field of regenerative medicine and tissue engineering due to their high self-renewal ability and multipotential differentiation lineage, as well as accessibility. Numerous studies have shown that they have been applied in repairing cartilage, bone, adipose, muscle, skin, liver, nerve, and other organs (Han et al., 2019). For instance, Wingate et al. (2012) obtained endothelial and muscle-like cells by culturing MSCs on a three-dimensional (3D) hydrogel; Duarte Campos et al. (2015) can accurately guide

MSCs toward osteogenic and adipogenic differentiation lineage. Those researches both utilized MSCs as seed cells to successfully harvest corresponding tissue cells, which will provide important cell sources and functional support for subsequent clinical treatment.

However, MSC-based tissue engineering still has its own shortcomings that cannot be ignored. One of the problems is that only a few injected MSCs can home and stabilize on the target tissue and play a therapeutic role (De Becker and Riet, 2016). More important, the uncertainty of the differentiation of MSCs after infusion complicates functional reconstruction. Currently, more and more studies documented that biomaterials could be used to protect transplanted MSCs, especially to maintain the viability of MSCs and accurately induce the MSC to differentiate into specific targeted cells. These potentials are mainly attributed to the ability of biomaterials to mimic a multitude and systematic extracellular milieu to guide MSCs in tissue regeneration. For example, engineered scaffolds derived from different biomaterials lead to the satisfying outcome of MSC-based repair in cartilage regeneration due to the excellent biocompatibility and chondrogenesis induction (Le et al., 2020). In addition, Li et al. (2005) fabricated a biodegradable synthetic scaffold that provides an important microenvironment for MSCs in cartilage repair. Subsequently, the cartilage formation was successfully observed on the scaffold, which provided a practical MSC-based tissue engineering approach for cartilage repair. In addition to the cartilage, Prabhakaran et al. (2009) fabricated a nanofibrous scaffold by electrospinning and successfully observed MSC-derived neural morphology and functional cells for nerve repair. Either as guidance cues or as delivery vehicles for controlling the fate of transplanted cells, biomaterials play a major role in the development of MSC-based therapy.

There is no doubt that numerous factors of biomaterials such as the cellular microenvironment can alter MSC behaviors. These factors include biophysical cues (e.g., stiffness, pore size, porosity, and topography) and biochemical cues (e.g., growth factors, growth factor derivatives, small bioactive molecules, and genetic regulators). Many biochemical cues have been determined over the past century, and a number of studies have reported that biochemical stimulation delivered by biomaterials can influence stem cell attachment, proliferation, and differentiation, and is generally effective and easy to deliver. However, biophysical cues have a longer lifetime and can be easily well defined. For instance, Gilbert et al. (2010) have demonstrated that stiffness of substrate has a significant effect on the fate of muscle stem cell. They elucidated that the soft hydrogel substrate mimics physiological elasticity and can obviously promote the propagation of muscle stem cell, and after transplantation, it contributed extensively to muscle regeneration. Gupte et al. (2018) demonstrated that the chondrogenesis and endochondral ossification of bone marrow stromal cells can be modulated by scaffold pore architecture, specifically pore size. Meanwhile, they found that the pore interconnectivity is essential for capillary ingrowth during bone formation. Thus, MSC-based tissue engineering will be greatly enhanced by the biomaterial design. However, the different designs in a variety of studies have led to difficulties in obtaining clear conclusions about the effects of the different cues and on regulating MSC behaviors. Therefore, it is necessary to focus on summarizing these biophysical and biochemical factors and their significant effects. An overall summary of topics covered in this review is presented in **Figure 1**. We propose that a deep understanding of various factors of biomaterials is of great significance to better release the potential of MSCs in tissue engineering, and the precise integration of cues according to the needs of different target tissues can open up new avenue for future MSC-based therapy.

BIOPHYSICAL CUES

Compared to biochemical cues of biomaterials, biophysical cues have a longer lifetime and can be easily defined. Biophysical cues, such as stiffness, pore size, porosity, topography, as well as stress relaxation, are often regarded as primary elements in biomaterial design for tissue engineering.

Stiffness

It is well known that, as Discher et al. (2005) claimed, cells can sensitively feel and respond to the stiffness of extracellular matrix. Similarly, the behavior of MSCs can also be altered by stiffness. Engler et al. (2006) cultured naive human MSCs (hMSCs) on matrix with three different levels of stiffness (0.1–1, 8–17, and 25–40 kPa). Finally, hMSCs cultured on the soft substrate, mimicking the brain stiffness at a level about 0.1–1 kPa, exhibited extensive branching and are filopodia-rich, much like primitive neuronal morphology. Stiffer materials that simulate muscle (8–17 kPa) and collagenous bone (25–40 kPa) guided hMSCs exhibiting myoblast-like and osteoblast-like morphology, causing cells to express myogenic marker (MyoD) and osteogenic marker (Runx-2), respectively. Meanwhile, different levels of stiffness can also produce changes in hMSC proliferation. Whitehead et al. seeded hMSCs on the surfaces of common cell culture dishes and polyethylene glycol (PEG)-based hydrogel platform, which have two different levels of stiffness (8–10 and 50–60 kPa). Ultimately, the stem cells on soft hydrogels exhibited more proliferation activity compared to stiffer hydrogels (Whitehead et al., 2018). Stiffness in 3D matrix also has a significant impact on behavior of MSCs. Wingate et al. (2012) synthesized a 3D nanofiber hydrogel matrix with tunable stiffness by varying the time of photopolymerization and stated that hMSCs on the rigid matrices (8–15 kPa) showed a larger extension area and more polarization compared to the soft matrices (2–5 kPa). Meanwhile, the smooth muscle marker (SMA) and SMA mRNA were significantly upregulated. By contrast, the expression of vascular-specific marker (FLK-1) and FLK-1 mRNA was significantly increased on soft substrate. Those results demonstrated that the stiffness of matrix can functionally regulate the behavior of MSCs, and the cells tend to exhibit corresponding morphology, proliferation rate, and differentiation lineages when they are cultured on substrate with similar stiffness to their native niches.

The mechanism of microenvironment affecting the behavior of MSCs mainly focuses on the direction of differentiation. Numerous studies have proposed that stiffness of matrices

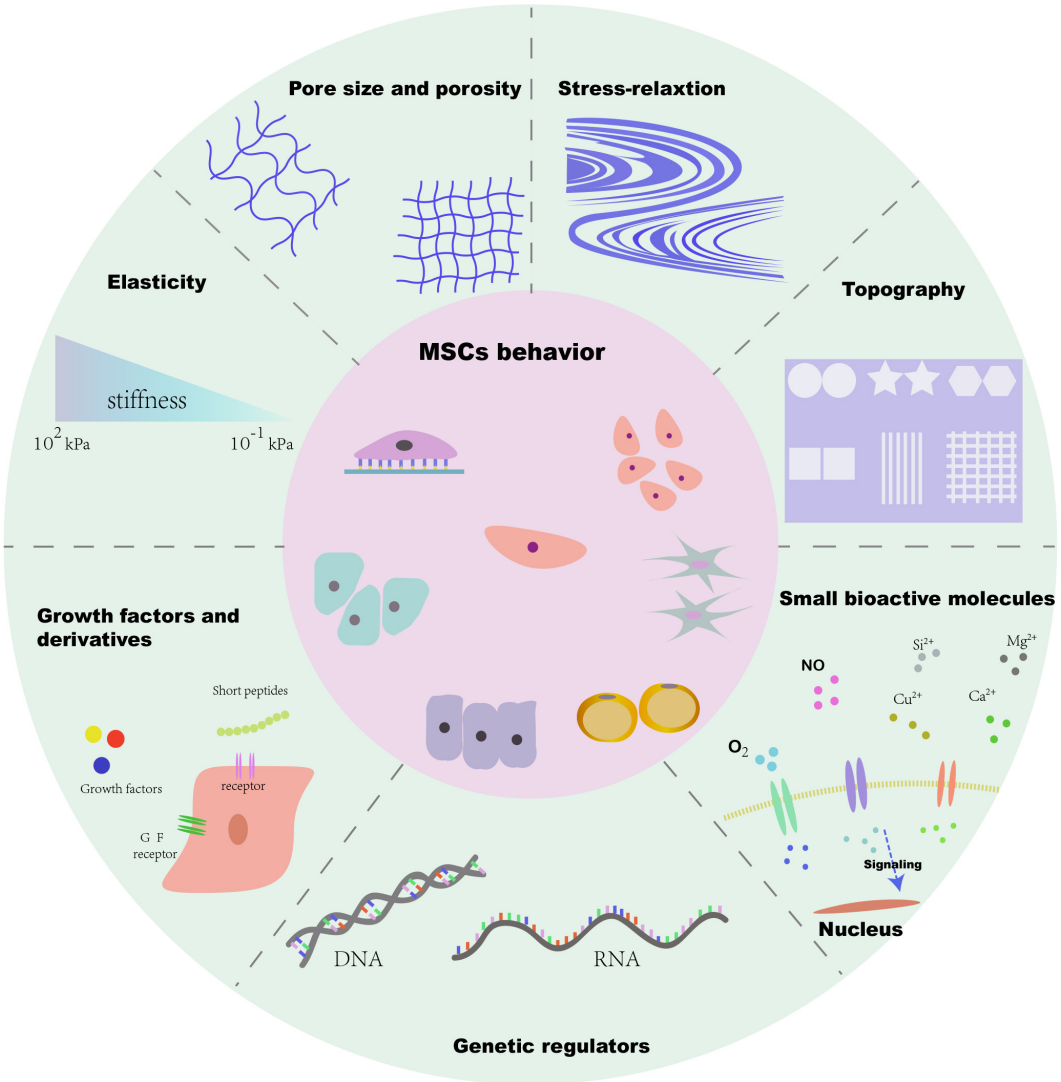

FIGURE 1 | Schematic diagram of biophysical and biochemical cues of microenvironment for MSC behavior.

can modulate self-renewal and differentiation of MSCs via the integrin-mediated signal pathways. Integrins are a family of heterodimeric surface molecules and the most important triggers located in the starting position of mechanotransduction (Du et al., 2011; Higuchi et al., 2013; Sun et al., 2018). For example, Shih et al. (2011) proved that activation of the α2-integrin-mediated Rho kinase (ROCK)–focal adhesion kinase (FAK)–ERK1/2 mechanotransduction pathway could significantly enhance osteogenic differentiation of MSCs, by cultured MSCs on hydrogels with different stiffness. Similarly, Du et al. demonstrated that β1-integrin activation was significantly enhanced in MSCs on soft hydrogels (0.1–1 kPa) compared to hard substrates (50–100 kPa). In addition, soft culture substrates can induce neural differentiation of MSCs by inhibiting the β1 integrin-modulated bone morphogenetic protein (BMP)–Smad pathway (Du et al., 2011). Currently, experts believe that the stiffness of substrate could provide different mechanical stimuli changes in focal adhesion protein (FAP) activities and remolding, and then MSCs sense the changes via integrins, the primary kind of FAP on cell membrane.

Stress Relaxation

Recently, increasing evidences have shown that stress relaxation of substrate is also a significant mechanical parameter in guiding the behavior of MSCs. Previous researches have mainly focused on the stiffness, which represents the characteristics of purely elastic biomaterials, while most ECMs and tissues are viscoelastic. During the compression process, viscoelastic tissues, such as brain, muscles, and cartilage, require a constantly decreased stress to maintain a certain strain. In other words, native ECM and tissues that maintain constant strain will exhibit stress relaxation or time-dependent deformation, which is another important mechanical property of biomaterials (Chaudhuri et al., 2015; Chaudhuri et al., 2016; Bauer et al., 2017).

Some excellent articles have elucidated the influence of stress relaxation on the behavior of MSCs. Chaudhuri et al. (2016) cultured murine MSC in the hydrogel with tunable stress relaxation but similar initial elastic modulus and found that the faster stress relaxation substrate strikingly enhanced both spreading and proliferation of MSCs compared to the low relaxation hydrogel. In addition, an interconnected, mineralized, and collagen-1-rich matrix was detected in the rapidly relaxing gel, which indicated that the rapid stress relaxation enhanced not only the osteogenesis of MSCs but also the bone-forming activity. In another study, Cameron et al. proposed a polyacrylamide gel system with constant storage moduli but varying loss moduli. The varying loss moduli ultimately changed the creep and deformation of the gel, which represented the stress relaxation property (Cameron et al., 2011). Eventually, they found that the spreading area of MSCs increased with the augmentation in modulus loss and stress relaxation of the substrate. Meanwhile, there was an obvious trend that the proliferation of MSCs was increased on the higher stress relaxation substrate. Furthermore, the differentiation potential of MSCs, such as adipogenesis, osteogenesis, and myogenesis, was also amplified on the higher loss moduli substrates compared to the low loss moduli substrates. Besides, in the calvarial defect repair test *in vivo*, Darnell et al. (2017) found that the rapid-relaxing hydrogel carrying MSCs promoted new bone formation better than the slow-relaxing but stiffness-matched hydrogel. Overall, those studies have shown that the stress relaxation or creep of the substrate can significantly affect the behavior of MSCs in tissue engineering.

With the deepening of the researches, the driving factors behind stress relaxation are gradually being exposed. Although the effects of matrix stiffness and stress relaxation on MSCs are all related to cell focal adhesion and the tension generated by the cytoskeleton or tension fiber, the molecular mechanisms and signal pathways behind them are not completely the same due to the different inherent physical properties. Cameron et al. (2014) demonstrated that the activated mechanotransductive signaling molecules (Rac1) pathway on rapid creep substrates exerted a valid mechanism, helping to the enhance the differentiation of hMSCs toward smooth muscle cell lineage. Chaudhuri et al. (2016) suggested that in the rapidly relaxing gel, the increased binding and clustering of integrins as well as the cell mechanoreceptor actomyosin contractility contributed to the osteogenesis of hMSCs. Compared with the mechanism of stiffness on MSCs, the mechanism of stress relation on cells is different, but there are some overlaps. Therefore, more researches are needed to explore the specific mechanism of stress release.

Topography

With the progress of the material manufacturing technology and the improvement of resolution, more and more biomaterials with different micro- and nano-patterned surfaces have been manufactured. To explore the influence of terrain on MSCs, various shapes and morphologies, such as squares, stars, stripes, and grids, have been reported (Tang et al., 2010; Tay et al., 2010; Wan et al., 2010). Meanwhile, there is increasing evidence that shows that the geometric characteristics or the topography of the extracellular microenvironment can directly alter the response of MSCs from proliferation, extension, differentiation, and paracrine.

The cell shapes, spreading area, cell–cell interaction, and orientation of arrangement direction are the main targets for biomaterial topography to influence MSCs. Due to the domestication of the surrounding topographical features, MSCs finally adapt to the micro- and nano-patterned surfaces by changing its own morphology, thus changing its own destiny. McBeath et al. (2004) cultured hMSCs on micropatterned materials with square shape ranging from 1000 to 10,000 μm^2, and cells with different spreading area and differentiation commitments were obtained after 1 week. Osteogenesis was observed mostly on larger micropatterned substrates, whereas adipogenesis was found on smaller substrates, suggesting that cell spreading area induced by the micropatterned microenvironment can change the fate of MSCs. However, the spreading area varies with the shape. Thanks to the development of print technique, we can decouple these two parameters. Kilian et al. seeded individual MSCs on different rectangles but with constant area using the microcontact printing technique. Eventually, they found that the osteogenic differentiation of MSCs increased with the aspect ratio (1:1, 3:2, and 4:1), indicating that the shape of materials can independently affect the fate of MSCs (Kilian et al., 2010). Moreover, the development of manufacturing technology also makes it possible to reveal the effects of the cell–cell interaction. Tang et al. (2010) designed five different micromodel domains composed of microisland, allowing a single MSC to bind to each microisland, so that the average number of cell contacts in each micromodel domain is different. Finally, they observed that the osteogenesis and adipogenesis of MSCs are linearly related to the number of cell–cell contacts and gap junctions. In addition, in order to study the effects of alignment direction, Zhu et al. (2005) aligned and cultured MSC-derived osteoblast-like cells along the direction of nanogrooves in the scaffold. Finally, they pointed out that the cells implanted in the laser-treated nanogrooves had a higher proliferation rate than those in normal disk, suggesting that the nanoscale alignment along the longitudinal direction can promote the aligned formation of bone tissue. However, contrary to the above results, Jahani et al. (2012) showed that random nanofibrous scaffolds were more suitable for the growth of rat MSCs than aligned scaffolds and had higher proliferation. The reason may be that the random fibers contain more interconnected pores for circulation of nutrients. In addition, the significance of topography, such as the mussel-inspired nanostructures of functionalized 3D-printed bioceramic scaffolds developed by Li et al. (2019), could accelerate tissue regeneration by regulating the paracrine of adipose-derived MSCs. Based on the above researches, the topography of the matrix can affect the behavior of MSCs in different ways.

Because the topography are mainly physical stimulations, the underlying mechanism is related to the cytoskeletal contractility and the response of MSCs to mechanical forces. Kilian et al. (2010) demonstrated that topographical features of substrates increased MSCs' actomyosin contractility so as to promote the osteogenesis of MSCs. At the same time, the increased

cytoskeletal tension is related to the enhanced c-Jun N-terminal kinase (JNK) and the activation of extracellular-related kinase (ERK1/2), as well as the elevated wingless-type (Wnt) signaling (Kilian et al., 2010). Thanks to the advance in biomaterials preparation, we can gain insight into the underlying mechanism of topography and give full play to its role in MSC-based regenerative medicine.

Pore Size and Porosity

The pore size and porosity have been valued by researchers for a long time. As early as 1971, Weber et al. (1971) pointed out that the structure of the porous medium is crucial. They stated that the interconnected pores with appropriate size, shape, and uniformity are essential for cell growth and adhesion. Since then, lots of experts have devoted themselves to studying the effects of pore characteristics on MSCs, in order to reveal its potential in the field of manufacturing biomaterials.

Although the optimal pore size of scaffolds varies with the biomaterials and cell type, the pore size and porosity are closely related to the cellular behavior of MSCs. Murphy et al. (2016) manufactured a series of collagen-glycosaminoglycan (CG) scaffolds with mean pore size ranging from 85 to 325 μm and found that the pore size exhibits a non-linear and bimodal effect on MSC adhesion. Specifically, MSCs adhered most to scaffolds with an average pore size of 325 μm, whereas another peak appeared at 120 μm. This phenomenon was due to the fact that the small pores have a larger surface area and the large pores have a higher ligand density. Similarly, Zhang et al. (2016) stated that the smaller pore size in the framework provided a larger surface area for cell adhesion. In addition, the pore size of biomaterials also changes the proliferation efficiency of MSCs. Zhang et al. fabricated a set of scaffolds with three different mean pore sizes (i.e., 215, 320, and 515 μm). Eventually, they claimed that the proliferation efficiency in the 515 μm scaffold was significantly lower than the other two groups. In other words, MSCs prefer to proliferate within the small pores of scaffolds. On the other hand, as demonstrated by O'Brien et al. (2007) the large pore size is superior to small pores in MSC migration or infiltration into the interior of the scaffold (Murphy et al., 2016). Therefore, when manufacturing the scaffold, we need to achieve a balance between utilizing large pores to improve cell migration and penetration and small pores to promote cell adhesion and proliferation. Meanwhile, the porosity also proved to be related to the behavior of MSCs. The highly porous patterns fabricated by electrospinning technology have been comprehensively assessed and proved to facilitate bone engineering (Ding et al., 2019). As we all know, the increase in porosity is beneficial to the nutrient diffusion and the waste removal within a certain range and achieves good proliferation of MSCs (Zhao et al., 2021). Kasten et al. (2008) implanted MSC-loaded β-tricalcium phosphate (TCP) scaffolds with different porosities (25, 65, and 75%) into SCID mice and found that the TCP 65 and TCP 75 with high porosity had higher ALP activity than the TCP 25 after 8 weeks. Obviously, the increase in porosity is conducive to the osteogenesis of MSCs *in vivo*. Like porosity, numerous studies have confirmed that the change of pore size can also guide the differentiation commitment of MSCs. Matsiko et al. (2015) cultured MSCs in Collagen-hyaluronic acid (CHyA) scaffolds with three different average pore sizes (94, 130, and 300 μm) and demonstrated that the maximum pore sizes (300 μm) significantly enhanced the expression of cartilage-forming genes and cartilage-like matrix deposition. In another research, Mygind et al. (2007) pointed out that the 200-μm pore hydroxyapatite scaffold exhibited faster osteogenic differentiation than the 500-μm pore scaffold, while the latter had a higher proliferation capability. It seems that there is an optimal pore range for MSC differentiation, and this range varies with the cell types and biomaterials. Pore size and porosity, as the specific form of pore structure, have a significant impact on the behavior of MSCs attached to biomaterials.

BIOCHEMICAL CUES

It has been many years since the biochemical modulation of stem cell growth and differentiation using small molecules and growth factors. However, due to the shortcomings of burst release and difficultly of long-term control or definition, biochemical factors have always been integrated into biomaterial-based scaffolds. Compared to biophysical cues, biochemical cues of biomaterials are easier to deliver. Besides growth factor and small bioactive molecules, genetic regulators have also been discussed in this section.

Growth Factor and Derivatives

Some progress has been made in promoting MSC-based regeneration by adding growth factors and derivatives, such as EGF, VEGF, FGF, and TGF β. For example, soluble EFG can not only promote the proliferation of MSCs without compromising its pluripotent differentiation but also increase paracrine secretion to accelerate tissue regeneration (Tamama et al., 2010). However, conventional administration methods deliver growth factors and derivatives in soluble form, leading to complications such as hypotension and nephrotoxicity (Ferrara and Alitalo, 1999). So, combination of scaffold with growth factors would become an alternative and effective method and has made clear progress in areas such as bone regeneration of osteonecrosis (Zhu et al., 2020). Therefore, as a novel delivery method, the integration of growth factors into biomaterials can recapitulate a more suitable environment for MSCs at a physiologically relevant concentration and duration.

Fan et al. (2007) fabricated a scaffold covalently modified with epidermal growth factor (EGF) to control the release of EGF more precisely, which could increase MSCs spreading and adhesion through elevated ERK signaling and enhanced resistance to FasL-mediated cell death relative to saturating concentrations of soluble EGF. These advances can be attributed to the combination of EGF molecules with structures that bind and activate EGF receptors and the production of local high concentrations of EGF at the cell–matrix interface. As we all know, basic fibroblast growth factor (bFGF) can not only enhance the proliferation of MSCs but also promote the differentiation of MSCs in different directions (Rodrigues et al., 2010). In order to accurately mimic the release concentration of bFGF in

injured ligament/tendon, Sahoo et al. (2010) incorporated bFGF-releasing PLGA fibers to the surface of the knitted silk scaffold, and the biological concentration of 6.5–13.5 pg/ml of bFGF in bioactive form was successfully recovered. Compared with bFGF (-) scaffold, MSCs in bFGF (+) scaffold exhibited higher viability (increased by 25%) during the whole culture process. Moreover, the gene expression level of ECM protein in the bFGF (+) scaffold such as type I and III collagens, fibronectin, and the deposition of soluble collagen were significantly increased. These results indicated that the released bFGF has broad application prospects in repairing tendon and ligament injury by promoting proliferation and tenogenic differentiation. On the other hand, vascularization of grafts plays a very important role in tissue repair and vascular endothelial growth factor (VEGF) is an essential growth factor in regular angiogenesis (Davies et al., 2008). Khojasteh et al. (2016) fabricated a porous scaffold with VEGF controlled release and proved that the proliferation and attachment of MSCs were significantly increased than those without VEGF. Meanwhile, they found that the gene expression of COL I and RUNX2 for osteogenesis and that of vWF and VEGFR2 for angiogenesis were statistically increased, demonstrating that VEGF not only promoted angiogenesis but also played an important role in bone repair. Besides, TGFβ is also a known superfamily that can affect the chondrogenic differentiation and matrix deposition of MSCs *in vivo* (Rodrigues et al., 2010). Therefore, lots of studies have integrated TGFβ into the scaffold to explore its prospects in cartilage repair. Re'em et al. (2012) developed a scaffold with TGFβ sustained release, and the chondrocytes with deposited type II collagen were only found in the TGFβ bound constructs compared to the naked one. Therefore, the use of biomaterials to deliver growth factors to regulate MSCs behavior provides a viable means for tissue regeneration.

Because MSCs are regulated by a variety of regulatory factors *in vivo*, the combination of multiple biological factors on a biomaterial or delivery system is also a promising approach. Moreover, the synergistic effect on target cells is the characteristic of integrating multiple factors into one system. For example, Simmons et al. (2004) fabricated a dual growth factor delivery alginate hydrogel scaffold in which bone morphogenetic protein-2 (BMP2) and transforming growth factor-β3 (TGF-β3) are incorporated. The scaffold supported the simultaneous release of important growth factors during osteogenesis from MSCs, and the dual delivery system showed more efficient and more effective tissue regeneration *in vivo* compared to the individual delivery. In another research, insulin-like growth factor-1 (IGF-1) and TGF-β1 were loaded together in gelatin microparticles (Park et al., 2009). Then, the gelatin microparticles and rabbit marrow MSCs were assembled into an injectable hydrogel. Over the culture time *in vitro*, TGF-β1 was gradually found to accelerate chondrogenic differentiation of MSCs, while IGF-1 promoted cell aggregation. The incorporation of the two growth factors showed a synergistic effect on chondrogenesis of MSCs, which provided a great potential for cartilage regeneration and repair. The above studies showed the advantages of multiple factor delivery biomaterials; thus, how to construct a novel system to provide appropriate combination of multiple growth factors or simulants is an inevitable trend in future researches and even clinical applications (Richardson et al., 2001).

However, due to the immunogenicity and short half-life, the integration of large protein growth factor into polymer scaffolds has certain limitations (Cai et al., 2014). Growth factor derivatives and peptides are short peptide sequences that mimic the receptor-binding or functional domains of growth factors (Liu et al., 2012). These short peptides can bind to corresponding receptors to activate intracellular pathways to achieve the effect of growth factors, while avoiding the obstacles of large proteins. Currently, it has been reported that short peptides such as QK, KLT, PRG, and the RGD can achieve this goal, and RGD sequence has been extensively tethered to biomaterials to regulate MSC behaviors for tissue repair (Liu et al., 2012; Lam and Segura, 2013; Cai et al., 2014; Rao et al., 2020). Yang et al. (2005) covalently incorporated different dosage adhesion peptides Arg-Gly-Asp (RGD) into hydrogel and found that the expression of bone-related markers ALP and OCN was significant higher in RGD-conjugated hydrogel than the control. Furthermore, the level of gene expression was positively correlated with the concentration of RGD. Consistent with Yang, the RGD peptide was bound to the surface of the scaffold by Qu et al. (2010). Compared with the unmodified scaffold, more MSCs adhered to RGD scaffolds after 4 h of culture. Moreover, after 14 days of culture, the RGD-modified scaffolds significantly promoted the osteogenesis of MSCs. These studies show that the growth factor derivatives and short peptide factor have good prospects and operability in regulating the behavior of MSCs.

Small Bioactive Molecules

Small bioactive molecules, such as nitric oxide, oxygen, and metallic ions, also have significant effects on MSCs behavior. Since 1977, Arnold et al. (1977) discovered that NO could participate in various physiological processes by activating the cyclic guanosine monophosphate (cGMP), and it has been intensively studied in cardiovascular homeostasis, tissue repair, and immunomodulation. Yao and his group cultured adipose-derived MSCs in a hydrogel that can release NO molecule continuously and transplanted the hydrogel into murine myocardial infarction (MI) models, which achieved positive therapeutic effects (Yao et al., 2015). It has been widely confirmed that the protective effect of MSCs on MI is mainly achieved through the pro-angiogenic cytokines it secreted (Berardi et al., 2011). Similarly, Yao and co-workers discovered that NO hydrogel remarkably enhanced the paracrine and the VEGF secretion of MSCs. Finally, these cytokines improved heart function by promoting vascularization and reducing ventricular remodeling. In another approach, the effects of NO on other aspects of MSCs was observed by Xing et al. (2013). He fabricated a gelatin hydrogel that can release nitric oxide at a physiological concentration, and lower attachment and proliferation efficiency of MSCs were obtained on the NO hydrogel compared to the control after incubating for 72 h. Therefore, utilizing NO to modify the scaffold can improve antithrombotic ability by reducing cell adhesion and proliferation, which can be used as a coating material for repairing vascular injury. However, the instability of NO and its oxidation potential to the toxic

nitrogen dioxide molecule is still the barrier to extremely exploit the therapeutic effects of NO (Xiao et al., 2017). So, the development of a more secure and stable delivery system becomes a breakthrough of the next-generation NO-based biomaterials.

Oxygen level is also a critical regulator of stem cell behavior. At present, MSCs are usually cultured in an incubator under an oxygen level of 20% pO_2, whereas the residing niche MSCs are in low oxygen tension (1–7% pO_2) (D'Ippolito et al., 2006). Therefore, more and more studies have examined the effects of oxygen level on MSCs. It is already known that low oxygen tension (hypoxia) can not only maintain the stemness of stem cells but also influence their proliferation and differentiation (Mohyeldin et al., 2010). Zhou et al. (2014) seeded bone marrow-derived MSCs into scaffold and cultured in different oxygen tension, and the MSCs under hypoxia (5% pO_2) exhibited a higher proliferation response compared with the others cultured under normoxic conditions (20% pO_2) on day 4 and 10. Meanwhile, higher levels of Runx2, Bmp2, BMP, and VEGF were observed in the hypoxia scaffold relative to the normoxic scaffold, suggesting that the hypoxia is conducive to the osteogenesis and angiogenesis of MSCs. In addition, Tong et al. (2016) demonstrated that hypoxic pretreated MSC-containing biomimetic scaffold observably accelerated wound healing in diabetic rat ulcer. The reason is that hypoxia pretreatment can enhance the secretion of proangiogenic factors and angiogenesis of MSCs.

As cofactors of enzymes, various metal ions are widely involved in tissue homeostasis and participated in lots of chain reactions related to cell signaling pathways (Gérard et al., 2010). In recent years, more and more evidences showed that metallic ions also play an important role in the field of regenerative medicine by regulating MSCs behavior. Meanwhile, the integration of metal ions into bioactive scaffolds generated a dual function for matrix and enhanced its therapeutic effect (Mouriño et al., 2012). The main reasons were due to the fact that these ions released from the scaffold can stimulate various processes, including proliferation, attachment, and differentiation. For example, the enhanced osteogenic differentiation was observed on a silicon-releasable scaffold, and the silicon species in the scaffold was regarded to promote the alkaline phosphatase (ALP) and osteogenesis (Obata and Kasuga, 2009). The silver nanoparticles were also found to promote the proliferation and osteogenesis of MSCs *in vitro*, and the improved bone fracture healing was obtained through a novel collagen reinforced by silver nanoparticles (Zhang et al., 2015). Therefore, a comprehensive understanding of the effects of metal particles on MSC behaviors is necessary for the development of metal ion-integrated biomaterials. **Table 1** summarizes the effects of different metallic ions on the behavior of MSCs. However, achieving sustained release of metal ions under suitable concentration and without systemic toxicity remains difficult as the complexity of manufacturing process is still a challenge for these strategies based on controlled metal release.

Genetic Regulators

Recently, great achievement has been made in regulating the behaviors of cells by integrating genetic regulatory factors into biomaterials. For example, the improved cell proliferation, enhanced osteogenesis, and high-quality healing of large-scale bone defects were obtained by a type of multi-functional scaffold containing phBMP-4 through controlled and sustained gene expression (Cui et al., 2020). The successful delivery of genes based on viral and non-viral means plays a great role in genetic-based tissue engineering (Huard et al., 2003; Giatsidis et al., 2013; Mellott et al., 2013). Currently, non-viral vectors are more preferred for gene therapy because viral vectors are immunogenic and carry the risk of infection and cytotoxicity (Giatsidis et al., 2013). Moreover, the physical non-viral transfection methods such as electroporation significantly improved the transfection efficiency to control the cellular behavior during tissue regeneration (Mellott et al., 2013). Here, we review the effects of genetic regulatory factors (such as complementary DNA and small interfering RNA) on MSCs.

Complementary DNA (cDNA) is a nucleic acid sequence that can encode specific proteins by reverse transcription in transfected cells. It has been reported that various specific proteins including VEGF (Huang et al., 2005), EGF (You and Nam, 2013), bFGF (Yau et al., 2007), BMP (Meinel et al., 2006; Wegman et al., 2011), and hepatocyte growth factors (HGFs) (Lu et al., 2013) can guide behaviors of MSCs through transfecting corresponding cDNA. Wegman et al. (2011) achieved osteogenic differentiation of MSCs *in vitro* and *in vivo* through prolonging expression of BMP-2 through plasmid DNA-based gene therapy. They incorporated the BMP-2 cDNA into an alginate hydrogel, and seeded MSCs into the hydrogel before implanting to naked mice. In the end, the continuous expression of BMP-2 protein significantly promoted the osteogenic differentiation of MSCs, which was also verified by the increased expression of ALP and the deposition of collagen I and osteocalcin. In another study, Moon et al. (2014) fabricated modified polyethyleneimine (PEI) conjugates to deliver VEGF cDNA and demonstrated that VEGF-MSCs enhanced capillary formation in the infarcted area and attenuated ventricular remodeling in the model of MI.

Small interfering RNA is a small double-stranded RNA sequence (21–23 nucleotides) that can silence and knock down target genes by complementary binding to the corresponding mRNA sequence. Therefore, siRNA may provide another effective intervention to guide stem cell behavior in regenerative medicine applications (Benoit and Boutin, 2012). Jia et al. (2014) integrated two small interfering RNAs into the chitosan sponge, one targeting casein kinase 2 interaction protein 1 (siCkip-1) and another targeting soluble VEGF receptor 1 (siFLT-1), and osteogenesis and angiogenesis were observed *in vitro* and *in vivo* after co-culturing with MSCs. Moreover, they pointed out that the osteogenesis may be due to the targeted knockdown of Ckip-1 that markedly activates the signaling pathways related to bone morphogenetic proteins. At the same time, silencing soluble VEGF receptor 1 gene eventually upregulated the release of VEGF, which promoted the angiogenesis of MSCs. Similarly, we can also see the same phenomenon in the research of Nagai (Nagane et al., 2010). The author transformed the osteogenesis of MSCs to adipogenesis through culturing MSCs with the siRNA-containing cationic dextran. The reason was that the siRNA here can knock down the activity of transcription coactivator

PDZ-binding motif (TAZ), thus significantly promoting the osteogenesis of MSCs rather than adipogenesis.

POTENTIAL OF COMBINING BIOCHEMICAL AND BIOPHYSICAL CUES

Because the biophysical and biochemical signals exist simultaneously and cooperate together *in vivo*, combining their effects *in vitro* as an alternative solution has become an increasingly clear and affirmative topic in the field of cellular therapy and regenerative medicine. More importantly, several groups have proved the feasibility of combining the effects of biophysical and biochemical signals *in vitro*. For example, a novel osteogenic polypeptide hydrogel (GelMA-c-OGP) in which GelMA enabled the formation of hydrogel with mechanical properties, combined with osteogenic growth peptides (OGP) through co-cross-linking that continuously release during the bone defect healing period, was created by Qiao et al. (2020). Finally, the interaction of the two parameters promoted the bone formation procedure of osteogenic precursor cells *in vitro*, and more collagen fibers were observed to connect with cortical bones after implantation. In another study, an *in vitro* model

TABLE 1 | Effects of metallic ions on MSCs.

Ion	Ionic form	Experimental trial	Effects on behaviors	References
Silicon	Glass microspheres (BGMs)	*In vitro*	Enhanced the attachment and proliferation of human MSCs	Lei et al., 2011
	Silicon-releasable scaffold	*In vitro*	Induce and enhance the osteogenic differentiation of MSCs	Obata and Kasuga, 2009
	Composite hydrogel	*In vitro/vivo*	Angiogenesis and adipogenesis	Wang et al., 2018
Calcium	Calcium phosphate composition	*In vitro*	High mobility of focal adhesion, osteogenesis without induce medium	Muller et al., 2008
Cobalt	Cobalt chloride composition	*In vitro*	Increase the chondrogenic markers such as SOX9, COL2A1, VCAN, ACAN	Teti et al., 2018
	Cobalt chloride composition	*In vitro*	Induce neuronal differentiation	Jeon et al., 2014
	Cobalt chloride solution	*In vitro*	Enhance migration of MSCs	Yu et al., 2013
Copper	Copper–histidine complex	*In vitro*	Modify differentiation and proliferation by different concentrations	Rodriguez et al., 2002
Zinc	Zinc-added bioactive glass	*In vitro*	Induce growth and osteogenic differentiation of MSCs	Oh et al., 2011
Vanadium	Vanadium-loaded collagen scaffold	*In vitro*	Adhesion, growth, differentiation	Cortizo et al., 2016
	Vanadium-released scaffold	*In vitro/vivo*	Endochondral ossification and angiogenesis *in vivo*.	Schussler et al., 2017
Strontium	Strontium-ranelate solution	*In vitro*	Osteogenic induction of MSCs at appropriate concentration	Sila-Asna et al., 2007
	Strontium-collagen scaffold	*In vitro/vivo*	Enhance osteogenic differentiation and bone formation	Yang et al., 2011
Iron	Iron oxide nanoparticles	*In vitro*	Accelerate cell cycle progression, promote cell growth	Huang et al., 2009
Magnesium	Magnesium-extract solution	*In vitro*	Cell proliferation, osteoblastic differentiation	Luthringer and Willumeit-Romer, 2016
	Magnesium alloys extracts	*In vitro*	Enhance proliferation and osteogenic differentiation	Li et al., 2014
Silver	Silver nanoparticles	*In vitro*	Induce MSCs activation at appropriate concentration	Greulich et al., 2009
	Silver nanoparticles	*In vitro/vivo*	Promote the proliferation and osteogenesis of MSCs	Zhang et al., 2015

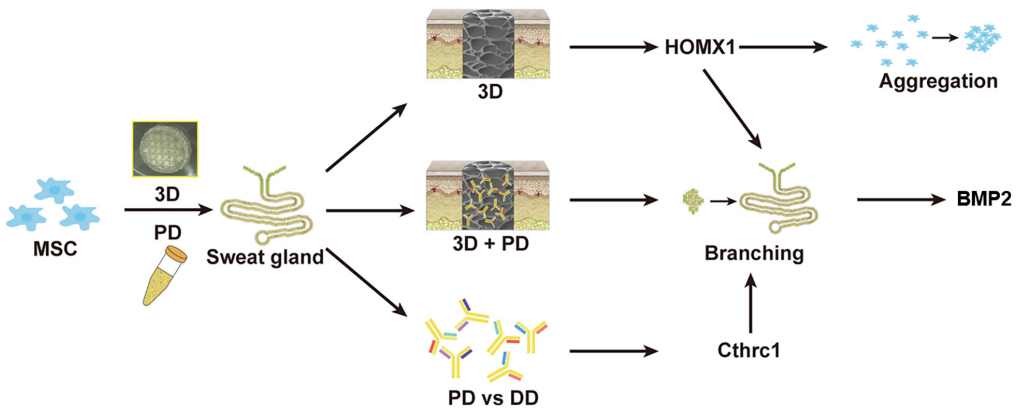

FIGURE 2 | The graphic illustration of 3D bioprinted matrix-directed MSC differentiation. CTHRC1 is the main biochemical cue during SG development and structural cues upregulated the expression of hmox1, synergistically initiating branching morphogenesis of SG.

system combining biochemical and biophysical factors was found to be more effective on cardiomyocyte differentiation from rat bone marrow-MSCs (BM-MSCs) than any single factor alone (Ge et al., 2009).

In recent years, 3D bioprinting offers a promising and alternative platform to fabricate tissue-specific constructs for tissue repair and regeneration. These 3D functional constructs are regarded as the most biomimetic module due to the fact that they can provide both biochemical cues and biophysical signals to regulate cell–cell and cell–ECM interaction. In our previous work, by 3D bioprinted specific sweat gland (SG) matrix, we can differentiate MSCs into functional SGs by combination of biochemical and structural cues (**Figure 2**). The 3D printed SG-like matrix provided a novel strategy to combine chemical factor, especially the collagen triple helix repeat containing 1 (CTHRC1), and 3D structural factor (Yao et al., 2020). These two cues synergistically directed MSCs' commitments into the glandular lineage and functional SG recovery *in vitro* and vivo. In addition, 3D bioprinting of tissue-specific decellularized extracellular matrix (dECM) bioink can provide a complex site-specific combination of biochemical and mechanical cues, which have been hypothesized to prove their potential application in tissue engineering.

In addition to the synergistic effects, some researches have revealed the competitive relationship between the biophysical cues and the biochemical cues. For example, human bone

TABLE 2 | Effects of biomaterials on MSCs.

Category		Effects on behaviors	References
Biophysical	Stiffness	Proliferation	Whitehead et al., 2018
		Spreading	Engler et al., 2006; Wingate et al., 2012
		Differentiation	Du et al., 2011; Shih et al., 2011; Higuchi et al., 2013; Sun et al., 2018
	Stress relaxation	Proliferation	Cameron et al., 2011; Chaudhuri et al., 2016
		Spreading	Cameron et al., 2011; Chaudhuri et al., 2016
		Differentiation	Cameron et al., 2011, 2014; Darnell et al., 2017
	Topography	Proliferation	Zhu et al., 2005; Jahani et al., 2012
		Spreading	McBeath et al., 2004
		Differentiation	McBeath et al., 2004; Kilian et al., 2010; Tang et al., 2010
		Paracrine	Li et al., 2019
	Pore size and porosity	Proliferation	Mygind et al., 2007; Zhang et al., 2016; Zhao et al., 2021
		Differentiation	Mygind et al., 2007; Kasten et al., 2008; Matsiko et al., 2015
		Adhesion	Murphy et al., 2016; Zhang et al., 2016
		Migration	O'Brien et al., 2007
Biochemical	Growth factor and derivatives	Proliferation	Rodrigues et al., 2010; Sahoo et al., 2010; Khojasteh et al., 2016
		Differentiation	Simmons et al., 2004; Park et al., 2009; Rodrigues et al., 2010; Sahoo et al., 2010; Re'em et al., 2012; Khojasteh et al., 2016; Rao et al., 2020; Zhu et al., 2020
		Paracrine	Tamama et al., 2010
		Spreading	Fan et al., 2007; Lam and Segura, 2013
		Adhesion	Fan et al., 2007; Qu et al., 2010; Khojasteh et al., 2016
	Small bioactive molecules (nitric oxide)	Immunomodulation	Yao et al., 2015
		Paracrine	Berardi et al., 2011
		Differentiation	Berardi et al., 2011
		Adhesion	Xing et al., 2013
		Proliferation	Xing et al., 2013
	Small bioactive molecules (oxygen level)	Proliferation	Zhou et al., 2014
		Differentiation	Zhou et al., 2014; Tong et al., 2016
		Paracrine	Tong et al., 2016
	Small bioactive molecules (metallic ions)	**Table 1**	
	Genetic regulators (cDNA)	Differentiation	Huang et al., 2005; Meinel et al., 2006; Yau et al., 2007; Lu et al., 2013
		Proliferation	You and Nam, 2013
		Migration	You and Nam, 2013
		Paracrine	Moon et al., 2014
	Genetic regulators (siDNA)	Differentiation	Nagane et al., 2010; Jia et al., 2014
Combined strategy	Mechanical property and polypeptides	Differentiation	Bauer et al., 2017
	Strain and biochemical extract factors	Differentiation	Ge et al., 2009
	3D microenvironment and biochemical extract factors	Differentiation	Yao et al., 2020

marrow-derived MSCs were cultured on the nanostructured surface in differentiation media by McMurray et al. (2011). Compared with the cells cultured in the inductive medium alone, one interesting phenomenon was that the cells on the surface of nano-patterned topography showed a higher degree of stemness maintenance and lower differentiation levels. The reason is probably that biophysical factors have a longer duration and lifetime, which could even convert the effects of biochemical stimulation (Ahsan and Nerem, 2010). However, it is not clear whether these two aspects will conflict with each other, as well as the extent and the underlying mechanism. Therefore, distinguishing the internal effects when biophysical and biochemical cues are used in combination is essential.

CONCLUSION AND FUTURE PROSPECTS

The key point of MSC-based therapy is to maintain the viability of MSCs and accurately guide their fate and functionalization at the injury site. However, once MSCs are separated from their niches, their phenotype, functionality, and viability can easily be distorted. Therefore, it is necessary to create highly mimicking native-room biomaterials or substrates for MSCs to maintain their properties and exhibit therapeutic effects. Here, the biophysical and biochemical factors that determine the behaviors of MSCs have been discussed. These different cues and different protocols utilized in a variety of studies have led to difficulties in obtaining clear conclusions about the effects on regulating the proliferation, adhesion, and differentiation of MSCs and ultimately affect the function of the target tissue. Therefore, a comprehensive and systematic understanding of these signals is essential for the synthesis of more advanced artificial biomaterials and tissue engineering. **Table 2** summarizes the factors that fall into some categories.

Recent advances in the design and manufacture of biomaterials with tailoring parameter not only provide a versatile toolbox for bioengineering [e.g., embedded 3D bioprinting (de Melo et al., 2019), co-fabrication (Jodat et al., 2020), and stereolithography (Kumar and Kim, 2020)] but also present a feasible approach for subsequent research. However, we believe that the development of the biomaterial for regenerative medicine needs to be combined with multidisciplinary research progress, and the biophysical and biochemical factors used to regulate MSC behaviors must be precisely integrated and adjusted according to the needs of the repair area. Just like Yasamin et al., they combined multi-material 3D bioprinting with electronic platform technology to synthesize a hybrid device that can not only reconstruct the mechanical structure of nasal cartilage but also sense odor (Jodat et al., 2020). The integration of the aforementioned multidisciplinary research can be a potential avenue toward achieving functional nasal regeneration and organ transplant. Therefore, we believe that the next-generation biomaterials with accurately integrated induction cues for MSCs will open a new window for perfect regeneration and simultaneous repair.

AUTHOR CONTRIBUTIONS

SH contributed to the conception of the study and edited the manuscript. JL and YL wrote the sections of the manuscript. All authors read and approved the submitted version.

FUNDING

This study was supported in part by the National Nature Science Foundation of China (81830064, 81721092, and 81701906), the National Key Research and Development Plan (2017YFC1103300), the CAMS Innovation Fund for Medical Sciences (CIFMS, 2019-I2M-5-059), the Military Medical Research and Development Projects (AWS17J005, 2019-126), the Fostering Funds of Chinese PLA General Hospital for National Distinguished Young Scholar Science Fund (2017-JQPY-002), and the National Natural Science Foundation of China (82002056).

REFERENCES

Ahsan, T., and Nerem, R. M. (2010). Fluid shear stress promotes an endothelial-like phenotype during the early differentiation of embryonic stem cells. *Tissue Eng. Part A* 16, 3547–3553. doi: 10.1089/ten.TEA.2010.0014

Arnold, W. P., Mittal, C. K., Katsuki, S., and Murad, F. (1977). Nitric oxide activates guanylate cyclase and increases guanosine 3':5'-cyclic monophosphate levels in various tissue preparations. *Proc. Natl. Acad. Sci. USA* 74, 3203–3207. doi: 10.1073/pnas.74.8.3203

Bauer, A., Gu, L., Kwee, B., Li, W. A., Dellacherie, M., Celiz, A. D., et al. (2017). Hydrogel substrate stress-relaxation regulates the spreading and proliferation of mouse myoblasts. *Acta Biomater.* 62, 82–90. doi: 10.1016/j.actbio.2017.08.041

Benoit, D. S. W., and Boutin, M. E. (2012). Controlling mesenchymal stem cell gene expression using polymer-mediated delivery of siRNA. *Biomacromolecules* 13, 3841–3849. doi: 10.1021/bm301294n

Berardi, G. R. M., Rebelatto, C. K., Tavares, H. F., Ingberman, M., Shigunov, P., Barchiki, F., et al. (2011). Transplantation of SNAP-treated adipose tissue-derived stem cells improves cardiac function and induces neovascularization after myocardium infarct in rats. *Exp. Mol. Pathol.* 90, 149–156. doi: 10.1016/j.yexmp.2010.11.005

Cai, L., Dinh, C. B., and Heilshorn, S. C. (2014). One-pot synthesis of elastin-like polypeptide hydrogels with grafted VEGF-mimetic peptides. *Biomater. Sci.* 2, 757–765. doi: 10.1039/C3BM60293A

Cameron, A. R., Frith, J. E., and Cooper-White, J. J. (2011). The influence of substrate creep on mesenchymal stem cell behaviour and phenotype. *Biomaterials* 32, 5979–5993. doi: 10.1016/j.biomaterials.2011.04.003

Cameron, A. R., Frith, J. E., Gomez, G. A., Yap, A. S., and Cooper-White, J. J. (2014). The effect of time-dependent deformation of viscoelastic hydrogels on myogenic induction and Rac1 activity in mesenchymal stem cells. *Biomaterials* 35, 1857–1868. doi: 10.1016/j.biomaterials.2013.11.023

Chaudhuri, O., Gu, L., Darnell, M., Klumpers, D., Bencherif, S. A., Weaver, J. C., et al. (2015). Substrate stress relaxation regulates cell spreading. *Nat. Commun.* 6:6364. doi: 10.1038/ncomms7365

Chaudhuri, O., Gu, L., Klumpers, D., Darnell, M., Bencherif, S. A., Weaver, J. C., et al. (2016). Hydrogels with tunable stress relaxation regulate stem cell fate and activity. *Nat. Mater.* 15, 326–334. doi: 10.1038/nmat4489

Cortizo, A. M., Ruderman, G., Mazzini, F. N., Molinuevo, M. S., and Mogilner, I. G. (2016). Novel vanadium-loaded ordered collagen scaffold promotes osteochondral differentiation of bone marrow progenitor cells. *Int. J. Biomater.* 2016:1486350. doi: 10.1155/2016/1486350

Cui, L., Zhang, J., Zou, J., Yang, X., Guo, H., Tian, H., et al. (2020). Electroactive composite scaffold with locally expressed osteoinductive factor for synergistic bone repair upon electrical stimulation. *Biomaterials* 230:119617. doi: 10.1016/j.biomaterials.2019.119617

Darnell, M., Young, S., Gu, L., Shah, N., Lippens, E., Weaver, J., et al. (2017). Substrate stress-relaxation regulates scaffold remodeling and bone formation in vivo. *Adv. Healthc. Mater.* 6:1601185. doi: 10.1002/adhm.201601185

Davies, N., Dobner, S., Bezuidenhout, D., Schmidt, C., Beck, M., Zisch, A. H., et al. (2008). The dosage dependence of VEGF stimulation on scaffold neovascularisation. *Biomaterials* 29, 3531–3538. doi: 10.1016/j.biomaterials.2008.05.007

De Becker, A., and Riet, I. V. (2016). Homing and migration of mesenchymal stromal cells: how to improve the efficacy of cell therapy? *World J. Stem Cells* 8, 73–87. doi: 10.4252/wjsc.v8.i3.73

de Melo, B. A., Jodat, Y. A., Mehrotra, S., Calabrese, M. A., Kamperman, T., Mandal, B. B., et al. (2019). 3D printed cartilage-like tissue constructs with spatially controlled mechanical properties. *Adv. Funct. Mater.* 29:1906330. doi: 10.1002/adfm.201906330

Ding, J., Zhang, J., Li, J., Li, D., Xiao, C., Xiao, H., et al. (2019). Electrospun polymer biomaterials. *Prog. Polym. Sci.* 90, 1–34.

Discher, D. E., Janmey, P., and Wang, Y. -L. (2005). Tissue cells feel and respond to the stiffness of their substrate. *Science* 310, 1139–1143. doi: 10.1126/science.1116995

Du, J., Chen, X., Liang, X., Zhang, G., Xu, J., He, L., et al. (2011). Integrin activation and internalization on soft ECM as a mechanism of induction of stem cell differentiation by ECM elasticity. *Proc. Natl. Acad. Sci. U.S.A.* 108, 9466–9471. doi: 10.1073/pnas.1106467108

Duarte Campos, D. F., Blaeser, A., Korsten, A., Neuss, S., Jäkel, J., Vogt, M., et al. (2015). The stiffness and structure of three-dimensional printed hydrogels direct the differentiation of mesenchymal stromal cells toward adipogenic and osteogenic lineages. *Tissue Eng. Part A* 21, 740–756. doi: 10.1089/ten.TEA.2014.0231

Engler, A. J., Sen, S., Sweeney, H. L., and Discher, D. E. (2006). Matrix elasticity directs stem cell lineage specification. *Cell* 126, 677–689.

Fan, V. H., Tamama, K., Au, A., Littrell, R., Richardson, L. B., Wright, J. W., et al. (2007). Tethered epidermal growth factor provides a survival advantage to mesenchymal stem cells. *Stem Cells* 25, 1241–1251.

Ferrara, N., and Alitalo, K. (1999). Clinical applications of angiogenic growth factors and their inhibitors. *Nat. Med.* 5, 1359–1364. doi: 10.1038/70928

Ge, D., Liu, X., Li, L., Wu, J., Tu, Q., Shi, Y., et al. (2009). Chemical and physical stimuli induce cardiomyocyte differentiation from stem cells. *Biochem. Biophy. Res. Commun.* 381, 317–321.

Gérard, C., Bordeleau, L.-J., Barralet, J., and Doillon, C. J. (2010). The stimulation of angiogenesis and collagen deposition by copper. *Biomaterials* 31, 824–831. doi: 10.1016/j.biomaterials.2009.10.009

Giatsidis, G., Venezia, E. D., and Bassetto, F. (2013). The role of gene therapy in regenerative surgery: updated insights. *Plast. Reconstr. Surg.* 131, 1425–1435. doi: 10.1097/PRS.0b013e31828bd153

Gilbert, P. M., Havenstrite, K. L., Magnusson, K. E. G., Sacco, A., Leonardi, N. A., Kraft, P., et al. (2010). Substrate elasticity regulates skeletal muscle stem cell self-renewal in culture. *Science* 329, 1078–1081. doi: 10.1126/science.1191035

Greulich, C., Kittler, S., Epple, M., Muhr, G., and Koller, M. (2009). Studies on the biocompatibility and the interaction of silver nanoparticles with human mesenchymal stem cells (hMSCs). *Langenbecks Arch. Surg.* 394, 495–502. doi: 10.1007/s00423-009-0472-1

Gupte, M. J., Swanson, W. B., Hu, J., Jin, X., Ma, H., Zhang, Z., et al. (2018). Pore size directs bone marrow stromal cell fate and tissue regeneration in nanofibrous macroporous scaffolds by mediating vascularization. *Acta Biomater.* 82, 1–11. doi: 10.1016/j.actbio.2018.10.016

Han, Y., Li, X., Zhang, Y., Han, Y., Chang, F., and Ding, J. (2019). Mesenchymal stem cells for regenerative medicine. *Cells* 8:886. doi: 10.3390/cells8080886

Higuchi, A., Ling, Q.-D., Chang, Y., Hsu, S.-T., and Umezawa, A. (2013). Physical cues of biomaterials guide stem cell differentiation fate. *Chem. Rev.* 113, 3297–3328. doi: 10.1021/cr300426x

Huang, D. M., Hsiao, J. K., Chen, Y. C., Chien, L. Y., Yao, M., Chen, Y. K., et al. (2009). The promotion of human mesenchymal stem cell proliferation by superparamagnetic iron oxide nanoparticles. *Biomaterials* 30, 3645–3651. doi: 10.1016/j.biomaterials.2009.03.032

Huang, Y.-C., Kaigler, D., Rice, K. G., Krebsbach, P. H., and Mooney, D. J. (2005). Combined angiogenic and osteogenic factor delivery enhances bone marrow stromal cell-driven bone regeneration. *J. Bone Miner. Res.* 20, 848–857.

Huard, J., Li, Y., Peng, H., and Fu, F. H. (2003). Gene therapy and tissue engineering for sports medicine. *J. Gene. Med.* 5, 93–108. doi: 10.1002/jgm.344

Jahani, H., Kaviani, S., Hassanpour-Ezatti, M., Soleimani, M., Kaviani, Z., and Zonoubi, Z. (2012). The effect of aligned and random electrospun fibrous scaffolds on rat mesenchymal stem cell proliferation. *Cell J.* 14, 31–38.

Jeon, E. S., Shin, J. H., Hwang, S. J., Moon, G. J., Bang, O. Y., and Kim, H. H. (2014). Cobalt chloride induces neuronal differentiation of human mesenchymal stem cells through upregulation of microRNA-124a. *Biochem. Biophys. Res. Commun.* 444, 581–587. doi: 10.1016/j.bbrc.2014.01.114

Jia, S., Yang, X., Song, W., Wang, L., Fang, K., Hu, Z., et al. (2014). Incorporation of osteogenic and angiogenic small interfering RNAs into chitosan sponge for bone tissue engineering. *Int. J. Nanomed.* 9, 5307–5316. doi: 10.2147/IJN.S70457

Jodat, Y. A., Kiaee, K., Vela Jarquin, D., De la Garza Hernández, R. L., Wang, T., Joshi, S., et al. (2020). A 3D-printed hybrid nasal cartilage with functional electronic olfaction. *Adv. Sci.* 7:1901878. doi: 10.1002/advs.201901878

Kasten, P., Beyen, I., Niemeyer, P., Luginbühl, R., Bohner, M., and Richter, W. (2008). Porosity and pore size of beta-tricalcium phosphate scaffold can influence protein production and osteogenic differentiation of human mesenchymal stem cells: an in vitro and in vivo study. *Acta Biomater.* 4, 1904–1915. doi: 10.1016/j.actbio.2008.05.017

Khojasteh, A., Fahimipour, F., Eslaminejad, M. B., Jafarian, M., Jahangir, S., Bastami, F., et al. (2016). Development of PLGA-coated β-TCP scaffolds containing VEGF for bone tissue engineering. *Mater. Sci. Eng. C Mater. Biol. Appl.* 69, 780–788. doi: 10.1016/j.msec.2016.07.011

Kilian, K. A., Bugarija, B., Lahn, B. T., and Mrksich, M. (2010). Geometric cues for directing the differentiation of mesenchymal stem cells. *Proc. Natl. Acad. Sci. U.S.A.* 107, 4872–4877. doi: 10.1073/pnas.0903269107

Kumar, H., and Kim, K. (2020). Stereolithography 3D Bioprinting. *Methods Mol. Biol.* 2140, 93–108. doi: 10.1007/978-1-0716-0520-2_6

Lam, J., and Segura, T. (2013). The modulation of MSC integrin expression by RGD presentation. *Biomaterials* 34, 3938–3947. doi: 10.1016/j.biomaterials.2013.01.091

Le, H., Xu, W., Zhuang, X., Chang, F., Wang, Y., and Ding, J. (2020). Mesenchymal stem cells for cartilage regeneration. *J. Tissue Eng.* 11:2041731420943839. doi: 10.1177/2041731420943839

Lei, B., Chen, X., Han, X., and Li, Z. (2011). Unique physical-chemical, apatite-forming properties and human marrow mesenchymal stem cells (HMSCs) response of sol-gel bioactive glass microspheres. *J. Mater. Chem.* 21, 12725–12734. doi: 10.1039/C1JM11547B

Li, R. W., Kirkland, N. T., Truong, J., Wang, J., Smith, P. N., Birbilis, N., et al. (2014). The influence of biodegradable magnesium alloys on the osteogenic differentiation of human mesenchymal stem cells. *J. Biomed. Mater. Res. A* 102, 4346–4357. doi: 10.1002/jbm.a.35111

Li, T., Ma, H., Ma, H., Ma, Z., Qiang, L., Yang, Z., et al. (2019). Mussel-inspired nanostructures potentiate the immunomodulatory properties and angiogenesis of mesenchymal stem cells. *ACS Appl. Mater. Interfaces* 11, 17134–17146. doi: 10.1021/acsami.8b22017

Li, W.-J. W.-J., Tuli, R., Okafor, C., Derfoul, A., Danielson, K. G. K. G., Hall, D. J. D. J., et al. (2005). A three-dimensional nanofibrous scaffold for cartilage tissue engineering using human mesenchymal stem cells. *Biomaterials* 26, 599–609. doi: 10.1016/j.biomaterials.2004.03.005

Liu, X., Wang, X., Horii, A., Wang, X., Qiao, L., Zhang, S., et al. (2012). *In vivo* studies on angiogenic activity of two designer self-assembling peptide scaffold hydrogels in the chicken embryo chorioallantoic membrane. *Nanoscale* 4, 2720–2727. doi: 10.1039/c2nr00001f

Lu, F., Zhao, X., Wu, J., Cui, Y., Mao, Y., Chen, K., et al. (2013). MSCs transfected with hepatocyte growth factor or vascular endothelial growth factor improve cardiac function in the infarcted porcine heart by increasing angiogenesis and

reducing fibrosis. *Int. J. Cardiol.* 167, 2524–2532. doi: 10.1016/j.ijcard.2012.06.052

Luthringer, B. J., and Willumeit-Romer, R. (2016). Effects of magnesium degradation products on mesenchymal stem cell fate and osteoblastogenesis. *Gene* 575, 9–20. doi: 10.1016/j.gene.2015.08.028

Matsiko, A., Gleeson, J. P., and O'Brien, F. J. (2015). Scaffold mean pore size influences mesenchymal stem cell chondrogenic differentiation and matrix deposition. *Tissue Eng. Part A* 21, 486–497. doi: 10.1089/ten.TEA.2013.0545

McBeath, R., Pirone, D. M., Nelson, C. M., Bhadriraju, K., and Chen, C. S. (2004). Cell shape, cytoskeletal tension, and RhoA regulate stem cell lineage commitment. *Dev. Cell* 6, 483–495.

McMurray, R. J., Gadegaard, N., Tsimbouri, P. M., Burgess, K. V., McNamara, L. E., Tare, R., et al. (2011). Nanoscale surfaces for the long-term maintenance of mesenchymal stem cell phenotype and multipotency. *Nat. Mater.* 10, 637–644. doi: 10.1038/nmat3058

Meinel, L., Hofmann, S., Betz, O., Fajardo, R., Merkle, H. P., Langer, R., et al. (2006). Osteogenesis by human mesenchymal stem cells cultured on silk biomaterials: comparison of adenovirus mediated gene transfer and protein delivery of BMP-2. *Biomaterials* 27, 4993–5002.

Mellott, A. J., Forrest, M. L., and Detamore, M. S. (2013). Physical non-viral gene delivery methods for tissue engineering. *Ann. Biomed. Eng.* 41, 446–468. doi: 10.1007/s10439-012-0678-1

Mohyeldin, A., Garzón-Muvdi, T., and Quiñones-Hinojosa, A. (2010). Oxygen in stem cell biology: a critical component of the stem cell niche. *Cell Stem Cell* 7, 150–161. doi: 10.1016/j.stem.2010.07.007

Moon, H.-H., Joo, M. K., Mok, H., Lee, M., Hwang, K.-C., Kim, S. W., et al. (2014). MSC-based VEGF gene therapy in rat myocardial infarction model using facial amphipathic bile acid-conjugated polyethyleneimine. *Biomaterials* 35, 1744–1754. doi: 10.1016/j.biomaterials.2013.11.019

Mouriño, V., Cattalini, J. P., and Boccaccini, A. R. (2012). Metallic ions as therapeutic agents in tissue engineering scaffolds: an overview of their biological applications and strategies for new developments. *J. R. Soc. Interface* 9, 401–419. doi: 10.1098/rsif.2011.0611

Muller, P., Bulnheim, U., Diener, A., Luthen, F., Teller, M., Klinkenberg, E. D., et al. (2008). Calcium phosphate surfaces promote osteogenic differentiation of mesenchymal stem cells. *J. Cell. Mol. Med.* 12, 281–291. doi: 10.1111/j.1582-4934.2007.00103.x

Murphy, C. M., Duffy, G. P., Schindeler, A., and O'Brien, F. J. (2016). Effect of collagen-glycosaminoglycan scaffold pore size on matrix mineralization and cellular behavior in different cell types. *J. Biomed. Mater. Res. A* 104, 291–304. doi: 10.1002/jbm.a.35567

Mygind, T., Stiehler, M., Baatrup, A., Li, H., Zou, X., Flyvbjerg, A., et al. (2007). Mesenchymal stem cell ingrowth and differentiation on coralline hydroxyapatite scaffolds. *Biomaterials* 28, 1036–1047.

Nagane, K., Jo, J. I., and Tabata, Y. (2010). Promoted adipogenesis of rat mesenchymal stem cells by transfection of small interfering RNA complexed with a cationized dextran. *Tissue Eng. Part A* 16, 21–31. doi: 10.1089/ten.TEA.2009.0170

O'Brien, F. J., Harley, B. A., Waller, M. A., Yannas, I. V., Gibson, L. J., and Prendergast, P. J. (2007). The effect of pore size on permeability and cell attachment in collagen scaffolds for tissue engineering. *Technol. Health Care* 15, 3–17.

Obata, A., and Kasuga, T. (2009). Stimulation of human mesenchymal stem cells and osteoblasts activities in vitro on silicon−releasable scaffolds. *J. Biomed. Mater. Res. Part A* 91, 11–17.

Oh, S. A., Kim, S. H., Won, J. E., Kim, J. J., Shin, U. S., and Kim, H. W. (2011). Effects on growth and osteogenic differentiation of mesenchymal stem cells by the zinc-added sol-gel bioactive glass granules. *J. Tissue Eng.* 2010:475260. doi: 10.4061/2010/475260

Park, H., Temenoff, J. S., Tabata, Y., Caplan, A. I., Raphael, R. M., Jansen, J. A., et al. (2009). Effect of dual growth factor delivery on chondrogenic differentiation of rabbit marrow mesenchymal stem cells encapsulated in injectable hydrogel composites. *J. Biomed. Mater. Res. Part A* 88, 889–897. doi: 10.1002/jbm.a.31948

Prabhakaran, M. P., Venugopal, J. R., and Ramakrishna, S. (2009). Mesenchymal stem cell differentiation to neuronal cells on electrospun nanofibrous substrates for nerve tissue engineering. *Biomaterials* 30, 4996–5003. doi: 10.1016/j.biomaterials.2009.05.057

Qiao, Y., Liu, X., Zhou, X., Zhang, H., Zhang, W., Xiao, W., et al. (2020). Gelatin templated polypeptide co-cross-linked hydrogel for bone regeneration. *Adv. Healthc. Mater.* 9:e1901239. doi: 10.1002/adhm.201901239

Qu, Z., Yan, J., Li, B., Zhuang, J., and Huang, Y. (2010). Improving bone marrow stromal cell attachment on chitosan/hydroxyapatite scaffolds by an immobilized RGD peptide. *Biomed. Mater.* 5:065001. doi: 10.1088/1748-6041/5/6/065001

Rao, F., Wang, Y., Zhang, D., Lu, C., Cao, Z., Sui, J., et al. (2020). Aligned chitosan nanofiber hydrogel grafted with peptides mimicking bioactive brain-derived neurotrophic factor and vascular endothelial growth factor repair long-distance sciatic nerve defects in rats. *Theranostics* 10, 1590–1603. doi: 10.7150/thno.36272

Re'em, T., Kaminer-Israeli, Y., Ruvinov, E., and Cohen, S. (2012). Chondrogenesis of hMSC in affinity-bound TGF-beta scaffolds. *Biomaterials* 33, 751–761. doi: 10.1016/j.biomaterials.2011.10.007

Richardson, T. P., Peters, M. C., Ennett, A. B., and Mooney, D. J. (2001). Polymeric system for dual growth factor delivery. *Nat. Biotechnol.* 19, 1029–1034. doi: 10.1038/nbt1101-1029

Rodrigues, M., Griffith, L. G., and Wells, A. (2010). Growth factor regulation of proliferation and survival of multipotential stromal cells. *Stem Cell Res. Ther.* 1:32. doi: 10.1186/scrt32

Rodriguez, J. P., Rios, S., and Gonzalez, M. (2002). Modulation of the proliferation and differentiation of human mesenchymal stem cells by copper. *J. Cell. Biochem.* 85, 92–100.

Sahoo, S., Toh, S. L., and Goh, J. C. H. (2010). A bFGF-releasing silk/PLGA-based biohybrid scaffold for ligament/tendon tissue engineering using mesenchymal progenitor cells. *Biomaterials* 31, 2990–2998. doi: 10.1016/j.biomaterials.2010.01.004

Schussler, S. D., Uske, K., Marwah, P., Kemp, F. W., Bogden, J. D., Lin, S. S., et al. (2017). Controlled release of vanadium from a composite scaffold stimulates mesenchymal stem cell osteochondrogenesis. *Aaps J.* 19, 1017–1028. doi: 10.1208/s12248-017-0073-9

Shih, Y. R. V., Tseng, K. F., Lai, H. Y., Lin, C. H., and Lee, O. K. (2011). Matrix stiffness regulation of integrin-mediated mechanotransduction during osteogenic differentiation of human mesenchymal stem cells. *J. Bone Miner. Res.* 26, 730–738. doi: 10.1002/jbmr.278

Sila-Asna, M., Bunyaratvej, A., Maeda, S., Kitaguchi, H., and Bunyaratavej, N. (2007). Osteoblast differentiation and bone formation gene expression in strontium-inducing bone marrow mesenchymal stem cell. *Kobe J. Med. Sci.* 53, 25–35.

Simmons, C. A., Alsberg, E., Hsiong, S., Kim, W. J., and Mooney, D. J. (2004). Dual growth factor delivery and controlled scaffold degradation enhance in vivo bone formation by transplanted bone marrow stromal cells. *Bone* 35, 562–569.

Sun, M., Chi, G., Xu, J., Tan, Y., Xu, J., Lv, S., et al. (2018). Extracellular matrix stiffness controls osteogenic differentiation of mesenchymal stem cells mediated by integrin α5. *Stem Cell Res. Ther.* 9:52. doi: 10.1186/s13287-018-0798-0

Tamama, K., Kawasaki, H., and Wells, A. (2010). Epidermal growth factor (EGF) treatment on multipotential stromal cells (MSCs). possible enhancement of therapeutic potential of MSC. *J. Biomed. Biotechnol.* 2010:795385. doi: 10.1155/2010/795385

Tang, J., Peng, R., and Ding, J. (2010). The regulation of stem cell differentiation by cell-cell contact on micropatterned material surfaces. *Biomaterials* 31, 2470–2476. doi: 10.1016/j.biomaterials.2009.12.006

Tay, C. Y., Yu, H., Pal, M., Leong, W. S., Tan, N. S., Ng, K. W., et al. (2010). Micropatterned matrix directs differentiation of human mesenchymal stem cells towards myocardial lineage. *Exp. Cell Res.* 316, 1159–1168. doi: 10.1016/j.yexcr.2010.02.010

Teti, G., Focaroli, S., Salvatore, V., Mazzotti, E., Ingra, L., Mazzotti, A., et al. (2018). The hypoxia-mimetic agent cobalt chloride differently affects human mesenchymal stem cells in their chondrogenic potential. *Stem Cells Int.* 2018:3237253. doi: 10.1155/2018/3237253

Tong, C., Hao, H., Xia, L., Liu, J., Ti, D., Dong, L., et al. (2016). Hypoxia pretreatment of bone marrow-derived mesenchymal stem cells seeded in a collagen-chitosan sponge scaffold promotes skin wound healing in diabetic rats with hindlimb ischemia. *Wound Repair Regen.* 24, 45–56. doi: 10.1111/wrr.12369

Wan, L. Q., Kang, S. M., Eng, G., Grayson, W. L., Lu, X. L., Huo, B., et al. (2010). Geometric control of human stem cell morphology and differentiation. *Integr. Biol. (Camb)* 2, 346–353. doi: 10.1039/c0ib00016g

Wang, X., Gao, L., Han, Y., Xing, M., Zhao, C., Peng, J., et al. (2018). Silicon-enhanced adipogenesis and angiogenesis for vascularized adipose tissue engineering. *Adv. Sci*. 5:1800776. doi: 10.1002/advs.201800776

Weber, J. N., White, E. W., and Lebiedzik, J. (1971). New porous biomaterials by replication of echinoderm skeletal microstructures. *Nature* 233, 337–339. doi: 10.1038/233337a0

Wegman, F., Bijenhof, A., Schuijff, L., Oner, F. C., Dhert, W. J. A., and Alblas, J. (2011). Osteogenic differentiation as a result of BMP-2 plasmid DNA based gene therapy in vitro and in vivo. *Eur. Cells Mater*. 21, 230–242.

Whitehead, A. K., Barnett, H. H., Caldorera-Moore, M. E., and Newman, J. J. (2018). Poly (ethylene glycol) hydrogel elasticity influences human mesenchymal stem cell behavior. *Regenerative Biomaterials* 5, 167–175. doi: 10.1093/rb/rby008

Wingate, K., Bonani, W., Tan, Y., Bryant, S. J., and Tan, W. (2012). Compressive elasticity of three-dimensional nanofiber matrix directs mesenchymal stem cell differentiation to vascular cells with endothelial or smooth muscle cell markers. *Acta Biomater*. 8, 1440–1449. doi: 10.1016/j.actbio.2011.12.032

Xiao, Y., Ahadian, S., and Radisic, M. (2017). Biochemical and biophysical cues in matrix design for chronic and diabetic wound treatment. *Tissue Eng. Part B Rev*. 23, 9–26. doi: 10.1089/ten.TEB.2016.0200

Xing, Q., Yates, K., Bailey, A., Vogt, C., He, W., Frost, M. C., et al. (2013). Effects of local nitric oxide release on human mesenchymal stem cell attachment and proliferation on gelatin hydrogel surface. *Surf. Innov*. 1, 224–232.

Yang, F., Williams, C. G., Wang, D. -A., Lee, H., Manson, P. N., and Elisseeff, J. (2005). The effect of incorporating RGD adhesive peptide in polyethylene glycol diacrylate hydrogel on osteogenesis of bone marrow stromal cells. *Biomaterials* 26, 5991–5998. doi: 10.1016/j.biomaterials.2005.03.018

Yang, F., Yang, D., Tu, J., Zheng, Q., Cai, L., and Wang, L. (2011). Strontium enhances osteogenic differentiation of mesenchymal stem cells and in vivo bone formation by activating Wnt/catenin signaling. *Stem Cells* 29, 981–991. doi: 10.1002/stem.646

Yao, B., Wang, R., Wang, Y., Zhang, Y., Hu, T., Song, W., et al. (2020). Biochemical and structural cues of 3D-printed matrix synergistically direct MSC differentiation for functional sweat gland regeneration. *Sci. Adv*. 6:eaaz1094. doi: 10.1126/sciadv.aaz1094

Yao, X., Liu, Y., Gao, J., Yang, L., Mao, D., Stefanitsch, C., et al. (2015). Nitric oxide releasing hydrogel enhances the therapeutic efficacy of mesenchymal stem cells for myocardial infarction. *Biomaterials* 60, 130–140. doi: 10.1016/j.biomaterials.2015.04.046

Yau, T. M., Kim, C., Li, G., Zhang, Y., Fazel, S., Spiegelstein, D., et al. (2007). Enhanced angiogenesis with multimodal cell-based gene therapy. *Ann. Thorac. Surg*. 83, 1110–1119.

You, D. H., and Nam, M. J. (2013). Effects of human epidermal growth factor gene-transfected mesenchymal stem cells on fibroblast migration and proliferation. *Cell Prolif*. 46, 408–415. doi: 10.1111/cpr.12042

Yu, X., Lu, C., Liu, H., Rao, S., Cai, J., Liu, S., et al. (2013). Hypoxic preconditioning with cobalt of bone marrow mesenchymal stem cells improves cell migration and enhances therapy for treatment of ischemic acute kidney injury. *PLoS One* 8:e62703. doi: 10.1371/journal.pone.0062703

Zhang, R., Lee, P., Lui, V. C. H., Chen, Y., Liu, X., Lok, C. N., et al. (2015). Silver nanoparticles promote osteogenesis of mesenchymal stem cells and improve bone fracture healing in osteogenesis mechanism mouse model. *Nanomed. Nanotechnol. Biol. Med*. 11, 1949–1959. doi: 10.1016/j.nano.2015.07.016

Zhang, Z. Z., Jiang, D., Ding, J. X., Wang, S. J., Zhang, L., Zhang, J. Y., et al. (2016). Role of scaffold mean pore size in meniscus regeneration. *Acta Biomater*. 43, 314–326. doi: 10.1016/j.actbio.2016.07.050

Zhao, D., Zhu, T., Li, J., Cui, L., Zhang, Z., Zhuang, X., et al. (2021). Poly(lactic-co-glycolic acid)-based composite bone-substitute materials. *Bioact. Mater*. 6, 346–360. doi: 10.1016/j.bioactmat.2020.08.016

Zhou, Y., Guan, X., Yu, M., Wang, X., Zhu, W., Wang, C., et al. (2014). Angiogenic/osteogenic response of BMMSCs on bone-derived scaffold: effect of hypoxia and role of PI3K/Akt-mediated VEGF-VEGFR pathway. *Biotechnol. J*. 9, 944–953. doi: 10.1002/biot.201300310

Zhu, B., Lu, Q., Yin, J., Hu, J., and Wang, Z. (2005). Alignment of osteoblast-like cells and cell-produced collagen matrix induced by nanogrooves. *Tissue Eng*. 11, 825–834.

Zhu, T., Cui, Y., Zhang, M., Zhao, D., Liu, G., and Ding, J. (2020). Engineered three-dimensional scaffolds for enhanced bone regeneration in osteonecrosis. *Bioact. Mater*. 5, 584–601. doi: 10.1016/j.bioactmat.2020.04.008

Conflict of Interest: The authors declare that the research was conducted in the absence of any commercial or financial relationships that could be construed as a potential conflict of interest.

frontiers in Cell and Developmental Biology

ORIGINAL RESEARCH
published: 01 April 2021
doi: 10.3389/fcell.2021.663037

Periodontal Inflammation-Triggered by Periodontal Ligament Stem Cell Pyroptosis Exacerbates Periodontitis

Qin Chen[1†], Xingguang Liu[2†], Dingyu Wang[3†], Jisi Zheng[1], Lu Chen[1], Qianyang Xie[1], Xiaohan Liu[1], Sujuan Niu[4], Guanlin Qu[5], Jianfeng Lan[6], Jing Li[7], Chi Yang[1] and Duohong Zou[1]**

[1] Shanghai Ninth People's Hospital, Shanghai Jiao Tong University School of Medicine; College of Stomatology, Shanghai Jiao Tong University; National Center for Stomatology; National Clinical Research Center for Oral Diseases; Shanghai Key Laboratory of Stomatology; Research Unit of Oral and Maxillofacial Regenerative Medicine, Chinese Academy of Medical Sciences, Shanghai, China, [2] National Key Laboratory of Medical Immunology, Navy Military Medical University, Shanghai, China, [3] State Key Laboratory of Pharmaceutical Biotechnology and Ministry of Education, Key Laboratory of Model Animal for Disease Study, Model Animal Research Center, Nanjing University, Nanjing, China, [4] College of Stomatology, Inner Mongolia Medical University, Hohhot, China, [5] Liaoning Provincial Key Laboratory of Oral Diseases, Department of Oral and Maxillofacial Surgery, School and Hospital of Stomatology, China Medical University, Shenyang, China, [6] Guangxi Key Laboratory of Molecular Medicine in Liver Injury and Repair, The Affiliated Hospital of Guilin Medical University, Guilin, China, [7] Shandong Provincial Key Laboratory of Oral Tissue Regeneration, School of Stomatology, Shandong University, Jinan, China

OPEN ACCESS

Edited by:
Zhouguang Wang,
Albert Einstein College of Medicine, United States

Reviewed by:
Ming Zhao,
University of Minnesota Twin Cities, United States
Xiaorui Luan,
Zhejiang University, China

***Correspondence:**
Chi Yang
yangchi63@hotmail.com
Duohong Zou
zdhyy@ahmu.edu.cn

[†]These authors have contributed equally to this work

Specialty section:
This article was submitted to Stem Cell Research, a section of the journal Frontiers in Cell and Developmental Biology

Received: *02 February 2021*
Accepted: *11 March 2021*
Published: *01 April 2021*

Citation:
Chen Q, Liu X, Wang D, Zheng J, Chen L, Xie Q, Liu X, Niu S, Qu G, Lan J, Li J, Yang C and Zou D (2021) Periodontal Inflammation-Triggered by Periodontal Ligament Stem Cell Pyroptosis Exacerbates Periodontitis. Front. Cell Dev. Biol. 9:663037. doi: 10.3389/fcell.2021.663037

Periodontitis is an immune inflammatory disease that leads to progressive destruction of bone and connective tissue, accompanied by the dysfunction and even loss of periodontal ligament stem cells (PDLSCs). Pyroptosis mediated by gasdermin-D (GSDMD) participates in the pathogenesis of inflammatory diseases. However, whether pyroptosis mediates PDLSC loss, and inflammation triggered by pyroptosis is involved in the pathological progression of periodontitis remain unclear. Here, we found that PDLSCs suffered GSDMD-dependent pyroptosis to release interleukin-1β (IL-1β) during human periodontitis. Importantly, the increased IL-1β level in gingival crevicular fluid was significantly correlated with periodontitis severity. The caspase-4/GSDMD-mediated pyroptosis caused by periodontal bacteria and cytoplasmic lipopolysaccharide (LPS) dominantly contributed to PDLSC loss. By releasing IL-1β into the tissue microenvironment, pyroptotic PDLSCs inhibited osteoblastogenesis and promoted osteoclastogenesis, which exacerbated the pathological damage of periodontitis. Pharmacological inhibition of caspase-4 or IL-1β antibody blockade in a rat periodontitis model lead to the significantly reduced loss of alveolar bone and periodontal ligament damage. Furthermore, Gsdmd deficiency alleviated periodontal inflammation and bone loss in mouse experimental periodontitis. These findings indicate that GSDMD-driven PDLSC pyroptosis and loss plays a pivotal role in the pathogenesis of periodontitis by increasing IL-1β release, enhancing inflammation, and promoting osteoclastogenesis.

Keywords: GSDMD, IL-1β, PDLSC, periodontitis, pyroptosis

INTRODUCTION

Periodontitis is one of the most prevalent infectious human inflammatory diseases and is distinguished by the progressive destruction of the tooth-supporting tissues and by the inflammatory reaction associated with gram-negative anaerobic bacteria (such as *Porphyromonas gingivalis* and *Treponema denticola*) in dental biofilms (Pihlstrom et al., 2005; Hajishengallis, 2015). Under this sustained inflammatory condition, the periodontal tissues (including alveolar bone, periodontal ligament, and root cementum) are destroyed, and the regeneration function of these attachment apparatuses is damaged, eventually leading to tooth loss and chewing dysfunction (Kinane et al., 2017). Recently, multiple studies have revealed that periodontitis accelerates the initiation or progression of various systemic diseases, including diabetes, cardiovascular disease, and Alzheimer's disease, through periodontal pathogen-induced inflammation (Polak and Shapira, 2018; Aoyama et al., 2019; Dominy et al., 2019). To date, the underlying mechanisms of inflammation amplification and persistence in periodontitis remain to be elucidated.

Periodontal ligament stem cells (PDLSCs) are a population of mesenchymal stem cells (MSCs) located in the periodontal ligament that show high self-renewal capability and have multiple differentiation potentials to regenerate lost/damaged periodontal tissues (Seo et al., 2004). Although PDLSCs have exhibited remarkable reconstruction effects in artificially created bone defects in various animal models, the regeneration of periodontal tissues does not achieve the desired effect in periodontitis-caused tissue loss (Liu et al., 2008; Mrozik et al., 2013; Chen F. M. et al., 2016). Increasing evidence indicates that the inflammatory environment caused by periodontitis could inhibit the differentiation potential of PDLSCs, and the loose pluripotency of PDLSCs is associated with the activation of NF-κB, mitogen-activated protein kinase (MAPK), and BMP/Smad signaling pathways by inflammatory cytokines (Mao et al., 2016). In addition, the expression of the inflammatory cytokine IL-1β is significantly increased in periodontitis tissues, and an *in vitro* study demonstrated that IL-1β-treated PDLSCs showed impaired osteogenesis potential (Fawzy El-Sayed et al., 2019). However, the molecular mechanism of PDLSC dysfunction and loss in periodontitis remains unclear, and whether abnormal PDLSCs are involved in the pathogenesis of periodontitis is also unknown.

Increasing evidence indicates that pro-IL-1β is processed into its biologically active form IL-1β during pyroptosis, which is a critical mechanism for host defense against infection (He et al., 2015). Pyroptosis, a pro-inflammatory form of cell death, is characterized by the activation of inflammatory caspases, cell swelling, and the release of the GSDMD-N terminus (1–275 aa) to form pores (10–14 nm) in the plasma membrane (Liu et al., 2016). This process results in the massive release of cellular contents, including danger-associated molecular patterns (DAMPs) and cytokines (IL-1β and IL-18), which trigger a robust inflammatory response (Man et al., 2017). Based on the different stimuli and inflammatory caspases, pyroptosis is divided into canonical and non-canonical pyroptosis (Aglietti and Dueber, 2017). For canonical pyroptosis, canonical inflammasomes (including NLRP3, NLRC4, AIM2, and Pyrin) activate caspase-1 to cleave both GSDMD and pro-IL-1β under DAMP stimulation (Xia et al., 2020). In non-canonical pyroptosis, cytoplasmic LPS directly activates caspase-4 (mouse counterpart caspase-11) to cleave GSDMD, which is independent of inflammasomes and caspase-1 (Kesavardhana et al., 2020). Although most pyroptosis studies focus on the role of pyroptosis in the pathogenesis of systemic inflammatory diseases (such as sepsis and inflammatory bowel disease), some clinical studies have reported a correlation of pyroptosis with periodontitis (Yamaguchi et al., 2017; García-Hernández et al., 2019; Ma et al., 2020). Additionally, Jun et al. (2018) have shown that human gingival fibroblasts infected with the periodontal pathogen *Treponema denticola* demonstrated obvious pyroptosis, accompanied by the activation of caspase-4 and the release of IL-1β. Moreover, increased expression of NLRP3 and caspase-1 were reported in human MSCs derived from the human umbilical cord under lipopolysaccharide (LPS) treatment (Wang et al., 2017). Whether PDLSCs undergo pyroptosis during periodontal pathogen infection is not known. How PDLSC pyroptosis is involved in the pathogenesis of periodontitis is also not clear.

In this study, combining human periodontitis specimens (n = 87), we found that PDLSCs underwent GSDMD-mediated pyroptosis with typical cell swelling and IL-1β release during periodontitis. Mechanistic investigation revealed that the caspase-4/GSDMD/IL-1β non-canonical pyroptosis pathway was the major contributor to the pathogenesis of periodontitis. Through the construction of animal periodontitis models, we demonstrated that GSDMD-mediated PDLSC pyroptosis participated in periodontal tissue destruction and could be therapeutically targeted.

MATERIALS AND METHODS

Study Participants

The patients in this study included 87 adults (43 females and 44 males, age 18–45 years) from the Department of Oral Surgery, Ninth People's Hospital, Shanghai Jiao Tong University. All participants were asked to give their consent in written form after being informed of the purpose and protocol of the study. This study was approved by the Research Ethics Committee of the Ninth People's Hospital (approval NO. SH9H-2020-TK60-1). Patients were divided based on clinical diagnosis into a severe periodontitis group and a healthy group. The patients in the severe periodontitis group (n = 16, 8 females and 8 males) were diagnosed by the following indices: clinical attachment level (CAL) $\geq$ 5 mm, alveolar crest bone loss (BL) $>$ 6 mm without reaching the tooth apex, positive pulpal sensitivity, the necessity of tooth extraction and reach stage III with potential for additional tooth loss (Caton et al., 2018). The healthy group (n = 22, 11 females and 11 males) consisted of patients with impacted or partially erupted third molars and teeth requiring removal for orthodontic therapy.

GCF and Periodontium Sampling

We obtained gingival crevicular fluid (GCF) from periodontitis patients (n = 65) and healthy patients (n = 10). For GCF collection, teeth were air dried and isolated with cotton rolls, supragingival plaque was removed, and then a collection strip was inserted into the sulcus for 1 min. Samples were eluted from the strip in 100 μl of phosphate-buffered saline (PBS) by centrifugation in centrifuge tubes. The eluates were stored at −80°C until assays were performed. Periodontium tissues were collected from 10 healthy (orthodontic) teeth and 10 teeth with severe periodontitis after extraction from patients. Periodontium tissues were isolated and prepared for protein extraction and western blot analysis. The antibodies used are given in **Supplementary Table 1**.

Immunohistochemistry (IHC), Immunofluorescence (IF)

Human teeth were obtained from 6 patients with severe periodontitis and 6 healthy (orthodontic) patients. The teeth were fixed with 4% paraformaldehyde (PFA) for 24 h, decalcified with 10% EDTA (pH = 7.2) for 10 weeks and then sectioned in sections. The sections were incubated at 4°C overnight with primary antibodies, then washed with PBS and incubated with secondary antibody for 1 h. For IHC, sections were visualized with a Diaminobenzidine (DAB) Kit (MXB, China) and restained with hematoxylin. For IF, sections were counterstained with 4′,6-diamidino-2-phenylindole (DAPI). Images were taken with a high-resolution digital camera (Olympus DP 73, Japan).

Cell Isolation, FACS Sorting and PDLSC Culture

Human periodontal ligament (PDL) tissues of third molars were obtained from 6 healthy donors (3 females and 3 males) undergoing tooth extraction for orthodontic reasons. Following the extraction, the PDL was minced into 1 mm^3 pieces and digested for 30 min at 37°C in 0.3% Type I collagenase (Sigma, United States). After centrifugation, the precipitate was transferred to culture flasks with α-minimum essential medium (HyClone, United States) supplemented with 20% fetal bovine serum (Gibco, United States), 100 U/mL penicillin and 100 mg/mL streptomycin (HyClone, United States) and then cultured at 37°C in a 5% CO_2 incubator. A total of 1×10^6 cells were harvested, and the single-cell suspension was incubated with mesenchymal stem cell surface markers: FITC CD90, PerCP-Cy5.5 CD105, APC CD73, and PE CD44 (BD, United States) (Bartold and Gronthos, 2017; Al-Habib and Huang, 2019; Trubiani et al., 2019). PDLSCs were acquired immediately after staining using a FACSCalibur flow cytometer (BD, United States) equipped with the Cell Quest program (BD, United States). Then, PDLSCs were expanded with α-MEM containing 10% FBS and 1% antibiotics at 37°C in a 5% CO_2 incubator.

Osteogenic Differentiation

To induce osteoblast differentiation, a total of 1×10^5 PDLSCs were seeded into each well of 6-well plates. Upon reaching a density of 70%, the PDLSCs were grown in osteogenic differentiation medium (Cyagen, United States) for 21 days. In some osteogenic induction assays, the PDLSCs were treated with recombinant human IL-1β protein (R&D, United States) at the indicated concentration every 2 days. After 21 days, the cells were fixed with 4% PFA in PBS and stained with 2% Alizarin red (pH = 4.2).

Adipogenic Differentiation

For adipogenic induction, PDLSCs were plated in 6-well plates. When the PDLSCs reached 100% confluence, the growth medium was changed to adipogenic differentiation medium (Cyagen, United States), and the manufacturer's protocol was followed. In some adipogenic induction assays, PDLSCs were treated with recombinant human IL-1β protein (R&D, United States) at the indicated concentration every 2 days. After 21 days, the cells were fixed in 4% PFA for 30 min and stained with Oil red O.

Chondrogenic Differentiation

To induce chondrogenic differentiation, a total of 2×10^5 PDLSCs were centrifuged in a 15 mL polypropylene tube (Corning, United States). Cell pellets were treated with chondrogenic differentiation medium (Cyagen, United States) according to the manufacturer's protocol. After 30 days, pellets were fixed with 4% PFA and then made into paraffin sections. Chondrogenic differentiation was evaluated by staining with Alcian blue solution (Cyagen, United States).

Osteoclast Differentiation and TRAP Staining

THP-1 (human monocyte) cells were purchased from the Shanghai Institute of Cell Biology, China. For osteoclast differentiation, 3×10^4 THP-1 cells were seeded in each well of 48-well plates and cultured with osteoclast differentiation medium, according to the previous studies (Li et al., 2017; Ren et al., 2019). In some osteoclastogenesis assays, THP-1 cells were treated with recombinant human IL-1β protein (R&D, United States) at the indicated concentration every 2 days. After 14 days of induction, cells were fixed with 4% PFA and stained with TRAP staining solution (Jiancheng Biotech, China). TRAP-positive cells with three or more nuclei were considered osteoclasts, and the number of osteoclasts in each well was counted under a microscope.

Bacterial Strains and Cell Stimulation

Porphyromonas gingivalis (*P. gingivalis*) strain ATCC 33,277 was obtained from the Shanghai Key Laboratory of Stomatology at Shanghai Jiao Tong University School of Medicine. *P. gingivalis* was grown on anaerobic blood agar plates with 80% N_2, 10% H_2, and 10% CO_2 for 3–5 days. It was then inoculated into brain heart infusion broth supplemented with 5 μg/mL hemin and 1 μg/mL vitamin K for 24 h until reaching an optical density of 0.04 at 660 nm, corresponding to 10^8 colony-forming units (CFU)/mL. The bacteria were washed and resuspended in α-MEM to infect the PDLSCs at multiplicities of infection (MOIs) of 1:10, 1:50, and 1:100 for 24 h. In some experiments, the PDLSCs were

pretreated with Z-VAD-FMK (Sellect, United States), Z-YVAD-FMK (BioVision, United States), Z-LEVD-FMK (BioVision, United States) and DMSO (Sigma, United States) at the indicated concentrations for 1 h before bacterial infection.

Stimulation of Canonical and Non-canonical Pyroptosis

To activate Caspase-4/11-mediated non-canonical pyroptosis, PDLSCs were transfected with 5 μg/mL LPS (Sigma, United States) by using 0.25% v/v FuGENE HD (Promega, United States). Activation of Caspase-1-mediated canonical pyroptosis: PDLSCs were pretreated with 50 ng/mL PMA (Sigma, United States) for 1 h and then stimulated with 10 μM nigericin (Sigma, United States) or 3 mM ATP (Sigma, United States) (Shi et al., 2015; Okondo et al., 2017; Wang et al., 2020). In some non-canonical pyroptosis activation experiments, the PDLSCs were pretreated with Z-VAD-FMK, Z-YVAD-FMK, Z-LEVD-FMK, and DMSO (Sigma, United States) at the indicated concentrations for 1 h.

Transwell Coculture Assay

PDLSCs were seeded into the lower 6-well transwell chamber at 1×10^5 cells per well and cultured to 80–90% confluence in growth medium. The medium was then replaced with osteogenic differentiation medium or adipogenic differentiation medium. PDLSCs were added to the upper chamber at 5×10^5/well with LPS treatment, with LPS^{FuGene} treatment or without treatment. The cells remaining in the upper transwell chambers were replaced every 2 days. After 21 days of coculture in the differentiation medium, the cells in the lower chamber were harvested for further analysis.

THP-1 cells were plated at 3×10^4 cells per well in the lower 48-well transwell chamber. The medium was then replaced with osteoclast differentiation medium. PDLSCs were added to the upper chamber at 1×10^4/well with LPS treatment, with LPS^{FuGene} treatment or without treatment. The cells remaining in the upper transwell chambers were replaced every 2 days. After 14 days of coculture, the cells in the lower chamber were harvested for osteoclastogenesis analysis.

Animal Studies

Gsdmd−/− mice were bred on a C57BL6/N background and provided by Jiangsu GemPharmatech Co., Ltd. (Nanjing, China). Sixteen male Sprague-Dawley (SD) rats (200–250 g, 8 weeks) were obtained from Shanghai Animal Experimental Center, China. In this study, all animals were maintained in a reserved facility and given free access to food and water under specific pathogen-free conditions. The animal welfare and experimental procedures were approved by the Animal Care and Use Committee of Shanghai Jiao Tong University Affiliated Ninth People's Hospital (approval NO. SH9H-2020-A132-1). To construct the experimental periodontitis model, a 4-0 silk ligature was placed around the left first molar of the animal maxilla for 14 days under anesthesia with sodium pentobarbital (Bhattarai et al., 2016; Santana et al., 2016; Marchesan et al., 2018). The ligatures remained in place throughout the experimental period and were checked every 2 days to ensure subgingival placement. Sixteen SD rats were randomly divided into four groups (n = 6/group): sham, ligature, ligature + Caspase-4 inhibitor (Z-LEVD-FMK, 50 ng/μl), and ligature + IL-1β antibody (25 pg/μl). The drugs were administered into the subperiosteum at the left buccal and palatal gingivae of the first maxillary molars every 2 days in a volume of 20 μl for 14 days. Mice were divided into three groups (n = 6/group): wild type (WT) + sham, WT + ligature, and Gsdmd-knockout + ligature. On day 14, all animals in each group were sacrificed by carbon dioxide inhalation for further experimental analyses.

Micro-Computed Tomography (Micro-CT) Imaging and Bone Parameter Analysis

All animals were anesthetized, and their maxillary specimens were scanned by a high-resolution micro-CT scanner SkyScan 1176 (Bruker, Belgium). The parameters used were 70 kV, 353 uA, and 360° rotations, with a 0.5 mm thick aluminum filter. The analyzer software CT Analyzer/CT Volume (Bruker, Belgium) was used for the visualization and quantification of 2D and 3D data. The distances from the cement-enamel junction (CEJ) to the alveolar bone crest (ABC) in the periodontitis-induced area in the images were measured to confirm alveolar bone loss and tissue damage. The bone mineral density (BMD, g/cm3) and bone/tissue volume (BV/TV, %) were calculated after the selection of a three-dimensional region of interest (ROI) around the first upper molar.

Histological Analysis

After scanning by micro-CT, the maxilla specimens were fixed in 4% PFA for 24 h and decalcified in 10% EDTA solution for 5 weeks, and then sectioned in sections. The sections were mounted on glass slides and stained with hematoxylin and eosin (H&E). Histopathological changes in stained tissues were observed using an optical microscope (Olympus, Japan).

RNA Extraction and Quantitative Real-Time PCR

Total RNA was extracted using RNAiso Plus (Takara, Japan) according to the manufacturer's instructions. The PrimerScript™ RT Reagent Kit with gDNA Eraser (Takara, Japan) was used to synthesize first-strand cDNA from equivalent amounts of RNA. Then, quantitative real-time PCR was performed using SYBR Premix EX Taq™ (Takara, Japan) following a real-time PCR detection system (Roche, CH). Relative gene expression was normalized to the housekeeping gene *36B4* using the $-\Delta\Delta$Ct method. Primer sequences are summarized in **Supplementary Table 2**.

LDH

LDH release was measured using a Cyto Tox 96 Non-Radioactive Cytotoxicity Assay Kit (Promega, United States) according to the manufacturer's protocol. All values represent the percentage of LDH release compared with a maximum lysis control (1% Triton X-100-lysed cells).

ELISA

The amount of IL-1β in gingival crevicular fluids and cell culture supernatants from different groups was measured by ELISA according to the manufacturer's guidelines. A Human IL-1 beta/IL-1F2 Quantikine ELISA Kit (R&D, United States) was used.

Statistical Analysis

All the results are shown as the mean ± SEM using GraphPad Prism version 8.01 (GraphPad Software, United States). The pairwise differences between two groups were evaluated for statistical significance using the unpaired Student's *t*-test with Welch's correction. For comparison of more than 2 groups, one-way ANOVA was used. *P*-values less than 0.05 were considered statistically significant ($^{*}P < 0.05$, $^{**}P < 0.01$, $^{***}P < 0.001$).

RESULTS

Inflammatory Lesions in Periodontitis Are Correlated With Pyroptosis in PDLSCs

We collected panoramic radiographs, gingival crevicular fluid (GCF), teeth and periodontal tissues from severe periodontitis patients and healthy patients. X-ray imaging combined with clinical examination demonstrated that periodontitis patients showed obvious alveolar bone resorption, gingival recession, and reduced periodontal tissue adhesion compared with healthy patients (**Figure 1A**). To look for the relationship between pyroptosis and periodontitis, first, a Pearson's correlation analysis was conducted between GCF IL-1β level (IL-1β release was the typical event of pyroptosis) and probing depth (clinical index of periodontitis), which demonstrated a significant positive correlation in the two parameters ($P < 0.0001$, $R = 0.6974$) (**Figure 1B**). Consistently, the active form of IL-1β was highly expressed in periodontal tissues and GCFs from periodontitis patients (**Figures 1C,D**). We next detected the expression of GSDMD (the key executor of pyroptosis) in periodontal tissues from periodontitis patients. In support of this hypothesis, we found that the GSDMD level was also upregulated, accompanied by increased release of the GSDMD N-terminal fragment (**Figures 1C,E**). Additionally, strong immunostaining for GSDMD was observed in the periodontal ligaments from periodontitis patients (**Figure 1F**). As shown in **Figure 1C**, caspase-4 was also highly expressed in the periodontal tissues of periodontitis patients. These findings suggested that caspase-4 was activated in periodontitis tissues, leading to GSDMD cleavage and IL-1β release.

As previous works proposed that IL-1β was a useful indicator for evaluating the host response during periodontitis and that human periodontal ligament cells released IL-1β under cyclic stretch (Zhuang et al., 2019; Aral et al., 2020), we detected the localization of IL-1β in periodontal ligament from periodontitis patients. Interestingly, immunofluorescence analysis showed that PDLSCs (CD90+) were the source of IL-1β production and the amount of PDLSCs was decreased in periodontitis patients (**Figure 1G**), which indicated the occurrence of pyroptosis in PDLSCs during periodontitis. To further prove PDLSC was the cell type that pyroptosis happened in periodontitis, we also examined the localization pattern of GSDMD. The co-staining results demonstrated that GSDMD was enriched in PDLSCs in periodontitis patients (**Figure 1H**). Taken together, the above results suggest that periodontitis primarily triggers the production of inflammatory cytokines by inducing PDLSC pyroptosis, which in turn has an important role in the pathogenesis of periodontitis.

P. gingivalis Induces PDLSC Pyroptosis Through Caspase-4 Activation

We used a flow cytometer to acquire PDLSCs based on surface molecules. PDLSCs positively expressed MSC markers, including CD90, CD44, CD105, and CD73 and were negative for hematopoietic progenitor cell surface markers (CD34, CD11b, CD19, CD45, and HLA-DR) (**Supplementary Figure 1A**). PDLSCs were grown in osteogenic, adipogenic and chondrogenic induction media for 21 or 30 days and assessed. Cells displayed calcium deposition positively stained by Alizarin red, cytoplasmic lipid accumulation positively stained by Oil red O, and acidic polysaccharide extracellular matrices positively stained by Alcian blue (**Supplementary Figures 1B–D**). Furthermore, the protein levels of osteogenic markers (ALP, RUNX2, and OPN) and adipogenic markers (APN, PPAR-γ, and C/EBP-α) were both significantly elevated under osteogenic or adipogenic differentiation (**Supplementary Figures 1E,F**). All of these results demonstrated that PDLSCs are stem cells of mesenchymal sources with powerful multipotency.

Periodontitis is a chronic inflammatory disease caused by major periodontopathogens. To determine whether PDLSCs undergo pyroptosis during periodontitis, we used *P. gingivalis* to mimic the pathogenetic process of periodontitis. We found that PDLSCs infected with *P. gingivalis* presented robust lactate dehydrogenase (LDH) release and increased IL-1β release, which were both gradually elevated in an MOI-dependent manner (**Figures 2A,B**). *P. gingivalis* activated caspase-4, and the amount of processed caspase-4 subunit in the culture supernatants was increased depending on the MOI of *P. gingivalis* (**Figure 2C**). In addition to caspase-4 activation, mature IL-1β release and GSDMD cleavage (indicators of terminal pyroptosis events) were both significantly increased under *P. gingivalis* infection (**Figure 2C**). In addition, the amount of activated caspase-1 did not show a marked increase in the culture supernatants compared with caspase-4 (**Figure 2C**). Furthermore, PDLSCs infected with MOI 100 *P. gingivalis* developed the typical pyroptotic morphology with cell swelling, membrane blebbing and propidium iodide (PI) uptake (**Figure 2D**). These results suggested that *P. gingivalis* promotes caspase-4 activation, GSDMD cleavage and mature IL-1β release.

To determine whether *P. gingivalis*-induced PDLSC pyroptosis was dependent on caspase-4 activation, cells were pretreated with the caspase pan inhibitor (Z-VAD-FMK), caspase-1 specific inhibitor (Z-YVAD-FMK) or caspase-4 specific inhibitor (Z-LEVD-FMK) prior to *P. gingivalis*

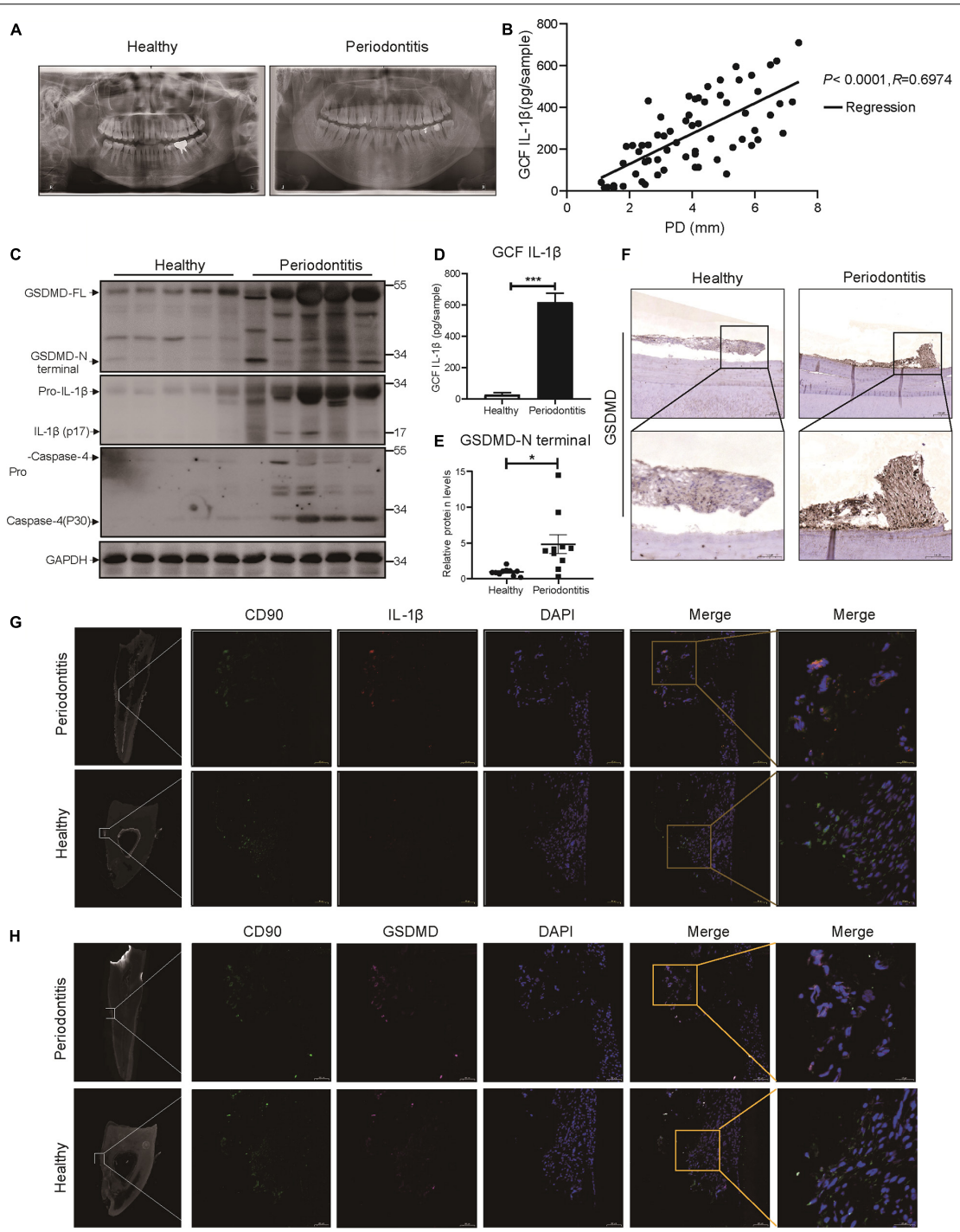

FIGURE 1 | The inflammatory lesions in periodontitis were correlated with the pyroptosis of PDLSCs. **(A)** Panoramic radiograph from healthy and periodontitis patients. **(B)** Scatter plot and regression line for the regression between GCF IL-1b level and probing depth (PD) from periodontitis patients (n = 65). **(C)** Periodontium tissues were collected from periodontitis patients and healthy individuals, and the expression of GSDMD, IL-1β, and Caspase-4 was analyzed by western blot. GAPDH was used as the loading control. **(D)** GCF from healthy subjects and periodontitis patients was analyzed to determine the concentrations of human IL-1β by ELISA. **(E)** The intensities of the GSDMD-N terminus were quantified using imaging software and normalized to that of GAPDH. Ten periodontium tissue specimens from periodontitis patients and healthy individuals were examined. **(F)** Representative immunohistochemical staining of GSDMD in human periodontal ligament sections from healthy and periodontitis patients. The signals of GSDMD appear brown in sections counterstained with hematoxylin (blue). Experiments were repeated independently more than three times. **(G)** Immunofluorescence staining of CD90 (green) and IL-1β (red) in human tooth longitudinal sections from severe periodontitis patients and healthy (orthodontic) patients. **(H)** Immunofluorescence staining of CD90 (green) and GSDMD (purple) in human tooth longitudinal sections from severe periodontitis patients and healthy patients. Nuclei were identified by staining with DAPI. Scale bars, 50 μm. The data are presented as the mean ± SEM. $^{*}P < 0.05$, $^{***}P < 0.001$.

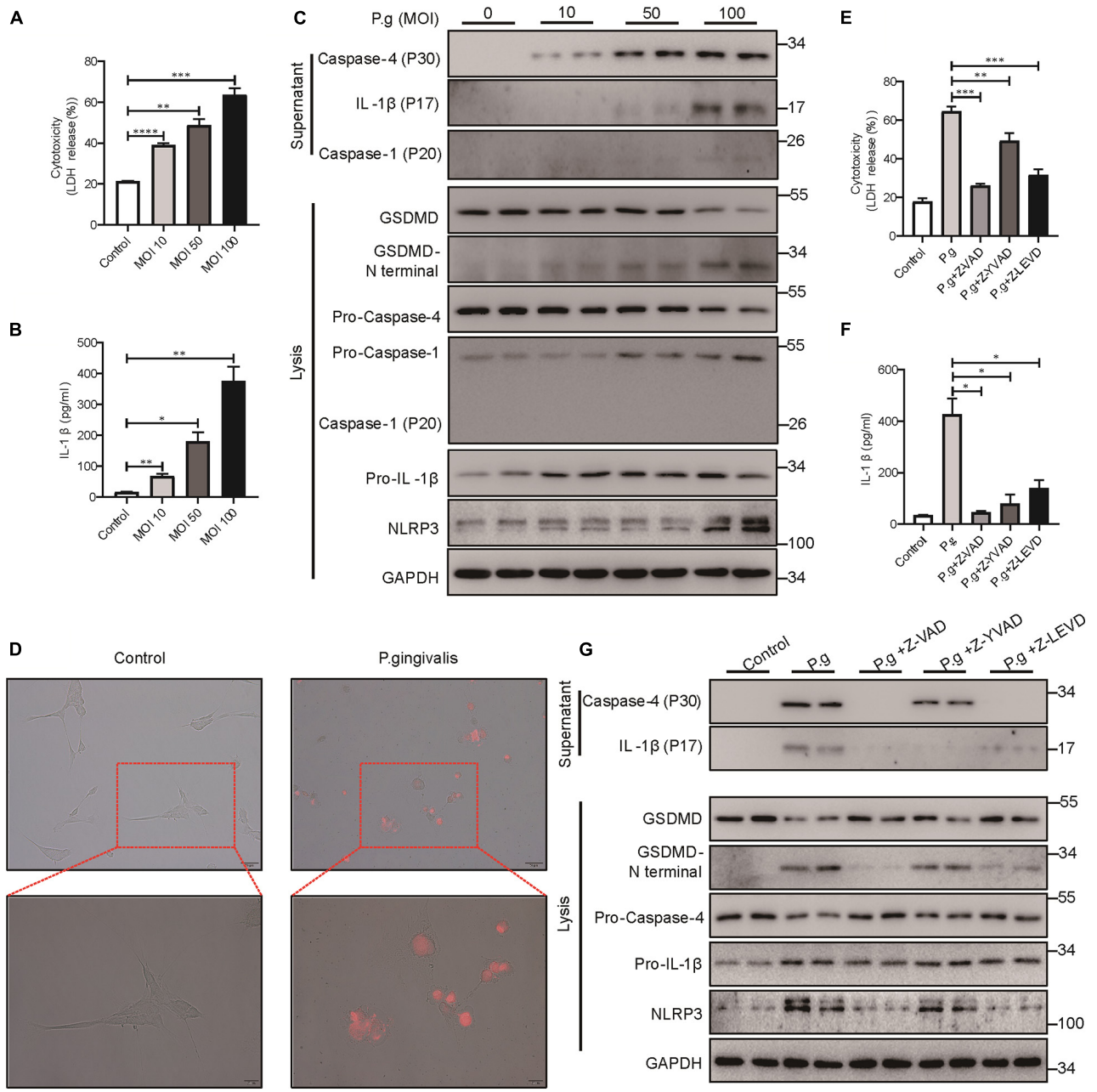

FIGURE 2 | *P. gingivalis* induced pyroptosis in PDLSCs dependent on caspase-4. **(A–C)** PDLSCs were infected with *P. gingivalis* (MOI, 10, 50, or 100) for 24 h. **(A)** The amount of cytoplasmic LDH released into the culture supernatant was measured by an LDH Cytotoxicity Assay Kit. **(B)** Cell culture supernatants were assayed for human IL-1β by ELISA. **(C)** The IL-1β, Caspase-4 and Caspase-1 secreted into the culture supernatants and the GSDMD cleavage, Pro-IL-1β, Pro-Caspase-4, Pro-Caspase-1, NLRP3, and GAPDH in the cell lysates (lysis) were detected by immunoblotting. **(D)** The morphology of PDLSCs with *P. gingivalis* (MOI, 100) infection. Cells were stained with propidium iodide (PI, red) and analyzed under a microscope. **(E–G)** PDLSCs were pretreated with the pan-caspase inhibitor Z-VAD-FMK (20 μM), the caspase-1 inhibitor Z-YVAD-FMK (20 μM), or the capase-4 inhibitor Z-LEVD-FMK (20 μM) for 1 h before *P. gingivalis* (MOI, 100) infection for 24 h. **(E,F)** Cell culture supernatant was collected and assayed for LDH release **(E)** and IL-1β secretion **(F)**. **(G)** The IL-1β and Caspase-4 secreted into the culture supernatants and the GSDMD cleavage, Pro-IL-1β, Pro-Caspase-4, NLRP3, and GAPDH in the cell lysates (lysis) were detected by immunoblotting. The data are presented as the mean ± SEM. $^{*}P < 0.05$, $^{**}P < 0.01$, $^{***}P < 0.001$, $^{****}P < 0.0001$.

challenge. As shown in **Figures 2E–G**, caspase pan inhibitor or caspase-4 specific inhibitor alleviated LDH release, IL-1β release and GSDMD cleavage, indicating that *P. gingivalis*-induced PDLSC pyroptosis was dependent on caspase-4 activation instead of caspase-1. Moreover, consistent with the important role of caspase-1 in IL-1β maturation (Monteleone et al., 2018), pretreatment with a caspase-1-specific inhibitor blocked the conversion of pro-IL-1β into its biologically

active form IL-1β in response to *P. gingivalis* infection (**Figures 2F,G**).

The Caspase-4-Mediated Non-canonical Pathway Dominantly Contributes to PDLSC Pyroptosis

Next, to further investigate the mechanism of PDLSC pyroptosis, both canonical pyroptosis and non-canonical pyroptosis were triggered *in vitro*. When canonical pyroptosis was triggered by PMA plus ATP or LPS plus nigericin in PDLSCs, the release of LDH and IL-1β did not show any significant change in the culture supernatants (**Figures 3A,B**). In addition, we did not detect any cleavage of GSDMD or the active form of IL-1β during canonical pyroptosis activation (**Figure 3C**). In contrast, when LPS (the major pathogenic factor of gram-negative bacteria) was transfected into PDLSCs to activate the non-canonical pyroptosis pathway, we found that the amounts of LDH and IL-1β in the culture supernatants were both significantly increased (**Figures 3D,E**). Consistent with the *P. gingivalis* infection, LPS-transfected PDLSCs also showed the activation of caspase-4, along with the cleavage of GSDMD and release of mature IL-1β (**Figure 3F**). Moreover, after LPS transfection, PDLSCs exhibited signature morphology of pyroptosis with cell swelling and rupture of the membrane (**Figure 3G**). To determine whether cytoplasmic LPS-induced non-canonical pyroptosis in PDLSCs was also dependent on caspase-4 activation, cells were pretreated with caspase inhibitors. Similar to the inhibitory effect of Z-LEVD-FMK in *P. gingivalis*-induced PDLSC pyroptosis, pretreatment with the caspase-4-specific inhibitor alleviated LDH release, GSDMD cleavage and mature IL-1β release in response to intracellular LPS stimulation (**Figures 3H–J**). Collectively, these data demonstrated that the caspase-4-mediated non-canonical pyroptosis pathway plays a dominant role in PDLSC pyroptosis.

PDLSC Pyroptosis Inhibits Osteoblast Differentiation and Promotes Osteoclast Differentiation

Previous works have demonstrated that the alveolar bone resorption of periodontitis was due to an imbalance between osteogenic differentiation and osteoclastogenic differentiation (Hienz et al., 2015), with increased osteoclasts and decreased osteoblasts. To evaluate whether pyroptotic PDLSCs affected the osteogenic differentiation of healthy PDLSCs (hPDLSCs), they were cocultured in osteogenic differentiation medium (**Figure 4A**). PDLSCs with LPS^{FuGene}-induced pyroptosis were seeded in the upper transwell chambers and replaced every 2 days. After 21 days of coculture, we subjected the lower chambers (hPDLSCs under osteogenic induction) to Alizarin red staining. A statistically significant decline in mineralization levels was found in hPDLSCs cocultured with pyroptotic PDLSCs, while hPDLSCs cocultured with empty or LPS-treated PDLSCs displayed no significant differences (**Figures 4B,C**). Additionally, the protein levels of the osteoblast markers ALP, RUNX2, and OPN were all significantly decreased in hPDLSCs cocultured with pyroptotic PDLSCs, and the transcription of these osteoblast markers was downregulated (**Figures 4D–H**). Similar to osteogenic differentiation, hPDLSCs cocultured with pyroptotic PDLSCs showed obvious inhibition of adipogenic differentiation, with decreased lipid droplet formation and downregulation of adipogenic markers (**Supplementary Figure 2**). The above data suggested an inhibitory effect of pyroptotic PDLSCs on the multipotential differentiation of hPDLSCs, which may reduce the regeneration of damaged periodontal tissues.

We used a coculture system of pyroptotic PDLSCs and THP-1 (human monocyte) cells to further investigate the functional role of pyroptotic PDLSCs in osteoclastogenesis (**Figure 4I**). Cells were cocultured with medium supplemented with RANKL and M-CSF for 14 days. Following removal of the Transwell inserts, the lower chambers consisting of THP-1 cells were subjected to TRAP staining to assess osteoclastogenic differentiation. While THP-1 cells cocultured with empty or LPS-treated PDLSCs induced abundant TRAP-positive multinucleated osteoclasts, THP-1 cells cocultured with pyroptotic PDLSCs induced significantly more multinucleated osteoclasts (**Figures 4J,K**). The mRNA expression levels of the osteoclast markers *TRAP*, *CTSK*, *DCSTAMP,* and *NFATC1* were also found to be significantly elevated in THP-1 cells cocultured with pyroptotic PDLSCs (**Figures 4L–O**). These results indicated the promotion effect of pyroptotic PDLSCs on osteoclastogenic differentiation, which may aggravate the destruction resulting from periodontitis.

PDLSC Pyroptosis-Mediated IL-1β Production Enhances Osteoclast Differentiation

As the most significant increase in IL-1β expression was detectable in the pyroptotic PDLSCs (**Figure 5A**), we examined whether the regulatory effect of PDLSC pyroptosis on osteogenic differentiation and osteoclastogenic differentiation was mediated by mature IL-1β release. Indeed, when the osteogenic differentiation of PDLSCs was induced by culturing in osteogenic media with or without recombinant human IL-1β protein, the osteogenic differentiation of PDLSCs was clearly inhibited by IL-1β treatment. This was evidenced by declining mineralization levels, decreased protein expression of osteoblast markers ALP, RUNX2, and OPN, and downregulation of the transcription of these osteoblast markers (**Figures 5B–G**). Analogously, the adipogenic differentiation of PDLSCs was significantly inhibited by IL-1β treatment (**Supplementary Figure 3**). The ability of PDLSCs to undergo osteogenic differentiation was greatly impaired by the addition of IL-1β protein, whereas the IL-1β antibody was able to rescue the inflammation-induced reduction in osteogenesis (**Supplementary Figure 4A**).

To test whether IL-1β also contributed to osteoclastogenesis, THP-1 cells were cultured in osteoclastogenic differentiation medium with or without IL-1β. After 14 days of IL-1β incubation, a marked increase in the number of multinucleated osteoclasts was observed through TRAP staining (**Figures 5H,I**). Furthermore, the expression levels of osteoclastogenic differentiation marker genes, such as *TRAP*, *CTSK*, *DCSTAMP*, and *NFATC1,* were significantly increased under IL-1β treatment (**Figures 5J–M**). When IL-1β antibody was added, the number of TRAP-positive multinucleated osteoclasts was markedly reduced

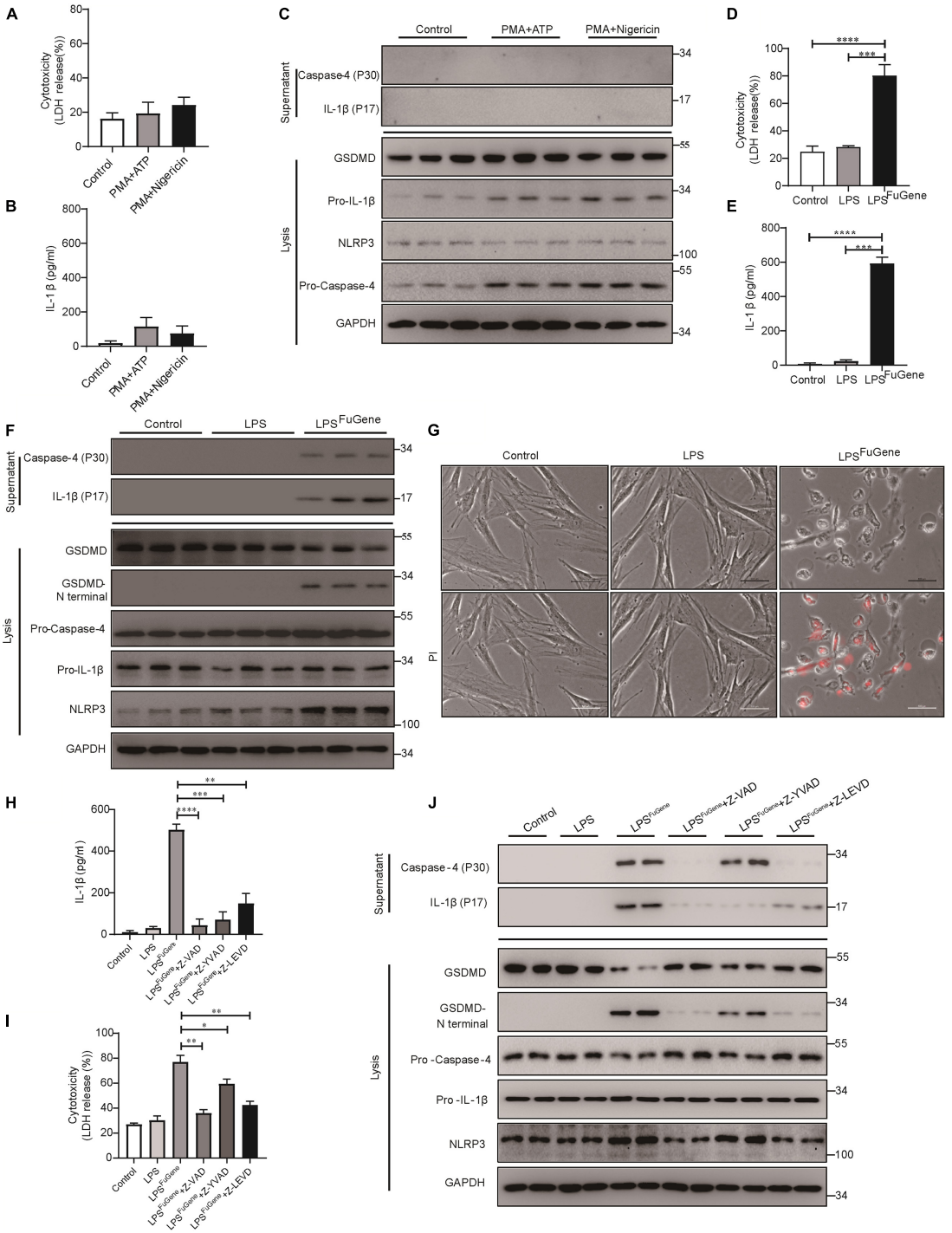

FIGURE 3 | PDLSC pyroptosis was mediated by the caspase-4-dependent non-canonical pyroptosis pathway. **(A–C)** PDLSCs were pretreated with PMA for 1 h and stimulated with ATP or nigericin for 4 h. **(A,B)** Cell culture supernatant was collected and assayed for LDH release **(A)** and IL-1β secretion **(B)**. **(C)** The IL-1β and Caspase-4 secreted into the culture supernatants and the GSDMD cleavage, Pro-IL-1β, Pro-Caspase-4, NLRP3, and GAPDH in the cell lysates (lysis) were detected by immunoblotting. **(D–G)** PDLSCs were treated with LPS or transfected with LPS using FuGene HD for 16 h. Cells without treatment were used as controls. **(D,E)** Cell culture supernatant was collected and assayed for LDH release **(D)** and IL-1β secretion **(E)**. **(F)** The IL-1β and Caspase-4 secreted into the culture supernatants and the GSDMD cleavage, Pro-IL-1β, Pro-Caspase-4, NLRP3, and GAPDH in the cell lysates (lysis) were detected by immunoblotting. **(G)** Representative images of propidium iodide (PI, red) uptake. **(H–J)** PDLSCs were pretreated with the pan-caspase inhibitor Z-VAD-FMK (20 μM), the caspase-1 inhibitor Z-YVAD-FMK (20 μM), or the capase-4 inhibitor Z-LEVD-FMK (20 μM) for 1 h before transfection with LPS (LPS^{FuGene}) for 16 h. **(H)** IL-1β ELISA in supernatants. **(I)** Percentage of LDH release in supernatants. **(J)** The IL-1β and Caspase-4 secreted into the culture supernatants and the GSDMD cleavage, Pro-IL-1β, Pro-Caspase-4, NLRP3, and GAPDH in the cell lysates (lysis) were detected by immunoblotting. The data are presented as the mean ± SEM. $^{*}P < 0.05$, $^{**}P < 0.01$, $^{***}P < 0.001$, $^{****}P < 0.0001$.

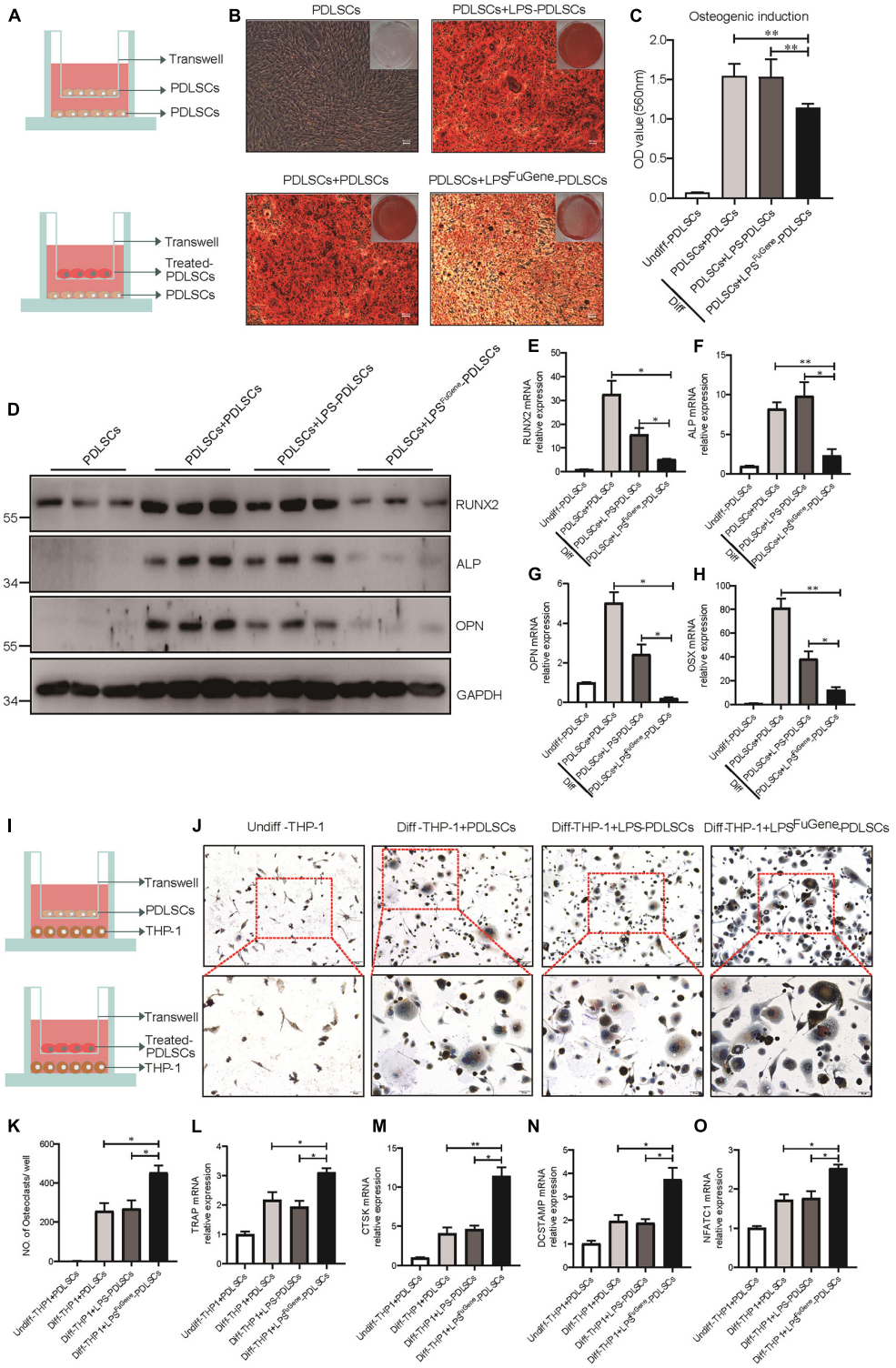

FIGURE 4 | The paracrine effect of PDLSC pyroptosis on osteoblast differentiation and osteoclast differentiation. **(A)** Schematic diagram of coculture design indicating the placement of PDLSCs with LPS, with LPS^{FuGene} treatment, or without treatment on the transwell insert with the lower chamber containing healthy PDLSCs. **(B–H)** Cells in the cocultured transwell system were maintained in osteogenic differentiation medium for 21 days. PDLSCs in a single culture (without coculture) were maintained in MEM-α medium as a control. **(B)** Entire plate views and micrographs of alizarin red staining after culturing in osteogenic differentiation medium. **(C)** Quantification of the alizarin red staining results. **(D)** Immunoblots for RUNX2, ALP, and OPN in whole-cell lysates. GAPDH was used as a loading control. *RUNX2* **(E)**, *ALP* **(F)**, *OPN* **(G)**, and *OSX* **(H)** mRNAs were subjected to real-time PCR analysis, and the expression levels were normalized to that of *36B4*.

(Continued)

FIGURE 4 | Continued
(I) Schematic diagram of coculture design indicating the placement of PDLSCs with LPS treatment, with LPS^{FuGene} treatment, or without treatment on transwell insert with the lower chamber containing THP-1 cells. **(J–O)** The THP-1 cells in the coculture system were cultured in osteoclast differentiation medium for 14 days. THP-1 cells in a single culture were maintained in RPMI-1640 medium as a control. **(J)** Micrographs of TRAP staining after culturing in osteoclast differentiation medium. **(K)** Quantification of TRAP-positive multinucleated cells (nuclei > 3). *TRAP* **(L)**, *CTSK* **(M)**, *DCSTAMP* **(N)**, and *NFATC1* **(O)** mRNAs were subjected to real-time PCR analysis, and the expression levels were normalized to that of *36B4*. The data are presented as the mean ± SEM. $^{*}P < 0.05$, $^{**}P < 0.01$.

(**Supplementary Figure 4B**). In brief, these results revealed that the regulatory effect of PDLSC pyroptosis on osteoblast and osteoclast differentiation was mediated by mature IL-1β release.

Caspase-4-Mediated Pyroptosis Promotes the Progression of Ligature-Induced Rat Periodontitis

To extend our *in vitro* findings, we next investigated the role of caspase-4-mediated non-canonical pyroptosis in ligature-induced rat periodontitis. A periodontitis rat model was generated by ligatures around the first maxillary molar and then treated with caspase-4 specific inhibitor (Z-LEVD-FMK) or IL-1β antibody for 14 days (**Figures 6A,B**). Similar to human periodontal tissues, Gsdmd cleavage, mature IL-1β release and caspase-4 activation were both significantly increased in ligature-induced rat periodontitis (**Figure 6C**). Representative sagittal 3D and bidimensional views of the rat maxillary molars from each group using micro-CT scanning are shown in **Figures 6D,E**. Compared with the sham group, the ligature group showed a greater distance between the cement-enamel junction (CEJ) and alveolar bone crest (ABC). However, administration of caspase-4 inhibitor or IL-1β antibody significantly inhibited periodontal destruction, showing a decreased CEJ-ABC distance (**Figures 6D,G**). Consistently, the bone mineral density (BMD, g/cm3) and bone/tissue volume (BV/TV, %) values in alveolar bone from the ligature group were both significantly lower than the corresponding values in the sham group, whereas the ligature-induced damage to BMD and BV/TV was rescued by treatment with caspase-4 inhibitor or IL-1β antibody (**Figures 6E,H,I**). Additionally, prominent loss of alveolar bone, periodontal ligament damage and infiltration of inflammatory cells were observed in ligatured rats, while treatment with caspase-4 inhibitor or IL-1β antibody showed improved periodontal conditions compared with the ligature group (**Figure 6F**). Collectively, either inhibiting the activation of caspase-4 or blocking the function of IL-1β can attenuate periodontitis-mediated tissue damage, which indicates the critical role of caspase-4-mediated non-canonical pyroptosis in rat periodontitis.

Gsdmd Deficiency Reduces Periodontal Inflammation and Bone Loss in a Mouse Model of Periodontitis

GSDMD, the key executor of pyroptosis, is cleaved by caspase-4 to mediate IL-1β release (Kayagaki et al., 2015). To better characterize the Caspase-4/GSDMD/IL-1β axis-mediated non-canonical pyroptosis as a potential driver of periodontitis, a mouse model with *Gsdmd* gene deficiency was used (**Supplementary Figure 5A**). In this model, the third codon of the *Gsdmd* gene was deleted by CRISPT/Cas-9 technology, and $Gsdmd^{-/-}$ mice were confirmed by genotyping and western blot (**Supplementary Figures 5B–D**). After 14 days of periodontitis induction, the WT-ligature mice showed an increased expression of osteoclast markers *Trap*, *Ctsk*, *Dcstamp,* and *Nfatc1* and decreased expression of osteoblast markers *Runx2*, *Alp*, *Opn,* and *Osx*, compared with the WT-sham group. Conversely, the $Gsdmd^{-/-}$ mice demonstrated fewer osteoclast markers expression and more osteoblast markers expression (**Figure 7A**). Histological analysis by H&E staining revealed that the WT-ligature mice showed a loss of alveolar bone, inflammatory cell infiltration and periodontal ligament damage after periodontitis induction, whereas $Gsdmd^{-/-}$ mice had attenuated periodontitis-mediated tissue damage (**Figure 7B**). We assessed bone loss by measuring CEJ-ABC distances and found that WT-ligament mice showed significant bone loss, but this loss was alleviated in $Gsdmd^{-/-}$ mice (**Figures 7C,D**). Meanwhile, BMD and BV/TV values were significantly decreased in the region between the first and second upper molars of WT-ligature mice compared with those of WT-sham mice. In contrast, the loss of BMD and BV/TV was attenuated significantly in $Gsdmd^{-/-}$ mice under periodontitis induction (**Figures 7E–G**). Furthermore, prominent loss of PDLSCs ($CD90^{+}$) was observed in WT-ligature mice, while Gsdmd-deficient mice demonstrated a rescue effect on PDLSC damage (**Figure 7H**). In brief, these data demonstrated that the genetic deletion of *Gsdmd* alleviated the loss of PDLSCs during experimental periodontitis and conferred protection from periodontal inflammatory bone loss. Therefore, GSDMD-mediated PDLSC pyroptosis was found to have a major contribution to periodontal inflammation and bone loss in this inflammatory disease, which supported a focus on PDLSC pyroptosis-targeted therapeutic approaches (**Figure 8**).

DISCUSSION

Periodontitis, the major cause of adult tooth loss, is an inflammatory disease caused by oral bacterial infection (Chen et al., 2020). Recently, new links have been established between oral microbe-induced pyroptosis and periodontitis. Pyroptosis is an important event in inflammatory processes and rapidly releases large amounts of activated cytokines, such as IL-1β, into the extracellular space (Kesavardhana et al., 2020). In this study, we provided a statistical correlation between IL-1β levels and the severity of periodontitis, which was consistent with previous reports that IL-1β in saliva or gingival crevicular fluid is a potential biomarker for periodontal disease (Gomes et al., 2016). Furthermore, GSDMD, the key executor of pyroptosis,

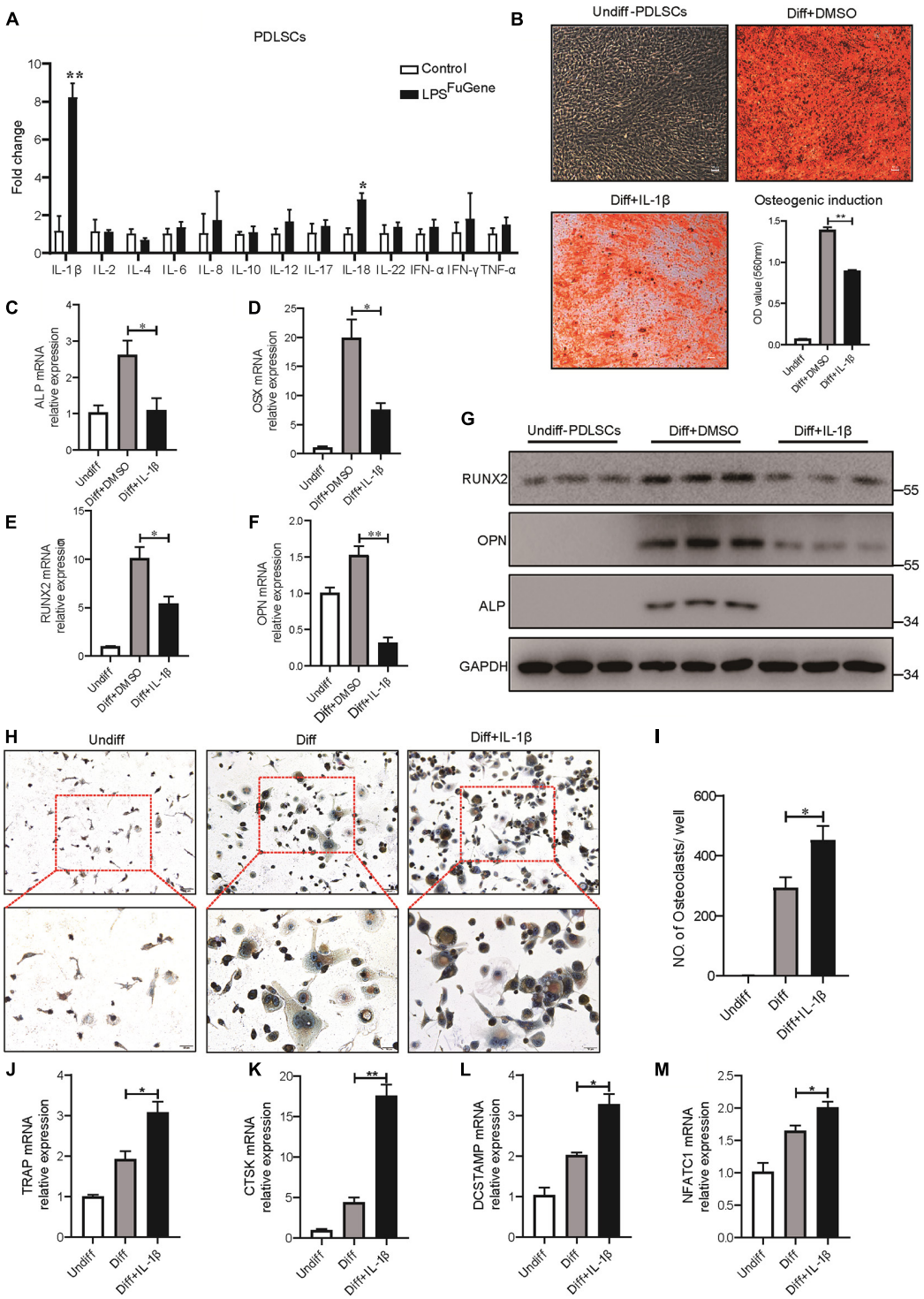

FIGURE 5 | IL-1β was the key factor in PDLSC pyroptosis to regulate osteoblast and osteoclast differentiation. **(A)** Expression profiles of several inflammatory cytokines in PDLSCs under LPS^{FuGene} treatment for 16 h. **(B–G)** PDLSCs were incubated with osteogenic differentiation medium for 21 days with or without 500 pg/mL IL-1β treatment. **(B)** Representative images of alizarin red staining and quantification of the staining results. *ALP* **(C)**, *OSX* **(D)**, *RUNX2* **(E)**, and *OPN* **(F)** mRNAs were subjected to real-time PCR analysis, and the expression levels were normalized to that of *36B4*. **(G)** Immunoblots for RUNX2, ALP, and OPN in whole-cell lysates. GAPDH was used as a loading control. **(H–M)** THP-1 cells were incubated with osteoclast differentiation medium for 14 days with or without 500 pg/mL IL-1β treatment. **(H)** Micrographs of TRAP staining after culturing in osteoclast differentiation medium. **(I)** Quantification of TRAP-positive multinucleated cells (nuclei > 3). *TRAP* **(J)**, *CTSK* **(K)**, *DCSTAMP* **(L)**, and *NFATC1* **(M)** mRNAs were subjected to real-time PCR analysis, and the expression levels were normalized to that of *36B4*. The data are presented as the mean ± SEM. $^{*}P < 0.05$, $^{**}P < 0.01$.

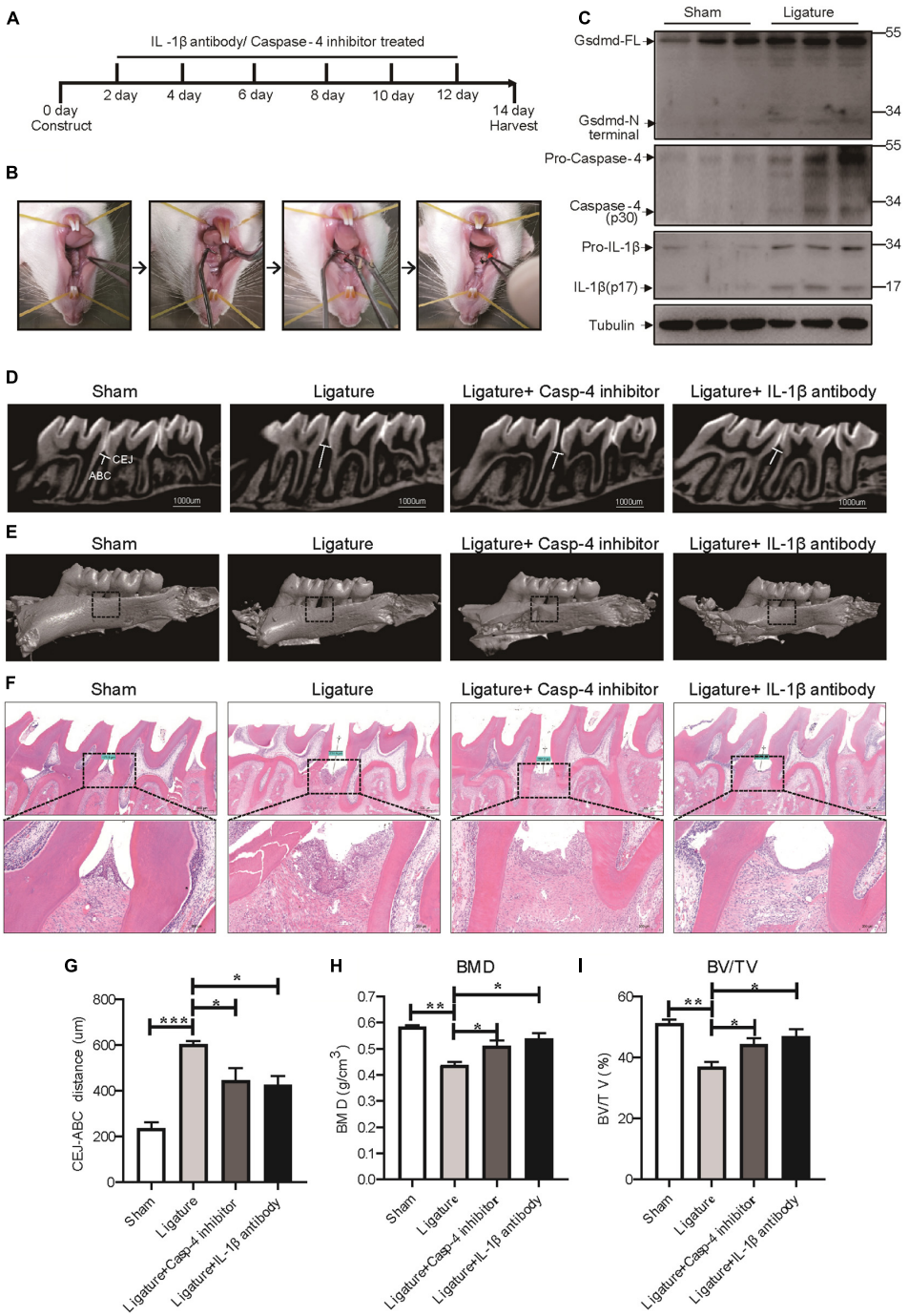

FIGURE 6 | Caspase-4-mediated non-canonical pyroptosis was involved in ligature-induced rat periodontitis. **(A–I)** Rats were divided randomly into a sham group, ligature-induced rat periodontitis group (ligature group), ligature with caspase-4 inhibitor injection into the subperiosteum at the left buccal and palatal gingivae of the first maxillary molars group (Ligature + Casp-4 inhibitor group), and ligature with IL-1b antibody injection into the subperiosteum at the first maxillary molar group (Ligature + IL-1b antibody group). **(A)** Timeline of the animal experiment. **(B)** Technical procedures of ligature-induced rat periodontitis. A 4-0 silk ligature was looped around the first molar of the rat maxilla under anesthesia and maintained for 14 days. The red arrow indicated the drugs injection site. **(C)** Periodontium tissues were collected from ligature-induced rat periodontitis group and sham group, and the expression of Gsdmd, IL-1β, and caspase-4 was analyzed by western blot. Tubulin was used as the loading control. **(D)** Representative micro-CT sagittal images of maxillary molars after insertion of ligature. CEJ, cement-enamel junction; ABC, alveolar bone crest. The line indicates the distance from the CEJ to the ABC on the buccal side of the ligature site. **(E)** The images show the reconstructed sagittal 3D images from the computerized tomography of the maxillary molars. The squares formed by the continuous dotted line show visual differences in alveolar bone from different animal groups. **(F)** Tissue sections from rats were prepared after 14 days of periodontitis induction and processed for hematoxylin and eosin (H&E) staining. **(G)** The distances (um) between CEJ and ABC were measured after periodontitis induction. The bone mineral density **(H)** and bone/tissue volume **(I)** of the selected squares regions on the ligature site were calculated. The data are presented as the mean ± SEM. $^{*}P < 0.05$, $^{**}P < 0.01$, $^{***}P < 0.001$.

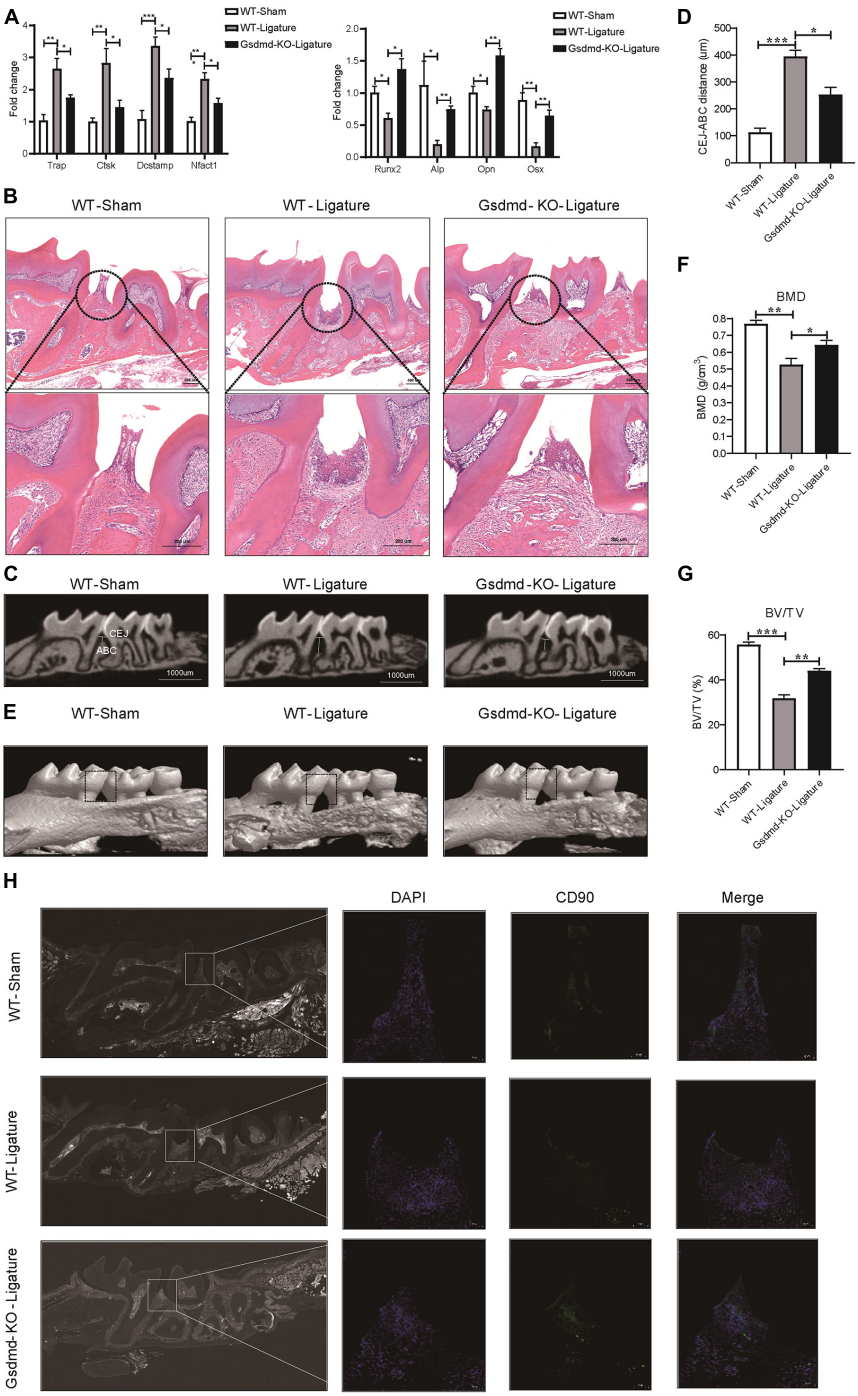

FIGURE 7 | *Gsdmd–/–* mice presented with reduced periodontal inflammation and bone loss in experimental periodontitis. **(A–H)** Mice were divided into the WT-sham group, WT-ligature group, and Gsdmd-KO-ligature group. Silk thread was used to form a ligature around the left maxillary first molar for 2 weeks to induce periodontitis. **(A)** Periodontium tissues were collected from each group, and the mRNA expression of osteoblast markers (including *Runx2*, *Alp*, *Opn,* and *Osx*) and osteoclast markers (including *Trap*, *Ctsk*, *Dcstamp,* and *Nfact1*) was analyzed by real-time PCR. *36b4* was used as an internal control. **(B)** Tissue sections from mice were prepared after 14 days of periodontitis induction and processed for hematoxylin and eosin (H&E) staining. **(C)** Representative micro-CT sagittal images of maxillary molars after insertion of ligature. CEJ, cement-enamel junction; ABC, alveolar bone crest. The line indicates the distance from the CEJ to the ABC on the buccal side of the ligature site. **(D)** The distances (μm) between CEJ and ABC were measured after periodontitis induction. **(E)** The images of bone surrounding first molars were analyzed by 3D micro-computed tomography. The squares formed by the continuous dotted line show visual differences in alveolar bone from animal groups. The bone mineral density **(F)** and bone/tissue volume **(G)** of the selected square regions on the ligature site were calculated. **(H)** Immunofluorescence staining of CD90 (green) in mouse maxillary molar longitudinal sections from the periodontitis model and sham group. Nuclei were identified by staining with DAPI. Scale bars, 50 μm. The data are presented as the mean ± SEM. $^{*}P < 0.05$, $^{**}P < 0.01$, $^{***}P < 0.001$.

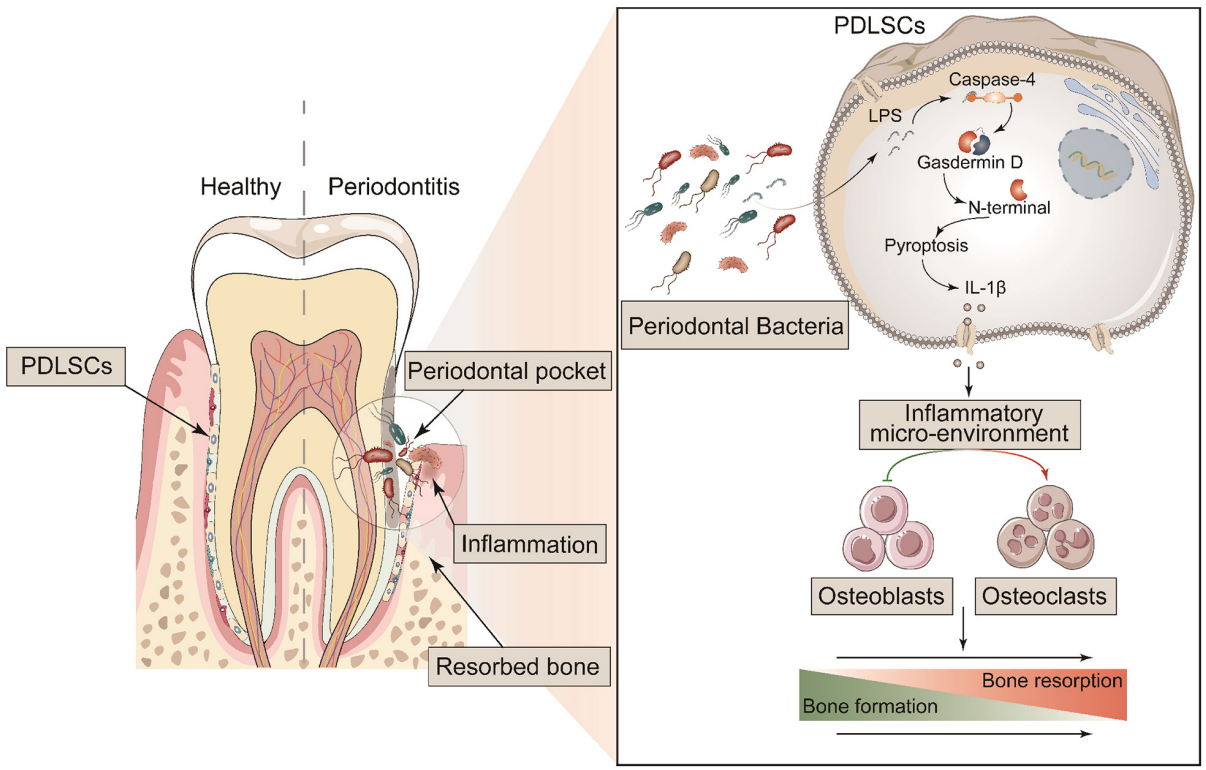

FIGURE 8 | Schematic diagram of the mechanism of GSDMD-mediated PDLSC pyroptosis in the promotion of periodontitis. PDLSCs commit Caspase-4/GSDMD-mediated non-canonical pyroptosis in periodontopathogen-induced periodontitis. The pyroptotic PDLSCs express IL-1β and release it to the cellular microenvironment following membrane rupture. IL-1β disrupts the homeostatic balance of bone formation and resorption by inhibiting osteoblastogenesis and promoting osteoclastogenesis, jointly aggravating the process of periodontitis.

was found to be highly expressed and activated in periodontitis tissues, and we reported for the first time that PDLSCs ($CD90^+$) were the source of IL-1β production in periodontitis patients. These data suggested that IL-1β release in GSDMD-mediated PDLSC pyroptosis played an important role in the process of periodontitis.

The molecular mechanisms of GSDMD-mediated PDLSC pyroptosis were subsequently investigated. Although the relationship between oral bacteria and periodontal destructive inflammation was already well documented clinically (Hasan and Palmer, 2014), the mechanisms of periodontopathogen-induced pathogenic inflammation in periodontitis were poorly demonstrated. *P. gingivalis*, an oral gram-negative anaerobic bacterium, was primarily found in deep periodontal pockets, especially in sites with active disease (Kuula et al., 2009). We infected PDLSCs with *P. gingivalis* to mimic the pathogenetic process of periodontitis and found typical pyroptosis morphology of PDLSCs with cell swelling and massive release of cellular contents. *P. gingivalis* stimulated the release of the cleaved GSDMD-N terminal domain and active IL-1β in an MOI-dependent manner and increased the activation of caspase-4. The inhibition of caspase-4 significantly decreased *P. gingivalis*-induced GSDMD cleavage and IL-1β secretion in PDLSCs, suggesting that *P. gingivalis*-induced PDLSC pyroptosis was mediated by caspase-4 activation. Furthermore, canonical pyroptosis and non-canonical pyroptosis were triggered based on previous works to investigate the preferential pyroptosis pathway in periodontitis (Kayagaki et al., 2015; Chen X. et al., 2016). These *in vitro* experiments revealed that the caspase-4/GSDMD/IL-1β axis-mediated non-canonical pyroptosis pathway dominantly contributed to PDLSC pyroptosis.

Currently, the standard treatment of periodontitis focuses on the removal of periodontitis-associated microbial communities and inflammatory tissues by means of mechanical dental debridement, and PDLSCs have been proposed and used in periodontal regeneration (American Academy of Periodontology, 2011; Sanz et al., 2012; Vandana et al., 2015; Tassi et al., 2017). However, the outcomes of clinical stem cell-based therapies did not achieve the desired outcome, most likely due to the local inflammatory microenvironment of the diseased periodontium (Fawzy El-Sayed et al., 2019; Jia et al., 2020). Indeed, we found that the differentiation potential of PDLSCs was significantly decreased in a pyroptosis-induced inflammatory microenvironment. These findings suggested that the paracrine effects of pyroptotic PDLSCs were responsible for the low efficiency of periodontium regeneration. IL-1β had previously been shown to be an important proinflammatory cytokine that drove the pathogenesis of periodontitis and often amplified the effect of other cytokines (Papathanasiou et al., 2020). Some studies reported that IL-1β inhibited the

osteogenesis of MSCs through the NF-κB and MAPK signaling pathway and exacerbated the destruction of alveolar bone by promoting osteoclast formation and activity (Mao et al., 2016; Aral et al., 2020). Consistently, IL-1β is the major inflammatory cytokine released in pyroptosis, and we found that it performed bidirectional regulation of osteogenic and osteoclastogenic differentiation. Overall, IL-1β release in PDLSC pyroptosis both damaged the differentiation capability of circumjacent PDLSCs and promoted the formation of osteoclasts, which jointly aggravated the process of periodontitis.

A previous study revealed that intracellular LPS or inflammatory caspases were required for the activation of GSDMD (Rathinam et al., 2019). As elevated levels of LPS from gram-negative bacterial and inflammatory caspases were often detected in patients with periodontitis and in murine periodontitis, this provided a prerequisite for the activation of GSDMD and IL-1β release (Cheng et al., 2017; Rocha et al., 2020). In this work, we also confirmed that the activation of caspase-4/11 was elevated in human periodontitis samples and in murine periodontitis models and that *P. gingivalis* (a gram-negative periodontopathogen) induced PDLSC pyroptosis with the cleavage of GSDMD and IL-1β release. Overall, our data demonstrated that GSDMD-dominant PDLSC pyroptosis played a pivotal role in the pathological damage of periodontitis.

GSDMD has been reported to execute pyroptosis in inflammation and to control proinflammatory cytokine IL-1β release (Ding et al., 2016). The induction of GSDMD in human periodontitis and ligature-induced rat periodontitis and the restorative effect of IL-1β antibody and caspase-4 inhibitor in rat periodontitis led us to hypothesize that GSDMD-driven pyroptosis was probably the key determinant of periodontitis. Thus, we further addressed the functional significance of pyroptosis in periodontitis by knocking out *Gsdmd*, which is the vital executor of pyroptosis. Our data showed that knockout of *Gsdmd* expression significantly reduce the loss of alveolar bone and periodontal ligament damage. This reduction was associated with increased expression of the osteogenic genes and downregulated expression of osteoclastogenic genes. Collectively, these results indicate that GSDMD-driven pyroptosis is an indispensable mechanism involved in the pathogenesis of periodontitis.

In summary, the most important finding in this study was revealing a direct link between PDLSC pyroptosis and human/murine periodontitis. The initiation of PDLSC pyroptosis disrupts the homeostatic balance of bone formation and resorption by releasing IL-1β, consequently aggravating the occurrence of periodontitis (**Figure 8**). Our study provides a novel insight into the pathogenic mechanism of periodontitis, which could potentially be valuable to treatment.

DATA AVAILABILITY STATEMENT

The raw data supporting the conclusions of this article will be made available by the authors, without undue reservation.

ETHICS STATEMENT

The studies involving human participants were reviewed and approved by the Research Ethics Committee of the Ninth People's Hospital (approval NO. SH9H-2020-TK60-1). The patients/participants provided their written informed consent to participate in this study. The animal study was reviewed and approved by Animal Care and Use Committee of Shanghai Jiao Tong University Affiliated Ninth People's Hospital (approval NO. SH9H-2020-A132-1). Written informed consent was obtained from the individual(s) for the publication of any potentially identifiable images or data included in this article.

AUTHOR CONTRIBUTIONS

QC, XGL, DZ, and CY: conception and design. JZ, LC, QX, XHL, SN, JLi, and GQ: provision of study material or patients. QC: collection and/or assembly of data. QC and DW: data analysis and interpretation. QC and XGL: manuscript writing. DZ and CY: final approval of manuscript. QC, JZ, JFL, and DZ: funding. All authors reviewed the results and approved the final version of the manuscript.

FUNDING

This work was supported by the National Natural Science Foundation of China (Grant Nos. 31870969, 32000513, 82001068, and 32000827), the China Postdoctoral Science Foundation (Grant No. 2020M671140), the CAMS Innovation Fund for Medical Sciences (CIFMS) (Project No. 2019-I2M-5-037), and the Shanghai Municipal Education Commission 200 Talent (Grant No. 20191816).

SUPPLEMENTARY MATERIAL

The Supplementary Material for this article can be found online at: https://www.frontiersin.org/articles/10.3389/fcell.2021.663037/full#supplementary-material

REFERENCES

Aglietti, R. A., and Dueber, E. C. (2017). Recent insights into the molecular mechanisms underlying pyroptosis and gasdermin family functions. *Trends Immunol.* 38, 261–271. doi: 10.1016/j.it.2017.01.003

Al-Habib, M., and Huang, G. T.-J. (2019). Dental mesenchymal stem cells: dental pulp stem cells, periodontal ligament stem cells, apical papilla stem cells, and primary teeth stem cells—isolation, characterization, and expansion for tissue engineering. *Methods Mol. Biol.* 1922, 59–76. doi: 10.1007/978-1-4939-9012-2_7

American Academy of Periodontology (2011). Comprehensive periodontal therapy: a statement by the American Academy of Periodontology. *J. Periodontol.* 82, 943–949. doi: 10.1902/jop.2011.117001

Aoyama, N., Kure, K., Minabe, M., and Izumi, Y. (2019). Increased heart failure prevalence in patients with a high antibody level against periodontal pathogen. *Int. Heart J.* 60, 1142–1146. doi: 10.1536/ihj.19-010

Aral, K., Milward, M. R., Kapila, Y., Berdeli, A., and Cooper, P. R. (2020). Inflammasomes and their regulation in periodontal disease: a review. *J. Periodontal Res.* 55, 473–487. doi: 10.1111/jre.12733

Bartold, P., and Gronthos, S. (2017). Standardization of criteria defining periodontal ligament stem cells. *J. Dent. Res.* 96, 487–490. doi: 10.1177/0022034517697653

Bhattarai, G., Poudel, S. B., Kook, S.-H., and Lee, J.-C. (2016). Resveratrol prevents alveolar bone loss in an experimental rat model of periodontitis. *Acta Biomater.* 29, 398–408.

Caton, J. G., Armitage, G., Berglundh, T., Chapple, I. L., Jepsen, S., Kornman, K. S., et al. (2018). A new classification scheme for periodontal and peri-implant diseases and conditions–Introduction and key changes from the 1999 classification. *J. Periodontol.* 89, S1–S8.

Chen, C., Feng, P., and Slots, J. (2020). Herpesvirus-bacteria synergistic interaction in periodontitis. *Periodontology* 2000, 42–64. doi: 10.1111/prd.12311

Chen, F.-M., Gao, L.-N., Tian, B.-M., Zhang, X.-Y., Zhang, Y.-J., Dong, G.-Y., et al. (2016). Treatment of periodontal intrabony defects using autologous periodontal ligament stem cells: a randomized clinical trial. *Stem Cell Res. Ther.* 7:33.

Chen, X., He, W.-T., Hu, L., Li, J., Fang, Y., Wang, X., et al. (2016). Pyroptosis is driven by non-selective gasdermin-D pore and its morphology is different from MLKL channel-mediated necroptosis. *Cell Res.* 26, 1007–1020. doi: 10.1038/cr.2016.100

Cheng, R., Liu, W., Zhang, R., Feng, Y., Bhowmick, N. A., and Hu, T. (2017). Porphyromonas gingivalis-derived lipopolysaccharide combines hypoxia to induce caspase-1 activation in periodontitis. *Front. Cell. Infect. Microbiol.* 7:474.

Ding, J., Wang, K., Liu, W., She, Y., Sun, Q., Shi, J., et al. (2016). Pore-forming activity and structural autoinhibition of the gasdermin family. *Nature* 535, 111–116. doi: 10.1038/nature18590

Dominy, S. S., Lynch, C., Ermini, F., Benedyk, M., Marczyk, A., Konradi, A., et al. (2019). Porphyromonas gingivalis in Alzheimer's disease brains: evidence for disease causation and treatment with small-molecule inhibitors. *Sci. Adv.* 5:eaau3333. doi: 10.1126/sciadv.aau3333

Fawzy El-Sayed, K. M., Elahmady, M., Adawi, Z., Aboushadi, N., Elnaggar, A., Eid, M., et al. (2019). The periodontal stem/progenitor cell inflammatory-regenerative cross talk: a new perspective. *J. Periodontal Res.* 54, 81–94. doi: 10.1111/jre.12616

García-Hernández, A. L., Muñoz-Saavedra, ÁE., González-Alva, P., Moreno-Fierros, L., Llamosas-Hernández, F. E., Cifuentes-Mendiola, S. E., et al. (2019). Upregulation of proteins of the NLRP3 inflammasome in patients with periodontitis and uncontrolled type 2 diabetes. *Oral Diseases* 25, 596–608.

Gomes, F. I. F., Aragão, M. G. B., Barbosa, F. C. B., Bezerra, M. M., Pinto, V. D. P. T., and Chaves, H. V. (2016). Inflammatory cytokines interleukin-1β and tumour necrosis factor-α-novel biomarkers for the detection of periodontal diseases: a literature review. *J. Oral Maxillofac. Res.* 7:e2.

Hajishengallis, G. (2015). Periodontitis: from microbial immune subversion to systemic inflammation. *Nat. Rev. Immunol.* 15, 30–44. doi: 10.1038/nri3785

Hasan, A., and Palmer, R. (2014). A clinical guide to periodontology: pathology of periodontal disease. *Br. Dent. J.* 216, 457–461. doi: 10.1038/sj.bdj.2014.299

He, W.-T., Wan, H., Hu, L., Chen, P., Wang, X., Huang, Z., et al. (2015). Gasdermin D is an executor of pyroptosis and required for interleukin-1β secretion. *Cell Res.* 25, 1285–1298. doi: 10.1038/cr.2015.139

Hienz, S. A., Paliwal, S., and Ivanovski, S. (2015). Mechanisms of bone resorption in periodontitis. *J. Immunol. Res.* 2015:615486.

Jia, R., Yi, Y., Liu, J., Pei, D., Hu, B., Hao, H., et al. (2020). Cyclic compression emerged dual effects on the osteogenic and osteoclastic status of LPS-induced inflammatory human periodontal ligament cells according to loading force. *BMC Oral Health* 20:7. doi: 10.1186/s12903-019-0987-y

Jun, H.-K., Jung, Y.-J., Ji, S., An, S.-J., and Choi, B.-K. (2018). Caspase-4 activation by a bacterial surface protein is mediated by cathepsin G in human gingival fibroblasts. *Cell Death Differ.* 25, 380–391. doi: 10.1038/cdd.2017.167

Kayagaki, N., Stowe, I. B., Lee, B. L., O'rourke, K., Anderson, K., Warming, S., et al. (2015). Caspase-11 cleaves gasdermin D for non-canonical inflammasome signalling. *Nature* 526, 666–671. doi: 10.1038/nature15541

Kesavardhana, S., Malireddi, R. S., and Kanneganti, T.-D. (2020). Caspases in cell death, inflammation, and pyroptosis. *Annu. Rev. Immunol.* 38, 567–595. doi: 10.1146/annurev-immunol-073119-095439

Kinane, D. F., Stathopoulou, P. G., and Papapanou, P. N. (2017). Periodontal diseases. *Nat. Rev. Dis. Primers* 3, 1–14.

Kuula, H., Salo, T., Pirilä, E., Tuomainen, A. M., Jauhiainen, M., Uitto, V.-J., et al. (2009). Local and systemic responses in matrix metalloproteinase 8-deficient mice during *Porphyromonas gingivalis*-induced periodontitis. *Infect. Immunity* 77, 850–859. doi: 10.1128/iai.00873-08

Li, Z. H., Si, Y., Xu, G., Chen, X. M., Xiong, H., Lai, L., et al. (2017). High-dose PMA with RANKL and MCSF induces THP-1 cell differentiation into human functional osteoclasts in vitro. *Mol. Med. Rep.* 16, 8380–8384. doi: 10.3892/mmr.2017.7625

Liu, X., Zhang, Z., Ruan, J., Pan, Y., Magupalli, V. G., Wu, H., et al. (2016). Inflammasome-activated gasdermin D causes pyroptosis by forming membrane pores. *Nature* 535, 153–158. doi: 10.1038/nature18629

Liu, Y., Zheng, Y., Ding, G., Fang, D., Zhang, C., Bartold, P. M., et al. (2008). Periodontal ligament stem cell−mediated treatment for periodontitis in miniature swine. *Stem Cells* 26, 1065–1073. doi: 10.1634/stemcells.2007-0734

Ma, C., Yang, D., Wang, B., Wu, C., Wu, Y., Li, S., et al. (2020). Gasdermin D in macrophages restrains colitis by controlling cGAS-mediated inflammation. *Sci. Adv.* 6:eaaz6717. doi: 10.1126/sciadv.aaz6717

Man, S. M., Karki, R., and Kanneganti, T. D. (2017). Molecular mechanisms and functions of pyroptosis, inflammatory caspases and inflammasomes in infectious diseases. *Immunol. Rev.* 277, 61–75. doi: 10.1111/imr.12534

Mao, C., Wang, Y., Zhang, X., Zheng, X., Tang, T., and Lu, E. (2016). Double-edged-sword effect of IL-1 β on the osteogenesis of periodontal ligament stem cells via crosstalk between the NF-κ B, MAPK and BMP/Smad signaling pathways. *Cell Death Dis.* 7:e2296. doi: 10.1038/cddis.2016.204

Marchesan, J., Girnary, M. S., Jing, L., Miao, M. Z., Zhang, S., Sun, L., et al. (2018). An experimental murine model to study periodontitis. *Nat. Protoc.* 13, 2247–2267. doi: 10.1038/s41596-018-0035-4

Monteleone, M., Stanley, A. C., Chen, K. W., Brown, D. L., Bezbradica, J. S., Von Pein, J. B., et al. (2018). Interleukin-1β maturation triggers its relocation to the plasma membrane for gasdermin-D-dependent and-independent secretion. *Cell Rep.* 24, 1425–1433. doi: 10.1016/j.celrep.2018.07.027

Mrozik, K. M., Wada, N., Marino, V., Richter, W., Shi, S., Wheeler, D. L., et al. (2013). Regeneration of periodontal tissues using allogeneic periodontal ligament stem cells in an ovine model. *Regenerative Med.* 8, 711–723. doi: 10.2217/rme.13.66

Okondo, M. C., Johnson, D. C., Sridharan, R., Go, E. B., Chui, A. J., Wang, M. S., et al. (2017). DPP8 and DPP9 inhibition induces pro-caspase-1-dependent monocyte and macrophage pyroptosis. *Nat. Chem. Biol.* 13, 46–53. doi: 10.1038/nchembio.2229

Papathanasiou, E., Conti, P., Carinci, F., Lauritano, D., and Theoharides, T. (2020). IL-1 superfamily members and periodontal diseases. *J. Dent. Res.* 99, 1425–1434. doi: 10.1177/0022034520945209

Pihlstrom, B. L., Michalowicz, B. S., and Johnson, N. W. (2005). Periodontal diseases. *Lancet* 366, 1809–1820.

Polak, D., and Shapira, L. (2018). An update on the evidence for pathogenic mechanisms that may link periodontitis and diabetes. *J. Clin. Periodontol.* 45, 150–166. doi: 10.1111/jcpe.12803

Rathinam, V. A., Zhao, Y., and Shao, F. (2019). Innate immunity to intracellular LPS. *Nat. Immunol.* 20, 527–533. doi: 10.1038/s41590-019-0368-3

Ren, X., Zhou, Q., Foulad, D., Tiffany, A. S., Dewey, M. J., Bischoff, D., et al. (2019). Osteoprotegerin reduces osteoclast resorption activity without affecting osteogenesis on nanoparticulate mineralized collagen scaffolds. *Sci. Adv.* 5:eaaw4991. doi: 10.1126/sciadv.aaw4991

Rocha, F. R. G., Delitto, A. E., De Souza, J. A. C., González-Maldonado, L. A., Wallet, S. M., and Junior, C. R. (2020). Relevance of Caspase-1 and Nlrp3 inflammasome on inflammatory bone resorption in A murine model of periodontitis. *Sci. Rep.* 10:7823.

Santana, J. B., Moraes, R. M., De Lima Zutin, E. A., De Fátima Santana Melo, G., Franco, G. C. N., and Anbinder, A. L. (2016). "The ligature-induced periodontitis model: literature overview and description of the technique," in *Periodontal Disease: Diagnosis, Management Options and Clinical Features*, 23–46.

Sanz, I., Alonso, B., Carasol, M., Herrera, D., and Sanz, M. (2012). Nonsurgical treatment of periodontitis. *J. Evid. Based Dent. Pract.* 12, 76–86.

Seo, B.-M., Miura, M., Gronthos, S., Bartold, P. M., Batouli, S., Brahim, J., et al. (2004). Investigation of multipotent postnatal stem cells from human periodontal ligament. *Lancet* 364, 149–155. doi: 10.1016/s0140-6736(04)16627-0

Shi, J., Zhao, Y., Wang, K., Shi, X., Wang, Y., Huang, H., et al. (2015). Cleavage of GSDMD by inflammatory caspases determines pyroptotic cell death. *Nature* 526, 660–665. doi: 10.1038/nature15514

Tassi, S., Sergio, N., Misawa, M., and Villar, C. (2017). Efficacy of stem cells on periodontal regeneration: systematic review of pre-clinical studies. *J. Periodontal Res.* 52, 793–812. doi: 10.1111/jre.12455

Trubiani, O., Pizzicannella, J., Caputi, S., Marchisio, M., Mazzon, E., Paganelli, R., et al. (2019). Periodontal ligament stem cells: current knowledge and future perspectives. *Stem Cells Dev.* 28, 995–1003. doi: 10.1089/scd.2019.0025

Vandana, K., Desai, R., and Dalvi, P. J. (2015). Autologous stem cell application in periodontal regeneration technique (SAI-PRT) using PDLSCs directly from an extracted tooth·an insight. *Int. J. Stem Cells* 8:235.

Wang, D., Zheng, J., Hu, Q., Zhao, C., Chen, Q., Shi, P., et al. (2020). Magnesium protects against sepsis by blocking gasdermin D N-terminal-induced pyroptosis. *Cell Death Differ.* 27, 466–481. doi: 10.1038/s41418-019-0366-x

Wang, L., Chen, K., Wan, X., Wang, F., Guo, Z., and Mo, Z. (2017). NLRP3 inflammasome activation in mesenchymal stem cells inhibits osteogenic differentiation and enhances adipogenic differentiation. *Biochem. Biophys. Res. Commun.* 484, 871–877. doi: 10.1016/j.bbrc.2017.02.007

Xia, S., Hollingsworth, L. R., and Wu, H. (2020). Mechanism and regulation of gasdermin-mediated cell death. *Cold Spring Harb. Perspect. Biol.* 12:a036400. doi: 10.1101/cshperspect.a036400

Yamaguchi, Y., Kurita-Ochiai, T., Kobayashi, R., Suzuki, T., and Ando, T. (2017). Regulation of the NLRP3 inflammasome in *Porphyromonas gingivalis*-accelerated periodontal disease. *Inflamm. Res.* 66, 59–65. doi: 10.1007/s00011-016-0992-4

Zhuang, J., Wang, Y., Qu, F., Wu, Y., Zhao, D., and Xu, C. (2019). Gasdermin-d played a critical role in the cyclic stretch–induced inflammatory reaction in human periodontal ligament cells. *Inflammation* 42, 548–558. doi: 10.1007/s10753-018-0912-6

Conflict of Interest: The authors declare that the research was conducted in the absence of any commercial or financial relationships that could be construed as a potential conflict of interest.

frontiers in Cell and Developmental Biology

ORIGINAL RESEARCH
published: 01 April 2021
doi: 10.3389/fcell.2021.654654

Titanium Nanotube Modified With Silver Cross-Linked Basic Fibroblast Growth Factor Improves Osteoblastic Activities of Dental Pulp Stem Cells and Antibacterial Effect

Abdullkhaleg Ali Albashari[1†], Yan He[2†], Mohammed A. Albaadani[1†], Yangfan Xiang[1], Jihea Ali[3], Fengting Hu[1], Yuan Zhang[1], Keke Zhang[1], Lihua Luo[1], Jianming Wang[2*] and Qingsong Ye[1,4*]*

[1] School and Hospital of Stomatology, Wenzhou Medical University, Wenzhou, China, [2] Laboratory for Regenerative Medicine, Tianyou Hospital, Wuhan University of Science and Technology, Wuhan, China, [3] College of Life and Environmental Science, Wenzhou University, Wenzhou, China, [4] Center of Regenerative Medicine, Renmin Hospital of Wuhan University, Wuhan, China

Titanium modifications with different silver loading methods demonstrate excellent antibacterial properties. Yet pure silver nanoparticles with limited bioactive properties may delay regeneration of bone surrounding the dental implant. Therefore, loading silver with bioactive drugs on titanium surfaces seems to be a very promising strategy. Herein, we designed a silver (Ag) step-by-step cross-linking with the basic fibroblast growth factor (bFGF) by polydopamine (PDA) and heparin on titanium nanotube (TNT) as its cargo (TNT/PDA/Ag/bFGF) to improve the implant surface. Our results showed that TNT/PDA/Ag/bFGF significantly enhanced the osteogenic differentiation of dental pulp stem cells (DPSCs). It also showed an excellent effect in bacterial inhibition and a reduction of pro-inflammatory factors through inhibition of M1 macrophage activity. These results showed that bFGF cross-linked silver coating on TNTs presented good osteogenic differentiation and early anti-infiammatory and antibacterial properties. Together, this novel design on titanium provides a promising therapeutic for dental implants.

Keywords: titanium nanotube, dental pulp stem cells, bFGF, implant, silver nanoparticles

OPEN ACCESS

Edited by:
Yidong Wang,
Xi'an Jiaotong University, China

Reviewed by:
Mingzhen Zhang,
Xi'an Jiaotong University, China
Ya Shen,
University of British Columbia, Canada
Xunwei Wu,
Shandong University, China

****Correspondence:***
Lihua Luo
luolihua81@126.com
Jianming Wang
wjm18jgm@aliyun.com
Qingsong Ye
qingsongye@hotmail.com;
qingsongye@foxmail.com

† These authors have contributed equally to this work

Specialty section:
This article was submitted to Stem Cell Research, a section of the journal Frontiers in Cell and Developmental Biology

Received: *17 January 2021*
Accepted: *04 March 2021*
Published: *01 April 2021*

Citation:
Albashari AA, He Y, Albaadani MA, Xiang Y, Ali J, Hu F, Zhang Y, Zhang K, Luo L, Wang J and Ye Q (2021) Titanium Nanotube Modified With Silver Cross-Linked Basic Fibroblast Growth Factor Improves Osteoblastic Activities of Dental Pulp Stem Cells and Antibacterial Effect. Front. Cell Dev. Biol. 9:654654. doi: 10.3389/fcell.2021.654654

INTRODUCTION

Despite that dental implants have been broadly used in clinics to replace missing teeth and restore oral functions, they have a poor success rate for application with low bone formation surrounding the implant with different surface modifications (Duyck and Vandamme, 2017; Yuan et al., 2019). To encourage the osteoblastic activities and implant osseointegration, numerous studies and attempts have focused on the alterations of surface features and morphology of implant materials via physical and chemical modifications (Marenzi et al., 2019; Siddiqui et al., 2019).

Dental pulp stem cells (DPSCs), a type of mesenchymal stem cells (MSCs), have been recognized as a good stem cell source in bone formation. Evidence indicates that initial stem cell adhesion to titanium surfaces is of essential importance in cell proliferation, differentiation, osteogenesis, and osseointegration surrounding the implant (Bandyopadhyay et al., 2019b). Proper surface modification of titanium (Ti) could facilitate the cell-to-Ti interaction and the early osseointegration of implants (Bandyopadhyay et al., 2019a). Also, studies have shown that many growth factors could support cell adhesion and osseointegration with the aid of chemical compounds like heparin, dextran, and hyaluronic acid (Subbiah and Guldberg, 2019). Also, growth factors can maintain and support the renewal and multipotency properties of stem cells (Choi et al., 2018). Bone morphogenetic protein 2 (BMP-2) is one of the most studied growth factors in bone formation that are used with Ti (Haimov et al., 2017). Except for the obvious osteogenic capacity of BMP-2, it does not have a strong supportive role in the proliferation and differentiation of stem cells as the basic fibroblast growth factor (bFGF) does (Kang et al., 2019). It has been proved that bFGF is one of the influential mitogens for many MSCs (Luo et al., 2020).

On the other hand, due to the naturally occurring oral microorganisms, it is important and challenging in clinical application to control the infection and promote osseointegration (Krastl and Amato, 2019). Many antibacterial drugs have been incorporated on titanium surfaces to prevent infections, such as amoxicillin, doxycycline, and cephalexin (Orapiriyakul et al., 2018). Limited by the potency of induced drug resistance, bioactivity, and loading capacity, the choice of drugs requires a sustained release of bioactive antibiotics (14–16). As a previous work indicated (Chouirfa et al., 2019), properly designed surface modification on Ti would be a possible solution to control-release the antibacterial agents, prohibit bacterial proliferation, and prevent biofilm formation. Because different nanoparticles are favorable bactericidal agents owing to their antibacterial wide-spectrum activity, good stability, low cytotoxicity, and high efficiency, Ag nanoparticles can penetrate biofilms and provide antimicrobial effects on both single-species biofilm of gram-positive and gram-negative bacteria and multi-species of oral biofilms (He et al., 2013, 2014; Peterson et al., 2015).

Current loading methods, including physical binding loading, dip loading, sputter loading, electrophoresis loading, and chemically conjugated loading, have several shortcomings like shape dependence, difficulty fabricating process, environmental pollution, expensive instruments, and harsh processing conditions. To get the better stability of loading multifactors on titanium, covalent cross-linking grafting has brought about step-by-step cross-linking, early cross-linking, and post-cross-linking. Unfortunately, this type of silver and bFGF step-by-step cross-linking delivery system on titanium nanotube (TNT) has not been developed. In this work, we fabricated TNTs coated with polydopamine (PDA) and Ag-bFGF cross-linking heparin binding. It is speculated that an Ag-bFGF cross-linking binding on titanium will control infection and sustainably promote bone formation. We believe that this strategy may inspire the design of step-by-step cross-linking loading for dental implants on titanium in the future.

MATERIALS AND METHODS

Materials and Chemicals

Titanium sheets (3 mm thick) were obtained from the Northwest Institute for Nonferrous Metal Research (Xi'an, China). Silver nitrate, ammonium fluoride, glycerol, heparin, paraformaldehyde (PFA), 2-(*N*-morpholino)ethanesulfonic acid, *n*-hydroxysuccinimide, 1-ethyl-3-(3-dimethylaminopropyl)carbodiimide, and toluidine blue were obtained from Aladdin Industrial Corporation (Shanghai, China). Dimethyl sulfoxide, Lysogeny broth (LB) medium, Triton X-100, 3-(4,5-dimethylthiazol-2-yl)-2,5-diphenyltetrazolium bromide (MTT), and Tris–HCl were obtained from Solarbio (China). Interleukin-6 (IL-6) detection IL-6 antibody was purchased from Affbiotech (DF6087, United States). Bicinchoninic acid kit (BCA kit), nitric oxide kit, 4′,6-diamidino-2-phenylindole (DAPI), and *p*-nitrophenyl phosphate assay kit were bought from Beyotime Institute of Biotechnology (Shanghai, China). Cell Counting Kit-8 (CCK-8) was purchased from Dojindo (Kumamoto, Japan). Recombinant bFGF, minimum essential medium α (MEM-α), Dulbecco modified Eagle's minimal essential medium (DMEM), phosphate-buffered saline (PBS), fetal bovine serum (FBS), and penicillin–streptomycin were bought from Gibco (Invitrogen, United States). Osteogenic medium was purchased from Cyagen, United States. ELISA kit for bFGF was purchased from Westang System (Shanghai, China). Sangon kit for RNA extraction was purchased from Sangon Biotech (Shanghai, China). Reverse RNA kit and PrimeScript RT kits were purchased from Takara Bio Inc (Kyoto, Japan).

Sample Preparation

As shown in **Figure 1**, sample surfaces went through a series of modifications to contain active components. Individual surface modifications are explained below.

Titanium Nanotube Preparation and Modification

The surface of the titanium (Ti) sheet was polished, smoothed, and then cleaned with acetone, ethanol, and distilled water in 300-W ultrasound for 15 min. Platinum foil and Ti sheet were placed as the cathode and anodic for oxidation modification, respectively. The distance between two electrodes was set at about 3 cm. TNT modification was performed in a glycerol electrolyte containing 0.51% wt ammonium fluoride and 8.1% wt water. First, the Ti sheet was oxidized at 20 V for 3 h followed by 2 min oxidation at 170 V. Then the Ti sheet was ultrasonicated (at 90 W, in water bath) for 5 min. Finally, the Ti sheet was oxidized for 20 min at 20 V to form nanotubes on the surface (Shen et al., 2019).

Ag Cross-Linking on Ti Surfaces

Silver ion was coated onto TNT surfaces in two methods, direct coating and via a PDA film. *Direct coating*: The TNT sheet was immersed in a silver nitrate solution (1.5 mg/ml) for 20 min in the dark, rinsed five times with deionized water, and air-dried. Then ultraviolet light was applied with a high-voltage Hg lamp for 20 min per side to receive TNT/Ag samples. *Coating via PDA*

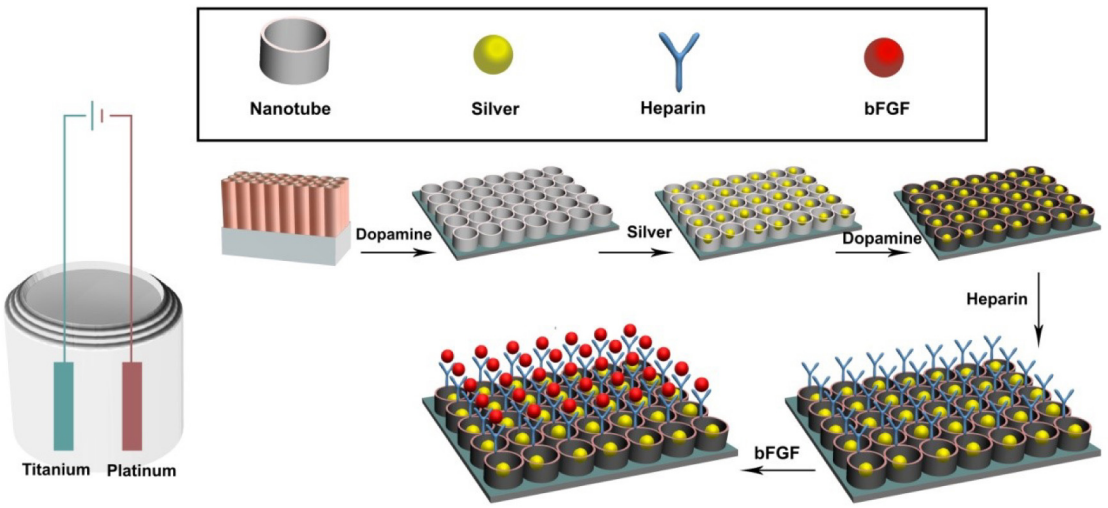

FIGURE 1 | Experimental design of the *in vitro* experiments. The titanium sheet was cut into the size of 1 cm × 1 cm pieces. Then the titanium surface was modified to titanium nanotube, coated with dopamine, and cross-linked with heparin and basic fibroblast growth factor (bFGF).

film: The TNT sheet was immersed in 2 mg/ml of dopamine in 10 mM of Tris–HCl buffer (pH 8.5) for 24 h at room temperature, washed by deionized water five times, and air-dried. Then this TNT/PDA sheet was coated with silver nitrate using the direct coating method to receive TNT/PDA/Ag samples.

Basic Fibroblast Growth Factor Functionalized Ti Samples via Heparin

To functionalize sample surfaces with bFGF, samples were immersed in 1 mg/ml of dopamine in 10 mM of Tris–HCl solution (pH = 8.5) for 12 h at room temperature in the dark, washed five times with deionized water, and air-dried. To aminate sample surface with heparin (HP), samples were immersed in a heparin solution [1 mg/ml heparin in 0.1 M of 2-(*N*-morpholino)ethanesulfonic acid solution (pH 5.6), 0.18 mg of *n*-hydroxysuccinimide, and 0.59 mg of 1-ethyl-3-(3-dimethylaminopropyl) carbodiimide] for 24 h followed by deionized water rinse and then air-dried. To functionalize samples with bFGF, 120 ng of bFGF was dissolved in 0.1 M of ethanesulfonic acid solution (pH 5.6), pipetted on the surface and left for 24 h at room temperature in the dark, washed by deionized water, and air-dried. To study the release of bFGF on heparinized sample (TNT/PDA/HP), bFGF-coated TNT and TNT/PDA/Ag samples were used as control.

Characterization of Ti Samples

The morphologic characterization of sample surfaces, coated with platinum, was examined by scanning electron microscopy (SEM; Hitachi, S2300, Japan) at the Wenzhou Institute of Biomaterials and Engineering, where the diameter of nanotubes was measured and compared. The composition of samples was assessed by the energy-dispersive X-ray spectroscopy (EDS). To evaluate the surface hydrophobicity, we performed contact angle studies on sample surfaces using deionized water.

Loading of Heparin Assay

To determine the quantity of coated heparin on sample surfaces, a toluidine blue protocol was adopted (Kim et al., 2011). Briefly, samples were immersed in 1 ml of PBS (pH 7.4) containing 0.005% toluidine blue solution for 40 min under gentle shaking at room temperature. Then the absorbance value of the solution was read using a spectrophotometric microplate reader at 620 nm (Varioskan LUX, Thermo Fisher Scientific, United States).

Protein Adsorption Assay

To evaluate protein adsorption on the substrates, bovine serum albumin (BSA) was used as a representative protein instead of bFGF (Kim et al., 2011). Five hundred microliters of 1 mg/ml BSA in PBS was added onto each sample for 2 h. Then, samples were washed once with PBS. BCA kit assay was performed, and the absorbance was measured at 570 nm using a microplate reader.

Release of Basic Fibroblast Growth Factor

To study the accumulative release of bFGF from assorted substrates (TNT, TNT/PDA/Ag, and TNT/PDA/HP), samples were soaked in 1 ml of PBS (pH 7.4) (100 rpm, 37°C). At established time points (0, 3, 6, 9, 12, 15, 18, and 21 days), the solution was collected and replaced with 1 ml of new PBS. Samples were kept at −20°C for quantitative analysis by bFGF ELISA kit according to the manufacturer's protocol.

Cellular Evaluations on Modified Ti Samples

Culture and Viability of Dental Pulp Stem Cells on Ti Samples

The isolation, culture, and identification of DPSCs were described in our previous paper (Luo et al., 2018). The use of DPSCs described in this paper was reviewed and approved by the

Ethics Committee of the School and Hospital of Stomatology, Wenzhou Medical University (No. WYKQ2018008). Sterile samples (1 cm × 1 cm) were placed in 24-well plates and seeded with DPSCs (1×10^4 cells/cm^2, passage 5) for 2 h at 37°C and 5% CO_2 humidified atmosphere. Then 1 ml/well of MEM-α medium supplemented with 10% FBS and 1% penicillin–streptomycin was used to start cell culture. The first passage of DPSCs was characterized by flow cytometry using the antibodies of human CD34, CD45, CD73, and CD105 according to standard protocols. The data were evaluated with CytoFLEX flow cytometers (Beckman Coulter, California, United States). The DPSCs were evaluated by immunofluorescence staining with CD44, CD146, and CD31. After 1 and 3 days, CCK-8 solution was applied to evaluate the viability of cells adhering to sample surfaces.

Morphology of Dental Pulp Stem Cells on Modified Ti Samples

To evaluate DPSCs on the surfaces, observation on cell morphology via SEM and immunofluorescence microscopy was performed. After 1-day culture of DPSCs on sample surfaces, cells were fixed with 4% PFA for 1 h, washed three times with PBS, dehydrated in a series of ethanol from 30 to 100%, and air-dried at 37°C. The samples were platinum coated and examined by SEM.

To visualize DPSCs on sample surfaces after 1- and 3-day culture, samples were washed with PBS three times, fixed with 4% PFA for 15 min, and rinsed with PBS three times. Cells were permeabilized by 0.1% Triton X-100 in PBS for 5 min and 5% BSA for 30 min at 37°C. Then DPSCs were labeled by 1 mg/ml of phalloidin-TRITC and 2 mg/ml DAPI. Five random locations per sample were photographed by a fluorescence microscope (Eclipse 80i, Nikon, Japan).

Osteogenic Capacity of Dental Pulp Stem Cells on Modified Ti Samples

Alkaline phosphatase activity

To evaluate the osteogenic differentiation of DPSCs on the sample surfaces, cells grown on sample surfaces were cultured with the osteogenic medium. On days 7 and 14, the alkaline phosphatase (ALP) activity of the cells was assessed. Briefly, cells were lysed by sonication within 1 ml of DNA-free H_2O containing 0.02% wt Triton X-100 for 45 min at room temperature. Total protein concentration and ALP activity of DPSCs were quantified with BCA kit (570 nm) and *p*-nitrophenyl phosphate assay kit (490 nm) by the microplate reader.

Mineralization level

Dental pulp stem cells grown on sample surfaces were cultured with osteogenic medium for 21 days. Then the samples were fixed with 4% PFA. To evaluate the formation of calcified nodules, samples were stained with Alizarin red S (pH 4.1), treated with 10% v/v acetic acid and 10% v/v ammonium hydroxide, and measured at 405 nm with the microplate reader. The cells were fixed for 30 min with 2.5% glutaraldehyde and dehydrated by gradient methanol (30, 40, 50, 70, 80, 90, 95, and 100%). The cells were observed using SEM.

Expression of osteogenic genes

Dental pulp stem cells were cultured on sample surfaces for 10 days using osteogenic medium. Total RNA was extracted using Sangon kit. RNA extractions were performed according to the manufacturer's protocol. Then 2 μg of extracted RNA was reversely transcribed to cDNA using cDNA Takara Reverse kits. Gene expression of ALP, runt-related transcription factor 2 (RUNX), osteocalcin (OCN), and osteopontin (OPN) were measured with corresponding primers (**Table 1**). Expression levels of all genes were normalized to GAPDH.

Antibacterial Property of Modified Ti Samples

Bacterial Culture and Short-Term Antibacterial Assay of Ti Samples

Escherichia coli ATCC25922 (*E. coli*) and *Staphylococcus aureus* ATCC35984 (*S. aureus*) were separately seeded on modified Ti surfaces at a density of 1×10^6/cm^2 and cultured with LB medium for 12 h at 37°C aerobically. Then, samples were fixed with 2.5% glutaraldehyde, dehydrated by gradient methanol, coated with platinum, and visualized by SEM. To qualitatively evaluate the antibacterial property of these Ti samples, disk diffusion assay was performed to compare the inhibition zone and bacterial colony free zone. One milliliter of 10^6 cells/ml bacterial solution per plate was inoculated on LB agar plate. Modified Ti samples were placed on the agar plates and incubated aerobically for 24 h at 37°C. The inhibition zone was photographed and compared (Cai et al., 2018).

Antibacterial Activity of Pre-released Ti Samples

To pre-release coated active components on modified Ti sheets, all samples were drenched in PBS (pH 7.4) for 1, 3, and 7 days. Then these pre-released Ti samples were placed in a 24-well plate and inoculated with *E. coli* or *S. aureus* (1×10^6/cm^2) using LB medium in an aerobic incubator at 37°C. After 24 h, the medium was replaced by a mixture of 50 μl of MTT (5 mg/ml) and 450 μl of fresh medium per well to evaluate the viability of the bacteria. After 2-h incubation at 37°C in the dark, the mixture was replaced with 500 μl of dimethyl sulfoxide and measured at 540 nm by the microplate reader.

TABLE 1 | Expression of osteogenic genes.

ALP-F	GCTATCCTGGCTCCGTGCT
ALP-R	ACAGATTTCCCAGCGTCCTT
OCN-F	GCAAAGGTGCAGCCTTTGTG
OCN-R	GGCTCCCAGCCATTGATACAG
Runx2-F	GCGGTGCAAACTTTCTCCAG
Runx2-R	TGCTTGCAGCCTTAAATGACTC
OPN-F	TTTTGCCTCCTAGGCATCACC
OPN-R	TGGAAGGGTCTGTGGGGCTA
GAPDH-F	ATGGGCAGCCGTTAGGAAAG
GAPDH-R	GATCTCGCTCCTGGAAGATGG

Titanium Modification on *Porphyromonas gingivalis* Associated With Peri-Implantitis

Porphyromonas gingivalis (ATCC 33277) was cultured in brain heart infusion (BHI) broth containing 0.001% hemin, 0.0001% vitamin K, and 5 mg/ml of yeast extraction in an anaerobic chamber (85% N_2, 10% H_2, and 5% CO_2 at 37°C; GeneScience Anaerobox IV, United States). For SEM and MTT assay, 1×10^6 colony-forming units (CFU) ml^{-1} of *P. gingivalis* was evaluated. All the modified titanium surfaces were cultured in 24-well plates with each well containing 1 ml of BHI, and then *P. gingivalis* is inoculated. The cells were fixed for 30 min with 2.5% glutaraldehyde and dehydrated by gradient methanol (30, 40, 50, 70, 80, 90, 95, and 100%). The cells were observed by using SEM after 24 h. To pre-release coated active components on modified Ti sheets, all samples were drenched in PBS (pH 7.4) for 1, 3, and 7 days. For MTT assay on days 1, 3, and 7, the medium was replaced by a mixture of 50 μl of MTT (5 mg/ml) and 450 μl of fresh medium per well for 2 h in the dark. Then, the mixture was replaced with 500 μl of dimethyl sulfoxide and measured at 540 nm by the microplate reader. All surfaces were placed in an anaerobic chamber (85% N_2, 10% H_2, and 5% CO_2 at 37°C).

Anti-inflammatory Property of Modified Ti Samples

RAW 264.7 Cell Culture and Pro-inflammatory Expression

RAW 264.7 cell was obtained from the Wenzhou Institute of Biomaterials and Engineering (Wenzhou, China) and cultured with DMEM containing 10% FBS and 1% penicillin–streptomycin. RAW 264.7 cells were seeded on Ti sample surfaces at 1×10^5 cells/cm^2 in 24-well plates and cultured for 24 h. Then the cells were challenged by culture medium supplemented with 500 ng/ml of lipopolysaccharide (LPS). After 12 h, cells were fixed with 4% PFA and washed with PBS thrice followed by 5 min permeabilization with 0.1% Triton X-100 and 30 min with 5% BSA at 37°C. Pro-inflammatory factor, IL-6, was stained by an immunofluorescence label. Nuclei were stained with 2 mg/ml of DAPI. Images were taken by the fluorescence microscope.

Expression of Pro-inflammatory Genes

RAW 264.7 cell was challenged the same way as above. Total RNA was extracted from cells. Relative mRNA expression of pro-inflammatory factors, IL-6, and TNF-α was assessed. cDNA was transcribed from RNA by using Prime Script RT kit. Quantitative PCR samples were performed using a total volume of 20 μl with identical primers (**Table 2**) and PCR SYBR Green Kit (95°C for 30 s, following by 39 cycles of 95°C for 5 s and 60°C for 30 s). Data were normalized with GAPDH, analyzed using the $2^{-\Delta\Delta CT}$ method, and expressed in the mean value of each group.

TABLE 2 | Expression of pro-inflammatory genes.

TNF-α-F	CCAGGCAGGTTCTGTCCCTT
TNF-α-R	ATAGGCACCGCCTGGAGTTC
IL-6-F	CTGGAGCCCACCAAGAACGA
IL-6-R	GCCTCCGACTTGTGAAGTGGT
GAPDH-F	GGATGCAGGGATGATGTTC
GAPDH-R	TGCACCACCAACTGCTTAG

Inhibition of Nitric Oxide Production

Nitric oxide production has been regarded as an effective indicator to study the inflammatory status of macrophages (Palmieri et al., 2020). To quantify the level of nitric oxide, RAW 264.7 cells were seeded at 1×10^5 cells/cm^2 in 24-well plates on sample surfaces and cultured overnight with DMEM containing 10% FBS and 1% penicillin–streptomycin. Then medium was replaced with FBS-free DMEM supplemented with 500 ng/ml of LPS for 1 and 3 days. The nitrite was determined in culture media according to protocol instruction kit (s0021, Beyotime, China). The total reaction was 50 μl of medium mixed with 50 μl of Griess Reagent I in 96-well plate and applying 50 μl of Griess Reagent II. Then the absorbance was measured at 540 nm in a microplate reader (Varioskan LUX, Thermo Fisher Scientific, United States).

Statistical Analysis

One-way analysis of variance (ANOVA) was used to analyze the data; then, we analyzed the homogeneity of variance by Levene test. If the significance of Levene test was >0.05, we used Tukey's test for multiple comparisons; if not, we checked the rest of the results. And statistical significance was set as $p < 0.05$. Statistical significance was defined as $^{*}p < 0.05$, $^{**}p < 0.01$, and $^{***}p < 0.001$.

RESULTS AND DISCUSSION

Characterization and Multipotency Analysis of Dental Pulp Stem Cells

Dental pulp stem cells are one type of MSCs and possessed the characteristics of MSCs; for example, DPSCs have multidifferentiation potentials and express MSC-like markers. For the DPSC identification, flow cytometry analysis was performed to examine the MSC-like properties of DPSCs. As presented in **Figure 2A**, the flow cytometry results showed that DPSCs positively expressed CD105 and CD73 phenotypic markers but negatively expressed CD34 and CD45. Also, the result proposed that DPSCs positively expressed the immunofluorescence for CD44 and CD164 but negatively expressed CD31 (**Figure 2B**). Studies showed that DPSCs have positively expressed MSC-like phenotypic markers such as STRO-1, CD146, CD105, CD90, and CD73 and negatively expressed hematopoietic lineage molecules, including HLA-DR, CD45, CD14, and CD34 (Gronthos et al., 2002; He et al., 2020).

Characterization of Samples

According to measurement on SEM images, the nanotube diameter of TNT, TNT/Ag, TNT/PDA/Ag, and TNT/PDA/Ag/bFGF was 79.8 ± 10.3, 70.6 ± 7.1, 60.6 ± 8.9, and 58.6 ± 7.4 nm, respectively (**Figure 3A**). The nanoparticles of Ag on pores could be detected at nanotube inner surfaces in

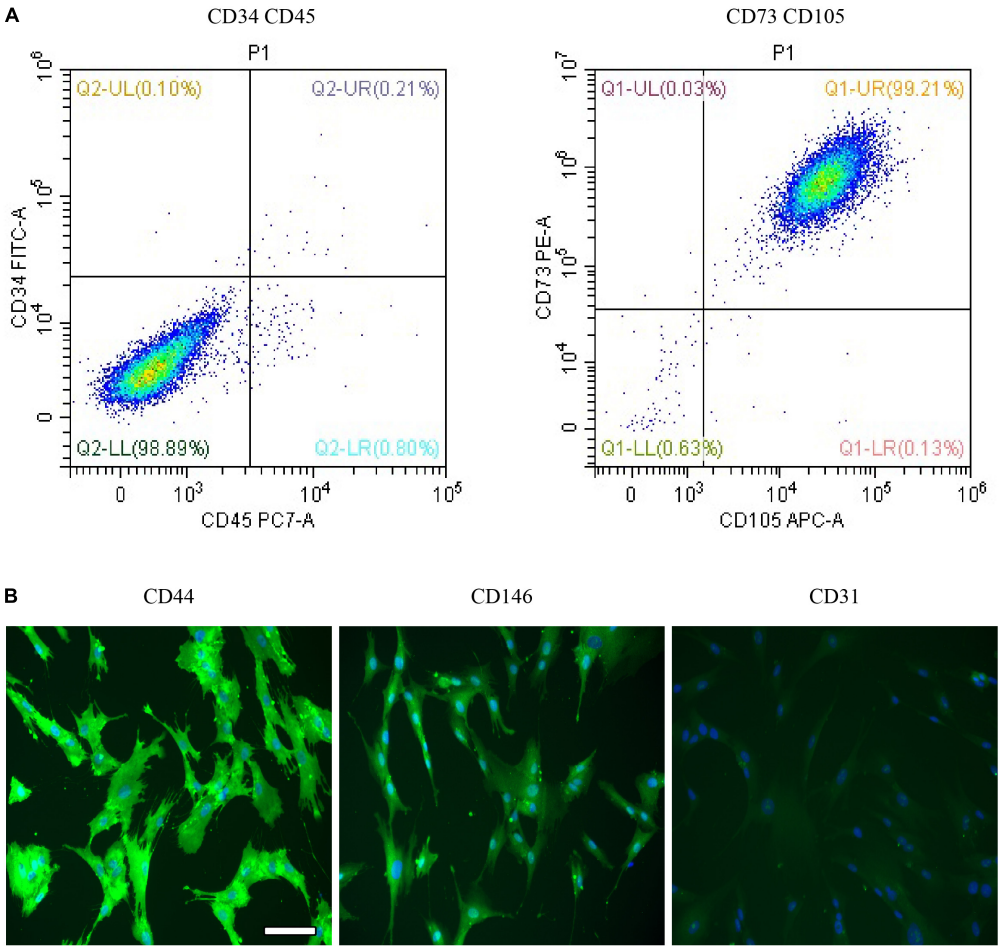

FIGURE 2 | Characterization and multipotency analysis of dental pulp stem cells (DPSCs). **(A)** The expression of surface markers of DPSCs. DPSCs positively expressed phenotypic markers CD105 and CD73 but negatively expressed CD34 and CD45. **(B)** Immunofluorescence expression of DPSC. DPSCs showed a positive expression for CD44 and CD164 but negative expression for CD31. Scale bar for **(B)**, 100 μm.

the TNT/Ag group. The wall thickness and pore size difference could be attributed to a different kind of coating structure. Some studies show different surface modifications of the TNT implants because of the excellent response to surface coating, which may encourage effective bonding between cells and implants and short healing of bone surrounding implants (Meyers and Grinstaff, 2012; Mokhtari et al., 2018; Bandyopadhyay et al., 2019b).

To study the formation of TNT/PDA/Ag/bFGF composite, EDS was performed. In the EDS study, different Ti modification samples were focused, and the peaks are shown in **Figure 3B**. All the Ti, C, O, and N could be seen in the EDS spectrum in all groups. Ag can be seen only in TNT/Ag, TNT/PDA/Ag, and TNT/PDA/Ag/bFGF.

From water contact angle study, there was a decrease of hydrophobicity on modified TNT surfaces ($p < 0.05$, **Figure 3C**), indicating that a cell adhesion-friendly surface on TNT samples was achieved with modifications introduced in this work. A previous work has shown that cell adhesion, proliferation, differentiation, and biologic activity of protein adhesion improved as the surface hydrophobicity of titanium decreased (Martin et al., 1995; Neoh et al., 2012).

In vitro Loading and Release Tests of Modified Ti Samples

To profile the heparin loaded onto Ti, TNT, TNT/Ag, and TNT/PDA, toluidine staining was performed. TNT/PDA/Ag surface showed the highest heparin release (**Figure 4A**), indicating that PDA could significantly facilitate heparin loading. This would greatly impact the release of bFGF in that bFGF was functionalized on modified Ti surfaces via heparin.

Instead of bFGF, BSA was applied to perform the protein adsorption on modified Ti surfaces using a BCA kit. We confirmed that TNT/PDA/HP was more effective in immobilizing BSA (1.55 $\mu g/cm^2$) than TNT (0.32 $\mu g/cm^2$), TNT/Ag (1.41 $\mu g/cm^2$), and TNT/PDA/Ag (0.60 $\mu g/cm^2$) (**Figure 4B**). Protein adsorption on titanium surface is important because it affects the early cell response to surfaces, including cell proliferation and differentiation (Mata et al., 2003;

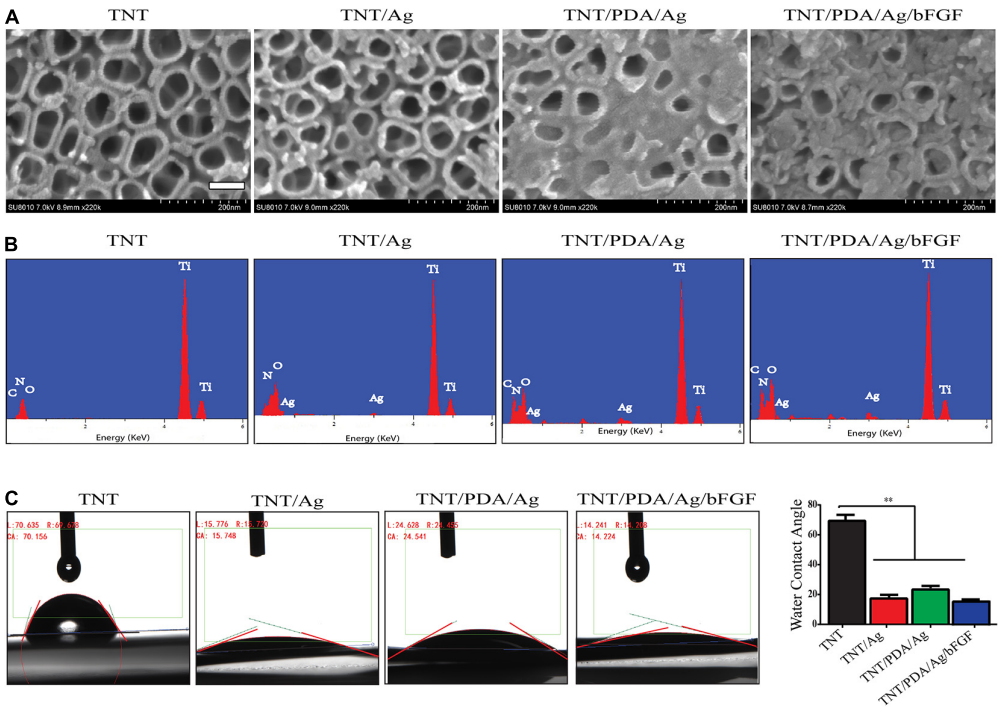

FIGURE 3 | Characterization of modified Ti samples. **(A)** SEM images of Ti challenged at 20 V: TNT, TNT/Ag, TNT/PDA/Ag, and TNT/PDA/Ag/bFGF. Ag nanoparticles on pores could be detected at nanotube inner surfaces in TNT/Ag. TNT/PDA/Ag and TNT/PDA/Ag/bFGF were partially covered with adherent particles, and the number of these particles increased in TNT/PDA/Ag/bFGF. Scale bar represents 500 nm. **(B)** Energy-dispersive X-ray spectroscopy (EDS) of modified Ti samples. TNT was mainly composed of titanium (Ti) with traces of nitrogen (N), oxygen (O), and carbon (C). Ag could be detected in TNT/Ag, TNT/PDA/Ag, and TNT/PDA/Ag/bFGF. **(C)** Water contact angle study indicated a hydrophilic surface feature in TNT/Ag, TNT/PDA/Ag, and TNT/PDA/Ag/bFGF. Data are presented as mean ± standard deviation; $^{**}p < 0.01$.

Grigoriou et al., 2005). Rivera and co-workers proved that cell adhesion and proliferation capacity increased as more protein adsorbed on titanium surfaces (Rivera-Chacon et al., 2013).

At predetermined time intervals, the release kinetics of bFGF immobilized on the TNT/PDA/Ag/HP was analyzed by ELISA kit (**Figure 4C**). TNT showed the fastest release of bFGF, reached the peak on day 9, and failed to maintain a plateau. On the contrary, TNT/PDA/Ag reached release peak on day 12 and TNT/PDA/HP on day 1. Both TNT/PDA/Ag and TNT/PDA/HP displayed a slow release with the latter being even more slowly. It seemed that heparin coating could further slow down the release of bFGF from Ti surface. Also, heparin has been known to protect growth factor from degradation by decreasing the noggin binding (Ruppert et al., 1996; Luo et al., 2018). It combatively inhibits the noggin binding to osteoblasts, resulting in a prolonged half-life of growth factor. The study reported that heparin could extend the lifetime of BMP-2 by 20 times longer (Zhao et al., 2006). Yang et al. (2015) showed that titanium coated with heparin and BMP-2 promoted the proliferation of MG-63 human osteosarcoma cells and their osteoblast differentiation.

Viability and Proliferation of Dental Pulp Stem Cells on Modified Ti Samples

The viability of DPSCs that adhered on modified Ti surfaces was examined using a CCK-8 assay after 1- and 3-day culture (**Figure 5A**). On both days 1 and 3, TNT/PDA/Ag/bFGF showed the highest viable results. Also, the CCK-8 results indicated an increase of cell number after 3 days growth on the surfaces. SEM image confirmed that DPSCs spread well on Ti surfaces after 1-day culture (**Figure 5B**). Immunofluorescence staining of DPSCs after 1- and 3-day culture visualized the cells on the surfaces (**Figures 5C,D**). Compared with that on day 1, the cell density was increased on day 3, corresponding to the CCK-8 results. Previous studies indicated that bFGF assisted cell adhesion on the hydrogel (Yan et al., 2010; Guo et al., 2019). On day 1, DPSCs on TNT/PDA/Ag showed alignment on the surface. This observation was also reported in others' work. PDA-coated TNTs decreased the pore size of the nanotube and supported cell adhesion (Ko et al., 2013; Kao et al., 2015). In our study, we discovered that DPSCs on all Ti surfaces aligned in one direction on day 3.

Osteogenic Differentiation of Dental Pulp Stem Cells on Modified Ti Samples

The ALP evolution of the DPSCs was investigated after 7 and 14 days on the modified samples. In **Figure 6A**, significant differences were shown between the ALP of DPSCs cultured on TNT containing silver with bFGF and other groups. The ALP activity of DPSCs co-cultured on the

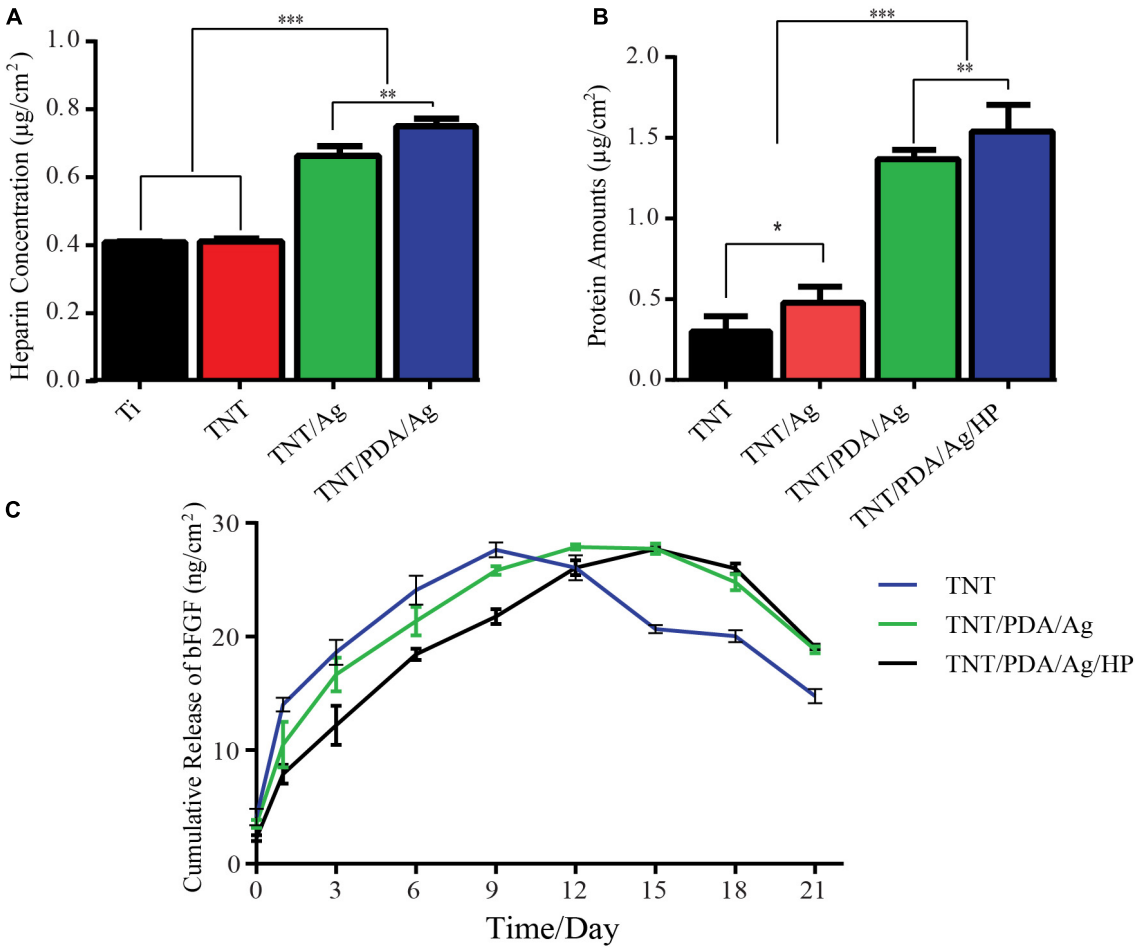

FIGURE 4 | *In vitro* loading and release tests of modified Ti samples. **(A)** Heparin loading assay: samples were immersed in 1 ml of phosphate-buffered saline (PBS) (pH 7.4) containing 0.005% toluidine blue solution for 40 min, and solutions were measured at 620 nm. TNT/PDA/Ag surface showed the highest heparin loading capacity. **(B)** Bovine serum albumin (BSA) release of modified Ti samples: a total of 500 μg of BSA per modified Ti samples was added and left for 2 h. The adsorbed amount of BSA was quantified using a bicinchoninic acid kit (BCA) kit assay (570 nm). TNT/PDA/Ag/HP showed the highest protein adsorption among all modified surfaces. **(C)** Cumulative release of basic fibroblast growth factor (bFGF) from modified Ti samples in PBS (pH: 7.4) at 37°C measured by ELISA. Both TNT/PDA/Ag and TNT/PDA/Ag/HP displayed a slow release, with the latter being even more slowly. TNT, TNT/PDA/Ag, and TNT/PDA/Ag/HP reached the release peak on days 9, 12, and 15, respectively. Data are presented as mean ± standard deviation; $*p < 0.05$, $**p < 0.01$, and $***p < 0.001$.

TNT/PDA/Ag/bFGF was higher than that of others cultured on TNT/PDA/Ag during the culture time. DPSCs grown on the TNT/PDA/Ag had significantly higher ALP activity than those grown on TNT/Ag for 7 and 14 days. The calcium amount deposited by DPSCs differentiated on each group was tested at 21 days of cell culture. By using SEM, the results of the amount of calcium deposition significantly show that DPSCs cultured on the TNT/PDA/Ag had higher amounts of calcium than the ones cultured on TNT/Ag (**Figure 6B**). Clearly, differences were shown in the calcium deposition level between DPSCs cultivated on TNT/PDA/Ag/bFGF and other surfaces (**Figure 6B**). The results of ALP, OPN, and OCN gene expression by DPSCs were evaluated by using real-time PCR after 14-day culture. In **Figure 6C**, significant differences were observed between gene expression by DPSCs that differed on the TNT/PDA/Ag and other groups. The ALP, OPN, and OCN by DPSCs cultivated on TNT/PDA/Ag were significantly greater than those cultivated on TNT/Ag.

Antibacterial Properties of Modified Ti Samples

Gram-negative bacteria, *E. coli*, and gram-positive bacteria, *S. aureus*, were used to examine the antibacterial properties of modified Ti samples. According to SEM observation (**Figure 7A**), after 12-h incubation on these Ti surfaces, a uniform layer of bacteria, biofilm, formed on TNT surfaces. A rod shape of *E. coli* and a circle shape of *S. aureus* were seen on TNT surfaces. On surfaces of TNT/Ag, TNT/PDA/Ag, and TNT/PDA/Ag/bFGF, the number of bacteria was reduced. Damaged membrane and deformed shape of bacteria were observed.

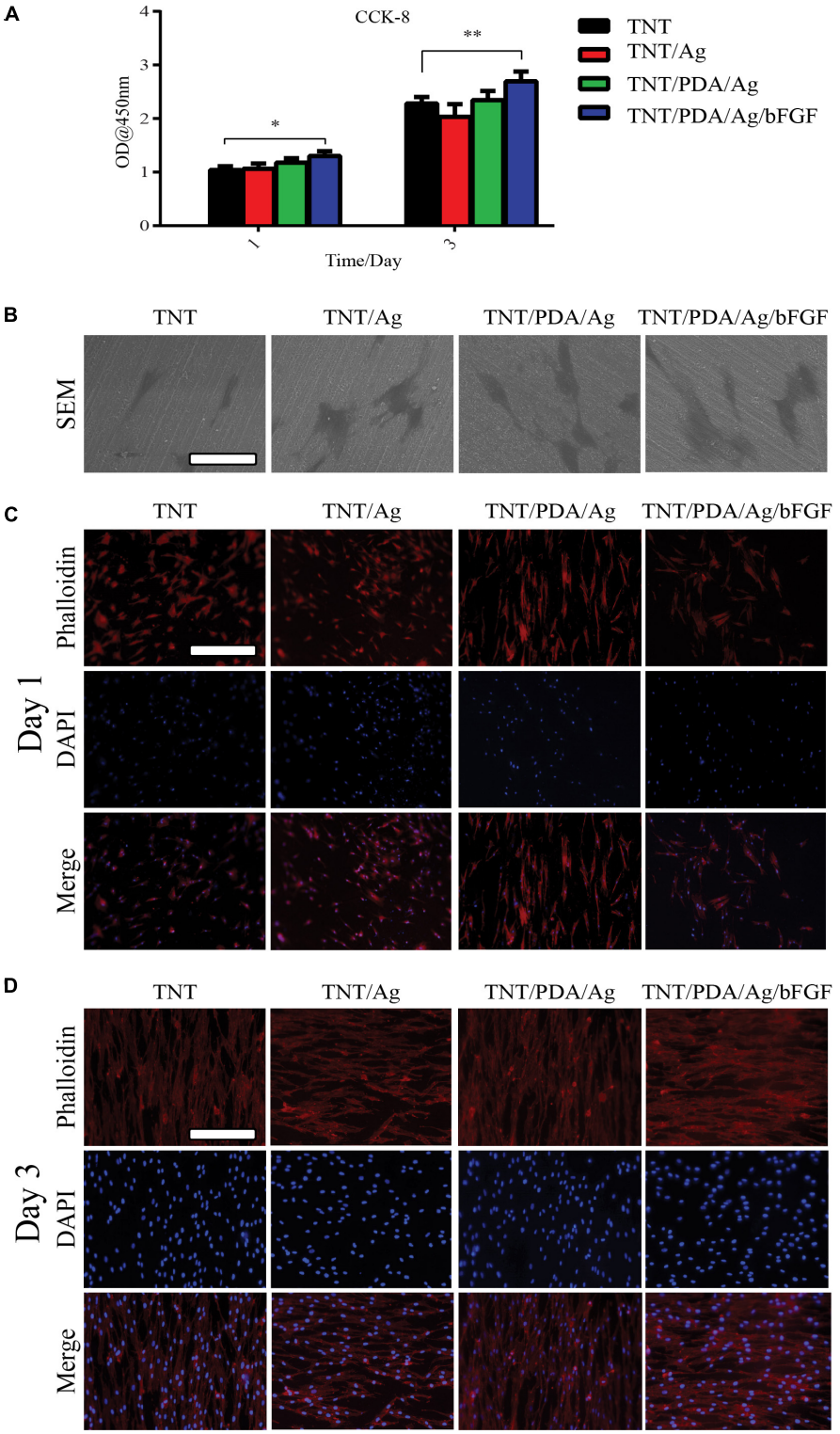

FIGURE 5 | Features of dental pulp stem cells (DPSCs) on modified Ti samples. **(A)** Determined by Cell Counting Kit-8 (CCK-8), on both days 1 and 3, DPSCs showed the highest viability on TNT/PDA/Ag/bFGF. **(B)** After 1-day culture of DPSCs on sample surfaces, cells were processed for SEM, which confirmed that DPSCs spread well on all modified Ti surfaces. Scale bar represents 20 μm. **(C,D)** To visualize DPSCs on sample surfaces after 1- and 3-day culture, cells were labeled by phalloidin-TRITC (red) and DAPI (blue). During the first day of culture of DPSCs on modified Ti surfaces, cells on TNT/PDA/Ag and TNT/PDA/Ag/bFGF were aligned. On day 3, DPSCs were well aligned in high density on all surfaces. Scale bar represents 20 μm. Data are presented as mean ± standard deviation; $^{*}p < 0.05$, $^{**}p < 0.01$.

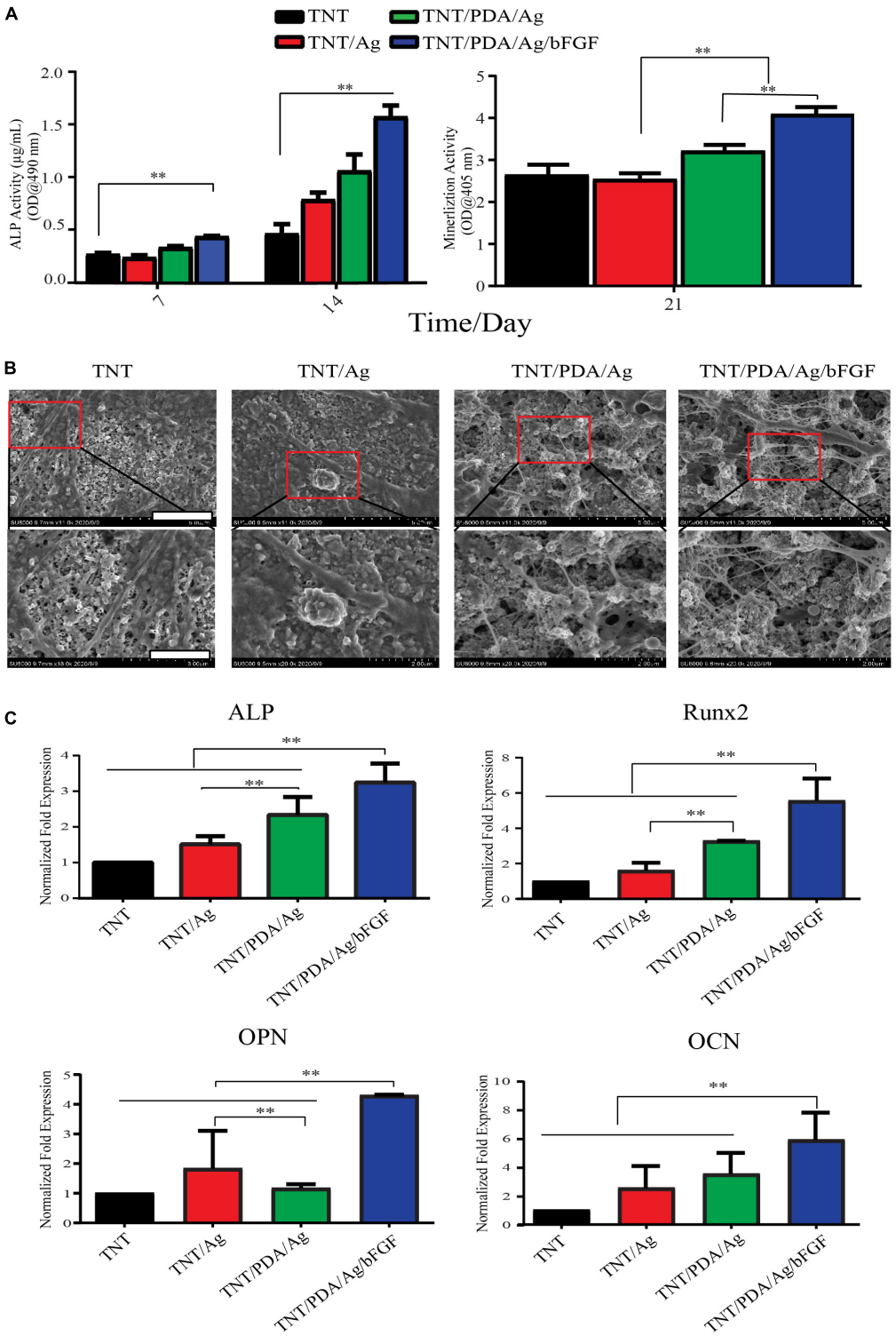

FIGURE 6 | Osteogenic differentiation of DPSCs on modified Ti samples. **(A)** ALP activity of DPSCs cultured on TNT/PDA/Ag/bFGF was significantly higher than that on other surfaces on days 7 and 14. Mineralization assay stained with Alizarin red S indicated that DPSCs grown on TNT/PDA/Ag/bFGF showed the highest calcium deposition among all surfaces. **(B)** After 21-day culture of DPSCs on sample surfaces, cells were prepared and examined by SEM. Calcium deposition on TNT/PDA/Ag/bFGF was significantly higher in all surfaces. Scale bars represent 5 and 2 μm in the upper and lower panels, respectively. **(C)** Relative mRNA expression of osteogenic genes (ALP, OPN, RUNX, and OCN) were normalized to GAPDH and compared among all groups. Osteogenic gene expression of DPSCs cultured on TNT/PDA/Ag/bFGF was the highest. Data are presented as mean ± standard deviation; $^{**}p < 0.01$. DPSCs, dental pulp stem cells; ALP, alkaline phosphatase; OPN, osteopontin; RUNX, runt-related transcription factor 2; OCN, osteocalcin.

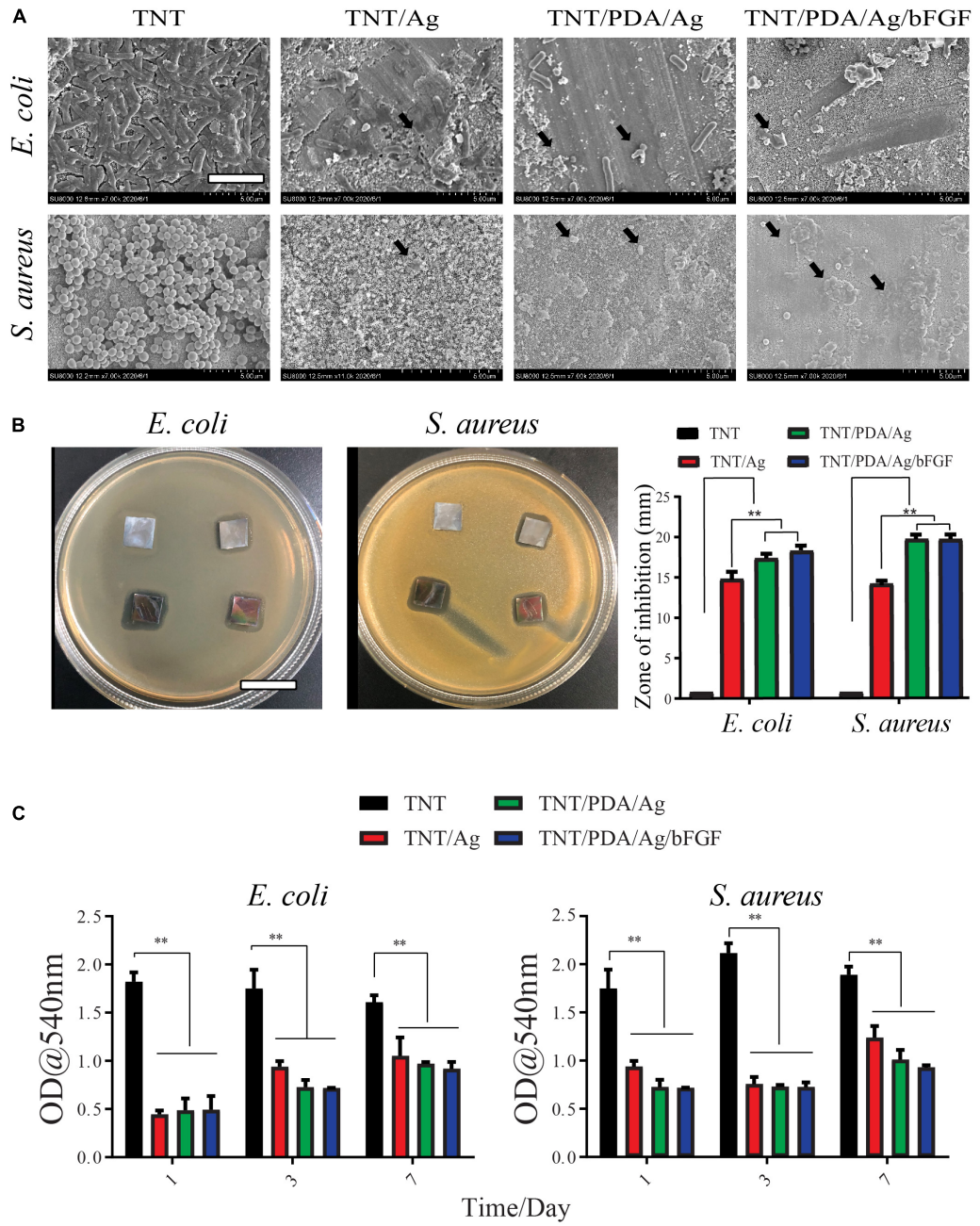

FIGURE 7 | Antibacterial properties of modified Ti samples. **(A)** *Escherichia coli* and *Staphylococcus aureus* were cultured on modified Ti surfaces for 12 h and imaged by SEM. Bacteria with damaged membrane and deformed shape were observed on TNT/Ag, TNT/PDA/Ag, and TNT/PDA/Ag/bFGF (black arrows). Scale bar represents 2 μm. **(B)** Inhibition zone of Ti samples. The bacterial suspension was inoculated, and modified Ti samples were placed on agar plates for 24-h incubation. Bacterial free zone was measured and compared. Both TNT/PDA/Ag and TNT/PDA/Ag/bFGF showed significantly larger inhibition zones. Scale bar represents 2 cm. **(C)** Quantitative analysis of antibacterial ability against *E. coli* and *S. aureus* of Ti samples after being pre-released in sterile phosphate-buffered saline (PBS) for 1, 3, and 7 days. These pre-released Ti samples were placed with bacteria for 24 h. Data are presented as mean ± standard deviation; $^{**}p < 0.01$.

Modified Ti samples were placed on agar plates for 24 h, where bacteria were inoculated. TNT/Ag, TNT/PDA/Ag, and TNT/PDA/Ag/bFGF have effectively inhibited the growth of *E. coli*, with TNT/PDA/Ag/bFGF being the most powerful. TNT/Ag, TNT/PDA/Ag, and TNT/PDA/Ag/bFGF were able to inhibit the growth of *S. aureus* (**Figure 7B**).

Ti samples were pre-released in sterile PBS for 1, 3, and 7 days to mimic an application situation, where bacteria arrive after the placement of the implant. These pre-released Ti samples were placed with bacteria for 24 h. Then the inhibition capacity of these pre-released Ti samples on bacterial metabolic activity was assessed by an MTT assay. We found that even after 7-day

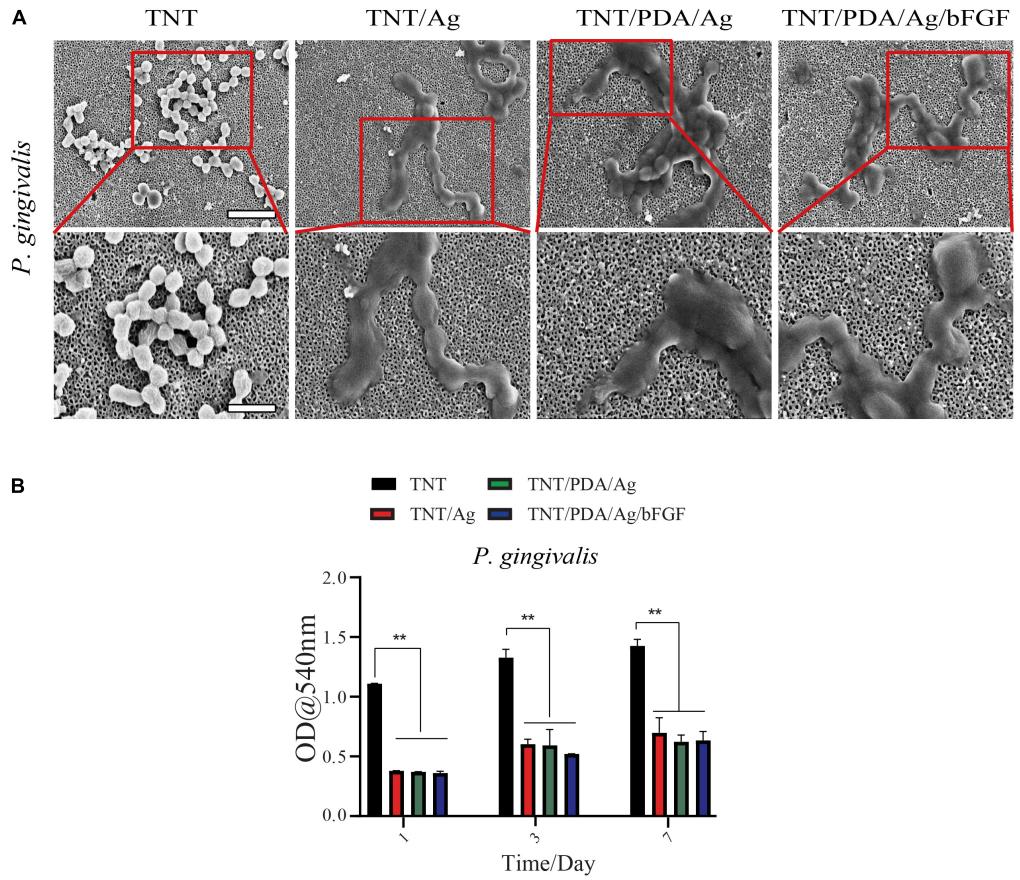

FIGURE 8 | *Porphyromonas gingivalis* associated with peri-implantitis. **(A)** SEM images of titanium-modified surfaces after immersion in *P. gingivalis* culture (scale bar, 5 and 2 μm). After 24 h of incubation with *P. gingivalis*, the TNT/Ag, TNT/PDA/Ag, and TNT/PDA/Ag/bFGF were occupied by clusters of *P. gingivalis*, which formed a visible biofilm. **(B)** Quantitative analysis of antibacterial ability against *P. gingivalis* of Ti for 1 and 3 days. Data are presented as mean ± standard deviation; $^{**}p < 0.01$.

pre-release, TNT/Ag, TNT/PDP/Ag, and TNT/PDP/Ag/bFGF were still able to suppress the metabolic activity significantly as compared with TNT (**Figure 7C**). Silver ions (Ag^+) and their combination have been used in different dental applications such as cement dental resin composites, coatings surfaces, and bone cement (Ai et al., 2017). Ag^+ and silver nanoparticles are strong bactericidal at low concentrations, presenting an "oligodynamic" impact during the subsistence of toxic ions (Rai et al., 2012). In our work, we adopted silver for its antibacterial and anti-inflammatory features (Feng et al., 2019; Kumar et al., 2019).

Effect of Titanium Modification on *Porphyromonas gingivalis* Associated With Peri-Implantitis

Scanning electron microscopy images of different titanium modifications are shown in **Figure 8A**. After 24 h of incubation with *Porphyromonas gingivalis*, the TNT/Ag, TNT/PDA/Ag, and TNT/PDA/Ag/bFGF were occupied by clusters of *P. gingivalis*, which formed a visible biofilm. Ti samples were pre-released in PBS for 1, 3, and 7 days to mimic an application situation. These pre-released Ti samples were placed with *P. gingivalis* for 24 h. Then the inhibition ability of these pre-released Ti samples on *P. gingivalis* metabolic activity was evaluated by an MTT. We found that even after 7-day pre-release, TNT/Ag, TNT/PDP/Ag, and TNT/PDP/Ag/bFGF were still able to suppress the metabolic activity significantly as compared with TNT (**Figure 8B**). Failures of dental titanium implantation due to a different type of bacterial infection have been increasing (Pye et al., 2009). Furthermore, around 10% of premature failures of titanium have occurred from some bacterial infection a year after implantation, and particularly it has been observed that the main cause for those failures of the implant was bone resorption and site inflammation by different kinds of bacteria such as *P. gingivalis* (van der Reijden et al., 2002). The antimicrobial activities of silver nanoparticles are quite known and broadly documented (Rai et al., 2014). Thus, step-by-step cross-linked silver-coated TNT was applied to decrease *P. gingivalis* infections.

Anti-inflammatory Properties of Modified Ti Samples

Macrophage RAW 264.7 was used to assess the anti-inflammatory effect of Ti samples. LPS-supplemented

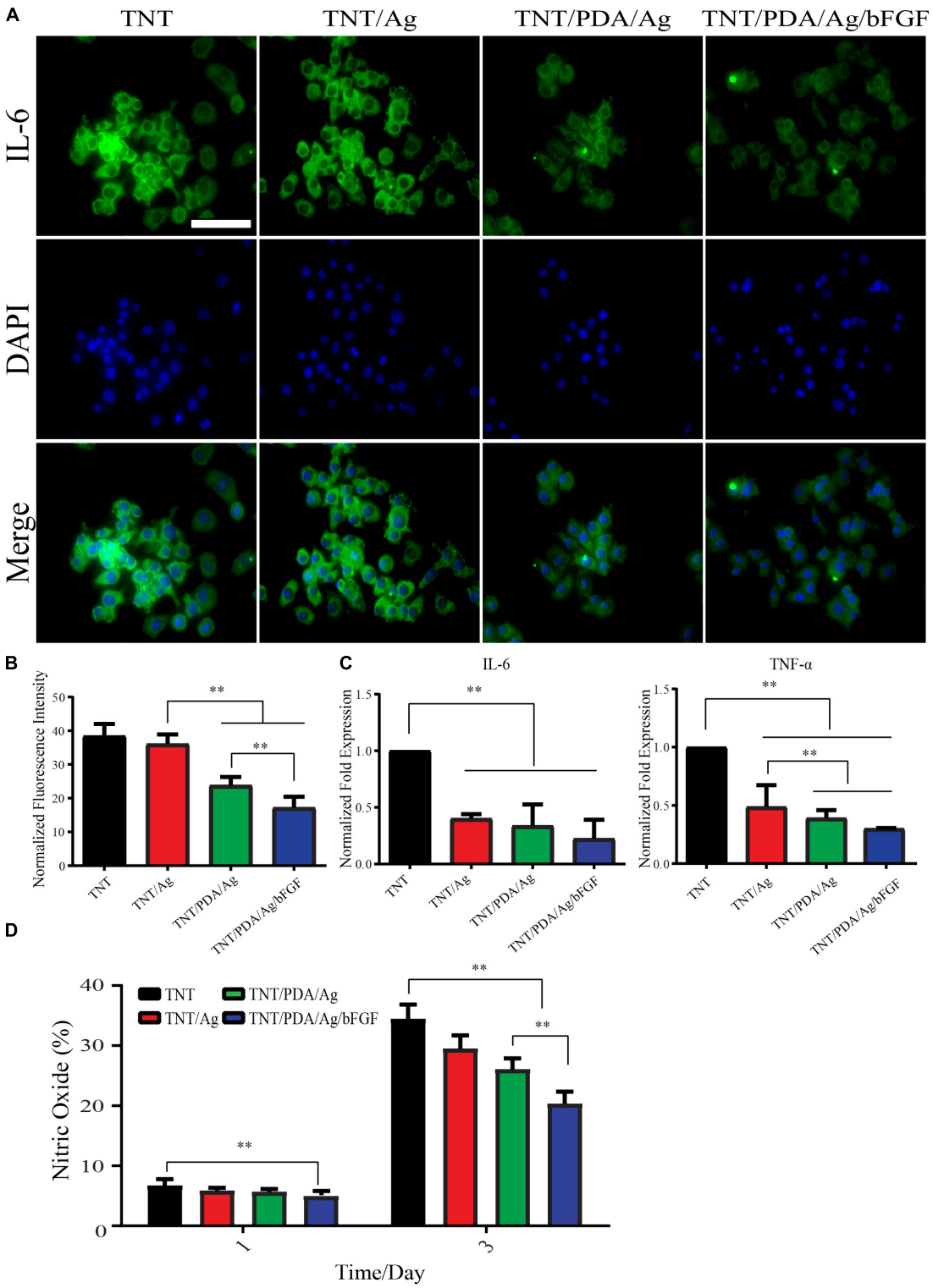

FIGURE 9 | Anti-inflammatory property of modified Ti samples on RAW 264.7 stimulated by lipopolysaccharide (LPS) (500 ng/ml). **(A,B)** LPS exposure of 12 h resulted in elevated expression of IL-6 in macrophages significantly. The expression of IL-6 decreased in the order of TNT, TNT/Ag, TNT/PDA/Ag, and TNT/PDA/Ag/bFGF. Scale bar represents 20 μm. **(C)** After 12 h LPS exposure of RAW 264.7, a significant reduction in gene expression of IL-6 and TNF-α was observed on TNT/Ag, TNT/PDA/Ag, and TNT/PDA/Ag/bFGF. **(D)** To quantify the level of nitric oxide, RAW 264.7 was seeded on sample surfaces with LPS for 1 and 3 days. It was found that TNT/PDA/Ag/bFGF had a good anti-inflammatory effect and decreased nitric oxide production on RAW 264.7. Data are presented as mean ± standard deviation; $^{**}p < 0.01$.

medium was applied to cell-adhered Ti surfaces for 12 h. Pro-inflammatory factor, IL-6, was visualized by fluorescence staining (**Figure 9A**). There was a decreasing trend of the expression of IL-6 in the order of TNT, TNT/Ag, TNT/PDA/Ag, and TNT/PDA/Ag/bFGF. Gene expression of IL-6 and TNF-α also confirmed a significant reduction on cells cultured on TNT/Ag, TNT/PDA/Ag, and TNT/PDA/Ag/bFGF. Both fluorescent and gene results pointed out that TNT/PDA/Ag/bFGF could effectively suppress the inflammatory reaction of macrophages upon an LPS challenge. Ti-modified samples evaluated NO accumulation inhibition in the LPS-activated RAW 264.7 cell. The nitrite production in the RAW 264.7 increased with the LPS at 1 and 3 days. Then NO production was read as nitrite concentration in the medium (50 μl). When compared with TNT/PDA/Ag/bFGF, LPS-induced RAW 264.7 cell released a lower production level of NO in the medium read. It is well-known that the secretion and expression of angiogenic factors such as bFGF are used to inhibit pro-inflammatory factor release. Also, bFGF has increased secretion at sites of acute and chronic inflammation (Shamloo et al., 2018; Albashari et al., 2020). Moreover, the level of bFGF is increasing in the serum and injury tissue of patients with diseases such as asthma, inflammatory bowel disease, and rheumatoid arthritis (Zittermann and Issekutz, 2006). In this article, the anti-inflammatory effects of samples are shown. From **Figure 9**, it was shown that the expression of pro-inflammatory protein IL-6 gradually increased. However, TNT/PDA/Ag/bFGF showed the opposite in the inflammation regulation (**Figures 6**, **9A**). Also, real-time PCR showed that TNT/Ag and TNT/PDA/Ag mainly decreased the TNF-α and IL-6 expression genes. It was found that TNT/PDA/Ag/bFGF had good anti-inflammatory activity and decreased nitric oxide production on RAW 264.7 (**Figures 9B,C**). bFGF can be a great positive regulator in acute and chronic inflammation. Furthermore, the IL-6 and TNF-α inhibition represent a positive part in the osteogenesis and without inducing prolonged inflammation (Bastidas-Coral et al., 2016). In *in vitro* works, it was found that Ag ions and nanoparticles decrease secretion of TNF-α from macrophage cells to suppress inflammation (Lappas, 2015). Another paper has shown that AgNPs on titanium surfaces mainly regulated the macrophage polarization (Pratsinis et al., 2013).

CONCLUSION

PDA/Ag/bFGF coating was successfully applied on the titanium surface. It was demonstrated that the surface modifications on Ti, including nanotube formation with coatings, could promote the slow release of bioactive bFGF. Our study also showed that cross-linking silver and bFGF on modified Ti surface at nanoscale had strong early anti-infiammatory and antibacterial properties. DPSCs cultured on this modified Ti (TNT/PDA/Ag/bFGF) could achieve an enhanced osteogenic differentiation. Together, our findings provide an alternative for the multifunctional titanium implants and expand the application of cross-linking of antibacterial with growth factor in bioengineering fields.

DATA AVAILABILITY STATEMENT

The original contributions presented in the study are included in the article/supplementary material, further inquiries can be directed to the corresponding author/s.

ETHICS STATEMENT

The studies involving human participants were reviewed and approved by the School and Hospital of Stomatology, Wenzhou Medical University (No. WYKQ2018008). The patients/participants provided their written informed consent to participate in this study.

AUTHOR CONTRIBUTIONS

QY and AA: design. AA, MA,YX, JA, and FH: methodology and validation. YZ, KZ, and LL: data curation and analysis. AA and YH: writing—original draft preparation. QY and JW: writing—review and editing. LL, YH, and QY: funding acquisition. All authors have read and agreed to the published version of the manuscript.

FUNDING

This research was supported by the National Natural Science Foundation of China under Grant Nos. 81701032 and 81871503, Wenzhou Science and Technology Association Project, Wenzhou Major Scientific and Technological Innovation Key Medical and Health Project under Grant No. ZY2019010, and Zhejiang Provincial Natural Science Foundation of China under Grant No. LGF21H140007.

ACKNOWLEDGMENTS

We thank the U-tooth Biotechnology Ltd., Co., for providing technical support in culturing DPSCs.

REFERENCES

Ai, M., Du, Z., Zhu, S., Geng, H., Zhang, X., Cai, Q., et al. (2017). Composite resin reinforced with silver nanoparticles–laden hydroxyapatite nanowires for dental application. *Dent. Mater.* 33, 12–22. doi: 10.1016/j.dental.2016.09.038

Albashari, A., He, Y., Zhang, Y., Ali, J., Lin, F., Zheng, Z., et al. (2020). Thermosensitive bFGF-Modified Hydrogel with dental pulp stem cells on neuroinflammation of spinal cord injury. *ACS Omega* 5, 16064–16075. doi: 10.1021/acsomega.0c01379

Bandyopadhyay, A., Mitra, I., Shivaram, A., Dasgupta, N., and Bose, S. (2019a). Direct comparison of additively manufactured porous titanium and tantalum

implants towards *in vivo* osseointegration. *Addit. Manuf.* 28, 259–266. doi: 10.1016/j.addma.2019.04.025

Bandyopadhyay, A., Shivaram, A., Mitra, I., and Bose, S. (2019b). Electrically polarized TiO2 nanotubes on Ti implants to enhance early-stage osseointegration. *Acta Biomater.* 96, 686–693. doi: 10.1016/j.actbio.2019.07.028

Bastidas-Coral, A. P., Bakker, A. D., Zandieh-Doulabi, B., Kleverlaan, C. J., Bravenboer, N., Forouzanfar, T., et al. (2016). Cytokines TNF-α, IL-6, IL-17F, and IL-4 differentially affect osteogenic differentiation of human adipose stem cells. *Stem Cells Int.* 2016:1318256.

Cai, N., Zeng, H., Fu, J., Chan, V., Chen, M., Li, H., et al. (2018). Synergistic effect of graphene oxide-silver nanofillers on engineering performances of polyelectrolyte complex nanofiber membranes. *J. Appl. Polym. Sci.* 135:46238. doi: 10.1002/app.46238

Choi, S. M., Lee, K.-M., Kim, H. J., Park, I. K., Kang, H. J., Shin, H.-C., et al. (2018). Effects of structurally stabilized EGF and bFGF on wound healing in type I and type II diabetic mice. *Acta Biomater.* 66, 325–334. doi: 10.1016/j.actbio.2017.11.045

Chouirfa, H., Bouloussa, H., Migonney, V., and Falentin-Daudré, C. (2019). Review of titanium surface modification techniques and coatings for antibacterial applications. *Acta Biomater.* 83, 37–54. doi: 10.1016/j.actbio.2018.10.036

Duyck, J., and Vandamme, K. (2017). "The effect of loading on peri-implant bone: a critical review of the literature," in *Bone Response to Dental Implant Materials*, ed. A. Piattelli (Amsterdam: Elsevier), 139–161. doi: 10.1016/b978-0-08-100287-2.00008-2

Feng, Y., Wang, G., Chang, Y., Cheng, Y., Sun, B., Wang, L., et al. (2019). Electron compensation effect suppressed silver ion release and contributed safety of Au@ Ag core–shell nanoparticles. *Nano Lett.* 19, 4478–4489. doi: 10.1021/acs.nanolett.9b01293

Grigoriou, V., Shapiro, I. M., Cavalcanti-Adam, E. A., Composto, R. J., Ducheyne, P., and Adams, C. S. (2005). Apoptosis and survival of osteoblast-like cells are regulated by surface attachment. *J. Biol. Chem.* 280, 1733–1739. doi: 10.1074/jbc.m402550200

Gronthos, S., Brahim, J., Li, W., Fisher, L., Cherman, N., Boyde, A., et al. (2002). Stem cell properties of human dental pulp stem cells. *J. Dent. Res.* 81, 531–535.

Guo, Y., Xu, B., Wang, Y., Li, Y., Si, H., Zheng, X., et al. (2019). Dramatic promotion of wound healing using a recombinant human-like collagen and bFGF cross-linked hydrogel by transglutaminase. *J. Biomater. Sci. Polym. Edition* 30, 1591–1603. doi: 10.1080/09205063.2019.1652416

Haimov, H., Yosupov, N., Pinchasov, G., and Juodzbalys, G. (2017). Bone morphogenetic protein coating on titanium implant surface: a systematic review. *J. Oral Maxillofac. Res.* 8:e1.

He, Y., Cao, Y., Xiang, Y., Hu, F., Tang, F., Zhang, Y., et al. (2020). An evaluation of norspermidine on anti-fungal effect on mature Candida albicans biofilms and angiogenesis potential of dental pulp stem cells. *Front. Bioeng. Biotechnol.* 8:948. doi: 10.3389/fbioe.2020.00948

He, Y., Peterson, B., Ren, Y., Van der Mei, H., and Busscher, H. (2014). Antimicrobial penetration in a dual-species oral biofilm after noncontact brushing: an in vitro study. *Clin. Oral Investig.* 18, 1103–1109.

He, Y., Peterson, B. W., Jongsma, M. A., Ren, Y., Sharma, P. K., Busscher, H. J., et al. (2013). Stress relaxation analysis facilitates a quantitative approach towards antimicrobial penetration into biofilms. *PLoS One* 8:e63750. doi: 10.1371/journal.pone.0063750

Kang, W., Liang, Q., Du, L., Shang, L., Wang, T., and Ge, S. (2019). Sequential application of bFGF and BMP-2 facilitates osteogenic differentiation of human periodontal ligament stem cells. *J. Periodontal Res.* 54, 424–434. doi: 10.1111/jre.12644

Kao, C.-T., Lin, C.-C., Chen, Y.-W., Yeh, C.-H., Fang, H.-Y., and Shie, M.-Y. (2015). Poly (dopamine) coating of 3D printed poly (lactic acid) scaffolds for bone tissue engineering. *Mater. Sci. Eng. C* 56, 165–173. doi: 10.1016/j.msec.2015.06.028

Kim, S. E., Song, S.-H., Yun, Y. P., Choi, B.-J., Kwon, I. K., Bae, M. S., et al. (2011). The effect of immobilization of heparin and bone morphogenic protein-2 (BMP-2) to titanium surfaces on inflammation and osteoblast function. *Biomaterials* 32, 366–373. doi: 10.1016/j.biomaterials.2010.09.008

Ko, E., Yang, K., Shin, J., and Cho, S.-W. (2013). Polydopamine-assisted osteoinductive peptide immobilization of polymer scaffolds for enhanced bone regeneration by human adipose-derived stem cells. *Biomacromolecules* 14, 3202–3213. doi: 10.1021/bm4008343

Krastl, G., and Amato, J. (2019). "Management of crown fractures and crown-root fractures," in *Management of Dental Emergencies in Children and Adolescents*, eds A. Lussi and K. W. Neuhaus (Hoboken, NJ: Wiley), 79–90. doi: 10.1002/9781119372684.ch2.2

Kumar, V., Singh, S., Srivastava, B., Bhadouria, R., and Singh, R. (2019). Green synthesis of silver nanoparticles using leaf extract of Holoptelea integrifolia and preliminary investigation of its antioxidant, anti-inflammatory, antidiabetic and antibacterial activities. *J. Environ. Chem. Eng.* 7:103094. doi: 10.1016/j.jece.2019.103094

Lappas, C. M. (2015). The immunomodulatory effects of titanium dioxide and silver nanoparticles. *Food Chem. Toxicol.* 85, 78–83. doi: 10.1016/j.fct.2015.05.015

Luo, L., Albashari, A. A., Wang, X., Jin, L., Zhang, Y., Zheng, L., et al. (2018). Effects of transplanted heparin-poloxamer hydrogel combining dental pulp stem cells and bFGF on spinal cord injury repair. *Stem Cells Int.* 2018:2398521.

Luo, L., Zhang, Y., Chen, H., Hu, F., Wang, X., Xing, Z., et al. (2020). Effects and mechanisms of basic fibroblast growth factor on the proliferation and regenerative profiles of cryopreserved dental pulp stem cells. *Cell Prolif.* 54:e12969.

Marenzi, G., Impero, F., Scherillo, F., Sammartino, J. C., Squillace, A., and Spagnuolo, G. (2019). Effect of different surface treatments on titanium dental implant micro-morphology. *Materials* 12:733. doi: 10.3390/ma12050733

Martin, J., Schwartz, Z., Hummert, T., Schraub, D., Simpson, J., Lankford, J. Jr., et al. (1995). Effect of titanium surface roughness on proliferation, differentiation, and protein synthesis of human osteoblast-like cells (MG63). *J. Biomed. Mater. Res.* 29, 389–401. doi: 10.1002/jbm.820290314

Mata, A., Su, X., Fleischman, A. J., Roy, S., Banks, B. A., Miller, S. K., et al. (2003). Osteoblast attachment to a textured surface in the absence of exogenous adhesion proteins. *IEEE Trans. Nanobiosci.* 2, 287–294. doi: 10.1109/tnb.2003.820268

Meyers, S. R., and Grinstaff, M. W. (2012). Biocompatible and bioactive surface modifications for prolonged *in vivo* efficacy. *Chem. Rev.* 112, 1615–1632. doi: 10.1021/cr2000916

Mokhtari, H., Ghasemi, Z., Kharaziha, M., Karimzadeh, F., and Alihosseini, F. (2018). Chitosan-58S bioactive glass nanocomposite coatings on TiO2 nanotube: structural and biological properties. *Appl. Surf. Sci.* 441, 138–149. doi: 10.1016/j.apsusc.2018.01.314

Neoh, K. G., Hu, X., Zheng, D., and Kang, E. T. (2012). Balancing osteoblast functions and bacterial adhesion on functionalized titanium surfaces. *Biomaterials* 33, 2813–2822. doi: 10.1016/j.biomaterials.2012.01.018

Orapiriyakul, W., Young, P. S., Damiati, L., and Tsimbouri, P. M. (2018). Antibacterial surface modification of titanium implants in orthopaedics. *J. Tissue Eng.* 9:2041731418789838.

Palmieri, E. M., Gonzalez-Cotto, M., Baseler, W. A., Davies, L. C., Ghesquière, B., Maio, N., et al. (2020). Nitric oxide orchestrates metabolic rewiring in M1 macrophages by targeting aconitase 2 and pyruvate dehydrogenase. *Nat. Commun.* 11:698.

Peterson, B. W., He, Y., Ren, Y., Zerdoum, A., Libera, M. R., Sharma, P. K., et al. (2015). Viscoelasticity of biofilms and their recalcitrance to mechanical and chemical challenges. *FEMS Microbiol. Rev.* 39, 234–245. doi: 10.1093/femsre/fuu008

Pratsinis, A., Hervella, P., Leroux, J. C., Pratsinis, S. E., and Sotiriou, G. A. (2013). Toxicity of silver nanoparticles in macrophages. *Small* 9, 2576–2584.

Pye, A., Lockhart, D., Dawson, M., Murray, C., and Smith, A. (2009). A review of dental implants and infection. *J. Hosp. Infect.* 72, 104–110. doi: 10.1016/j.jhin.2009.02.010

Rai, M., Kon, K., Ingle, A., Duran, N., Galdiero, S., and Galdiero, M. (2014). Broad-spectrum bioactivities of silver nanoparticles: the emerging trends and future prospects. *Appl. Microbiol. Biotechnol.* 98, 1951–1961. doi: 10.1007/s00253-013-5473-x

Rai, M. K., Deshmukh, S., Ingle, A., and Gade, A. (2012). Silver nanoparticles: the powerful nanoweapon against multidrug-resistant bacteria. *J. Appl. Microbiol.* 112, 841–852. doi: 10.1111/j.1365-2672.2012.05253.x

Rivera-Chacon, D., Alvarado-Velez, M., Acevedo-Morantes, C., Singh, S., Gultepe, E., Nagesha, D., et al. (2013). Fibronectin and vitronectin promote human fetal osteoblast cell attachment and proliferation on nanoporous titanium surfaces. *J. Biomed. Nanotechnol.* 9, 1092–1097. doi: 10.1166/jbn.2013.1601

Ruppert, R., Hoffmann, E., and Sebald, W. (1996). Human bone morphogenetic protein 2 contains a heparin-binding site which modifies its biological activity. *Eur. J. Biochem.* 237, 295–302. doi: 10.1111/j.1432-1033.1996.0295n.x

Shamloo, A., Sarmadi, M., Aghababaie, Z., and Vossoughi, M. (2018). Accelerated full-thickness wound healing via sustained bFGF delivery based on a PVA/chitosan/gelatin hydrogel incorporating PCL microspheres. *Int. J. Pharm.* 537, 278–289. doi: 10.1016/j.ijpharm.2017.12.045

Shen, X., Al-Baadani, M. A., He, H., Cai, L., Wu, Z., Yao, L., et al. (2019). Antibacterial and osteogenesis performances of LL37-loaded titania nanopores *in vitro* and *in vivo*. *Int. J. Nanomed.* 14:3043. doi: 10.2147/ijn.s198583

Siddiqui, D. A., Guida, L., Sridhar, S., Valderrama, P., Wilson, T. G. Jr., and Rodrigues, D. C. (2019). Evaluation of oral microbial corrosion on the surface degradation of dental implant materials. *J. Periodontol.* 90, 72–81. doi: 10.1002/jper.18-0110

Subbiah, R., and Guldberg, R. E. (2019). Materials science and design principles of growth factor delivery systems in tissue engineering and regenerative medicine. *Adv. Healthcare Mater.* 8:1801000. doi: 10.1002/adhm.201801000

van der Reijden, W., Vissink, A., Raghoebar, G., and Stegenga, B. (2002). Microbiota around root-formed endosseous implants. A review of the literature. *Int. J. Oral Maxillofac. Implants* 17, 829–838.

Yan, T., Sun, R., Li, C., Tan, B., Mao, X., and Ao, N. (2010). Immobilization of type-I collagen and basic fibroblast growth factor (bFGF) onto poly (HEMA-co-MMA) hydrogel surface and its cytotoxicity study. *J. Mater. Sci. Mater. Med.* 21, 2425–2433. doi: 10.1007/s10856-010-4094-5

Yang, D. H., Lee, D. W., Kwon, Y. D., Kim, H. J., Chun, H. J., Jang, J. W., et al. (2015). Surface modification of titanium with hydroxyapatite–heparin–BMP-2 enhances the efficacy of bone formation and osseointegration *in vitro* and *in vivo*. *J. Tissue Eng. Regen. Med.* 9, 1067–1077. doi: 10.1002/term.1973

Yuan, L., Ding, S., and Wen, C. (2019). Additive manufacturing technology for porous metal implant applications and triple minimal surface structures: a review. *Bioactive Mater.* 4, 56–70. doi: 10.1016/j.bioactmat.2018.12.003

Zhao, B., Katagiri, T., Toyoda, H., Takada, T., Yanai, T., Fukuda, T., et al. (2006). Heparin potentiates the *in vivo* ectopic bone formation induced by bone morphogenetic protein-2. *J. Biol. Chem.* 281, 23246–23253. doi: 10.1074/jbc.m511039200

Zittermann, S. I., and Issekutz, A. C. (2006). Basic fibroblast growth factor (bFGF, FGF-2) potentiates leukocyte recruitment to inflammation by enhancing endothelial adhesion molecule expression. *Am. J. Pathol.* 168, 835–846. doi: 10.2353/ajpath.2006.050479

Conflict of Interest: The authors declare that the research was conducted in the absence of any commercial or financial relationships that could be construed as a potential conflict of interest.

frontiers in Pharmacology

ORIGINAL RESEARCH
published: 23 April 2021
doi: 10.3389/fphar.2021.678322

Transforming Growth Factor-β3/ Recombinant Human-like Collagen/ Chitosan Freeze-Dried Sponge Primed With Human Periodontal Ligament Stem Cells Promotes Bone Regeneration in Calvarial Defect Rats

*Shiyi Huang[1†], Fenglin Yu[1†], Yating Cheng[1], Yangfan Li[1], Yini Chen[1], Jianzhong Tang[2], Yu Bei[2], Qingxia Tang[3], Yueping Zhao[3], Yadong Huang[1,2] and Qi Xiang[1,2]**

[1]Institute of Biomedicine and Guangdong Provincial Key Laboratory of Bioengineering Medicine, Jinan University, Guangzhou, China, [2]Biopharmaceutical R and D Center of Jinan University, Guangzhou, China, [3]Department of Stomatology, Jinan University Medical College, Guangzhou, China

OPEN ACCESS

Edited by:
Zhouguang Wang, Albert Einstein College of Medicine, United States

Reviewed by:
Wei Wang, Tianjin University, China
Yan Wang, Sun Yat-sen University, China

***Correspondence:**
Qi Xiang
txiangqi@jnu.edu.cn

†These authors have contributed equally to this work

Specialty section:
This article was submitted to Integrative and Regenerative Pharmacology, a section of the journal Frontiers in Pharmacology

Received: *09 March 2021*
Accepted: *06 April 2021*
Published: *23 April 2021*

Citation:
Huang S, Yu F, Cheng Y, Li Y, Chen Y, Tang J, Bei Y, Tang Q, Zhao Y, Huang Y and Xiang Q (2021) Transforming Growth Factor-β3/ Recombinant Human-like Collagen/ Chitosan Freeze-Dried Sponge Primed With Human Periodontal Ligament Stem Cells Promotes Bone Regeneration in Calvarial Defect Rats. Front. Pharmacol. 12:678322. doi: 10.3389/fphar.2021.678322

Patients with a skull defect are at risk of developing cerebrospinal fluid leakage and ascending bacterial meningitis at >10% per year. However, treatment with stem cells has brought great hope to large-area cranial defects. Having found that transforming growth factor (TGF)-β3 can promote the osteogenic differentiation of human periodontal ligament stem cells (hPDLSCs), we designed a hybrid TGF-β3/recombinant human-like collagen recombinant human collagen/chitosan (CS) freeze-dried sponge (TRFS) loading hPDLSCs (TRFS-h) to repair skull defects in rats. CFS with 2% CS was selected based on the swelling degree, water absorption, and moisture retention. The CS freeze-dried sponge (CFS) formed a porous three-dimensional structure, as observed by scanning electron microscopy. In addition, cytotoxicity experiments and calcein-AM/PI staining showed that TRFS had a good cellular compatibility and could be degraded completely at 90 days in the implantation site. Furthermore, bone healing was evaluated using micro-computed tomography in rat skull defect models. The bone volume and bone volume fraction were higher in TRFS loaded with hPDLSCs (TRFS-h) group than in the controls ($p < 0.01$, *vs.* CFS or TRFS alone). The immunohistochemical results indicated that the expression of Runx2, BMP-2, and collagen-1 (COL I) in cells surrounding bone defects in the experimental group was higher than those in the other groups ($p < 0.01$, *vs.* CFS or TRFS alone). Taken together, hPDLSCs could proliferate and undergo osteogenic differentiation in TRFS ($p < 0.05$), and TRFS-h accelerated bone repair in calvarial defect rats. Our research revealed that hPDLSCs could function as seeded cells for skull injury, and their osteogenic differentiation could be accelerated by TGF-β3. This represents an effective therapeutic strategy for restoring traumatic defects of the skull.

Abbreviations: CS, chitosan; CT, computed tomography; hPDLSCs, human periodontal ligament stem cells; MSC, mesenchymal stem cells; RHC, recombinant human-like collagen; SEM, scanning electron microscopy; TGF, transforming growth factor; TRFS, TGF-β3/RHC/CS freeze-dried sponge; TRFS-h, TRFS loading hPDLSCs.

Keywords: periodontal ligament stem cells, transforming growth factor 3, stem cell therapy, skull bone defect repair, freeze-dried sponge

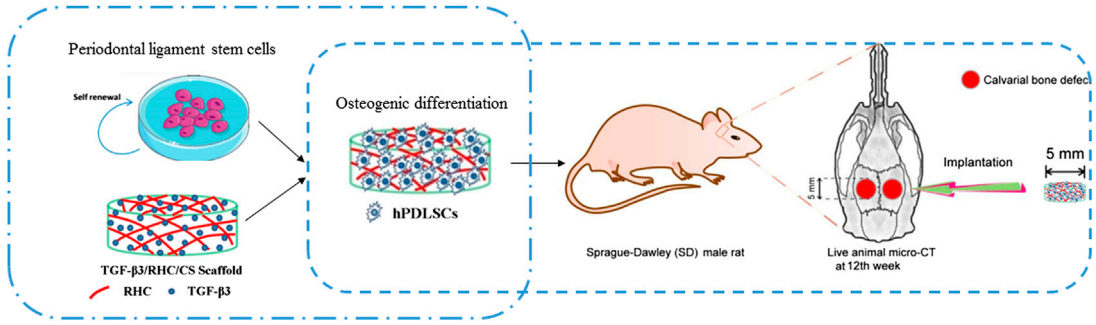

GRAPHICAL ABSTRACT |

INTRODUCTION

Craniocerebral injury is a global public health concern. In Australia, there are approximately 338,700 people with disabilities related to craniocerebral injuries (1.9% of the population). Large-scale skull defects are very difficult to repair and are associated with the risk of cerebrospinal fluid leakage and ascending bacterial meningitis, causing approximately 30% of deaths each year in the United States (Gardner and Zafonte, 2016). Survivors can have a variety of residual symptoms that affect their cognition, movement, and sensation (Xu et al., 2015). Autologous bone transplantation is a widely recognized clinical treatment method. However, sources of autologous bone are limited, and the required bone needs to be removed from other parts of the patient's body, increasing the risk of infection during surgery. In recent years, stem cell therapy has rapidly developed in bone defect repair. Bioactive materials loaded with mesenchymal stem cells (MSCs) are the most promising materials for the treatment of bone injuries.

Stem cells have ability to induce tissue regeneration and repair areas of injury (Zhang et al., 2015a). Among them, MSCs have strong application prospects in bone repair therapy because of their ability to self-replicate and to undergo multi-directional differentiation. Bone marrow mesenchymal stem cells (BMSCs), adipose mesenchymal stem cells, and umbilical cord mesenchymal stem cells (UC-MSCs) are examples of MSCs that are commonly used in bone repair therapy (Zhang et al., 2018). Human periodontal ligament stem cells (hPDLSCs), a type of MSC from the periodontal tissue of adult third molars, are considered to be relatively suitable MSC sources for bone tissue regeneration (Chalisserry et al., 2017). More interestingly, the acquisition of hPDLSCs is relatively simple, convenient, and less invasive, and some discarded teeth in clinical surgery can be used as a reliable source of stem cell banks (Luo et al., 2021). Zhang et al. (2018) reported that hPDLSCs and BMSCs exerted similar cell behaviors, both having the ability to induce colony formation and multi-directional differentiation. Thus, these stem cells could be promising potential seed cell population types for use in cell-based therapy and tissue regeneration (Luo et al., 2018). Recently, Professor Yan Wang and her laboratory fabricated zein/gelatin/nano-hydroxyapatite nanofiber membranes to load hPDLSCs, which is an effective strategy for the treatment of periodontitis in the future, as part of their research on odontogenic cells (Yang et al., 2017). Diomede et al. found that the combination of hPDLSCs and collagen membranes can effectively promote the repair of rat skull defects (Trubiani et al., 2019). Our group explored the osteogenic differentiation of hPDLSCs *in vitro* for applications in bone repair (Li et al., 2019; Li et al., 2020). Many studies have shown that hPDLSCs can maintain multi-differentiation performance in long-term culture, and are potentially ideal tissue-engineering seed cells (Ou et al., 2018). In summary, hPDLSCs can transfer generations many times *in vitro* while maintaining stemness, making them suitable for broad applications in bone injury repair.

Over the last decade, an increasing number of studies have focused on the development of natural, biodegradable, and biocompatible nanocomposites for bone replacement stem cell therapy. An ideal bio-nanocomposite should possess not only good mechanical properties but also an architecture that mimics the *in vitro* extracellular matrix (ECM) (Cheng et al., 2020). It provides a suitable habitat for stem cells and promotes the differentiation of stem cells to achieve tissue regeneration (Ma et al., 2020). Chitosan and collagen are the most widely used biological matrices owing to their biocompatibility and biodegradability. In particular, collagen is the most abundant matrix in the ECM and plays a decisive role in cell adhesion, migration, and differentiation, as well as promotes the growth of new tissues. However, the biodegradation rate and low mechanical strength of a single collagen-based or CS-based scaffold are crucial problems that limit their applications. The main obstacle in the wide use of collagen or CS alone is their almost complete lack of solubility in water and alkaline solutions. To overcome this obstacle, we united modified collagen and CS to achieve a relatively ideal scaffold material for bone repair and bone tissue engineering. Ramkumar et al. combined MSCs with a CS-collagen matrix to form a modular microstructure and repair

critical skull defects in rats (Annamalai et al., 2019). Natural collagen is difficult to prepare and the degradation rate cannot be controlled, while recombinant human-like collagen (RHC) redesigns and optimizes the main functional sequence of natural collagen, and the optimized gene sequence is reconstructed and expressed to obtain a new protein with collagen properties (Zhang et al., 2015b). In the last three decades, pioneering experiments have led to the expression of recombinant human or human-like collagens, providing a foundation for studies on the potential use of these proteins as substitutes for animal-derived collagens (Sionkowska et al., 2020). At present, RHC scaffold materials have been used in regenerative medicine, for example, as blood vessel scaffolds and artificial bones and skin tissues. Our group successfully constructed one type of RHC, derived from the cell adhesion domain of type I collagen, and achieved large-scale production in an *E. coli* expression system. Preliminary tests verified its safety and reliability, showing good water solubility, which is beneficial for the post-processing of preparation techniques for multiform scaffolds.

Stem cell therapy not only requires the growth and proliferation of stem cells on scaffolds but also the promotion of stem cell differentiation in repairing bone defects. In fact, understanding how the directional differentiation of stem cells is achieved remains elusive to researchers (Xiao et al., 2019; Liu et al., 2020; Shang et al., 2020). During the course of hPDLSC differentiation into osteogenic cells and endochondral ossification, specific growth and differentiation factors are needed to induce bone formation. Bone morphogenetic proteins (BMPs) are widely used in bone tissue engineering, including BMP-2 and transforming growth factor-β3 (TGF-β3) (Park et al., 2015). TGF-β3 has been used for cartilage repair, tissue regeneration, and wound healing *in vivo* (Liu et al., 2015). UgoRipamonti et al. confirmed that TGF-β3 significantly induced bone formation in primate baboon skull defect models and patients with segmental mandibular defects (Ripamonti et al., 2016a; Ripamonti et al., 2016b; Ripamonti et al., 2017). Our laboratory previously found that TGF-β3 facilitates the osteogenic differentiation of hPDLSCs *in vitro*. Based on the concept of bionic repair, we designed a hybrid TGF-β3/RHC/CS freeze-dried sponge (TRFS) for the loading of hPDLSCs (TRFS-h) to repair skull defects.

Although stem cell therapy has made considerable advances in animal experiments, it has a long way to go before its widespread use in clinical applications. For this reason, stem cell therapy is likely to remain a topic of interest in future studies. In the present study, the effects of RHC/CS scaffolds with hPDLSCs on the repair of critical-size skull injury in rats were studied with the aim of gaining insights into stem cell therapy for the development of novel therapeutic strategies in future studies.

MATERIALS AND METHODS

Materials

CS was supplied by Zhengzhou Corey Fine Chemical (MW 30–36 kDa) (with 55% deacetylation), TGF-β3 and RHC were provided by Jinan University Biopharmaceutical R and D Center (Guangzhou, China), and α-modified minimum essential medium (α-MEM), fetal bovine serum (FBS), and trypsin-EDTA were purchased from Gibco BRL. Penicillin and streptomycin (P/S) were purchased from MD Bio, China. MTT was purchased from MP Biomedicals (United States). Antibodies against collagen-1 (COL Ⅰ) were purchased from Affinity Biosciences (Cincinnati, OH, United States), BMP-2 and RUNX2 were purchased from Bioss (Boston, MA, United States), and GAPDH and an horseradish peroxidase-conjugated secondary antibody were purchased from Cell Signaling Technology (Boston, MA, United States).

Preparation and Characterization of TRFS

CS freeze-dried sponges were prepared as previously reported (Zang et al., 2014). Briefly, CS was dissolved in 1% (v/v) glacial acetic acid and lyophilized. It was placed in a 95% ethanol solution for 2 h, after which the ethanol was discarded. Next, the CS was immersed in a 10% sodium hydroxide solution for 2 h and repeatedly cleaned with deionized water until the pH was approximately 7. CFS was sterilized and stored for later use.

To obtain a suitable carrier, 1, 2, and 3% CFS were selected for optimization. The characteristics involved the water absorption rate, expansion rate, water vapor transmission rate, moisture retention, and porosity structure, which were calculated as reported previously (He et al., 2020). The surfaces of the freeze-dried sponges were coated with a thin layer of gold and observed using scanning electron microscopy (SEM) (XL30; Philips, Amsterdam, Netherlands).

The TGF-β3 freeze-dried sponges (TFS), RHC freeze-dried sponges (RFS), TGFβ3/RHC/CS freeze-dried sponges (TRFS) were prepared as follows: sterile CFS was immersed in sterile TGF-β3 (20 nmol/L) and RHC (1,000 nmol/L) with shaking overnight at 4°C; the freeze-dried sponges were fabricated by vacuum lyophilization.

Degradation of TRFS *in vitro* and Profile of TGF-β3 Release From TRFS

Next, the degradation rate of CFS was determined. Briefly, dried CFS of weight ^{0}W was added to a 50 ml centrifuge tube. Then, 50 ml of phosphate-buffered saline containing 20 μg/ml lysozyme was added and incubated at 37°C. Samples of each group were collected at 1, 2, 3, 4, 5, 6, 7, and 8 weeks and freeze-dried for weighing (Wt). The degradation rate was determined using the following formula:

$$D\% = (W0 - Wt)/W0 \times 100\%.$$

The release of TGF-β3 from TFS was measured using an ELISA kit (Cusabio, Wuhan, China). Briefly, the scaffold (three replicates/group) was placed in a 1.5 ml Eppendorf tube, and then 1 ml of minimum essential medium (MEM) was added, followed by incubation at 37°C for 360 h. Then, 1 ml of MEM was collected and 1 ml of fresh MEM was added at 1, 12, 48, 72, 168, and 360 h. The samples were stored at −80°C until measurement. ELISA was

performed according to the manufacturer's instructions. Light absorbance was read using a microplate reader (Thermo Lab Systems, Waltham, MA, United States) at a wavelength of 450 nm.

hPDLSC Growth and Osteogenic Differentiation in TRFS

hPDLSC Growth in TRFS

The cytotoxicity of TRFS was evaluated using an extraction test (Li et al., 2019). Briefly, hPDLSCs were cultured in a 96-well plate at a density of 1×10^4 cells/well in MEM and 10% FBS for 24 h. The cells were treated with 25, 50, 75, or 100% TRFS extract. The positive and negative groups were treated with 5% dimethyl sulfoxide and normal medium, respectively. After 24 and 48 h of culture, the MTT assay was used to evaluate the results.

The growth of hPDLSCs in TRFS was observed using SEM. The prepared cell suspension was added to the front and back sides of the freeze-dried sponges. Before observation, the sample was subjected to gold sputtering using a gold spray carbonator and observed using SEM (XL30; Philips).

To further study cell growth in TRFS, hPDLSCs (2.0×10^5 cells/mL) were cultured in TRFS for 3 days and then stained with calcein AM/PI (Calcein-AM/PI Double Stain Kit; Shanghai, China), followed by fluorescence microscopy (LSM700; Zeiss, Jena, Germany) to observe the staining by detecting red (535 nm, AM) and green (490 nm, PI) fluorescence.

hPDLSC Osteogenic Differentiation in TRFS

hPDLSCs were seeded in 24-well plates containing CFS, RFS, TFS, and TRFS at a density of 5×10^4 cells/well. Then, hPDLSCs were cultured in osteogenic differentiation medium consisting of α-MEM containing 10^{-8} M dexamethasone (Sigma-Aldrich, St. Louis, MO, United States), 10 mM ß-glycerophosphate (Sigma-Aldrich), 50 ng/ml ascorbic acid (Sigma-Aldrich), 10% FBS, and 1% penicillin-streptomycin. The osteogenic medium was changed every 2 days. After cultivation for 3, 7, and 14 days, the freeze-dried sponge was stained with an alkaline phosphatase (ALP) staining kit (Beyotime Institute of Biotechnology, Shanghai, China) to evaluate their osteogenic differentiation capacity.

In vivo Studies of Skull Defect SD Rat Model

All SD rats (male, 8 weeks old, 220 ± 20 g) used in this study were purchased from the animal center of Guangdong province (no. 44007200069979). Animals were caged under controlled room temperature, humidity, and light (12/12-h light-dark cycle) with access to water and food ad libitum. The experimental protocols used in this study were approved by the Institutional Animal Care and Use Committee of Jinan University (approval no. 2019228). Experiments were conducted according to the guidelines for animal care and use of China and were approved by the Animal Ethics Committee of the Chinese Academy of Medical Science.

An extreme skull defect model of SD rats was established to evaluate the repair properties of TRFS. SD rats (n = 6 per group) were randomly assigned to three groups (A) CFS group (B) TRFS group, and (C) TRFS loaded with hPDLSCs group (TRFS-h). TRFS-h was prepared as follows: hPDLSCs were seeded in TRFS at a density of 5×10^4 cells/well and cultured in osteogenic differentiation medium for 14 days. Then, the rats were anesthetized with an intraperitoneal injection of 2% sodium thiopental (40 mg/kg), and the hair in the skull region was shaved. Skull defects were generated on both sides of the rat skull (5 mm in diameter) using a medical dental drill. Subsequently, the implants of freeze-dried sponges were placed onto the defect on the right side as the experimental group, whereas the defect on the left side was considered as a model group without any implants. The animal skin was sutured, and the edge of the wound was sterilized. Penicillin (40,000 units/day) was administered for 3 days after the operation to prevent infection. The feeding, activity, and wound infection of the rats were monitored daily. At 12 weeks post-surgery, six mice were randomly selected from each group for micro-computed tomography (CT) examination. After observation, the animals were anesthetized and sacrificed by cervical dislocation to obtain excisional biopsies of the implant area, including sufficient normal surrounding area for paraffin section treatment, hematoxylin-eosin (HE) and Masson staining, and immunohistochemical analysis.

Micro-CT Examination

Animals selected at 12 weeks were evaluated with a micro-CT 80 scanner (Scanco Medical, Bassersdorf, Switzerland) for the analysis of new bone formation within defects. Three-dimensional (3D) reconstruction was then performed using micro-CT scanning to evaluate the reconstruction of skull defects. Bone volume (BV) and bone volume to total volume ratio (BV/TV) were analyzed using Mimics 17 software. BV/TV, indicating the proportion of mineralized tissue, was calculated for comparison.

Histochemical Staining

Briefly, the calvaria tissue was fixed with 4% paraformaldehyde and embedded in paraffin for histological sectioning. After dewaxing and hydration, the sections were examined with HE staining to analyze the formation of new bone. Masson's trichrome staining was performed to further analyze the formation of collagen. The sections were analyzed, and images were captured using a microscope (Olympus IX71; Tokyo, Japan).

In addition, the sections were used for immunohistochemical analysis to evaluate the expression of Runx2, BMP-2, and COL I. Lastly, the sections were dehydrated and sealed for microscopic observation (Olympus IX71).

Subcutaneous Implant Surgical Procedure

Kunming (KM) mice (male, 5 weeks old, 22 ± 2 g) used in this study were purchased from the animal center of Guangdong province (no. 44007200070156). The feeding conditions were the same as described above. Animals were anesthetized by intraperitoneal injection of 2% sodium pentobarbital (40 mg/ml). The dorsal area of the KM mice was shaved, and

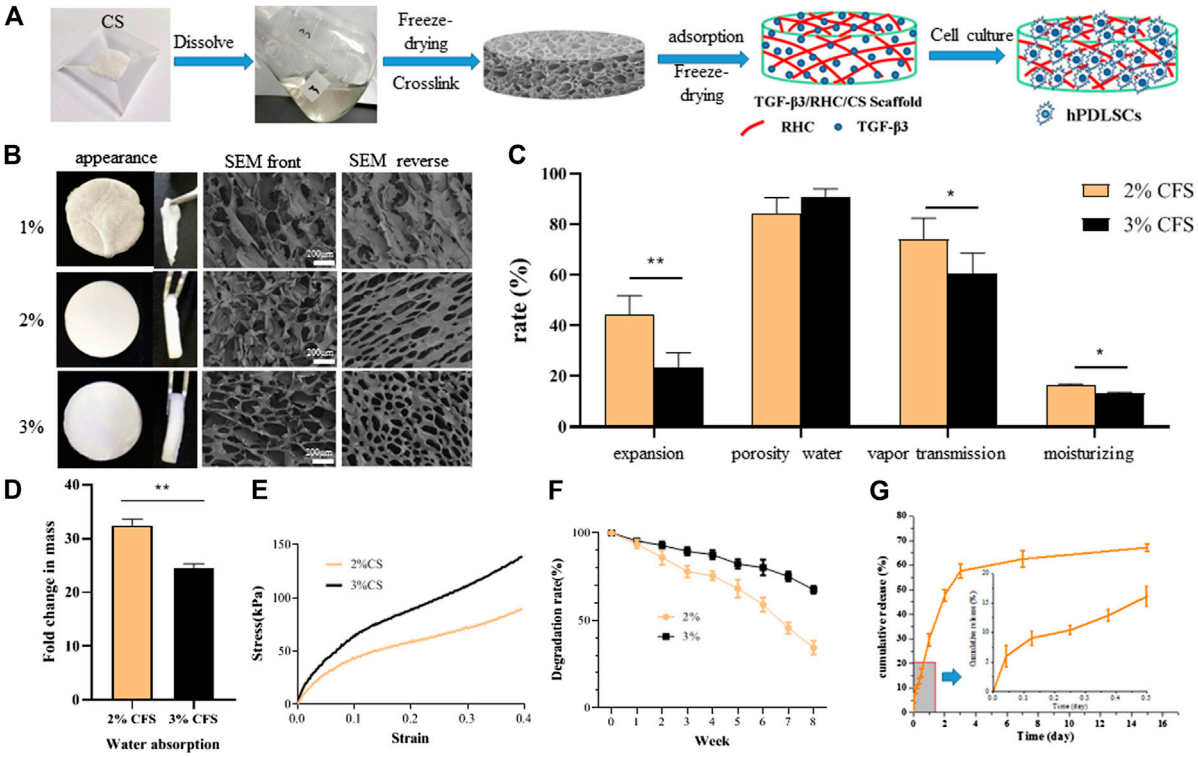

FIGURE 1 | Preparation and physicochemical properties of CFS **(A)** CFS preparation process **(B)**. SEM observation of freeze-dried sponge morphology **(C)** Expansion rate test; Porosity of freeze-dried sponge, Water vapor transmittance test and Moisture retention test **(D)** Water absorption capacity test ($n = 5$, $^{*}p < 0.05$, $^{**}p < 0.01$ *vs* 2% CS) **(E)** Mechanical properties **(F)** Degradation experiment **(G)** release curve of TGF-β3 from 2% freeze-dried sponge.

the animals were placed in the prone position on an aseptic operating platform. Longitudinal skin incisions with a maximum length of 1 cm were created along the dorsum of the mice. Within each incision, the subcutaneous space was dissected and irrigated with 0.9% sterile saline to expose each pocket. The materials were prepared in advance and implanted into the skin pocket, and the incisions were sutured. Animals were housed with free access to food and water and were administered 40,000 units of penicillin per day for 3 days post-surgery. At 4, 8, and 12 weeks post-surgery, the animals were sacrificed by cervical dislocation. The implanted materials were removed and evaluated for material degradation. The heart, liver, spleen, lung, and kidney of the rats were dissected 4, 8, and 12 weeks after subcutaneous implantation and examined with HE staining.

Statistical Analysis

All data are expressed as the mean ± standard deviation (SD) of at least three independent experiments. Statistical analyses were performed using GraphPad Prism 6 software (GraphPad Software Inc, La Jolla, CA, United States). Differences between more than two groups were analyzed using one-way ANOVA followed by Tukey's HSD comparison test. Statistical significance was set at $p < 0.05$.

RESULTS

Optimization of Chitosan Concentration in Freeze-Dried Sponges

The freeze-dried sponge preparation process is shown in **Figure 1A**. The CFS was characterized by the following indices: porosity, mechanical properties, water absorption, swelling degree, water vapor transmission, and moisture retention. **Figure 1B** shows that the 1% CFS structure collapsed without obvious pore formation. Therefore, subsequent studies on 1% CFS were not conducted. The 2 and 3% CFS had a porous three-dimensional structure and formed a staggered interconnected honeycomb structure on the front and a staggered network pore structure on the back. The surface of 2% CFS had ovoid pores with a pore size of 143 ± 33.1 μm, which is significantly higher than that of 3% CFS (87.6 ± 39.4 μm, $p < 0.01$). In **Figure 1C**, the expansion rate of 2% CFS was greater than 40% which was significantly different from that of 3% CFS ($p < 0.01$). Moreover, 2% CFS had better water vapor permeability ($p < 0.05$) than 3% CFS and better moisture retention rate (16.25 ± 1.37%) than 3% CFS (13.18 ± 0.97%) ($p < 0.01$). The porosity of 2% CFS was 84.9 ± 5.9% and that of 3% CFS was 90.2 ± 3.7%, which were not significantly different ($p > 0.05$). It

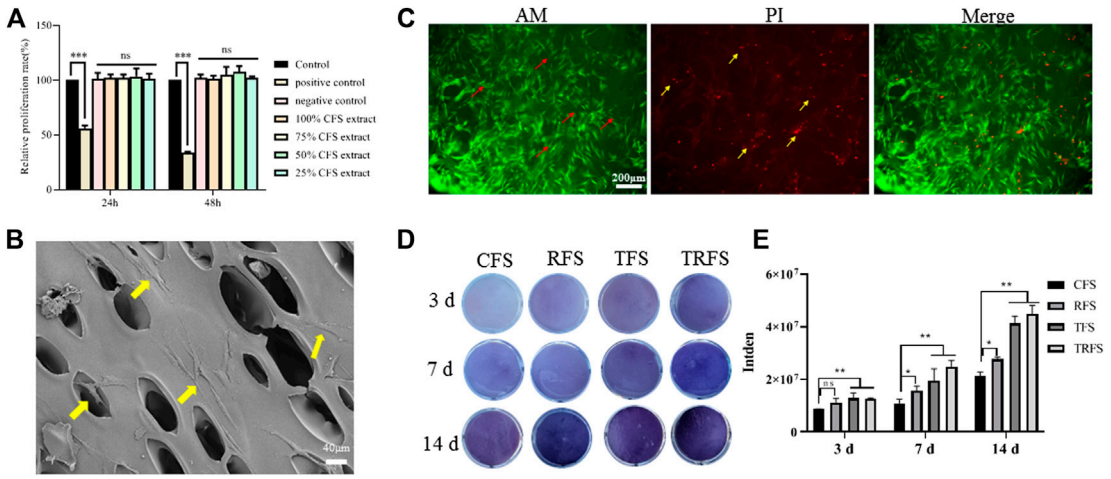

FIGURE 2 | Cell growth and osteogenic differentiation on TRFS **(A)** Detection of TRFS extract effect on the growth of hPDLSCs using MTT assay ($n = 6$, $^{*}p < 0.05$, $^{**}p < 0.01$, $^{***}p < 0.001$, ns means no significant difference *vs* control) **(B)** The growth of hPDLSCs on TRFS was observed using SEM **(C)** Calcein-AM/PI double staining was used to observe the survival of hPDLSCs cultured on TRFS for 7 days. Red arrows indicate living cells, and yellow arrows indicate dead cells **(D)** ALP staining (purple) was used to detect the ALP activity of hPDLSCs in CFS, RFS, TFS, and TRFS after 3, 7, and 14 days of osteogenic induction **(E)** Quantitative analysis of color depth ($n = 3$, $^{*}p < 0.05$, $^{**}p < 0.01$, ns means no significant difference *vs* CFS).

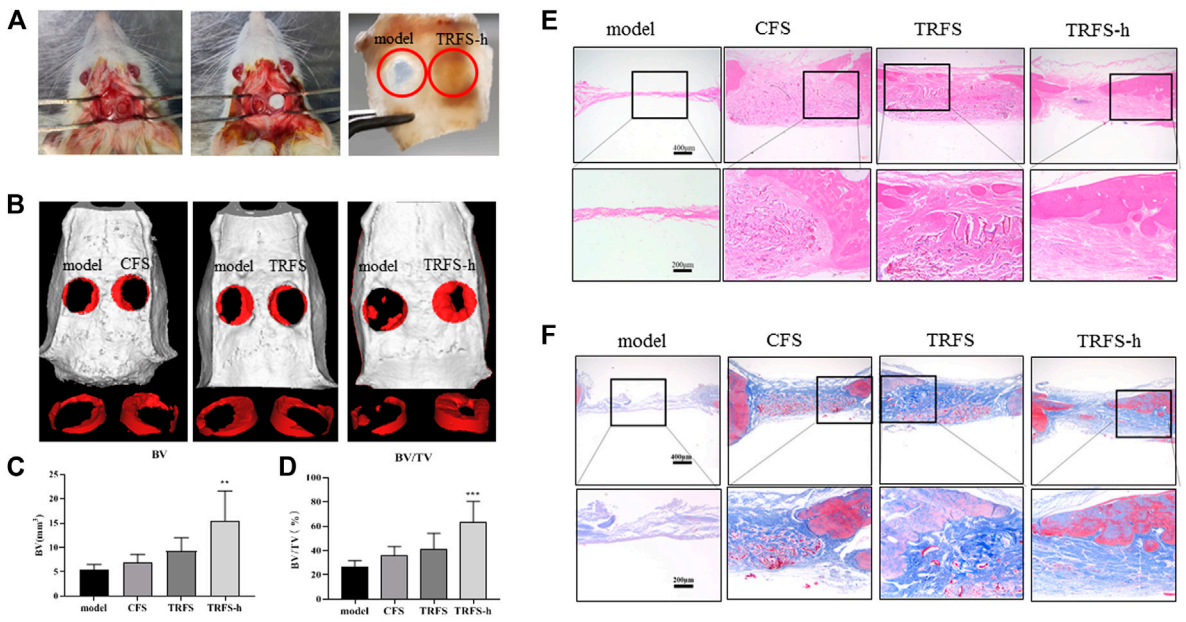

FIGURE 3 | TRFS containing hPDLSCs was used to repair skull injury in SD rats **(A)** Establishment and material implantation of ultimate skull defect (5 mm) model in rats **(B)** Micro-CT scanning and three-dimensional reconstruction of skull defects in SD rats **(C)** Analysis of new bone mass **(D)** Analysis of bone volume at the site of skull defect **(E)** HE staining of skull tissue after 12 weeks **(F)** Masson staining of skull tissue after 12 weeks ($n = 6$, $^{**}p < 0.01$, $^{***}p < 0.001$ *vs* model).

can be seen from **Figure 1D** that the 2% CFS can absorb more than 30 times its own weight in aqueous solution, which is significantly different from that of the 3% CFS ($p < 0.01$). **Figure 1E** shows that 2% CFS is approximately 90 kPa when the strain is equal to 40%, while the 3% CFS hydrogel is approximately 138 kPa, indicating that 2% sponge has lower mechanical properties than 3% sponge ($p < 0.01$).

In summary, while 3% CFS had slightly higher mechanical properties, 2% CFS had better water absorption, water vapor permeability, and moisture retention. As such, 2% CFS was selected for the preparation of TRFS and subsequent studies. TRFS was prepared from 2% CS and had the characteristics of 2% CS, including a porous three-dimensional structure with high water vapor permeability and moisture retention.

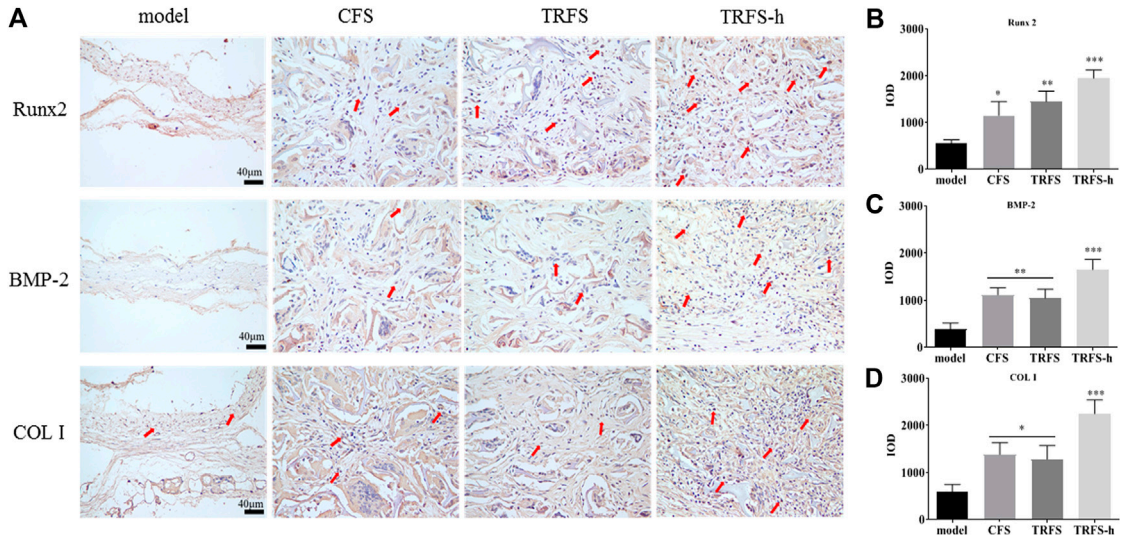

FIGURE 4 | Osteogenesis-associated protein immunohistochemical staining was performed in skull tissue sections at 12 weeks post-surgery **(A)** Immunohistochemical staining of osteogenesis-associated proteins Runx2, BMP-2, and COL I. Red arrows indicate positive cells **(B)** Runx2 positive statistics **(C)** BMP-2 positive statistics **(D)** COL I positive statistics ($n = 3$, $^{*}p < 0.05$, $^{**}p < 0.01$, $^{***}p < 0.001$ *vs* model).

Degradation of TRFS *in vitro* and Profile of TGF-β3 Release From TRFS

Figure 1F shows the *in vitro* degradation of TRFS. TRFS gradually degraded by approximately 65% at week 8. As shown in **Figure 1G**, TGF-β3 was stably released from TRFS. After a short initial burst (16.08%), TGF-β3 from the TRFS scaffold was released in a sustained manner, and the release rate decreased with time. By day 15, approximately 71.28% of the total TGF-β3 was released. This result suggested that the TRFS scaffold was a promising delivery carrier for TGF-β3 and allowed for a controlled release.

TRFS Promotes the Proliferation and Osteogenic Differentiation of hPDLSCs

TRFS Promotes the Proliferation of hPDLSCs *in vitro*

According to the results of the MTT *in vitro* cytotoxicity test (**Figure 2A**), there was no significant difference between the TRFS extract group and the control group ($p > 0.05$). **Figure 2B** shows the SEM image of hPDLSCs cultured in TRFS for 3 days hPDLSCs showed good adhesion and extension states on the surface of the material. **Figure 2C** shows the results of calcein-AM/PI double staining after hPDLSCs were cultured on TRFS for 7 days. The results showed that hPDLSCs grew well on TRFS with complete cell structure, and the number of living cells was far more than that of dead cells, indicating that TRFS is suitable for proliferation of hPDLSCs. These results indicated that TRFS was beneficial for cell growth.

TRFS Facilitates the Osteogenic Differentiation of hPDLSCs

hPDLSCs were cultivated in CFS, RFS, TFS, and TRFS, respectively, and the ALP values were determined at 3, 7, and 14 days after osteoblastic induction (**Figure 2D**). We observed significant differences between the TRFS and CFS groups at 3, 7, and 14 days ($p < 0.05$, *vs.* control; **Figure 2D**). The TFS and TRFS groups showed noticeably higher ALP levels than the CFS group. The results indicated that TRFS provided the most beneficial environment for hPDLSC differentiation.

TRFS Promotes Skull Defect Repair

Figure 3A shows the material implantation of the SD rat skull defect and the skull at 12 weeks post-surgery. The material implanted on the right side of the defect was noticeably filled with tissue, while the defect area on the left of the model was only a transparent film. As shown in **Figure 3B**, at 12 weeks after modeling, the effect of repairing bone defects in the TRFS-h group was significantly better than that in the other groups. In the TRFS-h group, a large amount of new bone formed, and the defect area was significantly reduced. By contrast, in the model, CFS and TRFS groups, only a few new bone tissues formed at the edge of the bone defect after 12 weeks **Figure 3C** shows the statistical results for the new BV at the defect site. The BV in the TRFS-h group was significantly higher than that in the model group at 12 weeks ($p < 0.01$). **Figure 3D** shows the new BV fractions. The BV fraction of the TRFS-h group was higher than that of the other groups at 12 weeks and significantly higher than that of the model group ($p < 0.01$).

HE staining of the skull specimen at 12 weeks (**Figure 3E**) showed that, in the model group, no new bone formation was found at the bone defect site, and only a small amount of tissue fiber filling was observed. In the TRFS-h group, there was significantly more new bone formed at the bone defect site than that in the other groups. The material in the bone defect was completely degraded, and a large amount of fibrous tissue was observed at the bone defect site with no inflammatory cell

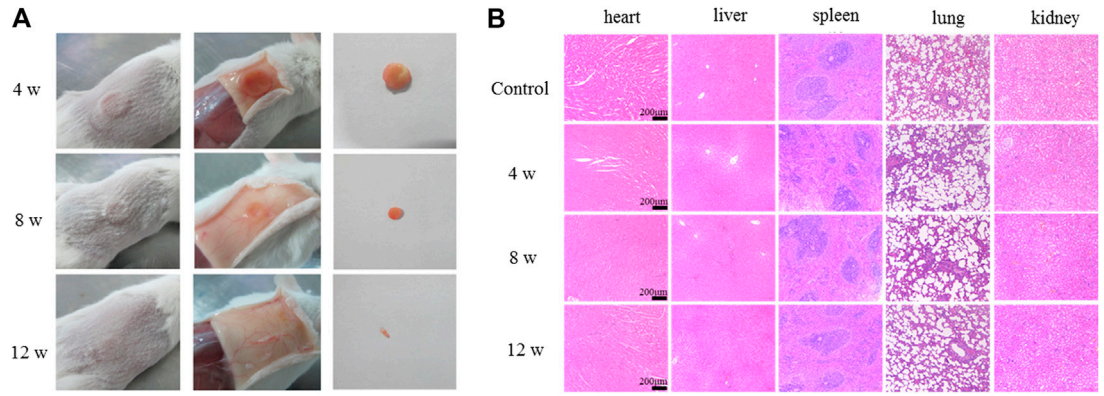

FIGURE 5 | Degradation of TRFS *in vivo* **(A)** Study on degradation of TRFS *in vivo* at 4, 8, and 12 weeks post-implantation into the dorsal subcutaneous tissue of male KM mice **(B)** HE staining of the heart, liver, spleen, lung, and kidney (n = 10).

infiltration. The Masson staining results (**Figure 3F**) showed that the bone defect in the model group only had a small amount of blue fibrous tissue filling, and no noticeable new bone formation in the bone defect site was observed. In the CFS, TRFS, and TRFS-h groups, compared with the model group, a large amount of blue fibrous tissue was found to fill the bone defect, and undegraded material was surrounded by blue fibrous tissue. The new bone tissue grew from the edge to the inside of the bone defect. The material was completely degraded, and many new blood vessels grew in the fibrous tissue of the bone defect, with no inflammatory cell infiltration.

TRFS Promotes the Expression of Osteogenesis-Associated Proteins

Figure 4A shows the Runx2, BMP-2, and COL I immunohistochemical staining of skull tissue sections at 12 weeks. In the model group, only a few cells showed positive expression reactions in bone defects. In the experimental groups, positive cell reactions were observed around the material, indicating that the material promoted the expression of osteogenesis-associated proteins in cells at the bone defect site. Among them, the number of positive reaction cells around the TRFS-h group was significantly higher than that in the other groups. The statistical results indicated that there was a significant difference between the experimental groups and the model group (**Figures 4B–D**; $p < 0.05$). In the TRFS-h group, the expression of Runx2, BMP-2, and COL I was significantly higher than that in the model group ($p < 0.001$), indicating that TRFS-h promoted osteoblast activity.

Degradation of TRFS *in vivo*

The degradation of the materials was observed at 4, 8, and 12 weeks (**Figure 5A**). The results showed that TRFS could be degraded gradually, and approximately, one-fourth was degraded at 8 weeks, and the degradation was basically complete at 12 weeks. The heart, liver, spleen, lung, and kidney of the rats were dissected 4, 8, and 12 weeks after subcutaneous implantation. The tissues were converted to paraffin sections and observed after HE staining. Compared with the tissue sections of control rats, there were no significant differences in those of experimental rats (**Figure 5B**).

DISCUSSION

Scaffold materials play a vital role in regenerative medicine and are bridges connecting seed stem cells and regenerative tissues. They provide structural and spatial support for the adhesion, proliferation, and differentiation of stem cells and serve as a template to guide tissue regeneration (Pérez-García et al., 2019; Zhai et al., 2020). In bone tissue engineering, scaffolds facilitate the delivery of biofactors and sustain mechanical forces until the regenerated tissue can bear them. Therefore, many factors need to be considered when designing scaffolds for the craniofacial region, including porosity, biocompatibility, degradability, surface morphology, and mechanical strength (Shakya and Kandalam, 2017). In this context, we used the vacuum freeze-drying method to design a hybrid TRFS to load hPDLSCs for the repair of calvarial defects in rats. We evaluated the main characteristics of CFS prepared with different CS concentrations, including apparent morphology, pore size, porosity, water absorption, expansion rate, moisture retention, water vapor transmission rate, mechanical properties, and *in vitro* degradation. Various reports have previously highlighted that pores smaller than 300 μm encourage endochondral ossification (Karageorgiou and Kaplan, 2005; Murphy et al., 2010). In our study, 2% CFS formed a porous three-dimensional sponge structure with higher porosity and more regular pores, interpenetrating the entire scaffold. They were found to be conducive to cell migration, nutrient transmission, and metabolite discharge. Biodegradation is an important criterion for the design of bone tissue engineering (BTE) scaffolds. The implanted BTE scaffolds should undergo degradation over time and should match the formation of new bone (Saravanan et al., 2016). The 2% CFS was gradually degraded by approximately 65% at week 8 *in vitro* and degraded almost completely after 12 weeks *in vivo*, which is consistent with the bone repair cycle.

Overall, 2% CFS was more suitable for the physical and chemical properties required for calvarial defect repair and thus was selected for further study.

Numerous reports have shown that CS-based materials not only exhibit the excellent activities of CS but also show other appealing performance of combined materials, giving rise to good synergistic properties of CS and its composite materials, such as RHC (Andonegi et al., 2020). RHC is a biological protein formed by high-density fermentation and separation processes through genetic engineering technology. RHC not only retains the excellent properties of collagen, but also has a high water solubility and processability and low immunogenicity compared to native collagen, without the risk of virus infection. It has been applied to various groups of biological scaffold materials. Cell adhesion is the primary condition for cell proliferation, migration, and differentiation. Crystalline violet staining and cytoskeleton staining showed that RHC effectively promoted the adhesion and spread of hPDLSCs (**Supplementary Figure S1**). Deng et al. reported that electrospun RHC/CS nanofibers crosslinked *in situ* are ideal candidates for use in wound healing applications (Deng et al., 2018). Yang et al. prepared recombinant collagen sponges loaded with BMP-2 as bone graft substitutes for the treatment of spinal instability caused by degenerative spondylosis (Yang et al., 2004). Zhou et al. successfully prepared a three-dimensional porous scaffold based on nanohydroxyapatite/RHC/poly (lactic acid) (nHA/RHC/PLA), which had the main component and hierarchical microstructure similar to that of natural bone. The nHA/RHC/PLA scaffold facilitated the healing of segmental bone defects and exhibited good osteoconductivity (Zhou et al., 2017). The hybrid RHC/CS scaffold also increased the adhesion of cells and promoted hPDLSC osteogenic differentiation, bone regeneration, and skull defect repair.

With advances in research, this ubiquitous polypeptide has been found to play an important role in bone remodeling and the regulation of bone differentiation. TGF-β3, an important regulatory molecule of MSCs, affects the proliferation, renewal, and differentiation of stem cells (Valdez et al., 2012). (Klar et al., 2013) found that TGF-β3 induced endochondral ossification by regulating BMP activity, thereby inducing bone formation (Klar et al., 2014). Deng et al. (2017) found that TGF-β3 may initiate the process of bone regeneration by recruiting endogenous stem cells. In a previous study, our research group found that TGF-β3 did not affect the proliferation of hPDLSCs but promoted their migration and differentiation into bone *in vitro*. To further demonstrate the effects of the above *in vivo*, a critical size skull defect SD rat model was used. Zhang et al. (2020) created two round defects on both sides of the rat skulls and implanted a gelatin-hydroxyapatite composite cryogel to investigate the regeneration efficiency of rat calvarial defects. Lam et al. (2019) transplanted MSCs loaded with polycaprolactone microvectors into rat skull defects to enhance bone healing in rat calvarial defects. After the operation, the rats showed normal physiological activities, such as eating and excretion, and no fatalities were recorded among the animals for the duration of the experiment. In the present study, the imaging and histological results at 12 weeks after surgery showed that few new bone tissues formed in the model group, and large defects remained. In the TRFS-h group, a large amount of new bone formation was observed, and the defect area was significantly reduced. Micro-CT was used to continuously observe skull defects in the experimental rats. Micro-CT is a non-traumatic detection tool with high resolution and good reconstruction accuracy and can continuously detect live animals. Three-dimensional reconstruction and analysis of the internal bone tissue structure can be performed to analyze the dynamic changes in sample bone density and mass. The results showed that the TRFS-h group significantly promoted the repair of rat skull defects. The volume and mass of new bone in the TRFS-h group were significantly higher than those in the other groups ($p < 0.05$). The results of the TRFS subcutaneous implantation experiment showed that TRFS did not cause noticeable inflammation in the body and degraded almost completely after 12 weeks, which is consistent with the bone repair cycle.

Based on the above experimental results, we further explored the mechanism by which TRFS promoted stem cell osteogenesis *in vivo*. The results of HE staining showed that after 12 weeks, the new bone morphology parameters at the bone defect site in the TRFS-h group were significantly higher than that in the other groups. A large number of thick new bones grew from the edge of the bone defect to the inside of the bone defect, and the materials in the bone defect were completely degraded. The Masson staining results showed that the bone defect in the TRFS-h group was filled with a large amount of blue fibrous tissue, and the undegraded sponge was surrounded by blue fibrous tissue. Further, the expression of Runx2, COL I, and BMP-2 was observed. Runx2 is the most specific and earliest expressed marker of osteoblasts. It is expressed by mesenchymal cells at the initial stage of bone development and exists throughout the differentiation process of osteoblasts (Zhang et al., 2003; Chen et al., 2014). Runx2 can control the transcription of many genes expressed on osteoblasts and is a necessary factor for osteoblast differentiation *in vivo* and *in vitro*. COL I is the main ECM protein secreted by the osteoblasts. It is the earliest product of osteoblasts in the formation of the bone matrix and is a characteristic marker of the osteoblast phenotype. BMP-2 is one of the most important cell signaling molecules that promotes bone formation, induces osteoblast differentiation, and plays an important role in bone formation. The results of immunohistochemical staining showed that the positive reactions of Runx2, COL I, and BMP-2 in the TRFS-h group were significantly higher than those in the other groups, indicating that the osteoblasts of the TRFS-h group were differentiated actively. Therefore, the above results indicate that TRFS loaded with hPDLSCs can effectively repair rat skull injuries.

PDLSCs have been proposed as the most promising cells for the regeneration of severely damaged PDL tissue, among other stem cells such as dental pulp stem cells, stem cells from human exfoliated deciduous teeth, and dental follicle stem cells (Tsumanuma et al., 2011). hPDLSCs have the ability to differentiate into osteoblasts, chondrocytes, cementoblasts, and adipocytes, as well as myocytes and neural cells (Tomokiyo et al., 2008; Song et al., 2012). Professor Qingsong Ye, the director of Wuhan University Regenerative Medicine Center, is the head of a research group that focuses on the clinical application and

transformation of odontogenic stem cells. Ye et al. prepared bioactive hydrogels combined with odontogenic stem cells to repair large space peripheral nerve injury and found that odontogenic stem cells could directly differentiate into new nerve tissue to repair the defect site (Luo et al., 2021). Many researchers are currently trying to develop innovative and critical methods for bone defect therapy from various perspectives to improve health and quality of life (Maeda, 2020). Both human dental pulp mesenchymal stem cells (hDPMSCs) and hPDLSCs originate from odontogenic tissue. An hDPMSC injection was recently approved for use in humans after a clinical trial (CXSL1700137), encouraging us to continue our research.

DATA AVAILABILITY STATEMENT

The raw data supporting the conclusion of this article will be made available by the authors, without undue reservation.

ETHICS STATEMENT

The animal study was reviewed and approved by the Institutional Animal Care and Use Committee of Jinan University.

AUTHOR CONTRIBUTIONS

QX and YH contributed to study conception and design. SH, and FY contributed to acquisition of data and study conduct. FY, YC, and YL contributed to analysis of data. YB, QT, YZ, and JT contributed materials. SH, YC, and YC helped perform the analysis with constructive discussions. SH and FY wrote the manuscript. QX and YH modified the manuscript.

FUNDING

This work was supported by grants from the Guangzhou Science and Technology Program Key Project (grant no. 201803010044), Guangdong Province Natural Sciences Fund Project (grant no. 2021A1515012480), the Special Innovation Projects of Universities in Guangdong Province (grant no. 2019KTSCX011), and Key Research and Development Program of Guangzhou (2021).

ACKNOWLEDGMENTS

The authors would like to acknowledge the faculty and staff at the Biopharmaceutical R&D Center of Jinan University and thank the research group of Professor Yang Yu from the Guangzhou University of Chinese Medicine.

SUPPLEMENTARY MATERIAL

The Supplementary Material for this article can be found online at: https://www.frontiersin.org/articles/10.3389/fphar.2021.678322/full#supplementary-material.

REFERENCES

Andonegi, M., Heras, K. L., Santos-Vizcaíno, E., Igartua, M., Hernandez, R. M., de la Caba, K., et al. (2020). Structure-properties Relationship of Chitosan/collagen Films with Potential for Biomedical Applications. *Carbohydr. Polym.* 237, 116159. doi:10.1016/j.carbpol.2020.116159

Annamalai, R. T., Hong, X., Schott, N. G., Tiruchinapally, G., Levi, B., and Stegemann, J. P. (2019). Injectable Osteogenic Microtissues Containing Mesenchymal Stromal Cells Conformally Fill and Repair Critical-Size Defects. *Biomaterials* 208, 32–44. doi:10.1016/j.biomaterials.2019.04.001

Chalisserry, E. P., Nam, S. Y., Park, S. H., and Anil, S. (2017). Therapeutic Potential of Dental Stem Cells. *J. Tissue Eng.* 8, 2041731417702531. doi:10.1177/2041731417702531

Chen, P., Wei, D., Xie, B., Ni, J., Xuan, D., and Zhang, J. (2014). Effect and Possible Mechanism of Network between microRNAs and RUNX2 Gene on Human Dental Follicle Cells. *J. Cel. Biochem.* 115, 340–348. doi:10.1002/jcb.24668

Cheng, Y., Li, Y., Huang, S., Yu, F., Bei, Y., Zhang, Y., et al. (2020). Hybrid Freeze-Dried Dressings Composed of Epidermal Growth Factor and Recombinant Human-like Collagen Enhance Cutaneous Wound Healing in Rats. *Front. Bioeng. Biotechnol.* 8, 742. doi:10.3389/fbioe.2020.00742

Deng, A., Yang, Y., Du, S., and Yang, S. (2018). Electrospinning of In Situ Crosslinked Recombinant Human Collagen Peptide/chitosan Nanofibers for Wound Healing. *Biomater. Sci.* 6, 2197–2208. doi:10.1039/c8bm00492g

Deng, M., Mei, T., Hou, T., Luo, K., Luo, F., Yang, A., et al. (2017). TGFβ3 Recruits Endogenous Mesenchymal Stem Cells to Initiate Bone Regeneration. *Stem Cel Res. Ther.* 8, 258. doi:10.1186/s13287-017-0693-0

Gardner, A. J., and Zafonte, R. (2016). Neuroepidemiology of Traumatic Brain Injury. *Handb. Clin. Neurol.* 138, 207–223. doi:10.1016/B978-0-12-802973-2.00012-4

He, Y., Hou, Z., Wang, J., Wang, Z., Li, X., Liu, J., et al. (2020). Assessment of Biological Properties of Recombinant Collagen-Hyaluronic Acid Composite Scaffolds. *Int. J. Biol. Macromol.* 149, 1275–1284. doi:10.1016/j.ijbiomac.2020.02.023

Karageorgiou, V., and Kaplan, D. (2005). Porosity of 3D Biomaterial Scaffolds and Osteogenesis. *Biomaterials* 26, 5474–5491. doi:10.1016/j.biomaterials.2005.02.002

Klar, R. M., Duarte, R., Dix-Peek, T., Dickens, C., Ferretti, C., and Ripamonti, U. (2013). Calcium Ions and Osteoclastogenesis Initiate the Induction of Bone Formation by Coral-Derived Macroporous Constructs. *J. Cel Mol Med* 17 (11), 1444–1457. doi:10.1111/jcmm.12125

Klar, R. M., Duarte, R., Dix-Peek, T., and Ripamonti, U. (2014). The Induction of Bone Formation by the Recombinant Human Transforming Growth Factor-B3. *Biomaterials* 35, 2773–2788. doi:10.1016/j.biomaterials.2013.12.062

Lam, A. T., Sim, E. J., Shekaran, A., Li, J., Teo, K. L., Goggi, J. L., et al. (2019). Sub-confluent Culture of Human Mesenchymal Stromal Cells on Biodegradable Polycaprolactone Microcarriers Enhances Bone Healing of Rat Calvarial Defect. *Cytotherapy* 21, 631–642. doi:10.1016/j.jcyt.2019.03.004

Li, Y., Qiao, Z., Yu, F., Hu, H., Huang, Y., Xiang, Q., et al. (2019). Transforming Growth Factor-β3/Chitosan Sponge (TGF-β3/CS) Facilitates Osteogenic Differentiation of Human Periodontal Ligament Stem Cells. *Int. J. Mol. Sci.* 20. doi:10.3390/ijms20204982

Li, Y., Yu, F., Liu, Y., Liang, Q., Huang, Y., Xiang, Q., et al. (2020). Sulfonated Chitosan Oligosaccharide Alleviates the Inhibitory Effect of Basic Fibroblast Growth Factor on Osteogenic Differentiation of Human Periodontal Ligament Stem Cells. *J. Periodontol.* 91, 975–985. doi:10.1002/JPER.19-0273

Liu, J., Yu, F., Sun, Y., Jiang, B., Zhang, W., Yang, J., et al. (2015). Concise Reviews: Characteristics and Potential Applications of Human Dental Tissue-Derived Mesenchymal Stem Cells. *Stem Cells* 33, 627–638. doi:10.1002/stem.1909

Liu, K., Tang, M., Liu, Q., Han, X., Jin, H., Zhu, H., et al. (2020). Bi-directional Differentiation of Single Bronchioalveolar Stem Cells during Lung Repair. *Cell Discov* 6, 1. doi:10.1038/s41421-019-0132-8

Luo, L., He, Y., Jin, L., Zhang, Y., Guastaldi, F. P., Albashari, A. A., et al. (2021). Application of Bioactive Hydrogels Combined with Dental Pulp Stem Cells for the Repair of Large Gap Peripheral Nerve Injuries. *Bioact. Mater.* 6, 638–654. doi:10.1016/j.bioactmat.2020.08.028

Luo, L., He, Y., Wang, X., Key, B., Lee, B. H., Li, H., et al. (2018). Potential Roles of Dental Pulp Stem Cells in Neural Regeneration and Repair. *Stem Cell Int* 2018, 1731289. doi:10.1155/2018/1731289

Ma, J., Zhong, L., Peng, X., Xu, Y., and Sun, R. (2020). Functional Chitosan-Based Materials for Biological Applications. *Curr. Med. Chem.* 27, 4660–4672. doi:10.2174/0929867327666200420091312

Maeda, H. (2020). Mass Acquisition of Human Periodontal Ligament Stem Cells. *World J. Stem Cell* 12, 1023–1031. doi:10.4252/wjsc.v12.i9.1023

Murphy, C. M., Haugh, M. G., and O'Brien, F. J. (2010). The Effect of Mean Pore Size on Cell Attachment, Proliferation and Migration in Collagen-Glycosaminoglycan Scaffolds for Bone Tissue Engineering. *Biomaterials* 31, 461–466. doi:10.1016/j.biomaterials.2009.09.063

Ou, Q., Wang, X., Wang, Y., Wang, Y., and Lin, X. (2018). Oestrogen Retains Human Periodontal Ligament Stem Cells Stemness in Long-Term Culture. *Cell Prolif* 51, e12396. doi:10.1111/cpr.12396

Pérez-García, S., Carrión, M., Gutiérrez-Cañas, I., Villanueva-Romero, R., Castro, D., Martínez, C., et al. (2019). Profile of Matrix-Remodeling Proteinases in Osteoarthritis: Impact of Fibronectin. *Cells.* 9, 40. doi:10.3390/cells9010040

Park, J. Y., Shim, J. H., Choi, S. A., Jang, J., Kim, M., Lee, S. H., et al. (2015). 3D Printing Technology to Control BMP-2 and VEGF Delivery Spatially and Temporally to Promote Large-Volume Bone Regeneration. *J. Mater. Chem.* B 3, 5415–5425. doi:10.1039/c5tb00637f

Ripamonti, U., Klar, R. M., Parak, R., Dickens, C., Dix-Peek, T., and Duarte, R. (2016a). Tissue Segregation Restores the Induction of Bone Formation by the Mammalian Transforming Growth Factor-B(3) in Calvarial Defects of the Non-human Primate *Papio ursinus*. *Biomaterials* 86, 21–32. doi:10.1016/j.biomaterials.2016.01.071

Ripamonti, U., Parak, R., Klar, R. M., Dickens, C., Dix-Peek, T., and Duarte, R. (2017). Cementogenesis and Osteogenesis in Periodontal Tissue Regeneration by Recombinant Human Transforming Growth Factor-β (3). *J. Clin. Periodontol.* 44, 83–95. doi:10.1111/jcpe.12642

Ripamonti, U., Parak, R., Klar, R. M., Dickens, C., Dix-Peek, T., and Duarte, R. (2016b). The Synergistic Induction of Bone Formation by the Osteogenic Proteins of the TGF-β Supergene Family. *Biomaterials* 104, 279–296. doi:10.1016/j.biomaterials.2016.07.018

Saravanan, S., Leena, R. S., and Selvamurugan, N. (2016). Chitosan Based Biocomposite Scaffolds for Bone Tissue Engineering. *Int. J. Biol. Macromol.* 93, 1354–1365. doi:10.1016/j.ijbiomac.2016.01.112

Shakya, A. K., and Kandalam, U. (2017). Three-dimensional Macroporous Materials for Tissue Engineering of Craniofacial Bone. *Br. J. Oral Maxillofac. Surg.* 55, 875–891. doi:10.1016/j.bjoms.2017.09.007

Shang, L., Ma, B., Wang, F., Li, J., Shen, S., Li, X., et al. (2020). Nanotextured Silk Fibroin/hydroxyapatite Biomimetic Bilayer Tough Structure Regulated Osteogenic/chondrogenic Differentiation of Mesenchymal Stem Cells for Osteochondral Repair. *Cel Prolif* 53, e12917. doi:10.1111/cpr.12917

Sionkowska, A., Michalska-Sionkowska, M., and Walczak, M. (2020). Preparation and Characterization of Collagen/hyaluronic Acid/chitosan Film Crosslinked with Dialdehyde Starch. *Int. J. Biol. Macromol.* 149, 290–295. doi:10.1016/j.ijbiomac.2020.01.262

Song, M., Kim, H., Choi, Y., Kim, K., and Chung, C. (2012). Skeletal Myogenic Differentiation of Human Periodontal Ligament Stromal Cells Isolated from Orthodontically Extracted Premolars. *Korean J. Orthod.* 42, 249–254. doi:10.4041/kjod.2012.42.5.249

Tomokiyo, A., Maeda, H., Fujii, S., Wada, N., Shima, K., and Akamine, A. (2008). Development of a Multipotent Clonal Human Periodontal Ligament Cell Line. *Differentiation* 76, 337–347. doi:10.1111/j.1432-0436.2007.00233.x

Trubiani, O., Marconi, G. D., Pierdomenico, S. D., Piattelli, A., Diomede, F., and Pizzicannella, J. (2019). Human Oral Stem Cells, Biomaterials and Extracellular Vesicles: A Promising Tool in Bone Tissue Repair. *Int. J. Mol. Sci.* 20, 4987. doi:10.3390/ijms20204987

Tsumanuma, Y., Iwata, T., Washio, K., Yoshida, T., Yamada, A., Takagi, R., et al. (2011). Comparison of Different Tissue-Derived Stem Cell Sheets for Periodontal Regeneration in a Canine 1-wall Defect Model. *Biomaterials* 32, 5819–5825. doi:10.1016/j.biomaterials.2011.04.071

Valdez, J. M., Zhang, L., Su, Q., Dakhova, O., Zhang, Y., Shahi, P., et al. (2012). Notch and TGFβ Form a Reciprocal Positive Regulatory Loop that Suppresses Murine Prostate Basal Stem/progenitor Cell Activity. *Cell Stem Cell* 11, 676–688. doi:10.1016/j.stem.2012.07.003

Xiao, B., Yang, W., Lei, D., Huang, J., Yin, Y., Zhu, Y., et al. (2019). PGS Scaffolds Promote the In Vivo Survival and Directional Differentiation of Bone Marrow Mesenchymal Stem Cells Restoring the Morphology and Function of Wounded Rat Uterus. *Adv. Healthc. Mater.* 8, e1801455. doi:10.1002/adhm.201801455

Xu, H., Niu, C., Fu, X., Ding, W., Ling, S., Jiang, X., et al. (2015). Early Cranioplasty vs. Late Cranioplasty for the Treatment of Cranial Defect: A Systematic Review. *Clin. Neurol. Neurosurg.* 136, 33–40. doi:10.1016/j.clineuro.2015.05.031

Yang, C., Hillas, P. J., Báez, J. A., Nokelainen, M., Balan, J., Tang, J., et al. (2004). The Application of Recombinant Human Collagen in Tissue Engineering. *BioDrugs* 18, 103–119. doi:10.2165/00063030-200418020-00004

Yang, F., Miao, Y., Wang, Y., Zhang, L. M., and Lin, X. (2017). Electrospun Zein/gelatin Scaffold-Enhanced Cell Attachment and Growth of Human Periodontal Ligament Stem Cells. *Materials (Basel)* 10, 1168. doi:10.3390/ma10101168

Zang, S., Dong, G., Peng, B., Xu, J., Ma, Z., Wang, X., et al. (2014). A Comparison of Physicochemical Properties of Sterilized Chitosan Hydrogel and its Applicability in a Canine Model of Periodontal Regeneration. *Carbohydr. Polym.* 113, 240–248. doi:10.1016/j.carbpol.2014.07.018

Zhai, P., Peng, X., Li, B., Liu, Y., Sun, H., and Li, X. (2020). The Application of Hyaluronic Acid in Bone Regeneration. *Int. J. Biol. Macromol.* 151, 1224–1239. doi:10.1016/j.ijbiomac.2019.10.169

Zhang, C., Chen, Y., and Fu, X. (2015a). Sweat Gland Regeneration after Burn Injury: Is Stem Cell Therapy a New Hope? *Cytotherapy* 17, 526–535. doi:10.1016/j.jcyt.2014.10.016

Zhang, J., Deng, A., Zhou, A., Yang, Y., Gao, L., Zhong, Z., et al. (2015b). Comparison of Two Proanthocyanidin Cross-Linked Recombinant Human Collagen-Peptide (RHC) - Chitosan Scaffolds. *J. Biomater. Sci. Polym. Ed.* 26, 585–599. doi:10.1080/09205063.2015.1047667

Zhang, X., Aubin, J. E., and Inman, R. D. (2003). Molecular and Cellular Biology of New Bone Formation: Insights into the Ankylosis of Ankylosing Spondylitis. *Curr. Opin. Rheumatol.* 15, 387–393. doi:10.1097/00002281-200307000-00004

Zhang, Y., Leng, H., Du, Z., Huang, Y., Liu, X., Zhao, Z., et al. (2020). Efficient Regeneration of Rat Calvarial Defect with Gelatin-Hydroxyapatite Composite Cryogel. *Biomed. Mater.* 15, 065005. doi:10.1088/1748-605X/ab9422

Zhang, Y., Xing, Y., Jia, L., Ji, Y., Zhao, B., Wen, Y., et al. (2018). An In Vitro Comparative Study of Multisource Derived Human Mesenchymal Stem Cells for Bone Tissue Engineering. *Stem Cell Dev* 27, 1634–1645. doi:10.1089/scd.2018.0119

Zhou, J., Guo, X., Zheng, Q., Wu, Y., Cui, F., and Wu, B. (2017). Improving Osteogenesis of Three-Dimensional Porous Scaffold Based on Mineralized Recombinant Human-like Collagen via Mussel-Inspired Polydopamine and Effective Immobilization of BMP-2-Derived Peptide. *Colloids Surf. B Biointerfaces* 152, 124–132. doi:10.1016/j.colsurfb.2016.12.041

Conflict of Interest: The authors declare that the research was conducted in the absence of any commercial or financial relationships that could be construed as a potential conflict of interest.

frontiers in Cell and Developmental Biology

ORIGINAL RESEARCH
published: 13 May 2021
doi: 10.3389/fcell.2021.671841

Validation of a Novel *Fgf10*$^{Cre-ERT2}$ Knock-in Mouse Line Targeting FGF10^{Pos} Cells Postnatally

Xuran Chu[1,2,3], *Sara Taghizadeh*[2,3], *Ana Ivonne Vazquez-Armendariz*[3,4], *Susanne Herold*[3,4], *Lei Chong*[5], *Chengshui Chen*[2], *Jin-San Zhang*[1,2]*, *Elie El Agha*[3,4]* and *Saverio Bellusci*[1,2,3]*

[1] School of Pharmaceutical Sciences, Wenzhou Medical University, Wenzhou, China, [2] Key Laboratory of Interventional Pulmonology of Zhejiang Province, Department of Pulmonary and Critical Care Medicine, The First Affiliated Hospital of Wenzhou Medical University, Wenzhou, China, [3] Department of Internal Medicine, Universities of Giessen and Marburg Lung Center (UGMLC), Cardio-Pulmonary Institute (CPI), Member of the German Center for Lung Research (DZL), Justus-Liebig University Giessen, Giessen, Germany, [4] Institute for Lung Health (ILH), Giessen, Germany, [5] National Key Clinical Specialty of Pediatric Respiratory Medicine, Discipline of Pediatric Respiratory Medicine, Institute of Pediatrics, The Second Affiliated Hospital of Wenzhou Medical University, Wenzhou, China

OPEN ACCESS

Edited by:
Zhouguang Wang, Albert Einstein College of Medicine, United States

Reviewed by:
Helen P. Makarenkova, The Scripps Research Institute, United States
Chen Li, Charité—Universitätsmedizin Berlin, Germany

***Correspondence:**
Jin-San Zhang
zhang.jinsan@WMU.edu.cn
Elie El Agha
Elie.El-Agha@innere.med.uni-giessen.de
Saverio Bellusci
saverio.bellusci@innere.med.uni-giessen.de

Specialty section:
This article was submitted to Stem Cell Research, a section of the journal Frontiers in Cell and Developmental Biology

Received: *24 February 2021*
Accepted: *25 March 2021*
Published: *13 May 2021*

Citation:
Chu X, Taghizadeh S, Vazquez-Armendariz AI, Herold S, Chong L, Chen C, Zhang J-S, El Agha E and Bellusci S (2021) Validation of a Novel Fgf10$^{Cre-ERT2}$ Knock-in Mouse Line Targeting FGF10^{Pos} Cells Postnatally. Front. Cell Dev. Biol. 9:671841. doi: 10.3389/fcell.2021.671841

Fgf10 is a key gene during development, homeostasis and repair after injury. We previously reported a knock-in *Fgf10*$^{Cre-ERT2}$ line (with the Cre-ERT2 cassette inserted in frame with the start codon of exon 1), called thereafter *Fgf10*$^{Ki-v1}$, to target FGF10^{Pos} cells. While this line allowed fairly efficient and specific labeling of FGF10^{Pos} cells during the embryonic stage, it failed to target these cells after birth, particularly in the postnatal lung, which has been the focus of our research. We report here the generation and validation of a new knock-in *Fgf10*$^{Cre-ERT2}$ line (called thereafter *Fgf10*$^{Ki-v2}$) with the insertion of the expression cassette in frame with the stop codon of exon 3. *Fgf10*$^{Ki-v2/+}$ heterozygous mice exhibited comparable *Fgf10* expression levels to wild type animals. However, a mismatch between *Fgf10* and *Cre* expression levels was observed in *Fgf10*$^{Ki-v2/+}$ lungs. In addition, lung and limb agenesis were observed in homozygous embryos suggesting a loss of *Fgf10* functional allele in *Fgf10*$^{Ki-v2}$ mice. Bioinformatic analysis shows that the 3′UTR, where the Cre-ERT2 cassette is inserted, contains numerous putative transcription factor binding sites. By crossing this line with tdTomato reporter line, we demonstrated that tdTomato expression faithfully recapitulated *Fgf10* expression during development. Importantly, *Fgf10*$^{Ki-v2}$ mouse is capable of significantly targeting FGF10^{Pos} cells in the adult lung. Therefore, despite the aforementioned limitations, this new *Fgf10*$^{Ki-v2}$ line opens the way for future mechanistic experiments involving the postnatal lung.

Keywords: *Fgf10*, knock-in Cre line, lipofibroblast, adult lung, lineage tracing

INTRODUCTION

The fibroblast growth factor (FGF) family consisting of 22 members is divided into three groups: the paracrine FGF group signaling through FGFR and heparin-sulfate proteoglycans, the endocrine FGF group signaling through FGFR with Klotho family of proteins as co-receptors, and the intracellular FGF group involved in FGFR independent signaling (Ornitz and Itoh, 2001). The FGF7 subgroup which contains FGF3, 7, 10, 22 belongs to the paracrine FGF group. These growth

factors interact mostly with the FGFR2b receptor. FGF10 in particular has been shown to play important roles during development, homeostasis and repair after injury (Yuan et al., 2018). In the lung, it plays a crucial role in regulating branching morphogenesis (Jones et al., 2020). Genetic deletion of either *Fgf10* or its predominant receptor *Fgfr2b* leads to agenesis of both the limb and the lung, specific portions of the gut, the pancreas as well as the mammary, lacrimal and salivary glands (Min et al., 1998; Sekine et al., 1999; Ohuchi et al., 2000; Mailleux et al., 2002; Jaskoll et al., 2005; Parsa et al., 2008). During homeostasis, Fgfr2b signaling has been shown to be critical for the regeneration of the incisors in mice as well as for the maintenance of the terminal end buds in the mammary gland (Parsa et al., 2008, 2010). Lineage tracing of FGF10^{Pos} during development indicated that these cells serve as progenitors for lipofibroblast as well as vascular and airway smooth muscle cells (El Agha et al., 2014).

In the context of the repair process, *Fgf10* deletion in peribronchial mesenchymal cells leads to impaired repair following injury to the bronchial epithelium using naphthalene (Volckaert et al., 2011; Moiseenko et al., 2020). On the other hand, overexpression of *Fgf10* reduces the severity of lung fibrosis in bleomycin-induced mice (Gupte et al., 2009). Given these diverse biological activities, it is important to generate and validate mouse knock-in lines allowing to monitor the localization, fate and status of FGF10^{Pos} cells during development, homeostasis and repair after injury.

We have previously generated a *Fgf10*$^{Cre-ERT2}$ knock-in mouse line, called thereafter *Fgf10*$^{KI-v1}$ mice, to monitor the fate of FGF10^{Pos} cells after tamoxifen (Tam) administration (El Agha et al., 2012). In these mice, the Tam-inducible Cre recombinase (Cre-ERT2-IRES-YFP) was inserted in frame with the start codon of the endogenous *Fgf10* gene. *Fgf10*$^{KI-v1}$ corresponds to a loss-of-function allele for *Fgf10* as evidenced by our observation that *Fgf10*$^{KI-v1/KI-v1}$ homozygous embryos die at birth from multi-organ agenesis, including the lung. In the *Fgf10*$^{KI-v1/+}$ lungs, the expression of *Cre* gradually decreases to almost undetectable levels postnatally, rendering the monitoring of FGF10^{Pos} cells postnatally impossible. This is likely due to the deletion of intronic sequences containing key transcription factor binding sites at the insertion site of the Cre-expression cassette.

In order to circumvent this problem, we therefore generated a new Cre-ERT2 knock-in line (named *Fgf10*$^{KI-v2}$) by targeting the 3′UTR of the endogenous *Fgf10* gene. We here provide experimental evidence for the validation of these mice. Besides a PCR-based strategy to genotype the *Fgf10*$^{KI-v2}$ allele, we have also established a qPCR-based approach to monitor the expression levels of *Fgf10* and *Cre* at different developmental stages in the lung. *Fgf10*$^{KI-v2/KI-v2}$ homozygous embryos have been generated to check for developmental defects. *Fgf10*$^{KI-v2/+}$ lines were crossed with the *tdTomato*^{flox} mice to validate, at two distinct embryonic stages, the expression patterns of tdTomato in previously known domains of *Fgf10* expression. Importantly, we validated the use of these mice in the adult stages to target FGF10^{Pos} cells in the lung. Flow cytometry analysis and immunofluorescence staining were carried out to further characterize the contribution of these cells to the lipofibroblast lineage. Bioinformatic analysis of the insertion site of the Cre-ERT2 cassette in the 3′UTR was also carried out. Altogether, our results indicate that the new *Fgf10*$^{Cre-ERT2}$ line can be successfully used to target FGF10^{Pos} cells both in embryonic and adult stages.

MATERIALS AND METHODS

Genotyping

Two pairs of primers were used to determine the genotype of *Fgf10*$^{Ki-v2}$ knock-in mice. Primer P1 (5′-AACACC TCTGCTCACTTCCTC-3′); and primer P2 (5′-AGGGTCCACC TTCCGCTTTT-3′) were used to detect the knock-in allele (252 bp band) whereas primer P3 (5′-GCAGGCAAA TGTATGTGGCA-3′) and primer P4 (5′-TGCTTGCGTGTCT TACTGCT-3′) were used to detect the wild-type allele (580 bp band). The PCR program consists of a denaturation step at 94°C for 3 min, followed by 34 cycles of denaturation (94°C for 1 min), annealing (60°C for 30 s) and extension steps (72°C for 300 s). The program ends with a completion step at 4°C for infinity hold. Each PCR tube contains 4.3 μL of H_2O, Taq DNA Polymerase in 5.5 μL of Qiagen Master Mix (QIAGEN, Hilden, Germany), 10 pmol of each primer, and 50 ng of genomic DNA in a final volume of 11 μL.

Mice and Tamoxifen Administration

All mice were kept under specific pathogen free (SPF) conditions with unlimited food and water. *tdTomato*$^{flox/flox}$ reporter mice were purchased from Jackson lab (B6; 129S6-Gt(ROSA)$^{26Sortm9(CAG-tdTomato)Hze}$/J, ref 007905). Embryonic day 0.5 (E0.5) was assigned to the day when a vaginal plug was detected. Animal experiments were approved by the Regierungspraesidium Giessen (approval number RP GI20/10-Nr. G47/2019). Tamoxifen stock solution was prepared by dissolving tamoxifen powder (Sigma, T5648-5G) in corn oil at a concentration of 20 mg/mL at room temperature and stored in −20°C. Adult mice received 3 successive intraperoneal (IP) injections of tamoxifen (0.25 mg/g body weight) before analysis. Pregnant mice received a single IP injection of tamoxifen (0.1 mg/g body weight) and pups also received a single subcutaneous injection of tamoxifen (0.2 mg/pup) before analysis. Dissected mice were examined using Leica M205 FA fluorescent stereoscope (Leica, Wetzlar, Germany) and images were acquired using Leica DFC360 FX camera. Figures were assembled in Adobe Photoshop and Illustrator.

Quantitative Real-Time PCR and Statistical Analysis

Freshly isolated embryos and lungs were lysed, and RNA was extracted using RNeasy kit (74106, Qiagen, Hilden, Germany). One microgram of RNA was used for cDNA synthesis using Quantitect Reverse Transcription kit (205311, Qiagen). Primers and probes for *Fgf10*, *Cre,* and *β2-Microglobulin* (*B2M*) were designed using NCBI Primer-BLAST[1]. More details about the used primers and probes can be found in **Supplementary Table 1**.

[1]https://www.ncbi.nlm.nih.gov/tools/primer-blast/

Quantitative real-time PCR (qPCR) was performed using LightCycler 480 real-time PCR machine (Roche Applied Science). Samples were run in doublets using *B2M* as a reference gene and the delta Ct method was used to calculate the relative quantification. GraphPad Prism 7.0 software was used to generate and analyze data. Statistical analyses were performed using Student's *t*-test (for comparing two groups) or One-way ANOVA (for comparing three or more groups). Data were considered significant if $P < 0.05$.

Flow Cytometry

Freshly dissected lung were washed with Hanks' balanced salt solution (HBSS, 14175-095, Thermo Fisher) and kept on ice. Sharp blades were used to cut the lung into small pieces and digested with 0.5% collagenase Type IV in HBSS (17104019, Life Technologies, Invitrogen) for 45 min at 37°C. Lung homogenates were then passed through 18, 21, and 24G needles followed by 70 and 40 μm cell strainers (542070 and 542040, Greiner Bio-one International). Lung homogenates were centrifuged at 200g at 4°C for 10 min and cell pellets were then re-suspended in HBSS. 20 (μL of sample is taken as an unstained control. Antibodies against CD45 (103114, APC-conjugated; 1:50), CD31 (102409, APC-conjugated; 1:50), EPCAM (APC-Cy7-conjugated; 1:50) and SCA1 (108120, Pacific blue-conjugated; 1:50) (all from Biolegend) as well as LipidTOX stain (FITC-conjugated, 1:200) (H34350, Life Technologies, Invitrogen) were applied for 30 min on ice in the dark. Samples were then washed with 1 mL of HBSS at 4°C for 5 min. FACSAria III cell sorter (BD Biosciences) was used to carry out the FACS measurements and sorting. Endogenous tdTomato signal was detected through PE channel. Gates were set up according to the unstained controls.

Bioinformatics

National Center of Biotechnology Information (https://www.ncbi.nlm.nih.gov/gene/) and rVista (rVista; http://rvista.dcode.org) were used to find the murine *Fgf10* sequence and the identification of putative transcription factor binding site (TFBS) was done by using PROMO software[2]. The list of putative TFBS located in the area including exon 3 and 3′UTR was further compared with previously identified transcription factors expressed in the lung mesenchyme (Herriges et al., 2012).

RESULTS

Generation of a Novel *Fgf10* Knock-in Line (*C57BL6-Fgf10*$^{tm2(YFP-Cre-ERT2)Sbel}$*/J* Aka *Fgf10*$^{KI-v2}$) With the Insertion of the Cre-ERT2 Cassette in Frame With the Stop Codon of Exon3

129Sv ES cells were electroporated with a targeting vector containing the first 3 kb of exon 3 of the *Fgf10* open reading frame (**Figures 1A,B**). Immediately downstream of the stop codon of exon 3 is the F2A sequence encoding for the self-cleaving peptide, followed by the coding sequence of eYFP, the self-cleaving peptide sequence T2A, the tamoxifen-inducible form of Cre recombinase (Cre-ERT2) (Feil et al., 1997), and the Neomycin-resistance gene (Neo), respectively. Resistant ES cell clones were selected, screened by PCR and then verified by Southern blotting. Selected ES clones were injected into C57BL/6J blastocysts to generate chimeric pups (**Figure 1C**). Chimeras were then crossed with C57BL/6J mice ubiquitously expressing Flp recombinase to generate heterozygous *Fgf10*$^{Ki-v2}$ knock-in mice where the Neo cassette was totally excised (**Figure 1D**). Genotyping strategy with primers P1/P2 (with P1 located just before the STOP codon and P2 being part of the F2A sequence) to detect the *Fgf10*$^{Ki-v2}$ mutant allele and P3/P4 (located before and after the STOP codon in exon 3, respectively) to detect the *Fgf10*$^{+}$ wild type allele (**Figure 1E**).

Fgf10^{Ki-v2} Is a Loss-of-Function Allele

Our initial design of the novel *Fgf10*$^{Ki-v2}$ knock-in line targeting the 3′UTR was conceived to allow normal expression of *Fgf10*. We carried out the initial validation for *Fgf10* expression in *Fgf10*$^{Ki-v2/+}$ vs. *Fgf10*$^{+/+}$ (WT) in the lung of embryonic and postnatal mice isolated at different time-points (**Figure 2A**). Our results indicated that *Fgf10* expression level in *Fgf10*$^{Ki-v2/+}$ lungs is comparable to the one observed in the *Fgf10*$^{+/+}$ lungs at all these time-points (**Figure 2B**). Next, we compared *Fgf10* vs. *Cre* expression in *Fgf10*$^{Ki-v2/+}$ lungs at different time-points (**Figure 2C**). Our results indicate a lower level of *Cre* compared to *Fgf10* at all these time-points (**Figure 2D**). This difference between *Cre* and *Fgf10* expression in *Fgf10*$^{Ki-v2/+}$ lungs suggests that the insertion of the Cre-ERT2 cassette in the 3′UTR disrupted the expression of the endogenous *Fgf10* gene produced from the recombined allele. Together with *Fgf10* expression in *Fgf10*$^{Ki-v2/+}$ vs. *Fgf10*$^{+/+}$ (WT), this result suggests that *Fgf10* expression from the non-recombined allele in *Fgf10*$^{Ki-v2/+}$ lungs is increased to compensate the loss of *Fgf10* expression from the recombined allele.

To determine whether the insertion of Cre-ERT2 in the endogenous *Fgf10* locus led to loss of function of *Fgf10*, *Fgf10*$^{Ki-v2}$ heterozygous animals were self-crossed and embryos were harvested at E15.5. *Fgf10*$^{Ki-v2/Ki-v2}$ homozygous embryos suffered from lung and limb agenesis, which is consistent with complete loss of function of *Fgf10* (**Figure 2E**). Analysis of *Fgf10* expression by qPCR at that stage indicated a drastic reduction in *Fgf10* expression in *Fgf10*$^{Ki-v2/Ki-v2}$ embryo ($n = 1$) compared to *Fgf10*$^{Ki-v2/+}$ or WT lungs (**Supplementary Figure 1**). We therefore conclude that the *Fgf10*$^{Ki-v2}$ allele corresponds to a *Fgf10* loss-of-function allele.

Validation of Cre Activity to Label FGF10^{Pos} Cells During Embryonic Development

In order to test the recombinase activity of Cre-ERT2, *Fgf10*$^{Ki-v2/+}$ heterozygous mice were crossed with *tdTomato*$^{flox/flox}$ reporter mice. Pregnant mice received a single intraperitoneal (IP) injection of tamoxifen at E11.5 (**Figure 3A**)

[2]http://alggen.lsi.upc.edu/recerca/menu_recerca.html

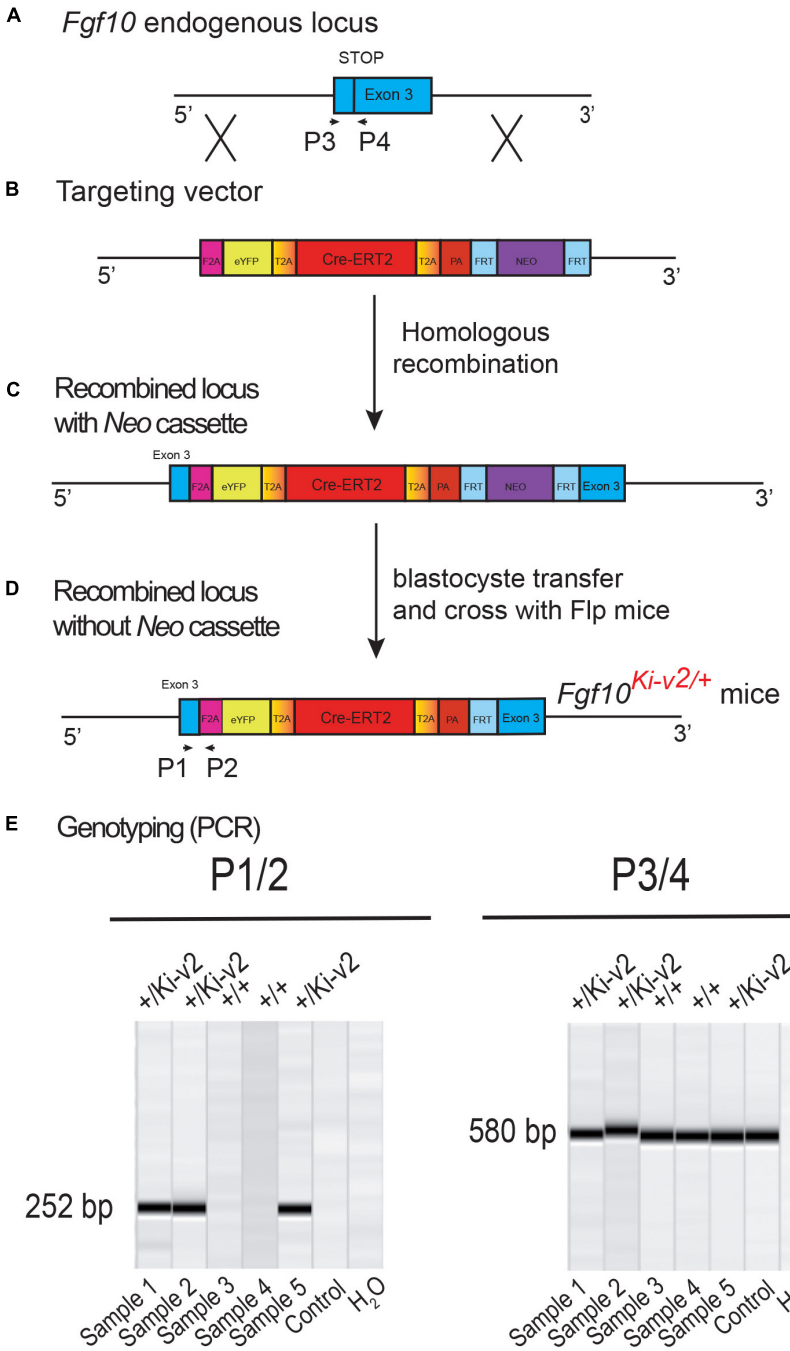

FIGURE 1 | Generation and genotyping of the novel *Fgf10*$^{Ki-v2}$ line. **(A,B)** Homologous recombination was carried out to insert the *F2A-eYFP-T2A-Cre-ERT2-T2A-PA-NEO* construct in frame with the stop codon of exon 3 of the mouse *Fgf10* gene. Neomycin resistance coding gene was used for the positive selection. **(C,D)** Recombined ES cell clones were treated with flipase to remove the Neo cassette and blastocyste transfer of the selected ES cells was carried out to generate chimera animals. **(E)** PCR strategy to genotype mutant and wild type animals. Primers 1 and 2 were used for the detection of the mutant *Fgf10*$^{Ki-v2}$ allele (252 bp) and Primers 3 and 4 were used for the detection of the wild type *Fgf10*$^{+}$ allele (580 bp).

or E15.5 (**Figure 4A**). Embryos were harvested at E18.5. No fluorescent signal was observed in *Fgf10*$^{+/+}$; *tdTomato*$^{flox/+}$ embryos (**Figures 3B**, **4B**; n = 4) indicating absence of recombination in control embryos and lack of leakiness of the *tdTomato*^{flox} allele. By contrast, tamoxifen treatment at E11.5 led to a strong fluorescent signal in the limbs, stomach, cecum, colon and lungs of *Fgf10*$^{Ki-v2/+}$; *tdTomato*$^{flox/+}$ embryos (n = 3). In the limb, the labeled cells were more abundant in the digit tip

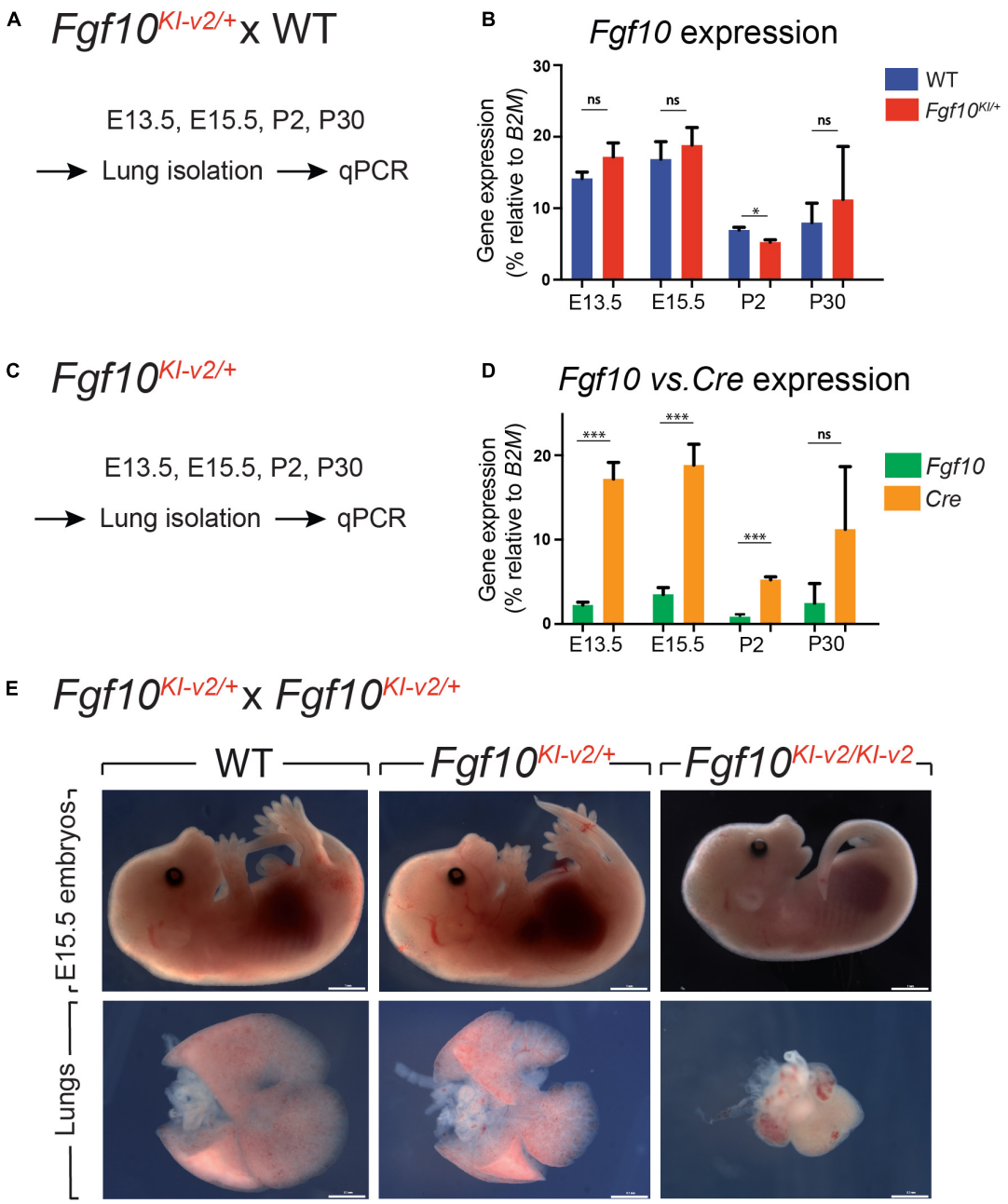

FIGURE 2 | *Fgf10*$^{Ki\text{-}v2}$ is a loss-of-function allele. **(A)** *Fgf10*$^{Ki\text{-}v2/+}$ and *Fgf10*$^{+/+}$ mice were crossed and lungs were isolated at E13.5, E15.5, P2, and P30 for qPCR analysis. **(B)** qPCR results for *Fgf10* expression in *Fgf10*$^{+/+}$ and *Fgf10*$^{Ki\text{-}v2/+}$ at these time points. **(C,D)** Lungs were isolated from *Fgf10*$^{Ki\text{-}v2/+}$ at different time points and the expression levels of *Fgf10* and *Cre* were analyzed by qPCR. **(E)** *Fgf10*$^{Ki\text{-}v2/+}$ animals were crossed to generate *Fgf10*$^{+/+}$, *Fgf10*$^{Ki\text{-}v2/+}$, and *Fgf10*$^{Ki\text{-}v2/Ki\text{-}v2}$ embryos at E13.5. Note the absence of limbs and lungs in the *Fgf10*$^{Ki\text{-}v2/Ki\text{-}v2}$ embryos. Scale bar in **(E)**: whole embryo: 1 mm; dissected lungs: 0.1 mm. $^{*}P \leq 0.05$, $^{***}P \leq 0.001$.

area, known to express high level of *Fgf10* (Danopoulos et al., 2013). Along the gastro-intestinal tract, labeled cells were located in the anterior part of the stomach as well as in duodenum (data not shown) which are both reported to express high level of *Fgf10* (Lv et al., 2019). A similar observation was made in the cecum and the distal colon (Lv et al., 2019). Throughout the lung, we found a robust tdTomato expression with a higher expression in the interlobular septa. This is similar to what was observed with the previously validated *Fgf10*^{LacZ} reporter line and *Fgf10*$^{KI-v1/+}$ line (Mailleux et al., 2005; El Agha et al., 2012, 2014). Interestingly, in the trachea, no labeled cells were observed in this experimental condition (**Figure 3C**).

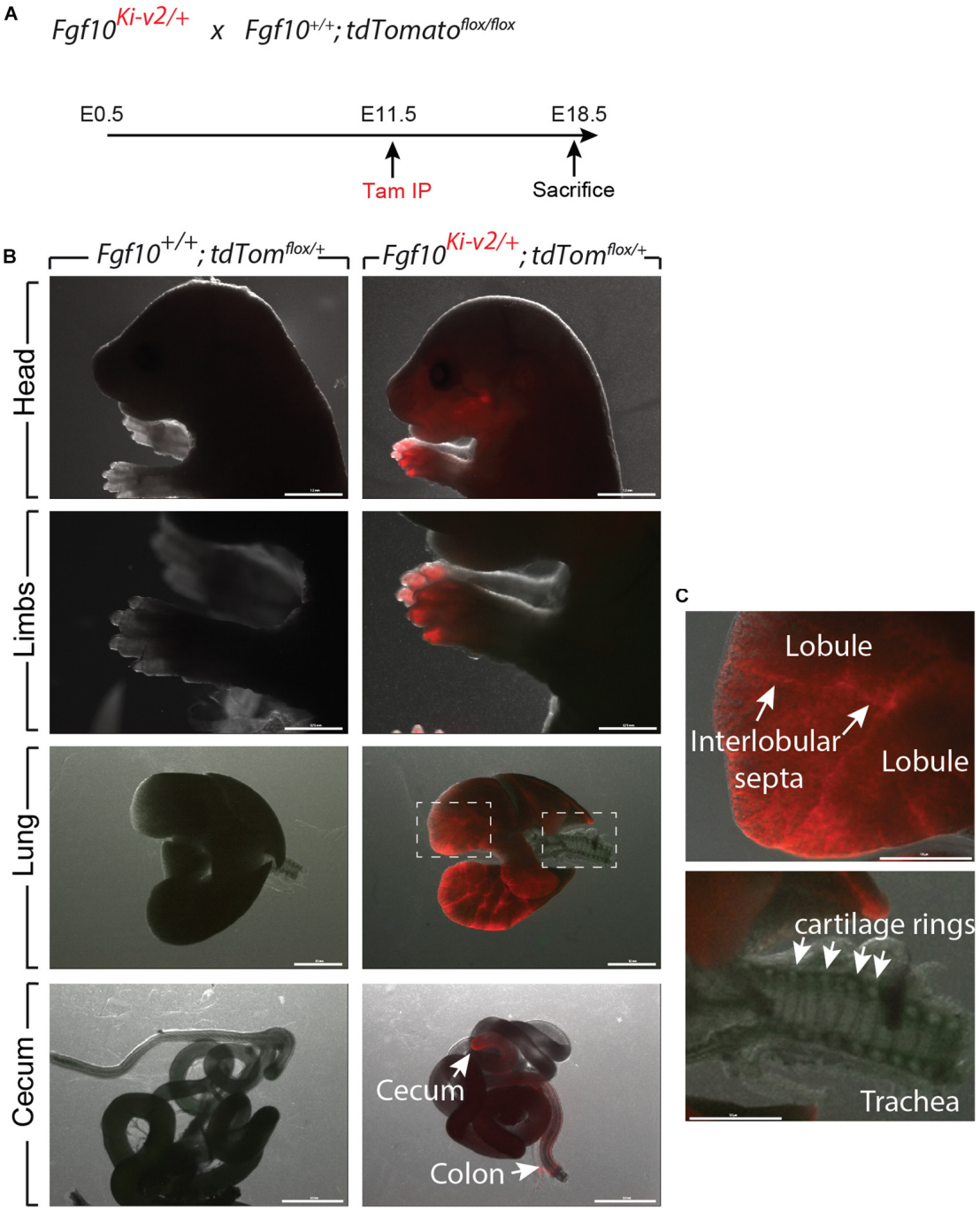

FIGURE 3 | Validation of the labeling of FGF10^{Pos} cells at E11.5. **(A)** *Fgf10*$^{Ki-v2/+}$ were crossed with *Fgf10*$^{+/+}$; *tdTom*$^{flox/flox}$ mice. Pregnant females received a single IP injection of tamoxifen when the embryos were at E11.5 and sacrificed at E18.5. **(B)** Head, limbs, lung and cecum of *Fgf10*$^{+/+}$; *tdTom*$^{flox/+}$ and *Fgf10*$^{Ki-v2/+}$; *tdTom*$^{flox/+}$ embryos are shown. Note the absence of fluorescence in the *Fgf10*$^{+/+}$; *tdTom*$^{flox/+}$ indicating that the non-recombined *LoxP-Stop-LoxP-tdTomato* allele is not leaky. **(C)** Higher magnification of lung and trachea showing enriched tdTomato expression in the interlobular septa and the lack of tdTomato expression between the cartilage rings, respectively. Scale bar in **(B)**: head: 1.5 mm, Limb: 0.75 mm, Lung: 0.5 mm, cecum: 0.5 mm. Scale bar in **(C)**: 125 μm.

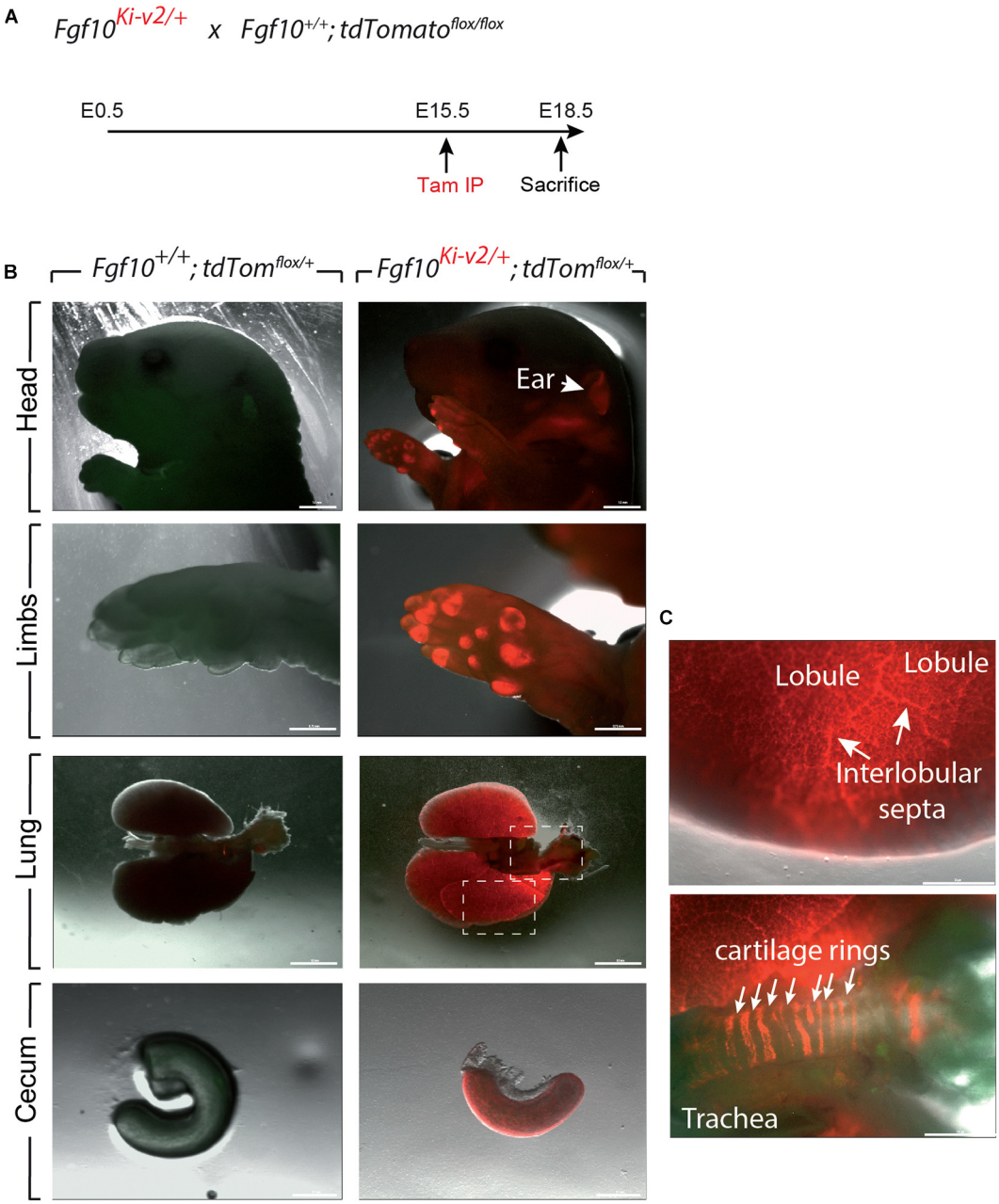

FIGURE 4 | Validation of the labeling of FGF10^{Pos} cells at E15.5. **(A)** *Fgf10*$^{Ki\text{-}v2/+}$ were crossed with *Fgf10*$^{+/+}$; *tdTom*$^{flox/flox}$ mice. Pregnant females received a single IP injection of tamoxifen when the embryos were at E15.5 and sacrificed at E18.5. **(B)** Head, limbs, lung and cecum of *Fgf10*$^{+/+}$; *tdTom*$^{flox/+}$ and *Fgf10*$^{Ki\text{-}v2/+}$; *tdTom*$^{flox/+}$ embryos are shown. Note the expression in the external ear (arrow). **(C)** Higher magnification of lung and trachea showing enriched tdTomato expression in the interlobular septa and the presence of tdTomato expression between the cartilage rings, respectively. Scale bar in **(B)**: head: 1.5 mm, Limb: 0.75 mm, Lung: 0.5 mm, Cecum: 0.1 mm. Scale bar in **(C)**: Lung 25 μm, Trachea 125 μm.

Additionally, tamoxifen treatment at E15.5 revealed strong fluorescent signal in the pinna of the developing ear as well as in the trachea and in between the cartilage rings (**Figure 4C**). These two additional expression domains are consistent with sites of *Fgf10* expression (Sala et al., 2011; Zhang et al., 2020). We therefore conclude that Cre expression reflects *Fgf10* expression and that this line can be used to target FGF10^{Pos} cells.

FGF10^{Pos} Cells Labeled After Birth Contribute to the Lipofibroblast Lineage but Not to the Smooth Muscle Cell Lineage

Using the previously generated *Fgf10*$^{Ki-v1/+}$ line, we demonstrated that FGF10^{Pos} cells labeled postnatally strongly

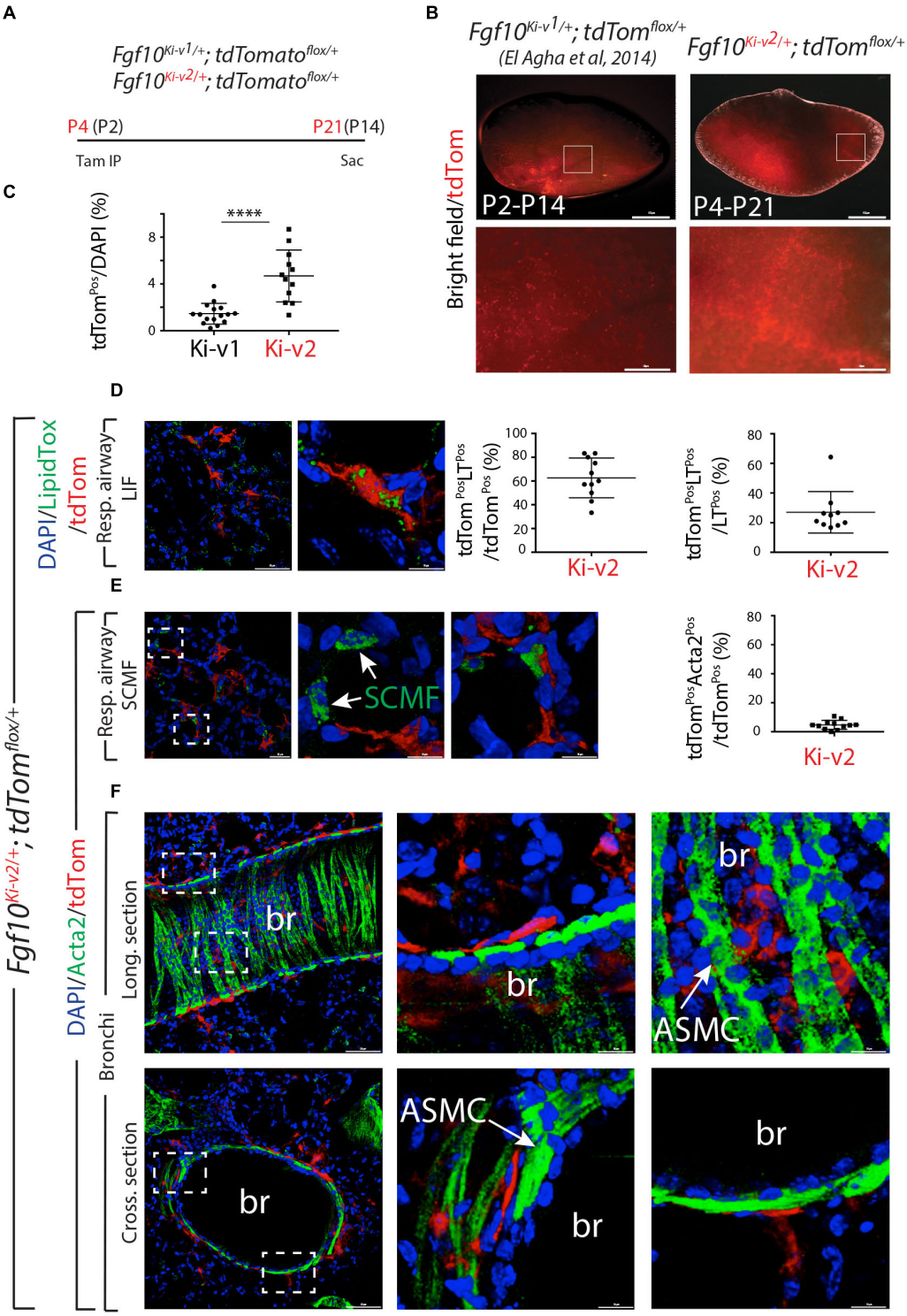

FIGURE 5 | FGF10^{Pos} cells labeled after birth do not contribute significantly to secondary crest myofibroblasts during alveologenesis. **(A)** FGF10^{Pos} cells in *Fgf10*$^{Ki\text{-}v2/+}$; *tdTomato*$^{flox/+}$ pups were labeled *in vivo* at P4 and analyzed at P21. We also used previously generated *Fgf10*$^{Ki\text{-}v1/+}$; *tdTomato*$^{flox/+}$ samples labeled between P2 and P14. **(B)** Whole-mount fluorescence images of *Fgf10*$^{Ki\text{-}v2/+}$; *tdTom*$^{flox/+}$ and *Fgf10*$^{Ki\text{-}v1/+}$; *tdTom*$^{flox/+}$ lungs showing more abundant labeled cells in *Fgf10*$^{Ki\text{-}v2/+}$ vs. *Fgf10*$^{Ki\text{-}v1/+}$ lungs. **(C)** ACTA2 IF on *Fgf10*$^{Ki\text{-}v2/+}$; *tdTom*$^{flox/+}$ lungs shows little contribution of FGF10^{Pos} cells to SCMF (ACTA2^{Pos}tdTom^{Pos}/ACTA2^{Pos}). **(D)** Quantification of tdTom^{Pos} cells. Br: bronchi. Scale bar in **(B)**: low magnification: 0.5 mm, High magnification: 50 μm. Scale bar in **(D)**: low magnification: 50 μm, High magnification: 10 μm. Scale bar in **(E)**: Llow magnification: 25 μm, High magnification: 10 μm. Scale bar in **(F)**: Low magnification: 50 μm, High magnification: 10 μm. ****$P \leq 0.0001$.

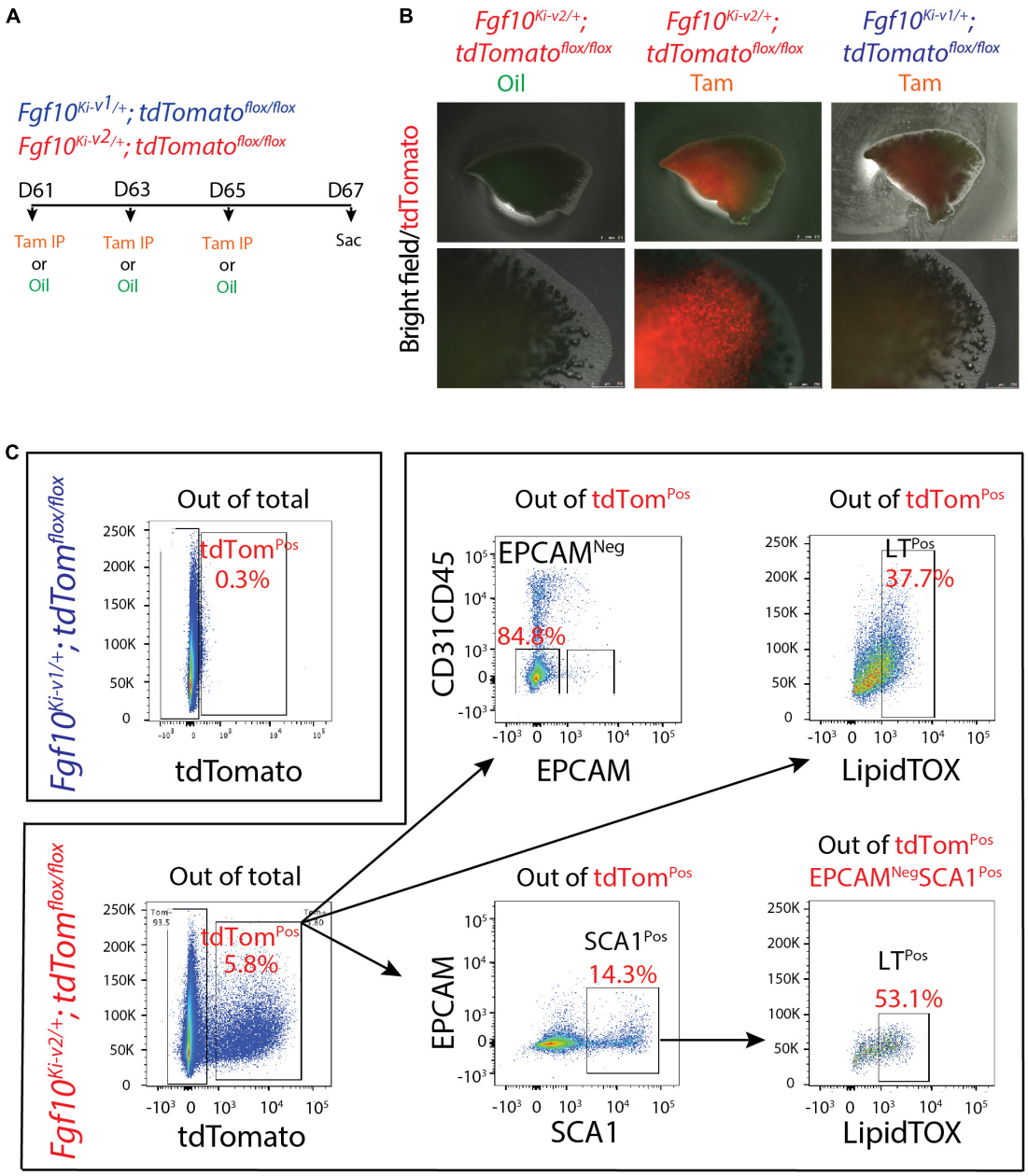

FIGURE 6 | *Fgf10*$^{Ki\text{-}v2/+}$; *tdTom*$^{flox/+}$ adult lungs display enhanced number of tdTom^{Pos} cells compared with to the *Fgf10*$^{Ki\text{-}v1/+}$; *tdTom*$^{flox/+}$ adult lungs. **(A)** 2-months-old; *Fgf10*$^{Ki\text{-}v1/+}$; *tdTom*$^{flox/+}$ and *Fgf10*$^{Ki\text{-}v2/+}$; *tdTom*$^{flox/+}$ mice received 3 Tam IPs or oil at P61, P63 and P65 and were sacrificed at P67. **(B)** Whole-mount fluorescence images of oil-treated *Fgf10*$^{Ki\text{-}v2/+}$; *tdTom*$^{flox/+}$, Tam-treated *Fgf10*$^{Ki\text{-}v2/+}$; *tdTom*$^{flox/+}$ *and* Tam-treated *Fgf10*$^{Ki\text{-}v1/+}$; *tdTom*$^{flox/+}$ lungs at P67. Higher magnification of the lungs are shown in the lower panel. **(C)** Flow cytometry analysis of *Fgf10*$^{Ki\text{-}v2/+}$; *tdTom*$^{flox/flox}$ lung homogenate. Scale bar in **(B)**: low magnification: 2.5 mm, High magnification: 0.75 mm.

contribute to the lipofibroblast (LIF) lineage but not the smooth muscle cell (SMC) lineage. In particular, they do not contribute in a major way to the ACTA2^{Pos} secondary crest myofibroblasts (SCMF) which are abundant during the first 2–3 weeks during alveologenesis which takes place from postnatal day 5 (P5) to -P28 (El Agha et al., 2014). To confirm this observation with the new *Fgf10*$^{Ki-v2/+}$ line, we labeled FGF10^{Pos} cells at P4 and examined the status of the labeled cells at P21, 1 week before the end of the alveologenesis phase (**Figure 5A**). Analysis of the whole lung by fluorescence stereomicroscopy indicated a much higher number of labeled cells in the *Fgf10*$^{Ki-v2}$; *tdTomato*$^{flox/+}$ lung compared with the *Fgf10*$^{Ki-v1}$; *tdTomato*$^{flox/+}$ lung (**Figure 5B**). Quantification of tdTom^{Pos} cells indicated that a higher percentile of tdTom^{Pos}/DAPI is observed on sections of *Fgf10*$^{Ki-v2}$; *tdTomato*$^{flox/+}$ vs. *Fgf10*$^{Ki-v1}$; *tdTomato*$^{flox/+}$ (4.7% ± 0.6% vs. 1.5% ± 0.2%, n = 2) thereby confirming the

fluorescence stereomicroscopy results (**Figure 5C**). LipidTOX staining of these lungs was used to visualize LIFs (**Figure 5D**). Quantification of this staining indicated that 62.6% ± 5.0% (n = 2) of the total tdTom^{Pos} are LT^{Pos} and that 27.0% ± 4.4% (n = 2) of the LT^{Pos} derive from tdTom^{Pos} cells. These data are in line with our results obtained with the previous *Fgf10*$^{Ki-v1/+}$ line. Immunofluorescence (IF) for ACTA2 on these lungs was also carried out (**Figures 5E,F**). First, we quantified the number of ACTA2^{Pos}/tdTom^{Pos} present in the respiratory airway (**Figure 5E**) and alveolar space (**Supplementary Figure 2**). ACTA2^{Pos} cells in the respiratory airway during alveologenesis mark secondary crest myofibroblasts (SCMF). We found 4.7% ± 0.9% (n = 2) tdTom^{Pos}ACTA2^{Pos}/tdTom^{Pos} indicating in our experimental conditions, a minimal commitment of the FGF10^{Pos} cells to the SCMF lineage. Second, we identified peribronchial tdTom^{Pos} cells both in longitudinal and cross sections of the bronchi (**Figure 5F**). Airway smooth muscle cells express ACTA2, display the typical bundle-like circular shape and are located in close proximity to the bronchial epithelium. tdTom^{Pos} cells are located close to ACTA2^{Pos}-ASMCs but are nevertheless negative for ACTA2. A similar observation was made for the perivascular tdTom^{Pos} cells (data not shown).

The New *Fgf10*$^{Ki-v2}$ Line Allows More Efficient Labeling of FGF10^{Pos} Cells in the Adult Lung Compared With the Previous *Fgf10*$^{Ki-v1}$ Line

Two months old *Fgf10*$^{K-v2/+}$; *tdTomato*$^{flox/flox}$ mice were treated with Tam IP or oil at day 1 (D61), 3 (D63), and 5(D65) and the lungs were collected at day 7 (D67) (**Figure 6A**). No fluorescent signal was observed in oil-treated *Fgf10*$^{K-v2/+}$; *tdTomato*$^{flox/flox}$ mice, indicating that the line is not leaky. By contrast, a solid signal was found in Tam-treated *Fgf10*$^{Ki-v2/+}$; *tdTomato*$^{flox/flox}$ lungs. A weak signal was detected in Tam-treated *Fgf10*$^{Ki-v1/+}$; *tdTomato*$^{flox/flox}$ lungs as described in a previously study (El Agha et al., 2014; **Figure 6B**). Flow cytometry analysis was also conducted to quantify the total number of tdTom^{Pos} cells in both conditions as well as their identity (El Agha et al., 2014; **Figure 6C**). Only 0.3% tdTom^{Pos} cells over total number of cells were detected in *Fgf10*$^{Ki-v1/+}$; *tdTomato*$^{flox/flox}$. This number is in line with the previously reported 0.1% (El Agha et al., 2014) and confirms that the *Fgf10*$^{Ki-v1/+}$ line is not efficient to target FGF10^{Pos} cells in the adult lung. By contrast, we observed 5.8% of tdTom^{Pos} cells over total cells in *Fgf10*$^{Ki-v2/+}$ lungs. Further analysis showed that these cells were mostly CD31^{Neg}CD45^{Neg}EPCAM^{Neg} cells (85%) identifying them as resident mesenchymal cells (rMC). 14.3% of the tdTom^{Pos} cells were also SCA1^{High}, a functional marker of the rMC subpopulation capable of sustaining the self-renewal of AT2 stem cells in the alveolosphere organoid model (Taghizadeh et al., 2021). Of note 53% of the SCA1^{High} were LipidTOX^{Pos} identifying them as lipofibroblasts (LIFs). Altogether these results suggest that tdTom^{Pos} cells are heterogeneous and comprise a significant percentile of LIFs as previously reported (El Agha et al., 2014).

The 3′UTR Region of the *Fgf10* Gene Contains Many Key Transcription Factor Binding Sites

The decrease in *Fgf10* expression in *Fg10*$^{Ki-v2}$ mice (**Figure 2D**) suggested that important transcription factor binding sites (TFBS) were impacted by the genetic manipulation in the 3′UTR of the *Fgf10* gene. We determined the identity of TFBS located at proximity of the 3′UTR of the *Fgf10* gene using an online TFBS prediction tool. We compared these TFBS with previously published TF expressed in the lung

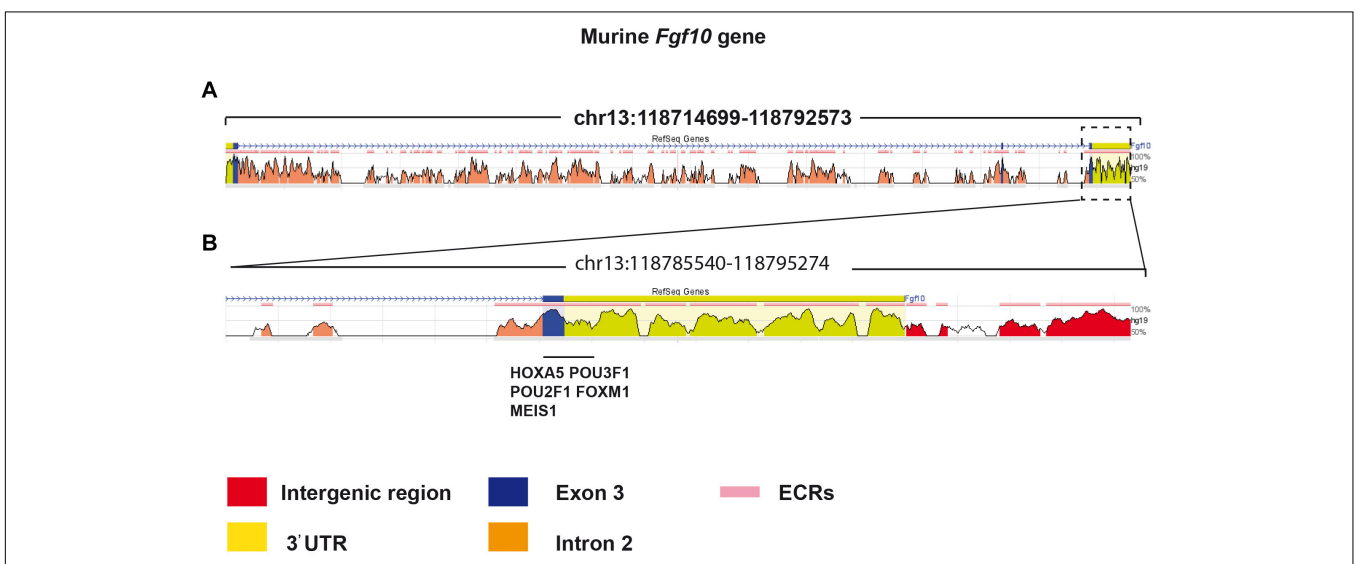

FIGURE 7 | Bioinformatic analysis identified potential transcriptional factors binding sites in the 3′UTR of Exon 3. **(A)** The murine *Fgf10* gene is made of 3 exons. **(B)** High magnification of Exon 3 and the associated 3′UTR. Several putative important transcriptional factor binding sites were found in this region.

mesenchyme (Herriges et al., 2012). We found several key TFBS matching the previously reported TF expression in the lung such as *Hoxa5*, *Pou3f1*, *Pou2f1*, *Foxm1,* and *Meis1* (**Figure 7**). Interestingly, all these transcription factors appear to play a functional role in the lung. Mutant *Hoxa5* mice display decreased surfactant production and disrupted tracheal cartilage, leading to respiratory distress and low survival rate at birth (Aubin et al., 1997; Kinkead et al., 2004; Mandeville et al., 2006). *Pou3F1*, also known as *Oct6* is primarily expressed in neural cells. *Pou3F1* deletion caused lethality at birth due to respiratory distress (Bermingham et al., 1996, 2002; Ghazvini et al., 2002). The deletion of the other related transcription factor, *Pou2f1*, is associated with smaller body size of embryos and full lethality at birth (Wang et al., 2004). *Foxm1* expression plays a crucial role in both the epithelium and the mesenchyme. Conditional inactivation of *Foxm1* in the lung mesenchyme leads to increased smooth muscles around the proximal airways and reduced pulmonary microvasculature (Kim et al., 2005). In the lung epithelium, *Foxm1* conditional inactivation causes reduction in sacculation and delayed differentiation of alveolar epithelial type I cells (Kalin et al., 2008). Knockout of *Meis1* caused lethality during the embryonic stage around E14.5 due to microvascular and hematopoietic defects in the lung (Hisa et al., 2004).

DISCUSSION

FGF10 is an essential morphogen underlying the developmental process of multiple organs including the lung. FGF10 signaling is also crucial during homeostasis and in the process of injury/repair in the adult lung. *FGF10* dysregulation in human has been implicated in some major respiratory diseases, such as bronchopulmonary dysplasia (BPD), Idiopathic pulmonary fibrosis (IPF) and chronic obstructive pulmonary disease (COPD) (Yuan et al., 2018). For example, increased FGF10 expression level in IPF patients has been found (El Agha et al., 2017). However, FGF10 expression is inversely correlated to the disease progression with higher levels in stable IPF vs. lower level in end-stage IPF. Higher FGF10 expression in the early, stable stage of IPF is most likely correlated with the repair process. Insufficient FGF10 level in prematurely newborn infants is associated with arrested lung development at the saccular stage (Prince, 2018). *Fgf10* deficiency in a newborn mouse model of hyperoxia-induced BPD led to drastic increase in lethality associated with abnormal alveolar epithelial type 2 (AT2) cell differentiation as well as surfactant production (Chao et al., 2017).

FGF10 also performs a key function for the repair of the bronchial epithelium after injury (Volckaert et al., 2011). Our knowledge about the sources of FGF10 in this context has been evolving. FGF10 was first described to be expressed by airway smooth muscle cells (ASMCs) (Volckaert et al., 2011), whereas more recent work identified a peribronchiolar mesenchymal population capable of producing FGF10 during the repair process, which is not derived from the ASMCs (Moiseenko et al., 2020).

In COPD, the conducting airway epithelium undergoes massive remodeling causing an irreversible airway obstruction (Decramer et al., 2012). Interestingly, we have reported that the FGF10-HIPPO epithelial mesenchymal crosstalk also maintains and recruits lung basal stem cells in the conducting airways (Volckaert et al., 2017). While transient *Fgf10* expression by ASMCs is critical for proper airway epithelial regeneration in response to injury, sustained FGF10 secretion by the ASMC niche, in response to chronic ILK/HIPPO inactivation, results in pathological changes in airway architecture resembling the abnormalities seen in COPD. The inhibition of FGF10/FGFR2b signaling may therefore be an interesting approach to treat chronic obstructive airway lung diseases. Conversely, the opposite situation might occur in the respiratory airways in that destruction of the alveolar compartments resulting in emphysema may be due to insufficient FGF signaling. Interestingly, recombinant FGF7 has been reported to induce *de novo*-alveologenesis in the elastase model of emphysema in mice (Yildirim et al., 2010).

The previous *Fgf10*$^{Ki-V1}$ model was mainly used to trace the FGF10^{Pos} cells during embryonic development. A near complete loss of the labeling capacity of FGF10^{Pos} cells during postnatal stages limited its utilization in the analysis of their cell fate in adult lung homeostasis and during the process of injury/repair. In order to overcome the limitations of the *Fgf10*$^{Ki-V1}$ line, we generated and validated this new knock-in *Fgf10*$^{Ki-V2}$ line. Upon crossing with a *tdTomato* reporter line, we demonstrated that the tdTomato expression domain faithfully reproduced the previously reported the *Fgf10* expression pattern (El Agha et al., 2012), and a more robust labeling of FGF10^{Pos} cells was achieved in the postnatal stages in spite of a mismatch between *Cre* and *Fgf10* expression, which could be explained by the disruption of critical TFBS located in the 3′UTR of the *Fgf10* gene. Therefore, this line will be a valuable tool to further define mesenchymal cell populations in the adult lung contributing to the repair process after injury. Combined crosses with existing or novel Dre-ERT2 recombinase driver lines may allow to capture subpopulations of FGF10^{Pos} cells/lineages based on the expression of two markers (Jones et al., 2019). The main FGF10^{Pos} subpopulation is represented by the lipid-containing alveolar interstitial fibroblasts (lipofibroblasts or LIFs). More and more studies have acknowledged LIFs as an essential piece of the AT2 stem cell niche in the rodent lungs. Despite the fact that LIFs were initially believed to only assist AT2 cells in surfactant production during neonatal life, recent studies have shown that these cells are important for self-renewal and differentiation of AT2 stem cells during adulthood (Barkauskas et al., 2013). In spite of the increasing interests in lipofibroblast biology, little is known about their cellular origin or the molecular pathways that control their formation during embryonic development. We have shown that in the developing mouse lung, FGF10^{Pos} cells labeled at E11.5 or E15.5 are progenitors for LIFs (El Agha et al., 2014). In addition, FGF10 is also essential for the differentiation of these progenitors into the LIF lineage (Al Alam et al., 2015). We have also reported the existence of FGF10^{Pos}-LIF as well as FGF10^{Neg}-LIFs

(Al Alam et al., 2015). The difference between these two populations is still unclear and will require further studies. In the context of bleomycin-induced lung fibrosis, *in vivo* lineage tracing indicates that LIFs transdifferentiate into activated myofibroblast during fibrosis formation and that a significant proportion of the labeled activated myofibroblasts transdifferentiate back to LIFs during fibrosis resolution (El Agha et al., 2017).

In conclusion, we have successfully generated a new $Fgf10^{Cre-ERT2}$ line with enhanced labeling efficiency of $FGF10^{Pos}$ cells postnatally. This line, which displays normal expression of *Fgf10* in $Fgf10^{Cre-ERT2/+}$, avoids many developmental defects linked to deficient *Fgf10* expression. Therefore, it paves the way for performing cell-autonomous based studies to investigate the role of these $FGF10^{Pos}$ cells as well as associated signaling pathways during lung development and disease.

DATA AVAILABILITY STATEMENT

The original contributions presented in the study are included in the article/**Supplementary Material**, further inquiries can be directed to the corresponding author/s.

ETHICS STATEMENT

Animal experiments were reviewed and approved by the Regierungspraesidium Giessen (approval number RP GI/47-2019).

AUTHOR CONTRIBUTIONS

XC, ST, AIV-A, and LC performed the experiments. SH, CC, and J-SZ contributed to methodology. EEA and SB conceived the study. XC and SB wrote the manuscript. J-SZ, EEA, and SB edited the manuscript. All authors contributed to the article and approved the submitted version.

FUNDING

EEA acknowledges the support of the Institute for Lung Health (ILH), the German Research Foundation (DFG; EL 931/4-1, KFO309 P7, and SFB CRC1213-project A04), the Cardio-Pulmonary Institute (CPI, EXC 2026, Project ID: 390649896) and the German Center for Lung Research (DZL). SB was supported by the CPI and by grants from the DFG (BE4443/1-1, BE4443/4-1, BE4443/6-1, KFO309 P7, and SFB1213-projects A02 and A04). CC was supported by the Interventional Pulmonary Key Laboratory of Zhejiang Province, the Interventional Pulmonology Key Laboratory of Wenzhou City, the Interventional Pulmonology Innovation Subject of Zhejiang Province, the National Nature Science Foundation of China (81570075 and 81770074), Zhejiang Provincial Natural Science Foundation (LZ15H010001), Zhejiang Provincial Science Technology Department Foundation (2015103253), and the National Key Research and Development Program of China (2016YFC1304000).

SUPPLEMENTARY MATERIAL

The Supplementary Material for this article can be found online at: https://www.frontiersin.org/articles/10.3389/fcell.2021.671841/full#supplementary-material

Supplementary Figure 1 | Comparative *Fgf10* expression in $Fgf10^{+/+}$ *and* $Fgf10^{Ki-v2/+}$ *lungs vs.* $Fgf10^{Ki-v2/Ki-v2}$ embryos at E15.5. qPCR was used to determine *Fgf10* expression.

Supplementary Figure 2 | Co-expression of ACTA2 and tdTomato in $FGF10^{Pos}$ cells. $Fgf10^{Ki-v1}$; $tdTomato^{flox/+}$ pups received one injection of Tam subcutaneously at P2 and were analyzed at P14.

REFERENCES

Al Alam, D., El Agha, E., Sakurai, R., Kheirollahi, V., Moiseenko, A., Danopoulos, S., et al. (2015). Evidence for the involvement of fibroblast growth factor 10 in lipofibroblast formation during embryonic lung development. *Development* 142, 4139–4150. doi: 10.1242/dev.109173

Aubin, J., Lemieux, M., Tremblay, M., Bérard, J., and Jeannotte, L. (1997). Early postnatal lethality in Hoxa-5 mutant mice is attributable to respiratory tract defects. *Dev. Biol.* 192, 432–445. doi: 10.1006/dbio.1997.8746

Barkauskas, C. E., Cronce, M. J., Rackley, C. R., Bowie, E. J., Keene, D. R., Stripp, B. R., et al. (2013). Type 2 alveolar cells are stem cells in adult lung. *J. Clin. Invest.* 123, 3025–3036.

Bermingham, J. R. Jr., Scherer, S. S., O'Connell, S., Arroyo, E., Kalla, K. A., Powell, F. L., et al. (1996). Tst-1/Oct-6/SCIP regulates a unique step in peripheral myelination and is required for normal respiration. *Genes Dev.* 10, 1751–1762. doi: 10.1101/gad.10.14.1751

Bermingham, J. R. Jr., Shumas, S., Whisenhunt, T., Sirkowski, E. E., O'Connell, S., Scherer, S. S., et al. (2002). Identification of genes that are downregulated in the absence of the POU domain transcription factor pou3f1 (Oct-6. Tst-1, SCIP) in sciatic nerve. *J. Neurosci.* 22, 10217–10231. doi: 10.1523/jneurosci.22-23-10217.2002

Chao, C. M., Yahya, F., Moiseenko, A., Tiozzo, C., Shrestha, A., Ahmadvand, N., et al. (2017). Fgf10 deficiency is causative for lethality in a mouse model of bronchopulmonary dysplasia. *J. Pathol.* 241, 91–103.

Danopoulos, S., Parsa, S., Al Alam, D., Tabatabai, R., Baptista, S., Tiozzo, C., et al. (2013). Transient Inhibition of FGFR2b-ligands signaling leads to irreversible loss of cellular beta-catenin organization and signaling in AER during mouse limb development. *PLoS One* 8:e76248. doi: 10.1371/journal.pone.0076248

Decramer, M., Janssens, W., and Miravitlles, M. (2012). Chronic obstructive pulmonary disease. *Lancet* 379, 1341–1351.

El Agha, E., Al Alam, D., Carraro, G., MacKenzie, B., Goth, K., De Langhe, S. P., et al. (2012). Characterization of a novel fibroblast growth factor 10 (Fgf10) knock-in mouse line to target mesenchymal progenitors during embryonic development. *PLoS One* 7:e38452. doi: 10.1371/journal.pone.0038452

El Agha, E., Herold, S., Al Alam, D., Quantius, J., MacKenzie, B., Carraro, G., et al. (2014). Fgf10-positive cells represent a progenitor cell population during lung development and postnatally. *Development* 141, 296–306. doi: 10.1242/dev.099747

El Agha, E., Moiseenko, A., Kheirollahi, V., De Langhe, S., Crnkovic, S., Kwapiszewska, G., et al. (2017). Two-way conversion between lipogenic and myogenic fibroblastic phenotypes marks the progression and resolution of lung fibrosis. *Cell Stem Cell* 20, 261.e3–273.e3.

Feil, R., Wagner, J., Metzger, D., and Chambon, P. (1997). Regulation of Cre recombinase activity by mutated estrogen receptor ligand-binding domains. *Biochem. Biophys. Res. Commun.* 237, 752–757. doi: 10.1006/bbrc.1997.7124

Ghazvini, M., Mandemakers, W., Jaegle, M., Piirsoo, M., Driegen, S., Koutsourakis, M., et al. (2002). A cell type-specific allele of the POU gene Oct-6 reveals Schwann cell autonomous function in nerve development and regeneration. *Embo J.* 21, 4612–4620. doi: 10.1093/emboj/cdf475

Gupte, V. V., Ramasamy, S. K., Reddy, R., Lee, J., Weinreb, P. H., Violette, S. M., et al. (2009). Overexpression of fibroblast growth factor-10 during both inflammatory and fibrotic phases attenuates bleomycin-induced pulmonary fibrosis in mice. *Am. J. Respir. Crit. Care Med.* 180, 424–436. doi: 10.1164/rccm.200811-1794oc

Herriges, J. C., Yi, L., Hines, E. A., Harvey, J. F., Xu, G., Gray, P. A., et al. (2012). Genome-scale study of transcription factor expression in the branching mouse lung. *Dev. Dyn.* 241, 1432–1453. doi: 10.1002/dvdy.23823

Hisa, T., Spence, S. E., Rachel, R. A., Fujita, M., Nakamura, T., Ward, J. M., et al. (2004). Hematopoietic, angiogenic and eye defects in Meis1 mutant animals. *Embo J.* 23, 450–459. doi: 10.1038/sj.emboj.7600038

Jaskoll, T., Abichaker, G., Witcher, D., Sala, F. G., Bellusci, S., Hajihosseini, M. K., et al. (2005). FGF10/FGFR2b signaling plays essential roles during in vivo embryonic submandibular salivary gland morphogenesis. *BMC Dev. Biol.* 5:11. doi: 10.1186/1471-213X-5-11

Jones, M., Zhang, J.-S., and Bellusci, S. (2019). Bronchioalveolar stem cells vindicated! *Biotarget* 3:4. doi: 10.21037/biotarget.2019.04.01

Jones, M. R., Chong, L., and Bellusci, S. (2020). Fgf10/Fgfr2b signaling orchestrates the symphony of molecular, cellular, and physical processes required for harmonious airway branching morphogenesis. *Front. Cell Dev. Biol.* 8:620667. doi: 10.3389/fcell.2020.620667

Kalin, T. V., Wang, I. C., Meliton, L., Zhang, Y., Wert, S. E., Ren, X., et al. (2008). Forkhead Box m1 transcription factor is required for perinatal lung function. *Proc. Natl. Acad. Sci. U.S.A.* 105, 19330–19335. doi: 10.1073/pnas.0806748105

Kim, I. M., Ramakrishna, S., Gusarova, G. A., Yoder, H. M., Costa, R. H., and Kalinichenko, V. V. (2005). The forkhead box m1 transcription factor is essential for embryonic development of pulmonary vasculature. *J. Biol. Chem.* 280, 22278–22286. doi: 10.1074/jbc.m500936200

Kinkead, R., LeBlanc, M., Gulemetova, R., Lalancette-Hébert, M., Lemieux, M., Mandeville, I., et al. (2004). Respiratory adaptations to lung morphological defects in adult mice lacking Hoxa5 gene function. *Pediatr. Res.* 56, 553–562. doi: 10.1203/01.pdr.0000139427.26083.3d

Lv, Y. Q., Wu, J., Li, X. K., Zhang, J. S., and Bellusci, S. (2019). Role of FGF10/FGFR2b signaling in mouse digestive tract development, repair and regeneration following injury. *Fron.t Cell Dev. Biol.* 7:326.

Mailleux, A. A., Kelly, R., Veltmaat, J. M., De Langhe, S. P., Zaffran, S., Thiery, J. P., et al. (2005). Fgf10 expression identifies parabronchial smooth muscle cell progenitors and is required for their entry into the smooth muscle cell lineage. *Development* 132, 2157–2166. doi: 10.1242/dev.01795

Mailleux, A. A., Spencer-Dene, B., Dillon, C., Ndiaye, D., Savona-Baron, C., Itoh, N., et al. (2002). Role of FGF10/FGFR2b signaling during mammary gland development in the mouse embryo. *Development* 129, 53–60.

Mandeville, I., Aubin, J., LeBlanc, M., Lalancette-Hébert, M., Janelle, M. F., Tremblay, G. M., et al. (2006). Impact of the loss of Hoxa5 function on lung alveogenesis. *Am. J. Pathol.* 169, 1312–1327. doi: 10.2353/ajpath.2006.051333

Min, H., Danilenko, D. M., Scully, S. A., Bolon, B., Ring, B. D., Tarpley, J. E., et al. (1998). Fgf-10 is required for both limb and lung development and exhibits striking functional similarity to Drosophila branchless. *Genes Dev.* 12, 3156–3161. doi: 10.1101/gad.12.20.3156

Moiseenko, A., Vazquez-Armendariz, A. I., Kheirollahi, V., Chu, X., Tata, A., Rivetti, S., et al. (2020). Identification of a repair-supportive mesenchymal cell population during airway epithelial regeneration. *Cell Rep.* 33:108549. doi: 10.1016/j.celrep.2020.108549

Ohuchi, H., Hori, Y., Yamasaki, M., Harada, H., Sekine, K., Kato, S., et al. (2000). FGF10 acts as a major ligand for FGF receptor 2 IIIb in mouse multi-organ development. *Biochem. Biophys. Res. Commun.* 277, 643–649. doi: 10.1006/bbrc.2000.3721

Ornitz, D. M., and Itoh, N. (2001). Fibroblast growth factors. *Genome Biol.* 2:Reviews3005.

Parsa, S., Kuremoto, K.-I., Seidel, K., Tabatabai, R., MacKenzie, B., Yamaza, T., et al. (2010). Signaling by FGFR2b controls the regenerative capacity of adult mouse incisors. *Development* 137, 3743–3752. doi: 10.1242/dev.051672

Parsa, S., Ramasamy, S. K., De Langhe, S., Gupte, V. V., Haigh, J. J., Medina, D., et al. (2008). Terminal end bud maintenance in mammary gland is dependent upon FGFR2b signaling. *Dev. Biol.* 317, 121–131. doi: 10.1016/j.ydbio.2008.02.014

Prince, L. S. (2018). FGF10 and human lung disease across the life spectrum. *Front. Genet.* 9:517. doi: 10.3389/fgene.2018.00517

Sala, F. G., Del Moral, P.-M., Tiozzo, C., Alam, D. A., Warburton, D., Grikscheit, T., et al. (2011). FGF10 controls the patterning of the tracheal cartilage rings via Shh. *Development* 138, 273–282. doi: 10.1242/dev.051680

Sekine, K., Ohuchi, H., Fujiwara, M., Yamasaki, M., Yoshizawa, T., Sato, T., et al. (1999). Fgf10 is essential for limb and lung formation. *Nat. Genet.* 21, 138–141. doi: 10.1038/5096

Taghizadeh, S., Heiner, M., Wilhelm, J., Herold, S., Chen, C., Zhang, J., et al. (2021). Characterization in mice of the stromal niche maintaining AT2 stem cell self-renewal in homeostasis and disease. *bioRxiv* [Preprint]. doi: 10.1101/2021.01.28.428090

Volckaert, T., Dill, E., Campbell, A., Tiozzo, C., Majka, S., Bellusci, S., et al. (2011). Parabronchial smooth muscle constitutes an airway epithelial stem cell niche in the mouse lung after injury. *J. Clin. Invest.* 121, 4409–4419. doi: 10.1172/jci58097

Volckaert, T., Yuan, T., Chao, C. M., Bell, H., Sitaula, A., Szimmtenings, L., et al. (2017). Fgf10-hippo epithelial-mesenchymal crosstalk maintains and recruits lung basal stem cells. *Dev. Cell* 43, 48.e5–59.e5.

Wang, V. E., Schmidt, T., Chen, J., Sharp, P. A., and Tantin, D. (2004). Embryonic lethality, decreased erythropoiesis, and defective octamer-dependent promoter activation in Oct-1-deficient mice. *Mol. Cell Biol.* 24, 1022–1032. doi: 10.1128/mcb.24.3.1022-1032.2004

Yildirim, A. O., Muyal, V., John, G., Müller, B., Seifart, C., Kasper, M., et al. (2010). Palifermin induces alveolar maintenance programs in emphysematous mice. *Am. J. Respir. Crit. Care Med.* 181, 705–717. doi: 10.1164/rccm.200804-573oc

Yuan, T., Volckaert, T., Chanda, D., Thannickal, V. J., and De Langhe, S. P. (2018). Fgf10 signaling in lung development, homeostasis, disease, and repair after injury. *Front. Genet.* 9:418. doi: 10.3389/fgene.2018.00418

Zhang, Y., Fons, J. M., Hajihosseini, M. K., Zhang, T., and Tucker, A. S. (2020). An essential requirement for Fgf10 in pinna extension sheds light on auricle defects in LADD syndrome. *Front. Cell Dev. Biol.* 8:609643. doi: 10.3389/fcell.2020.609643

Conflict of Interest: The authors declare that the research was conducted in the absence of any commercial or financial relationships that could be construed as a potential conflict of interest.

frontiers in Cell and Developmental Biology

REVIEW
published: 14 May 2021
doi: 10.3389/fcell.2021.672935

The Multifunctional Contribution of FGF Signaling to Cardiac Development, Homeostasis, Disease and Repair

Farhad Khosravi[1], Negah Ahmadvand[2], Saverio Bellusci[2] and Heinrich Sauer[1]*

[1] Department of Physiology, Justus Liebig University Giessen, Giessen, Germany, [2] Cardio-Pulmonary Institute, Justus Liebig University Giessen, Giessen, Germany

OPEN ACCESS

Edited by:
Jangho Kim,
Chonnam National University,
South Korea

Reviewed by:
Felix B. Engel,
University Hospital Erlangen, Germany
Myung Chul Lee,
Harvard Medical School,
United States

***Correspondence:**
Farhad Khosravi
farhad.khosravi@physiologie.med.uni-giessen.de

Specialty section:
This article was submitted to Stem Cell Research, a section of the journal Frontiers in Cell and Developmental Biology

Received: *26 February 2021*
Accepted: *20 April 2021*
Published: *14 May 2021*

Citation:
Khosravi F, Ahmadvand N, Bellusci S and Sauer H (2021) The Multifunctional Contribution of FGF Signaling to Cardiac Development, Homeostasis, Disease and Repair. Front. Cell Dev. Biol. 9:672935. doi: 10.3389/fcell.2021.672935

The current focus on cardiovascular research reflects society's concerns regarding the alarming incidence of cardiac-related diseases and mortality in the industrialized world and, notably, an urgent need to combat them by more efficient therapies. To pursue these therapeutic approaches, a comprehensive understanding of the mechanism of action for multifunctional fibroblast growth factor (FGF) signaling in the biology of the heart is a matter of high importance. The roles of FGFs in heart development range from outflow tract formation to the proliferation of cardiomyocytes and the formation of heart chambers. In the context of cardiac regeneration, FGFs 1, 2, 9, 16, 19, and 21 mediate adaptive responses including restoration of cardiac contracting rate after myocardial infarction and reduction of myocardial infarct size. However, cardiac complications in human diseases are correlated with pathogenic effects of FGF ligands and/or FGF signaling impairment. FGFs 2 and 23 are involved in maladaptive responses such as cardiac hypertrophic, fibrotic responses and heart failure. Among FGFs with known causative (FGFs 2, 21, and 23) or protective (FGFs 2, 15/19, 16, and 21) roles in cardiac diseases, FGFs 15/19, 21, and 23 display diagnostic potential. The effective role of FGFs on the induction of progenitor stem cells to cardiac cells during development has been employed to boost the limited capacity of postnatal cardiac repair. To renew or replenish damaged cardiomyocytes, FGFs 1, 2, 10, and 16 were tested in (induced-) pluripotent stem cell-based approaches and for stimulation of cell cycle re-entry in adult cardiomyocytes. This review will shed light on the wide range of beneficiary and detrimental actions mediated by FGF ligands and their receptors in the heart, which may open new therapeutic avenues for ameliorating cardiac complications.

Keywords: FGF (fibroblast growth factor), heart development, cardiac regeneration, cardiac diseases, cardiac adaptive and maladaptive responses, stem cells

INTRODUCTION

The ever-increasing threat of cardiac diseases accompanied by the modern, unhealthy lifestyle has prompted investigations on heart pathophysiology in order to develop novel therapeutic theories and options alleviating cardiac pathogenic symptoms and restoring physiological function. This progress, at least in part, profits from the understanding of cell signaling pathways governing embryonic cardiac development and cardiac physiology and pathophysiology. In the last two decades, cellular signaling networks in the heart, including fibroblast growth factors (FGFs) and their interplay with other growth factors and signaling contributors such as IGF1/2, VEGF, BMPs [as members of transforming growth factor-β (TGF-β) superfamily], Wnts, Notch and erythropoietin have been investigated in detail (Bruneau, 2013; Mascheck et al., 2015; Meganathan et al., 2015; Wilsbacher and McNally, 2016). Intriguingly, regardless of a 30–60% amino acid sequence homology between individual FGF family members, they contribute to distinct, and even contradictory actions, being either protective or pathogenic. Our current knowledge of FGF-dependent cardiac physiology is mainly based on loss- and gain-of-function studies provided through genetically modified animal models (transgenic or knockout), where the expression of FGFs and/or FGF receptors (FGFR) are impaired (Itoh et al., 2016). In addition, embryonic stem cells (ESCs) and induced pluripotent stem cells (iPSCs) serve as *in vitro* models for investigations on the implication of ligand–receptor interactions in cardiac cell differentiation (Kawai et al., 2004; Chan et al., 2010; Yamasaki et al., 2013; Mascheck et al., 2015).

FGF SUPERFAMILY

Fibroblast growth factors, consisting of a family of 22 identified members of pleiotropic proteins in human and mouse, mediate pivotal functions in the heart, ranging from development to homeostasis and disease. Since FGFs are among cardiac secreted proteins required for heart physiological and pathological responses, they are considered cardiomyokines (Doroudgar and Glembotski, 2011; Itoh et al., 2016). Based on a phylogenetic analysis, FGFs are categorized into 7 subfamilies, which are either intracellular or secreted factors with autocrine, paracrine, and/or endocrine functions (Ornitz and Itoh, 2015). The intracellular FGFs act in an intracrine manner and include members of the FGF11 subfamily (FGFs 11, 12, 13, and 14; Wang et al., 2011).

MECHANISM OF ACTION FOR SECRETED FGFS

Secreted FGF ligands form complex structures with cofactors (also termed coreceptors) and FGFRs enabling them to regulate cell signaling and mediate a wide variety of functions. These FGF members serve as ligands through specific interaction with one of the seven alternatively spliced tyrosine kinase receptors (FGFRs 1b, 1c, 2b, 2c, 3b, 3c, and 4) which are expressed on the cell surface and are encoded from four genes (*FGFR1-4*; Zhang et al., 2006). Binding to FGFRs is modulated by extracellular cofactors such as Klothos (in the endocrine subfamily of FGF 15/19) and heparin/heparan sulfates (in autocrine/paracrine members of the FGF 1, 4, 7, 8, and 9 subfamilies; Rapraeger et al., 1991; Goetz et al., 2012; Itoh et al., 2015). Cofactors (such as heparan sulfate) mediate the formation of a complex between FGF and FGFR, and this complex activates FGFR dimerization and underlying cell signaling cascades, including phosphoinositide 3-kinase (PI3K)/serine/threonine protein kinase B (AKT), Ras/mitogen-activated protein kinase (MAPK), signal transducer and activator of transcription (STAT), and phospholipase C (PLC)γ (Itoh et al., 2016).

In the characterization of FGF superfamily member effects, a putative redundancy in the function of distinct FGF ligands (e.g., FGFs 3 and 8 with FGF10) and receptors (e.g., between FGFR1c and 2c in interaction with FGF9 subfamily) in the process of heart development and the adult phase needs to be considered (Lavine et al., 2005; Marguerie et al., 2006; Watanabe et al., 2010; Urness et al., 2011; Krejci et al., 2016).

FGF SIGNALING IN HEART DEVELOPMENT

In the early stages of cardiac development, FGF signaling plays a central role for normal morphogenesis through profound effects on the second heart field (SHF) and the cardiac neuronal crest (CNC) cells which determine the outflow tract (OFT) formation (Hubert et al., 2018). Specifically, FGFs 2, 3, 4, 8, 10, 16, and 20 contribute to the communication between and within SHF cardiac progenitor stem cells, and this modulates the proliferation of SHF progenitor cells together with myocardial specification and finally the development of OFT (**Table 1**; Park et al., 2008; Felker et al., 2018). In the late phases of cardiac development, the myocardium grows and remodels coinciding with a proliferation shift from SHF progenitor cells to cardiomyocytes. These lead to the formation of ventricular and arterial heart chambers. FGF ligands were reported to be autocrinally or paracrinally involved in the modulation of fetal cardiomyocyte proliferation. FGFs 2, 4, 7, 8, 9, 10, 15/19 also appear to be involved in these cardiac morphologic events (**Table 1**).

Differential Expression of FGFs in Cardiac Development

In the early phase of heart development, FGF members are differentially expressed in distinct anatomical regions. For instance, *Fgf10* is expressed in the pharyngeal mesoderm [between embryonic day (E.) 8.5 and E.10.5], and therefore is known as an exclusive marker of SHF (Kelly et al., 2001). The expression of *Fgf8* is detectable at E.9.5 in the adjacent pharyngeal endoderm and ectoderm in addition to the SHF (Mesbah et al., 2012). FGF3 (between E.8.0 and E.10.0) is present in the pharyngeal endoderm. *Fgf3* is also expressed at E8.0 in the

TABLE 1 | Roles of secreted FGFs in heart development.

FGF ligands	Functional or structural effects of FGFs in heart development	References
FGF1	• Epicardial epithelial-mesenchymal transition (EMT) and coronary vasculogenesis • Inducer of angiogenesis	• Morabito et al., 2001 • Mori et al., 2013
FGF2	• Differentiation of stem cells to SHF progenitors, later generation of cardiac fibroblasts • Maintenance of pluripotency • Differentiation of cardiomyocytes	• Zhang et al., 2019 • Taelman et al., 2019 • Kawai et al., 2004; Yamasaki et al., 2013
	• Epicardial EMT and coronary vasculogenesis • Inducer of angiogenesis	• Morabito et al., 2001 • Sauer et al., 2013; Mori et al., 2017
FGF3	• Heart tube extension in SHF and OFT development	• Cohen et al., 2007; Urness et al., 2011
FGF4	• Proper left-right patterning of cardiac laterality	• Sempou et al., 2018; Guzzetta et al., 2020
	• Cardiac valve leaflet formation maturation • Heartbeat synchronization via effects on of cardiomyocytes and their aggregation with cardiac fibroblasts	• Sugi et al., 2003 • Jang et al., 2020
FGF7	• Heart wall thickness • Epicardial EMT and coronary vasculogenesis	• Vega-Hernández et al., 2011 • Morabito et al., 2001
FGF8	• Proliferation of SHF progenitor cells and arterial pole development • Cardiac loop formation and migratory CNC survival • OFT alignment, formation and septation • Anterior heart field development • Sufficient recruitment of SHF and neural crest cells for OFT remodeling • Proper left–right patterning of cardiac laterality	• Watanabe et al., 2010 • Abu-Issa et al., 2002 • Zhang R. et al., 2015 • Ilagan et al., 2006 • Zhang R. et al., 2015 • Sempou et al., 2018; Guzzetta et al., 2020
FGF9	• Cardiomyocyte differentiation and proliferation in the myocardium • Cardiac size and proliferation rate • Proliferative effect on cardiac fibroblasts • Coronary vessel development	• Lavine et al., 2005 • Lavine et al., 2005 • Jennbacken et al., 2019 • Lavine et al., 2006
FGF10	• Cardiomyocyte differentiation • Exclusive marker of SHF • SHF progenitor cell proliferation and arterial pole development • Heart tube extension	• Chan et al., 2010 • Cohen et al., 2007 • Watanabe et al., 2010 • Urness et al., 2011
	• Cardiomyocyte proliferation modulation especially in fetal right ventricle • Ventricle morphology • Cell migration toward compact myocardium • Cardiac wall thickness	• Rochais et al., 2014 • Rochais et al., 2014 • Vega-Hernández et al., 2011 • Vega-Hernández et al., 2011
FGF15/19	• Normal OFT formation and aorta alignment	• Vincentz et al., 2005
FGF16	• SHF and OFT development • Proliferative action on cardiac progenitor cells	• Cohen et al., 2007 • Jennbacken et al., 2019
	• Cardiomyocyte differentiation and proliferation in myocardium and from naïve cardiac progenitor cells • Cardiac weight and cardiomyocyte cell numbers	• Lavine et al., 2005; Hotta et al., 2008; Lu et al., 2008b • Hotta et al., 2008
FGF20	• SHF and OFT development	• Cohen et al., 2007
	• Cardiomyocyte differentiation and proliferation in the myocardium	• Lavine et al., 2005

ectoderm (Urness et al., 2011). FGF9 subfamily members (i.e., FGFs 9, 16, and 20 between E.10.5 and E.12.5) originate from the epicardium (i.e., FGF9 at E.10.5) and the endocardium (i.e., FGFs 9, 16, and 20 at E.10.5 and E.12.5; Lavine et al., 2005; Hotta et al., 2008; Lu et al., 2008b).

Mechanism of Action for FGFs in Cardiac Development

To fulfill these various and divergent functions, the contribution of other downstream pathways, i.e., PI3K/AKT (Luo et al., 2015) and Ras/extracellular signal-regulated kinase (ERK; Hutson et al., 2010) is a matter of significance for the understanding of FGF signaling (**Figure 1**). Importantly, the FGF-MAPK axis contributes to the continuance of cardiopharyngeal multipotency in cardiomyocyte-generating progenitor stem cells (Wang et al., 2019). Cardiac fibroblasts originate predominantly from the epicardium (up to 80% in the adult heart), the endocardium, SHF and neural crest. The differentiation of SHF progenitors from human pluripotent stem cells, which can later generate cardiac fibroblasts, is attributed to the effect of FGF2 as well as Wnt signaling cascades through the suppression of glycogen synthase kinase 3β (GSK3β; Zhang et al., 2019). This potential of FGF2 and Wnt is widely used in the maintenance of pluripotency in human ESCs (Taelman et al., 2019). Other proofs for the implication of FGF members in cardiomyogenic differentiation were provided in mouse ESC and iPSC models. For instance, FGF2 in combination with BMP2 promotes cardiomyocyte differentiation from ESCs and iPSCs (Kawai et al., 2004; Yamasaki et al., 2013). In this regard, FGF10 through interaction with its receptor FGFR2, expressed on

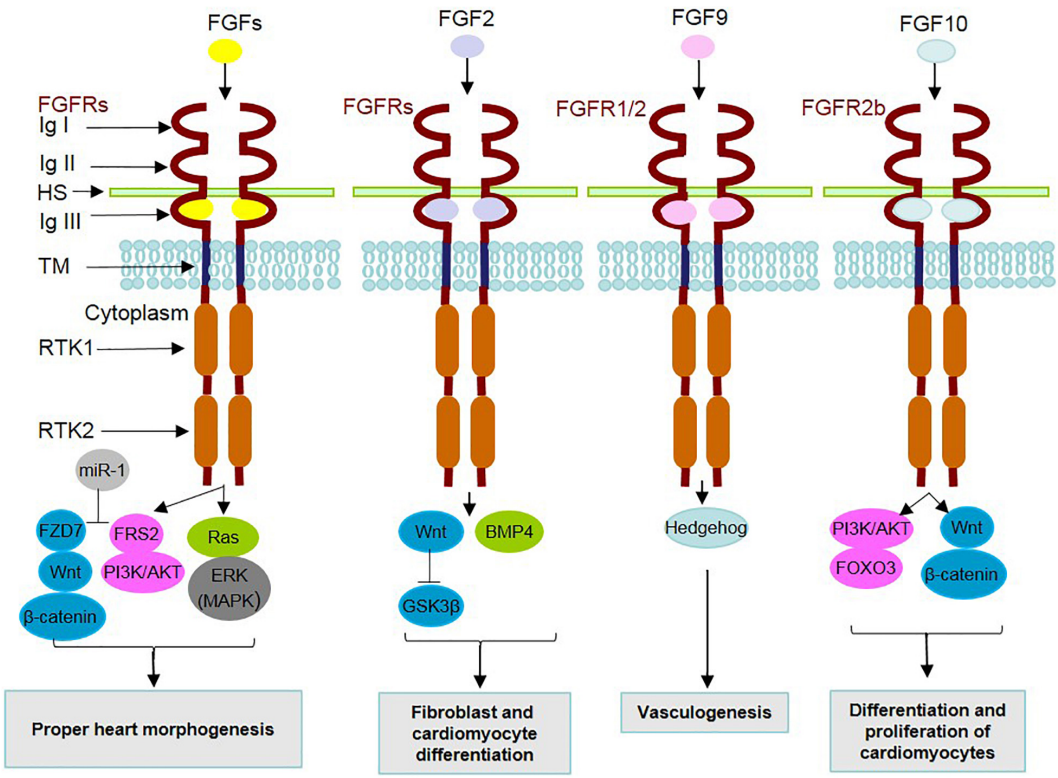

FIGURE 1 | Mechanism of action of secreted FGFs and identified underlying signaling contributors in heart development. During heart development, FGF ligands, through binding to FGF receptors (FGFRs) and cofactors [such as heparan sulfate (HS)] and dimerization, contribute to the activation/inhibition of related underlying intracellular signaling pathways. The FGFR family is composed of 7 FGFRs encoded by 4 genes expressing the alternative splicing forms 1b, 1c, 2b, 2c, 3b, 3c, and 4. FGFRs contain extracellular immunoglobulin-like domains (Ig I–III), a transmembrane domain (TM) and receptor tyrosine kinase domains (RTKs 1 and 2). MicroRNA-1 (miR-1) is positively involved in FGF actions through inhibition of FRS2 and FZD7. A summary of the effects related to the interactions of FGFs with underlying signaling mediators in cardiac development is listed in the boxes.

stem cells, mediates the differentiation of cardiomyocytes (Chan et al., 2010).

Regarding the interplay of FGF signaling with other underlying intracellular pathways (**Figure 1**), a mediating role is attributed to adaptor proteins such as FRS2 (at E.9.5), which transduce FGF signal to MAPK/PI3K (Zhang et al., 2008). Additionally, microRNA-1 (miR-1) is a mediator functioning in the differentiation of cardiomyocytes, by exerting inhibitory effects on FRS2 and FZD7, which acts as a linker of FGF to the Wnt signaling cascade (Lu et al., 2013).

During SHF and OFT development, the Wnt/β-catenin pathway is involved in myocardial progenitor cell differentiation through the modulation of *Fgf 3, 10, 16,* and *20* expression levels (at E.9.5; Cohen et al., 2007). The expression of *Fgf10* in the SHF is positively regulated by transcription factors (e.g., ISL1 and TBX1) in progenitor cells and negatively (e.g., NKX2-5) in cardiomyocytes (at E.9.5; Cohen et al., 2007; Watanabe et al., 2012). TBX1 plays the same activating role for FGF8 expression in the OFT (at E.9.5; Hu et al., 2004). Both FGFs 8 and 10 are involved in the proliferation of SHF progenitor cells, and thereby in the development of the arterial pole (at E.10.5 and between E.15.5 and E.18.5; Watanabe et al., 2010). Homozygous deletion of *Fgf10* in embryos, which is lethal after birth, mainly because of lung aplasia, results in cardiac malformation and ventricular transposition in the thoracic cavity (at E.17.5 and E.18.5; Marguerie et al., 2006; Rochais et al., 2014; Chao et al., 2017). However, normal arterial pole elongation and septation in the absence of *Fgf10* (at E.17.5) reflect its negligible effect on normal arterial development. Notably, the deletion of *Fgfr2b*, the major receptor of FGF10, impairs SHF deployment (at E.10.5), thus being different from the milder cardiac defects accompanied by *Fgf10* deletion (Marguerie et al., 2006). This and other severe heart malformations in the OFT and right ventricle occurring in the absence of both *Fgf10* and *Fgf8* indicate a functional redundancy between FGF10 and other mesodermal FGFs, such as FGF8, which engage the same FGFR2b receptor in the early stages of cardiac development (at E.9.5; Marguerie et al., 2006; Watanabe et al., 2010). Similarly, functional overlap of the FGF family members (FGF10 and FGF3) emerges during heart tube extension which is necessary for the coordination of cardiac progenitor cells. However, deletion of these two *Fgf* genes showed no impact on progenitor cell specification (at E.8.0–E.10.5; Urness et al., 2011).

FGF8 plays a critical role in cardiac loop formation and the survival of migratory CNCs (at E.10.5). The ablation of *Fgf8* perturbs OFT septation (at E.16.5; Abu-Issa et al., 2002).

Another essential function of FGF8 is in the development of the anterior heart field (between E.7.75 and E.10.5; Ilagan et al., 2006). Heparan sulfate, as a glycosaminoglycan and a major component present in the cardiac extracellular matrix, is necessary for the proper function of FGF8 in alignment and formation of OFT, together with the sufficient recruitment of SHF and neural crest cells for OFT remodeling (Zhang R. et al., 2015).

FGFR4 and its ligands (FGFs 4 and 8) are involved in the proper left-right patterning of cardiac laterality, which is impaired in congenital heart disease associated with heterotaxy syndrome (Sempou et al., 2018; Guzzetta et al., 2020). The functions of FGFs 4 and 8 in mesoderm migration and embryonic axis patterning are dependent on Hedgehog signaling activation (at E.9.5; Guzzetta et al., 2020).

FGF9 subfamily members (i.e., FGFs 9, 16, and 20) control cardiomyocyte differentiation and proliferation in the myocardium (Lavine et al., 2005; Hotta et al., 2008; Lu et al., 2008b). This effect on cardiac progenitor cells is mediated through interaction with two receptors (FGFR1c and 2c) with functional redundancy. Knockout of *Fgf9* reduces cardiac size and proliferation rate of cardiomyocytes (at E.12.5; Lavine et al., 2005). FGF16 is mainly encoded in embryonic cardiomyocytes (at E.14.5) and functions through interaction with heparin sulfate-FGFR1c (Hotta et al., 2008). Findings on the FGF16-associated implications seem to vary in different genetic backgrounds of selected mouse models (Lu et al., 2010). On the one hand, *Fgf16* (−/−) is lethal in Swiss black mice (at E.11.5) with severe cardiac malformations (Lu et al., 2008a). On the other hand, these mutants in C57 black 6 mice survive, yet with modest attenuation of cardiac weight and cardiomyocyte cell numbers (Hotta et al., 2008). Intriguingly, similarities with the cardiac phenotype in *Fgf9* (−/−) mice shed light on a possible synergistic effect of FGF9 and FGF16 on embryonic cardiomyocytes (Hotta et al., 2008). However, according to a recent study, FGFs 9 and 16 exert proliferative action on distinct targets (human cardiac fibroblasts versus cardiac progenitor cells, respectively) and receptors, and only FGF16 is specifically able to promote proliferation of mouse naïve cardiac progenitor cells and cardiomyocytes originated from human induced pluripotent stem cells (hiPSCs; Jennbacken et al., 2019).

In the last decade, a regulatory role in cardiomyocyte proliferation has been conferred to FGF10 after findings that ventricles are morphologically altered in this mutant model (E18.5). This study indicated, that FGF10 modulates cardiomyocyte proliferation in the fetal right ventricle in an autocrine fashion. FGF10 ligand and its receptor (FGFR2b) mediate this function through phosphorylation of the forkhead box O3 (FOXO3) transcription factor leading to diminished expression of cyclin-dependent kinase inhibitor $p27^{kip1}$ (Rochais et al., 2014). Myocardium-generated FGF10 affects epicardial cells paracrinally, activating their receptors (FGFR1 and FGFR2), and thereby contributes to the migration of cells toward the compact myocardium. Thus, FGF10 loss of function indirectly perturbs cardiomyocyte proliferating capacity and morphologically leads to the formation of a smaller thin-walled heart (at E17.5). The effect of FGF10 on cardiac wall formation requires functional redundancy between FGFs 7 and 10 over FGFR2b (Vega-Hernández et al., 2011).

FGF15 is present in the pharyngeal endoderm. For normal OFT formation, ortholog members of the endocrine subfamily, i.e., FGFs 15 (in mice)/19 (in humans) play a morphogenesis-related role. In fact, FGF15/19 is critical in developing pharyngeal arches, and the absence of FGF15 results in profound defects in OFT morphology and aorta alignment (at E.18.5; Vincentz et al., 2005). In a possible paracrine function, FGF15/19 may act independently from the typical endocrine cascade engaging FGFR4-βKlotho in cardiac development (Itoh et al., 2016). In this regard, however, the requirement of FGFR4-βKlotho for activation of this signaling in the heart needs to be further investigated (Yu et al., 2000; Ito et al., 2005; Dongiovanni et al., 2020).

Regardless of the known FGF4 contribution to the formation of the cardiac valve leaflet, little is known about other FGF4 functions in the heart (Sugi et al., 2003). Importantly, FGF4 may be involved in the maturation of cardiomyocytes and their aggregation with cardiac fibroblasts, therefore mediating functions in heartbeat synchronization (Jang et al., 2020).

The regulatory role of FGF during heart development was identified to be associated with the function of KLF2, which is a member of the Krüppel-like factor (KLF) family, in the communication between endocardium and myocardium. KLF2 acts as an important transcription factor expressed in the endocardium, and functions on the integrity of the myocardial wall which is correlated to FGF signaling (Rasouli et al., 2018).

FGF Role in the Vascular Network Formation

Concurrent with the loss of *Fgf9* vasculogenesis and development of coronary vessels is impaired. Mechanistically, this function of FGF9 in coronary development (at E.12.5–E.13.5) is related to the induction of the Hedgehog pathway (Lavine et al., 2006). Another process of epicardial/endocardial to myocardial FGF signal transduction in cardiovascular development occurs during the development of coronary vessels, induced by FGF ligands secreted from the endocardium and the epicardium. In this matter, myocardial originated FGFs 1, 2, and 7 stimulate epicardial epithelial-mesenchymal transition (EMT; Morabito et al., 2001). To fulfill this function in the coronary vasculature, Hedgehog signaling downstream of FGFR1 and FGFR2 is induced together with the expression of angiopoietin-2 and vascular endothelial growth factors (*Vegf-A*, *-B,* and *-C*), as proangiogenic growth factors (Lavine et al., 2006). FGFs are involved in vascular network formation, and this signaling is effective for neovasculogenesis and angiogenesis. In this regard, FGF1 and particularly FGF2 are known as inducers of angiogenesis, and this function is mediated by interaction with integrins (Mori et al., 2013, 2017; Sauer et al., 2013).

FGF SIGNALING IN CARDIAC HOMEOSTASIS

During cardiac homeostasis, FGFs play roles in the morphology and physiology of the heart. These actions range from cardiomyocyte proliferation to myocardial excitability together with angiogenesis and metabolic regulation of energy balance.

FGF Functions in Modulation of Cardiomyocyte Proliferation

In the postnatal developmental phase and adult heart, new cardiomyocytes still can proliferate, yet in a substantially decreased degree compared to embryonic heart development (Bergmann et al., 2015). This reduced cardiomyocyte renewal potential, which is albeit crucial for maintaining adult heart homeostasis, comprises annually 0.5–2% of total cardiomyocytes (Eschenhagen et al., 2017).

Fibroblast growth factor ligands (FGFs 1, 2, and 10) contribute to the modulation of adult cardiomyocyte proliferation (**Table 2**). The role of FGF2 in this matter is correlated to interaction with the specific receptor FGFR1 (Sheikh et al., 1999).

Fibroblast growth factor signaling during cardiac homeostasis in the adult zebrafish leads to the addition of cells from the epicardium to the myocardial wall of ventricles (Wills et al., 2008). Seemingly, FGF10 is involved in adult mice in the enlargement of ventricular wall thickness through modulation of cardiomyocyte cell cycle re-entry. This controlling function of FGF10 in cardiac cell proliferation is initiated by interaction with FGFR2b in the embryonic stage and with FGFR1b in the adult stage (Rochais et al., 2014).

Intracellular FGFs and Myocardial Excitability

The intracellular FGF11 subfamily members (including FGFs 11, 12, 13, and 14) regulate the performance of voltage-dependent sodium channel-related family members, as well as calcium channels. Thereby, they contribute to the generation of action potential and myocardial excitability (Hartung et al., 1997; Liu et al., 2003; Hennessey et al., 2013; Yang et al., 2016). Consequently, their absence can lead to cardiomyopathies and arrhythmias (Liu et al., 2003; Wang et al., 2011; Wang X. et al., 2017). In addition to the above-mentioned positive role in cardiac development and homeostasis, however, detrimental remodeling effects are attributed to FGF13 during cardiac hypertrophy. Mechanistically, to exert these adverse roles, FGF13 negatively regulates caveolae-associated cardioprotection (Wei et al., 2017). Added to this, FGF13 activates the inflammatory and pro-apoptotic NF-κB-p53 axis in cardiomyocytes (Sun J. et al., 2020). Despite a few mouse model studies, intracellular FGFs have still received less research attention.

FGF Effects on Angiogenesis

A wide range of FGFs including FGFs 1, 2, 5, 7, 8, 16, and 18 are present in vascular smooth muscle cells and endothelial cells. Although *Fgfr1* and *Fgfr2* are highly expressed in endothelial cells and were identified to be involved in the repair through injury-related angiogenesis, a double knockout condition for these two receptors did not lead to a significant alteration in the homeostatic function of the vascular system (Oladipupo et al., 2014; House et al., 2016). This finding, however, is contrary to the reported severe FGF inhibitor-associated defects, even in homeostasis, emphasizing the significance of FGF signaling for physiological vascular integrity and activity (Murakami et al., 2008; De Smet et al., 2014). These FGF studies on endothelial cells shed light on another functional redundancy between FGFRs.

Metabolic Functions of FGF21

In homeostasis, FGF21, which is another member of the FGF15/19 subfamily, exerts multifunctional roles in the metabolism of lipid and glucose (Yan et al., 2015). FGF21 is highly expressed in the liver, and endocrinally targets distant cells through blood cells (Kharitonenkov et al., 2005; Itoh et al., 2016). In addition to the liver, FGF21 expression is detected in adipose tissues (white and brown), pancreas, skeletal muscles, and heart, however, at a lower level (Yan et al., 2015). In fact, FGF21 functionally modulates energy balance and adaptation to oxidative stress (Gómez-Sámano et al., 2017). Moreover, FGF21 mediates functions in the heart via paracrine and autocrine fashions. A paracrine effect is attributed to FGF21 forming a complex with βKlotho-FGFR1c (**Figure 2**). Added to this, FGF21 possesses a low affinity to the heparan sulfate cofactor (Itoh et al., 2016).

ROLES OF FGF IN CARDIAC PATHOPHYSIOLOGY AND REPAIR

Fibroblast growth factors contribute to cardiac pathophysiology (**Figure 2**). This association was further revealed in genetically engineered rodent and cell culture models which elicit pathological conditions by triggering cardiac remodeling responses (e.g., cardiac hypertrophy, fibrosis and, as a later severe consequence, heart failure). FGFs are involved in the adaptive responses after myocardial infarction (MI) and induced hypertrophy. Moreover, FGFs are known to protect the heart against oxidative stress and diabetic cardiomyopathy. Additionally, FGFs contribute to maladaptive functions mediated by TGFβ1. In addition to these findings in experimental models, a variety of human diseases with cardiac complications affected by FGFs are discussed as follows.

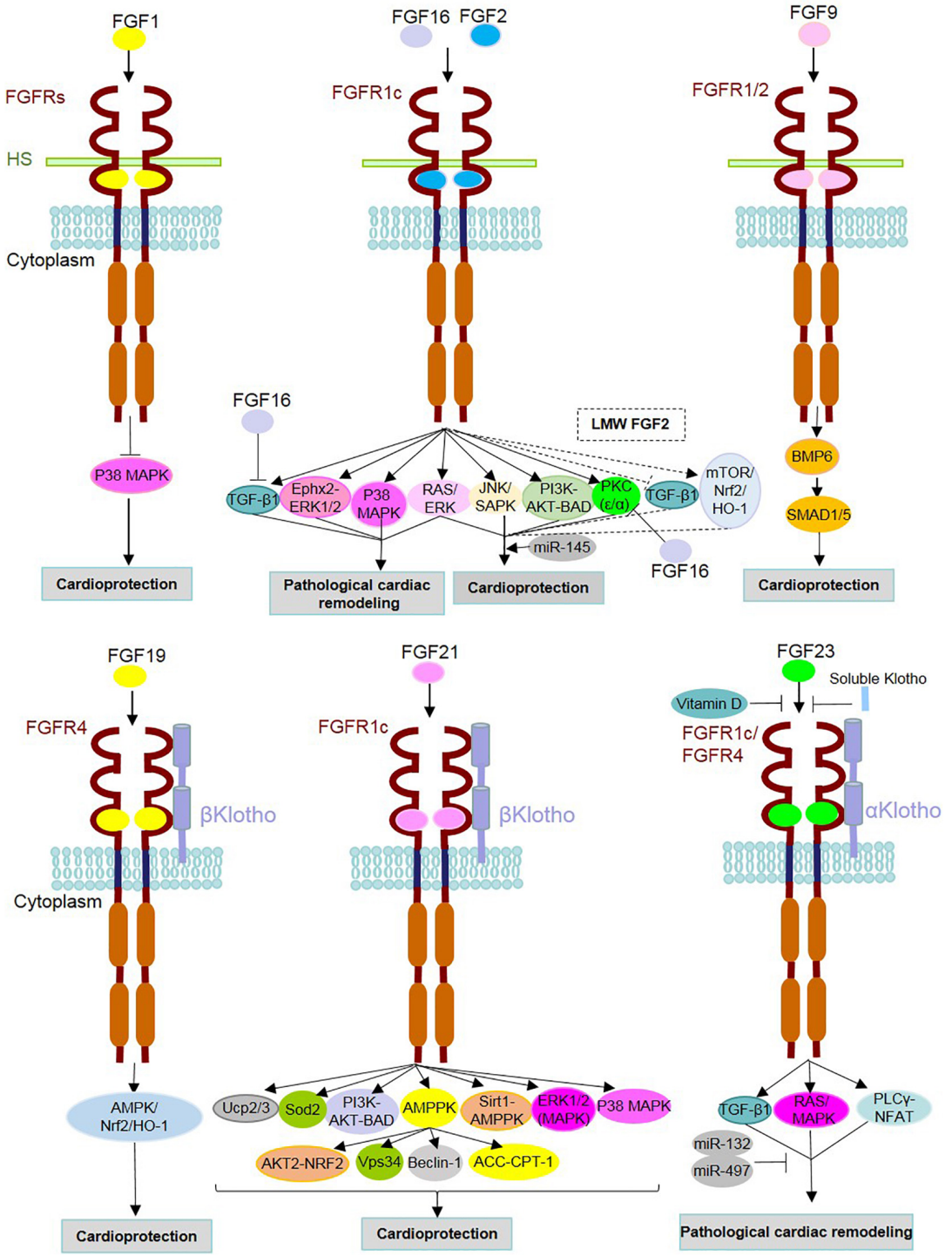

FIGURE 2 | Mechanism of action of FGFs and identified underlying signaling contributors in heart homeostasis, repair and diseases. FGF ligands (FGFs) are involved either in the protection or pathogenesis of the heart through binding with FGF receptors (FGFRs) and cofactors [i.e., heparan sulfate (HS) and α/β Klothos]. After dimerization, they contribute to the activation/inhibition of underlying intracellular signaling pathways. FGF16 and FGF2 can target the same receptor (FGFR1c), but with opposite functions. As an antagonist of FGF2, FGF16 inhibits TGFβ1 and PKC isoforms (PKC-α and PKC-ε). FGF2 is known to play both adaptive and maladaptive roles in cardiac events, and this could be due to the distinct effects of its isoforms [low- and high-molecular-weight isoforms (LMW and HMW)]. Dashed lines indicate signaling pathways and effects related to LMW FGF2. Vitamin D and soluble Klotho suppress the detrimental effects of FGF23-FGFR interactions. MicroRNAs (miR) mediate cardioprotective functions such as miR-145 in association with the Ras-MAPK and PI3K-AKT-related effects of FGF2 as well as miRs-132 and miR-497 through inhibition of FGF23-involved adverse cardiac events.

TABLE 2 | Cardioprotective and maladaptive effects of secreted FGFs on homeostasis and repair of heart detected in experimental injury models.

FGF ligands	Stage of action	Functional or structural roles	References
FGF1	Homeostasis	• Modulation of adult cardiomyocyte proliferation	• Sheikh et al., 1999
	Repair	• Regulation of cardiomyocyte proliferation, elevation of angiogenesis and recovery of MI-induced remodeling, systolic and diastolic heart activities	• Engel et al., 2006; Formiga et al., 2014; Garbayo et al., 2016
FGF2	Homeostasis	• Modulation of adult cardiomyocyte proliferation	• Sheikh et al., 1999
	Repair	• Proliferation of cardiomyocytes, alleviation of apoptosis, restoration of the cardiac contraction rate, suppression of endoplasmic reticulum stress, excessive autophagy reaction, and reduction of myocardial infarct size mainly through low-molecular-weight FGF2 • Suppression of the maladaptive functions of TGFβ1	• House et al., 2003; Rao et al., 2020 • Svystonyuk et al., 2015; Liguori et al., 2018
	Repair (maladaptive)	• Cardiac remodeling (i.e., cardiac hypertrophic, fibrotic responses and heart failure) probably through high-molecular-weight FGF2	• Liao et al., 2010; Wang Z. G. et al., 2015; Wang Z. et al., 2015
FGF9	Repair	• Restoration of systolic physiological activity by triggering vasculogenesis and hypertrophic effects in cardiomyocytes in the left ventricle • Modulation of inflammation, attenuation of the size of cardiac scar and fibrotic region after MI in diabetic cardiomyopathy (DCM)	• Korf-Klingebiel et al., 2008, 2011 • Singla et al., 2015
FGF10	Homeostasis	• Modulation of adult cardiomyocyte proliferation • Augmentation of ventricular wall thickness	• Sheikh et al., 1999 • Rochais et al., 2014
FGF16	Repair	• Myocardial regenerative responses post-injury, including cardiomyocyte replication • Support of cardiac adaptation, attenuation of cardiac scar size, fibrotic region, and modulation of inflammation after MI in DCM • Antagonist of FGF2 after hemodynamic stress	• Yu et al., 2016 • Hu et al., 2017 • Matsumoto et al., 2013
FGF17b	Repair	• Muscle regeneration by epithelial-mesenchymal transition and coronary neovascularization	• Lepilina et al., 2006
FGF19	Repair	• Protection against deleterious effects of reactive oxygen species (ROS) in DCM	• Li et al., 2018
FGF21	Repair	• Protection against damage of cardiomyocytes, ROS effects (also in DCM), hypertrophy, fibrosis and heart failure • Antiapoptotic effects • Rescue of pathological cardiac remodeling and improvement of left ventricular myocardial systolic dysfunction • Inhibition of eccentric hypertrophy progress, cardiac weight augmentation, dilatation and pro-inflammatory reactions	• Planavila et al., 2015a; Wang S. et al., 2017; Yang et al., 2018 • Zhang C. et al., 2015 • Joki et al., 2015 • Planavila et al., 2013

FGF Contributions to Adaptive Responses in Myocardial Infarction and Induced Hypertrophy

FGFs (mainly FGF2 as well as FGFs 1, 9, 17b, and 21) play important roles in cardiac repair after MI and their mechanism of action in injury models have been well characterized. In addition to cardiomyocytes, FGF2 is expressed in non-cardiomyocytes (i.e., mainly cardiac fibroblasts; Zhang et al., 2014) and exerts a paracrine role in the heart through a complex with heparan sulfate and FGFRs (predominantly FGFR1c; Tacer et al., 2010; Ornitz and Itoh, 2015). While knockout mice in the absence of *Fgf2* genes survive normally, their repair-related responses after MI are impaired. In contrast to these adverse effects and in a condition where *Fgf2* is overexpressed, left ventricular function is preserved after MI through induction of proliferation (in fibroblasts and endothelial cells) and hypertrophy (in cardiomyocytes; Virag et al., 2007). The contribution of FGF2 in these cardiac hypertrophic and fibrotic responses was also suggested in hypertrophy-inducing challenges caused by isoproterenol (House et al., 2010), as well as angiotensin II (Ang II) in a two-kidney one-clip model (Pellieux et al., 2001). However, the underlying signaling target of FGF2 for mediating these functions is controversially discussed ranging from p38 MAPK (Pellieux et al., 2001) to ERK in a mechanism that is independent of any correlation with the p38 MAPK signaling pathway (House et al., 2010). Added to these protection-associated pathways, FGF2 may induce ε isoform of protein kinase C (PKC) and, consequently, phosphorylation of connexin-43 as a major component of the cardiac gap junction (Srisakuldee et al., 2009). Later studies further strengthened the correlation of FGF2 with Ras-MAPK and PI3K-AKT (Wang Z. et al., 2015). In this regard, FGF2 and FGF21 elicit similar protective features in the heart as a result of an injury induced by ischemia−reperfusion or hypoxia-reoxygenation, which mimics MI (House et al., 2015; Ren et al., 2019). In an ischemia−reperfusion injury model, overexpression of *Fgf2* restores cardiac contracting rate and minimizes myocardial infarct size (House et al., 2003).

FGF2 in association with downstream cascades (Ras-MAPK and PI3K-AKT) and miR-145 suppresses endoplasmic reticulum stress, excessive autophagy reaction and expression of mitochondrial malfunction-associated proteins, but elevates the

removal of ubiquitinated protein (Wang Z. et al., 2015; Wang Z. G. et al., 2015). In contrast, FGF21 in a hypoxia-reoxygenation model recruited autophagic flux, together with elevation in the expression of autophagy modulator genes (Beclin-1 and Vps34), to limit cardiomyocyte damage (Hu et al., 2018; Ren et al., 2019).

FGF2 may be involved in the cardioprotective function of soluble epoxide hydrolase (Ephx2), a metabolizing enzyme required for the epoxidation of arachidonic acid. Since the hypertrophic potential of FGF2 is effectively counteracted upon gene inactivation of *Ephx2*, the cardiac remodeling role of FGF2 is attributed to the function of Ephx2, and subsequent activation of ERK1/2, but not AKT or p38 (Zhang et al., 2014). A similar interaction between FGF2 and ERK1/2 in cardiac fibroblasts plays a role in the development of lipopolysaccharide (LPS)-triggered cardiac adverse events, leading to fibrosis and heart failure (Chen et al., 2019). Along with an elevated number of cardiac mast cells in both ventricles under hypertrophic conditions, overexpression of *Fgf2* may denote its pro-fibrotic role in the progress of myocardial fibrosis (Kotov et al., 2020).

Inconsistent findings regarding the positive and inverse correlation of FGF2 and cardiac remodeling may be related to distinct functions of FGF2 isoforms including low- and high-molecular-weight isoforms (LMW and HMW; Okada-Ban et al., 2000). For instance, unlike the cardioprotective effect of LMW FGF2, HMW FGF2 mediates adverse cardiac functions under conditions of myocardial ischemia−reperfusion (Liao et al., 2010).

A mimicry myocardial ischemia-caused injury revealed that an endocrine interplay of upregulated hepatocyte- and adipocyte-derived FGF21 with activation of a βKlotho-FGFR1 complex, and consequently downstream activation of PI3K-AKT1-BAD in cardiomyocytes, ameliorates myocardial actions such as left ventricular function improvement, and exerts a long-term cardioprotective effect (Liu et al., 2013). Seemingly, FGF21 infusion rescues the pathological cardiac remodeling post-MI in a wild-type mouse model, and FGF21 exerts this protective action through an adipokine mediator, termed adiponectin. In other words, the adenoviral vector-based overexpression of FGF21 supports adaptation after MI with manifestations such as left ventricular systolic and dilation improvement (Joki et al., 2015). Another effective hormonal contribution of FGF21 and adiponectin, which are highly secreted due to methionine restriction (MR) in diet, prevents cardiac damages of hyperhomocysteinemia derived from dietary MR in mice (Ables et al., 2015).

Although a low level of FGF9 is encoded in adult cardiomyocytes, exogenous exposure of FGF9 from bone marrow or a transgenic-based stimulation of FGF9 expression in adult myocardium compensates MI-mediated cardiac defects. As a result, systolic physiological activity is restored, thus attenuating the mortality risk of MI (Korf-Klingebiel et al., 2008, 2011). To fulfill this compensatory role after MI, FGF9 triggers vasculogenesis through proliferative effects in endothelial cells and hypertrophic effects in cardiomyocytes, and in general, in the left ventricle. FGF9 mediates these functions through secretion of BMP6, which subsequently activates SMAD1/5 (Korf-Klingebiel et al., 2011).

Positive modulatory effects of FGF1 and FGF2 in the repair of induced ischemia-reperfusion injury and MI were revealed to be based on cardiomyocyte proliferation, stimulation of angiogenesis and the recovery of MI-induced remodeling, systolic and diastolic activities of the heart (Engel et al., 2006; Formiga et al., 2014; Garbayo et al., 2016; Rao et al., 2020). This repairing function of FGF1 is further improved by co-treatment of FGF1 with an inhibitor of p38 MAPK. This inhibitor hampers the activation of p38 MAPK correlated with the suppression of cardiomyocyte proliferation (Engel et al., 2005, 2006). Comparable effects of FGF1 were observed in combination with neuregulin1 (NRG1), which is a receptor tyrosine kinase agonist in the epidermal growth factor receptor family (Fuller et al., 2008; Formiga et al., 2014; Garbayo et al., 2016).

In injury models, FGF-FGFR signal transduction acts in coronary neovascularization required for muscle regeneration. This role in regeneration was evident in zebrafish following cardiac injury. In this process, an epithelial-mesenchymal transition occurs, where epicardial *fgfr2* and *fgfr4* expression is promoted when Fgf17b from the myocardium in its proximity is released (Lepilina et al., 2006). This function of FGFRs in neovascularization and vascular remodeling was further supported in mouse injury models upon transgenic deletion of *Fgfr1/2* from endothelial cells. However, the absence of FGFR1/2 did not impair normal cardiovascular function during homeostasis (Oladipupo et al., 2014; House et al., 2016). Another FGF-dependent induction of angiogenesis was reported in *Fgfr2* overexpressing endothelial cells after MI. The action of *Fgfr2* overexpression together with the reduction in cardiomyocyte apoptosis after MI is correlated to upregulation of *Fgf2* and its autocrine effect (Matsunaga et al., 2009). Anti-apoptotic and pro-angiogenic protective responses following FGF2 treatment after MI in mice were induced through activation of the AKT-hypoxia-inducible factor-1 alpha (HIF-1α)-VEGF axis (Rao et al., 2020). In cardiac regeneration of the zebrafish after injury, the active presence of the FGF-AKT signaling cascade is required for the survival of cardiomyocytes (Tahara et al., 2021). Nevertheless, in these injury model-based studies, differences in postnatal heart regeneration between zebrafish with a complete regeneration capacity and mammals in which the injury in the myocardium scar is mainly covered by fibrotic tissue, have to be considered (Kikuchi and Poss, 2012).

Cardioprotective Response of FGFs Against Oxidative Stress

Oxidative stress is another cardiac insult induced by reactive oxygen species (ROS), and causes deleterious structural and functional effects resulting in the development of heart failure, particularly after MI (Giordano, 2005). A protective role of FGF21 was evidenced against isoproterenol and LPS stimulated ROS generation in cardiac cells and subsequent hypertrophic and pro-inflammatory reactions (Planavila et al., 2015b). Upon gene inactivation of *Fgf21* (−/−), isoproterenol, which is a β adrenoreceptor agonist, induces progress of eccentric hypertrophy accompanied by pro-inflammatory reactions,

suppression of fatty acid oxidation and augmentation of cardiac weight and dilatation. These phenotypes are restored after administration of FGF21 (Planavila et al., 2013). Indeed, FGF21 secretion from cardiomyocytes is substantially increased in response to cardiac stress (e.g., in MI; Planavila et al., 2015b). Mechanistically, LPS-induced expression of *Fgf21* is regulated by the sirtuin-1 (Sirt1) pathway, and the FGF21 mediated reduction of ROS generation is attributable to the activation of antioxidative cascades, e.g., by upregulation of mitochondrial uncoupling proteins (Ucp) 2 and 3, together with superoxide dismutase-2 (Sod2; Planavila et al., 2015a). Thus, FGF21 is involved in protection against injuries from both systemic (in an endocrine fashion of enhanced production by hepatocytes post-MI) and local (paracrine signals by cardiomyocytes) resources (Planavila et al., 2013). Paracrine action of FGF21 in cardiomyocytes, particularly against hypertrophy, is associated with βKlotho-FGFR1c and leads to activation of the MAPK cascade (Planavila et al., 2013, 2015b).

Collectively, to combat cardiopathogenic stress, FGF21 negatively and positively modulates the expression of genes contributing to oxidative and antioxidative signaling cascades, respectively, thereby addressing cardiac remodeling and heart failure (Planavila et al., 2015a; Gómez-Sámano et al., 2017).

Cardioprotective Response of FGFs in Experimental Diabetic Cardiomyopathy

Fibroblast growth factors 9, 16, 19, and 21 protect the diabetic heart against maladaptive cardiac responses and modulate inflammatory reactions.

In a MI model and under a diabetes-inducing genetic modification (db/db), FGF9 and FGF16 suppressed pro-inflammatory responses (i.e., monocyte infiltration, M1 macrophage generation differentiated from monocytes and pro-inflammatory cytokine production). Conversely, anti-inflammatory reactions (i.e., differentiation of M2 macrophages from monocytes and anti-inflammatory cytokines) were augmented. Thus, FGFs 9 and 16 play a cardioprotective role through modulation of inflammation and support cardiac adaptation (e.g., attenuation in the size of the cardiac scar and fibrotic region) post-MI in diabetic patients (Singla et al., 2015; Hu et al., 2017).

Fgf21 ablation in type 1 diabetic mice leads to cardiac remodeling, lipid accumulation and oxidative stress. As a result of this, diabetic cardiomyopathy (DCM)- a severe abnormality in the structure and function of the myocardium- emerges earlier and is more severely deteriorating (Yan et al., 2015). In line with these findings, suppression of FGF21 induced fibrosis and hypertrophy in the heart, while the presence of FGF21 protected against these responses (Chen et al., 2018). Moreover, FGF21 was shown to inhibit the induction of apoptosis of cardiomyocytes occurring during type-1 diabetes. The antiapoptotic effect of FGF 21 was attributed to the activation of p38 MAPK, ERK1/2, and AMP-activated protein kinase (AMPK) pathways (Zhang C. et al., 2015).

Cardiac expression of FGF21 in type-1 diabetic mice and subsequent cardiac defensive actions against maladaptive cardiac events and inflammation are boosted by the administration of fenofibrate. Fenofibrate is a prominent medication for the control of systemic lipid levels and is considered an agonist of peroxisome-proliferator-activated receptor α (PPARα). The fenofibrate-induced cardioprotective function of FGF21 in type-1 diabetes is correlated to Sirt1, another upregulated target of fenofibrate, which rescues disrupted autophagy (Zhang et al., 2016). Similarly, treatment of type-2 diabetes patients with fenofibrate elevated FGF21 serum levels (Ong et al., 2012). FGF21 exerts this protective role against DCM in type 2 diabetes employing AMPK-associated anti-oxidative (AMPK-AKT2-NRF2) and lipid-diminishing (AMPK-ACC-CPT1) pathways (Yang et al., 2018). Similar protection against the deleterious effects of ROS in DCM is mediated by FGF19. To fulfill this anti-oxidative function, a target pathway consisting of AMPK/nuclear erythroid factor 2-related factor 2 (Nrf2)/heme oxygenase-1 (HO-1) is activated (Li et al., 2018).

Interplay of FGFs With TGFβ1-Induced Structural Heart Disorders

Profound extracellular matrix structural alteration, hypertrophy and fibrosis in the heart are induced after continuous exposure toward TGFβ1 and are mediated by miR-132. FGFs mediate contradictory actions on the adverse cardiac responses caused by TGFβ1 which include suppressing (LMW FGF2 and FGF16) versus boosting (FGFs 2 and 23) effects on TGFβ1 functions.

The inhibition of TGFβ1 maladaptive functions using FGF2 in human cardiac myofibroblasts proposes another cardioprotective role for FGF2 against progressive cardiac disorders, such as chamber remodeling and tissue fibrosis (Svystonyuk et al., 2015). Regarding the above-mentioned different actions of FGF2 isoforms, an anti-fibrotic function is induced by LMW FGF2 through antagonizing TGF-β1, thereby compensating the differentiation of fibroblasts to myofibroblasts and attenuating the generation of extracellular matrix (Liguori et al., 2018).

Conversely, FGF2 promotes the expression of *Tgf-β1* and thereby hypertrophic reaction and fibrosis. Intriguingly, this is abrogated in the presence of FGF16. In fact, cardiac remodeling upon exposure toward Ang II occurs in the lack of *Fgf16*, which is correlated to the activation of TGF-β1 as its underlying target (Matsumoto et al., 2013). Thus, *Fgf16*, which is predominantly encoded in cardiomyocytes, functions as an antagonist for FGF2, which is released from cardiac fibroblasts after hemodynamic stress in the context of cardiac adaptive responses (Kaye et al., 1996; Pellieux et al., 2001; Matsumoto et al., 2013). The antagonizing effect of FGF16 on FGF2 is mediated through competition over FGFR1c in cardiomyocytes (Matsumoto et al., 2013). By this virtue, FGF16 suppressed the proliferative role of FGF2 on cardiomyocytes. Mechanistically, FGF16 exerts inhibitory effects on FGF2-induced PKC isoforms (PKC-α and PKC-ε), but no limiting impact on other targets of FGF2

(e.g., p38 MAPK, ERK1/2, or JNK/SAPK; Lu et al., 2008b). To elicit myocardial regenerative responses post-injury, including cardiomyocyte replication, FGF16 is modulated by GATA4 – as a major cardiac transcription factor controlling the expression of specific genes in the heart (Yu et al., 2016).

In contrast, FGF23 in collaboration with TGFβ1, but not in its absence, induces myocardial fibrosis. In an animal model of experimental hypertrophy that triggers myocardial fibrosis, *Fgf23* and *Fgfr1* are highly expressed. Indeed, FGF23 originating from cardiomyocytes elicits a boosting effect on fibrosis in a paracrine manner through FGFR1 on cardiac fibroblasts (Kuga et al., 2020). In another hypertrophic and fibrotic model triggered by Ang II, the observed adverse structural and functional cardiac events are attributed to FGF23 activating the TGFβ1-miR-132 axis (Ding et al., 2019).

Cardiopathophysiological Roles of FGFs in Human Diseases

Impairment of FGF signaling is correlated with congenital and metabolic diseases, as well as a range of cancer types (Carter et al., 2015). In the context of cardiac disorders, either FGFs (e.g., 2, 21, and 23) are major contributors in the development of these diseases, or their serum levels are altered as a consequence of cardiac diseases (e.g., 15/19, 21, and 23). This introduces them as serum biomarkers for the prediction and diagnosis of cardiac diseases (Itoh et al., 2016; Emrich et al., 2019). In the following a range of FGF-related cardiac complications is explained (**Table 3**):

Pericardial Effusion

Pericardial effusion is mainly caused by inflammatory responses, and manifests in the malformation and accumulation of pericardial fluid, resulting in augmented intrapericardial pressure and consequently cardiac dysfunction (Karatolios et al., 2012). As a possible immune reaction under pathogenic conditions, FGF2 can be generated by immune cells (e.g., T-lymphocytes and macrophages; Kuwabara et al., 1995; Peoples et al., 1995). Thus, a higher level of FGF2 together with other inflammatory cytokines in the serum and pericardium of patients proposes a causative role for FGF2 in the pathogenesis of pericardial effusion (Karatolios et al., 2012).

Atrial Fibrillation

This atrial complication, which is associated with arrhythmia in atrial chambers, can develop to atrial fibrosis as a severe cardiac remodeling. Atrial fibrillation also occurs in rheumatic heart patients that is correlated to the elevation of FGFs 21 and 23 in their serum and atrial tissues. The negative modulatory effect of FGFs in the maintenance and progress of atrial fibrillation and fibrosis suggested the potential use of FGFs 21 and 23 as diagnostic and therapeutic biomarkers (Wang R. et al., 2015; Chua et al., 2019). Notably, atherosclerosis patients showed a positive correlation between the higher concentration of FGFs 21 and 23 in the serum and the incidence of atrial fibrillation (Mathew et al., 2014; Hui et al., 2018).

Congenital Heart Diseases (CHD)

Metacarpal 4–5 fusion (MF4) disease is identified as a hereditary disorder characterized by the fusion of the fourth and fifth metacarpal bone. Among its clinical manifestations, MI and atrial fibrillation occur which are attributed to *FGF16* mutations in the X-chromosome. Indeed, this finding reveals the link of nonsense mutations in *FGF16* with CHD (Laurell et al., 2014). Moreover, mutations in *FGF8* and *10* are correlated to conotruncal defects, which impair OFT development and are associated with a high mortality rate (Sun K. et al., 2020).

Cardiac Disorders Concomitant of Kidney Diseases

Life-threatening cardiovascular complications such as left ventricular hypertrophy are prevalently associated with chronic kidney disease (CKD) (Grabner et al., 2015). As a causative contributor to this cardiac pathogenicity a substantial increase in FGF23 levels was reported (Jimbo and Shimosawa, 2014; Wyatt and Drüeke, 2016). In kidney homeostasis, circulating FGF23 is predominantly derived from bone and modulates the metabolism of vitamin D and phosphate as well as sodium and chloride through interaction with αKlotho-FGFR1c (Andrukhova et al., 2014; Erben, 2016). Importantly, this hormonal FGF23 elevates sodium uptake and thereby can cause cardiovascular dysfunctions, e.g., hypertension and hypertrophy (Andrukhova et al., 2014). Added to its hypertrophic effect, FGF23 substantially increases intracellular calcium, induces arrhythmogenicity, and attenuates the contracting potential of cardiomyocytes. Notably, these adverse effects on cardiac cell function are prevented by the administration of soluble Klotho (sKlotho; Touchberry et al., 2013; Navarro-García et al., 2019). The sKlotho in the circulation, mainly provided by the kidney, is proteolytically cleaved from transmembrane Klotho and may interact with FGF23-FGFR1. However, the association of sKlotho with FGF23 is yet controversial (Seiler et al., 2013; Marçais et al., 2017; Memmos et al., 2019).

Additionally, the attenuated concentration of sKlotho in type 2 diabetic and hemodialysis patients (in the early and late stages of CKD, respectively) along with the elevated risk of cardiac events may imply this cardioprotective effect of sKlotho (Marçais et al., 2017; Memmos et al., 2019; Silva et al., 2019).

In addition, the expression of *Fgf23* and *Tgf*-β1 and, as a result, the detrimental cardiac outcomes are suppressed by administration of Klotho which inhibits the TGFβ1-miR-132 axis, thus suggesting therapeutic potential against cardiac remodeling (Ding et al., 2019). In this regard, the therapeutic administration of soluble αKlotho could be a treatment strategy to counteract Fgf23 and Tgf-β1-mediated adverse cardiac injury consequences, such as fibrosis and remodeling. Indeed, this coreceptor of FGF23 suppressed the apoptotic and fibrotic action of isoproterenol-caused injury on cardiomyocytes and endothelial cells, however, mechanistically independent of FGF23 contribution (Chen, 2020).

Cohort studies on end-stage renal disease patients with severe cardiac complications indicated enhanced serum levels of FGF23 and calcium. FGF23 elevation is accompanied by an

TABLE 3 | Secreted FGFs involved in/against cardiac pathogenicity and their potential as serum biomarker in diseases.

FGF ligands	Alteration	Effect/application	Diseases/complications	Other cardiac clinical manifestation	References
FGF2	Elevation	Causative	TGFβ1-induced heart disorders	• Hypertrophic reaction and fibrosis	• Matsumoto et al., 2013
		Causative	Pericardial effusion in coronary artery disease (CAD)	• Accumulation ofpericardial fluid, intrapericardial pressure and cardiac dysfunction	• Karatolios et al., 2012
		Biomarker	Type 4 cardiorenal syndrome (CRS)	• Cardiac hypertrophy and attenuated ejection fraction (EF)	• Liu et al., 2015
LMW FGF2*	Elevation	Protective	TGFβ1-induced heart disorders	• Against fibrosis and chamber remodeling	• Svystonyuk et al., 2015
FGFs 8 and 10	Mutation	Causative	Conotruncal defects	• Abnormal heart development	Sun K. et al., 2020
FGF 15/19	Attenuation	Protective/biomarker	Atherosclerosis and CAD	• Angina, myocardial infarction (MI), and sudden cardiac death	• Itoh et al., 2016
FGF16	Mutation	Causative	Congenital metacarpal 4–5 fusion	• MI and atrial fibrillation	• Laurell et al., 2014
	Elevation	Protective	TGFβ1-induced heart disorders	• Anti-hypertrophic and anti-fibrotic actions	• Matsumoto et al., 2013
FGF21	Elevation	Biomarker	Atrial fibrillation in rheumatic heart	• Atrial arrhythmia and fibrosis	• Wang R. et al., 2015; Hui et al., 2018
			Atherosclerosis and CAD	• Cardio-metabolic disorders	• Shen et al., 2013; Kim et al., 2015; Xiao et al., 2015; Wu et al., 2020
			Heart failure	• Reduced EF, cardiac cachexia, non-acute and acute MI	• Zhang W. et al., 2015; Refsgaard Holm et al., 2019
		Protective	DCM	• Attenuation of cardiac apoptosis, fibrosis lipotoxicity, and dysfunction	• Zhang C. et al., 2015; Chen et al., 2018; Yang et al., 2018
FGF23	Elevation	Causative	Myocardial fibrosis	• Induction of fibrosis in cardiac fibroblasts and adverse structural and functional cardiac events	• Ding et al., 2019
		Causative/biomarker	Atrial fibrillation, CAD and atherosclerosis	• Kawasaki syndrome cardiac complications and advanced vascular plaque calcification	• Falcini et al., 2013; Mathew et al., 2014; Chua et al., 2019; Holden et al., 2019
		Causative	Chronic kidney disease-associated cardiac complications	• Hypertension, left ventricular hypertrophy, reduced contracting potential, arrhythmogenicity and accelerated cardiac aging	• Touchberry et al., 2013; Andrukhova et al., 2014; Grabner et al., 2015, 2017; Navarro-García et al., 2019
		Biomarker	Heart failure, myocarditis and dilative cardiomyopathy	• Chronic systolic, congestive and acute decompensated heart failure, reduced and preserved EF and recurrent major cardiovascular events	• Lutsey et al., 2014; Richter M. H. et al., 2015; Wohlfahrt et al., 2015; Bergmark et al., 2018; von Jeinsen et al., 2019
	Temporary elevation	Biomarker	Type 4 CRS	• Hypertrophy and reduced EF	• Verhulst et al., 2017

**LMW FGF2, low-molecular-weight isoform of FGF2.*

inverse association between miR-497 and FGF23, thus suggesting another protective axis against detrimental cardiac effects of FGF23 (Xu et al., 2019; Liu et al., 2020).

In addition to this indirect endocrine effect, FGF23 can also be released from cardiomyocytes and acts in a paracrine manner (Leifheit-Nestler et al., 2016). In CKD patients, FGF23 is highly upregulated leading to left ventricular hypertrophy by interaction with FGFR4, and subsequently stimulating hypertrophy-inducing cascades of PLCγ-calcineurin-nuclear factor of activated T-cells (NFAT) and Ras/MAPK, however, without the contribution of Klotho cofactor (Faul et al., 2011; Leifheit-Nestler et al., 2016). This FGFR4-dependent hypertrophic effect of FGF23 was further confirmed in rats and mice since hypertrophy was suppressed either in presence of FGF23 blocking antibody or deletion of *Fgfr4* (−/−; Grabner et al., 2015).

Intriguingly, in a 5/6 nephrectomized rat renal injury model, FGF23-induced adverse left ventricular remodeling and consequently accelerated cardiac aging are reversible (Grabner et al., 2017). Seemingly, the administration of the vitamin D metabolite calcitriol (1,25-dihydroxyvitamin D), to the renal injury model diminishes this excessive FGF23-FGFR4 signal and thereby inhibits subsequent cardiovascular abnormalities. This indicates a synergic effect of vitamin D deficiency and FGF23 elevation in the development of cardiac hypertrophy (Leifheit-Nestler et al., 2017). These findings open a new avenue for a putative therapeutic strategy by blocking FGF23-FGFR4 in combination with vitamin D or its receptor to prevent or alleviate

the massive cardiovascular injuries in CKD patients (Grabner et al., 2017; Leifheit-Nestler et al., 2017).

Despite strong evidence on the effect of elevated FGF23 in cardiac complications followed by kidney disorders, two cohort studies on hemodialysis patients together with non-cardiovascular patients did not manifest any causal correlation between FGF23 levels and cardiovascular disease symptoms (Marthi et al., 2018; Takashi et al., 2020).

Type 4 Cardiorenal Syndrome (CRS)

This chronic class of CRS syndrome is identified by heart dysfunction and adverse remodeling as a consequence of a primary CKD (Clementi et al., 2013). Cardiac hypertrophy and attenuated ejection fraction (EF) in type 4 CRS patients are attributed to augmented oxidative stress. Mechanistically, this oxidative stress causes cardiac injury in a mimicry type 4 CRS rat model by activation nicotinamide adenine dinucleotide phosphate (NADPH) oxidase and subsequently ERK1/2 phosphorylation, leading to an increase in the expression of FGF2. The type 4 CRS injury and phenotypes are reversed by apocynin, a widely used antioxidant that inhibits NADPH oxidase (Liu et al., 2015). Additionally, type 4 CRS coincides with the temporary elevation of FGF23 serum levels (Verhulst et al., 2017).

Coronary Artery Anomalies

FGF15/19 contributes to the regulation of lipid and glucose metabolism and thereby, together with adiponectin, prevent atherosclerosis and other metabolic diseases (Wu and Li, 2011). Coronary artery disease (CAD) as the most prevalent cardiovascular disease with high mortality is an ischemia-related disease that can be accompanied by symptoms such as angina, MI, and sudden cardiac death (Itoh et al., 2016). The attenuated serum level of FGF19 and adiponectin in CAD patients imply a negative correlation of these factors and the severity of CAD, suggesting this factor as a serum biomarker of CAD (Hao et al., 2013).

FGF23 is elevated in CAD patients with a history of type 2 diabetes or a high risk of atherosclerosis (Lutsey et al., 2014; Tuñón et al., 2016; Holden et al., 2019). FGF23 is involved in atherosclerosis-related damage through advanced vascular plaque calcification (Holden et al., 2019). FGF23 levels are increased in the serum of patients with Kawasaki syndrome, as another type of coronary artery abnormality which is associated with severe cardiovascular complications in children (Falcini et al., 2013).

Similarly, FGF21 is elevated in the serum of CAD patients, correlated with pathogenic impaired metabolism of lipids (Lin et al., 2010; Shen et al., 2013; Kim et al., 2015). Excessive serum levels of FGF21 were reported in atherosclerosis patients with ischemic heart disease as well as in non-alcoholic fatty liver disease, type 2 diabetes, and metabolic disorders (Shen et al., 2013; Kim et al., 2015; Xiao et al., 2015; Wu et al., 2020).

FGF2 concentration is increased in the pericardial fluid (compared to the serum) of CAD patients (Karatolios et al., 2012). As mentioned above, FGF2 exerts a beneficial role in heart restoration after MI in mice, prompting its translation into clinical trials (House et al., 2003). However, intramyocardial injection of recombinant FGF2 in CAD patients did not significantly improve symptoms (Simons et al., 2002; Kukuła et al., 2011).

Heart Failure Syndrome Signs and Symptoms

According to the dysfunction level of the left ventricular EF heart failure syndrome can be further divided into two subtypes with preserved EF (≤50%) and reduced EF (≤40%; Tschöpe et al., 2018). An independent association was reported between elevated levels of FGF23 in the serum of heart failure patients with reduced EF or preserved EF (Koller et al., 2015; Almahmoud et al., 2018; Bergmark et al., 2019; Roy et al., 2020). This coincides with a substantial attenuation of plasmatic Klotho (Bergmark et al., 2019). A high concentration of FGF23 was reported in the serum of patients with chronic systolic and congestive heart failure (Wohlfahrt et al., 2015; von Jeinsen et al., 2019).

In up to 20% of heart failure patients with reduced EF, which is accompanied by an inflammatory losing weight syndrome, namely cardiac cachexia, the serum level of FGF21 is also increased (Refsgaard Holm et al., 2019). Augmented circulating FGF21 levels are also evident in other patients with non-acute and acute MI (Zhang W. et al., 2015).

Notably, a similar trend of elevated FGF23 concentration was detected in the serum of patients with recurrent major cardiovascular events, myocarditis, dilative cardiomyopathy and all-cause mortality (Lutsey et al., 2014; Richter M. H. et al., 2015; Bergmark et al., 2018). Mechanistically, the adverse FGF23 effect is associated with macrophage-oncostatin M (OSM) signaling, which is a prominent mediator of heart failure (Richter M. et al., 2015). This correlation is suggested since OSM stimulates the production of FGF23 in cardiomyocytes, but not in non-cardiomyocytes. OSM is a cytokine of the interleukin-6 family, secreted from infiltrated macrophages, and, unlike FGF23, is not considered as a proper biomarker due to its low serum concentration (Richter M. et al., 2015). Newly developed antibody therapies against the OSM receptor (Oβ) may open strategies to block the macrophage-OSM-Oβ cascade and suppress cardiac damages caused by increased FGF23 (Pöling et al., 2014; Richter M. et al., 2015).

Acute Decompensated Heart Failure (ADHF)

A substantially increased degree of FGF23 was detected in the serum of ADHF patients, but not in their myocardium, indicating an endocrine mechanism of FGF23 action in heart failure (Andersen et al., 2016). Thus, FGF23 can be considered a predictive marker of ADHF (Andersen et al., 2016; Emrich et al., 2019).

Diabetic Cardiomyopathy (DCM)

In line with the aforementioned association of FGFs and DCM in experimental models, this correlation was corroborated in clinical studies. In this regard, elevated levels of FGF21 in the serum of

DCM patients elicited a cardioprotective function (Ong et al., 2012; Cheng et al., 2016).

THE REGENERATIVE POTENTIAL OF FGFS THROUGH INDUCTION OF CARDIOMYOCYTE PROLIFERATION

Cardiovascular diseases are a major cause of death in the industrialized world. Indeed, unraveling the contribution of fetal FGF signaling to cardiac repair and especially cardiomyocyte proliferation may open new avenues to support cardiac regenerative processes.

A gradual attenuation in the proliferative capacity of cardiomyocytes during embryogenesis which exaggerates postnatally (after 1–3 days) with a significant and rapid reduction in the proliferative capacity, massively limits the adult cardiac regeneration rate (Li et al., 1996; Porrello et al., 2011; Ye et al., 2018). The idea of cardiac cell expansion has been tempting in the last decades, aiming for regenerative therapies applicable in cardiac treatment post-MI. Common strategies for cardiac regenerative medicine range from progenitor stem cell therapy (through injection or engineered tissue implantation) to stimulation of cell cycle re-entry in adult cardiomyocytes and direct reprogramming of them (El Agha et al., 2016; Tzahor and Poss, 2017). To this end, the proliferative potential of FGFs (e.g., FGFs 1, 2, 8, 10, and 16) on cardiomyocytes or their progenitor cells during development and homeostasis has been a center of research attention (Sheikh et al., 1999; Engel et al., 2006; Watanabe et al., 2010; Jennbacken et al., 2019).

FGF1 in combination with p38 MAPK inhibitor or NRG1 can promote the proliferation of cardiomyocytes (Engel et al., 2005, 2006; Formiga et al., 2014; Garbayo et al., 2016). This may occur by the interplay between FGF and MAPK signaling cascades in the alleviation of the limited mammalian cardiac repair potential.

A common problem in growth factor employment for clinical therapies is their low bioavailability, rapid elimination and degradation after treatment. To tackle the short stability and half-time issues, a drug delivery system was developed using biomaterials combined with FGFs. Preclinical studies in rats and pigs used biocompatible polymeric poly(lactic-co-glycolic acid) and polyethylene glycol microparticles loaded with FGF1. This beneficial delivery method prevented perturbation in the regenerative function of FGF1 post-MI after administration (Garbayo et al., 2016; Pascual-Gil et al., 2017).

FGF Potential in Cardiomyocyte Cell Cycle Reentry

Notably, FGF10 has been shown to modulate prenatal cardiomyocyte proliferation, while in the postnatal heart the proliferation together with the expression of FGF10 is suppressed. This suggests FGF10 as a putative candidate for the induction of cell cycle re-entry of cardiomyocytes, applicable for cardiac regenerative purposes. During cardiac injury in adult mice, FGF10 promoted the renewal of cardiomyocytes supporting the cardiac repairing function of FGF10 (Rochais et al., 2014). In contrast, a transgenic neonatal mouse model in which *Fgf10* in the myocardium was overexpressed was unable in epithelial to mesenchymal transition and improvement of the neonatal cardiac repair capacity after a cryoinjury, regardless of inducing effects on the epicardial cell number (Rubin et al., 2013).

FGF Application in Cell Replacement-Based Therapies

The stimulatory effects of FGFs can be employed to upscale cardiomyocyte cell numbers for stem cell-based clinical intervention and pharmaceutical tests. In the future, these ligands can be further used to enhance cardiomyocyte specification from cardiac progenitor cells, i.e., ESCs and iPSCs. For instance, FGF10 itself and FGF2 in the presence of BMP2 have been shown to be effective in cardiac cell differentiation, and FGF16 in the proliferation of cardiomyocytes from mouse and human ESCs and iPSCs (Kawai et al., 2004; Chan et al., 2010; Yamasaki et al., 2013; Jennbacken et al., 2019).

Another therapeutic model using the cell replacement approach is based on transplantation of engineered cardiac patches transferring ESCs- or hiPSCs-derived cardiomyocytes to the injured heart (Kolossov et al., 2006; Fan et al., 2020). Treatment of these patches with FGF1 and an inhibitor of GSK3 (CHIR99021), which activates Wnt signaling, leads to elevated hiPSCs derived cardiomyocyte cell divisions and increased grafting rate together with improved cardiac function following MI (Fan et al., 2020). Thus, FGF signaling could be exploited in the worldwide challenge of finding proper stem cell-based therapy for heart failure.

To improve cardiac repair after MI, secretome of progenitor cells containing FGFs in combination with other growth factors can be employed (Timmers et al., 2008; Sharma et al., 2017). A recent secretomic analysis study indicated a range of FGFs (1, 4, 9, 16, and 18) with presumed proliferative capacity. FGF16 may exert this capacity by specific targeting of cardiac progenitor cells, and thereby may be beneficial in the recovery from cardiac injuries (Jennbacken et al., 2019).

FGF Application in Direct Reprogramming Based Therapies

Direct reprogramming as another advanced therapeutic strategy aims to counteract MI detrimental effects and to replace lost cardiomyocytes (Yamakawa et al., 2015). FGFs combined with cardiac transcription factors (Gata4, Mef2c, Tbx5, and Hand2) serve in the transdifferentiation of somatic cells (e.g., fibroblasts) to cardiac progenitor cells (Li et al., 2015) or cardiomyocytes, thus bypassing the intermediate conversion step to pluripotent stem cells (Sadahiro et al., 2015). Co-administration of FGFs 2 and 10 together with VEGF induced the reprogramming of fibroblasts to cardiomyocyte-like cells through interplay with PI3K-AKT and p38 MAPK pathways (Yamakawa et al., 2015). Transplantation of FGF2-induced reprogrammed cardiac progenitor cells from dermal fibroblasts

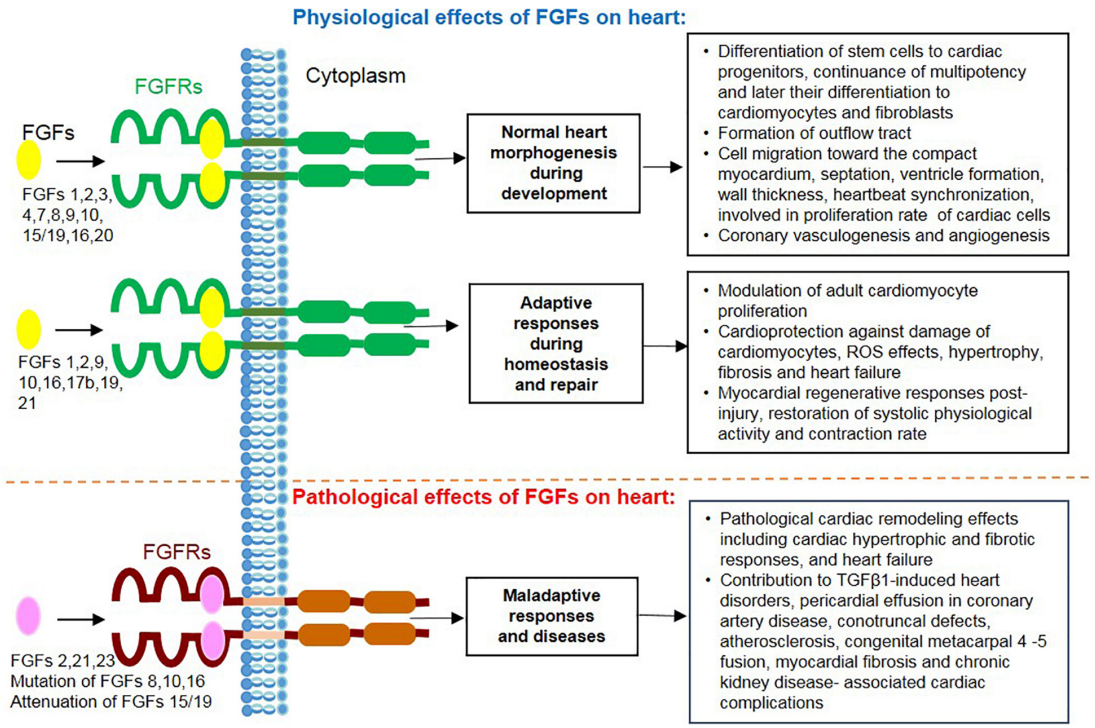

FIGURE 3 | Overview of actions mediated by secreted FGF ligands on the heart including physiological effects during cardiac development, homeostasis and repair together with their pathological and maladaptive effects during heart disease.

in a rat model post-MI effectively recovered cardiac damages (Li et al., 2015).

ANTI CARDIOTOXICITY POTENTIAL OF FGFS IN THERAPIES

Strong evidence has been provided by animal studies on the stimulation of cardioprotective function or minimizing the detrimental cardiac effects through modulation of FGF-FGR-coreceptors complex members which may be translated into human therapies.

The aforementioned cardioprotective capacity of FGFs 2, 16, and 21 can be used to counteract or limit the adverse cardiac side effects of drugs. In this regard, in a cardiomyocyte cell line and mouse model, severe cardiopathogenic damages of doxorubicin, a chemotherapy medication for cancer treatment, are alleviated (Wang et al., 2013, 2018; Koleini et al., 2017; Wang S. et al., 2017). This co-administration of doxorubicin with FGF21 induced anti-oxidative, anti-apoptotic, and anti-inflammatory (including enhanced Sirt1 function) responses (Wang S. et al., 2017). FGF2 mediates this anti-cardiotoxic action by its LMV isoforms through activation of antioxidant and detoxification cascades (mTOR/Nrf-2/HO-1 pathway; Koleini et al., 2017, 2019). This protective effect induced by the administration of exogenous LMW-FGF2 is replicated by endogenous LMW-FGF2 only if HMW FGF2 is neutralized or eliminated (Koleini et al., 2019).

CONCLUSION

Continued progress in the characterization of FGF family members with multipotential roles in cardiac events strengthened our knowledge regarding the necessity of these contributions for heart pathophysiology (**Figure 3**). These effects on the heart range from involvement in embryonic development to homeostasis after birth and in adulthood, from protective responses under pathophysiological attacks to correlation with maladaptations leading to detrimental cardiac effects. Importantly, an essential protective potential against cardiac insults could be conferred to FGFs 1, 2, 9, 16, 19, and 21. In attempts to employ this potential for regenerative purposes, FGFs 1, 2, 10, and 16 have been promisingly tested for the induction of cardiomyocyte differentiation and proliferation from pluripotent stem cells as well as transdifferentiation of cardiac fibroblasts. Interestingly, FGFs involved in the pathological events of the heart are either defensive contributors (e.g., FGFs 2, 15/19, 16, and 21) or considered as causative agents of cardiac diseases and complications (e.g., FGFs 2, 21, and 23) and diagnostic biomarkers (e.g., FGFs 15/19, 21, and 23). FGF ligands, receptors and their antagonists can serve to preclude or alleviate cardiac complications and promote repair. However, this promising body of evidence is predominantly inferred from experimental models. In the future, the beneficial effects of FGFs on the heart should be further investigated in the clinical context. This will result in the creation of new stem cell-based therapies through

up-scaling of cardiomyocytes, and the discovery of therapies counteracting detrimental cardiac effects of pathological FGFs by specific blockers.

AUTHOR CONTRIBUTIONS

FK made an original plan, wrote the manuscript, and discussed it. NA, SB, and HS wrote the manuscript and discussed it. All authors contributed to the article and approved the submitted version.

FUNDING

This study was supported by a research grant of the University Medical Center Giessen and Marburg (UKGM).

REFERENCES

Ables, G. P., Ouattara, A., Hampton, T. G., Cooke, D., Perodin, F., Augie, I., et al. (2015). Dietary methionine restriction in mice elicits an adaptive cardiovascular response to hyperhomocysteinemia. *Sci. Rep.* 5:8886. doi: 10.1038/srep08886

Abu-Issa, R., Smyth, G., Smoak, I., Yamamura, K. I., and Meyers, E. N. (2002). Fgf8 is required for pharyngeal arch and cardiovascular development in the mouse. *Development* 129, 4613–4625.

Almahmoud, M. F., Soliman, E. Z., Bertoni, A. G., Kestenbaum, B., Katz, R., Lima, J. A. C., et al. (2018). Fibroblast growth factor-23 and heart failure with reduced versus preserved ejection fraction: MESA. *J. Am. Heart Assoc.* 7:e008334. doi: 10.1161/JAHA.117.008334

Andersen, I. A., Huntley, B. K., Sandberg, S. S., Heublein, D. M., and Burnett, J. C. (2016). Elevation of circulating but not myocardial FGF23 in human acute decompensated heart failure. *Nephrol. Dial. Transplant.* 31, 767–772. doi: 10.1093/ndt/gfv398

Andrukhova, O., Slavic, S., Smorodchenko, A., Zeitz, U., Shalhoub, V., Lanske, B., et al. (2014). FGF23 regulates renal sodium handling and blood pressure. *EMBO Mol. Med.* 6, 744–759. doi: 10.1002/emmm.201303716

Bergmann, O., Zdunek, S., Felker, A., Salehpour, M., Alkass, K., Bernard, S., et al. (2015). Dynamics of cell generation and turnover in the human heart. *Cell* 161, 1566–1575. doi: 10.1016/j.cell.2015.05.026

Bergmark, B. A., Udell, J. A., Morrow, D. A., Cannon, C. P., Steen, D. L., Jarolim, P., et al. (2018). Association of fibroblast growth factor 23 with recurrent cardiovascular events in patients after an acute coronary syndrome A secondary analysis of a randomized clinical trial. *JAMA Cardiol.* 3, 473–480. doi: 10.1001/jamacardio.2018.0653

Bergmark, B. A., Udell, J. A., Morrow, D. A., Jarolim, P., Kuder, J. F., Solomon, S. D., et al. (2019). Klotho, fibroblast growth factor-23, and the renin–angiotensin system — an analysis from the PEACE trial. *Eur. J. Heart Fail.* 21, 462–470. doi: 10.1002/ejhf.1424

Bruneau, B. G. (2013). Signaling and transcriptional networks in heart development and regeneration. *Cold Spring Harb. Perspect. Biol.* 5:a008292. doi: 10.1101/cshperspect.a008292

Carter, E. P., Fearon, A. E., and Grose, R. P. (2015). Careless talk costs lives: fibroblast growth factor receptor signalling and the consequences of pathway malfunction. *Trends Cell Biol.* 25, 221–233. doi: 10.1016/j.tcb.2014.11.003

Chan, S. S. K., Li, H. J., Hsueh, Y. C., Lee, D. S., Chen, J. H., Hwang, S. M., et al. (2010). Fibroblast growth factor-10 promotes cardiomyocyte differentiation from embryonic and induced pluripotent stem cells. *PLoS One* 5:e14414. doi: 10.1371/journal.pone.0014414

Chao, C. M., Yahya, F., Moiseenko, A., Tiozzo, C., Shrestha, A., Ahmadvand, N., et al. (2017). Fgf10 deficiency is causative for lethality in a mouse model of bronchopulmonary dysplasia. *J. Pathol.* 241, 91–103. doi: 10.1002/path.4834

Chen, C., Meng, Z., Zheng, Y., Hu, B., and Shen, E. (2018). Fibroblast growth factor 21 inhibition aggravates cardiac dysfunction in diabetic cardiomyopathy by improving lipid accumulation. *Exp. Ther. Med.* 15, 75–84. doi: 10.3892/etm.2017.5375

Chen, L. C., Shibu, M. A., Liu, C. J., Han, C. K., Ju, D. T., Chen, P. Y., et al. (2019). ERK1/2 mediates the lipopolysaccharide-induced upregulation of FGF-2, uPA, MMP-2, MMP-9 and cellular migration in cardiac fibroblasts. *Chem. Biol. Interact.* 306, 62–69. doi: 10.1016/j.cbi.2019.04.010

Chen, W. Y. (2020). Soluble alpha-klotho alleviates cardiac fibrosis without altering cardiomyocytes renewal. *Int. J. Mol. Sci.* 21:2186. doi: 10.3390/ijms21062186

Cheng, P., Zhang, F., Yu, L., Lin, X., He, L., Li, X., et al. (2016). Physiological and pharmacological roles of FGF21 in cardiovascular diseases. *J. Diabetes Res.* 2016:1540267. doi: 10.1155/2016/1540267

Chua, W., Purmah, Y., Cardoso, V. R., Gkoutos, G. V., Tull, S. P., Neculau, G., et al. (2019). Data-driven discovery and validation of circulating blood-based biomarkers associated with prevalent atrial fibrillation. *Eur. Heart J.* 40, 1268–1276. doi: 10.1093/eurheartj/ehy815

Clementi, A., Virzì, G. M., Goh, C. Y., Cruz, D. N., Granata, A., Vescovo, G., et al. (2013). Cardiorenal syndrome type 4: a review. *Cardiorenal Med.* 3, 63–70. doi: 10.1159/000350397

Cohen, E. D., Wang, Z., Lepore, J. J., Min, M. L., Taketo, M. M., Epstein, D. J., et al. (2007). Wnt/β-catenin signaling promotes expansion of Isl-1-positive cardiac progenitor cells through regulation of FGF signaling. *J. Clin. Invest.* 117, 1794–1804. doi: 10.1172/JCI31731

De Smet, F., Tembuyser, B., Lenard, A., Claes, F., Zhang, J., Michielsen, C., et al. (2014). Fibroblast growth factor signaling affects vascular outgrowth and is required for the maintenance of blood vessel integrity. *Chem. Biol.* 21, 1310–1317. doi: 10.1016/j.chembiol.2014.07.018

Ding, J., Tang, Q., Luo, B., Zhang, L., Lin, L., Han, L., et al. (2019). Klotho inhibits angiotensin II-induced cardiac hypertrophy, fibrosis, and dysfunction in mice through suppression of transforming growth factor-β1 signaling pathway. *Eur. J. Pharmacol.* 859:172549. doi: 10.1016/j.ejphar.2019.172549

Dongiovanni, P., Crudele, A., Panera, N., Romito, I., Meroni, M., De Stefanis, C., et al. (2020). β-Klotho gene variation is associated with liver damage in children with NAFLD. *J. Hepatol.* 72, 411–419. doi: 10.1016/j.jhep.2019.10.011

Doroudgar, S., and Glembotski, C. C. (2011). The cardiokine story unfolds: ischemic stress-induced protein secretion in the heart. *Trends Mol. Med.* 17, 207–214. doi: 10.1016/j.molmed.2010.12.003

El Agha, E., Kosanovic, D., Schermuly, R. T., and Bellusci, S. (2016). Role of fibroblast growth factors in organ regeneration and repair. *Semin. Cell Dev. Biol.* 53, 76–84. doi: 10.1016/j.semcdb.2015.10.009

Emrich, I. E., Brandenburg, V., Sellier, A. B., Schauerte, J., Wiedenroth, J., Untersteller, K., et al. (2019). Strength of fibroblast growth factor 23 as a cardiovascular risk predictor in chronic kidney disease weaken by ProBNP adjustment. *Am. J. Nephrol.* 49, 203–211. doi: 10.1159/000497125

Engel, F. B., Hsieh, P. C. H., Lee, R. T., and Keating, M. T. (2006). FGF1/p38 MAP kinase inhibitor therapy induces cardiomyocyte mitosis, reduces scarring, and rescues function after myocardial infarction. *Proc. Natl. Acad. Sci. U.S.A.* 103, 15546–15551. doi: 10.1073/pnas.0607382103

Engel, F. B., Schebesta, M., Duong, M. T., Lu, G., Ren, S., Madwed, J. B., et al. (2005). p38 MAP kinase inhibition enables proliferation of adult mammalian cardiomyocytes. *Genes Dev.* 19, 1175–1187. doi: 10.1101/gad.1306705

Erben, R. G. (2016). Update on FGF23 and Klotho signaling. *Mol. Cell. Endocrinol.* 432, 56–65. doi: 10.1016/j.mce.2016.05.008

Eschenhagen, T., Bolli, R., Braun, T., Field, L. J., Fleischmann, B. K., Frisén, J., et al. (2017). Cardiomyocyte regeneration: a consensus statement. *Circulation* 136, 680–686. doi: 10.1161/CIRCULATIONAHA.117.029343

Falcini, F., Rigante, D., Masi, L., Covino, M., Franceschelli, F., Leoncini, G., et al. (2013). Fibroblast growth factor 23 (FGF23) gene polymorphism in children with Kawasaki syndrome (KS) and susceptibility to cardiac abnormalities. *Ital. J. Pediatr.* 39:69. doi: 10.1186/1824-7288-39-69

Fan, C., Tang, Y., Zhao, M., Lou, X., Pretorius, D., Menasche, P., et al. (2020). CHIR99021 and fibroblast growth factor 1 enhance the regenerative potency

of human cardiac muscle patch after myocardial infarction in mice. *J. Mol. Cell. Cardiol.* 141, 1–10. doi: 10.1016/j.yjmcc.2020.03.003

Faul, C., Amaral, A. P., Oskouei, B., Hu, M. C., Sloan, A., Isakova, T., et al. (2011). FGF23 induces left ventricular hypertrophy. *J. Clin. Invest.* 121, 4393–4408. doi: 10.1172/JCI46122

Felker, A., Prummel, K. D., Merks, A. M., Mickoleit, M., Brombacher, E. C., Huisken, J., et al. (2018). Continuous addition of progenitors forms the cardiac ventricle in zebrafish. *Nat. Commun.* 9:2001. doi: 10.1038/s41467-018-04402-6

Formiga, F. R., Pelacho, B., Garbayo, E., Imbuluzqueta, I., Díaz-Herráez, P., Abizanda, G., et al. (2014). Controlled delivery of fibroblast growth factor-1 and neuregulin-1 from biodegradable microparticles promotes cardiac repair in a rat myocardial infarction model through activation of endogenous regeneration. *J. Control. Release* 173, 132–139. doi: 10.1016/j.jconrel.2013.10.034

Fuller, S. J., Sivarajah, K., and Sugden, P. H. (2008). ErbB receptors, their ligands, and the consequences of their activation and inhibition in the myocardium. *J. Mol. Cell. Cardiol.* 44, 831–854. doi: 10.1016/j.yjmcc.2008.02.278

Garbayo, E., Gavira, J. J., De Yebenes, M. G., Pelacho, B., Abizanda, G., Lana, H., et al. (2016). Catheter-based intramyocardial injection of FGF1 or NRG1-loaded MPs improves cardiac function in a preclinical model of ischemia-reperfusion. *Sci. Rep.* 6:25932. doi: 10.1038/srep25932

Giordano, F. J. (2005). Oxygen, oxidative stress, hypoxia, and heart failure. *J. Clin. Invest.* 115, 500–508. doi: 10.1172/JCI200524408

Goetz, R., Ohnishi, M., Ding, X., Kurosu, H., Wang, L., Akiyoshi, J., et al. (2012). Klotho coreceptors inhibit signaling by paracrine fibroblast growth factor 8 subfamily ligands. *Mol. Cell. Biol.* 32, 1944–1954. doi: 10.1128/mcb.06603-11

Gómez-Sámano, M. Á., Grajales-Gómez, M., Zuarth-Vázquez, J. M., Navarro-Flores, M. F., Martínez-Saavedra, M., Juárez-León, Ó. A., et al. (2017). Fibroblast growth factor 21 and its novel association with oxidative stress. *Redox Biol.* 11, 335–341. doi: 10.1016/j.redox.2016.12.024

Grabner, A., Amaral, A. P., Schramm, K., Singh, S., Sloan, A., Yanucil, C., et al. (2015). Activation of cardiac fibroblast growth factor receptor 4 causes left ventricular hypertrophy. *Cell Metab.* 22, 1020–1032. doi: 10.1016/j.cmet.2015.09.002

Grabner, A., Schramm, K., Silswal, N., Hendrix, M., Yanucil, C., Czaya, B., et al. (2017). FGF23/FGFR4-mediated left ventricular hypertrophy is reversible. *Sci. Rep.* 7:1993. doi: 10.1038/s41598-017-02068-6

Guzzetta, A., Koska, M., Rowton, M., Sullivan, K. R., Jacobs-Li, J., Kweon, J., et al. (2020). Hedgehog–FGF signaling axis patterns anterior mesoderm during gastrulation. *Proc. Natl. Acad. Sci. U.S.A.* 117, 15712–15723. doi: 10.1073/pnas.1914167117

Hao, Y., Zhou, J., Zhou, M., Ma, X., Lu, Z., Gao, M., et al. (2013). Serum levels of fibroblast growth factor 19 are inversely associated with coronary artery disease in Chinese individuals. *PLoS One* 8:e72345. doi: 10.1371/journal.pone.0072345

Hartung, H., Feldman, B., Lovec, H., Coulier, F., Birnbaum, D., and Goldfarb, M. (1997). Murine FGF-12 and FGF-13: expression in embryonic nervous system, connective tissue and heart. *Mech. Dev.* 64, 31–39. doi: 10.1016/S0925-4773(97)00042-7

Hennessey, J. A., Wei, E. Q., and Pitt, G. S. (2013). Fibroblast growth factor homologous factors modulate cardiac calcium channels. *Circ. Res.* 113, 381–388. doi: 10.1161/CIRCRESAHA.113.301215

Holden, R. M., Hétu, M. F., Li, T. Y., Ward, E., Couture, L. E., Herr, J. E., et al. (2019). The heart and kidney: abnormal phosphate homeostasis is associated with atherosclerosis. *J. Endocr. Soc.* 3, 159–170. doi: 10.1210/js.2018-00311

Hotta, Y., Sasaki, S., Konishi, M., Kinoshita, H., Kuwahara, K., Nakao, K., et al. (2008). Fgf16 is required for cardiomyocyte proliferation in the mouse embryonic heart. *Dev. Dyn.* 237, 2947–2954. doi: 10.1002/dvdy.21726

House, S. L., Bolte, C., Zhou, M., Doetschman, T., Klevitsky, R., Newman, G., et al. (2003). Cardiac-specific overexpression of fibroblast growth factor-2 protects against myocardial dysfunction and infarction in a murine model of low-flow ischemia. *Circulation* 108, 3140–3148. doi: 10.1161/01.CIR.0000105723.91637.1C

House, S. L., Castro, A. M., Lupu, T. S., Weinheimer, C., Smith, C., Kovacs, A., et al. (2016). Endothelial fibroblast growth factor receptor signaling is required for vascular remodeling following cardiac ischemia-reperfusion injury. *Am. J. Physiol. Heart Circ. Physiol.* 310, H559–H571. doi: 10.1152/ajpheart.00758.2015

House, S. L., House, B. E., Glascock, B., Kimball, T., Nusayr, E., Schultz, J. E. J., et al. (2010). Fibroblast growth factor 2 mediates isoproterenol-induced cardiac hypertrophy through activation of the extracellular regulated kinase. *Mol. Cell. Pharmacol.* 2, 143–154. doi: 10.4255/mcpharmacol.10.20

House, S. L., Wang, J., Castro, A. M., Weinheimer, C., Kovacs, A., and Ornitz, D. M. (2015). Fibroblast growth factor 2 is an essential cardioprotective factor in a closed-chest model of cardiac ischemia-reperfusion injury. *Physiol. Rep.* 3:e12278. doi: 10.14814/phy2.12278

Hu, S., Cao, S., Tong, Z., and Liu, J. (2018). FGF21 protects myocardial ischemia-reperfusion injury through reduction of miR-145-mediated autophagy. *Am. J. Transl. Res.* 10, 3677–3688.

Hu, T., Yamagishi, H., Maeda, J., McAnally, J., Yamagishi, C., and Srivastava, D. (2004). Tbx1 regulates fibroblast growth factors in the anterior heart field through reinforcing autoregulatory loop involving forkhead transcription factors. *Development* 131, 5491–5502. doi: 10.1242/dev.01399

Hu, Y., Li, L., Shen, L., Gao, H., Yu, F., Yin, W., et al. (2017). FGF-16 protects against adverse cardiac remodeling in the infarct diabetic heart. *Am. J. Transl. Res.* 9, 1630–1640.

Hubert, F., Payan, S. M., and Rochais, F. (2018). FGF10 signaling in heart development, homeostasis, disease and repair. *Front. Genet.* 9:599. doi: 10.3389/fgene.2018.00599

Hui, T. H., McClelland, R. L., Allison, M. A., Rodriguez, C. J., Kronmal, R. A., Heckbert, S. R., et al. (2018). The relationship of circulating fibroblast growth factor 21 levels with incident atrial fibrillation: the Multi-Ethnic Study of Atherosclerosis. *Atherosclerosis* 269, 86–91. doi: 10.1016/j.atherosclerosis.2017.12.026

Hutson, M. R., Zeng, X. L., Kim, A. J., Antoon, E., Harward, S., and Kirby, M. L. (2010). Arterial pole progenitors interpret opposing FGF/BMP signals to proliferate or differentiate. *J. Cell Sci.* 123:e1. doi: 10.1242/jcs.079756

Ilagan, R., Abu-Issa, R., Brown, D., Yang, Y. P., Jiao, K., Schwartz, R. J., et al. (2006). Fgf8 is required for anterior heart field development. *Development* 133, 2435–2445. doi: 10.1242/dev.02408

Ito, S., Fujimori, T., Furuya, A., Satoh, J., Nabeshima, Y., and Nabeshima, Y. I. (2005). Impaired negative feedback suppression of bile acid synthesis in mice lacking βKlotho. *J. Clin. Invest.* 115, 2202–2208. doi: 10.1172/JCI23076

Itoh, N., Ohta, H., and Konishi, M. (2015). Endocrine FGFs: evolution, physiology, pathophysiology, and pharmacotherapy. *Front. Endocrinol.* 6:154. doi: 10.3389/fendo.2015.00154

Itoh, N., Ohta, H., Nakayama, Y., and Konishi, M. (2016). Roles of FGF signals in heart development, health, and disease. *Front. Cell Dev. Biol.* 4:110. doi: 10.3389/fcell.2016.00110

Jang, Y., Choi, S. C., Lim, D. S., Kim, J. H., Kim, J., and Park, Y. (2020). Modulating cardiomyocyte and fibroblast interaction using layer-by-layer deposition facilitates synchronisation of cardiac macro tissues. *Soft Matter* 16, 428–434. doi: 10.1039/c9sm01531k

Jennbacken, K., Wågberg, F., Karlsson, U., Eriksson, J., Magnusson, L., Chimienti, M., et al. (2019). Phenotypic screen with the human secretome identifies FGF16 as inducing proliferation of iPSC-derived cardiac progenitor cells. *Int. J. Mol. Sci.* 20:6037. doi: 10.3390/ijms20236037

Jimbo, R., and Shimosawa, T. (2014). Cardiovascular risk factors and chronic kidney disease - FGF23: a key molecule in the cardiovascular disease. *Int. J. Hypertens.* 2014:381082. doi: 10.1155/2014/381082

Joki, Y., Ohashi, K., Yuasa, D., Shibata, R., Ito, M., Matsuo, K., et al. (2015). FGF21 attenuates pathological myocardial remodeling following myocardial infarction through the adiponectin-dependent mechanism. *Biochem. Biophys. Res. Commun.* 459, 124–130. doi: 10.1016/j.bbrc.2015.02.081

Karatolios, K., Moosdorf, R., Maisch, B., and Pankuweit, S. (2012). Cytokines in pericardial effusion of patients with inflammatory pericardial disease. *Mediators Inflamm.* 2012:382082. doi: 10.1155/2012/382082

Kawai, T., Takahashi, T., Esaki, M., Ushikoshi, H., Nagano, S., Fujiwara, H., et al. (2004). Efficient cardiomyogenic differentiation of embryonic stem cell by fibroblast growth factor 2 and bone morphogenetic protein 2. *Circ. J.* 68, 691–702. doi: 10.1253/circj.68.691

Kaye, D., Pimental, D., Prasad, S., Mäki, T., Berger, H. J., McNeil, P. L., et al. (1996). Role of transiently altered sarcolemmal membrane permeability and basic fibroblast growth factor release in the hypertrophic response of adult rat

ventricular myocytes to increased mechanical activity in vitro. *J. Clin. Invest.* 97, 281–291. doi: 10.1172/JCI118414

Kelly, R. G., Brown, N. A., and Buckingham, M. E. (2001). The arterial pole of the mouse heart forms from fgf10-expressing cells in pharyngeal mesoderm. *Dev. Cell* 1, 435–440. doi: 10.1016/S1534-5807(01)00040-5

Kharitonenkov, A., Shiyanova, T. L., Koester, A., Ford, A. M., Micanovic, R., Galbreath, E. J., et al. (2005). FGF-21 as a novel metabolic regulator. *J. Clin. Invest.* 115, 1627–1635. doi: 10.1172/JCI23606

Kikuchi, K., and Poss, K. D. (2012). Cardiac regenerative capacity and mechanisms. *Annu. Rev. Cell Dev. Biol.* 28, 719–741. doi: 10.1146/annurev-cellbio-101011-155739

Kim, W. J., Kim, S. S., Lee, H. C., Song, S. H., Bae, M. J., Yi, Y. S., et al. (2015). Association between serum fibroblast growth factor 21 and coronary artery disease in patients with type 2 diabetes. *J. Korean Med. Sci.* 30, 586–590. doi: 10.3346/jkms.2015.30.5.586

Koleini, N., Nickel, B. E., Wang, J., Roveimiab, Z., Fandrich, R. R., Kirshenbaum, L. A., et al. (2017). Fibroblast growth factor-2-mediated protection of cardiomyocytes from the toxic effects of doxorubicin requires the mTOR/Nrf-2/HO-1 pathway. *Oncotarget* 8, 87415–87430. doi: 10.18632/oncotarget.20558

Koleini, N., Santiago, J. J., Nickel, B. E., Sequiera, G. L., Wang, J., Fandrich, R. R., et al. (2019). Elimination or neutralization of endogenous high-molecular-weight FGF2 mitigates doxorubicin-induced cardiotoxicity. *Am. J. Physiol. Heart Circ. Physiol.* 316, H279–H288. doi: 10.1152/ajpheart.00587.2018

Koller, L., Kleber, M. E., Brandenburg, V. M., Goliasch, G., Richter, B., Sulzgruber, P., et al. (2015). Fibroblast growth factor 23 is an independent and specific predictor of mortality in patients with heart failure and reduced ejection fraction. *Circ. Heart Fail.* 8, 1059–1067. doi: 10.1161/CIRCHEARTFAILURE.115.002341

Kolossov, E., Bostani, T., Roell, W., Breitbach, M., Pillekamp, F., Nygren, J. M., et al. (2006). Engraftment of engineered ES cell-derived cardiomyocytes but not BM cells restores contractile function to the infarcted myocardium. *J. Exp. Med.* 203, 2315–2327. doi: 10.1084/jem.20061469

Korf-Klingebiel, M., Kempf, T., Sauer, T., Brinkmann, E., Fischer, P., Meyer, G. P., et al. (2008). Bone marrow cells are a rich source of growth factors and cytokines: implications for cell therapy trials after myocardial infarction. *Eur. Heart J.* 29, 2851–2858. doi: 10.1093/eurheartj/ehn456

Korf-Klingebiel, M., Kempf, T., Schlüter, K. D., Willenbockel, C., Brod, T., Heineke, J., et al. (2011). Conditional transgenic expression of fibroblast growth factor 9 in the adult mouse heart reduces heart failure mortality after myocardial infarction. *Circulation* 123, 504–514. doi: 10.1161/CIRCULATIONAHA.110.989665

Kotov, G., Landzhov, B., Stamenov, N., Stanchev, S., and Iliev, A. (2020). Changes in the number of mast cells, expression of fibroblast growth factor-2 and extent of interstitial fibrosis in established and advanced hypertensive heart disease. *Ann. Anat.* 232:151564. doi: 10.1016/j.aanat.2020.151564

Krejci, E., Pesevski, Z., Nanka, O., and Sedmera, D. (2016). Physiological role of fgf signaling in growth and remodeling of developing cardiovascular system. *Physiol. Res.* 65, 425–435. doi: 10.33549/physiolres.933216

Kuga, K., Kusakari, Y., Uesugi, K., Semba, K., Urashima, T., Akaike, T., et al. (2020). Fibrosis growth factor 23 is a promoting factor for cardiac fibrosis in the presence of transforming growth factor-β1. *PLoS One* 15:e0231905. doi: 10.1371/journal.pone.0231905

Kukuła, K., Chojnowska, L., Dąbrowski, M., Witkowski, A., Chmielak, Z., Skwarek, M., et al. (2011). Intramyocardial plasmid-encoding human vascular endothelial growth factor A165/basic fibroblast growth factor therapy using percutaneous transcatheter approach in patients with refractory coronary artery disease (VIF-CAD). *Am. Heart J.* 161, 581–589. doi: 10.1016/j.ahj.2010.11.023

Kuwabara, K., Ogawa, S., Matsumoto, M., Koga, S., Clauss, M., Pinsky, D. J., et al. (1995). Hypoxia-mediated induction of acidic/basic fibroblast growth factor and platelet-derived growth factor in mononuclear phagocytes stimulates growth of hypoxic endothelial cells. *Proc. Natl. Acad. Sci. U.S.A.* 92, 4606–4610. doi: 10.1073/pnas.92.10.4606

Laurell, T., Nilsson, D., Hofmeister, W., Lindstrand, A., Ahituv, N., Vandermeer, J., et al. (2014). Identification of three novel fgf16 mutations in x-linked recessive fusion of the fourth and fifth metacarpals and possible correlation with heart disease. *Mol. Genet. Genomic Med.* 2, 402–411. doi: 10.1002/mgg3.81

Lavine, K. J., White, A. C., Park, C., Smith, C. S., Choi, K., Long, F., et al. (2006). Fibroblast growth factor signals regulate a wave of Hedgehog activation that is essential for coronary vascular development. *Genes Dev.* 20, 1651–1666. doi: 10.1101/gad.1411406

Lavine, K. J., Yu, K., White, A. C., Zhang, X., Smith, C., Partanen, J., et al. (2005). Endocardial and epicardial derived FGF signals regulate myocardial proliferation and differentiation *in vivo*. *Dev. Cell* 8, 85–95. doi: 10.1016/j.devcel.2004.12.002

Leifheit-Nestler, M., Grabner, A., Hermann, L., Richter, B., Schmitz, K., Fischer, D. C., et al. (2017). Vitamin D treatment attenuates cardiac FGF23/FGFR4 signaling and hypertrophy in uremic rats. *Nephrol. Dial. Transplant.* 32, 1493–1503. doi: 10.1093/ndt/gfw454

Leifheit-Nestler, M., Siemer, R. G., Flasbart, K., Richter, B., Kirchhoff, F., Ziegler, W. H., et al. (2016). Induction of cardiac FGF23/FGFR4 expression is associated with left ventricular hypertrophy in patients with chronic kidney disease. *Nephrol. Dial. Transplant.* 31, 1088–1099. doi: 10.1093/ndt/gfv421

Lepilina, A., Coon, A. N., Kikuchi, K., Holdway, J. E., Roberts, R. W., Burns, C. G., et al. (2006). A dynamic epicardial injury response supports progenitor cell activity during zebrafish heart regeneration. *Cell* 127, 607–619. doi: 10.1016/j.cell.2006.08.052

Li, F., Wang, X., Capasso, J. M., and Gerdes, A. M. (1996). Rapid transition of cardiac myocytes from hyperplasia to hypertrophy during postnatal development. *J. Mol. Cell. Cardiol.* 28, 1737–1746. doi: 10.1006/jmcc.1996.0163

Li, X., Wu, D., and Tian, Y. (2018). Fibroblast growth factor 19 protects the heart from oxidative stress-induced diabetic cardiomyopathy via activation of AMPK/Nrf2/HO-1 pathway. *Biochem. Biophys. Res. Commun.* 502, 62–68. doi: 10.1016/j.bbrc.2018.05.121

Li, X.-H., Li, Q., Jiang, L., Deng, C., Liu, Z., Fu, Y., et al. (2015). Generation of functional human cardiac progenitor cells by high-efficiency protein transduction. *Stem Cells Transl. Med.* 4, 1415–1424. doi: 10.5966/sctm.2015-0136

Liao, S., Bodmer, J. R., Azhar, M., Newman, G., Coffin, J. D., Doetschman, T., et al. (2010). The influence of FGF2 high molecular weight (HMW) isoforms in the development of cardiac ischemia-reperfusion injury. *J. Mol. Cell. Cardiol.* 48, 1245–1254. doi: 10.1016/j.yjmcc.2010.01.014

Liguori, T. T. A., Liguori, G. R., Moreira, L. F. P., and Harmsen, M. C. (2018). Fibroblast growth factor-2, but not the adipose tissue-derived stromal cells secretome, inhibits TGF-β1-induced differentiation of human cardiac fibroblasts into myofibroblasts. *Sci. Rep.* 8:16633. doi: 10.1038/s41598-018-34747-3

Lin, Z., Wu, Z., Yin, X., Liu, Y., Yan, X., Lin, S., et al. (2010). Serum levels of FGF-21 are increased in coronary heart disease patients and are independently associated with adverse lipid profile. *PLoS One* 5:e15534. doi: 10.1371/journal.pone.0015534

Liu, C. J., Dib-Hajj, S. D., Renganathan, M., Cummins, T. R., and Waxman, S. G. (2003). Modulation of the cardiac sodium channel Nav1.5 by fibroblast growth factor homologous factor 1B. *J. Biol. Chem.* 278, 1029–1036. doi: 10.1074/jbc.M207074200

Liu, D., Zhou, S., and Mao, H. (2020). MicroRNA-497/fibroblast growth factor-23 axis, a predictive indictor for decreased major adverse cardiac and cerebral event risk in end-stage renal disease patients who underwent continuous ambulatory peritoneal dialysis. *J. Clin. Lab. Anal.* 34:e23220. doi: 10.1002/jcla.23220

Liu, S. Q., Roberts, D., Kharitonenkov, A., Zhang, B., Hanson, S. M., Li, Y. C., et al. (2013). Endocrine protection of ischemic myocardium by FGF21 from the liver and adipose tissue. *Sci. Rep.* 3:2767. doi: 10.1038/srep02767

Liu, Y., Liu, Y., Liu, X., Chen, J., Zhang, K., Huang, F., et al. (2015). Apocynin Attenuates cardiac injury in type 4 cardiorenal syndrome via suppressing cardiac fibroblast growth factor-2 with oxidative stress inhibition. *J. Am. Heart Assoc.* 4:e001598. doi: 10.1161/JAHA.114.001598

Lu, S. Y., Jin, Y., Li, X., Sheppard, P., Bock, M. E., Sheikh, F., et al. (2010). Embryonic survival and severity of cardiac and craniofacial defects are affected by genetic background in fibroblast growth factor-16 null mice. *DNA Cell Biol.* 29, 407–415. doi: 10.1089/dna.2010.1024

Lu, S. Y., Sheikh, F., Sheppard, P. C., Fresnoza, A., Duckworth, M. L., Detillieux, K. A., et al. (2008a). FGF-16 is required for embryonic heart development. *Biochem. Biophys. Res. Commun.* 373, 270–274. doi: 10.1016/j.bbrc.2008.06.029

Lu, S. Y., Sontag, D. P., Detillieux, K. A., and Cattini, P. A. (2008b). FGF-16 is released from neonatal cardiac myocytes and alters growth-related signaling: a possible role in postnatal development. *Am. J. Physiol. Cell Physiol.* 294, C1242–C1249. doi: 10.1152/ajpcell.00529.2007

Lu, T. Y., Lin, B., Li, Y., Arora, A., Han, L., Cui, C., et al. (2013). Overexpression of microRNA-1 promotes cardiomyocyte commitment from human cardiovascular progenitors via suppressing WNT and FGF signaling pathways. *J. Mol. Cell. Cardiol.* 63, 146–154. doi: 10.1016/j.yjmcc.2013.07.019

Luo, W., Zhao, X., Jin, H., Tao, L., Zhu, J., Wang, H., et al. (2015). Akt1 signaling coordinates bmp signaling and β-catenin activity to regulate second heart field progenitor development. *Development* 142, 732–742. doi: 10.1242/dev.119016

Lutsey, P. L., Alonso, A., Selvin, E., Pankow, J. S., Michos, E. D., Agarwal, S. K., et al. (2014). Fibroblast growth factor-23 and incident coronary heart disease, heart failure, and cardiovascular mortality: the atherosclerosis risk in communities study. *J. Am. Heart Assoc.* 3:e000936. doi: 10.1161/JAHA.114.000936

Marçais, C., Maucort-Boulch, D., Drai, J., Dantony, E., Carlier, M. C., Blond, E., et al. (2017). Circulating klotho associates with cardiovascular morbidity and mortality during hemodialysis. *J. Clin. Endocrinol. Metab.* 102, 3154–3161. doi: 10.1210/jc.2017-00104

Marguerie, A., Bajolle, F., Zaffran, S., Brown, N. A., Dickson, C., Buckingham, M. E., et al. (2006). Congenital heart defects in Fgfr2-IIIb and Fgf10 mutant mice. *Cardiovasc. Res.* 71, 50–60. doi: 10.1016/j.cardiores.2006.03.021

Marthi, A., Donovan, K., Haynes, R., Wheeler, D. C., Baigent, C., Rooney, C. M., et al. (2018). Fibroblast growth factor-23 and risks of cardiovascular and noncardiovascular diseases: a meta-analysis. *J. Am. Soc. Nephrol.* 29, 2000–2013. doi: 10.1681/ASN.2017121334

Mascheck, L., Sharifpanah, F., Tsang, S. Y., Wartenberg, M., and Sauer, H. (2015). Stimulation of cardiomyogenesis from mouse embryonic stem cells by nuclear translocation of cardiotrophin-1. *Int. J. Cardiol.* 193, 23–33. doi: 10.1016/j.ijcard.2015.05.019

Mathew, J. S., Sachs, M. C., Katz, R., Patton, K. K., Heckbert, S. R., Hoofnagle, A. N., et al. (2014). Fibroblast growth factor-23 and incident atrial fibrillation: the multi-ethnic study of atherosclerosis (MESA) and the cardiovascular health study (CHS). *Circulation* 130, 298–307. doi: 10.1161/CIRCULATIONAHA.113.005499

Matsumoto, E., Sasaki, S., Kinoshita, H., Kito, T., Ohta, H., Konishi, M., et al. (2013). Angiotensin II-induced cardiac hypertrophy and fibrosis are promoted in mice lacking Fgf16. *Genes Cells* 18, 544–553. doi: 10.1111/gtc.12055

Matsunaga, S., Okigaki, M., Takeda, M., Matsui, A., Honsho, S., Katsume, A., et al. (2009). Endothelium-targeted overexpression of constitutively active FGF receptor induces cardioprotection in mice myocardial infarction. *J. Mol. Cell. Cardiol.* 46, 663–673. doi: 10.1016/j.yjmcc.2009.01.015

Meganathan, K., Sotiriadou, I., Natarajan, K., Hescheler, J., and Sachinidis, A. (2015). Signaling molecules, transcription growth factors and other regulators revealed from in-vivo and in-vitro models for the regulation of cardiac development. *Int. J. Cardiol.* 183, 117–128. doi: 10.1016/j.ijcard.2015.01.049

Memmos, E., Sarafidis, P., Pateinakis, P., Tsiantoulas, A., Faitatzidou, D., Giamalis, P., et al. (2019). Soluble Klotho is associated with mortality and cardiovascular events in hemodialysis. *BMC Nephrol.* 20:217. doi: 10.1186/s12882-019-1391-1

Mesbah, K., Rana, M. S., Francou, A., van duijvenboden, K., Papaioannou, V. E., Moorman, A. F., et al. (2012). Identification of a Tbx1/Tbx2/Tbx3 genetic pathway governing pharyngeal and arterial pole morphogenesis. *Hum. Mol. Genet.* 21, 1217–1229. doi: 10.1093/hmg/ddr553

Morabito, C. J., Dettman, R. W., Kattan, J., Collier, J. M., and Bristow, J. (2001). Positive and negative regulation of epicardial-mesenchymal transformation during avian heart development. *Dev. Biol.* 234, 204–215. doi: 10.1006/dbio.2001.0254

Mori, S., Hatori, N., Kawaguchi, N., Hamada, Y., Shih, T. C., Wu, C. Y., et al. (2017). The integrin-binding defective FGF2 mutants potently suppress FGF2 signalling and angiogenesis. *Biosci. Rep.* 37:BSR20170173. doi: 10.1042/BSR20170173

Mori, S., Tran, V., Nishikawa, K., Kaneda, T., Hamada, Y., Kawaguchi, N., et al. (2013). A dominant-negative FGF1 mutant (the R50E Mutant) suppresses tumorigenesis and angiogenesis. *PLoS One* 8:e57927. doi: 10.1371/journal.pone.0057927

Murakami, M., Nguyen, L. T., Zhang, Z. W., Moodie, K. L., Carmeliet, P., Stan, R. V., et al. (2008). The FGF system has a key role in regulating vascular integrity. *J. Clin. Invest.* 118, 3355–3366. doi: 10.1172/JCI35298

Navarro-García, J. A., Delgado, C., Fernández-Velasco, M., Val-Blasco, A., Rodríguez-Sánchez, E., Aceves-Ripoll, J., et al. (2019). Fibroblast growth factor-23 promotes rhythm alterations and contractile dysfunction in adult ventricular cardiomyocytes. *Nephrol. Dial. Transplant.* 34, 1864–1875. doi: 10.1093/ndt/gfy392

Okada-Ban, M. B., Thiery, J. P., and Jouanneau, J. (2000). Fibroblast growth factor-2. *Int. J. Biochem. Cell Biol.* 32, 263–267. doi: 10.1016/S1357-2725(99)00133-8

Oladipupo, S. S., Smith, C., Santeford, A., Park, C., Sene, A., Wiley, L. A., et al. (2014). Endothelial cell FGF signaling is required for injury response but not for vascular homeostasis. *Proc. Natl. Acad. Sci. U.S.A.* 111, 13379–13384. doi: 10.1073/pnas.1324235111

Ong, K. L., Rye, K. A., O'Connell, R., Jenkins, A. J., Brown, C., Xu, A., et al. (2012). Long-term fenofibrate therapy increases fibroblast growth factor 21 and retinol-binding protein 4 in subjects with type 2 diabetes. *J. Clin. Endocrinol. Metab.* 97, 4701–4708. doi: 10.1210/jc.2012-2267

Ornitz, D. M., and Itoh, N. (2015). The fibroblast growth factor signaling pathway. *Wiley Interdiscip. Rev. Dev. Biol.* 4, 215–266. doi: 10.1002/wdev.176

Park, E. J., Watanabe, Y., Smyth, G., Miyagawa-Tomita, S., Meyers, E., Klingensmith, J., et al. (2008). An FGF autocrine loop initiated in second heart field mesoderm regulates morphogenesis at the arterial pole of the heart. *Development* 135, 3599–3610. doi: 10.1242/dev.025437

Pascual-Gil, S., Simón-Yarza, T., Garbayo, E., Prósper, F., and Blanco-Prieto, M. J. (2017). Cytokine-loaded PLGA and PEG-PLGA microparticles showed similar heart regeneration in a rat myocardial infarction model. *Int. J. Pharm.* 523, 531–533. doi: 10.1016/j.ijpharm.2016.11.022

Pellieux, C., Foletti, A., Peduto, G., Aubert, J. F., Nussberger, J., Beermann, F., et al. (2001). Dilated cardiomyopathy and impaired cardiac hypertrophic response to angiotensin II in mice lacking FGF-2. *J. Clin. Invest.* 108, 1843–1851. doi: 10.1172/JCI13627

Peoples, G. E., Blotnick, S., Takahashii, K., Freeman, M. R., Klagsbrun, M., and Eberlein, T. J. (1995). T lymphocytes that infiltrate tumors and atherosclerotic plaques produce heparin-binding epidermal growth factor-like growth factor and basic fibroblast growth factor: a potential pathologic role. *Proc. Natl. Acad. Sci. U.S.A.* 92, 6547–6551. doi: 10.1073/pnas.92.14.6547

Planavila, A., Redondo, I., Hondares, E., Vinciguerra, M., Munts, C., Iglesias, R., et al. (2013). Fibroblast growth factor 21 protects against cardiac hypertrophy in mice. *Nat. Commun.* 4:2019. doi: 10.1038/ncomms3019

Planavila, A., Redondo-Angulo, I., Ribas, F., Garrabou, G., Casademont, J., Giralt, M., et al. (2015a). Fibroblast growth factor 21 protects the heart from oxidative stress. *Cardiovasc. Res.* 106, 19–31. doi: 10.1093/cvr/cvu263

Planavila, A., Redondo-Angulo, I., and Villarroya, F. (2015b). FGF21 and cardiac physiopathology. *Front. Endocrinol.* 6:133. doi: 10.3389/fendo.2015.00133

Pöling, J., Gajawada, P., Richter, M., Lörchner, H., Polyakova, V., Kostin, S., et al. (2014). Therapeutic targeting of the oncostatin M receptor-β prevents inflammatory heart failure. *Basic Res. Cardiol.* 109:396. doi: 10.1007/s00395-013-0396-3

Porrello, E. R., Mahmoud, A. I., Simpson, E., Hill, J. A., Richardson, J. A., Olson, E. N., et al. (2011). Transient regenerative potential of the neonatal mouse heart. *Science* 331, 1078–1080. doi: 10.1126/science.1200708

Rao, Z., Shen, D., Chen, J., Jin, L., Wu, X., Chen, M., et al. (2020). Basic fibroblast growth factor attenuates injury in myocardial infarction by enhancing hypoxia-inducible factor-1 Alpha accumulation. *Front. Pharmacol.* 11:1193. doi: 10.3389/fphar.2020.01193

Rapraeger, A. C., Krufka, A., and Olwin, B. B. (1991). Requirement of heparan sulfate for bFGF-mediated fibroblast growth and myoblast differentiation. *Science* 252, 1705–1708. doi: 10.1126/science.1646484

Rasouli, S. J., El-Brolosy, M., Tsedeke, A. T., Bensimon-Brito, A., Ghanbari, P., Maischein, H. M., et al. (2018). The flow responsive transcription factor Klf2 is required for myocardial wall integrity by modulating Fgf signaling. *eLife* 7:e38889. doi: 10.7554/eLife.38889

Refsgaard Holm, M., Christensen, H., Rasmussen, J., Johansen, M. L., Schou, M., Faber, J., et al. (2019). Fibroblast growth factor 21 in patients with cardiac

cachexia: a possible role of chronic inflammation. *ESC Heart Fail.* 6, 983–991. doi: 10.1002/ehf2.12502

Ren, Z., Xiao, W., Zeng, Y., Liu, M. H., Li, G. H., Tang, Z. H., et al. (2019). Fibroblast growth factor-21 alleviates hypoxia/reoxygenation injury in H9c2 cardiomyocytes by promoting autophagic flux. *Int. J. Mol. Med.* 43, 1321–1330. doi: 10.3892/ijmm.2019.4071

Richter, M., Lautze, H. J., Walther, T., Braun, T., Kostin, S., and Kubin, T. (2015). The failing heart is a major source of circulating FGF23 via oncostatin M receptor activation. *J. Heart Lung Transplant.* 34, 1211–1214. doi: 10.1016/j.healun.2015.06.007

Richter, M. H., Lautze, H., Skwara, W., Schönburg, M., Beiras-Fernandez, A., Werner, I., et al. (2015). Activation of oncostatin M receptor-β in cardiomyocytes increases serum levels of FGF23 during heart failure. *J. Heart Lung Transplant.* 34:S174. doi: 10.1016/j.healun.2015.01.475

Rochais, F., Sturny, R., Chao, C. M., Mesbah, K., Bennett, M., Mohun, T. J., et al. (2014). FGF10 promotes regional foetal cardiomyocyte proliferation and adult cardiomyocyte cell-cycle re-entry. *Cardiovasc. Res.* 104, 432–442. doi: 10.1093/cvr/cvu232

Roy, C., Lejeune, S., Slimani, A., de Meester, C., Ahn As, S. A., Rousseau, M. F., et al. (2020). Fibroblast growth factor 23: a biomarker of fibrosis and prognosis in heart failure with preserved ejection fraction. *ESC Heart Fail.* 7, 2494–2507. doi: 10.1002/ehf2.12816

Rubin, N., Darehzereshki, A., Bellusci, S., Kaartinen, V., and Lien, C. L. (2013). FGF10 signaling enhances epicardial cell expansion during neonatal mouse heart repair. *J. Cardiovasc. Dis. Diagnosis* 1:101. doi: 10.4172/2329-9517.1000101

Sadahiro, T., Yamanaka, S., and Ieda, M. (2015). Direct cardiac reprogramming: progress and challenges in basic biology and clinical applications. *Circ. Res.* 116, 1378–1391. doi: 10.1161/CIRCRESAHA.116.305374

Sauer, H., Ravindran, F., Beldoch, M., Sharifpanah, F., Jedelská, J., Strehlow, B., et al. (2013). A2-macroglobulin enhances vasculogenesis/angiogenesis of mouse embryonic stem cells by stimulation of nitric oxide generation and induction of fibroblast growth factor-2 expression. *Stem Cells Dev.* 22, 1443–1454. doi: 10.1089/scd.2012.0640

Seiler, S., Wen, M., Roth, H. J., Fehrenz, M., Flügge, F., Herath, E., et al. (2013). Plasma Klotho is not related to kidney function and does not predict adverse outcome in patients with chronic kidney disease. *Kidney Int.* 83, 121–128. doi: 10.1038/ki.2012.288

Sempou, E., Lakhani, O. A., Amalraj, S., and Khokha, M. K. (2018). Candidate Heterotaxy Gene FGFR4 is essential for patterning of the left-right organizer in Xenopus. *Front. Physiol.* 9:1705. doi: 10.3389/fphys.2018.01705

Sharma, S., Mishra, R., Bigham, G. E., Wehman, B., Khan, M. M., Xu, H., et al. (2017). A deep proteome analysis identifies the complete secretome as the functional unit of human cardiac progenitor cells. *Circ. Res.* 120, 816–834. doi: 10.1161/CIRCRESAHA.116.309782

Sheikh, F., Fandrich, R. R., Kardami, E., and Cattini, P. A. (1999). Overexpression of long or short FGFR-1 results in FGF-2-mediated proliferation in neonatal cardiac myocyte cultures. *Cardiovasc. Res.* 42, 696–705. doi: 10.1016/S0008-6363(99)00008-5

Shen, Y., Ma, X., Zhou, J., Pan, X., Hao, Y., Zhou, M., et al. (2013). Additive relationship between serum fibroblast growth factor 21 level and coronary artery disease. *Cardiovasc. Diabetol.* 12:124. doi: 10.1186/1475-2840-12-124

Silva, A. P., Mendes, F., Carias, E., Gonçalves, R. B., Fragoso, A., Dias, C., et al. (2019). Plasmatic klotho and fgf23 levels as biomarkers of ckd-associated cardiac disease in type 2 diabetic patients. *Int. J. Mol. Sci.* 20:1536. doi: 10.3390/ijms20071536

Simons, M., Annex, B. H., Laham, R. J., Kleiman, N., Henry, T., Dauerman, H., et al. (2002). Pharmacological treatment of coronary artery disease with recombinant fibroblast growth factor-2: double-blind, randomized, controlled clinical trial. *Circulation* 105, 788–793. doi: 10.1161/hc0802.104407

Singla, D. K., Singla, R. D., Abdelli, L. S., and Glass, C. (2015). Fibroblast growth factor-9 enhances M2 macrophage differentiation and attenuates adverse cardiac remodeling in the infarcted diabetic heart. *PLoS One* 10:e0120739. doi: 10.1371/journal.pone.0120739

Srisakuldee, W., Jeyaraman, M. M., Nickel, B. E., Tanguy, S., Jiang, Z. S., and Kardami, E. (2009). Phosphorylation of connexin-43 at serine 262 promotes a cardiac injury-resistant state. *Cardiovasc. Res.* 83, 672–681. doi: 10.1093/cvr/cvp142

Sugi, Y., Ito, N., Szebenyi, G., Myers, K., Fallon, J. F., Mikawa, T., et al. (2003). Fibroblast growth factor (FGF)-4 can induce proliferation of cardiac cushion mesenchymal cells during early valve leaflet formation. *Dev. Biol.* 258, 252–263. doi: 10.1016/S0012-1606(03)00099-X

Sun, J., Niu, C., Ye, W., An, N., Chen, G., Huang, X., et al. (2020). FGF13 is a novel regulator of NF-κB and potentiates pathological cardiac hypertrophy. *iScience* 23, 101627. doi: 10.1016/j.isci.2020.101627

Sun, K., Zhou, S., Wang, Q., Meng, Z., Peng, J., Zhou, Y., et al. (2020). Mutations in fibroblast growth factor (FGF8) and FGF10 identified in patients with conotruncal defects. *J. Transl. Med.* 18:283. doi: 10.1186/s12967-020-02445-2

Svystonyuk, D. A., Ngu, J. M. C., Mewhort, H. E. M., Lipon, B. D., Teng, G., Guzzardi, D. G., et al. (2015). Fibroblast growth factor-2 regulates human cardiac myofibroblast-mediated extracellular matrix remodeling. *J. Transl. Med.* 13:147. doi: 10.1186/s12967-015-0510-4

Tacer, K. F., Bookout, A. L., Ding, X., Kurosu, H., John, G. B., Wang, L., et al. (2010). Research resource: comprehensive expression atlas of the fibroblast growth factor system in adult mouse. *Mol. Endocrinol.* 24, 2050–2064. doi: 10.1210/me.2010-0142

Taelman, J., Popovic, M., Bialecka, M., Tilleman, L., Warrier, S., Van Der Jeught, M., et al. (2019). WNT inhibition and increased FGF signaling promotes derivation of less heterogeneous primed human embryonic stem cells, compatible with differentiation. *Stem Cells Dev.* 28, 579–592. doi: 10.1089/scd.2018.0199

Tahara, N., Akiyama, R., Wang, J., Kawakami, H., Bessho, Y., and Kawakami, Y. (2021). The FGF-AKT pathway is necessary for cardiomyocyte survival for heart regeneration in zebrafish. *Dev. Biol.* 472, 30–37. doi: 10.1016/j.ydbio.2020.12.019

Takashi, Y., Wakino, S., Minakuchi, H., Ishizu, M., Kuroda, A., Shima, H., et al. (2020). Circulating FGF23 is not associated with cardiac dysfunction, atherosclerosis, infection or inflammation in hemodialysis patients. *J. Bone Miner. Metab.* 38, 70–77. doi: 10.1007/s00774-019-01027-7

Timmers, L., Lim, S. K., Arslan, F., Armstrong, J. S., Hoefer, I. E., Doevendans, P. A., et al. (2008). Reduction of myocardial infarct size by human mesenchymal stem cell conditioned medium. *Stem Cell Res.* 1, 129–137. doi: 10.1016/j.scr.2008.02.002

Touchberry, C. D., Green, T. M., Tchikrizov, V., Mannix, J. E., Mao, T. F., Carney, B. W., et al. (2013). FGF23 is a novel regulator of intracellular calcium and cardiac contractility in addition to cardiac hypertrophy. *Am. J. Physiol. Endocrinol. Metab.* 304, E863–E873. doi: 10.1152/ajpendo.00596.2012

Tschöpe, C., Birner, C., Böhm, M., Bruder, O., Frantz, S., Luchner, A., et al. (2018). Heart failure with preserved ejection fraction: current management and future strategies: expert opinion on the behalf of the Nucleus of the "Heart Failure Working Group" of the German Society of Cardiology (DKG). *Clin. Res. Cardiol.* 107, 1–19. doi: 10.1007/s00392-017-1170-6

Tuñón, J., Fernández-Fernández, B., Carda, R., Pello, A. M., Cristóbal, C., Tarín, N., et al. (2016). Circulating fibroblast growth factor-23 plasma levels predict adverse cardiovascular outcomes in patients with diabetes mellitus with coronary artery disease. *Diabetes. Metab. Res. Rev.* 32, 685–693. doi: 10.1002/dmrr.2787

Tzahor, E., and Poss, K. D. (2017). Cardiac regeneration strategies: staying young at heart. *Science* 356, 1035–1039. doi: 10.1126/science.aam5894

Urness, L. D., Bleyl, S. B., Wright, T. J., Moon, A. M., and Mansour, S. L. (2011). Redundant and dosage sensitive requirements for Fgf3 and Fgf10 in cardiovascular development. *Dev. Biol.* 356, 383–397. doi: 10.1016/j.ydbio.2011.05.671

Vega-Hernández, M., Kovacs, A., de Langhe, S., and Ornitz, D. M. (2011). FGF10/FGFR2b signaling is essential for cardiac fibroblast development and growth of the myocardium. *Development* 138, 3331–3340. doi: 10.1242/dev.064410

Verhulst, A., Neven, E., and D'Haese, P. C. (2017). Characterization of an animal model to study risk factors and new therapies for the cardiorenal syndrome, a major health issue in our aging population. *Cardiorenal Med.* 7, 234–244. doi: 10.1159/000462984

Vincentz, J. W., McWhirter, J. R., Murre, C., Baldini, A., and Furuta, Y. (2005). Fgf15 is required for proper morphogenesis of the mouse cardiac outflow tract. *Genesis* 41, 192–201. doi: 10.1002/gene.20114

Virag, J. A. I., Rolle, M. L., Reece, J., Hardouin, S., Feigl, E. O., and Murry, C. E. (2007). Fibroblast growth factor-2 regulates myocardial infarct repair: effects

on cell proliferation, scar contraction, and ventricular function. *Am. J. Pathol.* 171, 1431–1440. doi: 10.2353/ajpath.2007.070003

von Jeinsen, B., Sopova, K., Palapies, L., Leistner, D. M., Fichtlscherer, S., Seeger, F. H., et al. (2019). Bone marrow and plasma FGF-23 in heart failure patients: novel insights into the heart–bone axis. *ESC Heart Fail.* 6, 536–544. doi: 10.1002/ehf2.12416

Wang, C., Hennessey, J. A., Kirkton, R. D., Wang, C., Graham, V., Puranam, R. S., et al. (2011). Fibroblast growth factor homologous factor 13 regulates Na+ channels and conduction velocity in murine hearts. *Circ. Res.* 109, 775–782. doi: 10.1161/CIRCRESAHA.111.247957

Wang, J., Nachtigal, M. W., Kardami, E., and Cattini, P. A. (2013). FGF-2 protects cardiomyocytes from doxorubicin damage via protein kinase C-dependent effects on efflux transporters. *Cardiovasc. Res.* 98, 56–63. doi: 10.1093/cvr/cvt011

Wang, J., Xiang, B., Dolinsky, V. W., Kardami, E., and Cattini, P. A. (2018). Cardiac Fgf-16 expression supports cardiomyocyte survival and increases resistance to doxorubicin cytotoxicity. *DNA Cell Biol.* 37, 866–877. doi: 10.1089/dna.2018.4362

Wang, R., Yi, X., Li, X., and Jiang, X. (2015). Fibroblast growth factor-21 is positively associated with atrial fibrosis in atrial fibrillation patients with rheumatic heart disease. *Int. J. Clin. Exp. Pathol.* 8, 14901–14908.

Wang, S., Wang, Y., Zhang, Z., Liu, Q., and Gu, J. (2017). Cardioprotective effects of fibroblast growth factor 21 against doxorubicin-induced toxicity via the SIRT1/LKB1/AMPK pathway. *Cell Death Dis.* 8:e3018. doi: 10.1038/cddis.2017.410

Wang, W., Niu, X., Stuart, T., Jullian, E., Mauck, W. M., Kelly, R. G., et al. (2019). A single-cell transcriptional roadmap for cardiopharyngeal fate diversification. *Nat. Cell Biol.* 21, 674–686. doi: 10.1038/s41556-019-0336-z

Wang, X., Tang, H., Wei, E. Q., Wang, Z., Yang, J., Yang, R., et al. (2017). Conditional knockout of Fgf13 in murine hearts increases arrhythmia susceptibility and reveals novel ion channel modulatory roles. *J. Mol. Cell. Cardiol.* 104, 63–74. doi: 10.1016/j.yjmcc.2017.01.009

Wang, Z., Wang, Y., Ye, J., Lu, X., Cheng, Y., Xiang, L., et al. (2015). bFGF attenuates endoplasmic reticulum stress and mitochondrial injury on myocardial ischaemia/reperfusion via activation of PI3K/Akt/ERK1/2 pathway. *J. Cell. Mol. Med.* 19, 595–607. doi: 10.1111/jcmm.12346

Wang, Z. G., Wang, Y., Huang, Y., Lu, Q., Zheng, L., Hu, D., et al. (2015). bFGF regulates autophagy and ubiquitinated protein accumulation induced by myocardial ischemia/reperfusion via the activation of the PI3K/Akt/mTOR pathway. *Sci. Rep.* 5:9287. doi: 10.1038/srep09287

Watanabe, Y., Miyagawa-Tomita, S., Vincent, S. D., Kelly, R. G., Moon, A. M., and Buckingham, M. E. (2010). Role of mesodermal FGF8 and FGF10 overlaps in the development of the arterial pole of the heart and pharyngeal arch arteries. *Circ. Res.* 106, 495–503. doi: 10.1161/CIRCRESAHA.109.201665

Watanabe, Y., Zaffran, S., Kuroiwa, A., Higuchi, H., Ogura, T., Harvey, R. P., et al. (2012). Fibroblast growth factor 10 gene regulation in the second heart field by Tbx1, Nkx2-5, and Islet1 reveals a genetic switch for down-regulation in the myocardium. *Proc. Natl. Acad. Sci. U.S.A.* 109, 18273–18280. doi: 10.1073/pnas.1215360109

Wei, E. Q., Sinden, D. S., Mao, L., Zhang, H., Wang, C., and Pitt, G. S. (2017). Inducible Fgf13 ablation enhances caveolae-mediated cardioprotection during cardiac pressure overload. *Proc. Natl. Acad. Sci. U.S.A.* 114, E4010–E4019. doi: 10.1073/pnas.1616393114

Wills, A. A., Holdway, J. E., Major, R. J., and Poss, K. D. (2008). Regulated addition of new myocardial and epicardial cells fosters homeostatic cardiac growth and maintenance in adult zebrafish. *Development* 135, 183–192. doi: 10.1242/dev.010363

Wilsbacher, L., and McNally, E. M. (2016). Genetics of cardiac developmental disorders: cardiomyocyte proliferation and growth and relevance to heart failure. *Annu. Rev. Pathol. Mech. Dis.* 11, 395–419. doi: 10.1146/annurev-pathol-012615-044336

Wohlfahrt, P., Melenovsky, V., Kotrc, M., Benes, J., Jabor, A., Franekova, J., et al. (2015). Association of fibroblast growth factor-23 levels and angiotensin-converting enzyme inhibition in chronic systolic heart failure. *JACC Heart Fail.* 3, 829–839. doi: 10.1016/j.jchf.2015.05.012

Wu, L., Qian, L., Zhang, L., Zhang, J., Zhou, J., Li, Y., et al. (2020). Fibroblast growth factor 21 is related to atherosclerosis independent of nonalcoholic fatty liver disease and predicts atherosclerotic cardiovascular events. *J. Am. Heart Assoc.* 9, e015226. doi: 10.1161/JAHA.119.015226

Wu, X., and Li, Y. (2011). Therapeutic utilities of fibroblast growth factor 19. *Expert Opin. Ther. Targets* 15, 1307–1316. doi: 10.1517/14728222.2011.624514

Wyatt, C. M., and Drüeke, T. B. (2016). Fibroblast growth factor receptor 4: The missing link between chronic kidney disease and FGF23-induced left ventricular hypertrophy? *Kidney Int.* 89, 7–9. doi: 10.1016/j.kint.2015.11.012

Xiao, Y., Liu, L., Xu, A., Zhou, P., Long, Z., Tu, Y., et al. (2015). Serum fibroblast growth factor 21 levels are related to subclinical atherosclerosis in patients with type 2 diabetes. *Cardiovasc. Diabetol.* 14:72. doi: 10.1186/s12933-015-0229-9

Xu, L., Hu, X., and Chen, W. (2019). Fibroblast growth factor-23 correlates with advanced disease conditions and predicts high risk of major adverse cardiac and cerebral events in end-stage renal disease patients undergoing continuous ambulatory peritoneal dialysis. *J. Nephrol.* 32, 307–314. doi: 10.1007/s40620-018-0557-4

Yamakawa, H., Muraoka, N., Miyamoto, K., Sadahiro, T., Isomi, M., Haginiwa, S., et al. (2015). Fibroblast growth factors and vascular endothelial growth factor promote cardiac reprogramming under defined conditions. *Stem Cell Rep.* 5, 1128–1142. doi: 10.1016/j.stemcr.2015.10.019

Yamasaki, S., Nabeshima, K., Sotomaru, Y., Taguchi, Y., Mukasa, H., Furue, M. K., et al. (2013). Long-term serial cultivation of mouse induced pluripotent stem cells in serum-free and feeder-free defined medium. *Int. J. Dev. Biol.* 57, 715–724. doi: 10.1387/ijdb.130173to

Yan, X., Chen, J., Zhang, C., Zhou, S., Zhang, Z., Chen, J., et al. (2015). FGF21 deletion exacerbates diabetic cardiomyopathy by aggravating cardiac lipid accumulation. *J. Cell. Mol. Med.* 19, 1557–1568. doi: 10.1111/jcmm.12530

Yang, H., Feng, A., Lin, S., Yu, L., Lin, X., Yan, X., et al. (2018). Fibroblast growth factor-21 prevents diabetic cardiomyopathy via AMPK-mediated antioxidation and lipid-lowering effects in the heart. *Cell Death Dis.* 9:227. doi: 10.1038/s41419-018-0307-5

Yang, J., Wang, Z., Sinden, D. S., Wang, X., Shan, B., Yu, X., et al. (2016). FGF13 modulates the gating properties of the cardiac sodium channel Nav1.5 in an isoform-specific manner. *Channels* 10, 410–420. doi: 10.1080/19336950.2016.1190055

Ye, L., D'Agostino, G., Loo, S. J., Wang, C. X., Su, L. P., Tan, S. H., et al. (2018). Early regenerative capacity in the porcine heart. *Circulation* 138, 2798–2808. doi: 10.1161/CIRCULATIONAHA.117.031542

Yu, C., Wang, F., Kan, M., Jin, C., Jones, R. B., Weinstein, M., et al. (2000). Elevated cholesterol metabolism and bile acid synthesis in mice lacking membrane tyrosine kinase receptor FGFR4. *J. Biol. Chem.* 275, 15482–15489. doi: 10.1074/jbc.275.20.15482

Yu, W., Huang, X., Tian, X., Zhang, H., He, L., Wang, Y., et al. (2016). GATA4 regulates Fgf16 to promote heart repair after injury. *Development* 143, 936–949. doi: 10.1242/dev.130971

Zhang, C., Huang, Z., Gu, J., Yan, X., Lu, X., Zhou, S., et al. (2015). Fibroblast growth factor 21 protects the heart from apoptosis in a diabetic mouse model via extracellular signal-regulated kinase 1/2-dependent signalling pathway. *Diabetologia* 58, 1937–1948. doi: 10.1007/s00125-015-3630-8

Zhang, H., Wang, T., Zhang, K., Liu, Y., Huang, F., Zhu, X., et al. (2014). Deletion of soluble epoxide hydrolase attenuates cardiac hypertrophy via down-regulation of cardiac fibroblasts-derived fibroblast growth factor-2. *Crit. Care Med.* 42, e345–e354. doi: 10.1097/CCM.0000000000000226

Zhang, J., Cheng, Y., Gu, J., Wang, S., Zhou, S., Wang, Y., et al. (2016). Fenofibrate increases cardiac autophagy via FGF21/SIRT1 and prevents fibrosis and inflammation in the hearts of Type 1 diabetic mice. *Clin. Sci.* 130, 625–641. doi: 10.1042/CS20150623

Zhang, J., Lin, Y., Zhang, Y., Lan, Y., Lin, C., Moon, A. M., et al. (2008). Frs2α-deficiency in cardiac progenitors disrupts a subset of FGF signals required for outflow tract morphogenesis. *Development* 135, 3611–3622. doi: 10.1242/dev.025361

Zhang, J., Tao, R., Campbell, K. F., Carvalho, J. L., Ruiz, E. C., Kim, G. C., et al. (2019). Functional cardiac fibroblasts derived from human pluripotent stem cells via second heart field progenitors. *Nat. Commun.* 10:2238. doi: 10.1038/s41467-019-09831-5

Zhang, R., Cao, P., Yang, Z., Wang, Z., Wu, J. L., Chen, Y., et al. (2015). Heparan sulfate biosynthesis enzyme, Ext1, contributes to outflow tract development

of mouse heart via modulation of FGF signaling. *PLoS One* 10:e0136518. doi: 10.1371/journal.pone.0136518

Zhang, W., Chu, S., Ding, W., and Wang, F. (2015). Serum level of fibroblast growth factor 21 is independently associated with acute myocardial infarction. *PLoS One* 10:e0129791. doi: 10.1371/journal.pone.0129791

Zhang, X., Ibrahimi, O. A., Olsen, S. K., Umemori, H., Mohammadi, M., and Ornitz, D. M. (2006). Receptor specificity of the fibroblast growth factor family: the complete mammalian FGF family. *J. Biol. Chem.* 281, 15694–15700. doi: 10.1074/jbc.M601252200

Conflict of Interest: The authors declare that the research was conducted in the absence of any commercial or financial relationships that could be construed as a potential conflict of interest.

frontiers in Cell and Developmental Biology

REVIEW
published: 26 May 2021
doi: 10.3389/fcell.2021.645400

FGF10 and Lipofibroblasts in Lung Homeostasis and Disease: Insights Gained From the Adipocytes

Yu-Qing Lv[1,2†], Qhaweni Dhlamini[2†], Chengshui Chen[1], Xiaokun Li[2], Saverio Bellusci[1,3] and Jin-San Zhang[1,2]**

[1]*Key Laboratory of Interventional Pulmonology of Zhejiang Province, Center for Precision Medicine, The First Affiliated Hospital of Wenzhou Medical University, Wenzhou, China,* [2]*International Collaborative Center on Growth Factor Research, School of Pharmaceutical Sciences, Wenzhou Medical University, Wenzhou, China,* [3]*Cardio-Pulmonary Institute, Institute of Lung Health and Department of Pulmonary and Critical Care Medicine and Infectious Diseases, Universities of Giessen and Marburg Lung Center (UGMLC), Member of the German Center for Lung Research (DZL), Justus-Liebig University Giessen, Giessen, Germany*

OPEN ACCESS

Edited by:
Ming Li,
Osaka University, Japan

Reviewed by:
Siegfried Ussar,
Helmholtz-Gemeinschaft Deutscher Forschungszentren (HZ), Germany
Jiqiu Wang,
Shanghai Jiao Tong University, China

***Correspondence:**
Saverio Bellusci
saverio.bellusci@innere.med.uni-giessen.de
Jin-San Zhang
zhang_jinsan@wmu.edu.cn

†These authors have contributed equally to this work

Specialty section:
This article was submitted to Stem Cell Research, a section of the journal Frontiers in Cell and Developmental Biology

Received: *23 December 2020*
Accepted: *28 April 2021*
Published: *26 May 2021*

Citation:
Lv Y-Q, Dhlamini Q, Chen C, Li X, Bellusci S and Zhang J-S (2021) FGF10 and Lipofibroblasts in Lung Homeostasis and Disease: Insights Gained From the Adipocytes. Front. Cell Dev. Biol. 9:645400. doi: 10.3389/fcell.2021.645400

Adipocytes not only function as energy depots but also secrete numerous adipokines that regulate multiple metabolic processes, including lipid homeostasis. Dysregulation of lipid homeostasis, which often leads to adipocyte hypertrophy and/or ectopic lipid deposition in non-adipocyte cells such as muscle and liver, is linked to the development of insulin resistance. Similarly, an altered secretion profile of adipokines or imbalance between calorie intake and energy expenditure is associated with obesity, among other related metabolic disorders. In lungs, lipid-laden adipocyte-like cells known as lipofibroblasts share numerous developmental and functional similarities with adipocytes, and similarly influence alveolar lipid homeostasis by facilitating pulmonary surfactant production. Unsurprisingly, disruption in alveolar lipid homeostasis may propagate several chronic inflammatory disorders of the lung. Given the numerous similarities between the two cell types, dissecting the molecular mechanisms underlying adipocyte development and function will offer valuable insights that may be applied to, at least, some aspects of lipofibroblast biology in normal and diseased lungs. FGF10, a major ligand for FGFR2b, is a multifunctional growth factor that is indispensable for several biological processes, including development of various organs and tissues such as the lung and WAT. Moreover, accumulating evidence strongly implicates FGF10 in several key aspects of adipogenesis as well as lipofibroblast formation and maintenance, and as a potential player in adipocyte metabolism. This review summarizes our current understanding of the role of FGF10 in adipocytes, while attempting to derive insights on the existing literature and extrapolate the knowledge to pulmonary lipofibroblasts.

Keywords: FGF10, adipocytes, adipocyte-like cells, stem cell, lipofibroblast, myofibroblast, lung regeneration/repair

INTRODUCTION

FGF10, a member of the FGF family, is a potent mitogen that is indispensable for proper development, regeneration, and health. In general, FGFs elicit biological responses by binding to and activating four highly conserved transmembrane tyrosine kinase receptors (FGFR1–4). Currently, the FGF family comprises at least 22 members that are classified into seven subfamilies

based on sequence homology, functional properties, and evolutionary phylogeny. FGF10 belongs to the FGF7 subfamily, a group consisting of FGF3, 7, 10, and 22 (Ornitz and Itoh, 2015), and binds with higher affinity to FGFR1b and FGFR2b compared to the other FGF receptors (Bellusci et al., 1997). More details regarding FGF10, including its protein structure and function, expression profile in tissues or during development, and signaling transduction mechanisms are comprehensively reviewed elsewhere (Ndlovu et al., 2018). Among the FGFs, Fgf10 is well-characterized for its roles in development of various organs and tissues, including the lung and white adipose tissue (WAT) (Gartside et al., 2009; Ohta and Itoh, 2014; Ornitz and Itoh, 2015). Mice lacking *Fgf10* or its primary receptor *Fgfr2b* display multiple organ defects, including complete lung agenesis (Min et al., 1998; De Moerlooze et al., 2000; Ohuchi et al., 2000). *FGF10* expression was observed in adipose tissue and has been strongly implicated in adipogenesis (Sakaue et al., 2002; Patel et al., 2005; Ohta and Itoh, 2014). Significantly, *Fgf10* knockout (KO) mice display impaired WAT development, indicating that Fgf10 expression is crucial for normal WAT development (Yamasaki et al., 1999; Sakaue et al., 2002). Herein, we summarize the current knowledge and gaps in our understanding of the role of FGF10 in adipocytes and adipocyte-like cells.

SUCCINCT BACKGROUND ON ADIPOSE TISSUE AND ADIPOGENESIS

The adipose tissue (AT) is a dynamic metabolic and endocrine organ that contributes to various crucial physiological processes, including regulation of energy balance and metabolic homeostasis. In mammals, AT is classified into two morphologically and functionally distinct types: WAT and brown adipose tissue (BAT) (Rosen and Spiegelman, 2000). WAT consists generally of spherical cells that contain a large uniocular lipid droplet occupying the majority of the cytosol and markedly lower mitochondria content than brown adipocytes (Cannon and Nedergaard, 2004; Cinti, 2005). WAT primarily stores excess energy in the form of triglycerides and mobilizes the energy depending on the state of energy balance and immediate physiological needs. Furthermore, WAT secretes several endocrine factors, such as adipokines and cytokines, that act on various targets to regulate multiple metabolic processes (Ahima and Lazar, 2008). BAT, in contrast to WAT, consists of ellipsoidal cells that contain multiple, small, multilocular lipid droplets, and higher content of UCP1-expressing mitochondria (Cannon and Nedergaard, 2004; Cinti, 2005). BAT mainly dissipates chemical energy *via* UCP1-mediated mitochondrial uncoupling, generating heat in the process; a phenomenon often dubbed "non-shivering thermogenesis" (Lowell and Flier, 1997; Cannon and Nedergaard, 2004; Richard and Picard, 2011).

Adipogenesis is a multi-step process by which mature adipocytes arise from mesenchymal stem cells (MSCs) through cell differentiation. This process is regulated by a complex network of transcription factors in concert with several extracellular mediators, such as hormones and growth factors, and occurs in two major phases. First, MSCs commit to preadipocytes, and second, preadipocytes terminally differentiate into mature, functional adipocytes (Rosen and Macdougald, 2006). Adipocytes represent the primary building blocks of adipose tissue, and three types of adipocytes deriving from distinct MSC lineages constitute two main types of adipose tissue. White adipocytes mainly derive from the Myf5-negative lineage, while brown adipocytes arise from the Myf5-positive lineage. Some studies, however, indicate that Myf5-positive precursors may give rise to a subset of white adipocytes as well (Sanchez-Gurmaches and Guertin, 2014; Sebo et al., 2018). In addition to classical brown adipocytes, a distinct type of thermogenic, brown adipocyte-like cells known as Beige adipocytes have been found in WAT depots (Cannon and Nedergaard, 2004; Wu et al., 2012). Beige adipocytes are thought to arise from: (a) mature white adipocytes *via* β3 adrenergic stimulation, chronic Peroxisome proliferator-activated receptor gamma (PPAR-γ) induction, and cold exposure-induced trans-differentiation (Barbatelli et al., 2010), (b) platelet-derived growth factor receptor α (PDGFRα) positive white preadipocytes *via* differentiation (**Figure 1**; Fischer et al., 2017), and (c) Myf5 negative MSCs (Sanchez-Gurmaches et al., 2016). Beige and brown adipocytes share several biochemical characteristics, specifically, they both contain abundant UCP1-expressing mitochondria and multilocular lipid droplets.

ROLE OF FGF10 IN ADIPOGENESIS AND WAT BROWNING

Autocrine/paracrine FGF10 signaling has been implicated in WAT development, remodeling, and metabolism (Ohta and Itoh, 2014). FGF10 is shown to play a crucial role in the differentiation of preadipocytes in WAT *via* activation of *PPAR-γ*, the key transcriptional regulator of adipogenesis (Sakaue et al., 2002; Asaki et al., 2004). KO mice studies revealed that loss of Fgf10 expression in embryonic WAT results in markedly reduced expression of *PPAR-γ*, indicating that FGF10 acts upstream of *PPAR-γ* to stimulate adipogenesis (Ohta et al., 2011). Furthermore, blockade of Fgf10 signaling inhibited the expression of C/EBPα, a major adipogenic transcription factor that is critical for the initiation of 3T3-L1 cell differentiation, thereby suppressing adipocyte development in differentiating 3T3-L1 preadipocytes (Lane et al., 1999; Sakaue et al., 2002). These data suggest that FGF10 expression or activity is critical for preadipocyte differentiation into mature adipocytes. Although FGF10 is shown to promote adipogenesis/terminal adipocyte differentiation *via* upregulation of the adipogenic genes *PPAR-γ*, C/EBPα, and lipoprotein lipase (LPL), it remains unclear whether FGF10 may induce/regulate adipogenic cell fate determination in undifferentiated MSCs, as most, if not all studies investigating the role of Fgf10 in adipogenesis have employed the 3 T3-L1 cell line, which is already committed to adipocyte lineage. Thus, further studies employing multipotent undifferentiated MSC cell lines, are warranted to investigate the potential effects of FGF10 on adipogenic cell fate commitment of MSCs *in vivo*.

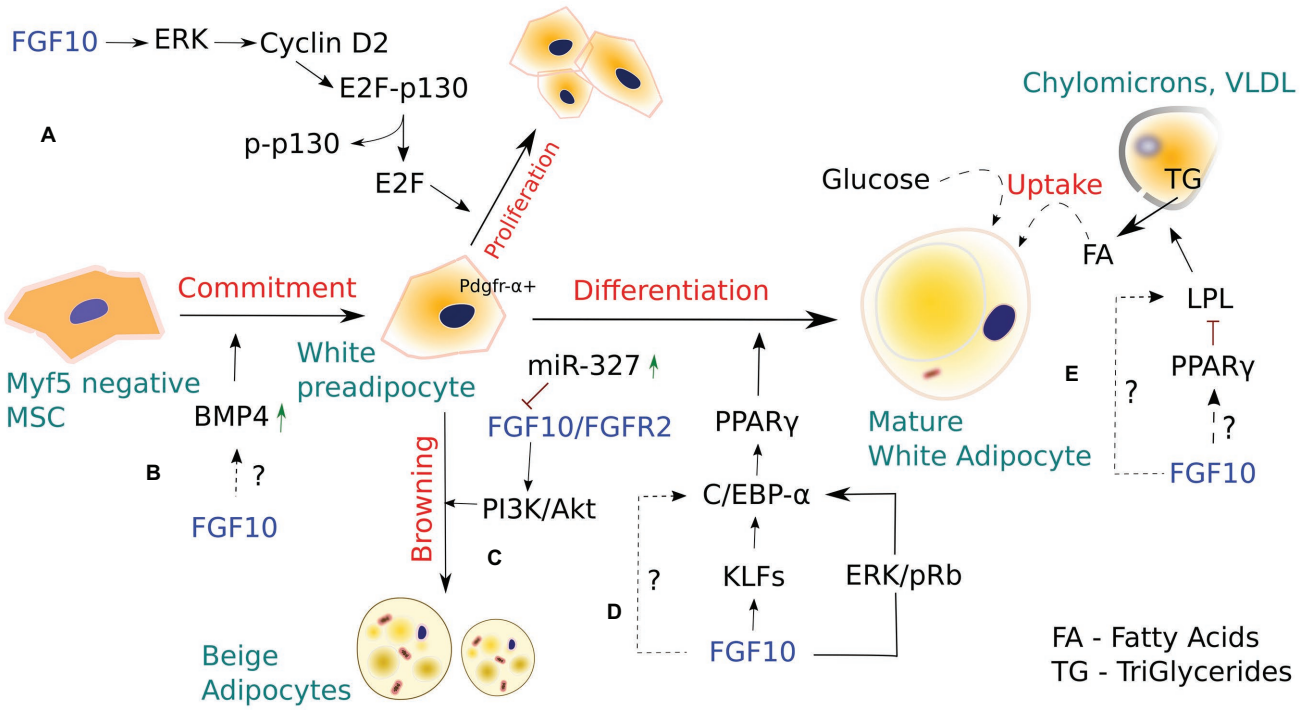

FIGURE 1 | The role of FGF10 in white and Beige adipocyte development. **(A)** FGF10-stimulated activation of the Ras/MAPK pathway induces proliferation of white preadipocytes *via* cyclin D2-dependent phosphorylation of p130. **(B)** Bone morphogenic protein 4 (BMP4), acting downstream of FGF10, is known to regulate FGF10-mediated bud outgrowth during branching morphogenesis of the developing lung, thus contributing to controlling bud size. In adipogenesis, BMP4 stimulates commitment of pluripotent stem cells toward the white adipocyte lineage. However, whether a dynamic interplay between FGF10 and BMP4 occurs in adipogenesis, similar to that seen in embryonic lung development, remains to be elucidated. **(C)** FGF10 is part of a miRNA-327-regulated autocrine loop that stimulates development of Beige adipocytes from Pdgfrα+ white preadipocytes. However, Beige adipocytes are also thought to arise from mature white adipocytes *via* β-3 adrenergic stimulation, cold exposure, and chronic PPAR-γ induction. **(D)** FGF10, *via* a number of signaling routes, activates downstream PPAR-γ, which in turn induces white adipocyte differentiation. **(E)** FGF10 overexpression in intramuscular adipocytes enhanced the expression of lipoprotein lipase (LPL) and LPL-induced lipid accumulation, suggesting a possible role for FGF10 in regulating adipocyte metabolism. However, LPL is also known to be regulated by PPAR-γ, and thus whether FGF10 would target LPL directly or *via* PPAR-γ to exert its effects in adipocyte metabolism remains to be determined.

FGF10 is abundantly expressed in the Stromal Vascular Fraction of WAT, which is comprised of adipocyte stem and progenitors among other cell types, suggesting that FGF10 is essential for adipogenesis *in vivo* (Yamasaki et al., 1999). Classical observations indicate that FGF10 expression in WAT stimulates both proliferation and differentiation of preadipocytes *via* the Ras/MAPK pathway (**Figure 1**; Asaki et al., 2004; Konishi et al., 2006; Ohta et al., 2011). In preadipocytes, FGF10/FGFR2b signaling *via* the Ras/MAPK cascade was shown to trigger pRb and subsequent Rb-C/EBP complex formation, leading to downstream activation of *PPAR-γ*, which in turn induces adipogenesis. FGF10 was also shown to mediate preadipocyte proliferation in WAT by inducing cyclin D2-dependent phosphorylation of P130 through the Ras/MAPK pathway. In support of these observations, *Fgf10* KO embryos exhibited aberrant *Cyclin D2* expression and P130 phosphorylation in the WAT and markedly impaired preadipocyte proliferation (Konishi et al., 2006; Ohta et al., 2011).

In addition, specific blockade of Fgf10/Fgfr2 and downstream AKT signaling with miR-327, a key regulator of preadipocyte differentiation into Beige adipocytes, resulted in impaired preadipocyte differentiation, indicating that Fgf10 may indeed drive preadipocyte differentiation *via* the Fgfr2-Akt axis. Furthermore, *miR-327* was shown to regulate *Fgf10*-mediated preadipocyte differentiation by inhibiting the Fgf10-activated Fgfr2-Akt signaling cascade (Fischer et al., 2017). However, using the established mouse 3T3-L1 cell line to investigate the effect of *Fgf10* and *miR-327* levels on preadipocyte proliferation, the researchers demonstrated that Fgf10 expression levels do not affect preadipocyte proliferation (Fischer et al., 2017).

Fischer et al. (2017) reported the existence of a *miRNA-327*-FGF10-FGFR2 autocrine regulatory loop in PDGFRα+ cells, which is critical for WAT browning. They demonstrated, for the first time, that a mechanism involving FGF10 could regulate PDGFRα+ preadipocyte differentiation into thermogenic Beige adipocytes. These findings are particularly intriguing because PDGFRα+ preadipocytes, similar to mesenchymal progenitors of pulmonary lipofibroblasts (LIFs), not only differentiate *via* a mechanism involving Fgf10 upregulation but also express a number of shared adipogenic genes. Considering the similarities between beige and LIF progenitors, we postulate that, similar to beige/white adipocyte- and bipotent PDGFRα+ progenitors, LIF progenitors, *via* Fgf10 upregulation, may also give rise to

distinct LIF cell subtypes that may play some as yet undiscovered roles in lung biology.

OTHER FGF FAMILY MEMBERS ARE IMPLICATED IN ADIPOSE TISSUE DEVELOPMENT, REMODELING, AND FUNCTION

Apart from FGF10, other FGF family members, including FGF21 and FGF9, play crucial roles as autocrine/paracrine adipokines in regulating energy homeostasis by influencing WAT or BAT/beige development, remodeling, and function. FGF21 has been shown to activate thermogenesis *via* induction of WAT browning and thermogenic genes, such as PGC1 and UCP1, following cold exposure (Fisher et al., 2012). FGF21 KO mice exhibited an impaired adaption to chronic cold exposure and diminished WA browning, suggesting that FGF21 is critical for normal adaptations to cold exposure. In addition, FGF21 *via* a feed-forward loop involving *PPAR-γ*, regulates insulin sensitivity and glucose homeostasis in WAT (Dutchak et al., 2012), suggesting that FGF21 contributes to the antidiabetic activities of *PPAR-γ*. On the contrary, FGF9 upregulation was shown to negatively regulate WAT browning and the expression of thermogenic genes, including PGC1and UCP1, and positively correlate with obesity (Sun et al., 2019). The inhibitory effects of FGF9 on WAT browning were accompanied with decreased expression of adipogenic markers including *C/EBPβ* and *PPAR-γ*, indicating that FGF9 upregulation inhibits adipogenesis. Besides FGF21 and FGF9, other FGFs such as FGF1, FGF16, and FGF19, also have important roles in adipogenesis; however, due to space limitations, these growth factors will not be covered here. Taken together, these findings provide new insights for FGFs as potential targets for treating obesity and its related metabolic disorders.

FGF10 IN THE REGULATION OF MULTIPLE ADIPOCYTE METABOLIC FACTORS

Lipoprotein Lipase

Lipoprotein lipase, a member of the lipase superfamily, is chiefly expressed in tissues that oxidize or store large amounts of fatty acids, such as WAT and BAT, and is an important early marker of adipocyte differentiation (Amri et al., 1996). LPL hydrolyzes triglycerides from circulating triglyceride-rich lipoproteins (VLDL and chylomicrons) into fatty acids, which are then taken up by adipocytes for storage or energy production *via* beta-oxidation (Mead et al., 2002). Specific siRNA-mediated knockdown of *Fgf10* in goat intramuscular preadipocytes inhibited lipid droplet accumulation, and impaired adipocyte development, suggesting that Fgf10 plays a pivotal role in adipocyte development and metabolism, as lipid accumulation represents a major functional characteristic of adipocytes (Xu et al., 2018). Beyond its adipogenesis activity, *PPAR-γ* is involved in various aspects of adipocyte lipid metabolism and regulates the expression of adipocyte-specific genes associated with lipid accumulation and metabolism, including LPL (Schoonjans et al., 1996; Kersten et al., 2000). Interestingly, Fgf10 overexpression in intramuscular adipocytes enhanced the expression of LPL among other transcription factors, while *Fgf10* knockdown using RNA interference suppressed the expression of LPL and LPL-induced lipid accumulation (Xu et al., 2018). These findings suggest a possible role for FGF10 in regulating adipocyte metabolism while raising the question of whether FGF10 would target LPL directly or *via PPAR-γ* to exert its effects in adipocyte metabolism.

Kruppel-Like Factors

Kruppel-like factors (KLFs) are a large family of zinc-finger proteins with functionally diverse roles in various physiological and cellular processes, including adipogenesis (Pearson et al., 2008; Pei et al., 2011). KLFs constitute the central transcriptional cascade that acts sequentially and upstream of the adipogenic master regulator *PPAR-γ* to negatively or positively regulate adipogenesis (Wu and Wang, 2013). Recently, *Fgf10* was shown to upregulate mRNA expression of KLF3, 9, and 13 in goat intramuscular preadipocytes, indicating a possibility that *Fgf10* may regulate adipocyte development, at least in part, by targeting KLF3, 9, and 13 (Xu et al., 2018). However, further studies are needed to clarify the precise effects of these KLFs on adipogenesis, and to establish the specific mechanisms involved (Xu et al., 2018).

Bone Morphogenic Proteins

Bone morphogenic proteins (BMPs) are known to play crucial roles in several hallmarks of adipogenesis, including adipocyte lineage commitment, preadipocyte differentiation, and support of adipocyte function (Fux et al., 2004; Huang et al., 2009; Schulz et al., 2011). BMPs are polypeptide growth factors that belong to the TGF-β superfamily and are involved in several aspects of embryonic lung patterning and adipogenesis. Among the BMP family members, BMP2, BMP4, and BMP7 are the most studied factors for their roles in adipogenesis. BMP2 and BMP4 are essential for white adipocyte development (Fux et al., 2004; Huang et al., 2009), while BMP7 is involved in brown adipocyte development (Schulz et al., 2011). BMP4 plays a critical role in adipogenesis and has been shown not only to stimulate commitment of pluripotent stem cells toward the white adipocyte lineage but also promote WAT differentiation (Otto et al., 2007). Interestingly, BMP4 was identified to act in concert with FGF10 during lung development. BMP4, acting downstream of FGF10, regulates branching and patterning of the developing lung, thus contributing to bud size control. During branching morphogenesis, FGF10 induces bud formation in proximal-distal regions and subsequent epithelial expression of BMP4, which in turn limits further FGF10-mediated bud outgrowth (Weaver et al., 2000). Given that both FGF10 and BMP4 have been implicated in

adipogenesis, it will be interesting to study whether a dynamic interplay between FGF10 and BMP4 occurs in adipogenesis, for instance, as similar to that seen in embryonic lung development.

THE ROLES OF FGF10 IN ADIPOCYTES MAY BE EXTRAPOLATED TO LIPOFIBROBLASTS

Lipofibroblasts and adipocytes share several common characteristics, despite their distinct anatomical locations. For one thing, both LIFs and adipocytes are lipid-laden cells that characteristically express an array of adipogenic genes and markers, such as Adrp, *PPAR-γ*, and LPL, associated with various aspects of their biological processes, including lipid metabolism and lipogenesis. The roles of some of these markers in LIF and adipocyte cellular biology are discussed in detail in other sections of this review. Furthermore, LIFs and adipocytes utilize shared developmental signaling pathways during their formation, including Fgf10, *PPAR-γ*, and PDGFRα signaling. Both cell types emerge from MSCs *via* Fgf10-mediated differentiation of their mesenchymal progenitors into mature cells (Ohta et al., 2011; Al Alam et al., 2015). In addition, like lipofibroblasts, adipocytes require *PPAR-γ* signaling during their maturation and for maintenance of their phenotype. Moreover, apart from FGF10 and *PPAR-γ*, the mesenchymal progenitors of both LIFs and adipocytes express PDGFRα, whose expression levels progressively decrease during their course of differentiation.

Given the many similarities between adipocytes and LIFs, it is plausible to draw a comparison between the two cells. We, therefore, postulate that the established and potential roles of FGF10 signaling in adipocytes can be extrapolated to pulmonary LIFs. While earlier studies have also predicted the role of Fgf10 in LIF formation by extrapolating from its role in adipogenesis (Al Alam et al., 2015), further studies to test whether, with regard to FGF10 signaling, the similarities between LIFs and adipocytes extend from cellular development to other aspects of their biology. Such studies may help unravel more mysteries of LIF biology and function in lung development, homeostasis, and regeneration.

During embryonic lung development, LIFs originate from several progenitor pools, including a subset of FGF10-expressing cells in the lung mesenchyme (Al Alam et al., 2015). Lineage tracing of Fgf10-positive (FGF10+) cells using *Fgf10* knock-in mice revealed that mesenchymal-derived FGF10+ progenitor cells give rise to multiple lineages, including myogenic and adipogenic lineages (El Agha et al., 2014). Furthermore, FGF10 signaling was shown to promote the adipogenic differentiation potential of MSCs through preferential induction of LIF (adipogenic) differentiation rather than alveolar MYF (myogenic) differentiation during lung development (El Agha et al., 2014), suggesting that FGF10 signaling may control early cell fate decisions of MSCs as well as induce conversions between established lineages. The possibility that FGF10 signaling may regulate MSC fate would have profound implications, especially in the context of lung repair and regeneration following injury or disease.

FGF10-FGFR2B SIGNALING IN LIPOFIBROBLASTS – ALVEOLAR TYPE 2 CELLS TWO-WAY COMMUNICATION

Pulmonary lipofibroblasts were first described five decades ago, and since this initial landmark report, various research groups have invested their efforts to characterize their development, morphology, and their biological roles *in vivo*. The capacity of LIFs to recruit, store, and supply alveolar type 2 (AT2) cells with lipid substrates for lung surfactant production (Rehan and Torday, 2014), has offered exciting opportunities to make important discoveries that will impact human health.

In vivo tracer studies have shown that LIF cells usually reside next to AT2 cells. Therefore, LIF cells are considered to be essential components of AT2 stem cell niches, and an essential factor in maintaining AT2 cell stemness (Barkauskas et al., 2013; El Agha and Bellusci, 2014; Al Alam et al., 2015). A myriad of studies indicate that AT2 cells and juxtaposed LIFs interact reciprocally *via* paracrine signaling pathways, such as the PPAR-γ pathway, in coordinating normal development, homeostasis, and regeneration/repair of the distal lung (Tordet et al., 1981; El Agha et al., 2014).

Apart from LIFs, FGF10 has been implicated in promoting AT2 lineage formation. Chao et al. (2017) found that lungs of *Fgf10*$^{+/-}$ mice had decreased total number of epithelial cells compared to wild-type mice, and unbalanced alveolar epithelial cell population, with a decreased proportion of AT2 cells and an increased proportion of AT1 cells. Furthermore, FGF10 hypomorphic mice with significantly reduced FGF10 expression levels exhibited marked AT2 defects compared to normal wild-type mice (Chao et al., 2017), further indicating that FGF10 plays a vital role in AT2 lineage formation.

AT2 cells normally play essential roles in host defense, barrier function, and normal lung homeostasis/repair. AT2 cells are generally small, rounded, or cuboidal cells containing characteristic lamellar bodies and apical microvilli (Mason, 2006), and distributed between alveolar epithelial type 1 cells (AT1) in the alveolar septa. In normal adult lungs, AT2 cells are more abundant than AT1 cells, accounting for 14–16% of all alveolar epithelial cells, and serve as an important progenitor during repair after lung injury and during normal lung homeostasis. AT1 cells appear to be more susceptible to injury from either endogenous or exogenous factors, while AT2 cells are more resistant. In severe cases of lung injury, such as the COVID-19 infection (Chen et al., 2020), the alveolar epithelium usually exhibits widespread AT1 cell necrosis, characterized by a denuded alveolar basement membrane and formation of hyaline membranes, one of the hallmark features of acute respiratory distress syndrome (ARDS).

Following epithelial injury resulting in loss of both AT1 and AT2 cells, surviving AT2 migrate and undergo compensatory proliferation along the alveolar septa, in an attempt to repopulate the denuded epithelial barrier, and eventually transdifferentiate

to replace lost AT1 cells (Kim et al., 2006). Recent findings, however, suggest that although AT2 cells can contribute to alveolar epithelial regeneration after injury, some of the newly generated alveolar epithelial cells (AECs) may arise from activated Bronchial epithelial stem cells (BESCs; Yuan et al., 2019). In a bleomycin model of lung injury, BESCs function as a source of alveolar epithelial regeneration and repair by differentiating toward AT1 and AT2 cell lineages over of Basal cells (BCs) in honeycomb cysts, in response to increased FGF10 signaling (Yuan et al., 2019). More on these findings will be further discussed in the FGF10 and respiratory disease section. Overall, these observations suggest that elevated FGF10 levels in BESCs may induce efficient epithelial repair *via* BESCs surrogacy for incapacitated AT2 progenitors in case of severe lung injury (**Figure 2A**) and that FGF10-based therapies based on this phenomenon may prove beneficial for ARDS and/or COVID-19 patients.

FGF10 IN THE LIF TO MYF SWITCH DURING FIBROSIS FORMATION AND RESOLUTION

Myofibroblasts (MYF) play an important role in both physiological and pathological repair processes (Kis et al., 2011; Hinz et al., 2012). In physiological repair, myofibroblasts are transiently activated to facilitate wound closure by producing extra cellular matrix (ECM) proteins, notably fibronectin and collagens type I and III (Tomasek et al., 2002; Klingberg et al., 2013). Successful wound repair is followed by degradation of the provisional matrix and disappearance of myofibroblasts *via* a number of mechanisms, including apoptosis. In pathological repair, however, myofibroblasts are continuously activated due to ongoing injury, often leading to excessive deposition of aberrant ECM and abnormal tissue repair. Moreover, these persistent myofibroblasts tend to resist apoptosis and, hence, their physiological clearance. Myofibroblast persistence leads to pathological scar formation, and ultimately organ fibrosis.

In pulmonary fibrosis, the origins of activated myofibroblasts remain speculative; however, several sources have been implicated. Recently, lineage-tracing studies implicated FGF10-expressing LIFs as a novel source of the activated MYFs (El Agha et al., 2017b). These studies not only indicated that LIFs transdifferentiate into activated MYFs following bleomycin-induced injury but also that a subpopulation of the myofibroblasts reverts to a quiescent phenotype characteristic of the pre-existing LIFs during fibrosis resolution. Unraveling the origins and/or fate of activated myofibroblasts during fibrosis resolution offers the unique opportunity to clearly define pathological hallmarks of lung fibrosis, and discover novel therapeutic interventions that may inhibit or even reverse the switch between lipogenic and myogenic phenotype, and ultimately accelerate fibrosis regression.

Furthermore, activation of PPAR-γ signaling *via* rosiglitazone (a potent PPAR-γ agonist) treatment antagonized TGF-β-mediated myofibroblast differentiation likely by reinforcing the lipogenic

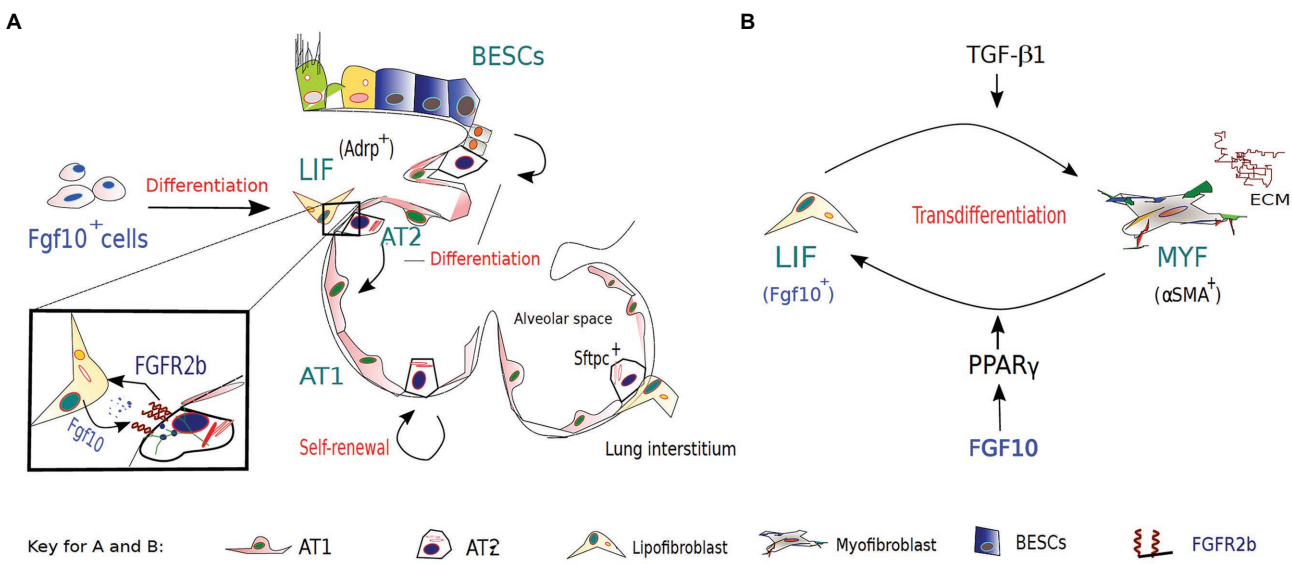

FIGURE 2 | The role of FGF10-FGFR2B signaling in lipofibroblast (LIF)-AT2 mediated alveolar repair and fibrosis development/resolution. **(A)**. During embryonic lung development, a subset of FGF10-expressing cells in the lung mesenchyme gives rise to LIFs, which are considered to be essential components of AT2 stem cell niches. AT2 cells and neighboring LIFs interact reciprocally *via* paracrine signaling pathways, such as the PPAR-γ pathway, in coordinating normal development, homeostasis, and regeneration/repair of the distal lung. Apart from other reserve stem cell populations for the alveolar epithelium, AT2 cells are important progenitors during repair after lung injury and during normal lung homeostasis. **(B)** The origins of activated myofibroblasts (MYF) in fibrotic lungs remain speculative; however, FGF10-expressing LIFs have been implicated as a novel source of the activated myofibroblasts. Following bleomycin-induced injury, lipofibroblasts are thought to transdifferentiate into activated myofibroblasts, from which a subpopulation reverts to a quiescent phenotype characteristic of the pre-existing LIFs during fibrosis resolution.

phenotype (El Agha et al., 2017b). Interestingly, TGF-β upregulation has been found to be induced by SARS-Cov-2 infection (Agrati et al., 2020; Chen, 2020; Ferreira-Gomes et al., 2021) and associated with several complications of severe COVID19, such as ARDS and pulmonary fibrosis. Thus, it is plausible that FGF10, likely *via PPAR-γ* activation, gets involved in an attempt to replenish LIFs lost to unrestrained MYF differentiation – driven by TGF-β upregulation and chronic epithelial injury (**Figure 2B**). The possibility that FGF10, *via PPAR-γ* signaling, can drive reinforcement of the lipogenic phenotype at the expense of the myogenic phenotype raises the potential that FGF10-based therapies could be beneficial in combating idiopathic pulmonary fibrosis (IPF) and/or COVID-19 related pulmonary fibrosis.

FGF10-FGFR2B SIGNALING AND OTHER ASSOCIATED RESPIRATORY DISEASES

Aberrant FGF10-FGFR2B signaling contributes to the pathophysiology of multiple respiratory diseases, including IPF and bronchopulmonary dysplasia (BPD). IPF is a chronic age-related respiratory disease of unknown etiology belonging to a heterogeneous group of interstitial lung diseases (ILDs) that are characterized by distorted pulmonary architecture, compromised lung function, and respiratory failure. By way of background, it is worth emphasizing that IPF differs from COVID-19 related pulmonary fibrosis in regard to certain etiological aspects, despite both being characterized by aberrant accumulation of myofibroblasts, reduced lung compliance, and excessive deposition of collagen and other ECM (Sime and O'Reilly, 2001; King et al., 2011; Steele and Schwartz, 2013). More importantly, pulmonary fibrosis is a common consequent manifestation of several acute and chronic ILDs such as ARDS – a major cause of morbidity and mortality in COVID-19 patients (Kruglikov and Scherer, 2020).

Interestingly, apart from fibrotic lungs, reduced lung compliance, as well as AT2 cells with altered surfactant protein expression, have been observed in different models of obesity (Inselman et al., 2004; Foster et al., 2010; Correll et al., 2019). The association of obesity with lung pathologies is gaining much attention, as obesity is increasingly implicated as a major risk factor in several lung disorders, including pulmonary fibrosis and severe COVID-19 infection. In an obese state, SARS-Cov-2 infection is thought to additionally modify the already-compromised adipocytes and adipocyte-like cells by altering their lipid metabolism and promoting their adoption of a differentiation-prone cell state, thus negatively affecting global metabolic homeostasis. In severe cases of SARS-Cov-2 infection, this may involve the lipogenic-to-myogenic switch, a key event in pulmonary fibrogenesis (Kruglikov and Scherer, 2020). Moreover, obese IPF patients have significantly higher waitlist mortality and post-transplant mortality of just over 3 months, compared with controls (Nathan et al., 2010; Gries et al., 2015). In addition, obesity is associated with worse outcome of COVID-19 infection, dysregulated lipid metabolism, and or ectopic lipid accumulation in non-adipocytes, such as pulmonary LIF and neighboring AT2 cells. Therefore, understanding LIF- and or AT2-cell behavior in the context of obesity and COVID-19 may unlock the mysteries associated with COVID-19 pathogenesis.

Dysregulated lipid metabolism in AT2 cells has been linked to an altered surfactant profile (Schmidt et al., 2002; Foster et al., 2010), which, we hypothesize, would increase AT2 cell susceptibility to COVID-19 infection, as surfactant proteins are known to participate in host defense against viral infection (Hsieh et al., 2018). Similarly, ectopic accumulation of lipid in AT2 cells has been shown to induce AT2 hyperplasia (Foster et al., 2010), which, we again hypothesize, may translate to more ACE2-expressing AT2 cells – the primary target of the COVID-19 virus (Zhao et al., 2020); that is, increased number of viral entry points, and thus, increased susceptibility of AT2 cells to COVID-19 infection. Furthermore, given the reciprocal interactions between LIFs and neighboring AT2 cells, in which LIFs traffic lipid substrates for surfactant production to AT2 cells (Rehan and Torday, 2014), it is highly plausible that aberrant lipid accumulation in AT2 cells and subsequent AT2 hyperplasia may also stem from impaired lipid trafficking from LIFs to AT2 cells.

In addition, obesity-associated AT2 hyperplasia may also explain the histologic features of samples derived from IPF lungs, as well as patients with severe COVID-19 cases (Mora et al., 2005; Selman and Pardo, 2006; Wigén et al., 2020), showing distinct foci of hyperplastic AT2 cells. Moreover, in obese lungs, LIFs, and AT2 cells alike, extensively accumulate lipid droplets (Foster et al., 2010), which in turn may lead to lipotoxicity, and lipotoxicity-mediated outcomes, such as cell cycle arrest and apoptosis, often observed in IPF among other lung pathologies.

FGF10-FGFR2b signaling has been shown to promote the resolution of pulmonary fibrosis *via* a number of mechanisms, including the one we mentioned earlier in this review (El Agha et al., 2017b). Although the precise role of FGF10 in IPF pathology remains unclear, studies found significantly elevated FGF10 expression levels in lung tissues of IPF patients compared to non-IPF donors. Strikingly, fibrotic foci, in contrast to fibrotic lesions, had detectable FGF10 protein expression, but rather at lower levels (El Agha et al., 2017a). Based on these observations, some have speculated that FGF10 is unlikely to be involved in the initial triggering events of IPF, but rather inducted to promote fibrosis resolution by counteracting the effects of TGF-β1 (Gupte et al., 2009; El Agha et al., 2017b).

In a more recent study using bleomycin injury models, FGF10 overexpression in BESCs was shown to enhance fibrosis resolution by promoting alveolar epithelial regeneration over the development of fibrotic honeycomb lesions, while inactivation of its receptor FGFR2b led to impaired epithelial regeneration by BESCs (Yuan et al., 2019). The need for elevated FGF10 levels to induce BESCs-driven AEC regeneration and fibrosis resolution following lung injury may explain why IPF is tightly correlated with aging, as FGF10 expression is known to decrease with age. Taken together, investigating the specific role of FGF10 and its receptor FGFR2B in IPF may help create effective

anti-fibrotic FGF10-based therapies that precisely target this signaling pathway with optimal efficacy.

Deficient FGF10 signaling during embryonic lung development is associated with BPD, a lethal lung developmental disorder of prematurely born infants. Hyperoxia injury models of BPD in *Fgf10* heterozygous pups resulted in complete postnatal lethality, starting at day 5, while in normoxia, no postnatal lethality was observed (Chao et al., 2017). This suggests that a potential beneficial effect of recombinant FGF10 treatment is likely to be effective in the context of BPD. This could, in turn, translate into the development of novel FGF10-based therapies that may improve the prognosis of BPD in preterm neonates.

CONCLUSION AND PERSPECTIVE

By looking at the numerous developmental and functional similarities between pulmonary LIFs and adipocytes, especially white adipocytes, a few lessons have emerged. We believe that these lessons, particularly the findings pertaining to adipocyte biology, including our knowledge about FGF10 signaling in these cells, can be extrapolated to explain, at least some aspects of LIF biology in normal and diseased lungs. To achieve this, further studies using scRNA-seq and lineage tracing tools are required to further explore the influence of FGF10 signaling in LIFs, examine the role of LIF progenitors beyond early developmental stages, and better assess the functional heterogeneity of pulmonary LIFs. For instance, the newly generated Fgf10-CreERT2 line that allows lineage tracing of Fgf10-pos cells during development and postnatally may be helpful. Such studies will contribute significantly to our understanding of the role of LIFs in lung health and disease. Also, given the importance of adipocytes and adipocyte-like cells in multiple physiological processes such as regulation of systemic energy homeostasis, and their implications for metabolic diseases such as obesity, a detailed understanding of the mechanisms by which FGF10 functions in these cells may provide profound insights into disease pathophysiology, and lead to development of novel FGF10-based therapies.

AUTHOR CONTRIBUTIONS

J-SZ and SB conceived the study and edited and revised the manuscript. Y-QL and QD drafted the manuscript and designed the figures. CC and XL provided the valuable intellectual input. All authors contributed to the article and approved the submitted version.

FUNDING

J-SZ was supported by a start-up package from Wenzhou Medical University and the Interventional Pulmonary Key Laboratory of Zhejiang Province. SB was supported by grants from the Deutsche Forschungsgemeinschaft (DFG; BE4443/6-1, KFO309 P7, and SFB CRC1213-projects A04) and the DZL. CC was supported by the National Key Research and Development Program of China (2016YFC1304000) and the Interventional Pulmonary Key Laboratory of Zhejiang Province.

REFERENCES

Agrati, C., Sacchi, A., Bordoni, V., Cimini, E., Notari, S., Grassi, G., et al. (2020). Expansion of myeloid-derived suppressor cells in patients with severe coronavirus disease (COVID-19). *Cell Death Differ.* 27, 3196–3207. doi: 10.1038/s41418-020-0572-6

Ahima, R. S., and Lazar, M. A. (2008). Adipokines and the peripheral and neural control of energy balance. *Mol. Endocrinol.* 22, 1023–1031. doi: 10.1210/me.2007-0529

Al Alam, D., El Agha, E., Sakurai, R., Kheirollahi, V., Moiseenko, A., Danopoulos, S., et al. (2015). Evidence for the involvement of fibroblast growth factor 10 in lipofibroblast formation during embryonic lung development. *Development* 142, 4139–4150. doi: 10.1242/dev.109173

Amri, E. Z., Teboul, L., Vannier, C., Grimaldi, P. A., and Ailhaud, G. (1996). Fatty acids regulate the expression of lipoprotein lipase gene and activity in preadipose and adipose cells. *Biochem. J.* 314, 541–546. doi: 10.1042/bj3140541

Asaki, T., Konishi, M., Miyake, A., Kato, S., Tomizawa, M., and Itoh, N. (2004). Roles of fibroblast growth factor 10 (Fgf10) in adipogenesis *in vivo*. *Mol. Cell. Endocrinol.* 218, 119–128. doi: 10.1016/j.mce.2003.12.017

Barbatelli, G., Murano, I., Madsen, L., Hao, Q., Jimenez, M., Kristiansen, K., et al. (2010). The emergence of cold-induced brown adipocytes in mouse white fat depots is determined predominantly by white to brown adipocyte transdifferentiation. *Am. J. Physiol. Endocrinol. Metab.* 298, E1244–E1253. doi: 10.1152/ajpendo.00600.2009

Barkauskas, C. E., Cronce, M. J., Rackley, C. R., Bowie, E. J., Keene, D. R., Stripp, B. R., et al. (2013). Type 2 alveolar cells are stem cells in adult lung. *J. Clin. Invest.* 123, 3025–3036. doi: 10.1172/JCI68782

Bellusci, S., Grindley, J., Emoto, H., Itoh, N., and Hogan, B. L. (1997). Fibroblast growth factor 10 (FGF10) and branching morphogenesis in the embryonic mouse lung. *Development* 124, 4867–4878. doi: 10.1242/dev.124.23.4867

Cannon, B., and Nedergaard, J. (2004). Brown adipose tissue: function and physiological significance. *Physiol. Rev.* 84, 277–359. doi: 10.1152/physrev.00015.2003

Chao, C. M., Yahya, F., Moiseenko, A., Tiozzo, C., Shrestha, A., Ahmadvand, N., et al. (2017). Fgf10 deficiency is causative for lethality in a mouse model of bronchopulmonary dysplasia. *J. Pathol.* 241, 91–103. doi: 10.1002/path.4834

Chen, W. A. (2020). Potential treatment of COVID-19 with TGF-β blockade. *Int. J. Biol. Sci.* 16, 1954–1955. doi: 10.7150/ijbs.46891

Chen, J., Wu, H., Yu, Y., and Tang, N. (2020). Pulmonary alveolar regeneration in adult COVID-19 patients. *Cell Res.* 30, 708–710. doi: 10.1038/s41422-020-0369-7

Cinti, S. (2005). The adipose organ. *Prostaglandins Leukot. Essent. Fat. Acids* 73, 9–15. doi: 10.1016/j.plefa.2005.04.010

Correll, K. A., Edeen, K. E., Zemans, R. L., Redente, E. F., Serban, K. A., Curran-Everett, D., et al. (2019). Transitional human alveolar type II epithelial cells suppress extracellular matrix and growth factor gene expression in lung fibroblasts. *Am. J. Phys. Lung Cell. Mol. Phys.* 317, L283–l294. doi: 10.1152/ajplung.00337.2018

De Moerlooze, L., Spencer-Dene, B., Revest, J. M., Hajihosseini, M., Rosewell, I., and Dickson, C. (2000). An important role for the IIIb isoform of fibroblast growth factor receptor 2 (FGFR2) in mesenchymal-epithelial signalling during mouse organogenesis. *Development* 127, 483–492. doi: 10.1242/dev.127.3.483

Dutchak, P. A., Katafuchi, T., Bookout, A. L., Choi, J. H., Yu, R. T., Mangelsdorf, D. J., et al. (2012). Fibroblast growth factor-21 regulates PPARγ activity and the antidiabetic actions of thiazolidinediones. *Cell* 148, 556–567. doi: 10.1016/j.cell.2011.11.062

El Agha, E., and Bellusci, S. (2014). Walking along the fibroblast growth factor 10 route: a key pathway to understand the control and regulation of epithelial and mesenchymal cell-lineage formation during lung development and repair after injury. *Scientifica* 2014:538379. doi: 10.1155/2014/538379

El Agha, E., Herold, S., Al Alam, D., Quantius, J., MacKenzie, B., Carraro, G., et al. (2014). Fgf10-positive cells represent a progenitor cell population during lung development and postnatally. *Development* 141, 296–306. doi: 10.1242/dev.099747

El Agha, E., Kramann, R., Schneider, R. K., Li, X., Seeger, W., Humphreys, B. D., et al. (2017a). Mesenchymal stem cells in fibrotic disease. *Cell Stem Cell* 21, 166–177. doi: 10.1016/j.stem.2017.07.011

El Agha, E., Moiseenko, A., Kheirollahi, V., De Langhe, S., Crnkovic, S., Kwapiszewska, G., et al. (2017b). Two-way conversion between lipogenic and myogenic fibroblastic phenotypes marks the progression and resolution of lung fibrosis. *Cell Stem Cell* 20, 261–273.e263. doi: 10.1016/j.stem.2016.10.004

Ferreira-Gomes, M., Kruglov, A., Durek, P., Heinrich, F., Tizian, C., Anne, H. G., et al. (2021). SARS-CoV-2 in severe COVID-19 induces a TGF-β-dominated chronic immune response that does not target itself. *Nat. Commun.* 12:1961. doi: 10.1038/s41467-021-22210-3

Fischer, C., Seki, T., Lim, S., Nakamura, M., Andersson, P., Yang, Y., et al. (2017). A miR-327-FGF10-FGFR2-mediated autocrine signaling mechanism controls white fat browning. *Nat. Commun.* 8:2079. doi: 10.1038/s41467-017-02158-z

Fisher, F. M., Kleiner, S., Douris, N., Fox, E. C., Mepani, R. J., Verdeguer, F., et al. (2012). FGF21 regulates PGC-1α and browning of white adipose tissues in adaptive thermogenesis. *Genes Dev.* 26, 271–281. doi: 10.1101/gad.177857.111

Foster, D. J., Ravikumar, P., Bellotto, D. J., Unger, R. H., and Hsia, C. C. (2010). Fatty diabetic lung: altered alveolar structure and surfactant protein expression. *Am. J. Phys. Lung Cell. Mol. Phys.* 298, L392–L403. doi: 10.1152/ajplung.00041.2009

Fux, C., Mitta, B., Kramer, B. P., and Fussenegger, M. (2004). Dual-regulated expression of C/EBP-alpha and BMP-2 enables differential differentiation of C2C12 cells into adipocytes and osteoblasts. *Nucleic Acids Res.* 32:e1. doi: 10.1093/nar/gnh001

Gartside, M. G., Chen, H., Ibrahimi, O. A., Byron, S. A., Curtis, A. V., Wellens, C. L., et al. (2009). Loss-of-function fibroblast growth factor receptor-2 mutations in melanoma. *Mol. Cancer Res.* 7, 41–54. doi: 10.1158/1541-7786.Mcr-08-0021

Gries, C. J., Bhadriraju, S., Edelman, J. D., Goss, C. H., Raghu, G., and Mulligan, M. S. (2015). Obese patients with idiopathic pulmonary fibrosis have a higher 90-day mortality risk with bilateral lung transplantation. *J. Heart Lung Transplant.* 34, 241–246. doi: 10.1016/j.healun.2014.09.031

Gupte, V. V., Ramasamy, S. K., Reddy, R., Lee, J., Weinreb, P. H., Violette, S. M., et al. (2009). Overexpression of fibroblast growth factor-10 during both inflammatory and fibrotic phases attenuates bleomycin-induced pulmonary fibrosis in mice. *Am. J. Respir. Crit. Care Med.* 180, 424–436. doi: 10.1164/rccm.200811-1794OC

Hinz, B., Phan, S. H., Thannickal, V. J., Prunotto, M., Desmoulière, A., Varga, J., et al. (2012). Recent developments in myofibroblast biology: paradigms for connective tissue remodeling. *Am. J. Pathol.* 180, 1340–1355. doi: 10.1016/j.ajpath.2012.02.004

Hsieh, I. N., De Luna, X., White, M. R., and Hartshorn, K. L. (2018). The role and molecular mechanism of action of surfactant protein D in innate host defense against influenza A virus. *Front. Immunol.* 9:1368. doi: 10.3389/fimmu.2018.01368

Huang, H., Song, T. J., Li, X., Hu, L., He, Q., Liu, M., et al. (2009). BMP signaling pathway is required for commitment of C3H10T1/2 pluripotent stem cells to the adipocyte lineage. *Proc. Natl. Acad. Sci. U. S. A.* 106, 12670–12675. doi: 10.1073/pnas.0906266106

Inselman, L. S., Chander, A., and Spitzer, A. R. (2004). Diminished lung compliance and elevated surfactant lipids and proteins in nutritionally obese young rats. *Lung* 182, 101–117. doi: 10.1007/s00408-003-1048-4

Kersten, S., Desvergne, B., and Wahli, W. (2000). Roles of PPARs in health and disease. *Nature* 405, 421–424. doi: 10.1038/35013000

Kim, K. K., Kugler, M. C., Wolters, P. J., Robillard, L., Galvez, M. G., Brumwell, A. N., et al. (2006). Alveolar epithelial cell mesenchymal transition develops in vivo during pulmonary fibrosis and is regulated by the extracellular matrix. *Proc. Natl. Acad. Sci. U. S. A.* 103, 13180–13185. doi: 10.1073/pnas.0605669103

King, T. E. Jr., Pardo, A., and Selman, M. (2011). Idiopathic pulmonary fibrosis. *Lancet* 378, 1949–1961. doi: 10.1016/S0140-6736(11)60052-4

Kis, K., Liu, X., and Hagood, J. S. (2011). Myofibroblast differentiation and survival in fibrotic disease. *Expert Rev. Mol. Med.* 13:e27. doi: 10.1017/S1462399411001967

Klingberg, F., Hinz, B., and White, E. S. (2013). The myofibroblast matrix: implications for tissue repair and fibrosis. *J. Pathol.* 229, 298–309. doi: 10.1002/path.4104

Konishi, M., Asaki, T., Koike, N., Miwa, H., Miyake, A., and Itoh, N. (2006). Role of Fgf10 in cell proliferation in white adipose tissue. *Mol. Cell. Endocrinol.* 249, 71–77. doi: 10.1016/j.mce.2006.01.010

Kruglikov, I. L., and Scherer, P. E. (2020). The role of adipocytes and adipocyte-like cells in the severity of COVID-19 infections. *Obesity (Silver Spring)* 28, 1187–1190. doi: 10.1002/oby.22856

Lane, M. D., Tang, Q. Q., and Jiang, M. S. (1999). Role of the CCAAT enhancer binding proteins (C/EBPs) in adipocyte differentiation. *Biochem. Biophys. Res. Commun.* 266, 677–683. doi: 10.1006/bbrc.1999.1885

Lowell, B. B., and Flier, J. S. (1997). Brown adipose tissue, beta 3-adrenergic receptors, and obesity. *Annu. Rev. Med.* 48, 307–316. doi: 10.1146/annurev.med.48.1.307

Mason, R. J. (2006). Biology of alveolar type II cells. *Respirology* 11, S12–S15. doi: 10.1111/j.1440-1843.2006.00800.x

Mead, J. R., Irvine, S. A., and Ramji, D. P. (2002). Lipoprotein lipase: structure, function, regulation, and role in disease. *J. Mol. Med.* 80, 753–769. doi: 10.1007/s00109-002-0384-9

Min, H., Danilenko, D. M., Scully, S. A., Bolon, B., Ring, B. D., Tarpley, J. E., et al. (1998). Fgf-10 is required for both limb and lung development and exhibits striking functional similarity to *Drosophila* branchless. *Genes Dev.* 12, 3156–3161. doi: 10.1101/gad.12.20.3156

Mora, A. L., Woods, C. R., Garcia, A., Xu, J., Rojas, M., Speck, S. H., et al. (2005). Lung infection with gamma-herpesvirus induces progressive pulmonary fibrosis in Th2-biased mice. *Am. J. Phys. Lung Cell. Mol. Phys.* 289, L711–L721. doi: 10.1152/ajplung.00007.2005

Nathan, S. D., Shlobin, O. A., Ahmad, S., Burton, N. A., Barnett, S. D., and Edwards, E. (2010). Comparison of wait times and mortality for idiopathic pulmonary fibrosis patients listed for single or bilateral lung transplantation. *J. Heart Lung Transplant.* 29, 1165–1171. doi: 10.1016/j.healun.2010.05.014

Ndlovu, R., Deng, L. C., Wu, J., Li, X. K., and Zhang, J. S. (2018). Fibroblast growth factor 10 in pancreas development and pancreatic cancer. *Front. Genet.* 9:482. doi: 10.3389/fgene.2018.00482

Ohta, H., and Itoh, N. (2014). Roles of FGFs as adipokines in adipose tissue development, remodeling, and metabolism. *Front. Endocrinol.* 5:18. doi: 10.3389/fendo.2014.00018

Ohta, H., Konishi, M., and Itoh, N. (2011). FGF10 and FGF21 as regulators in adipocyte development and metabolism. *Endocr Metab Immune Disord Drug Targets* 11, 302–309. doi: 10.2174/187153011797881166

Ohuchi, H., Hori, Y., Yamasaki, M., Harada, H., Sekine, K., Kato, S., et al. (2000). FGF10 acts as a major ligand for FGF receptor 2 IIIb in mouse multi-organ development. *Biochem. Biophys. Res. Commun.* 277, 643–649. doi: 10.1006/bbrc.2000.3721

Ornitz, D. M., and Itoh, N. (2015). The fibroblast growth factor signaling pathway. *Wiley Interdiscip. Rev. Dev. Biol.* 4, 215–266. doi: 10.1002/wdev.176

Otto, T. C., Bowers, R. R., and Lane, M. D. (2007). BMP-4 treatment of C3H10T1/2 stem cells blocks expression of MMP-3 and MMP-13. *Biochem. Biophys. Res. Commun.* 353, 1097–1104. doi: 10.1016/j.bbrc.2006.12.170

Patel, N. G., Kumar, S., and Eggo, M. C. (2005). Essential role of fibroblast growth factor signaling in preadipoctye differentiation. *J. Clin. Endocrinol. Metab.* 90, 1226–1232. doi: 10.1210/jc.2004-1309

Pearson, R., Fleetwood, J., Eaton, S., Crossley, M., and Bao, S. (2008). Krüppel-like transcription factors: a functional family. *Int. J. Biochem. Cell Biol.* 40, 1996–2001. doi: 10.1016/j.biocel.2007.07.018

Pei, H., Yao, Y., Yang, Y., Liao, K., and Wu, J. R. (2011). Krüppel-like factor KLF9 regulates PPARγ transactivation at the middle stage of adipogenesis. *Cell Death Differ.* 18, 315–327. doi: 10.1038/cdd.2010.100

Rehan, V. K., and Torday, J. S. (2014). The lung alveolar lipofibroblast: an evolutionary strategy against neonatal hyperoxic lung injury. *Antioxid. Redox Signal.* 21, 1893–1904. doi: 10.1089/ars.2013.5793

Richard, D., and Picard, F. (2011). Brown fat biology and thermogenesis. *Front. Biosci.* 16, 1233–1260. doi: 10.2741/3786

Rosen, E. D., and MacDougald, O. A. (2006). Adipocyte differentiation from the inside out. *Nat. Rev. Mol. Cell Biol.* 7, 885–896. doi: 10.1038/nrm2066

Rosen, E. D., and Spiegelman, B. M. (2000). Molecular regulation of adipogenesis. *Annu. Rev. Cell Dev. Biol.* 16, 145–171. doi: 10.1146/annurev.cellbio.16.1.145

Sakaue, H., Konishi, M., Ogawa, W., Asaki, T., Mori, T., Yamasaki, M., et al. (2002). Requirement of fibroblast growth factor 10 in development of white adipose tissue. *Genes Dev.* 16, 908–912. doi: 10.1101/gad.983202

Sanchez-Gurmaches, J., and Guertin, D. A. (2014). Adipocytes arise from multiple lineages that are heterogeneously and dynamically distributed. *Nat. Commun.* 5:4099. doi: 10.1038/ncomms5099

Sanchez-Gurmaches, J., Hung, C. M., and Guertin, D. A. (2016). Emerging complexities in adipocyte origins and identity. *Trends Cell Biol.* 26, 313–326. doi: 10.1016/j.tcb.2016.01.004

Schmidt, R., Meier, U., Markart, P., Grimminger, F., Velcovsky, H. G., Morr, H., et al. (2002). Altered fatty acid composition of lung surfactant phospholipids in interstitial lung disease. *Am. J. Phys. Lung Cell. Mol. Phys.* 283, L1079–L1085. doi: 10.1152/ajplung.00484.2001

Schoonjans, K., Staels, B., and Auwerx, J. (1996). The peroxisome proliferator activated receptors (PPARS) and their effects on lipid metabolism and adipocyte differentiation. *Biochim. Biophys. Acta* 1302, 93–109. doi: 10.1016/0005-2760(96)00066-5

Schulz, T. J., Huang, T. L., Tran, T. T., Zhang, H., Townsend, K. L., Shadrach, J. L., et al. (2011). Identification of inducible brown adipocyte progenitors residing in skeletal muscle and white fat. *Proc. Natl. Acad. Sci. U. S. A.* 108, 143–148. doi: 10.1073/pnas.1010929108

Sebo, Z. L., Jeffery, E., Holtrup, B., and Rodeheffer, M. S. (2018). A mesodermal fate map for adipose tissue. *Development* 145:dev166801. doi: 10.1242/dev.166801

Selman, M., and Pardo, A. (2006). Role of epithelial cells in idiopathic pulmonary fibrosis: from innocent targets to serial killers. *Proc. Am. Thorac. Soc.* 3, 364–372. doi: 10.1513/pats.200601-003TK

Sime, P. J., and O'Reilly, K. M. (2001). Fibrosis of the lung and other tissues: new concepts in pathogenesis and treatment. *Clin. Immunol.* 99, 308–319. doi: 10.1006/clim.2001.5008

Steele, M. P., and Schwartz, D. A. (2013). Molecular mechanisms in progressive idiopathic pulmonary fibrosis. *Annu. Rev. Med.* 64, 265–276. doi: 10.1146/annurev-med-042711-142004

Sun, Y., Wang, R., Zhao, S., Li, W., Liu, W., Tang, L., et al. (2019). FGF9 inhibits browning program of white adipocytes and associates with human obesity. *J. Mol. Endocrinol.* 62, 79–90. doi: 10.1530/JME-18-0151

Tomasek, J. J., Gabbiani, G., Hinz, B., Chaponnier, C., and Brown, R. A. (2002). Myofibroblasts and mechano-regulation of connective tissue remodelling. *Nat. Rev. Mol. Cell Biol.* 3, 349–363. doi: 10.1038/nrm809

Tordet, C., Marin, L., and Dameron, F. (1981). Pulmonary di-and-triacylglycerols during the perinatal development of the rat. *Experientia* 37, 333–334. doi: 10.1007/BF01959845

Weaver, M., Dunn, N. R., and Hogan, B. L. (2000). Bmp4 and Fgf10 play opposing roles during lung bud morphogenesis. *Development* 127, 2695–2704. doi: 10.1242/dev.127.12.2695

Wigén, J., Löfdahl, A., Bjermer, L., Elowsson-Rendin, L., and Westergren-Thorsson, G. (2020). Converging pathways in pulmonary fibrosis and Covid-19 - The fibrotic link to disease severity. *Respir. Med. X* 2:100023. doi: 10.1016/j.yrmex.2020.100023

Wu, J., Boström, P., Sparks, L. M., Ye, L., Choi, J. H., Giang, A. H., et al. (2012). Beige adipocytes are a distinct type of thermogenic fat cell in mouse and human. *Cell* 150, 366–376. doi: 10.1016/j.cell.2012.05.016

Wu, Z., and Wang, S. (2013). Role of kruppel-like transcription factors in adipogenesis. *Dev. Biol.* 373, 235–243. doi: 10.1016/j.ydbio.2012.10.031

Xu, Q., Lin, S., Wangsid, Y., Zhu, J., and Lin, Y. (2018). Fibroblast growth factor 10 (FGF10) promotes the adipogenesis of intramuscular preadipocytes in goat. *Mol. Biol. Rep.* 45, 1881–1888. doi: 10.1007/s11033-018-4334-1

Yamasaki, M., Emoto, H., Konishi, M., Mikami, T., Ohuchi, H., Nakao, K., et al. (1999). FGF-10 is a growth factor for preadipocytes in white adipose tissue. *Biochem. Biophys. Res. Commun.* 258, 109–112. doi: 10.1006/bbrc.1999.0594

Yuan, T., Volckaert, T., Redente, E. F., Hopkins, S., Klinkhammer, K., Wasnick, R., et al. (2019). FGF10-FGFR2B signaling generates basal cells and drives alveolar epithelial regeneration by bronchial epithelial stem cells after lung injury. *Stem Cell Rep.* 12, 1041–1055. doi: 10.1016/j.stemcr.2019.04.003

Zhao, Y., Zhao, Z., Wang, Y., Zhou, Y., Ma, Y., and Zuo, W. (2020). Single-cell RNA expression profiling of ACE2, the receptor of SARS-CoV-2. *Am. J. Respir. Crit. Care Med.* 202, 756–759. doi: 10.1164/rccm.202001-0179LE

Conflict of Interest: The authors declare that the research was conducted in the absence of any commercial or financial relationships that could be construed as a potential conflict of interest.

frontiers in Cell and Developmental Biology

REVIEW
published: 31 May 2021
doi: 10.3389/fcell.2021.656883

Cross-Talk Between Inflammation and Fibroblast Growth Factor 10 During Organogenesis and Pathogenesis: Lessons Learnt From the Lung and Other Organs

*Manuela Marega[1,2], Chengshui Chen[1] and Saverio Bellusci[1,2]**

[1] Key Laboratory of Interventional Pulmonology of Zhejiang Province, Department of Pulmonary and Critical Care Medicine, First Affiliated Hospital of Wenzhou Medical University, Wenzhou, China, [2] Member of the German Center for Lung Research (DZL), Department of Pulmonary and Critical Care Medicine and Infectious Diseases, Cardio-Pulmonary Institute (CPI), Universities of Giessen and Marburg Lung Center (UGMLC), Justus Liebig University Giessen, Giessen, Germany

OPEN ACCESS

Edited by:
Chen Zhang,
Capital Medical University, China

Reviewed by:
Lawrence S. Prince,
University of California, San Diego, United States
Ana Pardo,
Foundation for Applied Medical Research (FIMA), Spain
Barsha Dash,
University of California, San Diego, United States

***Correspondence:**
Saverio Bellusci
saverio.bellusci@innere.med.uni-giessen.de

Specialty section:
This article was submitted to Stem Cell Research, a section of the journal Frontiers in Cell and Developmental Biology

Received: 21 January 2021
Accepted: 19 April 2021
Published: 31 May 2021

Citation:
Marega M, Chen C and Bellusci S (2021) Cross-Talk Between Inflammation and Fibroblast Growth Factor 10 During Organogenesis and Pathogenesis: Lessons Learnt From the Lung and Other Organs. Front. Cell Dev. Biol. 9:656883. doi: 10.3389/fcell.2021.656883

The adult human lung is constantly exposed to irritants like particulate matter, toxic chemical compounds, and biological agents (bacteria and viruses) present in the external environment. During breathing, these irritants travel through the bronchi and bronchioles to reach the deeper lung containing the alveoli, which constitute the minimal functional respiratory units. The local biological responses in the alveoli that follow introduction of irritants need to be tightly controlled in order to prevent a massive inflammatory response leading to loss of respiratory function. Cells, cytokines, chemokines and growth factors intervene collectively to re-establish tissue homeostasis, fight the aggression and replace the apoptotic/necrotic cells with healthy cells through proliferation and/or differentiation. Among the important growth factors at play during inflammation, members of the fibroblast growth factor (Fgf) family regulate the repair process. Fgf10 is known to be a key factor for organ morphogenesis and disease. Inflammation is influenced by Fgf10 but can also impact Fgf10 expression *per se*. Unfortunately, the connection between Fgf10 and inflammation in organogenesis and disease remains unclear. The aim of this review is to highlight the reported players between Fgf10 and inflammation with a focus on the lung and to propose new avenues of research.

Keywords: inflammation, alveolar epithelial type 2 cell, lipofibroblast, immune cells, stromal niche, Fgf10

INTRODUCTION

In the past few years, the plasticity and dynamics of the immune cells in different organs and during development, homeostasis and repair after injury have become the focus of research. In particular, macrophages have been shown to be more than phagocytic cells and to display different behaviors based on the specific tissues where they are localized. Notably, many studies have demonstrated the heterogeneity of the macrophage subpopulations in different organs, such as the brain and lung. We propose that in the lung, alveolar epithelial cells and associated stromal cells

called lipofibroblasts (LIFs) are the main interlocutors of the immune cells. While LIFs are not yet well characterized, alveolar epithelial cells are known to display immune characteristics (e.g., expression of surface markers which allow their interaction with immune cells). Fibroblasts growth factors (Fgfs) are involved in many diseases with inflammatory features, suggesting a strong connection with the immune system. Among them, Fgf10 represents a promising molecule, due to its important role during lung morphogenesis and in the repair process after injury. It has been reported how different levels of *Fgf10* impacts the immune cell populations present in the lung during disease. Inflammation mediators, like NF-κB, could modify the expression level of *Fgf10*. Immune cells could express Fgf10 which acts in a paracrine and/or autocrine fashion. It remains to be clarified which immune cells are involved during development, homeostasis and repair, as well as the molecules at play, in terms of cytokines, chemokines or alarmins. In this review, we will explore what is known about the relationship between Fgf10 and inflammation and the possible approaches that we can develop to better understand and define the cross-talk between these two players. In particular, further studies are necessary to better characterize the role of Fgf10 in the context of inflammation, not only intended as a defense mechanism against aggression, but in the context of organogenesis and repair after injury.

FGF10 IS CRITICAL DURING ORGANOGENESIS

Fgf10 binds specifically to the Fgf receptor 2b (Fgfr2b), leading to the autophosphorylation of this tyrosine kinase receptor and the subsequent activation of a signaling cascade in the target cells. In the lung, *Fgf10* was first detected in the splanchnic mesoderm surrounding the foregut around E9.5 when the primary lung buds start to emerge (Yuan et al., 2018). From loss of function studies in mice, the importance of *Fgf10* in lung formation appears clear: the newborn mice die at birth due to a failure of lung formation. The primary buds corresponding to the main bronchi form but fail to elongate (Min et al., 1998). Strikingly, the trachea forms but displays abnormal patterning of the cartilage rings (Sala et al., 2011).

Other visceral organs including the pancreas, some specific portions of the gut, as well as ectoderm-derived organs such as the limb, mammary gland, and salivary and lacrimal glands are also impaired (Bellusci et al., 1997; Sekine et al., 1999; Itoh, 2016; Zepp and Morrisey, 2019). The last step of lung development is called alveologenesis, leading to the formation of the alveoli (Branchfield et al., 2015; Chao et al., 2016). In mice, this developmental phase starts shortly after birth [from postnatal day (P)5 through P36]. The alveolus is the basic functional structure containing several different cell types important for gas exchange, homeostasis and repair after injury. The role of Fgf10/Fgfr2b signaling in the alveolar epithelial progenitors giving rise to the alveolar type 1 and type 2 cells (AT1 and AT2, respectively) has been studied mostly from partial loss or gain of function approaches and it is still elusive (Chao et al., 2016). In the context of hyperoxia exposure to mouse pups, which models a human disease called bronchopulmonary dysplasia (BPD), decreased Fgf10 levels lead to premature death associated with profound alveolar defects (quantified by morphometry analysis for parameters such as mean linear intercept) and impaired AT2 differentiation and decreased surfactant production (Chao et al., 2017). Moreover, Kalymbetova et al. (2018) have proposed an active role for resident macrophages in pathological lung development, using a similar mouse model of BPD (85% oxygen). They identified a novel population of immune cells, named population 3 (Pop3), characterized by high expression of the major histocompatibility complex II (MHCII). Because of this high expression, the authors suggested that alveolar macrophages (AMs) can transdifferentiate into Pop3 after exposure of the animals to hyperoxia. At the same time, it was possible to observe arrested alveolar development, strongly suggesting a causative role in arrested lung development for this new macrophage population (Kalymbetova et al., 2018).

THE IMMUNE CELLS IN THE LUNG ARISE FROM DIFFERENT SOURCES

In the adult lung, the main immune cell type present is the macrophage. Lung macrophages belong to two different subgroups: alveolar macrophages and interstitial macrophages (IMs); the role of each group is still poorly understood, and research focuses mostly on AMs, due to their localization and their abundance. In the lung, AMs are localized in the lumen of the alveolus and are in direct contact with the epithelium. Their main function is phagocytosis of surfactant and irritants. On the other side, the IMs represent 30–40% of the total macrophages, and their role is primarily connected to tissue remodeling and homeostasis, as well as to antigen presentation (Evren et al., 2020).

The Origin of the Immune Cells Present in the Lung Has Been Clarified

During fetal life, the lung is populated by fetal lung myeloid populations that include fetal macrophages and fetal liver-derived monocytes (De Kleer et al., 2014; van de Laar et al., 2016). Shortly after birth, these immune cells mature into AMs, which are characterized by long-term survival. Throughout life, the population of AMs is maintained via their local proliferation and, therefore, does not normally require the recruitment of the circulating monocytes from the blood. AMs protect against viruses, bacteria, pollution and smoke. The exposure to these irritants, however, leads to a partial substitution of the local AMs with circulating monocytes, which then eventually become resident AMs themselves (Gordon and Plüddemann, 2017; Evren et al., 2020). Moreover, in the past, the proposed role of these cells was defined by the tissue or organ where they localized, with the assumption that all the macrophages originate from circulating monocytes derived from the bone marrow (Takahashi et al., 1989; Takeya and Takahashi, 1992). Over the years, this concept has drastically changed as the macrophages have been reported to originate from three independent sources: the previously mentioned bone marrow, but also the fetal yolk sac and the

fetal liver (Tan and Krasnow, 2016). This raises the possibility that, depending on their origin, the macrophages will react differently to their microenvironment. The developmental origin of AM and IM was recently addressed through a combination of immunofluorescence for specific markers, genetic lineage tracing, and parabiotic studies (Tan and Krasnow, 2016).

Three Different Macrophage Waves Were Described in the Mouse Lung

The macrophage cells constituting each wave are different but share nonetheless phagocytic abilities and antigen presentation capacity. The first wave gives rise to embryonic F4/80^{Pos} lineage macrophages and arises from the yolk sac. These cells spread in the lung interstitium, and during the first week of life, they change localization, moving to the perivascular and peripheral region of the lung. The second wave originates from the fetal liver, and the corresponding macrophages are characterized by the presence of Galectin 3 (aka Mac-2), a carbohydrate-binding protein marker present on their surface. These cells also spread in the interstitial space. During the first week postnatally, they enter in the alveoli as their final destination and display self-renewal capacity to maintain the cell pool size (Röszer, 2018). The third wave comes from circulating monocytes and leads to the formation of the mature interstitial macrophages. These cells replace the embryonic interstitial version, and they are eventually replaced when needed from circulating progenitors (Tan and Krasnow, 2016). Notably, the tissue microenvironment may be more important than the site of origin of the macrophages. A recent study shows that macrophages that arise from different sources can replace the vacant alveolar niche in what some authors have termed "niche competition model" (Guilliams and Scott, 2017). For example, yolk sac macrophages, fetal monocytes, and bone marrow monocytes are all capable of replacing AMs (Evren et al., 2020).

The origin of the interstitial macrophages present in the lung adds an additional level of understanding to the role of these cells. While the role of alveolar and canonical interstitial macrophages has been investigated, the presence of additional subpopulations requires further research for the in-depth characterization of these cellular pools of interstitial cells.

IM Represent a Minor Population Residing in the Parenchyma

Recently, an interesting work was published describing macrophages and their subpopulations in different tissues, including the lung (Chakarov et al., 2019). The authors identified two, not three, as previously described (Tan and Krasnow, 2016), subpopulations of resident macrophages, which derived from circulating monocytes and which displayed unique signatures based on their localization in different tissues, such as the heart, lung, skin, and in fat. They analyzed further the IMs in murine lung, with the rationale that AMs are the major embryonically-derived population and that IM represent a minor population residing in the parenchyma. IM are defined as Lyve^{hi}MHCII^{low}CX3CR1^{low} and Lyve^{low}MCHII^{hi}CX3CR1^{hi} based on the expression levels of these surface markers (Chakarov et al., 2019).

IM Lyve^{hi}MHCII^{low}CX3CR1^{low} and Lyve^{low}MCHII^{hi}CX3CR1^{hi} are characterized by distinctive gene profiles, phenotypes and functions. Focusing on the murine lung, the depletion of one of these two populations leads to the exacerbation of induced fibrosis, demonstrating the specific and relevant role of these cells in the inflammatory process taking place during fibrosis formation (Chakarov et al., 2019). Following activation by the inflammatory process, these dynamic cells could represent a source of Fgf10 and thus drive the repair process with their own plasticity. Therefore, further clarification is needed on the role of these respective immune populations in the lung in order to devise strategies to allow functional recovery of the lung following exposure to toxic biological or chemical agents. Different origins may be associated with different functions, and due to the localization of the embryonic F4/80^{Pos} macrophages, it is easy to speculate a role for these cells in stem cell renewal, combined with growth factor secretion.

INFLAMMATION AND EXTRACELLULAR MATRIX REMODELING: IMPACT ON FGF10 SIGNALING

Cleavage of heparan sulfate proteoglycans (HSPGs) during extracellular matrix remodeling (ECM) remodeling is a feature of inflammation as the leukocytes reach the site of injury. It has been reported that Fgf10 binds to HSPG, which can regulate Fgf10 activity (Watson and Francavilla, 2018). Inflammation could therefore release Fgf10 from the ECM and make it available for repair. Therefore, the changes in the microenvironment likely play a fundamental role in the modulation of Fgf10 activity. However, though it remains unclear how Fgf10 impacts the inflammatory process, ECM remodeling could represent another point of control and modulation of its activity, especially from the therapeutic point of view. In the lung, ECM could act as a chemoattractant where degraded ECM fragments mimic the effect of cytokines. Of note, elastin itself functions as a chemotactic factor for recruiting monocytes (Sorokin, 2010). Other evidence connects hyaluronic fragments with lung injury: the length of the chain determines the pro- or anti- inflammatory effect. Hyaluronic fragments originate from ECM after matrix metalloproteases digestion. They interact with the Toll like receptor 2/4 (Tlr2/4), whose expression can be inhibited by Fgf10 via Hmgb1 [see section "Lipopolysaccharides (LPS) Are Known to be a Potent Activator of the Innate Immune System and Have Been Used in the Context of *in vitro* Lung Explant Culture"].

INFLAMMATION AND FGF10 SIGNALING: LESSONS LEARNT FROM THE MAMMARY GLAND

Intriguingly, the development of the mammary gland is also regulated by Fgf10/Fgfr2b signaling: *Fgf10* deficiency leads to impaired mammary gland formation in mice (as well as the

lung, as previously mentioned) (Mailleux et al., 2002). *Fgf10* KO impairs the sprouting of the mammary epithelium into the adjacent fat pad. In addition, the fat pad itself is poorly developed in these KO mice, raising the question whether the defective sprouting is due to the mutant fat pad *per se* (Howlin et al., 2006).

Colony-Stimulating Factor 1 (*Csf-1*) Deficient Mice Display Delay in Fat Pad Development

Comparable to these results, *colony-stimulating factor 1* (*Csf-1*) deficient mice display an initial delay in fat pad development, but later, the fat pad resumes its growth and reaches a normal size (Gyorki et al., 2009). This last finding suggests that other mechanisms could be activated to compensate for the lack of *Csf-1* to allow fat pad development to resume; one of the possible candidates is the Fgf10/Fgfr2b axis. Studies in mice revealed that Csf-1/Csf-1 receptor signaling is an important chemotactic signaling pathway for the attraction of macrophages in different tissues. In the lung, the airway epithelium secretes Csf-1 thereby regulating the presence of macrophages and dendritic cells, especially in presence of allergens or irritants (Plaks et al., 2015). Tissue-resident macrophages are localized at distinct regions within the mammary gland and have been implicated in various stages of mammary gland development. Recent studies have also identified distinct myeloid cell populations, including $Cd11c^{Pos}$ antigen presenting cells and $Csf\text{-}1r^{Pos}$ macrophages that are localized in close association with ductal epithelial cells in mammary glands (Plaks et al., 2015; Stewart et al., 2019). Mammary gland analysis from *Csf-1* deficient mice demonstrated reduced ductal elongation and branching.

Fgf10/Fgfr2b Signaling Displays Multiple Roles in Mammary Gland Development and Homeostasis

Fgf10's initial expression in the somite controls the migration of surface ectoderm cells to form the mammary placodes as indicated by the observation that *Fgf10* null fail to form four of the five mammary placodes (Veltmaat et al., 2006). The unique placode still present in the *Fgf10* KO embryos reaches the bud stage but fails to elongate and ramify into the improperly differentiated mammary fat pad. Transplantation studies of mutant mammary bud epithelium into a cleared fat pad in the adult mice indicated that the mutant epithelium is perfectly capable to form a mature ramified structure when placed in a permissive environment (Veltmaat et al., 2006) [reviewed in Rivetti et al. (2020)]. Additionally, Fgfr2b ligands are also crucial in post-natal mammary gland development. *Fgfr2b* is highly expressed in mature mice, when puberty starts, and is needed to complete the maturation of the mammary gland with the development of the terminal end buds (TEBs) (Parsa et al., 2008). The mammary gland is composed of ducts, which are made of luminal epithelial cells surrounded by basal/myoepithelial cells. In mice, the TEBs appear as dilated structures at the duct tips around the first month postnatally. Mammary progenitors for both the luminal and basal/myoepithelial lineages are present in the TEBs. Transient inhibition of Fgfr2b signaling leads to the disappearance of the TEBs. However, the TEBs are only temporarily impacted as they reappear once Fgfr2b signaling is restored. It was demonstrated that luminal epithelial cell proliferation and survival is under control of Fgf10/Fgfr2b signaling, thereby allowing the formation and maintenance of the TEBs (Parsa et al., 2008). Interestingly, inactivation of *Csf-1* and *Fgf10* leads to comparable phenotypic alterations during mammary gland formation, suggesting a possible interaction between these two players in organogenesis.

Genetic Impairment of Macrophage Formation in Mice Leads to Alteration in the Terminal End Buds

As previously mentioned, genetic impairment of macrophage formation in mice leads to alteration in the terminal end buds, pointing out the importance of macrophages in the regulation of mammary gland branching (Gouon-Evans et al., 2000). Recently, a chemokine receptor called atypical chemokine receptor 2 (Ackr2) has been reported to be fundamental in the macrophage control of this process (Wilson et al., 2017). Ackr2 controls macrophage recruitment in the mammary gland (Wilson et al., 2020), and in concert with Ccr1 and its ligand Ccl7, regulates the number of macrophages present in the mammary gland, thereby impacting the process of mammary epithelial morphogenesis during puberty. In absence of Ccr1, macrophages cannot be stimulated by Ccl7; missing its receptor, Ccl7 is not able to guide the macrophages to the ductal epithelium, resulting in reduced presence of the immune cells. Consequently, the ductal epithelium is not stimulated by the macrophages resulting in delayed branching (Wilson et al., 2017). *Ackr2* null mice display increased levels of chemokines, which are attractants for monocytes and macrophages. This leads to an increased number of these cells in the mammary gland, which is associated with acceleration of the branching process. Ackr2's effect is likely indirect and the identification of *Ccr1* as a main player adds a new layer in our understanding of the relationship between branching and macrophage dynamics (Wilson et al., 2017).

The Relationship Between Csf-1 and Fgf10 Is Potentially Relevant for Many Diseases Linked to Developmental Defects

In the future, it will be interesting to determine whether the function assumed by macrophages and their impact on Fgf10 signaling observed in mammary gland could also be occurring in the developing lung. We also propose that these macrophages exhibit additional tissue-specific behaviors. For example, in the lung, AMs could regulate surfactant expression by AT2 cells; while it is already known that Csf-1 deficiency impacts the alveolar macrophage population in the lung of young mice: the $Csf\text{-}1^{op/op}$ (corresponding to a complete KO) mice have reduced AMs in the broncho-alveolar lavage compared to the control mice (Shibata et al., 2001); this difference is compensated during aging by higher expression of other molecules, like interleukin 3 (Il3) and matrix metalloproteinases (Mmps). Il3 expression may be the

main compensatory effect, but because it is associated with Mmp-2, Mmp-9, and Mmp-12 expression, it could cause structural damage to the lung. Supporting this possibility *Csf-1* null mice developed emphysema at later stages without displaying any sign of inflammation (Shibata et al., 2001).

INFLAMMATION MAY ALTER FGF10 EXPRESSION (AND VICE VERSA) IN BRONCHO-PULMONARY DYSPLASIA

The Inflammation Process Results From Unbalanced Organ Homeostasis and Is Initiated by Acute Injury, Chronic Damage and/or Infections

An excessive inflammatory response causes damage to the organs instead of repairing them. Bronchopulmonary dysplasia (BPD) is a chronic lung disease characterized by airway obstruction and defective gas exchange that affects preterm children. BPD is associated with a high risk of developing respiratory infections, right heart failure, and death during the first year of life (Lignelli et al., 2019). The definition of BPD has evolved, due to the development of new treatments, in particular oxygen ventilation. Currently, the lung structural hallmarks of BPD are fewer and larger alveoli. Therefore, aborted alveologenesis, the last phase of lung development, is an important characteristic of BPD (Lignelli et al., 2019). BPD pathogenesis is still unclear. Many factors, both cellular and molecular, could be involved in the early stage of the disease leading to impaired lung development. Infection and the associated inflammation during pregnancy and during the perinatal time increase the risk of developing BPD and negatively impact lung development. From a mechanistic point of view, studies have focused on FGF10 because of its importance throughout lung development. Interestingly, *FGF10* expression is reduced in BPD patients, suggesting that this growth factor is involved in BPD pathogenesis together with inflammation (Chao et al., 2017).

A Mouse Model of BPD Allows Studying Mechanistically the Significance of Reduction in *Fgf10* Expression

Contrary to humans, which are born normally with lungs at the alveolar stage, mice are born with lungs at the saccular stage. From a respiratory point of view, newborn mice therefore display an immature lung showing significant similarities with the lungs of prematurely born babies which are at high risk for developing BPD. When newborn mice are subjected to hyperoxia exposure (85% O_2 for 8 days), they exhibit an arrest in lung development and defects in alveolar development, similar to what is observed in human babies with BPD. These mice do survive but show permanent impairment in alveoli formation and therefore reduced respiratory function, among many other defects (Chao et al., 2017, 2019).

Interestingly, the exposure of *Fgf10* heterozygous newborn mice (with one copy of the *Fgf10* gene deleted) to hyperoxia injury causes the death of the mutant animals within 8 days (Chao et al., 2017). Analysis of the whole lung at E18.5 in wild type (WT), $Fgf10^{+/-}$ (50% *Fgf10* expression), and $Fgf10^{LacZ/-}$ (20–30% *Fgf10* expression) hypomorph mice by microarray revealed a dysregulation at many levels: genes that belong to the epithelium, nerve, immune system, muscle and ECM showed an up or down-regulation that correlated with the expression level of *Fgf10*. Analysis of the WT and *Fgf10* heterozygous isolated AT2s at postnatal day 3 in normoxia and hyperoxia by microarrays revealed a further strong dysregulation in genes involved in inflammation: for example, autoimmune diseases (systemic lupus erythematosus, auto-immune thyroid disease, and graft - versus- host disease) and antigen processing presentation. Therefore, these results suggest that AT2 cells display different immune status in *Fgf10* heterozygous compared to wild type control lungs, which could, in turn, differentially modulate the inflammatory response (Prince et al., 2001; Benjamin et al., 2007). Interestingly, as altered immune gene signature of the AT2 cells was observed in the *Fgf10* heterozygous neonate mice in the context of hyperoxia (Chao et al., 2017), it is likely that decreased Fgf10 expression is causative for the effects on inflammation.

AT2 Cells Can Impact Immune Cells via the Production of Chemokines, Alarmins as Well as via Antigen Presentation

The finding that Fgf10 regulates the expression of immune genes in AT2 cells adds an additional understanding to the proposed immune function played by Fgf10. Is all the activity of Fgf10 on the immune cells carried out via Fgf10 action on AT2s, or does Fgf10 mediate this action via the LIFs? We also cannot exclude that Fgf10 could directly act on immune cells. Further studies are therefore necessary to define the role of AT2s and associated LIFs and immune cells in BPD.

While the role of Fgf10 in controlling inflammation is still unclear, the role of another Fgfr2b ligand, Fgf7, has been reported (Prince et al., 2001). In primary cultures of human airway epithelial cells, recombinant FGF7 negatively affected the expression of many interferon-induced genes (Prince et al., 2001). In addition, different biological responses have been reported depending on the timing of epithelial *Fgf7* overexpression using transgenic mice. Short time overexpression impacts positively the repair process following acute lung injury, while long time expression causes inflammation (Tichelaar et al., 2007).

Deficiency of *Gm-csf* or Its Receptor Causes the Failure to Develop AMs Capable of Clearing Surfactant Proteins Made by AT2 Cells

In general, signals from the microenvironment regulate the maintenance and replacement of the AMs. One of these signals in particular, granulocyte-macrophage colony-stimulating factor (Gm-csf or Csf-2), is known to play an important role. Deficiency of Gm-csf or its receptor in mice mimics a human disease called pulmonary alveolar proteinosis, characterized by the

accumulation of surfactant in the alveoli leading to impaired gas exchange (Trapnell et al., 2009). Gm-csf expression is impacted by the level of expression of Fgf10 in the mouse model of BPD previously described (see section "A Mouse Model of BPD Allows Studying Mechanistically the Significance of Reduction in *Fgf10* Expression") (Chao et al., 2017). The physiological meaning of *Gm-Csf* expression changes in relation with Fgf10 expression should be further analyzed and contextualized in the inflammation process.

Il33 Is a Cytokine Secreted by AT2s Potentially Regulated by Fgf10

AMs as well as other immune cells responsible for type 2 immunity (Symowski and Voehringer, 2017), such as innate lymphoid cells (specifically ILC2), basophils, eosinophils, and mast cells are present at low numbers at birth but increase during alveologenesis in mice (Starkey et al., 2019). During mouse lung development, a peak in the numbers of these cell types is observed when pulmonary remodeling is at its climax, strongly suggesting that type 2 immunity actively participates in the process (de Kleer et al., 2016). This peak is associated with a local Il33 increased concentration, a cytokine secreted by AT2s, and which is potentially regulated by Fgf10. It is proposed that Il33 acts on type 2 immune cells, leading to the activation and increased number of ILC2s, stimulation of AMs, as well as inhibition in the dendritic cells of the expression of IL12p35 (de Kleer et al., 2016). Active ILC2s control the repair process in the lung. In addition, as mechanical stress associated with breathing has been reported to increase Il33 secreted by AT2s, as well as by fibroblasts, it has been suggested that this mechanical stress-based Il33 release, especially in the context of the first breath at birth, could regulate alveologenesis in mice (Saluzzo et al., 2017). Indeed, it has been reported in the context of BPD that reduced FGF10 expression and/or increased inflammation are associated with impaired alveologenesis (Chao et al., 2017). Il33 is also increased in the hyperoxia mouse model.

Lipopolysaccharides (LPS) Are Known to Be a Potent Activator of the Innate Immune System and Have Been Used in the Context of *in vitro* Lung Explant Culture

Lipopolysaccharides activate the inflammation through Toll-like receptors 2 and 4 (Tlr2/4), which in turn leads to inhibition of *Fgf10* expression (Benjamin et al., 2007). The conditioned medium from LPS-induced lung explants reduces the branching process when added to WT, as well as in *Tlr4* null lung explants. This indicated that LPS triggered its action on the lung via inflammatory mediators. This *in vitro* assay also demonstrated the existence of a remarkable link between *Fgf10* expression and inflammation. The NF-κB pathway is the major signaling pathway active in BPD patients. In general, NF-κB is considered a transcriptional activator; however, in the case of the *Fgf10* gene, the activation of the NF-κB pathway is associated with *Fgf10* inhibition (Benjamin et al., 2010). As there are no binding sites for NF-κB in the *Fgf10* promoter, it has been proposed that this inhibition is indirect and could be mediated through the activation of a transcriptional repressor. *Fgf10* promoter analysis revealed several GC-rich regions which could be Sp protein binding sites. NF-κB interferes with Sp1 binding on the *Fgf10* promoter, but also on other promoters (e.g., *Bmp4, TgfβRIII*, *Col1A2*, and *Col2A1*) (Benjamin et al., 2010). Sp1 normally induces *Fgf10* expression and NF-κB plays the unusual role of a repressor (**Figures 1A,B**). Interestingly, the inhibition of *Fgf10* expression is dose-dependent: the higher is the inflammation, the less *Fgf10* is expressed. Furthermore, NF-κB mediates the binding of Sp3, another Sp family member, which acts as a transcriptional factor that stimulates or represses transcription similarly to Sp1, and both bind to similar GC-rich sequences (Carver et al., 2013) and localize into the nucleus. Upon inflammatory stimuli, relA, a subunit of NF-κB, translocates into the nucleus, where it interacts physically with Sp3 to help binding the *Fgf10* promoter, thereby inhibiting *Fgf10* gene expression (Carver et al., 2013) (**Figure 1C**). The Sp1-*Fgf10* promoter binding, responsible for the positive *Fgf10* expression, is overcome by the relA action on the availability of Sp3, with the shift in the balance to *Fgf10* repression: inflammatory stimuli determine the downregulation of *Fgf10*.

This process links the inflammatory response to the expression of a key gene orchestrating organogenesis. What is unclear so far is how changes in *Fgf10* expression could impact inflammation. Tlr2/4 are receptors for many small inflammatory molecules, including the alarmin high-mobility group box 1 (Hmgb1) (Wang et al., 2020). It has been recently reported that in lung bronchial epithelial cells, recombinant FGF10 prevents the translocation of this alarmin from the nucleus to the cytoplasm/extracellular compartment (Liu et al., 2020). This resulted in the prevention of the activation of the toll-like receptors, thereby blunting the inflammatory cascade. It is still unclear whether Fgf10 can directly act on immune cells, or if its effect on inflammation is mostly via its impact on AT2 cells.

LINK BETWEEN INFLAMMATION AND AT2-LIF INTERACTION

Fgf10 Is Expressed by Resident Mesenchymal Cells in the Lung

As mentioned before, Fgf10 is expressed by mesenchymal progenitors as well as by differentiated LIFs and acts in a paracrine/autocrine fashion via Fgfr1b and Fgfr2b (Al Alam et al., 2015). Previously, it was reported that Fgf10 is essential to promote the differentiation of mesenchymal progenitor cells toward the LIF lineage. LIFs are mesenchymal cells, displaying a high density of lipid droplets (Torday and Rehan, 2016). In the adult lung, LIFs and AT2s closely interact, and we propose that Fgf10 takes center stage in this interaction. Through their close interaction with AT2 cells, LIFs transfer triglycerides to AT2 cells to produce surfactants (Torday and Rehan, 2016). LIFs are also capable of eliciting the self-renewal of a special subpopulation of

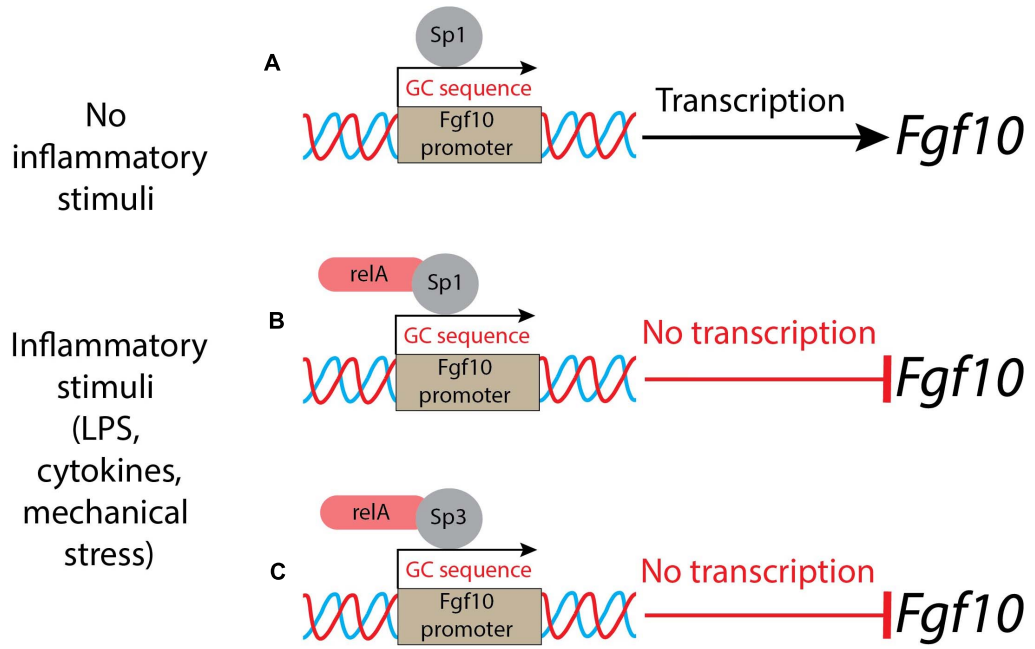

FIGURE 1 | A schematic representation of control of *Fgf10* expression during lung morphogenesis. **(A)** In normal conditions (no inflammatory stimuli), Sp1 binds the Fgf10 promoter leading to the transcription of the growth factor; **(B)** in presence of inflammatory stimuli, the relA subunit of NF-κB translocates into the nucleus and binds Sp1, acting as a repressor; **(C)** alternatively, the relA subunit of NF-κB interacts physically with Sp3 and the complex competes with Sp1: the result is a suppression of *Fgf10* transcription.

AT2s displaying stem cell capabilities (Barkauskas et al., 2013). This property has been explored and monitored, using the so-called "alveolosphere" assay, wherein AT2s and LIFs are isolated by flow cytometry and co-cultured in growth factor-reduced Matrigel for 2–3 weeks. During this time frame, organoids are formed which are made of Sftpc^{Pos}-AT2 cells as well as Podoplanin^{Pos}-AT1 cells (Barkauskas et al., 2013). Indeed, this reflects the property of AT2 stem cells which can proliferate to give rise to more AT2 stem cells, as well as differentiate toward the AT1 lineage. Therefore, it has been proposed that the LIF-AT2 interaction is critical for repair after injury (Nabhan et al., 2018; Zacharias et al., 2018). LIFs are quite poorly characterized and few markers are known to define LIFs: perilipin 2 (Plin2) (Ntokou et al., 2017), platelet derived growth factor receptor alpha (Pdgfrα) (Barkauskas et al., 2013), peroxisome proliferator-activated receptor gamma (Pparγ) (Rehan and Torday, 2012) and Fgf10 (Al Alam et al., 2015) in mice, and more recently, follistatin (FST) and APOE in humans (Travaglini et al., 2020).

Moreover, further characterization of the LIFs is required using approaches such as lineage tracing combined with single-cell RNA-seq data during development, homeostasis and repair after injury. These approaches will allow gathering important mechanistic information about potential cell surface markers capable of distinguishing between different sub-clusters of LIFs, as well as the signaling pathways involved in their differentiation and activation after injury. Our group has reported that in the postnatal mouse lung, *Fgf10* is only expressed by 30% of the LIFs, suggesting that LIFs are indeed heterogeneous (Al Alam et al., 2015). The difference between Fgf10^{Pos}-LIFs and Fgf10^{Neg}-LIFs from a biological point of view is still elusive. We propose that the Fgf10^{Pos}-LIFs are likely the ones capable of sustaining the self-renewal of AT2 stem cells in organoid assays.

The AT2-LIF Interaction *in vitro* Should be Investigated in Presence of Immune Cells

In the context of pneumonectomy in mice (which triggers a process of lung regeneration in the remaining lobes characterized by increased AT2 proliferation), it was reported that immune cells are essential for the expansion of AT2 cells (Lechner et al., 2017). The number of Cd115^{Pos} and Ccr2^{Pos} monocytes and M2-like macrophages increases at the peak of AT2 proliferation. Macrophages are recruited to the lung through the Ccl2/Ccr2 chemokine axis and are required for optimal AT2 proliferation and differentiation following pneumonectomy. It has been proposed that Il13, produced by type 2 innate lymphoid cells (ILC2), could promote lung regeneration, but its mode of action, direct or indirect on AT2s, is still unclear. These results support the concept that the manipulation of the immune cells could be a potential winning strategy to enhance the repair process (Lechner et al., 2017).

Mechanistically, candidate partners for the immune cells could be AT2s and/or LIFs. Use of *in vitro* organoid models bringing together AT2s, LIFs and immune cells should allow to decipher further the mechanistic aspects of such interactions. Like the LIFs, the AT2s are heterogeneous and contain a population of Wnt-responding cells displaying enhanced self-renewal capabilities *in vitro*, both in mice (Nabhan et al., 2018; Zacharias et al., 2018) and in humans (Travaglini

et al., 2020). In addition, our group has recently identified a subpopulation of AT2 cells, distinct from these Wnt-responding cells, which are normally quiescent in homeostasis, but which can proliferate upon injury (Ahmadvand et al., 2021). Of note, this subpopulation of AT2 cells preferentially express some genes related to the immune system. AT2s in general are known to play immunomodulatory functions; they can produce cytokines (IL33, IL17) and modulate the recruitment of immune cells, such as neutrophils, to the site of infection (Kalb et al., 1991; de Kleer et al., 2016; Wosen et al., 2018). Mouse and human AT2s express major histocompatibility complex 2 (MHC II) proteins at the cell surface, therefore acting as antigen presenting cells to the $CD4^{Pos}$ T-cells. Additionally, LIFs could also play a role in the modulation of the immune response. LIFs provide a source of neutral lipid (involved in surfactant production to alleviate the surface tension in the alveoli), which could be involved in mediating an immune response as well (Torday and Rehan, 2016; Duffney et al., 2018).

LINK BETWEEN INFLAMMATION AND FGF10 SIGNALING IN COPD

Chronic Obstructive Pulmonary Disease (COPD) Is the Third Major Cause of Lung Illness (and Death) in the World and Is Characterized by Chronic Lung Inflammation

Such an inflammatory response, overtime, leads to an obstruction of the conducting airways that is irreversible (Adeloye et al., 2015). Notably, the risk for COPD is also increased in humans displaying mutations in *FGF10* (Prince, 2018). Together with the branching defects which are the consequences of impaired lung development, constitutive *FGF10* insufficiency appears therefore to be associated with COPD. Macrophages and lymphocytes are the primary immune cells involved in the pathogenesis of this chronic disease (Nurwidya et al., 2016). Environmental causes are predominant in the pathogenesis of this disease. For instance, cigarette smoke and pollution mediated by particulate matter (PM) are guilty partners in COPD (Ling and van Eeden, 2009; Kelly and Fussell, 2011). Several studies have focused on PM (especially the ones equal or smaller to 2.5 μm than can easily reach the alveoli) that people breathe every day with long-term consequences (Ling and van Eeden, 2009).

Positive Effect of Treatment With Recombinant FGF10 in a Mouse Model of Airway Lung Injury

Recently, the treatment with recombinant FGF10 gave a positive effect in a mouse model of airway lung injury triggered by PM exposure. The authors analyzed the effects on the survival and the outcome of the administration of exogenous FGF10, resulting in a strong improvement of the animals (Liu et al., 2020). Ameliorated inflammatory response in FGF10-treated mice was observed, with a decrease in cell infiltration and decrease in proinflammatory cytokine expression (Il6, Il8, Tnfα, and Pge2). One of the possible downstream players of Fgf10 has been identified as Hmgb1, a nuclear and cytoplasmic small protein; after treatment with exogenous FGF10, the level of Hmgb1 was decreased in BALF (bronchoalveolar lavage fluid).

As mentioned earlier, Hmgb1 is considered an alarmin/damage-associated molecular pattern protein and is ubiquitously expressed (Yang et al., 2020). It is secreted into the extracellular space in response to inflammation and, via its binding to Toll-like receptors, activates the inflammatory cytokines cascade (Liu et al., 2020). It was already reported that FGF10 inhibits the release of Hmgb1 from the nucleus to the extracellular domain, and therefore prevents its binding with Tlr2/4 and the activation of the signaling pathway. TLR4 was up-regulated like HMGB1 in human bronchial epithelial cells after PM-treatment. Administration of recombinant FGF10 reduced TLR4 expression and the shuttling of HMGB1 from the nucleus to the cytoplasm and extracellular space (Liu et al., 2020). The molecular mechanism underlying this inhibition is still not known. Altered expression of proteins involved in the trafficking or degradation of HMGB1 could potentially represent the missing links between FGF10 and inflammation (see **Figure 2** for details). In addition, an increased number of inflammatory cells were detected, indicating that FGF10 is involved in the recruitment of immune cells to re-establish lung homeostasis (Liu et al., 2020).

Increased Infiltration of $Cd4^{Pos}Cd25^{Pos}Foxp3^{Pos}$ T Regulatory Cells in Fgf10 Overexpression Transgenic Mouse Model

The increase in inflammatory cell infiltration in the lungs of FGF10-treated mice in the context of PM exposure seems to occur also in other lung disease models. In a bleomycin-induced mouse model of lung fibrosis [a model for idiopathic pulmonary fibrosis (IPF)], alveolar epithelial Fgf10 overexpression using transgenic mice significantly increased the infiltration of $Cd4^{Pos}Cd25^{Pos}Foxp3^{Pos}$ T regulatory cells during the inflammation phase (Gupte et al., 2009). How these cells are recruited by Fgf10 (i.e., directly or indirectly) is still unclear. Regulatory T-cells are usually involved in the tolerance to self-antigens, and regulate the other immune cells (Okeke and Uzonna, 2019). During this phase, many chemoattractant and signaling molecules are released, with an increase of immune cells in the tissues.

Other T-cell subpopulations could be involved in the homeostasis of the lung and in the modulation of the inflammatory response. In smokers with preserved lung function, an upregulation of γδ T-cell numbers has been reported (Urboniene et al., 2013; Johnson et al., 2020). This is in sharp contrast with COPD patients, where this number is lowered. These γδ T-cells are distinct from $Cd4^{Pos}Cd25^{Pos}Foxp3^{Pos}$ T-regulatory cells. γδ T-cells are usually negative for Cd4 and Cd8 and express unique TCR receptors. γδ T-cells represent 8–20% of the total resident lymphocyte populations in the lung and are one

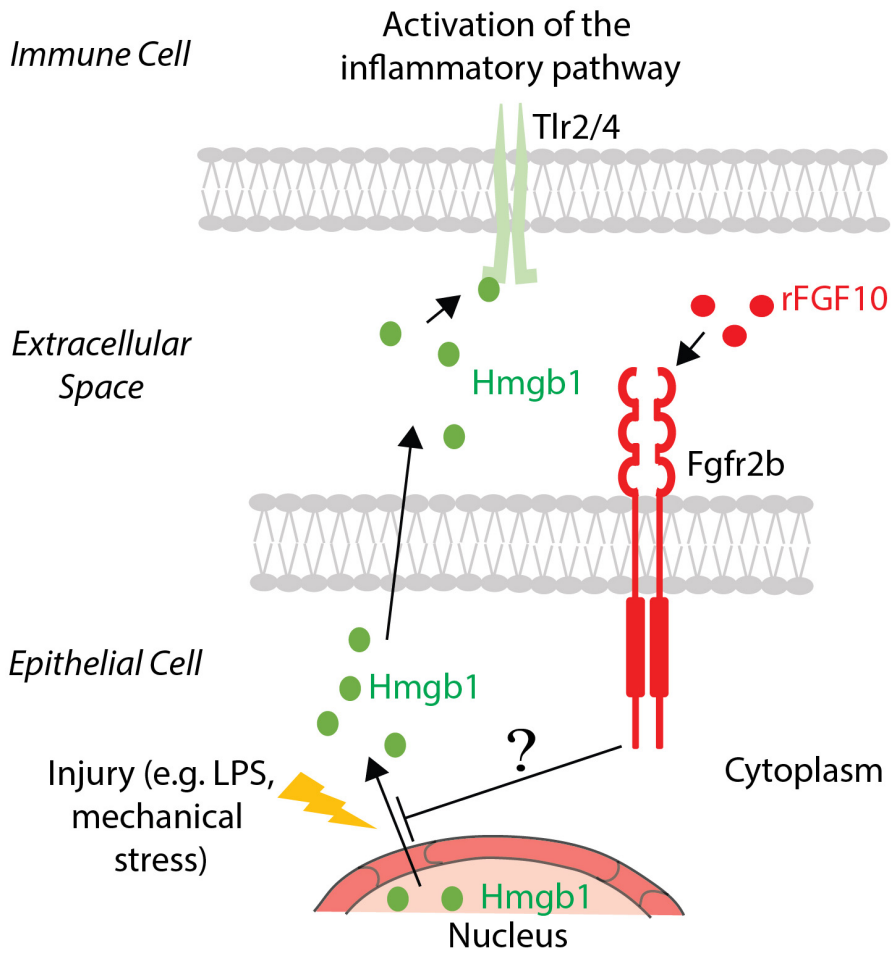

FIGURE 2 | FGF10 effect on Hmgb1. In the case of injury, Hmgb1 shuttles from nucleus to the cytoplasm of the epithelial cells to be released in the extracellular space, where it could bind its receptors Tlr2/4 present on the immune cell surface, causing an inflammatory response. Exogenous FGF10 blocks the release in the extracellular space, acting on the shuttling of Hmgb1 from the nucleus to the cytoplasm. The involved mechanism and the mediators are still unknown.

of the major coordinators for the inflammation that is established in case of injury (Urboniene et al., 2013). It is therefore not surprising that the increased number of γδ T-cells is related only to the active smokers with a normal lung: this observation is compatible with a physiological response aimed at protecting or repairing the lungs from the injury caused by tobacco smoking.

INFLAMMATION AND FGFS IN THE LUNG AND OTHER ORGANS

Apart from Fgf10, the role of other members of the Fgf family in regulating inflammation has also been reported. These Fgfs are expressed in organs where an active epithelial barrier function is required, such as the skin, gut, reproductive tract, and as already cited, the lung. These organs are characterized by the presence of cells able to produce and secrete Fgfs. Additionally, these organs also display the significant presence of specific γδ T-cells at the epithelial barrier (Cheng and Hu, 2017). Fgfs are also produced and secreted by different immune cells and act in a paracrine fashion to regulate the proliferation of epithelial cells, especially in cases where homeostasis needs to be re-established after injury.

FGF7 and Inflammation

A well-reported example of this process occurs in the gastrointestinal tract of adult mice. In the gut, intraepithelial lymphocytes (IEL) secrete Fgf7, thereby enhancing proliferation and differentiation of intestinal epithelial cells (Visco et al., 2009). Fgf7 is an Fgfr2b ligand which can potentially act redundantly with Fgf10. Several inflammatory disease models were used to investigate the impact of recombinant FGF7 on inflammation: in a model of colitis in rats and in mice, administration of recombinant FGF7 after colitis induction decreased the damage to the intestine mucosa and was associated with diminished cell death (Zeeh et al., 1996; Egger et al., 1999). When dextran-sulfate-sodium (DSS) induced-colitis was performed in *Fgf7* KO mice, as well as in *TCR*δ KO mice, the severity of the gut damage between the two models was comparable, but importantly both

KO lines displayed a higher susceptibility to the DSS-induced colitis compared to wild type mice used as controls. This study demonstrated the reparative role of Fgf7 in the intestinal mucosa, identifying also γδ intraepithelial T-lymphocytes as the cells producing and releasing the growth factor (Chen et al., 2002). Intriguingly, the damage in the intestinal barrier was slowly repaired, also in the absence of Fgf7 and TCRδ, suggesting the presence of compensatory mechanisms that may involve other growth factors.

FGF2 and Inflammation

Other Fgfs such as Fgf2 also modulate inflammation. *Fgf2* expression was detected in macrophages and T-cells, both players in acute and chronic inflammation (Song et al., 2015; Shao et al., 2017). Several human studies revealed that FGF2 blood level is increased in Crohn's disease and ulcerative colitis patients (Kanazawa et al., 2001) and that FGF2 could induce the expression of several proinflammatory genes in asthma (Tan et al., 2020). In inflammatory bowel disease (IBD) pathogenesis, the role of the inflammatory cytokines and the cells that produce them, T-helper1 and regulatory T-cells (specifically γδ T-cells), are well recognized. Administration of exogenous recombinant FGF2 alleviates DSS-induced colitis (Shao et al., 2017). Other studies dealing with lung diseases suggest that FGF2 may be associated with airway inflammation, bringing up the possibility of FGF2-targeted therapy. A recent review summarized the role of FGF2 as an immunomodulatory factor in COPD and severe asthma (Tan et al., 2020). In lung diseases, the inflammatory component is often responsible for the exacerbation of the pathology. Against this background, Song et al. (2015) investigated the relationship between Fgf2 and Il17 in the context of a DSS-colitis-induced model. In this model, a high number of infiltrating cells, specifically γδ T-cells, was observed. These cells produced both Il17 and Fgf2 which interact through nuclear factor NF-kappa-B activator 1 (Act1). Indeed, Act1 connects Fgf2 and Il17 signaling, allowing a synergistic action between these two pathways. In this study, dysregulated microbiota driven by the Tgfβ1-Fgf2 axis cooperates with Il17 to promote the repair of the damaged intestinal epithelial barrier, and Act1 bridges the direct signaling cross-talk between Fgf2 and Il17 for the cooperative effect. Such a synergistic effect was also tested in the context of rheumatoid arthritis (RA), an autoimmune disease (Zhang et al., 2019). In their collagen-induced arthritis (CIA) mouse model, ectopic expression of *Fgf2* caused a severe form of the disease, but in the *Il17* KO mice, these effects triggered by Fgf2 were blunted, thereby demonstrating that Fgf2 requires Il17 to mediate its effects. IL17 is also involved in the pathogenesis of different lung diseases such as COPD and IPF (Bozinovski et al., 2015). Innate and adaptive T-cells, as well as epithelial cells in the lung, have been proposed as a source for IL17. In lung fibrosis, IL17 seems to be primarily produced by γδ T-cells and the recruitment of those cells has been shown as a positive outcome. Recombinant FGF10 may recruit T-regulatory cells at the site of inflammation, similarly to Fgf2 in the DSS-colitis model, and thereby stimulate the release of IL17, to drive repair and homeostasis.

USE OF FGF10 AS A THERAPY IN INFLAMMATORY DISEASE

FGF10 and Dry Eye Disease

FGF10 modulates inflammation and as such, its administration in the context of disease could be beneficial. For example, local FGF10 administration via drops directly into the eye could represent a possible therapeutic solution to dry eye disease (Zheng et al., 2015). In a rabbit model of dry eye disease, such treatment resulted in the improvement of the general health of the eye. Indeed, the inflammatory process, which is visualized by the presence of necrotic areas, is clearly decreased in the context of FGF10 treatment. FGF10 increases the proliferation of the corneal epithelium and apoptosis is resolved (Zheng et al., 2015). In this context, the FGF10 effect on inflammation could be indirect; it probably ended the signals that sustained the apoptosis of the cells, a process that triggered and/or potentiated the inflammatory process. In addition, increasing the proliferation of the remaining healthy cells could also overcome the inflammatory signals, leading to the resolution of the damages (Zheng et al., 2015). Against this background, it is critical to mention that the alarmin Hmgb1 could be released from necrotic cells. As previously described, Hmgb1, after binding Tlr4, elicits the activation of a major inflammatory pathway, the NF-κB pathway.

FGF10 and Acute Kidney Injury

In the kidney, ischemia/reperfusion (I/R) causes acute kidney injury (AKI) and results in necrotic areas that could release inflammatory signals (Kezić et al., 2017). The impact of recombinant FGF10 pre-treatment in a mouse model of I/R, that mimics AKI, has been investigated. It was shown that FGF10 prevented the decrease of nuclear Hmgb1, implying that FGF10 stops the shuttling from the nucleus to the cytoplasm of the alarmin, thereby preventing the consequent binding with, and activation of, Tlr2/4, which thereby leads to the inhibition of the inflammatory cascade (Kezić et al., 2017). In agreement with this model of action, inhibition in pro-inflammatory cytokine production, like Il6 and Tnfα, was reported, revealing a similarity to what happens in the particulate matter-driven inflammation in the mouse lung.

FGF10 and Spinal Cord Injury

Tlr4 expression and the NF-κB pathway are also involved in spinal cord injury (SCI) (Chen et al., 2017). In this traumatic injury, microglia/macrophages and neurons produce Fgf10. In a mouse model of SCI, FGF10 treatment depressed the triggered inflammatory factors (Tnfα and Il6) and the NF-κB signaling pathway, and increased phosphorylation of the Pi3K/Akt signaling pathway. Notably, blockade of the Pi3K/Akt signaling pathway was not sufficient to impair the anti-inflammatory action of FGF10 (Chen et al., 2017). Once again, FGF10 appears to prevent inflammation through the inhibition of the NF-κB pathway and the associated inflammatory cytokines. Further studies investigated how recombinant FGF10 administration could affect the consequences of injury to

the central nervous system (CNS) (Li et al., 2016). It was demonstrated that FGF10 treatment inhibited the activation and proliferation of microglia/macrophages by inhibiting the Tlr4/NF-κB pathway, thereby attenuating the production and release of pro-inflammatory cytokines after SCI.

Moreover, increased expression of *Fgf10* from the neurons and microglia/macrophages after acute SCI has been reported. We propose that such increase could be an endogenous self-protective response, supporting the idea that Fgf10 ameliorates the inflammatory process at sites of injury. The involvement of Tlr4, one of the receptors for Hmgb1, opens the question whether the activity through this receptor could be modulated by Fgf10. *In vitro* assays identified the Tlr4/NF-κB pathway as the target of FGF10 anti-inflammatory effect; when LPS-induced BV2 cells (microglia cells) were pre-treated with FGF10, they displayed reduction in the expression of Trl4 and attenuation of NF-κB activation. FGF10 significantly impacts also on p65 (relA) nuclear translocation.

FGF10 and Chronic Inflammatory Skin Disease

The anti-inflammatory effect of FGF10 is not universal. It is known, for instance, that that while FGF10 plays an important role during organogenesis of the skin (Suzuki et al., 2000), in the context of psoriasis, a chronic inflammatory skin disease characterized by excessive proliferation of the keratinocytes, *Fgf10* together with *Fgf7* and their common receptor *Fgfr2b* were overexpressed (Kovacs et al., 2005). Psoriasis is characterized by the presence of a lymphocyte infiltrate that correlates with the level of *Fgf10* expression. In the corresponded animal model, blocking antibodies against Fgf10 ameliorate the inflammatory response, with a significant reduction (Xia et al., 2014). Taken together, evidence suggests that Fgf10 contributes to inflammation in the skin.

WHAT'S NEXT?

Better Characterization of the AT2 Cells

The reciprocal interaction between Fgf10 and inflammation both during organogenesis and the repair process after injury has been an important research topic. From a mechanistic aspect, emerging evidence points to the contribution of immune cells to the proliferation and differentiation of epithelial progenitor cells. Such activity of the immune cells qualifies them to be an integral part of the niche which supports the self-renewal and differentiation of these epithelial progenitor cells. In the context of the lung, AT2 cells are one of the most studied epithelial progenitor cells. These cells interact with mesenchymal cells as well as immune cells. An important aspect of these basic interactions is that each of these cell types represents a heterogeneous population. It is therefore extremely difficult to identify a specific role for each player. For the AT2 cells, our recently published work suggests that a subpopulation of quiescent and relatively undifferentiated AT2 cells, positive for the immune marker PD-L1, could be a major partner for the immune cells (Ahmadvand et al., 2021). In addition, Fgf10 signaling via Fgfr2b in AT2 cells appears to control the expression of immune markers (Chao et al., 2017). It is not clear from the reported study whether this regulation occurs in mature AT2 cells and/or in quiescent PD-L1^{Pos}-AT2 cells. One additional complication concerns the mesenchymal cells *per se*. LIFs, positive for Pdgfrα, have been reported to constitute the niche for AT2 cells in the alveolosphere organoid model (Barkauskas et al., 2013).

However, the LIFs are heterogenous, and more work needs to be done to identify the subset of LIFs responsible for the niche activity. As an example of such heterogeneity, only 30% of the LIFs express Fgf10 postnatally. It will be interesting to explore further, using the alveolosphere model, the functional difference between a Fgf10^{Pos}-LIF and a Fgf10^{Neg}-LIF. Fgf10 secreted by the Fgf10^{Pos}-LIF can either act in an autocrine fashion on the LIFs themselves to maintain their differentiation status, or act in a paracrine fashion on AT2 cells. The expected activity of Fgf10 signaling in the differentiated AT2 cells is still unclear. It may involve survival, proliferation, as well as differentiation (Gupte et al., 2009; Jones et al., 2019). The role of Fgf10 signaling on PD-L1^{Pos}-AT2 quiescent cells is equally unclear. However, in the context of pneumonectomy (PNX), these cells proliferate and differentiate toward mature AT2s. They also display an upregulation of *Fgfr2b* and *Etv5* expression in PNX versus Sham controls, suggesting increased Fgf signaling. In a SftpcCre-Tomato (Tom) mouse model, in which a tamoxifen Cre recombinase is under the control of the promoter of the surfactant protein C (Sftpc), it is possible to identify the AT2 cells using Tom expression/fluorescence. The positive cells display a different expression level of Tom. The isolation of these cells leads to the identification of two different populations, Tom^{hi} and Tom^{low}, based on the level of Tomato expression. Further analysis of these cells led to the discovery of Tom^{Low} cells displaying the expression of immune markers. It will be important to decipher the role of Fgf signaling on the expression of these markers in this AT2 sub-population using specific driver lines targeting these cells. This can be achieved using Dre/Rox and Cre/LoxP technology to generate two complementary driver lines, one under the control of the CD274 promoter and the other one under the control of the *Sftpc* promoter. Finally, the immune cells themselves are a big black box. The macrophages in the lung, for example, originate from at least three different sources (Tan and Krasnow, 2016). The subpopulation of resident or circulating macrophages interacting with AT2 or LIF subpopulations is so far unclear, and more work will have to be done in the context of development and repair after injury to tackle this important issue.

Better Characterization of the Interaction of AT2s With Immune Cells

Recently, many studies have focused on the identification of the specific signature of the type of cell responsible for the regeneration process of the lung in case of injury (e.g., LPS and bleomycin). Three studies converge on the identification of a transitional state, that characterizes AT2 cell differentiation into AT1, in order to re-establish tissue homeostasis. The authors named this new progenitor state with different names,

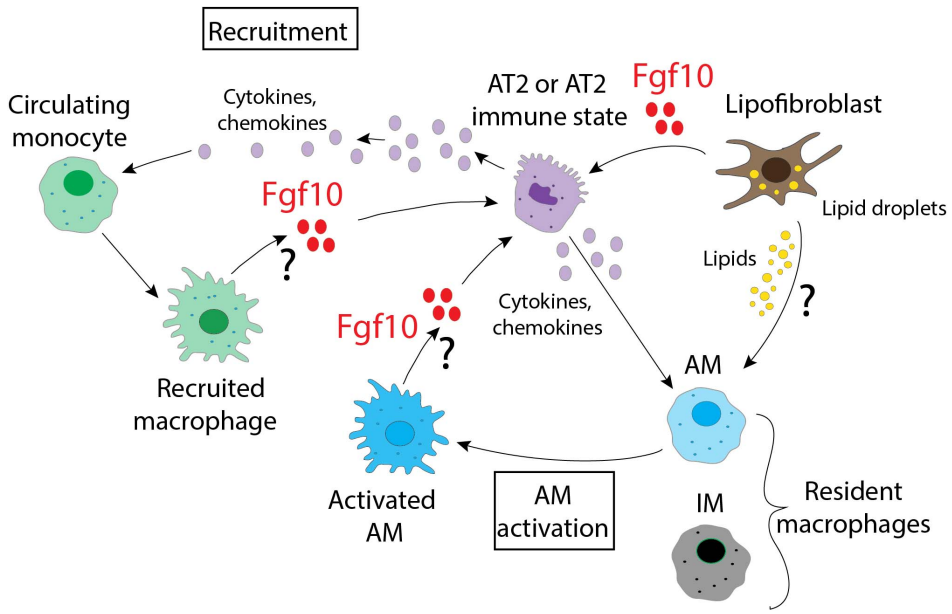

FIGURE 3 | A schematic representation of the possible interactions between different alveolar and immune cells in the lung. Fgf10, produced by lipofibroblasts, recruited macrophages and/or activated AMs, targets AT2 cells. Fgf10 can also orchestrate the production/release of chemokines and cytokines. Lipofibroblasts, via the secretion of lipids, can also activate the AMs.

including pre-alveolar type 1 transitional state (PATS), alveolar differentiation intermediate state (ADI) and damage associated transient progenitors (DATP) (Choi et al., 2020; Kobayashi et al., 2020; Strunz et al., 2020). Verheyden and Sun (2020) summarized and compared the features of these apparently different populations, highlighting how they are probably a picture of the same transitional state. PATS, ADI, and DATP are characterized by high expression of Krt8 and activation of TP53 genes and by a senescence signature. In Choi's paper, the authors, using as a model the bleomycin-treated mice, confirmed interleukin 1β (Il-1β) as a possible inducer of the transitional state. The gene signature of primed AT2 cells corresponded to an activated immune state, similar to what is reported in Ahmadvand's paper more recently (Ahmadvand et al., 2021). In Choi's paper, they identified IM as the source of Il-1β. Il-1β is secreted by IM after bleomycin treatment and acts on the AT2s that express the receptor Il1r1 leading to the acquisition of the transitional status. Il-1β administration on *ex vivo* AT2-derived organoids isolated from Sftpc+ lineage tracing mice leads to the activation of AT2s and pushes them into the transitional state, in which the cells display a specific expression profile, with an upregulation of the genes regulated by TP53, together with high expression of keratin 8 (Krt8) and claudin 4 (Cldn4). The fact that the induction of the transitional state comes from a cytokine secreted by macrophages is strong evidence of the impact of the immune system in tissue homeostasis. The inflammatory signals seem to have a prominent role in the regeneration process, and it is possible that they drive the regulation of the process itself, at least in part. In case of inflammation, the recruited circulating monocytes that arrive at the site show many IM features (Gibbings et al., 2017). At this point, it is overly reductive to consider only immune cells as players in the canonical inflammatory response. Macrophages in the lung already show heterogeneity and plasticity, and it appears that they could display different roles. Further research will be required to identify more subsets responsible for the homeostasis or repair processes. In the same way that AT2 cells are heterogeneous, it is more likely that macrophages, both alveolar and interstitial, with the additional contribution of the recruited-monocytes, could be characterized by different sets of genes, based on the type of environment they face: either healthy or compromised (such as after injury by chemical compound or by bacteria/virus).

Better Characterization of the Macrophages

Many different surface markers are used to identify the different macrophage subpopulations, including recruited-monocytes, but they are not yet sufficient to delineate the different subsets. However, among them, Cx3cr1 and Ccr2 appear to be good candidates to follow the fate and to explore the dynamics of circulating-monocytes. Recently, it has been shown that cells positive for Ccr2 in the subtissular niche of the lung are present in IMs which display variable Cx3cr1 expression (Chakarov et al., 2019). Using these two surface receptors, it is possible to identify macrophages derived from circulating monocytes: $Ccr2^{hi}Cx3cr1^{low}$ are usually considered to be classical or pro-inflammatory macrophages and $Ccr2^{low}Cx3cr1^{hi}$ are alternative or patrolling monocytes. The dual reporter system $Cx3cr1^{GFP/+}Ccr2^{RFP/+}$, which allows to study the fate of these peculiar cells, will be instrumental to follow the monocytes recruitment in the tissues in presence of damage/injury. The

identification at the same time of the change in expression of these two markers led to the possibility to discriminate different macrophage subpopulations based on the expression level of these receptors. This system has led to the discovery of the dynamic reprogramming of monocytes in different tissues, like the liver and the brain (Dal-Secco et al., 2015; Faustino et al., 2019). It is still unclear what induced the switch of expression in the surface markers and what happened to these cells when they reached their target tissues. Ccr2 seems to guide their recruitment following the gradient of Ccl2 (Ccr2 counterpart). Upon arrival in their target organ, they are proposed to undergo reprogramming quickly. Cx3cr1 expression characterized the cells involved in wound healing, but how and through what mechanism remains to be investigated. Moreover, due to the high heterogeneity of the macrophage population and the high variation in surface marker expression, in a context of regeneration, it could be interesting to adopt a depletion/deficiency approach; several models are available, and they are well summarized in a recent review (Hua et al., 2018). A depletion model, such as CD169-DNT, where a diphtheria toxin inducible system enclosing a fusion product of the human DNT receptor under control of the CD169 sialoadhesin gene promoter (Miyake et al., 2007), could clarify the role of this specific subset of macrophages. Similarly, additional studies on the different populations of lung macrophages, including AM and IM and recruited-monocytes, are required to specifically identify unique markers to target for transient depletion or genetic studies.

DISCUSSION

What emerges from this picture is the plasticity of the immune cells and their ability to adapt and follow new signals from the microenvironment which, in the lung, are likely generated by the heterogenous populations of LIFs and/or AT2s. It is therefore likely that multiple cell populations respond to stress as represented in **Figure 3**. Further studies are necessary to identify what guides the immune cells to sites of injury and the signals that later regulate them. From the data already published, Fgf10 is surely one of the most interesting candidates due to the evidence of its connection to several immune molecules, and it would therefore be important to decipher its role in detail by identifying the cells responsible for its production and release. This should be done not only in a context of injury/repair, but also during lung organogenesis, where Fgf10 controls the expression of many genes linked to the immune system. The possibility to use different mouse models that express different levels of Fgf10, together with the Cx3cr1/Ccr2 dual reporter system that identifies dynamic subpopulations of IM, could provide interesting clues about the complex interactions that are relevant in the cross-talk occurring in the microenvironment. In summary, Fgf10 is a key player during organogenesis, repair after injury, as well as in the inflammation, and its use, by clinicians, as a therapy to repair a damaged epithelial barrier may be more popular if beneficial effects on the inflammatory process are also robustly established.

AUTHOR CONTRIBUTIONS

MM and SB wrote the review and made the illustration. CC and SB edited the review. All authors contributed to the article and approved the submitted version.

FUNDING

SB was supported by the Cardio-Pulmonary Institute and by grants from the Deutsche Forschungsgemeinschaft (DFG; BE4443/1-1, BE4443/4-1, BE4443/6-1, KFO309 P7, and SFB1213-projects A02 and A04). CC was supported by the Interventional Pulmonary Key Laboratory of Zhejiang Province, the Interventional Pulmonology Key Laboratory of Wenzhou City, the Interventional Pulmonology Innovation Subject of Zhejiang Province, the National Natural Science Foundation of China (81570075 and 81770074), Zhejiang Provincial Natural Science Foundation (LZ15H010001), Zhejiang Provincial Science Technology Department Foundation (2015103253), and the National Key Research and Development Program of China (2016YFC1304000).

ACKNOWLEDGMENTS

We thank Matthew Jones for his help in editing this manuscript.

REFERENCES

Adeloye, D., Chua, S., Lee, C., Basquill, C., Papana, A., Theodoratou, E., et al. (2015). Global and regional estimates of COPD prevalence: systematic review and meta-analysis. *J. Glob. Health* 5:020415. doi: 10.7189/jogh.05.020415

Ahmadvand, N., Khosravi, F., Lingampally, A., Wasnick, R., Vazquez-Armendariz, I., Carraro, G., et al. (2021). Identification of a novel subset of alveolar type 2 cells enriched in PD-L1 and expanded following pneumonectomy. *Eur. Respir. J.* 16:2004168. doi: 10.1183/13993003.04168-2020

Al Alam, D., el Agha, E., Sakurai, R., Kheirollahi, V., Moiseenko, A., Danopoulos, S., et al. (2015). Evidence for the involvement of fibroblast growth factor 10 in lipofibroblast formation during embryonic lung development. *Development* 142:dev.109173. doi: 10.1242/dev.109173

Barkauskas, C. E., Cronce, M. J., Rackley, C. R., Bowie, E. J., Keene, D. R., Stripp, B. R., et al. (2013). Type 2 alveolar cells are stem cells in adult lung. *J. Clin. Invest.* 123, 3025–3036. doi: 10.1172/JCI68782

Bellusci, S., Grindley, J., Emoto, H., Itoh, N., and Hogan, B. L. (1997). Fibroblast growth factor 10 (FGF10) and branching morphogenesis in the embryonic mouse lung. *Development* 124, 4867–4878.

Benjamin, J. T., Carver, B. J., Plosa, E. J., Yamamoto, Y., Miller, J. D., Liu, J.-H., et al. (2010). NF-κB activation limits airway branching through inhibition of Sp1-mediated fibroblast growth Factor-10 expression. *J. Immunol.* 185, 4896–4903. doi: 10.4049/jimmunol.1001857

Benjamin, J. T., Smith, R. J., Halloran, B. A., Day, T. J., Kelly, D. R., and Prince, L. S. (2007). FGF-10 is decreased in bronchopulmonary dysplasia and suppressed by toll-like receptor activation. *Am. J. Physio. Lung Cell. Mol. Physiol.* 292, L550–L558. doi: 10.1152/ajplung.00329.2006

Bozinovski, S., Seow, H. J., Chan, S. P. J., Anthony, D., McQualter, J., Hansen, M., et al. (2015). Innate cellular sources of interleukin-17A regulate macrophage accumulation in cigarette smoke- induced lung inflammation in mice. *Clin. Sci.* 129, 785–796. doi: 10.1042/CS20140703

Branchfield, K., Li, R., Veheyden, J., McCulley, D., and Sun, X. (2015). A three-dimensional study of alveologenesis in mouse lung. *Dev. Biol.* 409, 429–441. doi: 10.1016/j.ydbio.2015.11.017

Carver, B. J., Plosa, E. J., Stinnett, A. M., Blackwell, T. S., and Prince, L. S. (2013). Interactions between NF-κB and SP3 connect inflammatory signaling with reduced FGF-10 expression. *J. Biol. Chem.* 288, 15318–15325. doi: 10.1074/jbc.M112.447318

Chakarov, S., Lim, H. Y., Tan, L., Lim, S. Y., See, P., Lum, J., et al. (2019). Two distinct interstitial macrophage populations coexist across tissues in specific subtissular niches. *Science* 363:aau0964. doi: 10.1126/science.aau0964

Chao, C. M., Moiseenko, A., Kosanovic, D., Rivetti, S., el Agha, E., Wilhelm, J., et al. (2019). Impact of Fgf10 deficiency on pulmonary vasculature formation in a mouse model of bronchopulmonary dysplasia. *Hum. Mol. Genet.* 28, 1429–1444. doi: 10.1093/hmg/ddy439

Chao, C.-M., Moiseenko, A., Zimmer, K.-P., and Bellusci, S. (2016). Alveologenesis: key cellular players and fibroblast growth factor 10 signaling. *Mol. Cell. Pediatr.* 3:17. doi: 10.1186/s40348-016-0045-7

Chao, C. M., Yahya, F., Moiseenko, A., Tiozzo, C., Shrestha, A., Ahmadvand, N., et al. (2017). Fgf10 deficiency is causative for lethality in a mouse model of bronchopulmonary dysplasia. *J. Pathol.* 241, 91–103. doi: 10.1002/path.4834

Chen, J., Wang, Z., Zheng, Z. M., Chen, Y., Khor, S., Shi, K. S., et al. (2017). Neuron and microglia/macrophage-derived FGF10 activate neuronal FGFR2/PI3K/Akt signaling and inhibit microglia/macrophages TLR4/NF-κB-dependent neuroinflammation to improve functional recovery after spinal cord injury. *Cell Death Dis.* 8:e3090. doi: 10.1038/cddis.2017.490

Chen, Y., Chou, K., Fuchs, E., Havran, W. L., and Boismenu, R. (2002). Protection of the intestinal mucosa by intraepithelial γδ T cells. *Proc. Natl. Acad. Sci. U.S.A.* 99, 14338–14343. doi: 10.1073/pnas.212290499

Cheng, M., and Hu, S. (2017). Lung-resident γδ T cells and their roles in lung diseases. *Immunology* 151:12764. doi: 10.1111/imm.12764

Choi, J., Park, J. E., Tsagkogeorga, G., Yanagita, M., Koo, B. K., Han, N., et al. (2020). Inflammatory signals induce AT2 cell-derived damage-associated transient progenitors that mediate alveolar regeneration. *Cell Stem Cell* 27, 366–382. doi: 10.1016/j.stem.2020.06.020

Dal-Secco, D., Wang, J., Zeng, Z., Kolaczkowska, E., Wong, C. H. Y., Petri, B., et al. (2015). A dynamic spectrum of monocytes arising from the in situ reprogramming of CCR2+ monocytes at a site of sterile injury. *J. Exper. Med.* 212, 447–456. doi: 10.1084/jem.20141539

De Kleer, I., Willems, F., Lambrecht, B., and Goriely, S. (2014). Ontogeny of myeloid cells. *Front. Immunol.* 5:423. doi: 10.3389/fimmu.2014.00423

de Kleer, I. M., Kool, M., de Bruijn, M. J. W., Willart, M., van Moorleghem, J., Schuijs, M. J., et al. (2016). Perinatal activation of the interleukin-33 pathway promotes Type 2 immunity in the developing lung. *Immunity* 45, 1285–1298. doi: 10.1016/j.immuni.2016.10.031

Duffney, P. F., Falsetta, M. L., Rackow, A. R., Thatcher, T. H., Phipps, R. P., and Sime, P. J. (2018). Key roles for lipid mediators in the adaptive immune response. *J. Clin. Invest.* 128, 2724–2731. doi: 10.1172/JCI97951

Egger, B., Procaccino, F., Sarosi, I., Tolmos, J., Buchler, M. W., and Eysselein, V. E. (1999). Keratinocyte growth factor ameliorates dextran sodium sulfate colitis in mice. *Digest. Dis. Sci.* 44, 836–844. doi: 10.1023/A:1026642715764

Evren, E., Ringqvist, E., and Willinger, T. (2020). Origin and ontogeny of lung macrophages: from mice to humans. *Immunology* 160, 126–138. doi: 10.1111/imm.13154

Faustino, J., Chip, S., Derugin, N., Jullienne, A., Hamer, M., Haddad, E., et al. (2019). CX3CR1-CCR2-dependent monocyte-microglial signaling modulates neurovascular leakage and acute injury in a mouse model of childhood stroke. *J. Cereb. Blood Flow Metab.* 39, 1919–1935. doi: 10.1177/0271678X18817663

Gibbings, S. L., Thomas, S. M., Atif, S. M., McCubbrey, A. L., Desch, A. N., Danhorn, T., et al. (2017). Three unique interstitial macrophages in the murine lung at steady state. *Am. J. Respir. Cell Mol. Biol.* 57, 66–76. doi: 10.1165/rcmb.2016-0361OC

Gordon, S., and Plüddemann, A. (2017). Tissue macrophages: heterogeneity and functions. *BMC Biol.* 15:53. doi: 10.1186/s12915-017-0392-4

Gouon-Evans, V., Rothenberg, M. E., and Pollard, J. W. (2000). Postnatal mammary gland development requires macrophages and eosinophils. *Development* 127, 2269–2282.

Guilliams, M., and Scott, C. L. (2017). Does niche competition determine the origin of tissue-resident macrophages? *Nat. Rev. Immunol.* 17, 451–460. doi: 10.1038/nri.2017.42

Gupte, V. V., Ramasamy, S. K., Reddy, R., Lee, J., Weinreb, P. H., Violette, S. M., et al. (2009). Overexpression of fibroblast growth factor-10 during both inflammatory and fibrotic phases attenuates bleomycin-induced pulmonary fibrosis in mice. *Am. J. Respir. Crit. Care Med.* 180, 424–436. doi: 10.1164/rccm.200811-1794OC

Gyorki, D. E., Asselin-Labat, M. L., van Rooijen, N., Lindeman, G. J., and Visvader, J. E. (2009). Resident macrophages influence stem cell activity in the mammary gland. *Breast Cancer Res.* 11:R62. doi: 10.1186/bcr2353

Howlin, J., McBryan, J., and Martin, F. (2006). Pubertal mammary gland development: insights from mouse models. *J. Mamm. Gland Biol. Neoplasia* 11, 283–297. doi: 10.1007/s10911-006-9024-2

Hua, L., Shi, J., Shultz, L. D., and Ren, G. (2018). Genetic models of macrophage depletion. *Methods Mol. Biol.* 1784, 243–258. doi: 10.1007/978-1-4939-7837-3_22

Itoh, N. (2016). FGF10: a multifunctional mesenchymal-epithelial signaling growth factor in development, health, and disease. *Cytokine Growth Fact. Rev.* 28, 63–69. doi: 10.1016/j.cytogfr.2015.10.001

Johnson, M. D., Witherden, D. A., and Havran, W. L. (2020). The Role of Tissue-resident γδ T cells in stress surveillance and tissue maintenance. *Cells* 9:686. doi: 10.3390/cells9030686

Jones, M. R., Dilai, S., Lingampally, A., Chao, C. M., Danopoulos, S., Carraro, G., et al. (2019). A comprehensive analysis of fibroblast growth factor receptor 2b signaling on epithelial tip progenitor cells during early mouse lung branching morphogenesis. *Front. Genet.* 10:746. doi: 10.3389/fgene.2018.00746

Kalb, T. H., Chuang, M. T., Marom, Z., and Mayer, L. (1991). Evidence for accessory cell function by class II MHC antigen-expressing airway epithelial cells. *Am. J. Respir. Cell Mol. Biol.* 4, 320–329. doi: 10.1165/ajrcmb/4.4.320

Kalymbetova, T. V., Selvakumar, B., Rodríguez-Castillo, J. A., Gunjak, M., Malainou, C., Heindl, M. R., et al. (2018). Resident alveolar macrophages are master regulators of arrested alveolarization in experimental bronchopulmonary dysplasia. *J. Pathol.* 245, 153–159. doi: 10.1002/path.5076

Kanazawa, S., Tsunoda, T., Onuma, E., Majima, T., Kagiyama, M., and Kikuchi, K. (2001). VEGF, basic-FGF, and TGF-beta in Crohn's disease and ulcerative colitis: a novel mechanism of chronic intestinal inflammation. *Am. J. Gastroenterol.* 96, 822–828. doi: 10.1111/j.1572-0241.2001.03527.x

Kelly, F. J., and Fussell, J. C. (2011). Air pollution and airway disease. *Clin. Exper. Allergy* 41, 1059–1071. doi: 10.1111/j.1365-2222.2011.03776.x

Kezić, A., Stajic, N., and Thaiss, F. (2017). Innate immune response in kidney ischemia/reperfusion injury: potential target for therapy. *J. Immunol. Res.* 2017:6305439. doi: 10.1155/2017/6305439

Kobayashi, Y., Tata, A., Konkimalla, A., Katsura, H., Lee, R. F., Ou, J., et al. (2020). Persistence of a regeneration-associated, transitional alveolar epithelial cell state in pulmonary fibrosis. *Nat. Cell Biol.* 22, 934–946. doi: 10.1038/s41556-020-0542-8

Kovacs, D., Falchi, M., Cardinali, G., Raffa, S., Carducci, M., Cota, C., et al. (2005). Immunohistochemical analysis of keratinocyte growth factor and fibroblast growth factor 10 expression in psoriasis. *Exper. Dermatol.* 14, 130–137. doi: 10.1111/j.0906-6705.2005.00261.x

Lechner, A. J., Driver, I. H., Lee, J., Conroy, C. M., Nagle, A., Locksley, R. M., et al. (2017). Recruited monocytes and Type 2 immunity promote lung regeneration following pneumonectomy. *Cell Stem Cell* 21, 120–134.e7. doi: 10.1016/j.stem.2017.03.024

Li, Y. H., Fu, H. L., Tian, M. L., Wang, Y. Q., Chen, W., Cai, L. L., et al. (2016). Neuron-derived FGF10 ameliorates cerebral ischemia injury via inhibiting NF-Ĭ B-dependent neuroinflammation and activating PI3K/Akt survival signaling pathway in mice. *Sci. Rep.* 6:19869. doi: 10.1038/srep19869

Lignelli, E., Palumbo, F., Myti, D., and Morty, R. E. (2019). Recent advances in our understanding of the mechanisms of lung alveolarization and bronchopulmonary dysplasia. *Am. J. Physiol. Lung Cell. Mol. Physiol.* 317, L832–L887. doi: 10.1152/ajplung.00369.2019

Ling, S. H., and van Eeden, S. F. (2009). Particulate matter air pollution exposure: role in the development and exacerbation of chronic obstructive pulmonary disease. *Intern. J. Chron. Obstruct. Pulm. Dis.* 4, 233–243. doi: 10.2147/copd.s5098

Liu, L., Song, C., Li, J., Wang, Q., Zhu, M., Hu, Y., et al. (2020). Fibroblast growth factor 10 alleviates particulate matter-induced lung injury by inhibiting the HMGB1-TLR4 pathway. *Aging* 12:102676. doi: 10.18632/aging.102676

Mailleux, A. A., Spencer-Dene, B., Dillon, C., Ndiaye, D., Savona-Baron, C., Itoh, N., et al. (2002). Role of FGF10/FGFR2b signaling during mammary gland development in the mouse embryo. *Development* 129, 53–60.

Min, H., Danilenko, D. M., Scully, S. A., Bolon, B., Ring, B. D., Tarpley, J. E., et al. (1998). Fgf-10 is required for both limb and lung development and exhibits striking functional similarity to *Drosophila* branchless. *Genes Dev*. 12, 3156–3161. doi: 10.1101/gad.12.20.3156

Miyake, Y., Asano, K., Kaise, H., Uemura, M., Nakayama, M., and Tanaka, M. (2007). Critical role of macrophages in the marginal zone in the suppression of immune responses to apoptotic cell-associated antigens. *J. Clin. Invest*. 117, 2268–2278. doi: 10.1172/JCI31990

Nabhan, A. N., Brownfield, D. G., Harbury, P. B., Krasnow, M. A., and Desai, T. J. (2018). Single-cell Wnt signaling niches maintain stemness of alveolar type 2 cells. *Science* 359:aam6603. doi: 10.1126/science.aam6603

Ntokou, A., Szibor, M., Rodríguez-Castillo, J. A., Quantius, J., Herold, S., Elagha, E., et al. (2017). A novel mouse Cre-driver line targeting Perilipin 2-expressing cells in the neonatal lung. *Genesis* 55:e23080. doi: 10.1002/dvg.23080

Nurwidya, F., Damayanti, T., and Yunus, F. (2016). The role of innate and adaptive immune cells in the immunopathogenesis of chronic obstructive pulmonary disease. *Tuberculos. Respir. Dis.* 79, 5–13. doi: 10.4046/trd.2016.79.1.5

Okeke, E. B., and Uzonna, J. E. (2019). The pivotal role of regulatory T cells in the regulation of innate immune cells. *Front. Immunol.* 10:680. doi: 10.3389/fimmu.2019.00680

Parsa, S., Ramasamy, S. K., de Langhe, S., Gupte, V. V., Haigh, J. J., Medina, D., et al. (2008). Terminal end bud maintenance in mammary gland is dependent upon FGFR2b signaling. *Dev. Biol.* 317, 121–131. doi: 10.1016/j.ydbio.2008.02.014

Plaks, V., Boldajipour, B., Linnemann, J. R., Nguyen, N. H., Kersten, K., Wolf, Y., et al. (2015). Adaptive immune regulation of mammary postnatal organogenesis. *Dev. Cell* 34, 493–504. doi: 10.1016/j.devcel.2015.07.015

Prince, L. S. (2018). FGF10 and human lung disease across the life spectrum. *Front. Genet.* 9:517. doi: 10.3389/fgene.2018.00517

Prince, L. S., Karp, P. H., Moninger, T. O., and Welsh, M. J. (2001). KGF alters gene expression in human airway epithelia: potential regulation of the inflammatory response. *Physiol. Genom.* 6, 81–89. doi: 10.1152/physiolgenomics.2001.6.2.81

Rehan, V. K., and Torday, J. S. (2012). PPARγ signaling mediates the evolution, development, homeostasis, and repair of the lung. *PPAR Res.* 2012:289867. doi: 10.1155/2012/289867

Rivetti, S., Chen, C., Chen, C., and Bellusci, S. (2020). Fgf10/Fgfr2b signaling in mammary gland development, homeostasis, and cancer. *Front. Cell Dev. Biol.* 8:415. doi: 10.3389/fcell.2020.00415

Röszer, T. (2018). Understanding the biology of self-renewing macrophages. *Cells* 7:103. doi: 10.3390/cells7080103

Sala, F. G., del Moral, P. M., Tiozzo, C., Al Alam, D., Warburton, D., Grikscheit, T., et al. (2011). FGF10 controls the patterning of the tracheal cartilage rings via Shh. *Development* 138:dev.051680. doi: 10.1242/dev.051680

Saluzzo, S., Gorki, A. D., Rana, B. M. J., Martins, R., Scanlon, S., Starkl, P., et al. (2017). First-breath-induced Type 2 pathways shape the lung immune environment. *Cell Rep.* 18, 1893–1905. doi: 10.1016/j.celrep.2017.01.071

Sekine, K., Ohuchi, H., Fujiwara, M., Yamasaki, M., Yoshizawa, T., Sato, T., et al. (1999). Fgf10 is essential for limb and lung formation. *Nat. Genet.* 21, 138–141. doi: 10.1038/5096

Shao, X., Chen, S., Yang, D., Cao, M., Yao, Y., Wu, Z., et al. (2017). FGF2 cooperates with IL-17 to promote autoimmune inflammation. *Sci. Rep*. 7:7024. doi: 10.1038/s41598-017-07597-8

Shibata, Y., Zsengeller, Z., Otake, K., Palaniyar, N., and Trapnell, B. C. (2001). Alveolar macrophage deficiency in osteopetrotic mice deficient in macrophage colony-stimulating factor is spontaneously corrected with age and associated with matrix metalloproteinase expression and emphysema. *Blood* 98, 2845–2852. doi: 10.1182/blood.V98.9.2845

Song, X., Dai, D., He, X., Zhu, S., Yao, Y., Gao, H., et al. (2015). Growth factor FGF2 cooperates with interleukin-17 to repair intestinal epithelial damage. *Immunity* 43, 488–501. doi: 10.1016/j.immuni.2015.06.024

Sorokin, L. (2010). The impact of the extracellular matrix on inflammation. *Nat. Rev. Immunol.* 10, 712–723. doi: 10.1038/nri2852

Starkey, M. R., McKenzie, A. N., Belz, G. T., and Hansbro, P. M. (2019). Pulmonary group 2 innate lymphoid cells: surprises and challenges. *Mucos. Immunol.* 12, 299–311. doi: 10.1038/s41385-018-0130-4

Stewart, T. A., Hughes, K., Hume, D. A., and Davis, F. M. (2019). Developmental stage-specific distribution of macrophages in mouse mammary gland. *Front. Cell Dev. Biol.* 7:250. doi: 10.3389/fcell.2019.00250

Strunz, M., Simon, L. M., Ansari, M., Kathiriya, J. J., Angelidis, I., Mayr, C. H., et al. (2020). Alveolar regeneration through a Krt8+ transitional stem cell state that persists in human lung fibrosis. *Nat. Commun.* 11:3559. doi: 10.1038/s41467-020-17358-3

Suzuki, K., Yamanishi, K., Mori, O., Kamikawa, M., Andersen, B., Kato, S., et al. (2000). Defective terminal differentiation and hypoplasia of the epidermis in mice lacking the Fgf10 gene. *FEBS Lett.* 481, 53–56. doi: 10.1016/S0014-5793(00)01968-2

Symowski, C., and Voehringer, D. (2017). Interactions between innate lymphoid cells and cells of the innate and adaptive immune system. *Front. Immunol.* 8:1422. doi: 10.3389/fimmu.2017.01422

Takahashi, K., Yamamura, F., and Naito, M. (1989). Differentiation, maturation, and proliferation of macrophages in the mouse yolk sac: a light-microscopic, enzyme-cytochemical, immunohistochemical, and ultrastructural study. *J. Leukocyte Biol.* 45, 87–96. doi: 10.1002/jlb.45.2.87

Takeya, M., and Takahashi, K. (1992). Ontogenic development of macrophage subpopulations and Ia-positive dendritic cells in fetal and neonatal rat spleen. *J. Leukocyte Biol.* 52, 516–523. doi: 10.1002/jlb.52.5.516

Tan, S. Y. S., and Krasnow, M. A. (2016). Developmental origin of lung macrophage diversity. *Development* 143, 1318–1327. doi: 10.1242/dev.129122

Tan, Y., Qiao, Y., Chen, Z., Liu, J., Guo, Y., Tran, T., et al. (2020). FGF2, an immunomodulatory factor in asthma and chronic obstructive pulmonary Disease (COPD). *Front. Cell Dev. Biol.* 8:223. doi: 10.3389/fcell.2020.00223

Tichelaar, J. W., Wesselkamper, S. C., Chowdhury, S., Yin, H., Berclaz, P. Y., Sartor, M. A., et al. (2007). Duration-dependent cytoprotective versus inflammatory effects of lung epithelial fibroblast growth factor-7 expression. *Exper. Lung Res.* 33, 385–417. doi: 10.1080/01902140701703226

Torday, J. S., and Rehan, V. K. (2016). On the evolution of the pulmonary alveolar lipofibroblast. *Exper. Cell Res.* 340, 215–219. doi: 10.1016/j.yexcr.2015.12.004

Trapnell, B. C., Carey, B. C., Uchida, K., and Suzuki, T. (2009). Pulmonary alveolar proteinosis, a primary immunodeficiency of impaired GM-CSF stimulation of macrophages. *Curr. Opin. Immunol.* 21, 514–521. doi: 10.1016/j.coi.2009.09.004

Travaglini, K. J., Nabhan, A. N., Penland, L., Sinha, R., Gillich, A., Sit, R. V., et al. (2020). A molecular cell atlas of the human lung from single-cell RNA sequencing. *Nature* 587, 619–625. doi: 10.1038/s41586-020-2922-4

Urboniene, D., Babusyte, A., Lötvall, J., Sakalauskas, R., and Sitkauskiene, B. (2013). Distribution of γδ and other T-lymphocyte subsets in patients with chronic obstructive pulmonary disease and asthma. *Respir. Med.* 107, 413–423. doi: 10.1016/j.rmed.2012.11.012

van de Laar, L., Saelens, W., De Prijck, S., Martens, L., Scott, C. L., Van Isterdael, G., et al. (2016). Yolk sac macrophages, fetal Liver, and adult monocytes can colonize an empty niche and develop into functional tissue-resident macrophages. *Immunity* 44, 755–768. doi: 10.1016/j.immuni.2016.02.017

Veltmaat, J. M., Relaix, F., Le, L. T., Kratochwil, K., Sala, F. G., van Veelen, W., et al. (2006). Gli3-mediated somitic Fgf10 expression gradients are required for the induction and patterning of mammary epithelium along the embryonic axes. *Development* 133, 2325–2335. doi: 10.1242/dev.02394

Verheyden, J. M., and Sun, X. (2020). A transitional stem cell state in the lung. *Nat. Cell Biol.* 22, 1025–1026. doi: 10.1038/s41556-020-0561-5

Visco, V., Bava, F. A., D'Alessandro, F., Cavallini, M., Ziparo, V., and Torrisi, M. R. (2009). Human colon fibroblasts induce differentiation and proliferation of intestinal epithelial cells through the direct paracrine action of keratinocyte growth factor. *J. Cell. Physiol.* 220, 204–213. doi: 10.1002/jcp.21752

Wang, J., Li, R., Peng, Z., Hu, B., Rao, X., and Li, J. (2020). HMGB1 participates in LPS-induced acute lung injury by activating the AIM2 inflammasome in macrophages and inducing polarization of M1 macrophages via TLR2, TLR4, and RAGE/NF-κB signaling pathways. *Intern. J. Mol. Med.* 45, 61–80. doi: 10.3892/ijmm.2019.4402

Watson, J., and Francavilla, C. (2018). Regulation of FGF10 signaling in development and disease. *Front. Genet.* 9:500. doi: 10.3389/fgene.2018.00500

Wilson, G. J., Fukuoka, A., Love, S. R., Kim, J., Pingen, M., Hayes, A. J., et al. (2020). Chemokine receptors coordinately regulate macrophage dynamics and

mammary gland development. *Development* 147:dev187815. doi: 10.1242/dev.187815

Wilson, G. J., Hewit, K. D., Pallas, K. J., Cairney, C. J., Lee, K. M., Hansell, C. A., et al. (2017). Atypical chemokine receptor ACKR2 controls branching morphogenesis in the developing mammary gland. *Development* 144, 74–82. doi: 10.1242/dev.139733

Wosen, J. E., Mukhopadhyay, D., MacAubas, C., and Mellins, E. D. (2018). Epithelial MHC class II expression and its role in antigen presentation in the gastrointestinal and respiratory tracts. *Front. Immunol.* 9:2144. doi: 10.3389/fimmu.2018.02144

Xia, J. X., Mei, X. L., Zhu, W. J., Li, X., Jin, X. H., Mou, Y., et al. (2014). Effect of FGF10 monoclonal antibody on psoriasis-like model in guinea pigs. *Intern. J. Clin. Exper. Pathol.* 7, 2219–2228.

Yang, H., Wang, H., and Andersson, U. (2020). Targeting inflammation driven by HMGB1. *Front. Immunol.* 11:484. doi: 10.3389/fimmu.2020.00484

Yuan, T., Volckaert, T., Chanda, D., Thannickal, V. J., and de Langhe, S. P. (2018). Fgf10 signaling in lung development, homeostasis, disease, and repair after injury. *Front. Genet.* 9:418. doi: 10.3389/fgene.2018.00418

Zacharias, W. J., Frank, D. B., Zepp, J. A., Morley, M. P., Alkhaleel, F. A., Kong, J., et al. (2018). Regeneration of the lung alveolus by an evolutionarily conserved epithelial progenitor. *Nature* 555, 251–255. doi: 10.1038/nature25786

Zeeh, J. M., Procaccino, F., Hoffmann, P., Aukerman, S. L., McRoberts, J. A., Soltani, S., et al. (1996). Keratinocyte growth factor ameliorates mucosal injury in an experimental model of colitis in rats. *Gastroenterology* 110, 1077–1083. doi: 10.1053/gast.1996.v110.pm8612996

Zepp, J. A., and Morrisey, E. E. (2019). Cellular crosstalk in the development and regeneration of the respiratory system. *Nat. Rev. Mol. Cell Biol.* 20, 551–566. doi: 10.1038/s41580-019-0141-3

Zhang, J., Wang, D., Wang, L., Wang, S., Roden, A. C., Zhao, H., et al. (2019). Profibrotic effect of IL-17A and elevated IL-17RA in idiopathic pulmonary fibrosis and rheumatoid arthritis-associated lung disease support a direct role for IL-17A/IL-17RA in human fibrotic interstitial lung disease. *Am. J. Physiol. Lung Cell. Mol. Physiol.* 316, L487–L497. doi: 10.1152/ajplung.00301.2018

Zheng, W., Ma, M., Du, E., Zhang, Z., Jiang, K., Gu, Q., et al. (2015). Therapeutic efficacy of fibroblast growth factor 10 in a rabbit model of dry eye. *Mol. Med. Rep.* 12, 7344–7350. doi: 10.3892/mmr.2015.4368

Conflict of Interest: The authors declare that the research was conducted in the absence of any commercial or financial relationships that could be construed as a potential conflict of interest.

frontiers in Pharmacology

ORIGINAL RESEARCH
published: 03 June 2021
doi: 10.3389/fphar.2021.690535

PPARγ Mediates the Anti-Epithelial-Mesenchymal Transition Effects of FGF1$^{\Delta HBS}$ in Chronic Kidney Diseases via Inhibition of TGF-β1/SMAD3 Signaling

Dezhong Wang[1,2†], Tianyang Zhao[3†], Yushuo Zhao[4†], Yuan Yin[4], Yuli Huang[3], Zizhao Cheng[3], Beibei Wang[3], Sidan Liu[3], Minling Pan[1], Difei Sun[1], Zengshou Wang[4]* and Guanghui Zhu[2,4]**

[1]Institute of Life Sciences and Engineering Laboratory of Zhejiang Province for Pharmaceutical Development of Growth Factors, Wenzhou University, Wenzhou, China, [2]The First Affiliated Hospital of Wenzhou Medical University, Wenzhou, China, [3]School of Pharmaceutical Sciences, Wenzhou Medical University, Wenzhou, China, [4]The Second Affiliated Hospital and Yuying Children's Hospital of Wenzhou Medical University, Wenzhou, China

Podocytes are essential components of the glomerular basement membrane. Epithelial-mesenchymal-transition (EMT) in podocytes results in proteinuria. Fibroblast growth factor 1 (FGF1) protects renal function against diabetic nephropathy (DN). In the present study, we showed that treatment with an FGF1 variant with decreased mitogenic potency (FGF1$^{\Delta HBS}$) inhibited podocyte EMT, depletion, renal fibrosis, and preserved renal function in two nephropathy models. Mechanistic studies revealed that the inhibitory effects of FGF1$^{\Delta HBS}$ podocyte EMT were mediated by decreased expression of transforming growth factor β1 via upregulation of PPARγ. FGF1$^{\Delta HBS}$ enhanced the interaction between PPARγ and SMAD3 and suppressed SMAD3 nuclei translocation. We found that the anti-EMT activities of FGF1$^{\Delta HBS}$ were independent of glucose-lowering effects. These findings expand the potential uses of FGF1$^{\Delta HBS}$ in the treatment of diseases associated with EMT.

Keywords: fibrosis, FGF1, PPARγ, chronic kidney disease, epithelial-mesenchymal transition

OPEN ACCESS

Edited by:
Zhouguang Wang, Albert Einstein College of Medicine, United States

Reviewed by:
Shuhui Liu, Icahn School of Medicine at Mount Sinai, United States
Weiguo Fan, Stanford University Medical Center, United States

***Correspondence:**
Guanghui Zhu
lcylhy@126.com
Zengshou Wang
wzwangzs@126.com
Difei Sun
sundifei0625@163.com

†These authors have contributed equally to this work

Specialty section:
This article was submitted to Integrative and Regenerative Pharmacology, a section of the journal Frontiers in Pharmacology

Received: *03 April 2021*
Accepted: *21 May 2021*
Published: *03 June 2021*

Citation:
Wang D, Zhao T, Zhao Y, Yin Y, Huang Y, Cheng Z, Wang B, Liu S, Pan M, Sun D, Wang Z and Zhu G (2021) PPARγ Mediates the Anti-Epithelial-Mesenchymal Transition Effects of FGF1$^{\Delta HBS}$ in Chronic Kidney Diseases via Inhibition of TGF-β1/SMAD3 Signaling. Front. Pharmacol. 12:690535. doi: 10.3389/fphar.2021.690535

INTRODUCTION

Podocytes are an essential part of the glomerular filtration barrier. Their injury leads to several glomerular diseases that develop to end-stage renal disease (ESRD) (Fishel Bartal et al., 2020). Podocytes are highly specialized epithelial cells; epithelial-mesenchymal-transition (EMT) in podocytes has been observed in chronic kidney disease (CKD) (Liu, 2010; Asfahani et al., 2018; Yin et al., 2018). The expression of nephrin, podocin, and ZO-1 was decreased during podocyte EMT, resulting in the abnormal glomerular basement membrane (GBM) and fibrosis (He et al., 2011; Choi et al., 2020). Owing to its pivotal role in renal function, podocyte homeostatic regulation is a promising strategy for treating CKD.

Studies confirmed that EMT is an essential mechanism of the accumulation and deposition of the extracellular matrix that leads to renal fibrosis (Wynn and Ramalingam, 2012; Kang et al., 2020). Transforming growth factor-β1 (TGF-β1) is the most potent EMT inducer, and enhanced expression of TGF-β1 was noted in renal tissues in the context of CKD (Chen et al., 2021). Biological functions

induced by TGF-β1 depend on accelerating the phosphorylation of Smad3 and nuclei translocation that activates the transcription of target genes (Meng et al., 2016). Bone morphogenetic protein 2 (BMP2) is a sub-member of the TGF-β superfamily. Defective signaling transduction in this pathway is present in hereditary, idiopathic, and other forms of CKD (Orriols et al., 2017). BMP2 antagonizes the TGF-β1/TGF-βR pathway through peroxisome proliferator-activated receptor γ (PPARγ), which participates in cardiovascular homeostasis and glucose metabolism (Tyagi et al., 2011; Chen et al., 2012; Calvier et al., 2017). Several lines of evidence suggested podocyte protection *via* activation of PPARγ (Kanjanabuch et al., 2007; Henique et al., 2016; Zhou et al., 2017). Nevertheless, the side effects of PPARγ agonists such as thiazolidinedione (TZD) limit its use in CKD treatment.

Fibroblast growth factor 1 (FGF1) mediates wound healing, angiogenesis, embryonic development, and neurogenesis (Xie et al., 2020). Recently, FGF1 was found to function as a critical metabolic hormone that is pivotal for regulating insulin sensitivity, glycemic control, and nutrient stress (Beenken and Mohammadi, 2009; Gasser et al., 2017). FGF1 treatment increased insulin sensitization, maintained normoglycemia, and prevented diabetic complications, including hepatic steatosis and podocyte injury (Suh et al., 2014; Gasser et al., 2017; Liang et al., 2018; Lin et al., 2020). Nevertheless, the underlying mechanism of FGF1 or its variant's protective effects on podocyte EMT remains unclear.

FGF1 exerts its biological function *via* heparin sulfate-assisted FGF receptor dimerization and downstream signal transduction. Previously, we obtained an FGF1 variant (FGF1$^{\Delta HBS}$) by replacing 3 residues from heparin sulfate binding site (Lys127Asp, Lys128Gln and Lys133Val) that exhibited full metabolic capacity and much less proliferative potential than wild-type FGF1 (Huang et al., 2017). We employed two murine models of CKD to investigate the protective role and underlying mechanisms preventing podocyte EMT.

MATERIALS AND METHODS

Regents and Antibodies

Doxorubicin (adriamycin) was purchased from Selleck (Cat# S1208). RPMI-1640 medium and penicillin-streptomycin were purchased from Gibco. Fetal bovine serum (FBS) was purchased from ScienCell. Hydroxyproline content assay kit was purchased from Solarbio (Cat# BC0255). Mouse interferon was purchased from Cell Signaling Technology (Cat# 39127). PPARγ siRNA was purchased from Santa Cruz (Cat# sc-29456). Serum levels of blood urea nitrogen (BUN), ALB and creatinine were measured using assay kits according to the manufacturer's instructions (Jiancheng, Nanjing, China). Kits for Sirius red staining, Masson trichrome staining and hematoxylin and eosin (H&E) were purchased from Beyotime Biotech (Nantong, China). BCA kits were used to measure protein concentration (Transgen, Cat# DQ111). The SuperSignal™ West Pico PLUS (Thermo, Cat# 34577) was chosen to visualize the immunoreactive bands.

The following antibodies were used to measure the proteins of interest: COL 1 (Abcam; Cat# ab34710, dilution: 1:800), COL 4 (Proteintech; Cat# 55131-1-AP, dilution: 1:800), α-Smooth Muscle Actin (Abcam; Cat# 19245, dilution: 1:1,000), TGF-β1 (Abcam; Cat# ab215715; dilution: 1:800), phospho-SMAD3 (Cell Signaling; Cat# 9520, dilution: 1:1,000. Abcam, Cat# ab52903, dilution: 1:100), SMAD3 (Proteintech; Cat# 66516-1, dilution: 1:1,000), GAPDH (Cell Signaling; Cat# 5174, dilution: 1:1,000), PPARγ (Santa Cruz; Cat# sc-7273, dilution: 1:1,000), goat anti-rabbit secondary antibody (Abcam; Cat# ab150080, dilution: 1:200), goat anti-mouse secondary antibody (Abcam; Cat# ab6717, dilution: 1:200), HRP-conjugated antibodies (Cell Signaling; Cat# 7074 or 7076, 1:3,000), and biotinylated antibody (Zhongshan Golden Bridge; Cat# ZB-2010, 1:80). Transfection reagent was purchased from Invitrogen (Cat# 13778030). FGF1$^{\Delta HBS}$ was expressed and purified as described (Wang et al., 2019).

Cell Culture

Cell culture and treatment were performed as described (Wang et al., 2019). Briefly, conditionally immortalized mouse podocyte cell line were cultured at 33°C for proliferation. Cell differentiation was induced for 10 days at 37°C, and then starved for 12 h and pretreated with FGF1$^{\Delta HBS}$ (100 ng/ml) for 1 h. Then the cells were incubated in high glucose (HG, 25 mM) (with D-mannitol as an osmotic control) or ADR (0.5 μ g/ml) for 12 h. For PPARγ knockdown experiments, specific siRNA was transfected using transfection reagent Lipofectamine 3000 according to the manufacturer's protocol.

Animals

8 week-old male d*b*/d*b* mice, their d*b*/*m* littermates, and male BALB/c mice were purchased from the GemPharmatech Co., Ltd., (Nanjing China). Animals were maintained in a controlled environment (12 h light/dark cycle at 23°C) with free access to food and water. The experiments were performed following the National Institutes of Health guidelines and with approval from the Animal Care and Use Committee of Wenzhou Medical University, China.

For the DN model, d*b*/d*b* mice were intraperitoneally (i.p.) injected with FGF1$^{\Delta HBS}$ at 0.5 mg/kg body weight every other day for 8 weeks while d*b*/*m* and d*b*/d*b* mice were received 0.9% normal saline as controls. Blood glucose levels were measured using a blood glucose monitor (Roche).

For the adriamycin-induced nephropathy (AN) model, mice were injected with a single dose of ADR (11 mg/kg) through the tail vein. FGF1$^{\Delta HBS}$ (0.5 mg/kg body weight) or normal saline was administered i.p. every other day starting one week before ADR injection and lasting for 5 weeks. Metabolic cages (TSE Systems, MO) were chosen to collect mice urine for 24 h.

Histological Analysis

Renal tissues were fixed and sectioned at 5–6 μm thickness. For immunohistochemistry analysis, sections were incubated with antibody overnight and incubated with the biotinylated antibody for 1 h and stained with DAPI. Stained sections were evaluated for histopathological damage (Nikon, Japan).

For transmission electron microscope analysis, renal samples were fixed using a triple aldehyde fixative overnight at 4°C.

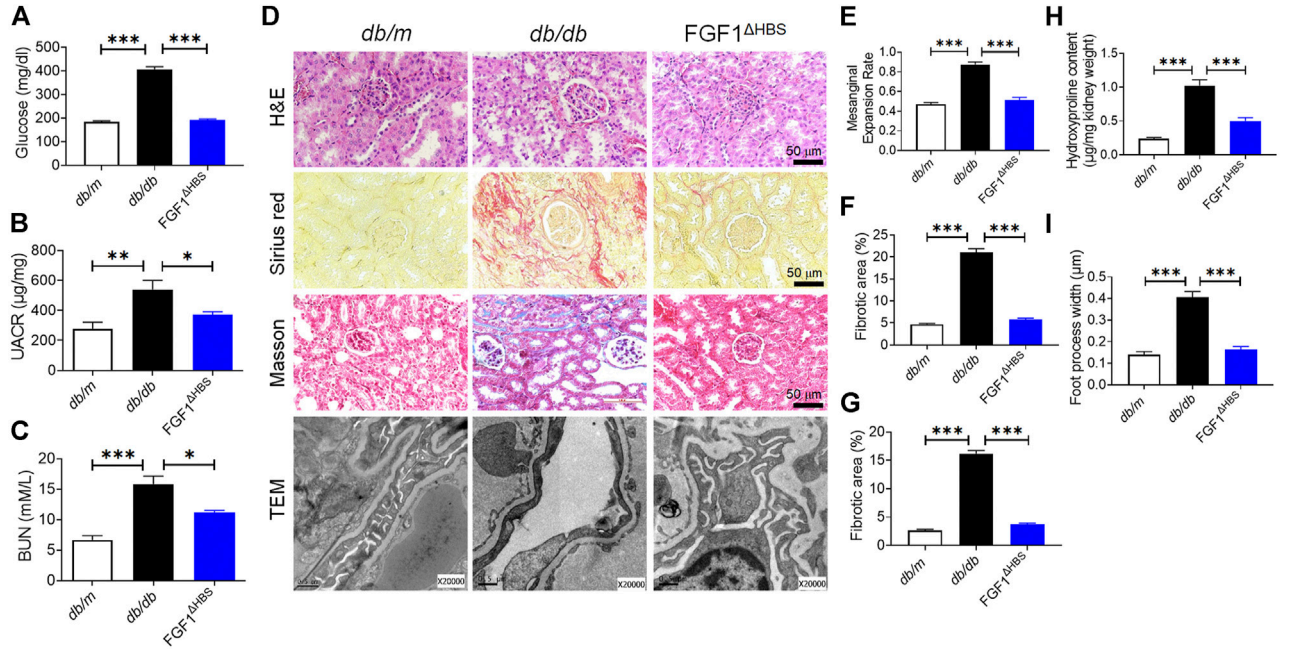

FIGURE 1 | FGF1$^{\Delta HBS}$ prevented renal remodeling and dysfunction in d*b*/d*b* mice. **(A)** Blood glucose levels. **(B)** Urine albumin-to-creatinine ratio (UACR). **(C)** Blood urea nitrogen (BUN) levels. **(D)** Representative images of hematoxylin and eosin (H&E) staining, Sirius red staining, Masson's trichrome staining and transmission electron microscopy (TEM) images of renal tissues. **(E)** Quantification of mesangial expansion. **(F)** Quantification of the fibrotic area in Sirius red staining. **(G)** Quantification of the fibrotic area in Masson staining. **(H)** Hydroxyproline content in renal tissues. **(I)** Quantification of podocyte foot process effacement. Data are presented as the mean ± SEM (n = 6); $^{*}p < 0.05$, $^{**}p < 0.01$, $^{***}p < 0.001$.

Specimens were incubated with uranyl acetate and embedded in epoxy resin after rinsing. Sections were stained and observed under an electron microscope (JEOL, Japan).

For immunofluorescence staining, renal tissues or cells were fixed with 4% paraformaldehyde for15 min, permeabilized with 0.1% Triton X-100 for 10 min, and incubated with anti-PPARγ and anti-SMAD3 antibody overnight at 4°C in a humidified atmosphere in the dark. Following incubation with a secondary antibody, the cells were evaluated using a Nikon confocal microscope (Nikon, Japan).

Real-Time PCR Analysis

MiniBEST Universal RNA Extraction Kit (Takara, Cat# 9767) were used to extract total RNA and RNA was reverse transcribed using PrimeScript™ RT Master Mix (Takara, Cat# RR036A). Real-time PCR was conducted using a QuantStudio3 system with TB Green qPCR Master Mix (Clontech, Cat# 639676). Primers are listed in **Supplementary Table S1.**

Western Blot Analysis

Renal tissues (25–40 mg) or cells were lysed and protein concentrations were determined using the BCA kit (Thermo, Cat# 23225) per the manufacturer's introduction. Equal amounts of samples were subjected to electrophoresis, transferred to nitrocellulose membranes, and blocked. After incubation with antibodies, the blots were incubated using commercial kits to visualize. Densitometric analysis was performed using ImageJ (NIH, United States of America).

Statistical Analysis

All data were expressed as mean ± SEM. *In vitro* experiments were repeated in triplicate (biological repeat) for each experiment. One-way ANOVA followed by the Tukey post hoc test was used to compare more than two groups' mean values. Two-way ANOVA followed by Turkey post hoc test was used to compare the effects of PPARγ knockdown in response to FGF1$^{\Delta HBS}$ treatment. GraphPad Prism was used to analysis the statistical tests. p-values less than 0.05 were considered statistically significant.

RESULTS

FGF1$^{\Delta HBS}$ Prevents Renal Remodeling in *db/db* Mice

To explore the anti-fibrotic effects of FGF1$^{\Delta HBS}$ against diabetes-induced CKD, d*b*/d*b* mice received FGF1$^{\Delta HBS}$ every other day for 8 weeks. As shown in **Figure 1A**, FGF1$^{\Delta HBS}$ decreased blood glucose in d*b*/d*b* mice, consistent with our previous findings (Wang et al., 2021). The increase of urine albumin-to-creatinine ratio (UACR) was ameliorated in FGF1$^{\Delta HBS}$-treated group and serum levels of BUN were lower following FGF1$^{\Delta HBS}$ treatment as well (**Figures 1B,C**).

DN is characterized by mesangial expansion, collagen accumulation, and podocyte loss (Alicic et al., 2021). H&E staining revealed that mesangial expansion was relieved by FGF1$^{\Delta HBS}$ treatment (**Figures 1D,E**), and renal fibrosis was

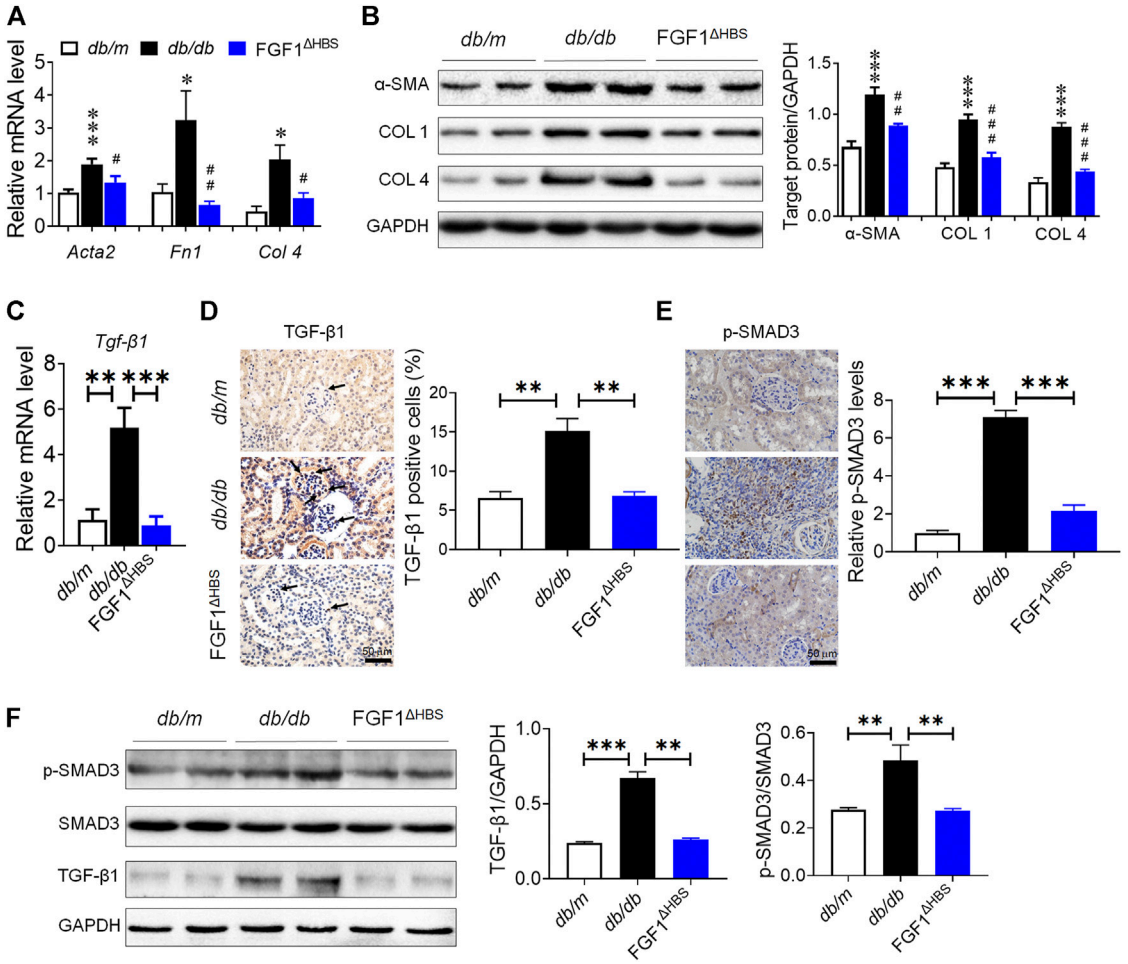

FIGURE 2 | FGF1$^{\Delta HBS}$ suppressed renal fibrosis and TGF-β1 signaling in d*b*/d*b* mice. **(A)** Real-time PCR analysis of *Acta2*, *Fn1*, and *Col 4* mRNA expression. **(B)** Expression levels of α-SMA, COL 1, and COL 4 as determined by western blot analysis and quantitation using ImageJ. **(C)** Real-time PCR analysis of TGF-β1 mRNA expression levels. **(D)** Representative images of TGF-β1 immunohistochemical staining of renal tissues and quantitation using ImageJ. (**E**) Representative images of phosphorylated SMAD3 immunohistochemical staining of renal tissues and quantitation using ImageJ. **(F)** Expression levels of phosphorylated SMAD3, SMAD3, and TGF-β1 as determined by western blot analysis and quantitation using ImageJ. Data are presented as the mean ± SEM (n = 6); Panels A and B, $^{*}p < 0.05$, $^{***}p < 0.001$ vs. d*b*/*m*; $^{\#}p < 0.05$, $^{\#\#}p < 0.01$, $^{\#\#\#}p < 0.001$ vs. d*b*/d*b*; Panels C–F, $^{**}p < 0.01$, $^{***}p < 0.001$.

significantly reduced (**Figures 1D–H**). Podocyte injury is associated with proteinuria, and podocyte loss is the primary starting point of glomerular damage (Koga et al., 2015). Disruption of podocyte foot processes and thickening of basement membranes were found in d*b*/d*b* mice (**Figures 1D–I**). These pathological findings were ameliorated in the FGF1$^{\Delta HBS}$-treated group (**Figures 1D–I**). These data suggest that FGF1$^{\Delta HBS}$ mitigates renal remodeling, fibrosis, and podocyte injury in diabetic mice.

FGF1$^{\Delta HBS}$ Decreases Expression of TGF-β1 and SMAD3 Phosphorylation in Renal Tissues of Diabetic Mice

Given the significantly decreased deposition of extracellular matrix in kidneys by FGF1$^{\Delta HBS}$ treatment, we measured mRNA expression levels of fibrotic genes. As shown in **Figure 2A**, there was diabetes-induced upregulation of *Acta2* (an indicator of fibrosis), *Fn1* (participates in extracellular matrix formation), and *Col 4* (main component of the glomerular basement membrane) in renal tissues. FGF1$^{\Delta HBS}$ inhibited the mRNA levels of these genes (**Figure 2A**). These results were further confirmed by western blot analysis in which protein levels of α-SMA, COL 1, and COL 4 were increased in renal tissues from d*b*/d*b* mice and were remarkably restored by FGF1$^{\Delta HBS}$ treatment (**Figure 2B**).

Since TGF-β1 participates in promoting the deposition of extracellular matrix, podocyte EMT, and apoptosis (Liu, 2004), we used immunohistochemistry to analyze the expression of TGF-β1. We first measured the mRNA expression of TGF-β1. As shown in **Figure 2C**, FGF1$^{\Delta HBS}$ decreased diabetes-induced upregulation of Tgf-β1 in renal tissues. Increased expression of TGF-β1 in the glomeruli was observed in buffer-treated mice, and FGF1$^{\Delta HBS}$ treatment substantially reduced positive cell numbers

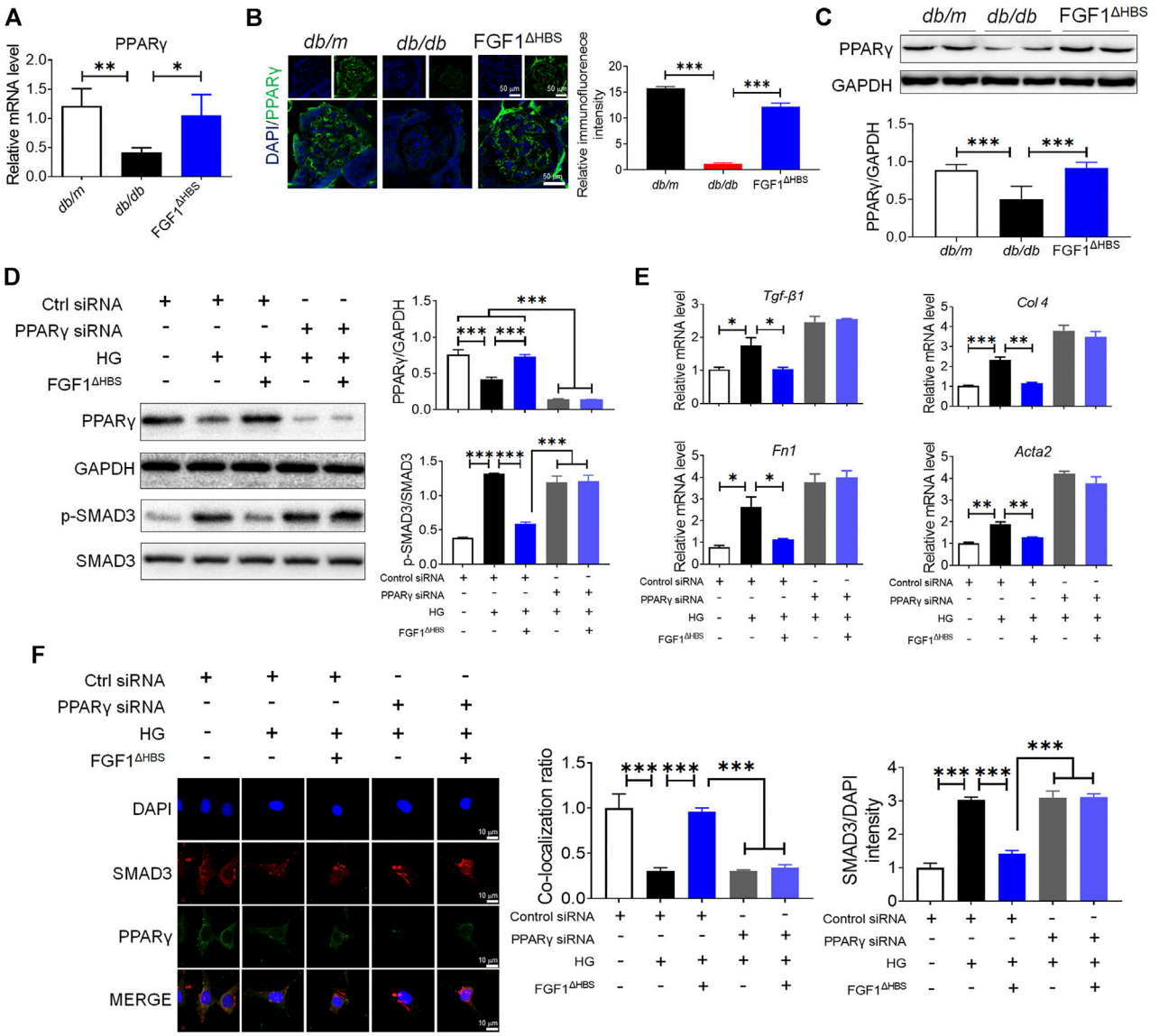

FIGURE 3 | PPARγ mediated the protective effects of FGF1$^{\Delta HBS}$ on podocyte EMT in diabetic conditions. **(A)** Real-time PCR analysis of PPARγ mRNA expression. **(B)** Representative images and quantitation of immunofluorescence staining for PPARγ. **(C)** Expression levels of PPARγ as determined by western blot analysis and quantitation using ImageJ. **(D)** Phosphorylation levels of SMAD3 and protein expression of PPARγ as determined by western blot analysis and quantitation using ImageJ. **(E)** Real-time PCR analysis of *TGF-β1*, *Fn1*, *Col 4*, and *Acta2* mRNA expression. (**F**) Representative images and quantitation of immunofluorescence staining of SMAD3 and PPARγ. In panels **(A–C)**, data are presented as the mean ± SEM (n = 6). In panels **(D–F)**, data from three independent measurements are presented as the mean ± SEM; $^{*}p < 0.05$, $^{**}p < 0.01$, $^{***}p < 0.001$.

(**Figure 2D**). SMAD3 mediated the intracellular signaling of TGF-β1 by shuttling into the nuclei and promoting transcription of target genes for which phosphorylation is essential (Le et al., 2020). We next analyzed the phosphorylation levels of SMAD3 by immunohistochemistry staining (**Figure 2E**) and found that the increased phosphorylation of SMAD3 was strongly suppressed, along with decrease of protein expression of TGF-β1 by FGF1$^{\Delta HBS}$ treatment (**Figures 2E,F**). These data suggest that FGF1$^{\Delta HBS}$ prevents renal fibrosis and podocytes injury *via* downregulation of TGF-β1 and SMAD3 phosphorylation expression.

PPARγ Mediated the Anti-EMT Effects of FGF1$^{\Delta HBS}$ in Diabetes

The crosstalk between TGF-β and BMP signaling pathways tunes the accumulation of extracellular matrix and EMT (Munoz-Felix et al., 2015; Kim et al., 2020). Several lines of evidence suggest that PPARγ participates in maintaining podocyte homeostasis and renal function (Agrawal et al., 2021). We then measured mRNA levels of PPARγ in d*b*/d*b* mice. As shown in **Figure 3A**, diabetes downregulated renal PPARγ expression in d*b*/d*b* mice and FGF1$^{\Delta HBS}$ treatment significantly increased PPARγ

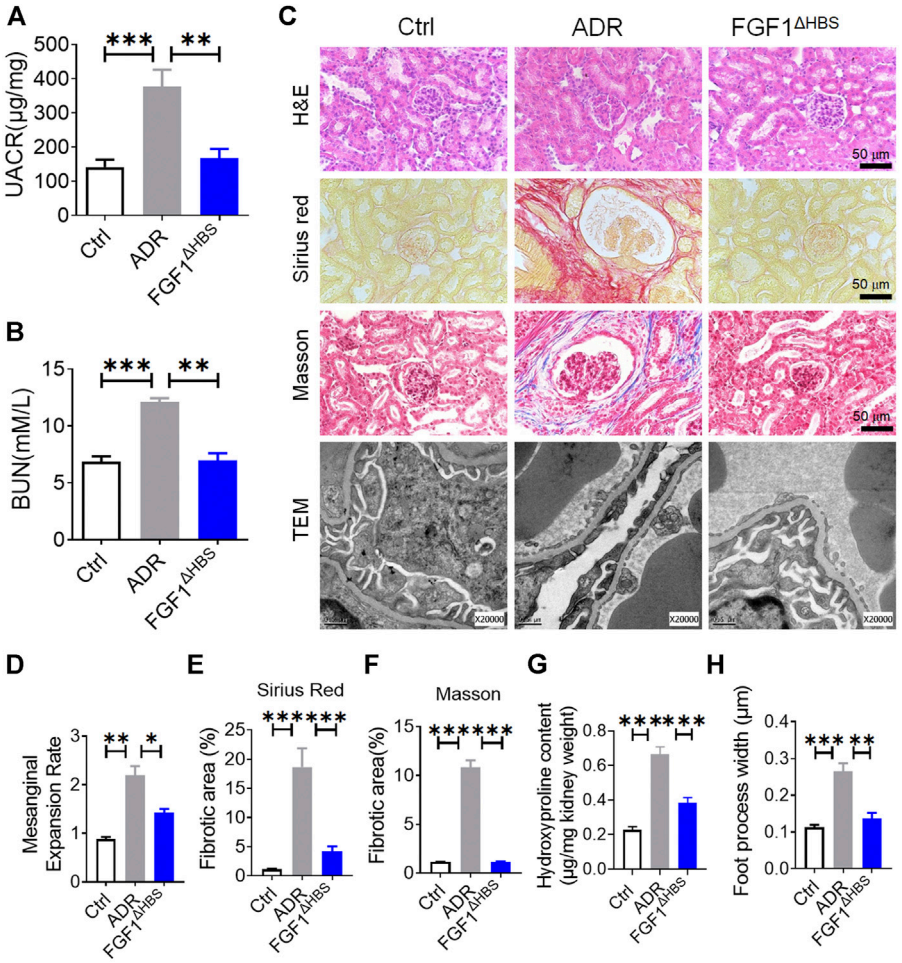

FIGURE 4 | FGF1$^{\Delta HBS}$ inhibited ADR-induced renal remodeling and dysfunction. **(A)** Urine albumin-to-creatinine ratio (UACR). **(B)** Blood urea nitrogen (BUN) levels. **(C)** Representative images of hematoxylin and eosin (H&E) staining, Sirius red staining, Masson's trichrome staining, and transmission electron microscopy (TEM) images of renal tissues. **(D)** Quantification of mesangial expansion. **(E)** Quantification of the fibrotic area in Sirius red staining. **(F)** Quantification of the fibrotic area in Masson staining. **(G)** Hydroxyproline content in renal tissues. **(H)** Quantification of podocyte foot process effacement. Data are presented as the mean ± SEM (n = 6); $^{*}p < 0.05$, $^{**}p < 0.01$, $^{***}p < 0.001$.

transcription. Consistent with these findings, immunofluorescence confirmed reduced expression of PPARγ in glomeruli of d*b*/d*b* mice (**Figure 3B**). FGF1$^{\Delta HBS}$ enhanced fluorescence intensity (**Figure 3B**). The protein expression of PPARγ was also measured using western blot, confirming upregulation by FGF1$^{\Delta HBS}$ treatment (**Figure 3C**).

Podocyte depletion caused by EMT is one of the critical determinants of CKD (Dai et al., 2017). To determine the role of PPARγ in FGF1$^{\Delta HBS}$-preserved podocytes, we used specific PPARγ siRNA to knock down protein expression. We found that HG treatment increased the phosphorylation of SMAD3 and downregulated PPARγ expression (**Figure 3D**). Podocytes treated with FGF1$^{\Delta HBS}$ inhibited SMAD3 phosphorylation in a PPARγ-dependent manner (**Figure 3D**). Real-time PCR showed that the expression of *Tgf-β1*, *Col 4*, *Fn1*, and *Acta2* were attenuated by FGF1$^{\Delta HBS}$ treatment under HG challenge, while these inhibitory effects were abolished in the presence of PPARγ siRNA (**Figure 3E**). The inhibitory effects of FGF1$^{\Delta HBS}$ on nuclei translocation of SMAD3 was PPARγ dependent (**Figure 3F**). Enhanced interaction between SMAD3 and PPARγ was also observed after FGF1$^{\Delta HBS}$ treatment (**Figure 3F**). Taken together, these data suggest that FGF1$^{\Delta HBS}$ protects podocytes from HG-induced EMT and injury, highlighting the importance of PPARγ in the maintenance of podocyte homeostasis and renal function.

FGF1$^{\Delta HBS}$ Inhibited Renal Remodeling in Adriamycin-Induced CKD

To explore whether the inhibitory effect of podocyte EMT by FGF1$^{\Delta HBS}$ applied to other types of CKD, we used an ADR-induced nephropathy model to investigate the anti-EMT effects of FGF1$^{\Delta HBS}$. Consistent with our previous findings (Wang et al., 2019), renal function was restored by FGF1$^{\Delta HBS}$ treatment, as evidenced by decreased UACR and BUN levels

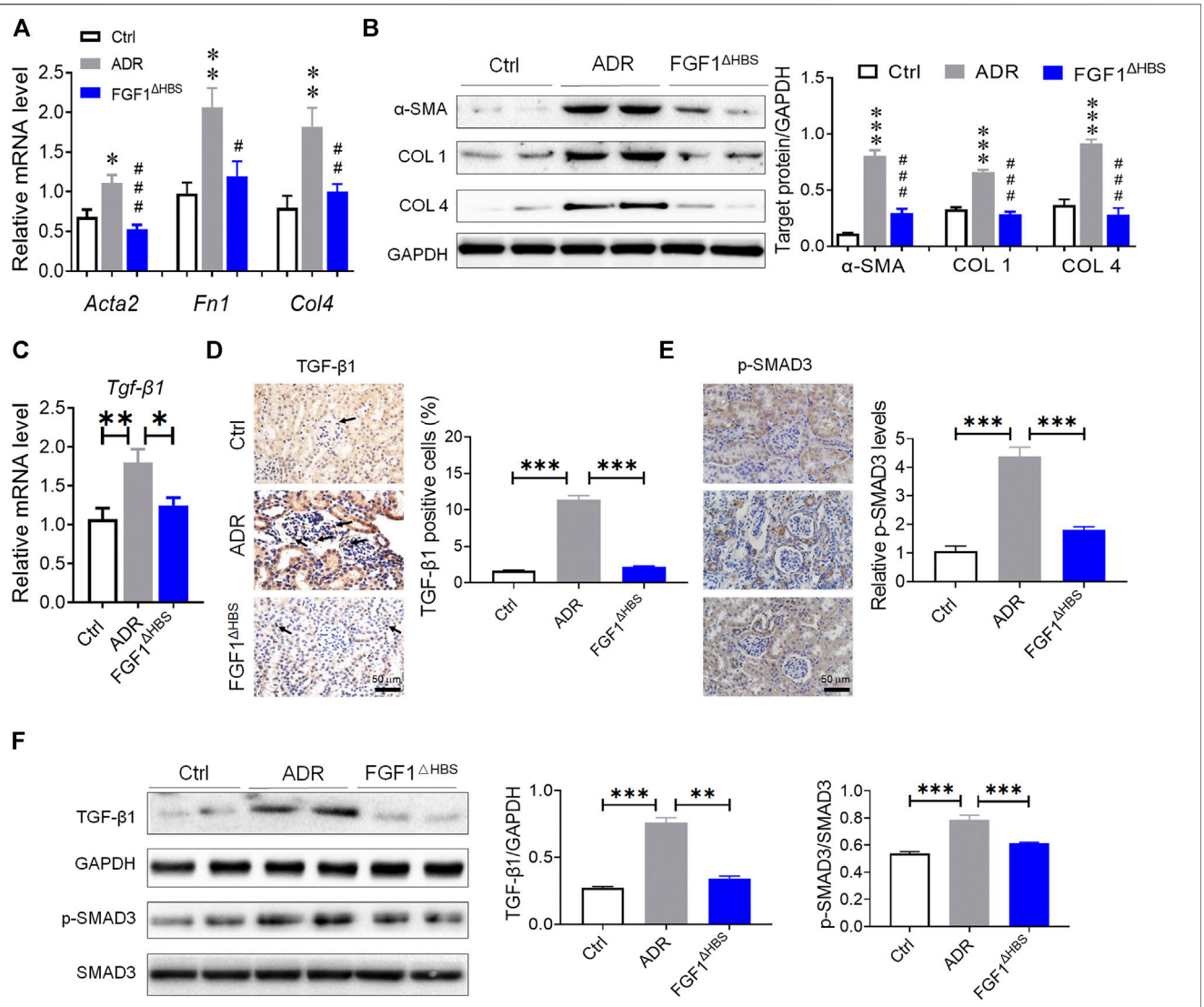

FIGURE 5 | FGF1$^{\Delta HBS}$ inhibited ADR-induced the upregulation of TGF-β1 and phosphorylation of SMAD3. **(A)** Real-time PCR analysis of *Acta2*, *Fn1*, and *Col 4* mRNA expression. **(B)** Expression levels of α-SMA, COL 1, and COL 4 as determined by western blot analysis and quantitation using ImageJ. **(C)** Real-time PCR analysis of TGF-β1 mRNA expression levels. **(D)** Representative images of TGF-β1 immunohistochemical staining of renal tissues and quantitation using ImageJ. **(E)** Representative images of phosphorylated SMAD3 immunohistochemical staining of renal tissues and quantitation using ImageJ. (**F**) Expression levels of phosphorylated SMAD3, SMAD3, and TGF-β1 as determined by western blot analysis and quantitation using ImageJ. Data are presented as the mean ± SEM (n = 6); Panels **(A,B)**, $^{*}p < 0.05$, $^{**}p < 0.01$, $^{***}p < 0.001$ vs. *db/m*; $^{\#}p < 0.05$, $^{\#\#}p < 0.01$, $^{\#\#\#}p < 0.001$ vs. *db/db*; Panels **(C–F)**, $^{*}p < 0.05$, $^{**}p < 0.01$, $^{***}p < 0.001$.

(**Figures 4A,B**). ADR-induced mesangial expansion was inhibited in the FGF1$^{\Delta HBS}$-treated group (**Figures 4C,D**). In addition, tissue remodeling was significantly prevented as renal fibrosis and collagen deposition was attenuated, and foot process loss was alleviated (**Figures 4C,E–H**).

FGF1$^{\Delta HBS}$ Inhibited ADR-Induced the Upregulation of TGF-β1 and Phosphorylation of SMAD3

Consistent with the increase of mRNA levels of EMT markers in DN, we found significantly upregulated gene transcription of *Acta2*, *Fn1*, and *Col 4* by ADR treatment while FGF1$^{\Delta HBS}$ treatment restored them to normal levels (**Figure 5A**). Furthermore, there were significant reductions in protein expression of α-SMA, COL 1, and COL 4 associated with FGF1$^{\Delta HBS}$ treatment (**Figure 5B**). Consistent with reduced mRNA expression, FGF1$^{\Delta HBS}$ also reduced TGF-β1-positive cells in renal tissues of ADR-treated mice (**Figures 5C,D**). And the phosphorylation levels of SMAD3 were attenuated by FGF1$^{\Delta HBS}$ treatment (**Figure 5E**). Immune blotting analysis showed that ADR treatment increased TGF-β1 expression and SMAD3 phosphorylation that was significantly restored with FGF1$^{\Delta HBS}$ treatment (**Figure 5F**). These results suggest that FGF1$^{\Delta HBS}$ suppresses TGF-β1-mediated renal fibrosis and EMT.

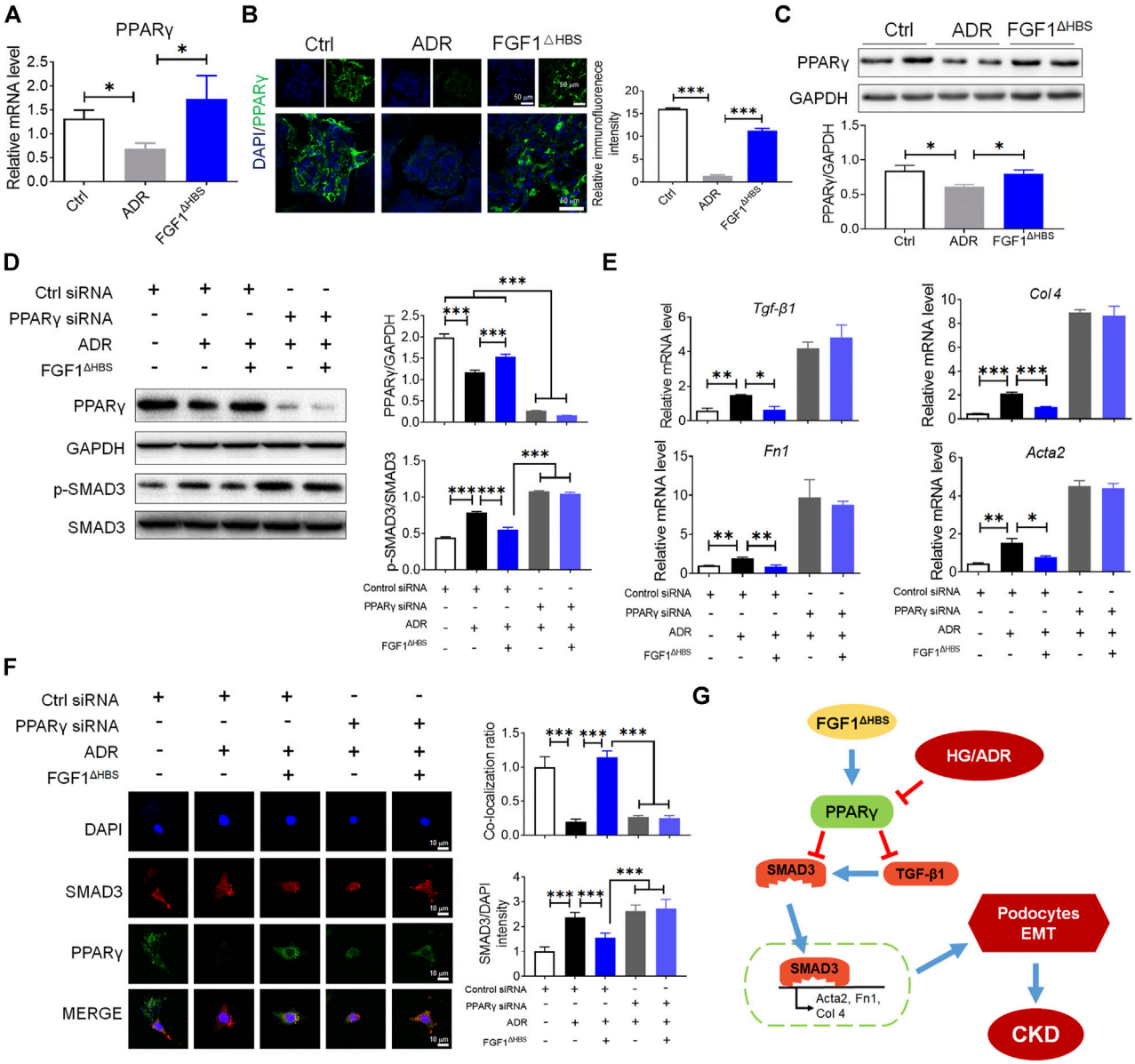

FIGURE 6 | FGF1$^{\Delta HBS}$ suppressed podocytes EMT via upregulation of PPARγ under ADR challenge. **(A)** Real-time PCR analysis of PPARγ mRNA expression. **(B)** Representative images and quantitation of immunofluorescence staining for PPARγ. **(C)** Expression levels of PPARγ as determined by western blot analysis and quantitation using ImageJ. **(D)** Phosphorylation levels of SMAD3 and protein expressions of PPARγ as determined by western blot analysis and quantitation using ImageJ. **(E)** Real-time PCR analysis of *TGF-β1*, *Fn1*, *Col 4*, and *Acta2* mRNA expression. **(F)** Representative images and quantitation of immunofluorescence staining of SMAD3 and PPARγ. **(G)** A mechanistic illustration of FGF1$^{\Delta HBS}$ protection from diabetes or chemical induced podocyte EMT and CKD. In panels **(A–C)**, Data are presented as the mean ± SEM (n = 6). In panels **(D–F)**, data from three independent measurements are presented as the mean ± SEM; $^{*}p < 0.05$, $^{**}p < 0.01$, $^{***}p < 0.001$.

FGF1$^{\Delta HBS}$ Suppressed Podocyte EMT Via Upregulation of PPARγ Under ADR Challenge

To determine whether PPARγ mediated the protective effects of FGF1$^{\Delta HBS}$ in AN, we investigated the expression of PPARγ using various methods. The mRNA and protein levels of PPARγ were decreased by ADR treatment (**Figures 6A–C**). FGF1$^{\Delta HBS}$ treatment significantly enhanced the transcription and protein levels of PPARγ (**Figures 6A–C**). Mouse podocytes were used to analyze the *in vitro* protective effects of FGF1$^{\Delta HBS}$. As shown in **Figure 6D**, we found that FGF1$^{\Delta HBS}$ upregulated PPARγ expression and suppressed SMAD3 phosphorylation under ADR challenge. The suppression effect was abolished when cells were treated with PPARγ siRNA. ADR increased the expression of pro-EMT genes (*Tgf-β1*, *Fn1*, *Col 4*, and *Acta2*), and FGF1$^{\Delta HBS}$ attenuated this induction in a

PPARγ-dependent manner (**Figure 6E**). Consistent with the results of HG treatment, SMAD3 nuclei translocation was decreased, and enhanced interactions between PPARγ and SMAD3 were observed following FGF1$^{\Delta HBS}$ treatment (**Figure 6F**). These results suggest that the protective effects of FGF1$^{\Delta HBS}$ against podocyte EMT were independent of glucose control.

DISCUSSION

The characteristics of CKD where GBM composition is impaired are associated with progressive renal dysfunction, highlighting the importance of podocyte integrity in maintaining normal filtration (Kriz and Lemley, 2015). Activation of TGF-β1/SMAD3 signaling accelerates the overproduction of ECM, promotes podocyte EMT, and participates in the pathogenesis of CKD (Meng et al., 2016). Previously, we reported the protective effects of FGF1 against DN via anti-inflammatory signal transduction (Liang et al., 2018). The present study elucidated a novel mechanism by which FGF1$^{\Delta HBS}$ protects podocytes from diabetes- or drug-induced EMT and renal fibrosis. We found that FGF1$^{\Delta HBS}$ suppressed TGF-β1 expression and SMAD3 nuclei translocation via activation of PPARγ (**Figure 6G**).

Inhibition of the TGF-β1/SMAD3 signaling pathway ameliorates non-alcoholic steatohepatitis, tubulointerstitial fibrosis, and myocardium infraction (Chen et al., 2019; He et al., 2020; Okina et al., 2020). Increased EMT of podocytes induced by diabetes and ADR is closely related to end-stage renal disease and glomerular fibrosis. Several lines of evidence demonstrated that TGF-β1/SMAD3 signaling contributes to EMT in podocytes (Kang et al., 2010; Yin et al., 2018). Renal injuries, including mesangial expansion, matrix accumulation, proteinuria, and GBM thickening, were alleviated in SMAD3-null mice treated by streptozotocin (Lin et al., 2009; Yadav et al., 2011). Proteinuria and kidney dysfunction were found in TGF-β1-overexpressing mice (Kopp et al., 1996; Schiffer et al., 2001). In the present study, we found that the upregulation of TGF-β1 induced by diabetic conditions or ADR was inhibited by FGF1$^{\Delta HBS}$ treatment. *In vitro* studies showed that FGF1$^{\Delta HBS}$ suppressed the expression of EMT markers (*Fn1*, *Atca2*, and *Col 1*). Taken together, these data suggest that the protective effects of FGF1$^{\Delta HBS}$ on podocyte EMT are mediated by inhibition of TGF-β1.

PPARγ participates in adipogenesis and exerts diverse effects in other tissues, including liver, skeletal muscle, brain, bone, blood vessels, and kidney (Kawai and Rosen, 2010; Brun et al., 2017). As a transcription factor, PPARγ regulates expression of such genes as *Il-1β*, *Tnf-α*, *Tgf-β*, *Ho-1*, and *Bcl-2* in transactivation- or transrepression-manners (Schmidt et al., 2010; Quelle and Sigmund, 2013; Gross et al., 2017). In addition to transcriptional activity, PPARγ binds to other proteins and regulates their function. Yang et al. (2020) found that decreased interaction between PPARγ and Nur77 resulted in enhanced stability of Nur77 and inhibited metabolic reprogramming in breast cancer. Interactions between PPARγ and NLRP3, β-arrestin-1, and UBR5 regulated inflammatory responses of macrophages, adipogenesis, and endothelial homeostasis (Zhuang et al., 2011; Li et al., 2019; Yang et al., 2021). We found enhanced interactions between PPARγ and SMAD3 and suppressed EMT in podocytes following FGF1$^{\Delta HBS}$ treatment. These findings are consistent with a previous report in which a PPARγ agonist reversed pulmonary arterial hypertension (PAH) via inhibition of SMAD3 nuclei translocation in TGF-β1 transgenic mice (Calvier et al., 2017).

FGF1 is a promising agent for the treatment of type 2 diabetes by improving insulin sensitivity. FGF1-null mice displayed an aggressive diabetic phenotype upon a high-fat diet challenge (Jonker et al., 2012; Suh et al., 2014). The glucose-lowering effects of FGF1 or its variants have been reported (Suh et al., 2014; Huang et al., 2017). A high-glucose environment has been suggested to be involved in podocyte EMT. In the current study, we showed that the inhibitory effects of FGF1$^{\Delta HBS}$ on podocyte EMT and renal protection were independent of its glucose-lowering activity. Expression of EMT markers was significantly reduced by FGF1$^{\Delta HBS}$ treatment *in vivo* and *in vitro*.

CONCLUSION

We found inhibitory effects of FGF1$^{\Delta HBS}$ on podocyte EMT. The protective mechanism conferred by FGF1$^{\Delta HBS}$ is mediated by downregulation of TGF-β1 expression and reduced nuclei translocation of SMAD3 via restoration and enhancement of PPARγ expression. We conclude that this is a novel signaling mechanism by which FGF1$^{\Delta HBS}$ maintains podocyte homeostasis, resulting in protection against decreased glomerular filtration and proteinuria. The findings suggest that FGF1$^{\Delta HBS}$ is a promising therapeutic strategy for the prevention of podocyte EMT in CKD.

DATA AVAILABILITY STATEMENT

The original contributions presented in the study are included in the article/**Supplementary Material**, further inquiries can be directed to the corresponding authors.

ETHICS STATEMENT

The animal study was reviewed and approved by the Animal Care and Use Committee of Wenzhou Medical University, China.

AUTHOR CONTRIBUTIONS

DW, GZ, and ZW contributed to the initial design and discussion of the project. DW, TZ, YZ, YY, YH, ZC, BW, SL, and MP researched the data. DS, GZ, and ZW wrote the manuscript. All Authors discussed the results and commented on the manuscript.

FUNDING

This work was supported by grants from the Zhejiang Provincial Natural Science Foundation of China (LGF19H300004 to DW,

LWY20H070001 to GZ), the Natural Science Foundation of China (81903532 to DW), the Science and Technology Project of Wenzhou (Y20180155 to GZ) and the College Students' innovation of Science and Technology activities plan of Zhejiang Province (2020R413081 to YH).

SUPPLEMENTARY MATERIAL

The Supplementary Material for this article can be found online at: https://www.frontiersin.org/articles/10.3389/fphar.2021.690535/full#supplementary-material

REFERENCES

Agrawal, S., He, J. C., and Tharaux, P.-L. (2021). Nuclear Receptors in Podocyte Biology and Glomerular Disease. *Nat. Rev. Nephrol.* 17, 185–204. doi:10.1038/s41581-020-00339-6

Alicic, R. Z., Cox, E. J., Neumiller, J. J., and Tuttle, K. R. (2021). Incretin Drugs in Diabetic Kidney Disease: Biological Mechanisms and Clinical Evidence. *Nat. Rev. Nephrol.* 17, 227–244. doi:10.1038/s41581-020-00367-2

Asfahani, R. I., Tahoun, M. M., Miller-Hodges, E. V., Bellerby, J., Virasami, A. K., Sampson, R. D., et al. (2018). Activation of Podocyte Notch Mediates Early Wt1 Glomerulopathy. *Kidney Int.* 93, 903–920. doi:10.1016/j.kint.2017.11.014

Beenken, A., and Mohammadi, M. (2009). The FGF Family: Biology, Pathophysiology and Therapy. *Nat. Rev. Drug Discov.* 8, 235–253. doi:10.1038/nrd2792

Brun, J., Berthou, F., Trajkovski, M., Maechler, P., Foti, M., and Bonnet, N. (2017). Bone Regulates Browning and Energy Metabolism through Mature Osteoblast/Osteocyte PPARγ Expression. *Diabetes* 66, 2541–2554. doi:10.2337/db17-0116

Calvier, L., Chouvarine, P., Legchenko, E., Hoffmann, N., Geldner, J., Borchert, P., et al. (2017). PPARγ Links BMP2 and TGFβ1 Pathways in Vascular Smooth Muscle Cells, Regulating Cell Proliferation and Glucose Metabolism. *Cel Metab.* 25, 1118–1134.e7. doi:10.1016/j.cmet.2017.03.011

Chen, G., Deng, C., and Li, Y.-P. (2012). TGF-β and BMP Signaling in Osteoblast Differentiation and Bone Formation. *Int. J. Biol. Sci.* 8, 272–288. doi:10.7150/ijbs.2929

Chen, B., Huang, S., Su, Y., Wu, Y.-J., Hanna, A., Brickshawana, A., et al. (2019). Macrophage Smad3 Protects the Infarcted Heart, Stimulating Phagocytosis and Regulating Inflammation. *Circ. Res.* 125, 55–70. doi:10.1161/circresaha.119.315069

Chen, Y. T., Jhao, P. Y., Hung, C. T., Wu, Y. F., Lin, S. J., Chiang, W. C., et al. (2021). Endoplasmic Reticulum Protein TXNDC5 Promotes Renal Fibrosis by Enforcing TGF-Beta Signaling in Kidney Fibroblasts. *J. Clin. Invest.* 131, e143645. doi:10.1172/jci143645

Choi, D., Kim, C.-L., Kim, J. E., Mo, J.-S., and Jeong, H.-S. (2020). Hesperetin Inhibit EMT in TGF-β Treated Podocyte by Regulation of mTOR Pathway. *Biochem. Biophys. Res. Commun.* 528, 154–159. doi:10.1016/j.bbrc.2020.05.087

Dai, H., Liu, Q., and Liu, B. (2017). Research Progress on Mechanism of Podocyte Depletion in Diabetic Nephropathy. *J. Diabetes Res.* 2017, 2615286. doi:10.1155/2017/2615286

Fishel Bartal, M., Lindheimer, M. D., and Sibai, B. M. (2020). Proteinuria during Pregnancy: Definition, Pathophysiology, Methodology, and Clinical Significance. *Am. J. Obstet. Gynecol.* S0002-9378 (20), 30989–3. doi:10.1016/j.ajog.2020.08.108

Gasser, E., Moutos, C. P., Downes, M., and Evans, R. M. (2017). FGF1 - a New Weapon to Control Type 2 Diabetes Mellitus. *Nat. Rev. Endocrinol.* 13, 599–609. doi:10.1038/nrendo.2017.78

Gross, B., Pawlak, M., Lefebvre, P., and Staels, B. (2017). PPARs in Obesity-Induced T2DM, Dyslipidaemia and NAFLD. *Nat. Rev. Endocrinol.* 13, 36–49. doi:10.1038/nrendo.2016.135

He, W., Kang, Y. S., Dai, C., and Liu, Y. (2011). Blockade of Wnt/β-Catenin Signaling by Paricalcitol Ameliorates Proteinuria and Kidney Injury. *Jasn* 22, 90–103. doi:10.1681/asn.2009121236

He, X., Cheng, R., Huang, C., Takahashi, Y., Yang, Y., Benyajati, S., et al. (2020). A Novel Role of LRP5 in Tubulointerstitial Fibrosis through Activating TGF-beta/Smad Signaling. *Signal. Transduct Target. Ther.* 5, 45. doi:10.1038/s41392-020-0142-x

Henique, C., Bollee, G., Lenoir, O., Dhaun, N., Camus, M., Chipont, A., et al. (2016). Nuclear Factor Erythroid 2-Related Factor 2 Drives Podocyte-specific Expression of Peroxisome Proliferator-Activated Receptor γ Essential for Resistance to Crescentic GN. *Jasn* 27, 172–188. doi:10.1681/asn.2014111080

Huang, Z., Tan, Y., Gu, J., Liu, Y., Song, L., Niu, J., et al. (2017). Uncoupling the Mitogenic and Metabolic Functions of FGF1 by Tuning FGF1-FGF Receptor Dimer Stability. *Cel Rep.* 20, 1717–1728. doi:10.1016/j.celrep.2017.06.063

Jonker, J. W., Suh, J. M., Atkins, A. R., Ahmadian, M., Li, P., Whyte, J., et al. (2012). A PPARγ-FGF1 axis Is Required for Adaptive Adipose Remodelling and Metabolic Homeostasis. *Nature* 485, 391–394. doi:10.1038/nature10998

Kang, Y. S., Li, Y., Dai, C., Kiss, L. P., Wu, C., and Liu, Y. (2010). Inhibition of Integrin-Linked Kinase Blocks Podocyte Epithelial-Mesenchymal Transition and Ameliorates Proteinuria. *Kidney Int.* 78, 363–373. doi:10.1038/ki.2010.137

Kang, M. K., Kim, S. I., Oh, S. Y., Na, W., and Kang, Y. H. (2020). Tangeretin Ameliorates Glucose-Induced Podocyte Injury through Blocking Epithelial to Mesenchymal Transition Caused by Oxidative Stress and Hypoxia. *Int. J. Mol. Sci.* 21, 8577. doi:10.3390/ijms21228577

Kanjanabuch, T., Ma, L.-J., Chen, J., Pozzi, A., Guan, Y., Mundel, P., et al. (2007). PPAR-γ Agonist Protects Podocytes from Injury. *Kidney Int.* 71, 1232–1239. doi:10.1038/sj.ki.5002248

Kawai, M., and Rosen, C. J. (2010). PPARγ: a Circadian Transcription Factor in Adipogenesis and Osteogenesis. *Nat. Rev. Endocrinol.* 6, 629–636. doi:10.1038/nrendo.2010.155

Kim, S., Shin, D. H., Nam, B. Y., Kang, H. Y., Park, J., Wu, M., et al. (2020). Newly Designed Protein Transduction Domain (PTD)-mediated BMP-7 Is a Potential Therapeutic for Peritoneal Fibrosis. *J. Cel. Mol. Med.* 24, 13507–13522. doi:10.1111/jcmm.15992

Koga, K., Yokoi, H., Mori, K., Kasahara, M., Kuwabara, T., Imamaki, H., et al. (2015). MicroRNA-26a Inhibits TGF-β-Induced Extracellular Matrix Protein Expression in Podocytes by Targeting CTGF and Is Downregulated in Diabetic Nephropathy. *Diabetologia* 58, 2169–2180. doi:10.1007/s00125-015-3642-4

Kopp, J. B., Factor, V. M., Mozes, M., Nagy, P., Sanderson, N., Böttinger, E. P., et al. (1996). Transgenic Mice with Increased Plasma Levels of TGF-Beta 1 Develop Progressive Renal Disease. *Lab. Invest.* 74, 991–1003.

Kriz, W., and Lemley, K. V. (2015). A Potential Role for Mechanical Forces in the Detachment of Podocytes and the Progression of CKD. *Jasn* 26, 258–269. doi:10.1681/asn.2014030278

Le, B. V., Podszywalow-Bartnicka, P., Maifrede, S., Sullivan-Reed, K., Nieborowska-Skorska, M., Golovine, K., et al. (2020). TGFβR-SMAD3 Signaling Induces Resistance to PARP Inhibitors in the Bone Marrow Microenvironment. *Cel Rep.* 33, 108221. doi:10.1016/j.celrep.2020.108221

Li, C. G., Mahon, C., Sweeney, N. M., Verschueren, E., Kantamani, V., Li, D., et al. (2019). PPARγ Interaction with UBR5/ATMIN Promotes DNA Repair to Maintain Endothelial Homeostasis. *Cel Rep.* 26, 1333–1343.e7. doi:10.1016/j.celrep.2019.01.013

Liang, G., Song, L., Chen, Z., Qian, Y., Xie, J., Zhao, L., et al. (2018). Fibroblast Growth Factor 1 Ameliorates Diabetic Nephropathy by an Anti-inflammatory Mechanism. *Kidney Int.* 93, 95–109. doi:10.1016/j.kint.2017.05.013

Lin, H.-M., Lee, J.-H., Yadav, H., Kamaraju, A. K., Liu, E., Zhigang, D., et al. (2009). Transforming Growth Factor-β/Smad3 Signaling Regulates Insulin Gene Transcription and Pancreatic Islet β-Cell Function. *J. Biol. Chem.* 284, 12246–12257. doi:10.1074/jbc.m805379200

Lin, Q., Huang, Z., Cai, G., Fan, X., Yan, X., Liu, Z., et al. (2020). Activating AMP-Activated Protein Kinase Mediates Fibroblast Growth Factor 1 Protection from Nonalcoholic Fatty Liver Disease in Mice. *Hepatology* 2020, 31568. doi:10.1002/hep.31568

Liu, Y. (2004). Epithelial to Mesenchymal Transition in Renal Fibrogenesis: Pathologic Significance, Molecular Mechanism, and Therapeutic Intervention. *J. Am. Soc. Nephrol.* 15, 1–12. doi:10.1097/01.asn.0000106015.29070.e7

Liu, Y. (2010). New Insights into Epithelial-Mesenchymal Transition in Kidney Fibrosis. *Jasn* 21, 212–222. doi:10.1681/asn.2008121226

Meng, X.-m., Nikolic-Paterson, D. J., and Lan, H. Y. (2016). TGF-β: the Master Regulator of Fibrosis. *Nat. Rev. Nephrol.* 12, 325–338. doi:10.1038/nrneph.2016.48

Muñoz-Félix, J. M., González-Núñez, M., Martínez-Salgado, C., and López-Novoa, J. M. (2015). TGF-β/BMP Proteins as Therapeutic Targets in Renal Fibrosis. Where Have We Arrived after 25years of Trials and Tribulations? *Pharmacol. Ther.* 156, 44–58. doi:10.1016/j.pharmthera.2015.10.003

Okina, Y., Sato-Matsubara, M., Matsubara, T., Daikoku, A., Longato, L., Rombouts, K., et al. (2020). TGF-β1-driven Reduction of Cytoglobin Leads to Oxidative DNA Damage in Stellate Cells during Non-alcoholic Steatohepatitis. *J. Hepatol.* 73, 882–895. doi:10.1016/j.jhep.2020.03.051

Orriols, M., Gomez-Puerto, M. C., and Ten Dijke, P. (2017). BMP Type II Receptor as a Therapeutic Target in Pulmonary Arterial Hypertension. *Cell. Mol. Life Sci.* 74, 2979–2995. doi:10.1007/s00018-017-2510-4

Quelle, F. W., and Sigmund, C. D. (2013). PPARγ: no SirT, no Service. *Circ. Res.* 112, 411–414. doi:10.1161/circresaha.113.300870

Schiffer, M., Bitzer, M., Roberts, I. S. D., Kopp, J. B., ten Dijke, P., Mundel, P., et al. (2001). Apoptosis in Podocytes Induced by TGF-β and Smad7. *J. Clin. Invest.* 108, 807–816. doi:10.1172/jci200112367

Schmidt, M. V., Brüne, B., and von Knethen, A. (2010). The Nuclear Hormone Receptor PPARγas a Therapeutic Target in Major Diseases. *The Sci. World J.* 10, 2181–2197. doi:10.1100/tsw.2010.213

Suh, J. M., Jonker, J. W., Ahmadian, M., Goetz, R., Lackey, D., Osborn, O., et al. (2014). Endocrinization of FGF1 Produces a Neomorphic and Potent Insulin Sensitizer. *Nature* 513, 436–439. doi:10.1038/nature13540

Tyagi, S., Sharma, S., Gupta, P., Saini, A., and Kaushal, C. (2011). The Peroxisome Proliferator-Activated Receptor: A Family of Nuclear Receptors Role in Various Diseases. *J. Adv. Pharm. Tech. Res.* 2, 236–240. doi:10.4103/2231-4040.90879

Wang, D., Jin, M., Zhao, X., Zhao, T., Lin, W., He, Z., et al. (2019). FGF1(DeltaHBS) Ameliorates Chronic Kidney Disease via PI3K/AKT Mediated Suppression of Oxidative Stress and Inflammation. *Cell Death Dis* 10, 464. doi:10.1038/s41419-019-1696-9

Wang, D., Yin, Y., Wang, S., Zhao, T., Gong, F., Zhao, Y., et al. (2021). FGF1(DeltaHBS) Prevents Diabetic Cardiomyopathy by Maintaining Mitochondrial Homeostasis and Reducing Oxidative Stress via AMPK/Nur77 Suppression. *Signal. Transduct Target. Ther.* 6, 133. doi:10.1038/s41392-021-00542-2

Wynn, T. A., and Ramalingam, T. R. (2012). Mechanisms of Fibrosis: Therapeutic Translation for Fibrotic Disease. *Nat. Med.* 18, 1028–1040. doi:10.1038/nm.2807

Xie, Y., Su, N., Yang, J., Tan, Q., Huang, S., Jin, M., et al. (2020). FGF/FGFR Signaling in Health and Disease. *Signal. Transduct Target. Ther.* 5, 181. doi:10.1038/s41392-020-00222-7

Yadav, H., Quijano, C., Kamaraju, A. K., Gavrilova, O., Malek, R., Chen, W., et al. (2011). Protection from Obesity and Diabetes by Blockade of TGF-β/Smad3 Signaling. *Cel Metab.* 14, 67–79. doi:10.1016/j.cmet.2011.04.013

Yang, C.-C., Wu, C.-H., Lin, T.-C., Cheng, Y.-N., Chang, C.-S., Lee, K.-T., et al. (2021). Inhibitory Effect of PPARγ on NLRP3 Inflammasome Activation. *Theranostics* 11, 2424–2441. doi:10.7150/thno.46873

Yang, P. B., Hou, P. P., Liu, F. Y., Hong, W. B., Chen, H. J., Sun, X. Y., et al. (2020). Blocking PPARgamma interaction facilitates Nur77 interdiction of fatty acid uptake and suppresses breast cancer progression. *Proc. Natl. Acad. Sci. U S A* 117, 27412–27422.

Yin, J., Wang, Y., Chang, J., Li, B., Zhang, J., Liu, Y., et al. (2018). Apelin Inhibited Epithelial-Mesenchymal Transition of Podocytes in Diabetic Mice through Downregulating Immunoproteasome Subunits Beta5i. *Cel Death Dis* 9, 1031. doi:10.1038/s41419-018-1098-4

Zhou, Z., Wan, J., Hou, X., Geng, J., Li, X., and Bai, X. (2017). MicroRNA-27a Promotes Podocyte Injury via PPARγ-Mediated β-catenin Activation in Diabetic Nephropathy. *Cel Death Dis* 8, e2658. doi:10.1038/cddis.2017.74

Zhuang, L.-n., Hu, W.-x., Xin, S.-m., Zhao, J., and Pei, G. (2011). β-Arrestin-1 Protein Represses Adipogenesis and Inflammatory Responses through its Interaction with Peroxisome Proliferator-Activated Receptor-γ (PPARγ). *J. Biol. Chem.* 286, 28403–28413. doi:10.1074/jbc.m111.256099

Conflict of Interest: The authors declare that the research was conducted in the absence of any commercial or financial relationships that could be construed as a potential conflict of interest.

frontiers in Pharmacology

ORIGINAL RESEARCH
published: 07 June 2021
doi: 10.3389/fphar.2021.655281

Keratinocyte Growth Factor 2 Ameliorates UVB-Induced Skin Damage *via* Activating the AhR/Nrf2 Signaling Pathway

Shuang Gao[1†], Keke Guo[2†], Yu Chen[2†], Jungang Zhao[2], Rongrong Jing[2], Lusheng Wang[2], Xuenan Li[2], Zhenlin Hu[2], Nuo Xu[2] and Xiaokun Li[1*]*

[1]School of Pharmaceutical Sciences, Wenzhou Medical University, Wenzhou, China, [2]College of Life and Environmental Sciences, Wenzhou University, Wenzhou, China

OPEN ACCESS

Edited by:
Thomas Haarmann-Stemmann, Leibniz-Institut für Umweltmedizinische Forschung (IUF), Germany

Reviewed by:
Medardo Hernández, Complutense University of Madrid, Spain
Robert Lust, The Brody School of Medicine at East Carolina University, United States

***Correspondence:**
Xiaokun Li
xiaokunli@wmu.edu.cn
Nuo Xu
seer.sino@hotmail.com

[†]These authors have contributed equally to this work

Specialty section:
This article was submitted to Integrative and Regenerative Pharmacology, a section of the journal Frontiers in Pharmacology

Received: 18 January 2021
Accepted: 24 May 2021
Published: 07 June 2021

Citation:
Gao S, Guo K, Chen Y, Zhao J, Jing R, Wang L, Li X, Hu Z, Xu N and Li X (2021) Keratinocyte Growth Factor 2 Ameliorates UVB-Induced Skin Damage via Activating the AhR/Nrf2 Signaling Pathway. Front. Pharmacol. 12:655281. doi: 10.3389/fphar.2021.655281

Objective: Exposure to ultraviolet B (UVB) can cause skin damage through oxidative stress, DNA damage, and apoptosis. Keratinocyte growth factor (KGF) has been shown to reduce the content of intracellular reactive oxygen species (ROS) following UVB exposure, a role that is crucial for the efficient photoprotection of skin. The present study evaluated the photoprotective effect of KGF-2 on UVB-induced skin damage and explored its potential molecular mechanism.

Methods: To evaluate the effect of KGF-2 on UVB-induced damage *ex vivo*, a human epidermal full-thickness skin equivalent was pretreated without or with KGF-2 and then exposed to UVB and the levels of histopathological changes, DNA damage, inflammation, and apoptosis were then evaluated. The ability of KGF-2 to protect the cells against UVB-inflicted damage and its effect on ROS production, apoptosis, and mitochondrial dysfunction were determined in HaCaT cells.

Results: Pretreatment of the epidermis with KGF-2 ameliorated the extent of photodamage. At the cellular level, KGF-2 could attenuate ROS production, apoptosis, DNA damage, and mitochondrial dysfunction caused by UVB exposure. KGF-2 could also activate the aryl hydrocarbon receptor (AhR) to trigger the Nrf2 signaling pathway.

Conclusion: Taken together, our findings suggested that KGF-2 could ameliorate UVB-induced skin damage through inhibiting apoptosis, reducing oxidative stress, and preventing DNA damage and mitochondrial dysfunction *via* regulating AhR/Nrf2 signaling pathway.

Keywords: keratinocyte growth factor 2, ultraviolet B, photoprotective, aryl hydrocarbon receptor, Nrf2

INTRODUCTION

The skin, the largest organ of the human body, is divided into three different layers, called subcutis, dermis, and epidermis. The outermost epidermis is mainly composed of keratinocytes and it provides a selective physical barrier to protect human beings from harmful substances that come from the environment (Eckhart and Zeeuwen 2018). Ultraviolet (UV) radiation is the most ubiquitous environmental threat that affects human skin (Perluigi et al., 2010). UV is composed of three different types classified by wavelengths: UVA (320–400 nm), UVB (280–320 nm), and UVC

(200–280 nm). UVC is effectively blocked from reaching the Earth's surface by the ozone layer of the atmosphere. UVA can penetrate deeply into the dermis to cause aging and wrinkling of the skin. UVB on the other hand is regarded as "burning rays" and it is almost completely absorbed by the epidermis, where it can induce oxidative damage, inflammation, DNA damage, photoaging, and apoptosis (Tomaino et al., 2006; Oh et al., 2016; D'Orazio et al., 2013; de Gruijl 2000).

The hallmark of UVB-induced skin damage is the formation of apoptotic keratinocytes within the epidermis once the dose of UV exceeds a certain threshold (Takahashi et al., 1997). Such apoptotic keratinocytes, which can be identified by their pyknotic nuclei and cytoplasmic shrinkage (Bayerl et al., 1995; D'Orazio et al., 2013). UVB-induced DNA damage and the formation of reactive oxygen species (ROS) are thought to be crucial factors that trigger the apoptotic machinery (Wang et al., 1999). Direct UVB-induced DNA damage in keratinocytes consists of two major forms of lesions: cyclobutane pyrimidine dimers (CPDs) and 6–4 pyrimidine photoproducts (6–4 PPs) (Garinis et al., 2005; Rastogi et al., 2010). Such DNA damage can also induce an inflammatory response through mediating the release of interleukin 1β (IL-1β), IL-6 and tumor necrosis factor α (TNF-α) (Piotrowska et al., 2016; Prasad and Katiyar 2017). UVB can promote the excessive production of ROS in keratinocytes, and the increased level of ROS can in turn, inhibit the antioxidant defense mechanism as well as stimulate the inflammatory response in skin (Darr and Fridovich, 1994; Kuanpradit et al., 2017). Meanwhile, ROS can attack the mitochondrial membranes and mitochondrial DNA directly, causing mitochondrial dysfunctions (Kudryavtseva et al., 2016).

Keratinocyte growth factor (KGF) is a fibroblast growth factor (FGF) family member and it is known to protect skin against oxidant injury (Werner et al., 2007). KGF-1 plays a crucial protective role in keratinocytes through reducing the level of intracellular ROS and apoptosis following UVB exposure (Braun et al., 2006; Kovacs et al., 2009). A previous study has reported that exposure to UVB and oxidant stimuli can trigger the activation and internalization of KGFR, similar to those induced by KGF-1 (Marchese et al., 2003). Fibroblast growth factor-10 (KGF-2), another member of the FGF family, is similar to KGF-1 in structure and function. KGF-2 promotes both the growth and differentiation of keratinocyte cells (Soler et al., 1999). KGF-2 can suppress excessive oxidative stress-induced cell apoptosis to promote cell/tissue regeneration (Dong et al., 2019). Additionally, KGF-2 can augment the repair of oxidant-induced DNA damage in alveolar epithelial cells (Takeoka et al., 1997; Upadhyay et al., 2004). We, therefore, hypothesized that KGF-2 would protect the skin against UVB-induced damage following its exposure. In this study, the involvement of KGF-2 in UVB-induced skin damage was evaluated and the underlying mechanism was explored.

MATERIALS AND METHODS

Reagents

KGF-2 was expressed in *Escherichia coli* and purified in our laboratory. GNF 351 was purchased from Selleck (Shanghai, China).

Detection of Human Epidermal Equivalents After Ultraviolet B Irradiation

Human epidermal equivalent (HEE) is an *in vitro* reconstructed human epidermis from normal human keratinocytes cultured on an inert polycarbonate filter at the air-liquid interface, in a chemically defined medium. This model exists at different stages of maturity. This model is histologically similar to *in vivo* human epidermis. HEE (Biocell Biotechnology, Guangdong, China) was placed in a six-well cultured plate and equilibrated in HEE medium for 24 h at 37°C in a 5% CO_2 incubator before use. The HEE was treated with KGF-2 for 4 h *via* topical application. The medium was then replaced with PBS, the HEE was then exposed to 200 mJ/cm^2 of UVB radiation. After exposure, it was cultured in fresh medium for 36 h and then harvested. The HEE was fixed in 4% paraformaldehyde, dehydrated, and then embedded in paraffin, followed by sectioning into 5 μm-thick coronal slices. The slices were then subjected to the following analyses.

Histological Examination

For histological examination, the HEE slices were stained with hematoxylin-eosin and then examined by fluorescence microscopy using a DM3000 microscope (Leica, Wetzlar, Germany) to assess the histological changes. The number of epidermal UVB-damaged keratinocyte characterized by the presence of pyknotic condensed nuclei in the HEE sample was quantified.

Immunofluorescence Assay

For immunofluorescence assay, the HEE slices were dewaxed, rehydrated, and incubated in 3% H_2O_2/methanol solution for 25 min and then blocked with 5% BSA for 4 h at 37°C. After that, the slices were incubated with the immunofluorescence markers: phospho-H2AX (1:1,000) (Cell Signaling Technology, Beverly, MA, United States) and anti-CPD (1:200) (Cosmo Bio, Tokyo, Japan) overnight at 4°C in a humidified chamber. The samples were then washed three times with PBS, followed by incubation with Alexa Flour 488 (green) donkey anti-rabbit secondary antibody and Alexa Flour 568 (red) donkey anti-mouse secondary antibody for 1 h at room temperature in the dark. Finally, the samples were stained with ProLong Gold Antifade reagent containing DAPI (Life Technologies Corporation, NY, United States) and then mounted on glass slides and examined under a Ti2-E&CSU-W1 confocal microscope (Nikon, Tokyo, Japan). The 488 nm laser intensity is 2% with the detector voltage of 430 V. The 561 nm laser intensity is 4% with the detector voltage of 550 V.

TUNEL Assay

TUNEL assay carried out for the HEE slices according to the instructions of manufacturer (Roche, Penzberg, Germany) and examined under a Ti2-E&CSU-W1 confocal microscope (Nikon, Tokyo, Japan). The 488 nm laser intensity is 5% with the detector voltage of 500 V.

Cells Culture

Immortalized human keratinocytes were supplied by Zhong Qiao Xin Zhou Biotechnology Co., Ltd. (Shanghai, China). The cells

were cultured in Dulbecco's modified Eagle's medium (DMEM) (GIBCO, Life Technologies Corporation, NY, United States) containing 10% fetal bovine serum (FBS) (GIBCO, Life Technologies Corporation, NY, United States) at 37°C in a 5% CO_2 incubator.

Ultraviolet B Irradiation

HaCaT cells were incubated with KGF-2 at different concentrations (0, 50, 200 ng/ml) for 4 h, and then washed with PBS. The cells were then exposed to UVB (200 mJ/cm^2) in PBS using a VL6-M Biotronic device (Vilber Lourmat, Marne La Vallee, France). After UVB exposure, the cells were incubated with fresh DMEM at 37°C in a 5% CO_2 incubator for different times depending on the experiment.

Intracellular Reactive Oxygen Species Measurement

HaCaT cells were treated under the designated experimental conditions. An assay kit (Beyotime, China) was employed to measure ROS production according to the manufacturer's protocol. Briefly, after 1 h of UVB (200 mJ/cm^2) irradiation, the cells were washed twice with PBS, and then incubated with DCFH-DA at a final concentration of 5 μM for 20 min at 37°Cin a 5% CO_2 incubator. After that, the cells were digested and washed three times with PBS, and intracellular ROS production was then measured with an ACEA NovoCyte flow cytometer (Agilent, Santa Clara, CA, United States), and the result was analyzed using NovoExpress software.

Apoptosis Assay

HaCaT cells were cultured in a 6-well plates at a density of 5×10^4 cells/well for 24 h and then incubated with KGF-2 at different concentrations (0, 50, 200 ng/ml) for 4 h followed by exposure to UVB (200 mJ/cm^2). After that, the cells were incubated with fresh DMEM at 37°C in a 5% CO_2 incubator for 6 h. An annexin V &FITC apoptosis detection kit (Dojindo Laboratories, Kumamoto, Japan) was used to stain the cells according to the manufacturer's protocol. The stained cells were quantified with an ACEA NovoCyte flow cytometer (Agilent, Santa Clara, CA, United States). The apoptotic frequency was expressed as the percentage of Annexin V-FITC positive cells.

JC-1 Staining

JC-1 fluorescent probes (Beyotime, Jiangsu, China) was used to determine the mitochondrial membrane potential (MMP). First, HaCaT cells were cultured for 24 h in 6-well plates at a density of 5×10^4/well. Next, the cells were treated with the different concentrations of KGF-2 (0, 50, 200 ng/ml) for 4 h and then irradiated with UVB followed by 1 h of incubation. After that, the cells were washed with PBS and incubated with DMEM containing 5 μM of JC-1 for 20 min. Finally, the cell nuclei were stained with 40,6-diamidino-2-phenylindole (DAPI), and the MMP of the cells was monitored with a fluorescence microscope (Nikon, Tokyo, Japan) (Red: excitation/emission 530 nm/590 nm, exposure time: 180 ms; Green: excitation/emission 490/530 nm, exposure time: 200 ms).

TABLE 1 | Primer sequences used in this study.

Gene name	Primer sequences
β-ACTIN	F: 5′- CTC CAT CCT GGC CTC GCT GT -3′
	R: 5′- GCT GTC ACC TTC ACC GTT -3′
TNF-α	F: 5′-CCT GTA GCC CAC GTC GTA GC-3′
	R: 5′-TTG ACC TCA GCG CTG AGT TG-3′
IL-1β	F: 5′-TGG CAA TGA GGA TGA CTT GT-3′
	R: 5′-GTG GTG GTC GGA GAT TCG TA-3′
IL-6	F: 5′-CCG AGA AGG AGA CTT CAC AG-3′
	R: 5′-TCC ACG ATT TCC CAG AGA AC-3′

Mitochondrial Mass Analysis

HaCaT cells were treated in the same way as described for JC-1 staining. The fluorescent probe Mito-Tracker Green (Beyotime, Jiangsu, China) was used to determine the mitochondrial mass of HaCaT cells. In brief, the cells were first incubated with 50 nm Mito-Tracker Green in DMEM for 1 h at 37°C in the dark. After that, they were washed with PBS, and the nuclei were stained with DAPI, while the fluorescence of the mitochondria was measured with a Ti2-E&CSU-W1 confocal microscope (Nikon, Tokyo, Japan) using λEm and λEx of 488 and 590 nm, respectively. The 488 nm laser intensity is 3% with the detector voltage of 450 V.

Quantitative Real-Time PCR

HEE was treated without or with KGF-2 followed by UVB irradiation as described above and total RNA was then isolated from the sample using TRIzol reagent (Invitrogen, Carlsbad, CA, United States) according to the manufacturer's instructions. At the same time, total RNA was also isolated from HaCaT cells treated without or with KGF-2 and followed by UVB irradiation. The concentration of total RNA obtained was determined with a NanoQuant Plate (Tecan, Mannedorf, Switzerland). Reverse transcription was performed with PrimeScript RT reagent Kit (Takara, Dalian, China) using 1 μg of total RNA as template. *q*RT-PCR was performed using the SYBR Green Master Mix (Applied Biosystems, Foster City, CA) and the LC96 system (Roche, Basel, Switzerland). The sequences of all the primers used are shown in **Table 1**. The expression of target genes was normalized to the level of β-actin, which served as an endogenous control. The relative expression of each targeted gene was analyzed using the $2^{-\Delta\Delta Ct}$ method.

Immunofluorescence Staining for Detection of γ-H2AX and CPD

HaCaT cells grown on coverslips (WHB Scientific, Shanghai, China) for 24 h and treated with KGF-2 or exposed to UVB as described above and allowed to recover for 1 h at 37°C in a 5% CO_2 incubator. The cells were then washed three times with PBS and immediately fixed in 4% paraformaldehyde for 15 min at room temperature. The fixed cells were permeabilized with 0.5% Triton X-100 in PBS and immersed in 2 M HCl for 30 min at room temperature. After being washed with TBS, the cells were blocked with 5% BSA in TBST (TBS + 0.1% Triton X-100) for 30 min at 37°C with gentle shaking. For the double staining

experiments, the cells were incubated with γ-H2AX and anti-CPD in 5% BSA for overnight at 4°C. After that, the cells were washed three times with TBST, incubated with a secondary antibody, and then mounted with an antifade reagent containing DAPI. The fluorescence of the cells was measured using a Ti2-E&CSU-W1 confocal microscope (Nikon, Tokyo, Japan). The 488 nm laser intensity is 1% with the detector voltage of 450 V. The 561 nm laser intensity is 3% with the detector voltage of 500 V.

Western Blot

HaCaT cells were cultured in a 6-well plates at a density of 5×10^4/well for 24 h and then treated with different concentrations of KGF-2 (0, 50, and 200 ng/ml) for 4 h followed by exposure to UVB. After UVB irradiation, the cells were incubated at 37°C in a 5% CO_2 incubator for 30 min. Cytoplasmic and nuclear proteins were extracted from the cells using NE-PER™ Reagents (Thermo scientific, NY, United States) according to the manufacturer's instructions. The samples were then subjected to SDS-PAGE and the protein bands in the gel were transferred to a PVDF membrane. The membrane was immunolabeled with one of the following primary antibodies: anti-Nrf2, anti-AHR, anti-capase-3, anti-capase-9, anti-CYP1A1, anti-LaminB1, or anti-Tubulin (Cell Signaling Technology, Beverly, MA, United States) followed by washing and further incubation with a secondary antibody (Cell Signaling Technology, Beverly, MA). The immune complexes were finally detected with a chemiluminescence substrate (Thermo scientific, NY, United States) and the image was captured with an Amersham Imager (GE Healthcare Biosciences, Pittsburgh, PA, United States).

Statistical Analysis

All quantitative data were presented as means ± SD from at least three independent experiments. A comparison of multi-group data was carried out with a One-way analysis of variance (ANOVA) followed by Dunnett's test. Statistical significance was considered at either the $p < 0.05$ or $p < 0.01$ level. All graphical presentations were done using GraphPad Prism 5.01 (GraphPad, San Diego, CA, United States).

RESULTS

Keratinocyte Growth Factor-2 Ameliorated the Extent of Photodamage of Epidermis

HEE irradiated with 200 mJ/cm^2 dose of UVB followed by 24 h of culturing revealed a significant increase in the number of UVB-damaged keratinocyte (as shown by HE staining) compared with control (non-irradiated) HEE, but the number of UVB-damaged keratinocyte was reduced when HEE was pretreated with KFG-2 before UVB irradiation (**Figure 1A**). Consistent with the result obtained from HE staining, the result obtained from TUNEL assay also showed that KGF-2 could prevent the keratinocytes from undergoing apoptosis in the UVB-irradiated HEE (**Figure 1B**). UVB-induced DNA damage is crucial to the initiation of apoptosis. In general, DNA damage can be detected by looking at the formation of CPD and γ-H2AX within the HEE cells. DNA damage in the UVB-irradiated HEE was detected by the formation of CPD and γ-H2AX using immunofluorescence staining. No foci of CPD and γ-H2AX were observed within the cell nuclei of the control HEE, whereas many CPD and γ-H2AX foci were detected in the cell nuclei of UVB-irradiated HEE. The number of CPD and γ-H2AX foci in the cell nuclei was significantly reduced when the HEE was treated with KGF-2 before UVB irradiation (**Figure 1C**). UVB-irradiated keratinocytes are known to release various proinflammatory cytokines such as IL-1β, IL-6, and TNF-α (Kim et al., 2013). The mRNA levels of IL-1β,IL-6, and TNF-α were notably increased in UVB-irradiated HEE (**Figure 1D**). However, pretreatment with KGF-2 led to a reduction in the mRNA levels of all these proinflammatory cytokines. These results suggested that KGF-2 could prevent or reduce the extent of DNA damage and formation of associated cytokines in UVB-irradiated HEE, demonstrating the protective effect of KGF-2 against UVB-induced damage on the skin.

Keratinocyte Growth Factor-2 Attenuates Apoptosis, Reactive Oxygen Species Production, and DNA Damage Caused by Ultraviolet B Exposure in Keratinocytes

At the cellular level, the exposure of keratinocytes to excessive UVB radiation can cause irreversible DNA damages and induce ROS production, which will eventually lead to apoptosis (Wang et al., 1999; Afaq et al., 2007). After UVB irradiation, the number of apoptotic cells was significantly elevated compared with the control (non-irradiated) sample, but the apoptotic rate was significantly repressed when the cells were treated with KGF-2 before UVB irradiation, indicating that KGF-2 could protect HaCaT cells against UVB-induced apoptosis (**Figure 2A**). UVB irradiation also stimulated the high production of intracellular ROS compared with the control cells. Treatment with 50 or 200 ng/ml KGF-2 before UVB irradiation significantly reduced ROS production (**Figure 2B**). Interestingly, KGF-2 pretreatment reversed the loss of key antioxidant enzymes, e.g., superoxide dismutase (SOD), in UVB-injured HaCaT cells (**Figure 2C**). The level of CPD and γ-H2AX in UVB-irradiated HaCaT cells increased significantly compared with the control cells. Pretreatment of HaCaT cells with KGF-2 significantly decreased the formation of CPD and γ-H2AX (**Figure 2D**). These results indicated that KGF-2 could protect keratinocytes from UVB-induced cell damage.

Keratinocyte Growth Factor-2 Ameliorates Mitochondrial Dysfunction Caused by Ultraviolet B Irradiation

UVB-induced ROS overproduction can result in mitochondrial dysfunction, a major cause of apoptosis. To evaluate the effect of KGF-2 on mitochondrial function, the mitochondrial membrane potential (MMP) and mitochondrial mass of HaCaT cells were measured following UVB irradiation. HaCaT cells irradiated with

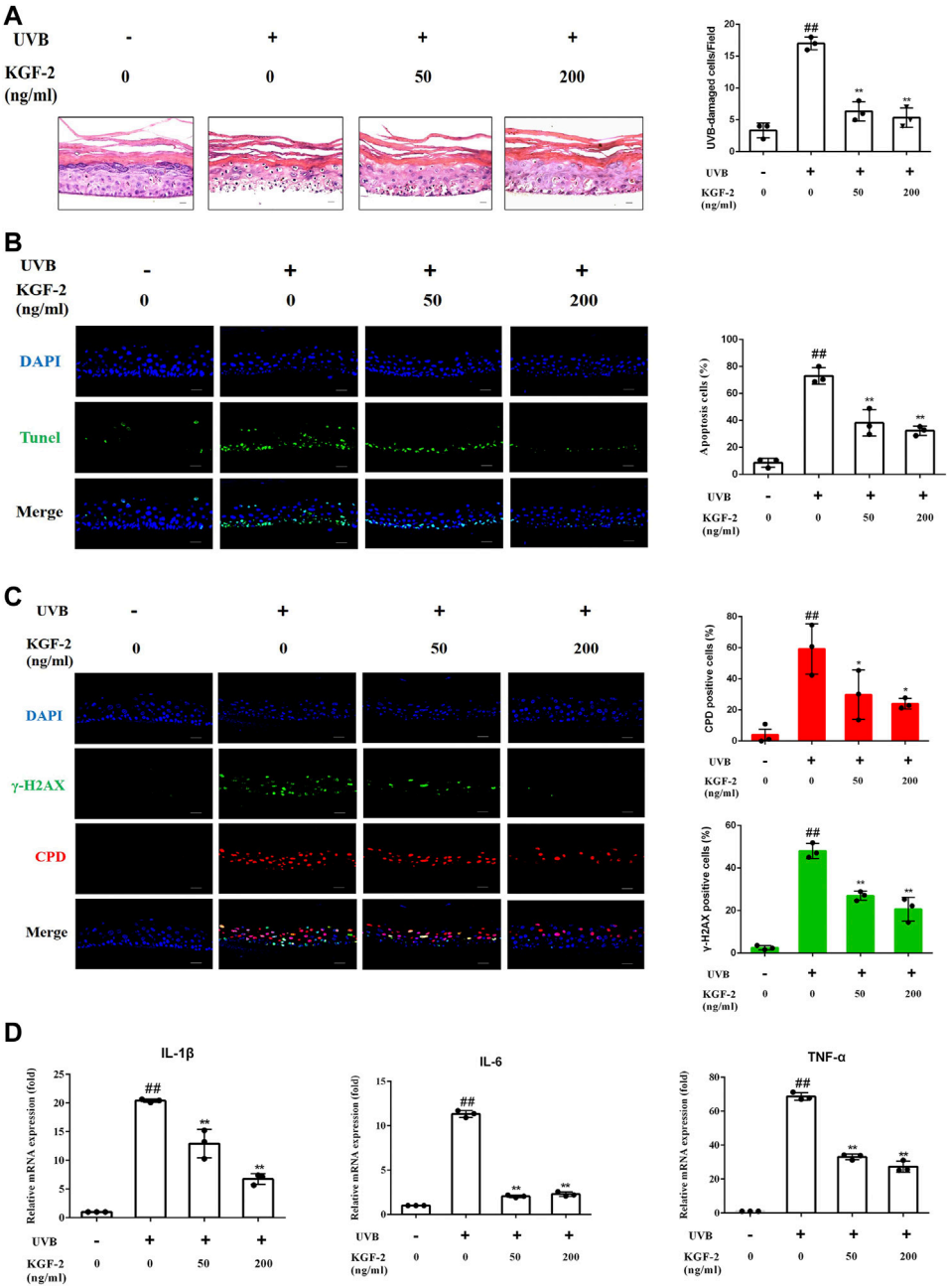

FIGURE 1 | Effect of KGF-2 on UVB-irradiated HEE. HEE was treated with or without KGF-2 (0, 50, 200 ng/ml) for 4 h, and then irradiated with 200 mJ/cm^2 dose of UVB. 24 h later, the HEE was collected and subjected to a series of analyses. **(A)** Specimens of HEE stained with HE, the plot compares the UVB-damaged cell counts taken from three independent HEE cultures. UVB only *vs.* untreated control group, $p < 0.0001$; KGF-2 (50 ng/ml) *vs.* UVB only group, $p < 0.0001$; KGF-2 (200 ng/ml) *vs.* UVB only group, $p < 0.0001$. **(B)** Representative image of immunofluorescence staining of apoptotic keratinocytes; the plot compares the apoptotic cell number within HEEs from three different treatments. UVB only *vs.* untreated control group, $p < 0.0001$; KGF-2 (50 ng/ml) *vs.* UVB only group, $p = 0.0004$; KGF-2 (200 ng/ml) *vs.* UVB only group, $p = 0.0001$ **(C)** Representative immunofluorescence images of HEEs stained with anti-CPD and anti-γ-H2AX antibodies, the first plot compares the formation of CPD of HEEs from three different treatments, UVB only *vs.* untreated control group, $p = 0.0012$; KGF-2 (50 ng/ml) *vs.* UVB only group, $p = 0.0393$; KGF-2 (200 ng/ml) *vs.* UVB only group, $p = 0.0166$. The second plot compares the formation of γ-H2AX of HEEs from three different treatments, UVB only *vs.* untreated control group, $p < 0.0001$; KGF-2 (50 ng/ml) *vs.* UVB only group, $p = 0.0002$; KGF-2 (200 ng/ml) *vs.* UVB only group, $p < 0.0001$. **(D)** qRT-PCR analysis of IL-1β,IL-6, and TNF-α mRNA levels in HEEs subjected to different treatments. For IL-1β, UVB only *vs.* untreated control group, $p < 0.0001$; KGF-2 (50 ng/ml) *vs.* UVB only group, $p = 0.0004$; KGF-2 (200 ng/ml) *vs.* UVB only group, $p < 0.0001$. For IL-6, UVB only *vs.* untreated control group, $p < 0.0001$; KGF-2 (50 ng/ml) *vs.* UVB only group, $p < 0.0001$; KGF-2 (200 ng/ml) *vs.* UVB only group, $p < 0.0001$. For TNF-α, UVB only *vs.* untreated control group, $p < 0.0001$; KGF-2 (50 ng/ml) *vs.* UVB only group, $p < 0.0001$; KGF-2 (200 ng/ml) *vs.* UVB only group, $p < 0.0001$. All graphical data are the means ± SD from three independent experiments, "#" and "##" indicate significantly different from the untreated control group at the $p < 0.05$ and $p < 0.01$ levels, respectively, "*" and "**" indicate significantly different from the UVB only control group at the $p < 0.05$ and $p < 0.01$ levels, respectively.

UVB displayed a loss of MMP while those that had been treated with KGF-2 before UVB irradiation showed an elevated level of MMP (**Figure 3A**). In agreement with the result of MMP, KGF-2 also significantly attenuated the loss of mitochondrial mass caused by UVB irradiation (**Figure 3B**). Thus, KGF-2 could prevent mitochondrial dysfunction in HaCaT cells induced by UVB irradiation.

Keratinocyte Growth Factor-2 Activates the Aryl Hydrocarbon Receptor/Nrf2 Signaling Pathway

Apoptosis-related caspase-3 and caspase-9 can be activated in UVB-irradiated keratinocytes (Kamarajan and Chao 2000; Itoh and Horio 2001). Pretreatment of HaCaT cells with KGF-2 resulted in a reduction of the caspase-3 and caspase-9 activation, indicating that KGF-2 could effectively inhibit UVB-induced apoptosis (**Figure 4A**). It has been reported that the aryl hydrocarbon receptor (AhR) is a crucial mediator of the UVB stress response in human keratinocytes following UVB exposure (Fritsche et al., 2007). In unstressed cells, ligand-free AhRs are maintained in an inactive complex in the cytosol. In the epidermal compartment, UVB is absorbed by the aromatic amino acid L-tryptophan, leading to the formation of 6-formylindolo (3,2-b)carbazole (FICZ), which binds AhR with high affinity and induces pp60src to dissociate from the complex. The AhR is then translocated from the cytoplasm to the nucleus where it heterodimerizes with ARNT and induces the expression of monooxygenase cytochrome P450 (CYP1A1) (Villard et al., 2002; Agostinis et al., 2007; Fritsche et al., 2007; Diani-Moore et al., 2011). HaCaT cells that were irradiated with UVB exhibited a significant increase in the level of AhR in the nuclei compared with the untreated cells. However, when the cells were pretreated with KGF-2, the translocation of AhR into the nucleus was promoted (**Figure 4A**). Furthermore, these cells also displayed a marked increase in CYP1A1 expression compared with those irradiated with UVB without KGF-2 pretreatment (**Figure 4A**). In inactive state, Nrf2 is anchored to Kelch-like ECH associated protein 1 (Keap1) in the cytoplasm. Once activated, Nrf2 departs from Keap1, leading to its stabilization, accumulation, and translocation to nuclei (Itoh et al., 2004; Li and Kong 2009; Suzuki and Yamamoto 2015). Our data showed that KGF-2 could promote the translocation of Nrf2 to the nucleus, indicating that KGF-2 could activate the Nrf2 signaling pathway. In order to clarify whether KGF-2 could activate Nrf2 through activating AhR, HaCaT cells were pretreated with GNF351 (AhR antagonist) for 12 h prior to treatment with KGF-2 in order to block the translocation of AhR into the nucleus. After UVB irradiation, the expression of AhR in the nucleus of these cells was significantly inhibited compared with the cells that were not treated with GNF351, indicating that UVB induced AhR activation was effectively blocked by GNF351. The result also demonstrated when the activation of AhR was blocked, KGF-2 could not elevate the expression of CYP1A1 and inhibit the expression of caspase-3 and caspase-9 after UVB irradiation. More importantly, KGF-2 could not trigger Nrf2 activation once the activation of AhR was blocked, demonstrating that KGF-2 could stimulate the activation of Nrf2 *via* activating the AhR pathways (**Figure 4B**).

Keratinocyte Growth Factor-2 Protects HaCaT Cells From Ultraviolet B-Induced Damage Through Activating Aryl Hydrocarbon Receptor/Nrf2 Signaling Pathway

In order to clarify whether KGF-2 could protect the keratinocytes from UVB-induced damage through activating AhR/Nrf2 signaling pathway, HaCaT cells were pretreated with or without GNF351 for 12 h prior to KGF-2 treatment. The extent of UVB-induced keratinocytes apoptosis was then determined by flow cytometry. The result showed that KGF-2 could not inhibit the apoptotic rate induced by UVB irradiation when the cells were pretreated with GNF351, suggesting that blocking the activation of AhR prevented the KGF-2 from conferring its protective effect against UVB-induced apoptosis (**Figure 5A**). Pretreatment of HaCaT cells with GNF351 followed by KGF-2 treatment also led to the lack of reduction of ROS production following UVB irradiation compared with no GNF351 pretreatment, indicating that the ability of KGF-2 to reduce the production of ROS induced by UVB irradiation was abolished once the activation of AhR was blocked (**Figure 5B**). Under this condition, KGF-2 could not prevent the reduction of SOD and formation of CPD and γ-H2AX and protect the mitochondria against the loss function induced by UVB irradiation (**Figures 5C–F**), suggesting that KGF-2 might protect the HaCaT cells from UVB-induced damage *via* activating AhR/Nrf2 pathway.

DISCUSSION

UV radiation is the most prominent and ubiquitous physical stressor in our environment and the gradual depletion of the stratospheric ozone over the past many decades has resulted in more intensive UV radiation reaching the Earth's surface. This has translated into more UV-induced damage to individuals without proper protection while exposing their skins to direct sunlight, especially in summertime. Such UV-induced damages include erythema, oedema, heat, burn, and pruritus.

KGF might provide efficient photoprotection of the human skin against UV radiation because it could markedly reduce cell death and the intracellular level of ROS, while preventing the loss of catalase activity in the epidermis after UVB irradiation (Braun et al., 2006; Kovacs et al., 2009). KGF-2 is a typical paracrine growth factor, and it has been shown to possess anti-inflammatory and antioxidation activities, increase cell proliferation as well as reducing apoptosis through initiating the activation of intracellular signaling cascades. These signaling cascades include the extracellular signal-regulated kinase (ERK) 1/2 signaling pathway, phosphatidylinositol-3 kinase/protein kinase B (PI3K/Akt) signaling pathway, and Nrf2 signaling pathway (Upadhyay et al., 2005; Shi et al.,

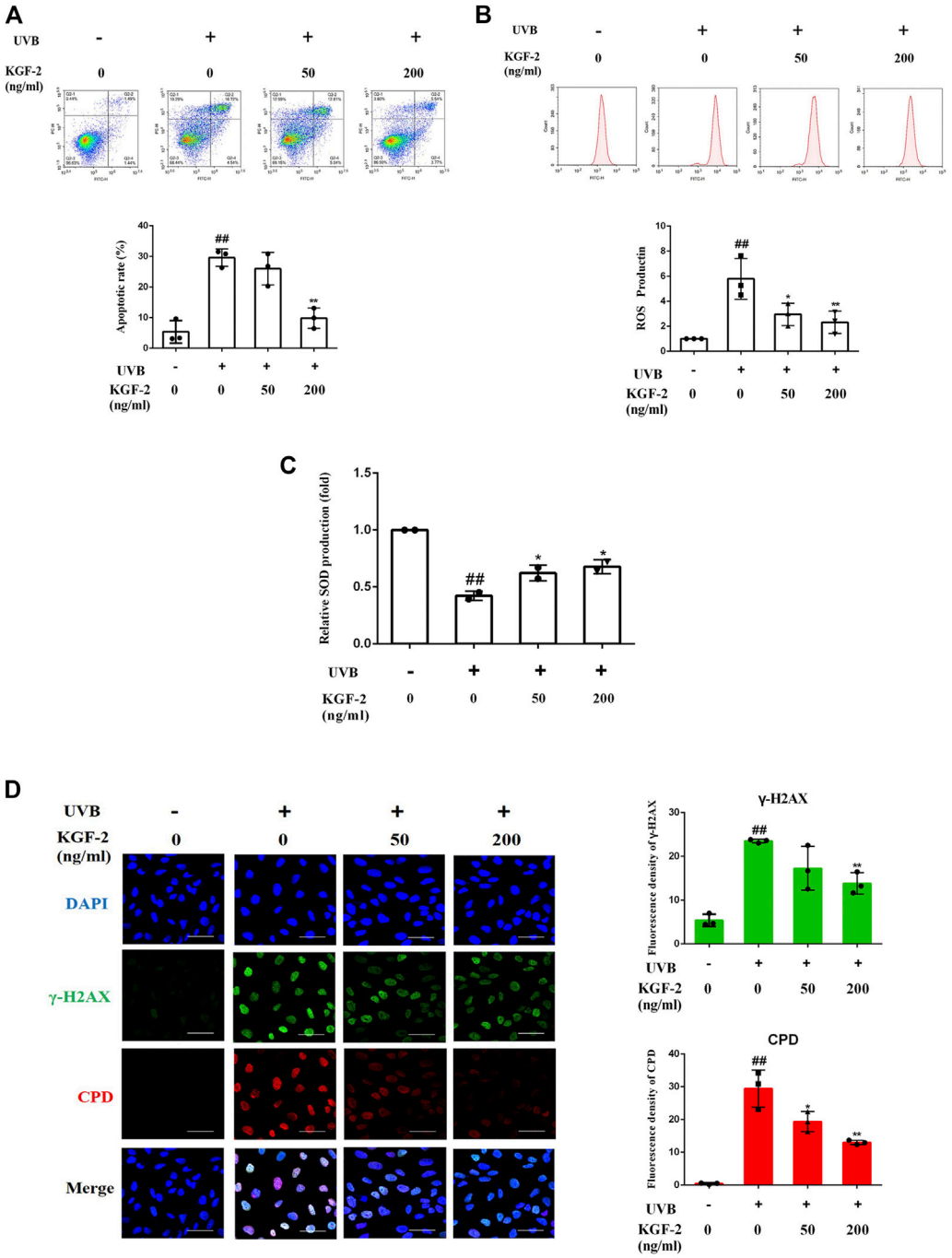

FIGURE 2 | Effects of KGF-2 on the apoptosis, ROS, and SOD production as well as DNA damage of UVB-irradiated HaCaT cells. HaCaT cells were incubated with KGF-2 (0, 50, 200 ng/ml) for 4 h, then exposed to UVB (200 mJ/cm^2) and further incubation for the indicated times. **(A)** Flow cytometry analysis of apoptotic HaCaT cells stained with Annexin V/PI after 6-h incubation following UVB irradiation, the plot compares the apoptotic rate from three different treatments. UVB only *vs.* untreated control group, $p = 0.0002$; KGF-2 (50 ng/ml) *vs.* UVB only group, $p = 0.5635$; KGF-2 (200 ng/ml) *vs.* UVB only group, $p = 0.0007$. **(B)** Intracellular ROS levels as measured by flow cytometry using the oxidant-sensitive probe DCFH-DA after 1-h incubation following UVB irradiation, the plot compares the relative ROS production from three different treatments. UVB only *vs.* untreated control group, $p = 0.0012$; KGF-2 (50 ng/ml) *vs.* UVB only group, $p = 0.0242$; KGF-2 (200 ng/ml) *vs.* UVB only group, $p = 0.0084$. **(C)** The SOD levels were measured after 6-h incubation following UVB irradiation. UVB only *vs.* untreated control group, $p = 0.0008$**;** KGF-2 (50 ng/ml) *vs.* UVB only group, $p = 0.0385$; KGF-2 (200 ng/ml) *vs.* UVB only group, $p = 0.0168$. **(D)** Representative image of immunofluorescence staining of CPD and γ-H2AX were obtained after incubating for 1-h following UVB irradiation, the plot compares the formation of CPD and γ-H2AX from three different treatments. For γ-H2AX, UVB only *vs.* untreated control group, $p = 0.0002$; KGF-2 (50 ng/ml) *vs.* UVB only group, $p = 0.0703$; KGF-2 (200 ng/ml) *vs.* UVB only group, $p = 0.0085$. For CPD, UVB only *vs.* untreated control group, $p < 0.0001$; KGF-2 (50 ng/ml) *vs.* UVB only group, $p = 0.0132$; KGF-2 (200 ng/ml) *vs.* UVB only group, $p = 0.0007$. All graphical data are the means ± SD from three independent experiments, "#" and "##" indicate significantly different from the untreated control group at the $p < 0.05$ and $p < 0.01$ levels, respectively, "*" and "**" indicate significantly different from the UVB only control group at the $p < 0.05$ and $p < 0.01$ levels, respectively.

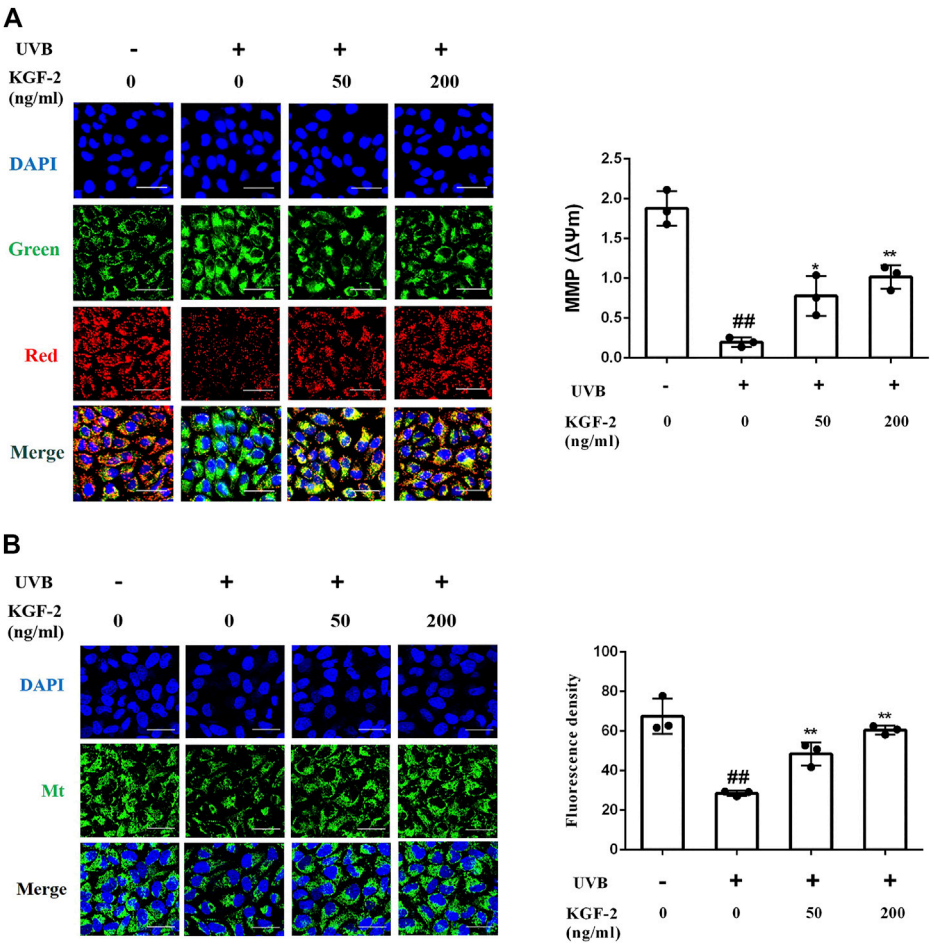

FIGURE 3 | Effect of KGF-2 on the mitochondrial dysfunction induced by of UVB irradiation. HaCaT cells were incubated with KGF-2 (0, 50, 200 ng/ml) for 4 h, then exposed to UVB (200 mJ/cm^2) and a further 1-h incubation. **(A)** Representative image of mitochondrial membrane potential (MMP) in HaCaT cells, the plot compares the MMP of HaCaT cells from three different treatments. UVB only *vs.* untreated control group, $p < 0.0001$; KGF-2 (50 ng/ml) *vs.* UVB only group, $p = 0.0125$; KGF-2 (200 ng/ml) *vs.* UVB only group, $p = 0.0016$. **(B)** Representative image of mitochondrial mass, the plot compares the mitochondrial mass of HaCaT cells from three different treatments. UVB only *vs.* untreated control group, $p < 0.0001$; KGF-2 (50 ng/ml) *vs.* UVB only group, $p = 0.0057$; KGF-2 (200 ng/ml) *vs.* UVB only group, $p = 0.0003$. All graphical data are the means ± SD from three independent experiments, "#" and "##" indicate significantly different from the untreated control group at the $p < 0.05$ and $p < 0.01$ levels, respectively, "*" and "**" indicate significantly different from the UVB only control group at the $p < 0.05$ and $p < 0.01$ levels, respectively.

2018; Dong et al., 2019; Tan et al., 2020). Previous studies have focused on the role of KGF-2 in embryonic development, wound healing, and tissue regeneration. However, the effect of KGF-2 on UVB-induced skin damage was not clear. We have shown that KGF-2 could ameliorate UVB-induced skin damage through inhibiting oxidative stress, DNA damage, apoptosis, and mitochondrial dysfunction.

The ability of KGF-2 to ameliorate the extent of UVB-induced epidermis damage was demonstrated using human epidermal equivalent (HEE) as a skin substitute. HEE was used instead of animals because it could faithfully mimic the *in vivo* epidermis (Smits et al., 2017; Yoshida et al., 2012). A number of parameters were monitored to demonstrate the level of damage sustained by HEE following UVB irradiation. HEE irradiated with UVB clearly exhibited an increase in the number of UVB-damaged cells accompanied by DNA damage and inflammation. However, treatment of the HEE with KGF-2 before UVB irradiation resulted in marked protection against the UVB radiation-induced damage, as seen by the reduced number of UVB-damaged cells, lesser DNA damage as well as lower inflammation response. UV radiation can cause inflammation, aging, and cell damage (Kim et al., 2019). If the dose of UVB sustained by the keratinocytes exceeds a threshold damage response, apoptosis will be activated, leading to the death of these cells as a mean to prevent the accumulation of potentially mutagenic keratinocytes within the skin (Van Laethem et al., 2005; Nakanishi et al., 2009; Deshmukh et al., 2017). DNA is the most abundant chromophore present in the epidermis, UVB is directly absorbed by DNA which causes molecular rearrangements forming the photoproducts such as CPD and 6–4 photoproducts (D'Orazio et al., 2013; Chen et al., 2014). CPDs are the main DNA damage lesions responsible for cell death following UV exposure (Kciuk and Marciniak 2020). Increased formation of CPD can lead to an increase in the phosphorylation of the histone protein H2AX at Ser139. The phosphorylated H2AX, termed γ-H2AX, is not only an

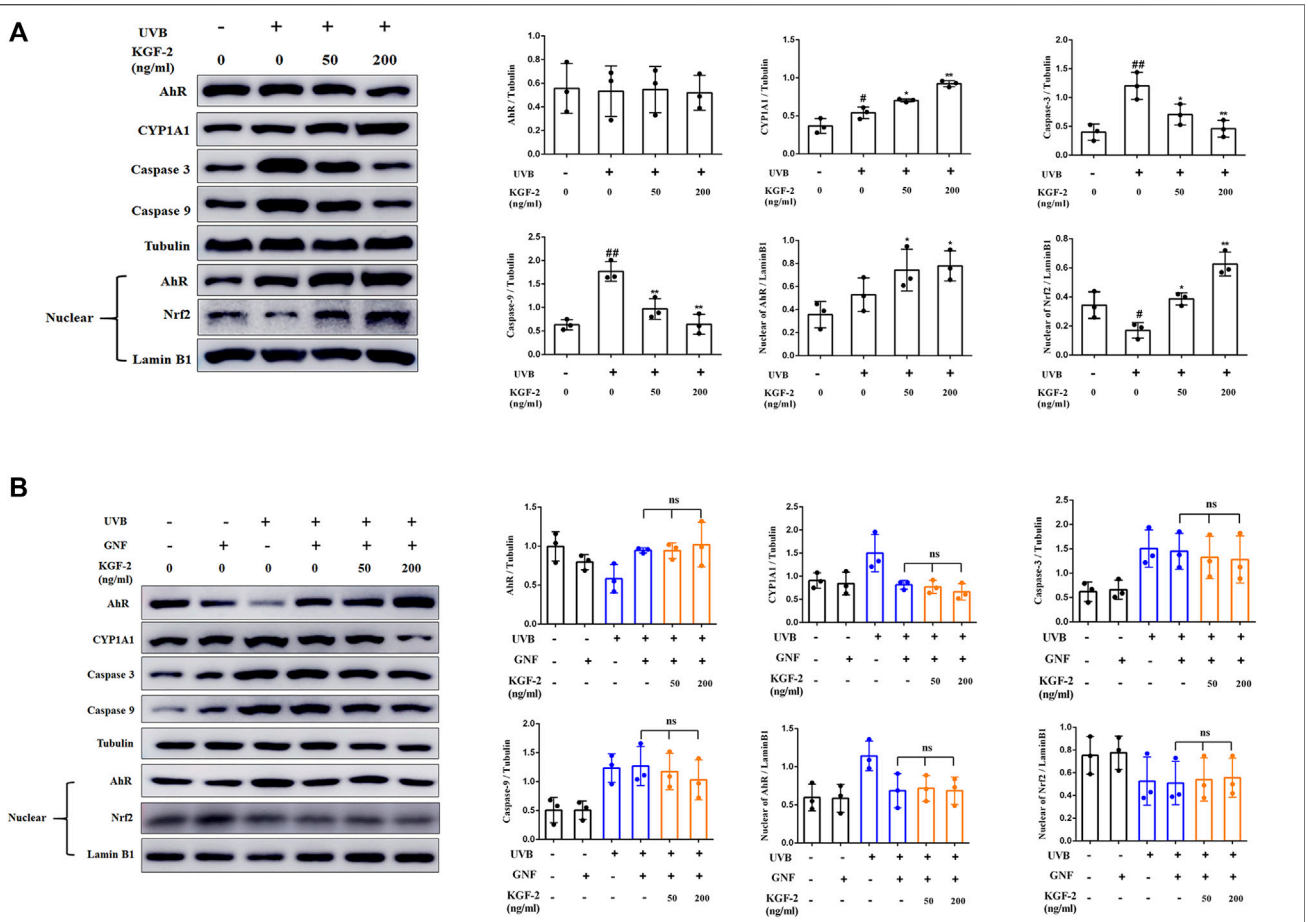

FIGURE 4 | Effects of KGF-2 on the AhR/Nrf2 signaling pathway in keratinocytes following UVB irradiation. **(A)** HaCaT cells were treated with or without KGF-2 for 4 h followed by exposure to UVB (200 mJ/cm^2) and a further 30-min incubation. The cells were then subjected to western blot analysis to measure the levels of AhR, CYP1A1, caspase 3, caspase 9 in cytoplasm and the levels of AhR, and Nrf2 in nucleus, the plot compares the protein level of HaCaT cells from three different experiments. AhR: UVB only *vs.* untreated control group, $p = 0.9976$; KGF-2 (50 ng/ml) *vs.* UVB only group, $p = 0.9995$; KGF-2 (200 ng/ml) *vs.* UVB only group, $p = 0.9995$. CYP1A1: UVB only *vs.* untreated control group, $p = 0.0288$; KGF-2 (50 ng/ml) *vs.* UVB only group, $p = 0.0378$; KGF-2 (200 ng/ml) *vs.* UVB only group, $p = 0.0003$. Caspase 3: UVB only *vs.* untreated control group, $p = 0.0015$; KGF-2 (50 ng/ml) *vs.* UVB only group, $p = 0.0237$; KGF-2 (200 ng/ml) *vs.* UVB only group, $p = 0.0025$. Caspase 9: UVB only *vs.* untreated control group, $p = 0.0003$; KGF-2 (50 ng/ml) *vs.* UVB only group, $p = 0.0025$; KGF-2 (200 ng/ml) *vs.* UVB only group, $p = 0.0003$. AhR in nucleus: UVB only *vs.* untreated control group, $p = 0.3802$; KGF-2 (50 ng/ml) *vs.* UVB only group, $p = 0.2422$; KGF-2 (200 ng/ml) *vs.* UVB only group, $p = 0.1558$. Nrf2 in nucleus: UVB only *vs.* untreated control group, $p = 0.0390$; KGF-2 (50 ng/ml) *vs.* UVB only group, $p = 0.0131$; KGF-2 (200 ng/ml) *vs.* UVB only group, $p = 0.0001$. **(B)** HaCaT cells were pretreated with or without GNF351 for 12 h followed by identical treatment as western blot analysis as in A. AhR: KGF-2 (50 ng/ml) *vs.* UVB + GNF group, $p = 0.9999$; KGF-2 (200 ng/ml) *vs.* UVB + GNF group, $p = 0.9746$. CYP1A1: KGF-2 (50 ng/ml) *vs.* UVB + GNF group, $p = 0.9987$; KGF-2 (200 ng/ml) *vs.* UVB + GNF group, $p = 0.9746$. Caspase 3: KGF-2 (50 ng/ml) *vs.* UVB + GNF group, $p = 0.9898$; KGF-2 (200 ng/ml) *vs.* UVB + GNF group, $p = 0.9650$. Caspase 9: KGF-2 (50 ng/ml) *vs.* UVB + GNF group, $p = 0.9904$; KGF-2 (200 ng/ml) *vs.* UVB + GNF group, $p = 0.7419$. AhR in nucleus: KGF-2 (50 ng/ml) *vs.* UVB + GNF group, $p = 0.9997$; KGF-2 (200 ng/ml) *vs.* UVB + GNF group, $p = 0.9999$. Nrf2 in nucleus: KGF-2 (50 ng/ml) *vs.* UVB + GNF group, $p = 0.9997$; KGF-2 (200 ng/ml) *vs.* UVB + GNF group, $p = 0.9971$. All graphical data are the means ± SD from three independent experiments, "#" and "##" indicate significantly different from the untreated control group at the $p < 0.05$ and $p < 0.01$ levels, respectively, "*" and "**" indicate significantly different from the UVB only control group at the $p < 0.05$ and $p < 0.01$ levels, respectively.

important biomarker of DNA damage, but is also an important marker of apoptosis (Zhao et al., 2014; Huang et al., 2003). KGF-2 also decreased the formation of CPD and γ-H2AX in HEE and HaCaT cell (**Figures 1C**, **2D**), indicating that KGF-2 could protect the epidermis from UVB induced DNA damage. One of the most obvious acute effects of UV on the skin is the induction of inflammation. Several studies have shown that UVB stimulates release of IL-1β, IL-6, and TNF-α in epidermis, which cause pain and redness (Rabe et al., 2006; Oh et al., 2014; Prasad and Katiyar 2017). Our data explicitly showed that KGF-2 was able to inhibit the production of proinflammatory cytokines (IL-1β, IL-6, and TNF-α) in UVB-irradiated HEEs, consistent with our expectation (**Figure 1D**).

Changes in the skin following UV exposure are associated with changes at the cellular level. HaCaT, a spontaneously immortalized human keratinocyte cell line, possesses similar biological characteristics as those found in primary keratinocytes, making them suitable for studying UVB-induced epidermal damage *in vitro*. Several experiments were performed to determine

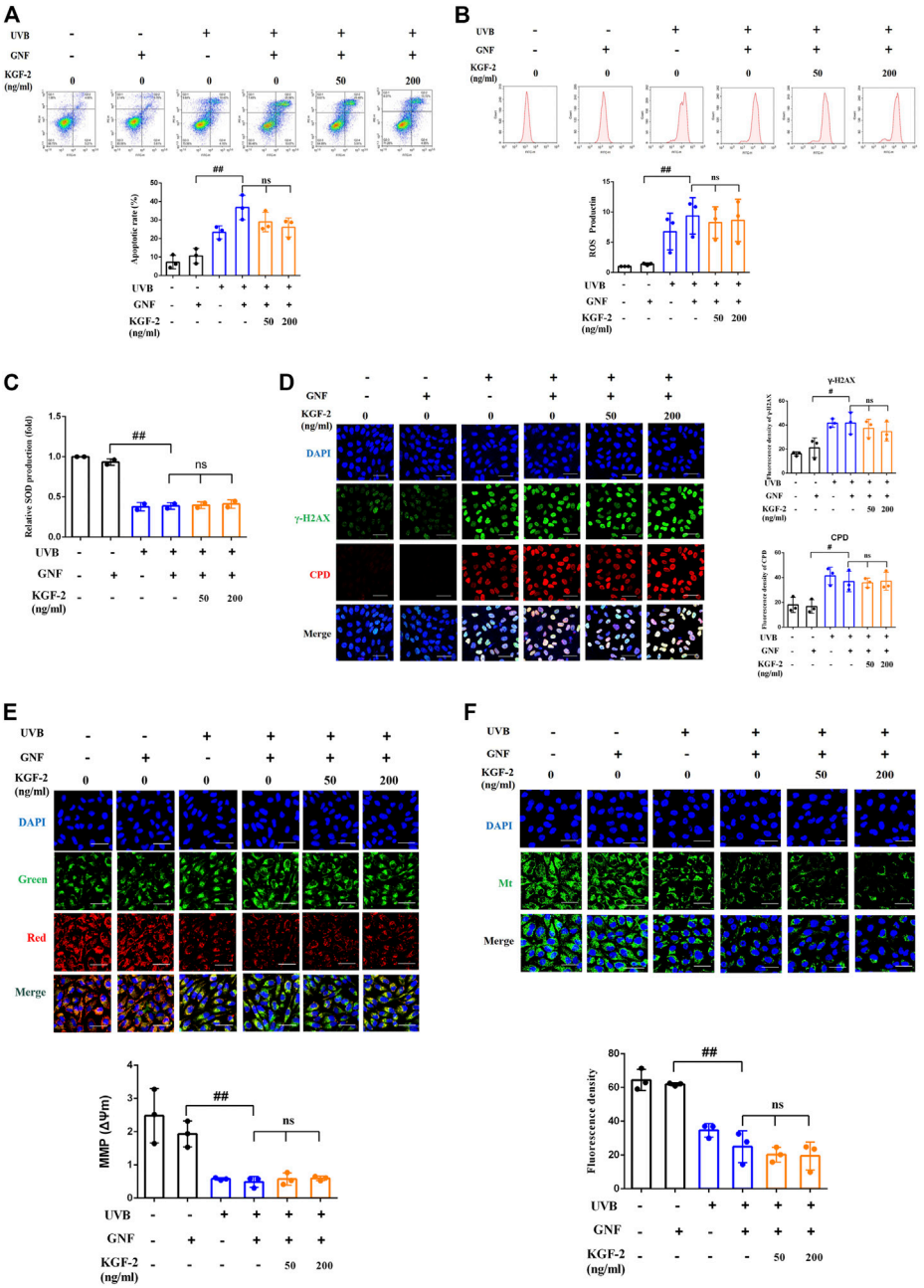

FIGURE 5 | HaCaT cells were pretreated with or without GNF351 for 12 h prior and then treated with KGF-2. After that, the cells were treated with or without KGF-2 for 4 h, and then exposed to UVB (200 mJ/cm^2). The protective effect of KGF-2 on the UVB-induced cell damage was then determined. **(A)** Flow cytometric analysis of apoptotic HaCaT cells, the plot compares the apoptotic rates from three different treatments. UVB + GNF *vs.* GNF group, $p = 0.0001$; KGF-2 (50 ng/ml) *vs.* UVB + GNF group, $p = 0.2314$; KGF-2 (200 ng/ml) *vs.* UVB + GNF group, $p = 0.0675$. **(B)** Representative image of intracellular ROS levels; The plot compares the relative ROS production from three different treatments. UVB + GNF *vs.* GNF group, $p = 0.0083$; KGF-2 (50 ng/ml) *vs.* UVB + GNF group, $p = 0.9729$; KGF-2 (200 ng/ml) *vs.* UVB + GNF group, $p = 0.9952$. **(C)** SOD levels from different treatments. UVB + GNF *vs.* GNF group, $p < 0.0001$; KGF-2 (50 ng/ml) *vs.* UVB + GNF group, $p = 0.9988$; KGF-2 (200 ng/ml) *vs.* UVB + GNF group, $p = 0.9588$. **(D)** Representative image of immunofluorescence staining of CPD and γ-H2AX, the plot compares the formation of CPD and γ-H2AX from three different treatments. γ-H2AX: UVB + GNF *vs.* GNF group, $p = 0.0128$; KGF-2 (50 ng/ml) *vs.* UVB + GNF group, $p = 0.8935$; KGF-2 (200 ng/ml) *vs.* UVB + GNF group, $p = 0.6063$. CPD: UVB + GNF *vs.* GNF group, $p = 0.0155$; KGF-2 (50 ng/ml) *vs.* UVB + GNF group, $p = 0.9997$; KGF-2 (200 ng/ml) *vs.* UVB + GNF group, $p = 0.9999$. **(E)** Representative image of mitochondrial membrane potential (MMP) in HaCaT cells, the plot compares the MMP of HaCaT cells from three different treatments. UVB + GNF *vs.* GNF group, $p = 0.0002$; KGF-2 (50 ng/ml) *vs.* UVB + GNF group, $p = 0.99855$; KGF-2 (200 ng/ml) *vs.* UVB + GNF group, $p = 0.9961$. **(F)** Representative image of mitochondrial mass, the plot compares the mitochondrial mass of HaCaT cells from three different treatments. UVB + GNF *vs.* GNF group, $p < 0.0001$; KGF-2 (50 ng/ml) *vs.* UVB + GNF group, $p = 0.8163$; KGF-2 (200 ng/ml) *vs.* UVB + GNF group, $p = 0.7211$. All graphical data are the means ± SD from three independent experiments, "#" and "##" indicate significantly different from the GNF only control group at the $p < 0.05$ and $p < 0.01$ levels, respectively, "*" and "**" indicate significantly different from the UVB + GNF group at the $p < 0.05$ and $p < 0.01$ levels, respectively.

whether KGF-2 could reduce UVB-induced damage in HaCaT cell. HaCaT cells irradiated with UVB clearly exhibited increased apoptotic rate and DNA damage, ROS overproduction and loss of SOD as well as the presence of mitochondrial dysfunction. The concurrent increase in ROS production and inhibition of antioxidant defense mechanism could result in mitochondrial dysfunctions (Yoon et al., 2010; Hwang et al., 2014; Kudryavtseva et al., 2016). These effects appeared to be suppressed by KGF-2, clearly demonstrating a protective role for KGF-2 in the reduction of oxidative stress, DNA damage, apoptosis, and mitochondrial dysfunction in HaCaT cells, providing a further evidence that KGF-2 may be crucial for an efficient skin photoprotection.

UVB is absorbed by the aromatic amino acid tryptophan present in the cells, leading to the formation of FICZ that binds AhR with high affinity to regulate the expression of several genes with toxic or protective effects (Fritsche et al., 2007; Diani-Moore et al., 2011), (Nebert 2017; Rothhammer and Quintana 2019). UVB irradiation could trigger the translocation of AhR from the cytosol to the nucleus in HaCaT cells, suggesting its activation by UVB. Surprisingly, KGF-2 pretreatment followed by UVB-irradiation resulted in further increase in nuclear AhR, indicating that the activation of AhR was enhanced by KGF-2 (**Figure 4A**). AhR mediates the cutaneous stress response toward a variety of environmental noxae and therefore it has attracted great interest in the field of modern preventive medicine (Haarmann-Stemmann et al., 2012). Several studies have demonstrated that AhR can contribute to the pathogenesis of some skin diseases. Indeed, the activation of AhR might be advantageous to inflammation, skin barrier function, and oxidative stress. AhR has been considered as a possible therapeutic target for the treatment of skin diseases such as atopic dermatitis, psoriasis, acne, and vitiligo (Napolitano and Patruno 2018). The antioxidant response of AhR is thought to be mediated through the activation of Nrf2, since the transcription of Nrf2 is directly regulated by AhR (Miao et al., 2005). In the inactive state, Nrf2 is anchored to Keap1 in the cytoplasm. Once activated, Nrf2 departs from Keap1, leading to its stabilization, accumulation and translocation to nuclei, where it will bind to the antioxidant responsive element (ARE) on a number of antioxidant genes and regulate their expression (Itoh et al., 2004; Li and Kong 2009; Suzuki and Yamamoto 2015). The ability of KGF-2 to promote the translocation of Nrf2 to the nucleus and increase the expression of CYP1A1 suggested that KGF-2 could activate Nrf2 (**Figure 4A**). Previous studies have shown that Nrf2 plays a beneficial role in protecting skin against UVB-induced inflammation, oxidative damage, cellular dysfunction, and sunburn reaction in the skin (Saw et al., 2011; Ikehata and Yamamoto 2018). Nrf2 activation plays a critical role in the photoprotection of skin. Nrf2 deficiency exacerbates UVB-induced skin damage such as inflammation, DNA damage, and extracellular matrix damage, while the activation of Nrf2 can protect against UV-triggered skin carcinogenesis (Saw et al., 2014; Knatko et al., 2015), (Li et al., 2017; Rojo de la Vega et al., 2018; Gęgotek et al., 2018; Chaiprasongsuk et al., 2019). The AhR antagonist GNF351 can interact directly with the ligand-binding pocket and compete with a well-characterized photoaffinity AhR ligand for binding with AhR that ultimately results in the blocking of AhR nuclear translocation (van den Bogaard et al., 2015). The activation of Nrf2 triggered by KGF-2 was substantially suppressed by the AhR antagonist GNF351, indicating that KGF-2 could activate Nrf2 to exert its antioxidant effect through activating AhR after UVB irradiation. Furthermore, the ability of KGF-2 to reduce cell apoptosis and ROS production, elevate the SOD production, ameliorate DNA damage, and mitochondrial dysfunctions was completely abolished once the activation of AhR was blocked. These results demonstrated for the first time that KGF-2 may stimulate the activation of Nrf2 *via* activating the AhR pathway, thereby protecting the keratinocytes from UVB-induced cell damage. However, the precise mechanism of how KGF-2 might activate AhR is a subject of further investigation.

CONCLUSION

KGF-2 could successfully prevent UVB-induced HEE damage and significantly inhibit UVB-induced DNA damage and inflammatory response. In addition, KGF-2 could alleviate UVB-induced keratinocytes apoptosis, ROS production, DNA damage, and mitochondrial dysfunction and up-regulate SOD production in HaCaT cells. The protective mechanism of KGF-2 on UVB-induced skin damage might involve AhR-activated Nrf2 signaling. Our research could serve as a theoretical and experimental basis for the development and application of KGF-2 in protecting human skin against UVB irradiation.

DATA AVAILABILITY STATEMENT

The raw data supporting the conclusions of this article will be made available by the authors, without undue reservation, to any qualified researcher.

AUTHOR CONTRIBUTIONS

NX and XiL conceived and designed the experiments. SG, KG, and YC performed the experiments. SG, RJ, and JZ analyzed the data. SG, XuL, and LW prepared the manuscript. ZH, and NX revised the manuscript.

FUNDING

The work was supported by the Scientific and Technological Plan Project of Wenzhou (No. N20180002).

ACKNOWLEDGMENTS

We thank Alan K Chang (Wenzhou University) for his valuable work in revising the language of the manuscript.

REFERENCES

Afaq, F., Syed, D. N., Malik, A., Hadi, N., Sarfaraz, S., Kweon, M.-H., et al. (2007). Delphinidin, an Anthocyanidin in Pigmented Fruits and Vegetables, Protects Human HaCaT Keratinocytes and Mouse Skin against UVB-Mediated Oxidative Stress and Apoptosis. *J. Invest. Dermatol.* 127 (1), 222–232. doi:10.1038/sj.jid.5700510

Agostinis, P., Garmyn, M., and Van Laethem, A. (2007). The Aryl Hydrocarbon Receptor: an Illuminating Effector of the UVB Response. *Science's STKE* 2007 (403), pe49. doi:10.1126/stke.4032007pe49

Bayerl, C., Taake, S., Moll, I., and Jung, E. G. (1995). Characterization of Sunburn Cells after Exposure to Ultraviolet Light. *Photodermatol. Photoimmunol Photomed.* 11 (4), 149–154. doi:10.1111/j.1600-0781.1995.tb00157.x

Braun, S., Krampert, M., Bodó, E., Kümin, A., Born-Berclaz, C., Paus, R., et al. (2006). Keratinocyte Growth Factor Protects Epidermis and Hair Follicles from Cell Death Induced by UV Irradiation, Chemotherapeutic or Cytotoxic Agents. *J. Cel Sci no* 119 (Pt 23), 4841–4849. doi:10.1242/jcs.03259

Chaiprasongsuk, A., Janjetovic, Z., Kim, T.-K., Jarrett, S. G., D'Orazio, J. A., Holick, M. F., et al. (2019). Protective Effects of Novel Derivatives of Vitamin D3 and Lumisterol against UVB-Induced Damage in Human Keratinocytes Involve Activation of Nrf2 and P53 Defense Mechanisms. *Redox Biol.* 24, 101206. doi:10.1016/j.redox.2019.101206

Chen, H., Weng, Q. Y., and Fisher, D. E. (2014). UV Signaling Pathways within the Skin. *J. Invest. Dermatol.* 134 (8), 2080–2085. doi:10.1038/jid.2014.161

D'Orazio, J., Jarrett, S., Amaro-Ortiz, A., and Scott, T. (2013). UV Radiation and the Skin. *Int. J. Mol. Sci.* 14 (6), 12222–12248. doi:10.3390/ijms140612222

Darr, D., and Fridovich, I. (1994). Free Radicals in Cutaneous Biology. *J. Invest. Dermatol.* 102 (5), 671–675. doi:10.1111/1523-1747.ep12374036

de Gruijl, F. R. (2000). [33] Photocarcinogenesis: UVA vs UVB. *Methods Enzymol.* 319, 359–366. doi:10.1016/s0076-6879(00)19035-4

Deshmukh, J., Pofahl, R., and Haase, I. (2017). Epidermal Rac1 Regulates the DNA Damage Response and Protects from UV-Light-Induced Keratinocyte Apoptosis and Skin Carcinogenesis. *Cell Death Dis* 8 (3), e2664. doi:10.1038/cddis.2017.63

Diani-Moore, S., Ma, Y., Labitzke, E., Tao, H., David Warren, J., Anderson, J., et al. (2011). Discovery and Biological Characterization of 1-(1h-Indol-3-Yl)-9h-Pyrido[3,4-B]indole as an Aryl Hydrocarbon Receptor Activator Generated by Photoactivation of Tryptophan by Sunlight. *Chemico-Biological Interactions* 193 (2), 119–128. doi:10.1016/j.cbi.2011.05.010

Dong, L., Li, R., Li, D., Wang, B., Lu, Y., Li, P., et al. (2019). FGF10 Enhances Peripheral Nerve Regeneration *via* the Preactivation of the PI3K/Akt Signaling-Mediated Antioxidant Response. *Front. Pharmacol.* 10, 1224. doi:10.3389/fphar.2019.01224

Eckhart, L., and Zeeuwen, P. L. J. M. (2018). The Skin Barrier: Epidermis vs Environment. *Exp. Dermatol.* 27 (8), 805–806. doi:10.1111/exd.13731

Fritsche, E., Schäfer, C., Calles, C., Bernsmann, T., Bernshausen, T., Wurm, M., et al. (2007). Lightening up the UV Response by Identification of the Arylhydrocarbon Receptor as a Cytoplasmatic Target for Ultraviolet B Radiation. *Proc. Natl. Acad. Sci.* 104 (21), 8851–8856. doi:10.1073/pnas.0701764104

Gęgotek, A., Jastrząb, A., Jarocka-Karpowicz, I., Muszyńska, M., and Skrzydlewska, E. (2018). The Effect of Sea Buckthorn (Hippophae Rhamnoides L.) Seed Oil on UV-Induced Changes in Lipid Metabolism of Human Skin Cells. *Antioxidants (Basel)* 7 (9). 110. doi:10.3390/antiox7090110

Garinis, G. A., Mitchell, J. R., Moorhouse, M. J., Hanada, K., de Waard, H., Vandeputte, D., et al. (2005). Transcriptome Analysis Reveals Cyclobutane Pyrimidine Dimers as a Major Source of UV-Induced DNA Breaks. *Embo J.* 24 (22), 3952–3962. doi:10.1038/sj.emboj.7600849

Haarmann-Stemmann, T., Abel, J., Fritsche, E., and Krutmann, J. (2012). The AhR-Nrf2 Pathway in Keratinocytes: on the Road to Chemoprevention? *J. Invest. Dermatol.* 132 (1), 7–9. doi:10.1038/jid.2011.359

Huang, X., Traganos, F., and Darzynkiewicz, Z. (2003). DNA Damage Induced by DNA Topoisomerase I- and Topoisomerase II-Inhibitors Detected by Histone H2AX Phosphorylation in Relation to the Cell Cycle Phase and Apoptosis. *Cell Cycle* 2 (6), 614–619. doi:10.4161/cc.2.6.565

Hwang, E., Park, S.-Y., Lee, H. J., Lee, T. Y., Sun, Z.-w., and Yi, T. H. (2014). Gallic Acid Regulates Skin Photoaging in UVB-Exposed Fibroblast and Hairless Mice. *Phytother. Res.* 28 (12), 1778–1788. doi:10.1002/ptr.5198

Ikehata, H., and Yamamoto, M. (2018). Roles of the KEAP1-NRF2 System in Mammalian Skin Exposed to UV Radiation. *Toxicol. Appl. Pharmacol.* 360, 69–77. doi:10.1016/j.taap.2018.09.038

Itoh, K., Tong, K. I., and Yamamoto, M. (2004). Molecular Mechanism Activating Nrf2-Keap1 Pathway in Regulation of Adaptive Response to Electrophiles. *Free Radic. Biol. Med.* 36 (10), 1208–1213. doi:10.1016/j.freeradbiomed.2004.02.075

Itoh, T., and Horio, T. (2001). DNA-dependent Protein Kinase Catalytic Subunit Is Cleaved during UV-Induced Apoptosis. *J. Dermatol. Sci.* 25 (1), 72–77. doi:10.1016/s0923-1811(00)00107-9

Kamarajan, P., and Chao, C. C.-K. (2000). UV-induced Apoptosis in Resistant HeLa Cells. *Biosci. Rep. No* 20 (2), 99–108. doi:10.1023/a:1005515400285

Kciuk, M., Marciniak, B., Mojzych, M., and Kontek, R. (2020). Focus on UV-Induced DNA Damage and Repair-Disease Relevance and Protective Strategies. *Int. J. Mol. Sci.* 21 (19), 7264. doi:10.3390/ijms21197264

Kim, K. M., Im, A.-R., Park, S. K., Shin, H. S., and Chae, S.-w. (2019). Protective Effects of Timosaponin AIII against UVB-Radiation Induced Inflammation and DNA Injury in Human Epidermal Keratinocytes. *Biol. Pharm. Bull.* 42 (9), 1524–1531. doi:10.1248/bpb.b19-00222

Kim, Y., Lee, S. K., Bae, S., Kim, H., Park, Y., Chu, N. K., et al. (2013). The Anti-inflammatory Effect of Alloferon on UVB-Induced Skin Inflammation through the Down-Regulation of Pro-inflammatory Cytokines. *Immunol. Lett.* 149 (1-2), 110–118. doi:10.1016/j.imlet.2012.09.005

Knatko, E. V., Ibbotson, S. H., Zhang, Y., Higgins, M., Fahey, J. W., Talalay, P., et al. (2015). Nrf2 Activation Protects against Solar-Simulated Ultraviolet Radiation in Mice and Humans. *Cancer Prev. Res.* 8 (6), 475–486. doi:10.1158/1940-6207.capr-14-0362

Kovacs, D., Raffa, S., Flori, E., Aspite, N., Briganti, S., Cardinali, G., et al. (2009). Keratinocyte Growth Factor Down-Regulates Intracellular ROS Production Induced by UVB. *J. Dermatol. Sci.* 54 (2), 106–113. doi:10.1016/j.jdermsci.2009.01.005

Kuanpradit, C., Jaisin, Y., Jungudomjaroen, S., Mitu, S. A., Puttikamonkul, S., Sobhon, P., et al. (2017). Attenuation of UV-B Exposure-Induced Inflammation by Abalone Hypobranchial Gland and Gill Extracts. *Int. J. Mol. Med. No* 39 (5), 1083–1090. doi:10.3892/ijmm.2017.2939

Kudryavtseva, A. V., Krasnov, G. S., Dmitriev, A. A., Alekseev, B. Y., Kardymon, O. L., Sadritdinova, A. F., et al. (2016). Mitochondrial Dysfunction and Oxidative Stress in Aging and Cancer. *Oncotarget* 7 (29), 44879–44905. doi:10.18632/oncotarget.9821

Laethem, A. V., Claerhout, S., Garmyn, M., and Agostinis, P. (2005). The Sunburn Cell: Regulation of Death and Survival of the Keratinocyte. *Int. J. Biochem. Cel Biol.* 37 (8), 1547–1553. doi:10.1016/j.biocel.2005.02.015

Li, H., Jiang, N., Liang, B., Liu, Q., Zhang, E., Peng, L., et al. (2017). Pterostilbene Protects against UVB-Induced Photo-Damage through a Phosphatidylinositol-3-kinase-dependent Nrf2/ARE Pathway in Human Keratinocytes. *Redox Rep.* 22 (6), 501–507. doi:10.1080/13510002.2017.1329917

Li, W., and Kong, A.-N. (2009). Molecular Mechanisms of Nrf2-Mediated Antioxidant Response. *Mol. Carcinog.* 48 (2), 91–104. doi:10.1002/mc.20465

Marchese, C., Maresca, V., Cardinali, G., Belleudi, F., Ceccarelli, S., Bellocci, M., et al. (2003). UVB-induced Activation and Internalization of Keratinocyte Growth Factor Receptor. *Oncogene* 22 (16), 2422–2431. doi:10.1038/sj.onc.1206301

Miao, W., Hu, L., Scrivens, P. J., and Batist, G. (2005). Transcriptional Regulation of NF-E2 P45-Related Factor (NRF2) Expression by the Aryl Hydrocarbon Receptor-Xenobiotic Response Element Signaling Pathway. *J. Biol. Chem.* 280 (21), 20340–20348. doi:10.1074/jbc.M412081200

Nakanishi, M., Niida, H., Murakami, H., and Shimada, M. (2009). DNA Damage Responses in Skin Biology-Implications in Tumor Prevention and Aging Acceleration. *J. Dermatol. Sci.* 56 (2), 76–81. doi:10.1016/j.jdermsci.2009.09.001

Napolitano, M., and Patruno, C. (2018). Aryl Hydrocarbon Receptor (AhR) a Possible Target for the Treatment of Skin Disease. *Med. Hypotheses* 116, 96–100. doi:10.1016/j.mehy.2018.05.001

Nebert, D. W. (2017). Aryl Hydrocarbon Receptor (AHR): "pioneer Member" of the basic-helix/loop/helix Per - Arnt - Sim (bHLH/PAS) Family of "sensors" of Foreign and Endogenous Signals. *Prog. Lipid Res.* 67, 38–57. doi:10.1016/j.plipres.2017.06.001

Oh, J. E., Kim, M. S., Jeon, W.-K., Seo, Y. K., Kim, B.-C., Hahn, J. H., et al. (2014). A Nuclear Factor Kappa B-Derived Inhibitor Tripeptide Inhibits UVB-Induced

Photoaging Process. *J. Dermatol. Sci.* 76 (3), 196–205. doi:10.1016/j.jdermsci.2014.10.002

Oh, Y., Lim, H.-W., Huang, Y.-H., Kwon, H.-S., Jin, C. D., Kim, K., et al. (2016). Attenuating Properties of Agastache Rugosa Leaf Extract against Ultraviolet-B-Induced Photoaging *via* Up-Regulating Glutathione and Superoxide Dismutase in a Human Keratinocyte Cell Line. *J. Photochem. Photobiol. B: Biol.* 163, 170–176. doi:10.1016/j.jphotobiol.2016.08.026

Perluigi, M., Di Domenico, F., Blarzino, C., Foppoli, C., Cini, C., Giorgi, A., et al. (2010). Effects of UVB-Induced Oxidative Stress on Protein Expression and Specific Protein Oxidation in normal Human Epithelial Keratinocytes: a Proteomic Approach. *Proteome Sci.* 8, 13. doi:10.1186/1477-5956-8-13

Piotrowska, A., Wierzbicka, J., Ślebioda, T., Woźniak, M., Tuckey, R. C., Slominski, A. T., et al. (2016). Vitamin D Derivatives Enhance Cytotoxic Effects of H2O2 or Cisplatin on Human Keratinocytes. *Steroids* 110, 49–61. doi:10.1016/j.steroids.2016.04.002

Prasad, R., and Katiyar, S. K. (2017). Crosstalk Among UV-Induced Inflammatory Mediators, DNA Damage and Epigenetic Regulators Facilitates Suppression of the Immune System. *Photochem. Photobiol.* 93 (4), 930–936. doi:10.1111/php.12687

Rabe, J. H., Mamelak, A. J., McElgunn, P. J. S., Morison, W. L., and Sauder, D. N. (2006). Photoaging: Mechanisms and Repair. *J. Am. Acad. Dermatol.* 55 (1), 1–19. doi:10.1016/j.jaad.2005.05.010

Rastogi, R. P., Richa, A. Kumar, M. B. Tyagi., Kumar, A., Tyagi, M. B., and Sinha, R. P. (2010). Molecular Mechanisms of Ultraviolet Radiation-Induced DNA Damage and Repair. *J. Nucleic Acids* 2010, 1–32. doi:10.4061/2010/592980

Rojo de la Vega, M., Zhang, D. D., and Wondrak, G. T. (2018). Topical Bixin Confers NRF2-dependent Protection against Photodamage and Hair Graying in Mouse Skin. *Front. Pharmacol.* 9, 287. doi:10.3389/fphar.2018.00287

Rothhammer, V., and Quintana, F. J. (2019). The Aryl Hydrocarbon Receptor: an Environmental Sensor Integrating Immune Responses in Health and Disease. *Nat. Rev. Immunol.* 19 (3), 184–197. doi:10.1038/s41577-019-0125-8

Saw, C. L., Huang, M.-T., Liu, Y., Khor, T. O., Conney, A. H., and Kong, A.-N. (2011). Impact of Nrf2 on UVB-Induced Skin Inflammation/photoprotection and Photoprotective Effect of Sulforaphane. *Mol. Carcinog.* 50 (6), 479–486. doi:10.1002/mc.20725

Saw, C. L., Yang, A., Huang, M.-T., Liu, Y., Lee, J., Khor, T., et al. (2014). Nrf2 Null Enhances UVB-Induced Skin Inflammation and Extracellular Matrix Damages. *Cell Biosci* 4, 39. doi:10.1186/2045-3701-4-39

Shi, X., Liu, H.-y., Li, S.-p., and Xu, H.-b. (2018). Keratinocyte Growth Factor Protects Endometrial Cells from Oxygen Glucose Deprivation/re-Oxygenation *via* Activating Nrf2 Signaling. *Biochem. Biophysical Res. Commun.* 501 (1), 178–185. doi:10.1016/j.bbrc.2018.04.208

Smits, J. P. H., Niehues, H., Rikken, G., van Vlijmen-Willems, I. M. J. J., van de Zande, G. W. H. J. F., Zeeuwen, P. L. J. M., et al. (2017). Immortalized N/TERT Keratinocytes as an Alternative Cell Source in 3D Human Epidermal Models. *Sci. Rep.* 7 (1), 11838. doi:10.1038/s41598-017-12041-y

Soler, P. M., Wright, T. E., Smith, P. D., Maggi, S. P., Hill, D. P., Ko, F., et al. (1999). *In Vivo* characterization of Keratinocyte Growth Factor-2 as a Potential Wound Healing Agent. *Wound Repair Regen.* 7 (3), 172–178. doi:10.1046/j.1524-475x.1999.00172.x

Suzuki, T., and Yamamoto, M. (2015). Molecular Basis of the Keap1-Nrf2 System. *Free Radic. Biol. Med.* 88 (Pt B), 93–100. doi:10.1016/j.freeradbiomed.2015.06.006

Takahashi, H., Kinouchi, M., and Iizuka, H. (1997). Interleukin-1β-Converting Enzyme and CPP32 Are Involved in Ultraviolet B-Induced Apoptosis of SV40-Transformed Human Keratinocytes. *Biochem. Biophysical Res. Commun.* 236 (1), 194–198. doi:10.1006/bbrc.1997.6931

Takeoka, M., Ward, W. F., Pollack, H., Kamp, D. W., and Panos, R. J. (1997). KGF Facilitates Repair of Radiation-Induced DNA Damage in Alveolar Epithelial Cells. *Am. J. Physiology-Lung Cell Mol. Physiol.* 272 (6 Pt 1), L1174–L1180. doi:10.1152/ajplung.1997.272.6.L1174

Tan, X., Yu, L., Yang, R., Tao, Q., Xiang, L., Xiao, J., et al. (2020). Fibroblast Growth Factor 10 Attenuates Renal Damage by Regulating Endoplasmic Reticulum Stress after Ischemia-Reperfusion Injury. *Front. Pharmacol.* 11, 39. doi:10.3389/fphar.2020.00039

Tomaino, A., Cristani, M., Cimino, F., Speciale, A., Trombetta, D., Bonina, F., et al. (2006). *In Vitro* protective Effect of a Jacquez Grapes Wine Extract on UVB-Induced Skin Damage. *Toxicol. Vitro* 20 (8), 1395–1402. doi:10.1016/j.tiv.2006.06.005

Upadhyay, D., Bundesmann, M., Panduri, V., Correa-Meyer, E., and Kamp, D. W. (2004). Fibroblast Growth Factor-10 Attenuates H2O2-Induced Alveolar Epithelial Cell DNA Damage. *Am. J. Respir. Cel Mol Biol* 31 (1), 107–113. doi:10.1165/rcmb.2003-0064OC

Upadhyay, D., Panduri, V., and Kamp, D. W. (2005). Fibroblast Growth Factor-10 Prevents Asbestos-Induced Alveolar Epithelial Cell Apoptosis by a Mitogen-Activated Protein Kinase-dependent Mechanism. *Am. J. Respir. Cel Mol Biol* 32 (3), 232–238. doi:10.1165/rcmb.2004-0242OC

van den Bogaard, E. H., Podolsky, M. A., Smits, J. P., Cui, X., John, C., Gowda, K., et al. (2015). Genetic and Pharmacological Analysis Identifies a Physiological Role for the AHR in Epidermal Differentiation. *J. Invest. Dermatol.* 135 (5), 1320–1328. doi:10.1038/jid.2015.6

Villard, P. H., Sampol, E., Elkaim, J. L., Puyoou, F., Casanova, D., Sérée, E., et al. (2002). Increase of CYP1B1 Transcription in Human Keratinocytes and HaCaT Cells after UV-B Exposure. *Toxicol. Appl. Pharmacol.* 178 (3), 137–143. doi:10.1006/taap.2001.9335

Wang, E., Marcotte, R., and Petroulakis, E. (1999). Signaling Pathway for Apoptosis: a Racetrack for Life or Death. *J. Cel. Biochem.* 75 (Suppl. 32-33), 95–102. doi:10.1002/(sici)1097-4644(1999)75:32+<95::aid-jcb12>3.0.co;2-f

Werner, S., Krieg, T., and Smola, H. (2007). Keratinocyte-fibroblast Interactions in Wound Healing. *J. Invest. Dermatol.* 127 (5), 998–1008. doi:10.1038/sj.jid.5700786

Yoon, S., Woo, S. U., Kang, J. H., Kim, K., Kwon, M.-H., Park, S., et al. (2010). STAT3 Transcriptional Factor Activated by Reactive Oxygen Species Induces IL6 in Starvation-Induced Autophagy of Cancer Cells. *Autophagy* 6 (8), 1125–1138. doi:10.4161/auto.6.8.13547

Yoshida, N., Sawada, E., and Imokawa, G. (2012). A Reconstructed Human Epidermal Keratinization Culture Model to Characterize Ceramide Metabolism in the Stratum Corneum. *Arch. Dermatol. Res.* 304 (7), 563–577. doi:10.1007/s00403-012-1232-6

Zhao, X., Toyooka, T., and Ibuki, Y. (2014). Silver Ions Enhance UVB-Induced Phosphorylation of Histone H2AX. *Environ. Mol. Mutagen.* 55 (7), 556–565. doi:10.1002/em.21875

Conflict of Interest: The authors declare that the research was conducted in the absence of any commercial or financial relationships that could be construed as a potential conflict of interest.

frontiers in Cell and Developmental Biology

ORIGINAL RESEARCH
published: 14 June 2021
doi: 10.3389/fcell.2021.693694

Hypoxia Response Element-Directed Expression of aFGF in Neural Stem Cells Promotes the Recovery of Spinal Cord Injury and Attenuates SCI-Induced Apoptosis

Yibo Ying[1,2†], Yifan Zhang[1†], Yurong Tu[1†], Min Chen[1†], Zhiyang Huang[1], Weiyang Ying[3], Qiuji Wu[1], Jiahui Ye[1], Ziyue Xiang[1], Xiangyang Wang[1], Zhouguang Wang[1,2*] and Sipin Zhu[1,2*]*

[1] Department of Orthopaedics, The Second Affiliated Hospital and Yuying Children's Hospital of Wenzhou Medical University, Wenzhou, China, [2] Molecular Pharmacology Research Center, School of Pharmaceutical Science, Wenzhou Medical University, Wenzhou, China, [3] Department of Pain Medicine, The Second Affiliated Hospital and Yuying Children's Hospital of Wenzhou Medical University, Wenzhou, China

Reducing neuronal death after spinal cord injury (SCI) is considered to be an important strategy for the renovation of SCI. Studies have shown that, as an important regulator of the development and maintenance of neural structure, acidic fibroblast growth factor (aFGF) has the role of tissue protection and is considered to be an effective drug for the treatment of SCI. Neural stem cells (NSCs) are rendered with the remarkable characteristics to self-replace and differentiate into a variety of cells, so it is promising to be used in cell transplantation therapy. Based on the facts above, our main aim of this research is to explore the role of NSCs expressing aFGF meditated by five hypoxia-responsive elements (5HRE) in the treatment of SCI by constructing AAV–5HRE–aFGF–NSCs and transplanting it into the area of SCI. Our research results showed that AAV–5HRE–aFGF–NSCs can effectively restore the motor function of rats with SCI. This was accomplished by inhibiting the expression of caspase 12/caspase 3 pathway, EIF2α–CHOP pathway, and GRP78 protein to inhibit apoptosis.

Keywords: spinal cord injury, acidic fibroblast growth factor, adeno-associated virus, neural stem cell, endoplasmic reticulum stress, apoptosis

OPEN ACCESS

Edited by:
Yidong Wang,
Xian Jiaotong University, China

Reviewed by:
Lin Zhou,
Guangzhou Medical University, China
Fangming Song,
Guangxi Medical University, China

***Correspondence:**
Xiangyang Wang
xiangyangwang@wmu.edu.cn
Zhouguang Wang
wzhouguang@gmail.com
Sipin Zhu
sipinzhu@163.com

† These authors have contributed equally to this work

Specialty section:
This article was submitted to Stem Cell Research, a section of the journal Frontiers in Cell and Developmental Biology

Received: *11 April 2021*
Accepted: *10 May 2021*
Published: *14 June 2021*

Citation:
Ying Y, Zhang Y, Tu Y, Chen M, Huang Z, Ying W, Wu Q, Ye J, Xiang Z, Wang X, Wang Z and Zhu S (2021) Hypoxia Response Element-Directed Expression of aFGF in Neural Stem Cells Promotes the Recovery of Spinal Cord Injury and Attenuates SCI-Induced Apoptosis. Front. Cell Dev. Biol. 9:693694. doi: 10.3389/fcell.2021.693694

INTRODUCTION

Spinal cord injury (SCI) is a catastrophic traumatic illness in the central nervous system (CNS), which can lead to impaired movement, sensation, and other functions (Ahuja et al., 2017; Chhabra and Sarda, 2017; Bradbury and Burnside, 2019; Song et al., 2019). It is estimated that 2.5 million people worldwide suffer from SCI, and over 130,000 new cases are reported each year (Thuret et al., 2006). Due to the non-regeneration of the CNS, SCI may lead to permanent functional damage (Sofroniew, 2018). Apoptosis can result in the loss of numerous neurons, which contributes to the

sensory and motor function loss (Crowe et al., 1997; Beattie, 2004; Abbaszadeh et al., 2020; Shi et al., 2021). Therefore, it is of great significance to take apoptosis as the target for the renovation of SCI.

At present, the treatment of acute SCI is limited to surgery and hormone therapy, and its clinical effect is not ideal (Ramer et al., 2014). Studies have shown that the CNS is very difficult to repair, and scientists hope that advances in stem cell research may eventually restore neurocirculation in people with SCI, putting the hope of future treatment on stem cells (Bourzac, 2016). NSCs isolated from the developing CNS and peripheral nervous system have aroused increasing interest of researchers (Peruzzotti-Jametti et al., 2018; Deng et al., 2019). NSCs have the ability to self-replace and differentiate into a variety of cells (Navarro Negredo et al., 2020). Some experiments have shown that after transplantation, most of the NSCs differentiate into corresponding cells and migrate and integrate into the host tissue due to the regulation of signal factors (Denoth-Lippuner and Jessberger, 2021). Thus, the neural loop is reconstructed, and the relay station between the regenerated axons of the host and the denervated neurons is provided (Xu et al., 2011; Li et al., 2020; Zheng et al., 2020). As an immune exemption organ, the CNS has almost no rejection in neural stem cell transplantation between different individuals and even between different species (Xu et al., 2011). Therefore, NSCs are a good choice for stem cell transplantation in the treatment of SCI.

AFGF has been proved to be an important molecule in the growth and development of spinal cord (Tsai et al., 2006; Kuo et al., 2011; Wang et al., 2018). AFGF plays a significant role in expressing mitosis and pluripotent activity, which is closely related to the development and maintenance of neural structure (Nurcombe et al., 1993). Some studies have shown that aFGF has a tissue-protective effect and can promote the repair of SCI (Eckenstein et al., 1991; Maquet et al., 2001; Wang et al., 2017). However, previous studies have shown that the effect of using conventional methods to apply aFGF to the site of SCI is not ideal. The possible reason is that direct injection has the problems of short half-life and easy degradation. Therefore, the main purpose of this study is to improve the concentration of aFGF in the injured area by combining regulated aFGF with transplanted NSCs, so as to achieve the purpose of repairing SCI.

Adeno-associated virus (AAV) vectors are the main platform for *in vivo* gene therapy delivery. AAV is safe and can deliver its single-stranded DNA (ssDNA) vector genome to various tissues and cell types, and can be expressed for a long time (Wang et al., 2019, 2020). Hypoxia-response element (HRE) is the main regulator of cell response to hypoxia, which can regulate the transcription of specific genes under hypoxia, so it is widely used in the construction of hypoxia-regulated expression genes (Wu et al., 2015; Zhu et al., 2021). In this study, we used AAV with HRE, to induce HRE-mediated expression of aFGF of NSCs in hypoxic environment, which effectively reduced the tumorigenicity and short half-life emulated with direct injection of aFGF. Thus, AAV–5HRE–aFGF–NSCs is brought about and transplanted to the original injured site of SCI. We used video camera recording (VCR), inclined plate test, footprint analysis, and Basso–Beattie–Bresnahan (BBB) score scale to study the role of AAV–5HRE–aFGF–NSCs in the restoration of locomotion in SCI rats. In order to study the regulation of endoplasmic reticulum (ER) stress-induced apoptosis, we detected the expression of caspase 12–caspase 3, EIF2α–CHOP pathway, and GRP78. Our research shows that AAV–5HRE–aFGF–NSCs can promote the repair of SCI by inhibiting ER stress.

MATERIALS AND METHODS

Reagents and Antibodies

The primary antibodies, including aFGF (ab169748), NeuN (ab177487), caspase 12 (ab62484), caspase3 (EPR18297), EIF–2α (ab169528), CHOP (ab11419), and GRP78 [EPR4041 (2)] and the secondary antibodies: goat anti-rabbit 488 (ab150077), goat anti-mouse 488 (ab150113), goat anti-rabbit (HRP) (ab6721), and rabbit anti-mouse (HRP) (ab6728) were all bought from Abcam. The DAPI is also provided by Abcam (MC, United Kingdom).

Isolation and Culture of Neural Stem Cells

The cerebral cortex of SD rat embryos of 14–16 days were separated and immersed in D-Hanks solution. We carefully removed the cerebrovascular and meninges under the microscope. After trimming, the tissue was digested in trypsin (0.125%) and ethylenediaminetetraacetic acid (0.102%). After terminating the digestion with complete medium, we centrifuged the liquid at 1,000 rpm for 3 min and collected the cell suspension.

The components of neural stem cell culture medium (100 mL) were as follows: DMEM 96 mL, B27 2 mL, glutamine 1 mL, horse serum 1 mL, glutamine 2 mmol/L, penicillin, heparin 100 μL, basic fibroblast growth factor (bFGF) 20 μL, and epidermal growth factor (EGF) 10 μL cultured in 5% CO_2 and 37°C humidified incubator.

Polylysine Coating of Neural Stem Cells

The polylysine solution was diluted to 0.1 mg/mL with sterile water. Before use, the diluted polylysine solution was placed in a room, and the temperature was set to room temperature. Then, the slide was immersed in the diluted polylysine solution for 5 min. After completion, it was dried overnight at room temperature. Before immunofluorescence staining, the cell suspension was dropped on the glass slide and cultured in a 37°C incubator.

In vitro Scratch Motility Assay

All the cells were randomly divided into four groups, including Sham, thapsigargin (TG), 4-phenylbutyric acid (4–PBA), AAV–5HRE–NSCs, and AAV–5HRE–aFGF–NSCs group. All cells are fixed to the well plate with polylysine. The doses of Tg and 4–PBA were 100 and 500 nM, respectively.

A 200-μL tip was utilized to draw a linear scratch on the cell monolayer to generate a cell-free area. After that, the cells were

rinsed twice in PBS. At 0, 12, and 24 h, the wound was analyzed and photographed by an inverted microscope. After exporting the data, the injured area was analyzed by Image J.

Virus Construction

We used the H4409 AAV–5HRE–CMVmp vector (Obio, Shanghai, China) and then introduced aFGF into the vector through the seamless connection kit (Obio, Shanghai, China) to construct AAV–5HRE–aFGF. It was tested whether stocks of AAV–5HRE–aFGF and AAV–5HRE contain virus particles with a titer of 2.56×10^{12} and 2.32×10^{12}/mL, respectively.

Cell Transformation

After that, NSC was transduced with the multiplicity of infection of 1×10^5 AAV–5HRE–aFGF and AAV–5HRE virus particles, reaching a transduction rate of 90%. The transduced cells were cultured under hypoxia (<1% O_2) conditions for at least 6 h.

Spinal Cord Injury Model

Adult female SD rats (48) were randomly separated into four groups: Sham, SCI, AAV–5HRE–NSCs, and AAV–5HRE–aFGF–NSCs groups. The rats were placed in 5% isoflurane (220–250 g) till they lost consciousness, and then they were continuously anesthetized with 3% isoflurane. The skin of SD rats was cut along the middle of the back, and after the spinous process and lamina process of T9–T10 were cut, the spinal cords were exposed. After the midline as the center, a 10-g hammer was utilized to hit T9 segment from 25-mm high to produce acute SCI injury. The sham group went through the operation similarly without SCI by collision. The rats were given bladder massage every morning and evening to help them urinate.

Cell Transplantation

The extracted NSCs were transduced in advance with 1×10^5 multiplicity of infection of AAV–5HRE–aFGF or AAV–5HRE virus particles for over 48 h. Seven days past SCI, another operation was performed to expose the injured spinal cord. NSCs, 5×10^5 were resuspended in 10 μL at 0–4°C PBS were syringed into the SCI center (depth: 1 mm) through a stereotaxic device and a micro syringe pump. After transplantation, the mice were injected intraperitoneally (i.p.) with cyclosporine (10 mg/kg dose) for immunosuppression, which was continued every day after transplantation (Yoo et al., 2014).

Western Blot Analysis

For protein analysis, tissues were taken from the upper and lower 0.5 cm of the SCI area and quickly stored in −80°C for Western blotting analysis. The tissue was homogenized in a modified radioimmunoprecipitation assay (RIPA) buffer (25 mM Tris-HCl, 150 mM NaCl, 1% Nonidet Pmur40, 1% sodium deoxycholate, and 0.1% SDS). The extract was quantitatively analyzed by dicarboxylic acid (BCA) reagent (Thermo, Rockford, IL, United States). Gel, 11.5%, was configured, and 50 μg of protein was placed in it. Then, it was transferred to a PVDF membrane (Bio-Rad, Hercules, CA, United States). The membrane was blocked with 5% milk (Bio-Rad) in TBS containing 0.05% Tween 20 for 1 h. The membrane was incubated in anti-aFGF antibody and placed in a refrigerator at 4°C overnight. The membrane was washed in TBS three times and incubated with horseradish peroxidase-coupled secondary antibody at room temperature for 1 h. The experimental results were visualized through the ChemiDocXRS^{TM} imaging system (Bio-Rad), and the strip density was quantitatively measured using the Multigauge software of 2006 Science Lab (FUJIFILM Corporation, Tokyo, Japan). We used the analyzing Software, Quantity One (Bio-Rad) to analyze the relative density of stripes and use GAPDH to normalize them.

Locomotion Assessment

In order to evaluate the motor function after SCI, two trained researchers used the Basso–Beattie–Bresnahan (BBB) scale for behavior analysis. They knew the scoring criteria well, but did not understand the experimental conditions. Scores range from 0 (lower limb paralysis) to 21 (responding to normal locomotion). The inclined board test is the maximum angle at which rats cannot fall for 5 s through equipment, testing, and recording. Footprint analysis was carried out by soaking the hind feet of rats with red dye and making them climb over a frame of appropriate size (1 m × 7 cm). Then results were scanned and processed.

Video Imaging of Locomotion

Six rats were randomly selected from the Sham group, SCI group, AAV–5HRE–NSCs group, and AAV–5HRE–aFGF–NSCs group. Using the camera (Leica), each group of rats walked on a 1-m-long glass track with markings on their hind legs to take pictures of the hips, knees, ankles, and feet and estimate their positions. The exercise of rats was evaluated by the following parameters: (1) weight support (height; the height of the torso from the ground), (2) leg extensor spasm (quantified by the time the foot was overstretched and dragged and the leg staying on the back), (3) the number of footprints (the number of previous steps as a reference), and (4) the posture of the foot (the distance between the beginning of the ankle and the rear of the hip). Pace was determined through the front legs (steps in the front legs per second) (Li et al., 2017).

Hematoxylin and Eosin Staining and Nissl Staining

In order to obtain the samples, rats with SCI for 60 days were anesthetized with the 1% pentobarbital (40–50 mg/kg, intraperitoneal injection). After thoracotomy, the whole body was perfused with 500 mL of 0.9% NaCl and then 100 mL of paraformaldehyde phosphate buffer solution. The spinal cord at the level of T8–10 was removed and spent the night in 4% paraformaldehyde. After paraffin embedding, the paraffin sections (5 μm) were stained in hematoxylin and eosin (H&E) and Nissl for further evaluation.

Immunohistochemistry

Spinal cord slices were incubated in 80% methanol and 3% H_2O_2 for 30 min, and then placed in a closed solution at 25°C for 1 h. The sample and the first antibody were then incubated overnight

in a refrigerator at 4°C: caspase 12 (1:4,000), caspase 3 (1:500), Eif–2 α (1:100), CHOP (1:200), and GRP78 (1:200). After washing with PBS three times, the second antibody bound to horseradish peroxidase was incubated at 37°C for 2 h. We terminated the reaction by 3pyr3-diaminobenzidine (DAB). Finally, the nucleus is stained with hematoxylin. Six regions were randomly selected in each sample, and the densities of caspase 12, caspase 3, Eif–2 α, CHOP, and GRP78-positive neurons were counted. We display the results through Nikon ECLPSE 80i (Nikon, Tokyo, Japan).

Immunofluorescence Staining

When finished with dewaxing, rehydration, and antigen retrieval, all the slices were incubated at 37°C in PBS containing 5% bovine serum albumin (BSA) and 0.1% Triton X–100 for 1 h. The slices were incubated with suitable primary antibody at 4°C overnight and stained with DAPI (0.25 μg/mL) dye to observe the nucleus. In order to evaluate neurons and aFGF, we used anti-NeuN (1:200) and anti-aFGF (10 μg/mL) antibodies, respectively. After incubation, the slices were then washed with PBS three times at room temperature, and the samples were incubated with the secondary antibody (1:500) at 37°C for 1 h. When finished, the slices were washed with PBS three times for 5 min each time. All pictures were shot with Nikon ECLIPSE Ti microscope (Nikon, Tokyo, Japan) and counted with ImageJ software, and then analyzed with Prism 7 (GraphPad, San Diego, CA, United States) to generate statistical charts.

Statistical Analysis

Statistically, the data are expressed as the average ± SD. When comparing the two groups of data, the double-sided Student *t*-test was carried out. When there are more than two sets of data, Dunnett and the ex-post test of one-way analysis of variance (ANOVA) were utilized to assess the data. $P < 0.05$ indicates significant difference.

RESULTS

Expression of Adeno-Associated Virus–Five Hypoxia-Responsive Elements–Acidic Fibroblast Growth Factor in Neural Stem Cells

In order to detect whether AAV-mediated aFGF was directly regulated by HRE under hypoxia, AAV–5HRE–aFGF was structured and transduced into NSCs (**Figure 1A**). From the immunofluorescence staining, it could be seen that AAV–5HRE–aFGF in nerve cells successfully expressed aFGF under hypoxia (**Figure 1B**). In addition, the level of aFGF protein was evaluated by Western blotting. We found that under normoxia, the expression of aFGF was weak, while the expression of aFGF of AAV–5HRE–aFGF–NSCs under hypoxia was significantly higher than that of other groups (**Figures 1C,D**). All our findings showed that AAV–5HRE–aFGF was successfully transfected into NSCs, while aFGF was expressed only under hypoxia.

Expression of Acidic Fibroblast Growth Factor in Adeno-Associated Virus–Five Hypoxia-Responsive Elements–Acidic Fibroblast Growth Factor–Neural Stem Cells Group *in vivo*

To study the expression of aFGF after transplantation of AAV–5HRE–aFGF–NSCs, we performed immunofluorescence staining of aFGF protein on tissue samples for 14 days. The results showed that the positive rate of aFGF in the AAV–5HRE–aFGF–NSCs group was significantly higher than the positive rate in the other groups, and the positive rate in the injured area was much higher than the positive rate in the non-injured area (**Figure 2**). In summary, AAV–5HRE–aFGF–NSCs expressed high levels of aFGF *in vivo* and were regulated by hypoxia.

Adeno-Associated Virus–Five Hypoxia-Responsive Elements–Acidic Fibroblast Growth Factor–Neural Stem Cells Promotes the Recovery of Motor Function to a Great Extent

AAV–5HRE–aFGF–NSCs treatment could reduce nerve death after SCI and enhanced the restoration of motor function in SCI rats. In order to evaluate the effect of the therapy of AAV–5HRE–aFGF–NSCs on SCI rats, we took visual images of spinal cord morphology. Compared with the large area blackening of the spinal cord of SCI group, the blackening degree in the AAV–5HRE–aFGF–NSCs group was particularly lower, showing the appearance of the SCI group closest to the Sham group (**Figure 3A**). Through footprint analysis, compared with the SCI group, the motor function of the AAV–5HRE–aFGF–NSCs group was improved (**Figure 3B**). Similarly, through the BBB score and the inclined plate test, the AAV–5HRE–aFGF–NSCs group showed significant recovery (**Figures 3C,D**). In addition, the video camera recording also showed that the foot error index of the AAV–5HRE–aFGF–NSCs group was lower, while the height and plantar step index were higher, which indicated that the functional recovery was better (**Figure 3E**). In addition, compared with the SCI group, the foot position error of the AAV–5HRE–aFGF–NSCs group decreased, and the height of the torso on the ground and the number of plantar steps increased (**Figures 3F–H**).

Adeno-Associated Virus–Five Hypoxia-Responsive Elements–Acidic Fibroblast Growth Factor–Neural Stem Cells Improves Neuronal Regeneration and Promotes the Repair of Spinal Cord Injury

After 60 days of contusion, the spinal cord samples were examined by cross-sectional Nissl staining and H&E staining to evaluate the structure of spinal cord tissue. Emulated with the Sham group, some tissues in the SCI group were harmed, accompanied by a significant decline in the quantity

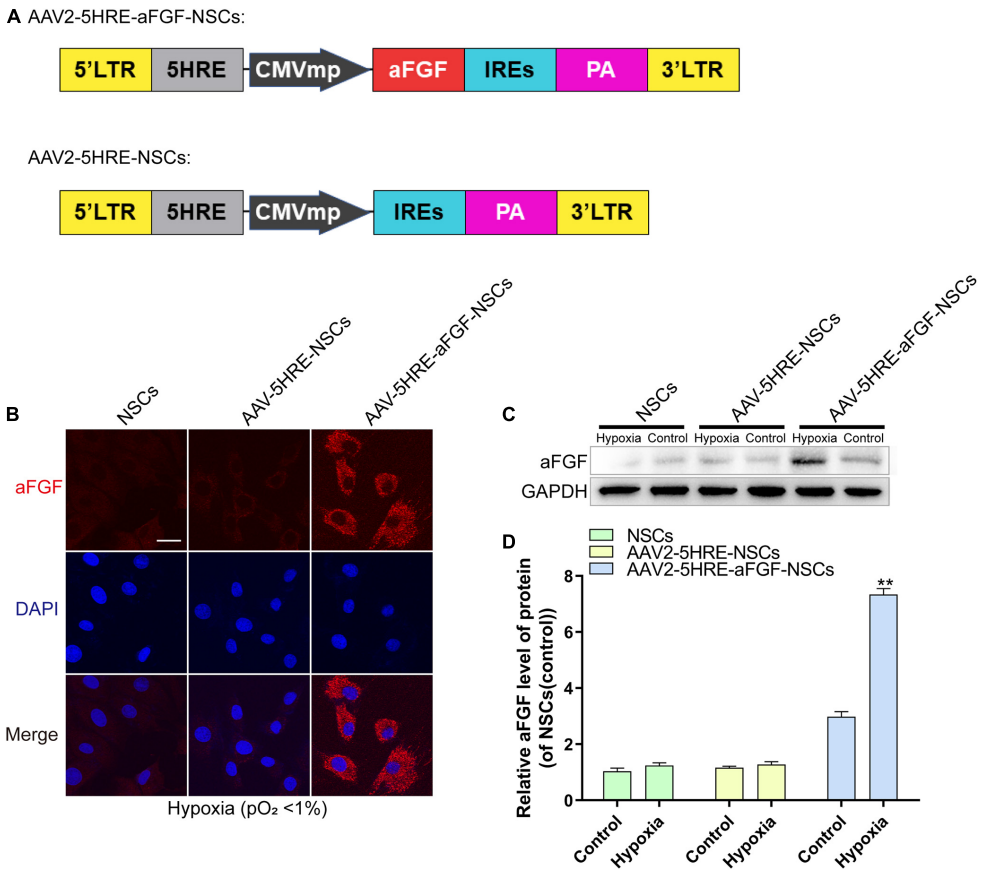

FIGURE 1 | The preparation and identification of AAV–5HRE–aFGF–NSCs. **(A)** The schematic diagrams of the vector construction: AAV–5HRE–aFGF and AAV–5HRE. **(B)** The immunofluorescence shows the expression of aFGF (red) and DAPI (blue) in different groups. Magnification: 40×; Scale: 50 μm. **(C)** Western blotting showing the expression of aFGF in each group. **(D)** The quantitative analysis of aFGF protein expression. $^{**}P < 0.01$. Data are represented as mean ± SD ($n = 6$). AAV, adeno-associated virus; 5HRE, five hypoxia-responsive elements; aFGF, acidic fibroblast growth factor; NSCs, neural stem cells.

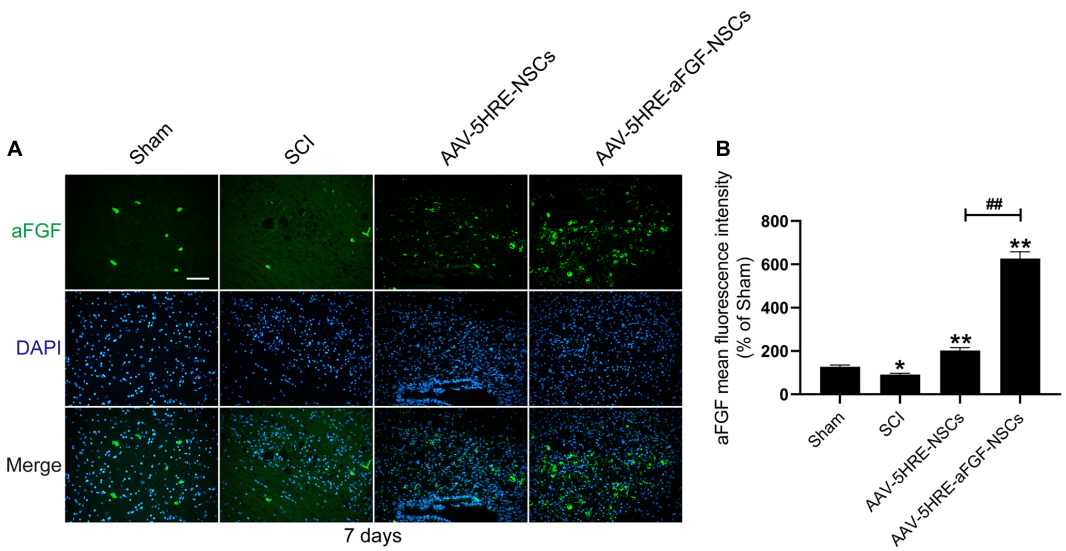

FIGURE 2 | Detection of aFGF production *in vivo*. **(A)** The immunofluorescence shows the expression of aFGF (green) and DAPI (blue) in different groups. Magnification: 20×; Scale: 100 μm. **(B)** Mean fluorescence intensity of aFGF. ##,$^{*}P < 0.05$. $^{**}P < 0.01$. Data are represented as mean ± SD ($n = 6$).

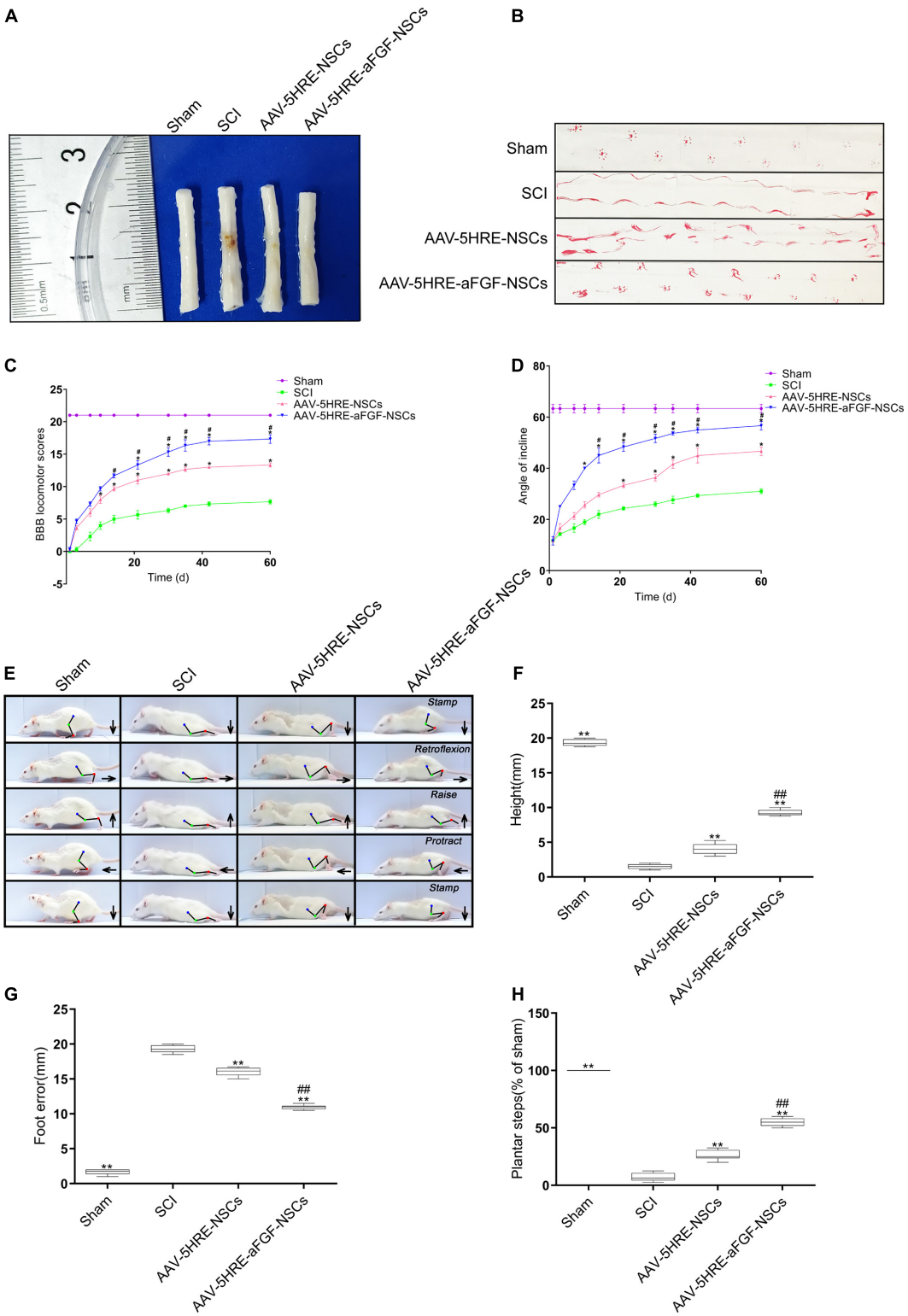

FIGURE 3 | AAV–5HRE–aFGF–NSCs enhance the recovery of motor function in SCI rats. **(A)** Image showing varying degrees of damage of spinal cords in different groups. **(B)** Footprint analysis of the Sham, SCI group, AAV–5HRE–NSCs group, and AAV–5HRE–aFGF–NSCs group in 30 d.a.t. **(C)** The BBB scores in the Sham, SCI, AAV–5HRE–NSCs, and AAV–5HRE–aFGF–NSCs rats. **(D)** The inclined plane test scores of rats in the Sham, SCI group, AAV–5HRE–NSCs group, and AAV–5HRE–aFGF–NSCs group. **(E)** Images from videos showing rats' walk in 30 d.a.t. The weight support, slow steps, leg extensor spasms, and foot placement were processed. The direction of the foot movement is marked by arrows. The initial position of the move is highlighted by red dots. **(F)** Weight support. **(G)** Foot error. **(H)** The spasm. #,*$P < 0.05$. ##,**$P < 0.01$. All the data are represented as mean ± SD ($n = 6$). SCI, spinal cord injury; BBB, Basso–Beattie–Bresnahan.

of neurons and the formation of cavities. In the AAV–5HRE–aFGF–NSCs group, there were a few gaps, but no obvious necrosis, showing a more complete tissue structure (**Figures 4A,B**). From immunofluorescence staining of NeuN, we knew that the fluorescence signal density of the AAV–5HRE–aFGF–NSCs-treated group was even higher than that of the SCI group, which revealed a fine recovery of the nerves (**Figures 4C,D**). This showed that AAV–5HRE–aFGF–NSCs plays a positive role in axonal survival and regeneration.

Adeno-Associated Virus–Five Hypoxia-Responsive Elements–Acidic Fibroblast Growth Factor–Neural Stem Cells Inhibits Endoplasmic Reticulum Stress-Induced Apoptosis and Enhances the Restoration of Spinal Cord Injury

In order to figure out if AAV–5HRE–aFGF–NSCs promotes the recovery of SCI by inhibiting apoptosis that was induced by ER stress, we detected the caspase 12–caspase 3 pathway, EIF2α–CHOP pathway, and GRP78 expression of ER stress (**Figure 5**) by immunohistochemical staining. As is shown in the figure, emulated with the SCI group, the AAV–5HRE–NSCs group could reduce the expression level of caspase 12. However, the decrease in the AAV–5HRE–aFGF–NSCs group was greater than the decrease in the AAV–5HRE–NSCs group. The caspase 3 expression level in the AAV–5HRE–NSCs group was even lower than the expression level in the SCI group. At the same time, the production of caspase 3 in the AAV–5HRE–aFGF–NSCs group was more significantly inhibited. This suggests that AAV–5HRE–aFGF–NSCs could further inhibit caspase 12–caspase 3–mediated apoptosis in SCI, thus, promoting the recovery of SCI. In the determination of EIF–2α, although there was a significant decrease in the AAV–5HRE–NSCs group compared with the SCI group, the degree of the decrease in the AAV–5HRE–aFGF–NSCs group was even obvious. Similarly, emulated with the SCI group, the AAV–5HRE–NSCs group could reduce the expression of CHOP, but the decrease in the AAV–5HRE–aFGF–NSCs group was more significant. Therefore, in the EIF–2α/CHOP pathway, treatment of NSC alone could also reduce the expression of EIF–2α and CHOP. Compared with the AAV–5HRE–NSCs group, the therapeutic effect of AAV–5HRE–aFGF–NSCs was better. Finally, we also detected the expression of GRP78 in each group. We observed that although the level of GRP78 in the AAV–5HRE–NSCs group was still better than the level in the SCI group, the improvement in the AAV–5HRE–aFGF–NSCs group was more significant. To sum up, through the treatment of AAV–5HRE–aFGF–NSCs, the levels of caspase 12–caspase 3 pathway, EIF2α–CHOP pathway, and GRP78 induced by ER stress decreased, which effectively inhibited the apoptosis and finally enhanced the recovery of SCI.

Adeno-Associated Virus–Five Hypoxia-Responsive Elements–Acidic Fibroblast Growth Factor Increases the Migration and Restoration Ability of Neural Stem Cells by Inhibiting Endoplasmic Reticulum Stress

The results of the cell migration test in different groups are showed at 0, 12, and 24 h after scratch (**Figure 6**), respectively. With the passage of time, the acellular area of each group declined. Emulated with the control group, the acellular area in the TG group was larger, which indicated that apoptosis had an effect and inhibited cell migration. Compared with the TG group, the wound area of the AAV–5HRE–aFGF–NSCs group was significantly smaller, and the migration speed was faster. This result is the same as the recovery trend of the 4–PBA group, but the migration rate is higher, which indicates that AAV–5HRE–aFGF–NSCs can inhibit cell apoptosis more effectively than 4–PBA.

DISCUSSION

Due to the non-renewability of the CNS, it is difficult to regenerate neurons through its own repair (McDonald and Sadowsky, 2002; Tran et al., 2018). Therefore, exogenous neurons are needed to supplement the missing parts. Current research is mainly focused on stem cell transplantation (Desgres and Menasché, 2019; Lindsay et al., 2020). NSCs are able to self-replace and differentiate into a variety of cells (Kumamaru et al., 2018). After transplantation, most NSCs can differentiate and migrate into the host tissue, providing an important supplement for the loss of neurons (Assinck et al., 2017). Literature has shown that transplanted NSCs also have the capability to secrete neurotrophic factors, which can protect neurons (Fan et al., 2018). In the research of this article, we found that the effect of neural stem cell therapy alone is not good, and it needs to be combined with other treatments to achieve better results.

AFGF has been proven to play a significant role in neuroprotection and axon regeneration, and its feasibility has been verified in clinical trials (Lee et al., 2011). Experiments have confirmed that aFGF has a good neurotrophic effect. At present, the research on aFGF is mostly focused on promoting the growth and differentiation of neurons and neurotrophic effects, but its role in ER stress-induced apoptosis is still unknown (Garré et al., 2010; Kuo et al., 2011). Moreover, as a macromolecular protein, it is easy to decompose in the body and has a short half-life, so a carrier is needed to solve this problem (Zakrzewska et al., 2008; Haenzi and Moon, 2017).

Although scientists have made considerable progress in the research of SCI, single-factor research has great limitations in the repair of SCI (Fouad et al., 2021). Therefore, the organic combination of aFGF and NSCs to achieve a better repair effect on SCI is an important goal of our current research.

In recent years, AAV has been widely used in neuroscience research (Leborgne et al., 2020; Wang et al., 2020). Emulated with adenovirus and lentivirus, AAV is rendered with more

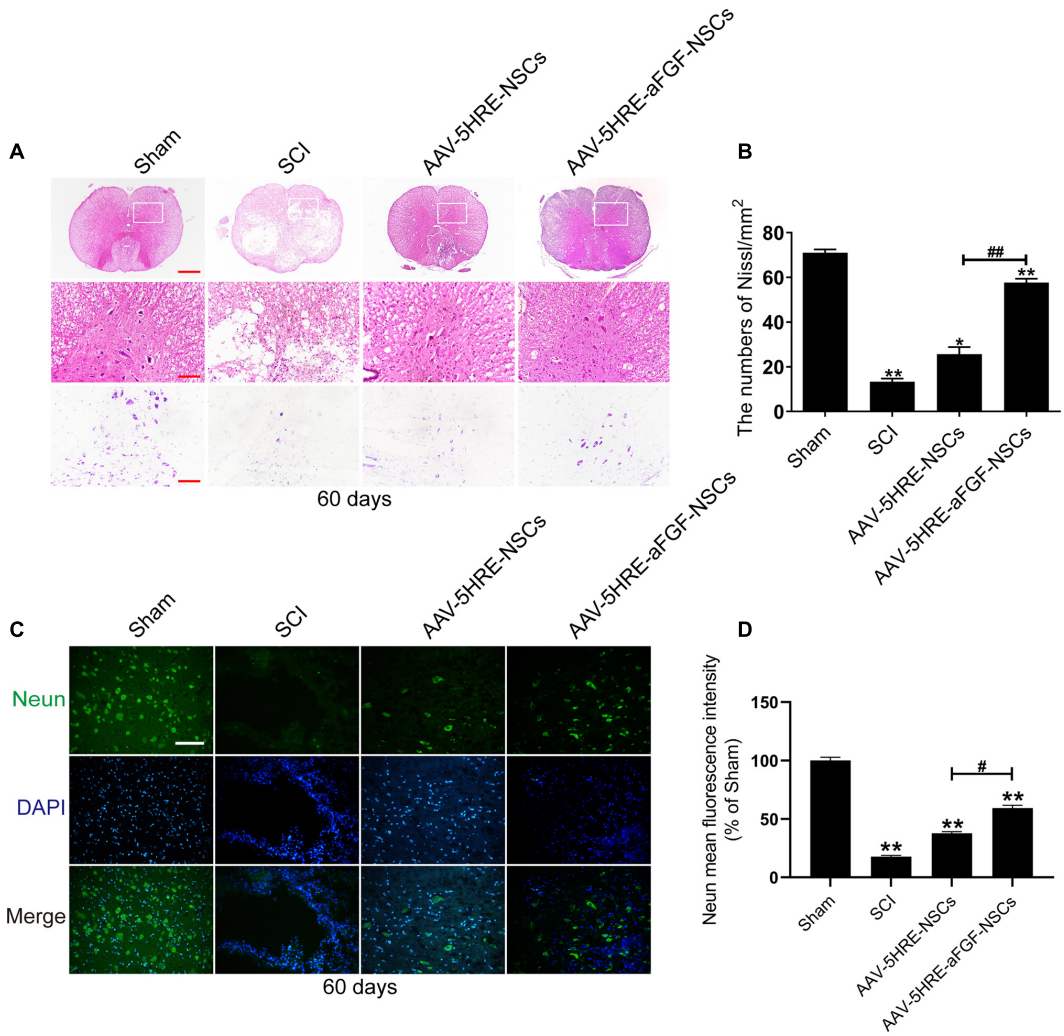

FIGURE 4 | AAV–5HRE–aFGF–NSCs treatment improved the structural integrity of the spinal cord and the restoration of neurons. **(A)** Images of whole cross section after hematoxylin and eosin (H&E) staining and Nissl staining. Magnification: 4×; Scale: 500 μm. The scale bar of Nissl staining images are 100 μm. **(B)** Quantification of Nissl staining in different groups. $^{*}P < 0.05$. $^{**}P < 0.01$. Data are represented as mean ± SD ($n = 6$). **(C)** Immunofluorescence to show the expression of NeuN (green) and DAPI (blue) in different groups. Magnification: 40×; Scale: 50 μm. **(D)** Mean intensity of fluorescence of NeuN in different groups. #,$^{*}P < 0.05$. ##,$^{**}P < 0.01$. Data are represented as mean ± SD ($n = 6$).

stable expression ability and higher immunocompatibility in nerve cells (Li and Samulski, 2020). The HRE can induce the expression of specific genes under hypoxic conditions (Schörg et al., 2015; Zhang et al., 2016). We used AAV to carry 5HRE–aFGF into NSCs and achieved a high expression of aFGF induced by hypoxia. In this study, we built AAV–5HRE–aFGF–NSCs and transplanted them to the SCI, and verified their repairing effect on the locomotion of the SCI rats.

In order to further explore its role after SCI, we focused our attention on apoptosis. Apoptosis, as one of the four types of programmed death, is activated after cells are damaged by the outside world, and induces the autonomous and orderly death of cells through the activation of specific pathways (Bedoui et al., 2020). After SCI, ischemia and hypoxia can impair the function of the ER, causing the accumulation and aggregation of unfolded proteins (Hetz, 2012; Cybulsky, 2017; Hetz and Saxena, 2017; Ren et al., 2021). This condition is ER stress. Although the body can reduce the harmful effects of ER stress through the unfolded protein response (UPR), after SCI, UPR is out of controllable range of protein folding and is not compensated (Ohri et al., 2011). It will stimulate the apoptosis signaling pathway, thereby exacerbating SCI. After accumulation of unfolded protein, it induces the activation of the PERK signal. It will lead to the upregulation of EIF–2α expression, and eventually activate CHOP and other proteins to cause cell apoptosis. Moreover, chaperone proteins such as GRP78 and the caspase 12/caspase 3 pathway will also be activated to induce cell apoptosis (Lee et al., 2014). Studies have shown that SCI can cause numerous neuron deaths, myelin sheath loss, axon damage, and neural circuit defects (Fancy et al., 2011; Sas et al., 2020). Among them,

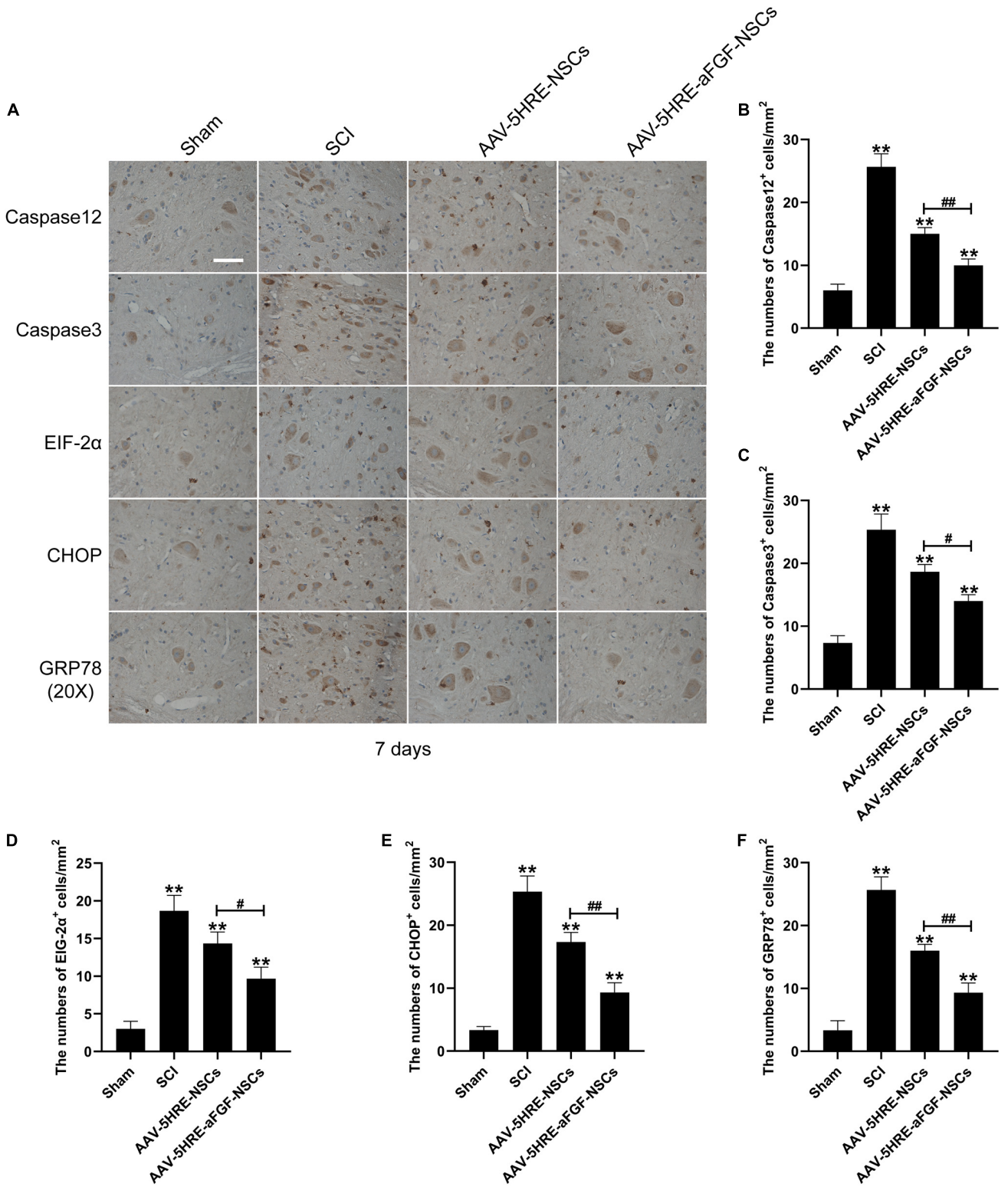

FIGURE 5 | The regulation signals are significant for the neuroprotective effect of AAV–5HRE–aFGF–NSCs. **(A)** Immunohistochemistry for caspase 12, caspase 3, EIF–2α–CHOP, and GRP78 in the Sham, SCI, AAV–5HRE–NSCs, and AAV–5HRE–aFGF–NSCs group. Magnification: 20 × ; Scale: 100 μm. **(B–F)** Analysis of immunohistochemistry positive cells. $^{**}P < 0.01$. $^{\#}P < 0.05$. $^{\#\#}P < 0.01$. Data are represented as mean ± SD ($n = 6$).

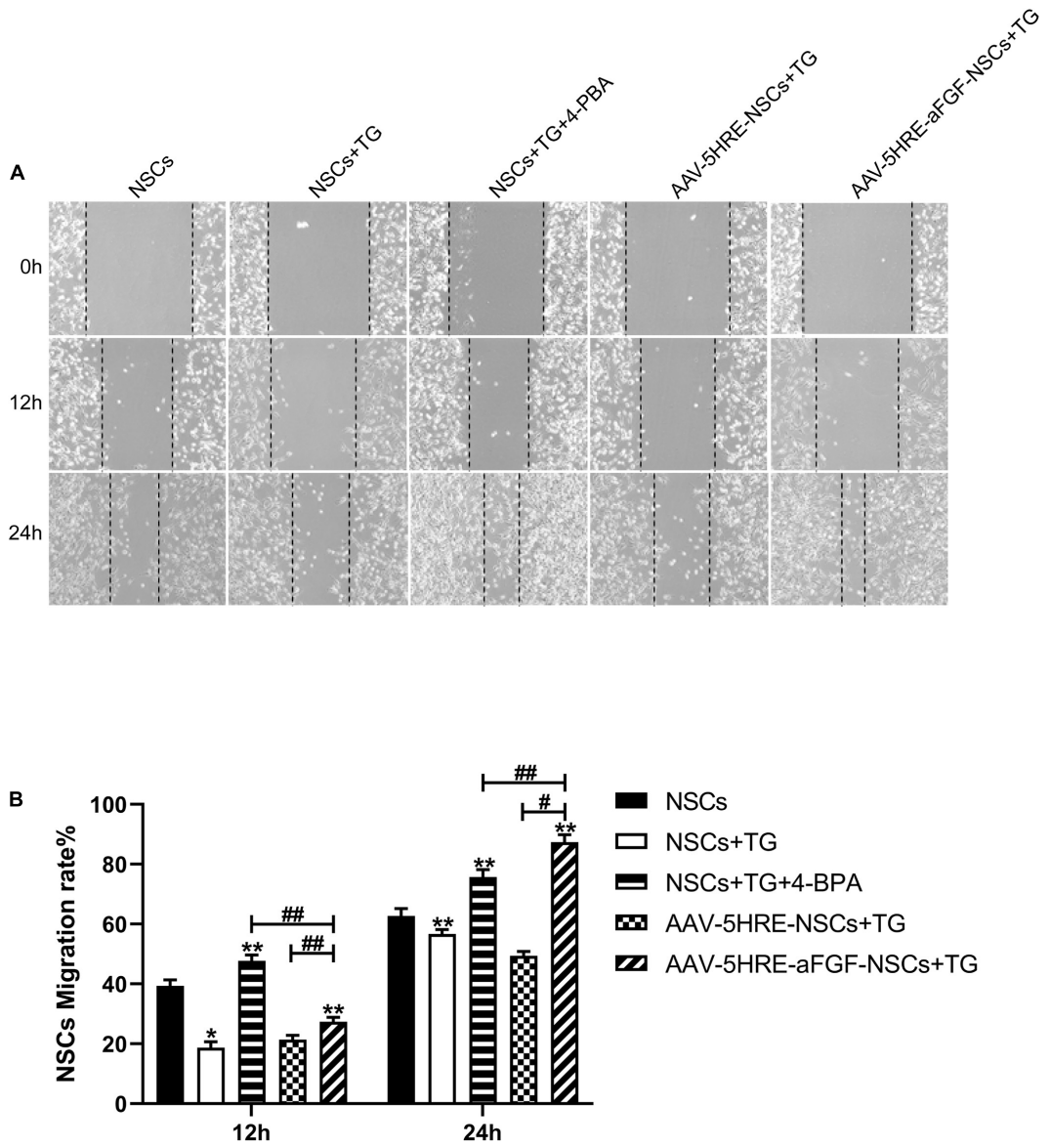

FIGURE 6 | AAV–5HRE–aFGF–NSCs promote NSC migration by inhibiting endoplasmic reticulum (ER) stress. **(A)** Cell migrating images in control, TG, TG^+ 4–PBA, TG^+ 4–BPA, AAV–5HRE–NSCs, and AAV–5HRE–aFGF–NSCs group. These images are 0-, 12-, and 24-h inspection images taken by an inverted phase-contrast microscope. **(B)** The NSCs migration rate for 12 and 24 h. #, $^*P < 0.05$. ##, $^{**}P < 0.01$. The data were processed by ImageJ and presented as the mean values ± SD, $n = 6$. TG, thapsigargin; PBA, phenylbutyric acid.

the loss of neurons is an important factor leading to motor dysfunction. Studies have confirmed that a series of biochemical reactions triggered by ER stress may play an important role in neuronal apoptosis after SCI (Springer et al., 1999). Since neurons are difficult to regenerate, reducing their apoptosis becomes an ideal strategy to reduce neuron loss. Therefore, inhibiting the stress of the ER to conserve neurons from apoptosis may be a sensible treatment for SCI.

Pharmacological intervention to inhibit apoptosis has been considered an important direction to reduce neuronal death (Cheng et al., 2018; Song et al., 2019). As an acute stress response, apoptosis mainly occurs in the acute phase of SCI. Consistently, we found that AAV–5HRE–aFGF–NSCs had effectively inhibited the caspase 12/caspase 3 pathway, EIF2α–CHOP pathway, and GRP78 in 7 days, thereby attenuating the apoptosis after SCI and promoting the recovery of the rat's motor function. After accumulation of unfolded protein, it induces the stimulation of the PERK signaling pathway. The activation of it will increase the expression of EIF–2α/CHOP, leading to cell apoptosis. In addition, the expression of the caspase 12/caspase 3 pathway and GRP78 and other chaperone proteins will also be upregulated, thereby inducing apoptosis. Our research shows that contrasted

with the SCI group, the expression of apoptosis-related proteins (such as CHOP, GRP78, and caspase 3) in the NSC-only treatment group was downregulated, which may be owed to the fact that NSCs secrete a small amount of aFGF when stimulated. It has a protective effect on nerve cells, but its expression is far less than the concentration to achieve the best effect, so it needs to be supplemented by exogenous aFGF. Compared with the simple NSCs treatment group, the expression of apoptosis-related proteins in the combined treatment group of aFGF and NSCs is lower, which indicates that the supplementation of exogenous aFGF has a better regulatory effect on ER stress-induced apoptosis.

We used the Basso–Beattie–Bresnahan (BBB) scale and inclined plate test to detect the recovery of the rat's motor function. In addition, we tested the expression levels of NeuN and apoptosis-related proteins (such as GRP78, caspase 12, and CHOP) induced by ER stress. Data showed that AAV–5HRE–aFGF–NSCs can repair SCI by lessening the ER stress-induced apoptosis.

In short, our research shows that the combined action of aFGF and NSCs protects neurons and promotes the restoration of motor function in SCI rats. This is achieved by reducing apoptosis induced by ER stress.

DATA AVAILABILITY STATEMENT

The original contributions presented in the study are included in the article/supplementary material, further inquiries can be directed to the corresponding author/s.

ETHICS STATEMENT

The animal study was reviewed and approved by Animal Care and Use Committee of Wenzhou Medical College (wydw2014-0074).

AUTHOR CONTRIBUTIONS

YY, YZ, MC, and YT coordinated and carried out most of the experiments and data analysis, and participated in drafting the manuscript. MC, ZH, WY, and QW provided technical assistance. JY and ZX carried out assistance on data analysis and manuscript preparation. SZ and ZW supervised the project and experimental designs and data analysis. SZ, ZW, and XW supervised the project and revised the manuscript. All authors approved the final manuscript.

FUNDING

This study was partly funded by a grant from the National Natural Science Foundation of China (81802235), Zhejiang Medical and Health Science and Technology Plan Project (2021KY212), Wenzhou Basic Science Research Plan Project (Y2020050), XinMiao Project of Science and Technology Department of Zhejiang Province (2020R413002), and Research Grant for Students of Wenzhou Medical University (wyx2020102082).

REFERENCES

Abbaszadeh, F., Fakhri, S., and Khan, H. (2020). Targeting apoptosis and autophagy following spinal cord injury: therapeutic approaches to polyphenols and candidate phytochemicals. *Pharmacol. Res.* 160:105069. doi: 10.1016/j.phrs.2020.105069

Ahuja, C., Wilson, J., Nori, S., Kotter, M., Druschel, C., Curt, A., et al. (2017). Traumatic spinal cord injury. *Nat. Rev. Dis. Primers* 3:17018. doi: 10.1038/nrdp.2017.18

Assinck, P., Duncan, G., Hilton, B., Plemel, J., and Tetzlaff, W. (2017). Cell transplantation therapy for spinal cord injury. *Nat. Neurosci.* 20, 637–647. doi: 10.1038/nn.4541

Beattie, M. (2004). Inflammation and apoptosis: linked therapeutic targets in spinal cord injury. *Trends Mol. Med.* 10, 580–583. doi: 10.1016/j.molmed.2004.10.006

Bedoui, S., Herold, M., and Strasser, A. (2020). Emerging connectivity of programmed cell death pathways and its physiological implications. *Nat. Rev. Mol. Cell Biol.* 21, 678–695. doi: 10.1038/s41580-020-0270-8

Bourzac, K. (2016). Neuroscience: new nerves for old. *Nature* 540, S52–S54. doi: 10.1038/540S52a

Bradbury, E., and Burnside, E. (2019). Moving beyond the glial scar for spinal cord repair. *Nat Commun.* 10:3879. doi: 10.1038/s41467-019-11707-7

Cheng, J., Korte, N., Nortley, R., Sethi, H., Tang, Y., and Attwell, D. (2018). Targeting pericytes for therapeutic approaches to neurological disorders. *Acta. Neuropathol.* 136, 507–523. doi: 10.1007/s00401-018-1893-0

Chhabra, H., and Sarda, K. (2017). Clinical translation of stem cell based interventions for spinal cord injury - Are we there yet? *Adv. Drug Deliv. Rev.* 120, 41–49. doi: 10.1016/j.addr.2017.09.021

Crowe, M., Bresnahan, J., Shuman, S., Masters, J., and Beattie, M. (1997). Apoptosis and delayed degeneration after spinal cord injury in rats and monkeys. *Nat. Med.* 3, 73–76. doi: 10.1038/nm0197-73

Cybulsky, A. (2017). Endoplasmic reticulum stress, the unfolded protein response and autophagy in kidney diseases. *Nat. Rev. Nephrol.* 13, 681–696. doi: 10.1038/nrneph.2017.129

Deng, W., Shao, F., He, Q., Wang, Q., Shi, W., Yu, Q., et al. (2019). EMSCs build an all-in-one niche via cell-cell lipid raft assembly for promoted neuronal but suppressed astroglial differentiation of neural stem cells. *Adv. Mater.* 31:e1806861. doi: 10.1002/adma.201806861

Denoth-Lippuner, A., and Jessberger, S. (2021). Formation and integration of new neurons in the adult hippocampus. *Nat. Rev. Neurosci.* 22, 223–236. doi: 10.1038/s41583-021-00433-z

Desgres, M., and Menasché, P. (2019). Clinical translation of pluripotent stem cell therapies: challenges and considerations. *Cell Stem Cell* 25, 594–606. doi: 10.1016/j.stem.2019.10.001

Eckenstein, F., Shipley, G., and Nishi, R. (1991). Acidic and basic fibroblast growth factors in the nervous system: distribution and differential alteration of levels after injury of central versus peripheral nerve. *J. Neurosci.* 11, 412–419. doi: 10.1523/jneurosci.11-02-00412.1991

Fan, W., Liu, P., Wang, G., Pu, J., Xue, X., and Zhao, J. (2018). Transplantation of hypoxic preconditioned neural stem cells benefits functional recovery via enhancing neurotrophic secretion after spinal cord injury in rats. *J. Cell Biochem.* 119, 4339–4351. doi: 10.1002/jcb.26397

Fancy, S., Harrington, E., Yuen, T., Silbereis, J., Zhao, C., Baranzini, S., et al. (2011). Axin2 as regulatory and therapeutic target in newborn brain injury and remyelination. *Nat. Neurosci.* 14, 1009–1016. doi: 10.1038/nn.2855

Fouad, K., Popovich, P., Kopp, M., and Schwab, J. (2021). The neuroanatomical-functional paradox in spinal cord injury. *Nat. Rev. Neurol.* 17, 53–62. doi: 10.1038/s41582-020-00436-x

Garré, J., Retamal, M., Cassina, P., Barbeito, L., Bukauskas, F., Sáez, J., et al. (2010). FGF-1 induces ATP release from spinal astrocytes in culture and

opens pannexin and connexin hemichannels. *Proc. Natl. Acad. Sci. U.S.A* 107, 22659–22664. doi: 10.1073/pnas.1013793107

Haenzi, B., and Moon, L. (2017). The function of FGFR1 signalling in the spinal cord: therapeutic approaches using FGFR1 ligands after spinal cord injury. *Neural Plast.* 2017:2740768. doi: 10.1155/2017/2740768

Hetz, C. (2012). The unfolded protein response: controlling cell fate decisions under ER stress and beyond. *Nat. Rev. Mol. Cell Biol.* 13, 89–102. doi: 10.1038/nrm3270

Hetz, C., and Saxena, S. (2017). ER stress and the unfolded protein response in neurodegeneration. *Nat. Rev. Neurol.* 13, 477–491. doi: 10.1038/nrneurol.2017.99

Kumamaru, H., Kadoya, K., Adler, A., Takashima, Y., Graham, L., Coppola, G., et al. (2018). Generation and post-injury integration of human spinal cord neural stem cells. *Nat. methods* 15, 723–731. doi: 10.1038/s41592-018-0074-3

Kuo, H., Tsai, M., Huang, M., Chiu, C., Tsai, C., Lee, M., et al. (2011). Acid fibroblast growth factor and peripheral nerve grafts regulate Th2 cytokine expression, macrophage activation, polyamine synthesis, and neurotrophin expression in transected rat spinal cords. *J. Neurosci.* 31, 4137–4147. doi: 10.1523/jneurosci.2592-10.2011

Leborgne, C., Barbon, E., Alexander, J., Hanby, H., Delignat, S., Cohen, D., et al. (2020). IgG-cleaving endopeptidase enables in vivo gene therapy in the presence of anti-AAV neutralizing antibodies. *Nat. Med.* 26, 1096–1101. doi: 10.1038/s41591-020-0911-7

Lee, J., Maeng, S., Kang, S., Choi, H., Oh, T., Ju, B., et al. (2014). Valproic acid protects motor neuron death by inhibiting oxidative stress and endoplasmic reticulum stress-mediated cytochrome C release after spinal cord injury. *J. Neurotrauma* 31, 582–594. doi: 10.1089/neu.2013.3146

Lee, M., Chen, C., Huang, W., Huang, M., Chang, W., Kuo, H., et al. (2011). Regulation of chondroitin sulphate proteoglycan and reactive gliosis after spinal cord transection: effects of peripheral nerve graft and fibroblast growth factor 1. *Neuropathol. Appl. Neurobiol.* 37, 585–599. doi: 10.1111/j.1365-2990.2011.01182.x

Li, C., and Samulski, R. (2020). Engineering adeno-associated virus vectors for gene therapy. *Nat. Rev. Genet.* 21, 255–272. doi: 10.1038/s41576-019-0205-4

Li, X., Peng, Z., Long, L., Tuo, Y., Wang, L., Zhao, X., et al. (2020). Wnt4-modified NSC transplantation promotes functional recovery after spinal cord injury. *FASEB J.* 34, 82–94. doi: 10.1096/fj.201901478RR

Li, Y., Lucas-Osma, A., Black, S., Bandet, M., Stephens, M., Vavrek, R., et al. (2017). Pericytes impair capillary blood flow and motor function after chronic spinal cord injury. *Nat. Med.* 23, 733–741. doi: 10.1038/nm.4331

Lindsay, S., McCanney, G., Willison, A., and Barnett, S. (2020). Multi-target approaches to CNS repair: olfactory mucosa-derived cells and heparan sulfates. *Nat. Rev. Neurol.* 16, 229–240. doi: 10.1038/s41582-020-0311-0

Maquet, V., Martin, D., Scholtes, F., Franzen, R., Schoenen, J., Moonen, G., et al. (2001). Poly(D,L-lactide) foams modified by poly(ethylene oxide)-block-poly(D,L-lactide) copolymers and a-FGF: in vitro and in vivo evaluation for spinal cord regeneration. *Biomaterials* 22, 1137–1146. doi: 10.1016/s0142-9612(00)00357-4

McDonald, J., and Sadowsky, C. (2002). Spinal-cord injury. *Lancet* 359, 417–425. doi: 10.1016/s0140-6736(02)07603-1

Navarro Negredo, P., Yeo, R., and Brunet, A. (2020). Aging and rejuvenation of neural stem cells and their niches. *Cell Stem Cell* 27, 202–223. doi: 10.1016/j.stem.2020.07.002

Nurcombe, V., Ford, M., Wildschut, J., and Bartlett, P. (1993). Developmental regulation of neural response to FGF-1 and FGF-2 by heparan sulfate proteoglycan. *Science* 260, 103–106. doi: 10.1126/science.7682010

Ohri, S., Maddie, M., Zhao, Y., Qiu, M., Hetman, M., and Whittemore, S. (2011). Attenuating the endoplasmic reticulum stress response improves functional recovery after spinal cord injury. *Glia* 59, 1489–1502. doi: 10.1002/glia.21191

Peruzzotti-Jametti, L., Bernstock, J., Vicario, N., Costa, A., Kwok, C., Leonardi, T., et al. (2018). Macrophage-derived extracellular succinate licenses neural stem cells to suppress chronic neuroinflammation. *Cell Stem Cell* 22, 355-368.e13. doi: 10.1016/j.stem.2018.01.020

Ramer, L., Ramer, M., and Bradbury, E. (2014). Restoring function after spinal cord injury: towards clinical translation of experimental strategies. *Lancent Neurol.* 13, 1241–1256. doi: 10.1016/s1474-4422(14)70144-9

Ren, J., Bi, Y., Sowers, J., Hetz, C., and Zhang, Y. (2021). Endoplasmic reticulum stress and unfolded protein response in cardiovascular diseases. *Nat. Rev. Dardiol.* [preprint]. doi: 10.1038/s41569-021-00511-w

Sas, A., Carbajal, K., Jerome, A., Menon, R., Yoon, C., Kalinski, A., et al. (2020). A new neutrophil subset promotes CNS neuron survival and axon regeneration. *Nat. Immunol.* 21, 1496–1505. doi: 10.1038/s41590-020-00813-0

Schörg, A., Santambrogio, S., Platt, J., Schödel, J., Lindenmeyer, M., Cohen, C., et al. (2015). Destruction of a distal hypoxia response element abolishes trans-activation of the PAG1 gene mediated by HIF-independent chromatin looping. *Nucleic Acids Res.* 43, 5810–5823. doi: 10.1093/nar/gkv506

Shi, Z., Yuan, S., Shi, L., Li, J., Ning, G., Kong, X., et al. (2021). Programmed cell death in spinal cord injury pathogenesis and therapy. *Cell Prolif.* 54:e12992. doi: 10.1111/cpr.12992

Sofroniew, M. (2018). Dissecting spinal cord regeneration. *Nature* 557, 343–350. doi: 10.1038/s41586-018-0068-4

Song, Y., Agrawal, N., Griffin, J., and Schmidt, C. (2019). Recent advances in nanotherapeutic strategies for spinal cord injury repair. *Adv. Drug Deliv. Rev.* 148, 38–59. doi: 10.1016/j.addr.2018.12.011

Springer, J., Azbill, R., and Knapp, P. (1999). Activation of the caspase-3 apoptotic cascade in traumatic spinal cord injury. *Nat. Med.* 5, 943–946. doi: 10.1038/11387

Thuret, S., Moon, L., and Gage, F. (2006). Therapeutic interventions after spinal cord injury. *Nat. Rev. Neurosci.* 7, 628–643. doi: 10.1038/nrn1955

Tran, A., Warren, P., and Silver, J. (2018). The biology of regeneration failure and success after spinal cord injury. *Physiol. Rev.* 98, 881–917. doi: 10.1152/physrev.00017.2017

Tsai, E., Dalton, P., Shoichet, M., and Tator, C. (2006). Matrix inclusion within synthetic hydrogel guidance channels improves specific supraspinal and local axonal regeneration after complete spinal cord transection. *Biomaterials* 27, 519–533. doi: 10.1016/j.biomaterials.2005.07.025

Wang, D., Tai, P., and Gao, G. (2019). Adeno-associated virus vector as a platform for gene therapy delivery. *Nat. Rev. Drug Discov.* 18, 358–378. doi: 10.1038/s41573-019-0012-9

Wang, D., Zhang, F., and Gao, G. (2020). CRISPR-based therapeutic genome editing: strategies and in vivo delivery by AAV vectors. *Cell* 181, 136–150. doi: 10.1016/j.cell.2020.03.023

Wang, Q., He, Y., Zhao, Y., Xie, H., Lin, Q., He, Z., et al. (2017). A thermosensitive heparin-poloxamer hydrogel bridges aFGF to treat spinal cord injury. *ACS Appl. Mater. Interfaces* 9, 6725–6745. doi: 10.1021/acsami.6b13155

Wang, Q., Zhang, H., Xu, H., Zhao, Y., Li, Z., Li, J., et al. (2018). Novel multi-drug delivery hydrogel using scar-homing liposomes improves spinal cord injury repair. *Theranostics* 8, 4429–4446. doi: 10.7150/thno.26717

Wu, D., Potluri, N., Lu, J., Kim, Y., and Rastinejad, F. (2015). Structural integration in hypoxia-inducible factors. *Nature* 524, 303–308. doi: 10.1038/nature14883

Xu, C., Xu, L., Huang, L., Li, Y., Yu, P., Hang, Q., et al. (2011). Combined NgR vaccination and neural stem cell transplantation promote functional recovery after spinal cord injury in adult rats. *Neuropathol. Appl. Neurobiol.* 37, 135–155. doi: 10.1111/j.1365-2990.2010.01117.x

Yoo, M., Lee, G., Park, C., Cohen, R., and Schachner, M. (2014). Analysis of human embryonic stem cells with regulatable expression of the cell adhesion molecule l1 in regeneration after spinal cord injury. *J. Neurotrauma* 31, 553–564. doi: 10.1089/neu.2013.2886

Zakrzewska, M., Marcinkowska, E., and Wiedlocha, A. (2008). FGF-1: from biology through engineering to potential medical applications. *Crit. Rev. Clin. Lab. Sci.* 45, 91–135. doi: 10.1080/10408360701713120

Zhang, H., Liang, C., Hou, X., Wang, L., and Zhang, D. (2016). Study of the combined treatment of lung cancer using gene-loaded immunomagnetic

albumin nanospheres in vitro and in vivo. *Int. J. Nanomed.* 11, 1039–1050. doi: 10.2147/ijn.s98519

Zheng, Y., Mao, Y., Yuan, T., Xu, D., and Cheng, L. (2020). Multimodal treatment for spinal cord injury: a sword of neuroregeneration upon neuromodulation. *Neural Regen. Res.* 15, 1437–1450. doi: 10.4103/1673-5374.274332

Zhu, S., Ying, Y., Ye, J., Chen, M., Wu, Q., Dou, H., et al. (2021). AAV2-mediated and hypoxia response element-directed expression of bFGF in neural stem cells showed therapeutic effects on spinal cord injury in rats. *Cell Death Dis.* 12:274. doi: 10.1038/s41419-021-03546-6

Conflict of Interest: The authors declare that the research was conducted in the absence of any commercial or financial relationships that could be construed as a potential conflict of interest.

frontiers in Pharmacology

ORIGINAL RESEARCH
published: 14 June 2021
doi: 10.3389/fphar.2021.658040

TMT-Based Quantitative Proteomic Analysis Reveals the Effect of Bone Marrow Derived Mesenchymal Stem Cell on Hair Follicle Regeneration

Chao Zhang[1,2,3], *YuanHong Li*[1,2,3], *Jie Qin*[1,2,3], *ChengQian Yu*[1,2,3], *Gang Ma*[4], *HongDuo Chen*[1,2,3]* *and XueGang Xu*[1,2,3]*

[1]*Department of Dermatology, The First Hospital of China Medical University, Shenyang, China,* [2]*NHC Key Laboratory of Immunodermatology (China Medical University), Shenyang, China,* [3]*Key Laboratory of Immunodermatology (China Medical University), Ministry of Education, Shenyang, China,* [4]*Key Laboratory for the Genetics of Developmental and Neuropsychiatric Disorders (Ministry of Education), Bio-X Institutes, Shanghai Jiao Tong University, Shanghai, China*

OPEN ACCESS

Edited by:
Zhouguang Wang,
Albert Einstein College of Medicine,
New York, NY, United States

Reviewed by:
Xiaohua Lei,
Chinese Academy of Sciences,
Shenzhen, China
Jian Zhong,
Shanghai Ocean University, China

***Correspondence:**
XueGang Xu
xuxuegang2749290@163.com
HongDuo Chen
hongduochen@hotmail.com

Specialty section:
This article was submitted to Integrative and Regenerative Pharmacology, a section of the journal Frontiers in Pharmacology

Received: *25 January 2021*
Accepted: *12 March 2021*
Published: *14 June 2021*

Citation:
Zhang C, Li Y, Qin J, Yu C, Ma G, Chen H and Xu X (2021) TMT-Based Quantitative Proteomic Analysis Reveals the Effect of Bone Marrow Derived Mesenchymal Stem Cell on Hair Follicle Regeneration. Front. Pharmacol. 12:658040. doi: 10.3389/fphar.2021.658040

Hair loss (HL) is a common chronic problem of poorly defined etiology. Herein, we explored the functionality of bone marrow-derived mesenchymal stem cell (BMSC) and conditioned medium (MSC-CM) as regulators of hair follicle proliferation and regeneration, and the mechanistic basis for such activity. BMSC were cultured and identified *in vitro* through the induction of multilineage differentiation and the use of a CCK-8 kit. The dorsal skin of mice was then injected with BMSC and MSC-CM, and the impact of these injections on hair cycle transition and hair follicle stem cell (HFSC) proliferation was then evaluated via hematoxylin and eosin (H&E) staining and immunofluorescent (IF) staining. We then conducted a tandem mass tags (TMT)-based quantitative proteomic analysis of control mice and mice treated with BMSC or MSC-CM to identify differentially expressed proteins (DEPs) associated with these treatments. Parallel reaction monitoring (PRM) was utilized as a means of verifying our proteomic analysis results. Herein, we found that BMSC and MSC-CM injection resulted in the transition of telogen hair follicles to anagen hair follicles, and we observed the enhanced proliferation of HFSCs positive for Krt15 and Sox9. Our TMT analyses identified 1,060 and 770 DEPs (fold change > 1.2 or < 0.83 and $p < 0.05$) when comparing the BMSC vs. control and MSC-CM vs. control groups, respectively. Subsequent PRM validation of 14 selected DEPs confirmed these findings, and led to the identification of Stmn1, Ncapd2, Krt25, and Ctps1 as hub DEPs in a protein-protein interaction network. Together, these data suggest that BMSC and MSC-CM treatment can promote the proliferation of HFSCs, thereby facilitating hair follicle regeneration. Our proteomics analyses further indicate that Krt25, Cpm, Stmn1, and Mb may play central roles in hair follicle transition in this context and may represent viable clinical targets for the treatment of HL.

Keywords: bone marrow-derived mesenchymal stem cell, hair follicle stem cell, hair follicle regeneration, TMT-based quantitative proteomics analysis, parallel reaction monitoring

INTRODUCTION

Hair loss (HL) is a common cosmetic condition that can have a significant adverse impact on the quality of life (QOL) and well-being of affected individuals. Hair follicles function as miniature organs, and are generally relatively synchronous, undergoing three primary stages of growth: a growth (anagen) phase, a rest (telogen) phase, and an apoptosis-mediated regression (catagen) stage (Paus, 1998). Aside from scar tissue- or wound-induced alopecia, the majority of HL-related disorders are attributable to aberrant hair follicle morphology or dysregulating cycling, including the shortening of the anagen stage or the prolongation of the telogen stage (Cotsarelis and Millar, 2001; Varothai and Bergfeld, 2014).

Hair follicle stem cells (HFSCs) are essential for the regeneration of hair follicles and the transition of these follicles from the telogen to anagen stage. These HFSCs exist as a small cellular subpopulation within the midportion of the follicle at the arrector pili muscle attachment site (Cotsarelis et al., 1990; Blanpain et al., 2004), and can be identified at the molecular level owing to their staining for Krt15(Lyle et al., 1998; Liu et al., 2003) and Sox9 (Vidal et al., 2005; Nowak et al., 2008; Chacón-Martínez et al., 2017).

Bone marrow-derived mesenchymal stem cells (BMSC) are multipotent stem cells (Friedenstein et al., 1974), and they can be readily obtained, grown, and expanded, all while exhibiting minimal immunogenicity (Le Blanc et al., 2003; Bara et al., 2014). Importantly, BMSC can also differentiate into diverse cell types *in vitro* (Prockop, 1997; Pittenger et al., 1999). These properties make BMSC promising candidates for use in the context of regenerative medicine and other tissue engineering applications (Bianco et al., 2001; Lane et al., 2014).

To date, BMSC and conditioned medium (MSC-CM) have been studied in-depth in the context of wound healing assays in animal skin wound model or diabetic foot ulcers, and have been shown to promote wound repair, neoangiogenesis and to accelerate re-epithelialization. Meanwhile, the regeneration of cutaneous appendages, such as hair follicles and sebaceous glands, were also found. The ability and mechanism of BMSC and MSC-CM to induce the regeneration of hair follicles in mice intradermal injection model, however, remains to be studied in detail.

While genomic and transcriptomic analyses can provide insight into the mechanistic basis for hair follicle regeneration, such mRNA-level data may not align with true phenotypic findings given that protein expression levels are determined by multiple factors including mRNA stability, mRNA localization, protein degradation, and posttranslational modifications. Detailed proteomic analyses are therefore essential in order to fully understand the mechanisms whereby BMSC and MSC-CM influence the growth of hair follicles. Tandem mass spectrometry (MS/MS)-based approaches have emerged as a reliable approach to accurately quantifying relative protein levels in complex samples. The use of isotopomer labels to perform tandem mass tag (TMT) MS/MS analyses is increasingly common (Thompson et al., 2003), offering key advantages including high sensitivity, good reproducibility, a high signal-to-noize ratio, and the ability to multiplex up to 11 samples.

Herein, we intradermally transplanted BMSC and MSC-CM into mice and then evaluated hair cycle transition, hair follicle regeneration, and HFSC phenotypes. We additionally employed a TMT-based proteomics approach coupled with PRM to better identify key hair regeneration-related protein targets in this therapeutic context.

MATERIALS AND METHODS

BMSC Isolation and Culture

Female C57BL/6 mice (4–6 weeks old; Beijing Vital River Laboratory Animal Technology Co., Ltd., China) were euthanized, and BMSC were isolated from the femurs of these animals. After isolation, BMSC were cultured in complete DMEM (Sigma-Aldrich, D6046) containing 10% fetal bovine serum (FBS) (Sigma-Aldrich, F2442), 2 mM L-glutamine, and penicillin/streptomycin at 37°C in 5% humidified CO_2. Cells were grown until 80–90% confluent at which time they were passaged. Cells were passaged three times for use in downstream analyses. Supernatants were collected from cells on the fifth day of the third-passage culture, and were used as conditioned media for cell-free MSC-CM assays.

BMSC *in vitro* Differentiation

BMSC were induced to undergo osteogenesis by treating them with low-glucose DMEM containing 10% FBS, 50 μg/ml ascorbic acid, 100 nM dexamethasone 10 mM β-glycerophosphate, and penicillin/streptomycin. Osteogenic differentiation was assessed by measuring alkaline phosphatase (ALP) activity through an azo coupling approach on day 7 following induction, and via Alizarin red staining on day 21 following induction.

Adipogenesis was induced by treating BMSC with low-glucose DMEM containing 10% FBS, 500 mM 1-methyl-3-isobutylxanthine, 1 μM dexamethasone, 200 μM indomethacin, and 10 μM insulin. After three days, this media was exchanged for adipogenic maintenance medium and cells were cultured for one additional day. This process was repeated thrice, after which oil red O staining was performed to evaluate lipid accumulation within these cells.

CCK-8 Assay

A CCK-8 kit was used to gage BMSC proliferation. Briefly, cells were plated in 96-well plates (2000/well in 100 μL), and 10 μL of CCK8 reagent was added per well. Plates were then incubated for 2 h at 37°C, after which absorbance (OD) at 450 nm was measured, and growth curves were established by plotting time against OD values.

Animals

Female C57BL/6 mice (18–20 g, 7 weeks old, Beijing Vital River Laboratory Animal Technology Co., Ltd.) were used for all *in vivo* experiments, which were conducted in accordance with the China Medical University Guidelines for the Care and Use of Laboratory Animals.

Intradermal Injections

Hair clippers and an electric razor were used to remove hair from the dorsal flank of all 60 mice, which were subsequently randomized into three treatment groups (n = 20 each): a control group, an MSC-CM group, and a BMSC group. Control mice were administered media containing no cells, while mice in the MSC-CM group were administered cell-free MSC-CM, and mice in the BMSC group were administered 1×10^6 BMSC in fresh CM. A 250 μL total injection volume was used for a mouse, with 16 separate intradermal injections being made on the dorsal skin of treated mice. One injection was made every other day for two weeks in total.

Histological Analyses

On days 0, 7, 10, and 15 after the initial injection, mice in each group were euthanized and samples of full-thickness dorsal skin were collected, fixed for 24 h with 4% paraformaldehyde (PFA), and paraffin-embedded prior to slicing into 5 μm sections that were subjected to hematoxylin and eosin staining (H&E) based upon standard protocols.

Hair follicle length in each section was quantified by randomly selecting three fields of view per section and measuring the follicle length from papilla to epidermis with the ImageJ program. A total of 20 follicles were measured per mouse, with five mice per group being analyzed at each time point.

Immunofluorescent Staining

The paraffin-embedded 5 μm-thick sections prepared above were used for IF staining. Antigen retrieval was first achieved by treating samples for 4 min with citrate buffer at 100°C, followed by blocking for 1 h with 5% BSA at room temperature. Sections were then probed overnight with primary rabbit anti-Krt15 (1:100 dilution, Abcam, ab52816) and anti-Ki67 (1:100 dilution, Novus Biologicals, NBP2-22112) or anti-Sox9 (1:250 dilution, Abcam, ab185966) and anti-Ki67 (1:100 dilution, Novus Biologicals, NBP2-22112) at 4°C, followed by incubation for 1 h with goat anti-rabbit IgG conjugated to AF594 (1:500 dilution, Cell Signaling, #8889) or goat anti-mouse IgG conjugated to AF488 (1:200 dilution, Abcam, ab150113) at room temperature. DAPI was then used to stain cell nuclei, and a Fluoview FV1000 confocal laser scanning fluorescence microscope (Olympus, Tokyo, Japan) was employed to image cells.

Protein Extraction, Trypsin Digestion, and TMT Proteomic Labeling

A total of four full-thickness dorsal skin samples from each group on day 7 post-injection were collected and subjected to total protein extraction with the MinuteTM Total Protein Extraction Kit for Skin Tissue (Invent Biotechnologies, lnc. Beijing, China). Trypsin digestion was then performed by reducing the protein lysate with a 5 mM dithiothreitol (DTT) solution for 30 min at 56°C, followed by alkylation with 11 mM iodoacetamide (IAA) for 15 min at room temperature protected from light. Next, 200 mM tetraethylammonium bromide (TEAB) was used to dilute samples to a urea concentration of <2 M, and trypsin was added at a 1:50 trypsin-to-protein mass ratio overnight at 37°C, followed by a second digestion for 4 h at a 1:100 trypsin-to-protein mass ratio. Once digestion was complete, a Strata X C18 SPE column (Phenomenex, CA, United States) was used to achieve protein desalting, and samples were vacuum-dried. These peptides were then resuspended in 0.5 M TEAB and processed with a 6-plex TMT kit (Thermo Fisher Scientific, CA, United States) based on provided directions. Briefly, one unit of TMT reagent, which was required to label 100 μg of peptide was thawed and reconstituted in acetonitrile (ACN). The peptide mixtures were then incubated with the prepared TMT reagent for 2 h at room temperature. Finally, TMT-labeled peptide mixtures were pooled, desalted and dried by vacuum centrifugation.

HPLC Fractionation, LC-MS/MS Analysis, and Database Search

TMT-labeled peptides were fractionated via high pH reverse-phase high-performance liquid chromatography (HPLC) with an Agilent 300Extend C18 column (5 μm particles, 4.6 mm ID, 250 mm long). Briefly, TMT-labeled peptide mixture was first separated into 60 fractions with a gradient of 8–32% acetonitrile (ACN, pH 9.0) over 60 min. Then, the fractions were combined into nine fractionated simplified samples and dried by vacuum centrifuging.

Liquid chromatography-tandem mass spectrometry (LC-MS/MS) was performed at PTM Biolab Hangzhou (Hangzhou, China). All fragments were dissolved in solvent A (0.1% formic acid and 2% acetonitrile), directly loaded onto a home-made reversed-phase analytical column (15 cm length, 75 μm i.d.). The gradient was comprised of an increase from 6 to 23% solvent B (0.1% formic acid in 100% acetonitrile) over 42 min, 23–35% solvent B in 12 min and climbing to 80% solvent B in 3 min. Finally, a holding phase at 80% solvent B for the last 3 min was performed, all at a constant flow rate of 450 nL/min on a NanoElute ultraperformance liquid chromatography (UPLC) system. The peptides were subjected to Capillary source followed by tandem mass spectrometry (MS/MS) in tims-TOF Pro coupled online to the UPLC. The electrospray voltage applied was 2.0 kV and intact peptides were detected in the TOF. The secondary mass spectrometry scan range was from 100 to 1700 m/z. Data collection was acquired in parallel accumulation-serial fragmentation (PASEF) mode. A first mass spectrometry was collected and PASEF mode was used for 10 times to collect the secondary mass spectrometry with the charge of the parent ion in the range of 0–5. The dynamic exclusion was set at 30 s to avoid repeated scanning of parent ions.

The Maxquant search engine (v.1.6.6.0) was used to analyze the resultant data, with MS/MS spectra being searched against the *Mus*_musculus_10,090 database (17,045 sequences) concatenated with a reverse decoy database. Trypsin/*p* was specified as cleavage enzyme allowing up to two missing cleavages. The mass tolerance for precursor ions was set as 20 ppm in First search and 5 ppm in Main search, respectively, and 0.02 Da was set for fragment ions. Carbamidomethyl on Cys

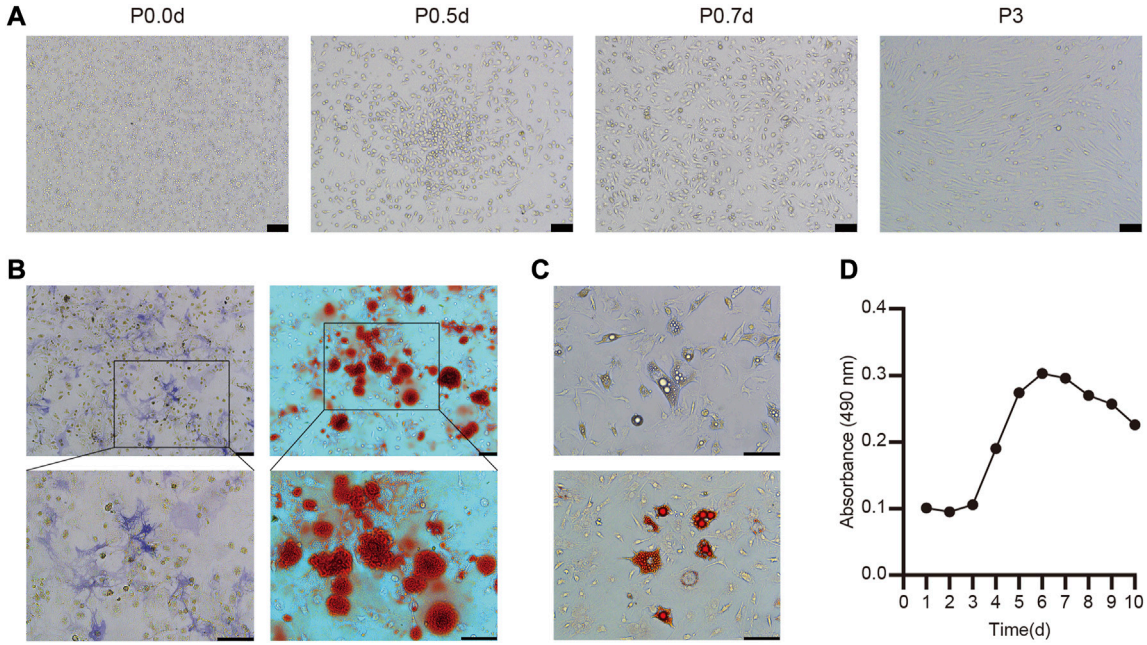

FIGURE 1 | Culture, identification and biological characteristics of BMSC **(A)** The morphology of primary and the third-passage BMSC from C57BL/6 mice was observed under light microscopy **(B)** Osteogenic differentiation was stained with ALP and Alizarin red **(C)** Adipogenic differentiation of BMSC and stained with oil red O **(D)** Cell growth curve of the third passage BMSC.

was specified as fixed modification and oxidation on Met was specified as variable modifications. FDR was adjusted to <1% and minimum score for peptides was set >40.

Parallel Reaction Monitoring Analyses

Protein isolation and trypsinization were conducted as above, after which a PRM mass spectrometric analysis was performed via MS/MS with Q Exactive Plus (Thermo) coupled online to the UPLC. The LC parameters, electrospray voltage, scan range, and Orbitrap resolution were identical to those used for TMT analyses. Automatic gain control was set to 3E6 for full MS and 1E5 for MS/MS, with a maximum IT of 20 ms for full MS and auto for MS/MS. An MS/MS isolation window of 2.0 m/z was used, and the resultant MS data were analyzed with Skyline (v.3.6). Peptide settings: enzyme was set as Trypsin [KR/P], Max missed cleavage set as 2. The peptide length was set as 8–25, Variable modification was set as Carbamidomethyl on Cys and oxidation on Met, and max variable modifications was set as 3. Transition settings: precursor charges were set as 2, 3, ion charges were set as 1, 2, ion types were set as b, y, *p*. The product ions were set as from ion three to last ion, the ion match tolerance was set as 0.02 Da.

Bioinformatics Analyses

DEPs were subjected to functional annotation based upon Gene Ontology (GO) classifications, subcellular localization, and COG/KOG categories, using the UniProt-GOA database and InterProScan, Wolfpsort, and the COG/KOG database.

The enrichment of DEPs for particular GO terms, KEGG pathways, and protein domains were assessed using the GO annotations, KEGG, and InterPro databases, respectively, using two-tailed Fisher's exact test with a $p < 0.05$ as the threshold of significance.

A protein-protein interaction (PPI) network incorporating identified DEPs was prepared with the STRING database (https://string-db.org), using a score >0.4 as the significance threshold for identified interactions.

Statistical Analysis

Data are means ± SD from three or more experiments, and were compared via one- or two-way ANOVAs with Tukey's test. $p < 0.05$ was the significance threshold.

RESULTS

BMSC Characterization

Cultured BMSC exhibit a normal round morphology when cultured at 10^6 cells/mL. Within 24–48 h of isolation, these cells began to adhere and form radial colonies that were evidence within 5 days, growing to 80–90% confluence within 7 days. At the end of this 7-day period, cells exhibited polygonal, triangular, and spindle-like morphology, and were subsequently passaged. Remaining erythrocytes and other non-adherent cells were removed by repeatedly changing the media and passaging these cells, and BMSC from the third passage exhibited uniform fibroblast-like spindle-shaped morphology and were considered suitable for *in vivo* use (**Figure 1A**).

To explore the ability of these BMSC to undergo osteogenesis *in vitro,* they were treated with osteogenic differentiation

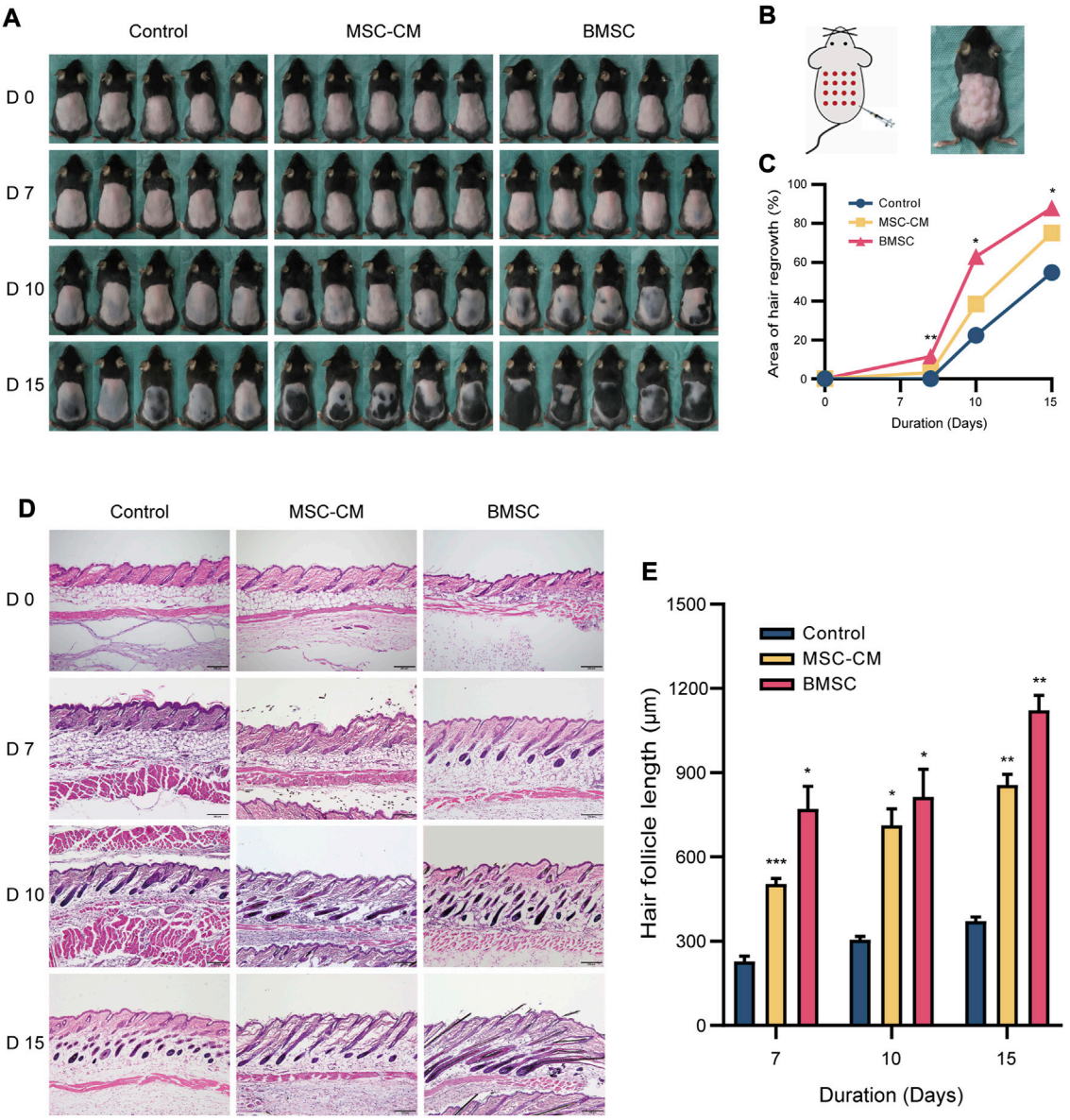

FIGURE 2 | Macroscopic and histologic assessment of mice on 0, 7, 10, 15 days after intradermally injection of MSC-CM and BMSC **(A)** The dorsal skin of control, MSC-CM treated and BMSC treated mice was photographed on 0, 7, 10, and 15 days **(B)** Schematic representation of injection sites and photos of mouse after injection **(C)** Quantification of area of hair regrowth. values are represented in percentage. $^{*}p < 0.05$, $^{**}p < 0.01$ **(D)** Representative H&E staining images of dorsal skin sections on 0, 7, 10, and 15 days for determination of hair follicle cycle and length. Scale bar: 200 μm **(E)** Graph represents length of hair follicle of the visible microscopic field (at-least three fields) with 20 measurements was taken in all three groups. Values are represented in μm. Data are expressed as mean ± SD. $^{*}p < 0.05$, $^{**}p < 0.01$, $^{***}p < 0.001$.

medium and ALP staining was conducted after 7 days via the azo coupling approach, revealing positively stained (blue-purple) cytoplasmic precipitates. Furthermore, Alizarin red staining was used to confirm the differentiation of these cells based on the presence of calcium nodules and bone mineralization on day 21 (**Figure 1B**). We also determined that these BMSC were able to differentiate into adipocytes, as evidenced by the presence of lipid droplets within 4 days and the presence of clear lipid vacuoles upon oil red O staining on day 12 of the differentiation process (**Figure 1C**).

Overall, these findings thus confirmed that these isolated cells were functionally and morphologically consistent with BMSC, making them ideal for use in our experimental model system.

BMSC Growth Kinetics

A CCK-8 assay was next used to evaluate the growth kinetics of third-passage BMSC, revealing a standard "S"-shaped curve with a lag phase from days 1–3, followed by logarithmic growth from days 3–6, a plateau beginning on day 6, and a slight decrease in cell numbers beginning on day 8 (**Figure 1D**). Based upon this

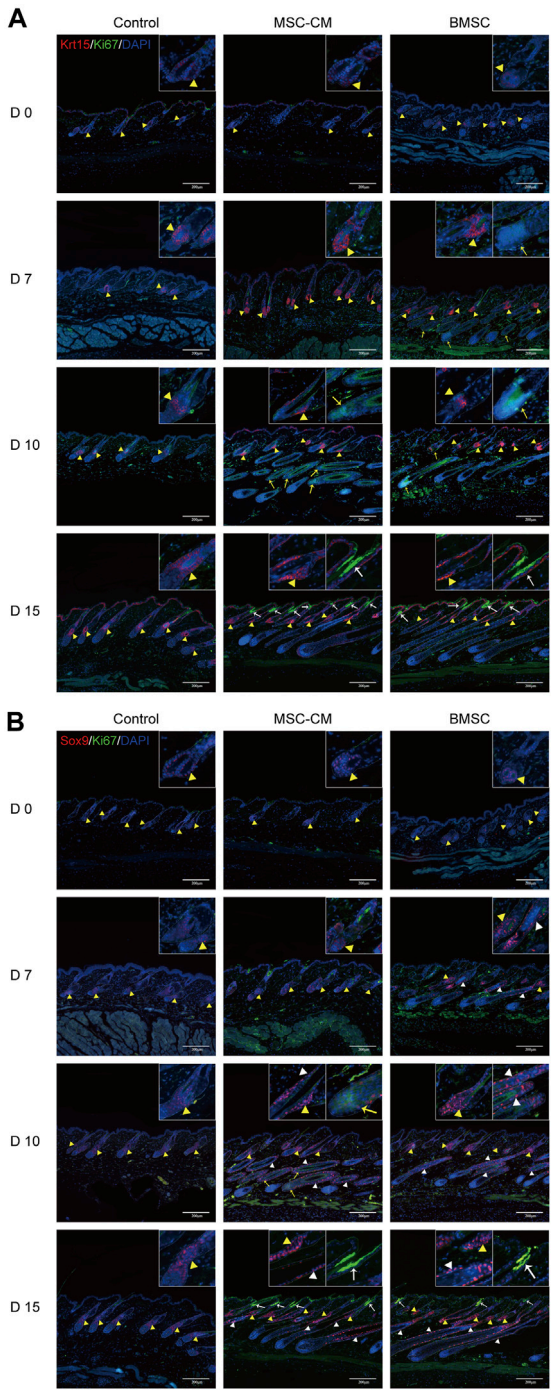

FIGURE 3 | Proliferation of hair follicle stem cells after BMSC and MSC-CM treatment **(A)** Krt15 (red fluorescence) was observed in the Bu region and Ki67 (green fluorescence) was observed in the bulb area and infundibulum of hair follicle at 0, 7, 10 and 15 days **(B)** Sox9 fluorescence (red fluorescence) in the Bu and ORS region and Ki67 (green fluorescence) in the bulb area and infundibulum at 0, 7, 10 and 15 days. Nuclei were stained with DAPI (blue). The dashed line delineates the hair follicle structure. The yellow triangles show the expression site of the bulge (Bu) region and white triangles show the expression site of outer root sheaths (ORS). The bulb areas are indicated by yellow arrows and infundibula are indicated by white arrows. Scale bar: 200 μm.

curve, we elected to utilize third-passaged BMSC collected on the fifth day of culture for all intradermal injection experiments.

The Impact of BMSC and MSC-CM on Hair Follicle Transition *in vivo*

For C57BL/6 mice, shaved skin typically appears pink during the telogen stage but darkens upon anagen initiation (Sato et al., 1999). All mice appeared to be in the telogen phase prior to injection. On day 7 post-injection, however, dark punctate spots were evident in the skin of mice in the BMSC and MSC-CM treatment groups but not in control animals. On day 10 post-injection, the majority of mice in the BMSC and MSC-CM treatment groups had entered the anagen phase, with the tips of hair shafts having begun to emerge from the epidermal layer and with dorsal pigmentation having increased substantially in both groups, with some darkening beginning to appear in the control group as well. On day 15 post-injection, hair growth was nearly complete in the BMSC group, and the majority of the dorsal skin of MSC-CM-treated mice was dark, whereas in control mice this pigmentation and hair growth was sporadic and uneven (**Figure 2A**). The schematic representation of injection sites and photos of mouse after injection were shown in **Figure 2B**. Together, these data revealed that BMSC and MSC-CM treatment were sufficient to induce hair cycle transition in mice. Quantification of these data confirmed that BMSC treatment significantly enhanced hair growth relative to control treatment on days 7, 10, and 15 post-treatment ($^{*}p < 0.05$, $^{**}p < 0.01$) (**Figure 2C**).

Histopathological Staining

We next conducted the H&E staining of tissue samples from these mice, which revealed that samples of control, MSC-CM and BMSC groups were all in telogen on day 0. On day 7 post-injection, control group samples were still in the telogen phase, whereas BMSC- and MSC-CM-treated samples had entered the anagen phase and exhibited increased numbers of hair matrix cells. On day 10 post-injection, control group samples exhibited an increase in the volume of the hair follicle dermal papilla, while the dermal papilla in the MSC-CM-treated samples was largely surrounded by hair matrix cells, and was surrounded by dermal papilla in the BMSC-treated samples with clear evidence of hair shaft development. On day 15 post-injection, most follicles in the control group had entered the anagen phase, while there was a clear increase in hair follicle density in the BMSC group and the BMSC-CM group (**Figure 2D**). Quantitative analyses confirmed that hair follicle length increased over time after injection, with significantly longer hair follicles being observed in the BMSC and MSC-CM treatment groups relative to the control group ($^{*}p < 0.05$, $^{**}p < 0.01$, $^{***}p < 0.001$) (**Figure 2E**).

BMSC and MSC-CM Treatments Induce HFSC Activation

HFSCs are key mediators of hair regeneration, and their ability to proliferate is closely linked to hair follicle transition and overall hair growth. As such, we next analyzed the expression of the HFSC markers Krt15 and Sox9 in the dorsal skin of our treated mice via IF staining. This approach revealed that there was no difference in the fluorescence intensity between three groups on

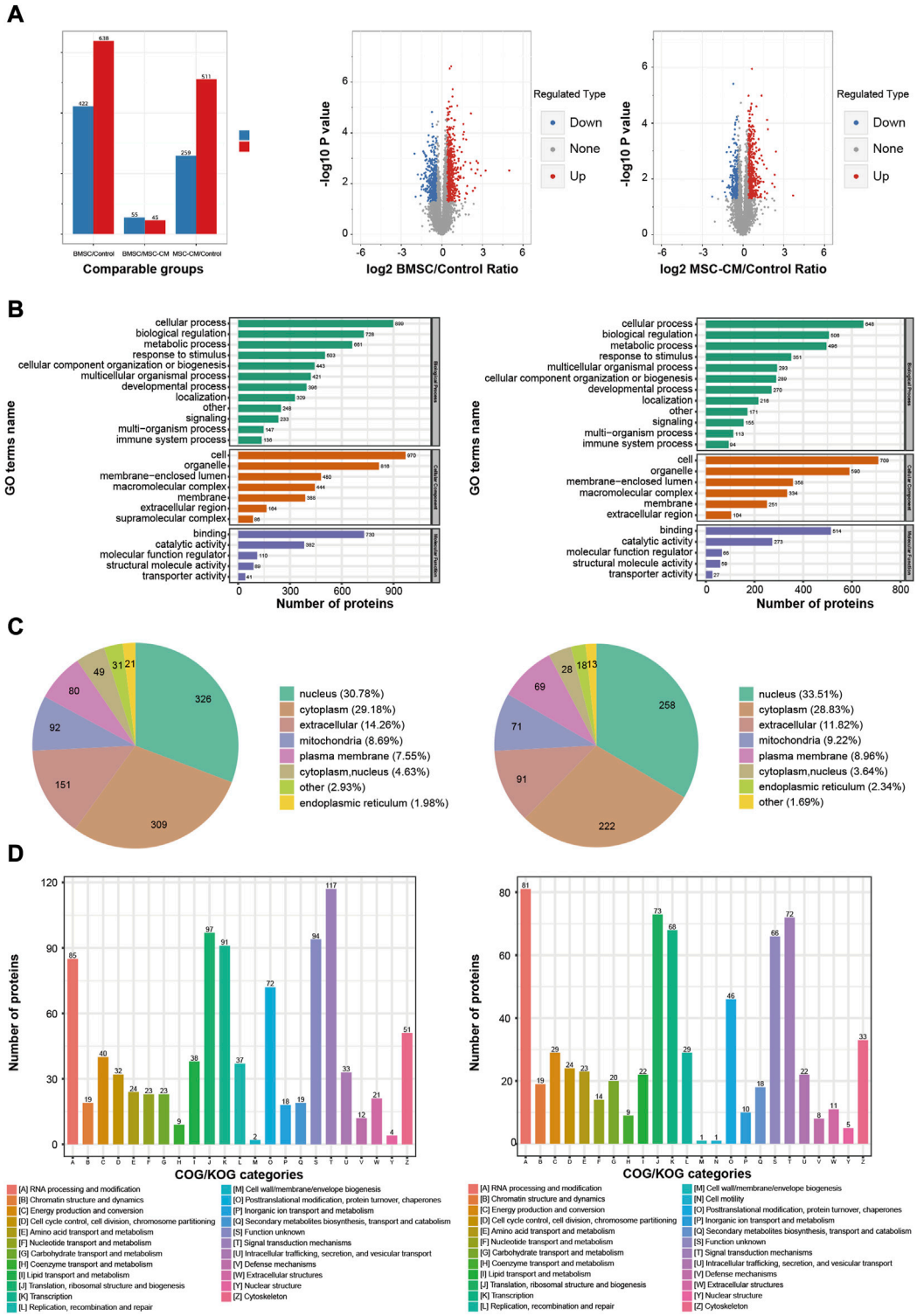

FIGURE 4 | Functional annotations and classification of the DEPs in BMSC/Control group and MSC-CM/Control group **(A)** Statistics and volcano plots of the DEPs **(B)** Statistical distribution chart of the DEPs under each GO category (second Level) **(C)** Subcellular localization chart of the DEPs **(D)** COG/KOG functional classification chart of the DEPs. Note: DEPs: Differentially Expressed Proteins.

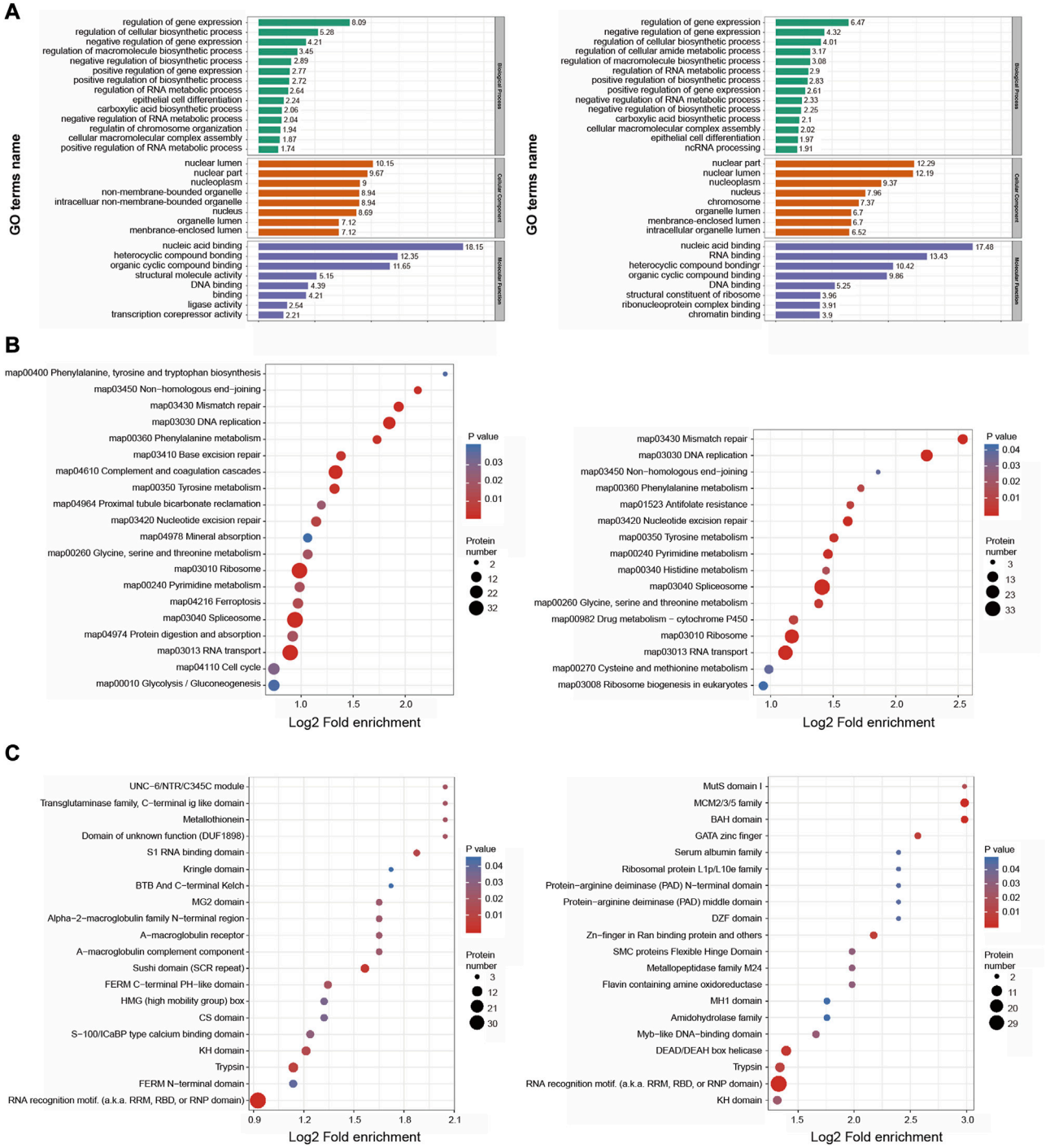

FIGURE 5 | Functional enrichment analysis of the DEPs in BMSC/Control group and MSC-CM/Control group **(A)** GO enrichment analysis of the DEPs were annotated and enriched by biological process, cell component and molecular function **(B)** KEGG pathway enrichment analysis of the DEPs **(C)** Protein domain enrichment analysis of the DEPs.

days 0 and there were significantly more Krt15 + proliferating cells in the bulge region and Ki67 + proliferating cells in the bulb area and infundibulum of hair follicles in the BMSC and MSC-CM treatment groups on days 7, 10, and 15 of treatment relative to the control group (**Figure 3A**). We also detected a significant increase in Sox9 expression in the bulge and outer root sheath (ORS) region and Ki67 expression in the bulb area and infundibulum of follicles from BMSC- and MSC-CM-treated mice (**Figure 3B**). Together, these data show that treatment with BMSC or MSC-CM can trigger HFSC activation and thereby promote hair regrowth.

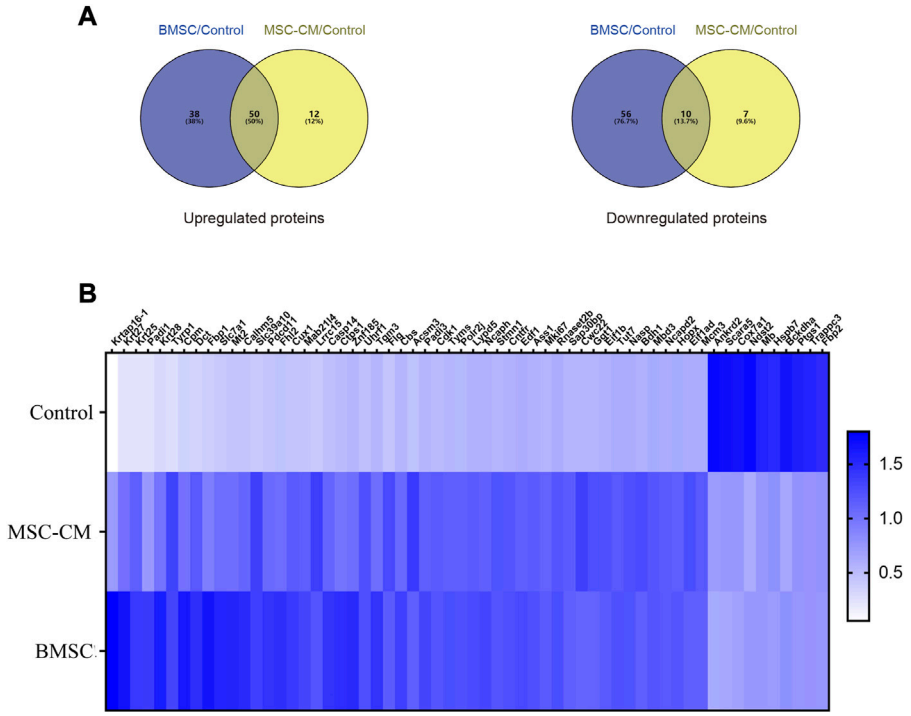

FIGURE 6 | Discovery of candidate hair follicle regeneration related proteins **(A)** Venn diagrams of differentially expressed proteins between BMSC vs. control and MSC-CM vs. control groups. Fold change >1.85 or <0.54 and *p*-value < 0.05 **(B)** Heatmap of the 60 optimized DEPs in the Control, MSC-CM, and BMSC groups. The X-coordinate stands for the DEPs, while Y-coordinate stands for the different groups.

Identification of Proteins Differentially Expressed in Response to BMSC and MSC-CM Treatment

We next conducted a TMT labeling-based proteomic analysis of dorsal skin samples from mice in our control, BMSC, and MSC-CM treatment groups. In total, we identified 63,131 peptides, of which 60,598 were unique, leading to the identification of 5,046 quantifiable proteins. Those proteins with a fold change (FC) > 1.30 or <0.77 and $p < 0.05$ when comparing the BMSC or MSC-CM groups to the control group were identified as differentially expressed proteins (DEPs).

In total, we identified 1,060 DEPs when comparing the BMSC and control group samples (638 upregulated, 422 downregulated), while 770 were identified when comparing the MSC-CM and control group samples (511 upregulated, 259 downregulated) (**Figure 4A**).

In the BMSC vs. control and MSC-CM vs. control groups, overall DEPs were classified based upon their enrichment in specific GO biological process (BP), molecular function (MF), and cellular component (CC) terms. With respect to BPs, DEPs were primarily involved in cellular processes (899 proteins; 648 proteins), biological regulation (728 proteins; 506 proteins), and metabolic processes (661 proteins; 496 proteins). With respect to CCs, these DEPs were primarily enriched in cell (970 proteins; 709 proteins), organelle (816 proteins; 590 proteins), and membrane-enclosed lumen (480 proteins; 358 proteins). With respect to MFs, DEPs were mainly enriched for binding (730 proteins; 514 proteins), catalytic activity (382 proteins; 273 proteins), and molecular function regulation (110 proteins; 66 proteins) (**Figure 4B**).

Wolfpsort was used to predict the subcellular localization of these DEPs, which were primarily localized to the nucleus (30.78%; 33.51%), cytoplasm (29.18%; 28.83%), and extracellular compartment (14.26%; 11.82%) (**Figure 4C**).

COG/KOG functional classification analyses assigned these DEPs to 23 functional KOG classifications that were primarily associated with signal transduction (117 proteins; 72 proteins), translation, ribosomal structure, and biogenesis (97 proteins; 73 proteins), and transcription (91 proteins; 68 proteins) (**Figure 4D**).

Functional Enrichment Analyses of Treatment-Related DEPs

To better understand the relationship between identified DEPs and hair regrowth, we next conducted functional enrichment analyses of proteins that were differentially expressed between the BMSC or MSC-CM groups and the control group based upon GO, KEGG pathway, and protein domain analyses.

With respect to GO biological processes, DEPs were enriched in the regulation of gene expression, regulation of cellular biosynthetic processes, and negative regulation of gene expression. They were additionally enriched for cellular components including the nuclear lumen, nuclear part, and nucleoplasm, and for molecular functions including nucleic

TABLE 1 | The 50 optimized up-regulated expressed proteins.

Protein ID	Protein name	Gene name	Fold change (BMSCs/ control)	*p*-value (BMSCs/ control)	Fold change (mscs-cm/ control)	*p*-value (mscs-cm/ control)
A2A5X5	Keratin-associated protein 16–1	Krtap16–1	31.561	3.03E-03	12.86	3.92E-02
Q9Z320	Keratin, type I cytoskeletal 27	Krt27	7.373	4.80E-03	4.436	1.46E-02
Q8VCW2	Keratin, type I cytoskeletal 25	Krt25	6.192	2.77E-03	5.027	7.05E-03
Q9Z185	Protein-arginine deiminase type-1	Padi1	5.635	3.89E-03	5.357	1.04E-03
A6BLY7	Keratin, type I cytoskeletal 28	Krt28	5.455	1.45E-02	3.406	3.25E-02
P07147	5,6-Dihydroxyindole-2-carboxylic acid oxidase	Tyrp1	4.899	1.91E-02	5.007	1.92E-02
Q80V42	Carboxypeptidase M	Cpm	4.572	2.74E-03	2.833	1.26E-02
P29812	L-dopachrome tautomerase	Dct	4.457	1.73E-05	3.564	1.64E-04
Q9QXD6	Fructose-1,6-bisphosphatase 1	Fbp1	4.31	1.53E-03	2.421	4.01E-02
Q09143	High affinity cationic amino acid transporter 1	Slc7a1	3.674	1.24E-02	2.487	3.50E-02
P02798	Metallothionein-2	Mt2	3.479	1.81E-04	2.281	8.23E-03
Q8R100	Calcium homeostasis modulator protein 5	Calhm5	3.469	2.35E-02	2.506	4.53E-02
Q6P5F6	Zinc transporter ZIP10	Slc39a10	3.342	1.39E-03	3.357	4.21E-03
Q6NS46	Protein RRP5 homolog	Pdcd11	3.295	3.84E-02	2.426	9.72E-03
O70433	Four and a half LIM domains protein 2	Fhl2	3.118	9.26E-05	2.224	9.31E-04
P53564	Homeobox protein cut-like 1	Cux1	3.062	5.87E-03	2.587	1.01E-05
Q8CEZ4	Protein mab-21-like 4	Mab21l4	3.039	1.93E-03	2.685	2.16E-03
Q80 × 72	Leucine-rich repeat-containing protein 15	Lrrc15	3.02	4.49E-05	3.42	7.61E-05
O89094	Caspase-14	Casp14	3.016	1.71E-04	2.303	1.84E-03
P70698	CTP synthase 1	Ctps1	2.984	1.16E-04	1.981	2.51E-02
Q62394	Zinc finger protein 185	Znf185	2.764	5.70E-04	1.883	1.09E-02
Q8VDF2	E3 ubiquitin-protein ligase UHRF1	Uhrf1	2.619	2.69E-03	2.57	1.46E-03
Q08189	Protein-glutamine gamma-glutamyltransferase E	Tgm3	2.614	5.94E-03	1.854	3.75E-02
P11088	Filaggrin (fragment)	Flg	2.587	5.12E-03	2.896	3.02E-03
Q91WT9	Cystathionine beta-synthase	Cbs	2.47	5.79E-03	1.931	3.65E-02
Q3UNX5	Acyl-coenzyme a synthetase ACSM3, mitochondrial	Acsm3	2.459	4.44E-02	3.024	2.87E-02
Q9Z184	Protein-arginine deiminase type-3	Padi3	2.384	2.05E-02	2.078	1.38E-02
P11440	Cyclin-dependent kinase 1	Cdk1	2.359	1.04E-03	2.308	8.70E-04
P07607	Thymidylate synthase	Tyms	2.327	6.90E-03	2.11	2.64E-02
O08740	DNA-directed RNA polymerase II subunit RPB11	Polr2j	2.298	7.26E-03	2.125	8.61E-03
Q9D7Z7	Ly6/PLAUR domain-containing protein 5	Lypd5	2.255	3.05E-02	2.055	3.75E-02
Q8C156	Condensin complex subunit 2	Ncaph	2.211	6.54E-03	1.908	3.10E-02
P54227	Stathmin OS = *Mus musculus*	Stmn1	2.209	8.55E-06	2.219	3.69E-04
O88507	Ciliary neurotrophic factor receptor subunit alpha	Cntfr	2.207	1.66E-02	2.102	1.54E-02
Q9JMG1	Endothelial differentiation-related factor 1	Edf1	2.16	1.18E-02	1.908	2.87E-02
P16460	Argininosuccinate synthase	Ass1	2.114	2.85E-03	1.958	9.77E-03
E9PVX6	Proliferation marker protein Ki-67	Mki67	2.091	3.10E-03	2.005	4.46E-03
C0HKG6	Ribonuclease T2-B	Rnaset2b	2.081	3.82E-03	1.975	3.23E-02
Q02614	SAP30-binding protein	Sap30bp	2.076	1.55E-03	2.116	2.68E-03
Q8C5N3	Pre-mRNA-splicing factor CWC22 homolog	Cwc22	2.006	4.81E-02	2.492	1.23E-02
Q60928	Glutathione hydrolase 1 proenzyme	Ggt1	2.005	1.64E-02	2.247	1.99E-02
Q9CXU9	Eukaryotic translation initiation factor 1 b	Eif1b	2.003	2.29E-02	2.093	4.62E-02
Q5BLK4	Terminal uridylyltransferase 7	Tut7	2.002	6.58E-03	1.924	6.56E-03
Q99MD9	Nuclear autoantigenic sperm protein	Nasp	1.991	2.30E-03	2.022	2.47E-03
Q80XN0	D-beta-hydroxybutyrate dehydrogenase, mitochondrial	Bdh1	1.962	2.41E-02	2.199	1.16E-02
Q9Z2D8	Methyl-CpG-binding domain protein 3	Mbd3	1.959	1.27E-02	1.926	1.73E-02
Q8K2Z4	Condensin complex subunit 1	Ncapd2	1.951	1.92E-04	1.93	5.00E-04
Q8R1H0	Homeodomain-only protein	Hopx	1.926	1.61E-02	1.858	1.23E-02
Q3THJ3	Probable RNA-binding protein EIF1AD	Eif1ad	1.881	1.54E-02	2.096	1.14E-02
P25206	DNA replication licensing factor MCM3	Mcm3	1.858	1.51E-03	1.955	7.45E-04

acid binding, heterocyclic compound binding, and organic cyclic compound binding (**Figure 5A**).

KEGG pathway enrichment analyses revealed these DEPs to be enriched in DNA replication, mismatch repair, splicesome, and ribosome pathways (**Figure 5B**).

Protein domain enrichment analyses revealed these DEPs to be enriched in RNA recognition motifs and trypsin domain (**Figure 5C**).

Together, based on functional classifications and enrichment analyses, these DEPs are involved in genetic material replication, cell cycle control, and metabolic regulation, which are related to hair cycle transition.

PRM Validation

DEPs that were shared between the BMSC vs. control and MSC-CM vs. control datasets (FC > 1.85 or <0.54 and $p < 0.05$) were identified

TABLE 2 | The 10 optimized down-regulated expressed proteins.

Protein ID	Protein name	Gene name	Fold change (BMSCs/ control)	*p*-value (BMSCs/ control)	Fold change (mscs-cm/ control)	*p*-value (mscs-cm/ control)
Q9WV06	Ankyrin repeat domain-containing protein 2	Ankrd2	0.358	1.33E-02	0.418	4.21E-02
Q8K299	Scavenger receptor class a member 5	Scara5	0.386	5.30E-04	0.437	1.10E-03
P56392	Cytochrome c oxidase subunit 7A1, mitochondrial	Cox7a1	0.399	1.68E-02	0.447	2.00E-02
P52850	Bifunctional heparan sulfate N-deacetylase/N-sulfotransferase 2	Ndst2	0.428	1.64E-02	0.352	1.18E-02
P04247	Myoglobin	Mb	0.473	2.13E-02	0.482	1.72E-02
P35385	Heat shock protein beta-7	Hspb7	0.487	7.50E-03	0.53	7.28E-03
P50136	2-Oxoisovalerate dehydrogenase subunit alpha, mitochondrial	Bckdha	0.489	4.80E-02	0.396	3.00E-02
P22437	Prostaglandin G/H synthase 1	Ptgs1	0.49	2.22E-02	0.499	1.93E-02
O55013	Trafficking protein particle complex subunit 3	Trappc3	0.503	3.45E-02	0.499	2.09E-02
P70695	Fructose-1,6-bisphosphatase isozyme 2	Fbp2	0.51	1.29E-03	0.531	3.51E-03

using Venn diagrams, leading to the identification of 60 optimized DEPs, of which 50 and 10 were up- and down-regulated, respectively (**Figure 6A**; **Tables 1**, **2**). These proteins are shown in a heatmap in **Figure 6B**. Of these 60 DEPs, we selected nine upregulated DEPs (Krt25, Cpm, Ctps1, Flg, Ncapd2, Tyrp1, Dct, Tgm3, Stmn1) (**Figures 7A**,**B**) and five downregulated DEPs (Mb, Hspb7, Cox7a1, Scara5, Fbp2) (**Figure 7C**) for subsequent PRM validation. Our quantitative PRM results confirmed that these candidate DEPs exhibited trends comparable to those observed upon TMT analysis, confirming the reliability of our proteomics data (**Table 3**).

PPI Network Analysis

Lastly, we constructed a PPI network incorporating DEPs that were shared between the BMSC vs. control and MSC-CM vs. control datasets, including some of the proteins from our PRM validation analysis. Several of our PRM validation proteins were identified as hub proteins within this PPI network, including Stathmin 1 (Stmn1), Non-SMC condensin I complex subunit D2 (Ncapd2), Keratin, type I cytoskeletal 25 (Krt25), and Cytidine triphosphate synthetase 1 (Ctps1) (**Figure 8**). These proteins may thus play key roles in mitosis and migration, stem cell proliferation, hair follicle regeneration, and hair cycle transition.

DISCUSSION

BMSC and derivatives thereof are frequently studied as a potential resource for use in therapeutic applications as a means of repairing damaged tissue (Zhang et al., 2018), treating inflammatory diseases (Shi et al., 2018; Harrell et al., 2019), or normalizing aberrant immunological and inflammatory responses in a range of contexts. BMSC are particularly promising in these therapeutic contexts as they can undergo self-renewal, multipotent differentiation, and enable patient-specific tissue regeneration without any significant ethical concerns (Park et al., 2019).

Significant progress has been made in applying BMSC and conditioned medium as a means of treating androgenic alopecia and alopecia areata (Elmaadawi et al., 2018). BMSC-conditioned medium collected during BMSC culture has been used as a cell-free therapeutic approach in stem cell therapy. Paracrine factors including basic fibroblast growth factor (bFGF), vascular endothelial growth factor (VEGF), epidermal growth factor (EGF), hepatocyte growth factor (HGF), insulin-like growth factor-1 (IGF-1), and platelet-derived growth factor (PDGF) are present in MSC-CM preparations and are likely to contribute to tissue follicle regeneration (Fu et al., 2019).

The mechanisms whereby BMSC can facilitate hair regeneration, however, remain poorly understood. As such, in the present study, we injected BMSC and MSC-CM into the dorsal side of 7-week-old C57BL/6 mice and explored the biological basis of BMSC-induced hair regrowth. We confirmed that both of these treatment approaches were able to expedite the telogen-to-anagen transition necessary to enhance hair growth.

Hair loss can be classified as being either permanent, cicatricial, non-reversible scarring alopecia, or temporary, non-cicatricial, reversible non-scarring alopecia. In cases of scarring alopecia, as in patients with cutaneous lupus erythematosus and lichen planus, inflammation leads to irreversible HFSC loss. In contrast, forms of non-scarring alopecia such as alopecia areata (AA) and androgenic alopecia (AGA) are characterized by the loss of progenitor cells but the preservation of HFSCs, allowing for the restoration of hair growth (Garza et al., 2011). Promoting the proliferation and differentiation of HFSCs is thus necessary to facilitate hair regeneration and telogen-to-anagen transition. Several signaling pathways regulate HFSCs activation and they include Wnt/β-catenin (Deschene et al., 2014), BMP, and mTOR (Deng et al., 2015) signaling pathways.

HFSCs are activated via a two-step process during hair regeneration: Secondary hair germ cells are first activated by dermal papilla at anagen onset, followed by bulge HFSC during the anagen III phase (Greco et al., 2009). Cytokeratin 15 (Krt15) is an HFSC marker protein (Lyle et al., 1998; Liu et al., 2003), and is used together with CD200 and CD34 to monitor the efficacy of AA and AGA treatment (Elmaadawi et al., 2018). Sox9 (Vidal et al., 2005; Nowak et al., 2008) is also a potential HFSC marker. Herein, we found that the levels of Krt15-and Sox9-positive cells rose in bulge and ORS regions following BMSC and MSC-CM injection, confirming that these treatments were able to induce

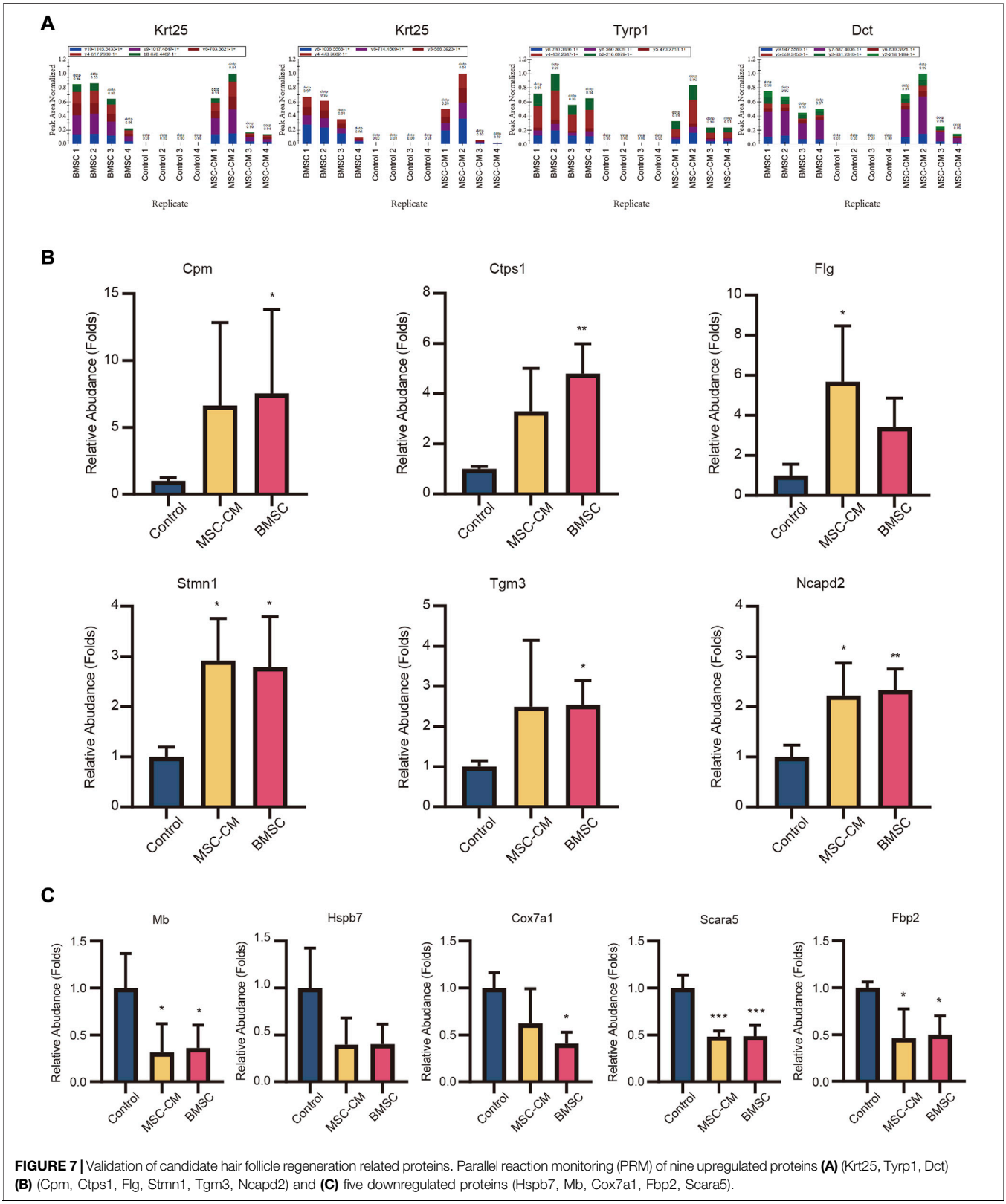

FIGURE 7 | Validation of candidate hair follicle regeneration related proteins. Parallel reaction monitoring (PRM) of nine upregulated proteins **(A)** (Krt25, Tyrp1, Dct) **(B)** (Cpm, Ctps1, Flg, Stmn1, Tgm3, Ncapd2) and **(C)** five downregulated proteins (Hspb7, Mb, Cox7a1, Fbp2, Scara5).

TABLE 3 | PRM analysis of 14 candidate proteins.

Protein ID	Prorein name	Gene name	Peptide sequence	BMSCs/ Control Ratio	BMSCs/ Control ratio (TMT)	MSCs-CM/ Control Ratio	MSCs-CM/ Control Ratio (TMT)
Q8VCW2	Keratin, type I cytoskeletal 25	Krt25	LASYLDNVQALQEANADLEQK LEYEQLLNVK	∞	6.19	∞	5.03
P07147	5,6-Dihydroxyindole-2-carboxylic acid oxidase	Tyrp1	NTVEGYSAPTGK	∞	4.90	∞	5.01
P29812	L-dopachrome tautomerase	Dct	EQFLGALDLAK	∞	4.46	∞	3.56
Q80V42	Carboxypeptidase M	Cpm	LPLFWNDNK	7.51	4.57	6.65	2.83
P70698	CTP synthase 1	Ctps1	GLGLSPDLVVCR NVLGWQDANSTEFDPK	4.74	2.98	3.24	1.98
P11088	Filaggrin (fragment)	Flg	AGSSSGSGVQGASAGGLAADASR GQSPDASGR	3.42	2.59	5.66	2.90
P54227	Stathmin	Stmn1	ASGQAFELILSPR ESVPDFPLSPPK	2.79	2.21	2.92	2.22
Q08189	Protein-glutamine gamma-glutamyltransferase E	Tgm3	VITNFNSAHDTDR IAYSQYER	2.87	2.61	1.80	1.85
Q8K2Z4	Condensin complex subunit 1	Ncapd2	HSQELSSILDDAALSGSDR GFAAFLTELAER	2.34	1.95	2.22	1.93
P04247	Myoglobin	Mb	VEADLAGHGQEVLIGLFK GQHAAEIQPLAQSHATK	0.36	0.47	0.31	0.48
P35385	Heat shock protein beta-7	Hspb7	CQLPEDVDPTSVTSALR	0.40	0.49	0.40	0.53
P56392	Cytochrome c oxidase subunit 7A1, mitochondrial	Cox7a1	LFQADNDLPVHLK	0.41	0.40	0.62	0.45
Q8K299	Scavenger receptor class a member 5	Scara5	LLQAPLQADLTEQVWK VGVLGEELADVGGALR	0.49	0.39	0.48	0.44
P70695	Fructose-1,6-bisphosphatase isozyme 2	Fbp2	EAVITAQER VPLILGSPEDVQEYLSCVQR	0.50	0.51	0.46	0.53

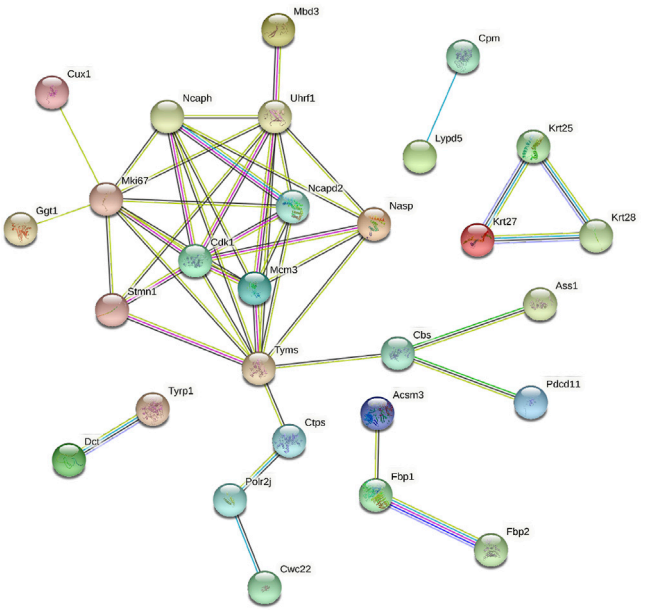

FIGURE 8 | (A) PPI network of some of the optimized upregulated and downregulated proteins.

telogen-to-anagen hair cycling via promoting HFSC proliferation.

We also found that BMSC and MSC-CM treatment were associated with significant increases in the expression of certain key hair structure- and induction-related proteins. For example, keratins, which encode intermediate filaments, are involved in several key processes. The type I keratin gene Krt25 is expressed in the hair medulla and all three layers of the inner root sheath (IRS) (Langbein et al., 2006), wherein it is involved in protecting, supporting, and molding the hair shaft. Ansar (Ansar et al., 2015) and Zernov (Zernov et al., 2016) et al. found that Krt25 mutations were damaging to intermediate filament formation and hair follicle development, resulting in autosomal recessive hypotrichosis. Moreover, the transglutaminase (TGase) isoform TGase-3 is expressed within the cuticle and cortex of growing hair fibers wherein it is involved in progressive hair shaft scaffolding via driving the formation of isopeptide bonds between intermediate filaments and keratin-associated proteins (KAPs). Tarsca et al. have also shown this enzyme to play a role in regulating mouse anagen hair fiber rigidity (Tarcsa et al., 1997), and Sebastien et al. have referred to is as a possible mediator in the context of hair shaft scaffolding (Thibaut et al., 2009). Susan et al. also showed that hair lacking TGase-3 was thinner and that there were clear cuticle cell alterations in mice lacking TGase-3 (John et al., 2012). We also found the expression of the hair melanin biosynthetic proteins 5,6-dihydroxyindole-2-carboxylic acid oxidase (Tyrp1) (Zdarsky et al., 1990; Kobayashi et al., 1994) and L-dopachrome tautomerase (Dct) (Jackson et al., 1992; Tsukamoto et al., 1992) to be significantly increased in skin samples following BMSC and MSC-CM treatment.

Many studies have shown T cells and macrophages to be recruited and to induce hair regeneration via the activation of

HFSC differentiation (Rahmani et al., 2020) during physiologic hair cycling (Castellana et al., 2014; Ali et al., 2017), wounding, and depilation-induced hair growth (Chen et al., 2015; Lee et al., 2017; Wang et al., 2017; Rahmani et al., 2018). Notably, one of our validated DEPs identified in this study, carboxypeptidase M (Cpm), is often used as a marker for the differentiation of monocytes into macrophages (Rehli et al., 1995; Krause et al., 1998). We observed significant Cpm upregulation following BMSC and MSC-CM injection, suggesting that such treatment may be involved in macrophage recruitment and consequent anagen onset. We also identified cytidine triphosphate (CTP) synthetase 1 (Ctps1) to be significantly upregulated in this experimental system, which is noteworthy given that it is involved in activated T cell proliferation (Martin et al., 2014). Our data thus suggested that BMSC and MSC-CM treatment induce hair follicle regeneration through mechanisms associated with immunomodulation.

We additionally identified multiple upregulated proteins related to the cell cycle and proliferation. Filaggrin (Flg), for example, is involved in mechanical barrier function in healthy skin, with Salerno et al. having shown melanoma cells to upregulate Flg (Salerno et al., 2016). Leick et al. also successfully knocked out Flg in DM93 human melanoma cells via a CRISPR/Cas9 approach and thereby clarified its role in the context of cellular growth (Leick et al., 2019). Stathmin 1 (Stmn1) is a protein involved in destabilizing microtubules that it is involved in mitosis and migration by controlling free tubulin dimer availability within cells (Ringhoff and Cassimeris, 2009). Stmn1 depletion has been shown to contribute to cell cycle arrest (Chen et al., 2007) and enhanced apoptotic death (Alli et al., 2007; Ma et al., 2017). Bichsel et al. also previously demonstrated that Stmn1 deletion promoted expedited catagen transition and prematurely suppressed follicular proliferation, suggesting it plays a critical role in hair follicle cycling (Bichsel et al., 2016). Non-SMC condensin I complex subunit D2 (Ncapd2) is a condensin I complex subunit encoded on chromosome 12p13.3 that is primarily involved in chromosome condensation and segregation. Zhang et al. determined that Ncapd2 is an essential mediator of cell cycle progression and triple-negative breast cancer (TNBC) cell migration such that when it was knocked down, TNBC cells failed to proliferate or exhibit invasive activity, and instead underwent apoptotic death (Zhang et al., 2020).

In addition to these upregulated proteins, we also validated multiple proteins that were downregulated in the BMSC and MSC-CM groups relative to control mice (Hspb7, Mb, Cox7a1, Fbp2, Scara5). Hspb7, Mb, Cox7a1, Fbp2, and Scara5 have all previously been identified as tumor suppressor genes (Naderi, 2018) in breast cancer (Braganza et al., 2019), non-small cell lung cancer (Zhao et al., 2019), gastric cancer (Li et al., 2013), sarcoma (Huangyang et al., 2020), and hepatocellular carcinoma (Huang et al., 2010), wherein they can suppress tumor cell invasion, proliferation, and migration. In contrast, our data suggest that BMSC and MSC-CM treatment can enhance proliferation and hair follicle regeneration via reducing the expression of these key proteins.

CONCLUSION

In summary, we herein evaluated the ability of BMSC and MSC-CM to promote the regeneration of hair follicles. We found that both of these treatments were capable of promoting follicle telogen-to-anagen transition in C57BL/6 mice, increasing follicle length and driving HFSC proliferation. Our TMT-based proteomics approach identified Krt25, Cpm, Stmn1, and Mb as candidate follicle regeneration-related proteins, and these findings were validated via PRM. Overall, these data thus suggest that BMSC and MSC-CM may represent ideal therapeutic approaches to anagen induction and hair growth stimulation as a means of treating HL.

DATA AVAILABILITY STATEMENT

The datasets presented in this study can be found in online repositories. The names of the repository/repositories and accession number(s) can be found in the article/ **Supplementary material**.

ETHICS STATEMENT

The animal study was reviewed and approved by the Ethics Committee of the China Medical University.

AUTHOR CONTRIBUTIONS

CZ carried out all the experiments, collection and analysis of data, and wrote the manuscript. HC, and XX performed experimental guidance and data analysis. YL, JQ, CY, and GM contributed to BMSC culture and data collection. All authors read and approved the final manuscript.

FUNDING

This work was supported by the National Natural Science Foundation of China (81972956), the National Key Research and Development Program of China (No.2016YFC0901504) and the 111 Project (D18011).

ACKNOWLEDGMENTS

The authors would like to thank all the reviewers who participated in the review and MJEditor (www.mjeditor.com) for its linguistic assistance during the preparation of this manuscript.

SUPPLEMENTARY MATERIAL

The Supplementary Material for this article can be found online at: https://www.frontiersin.org/articles/10.3389/fphar.2021.658040/full#supplementary-material.

REFERENCES

Ali, N., Zirak, B., Rodriguez, R. S., Pauli, M. L., Truong, H.-A., Lai, K., et al. (2017). Regulatory T cells in skin facilitate epithelial stem cell differentiation. *Cell* 169 (6), 1119. doi:10.1016/j.cell.2017.05.002

Alli, E., Yang, J.-M., and Hait, W. N. (2007). Silencing of stathmin induces tumor-suppressor function in breast cancer cell lines harboring mutant p53. *Oncogene* 26 (7), 1003–1012. doi:10.1038/sj.onc.1209864

Ansar, M., Raza, S. I., Lee, K., Irfanullah, S., Shahi, A., Dai, H., et al. (2015). A homozygous missense variant in type I keratinKRT25causes autosomal recessive woolly hair. *J. Med. Genet.* 52 (10), 676–680. doi:10.1136/jmedgenet-2015-103255

Bara, J. J., Richards, R. G., Alini, M., and Stoddart, M. J. (2014). Concise review: bone marrow-derived mesenchymal stem cells change phenotype following *in vitro* culture: implications for basic research and the clinic. *Stem Cells* 32 (7), 1713–1723. doi:10.1002/stem.1649

Bianco, P., Riminucci, M., Gronthos, S., and Robey, P. G. (2001). Bone marrow stromal stem cells: nature, biology, and potential applications. *Stem Cells* 19 (3), 180–192. doi:10.1634/stemcells.19-3-180

Bichsel, K. J., Hammiller, B., Trempus, C. S., Li, Y., and Hansen, L. A. (2016). The epidermal growth factor receptor decreases Stathmin 1 and triggers catagen entry in the mouse. *Exp. Dermatol.* 25 (4), 275–281. doi:10.1111/exd.12921

Blanpain, C., Lowry, W. E., Geoghegan, A., Polak, L., and Fuchs, E. (2004). Self-renewal, multipotency, and the existence of two cell populations within an epithelial stem cell niche. *Cell* 118 (5), 635–648. doi:10.1016/j.cell.2004.08.012

Braganza, A., Quesnelle, K., Bickta, J., Reyes, C., Wang, Y., Jessup, M., et al. (2019). Myoglobin induces mitochondrial fusion, thereby inhibiting breast cancer cell proliferation. *J. Biol. Chem.* 294 (18), 7269–7282. doi:10.1074/jbc.RA118.006673

Castellana, D., Paus, R., and Perez-Moreno, M. (2014). Macrophages contribute to the cyclic activation of adult hair follicle stem cells. *Plos Biol.* 12 (12), e1002002. doi:10.1371/journal.pbio.1002002

Chacón-Martínez, C. A., Klose, M., Niemann, C., Glauche, I., and Wickström, S. A. (2017). Hair follicle stem cell cultures reveal self-organizing plasticity of stem cells and their progeny. *EMBO J.* 36 (2), 151–164. doi:10.15252/embj.201694902

Chen, C.-C., Wang, L., Plikus, M. V., Jiang, T. X., Murray, P. J., Ramos, R., et al. (2015). Organ-level quorum sensing directs regeneration in hair stem cell populations. *Cell* 161 (2), 277–290. doi:10.1016/j.cell.2015.02.016

Chen, Y., Lin, M. C., Yao, H., Wang, H., Zhang, A.-Q., Yu, J., et al. (2007). Lentivirus-mediated RNA interference targeting enhancer of zeste homolog 2 inhibits hepatocellular carcinoma growth through down-regulation of stathmin. *Hepatology* 46 (1), 200–208. doi:10.1002/hep.21668

Cotsarelis, G., and Millar, S. E. (2001). Towards a molecular understanding of hair loss and its treatment. *Trends Mol. Med.* 7 (7), 293–301. doi:10.1016/s1471-4914(01)02027-5

Cotsarelis, G., Sun, T.-T., and Lavker, R. M. (1990). Label-retaining cells reside in the bulge area of pilosebaceous unit: implications for follicular stem cells, hair cycle, and skin carcinogenesis. *Cell* 61 (7), 1329–1337. doi:10.1016/0092-8674(90)90696-c

Deng, Z., Lei, X., Zhang, X., Zhang, H., Liu, S., Chen, Q., et al. (2015). mTOR signaling promotes stem cell activation via counterbalancing BMP-mediated suppression during hair regeneration. *J. Mol. Cell Biol.* 7 (1), 62–72. doi:10.1093/jmcb/mjv005

Deschene, E. R., Myung, P., Rompolas, P., Zito, G., Sun, T. Y., Taketo, M. M., et al. (2014). -Catenin activation regulates tissue growth non-cell autonomously in the hair stem cell niche. *Science* 343 (6177), 1353–1356. doi:10.1126/science.1248373

Elmaadawi, I. H., Mohamed, B. M., Ibrahim, Z. A. S., Abdou, S. M., El Attar, Y. A., Youssef, A., et al. (2018). Stem cell therapy as a novel therapeutic intervention for resistant cases of alopecia areata and androgenetic alopecia. *J. Dermatol. Treat.* 29 (5), 431–440. doi:10.1080/09546634.2016.1227419

Friedenstein, A. J., Chailakhyan, R. K., Latsinik, N. V., Panasyuk, A. F., and Keiliss-Borok, I. V. (1974). Stromal cells responsible for transferring the microenvironment of the hemopoietic tissues. *Transplantation* 17 (4), 331–340. doi:10.1097/00007890-197404000-00001

Fu, X., Liu, G., Halim, A., Ju, Y., Luo, Q., Song, A. G., et al. (2019). Mesenchymal stem cell migration and tissue repair. *Cells* 8 (8), 784. doi:10.3390/cells8080784

Garza, L. A., Yang, C.-C., Zhao, T., Blatt, H. B., Lee, M., He, H., et al. (2011). Bald scalp in men with androgenetic alopecia retains hair follicle stem cells but lacks CD200-rich and CD34-positive hair follicle progenitor cells. *J. Clin. Invest.* 121 (2), 613–622. doi:10.1172/JCI44478

Greco, V., Chen, T., Rendl, M., Schober, M., Pasolli, H. A., Stokes, N., et al. (2009). A two-step mechanism for stem cell activation during hair regeneration. *Cell stem Cell* 4 (2), 155–169. doi:10.1016/j.stem.2008.12.009

Harrell, C. R., Jovicic, N., Djonov, V., Arsenijevic, N., and Volarevic, V. (2019). Mesenchymal stem cell-derived exosomes and other extracellular vesicles as new remedies in the therapy of inflammatory diseases. *Cells* 8 (12), 1605. doi:10.3390/cells8121605

Huang, J., Zheng, D.-L., Qin, F.-S., Cheng, N., Chen, H., Wan, B.-B., et al. (2010). Genetic and epigenetic silencing of SCARA5 may contribute to human hepatocellular carcinoma by activating FAK signaling. *J. Clin. Invest.* 120 (1), 223–241. doi:10.1172/JCI38012

Huangyang, P., Li, F., Lee, P., Nissim, I., Weljie, A. M., Mancuso, A., et al. (2020). Fructose-1,6-Bisphosphatase 2 inhibits sarcoma progression by restraining mitochondrial biogenesis. *Cel Metab.* 31 (1), 174. doi:10.1016/j.cmet.2019.10.012

Jackson, I. J., Chambers, D. M., Tsukamoto, K., Copeland, N. G., Gilbert, D. J., Jenkins, N. A., et al. (1992). A second tyrosinase-related protein, TRP-2, maps to and is mutated at the mouse slaty locus. *EMBO J.* 11 (2), 527–535. doi:10.1002/j.1460-2075.1992.tb05083.x

John, S., Thiebach, L., Frie, C., Mokkapati, S., Bechtel, M., Nischt, R., et al. (2012). Epidermal transglutaminase (TGase 3) is required for proper hair development, but not the formation of the epidermal barrier. *PLoS One* 7 (4), e34252. doi:10.1371/journal.pone.0034252

Kobayashi, T., Urabe, K., Winder, A., Jiménez-Cervantes, C., Imokawa, G., Brewington, T., et al. (1994). Tyrosinase related protein 1 (TRP1) functions as a DHICA oxidase in melanin biosynthesis. *EMBO J.* 13 (24), 5818–5825. doi:10.1002/j.1460-2075.1994.tb06925.x

Krause, S. W., Rehli, M., and Andreesen, R. (1998). Carboxypeptidase M as a marker of macrophage maturation. *Immunol. Rev.* 161, 119–127. doi:10.1111/j.1600-065x.1998.tb01576.x

Lane, S. W., Williams, D. A., and Watt, F. M. (2014). Modulating the stem cell niche for tissue regeneration. *Nat. Biotechnol.* 32 (8), 795–803. doi:10.1038/nbt.2978

Langbein, L., Rogers, M. A., Praetzel-Wunder, S., Helmke, B., Schirmacher, P., and Schweizer, J. (2006). K25 (K25irs1), K26 (K25irs2), K27 (K25irs3), and K28 (K25irs4) represent the type I inner root sheath keratins of the human hair follicle. *J. Invest. Dermatol.* 126 (11), 2377–2386. doi:10.1038/sj.jid.5700494

Le Blanc, K., Tammik, C., Rosendahl, K., Zetterberg, E., and Ringdén, O. (2003). HLA expression and immunologic propertiesof differentiated and undifferentiated mesenchymal stem cells. *Exp. Hematol.* 31 (10), 890–896. doi:10.1016/s0301-472x(03)00110-3

Lee, P., Gund, R., Dutta, A., Pincha, N., Rana, I., Ghosh, S., et al. (2017). Stimulation of hair follicle stem cell proliferation through an IL-1 dependent activation of γδT-cells. *eLife* 6, e28875. doi:10.7554/eLife.28875

Leick, K. M., Rodriguez, A. B., Melssen, M. M., Benamar, M., Lindsay, R. S., Eki, R., et al. (2019). The barrier molecules junction plakoglobin, filaggrin, and dystonin play roles in melanoma growth and angiogenesis. *Ann. Surg.* 270 (4), 712–722. doi:10.1097/SLA.0000000000003522

Li, H., Wang, J., Xu, H., Xing, R., Pan, Y., Li, W., et al. (2013). Decreased fructose-1,6-bisphosphatase-2 expression promotes glycolysis and growth in gastric cancer cells. *Mol. Cancer* 12 (1), 110. doi:10.1186/1476-4598-12-110

Liu, Y., Lyle, S., Yang, Z., and Cotsarelis, G. (2003). Keratin 15 promoter targets putative epithelial stem cells in the hair follicle bulge. *J. Invest. Dermatol.* 121 (5), 963–968. doi:10.1046/j.1523-1747.2003.12600.x

Lyle, S., Christofidou-Solomidou, M., Liu, Y., Elder, D. E., Albelda, S., and Cotsarelis, G. (1998). The C8/144B monoclonal antibody recognizes cytokeratin 15 and defines the location of human hair follicle stem cells. *J. Cell Sci.* 111 (Pt 21), 3179–3188.

Ma, H.-L., Jin, S.-F., Ju, W.-T., Fu, Y., Tu, Y.-Y., Wang, L.-Z., et al. (2017). Stathmin is overexpressed and regulated by mutant p53 in oral squamous cell carcinoma. *J. Exp. Clin. Cancer Res.* 36 (1), 109. doi:10.1186/s13046-017-0575-4

Martin, E., Palmic, N., Sanquer, S., Lenoir, C., Hauck, F., Mongellaz, C., et al. (2014). CTP synthase 1 deficiency in humans reveals its central role in lymphocyte proliferation. *Nature* 510 (7504), 288–292. doi:10.1038/nature13386

Naderi, A. (2018). SRARP and HSPB7 are epigenetically regulated gene pairs that function as tumor suppressors and predict clinical outcome in malignancies. *Mol. Oncol.* 12 (5), 724–755. doi:10.1002/1878-0261.12195

Nowak, J. A., Polak, L., Pasolli, H. A., and Fuchs, E. (2008). Hair follicle stem cells are specified and function in early skin morphogenesis. *Cell stem Cell* 3 (1), 33–43. doi:10.1016/j.stem.2008.05.009

Park, J., Jun, E. K., Son, D., Hong, W., Jang, J., Yun, W., et al. (2019). Overexpression of Nanog in amniotic fluid-derived mesenchymal stem cells accelerates dermal papilla cell activity and promotes hair follicle regeneration. *Exp. Mol. Med.* 51 (7), 1. doi:10.1038/s12276-019-0266-7

Paus, R. (1998). Principles of hair cycle control. *J. Dermatol.* 25 (12), 793–802. doi:10.1111/j.1346-8138.1998.tb02507.x

Pittenger, M. F., Mackay, A. M., Beck, S. C., Jaiswal, R. K., Douglas, R., Mosca, J. D., et al. (1999). Multilineage potential of adult human mesenchymal stem cells. *Science (New York, N.Y.)* 284 (5411), 143–147. doi:10.1126/science.284.5411.143

Prockop, D. J. (1997). Marrow stromal cells as stem cells for nonhematopoietic tissues. *Science.* 276 (5309), 71–74. doi:10.1126/science.276.5309.71

Rahmani, W., Liu, Y., Rosin, N. L., Kline, A., Raharjo, E., Yoon, J., et al. (2018). Macrophages promote wound-induced hair follicle regeneration in a CX3CR1- and TGF-β1-dependent manner. *J. Invest. Dermatol.* 138 (10), 2111–2122. doi:10.1016/j.jid.2018.04.010

Rahmani, W., Sinha, S., and Biernaskie, J. (2020). Immune modulation of hair follicle regeneration. *Npj Regen. Med.* 5, 9. doi:10.1038/s41536-020-0095-2

Rehli, M., Krause, S. W., Kreutz, M., and Andreesen, R. (1995). Carboxypeptidase M is identical to the MAX.1 antigen and its expression is associated with monocyte to macrophage differentiation. *J. Biol. Chem.* 270 (26), 15644–15649. doi:10.1074/jbc.270.26.15644

Ringhoff, D. N., and Cassimeris, L. (2009). Stathmin regulates centrosomal nucleation of microtubules and tubulin dimer/polymer partitioning. *MBoC* 20 (15), 3451–3458. doi:10.1091/mbc.E09-02-0140

Salerno, E. P., Bedognetti, D., Mauldin, I. S., Deacon, D. H., Shea, S. M., Pinczewski, J., et al. (2016). Human melanomas and ovarian cancers overexpressing mechanical barrier molecule genes lack immune signatures and have increased patient mortality risk. *Oncoimmunology* 5 (12), e1240857. doi:10.1080/2162402X.2016.1240857

Sato, N., Leopold, P. L., and Crystal, R. G. (1999). Induction of the hair growth phase in postnatal mice by localized transient expression of Sonic hedgehog. *J. Clin. Invest.* 104 (7), 855–864. doi:10.1172/jci7691

Shi, Y., Wang, Y., Li, Q., Liu, K., Hou, J., Shao, C., et al. (2018). Immunoregulatory mechanisms of mesenchymal stem and stromal cells in inflammatory diseases. *Nat. Rev. Nephrol.* 14 (8), 493–507. doi:10.1038/s41581-018-0023-5

Tarcsa, E., Marekov, L. N., Andreoli, J., Idler, W. W., Candi, E., Chung, S.-I., et al. (1997). The fate of trichohyalin. *J. Biol. Chem.* 272 (44), 27893–27901. doi:10.1074/jbc.272.44.27893

Thibaut, S., Cavusoglu, N., de Becker, E., Zerbib, F., Bednarczyk, A., Schaeffer, C., et al. (2009). Transglutaminase-3 enzyme: a putative actor in human hair shaft scaffolding? *J. Invest. Dermatol.* 129 (2), 449–459. doi:10.1038/jid.2008.231

Thompson, A., Schäfer, J., Kuhn, K., Kienle, S., Schwarz, J., Schmidt, G., et al. (2003). Tandem mass tags: a novel quantification strategy for comparative analysis of complex protein mixtures by MS/MS. *Anal. Chem.* 75 (8), 1895–1904. doi:10.1021/ac0262560

Tsukamoto, K., Jackson, I. J., Urabe, K., Montague, P. M., and Hearing, V. J. (1992). A second tyrosinase-related protein, TRP-2, is a melanogenic enzyme termed DOPAchrome tautomerase. *EMBO J.* 11 (2), 519–526. doi:10.1002/j.1460-2075.1992.tb05082.x

Varothai, S., and Bergfeld, W. F. (2014). Androgenetic alopecia: an evidence-based treatment update. *Am. J. Clin. Dermatol.* 15 (3), 217–230. doi:10.1007/s40257-014-0077-5

Vidal, V. P. I., Chaboissier, M.-C., Lützkendorf, S., Cotsarelis, G., Mill, P., Hui, C.-C., et al. (2005). Sox9 is essential for outer root sheath differentiation and the formation of the hair stem cell compartment. *Curr. Biol.* 15 (15), 1340–1351. doi:10.1016/j.cub.2005.06.064

Wang, X., Chen, H., Tian, R., Zhang, Y., Drutskaya, M. S., Wang, C., et al. (2017). Macrophages induce AKT/β-catenin-dependent Lgr5+ stem cell activation and hair follicle regeneration through TNF. *Nat. Commun.* 8, 14091. doi:10.1038/ncomms14091

Zdarsky, E., Favor, J., and Jackson, I. J. (1990). The molecular basis of brown, an old mouse mutation, and of an induced revertant to wild type. *Genetics* 126 (2), 443–449.

Zernov, N. V., Skoblov, M. Y., Marakhonov, A. V., Shimomura, Y., Vasilyeva, T. A., Konovalov, F. A., et al. (2016). Autosomal recessive hypotrichosis with woolly hair caused by a mutation in the keratin 25 gene expressed in hair follicles. *J. Invest. Dermatol.* 136 (6), 1097–1105. doi:10.1016/j.jid.2016.01.037

Zhang, S., Chuah, S. J., Lai, R. C., Hui, J. H. P., Lim, S. K., and Toh, W. S. (2018). MSC exosomes mediate cartilage repair by enhancing proliferation, attenuating apoptosis and modulating immune reactivity. *Biomaterials* 156, 16–27. doi:10.1016/j.biomaterials.2017.11.028

Zhang, Y., Liu, F., Zhang, C., Ren, M., Kuang, M., Xiao, T., et al. (2020). Non-SMC condensin I complex subunit D2 is a prognostic factor in triple-negative breast cancer for the ability to promote cell cycle and enhance invasion. *Am. J. Pathol.* 190 (1), 37–47. doi:10.1016/j.ajpath.2019.09.014

Zhao, L., Chen, X., Feng, Y., Wang, G., Nawaz, I., Hu, L., et al. (2019). COX7A1 suppresses the viability of human non-small cell lung cancer cells via regulating autophagy. *Cancer Med.* 8 (18), 7762–7773. doi:10.1002/cam4.2659

Conflict of Interest: The authors declare that the research was conducted in the absence of any commercial or financial relationships that could be construed as a potential conflict of interest.

frontiers in Cell and Developmental Biology

ORIGINAL RESEARCH
published: 22 June 2021
doi: 10.3389/fcell.2021.648627

SIRT6 Promotes Osteogenic Differentiation of Adipose-Derived Mesenchymal Stem Cells Through Antagonizing DNMT1

Bo Jia[1,2†], Jun Chen[1†], Qin Wang[1], Xiang Sun[1], Jiusong Han[1], Fernando Guastaldi[3], Shijian Xiang[4], Qingsong Ye[5,6] and Yan He[7*]*

[1] Department of Oral Surgery, Stomatological Hospital, Southern Medical University, Guangzhou, China, [2] Department of Stomatology, Shunde Hospital, Southern Medical University, Foshan, China, [3] Skeletal Biology Research Center, Department of Oral and Maxillofacial Surgery, Massachusetts General Hospital, Harvard School of Dental Medicine, Boston, MA, United States, [4] The Seventh Affiliated Hospital, Sun Yat-sen University, Shenzhen, China, [5] School of Stomatology and Medicine, Foshan University, Foshan, China, [6] Center of Regenerative Medicine, Renmin Hospital of Wuhan University, Wuhan University, Wuhan, China, [7] Laboratory of Regenerative Medicine, Tianyou Hospital, Wuhan University of Science and Technology, Wuhan, China

OPEN ACCESS

Edited by:
Yidong Wang,
Xi'an Jiaotong University, China

Reviewed by:
Oleh Akchurin,
Weill Cornell Medical Center, United States
Yinghong Zhou,
Queensland University of Technology, Australia

***Correspondence:**
Qingsong Ye
qingsongye@foxmail.com
Yan He
helen-1101@hotmail.com

† These authors have contributed equally to this work

Specialty section:
This article was submitted to Stem Cell Research, a section of the journal Frontiers in Cell and Developmental Biology

Received: *01 January 2021*
Accepted: *22 March 2021*
Published: *22 June 2021*

Citation:
Jia B, Chen J, Wang Q, Sun X, Han J, Guastaldi F, Xiang S, Ye Q and He Y (2021) SIRT6 Promotes Osteogenic Differentiation of Adipose-Derived Mesenchymal Stem Cells Through Antagonizing DNMT1. Front. Cell Dev. Biol. 9:648627. doi: 10.3389/fcell.2021.648627

Background: Adipose-derived stem cells (ADSCs) are increasingly used in regenerative medicine because of their potential to differentiate into multiple cell types, including osteogenic lineages. Sirtuin protein 6 (SIRT6) is a nicotinamide adenine dinucleotide (NAD)-dependent deacetylase that plays important roles in cell differentiation. NOTCH signaling has also been reported to involve in osteogenic differentiation. However, the function of SIRT6 in osteogenic differentiation of ADSCs and its relation to the NOTCH signaling pathways are yet to be explored.

Methods: The *in vitro* study with human ADSCs (hADSCs) and *in vivo* experiments with nude mice have been performed. Alkaline phosphatase (ALP) assays and ALP staining were used to detect osteogenic activity. Alizarin Red staining was performed to detect calcium deposition induced by osteogenic differentiation of ADSCs. Western blot, RT-qPCR, luciferase reporter assay, and co-immunoprecipitation assay were applied to explore the relationship between of SIRT6, DNA methyltransferases (DNMTs) and NOTCHs.

Results: SIRT6 promoted ALP activity, enhanced mineralization and upregulated expression of osteogenic-related genes of hADSCs *in vitro* and *in vivo*. Further mechanistic studies showed that SIRT6 deacetylated DNMT1, leading to its unstability at protein level. The decreased expression of DNMT1 prevented the abnormal DNA methylation of NOTCH1 and NOTCH2, resulting in the upregulation of their transcription. SIRT6 overexpression partially suppressed the abnormal DNA methylation of NOTCH1 and NOTCH2 by antagonizing DNMT1, leading to an increased capacity of ADSCs for their osteogenic differentiation.

Conclusion: This study demonstrates that SIRT6 physical interacts with the DNMT1 protein, deacetylating and destabilizing DNMT1 protein, leading to the activation of NOTCH1 and NOTCH2, Which in turn promotes the osteogenic differentiation of ADSCs.

Keywords: sirtuin proteins 6, osteogenic differentiation, adipose-derived mesenchymal stem cells, NOTCH signaling, DNMT1

INTRODUCTION

Adipose-derived stem cells (ADSCs), a type of mesenchymal stem cells, are being increasingly accepted as an attractive cell type for regenerative medicine because of their potential to differentiate into multiple cell types, including adipogenic, osteogenic, and chondrogenic lineages (Caplan, 2007; Bianco et al., 2008; Worthley et al., 2015). Owing to their osteogenic capacity and ease of acquisition and culture, human ADSCs (hADSCs) are considered a suitable cellular source for the regeneration of bone loss and fractures (Schubert et al., 2013; Heilmeier et al., 2016). However, the exact underlying mechanisms for osteogenic differentiation of ADSCs remain largely unknow.

Sirtuin protein 6 (SIRT6) is a nicotinamide adenine dinucleotide (NAD)+-dependent protein deacetylase involved in several important biological processes including genomic stability, transcriptional silencing, and DNA repair (Mostoslavsky et al., 2006; Kanfi et al., 2012). SIRT6 has a high affinity for chromatin and it universally deacetylates histone H3 lysine 9 (H3K9) and H3 lysine 56 (H3K56) in an NAD+-dependent manner (Kawahara et al., 2009). The deacetylation of telomeric H3K9 by SIRT6 is necessary for the function and structural stability of telomeric chromatin (Michishita et al., 2008).

Recent studies imply that SIR6 is associated with stem cell regulation. SIRT6 deacetylates the H3K56ac and H3K9ac of Oct4, Sox2, and Nanog at the promoter regions, and in turn controls embryonic stem cell differentiation (Etchegaray et al., 2015). SIRT6 deficiency leads the histone hyperacetylation at the imprinting control region of long non-coding RNA H19, and the activation of H19 delays neuronal differentiation (Zhang et al., 2018). These studies suggest the role of SIRT6 in the regulation of stem cell differentiation.

Previous studies reported SIRT1 could deacetylase DNA methyltransferases (DNMTs) and alter their activities (O'Hagan et al., 2008; Peng et al., 2011). DNA methylation is necessary for fundamental biological processes, including embryonic development, gene regulation, developmental potential of stem cells, and genomic imprinting (Jaenisch and Bird, 2003; Hayashi and Surani, 2009; Lee and Bartolomei, 2013), DNA methylation is catalyzed by DNMTs at 5 mC of CpG dinucleotides, DNMT1, DNMT3A, DNMT3B, and DNMT3L are responsible for *de novo* DNA methylation (Cedar and Bergman, 2009). Among them, DNMT1 often methylates newly replicated DNA and is regarded as a maintenance enzyme. DNMTs have been reported to involve in osteogenic differentiation of bone mesenchymal stem cell (Liu et al., 2016; Li et al., 2019). Furthermore, DNA methylation of the NOTCH family protein has been reported in stem cells (Chattapadhyaya et al., 2020; Wei et al., 2020). However, the association between SIRT6, DNMT1, and NOTCH signaling in ADSCs differentiation was yet to be elucidated.

In this study, we aim to investigate the effect of SIRT6 on the osteogenic differentiation of hADSCs and exam whether SIRT6 could modify the histone acetylation status of the DNMT1 and increasing the expression of NOTCH1 and NOTCH2. Our study may further strengthen the understanding of the mechanism underlying the osteogenic differentiation capacity of ADSCs.

Abbreviations: ADSCs, Adipose-derived stem cells; ALP, Alkaline phosphatase; SIRT6, Sirtuin proteins 6; DNMTs, DNA methyltransferases; ARS, Alizarin red S; CHX, cycloheximide.

MATERIALS AND METHODS

Cell Lines and Reagents

The hADSCs were purchased from Cyagen Biosciences Inc. (Guangzhou, China). Briefly, the hADSCs were isolated and purified from fresh human adipose tissues donated from healthy adults less than 45 years of age after liposuction. The cells were cultured in Dulbecco's modified Eagle's medium (Gibco, Carlsbad, CA, United States) containing 10% fetal bovine serum and cultured at 37°C in a humidified atmosphere of 5% CO_2. Osteogenic induction medium was purchased from SALILA (SALILA, Guangzhou, China). The medium was changed every 2 days. To inhibit DNA methylation, hADSCs were treated with 5 μmol/L 5-aza-2′-deoxycytidine (DAC, Sigma Aldrich, Munich, Germany). To inhibit NOTCH signaling, cells were treated with 2 μM DAPT (Selleck). Protein deacetylation was inhibited using 20 μM OSS_128167 (Selleck). For the cycloheximide (CHX)-chase assay, cells were treated with 100 g/mL CHX (Sigma-Aldrich, St. Louis, MO, United States) for the indicated hours in the absence or presence of 5 g/mL actinomycin D (Sigma-Aldrich, St. Louis, MO, United States) and western blot analysis was performed.

Western Blot

The hADSCs were lysed on ice for 15 min using Radio Immunoprecipitation Assay (RIPA) lysis buffer (BeyoTime, Shanghai, China) supplemented with protease inhibitor cocktail (Roche, Basel, Switzerland). The protein concentration of the lysate was then measured using the BCA Protein Assay Kit (BeyoTime, Shanghai, China) according to the manufacturer's protocol. Protein sample were subjected to SDS-PAGE and transferred to polyvinylidene difluoride membranes (Millipore, Billerica, United States), which were blocked with 5% fat-free milk and then incubated with specific primary antibodies

overnight at 4°C An anti-rabbit-horseradish peroxidase (HRP) secondary antibody was added, and the staining was visualized using an enhanced chemiluminescence detection system (Millipore, Billerica, United States). The primary antibodies used in this study were as follows: SIRT6, RUNX2, SP7, COL1A1, NOTCH1, NOTCH2, NOTCH3, NOTCH4, JAG1, HEY1 (Abcam, Cambering, United Kingdom), HA, Flag, GAPDH (BeyoTime, Shanghai, China) DNMT1, Acetylated Lysine (Ac-K) (Cell Signaling Technology, Danvers, MA, United States).

Quantitative Reverse Transcription (RT)-PCR

Total RNA was extracted using Trizol reagent (Invitrogen, Carlsbad, CA, United States). cDNA was synthesized using a Reverse Transcription Kit (Promega, Madison, WI, United States). cDNA was used for quantitative PCR reactions to determine the expression of specific genes with SYBR Green Real-Time PCR Master Mix Kit (Invitrogen, Carlsbad, CA, United States) according to the manufacturer's instructions. GAPDH mRNA was applied as endogenous control. Primer sequences are shown in **Supplementary Table 1**. The total cycles for RT-PCR was set as 40.

Lentivirus, siRNAs, and shRNAs Transfection

Lentivirus particles for the SIRT6 overexpression or knockdown of genes were purchased from GeneChem (GeneChem, Shanghai, China). The overexpressed plasmid was purchased from (Vigenebio, Jinan, China). The hADSCs in 24-well plates were infected with lentiviral vectors fixed with 10 mg/mL polybrene (GeneChem) in DMEM (Invitrogen, Carlsbad, CA, United States). Stable clones were selected using 0.5 μg/mL puromycin. Short hairpin RNAs (**Supplementary Table 2**) were synthesized by RiboBio (Guangzhou, China). hADSCs in 6-well plates were treated with 50 nM siRNAs or 4 μg shRNAs or 5 μg overexpression plasmid using Lipofectamine 3000 reagent (Invitrogen, Carlsbad, CA, United States) according to the manufacturer's instructions and then harvested for assays.

Alkaline Phosphatase Staining and Activity

Alkaline phosphatase (ALP) staining was performed in cells seeded in 24-well plates. After treatment with osteogenic differentiation medium for 7 days, the cells were fixed in 70% ethanol and incubated with a staining solution containing 0.1% naphthol AS-TR phosphate and 2% fast violet B (Sigma-Aldrich, St. Louis, MO, United States) for 1 h at room temperature. ALP activity was calculated quantitatively using a commercial ALP kit (Cell Biolab, San Diego, CA, United States) according to the manufacturer's protocol.

Alizarin Red Staining

Human ADSCs were incubated with osteogenic red S (pH 4.2, Sigma) for 10 min. For the quantitative assessment of the mineralization, the mineralized bone nodules were eluted with 10% (w/v) cetylpyridinium chloride (Sigma-Aldrich) for 1 h and analyzed by measuring the absorbance at 562 nm.

Animal Experiments and Masson's Trichrome Staining

Transplantation of *in vivo* experiment has been previously described (Jia et al., 2019). In brief, 4 weeks old nude mice were purchased from the Provincial Animal Center (Guangdong, China, No. 44002100023792). The mice were kept under a 12 h light/dark cycle in a drafty room at temperature of 22–26°C. Hydroxyapatite/tricalcium phosphate (HA-TCP; Sigma, St. Louis, MO, United States) was treated with 75% ethanol for sterilization for 12 h, washed by PBS for 6 times. Cut them into pieces and seeded with 200 ml of osteogenic differentiation-induced ADSCs suspension at a density of 5×10^6 cells/ml. The mixed cells were subcutaneously inoculated into the right dorsal region of mice (5 mice per group). Four weeks later, the mice were sacrificed and the transplants were removed as previously described (Jia et al., 2019). The group implanted the mock vector was used as the control groups. The Animal experiments were approved by the Animal Care Committee of Southern Medical University. The samples were collected, fixed with 4% paraformaldehyde, and decalcified in 10% EDTA (pH 6.0) for 7 days. Paraffin sections were prepared and stained with hematoxylin and eosin, and Masson's trichrome stain (Sigma-Aldrich, St. Louis, MO, United States) according to the manufacturers' protocols.

Luciferase Reporter Assay

The 2 kb region upstream of the transcription starting site of NOTCH1, NOTCH 2, and DNMT1 were synthesized and cloned upstream of the luciferase gene in the pmirGLO luciferase vector (GeneChem, Shanghai, China). hADSCs and 293T cells were treated with the indicated transfection particles using Lipofectamine 2000 (Invitrogen, Carlsbad, CA, United States). Promoter activity was measured using the luciferase assay kit (Promega, Madison, WI, United States) and normalized to the Firefly and Renilla luciferase activities 48 h after transfection.

Co-immunoprecipitation

NP-40-containing lysis buffer supplemented with protease inhibitor cocktail was used to lyse cells (Roche, Basel, Switzerland), and the immunoprecipitated complexes were recovered with ChIP grade antibodies against acetylated lysine (Ac-K) (Cell Signaling Technology, Danvers, MA, United States), HA epitope (Beyotime, Shanghai, China), Flag epitope (Beyotime, Shanghai, China), rabbit immunoglobulin (Ig)G control antibodies (Sigma-Aldrich, St. Louis, MO, United States), which were incubated with protein A/G Sepharose beads (Santa Cruz, CA, United States), and then rinsed with wash buffer. The eluted immune complexes were denatured and subjected to western blot assay.

Statistical Analysis

The data were presented as the mean ± SD. All data were analyzed using one- or two-way ANOVA with Bonferroni

post hoc tests. SPSS 18.0 was used to perform all analyses. Statistical significance was defined as $p < 0.05$.

RESULTS

SIRT6 Promoted Osteogenic Differentiation of hADSCs Both *in vitro* and *in vivo*

In order to elucidate the role of SIRT6 in osteogenic differentiation, hADSCs were cultured under osteogenic inductive conditions. The hADSCs sustained their capacity for osteogenic differentiation, as indicated by gradually increased in the expression of osteogenic markers RUNX2, SP7 and ALP. The SIRT6 expression was increased after osteogenic induction (**Figures 1A,B**). Then, we constructed stable SIRT6-overexpression or knockdown hADSCs, confirmed by RT-qPCR and Western blot (**Figures 1C,D**). Alizarin red S (ARS) staining, ALP staining and activity assays revealed that upregulated SIRT6 promoted mineralized bone matrix formation and ALP activity in hADSCs, SIRT6 knockdown inhibited osteogenic differentiation in hADSCs (**Figures 1E–G**). To further evaluate the osteogenic function of SIRT6 in hADSCs. SIRT6 overexpressing hADSCs were cultured in osteogenic differentiation medium for 2 weeks and then implanted into immunocompromised mice subcutaneously using HA/TCP as a carrier. The hADSCs with SIRT6 overexpression exhibited significantly increased capacities to generate new bone as shown through Masson's trichrome stain (**Figure 1H**). These results strongly suggest that SIRT6 promoted the osteogenesis of hADSCs both *in vitro* and *in vivo*.

NOTCH Signaling Contributed to SIRT6-Mediated Promotion of Osteogenic Differentiation in hADSCs

NOTCH signaling has been reported to regulate bone mesenchymal cell differentiation (Dong et al., 2010).Also, previous studies revealed that the SIRT family may interact with NOTCH during differentiation (Bai et al., 2018; Okasha et al., 2020).Therefore, we hypothesized that NOTCH signaling was regulated by SIRT6 in the process of osteogenic differentiation in hADSCs. To test this hypothesis, we determined the expression of NOTCH family members in SIRT-overexpressed or silenced hADSCs, the results showed that the expression of NOTCH1 and NOTCH2 were increased following SIRT6 overexpression and decreased following SIRT6 knockdown both at mRNA and protein levels (**Figures 2A,B**). Then, we overexpressed NOTCH1 and NOTCH2 in hADSCs and found that the expression of osteogenic markers RUNX2, SP7, and ALP were increased consequently (**Figures 2C–F**). Mineralized bone matrix formation and ALP activity in hADSCs were also elevated in NOTCH1 and NOTCH2 overexpressing hADSCs as shown using ARS staining, ALP staining and activity assays (**Figures 2G–L**).

To identify the role of NOTCH signaling in SIRT6-mediated promotion of osteogenic differentiation, the NOTCH signaling inhibitor, DAPT, was applied in SIRT6-overexpressed hADSCs. DAPT treatment reversed the increase in the expression of NOTCH1, NOTCH2, JAG1, HEY1 induced by SIRT6 (**Figures 3A,B**). In addition, DAPT partially restrained the SIRT6-induced osteogenic differentiation capacity, as indicated by mineralized nodule formation and ALP activity (**Figures 3C–E**). In the *in vivo* experiment, DAPT also impaired the promoting effect of SIRT6 on hADSCs' function in mineralized nodule formation, as illustrated using Masson's trichrome staining (**Figure 3F**). To further confirm the role of NOTCH signaling in the regulation of hADSCs osteogenic differentiation, SIRT6-overexpression hADSCs were transfected with NOTCH1 or NOTCH2 shRNAs. ARS staining, ALP staining and activity assays demonstrated that silencing NOTCH1 or NOTCH2 could abolish the increased capacity of osteogenic differentiation by SIRT6 (**Figures 3G–I**). These data indicate that NOTCH signaling play an important role in the SIRT6-induced promotion of osteogenic differentiation in hADSCs.

DNMT1 Suppressed Osteogenic Differentiation in hADSCs by Inducing Hypermethylation of the NOTCH1 and NOTCH2

Epigenetic regulation, such as DNA methylation, is essential for the self-renewal and differentiation of stem cells (Challen et al., 2011; Tsai et al., 2012). DNA methylation of CpG dinucleotides is regulated by DNMTs, including DNMT1, DNMT3A and DNMT3B and DNMT3L (Denis et al., 2011). We examined whether DNA methylation was involved in osteogenic differentiation of hADSCs. ShRNAs targeting DNMT1, DNMT3A and DNMT3B, and DNMT3L were transfected into hADSCs and the capacity of osteogenic differentiation were assessed. We found DNMT1, rather than DNMT3A and DNMT3B or DNMT3L, was verified as a potential regulator in osteogenic differentiation of hADSCs (**Figures 4A,B**). Following overexpression of DNMTs, only DNMT1 significantly decreased the expression of osteogenic marker and impaired the capacity of osteogenic differentiation in hADSCs, as confirmed through ARS staining, ALP staining, and activity assays (**Figures 4C–E**). DNMT1 silencing increased mineralized nodule formation and ALP activity *in vitro* (**Figures 4F–H**).

To gain insights into weather the hypermethylation of the NOTCH1 promoters was regulated by DNMT1, the expression of NOTCH1, NOTCH2, the upstream ligand of NOTH signaling JAG1, and the import downstream target HEY1 were detected. The result implied that NOTCH1, NOTCH2, JAG1, and HEY1 expression was remarkably increased in DNMT1 silenced hADSCs at both transcription and protein levels (**Figures 5A,B**). In contrast, DNMT1 overexpression suppressed the NOTCH signal (**Figures 5C,D**). Moreover, when co-transfection with NOTCH1 or NOTCH2 overexpression plasmid in DNMT1-overexpressed hADSCs partially rescued the DNMT1 induced impairment of osteogenic differentiation hADSCs, as indicated by expression of RUNX2, and SP7 the mineralized nodule formation capacity and ALP activity (**Figures 5E–H**). These data showed that DNMT1 could promote osteogenic differentiation of hADSCs by inducing the hypermethylation of the NOTCH1 and NOTCH2.

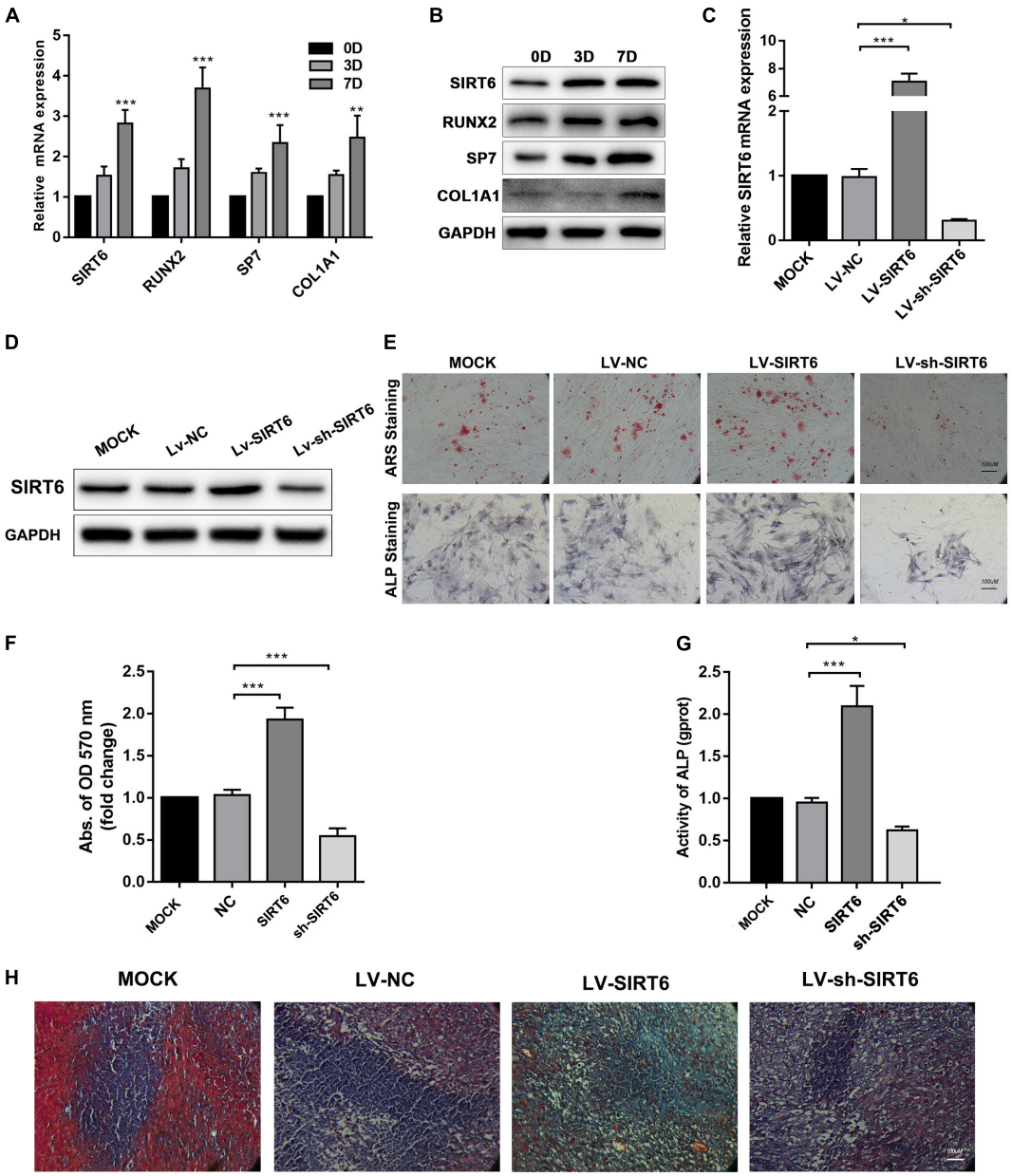

FIGURE 1 | SITR6 promoted osteogenic differentiation of hADSCs. **(A,B)** Relative expression of SIRT6, RUNX2, SP7, and COL1A1 during osteogenic differentiation of hADSCs at day 0, 3, 7, determined by RT-qPCR and Western blot. **(C)** RT-qPCR analysis of SIRT6 in overexpression or knockdown hADSCs. **(D)** Western blot analysis of SIRT6 in overexpression or knockdown hADSCs. **(E)** Images of Alizarin red staining and ALP staining in SIRT6 overexpressed or silenced hADSCs. Cells were cultured in osteogenic differentiation media for 14 days. Alizarin red staining was quantified by spectrophotometry **(F)** Activity of ALP **(G)** (normalized to the NC groups). **(H)** SIRT6 promoted the osteogenesis of hADSCs *in vivo*. hADSCs loaded on HA-TCP were transplanted into the dorsal region of nude mice for 4 weeks. Then, sections of transplants were stained by Masson's trichrome. Data were shown as means ± SD. $^{*}p < 0.05$, $^{**}p < 0.01$, $^{***}p < 0.001$.

SIRT6 Suppressed the DNMT1 Transcription and Deacetylated the DNMT1 Protein via Physical Interactions

Based on the above results, we proposed a hypothesis that regulation of DNMT1 expression by the SIRT6 protein was responsible for the inhibition of NOTCH signaling in osteogenic differentiation of hADSCs. Consistent with the above result, DNMT1 overexpression could abolish the SIRT6-induced increase of NOTCH1, NOTCH2, JAG and HEY1 expression (**Figure 6A**). In order to assess whether SIRT6 could suppress DNMT1 transcription, a luciferase vector was constructed upstream of the transcription starting site of DNMT1 was constructed. We confirmed that SIRT6 overexpression suppressed the DNMT1 promoter activity, in contrast, SIRT6 knockdown increased the luciferase activity (**Figures 6B,C**). As

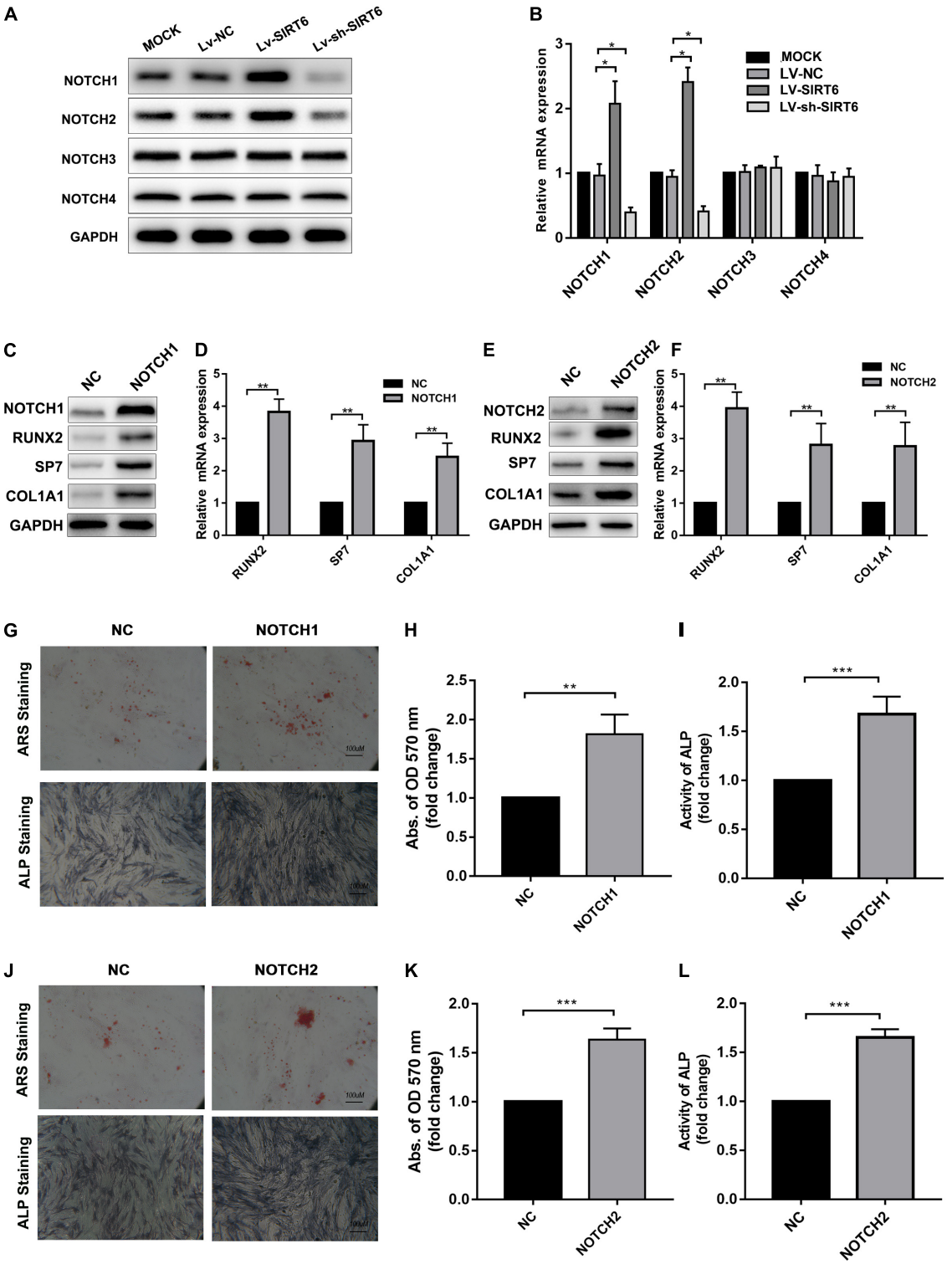

FIGURE 2 | (A,B) Western blot and RT-qPCR showed the expression of NOTCH1, NOTCH2 was increased by SIRT6 overexpression and decreased by SIRT6 knockdown. **(C,D)** High expression of NOTCH1, RUNX2, SP7 and COL1A1 in NOTCH1 overexpressed hADSCs, was determined by Western blot and RT-qPCR. **(E,F)** Expression of NOTCH1, RUNX2, SP7, and COL1A1 in NOTCH2 overexpressed hADSCs, determined by Western blot and RT-qPCR. **(G–I)** Images of Alizarin red staining and ALP staining in NOTCH1 overexpressed hADSCs. Histograms show ALP activity and quantification of Alizarin red staining by spectrophotometry. **(J–L)** Images of Alizarin red staining and ALP staining in NOTCH2 overexpressed hADSCs. Histograms show ALP activity and quantification of Alizarin red staining by spectrophotometry. Data were shown as mean ± SD. $^{*}p < 0.05$, $^{**}p < 0.01$, $^{***}p < 0.001$.

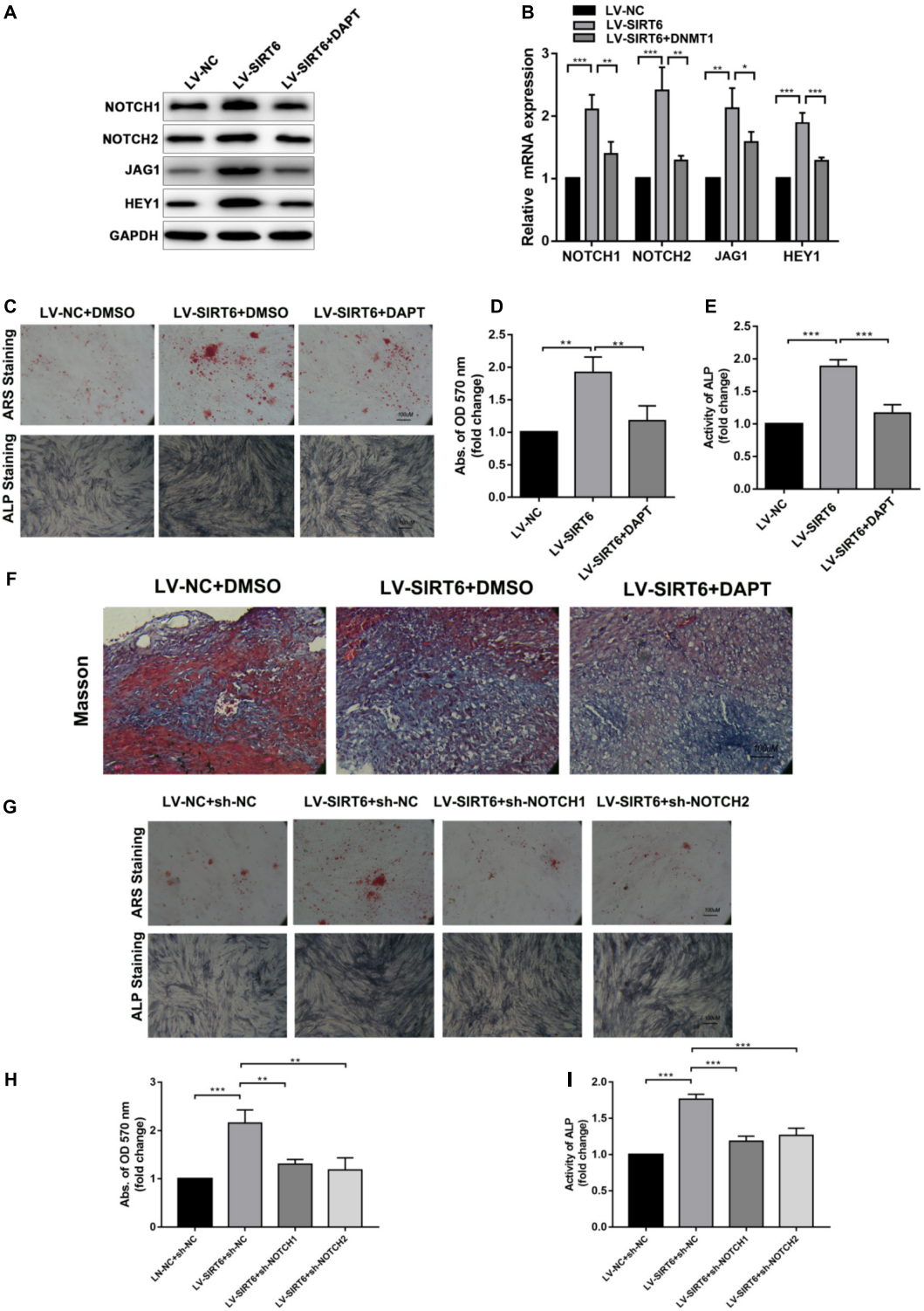

FIGURE 3 | (A,B) SIRT6 overexpressed hADSCs were administered with DAPT, expression of NOTCH1, NOTCH2, JAG1, HEY1 were determined by Western blot and RT-qPCR. **(C–E)** SIRT6 overexpressed hADSCs were administered with DAPT and osteogenic differentiation medium for 14 days, Alizarin red staining and ALP staining showed mineralized nodule formation. ALP activity and quantification of Alizarin red staining by spectrophotometry were determined. **(F)** SIRT6 overexpressed hADSCs loaded on HA-TCP were transplanted into the dorsal region of nude mice, the mice were intraperitoneal injected with DAPT for 4 weeks. Then, the removed samples were measured by Masson's trichrome staining. **(G–I)** SIRT6 overexpressed hADSCs were transfected with NOTCH1 or NOTCH2 shRNAs and cultured in osteogenic differentiation medium for 14 days, Alizarin red staining and ALP staining showed mineralized nodule formation. ALP activity and quantification of Alizarin red staining by spectrophotometry were determined. Data are shown as means ± SD. $^{*}p < 0.05$, $^{**}p < 0.01$, $^{***}p < 0.001$.

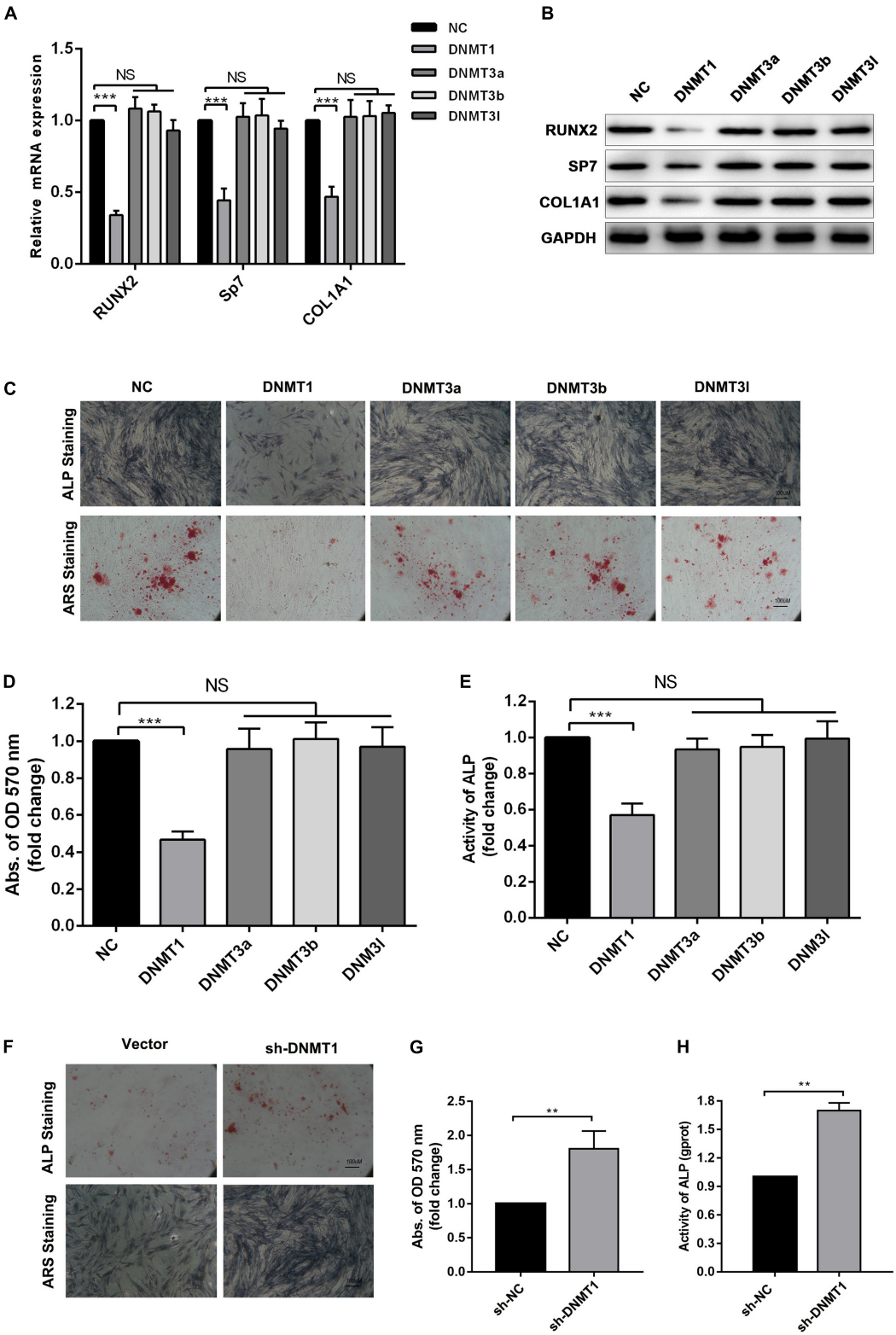

FIGURE 4 | (A,B) Expression of RUNX2, SP7 and COL1A1 4 in DNMT1, DNMT3A, DNMT3B, DNMT3L overexpressed hADSCs were determined by Western blot and RT-qPCR. **(C–E)** hADSCs were transfected with DNMTs plasmid and cultured in osteogenic differentiation medium for 14 days, Alizarin red staining and ALP staining showed mineralized nodule formation, ALP activity and quantification of Alizarin red staining by spectrophotometry were determined. **(F–H)** DNMT1 silenced hADSCs were cultured in osteogenic differentiation medium for 14 days, Alizarin red staining and ALP staining showed mineralized nodule formation, ALP activity and quantification of Alizarin red staining by spectrophotometry were determined. Data are shown as means ± SD. $^{**}p < 0.01$, $^{***}p < 0.001$.

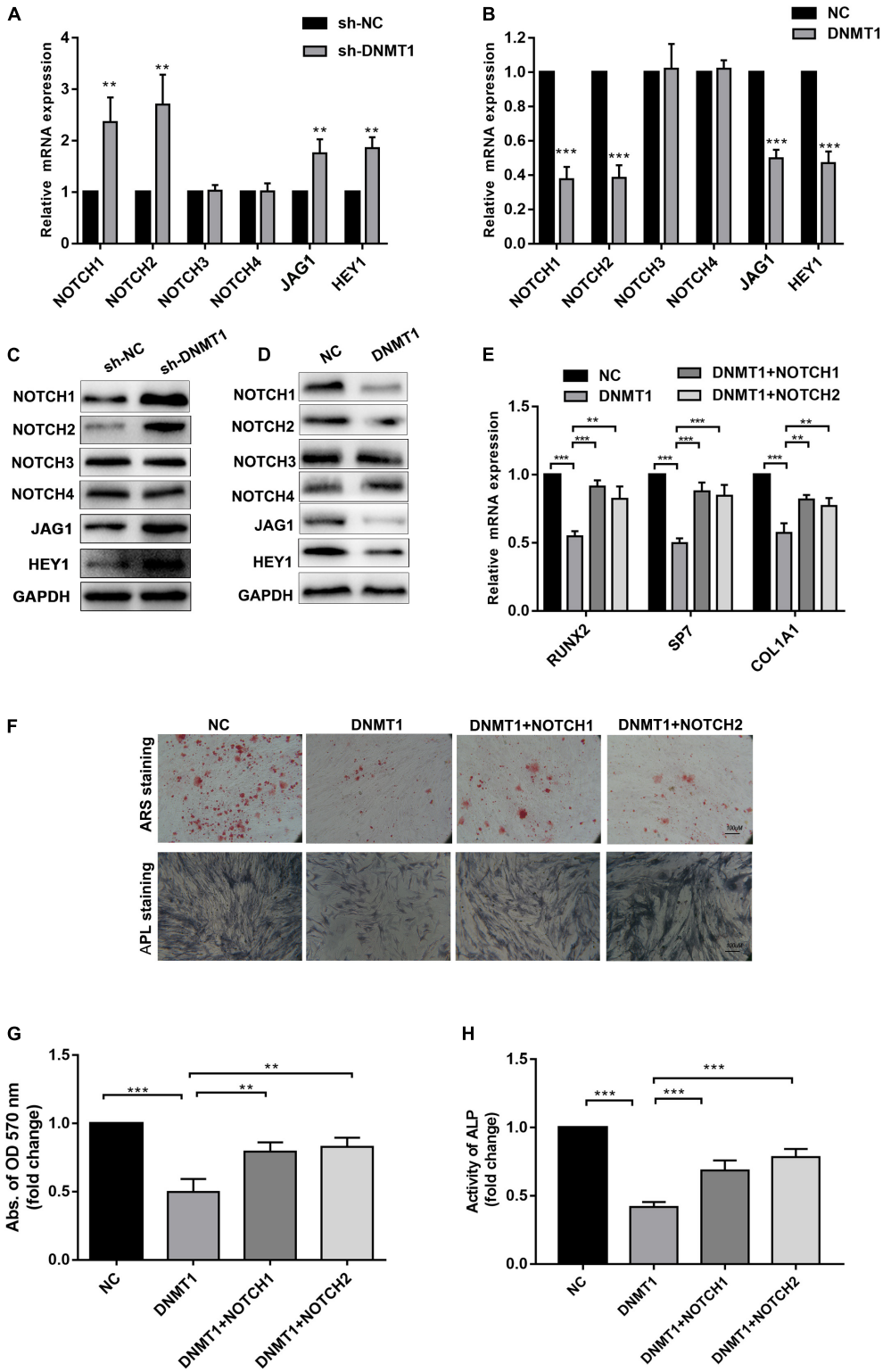

FIGURE 5 | (A,B) Human ADSCs were transfected with DNMT1 shRNA plasmid, expression of NOTCH1, NOTCH2, NOTCH2, NOTCH3,NOTCH4, JAG1, HEY1, were determined by Western blot and RT-qPCR. **(C,D)** hADSCs were transfected with DNMT1 overexpression plasmid, expression of NOTCH1, NOTCH2, NOTCH2, NOTCH3, NOTCH4, JAG1, HEY1, were determined by Western blot and RT-qPCR. **(E)** DNMT1 overexpressed hADSCs were transfected with NOTCH1 or NOTCH2 overexpression plasmids, expression of RUNX2, SP7, and COL1A1 were determined by Western blot and RT-qPCR. **(F–H)** DNMT1 stably overexpressed hADSCs were transfected with NOTCH1 and NOTCH2. After differentiation medium for 14 days, Alizarin red staining and ALP staining showed mineralized nodule formation, ALP activity and quantification of Alizarin red staining by spectrophotometry were determined. Data are shown as means ± SD. $^{**}p < 0.01$, $^{***}p < 0.001$.

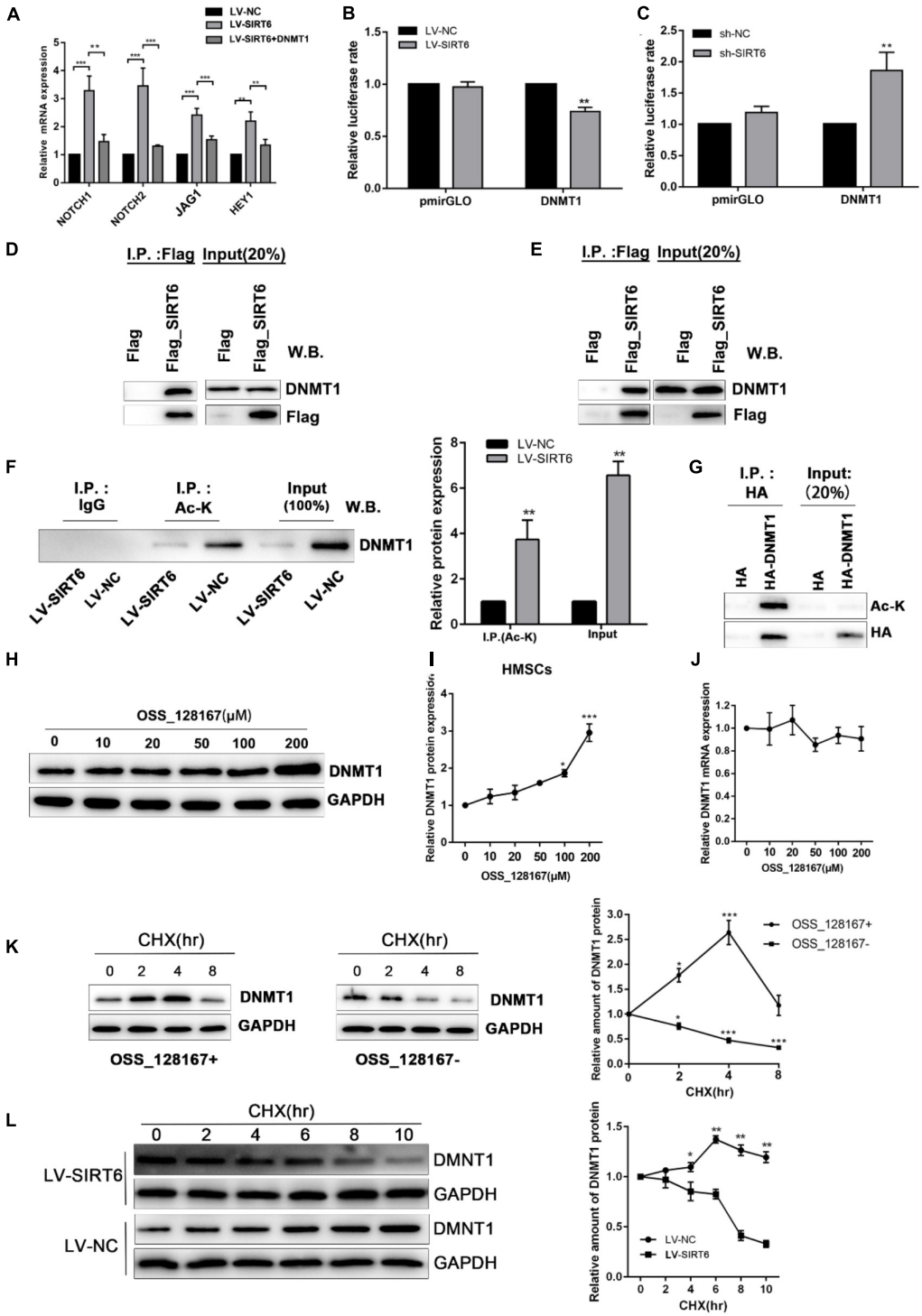

FIGURE 6 | (A) SIRT6 overexpressed hADSCs were transfected with DNMT1 plasmid, the expression of NOTCH1, NOTCH2, NOTCH2, JAG1, HEY1 were determined by RT-qPCR. **(B,C)** Promoter activity was assessed for DNMT1 in SIRT6 overexpressed of silenced hADSCs ($n = 3$). **(D,E)** Immunoprecipitation (IP) analysis was performed in Flag-SIRT1-overexpressing hADSCs and 293T cells. A stable empty vector transfected cell line was established as control group. **(F)** IP analysis was performed with an acetylated lysine (Ac-K) antibody using flag-SIRT6-overexpressing hADSCs nuclear extracts. DNMT1 proteins levels in the Ac-K IP is shown as mean ± SEM. **(G)** HA-tagged Dnmt1 proteins were immunoprecipitated (IP) using an HA antibody. Acetylated proteins in the IP products were detected by western blot. **(H,I)** The change of DNMT1 protein expression are shown during treatment of OSS_128167. **(J)** The change of DNMT1 mRNA expression is shown during treatment of OSS_128167. (K) DNMT1 proteins stability in hADSCs in the present or absent of OSS_128167 was measured using a cycloheximide (CHX)-chase assay (100 mg/mL CHX) for the indicated hours. **(L)** Stability of the DNMT1 proteins in SIRT6 overexpressed or control hADSCs was measured using a CHX-chase assay involving 100 mg/mL CHX for the indicated hours. Data are shown as means ± SD. $^{*}p < 0.05$, $^{**}p < 0.01$, $^{***}p < 0.001$.

reported, the SIRT1 protein physically interacted with DNMT3L and regulates its activity by protein deacetylation. In this study, we assessed the potential physical interactions between SIRT6 and DNMT1 proteins. Co-immunoprecipitation assay was performed in hADSCs and 293T cells with flag tagged SIRT6 protein. Endogenous DNMT1 protein was identified in the SIRT6 protein complex (**Figures 6D,E**).

To identify whether SIRT6 deacetylate DNMT1, we examined the acetylation status of the DNMT1 protein in hADSCs via immunoprecipitation assays. The results demonstrated that an amount of DNMT1 protein was acetylated in hADSCs, and acetylated DNMT1 was found at a remarkably lower level in SIRT6 overexpressed hADSCs (**Figures 6F,G**). These results suggest that DNMT1 protein could be acetylated by SIRT6 in hADSCs.

Next, we determined the biological significance of the acetylation status in DNMT1, SIRT6 overexpressing hADSCs were administrated with OSS_128167, a chemical inhibitor of SIRT6. Treatment with OSS_128167 increased the protein and mRNA levels of DNMT1 (**Figures 6H–J**). Then, we performed a CHX chasing assay to check the stability of the DNMT1 protein with or without OSS_128167 treatment. As shown in **Figure 6K**, blocking the SIRT6 deacetylase activity dramatically increased the stability of DNMT1. In addition, the DNMT1 protein stability was weaker in SIT6 overexpressing hADSCs than in control cells (**Figure 6L**). These results indicate that SIRT6 regulates DNMT1 protein stability via a posttranslational modification mechanism. A diagram was show in **Figure 7** to visualize the detail mechanism in our study.

DISCUSSION

SIRT6 has been identified as an NAD1-dependent deacetylase and it is crucial for genome stability, telomere integrity, and life span (Michishita et al., 2005). Recently SIRT6 deficiency was found to be involved in several bone metabolism disease, such as osteoporosis and osteoarthritis, which may due to the broken balance of bone homeostasis (Sugatani et al., 2015; Zhang et al., 2018). Further, knockdown of SIRT6 accelerated the aging of the marrow mesenchymal stem cells (BMSCs) while its overexpression could promote the osteogenic differentiation (Zhai et al., 2016). SIRT6 reported to promote the osteogenic differentiation via modifying the BMP signaling in a PCAF dependent manner (Zhang et al., 2017). In the present study, we demonstrated that SIRT6 expression was increased after osteogenic induction of hADSCs, SIRT6 overexpression significantly increased the expression of osteogenic markers and promoted mineralized bone matrix formation and ALP activity. The effects of SIRT6 overexpression on osteogenic differentiation could be offset by NOTCH1/2 shRNAs or DAPT. The expression of NOTCH1 and NOTCH2 was epigenetic regulated by DNMT1. DNMT1 impaired the capacity of osteogenic differentiation in hADSCs as confirmed by ARS staining, ALP staining and activity assays, which could be rescued by through SIRT6 overexpression as well as NOTCH1 and NOTCH2 plasmid transfection. SIRT6 promoted osteogenic differentiation by preventing abnormal DNA methylation of NOTCH1 and NOTCH2 via antagonizing DNMT1.

Altered DNA methylation of the NOTCH family protein has been observed in stem cells (Liu et al., 2015; Yan et al., 2018). Consistent with these reports, we identified that NOTCH1 and NOTCH2 were regulated by DNMT1. However, we were unable to explain why DNMT1 selectively hypermethylated NOTCH family members. DNA methylation of these two genes resulted in increased ALP activity, enhanced mineralization and elevated expression level of osteogenic-related genes. Inhibition of NOTCH signaling via silencing JAG1 caused an impairment of osteogenic differentiation (Qu et al., 2017). Tetrahedral DNA nanostructures could dramatically enhance

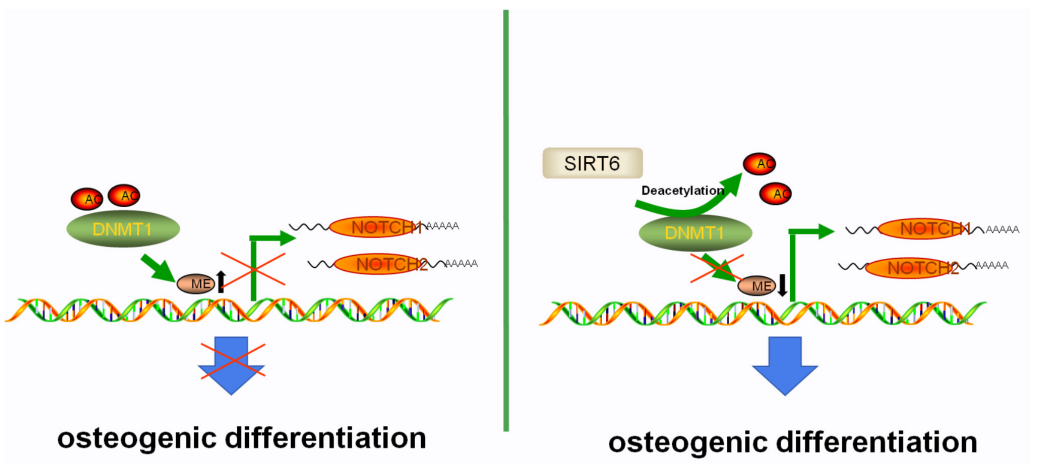

FIGURE 7 | The proposed mechanism of SIRT6-induced osteogenic differentiation of adipose-derived mesenchymal stem cells. SIRT6 tightly regulates the level of NOTCHs by antagonizing the DNMT1 protein at the level of protein stability. Abnormal DNA methylation status of NOTCHs caused by DNMT1 in SIRT6 deficiency impairs the osteogenic differentiation potential of ADSCs. In the present of SIRT6, the histone acetylation status of the DNMT1 was upregulated, leading to the increased expression of NOTCH1 and NOTCH2, which further promotes the osteogenic differentiation capability of ADSCs.

the proliferation and osteogenic differentiation of dental pulp stem cells by upregulating the NOTCH signaling (Zhou et al., 2018). Similar mechanism was reported in BMSCs and it seems that microenvironment plays an important role (Chen et al., 2013; Xie et al., 2018). In this study, overexpression of NOTCH1 and NOTCH2 promoted the osteogenic differentiation of hADSCs and DNMT1 rather than DNMT3A, DNMT3B or DNMT3L could restrain this effect. Hence, we speculated that the specificity of SIRT6 targets could be determined by their association with the DNMT1 protein. In our study, the SIRT6 protein deacetylated and destabilized DNMT1 protein via physical interaction. Peng et al. Reported that DNMT3L is a substrate of the SIRT1 protein (Peng et al., 2011), and DNMT3L expression and the protein stability were regulated by SIRT1 (Heo et al., 2017). Here, we identified that SIRT6 protein strongly interacted with DNMT1. DNMT1 overexpression significantly suppressed NOTCH1 and NOTCH2 and impaired the osteogenic differentiation. This suggested that DNMT1, a crucial target of SIRT6, involved in regulation of DNA methylation of NOTCH1 and NOTCH2 in hADSCs. Thus, SIRT6 might affect distinct downstream targets via DNMT1, which regulated the DNA methylation status of this gene. Here, we revealed that DNMT1 is a substrate of SIRT6 deacetylase in hADSCs and identification of the proteins directly modified by SIRT6 would be helpful in understanding the biological significance of the SIRT6-DNMT1 complex in the multi-directional differentiations of hADSCs (**Figure 7**). Our data reemphasized the import role for SIRT6 in regulating osteogenesis found in other marrow mesenchymal stem cells, while also establish a previously unconfirmed underlying mechanism. The new mechanism we discovered may support a potential therapeutic application through a SIRT6 agonist or DNA methyltransferase inhibitor in the bone metabolism diseases.

CONCLUSION

In our study, we identified the regulation of osteogenic potential of hADSCs composed of SIRT6/DNMT1/NOTCHs axis. SIRT6 increased the levels of NOTCH1 and NOTCH2 via acetylated DNMT1, which could hypermethylated NOTCH1 and NOTCH2. Our study demonstrated the promotion of SIRT6 in osteogenic differentiation and its potential role in the treatment of osteogenesis disorders.

DATA AVAILABILITY STATEMENT

The original contributions presented in the study are included in the article/**Supplementary Materials**, further inquiries can be directed to the corresponding authors.

ETHICS STATEMENT

The animal study was reviewed and approved by Animal Ethics Committee of the Southern Medical University.

AUTHOR CONTRIBUTIONS

BJ, YH, and QY conceived the research idea and designed the whole experimental plan. JC, QW, and XS isolated and characterized the adipose-derived mesenchymal stem cells. BJ, JH, and SX performed the animal study. BJ and YH analyzed the *in vitro* and *in vivo* results and discussed the findings with YH. BJ wrote the initial draft of the manuscript. YH and QY revised the manuscript. FG provided constructive suggestion on the discussion and proofread the language of the manuscript. All authors have approved the final version of this manuscript.

FUNDING

This study was financially supported by the Guangzhou Science and Technology Program key Projects (201802020018), the China Postdoctoral Science Foundation (2019M652979), the Guangdong Science and Technology Program (2019A1515010408), and the program of Stomatological Hospital, Southern Medical University, China (PY2019003).

SUPPLEMENTARY MATERIAL

The Supplementary Material for this article can be found online at: https://www.frontiersin.org/articles/10.3389/fcell.2021.648627/full#supplementary-material

REFERENCES

Bai, X., He, T., Liu, Y., Zhang, J., Li, X., Shi, J., et al. (2018). Acetylation-dependent regulation of notch signaling in macrophages by SIRT1 affects sepsis development. *Front. Immunol.* 9:762.

Bianco, P., Robey, P. G., and Simmons, P. J. (2008). Mesenchymal stem cells: revisiting history, concepts, and assays. *Cell Stem Cell* 2, 313–319. doi: 10.1016/j.stem.2008.03.002

Caplan, A. I. (2007). Adult mesenchymal stem cells for tissue engineering versus regenerative medicine. *J. Cell Physiol.* 213, 341–347. doi: 10.1002/jcp.21200

Cedar, H., and Bergman, Y. (2009). Linking DNA methylation and histone modification: patterns and paradigms. *Nat. Rev. Genet.* 10, 295–304. doi: 10.1038/nrg2540

Challen, G. A., Sun, D., Jeong, M., Luo, M., Jelinek, J., Berg, J. S., et al. (2011). Dnmt3a is essential for hematopoietic stem cell differentiation. *Nat. Genet.* 44, 23–31.

Chattapadhyaya, S., Haldar, S., and Banerjee, S. (2020). Microvesicles promote megakaryopoiesis by regulating DNA methyltransferase and methylation of Notch1 promoter. *J. Cell Physiol.* 235, 2619–2630. doi: 10.1002/jcp.29166

Chen, X., Zhang, T., Shi, J., Xu, P., Gu, Z., Sandham, A., et al. (2013). Notch1 signaling regulates the proliferation and self-renewal of human dental follicle cells by modulating the G1/S phase transition and telomerase activity. *PLoS One* 8:e69967. doi: 10.1371/journal.pone.0069967

Denis, H., Ndlovu, M. N., and Fuks, F. (2011). Regulation of mammalian DNA methyltransferases: a route to new mechanisms. *EMBO Rep.* 12, 647–656. doi: 10.1038/embor.2011.110

Dong, Y., Jesse, A. M., Kohn, A., Gunnell, L. M., Honjo, T., Zuscik, M. J., et al. (2010). RBPjkappa-dependent Notch signaling regulates mesenchymal progenitor cell proliferation and differentiation during skeletal development. *Development* 137, 1461–1471. doi: 10.1242/dev.042911

Etchegaray, J. P., Chavez, L., Huang, Y., Ross, K. N., Choi, J., Martinez-Pastor, B., et al. (2015). The histone deacetylase SIRT6 controls embryonic stem cell fate via TET-mediated production of 5-hydroxymethylcytosine. *Nat. Cell Biol.* 17, 545–557. doi: 10.1038/ncb3147

Hayashi, K., and Surani, M. A. (2009). Resetting the epigenome beyond pluripotency in the germline. *Cell Stem Cell* 4, 493–498. doi: 10.1016/j.stem.2009.05.007

Heilmeier, U., Hackl, M., Skalicky, S., Weilner, S., Schroeder, F., Vierlinger, K., et al. (2016). Serum miRNA signatures are indicative of skeletal fractures in postmenopausal women with and without Type 2 diabetes and influence osteogenic and adipogenic differentiation of adipose tissue-derived mesenchymal stem cells in vitro. *J. Bone Miner. Res.* 31, 2173–2192. doi: 10.1002/jbmr.2897

Heo, J., Lim, J., Lee, S., Jeong, J., Kang, H., Kim, Y., et al. (2017). Sirt1 regulates DNA methylation and differentiation potential of embryonic stem cells by antagonizing Dnmt3l. *Cell Rep.* 18, 1930–1945. doi: 10.1016/j.celrep.2017.01.074

Jaenisch, R., and Bird, A. (2003). Epigenetic regulation of gene expression: how the genome integrates intrinsic and environmental signals. *Nat. Genet.* 33(Suppl.), 245–254. doi: 10.1038/ng1089

Jia, B., Qiu, X., Chen, J., Sun, X., Zheng, X., Zhao, J., et al. (2019). A feed-forward regulatory network lncPCAT1/miR-106a-5p/E2F5 regulates the osteogenic differentiation of periodontal ligament stem cells. *J. Cell Physiol.* 234, 19523–19538. doi: 10.1002/jcp.28550

Kanfi, Y., Naiman, S., Amir, G., Peshti, V., Zinman, G., Nahum, L., et al. (2012). The sirtuin SIRT6 regulates lifespan in male mice. *Nature* 483, 218–221. doi: 10.1038/nature10815

Kawahara, T. L., Michishita, E., Adler, A. S., Damian, M., Berber, E., Lin, M., et al. (2009). SIRT6 links histone H3 lysine 9 deacetylation to NF-kappaB-dependent gene expression and organismal life span. *Cell* 136, 62–74. doi: 10.1016/j.cell.2008.10.052

Lee, J. T., and Bartolomei, M. S. (2013). X-inactivation, imprinting, and long noncoding RNAs in health and disease. *Cell* 152, 1308–1323. doi: 10.1016/j.cell.2013.02.016

Li, L., Ling, Z., Dong, W., Chen, X., Vater, C., Liao, H., et al. (2019). Dnmt3a-mediated DNA methylation changes regulate osteogenic differentiation of hMSCs cultivated in the 3D scaffolds under oxidative stress. *Health Med.* 2019:4824209.

Liu, S., Liu, D., Chen, C., Hamamura, K., Moshaverinia, A., Yang, R., et al. (2015). MSC transplantation improves osteopenia via epigenetic regulation of notch signaling in lupus. *Cell Metab.* 22, 606–618. doi: 10.1016/j.cmet.2015.08.018

Liu, Z., Chen, T., Sun, W., Yuan, Z., Yu, M., Chen, G., et al. (2016). DNA demethylation rescues the impaired osteogenic differentiation ability of human periodontal ligament stem cells in high glucose. *Sci. Rep.* 6:27447.

Michishita, E., Mccord, R. A., Berber, E., Kioi, M., Padilla-Nash, H., Damian, M., et al. (2008). SIRT6 is a histone H3 lysine 9 deacetylase that modulates telomeric chromatin. *Nature* 452, 492–496. doi: 10.1038/nature06736

Michishita, E., Park, J. Y., Burneskis, J. M., Barrett, J. C., and Horikawa, I. (2005). Evolutionarily conserved and nonconserved cellular localizations and functions of human SIRT proteins. *Mol. Biol. Cell* 16, 4623–4635. doi: 10.1091/mbc.e05-01-0033

Mostoslavsky, R., Chua, K. F., Lombard, D. B., Pang, W. W., Fischer, M. R., Gellon, L., et al. (2006). Genomic instability and aging-like phenotype in the absence of mammalian SIRT6. *Cell* 124, 315–329. doi: 10.1016/j.cell.2005.11.044

O'Hagan, H. M., Mohammad, H. P., and Baylin, S. B. (2008). Double strand breaks can initiate gene silencing and SIRT1-dependent onset of DNA methylation in an exogenous promoter CpG island. *PLoS Genet.* 4:e1000155. doi: 10.1371/journal.pgen.1000155

Okasha, S. M., Itoh, M., and Tohda, S. (2020). Sirtuin 1 activation suppresses the growth of T-lymphoblastic leukemia cells by inhibiting NOTCH and NF-κB Pathways. *Anticancer Res.* 40, 3155–3161. doi: 10.21873/anticanres.14297

Peng, L., Yuan, Z., Ling, H., Fukasawa, K., Robertson, K., Olashaw, N., et al. (2011). SIRT1 deacetylates the DNA methyltransferase 1 (DNMT1) protein and alters its activities. *Mol. Cell Biol.* 31, 4720–4734. doi: 10.1128/mcb.06147-11

Qu, X., Chen, Z., Fan, D., Sun, C., Zeng, Y., Guo, Z., et al. (2017). MiR-199b-5p inhibits osteogenic differentiation in ligamentum flavum cells by targeting JAG1 and modulating the Notch signalling pathway. *J. Cell Mol. Med.* 21, 1159–1170. doi: 10.1111/jcmm.13047

Schubert, T., Lafont, S., Beaurin, G., Grisay, G., Behets, C., Gianello, P., et al. (2013). Critical size bone defect reconstruction by an autologous 3D osteogenic-like tissue derived from differentiated adipose MSCs. *Biomaterials* 34, 4428–4438. doi: 10.1016/j.biomaterials.2013.02.053

Sugatani, T., Agapova, O., Malluche, H. H., and Hruska, K. A. (2015). SIRT6 deficiency culminates in low-turnover osteopenia. *Bone* 81, 168–177. doi: 10.1016/j.bone.2015.07.018

Tsai, C. C., Su, P. F., Huang, Y. F., Yew, T. L., and Hung, S. C. (2012). Oct4 and Nanog directly regulate Dnmt1 to maintain self-renewal and undifferentiated state in mesenchymal stem cells. *Mol. Cell* 47, 169–182. doi: 10.1016/j.molcel.2012.06.020

Wei, H., Yin, X., Tang, H., Gao, Y., Liu, B., Wu, Q., et al. (2020). Hypomethylation of Notch1 DNA is associated with the occurrence of uveitis. *Clin. Exp. Immunol.* 201, 317–327. doi: 10.1111/cei.13471

Worthley, D. L., Churchill, M., Compton, J. T., Tailor, Y., Rao, M., Si, Y., et al. (2015). Gremlin 1 identifies a skeletal stem cell with bone, cartilage, and reticular stromal potential. *Cell* 160, 269–284.

Xie, H., Gu, Z., He, Y., Xu, J., Xu, C., Li, L., et al. (2018). Microenvironment construction of strontium–calcium-based biomaterials for bone tissue regeneration: the equilibrium effect of calcium to strontium. *J. Mater. Chem .B* 6, 2332–2339. doi: 10.1039/c8tb00306h

Yan, J., Tie, G., Wang, S., Tutto, A., Demarco, N., Khair, L., et al. (2018). Diabetes impairs wound healing by Dnmt1-dependent dysregulation of hematopoietic stem cells differentiation towards macrophages. *Nat. Commun.* 9:33.

Zhai, X. Y., Yan, P., Zhang, J., Song, H. F., Yin, W. J., Gong, H., et al. (2016). Knockdown of SIRT6 enables human bone marrow mesenchymal stem cell senescence. *Rejuvenation Res.* 19, 373–384. doi: 10.1089/rej.2015.1770

Zhang, P., Liu, Y., Wang, Y., Zhang, M., Lv, L., Zhang, X., et al. (2017). SIRT6 promotes osteogenic differentiation of mesenchymal stem cells through BMP signaling. *Sci. Rep.* 7:10229.

Zhang, W., Wan, H., Feng, G., Qu, J., Wang, J., Jing, Y., et al. (2018). SIRT6 deficiency results in developmental retardation in cynomolgus monkeys. *Nature* 560, 661–665. doi: 10.1038/s41586-018-0437-z

Zhou, M., Liu, N. X., Shi, S. R., Li, Y., Zhang, Q., Ma, Q. Q., et al. (2018). Effect of tetrahedral DNA nanostructures on proliferation and osteo/odontogenic differentiation of dental pulp stem cells via activation of the notch signaling pathway. *Nanomedicine* 14, 1227–1236. doi: 10.1016/j.nano.2018.02.004

Conflict of Interest: The authors declare that the research was conducted in the absence of any commercial or financial relationships that could be construed as a potential conflict of interest.

frontiers in Pharmacology

ORIGINAL RESEARCH
published: 07 July 2021
doi: 10.3389/fphar.2021.666860

Suppression of FGF5 and FGF18 Expression by Cholesterol-Modified siRNAs Promotes Hair Growth in Mice

Jungang Zhao[1†], Haojie Lin[1†], Lusheng Wang[1†], Keke Guo[1], Rongrong Jing[1], Xuenan Li[1], Yu Chen[1], Zhenlin Hu[1], Shuang Gao[2] and Nuo Xu[1]**

[1]College of Life and Environmental Sciences, Wenzhou University, Wenzhou, China, [2]School of Pharmaceutical Sciences, Wenzhou Medical University, Wenzhou, China

OPEN ACCESS

Edited by:
Zhouguang Wang,
Albert Einstein College of Medicine,
United States

Reviewed by:
Song Hui Jia,
St. Michael's Hospital, Canada
Yong Miao,
Southern Medical University, China

***Correspondence:**
Shuang Gao
gaoshuangphu@163.com
Nuo Xu
seer.sino@hotmail.com

[†]These authors have contributed equally to this work

Specialty section:
This article was submitted to Integrative and Regenerative Pharmacology, a section of the journal Frontiers in Pharmacology

Received: 11 February 2021
Accepted: 28 June 2021
Published: 07 July 2021

Citation:
Zhao J, Lin H, Wang L, Guo K, Jing R, Li X, Chen Y, Hu Z, Gao S and Xu N (2021) Suppression of FGF5 and FGF18 Expression by Cholesterol-Modified siRNAs Promotes Hair Growth in Mice. Front. Pharmacol. 12:666860. doi: 10.3389/fphar.2021.666860

FGF5 and FGF18 are key factors in the regulation of the hair follicle cycle. FGF5 is overexpressed during the late anagen phase and serves as a crucial regulatory factor that promotes the anagen-to-catagen transition in the hair follicle cycle. FGF18, which is overexpressed during the telogen phase, mainly regulates the hair follicle cycle by maintaining the telogen phase and inhibiting the entry of hair follicles into the anagen phase. The inhibition of FGF5 may prolong the anagen phase, whereas the inhibition of FGF18 may promote the transition of the hair follicles from the telogen phase to the anagen phase. In the present study, we used siRNA to suppress FGF5 or FGF18 expression as a way to inhibit the activity of these genes. Using qPCR, we showed that FGF5-targeting siRNA modified by cholesterol was more effective than the same siRNA bound to a cell-penetrating peptide at suppressing the expression of FGF5 both *in vitro* and *in vivo*. We then investigated the effects of the cholesterol-modified siRNA targeting either FGF5 or FGF18 on the hair follicle cycle in a depilated area of the skin on the back of mice. The cholesterol-modified siRNA, delivered by intradermal injection, effectively regulated the hair follicle cycle by inhibiting the expression of FGF5 and FGF18. More specifically, intradermal injection of a cholesterol-modified FGF5-targeted siRNA effectively prolonged the anagen phase of the hair follicles, whereas intradermal injection of the cholesterol-modified FGF18-targeted siRNA led to the mobilization of telogen follicles to enter the anagen phase earlier. The inhibitory effect of the cholesterol-modified FGF18-targeted siRNA on FGF18 expression was also evaluated for a topically applied siRNA. Topical application of a cream containing the cholesterol-modified FGF18-targeted siRNA on a depilated area of the skin of the back of mice revealed comparable inhibition of FGF18 expression with that observed for the same siRNA delivered by intradermal injection. These findings suggested that alopecia could be prevented and hair regrowth could be restored either through the intradermal injection of cholesterol-modified siRNA targeting FGF5 or FGF18 or the topical application of FGF18 siRNA.

Keywords: fibroblast growth factors, FGF5, FGF18, hair follicle cycle, cholesterol-modified siRNA

INTRODUCTION

Hair follicles, which are major accessory organs of the skin, control the cyclic growth of hairs (Chen et al., 2013). They can regenerate and undergo cyclical changes in growth. The growth cycle of hair follicles supports the self-renewal of hair follicles and regulates hair growth and shedding. Hair follicles consist of an upper permanent portion and a lower cyclical portion. Based on the changes that occur in the cyclical portion, the hair follicle cycle is divided into the anagen, catagen, and telogen phases (Higgins et al., 2014). Abnormalities in the hair follicle cycle are a key mechanism in the pathogenesis of alopecia. The anagen phase in normal scalp hair follicles lasts for 2–6 years, but this may be shortened to several months to a year for the hair follicles on the crown in androgenetic alopecia, which is the most common form of alopecia (Ben David-Naim et al., 2017). Continuous shortening of the anagen phase leads to progressive hair follicle miniaturization, thus prolonging the telogen phase. Ultimately, the hair follicles become arrested at the telogen phase, which results in alopecia. Shortening of the anagen phase is caused by premature termination of the anagen phase followed by premature entry into the catagen phase. Therefore, the key to preventing alopecia is to prevent the progressive shortening and premature termination of the anagen phase, and the key to restoring hair growth is the mobilization of telogen follicles to enter the anagen phase.

The mechanisms involved in the regulation of hair growth are extremely complex. Research in recent years has revealed that many growth factors, including fibroblast growth factors (FGFs), participate in the regulation of the hair follicle cycle (Kawano et al., 2005). FGFs, a large 23-member family of growth factors, mediate FGF signal transduction by binding to FGF receptors (FGFRs) and forming ternary complexes with heparan sulfate proteoglycans (HSPGs) or members of the Klotho family. Various members of the FGF family participate in the regulation of the hair follicle cycle, with FGF1, FGF2, FGF7, and FGF10 being highly expressed and promoting hair growth during the anagen phase. Notably, FGF5, which is an inhibitor of hair growth, is highly expressed during the late anagen phase. It is currently regarded as the most effective factor for promoting the anagen-to-catagen transition of hair follicles (Kehler et al., 2007; He et al., 2016; Jin and Zhang 2018). FGF5 was first discovered in angora mice, which carry a spontaneous mutation in the FGF5 gene. Angora mice were characterized by a prolonged anagen phase for the hair follicles, an abnormal increase in the proportion of anagen hair follicles, and a 50% longer hair coat length compared with that of the wild-type mice. Mutations in the FGF5 gene form the genetic basis for familial trichomegaly, which is manifested as increased hair growth and abnormally long and thick eyelashes for the carriers of the mutated FGF5 gene. FGF5-deficient or knockout animals (including mice, sheep, cats, dogs and guinea pigs) also have abnormally thick and long hair (Yu et al., 2018). A previous study has shown that an FGF5-derived decapeptide that possesses FGF5-antagonizing activity can promote hair growth in mice (Ito et al., 2003). Therefore, inhibiting the expression of the FGF5 gene or antagonizing its activity will prevent the premature termination of the anagen phase of the hair follicles, thereby preventing alopecia.

FGF18 is overexpressed during the telogen phase to maintain the quiescent stage of the hair follicles and to facilitate their entry into the anagen phase. When the hair follicles are in the late anagen phase, subcutaneous injection of FGF18 into skin of mice can effectively inhibit the growth of hair follicles (Blanpain et al., 2004). When the FGF18 gene was conditionally knocked out in keratin 5-positive epithelial cells in mice, the telogen phase was dramatically shortened, causing a strikingly rapid succession of hair cycles, demonstrating that the absence of FGF18 signaling significantly accelerates the start of anagen phase (Kimura-Ueki et al., 2012). These studies indicate that FGF18 is a key regulatory factor in the maintenance of the telogen phase in hair follicles and that inhibition of its expression or antagonism of its activity can promote the telogen-to-anagen transition, which will ultimately lead to hair regrowth.

Small interfering RNA (siRNA)-mediated inhibition of gene expression, which is characterized by its high specificity and high efficiency, has become an important technique for studying gene function and for drug target discovery research. Dozens of siRNA drugs are currently being studied in clinical trials for the treatment of a wide variety of diseases such as malignant tumors, viral infections, diabetic macular edema, asthma, eye diseases, and skin diseases (Sajid and Moazzam 2020; Saw and Song 2020). However, two major barriers exist in the local application of siRNA to the skin, namely the inability of siRNA to penetrate the stratum corneum barrier and poor efficiency in the uptake of the siRNA by the skin cells. The stratum corneum, which is the outermost layer of the skin, has a thickness of 10–20 μm and is composed of multiple layers of corneocytes (i.e., keratinocytes in their last stage of differentiation). Hydrophilic compounds with a molecular weight of >500 Da are therefore unable to penetrate the stratum corneum freely (Steven and Steinert, 1994). As siRNA molecules generally have a molecular weight of >13,000 Da, a negative charge, and a high degree of hydrophilicity, they are incapable of penetrating the stratum corneum barrier in the absence of an assisted delivery method. Assuming that the stratum corneum barrier could be overcome, the lipid bilayer structure of the cell membrane still makes it difficult for the negatively charged siRNAs to enter the skin cell. Previous research has indicated that transfection agents such as cationic liposomes must be used during *in vitro* cell experiments to allow the siRNA to enter the cell and exert its intended effects (Hickerson et al., 2011). Studies have found that the covalent conjugation of a cholesterol molecule to the 3′ or 5′ end of siRNA greatly enhances its *in vivo* stability and increases its hydrophobicity and ability to penetrate the membrane (Soutschek et al., 2004; Chong et al., 2013). The cholesterol-modified siRNA, which has a high transfection efficiency is safe and can act as a self-delivering siRNA that can effectively interfere with the expression of target genes. One recent study has revealed that topical application of a cream containing a cholesterol-modified siRNA can efficiently deliver the siRNA through the stratum corneum barrier to allow its subsequent entry into the epithelial cells, thereby effectively inhibiting the expression of the

target gene in the epithelial cells to <50% without producing any obvious adverse effect (Wolfrum et al., 2007). Such cholesterol-modified siRNA creams may potentially be developed into a simple, convenient, efficient, and safe RNA interference-based product for the treatment of skin diseases.

Cell-penetrating peptides (CPPs) are short peptides that are capable of carrying macromolecules such as proteins and nucleic acids across the cell membrane and into the cell (Beloor et al., 2015). The non-covalent interaction between CPPs and siRNAs can lead to the formation of stable nanocomposites (Falato et al., 2021). These nanocomposites have been demonstrated to have a good delivery efficiency in various cell lines (Nakase et al., 2013). Besides efficiently transporting the siRNAs into the cells, CPPs can also facilitate the penetration of siRNAs across the stratum corneum barrier (Uchida et al., 2011; Chen et al., 2014).

In the present study, FGF5 and FGF18, which are key factors that negatively regulate the hair follicle cycle, were selected for inhibition by targeted siRNAs and the effects of these siRNAs on the hair follicle growth cycle were examined. Different formulations of the siRNAs (cholesterol-conjugated or CPP-bound) were compared. In addition, delivery by intradermal injection and via topical application were also evaluated. The results of this study may provide a scientific basis for the development of novel hair loss prevention products suitable for topical application.

MATERIALS AND METHODS

Preparation of siRNA Samples

Synthesis of the candidate siRNAs and the subsequent covalent modifications at the 5′end with cholesterol were performed by GenePharma (Shanghai, China). Three FGF5-targeting siRNAs were designed: 567–25/27, 635–25/27 and 565–25/27. The numbers 567, 653 and 565 indicate the start of the binding site in the target gene, while 25/27 indicates the length of the siRNA sequence. The sequences of the siRNAs are as follows: FGF5 siRNA-635–25/27-sense 5′-GCAACAAAUUUUUAGCGAUGU CAAA-3′ and antisense 5′-UUUGACAUCGCUAAAAAUUUG UUGCUG-3’; FGF5 siRNA-565–25/27-sense 5′-GCCAGAGAG UUAAGUAUUUUGGAAA-3′ and antisense 5′-UUUCCAAAA UACUUAACUCUCUGGCUU-3’; FGF5 siRNA-567–25/27-sense5′-CAGUGUGUUAAGUAUUUUGGAAAUA-3′ and antisense 5′-UAUUUCCAAAAUACUUAACACACUGGC-3’; FGF5 siRNA-567–25/27-NC-sense 5′-GUUGUAAUCUUGAUG AUAAUGAGUA-3′ and antisense 5′-UACUCAUUAUCAUCA AGAUUACAACGC-3’; FGF8 siRNA-502–25/27-sense 5′-GGA GUGCGUGUUCAUUGAGAAGGUU-3′ and antisense 5′-AAC CUUCUCAAUGAACACGCACUCCUU-3’; FGF8 siRNA-502–25/27-NC-sense 5′-GUCAUUGAGAAGGUGAGUGCG UGUU-3′ and antisense 5′-AACACGCACUCACCUUCUCAA UGACUU-3’.

For intradermal injection, the cholesterol-modified siRNA and the siRNA containing a negative control sequence were each diluted 20 μM. To prepare the siRNA cream for topical application, 330 μg cholesterol-modified siRNA was first dissolved in 0.25 g of azone and 2.0 g of 2-ethylhexyl palmitate to form an oil phase. Next, 1.0 g of propylene glycol and 0.25 g of benzethonium chloride were dissolved in water to form an aqueous phase. After that, an emulsifier was added to the oil phase and stirred slowly to achieve a uniform mixture. Finally, the aqueous phase was slowly added to the oil phase in a batch-wize manner and stirred to obtain a uniform mixture, which was then stored in a separate container.

Cell Line and Cell Culture

NIH-3T3 cells (mouse embryonic cell line) were obtained from the Cell Bank of the Chinese Academy of Sciences (Shanghai, China) and cultured in Dulbecco's modified Eagle's medium (DMEM) containing 10% fetal bovine serum (FBS) (Gibco, Life Technologies Corporation, NY, United States) and 1% penicillin/streptomycin at 37°C in a 5% CO_2 incubator.

Animal and Housing

Healthy C57BL/6 mice (female, 18–22 g) were purchased from Shanghai SLAC Laboratory Animal Co., Ltd. (Shanghai, China). Animal care was performed in accordance with international ethical guidelines and the National Institutes of Health Guide for the Care and Use of Laboratory Animals. All animals were housed under controlled temperature (20 ± 2°C) with a 12 h light/12 h dark cycle.

Transfection of NIH/3T3 Cells With FGF5/FGF18 Plasmid and Liposome-Encapsulated, Cholesterol-Modified, and CPP-Bound siRNAs

NIH/3T3 cells that overexpressed either FGF5 or FGF18 were prepared by inoculating the cells onto 6-well plates at a density of 1×10^5 cells/well in 2 ml complete medium containing serum and penicillin/streptomycin. When the cells reached 80% confluence, the medium was replaced with 2 ml fresh medium without penicillin/streptomycin. Next,1.6 μg of FGF5 or FGF18 expression plasmid DNA and 4 μL lipofectamine 2000 were mixed in 200 μL DMEM medium without serum and penicillin/streptomycin and left to stand for 5 min. After that, the sample was added to the cells and the plate was then incubated at 37°C for 6 h in a 5% CO_2 incubator. The culture medium was replaced with fresh medium and the cells were transfected with siRNA as described below. NIH/3T3 cells that did not overexpress FGF5 or FGF18 were also prepared in the same way, but the cells were instead transfected with the empty plasmid DNA.

To prepare the Lipofectamine 2000-mediated siRNA, 200 pmol siRNA was first diluted in 100 μL of serum-free medium without penicillin/streptomycin, while 4 μL of Lipofectamine 2000 was added to a separate 100 μL of serum-free medium, and the two samples were each stirred gently, left to stand for 5 min, and then thoroughly mixed and left to stand for another 20 min. To prepare the cholesterol-modified siRNA, 200 pmol of the cholesterol-modified siRNA was diluted and gently mixed with 200 μL of serum-free medium without penicillin/streptomycin and left to stand for 5 min. To prepare the CPP-bound siRNA, 200 pmol of siRNA was diluted in 100 ml of culture medium without serum and penicillin/streptomycin,

while 600 pmol of CPP stearyl-R8 was diluted in a separate 100 ml of serum-free medium without penicillin/streptomycin. Each sample was gently stirred, left to stand for 5 min and then thoroughly mixed and left to stand for a further 20 min. To perform the transfection, each of the siRNA preparation was added to separate wells in a 6-well plate containing the NIH/3T3 cells, and the plate was then incubated at 37°C for 24 h in a 5% CO_2 incubator.

Administration of FGF5 siRNA to the Skin and Collection of Tissue Samples

Seven-week-old female C57BL/6 mice were anesthetized using a small animal inhalation anesthesia machine. Depilation wax was prepared by mixing rosin and paraffin wax in a 1:1 ratio. The mixture was melted by heating, and then evenly applied to the back of each animal. After complete solidification, the depilation wax was slowly peeled off using a pair of tweezers to completely remove the hairs, and the date of depilation was recorded as Day 0. the purpose of using depilatory wax to completely remove hair is to stimulate hair follicles to enter the growth phase on the next day. The back of each animal was divided into two zones, left and right zones. The left zone was injected with the siRNA containing a negative control sequence, while the right zone was injected with the cholesterol-modified siRNA. For each injection, 50 μL of each siRNA sample was intradermally injected at five points in the appropriate skin region for even distribution of the siRNA. For the mice in this part of the experiment, we observed for 29 days. The siRNA was injected on days 14, 17, and 20 following depilation. From Day 15 to Day 29, skin specimens were collected from the regions of siRNA injection once every 2 days. The specimens were obtained from three mice at each collection time point. Each skin tissue specimen was divided into three portions, with one portion fixed in 4% paraformaldehyde solution for histochemical staining and microscopic observation while the remaining portions were stored in two separate 1.5 ml EP tubes at −80°C for quantitative polymerase chain reaction (qPCR) and western blot assays.

Administration of FGF18 siRNA and Collection of Skin Tissue Samples

Seven-week-old female C57BL/6 mice were anesthetized using a small animal inhalation anesthesia machine. Surface hairs on the skin of the back of each animal were removed using an electric shaver. Subsequently, depilation wax was applied to the shaved region, left on for 10 min, and removed by gentle rubbing with a piece of gauze to achieve complete surface hair removal. The purpose of using depilatory wax to surface hair removal is for topical application and to observe the black spots in the skin of the depilated regions. The back-depilated mice were randomly divided into two groups, which were separately administered siRNAs by intradermal injections or with topical application to compare the *in vivo* pharmacological effects of the two drug administration methods. The back of each animal was divided into two zones, left and right zones. The left zone was injected with the siRNA containing a negative control sequence or smeared with a cream containing the same siRNA, whereas the right zone was injected with the cholesterol-modified FGF18-targeting siRNA or smeared with a cream containing the same siRNA. Topical application was commenced on Day 1 following depilation and performed once daily for 15 consecutive days. For injection, 50 μL of the siRNA was intradermally injected at five points in the corresponding skin region. For the mice in this part of the experiment, we observed for 15 days. The siRNA was injected on Days 1, 4, 7 and 10 following depilation. From Day 3 to Day 15, hair growth in the siRNA-administered regions of the skin was recorded by photographing with a digital camera and a hair follicle detector once every 3 days. Skin tissue specimens were also collected at the time of recording. Each skin tissue specimen was divided into three portions as treated as described in Administration of FGF5 siRNA to the skin and collection of tissue samples.

ELISA

NIH-3T3 cultures, both plasmids or siRNAs-treated, were centrifuged to obtain the culture supernatants, and the extent of FGF5 secretion in the supernatants was then measured with an ELISA kit (HUAMEI, Wuhan, China) according to the manufacturer's instruction.

Reverse Transcription-Quantitative Polymerase Chain Reaction

Total RNA was extracted from skin specimens Using TRIzol® Reagent (Thermo Fisher Scientific, Waltham, MA, United States). And total RNA was extracted from cultured cells using an RNA isolation kit (Biomiga, San Diego, CA, United States) according to the manufacturer's instruction. The extracted RNA was used as a template for reverse transcription performed with the PrimeScript RT reagent Kit (Takara, Dalian, China). Reverse transcription was carried out on an LC96 system (Roche, Basel, Switzerland) using the SYBR Green Master Mix (Applied Biosystems, Foster City, CA, United States). The following primers used: FGF5-forward, 5′-AAGTCAATGGCTCCCACGAAGC-3′and reverse 5′-CCG TAAATTTGGCACTTGCATGG-3'; FGF18-forward, 5′-GGAGCAGGTGACCTTTGATGAG-3′and reverse 5′-GAG AGGTGCCAGTTGATGATGG-3'; GAPDH-forward5′-AGAAGGTGGTGAAGCAGGCATC-3′and reverse-5′-CGAAGGTGGAAGAGTGGGAGTTG-3'. The relative level of FGF5 or FGF18 mRNA was calculated using the comparative Ct method with GAPDH mRNA as an endogenous control. All data were normalized to that of the non-treated control.

Western Blot

Extracts of the skin tissue or NIH-3T3 cells were prepared and then centrifuged at 12,000 × g to precipitate the insoluble materials. The protein concentration in the supernatant was determined and samples containing equal amounts (25/40 μg) of protein were separated by SDS-PAGE using 12% gel. The protein in the gel was then transferred to polyvinylidene difluoride (PVDF) membrane and blocked with 5% skim milk for 1 h followed by incubation with rabbit anti-FGF5

(Proteintech, Chicago, IL, United States), anti-FGF18 (Proteintech, Chicago, IL, United States), or anti-tubulin (Cell Signaling Technology, Beverly, MA, United States) for overnight at 4°C. After washing the blot was incubated with goat anti-rabbit antibody (Cell Signaling Technology, Beverly, MA). The blot was visualized with a chemiluminescence substrate (Pierce, Rockford, IL, United States) and images of the blot were captured with an Amersham Imager (GE Healthcare Biosciences, Pittsburgh, PA, United States) and analyzed using the ImageJ software (U. S. National Institutes of Health, Bethesda, Maryland, United States).

Histological Examination

The skin tissue was soaked in 4% paraformaldehyde and stored in a 4°C refrigerator for 24–48 h. After that, it was dehydrated in ethanol solutions containing increasing concentrations of ethanol, and then embedded in paraffin, and subsequently sliced into 10-mm thick sections. The sections were stained with hematoxylin and eosin (HE) solution and observed under a Leica Microsystem (Wetzlar, Germany). To evaluate the expression of FGF5 and FGF18 in the hair follicles by immunohistochemistry, the sections were incubated in 3% H_2O_2 for 25 min and then blocked with 3% BSA for 4 h. They were then incubated with anti-FGF5 antibody (1: 500 dilution; Proteintech, Wuhan, China) or anti-FGF18 antibody (1:500 dilution; Proteintech, Wuhan, China) overnight at 4°C. After three washes with PBS, the sections were incubated with horseradish peroxidase-conjugated secondary antibodies for 4 h at 37°C and then with 3,3-diaminobenzidine (DAB) for about 3 min. All stained sections were examined with a DM3000 microscope (Leica, Wetzlar, Germany) to determine the histological changes.

Statistical Analysis

All statistical analyses were performed with GraphPad Prism 6.0 software. The statistical differences between treatment groups and control were determined using one-way analysis of variance (ANOVA). All data were expressed as mean ± SD, and statistical significance was considered at the $p < 0.05$ level.

RESULTS

Effects of Different Delivery Methods for FGF5-Targeted siRNAs at the Cellular and Tissue Levels

Three candidates of FGF5-targeting siRNAs were tested and all were found to effectively inhibit the expression of FGF5 as evaluated using FGF5-overexpressing NIH/3T3 cells. Subsequently, each siRNA was separately subjected to liposome (Lipofectamine 2000) encapsulation, binding with CPP (stearyl-R8) and cholesterol modification. Compared with the naked siRNA, the liposome-encapsulated, CPP-bound and cholesterol-modified siRNAs all caused a significant decrease in FGF5 mRNA level, indicating that all three delivery methods allowed the siRNA to enter the cells to inhibit the expression of FGF5. However, the cholesterol-modified siRNA exerted a stronger inhibition than the CPP-bound siRNAs (**Figure 1A**), and 567–25/27 was the most potent. As FGF5 is an secretory protein, we used ELISA to detect FGF5 produced by NIH-3T3 cells. Compared with the cells transfected with the empty vector, those transfected with FGF5 containing plasmid produced significantly more FGF5. However, the amount of FGF5 produced by the cells that did not overexpress FGF5 did not change significantly when they were also transfected with the cholesterol-modified negative control siRNA or FGF5 siRNA (567–25/27) (**Figure 1B**). In contrast, cells that overexpressed FGF5 displayed a significant decrease in FGF5 production when they were transfected with the cholesterol-modified FGF5 siRNA (567–25/27), consistent with the qPCR result. Although Lipofectamine 2000 is commonly used in a laboratory for the transfection of cells with siRNAs, it cannot be used for *in vivo* experimentation because of its cytotoxicity. The efficiency of FGF5 knockdown by the cholesterol-modified and CPP-bound siRNAs in the mice skin was then determined. Both cholesterol-modified and CPP-bound siRNAs effectively reduced the level of FGF5 mRNA compared with the negative control siRNA (**Figure 1C**), with the cholesterol-modified siRNA 567–25/27 exerting a strongest effect. Thus, 567–25/27 was chosen for subsequent investigation of the mouse hair follicle cycle. To determine the duration of the inhibition of FGF5 expression by siRNA in mice, we measured the level of FGF5 mRNA at 24, 72, and 120 h after intradermal injection of the cholesterol-modified 567–25/27. The level of FGF5 mRNA dropped by as much as 55.37 ± 7.64% 24 h after injection, and 73.62 ± 0.69% 72 h after injection compared with the level of FGF5 mRNA in the skin injected with the negative control siRNA. The suppressive effects of siRNA had almost completely disappeared 120 h after injection (**Figure 1D**), indicating that the intradermally injected cholesterol-modified siRNA exerted a continuous inhibitory effect on the target gene for up to 72 h post-injection. Therefore, the cholesterol-modified 567–25/27 was injected intradermally once every 72 h to further investigate the effect of inhibition of FGF5 on the hair follicle cycle in mouse skin.

Effects of Chol-FGF5-siRNA on FGF5 Expression and Hair Follicle Cycle Status in Mouse Skin

Figure 2A shows the timeline for the depilation of mice skin, administration of siRNA and collection of skin samples for further analysis. According to the qPCR result, the level of FGF5 mRNA in the skin tissue of mice injected with the cholesterol-modified FGF5 siRNA was reduced by 59.32 ± 4.37%, 91.08 ± 2.13%, and 55.14 ± 0.48% on days 15, 19, and 23 respectively, compared with mice intradermally injected with the cholesterol-modified negative control siRNA. Consistently, the level of FGF5 protein in the skin injected with the FGF5 siRNA was also significantly reduced on days 15, 19 and 23 compared the negative control siRNA (**Figure 2C**). Immunohistochemical analysis of the skin tissue further confirmed that injection with FGF5 siRNA effectively inhibited the expression of FGF5 in the skin (**Figure 2D**). Histochemical

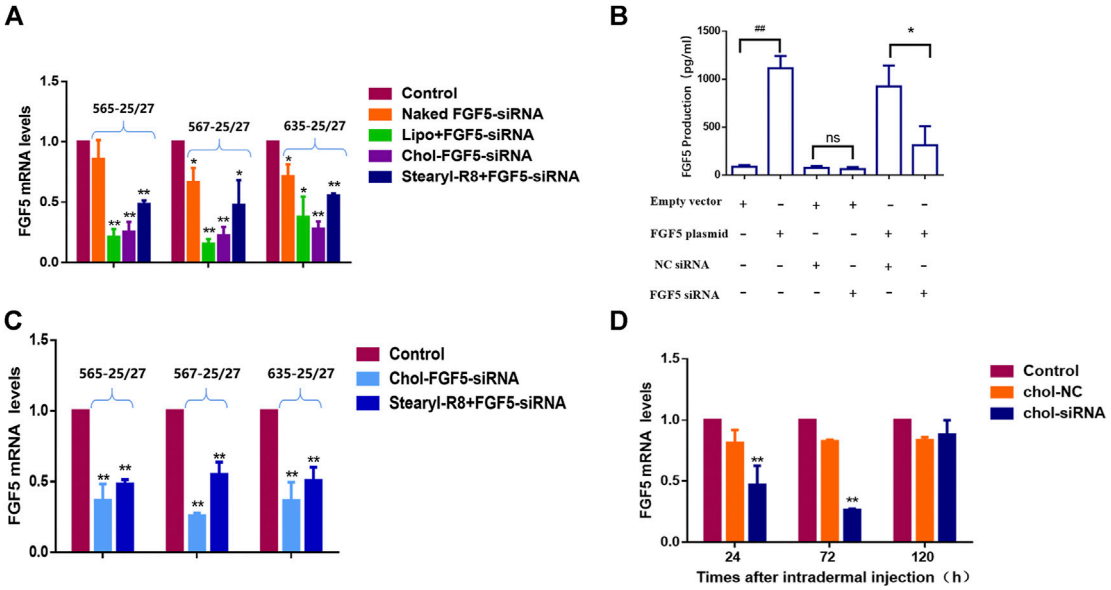

FIGURE 1 | Effects of different FGF5-targeting siRNA delivery methods on the expression of FGF5 **(A)** Changes in FGF5 mRNA level in NIH-3T3 cells overexpressing the FGF5 gene that were transfected with different preparations of FGF5-targeting siRNA as determined by qPCR. NIH-3T3 cells were incubated without (control) or with naked FGF5 siRNA, lipo + FGF5 siRNA, chol-FGF5-siRNA or Stearyl-R8+FGF5-siRNA for 24 h and the levels of FGF5 mRNA in these cells were measured by qPCR. Data are mean ± SD from three experiments. $^{*}p < 0.05$, $^{**}p < 0.01$ vs. control **(B)** Effect of FGF5 siRNA on the expression of FGF5 in NIH-3T3 cells. NIH-3T3 cells were transfected with an empty vector or vector containing the FGF5 gene and the level of FGF5 secreted by the cells was then measured by ELISA following transfection with the cholesterol-modified negative control siRNA (NC siRNA) or cholesterol-modified FGF5 siRNA. Data are mean ± SD from three experiments. $^{\#\#}p < 0.05$, $^{**}p < 0.01$ **(C)** Effect of FGF5 siRNA on FGF5 mRNA level in mouse skin. The skin of the animal was either not treated with siRNA (control) or treated with Chol-FGF5-siRNA or the Stearyl-R8 bound FGF5-siRNA by intradermal injections, and the level of FGF5 mRNA in the skin was measured by qPCR after 24 h. Data are mean ± SD ($n = 3$). $^{**}p < 0.01$ vs. control **(D)** Changes in FGF5 mRNA level in mouse skin over time following the administration of FGF5 siRNA. Chol-FGF5-siRNA or Chol-NC-siRNA was administered to the skin of mice by intradermal injection, and the mRNA level of FGF5 in the skin was measured after 24, 72, 120 h, respectively, using qPCR. Data are mean ± SD ($n = 3$). $^{**}p < 0.01$ vs. control.

staining of the hair follicles in both groups revealed thick hair bulbs located at the dermal-subcutaneous junction on days 15, 17 and 19, indicating that the hair follicles were in the anagen phase, with the presence of vigorous hair growth. From day 21 onwards, the hair follicles of the negative control group started to diminish in size while the hair bulbs at the base of the follicles shrank and migrated upwards, indicating that these hair bulbs were undergoing the anagen-to-catagen transition. By day 23, the hair follicles were in the catagen phase. However, in the FGF5 siRNA group, the hair follicles began to exhibit signs of the anagen-to-catagen transition (i.e., shrinkage and upward migration) only from day 23 onwards (**Figure 2E**). The result indicated that intradermal injection of the cholesterol-modified FGF5 siRNA (567–25/27) into mouse skin could effectively inhibit the expression of FGF5, prolonging the anagen phase of hair follicles by two days, and delaying the entry of hair follicles into the catagen phase.

Effects of Intradermal Injection of a Cholesterol-Modified FGF18-Targeted siRNA in Mouse Skin Tissue

The effect of FGF18 siRNA on the expression of FGF18 was determined essentially following the same approach as that of FGF5. NIH-3T3 cells were either transfected with the empty vector or FGF18 containing plasmid without or with subsequent transfection with the cholesterol-modified negative control siRNA or FGF18 siRNA, and the level of FGF18 protein was then measured by western blot. Again, cells that transfected with the FGF18 containing plasmid showed significantly higher level of FGF18 protein than those transfected with the empty vector, confirming the overexpression of FGF18 in these cells (**Figure 3A**). Following the transfection with the negative control siRNA or FGF18 siRNA, the cells that did not overexpress FGF18 showed not significant change in FGF18 protein level, but the cells that overexpressed FGF18 displayed a significant decrease in FGF18 protein. This result confirmed that FGF18 siRNA could specifically interfere with the expression of FGF18 in the cells. **Figure 3B** shows the timeline for the depilation of mice skin, administration of FGF18 siRNA and collection of skin samples for further analysis to assess the impact on the hair follicles. The level of FGF18 mRNA in the skin tissue samples of mice given the FGF18 siRNA was significantly lower than in the mice given the negative control siRNA (**Figure 3C**). At the same time, western blot also revealed a significant decrease in the level of FGF18 protein in the skin injected with FGF18 siRNA compared with that in the skin injected with the negative control siRNA (**Figure 3D**). On day 9, the hair follicles in the group injected with the FGF18 siRNA exhibited hair growth and plump papillae that were located at the dermal-subcutaneous

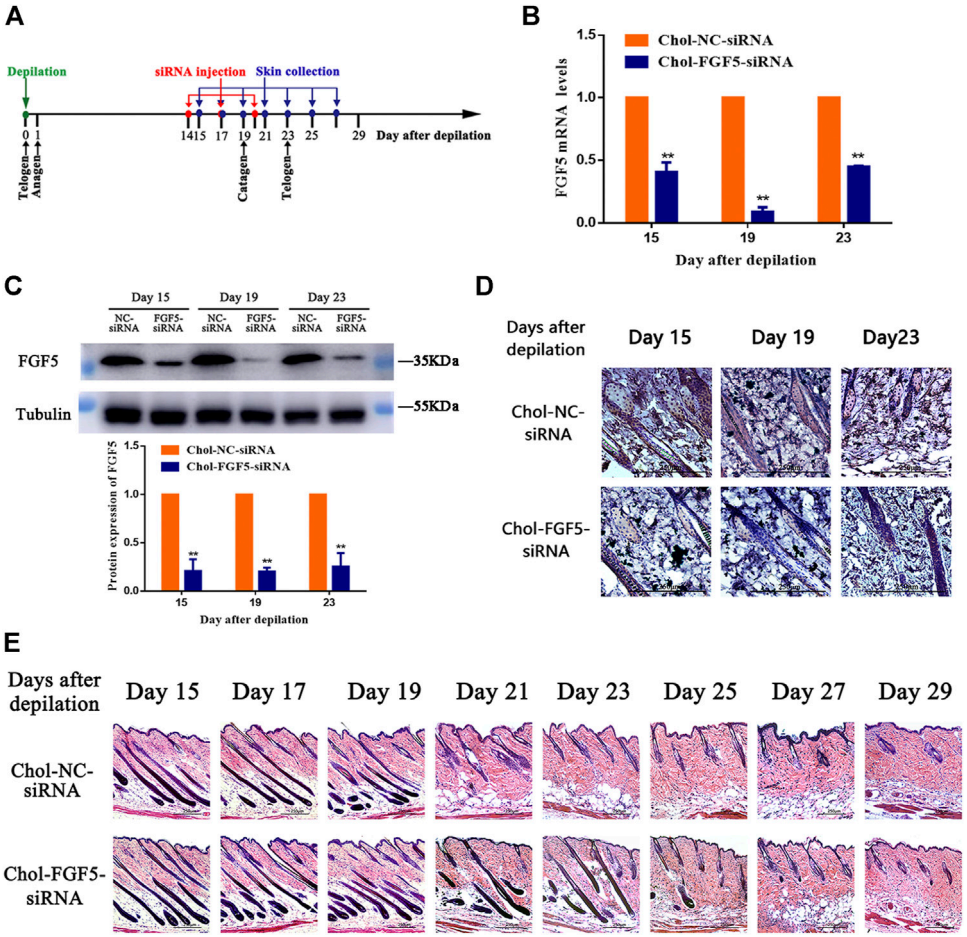

FIGURE 2 | Effects of Chol-FGF5-siRNA on the expression of FGF5 and hair follicle cycle in mouse skin **(A)** Diagram depicting the timeline in the establishment of the model used for the administration of Chol-siRNA and collection of skin samples. **(B)** Changes in FGF5 mRNA expression in mouse skin as determined by qPCR. Chol-FGF5-siRNA or Chol-NC-siRNA was delivered to the mouse skin by intradermal injection 14 days after depilation, and the mRNA level of FGF5 in the skin was measured by qPCR at the indicated times **(C)** Changes in FGF5 protein expression in mouse skin as determined by western blot. Chol-FGF5-siRNA or Chol-NC-siRNA was delivered to the mouse skin by intradermal injection 14 days after depilation, and the expression of FGF5 protein in the skin was measured by western blot at the indicated times. The plot below the blot shows the quantitation of the protein in the blot as determined by gray analysis. **(D)** Immunohistochemical staining of the skin tissue **(E)** HE staining of skin tissue showing the different phases of the hair follicle cycle. All graphical data are mean ± SD (n = 3). $^{**}p < 0.01$ vs. Chol-NC-siRNA.

junction, indicating that the hair follicles were in the anagen phase. Similar growth was only achieved on day 12 in the hair follicles of the group injected with the negative control siRNA (**Figure 3E**), demonstrating FGF18 siRNA could result in earlier transition of the telogen-to-anagen phase for the hair follicles. On day 9, photographs taken through hair follicle detector and ordinary digital camera show photographs and a hair follicle detector showed the presence of black spots in FGF18 siRNA-administered zone. Obvious hair growth occurred by day 12 and thick hair appeared on day 15. In contrast, the zone of the skin that was injected with the negative control siRNA zone remained pink on day 9 and did not exhibit obvious hair growth on day 12. Hair growth finally occurred on day 15, but the regrown hair was relatively sparse (**Figures 3F**,G). Taken together, the results showed that following the intradermal injection of a cholesterol-modified FGF18 siRNA, there was an effective reduction in FGF18 gene expression in the skin tissue, the telogen-to-anagen transition was shorten by 3 days, with was the stimulation of hair growth.

Effects of siRNA Application of a Cholesterol-Modified FGF18-Targeted siRNA Cream in Mouse Skin Tissue

Figure 4A shows the timeline for the depilation of mice skin, the topical application of FGF18 siRNA and collection of skin samples for further analysis to assess the impact on the hair follicles. Topical application with a cholesterol-modified FGF18 siRNA cream resulted in significantly lower level of FGF18 mRNA compared with the application of a cholesterol-modified negative control siRNA cream (**Figure 4B**). Similarly, western blot also revealed a significant decrease in the level of FGF18 protein in skin that was applied with the FGF18 siRNA cream. (**Figure 4C**). Immunohistochemical analysis of the skin

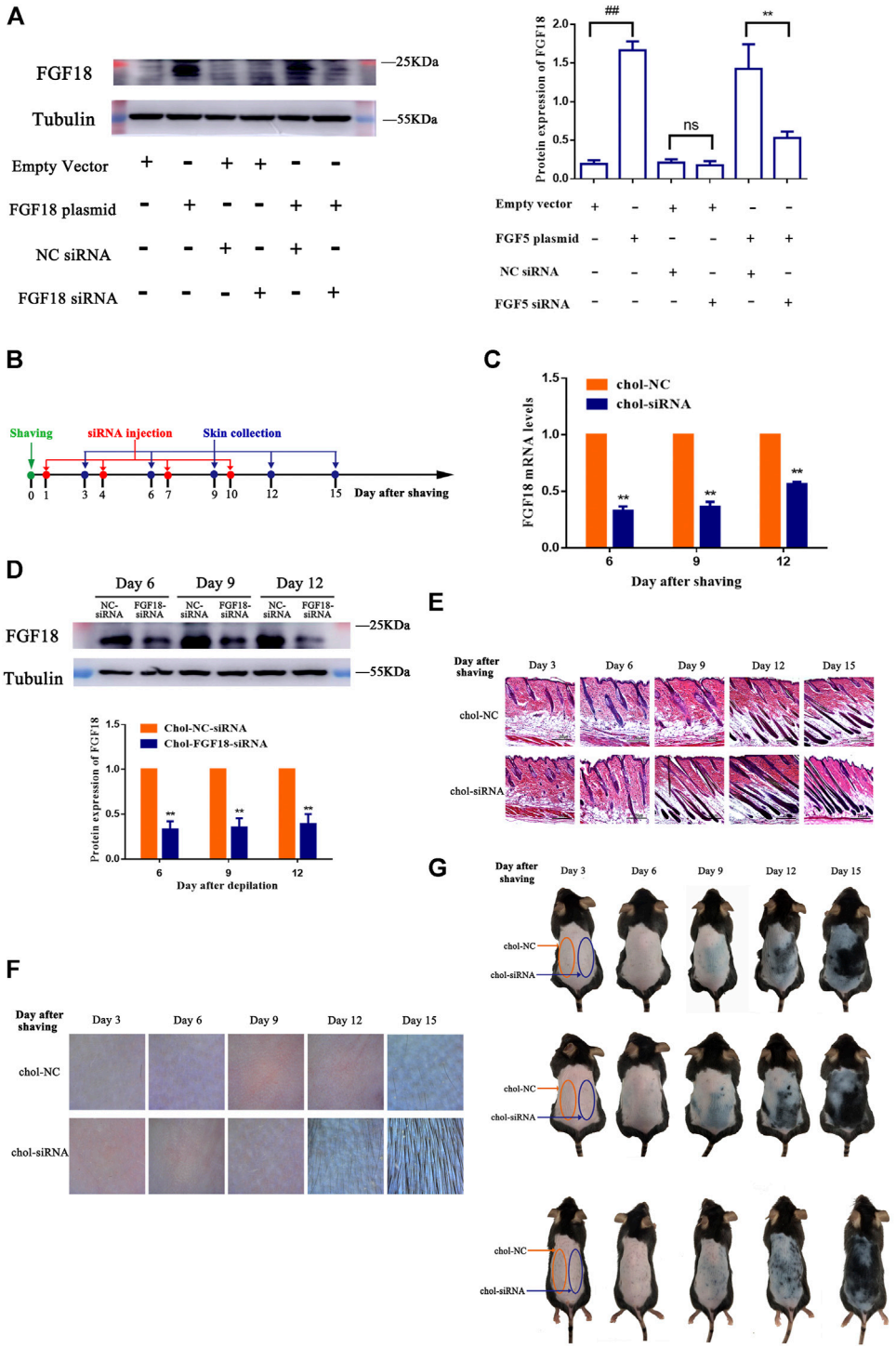

FIGURE 3 | Effect of FGF8 siRNA on the expression of FGF8 in mouse skin **(A)** Effect of FGF18 siRNA on the expression of FGF18 in NIH-3T3 cells. NIH-3T3 cells were transfected with an empty vector or vector containing the FGF18 gene and the level of FGF18 secreted by the cells was then measured by western blot following transfection with the cholesterol-modified negative control siRNA (NC siRNA) or cholesterol-modified FGF18 siRNA. The plot shows the corresponding western blot result. Data are mean ± SD ($n = 3$). $^{**}p < 0.01$, $^{\#\#}p < 0.01$ **(B)** Diagram depicting the timeline in the establishment of the model used for the administration of Chol-FGF18-siRNA and collection of skin samples. Chol-FGF18-siRNA or Chol-NC-siRNA was delivered to the mouse skin by intradermal injection one day after depilation, and the mRNA level of FGF18 in the skin tissue was measured by PCR **(C)** whereas the protein level of FGF18 was measured by western blot **(D)** at the indicated times. The plot below the blot in **(D)** shows the quantitation of the protein bands in the blot as determined by grayscale. Data are mean ± SD ($n = 3$). $^{**}p < 0.01$ vs. Chol-NC siRNA **(E)** HE staining of skin tissue showing the different phases of the hair follicle cycle. **(F)** Digital images showing the extent of hair growth on the skin as detected by a hair follicle detector at 200× magnification following injection of siRNA. **(G)** Digital images showing the back of the mice after injection with FGF18-targeted siRNA and NC-siRNA following depilation.

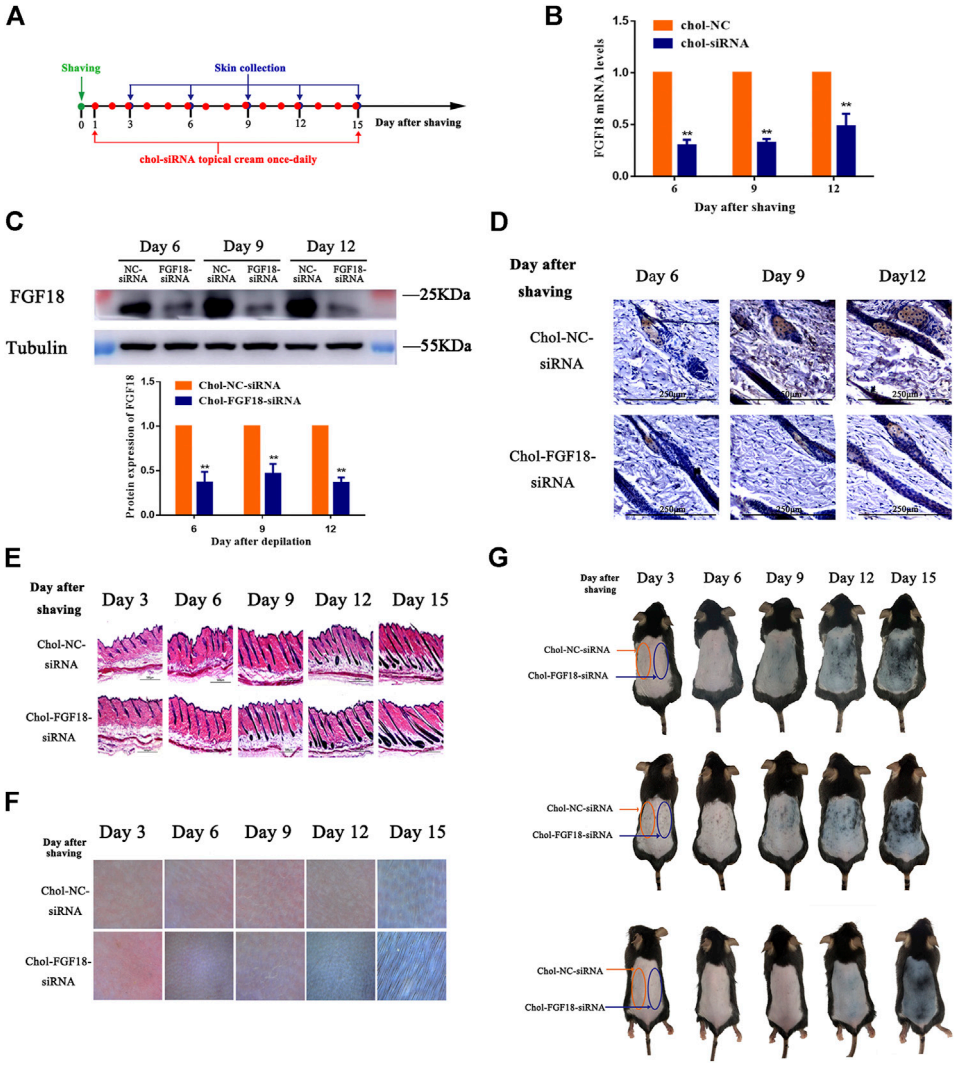

FIGURE 4 | Effects of topical application of FGF18-targeted siRNA cream on hair growth on mouse skin following depilation **(A)** Diagram depicting the timeline in the establishment of the model used for the topical application of Chol-FGF18-siRNA containing cream and collection of skin samples. A cream containing Chol-FGF18-siRNA or Chol-NC-siRNA was applied onto the skin one day after depilation, and changes in the mRNA level of FGF18 in the skin tissue were measured by qPCR **(B)** whereas changes in the protein level of FGF18 were measured by western blot **(C)** at the indicated times. The plot below the blot in **(C)** shows the quantitation of the protein bands in the blot as determined by the gray scale. Data are mean ± SD (n = 3). $^{**}p < 0.01$ vs. Chol-NC siRNA **(D)** Immunohistochemical staining of the skin tissue. **(E)** HE staining of skin tissue showing the different phases of the hair follicle cycle **(F)** Representative images showing the extent of hair growth on the skin as detected by a hair follicle detector at 200× magnification. **(G)** Representative images showing the back of the mice after depilation and administration of FGF18-targeted siRNA and NC-siRNA.

sample confirmed that topical application of FGF18 siRNA could effectively inhibit the expression of FGF18 in the skin, resulting in significantly lower level of FGF5 on days 6, 9 and 12 compared with the application of the negative control siRNA (**Figure 4D**). On day 9, the hair follicles of the skin applied with the FGF18 siRNA cream exhibited hair growth and plump papillae that were located at the dermal-subcutaneous junction, indicating that the hair follicles had entered the anagen phase. As for the skin treated with the negative control siRNA, similar levels of hair growth were only achieved on day 12 (**Figure 4E**), demonstrating that the telogen-to-anagen transition occurred significantly earlier when cholesterol-modified siRNA was topically applied onto the skin. Digital images taken of the skin zone where FGF18 siRNA was applied revealed the presence of black spots on day 9, followed by obvious hair growth on day 12 and patches of thick hairs by day 15. In contrast, the zone applied with the negative control siRNA remained pink on day 9 and exhibited little hair growth on day 12. Significant hair growth only appeared on day 15 (**Figures 4F**,G). These results showed that the topical application of a cholesterol-modified FGF18 siRNA-containing cream could produce effects comparable to those of an intradermal injection. FGF18 gene expression in skin tissue was effectively suppressed, and as a result, the time taken to reach the telogen-to-anagen transition was shortened by 3 days, effectively promoting hair growth.

DISCUSSION

Hair follicle cycle abnormalities constitute an important pathological feature and a key pathogenic mechanism of alopecia. The key to preventing alopecia is the prevention of the progressive shortening and premature termination of the anagen phase of the hair follicles, and the key to hair growth is the triggering of entry into the anagen phase. Presently, there is abundant research evidence showing that FGF5 is the most crucial regulatory factor that promotes the anagen-to-catagen transition of the hair follicles. As abnormally thick and long hair has been observed in FGF5-deficient animals, FGF5 has become the main target of research seeking to improve the length and quality of the hair coat in animals. Besides prolonging the anagen phase of the hair follicles to promote continuous hair growth, the mobilization of hair follicles in the telogen phase toward the anagen phase is also a key aspect of alopecia treatment. It is worth noting that FGF18 is a key regulatory factor in the maintenance of the telogen phase of hair follicles. Therefore, targeting the regulation of FGF5 and FGF18 could be a potential strategy for preventing hair loss and promoting hair growth.

Finasteride and minoxidil have been approved to use in clinic to promote the hair growth. Finasteride is a dihydrotestosteron-suppressing 5 α-reductase inhibitor, it stimulates hair growth by decreasing the serum levels of dihydrotestosterone. Minoxidil is a vasodilator, it slows or stops hair loss and promotes hair growth via increaseing the cutaneous blood flow to the scalp, allowing more oxygen, blood and nutrients to reach the follicle. Different from the mechanism of minoxidil and finasteride, the objective of this study is use cholesterol-modified siRNA to promote hair growth through changing the hair follicle cycle. In the present study, we inhibited the expression of the FGF5 gene in the skin tissue on the back of mice using a cholesterol-modified FGF5-targeting siRNA. This modified siRNA prolonged the anagen phase of the hair follicles and delayed the anagen-to-catagen transition by 2 days, suggesting that hair follicles are extremely sensitive to changes in the expression of FGF5, as the extension of the anagen phase could be effectively achieved by partially inhibiting FGF5 expression, eliminating the need to perform complex gene editing at the DNA level or targeted gene inactivation. This observation is consistent with the findings reported by Burg (Burg et al., 2017), who found that certain traditional Chinese medicine (TCM) extracts such as *Ginkgo biloba* leaf extract, *Eriobotrya japonica* leaf extract, and *Sanguisorba officinalis* extract can specifically inhibit the activity of FGF5 and prevent hair loss and enhance hair growth. On this basis, hair care products containing FGF5-inhibiting *Ginkgo biloba* leaf extract and *Eriobotrya japonica* leaf extract have been developed by these researchers. Besides, a number of monoterpenoids with FGF5 inhibitory activity were found in the aforementioned TCM extracts, and these monoterpenoids can also prevent hair loss and enhance hair growth in a clinical study. However, the siRNA-mediated inhibition of mRNA expression that we observed was quite effective and more specific compared with the TCM extracts. Taken together, the findings from previous research and our experimental observations could suggest that the use of an FGF5-targeted siRNA may be an optimum method for prolonging the anagen phase of hair follicles and promoting hair regrowth.

FGF18-targeted siRNA also effectively suppressed the expression of the FGF18 gene *in vivo*. Consequently, the telogen-to-anagen transition was shortened by 3 days, suggesting that targeting FGF18 could mobilize the hair follicles in the telogen phase to enter the anagen phase. Considerable research evidence has shown that FGF18 is not the only factor responsible for maintaining the telogen phase of the hair follicles, but that it also interacts with bone morphogenetic protein (BMP) and Sost signaling to maintain the quiescent state of the hair follicles (Kimura-Ueki et al., 2012). Interestingly, although FGF18 and BMPs are key regulatory factors for maintaining hair follicles in the telogen phase and are overexpressed during the refractory telogen, both factors seem to exert their effects independently of each other. Our data have also confirmed this conjecture, i.e., precocious anagen initiation could also be induced by merely blocking FGF18 signaling (**Figure 3**). However, the possibility that the simultaneous inhibition of FGF18 and BMPs might result in synergistic or additive effects cannot be ruled out.

The cholesterol-modified siRNAs were found to have better activity and stability compared with the CPP-bound siRNAs in both the *in vivo* and *in vitro* experiments. Therefore, in subsequent animal experiments that investigated the regulation of the hair follicle cycle by siRNAs, we selected the cholesterol-modified siRNA as the sole means for the delivery of the siRNA. Our results indicated that the expression of FGF5 or FGF18 remained inhibited for 24–72 h, with more than 50% inhibition after a single injection of the siRNA. Prolonged inhibition of FGF5 or FGF18 expression mediated by multiple injections of the corresponding cholesterol-modified siRNA appeared to prolong the anagen phase of the hair follicles and hastened the entry of the hair follicles in the telogen phase into the anagen phase.

When siRNA first entered clinical trials, the method of administration was intradermal injection. However, intradermal injection was found to cause intolerable pain and result in low siRNA penetration efficiency (Hickerson et al., 2011). To investigate the convenience and effectiveness of minimally invasive and noninvasive siRNA delivery methods, we compared the *in vivo* pharmacological effects of the cholesterol-modified FGF18 siRNA, administered either by intradermal injection or by topical application on the hair follicle cycle in mice. In the depilated mouse model established using seven-week-old C57BL/6 mice, the hair follicles were in the telogen phase, implying the presence of a high level of FGF18 expression in the skin. Therefore, the application of siRNA was performed on the day after depilation, and the inhibitory effect of the FGF18 siRNA was assessed at the appropriate time points. During the telogen phase of the hair follicles, the melanocytic stem cells in the skin were also in a quiescent state, giving rise to a pink appearance in the skin on the back of the depilated mice (**Figure 4G**). Upon entry into the anagen phase, the melanocytic stem cells were simultaneously activated, which were manifested as the appearance of black patches in the skin of the depilated regions. Therefore, the anagen-inducing effect of the

administered siRNA could be determined from the time elapsed between the injection of siRNA and the appearance of these black patches in the depilated skin as well as by the observation of hair growth after depilation. In contrast, to prolong the anagen phase via targeting FGF5, it was necessary to inhibit the expression of FGF5 at the late anagen phase. In the depilation mouse model that we used, the hair follicles in the back skin were able to enter the anagen phase within 24 h after depilation. Consequently, drug administration could only be initiated during the late anagen phase, i.e., Day 14 after depilation, and the mice needed to be observed for a certain period after the late anagen phase (around Day 27; a normal anagen phase lasts approximately 21 days) to determine if the anagen phase had been prolonged by the administered drug. However, the hair coat of the animal became extremely thick by the late anagen phase, making it difficult to determine the end of the anagen phase by naked-eye observations or by the aid of dermatoscope. Thus, it was difficult to observe the regulation of the hair follicles following the disruption of FGF5 expression than the disruption of FGF18 expression. Therefore, we only tried the topical cream experiment for FGF18 siRNA.

Considerable evidence has shown that lipophilic liposomes and cream formulations are capable of delivering large molecules to the hair follicles, which promote transdermal delivery in conjunction with sebaceous glands and facilitate the distribution of macromolecules within the dermis (Dokka et al., 2005)-(Colombo et al., 2019). Previous research has reported that the topical application of an emulsified siRNA on the skin surface can lead to the efficient suppression of the target gene in the epidermis, and this can be further improved by the addition of a penetration-enhancing agent. Therefore, we designed a cholesterol-modified siRNA-containing lipophilic cream that can be topically applied to the skin using azone as the penetration-enhancing agent. The inhibition of FGF18 expression exerted by the topical application of the FGF18 siRNA specific cream was comparable with that exerted by the intradermal injection of the same siRNA. Both were able to reduce the time required for the telogen-to-anagen transition by 3 days, suggesting that differences in the formulation of the cream and the relative number and functional integrity of the hair follicles play a key role in the success of this delivery method. Compared with intradermal injections, topical medications possess the key advantages of being noninvasive, less irritating to the skin, and safer to use. The findings from previous studies and those of our experiments jointly demonstrate that the topical application of a cholesterol-modified siRNA-containing cream could potentially be used as a long-term, convenient, and economical method of siRNA administration for regulating target genes in the skin that associated with skin conditions such as alopecia. As the present study is a proof-of-concept study, further research is required to validate the effects of the cholesterol-modified siRNA-containing lipophilic cream in humans, especially in alopecia patients.

CONCLUSION

Cholesterol modification of siRNAs targeting FGF5 or FGF18 could facilitate their efficient entry into skin cells and subsequent inhibition of FGF5 or FGF18 expression. Intradermal injections of a cholesterol-modified FGF5 siRNA effectively prolonged the anagen phase of the hair follicles, while intradermal injections of a cholesterol-modified FGF18 siRNA or direct topical application of a cream containing the cholesterol-modified FGF18 siRNA to the skin was found to effectively inhibit the expression of FGF18, thereby promoting the telogen-to-anagen transition by hair follicles. Thus, the prevention of hair loss and promotion of hair regrowth could be achieved through the injection of cholesterol-modified siRNA or topical application of a cholesterol-modified siRNA-containing cream that would inhibit the expression of FGF5 or FGF18 expression. Both types of siRNA formulations could, therefore, be used in the development of novel treatments for alopecia as well as for production of hair growth products.

DATA AVAILABILITY STATEMENT

The raw data supporting the conclusions of this article will be made available by the authors, without undue reservation, to any qualified researcher

ETHICS STATEMENT

The animal study was reviewed and approved by Animal Care and Use Committee of Wenzhou Medical University.

AUTHOR CONTRIBUTIONS

NX and SG conceived and designed the experiments. JZ, HL and LW performed the experiments. KG and RJ analyzed the data. YC, XL and ZH prepared the manuscript. SG and NX revised the manuscript.

FUNDING

The work was supported by Scientific and Technological Plan Project of Wenzhou (N20180002).

ACKNOWLEDGMENTS

We thank Alan K. Chang (Wenzhou University) for valuable discussion and critical comments.

REFERENCES

Beloor, J., Zeller, S., Choi, C. S., Lee, S.-K., and Kumar, P. (2015). Cationic Cell-Penetrating Peptides as Vehicles for siRNA Delivery. *Ther. Deliv.* 6 (4), 491–507. doi:10.4155/tde.15.2

Ben David-Naim, M., Grad, E., Aizik, G., Nordling-David, M. M., Moshel, O., Granot, Z., et al. (2017). Polymeric Nanoparticles of siRNA Prepared by a Double-Emulsion Solvent-Diffusion Technique: Physicochemical Properties, Toxicity, Biodistribution and Efficacy in a Mammary Carcinoma Mice Model. *Biomaterials* 145, 154–167. doi:10.1016/j.biomaterials.2017.08.036

Blanpain, C., Lowry, W. E., Geoghegan, A., Polak, L., and Fuchs, E. (2004). Self-renewal, Multipotency, and the Existence of Two Cell Populations within an Epithelial Stem Cell Niche. *Cell* 118 (5), 635–648. doi:10.1016/j.cell.2004.08.012

Burg, D., Yamamoto, M., Namekata, M., Haklani, J., Koike, K., and Halasz, M. (2017). Promotion of Anagen, Increased Hair Density and Reduction of Hair Fall in a Clinical Setting Following Identification of FGF5-Inhibiting Compounds via a Novel 2-stage Process. *Clin. Cosmet. Investig. Dermatol.* 10, 71–85. doi:10.2147/ccid.s123401

Chen, M., Zakrewsky, M., Gupta, V., Anselmo, A. C., Slee, D. H., Muraski, J. A., et al. (2014). Topical Delivery of siRNA into Skin Using SPACE-Peptide Carriers. *J. Controlled Release* 179, 33–41. doi:10.1016/j.jconrel.2014.01.006

Chen, Z., Wang, Z., Xu, S., Zhou, K., and Yang, G. (2013). Characterization of Hairless (Hr) and FGF5 Genes Provides Insights into the Molecular Basis of Hair Loss in Cetaceans. *BMC Evol. Biol.* 13, 34. doi:10.1186/1471-2148-13-34

Chong, R. H. E., Gonzalez-Gonzalez, E., Lara, M. F., Speaker, T. J., Contag, C. H., Kaspar, R. L., et al. (2013). Gene Silencing Following siRNA Delivery to Skin via Coated Steel Microneedles: *In Vitro* and *In Vivo* Proof-Of-Concept. *J. Controlled Release* 166 (3), 211–219. doi:10.1016/j.jconrel.2012.12.030

Colombo, S., Harmankaya, N., Water, J. J., and Bohr, A. (2019). Exploring the Potential for Rosacea Therapeutics of siRNA Dispersion in Topical Emulsions. *Exp. Dermatol.* 28 (3), 261–269. doi:10.1111/exd.13881

Dokka, S., Cooper, S. R., Kelly, S., Hardee, G. E., and Karras, J. G. (2005). Dermal Delivery of Topically Applied Oligonucleotides via Follicular Transport in Mouse Skin. *J. Invest. Dermatol.* 124 (5), 971–975. doi:10.1111/j.0022-202X.2005.23672.x

Falato, L., Gestin, M., and Langel., Ü. (2021). Cell-Penetrating Peptides Delivering siRNAs: An Overview. *Methods Mol. Biol.* 2282, 329–352. doi:10.1007/978-1-0716-1298-9_18

He, X., Chao, Y., Zhou, G., and Chen, Y. (2016). Fibroblast Growth Factor 5-short (FGF5s) Inhibits the Activity of FGF5 in Primary and Secondary Hair Follicle Dermal Papilla Cells of cashmere Goats. *Gene* 575 (2 Pt 2), 393–398. doi:10.1016/j.gene.2015.09.034

Hickerson, R. P., Flores, M. A., Leake, D., Lara, M. F., Contag, C. H., Leachman, S. A., et al. (2011). Use of Self-Delivery siRNAs to Inhibit Gene Expression in an Organotypic Pachyonychia Congenita Model. *J. Invest. Dermatol.* 131 (5), 1037–1044. doi:10.1038/jid.2010.426

Higgins, C. A., Petukhova, L., Harel, S., Ho, Y. Y., Drill, E., Shapiro, L., et al. (2014). FGF5 Is a Crucial Regulator of Hair Length in Humans. *Proc. Natl. Acad. Sci.* 111 (29), 10648–10653. doi:10.1073/pnas.1402862111

Ito, C., Saitoh, Y., Fujita, Y., Yamazaki, Y., Imamura, T., Oka, S., et al. (2003). Decapeptide with Fibroblast Growth Factor (FGF)-5 Partial Sequence Inhibits Hair Growth Suppressing Activity of FGF-5. *J. Cel. Physiol.* 197 (2), 272–283. doi:10.1002/jcp.10369

Jin, M., Zhang, J.-y., Chu, M.-x., Piao, J., Piao, J.-a., and Zhao, F.-q. (2018). Cashmere Growth Control in Liaoning cashmere Goat by Ovarian Carcinoma Immunoreactive Antigen-like Protein 2 and Decorin Genes. *Asian-australas J. Anim. Sci.* 31 (5), 650–657. doi:10.5713/ajas.17.0517

Kawano, M., Komi-Kuramochi, A., Asada, M., Suzuki, M., Oki, J., Jiang, J., et al. (2005). Comprehensive Analysis of FGF and FGFR Expression in Skin: FGF18 Is Highly Expressed in Hair Follicles and Capable of Inducing Anagen from Telogen Stage Hair Follicles. *J. Invest. Dermatol.* 124 (5), 877–885. doi:10.1111/j.0022-202X.2005.23693.x

Kehler, J. S., David, V. A., Schäffer, A. A., Bajema, K., Eizirik, E., Ryugo, D. K., et al. (2007). Four Independent Mutations in the Feline Fibroblast Growth Factor 5 Gene Determine the Long-Haired Phenotype in Domestic Cats. *J. Hered.* 98 (6), 555–566. doi:10.1093/jhered/esm072

Kimura-Ueki, M., Oda, Y., Oki, J., Komi-Kuramochi, A., Honda, E., Asada, M., et al. (2012). Hair Cycle Resting Phase Is Regulated by Cyclic Epithelial FGF18 Signaling. *J. Invest. Dermatol.* 132 (5), 1338–1345. doi:10.1038/jid.2011.490

Nakase, I., Tanaka, G., and Futaki, S. (2013). Cell-penetrating Peptides (CPPs) as a Vector for the Delivery of siRNAs into Cells. *Mol. Biosyst.* 9 (5), 855–861. doi:10.1039/c2mb25467k

Sajid, M. I., Moazzam, M., Kato, S., Yeseom Cho, K., and Tiwari, R. K. (2020). Overcoming Barriers for siRNA Therapeutics: From Bench to Bedside. *Pharmaceuticals* 13 (10), 294. doi:10.3390/ph13100294

Saw, P. E., and Song, E.-W. (2020). siRNA Therapeutics: a Clinical Reality. *Sci. China Life Sci.* 63 (4), 485–500. doi:10.1007/s11427-018-9438-y

Soutschek, J., Akinc, A., Bramlage, B., Charisse, K., Constien, R., Donoghue, M., et al. (2004). Therapeutic Silencing of an Endogenous Gene by Systemic Administration of Modified siRNAs. *Nature* 432 (7014), 173–178. doi:10.1038/nature03121

Steven, A. C., and Steinert, P. M. (1994). Protein Composition of Cornified Cell Envelopes of Epidermal Keratinocytes. *J. Cel. Sci.* 107 (Pt 2), 693–700. doi:10.1242/jcs.107.2.693

Uchida, T., Kanazawa, T., Kawai, M., Takashima, Y., and Okada, H. (2011). Therapeutic Effects on Atopic Dermatitis by Anti-RelA Short Interfering RNA Combined with Functional Peptides Tat and AT1002. *J. Pharmacol. Exp. Ther.* 338 (2), 443–450. doi:10.1124/jpet.111.180042

Wolfrum, C., Shi, S., Jayaprakash, K. N., Jayaraman, M., Wang, G., Pandey, R. K., et al. (2007). Mechanisms and Optimization of *In Vivo* Delivery of Lipophilic siRNAs. *Nat. Biotechnol.* 25 (10), 1149–1157. doi:10.1038/nbt1339

Yu, F., Liu, Z., Jiao, S., Zhang, X., Bai, C., Zhang, J., et al. (2018). A Nonsense Mutation in the FGF5 Gene Is Associated with the Long-Haired Phenotype in Domestic guinea Pigs (*Cavia porcellus*). *Anim. Genet.* 49 (3), 269. doi:10.1111/age.12656

Conflict of Interest: The authors declare that the research was conducted in the absence of any commercial or financial relationships that could be construed as a potential conflict of interest.

frontiers in Pharmacology

REVIEW
published: 20 July 2021
doi: 10.3389/fphar.2021.680209

The Regenerative Potential of bFGF in Dental Pulp Repair and Regeneration

*Keyue Liu, Sijing Yu, Ling Ye and Bo Gao**

State Key Laboratory of Oral Diseases, National Clinical Research Center for Oral Diseases, West China Hospital of Stomatology, Sichuan University, Chengdu, China

Regenerative endodontic therapy intends to induce the host's natural wound-healing process, which can restore the vitality, immunity, and sensitivity of the inflammatory or necrotic pulp tissue destroyed by infection or trauma. Myriads of growth factors are critical in the processes of pulp repair and regeneration. Among the key regulatory factors are the fibroblast growth factors, which have turned out to be the master regulators of both organogenesis and tissue homeostasis. Fibroblast growth factors, a family composed of 22 polypeptides, have been used in tissue repair and regeneration settings, in conditions as diverse as burns, ulcers, bone-related diseases, and spinal cord injuries. Meanwhile, in dentistry, the basic fibroblast growth factor is the most frequently investigated. Thereby, the aim of this review is 2-fold: 1) foremost, to explore the underlying mechanisms of the bFGF in dental pulp repair and regeneration and 2) in addition, to shed light on the potential therapeutic strategies of the bFGF in dental pulp–related clinical applications.

Keywords: fibroblast growth factors, basic fibroblast growth factor, regenerative endodontic therapy, regenerative endodontics, pulp repair, pulp regeneration

OPEN ACCESS

Edited by:
Q. Adam Ye,
Harvard Medical School,
United States

Reviewed by:
Xiaogang Xu,
Zhejiang University, China
Wenguo Cui,
Shanghai Jiao Tong University, China

****Correspondence:***
Bo Gao
gaob@scu.edu.cn

Specialty section:
This article was submitted to Integrative and Regenerative Pharmacology, a section of the journal Frontiers in Pharmacology

Received: *13 March 2021*
Accepted: *22 June 2021*
Published: *20 July 2021*

Citation:
Liu K, Yu S, Ye L and Gao B (2021) The Regenerative Potential of bFGF in Dental Pulp Repair and Regeneration. Front. Pharmacol. 12:680209. doi: 10.3389/fphar.2021.680209

INTRODUCTION

With the advancement of our knowledge in pulp biology, the concept of treatment of endodontic diseases changes accordingly. "Regenerative endodontics" has been defined as "biologically based procedure designed to replace damaged structures, including dentin and root structures, as well as cells of the pulp-dentin complex" (Murray et al., 2007). The new era of regenerative endodontic therapy intends to induce the host's natural wound-healing process, which can restore the vitality, immunity, and sensitivity of the inflammatory or necrotic pulp tissue destroyed by infection or trauma (Yang et al., 2016).

Both pulp repair and regeneration processes are orchestrated by a highly coordinated interplay of different growth factors and cytokines (Orti et al., 2018). These myriads of growth factors create a favorable microenvironment conducive to tissue repair and/or regeneration taking place and act as signaling molecules that regulate cell behaviors, including migration, proliferation, and differentiation (Kim et al., 2018). Among the key regulatory factors are the fibroblast growth factors (FGFs), which have turned out to be the master regulators of both organogenesis and tissue homeostasis (Maddaluno et al., 2017). FGFs are a family of growth factors, consisting of 22 members that share 13–71% sequence homology in mammals (Ornitz and Itoh, 2001). Major attention has been paid to the use of FGFs in tissue repair and regeneration settings, in conditions as diverse as burns, ulcers, bone-related diseases, and spinal cord injuries, just to name a few (EL Agha et al., 2016; Nunes et al., 2016; Zhou et al., 2018; Wang J. et al., 2019). Meanwhile, in dentistry, the basic fibroblast growth factor (bFGF), also termed FGF-2, is the most frequently investigated (Vaseenon et al., 2020). As a member of the FGF family, the bFGF has been implicated as a signaling molecule that contributes to the regulation of virtually all aspects of tooth

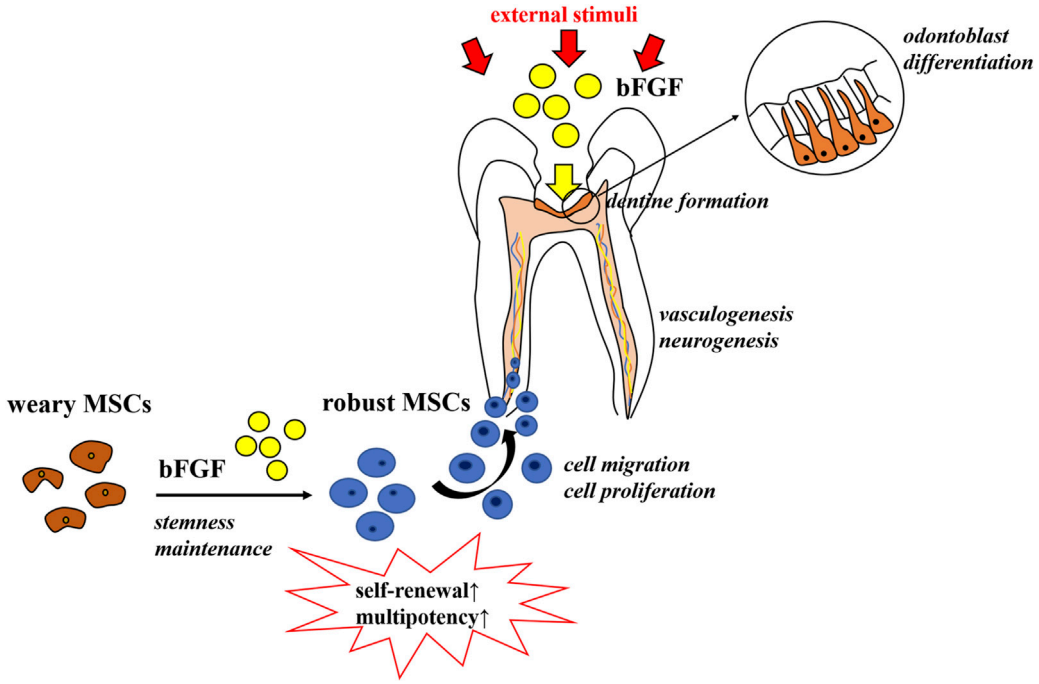

FIGURE 1 | Role of the bFGF in pulp repair and regeneration. The bFGF contributes to the regulation of virtually all aspects of tooth development, repair, and regeneration, including mesenchymal stem cells' stemness maintenance, migration, and proliferation, as well as dentine formation, vasculogenesis, and neurogenesis.

development, repair, and regeneration (Li et al., 2014; Vaseenon et al., 2020), including mesenchymal stem cell migration, proliferation, and stemness maintenance, as well as dentine formation, vasculogenesis, and neurogenesis (as shown in **Figure 1**) (Galler et al., 2012; Chang et al., 2017).

To figure out the role of the bFGF in regenerative endodontics, this review aims to give a comprehensive summary of the underlying mechanisms associated with the bFGF in promoting dental pulp repair and regeneration and shed light on the potential therapeutic strategies of the bFGF in dental pulp–related clinical applications.

THE UNDERLYING MECHANISMS OF BASIC FIBROBLAST GROWTH FACTOR IN DENTAL PULP REPAIR AND REGENERATION

According to the mode of action, the bFGF acts through binding to tyrosine kinase FGF receptors 1–4 (FGFR1–4) on the cell membrane (Müller et al., 2012). When the bFGF binds to its receptors, phosphorylation occurs and subsequently triggers a cascade of intracellular signaling pathways, such as the RAS-MAPK, PI3K-AKT, PLCγ, and JAK/STAT signaling pathways, initiating cell migration, proliferation, and differentiation (Müller et al., 2012). These findings lead to the hypothesis that the bFGF may use different intracellular signaling pathways to control specific biological processes in dental pulp repair and regeneration (Nowwarote et al., 2020). In this regard, we try to elucidate the potential roles of the bFGF in the specific biological processes, respectively.

Cell Migration

Before the regeneration occurs, cells must migrate to the sites where they are required to function (Adam and Richard, 1999). The migration process is initiated by more than 50 chemotactic factors which have been identified in mammals (Horuk, 2001). Among those chemotactic factors, the bFGF has been reported to induce the migration of certain types of mesenchymal stem cells (MSCs) which are critical for pulp regeneration, including adult dental pulp stem cells (DPSCs), stem cells from human exfoliated deciduous teeth (SHEDs), stem cells from apical papilla (SCAPs), bone marrow–derived mesenchymal stem cells (BMMSCs), and so on (Peng et al., 2009). Several cytokines were examined to enhance the migratory ability of BMMSCs, while the bFGF in particular was able to initiate the migration of BMMSCs in a dose-dependent manner *via* the Akt/protein kinase B (PKB) pathway (Schmidt et al., 2006). It was reported that low concentrations of the bFGF attracted BMMSCs, whereas higher concentrations resulted in an ambivalent effect (Schmidt et al., 2006). The ability of the bFGF to induce the migration of DPSCs was also verified (Howard et al., 2010), which agreed with the later study that reported that the bFGF significantly recruited more DPSCs seeded on the surface of 3D collagen gel cylinders into the deep (Suzuki et al., 2011). Coincidentally, Fayazi et al. claimed that the number of SCAPs recruited by the G-CSF and bFGF was approximately 2-fold greater than that of other tested factors (Fayazi et al., 2017), and there was no apparent difference between the G-CSF and the bFGF in homing effect (Takeuchi et al., 2015). The periodontal ligament

was also reported as a good source of MSCs (PDLSCs), which have a similar feature to that of BMMSCs and DPSCs, and could also contribute to the regenerative dentistry (Trubiani et al., 2008). In this regard, Zhang et al. verified that the bFGF promoted PDLSC migration and adhesion with more prominent ability than the VEGF (Zhang et al., 2013). Furthermore, the implantation of collagen scaffolds containing the bFGF resulted in abundant cell ingrowth, recellularization, and revascularization in endodontically treated root canals (Kim J. Y. et al., 2010).

Collectively, the bFGF is an efficacious chemotactic factor to facilitate the motility of MSCs and the following tissue remodeling processes, thereby providing a therapeutic basis for the cell homing strategy (Kim J. Y. et al., 2010; Galler et al., 2014).

Cell Proliferation

Generally, stem cell populations of various oral cells would dramatically decrease during the culture period (Min et al., 2011), which greatly limited their applications in tissue regeneration.

The mitogenic ability of the bFGF has attracted much attention. Morito et al. showed that the ratio of dental pulp cells in the S-phase and the ratio of hDPCs expressing STRO-1 were significantly higher when in the presence of the bFGF (Morito et al., 2009). The mitogenic effect of the bFGF on dental pulp cells was also supported recently by adding it in culture medium. Promising results were received in that the bFGF significantly promoted the proliferation of DPSCs through activating the ERK pathway without comprising cell stemness and pluripotency (Luo et al., 2021). With no exceptions, the mitogenic potential of the bFGF on SHEDs was also found (Sukarawan et al., 2014), and further study revealed that the bFGF promoted SHED colony-forming units *via* the FGFR/PI3K pathway (Nowwarote et al., 2020). In the gene level, the bFGF was reported to be in charge of controlling the cell cycle progression by significantly increasing the MKI67 mRNA and Ki67 protein level in SHEDs (Nowwarote et al., 2020) and regulating the cdc2 and cyclin B1 expression in HDPCs and SCAPs in a dose-dependent manner *via* the MEK/ERK pathway (Chang et al., 2017; Chang et al., 2020), leading to a higher G2/M subpopulation and promoting the cell proliferation process (Nowwarote et al., 2020).

Taking those pieces of evidence together, the bFGF has the superiority to promote cell proliferation and control the cell cycle progression *via* stimulating the expression of related genes and proteins, including Ki67, cdc2, and cyclin B1. Therefore, its mitogenic effect can be put into use to amplify the cell number in order to obtain the sufficient amount of stem cells required for endodontic regenerative treatments and can also brighten the future of stem cell banking and tissue engineering (Luo et al., 2021).

Stemness Maintenance

Stemness maintenance has emerged to preserve the two defined features of stem cells, self-renewal and multipotency, which would become limited when these cells are introduced in long-term culture (Kong et al., 2019). Interestingly, the bFGF added in growth medium was proven to be able to support the self-renewal of human embryonic stem cells and maintain them in a multipotent state (Ehman et al., 2006; Diecke et al., 2008). In addition, the bFGF has also been demonstrated to maintain MSC potential in multilineage differentiation. Correspondingly, the bFGF, in low-density cultures, was reported to retain the osteogenic, adipogenic (Tsutsumi et al., 2001), and chondrogenic potential (Solchaga et al., 2005) of BMMSCs through the regulation of the MAPK and Wnt signaling pathways (Solchaga et al., 2005). Although the expression of mesenchymal stem cell markers was generally decreased during culture, treatment with the bFGF could delay their decrements and maintain their expressions in oral stem cells during culture (Lee et al., 2015). Additional studies demonstrated that the bFGF regulated stemness maintenance by increasing the gene expression of pluripotent stem cell markers including NANOG, OCT4, and REX1 on SCAPs, DPSCs, and SHEDs (Wu et al., 2012; Osathanon et al., 2011; Sukarawan et al., 2014). It was further revealed that the bFGF induced REX1 expression *via* the FGFR/Akt pathway with IL-6 as a middle regulator (Nowwarote et al., 2017).

Taken together, these investigations imply the important role of the bFGF in maintaining human stem cells' stemness, which is a critical step toward the clinical application of MSCs in regenerative endodontics.

Dentinogenesis

Once subjected to external injuries, the pulp cells may go through proliferation and differentiation, developing into odontoblast-like cells to elicit reparative dentinogenesis, which is critical for the pulpal wound-healing process (Yamamura, 1985). Dentinogenesis is a complex and multistep process, which is regulated by various growth factors including the bFGF (Cooper et al., 2010). However, the effects of the bFGF on mineralization and odontoblast differentiation remain elusive, while both stimulatory and inhibitory effects of the bFGF on dentinogenesis have been reported. Several studies have shown that the bFGF inhibited dentinogenesis and the expression of dentin sialophosphoprotein (Dspp) and alkaline phosphatase (ALP) (Tsuboi et al., 2003; Takedachi et al., 2009; Kim et al., 2014). On the other hand, other studies have shown that the bFGF stimulated the formation of osteodentin and the expression of Dspp and ALP (Kikuchi et al., 2007; Ishimatsu et al., 2009; Kim Y.-S. et al., 2010). Thus, to gain better insight into the biphasic role of the bFGF in dentinogenesis and cell differentiation in the odontoblast lineage, the underlying mechanisms of these controversial results need to be elaborated upon.

Dental pulp cells at different stages of odontoblast differentiation were identified by using a series of transgenic mice (Sagomonyants and Mina, 2014a). Studies have shown that 2.3-GFP and 3.6-GFP transgenes were activated at early stages of odontoblast differentiation (polarizing odontoblasts), and DMP1-GFP first emerged in functional/secretory odontoblasts. Meanwhile, all three transgenes (2.3-GFP, 3.6-GFP, and DMP1-GFP) were expressed at high levels in fully differentiated/mature odontoblasts (Braut et al., 2003; Balic et al., 2010; Balic and Mina, 2011). In addition, researchers have generated a new kind of transgenic mouse using the bacterial artificial chromosome

(BAC), directing the expression of the DSPP-Cerulean transgene that can be used to identify fully differentiated odontoblasts in the heterogeneous pulp cultures (Sagomonyants and Mina, 2014a). Cells were isolated and first grown for 7 days in medium supporting their proliferation (proliferation phase) and then for an additional 7 days in medium inducing their mineralization (differentiation/mineralization phase) (Sagomonyants and Mina, 2014b). Experiments conducted showed that the effects of the bFGF on odontogenic differentiation of pulp cells were stage-specific and depended on the stage of maturity of cells (Sagomonyants and Mina, 2014a). During the proliferation phase of *in vitro* growth, early and limited exposure to the bFGF increased the expression of the markers of dentinogenesis and the percentage of DMP1-GFP + functional odontoblasts, showing the differentiation of early progenitors into functional odontoblasts. During the mineralization/differentiation phase, additional/continuous exposure to the bFGF decreased the expression of the markers of dentinogenesis and the expression of DMP1-GFP and DSPP-Cerulean transgenes, indicating the shrinkage of the extent of mineralization and the failure of mature odontoblast differentiation. However, immediate withdrawal of bFGF for 7 days rapidly and mostly completed the recovery of mineralization and the expression of various GFP transgenes and dentinogenic markers (Sagomonyants and Mina, 2014a). Collectively, these results suggested a positive role of the bFGF in early differentiation into functional odontoblasts but a negative role in further differentiation into fully differentiated/mature odontoblasts.

Additional experiments were in progress to examine the underlying mechanisms mediating the biphasic effects of the bFGF on odontogenic differentiation. Studies revealed that the effects of the bFGF on odontoblast differentiation were mediated through the activation of FGFR/MEK/Erk1/2 signaling (Sagomonyants et al., 2015; Sagomonyants et al., 2017), and additional research examined that the BMP and Wnt signaling pathways also participated in the process (Sagomonyants and Mina, 2014b). Early and limited bFGF treatment promoting odontogenic differentiation during the proliferation phase was associated with increased levels of the components of the BMP (Bmp2, Dlx5, Msx2, and Osx) and Wnt (Wnt10a and Wisp2) pathways and with a decreased expression of the Wnt signaling inhibitor (Nkd2). Further addition of the bFGF suppressing the terminal odontogenic differentiation during the differentiation/mineralization phase was accompanied by decreased expression of the components of the BMP signaling (Bmp2, Runx2, and Osx) and lower levels of Wnt inhibitors (Nkd2 and Dkk3) but increased expression of the Wnt signaling (Wnt10a). Taken together, these observations suggested that the BMP signaling could act as a positive regulator during odontoblast differentiation, while Wnt signaling stimulated early odontoblast differentiation but inhibited the terminal odontoblast differentiation (Sagomonyants et al., 2017). Furthermore, Vining et al. also revealed the possible mechanism of the early and limited exposure to the bFGF promoting odontogenic differentiation by expanding αSMA-tdTomato$^+$ cells and accelerating their differentiation into odontoblasts (Vining et al., 2018). IFT80 (intraflagellar transport protein 80) may also be involved in the positive differentiation process by maintaining cilia formation and FGFR1 expression and subsequently activating the AKT, Hh, and BMP2 signaling pathways to drive DPSCs differentiating into the odontogenic lineage (Yuan et al., 2019a). Nevertheless, the attenuation of ITGA11, CTGF, and ATF4 levels (Novais et al., 2019) and the downregulation of the Pi/PPi ratio (Nowwarote et al., 2018) in bFGF-treated SHEDs may participate in the negative regulatory mechanisms of the bFGF in odontogenic differentiation.

These observations together show the stage-specific effects of the bFGF on dentinogenesis through dental pulp cells (as shown in **Figure 2**) and provide a better insight into the treatments for vital pulp therapy and dentinal regeneration by priming the dental pulp tissue with the bFGF to achieve the desired mineralization state, which may be able to impede the excessive calcification in the pulp (Qian et al., 2015).

Neurogenesis

Neural regeneration is critical for ideal regenerative endodontic treatment so as to regain the normal sensation of the affected teeth (Kim et al., 2018). The bFGF is an important neurotrophin which possesses superior properties to promote neural stem cell (NSC) migration, proliferation, and self-renewal (Yeoh and de Haan, 2007). Ye et al. further informed that the bFGF could promote the survival and differentiation of NSCs to reduce brain damage and restore sensorimotor function after neonatal hypoxia-ischemia (Ye et al., 2018). The bFGF has also been reported to be able to maintain the survival of neuronal and glial cells, probably by protecting neurons from ROS-induced cell death and antagonizing the neuronal apoptosis induced by glutamate (Liu and Zhu, 1999). Indirectly, bFGF priming could protect cultured DPCs from hydrogen peroxide–induced cell death and increased the number of DPCs surviving so as to provide neurotrophic factors, thereby promoting axonal regeneration and locomotor function recovery (Nagashima et al., 2017).

DPSCs, deriving from the neural crest, retain remarkable characteristics that are similar to those of neural cells and have the potential to undergo neural differentiation to help crushed nerves achieve functional recovery and anatomical repair *in vivo* (Wang et al., 2020). The neurotrophic and neuroprotective merits of DPSCs make it an ideal stem cell source for neural repair and regeneration (Luo et al., 2018b; Wang D. et al., 2019). Accordingly, the implanted DPSCs could promote endogenous neural stem/progenitor cell proliferation, recruitment, and maturation through modulating the local microenvironment *via* secreting multiple factors, especially the bFGF (Huang et al., 2008). On the other hand, numerous protocols have documented that the exogeneous application of the bFGF could facilitate DPSCs differentiating into neurons. Studies discovered that the supplementation of the bFGF increased the neurosphere size and the neurogenic markers of DPSCs (Osathanon et al., 2011; Kang Y.-H. et al., 2019) and simultaneously revealed that the bFGF induced neuronal differentiation of DPSCs through the PLCγ signaling pathway

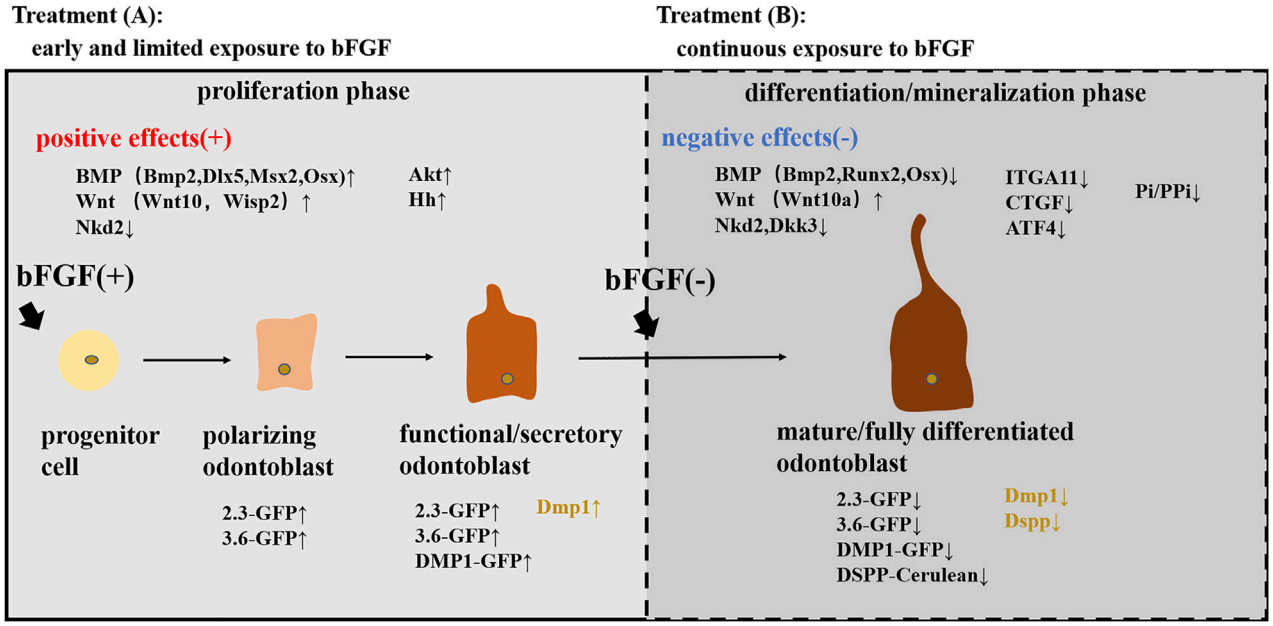

FIGURE 2 | Stage-specific effects of the bFGF on odontoblast differentiation. Treatment **(A)**: early and limited exposure to the bFGF during the proliferation phase stimulated the differentiation into functional/secretory odontoblasts and increased the expression of various GFP transgenes (2.3-GFP, 3.6-GFP, and DMP1-GFP) and dentinogenic markers (Dmp1) by activating the BMP, Wnt, and Akt pathways. Treatment **(B)**: continuous exposure to the bFGF during the differentiation/mineralization phase inhibited the differentiation into mature odontoblasts and decreased the expression of GFP transgenes (2.3-GFP, 3.6-GFP, and DSPP-Cerulean) and dentinogenic markers (Dmp1 and Dspp) by activating the Wnt pathway while suppressing the BMP pathway and downregulating ITGA11, CTGF, and ATF4 levels and the Pi/PPi ratio.

(Osathanon et al., 2011). Meanwhile, Zheng et al. recognised the phospho-ERK (*p*-ERK) activation as a major mediator in such a process (Zheng et al., 2020). In addition, the bFGF and NGF were shown to have a synergistic effect to increase neural differentiation of DPSCs by upregulating the levels of Sirt1 and activating the ERK and Akt signaling pathways (Zhang et al., 2017). Coincidentally, the bFGF and NGF–co-transfected BMMSCs were also inclined to differentiate into neurons with the manipulation of the ERK and Akt signaling pathways (Hu et al., 2016). In the preliminary study, it is noteworthy that when exogenously supplied with the bFGF, the CD81 and nestin double-positive dental pulp cells localized in the apical portion were deemed to be mainly responsible for the neural regeneration (Sasaki et al., 2008).

In summary, the results from the aforementioned studies emphasize the important role of the bFGF in neural differentiation and promise new therapeutic strategies by using the bFGF to treat neurological diseases and repair neuronal damage, such as spinal cord injury (SCI), Parkinson's disease, neonatal hypoxia-ischemia (NHI), and Alzheimer's disease (Barzilay et al., 2008; Zhang et al., 2014; Luo et al., 2018a; Ye et al., 2018). However, achieving the neurite growth in root canals with the treatment of the bFGF needs more experimental reports.

Vasculogenesis/Angiogenesis

Angiogenesis is important for tissue regeneration, especially for the dental pulp, since the nutrition of dental pulp could only be provided from the apical foramen of the tooth. The greatest challenge of tissue engineering the "pulp" is to achieve *in vivo* revascularization from the host blood supply (Wigler et al., 2013). The angiogenesis process refers to the migration, proliferation, and differentiation (tube formation) of vascular endothelial cells and is mediated by various angiogenic factors acting on endothelial cells and pericytes (mural cells) (Chung and Ferrara, 2011).

The bFGF was generally described as a protective factor that protects endothelial cells from the programmed cell death process (Karsan et al., 1997; Takeuchi et al., 2015) and was also recognized as one of the potent angiogenesis inducers that prompt vascular formation by stimulating the migration, proliferation, and differentiation of endothelial cells in a dose- and time-dependent manner (Kanda et al., 1999; Kitamura et al., 2014; Zbinden et al., 2018). The angiogenic effect of the bFGF was evaluated similar to that of the VEGF when at the same dosage (Mullane et al., 2008).

DPSCs were shown to locate adjacent to vascular tubes assuming a pericyte location and have also been demonstrated to display potential pericyte-like topography and function. It was reported that the majority of DPSCs expressed the typical pericyte markers including alpha-smooth muscle actin (α-SMA), NG2, PDGFRβ, CD146, and 3G5 (Nam et al., 2017). The pericyte-like properties of DPSCs were investigated to enhance angiogenesis by stabilizing the preexisting vessel-like structures formed by endothelial cells and increasing their longevity, leading to more mature tube-like structures' formation *in vitro via* the EphrinB2/EphB4 signaling pathway (Dissanayaka et al., 2012;

Janebodin et al., 2013; Gong et al., 2019). Meanwhile, the bFGF treatment was able to augment the expression of NG2 and α-SMA of DPSCs and finally, supported the stabilization of HUVEC tubes for a longer time (Delle et al., 2019). In addition, bFGF priming had a stronger impact on DPSCs than hypoxia and enhanced the proangiogenic effect of DPSCs through the secretion of the HGF (hepatocyte growth factor) and the VEGF (Gorin et al., 2016).

In conclusion, the bFGF is an angiogenic factor targeting endothelial cells directly and is capable of facilitating angiogenesis by enhancing the pericyte-like properties of DPSCs.

Cytokine Production, Matrix Turnover, and Anti-Apoptosis

Beyond that, available studies replenished the bFGF with the abilities of cytokine production, matrix turnover, and anti-apoptosis.

It was stated that the bFGF enhanced dental pulp repair/regeneration by upregulating the expression of several cytokines, including IL-6, IL-8, MCP-1, MIP-1α, and CCL20, *via* the PKC/PI3K-AKT/MAPK signaling pathways. The bFGF-induced cytokines could trigger the innate cellular responses in dental pulp to promote cell differentiation and dentin formation (Kim Y.-S. et al., 2010).

The bFGF may also influence the extracellular matrix turnover through stimulating TIMP-1 expression in HDPCs and SCAPs (Chang et al., 2017; Chang et al., 2020) while inhibiting the expression of type I collagen and downregulating related genes in SHEDs (COL5A1, COL8A2, COL11A1, and COL15A1) and periodontal ligament stem/progenitor cells (COL1A1, COL3A1, ACTA2, and FBN1) (Nowwarote et al., 2020). The influence of the bFGF on collagen genes raised a hypothesis that the bFGF may act as an anti-fibrotic agent in several cell types (Grella et al., 2016). How the bFGF affects pulp repair and regeneration through matrix turnover awaits further investigation.

Besides, the bFGF was reputed to be a survival factor which inhibited cellular senescence and apoptosis in adipose-derived mesenchymal stromal cells (ASCs), probably by diminishing the expression of SA-βgal, p21, and p53 (Nawrocka et al., 2017). A similar anti-apoptosis impact of the bFGF was also underscored when being applied to neural precursor cells (NPCs) (Mellisa and Kristi, 2006), indicating that the bFGF is a potential therapeutic agent in stem cell–based tissue regeneration, while the anti-senescence and anti-apoptosis properties of the bFGF in dental stem cells need more elaboration.

THE POTENTIAL THERAPEUTIC STRATEGIES OF BASIC FIBROBLAST GROWTH FACTOR IN PULP REPAIR AND REGENERATION

The bFGF is certified for safe usage and has already been applied in the treatment of ulcer and burns (Akita et al., 2008). The bFGF has also contributed much to the field of nerve (Matsumine et al., 2016), muscle (Goto et al., 2020), and bone regeneration (Chen et al., 2011) based on its prominent regenerative potential. As mentioned above, the bFGF has combinatorial trophic effects on dental stem cells for pulp repair/regeneration to either induce cell migration, proliferation, and differentiation or regulate matrix turnover, cytokine production, and the apoptosis procedure. Therefore, the bFGF can be confirmed to be a safe and competent candidate for clinical applications in pulp regeneration therapy. To sustain this view, we collect the therapeutic protocols which have been developed to apply the bFGF in pulp repair and regeneration therapy.

The regenerative endodontic treatment (RET) contains two different clinical approaches. The first aims to achieve local pulpal regeneration and dentin bridge formation *via* pulp-capping agent usage to stimulate the healing process and preserve the pulp vitality (referred to as "pulp repair"). Another approach strives to induce the growth of new pulp-like tissue in the entire disinfected root canal space in order to revitalize the teeth (referred to as "pulp regeneration") (Orti et al., 2018).

Pulp Repair

When the dental pulp is exposed to external stimuli such as caries infection or traumatic injuries, the preservation of dental pulp or the dentin-pulp complex and the maintenance of its viability are essential to avoid serious consequences such as tooth extraction (Kitamura et al., 2012). The formation of new dentin in the site of dentin defects is essential to the local regeneration of the dentin-pulp complex (Kitamura et al., 2012).

For the pulp exposures, at the reversible stage, pulpal inflammation is treated using a direct pulp-capping technique. Calcium hydroxide and mineral trioxide aggregate (MTA) are widely used as pulp-capping materials due to their properties of mobilizing extracellular molecules which then initiate specific biological actions and promote dentin bridge formation (Graham et al., 2006; Li et al., 2015; Tomson et al., 2017; Torabinejad et al., 2018). However, the materials above have been criticized for their limited capacity in tissue regeneration (Chakka et al., 2020) and the tunnel defects in the formed dentin bridge (Chen et al., 2017). Moreover, the treatments elicit the formation of a thin layer of necrotic tissue underneath the capping material (de Souza Costa et al., 2008). Therefore, it is clear that in the future, pulp-capping procedures will rely on a more biological approach (Chakka et al., 2020). Promisingly, bFGF-loaded MesoCS nanoparticles have been shown to be capable of upregulating the odontogenic-related protein of hDPCs (Huang et al., 2017). Following studies have correspondingly reported the local applications of the bFGF as a bioactive molecule that received promising results under the pulp exposure condition. Research has succeeded in treating the pulp exposure through combining the bFGF with the HAP nanoparticle–assembled powder (nano-HAP) and applying this compound to the exposed dental pulp of rat molars. Histological and radiological results showed that the application of the nano-HAP/bFGF induced the invasion of dental pulp cells and vessels, indicating the regeneration of pulp tissue, and stimulated the formation of a dentinal bridge containing numerous dentinal tubules (Imura et al., 2019). It was

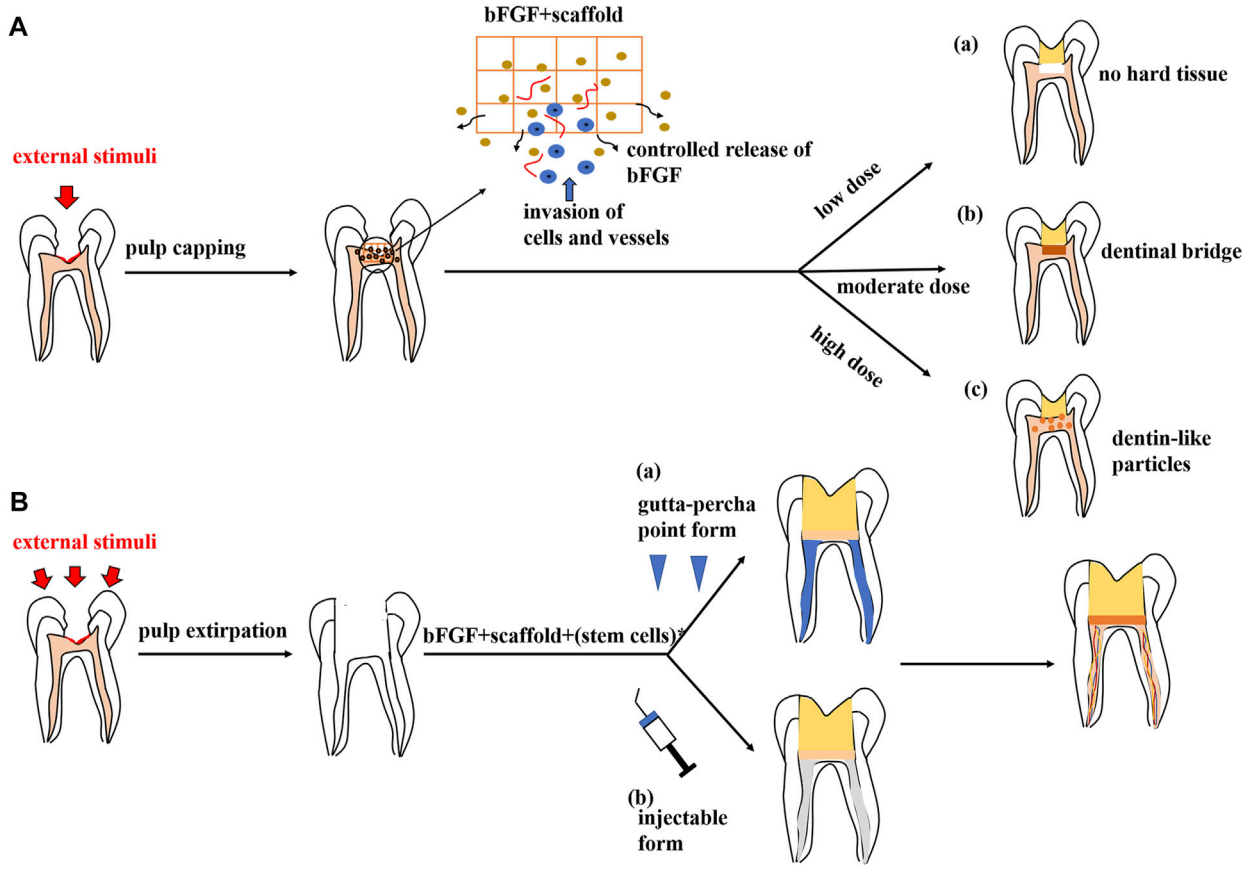

FIGURE 3 | Potential therapeutic strategies of the bFGF in regenerative endodontic therapy. **(A)** Pulp repair. The bFGF could be prepared as a pulp-capping agent when combined with a customized scaffold. This drug carrier system could provide controlled release of the bFGF and induce the ingrowth of cells and vessels, resulting in local pulp regeneration and dentine formation. The outcomes are dose-dependent: (a) low dose of the bFGF (0,0.05 mg/ml), no calcified tissue formation; (b) moderate dose of the bFGF (0.5 mg/ml), dentinal bridge–like structure on the dentin defect surface; and (c) high dose of the bFGF (1.0, 5.0 mg/ml), dentin-like particles in the proliferating pulp. **(B)** Pulp regeneration. A specific scaffold in the gutta-percha point or an injectable form loads the bFGF or the combinatory group of factors, with or without stem cells, which could be applied in pulp regeneration therapy, leading to pulp-like tissue formation in root canals.

also validated that the appropriate dosage of the bFGF releasing from gelatin hydrogels could induce the formation of the dentinal bridge-like osteodentin on the surface of the regenerated pulp (Kitamura et al., 2012). The result with this perspective was in accordance with the report provided by Ishimatsu et al., who found that the structures of newly formed calcified tissue in the dentin defect were dependent on the dose of the bFGF incorporated in gelatin hydrogels (Ishimatsu et al., 2009). As far as the studies demonstrated, a high dose (1.0, 5.0 mg/ml) of the bFGF induced calcified particles in the proliferating pulp, which was consistent with the previous results (Kikuchi et al., 2007), whereas a moderate dose (0.5 mg/ml) of the bFGF induced a dentinal bridge–like structure on the surface of the dentin defect. Meanwhile, at a low dose (0, 0.05 mg/ml) of the bFGF, there was no calcified tissue formation (Ishimatsu et al., 2009) (as shown in **Figure 3A**).

Intriguingly, we find that all experimental models depicted above have used specific scaffolds as drug carriers to load the bFGF, including MesoCS nanoparticles, nano-HAP powder, and gelatin hydrogels, respectively. More scaffold materials can be established for pulp engineering, such as extracellular matrices, self-assembling peptides, and bio-ceramics (Galler et al., 2011). Research studies have shown that scaffold usage could provide sustained (controlled) release of the bFGF, avoiding a large usage of the bFGF protein because of its rapid release (Huang et al., 2017). Furthermore, the comparison of the free-bFGF with the loaded-bFGF was made by putting them into dentin defects above amputated pulp, and it was found that a noncontrolled release of the bFGF only accelerated reparative dentin formation in the residual dental pulp, whereas a controlled release of the bFGF from specific scaffolds induced the formation of DMP-1–positive and nestin-negative osteodentin in the pulp proliferating at the dentin defects, which indicated dentin regeneration (Ishimatsu et al., 2009; Kitamura et al., 2012).

As alluded to above, the application of a moderate dosage (0.5 mg/ml) of the bFGF with a specific scaffold as a drug carrier could induce local pulp regeneration and dentin bridge–like

osteodentin formation, which is distinct from the conventional calcium hydroxide or mineral trioxide aggregate treatments. Considering the cost-effectiveness and the short half-life of the bFGF protein, a more current and efficient approach has been proposed to utilize gene-activated scaffolds for dental pulp capping. Chakka et al. transfected DPSCs with nanoplexes comprising polyethyleneimine (PEI) and plasmid DNA (pDNA) encoding for the bFGF and/or BMP-2. Loaded with collagen scaffolds, these nanoplexes resulted in increased expression of the bFGF and/or BMP-2 and enhanced the proliferation and mineralization properties of DPSCs (Chakka et al., 2020). This biological gene delivery approach in pulp capping is expected to facilitate a better pulp regeneration *in vivo* (Chakka et al., 2020).

Pulp Regeneration

When the external stimuli cause irreversible damage to dental pulp, the affected teeth can be traditionally treated with root canal therapy (RCT), which controls the infection while depriving the teeth of sensitivity and decreasing the resistance of the teeth because of pulp extirpation and malnutrition (Sjögren et al., 1990). In this situation, the pulp regeneration strategy is needed to regenerate a new vital tissue, which ideally mimics the dental pulp in order to extend the longevity of the teeth and improve the patients' life quality (Simon et al., 2011).

Appropriate cells (stem or progenitor cells), customized scaffolds, and appropriate signaling molecules are required for tissue engineering. Accordingly, this concept can be applied to dental pulp regeneration (Orti et al., 2018). Several reports have documented the regeneration of pulp-like tissue *in vitro via* transplantation of dental pulp stem cells with scaffolds incorporating the bFGF. Self-assembling peptide nanofibers were fabricated to encapsulate dental pulp stem cells and growth factors, including the bFGF, TGF-β1, and VEGF. Subcutaneous transplantation of the component within dentin cylinders into immunocompromised mice showed the formation of a vascularized soft connective tissue similar to dental pulp (Galler et al., 2012). In another approach, the combination of the bFGF and BMP-4 was mixed with DPSCs in a collagen scaffold and was transplanted into a special tissue-engineering chamber. Newly formed tissue with blood vessel formation and DSPP-positive matrix production was later observed in this chamber (Srisuwan et al., 2012). A similar result was acquired in an ectopic root canal transplantation model in which the bFGF and DPSCs were packaged in a silk fibroin scaffold (Yang et al., 2015). It is also noteworthy that even without stem cell transplantation, the bFGF alone or with a combinatory group of growth factors could induce pulp regeneration due to their chemotactic properties. For example, the bFGF was shown to be able to yield recellularization and revascularization in endodontically treated human teeth which were implanted into the dorsum of rats (Suzuki et al., 2011). Meanwhile, the bFGF combined with a basal set of growth factors (NGF and BMP-7) also induced the regeneration of pulp-like tissue in the entire root canal from the root apex to the pulp chamber (Kim J. Y. et al., 2010). Thus, it is plausible to postulate a cell-free therapy which works by using selective chemotactic cytokines to recruit stem cells from residual pulp or from the periapical region and subsequently induce the regeneration of dental pulp. If this concept proved to be successful, cell-free therapy may be an advantageous approach that means a more reliable, feasible, and affordable alternative to the cell transplantation method (Galler et al., 2014). It is also thought-provoking that the bFGF was usually applied with a combination of other growth factors in the pulp regeneration therapy. These growth factors (like VEGF, BMP-2, and TGF-β1) were said to have positive effects on pulp regeneration or proved to have a synergistic effect with the bFGF to enhance specific biological effects (He et al., 2008; Kang W. et al., 2019; Zhang et al., 2020). Other than the reciprocal growth factors, the supplementation of inorganic polyphosphate [poly(P)] was confirmed to facilitate the autocrine of the bFGF and enhance the function of the bFGF by promoting its stability and receptor affinity, resulting in the enhancement of the proliferation of HDPCs (Kawazoe et al., 2008). Intraflagellar transport protein 80 (IFT80) (Yuan et al., 2019b) and FGF-binding protein 1 (FGF-BP1) (Tassi et al., 2001) were also proposed as positive modulators in bFGF signal transduction. Therefore, future studies need to be carried out to understand the interplayed relationships among these key players and develop an optimal mixture of molecules for pulp regeneration (Schmalz et al., 2017). Besides, ongoing work is also required to determine whether the bFGF, a single cytokine, is sufficient for the regeneration of dental pulp (Kim J. Y. et al., 2010). For clinical concerns, Bhoj et al. took a first step to fabricate an RGD-bearing alginate scaffold that replicated the shape of gutta-percha. With the encapsulation of DPSCs and dual growth factors involving the bFGF and the VEGF, the customized RGD-bearing alginate framework could be simply shaped to fill the pulp space (Bhoj et al., 2015). In terms of future clinical application, scaffold materials could also be developed into an injectable form to achieve a more efficient root canal obturation (Marler et al., 2000) (as shown in **Figure 3B**).

Collectively, these reports support that the bFGF is a validated candidate for future treatment in pulp regeneration.

SUMMARY

To sum up, the bFGF is known to be involved in all stages of pulp repair/regeneration and uses different intracellular signaling pathways to control specific biological processes, which may be determined by cell origins and treatment durations (Lee et al., 2015; Novais et al., 2019; Nowwarote et al., 2020). Abundant molecules and proteins are involved in such processes. In terms of clinical use, a moderate dose of the bFGF combined with a customized scaffold could be prepared as pulp-capping agents to preserve the vitality of the dentine-pulp complex. Furthermore, the bFGF combined with stem cells and specific scaffolds is put into use in pulp regeneration therapy. In the near future, it is more advisable to begin a new paradigm in pulp regeneration with the cell-free approach (without exogeneous cell transplantation), cytokine reduction

strategy (using only one or a minimum subset of cytokines), and injectable scaffold form (Kim J. Y. et al., 2010; Galler et al., 2011; Galler et al., 2014). At last, since the bFGF has attracted much attention in regenerative endodontic therapy, it is a wise choice to focus on its siblings. Not surprisingly, other FGFs, like FGF-8 (Tsikandelova et al., 2018), FGF-9 (Dai et al., 2012), and aFGF in particular (Cam et al., 1992; Li and Sae-Lim, 2007), are confirmed to own non-negligible regenerative potential in dentistry and tissue engineering. Therefore, greater effort should be put forward to exploit more regenerative properties of FGFs to reinforce their role in pulp repair and regeneration.

AUTHOR CONTRIBUTIONS

KL and SY conceived and drafted the original article. LY and BG instructed with regard to and reviewed the article. All authors approved the final article.

FUNDING

This work was supported by the Department of Science and Technology of Sichuan Province (CN) (Grant no. 2020YFS0202).

REFERENCES

Adam, J. S., and Richard, A. F. C. (1999). Cutaneous Woung Healing. *N. Engl. J. Med.* 341, 738–746. doi:10.1056/NEJM199909023411006

Akita, S., Akino, K., Imaizumi, T., and Hirano, A. (2008). Basic Fibroblast Growth Factor Accelerates and Improves Second-Degree Burn Wound Healing. *Wound Repair Regen.* 16, 635–641. doi:10.1111/j.1524-475X.2008.00414.x

Balic, A., Aguila, H. L., and Mina, M. (2010). Identification of Cells at Early and Late Stages of Polarization during Odontoblast Differentiation Using pOBCol3.6GFP and pOBCol2.3GFP Transgenic Mice. *Bone* 47, 948–958. doi:10.1016/j.bone.2010.08.009

Balic, A., and Mina, M. (2011). Identification of Secretory Odontoblasts Using DMP1-GFP Transgenic Mice. *Bone* 48, 927–937. doi:10.1016/j.bone.2010.12.008

Barzilay, R., Kan, I., Ben-Zur, T., Bulvik, S., Melamed, E., and Offen, D. (2008). Induction of Human Mesenchymal Stem Cells into Dopamine-Producing Cells with Different Differentiation Protocols. *Stem Cell Dev.* 17, 547–554. doi:10.1089/scd.2007.0172

Bhoj, M., Zhang, C., and Green, D. W. (2015). A First Step in De Novo Synthesis of a Living Pulp Tissue Replacement Using Dental Pulp MSCs and Tissue Growth Factors, Encapsulated within a Bioinspired Alginate Hydrogel. *J. Endodontics* 41, 1100–1107. doi:10.1016/j.joen.2015.03.006

Braut, A., Kollar, E. J., and Mina, M. (2003). Analysis of the Odontogenic and Osteogenic Potentials of Dental Pulp *In Vivo* Using a Col1a1-2.3-GFP Transgene. *Int. J. Dev. Biol.* 47, 281–292. doi:10.1387/ijdb.12755333

Cam, Y., Neumann, M. R., Oliver, L., Raulais, D., Janet, T., and Ruch, J. V. (1992). Immunolocalization of Acidic and Basic Fibroblast Growth Factors during Mouse Odontogenesis. *Int. J. Dev. Biol.* 36, 381–389. doi:10.1387/ijdb.1280156

Chakka, L. R. J., Vislisel, J., Vidal, C. d. M. P., Biz, M. T., Salem, A., Cavalcanti, B. N., et al. (2020). Application of BMP-2/FGF-2 Gene-Activated Scaffolds for Dental Pulp Capping. *Clin. Oral Invest.* 24, 4427–4437. doi:10.1007/s00784-020-03308-2

Chang, M.-C., Chen, C.-Y., Chang, Y.-C., Zhong, B.-H., Wang, Y.-L., Yeung, S.-Y., et al. (2020). Effect of bFGF on the Growth and Matrix Turnover of Stem Cells from Human Apical Papilla: Role of MEK/ERK Signaling. *J. Formos. Med. Assoc.* 119, 1666–1672. doi:10.1016/j.jfma.2019.12.013

Chang, Y.-C., Chang, M.-C., Chen, Y.-J., Liou, J.-U., Chang, H.-H., Huang, W.-L., et al. (2017). Basic Fibroblast Growth Factor Regulates Gene and Protein Expression Related to Proliferation, Differentiation, and Matrix Production of Human Dental Pulp Cells. *J. Endodontics* 43, 936–942. doi:10.1016/j.joen.2017.01.024

Chen, J., Cui, C., Qiao, X., Yang, B., Yu, M., Guo, W., et al. (2017). Treated Dentin Matrix Paste as a Novel Pulp Capping Agent for Dentin Regeneration. *J. Tissue Eng. Regen. Med.* 11, 3428–3436. doi:10.1002/term.2256

Chen, M., Song, K., Rao, N., Huang, M., Huang, Z., and Cao, Y. (2011). Roles of Exogenously Regulated bFGF Expression in Angiogenesis and Bone Regeneration in Rat Calvarial Defects. *Int. J. Mol. Med.* 27, 545–553. doi:10.3892/ijmm.2011.619

Chung, A. S., and Ferrara, N. (2011). Developmental and Pathological Angiogenesis. *Annu. Rev. Cel Dev. Biol* 27, 563–584. doi:10.1146/annurev-cellbio-092910-154002

Cooper, P. R., Takahashi, Y., Graham, L. W., Simon, S., Imazato, S., and Smith, A. J. (2010). Inflammation-regeneration Interplay in the Dentine-Pulp Complex. *J. Dentistry* 38, 687–697. doi:10.1016/j.jdent.2010.05.016

Dai, J., Wang, J., Lu, J., Zou, D., Sun, H., Dong, Y., et al. (2012). The Effect of Co-culturing Costal Chondrocytes and Dental Pulp Stem Cells Combined with Exogenous FGF9 Protein on Chondrogenesis and Ossification in Engineered Cartilage. *Biomaterials* 33, 7699–7711. doi:10.1016/j.biomaterials.2012.07.020

de Souza Costa, C. A., Duarte, P. T., de Souza, P. P., Giro, E. M. A., and Hebling, J. (2008). Cytotoxic Effects and Pulpal Response Caused by a mineral Trioxide Aggregate Formulation and Calcium Hydroxide. *Am. J. Dent.* 21, 255–261.

Delle, M. S., Martellucci, S., Clementi, L., Pulcini, F., Santilli, F., Mei, C., et al. (2019). In Vitro *Conditioning Determines Capacity Dental Pulp Stem Cell Funct. as Pericyte-Like Cell Stem Cell Dev.* 28, 695–706. doi:10.1089/scd.2018.0192

Diecke, S., Quiroga-Negreira, A., Redmer, T., and Besser, D. (2008). FGF2 Signaling in Mouse Embryonic Fibroblasts Is Crucial for Self-Renewal of Embryonic Stem Cells. *Cells Tissues Organs* 188, 52–61. doi:10.1159/000121282

Dissanayaka, W. L., Zhan, X., Zhang, C., Hargreaves, K. M., Jin, L., and Tong, E. H. Y. (2012). Coculture of Dental Pulp Stem Cells with Endothelial Cells Enhances Osteo-/Odontogenic and Angiogenic Potential *In Vitro*. *J. Endodontics* 38, 454–463. doi:10.1016/j.joen.2011.12.024

Ehman, E. C., Johnson, G. B., Villanueva-meyer, J. E., Cha, S., Leynes, A. P., Eric, P., and et al (2006). Basic FGF Support of Human Embryonic Stem Cell Self-Renewal. *Stem Cells.* 24, 568–574. doi:10.1634/stemcells.2005-0247

El Agha, E., Kosanovic, D., Schermuly, R. T., and Bellusci, S. (2016). Role of Fibroblast Growth Factors in Organ Regeneration and Repair. *Semin. Cel Dev. Biol.* 53, 76–84. doi:10.1016/j.semcdb.2015.10.009

Fayazi, S., Takimoto, K., and Diogenes, A. (2017). Comparative Evaluation of Chemotactic Factor Effect on Migration and Differentiation of Stem Cells of the Apical Papilla. *J. Endodontics* 43, 1288–1293. doi:10.1016/j.joen.2017.03.012

Galler, K. M., D'Souza, R. N., Hartgerink, J. D., and Schmalz, G. (2011). Scaffolds for Dental Pulp Tissue Engineering. *Adv. Dent Res.* 23, 333–339. doi:10.1177/0022034511405326

Galler, K. M., Eidt, A., and Schmalz, G. (2014). Cell-free Approaches for Dental Pulp Tissue Engineering. *J. Endodontics* 40, S41–S45. doi:10.1016/j.joen.2014.01.014

Galler, K. M., Hartgerink, J. D., Cavender, A. C., Schmalz, G., and D'Souza, R. N. (2012). A Customized Self-Assembling Peptide Hydrogel for Dental Pulp Tissue Engineering. *Tissue Eng. A* 18, 176–184. doi:10.1089/ten.tea.2011.0222

Gong, T., Xu, J., Heng, B., Qiu, S., Yi, B., Han, Y., et al. (2019). EphrinB2/EphB4 Signaling Regulates DPSCs to Induce Sprouting Angiogenesis of Endothelial Cells. *J. Dent Res.* 98, 803–812. doi:10.1177/0022034519843886

Gorin, C., Rochefort, G. S., Bascetin, R., Ying, H., Lesieur, J., Sadoine, J., and et al (2016). Priming Dental Pulp Stem Cells with Fibroblast Growth Factor-2 Increases Angiogenesis of Implanted Tissue-Engineered Constructs through Hepatocyte Growth Factor and Vascular Endothelial Growth Factor Secretion. *Stem Cell Transl. Med.* 5, 392–404.

Goto, T., Ueha, R., Sato, T., Fujimaki, Y., Nito, T., and Yamasoba, T. (2020). Single, High-dose Local Injection of bFGF Improves Thyroarytenoid Muscle Atrophy after Paralysis. *The Laryngoscope* 130, 159–165. doi:10.1002/lary.27887

Graham, L., Cooper, P. R., Cassidy, N., Nor, J. E., Sloan, A. J., and Smith, A. J. (2006). The Effect of Calcium Hydroxide on Solubilisation of Bio-Active Dentine Matrix Components. *Biomaterials* 27, 2865–2873. doi:10.1016/j.biomaterials.2005.12.020

Grella, A., Kole, D., Holmes, W., and Dominko, T. (2016). FGF2 Overrides TGFβ1-Driven Integrin ITGA11 Expression in Human Dermal Fibroblasts. *J. Cel. Biochem.* 117, 1000–1008. doi:10.1002/jcb.25386

He, H., Yu, J., Liu, Y., Lu, S., Liu, H., Shi, J., et al. (2008). Effects of FGF2 and TGFβ1 on the Differentiation of Human Dental Pulp Stem Cells *In Vitro*. *Cel Biol. Int.* 32, 827–834. doi:10.1016/j.cellbi.2008.03.013

Horuk, R. (2001). Chemokine Receptors. *Cytokine Growth Factor. Rev.* 12, 313–335. doi:10.1016/S1359-6101(01)00014-4

Howard, C., Murray, P. E., and Namerow, K. N. (2010). Dental Pulp Stem Cell Migration. *J. Endodontics* 36, 1963–1966. doi:10.1016/j.joen.2010.08.046

Hu, Y., Zhang, Y., Tian, K., Xun, C., Wang, S., and Lv, D. (2016). Effects of Nerve Growth Factor and Basic Fibroblast Growth Factor Dual Gene Modification on Rat Bone Marrow Mesenchymal Stem Cell Differentiation into Neuron-like Cells *In Vitro*. *MOLECULAR MEDICINE REPORTS.* 13, 49–58. doi:10.3892/mmr.2015.4553

Huang, A. H.-C., Snyder, B. R., Cheng, P.-H., and Chan, A. W. S. (2008). Putative Dental Pulp-Derived Stem/Stromal Cells Promote Proliferation and Differentiation of Endogenous Neural Cells in the Hippocampus of Mice. *Stem Cells* 26, 2654–2663. doi:10.1634/stemcells.2008-0285

Huang, C.-Y., Huang, T.-H., Kao, C.-T., Wu, Y.-H., Chen, W.-C., and Shie, M.-Y. (2017). Mesoporous Calcium Silicate Nanoparticles with Drug Delivery and Odontogenesis Properties. *J. Endodontics* 43, 69–76. doi:10.1016/j.joen.2016.09.012

Imura, K., Hashimoto, Y., Okada, M., Yoshikawa, K., and Yamamoto, K. (2019). Application of Hydroxyapatite Nanoparticle-Assembled Powder Using Basic Fibroblast Growth Factor as a Pulp-Capping Agent. *Dent. Mater. J.* 38, 713–720. doi:10.4012/dmj.2018-198

Ishimatsu, H., Kitamura, C., Morotomi, T., Tabata, Y., Nishihara, T., Chen, K.-K., et al. (2009). Formation of Dentinal Bridge on Surface of Regenerated Dental Pulp in Dentin Defects by Controlled Release of Fibroblast Growth Factor-2 from Gelatin Hydrogels. *J. Endodontics* 35, 858–865. doi:10.1016/j.joen.2009.03.049

Janebodin, K., Zeng, Y., Buranaphatthana, W., Ieronimakis, N., and Reyes, M. (2013). VEGFR2-dependent Angiogenic Capacity of Pericyte-like Dental Pulp Stem Cells. *J. Dent Res.* 92, 524–531. doi:10.1177/0022034513485599

Kanda, S., Tomasini-Johansson, B., Klint, P., Dixelius, J., Rubin, K., and Claesson-Welsh, L. (1999). Signaling via Fibroblast Growth Factor Receptor-1 Is Dependent on Extracellular Matrix in Capillary Endothelial Cell Differentiation. *Exp. Cel Res.* 248, 203–213. doi:10.1006/excr.1999.4400

Kang, W., Liang, Q., Du, L., Shang, L., Wang, T., and Ge, S. (2019a). Sequential Application of bFGF and BMP-2 Facilitates Osteogenic Differentiation of Human Periodontal Ligament Stem Cells. *J. Periodontal Res.* 54, 424–434. doi:10.1111/jre.12644

Kang, Y.-H., Shivakumar, S. B., Son, Y.-B., Bharti, D., Jang, S.-J., Heo, K.-S., et al. (2019b). Comparative Analysis of Three Different Protocols for Cholinergic Neuron Differentiation *In Vitro* Using Mesenchymal Stem Cells from Human Dental Pulp. *Anim. Cell Syst.* 23, 275–287. doi:10.1080/19768354.2019.1626280

Karsan, A., Yee, E., Poirier, G. G., Zhou, P., Craig, R., and Harlan, J. M. (1997). Fibroblast Growth Factor-2 Inhibits Endothelial Cell Apoptosis by Bcl- 2-dependent and Independent Mechanisms. *Am. J. Pathol.* 151, 1775–1784.

Kawazoe, Y., Katoh, S., Onodera, Y., Kohgo, T., Shindoh, M., and Shiba, T. (2008). Activation of the FGF Signaling Pathway and Subsequent Induction of Mesenchymal Stem Cell Differentiation by Inorganic Polyphosphate. *Int. J. Biol. Sci.* 4, 37–47. doi:10.7150/ijbs.4.37

Kikuchi, N., Kitamura, C., Morotomi, T., Inuyama, Y., Ishimatsu, H., Tabata, Y., et al. (2007). Formation of Dentin-like Particles in Dentin Defects above Exposed Pulp by Controlled Release of Fibroblast Growth Factor 2 from Gelatin Hydrogels. *J. Endodontics* 33, 1198–1202. doi:10.1016/j.joen.2007.07.025

Kim, J., Park, J.-C., Kim, S.-H., Im, G.-I., Kim, B.-S., Lee, J.-B., et al. (2014). Treatment of FGF-2 on Stem Cells from Inflamed Dental Pulp Tissue from Human Deciduous Teeth. *Oral Dis.* 20, 191–204. doi:10.1111/odi.12089

Kim, J. Y., Xin, X., Moioli, E. K., Chung, J., Lee, C. H., Chen, M., et al. (2010a). Regeneration of Dental-pulp-like Tissue by Chemotaxis-Induced Cell Homing. *Tissue Eng. Part A* 16, 3023–3031. doi:10.1089/ten.tea.2010.0181

Kim, S. G., Malek, M., Sigurdsson, A., Lin, L. M., and Kahler, B. (2018). Regenerative Endodontics: a Comprehensive Review. *Int. Endod. J.* 51, 1367–1388. doi:10.1111/iej.12954

Kim, Y.-S., Min, K.-S., Jeong, D.-H., Jang, J.-H., Kim, H.-W., and Kim, E.-C. (2010b). Effects of Fibroblast Growth Factor-2 on the Expression and Regulation of Chemokines in Human Dental Pulp Cells. *J. Endodontics* 36, 1824–1830. doi:10.1016/j.joen.2010.08.020

Kitamura, C., Nishihara, T., Terashita, M., Tabata, Y., and Washio, A. (2012). Local Regeneration of Dentin-Pulp Complex Using Controlled Release of FGF-2 and Naturally Derived Sponge-like Scaffolds. *Int. J. Dentistry* 2012, 1–8. doi:10.1155/2012/190561

Kitamura, N., Hasebe, T., Matsumoto, T., Hotta, A., Suzuki, T., Yamagami, T., et al. (2014). Basic Fibroblast Growth Factor as a Potential Stent Coating Material Inducing Endothelial Cell Proliferation. *Jat* 21, 477–485. doi:10.5551/jat.20404

Kong, Y., Ma, B., Liu, F., Chen, D., Zhang, S., Duan, J., et al. (2019). Cellular Stemness Maintenance of Human Adipose-Derived Stem Cells on ZnO Nanorod Arrays. *Small* 15, 1–11. doi:10.1002/smll.201904099

Lee, T.-H., Kim, W.-T., Ryu, C. J., and Jang, Y.-J. (2015). Optimization of Treatment with Recombinant FGF-2 for Proliferation and Differentiation of Human Dental Stem Cells, Mesenchymal Stem Cells, and Osteoblasts. *Biochem. Cel Biol.* 93, 298–305. doi:10.1139/bcb-2014-0140

Li, C.-Y., Prochazka, J., Goodwin, A. F., and Klein, O. D. (2014). Fibroblast Growth Factor Signaling in Mammalian Tooth Development. *Odontology* 102, 1–13. doi:10.1007/s10266-013-0142-1

Li, Z., Cao, L., Fan, M., and Xu, Q. (2015). Direct Pulp Capping with Calcium Hydroxide or Mineral Trioxide Aggregate: A Meta-Analysis. *J. Endod.* 41, 1412–1417. doi:10.1016/j.joen.2015.04.012

Li, Z., and Sae-Lim, V. (2007). Comparison of Acidic Fibroblast Growth Factor on Collagen Carrier with Calcium Hydroxide as Pulp Capping Agents in Monkeys. *Dent Traumatol.* 23, 278–286. doi:10.1111/j.1600-9657.2006.00459.x

Liu, X., and Zhu, X. (1999). Roles of P53, C-Myc, Bcl-2, Bax and Caspases in Glutamate-Induced Neuronal Apoptosis and the Possible Neuroprotective Mechanism of Basic Fibroblast Growth Factor. *Mol. Brain Res.* 71, 210–216. doi:10.1016/s0169-328x(99)00186-2

Luo, L., Albashari, A. A., Wang, X., Jin, L., Zhang, Y., Zheng, L., et al. (2018a). Effects of Transplanted Heparin-Poloxamer Hydrogel Combining Dental Pulp Stem Cells and bFGF on Spinal Cord Injury Repair. *Stem Cell Int.* 2018, 1–13. doi:10.1155/2018/2398521

Luo, L., He, Y., Wang, X., Key, B., Lee, B. H., Li, H., et al. (2018b). Potential Roles of Dental Pulp Stem Cells in Neural Regeneration and Repair. *Stem Cell Int.* 2018, 1–15. doi:10.1155/2018/1731289

Luo, L., Zhang, Y., Chen, H., Hu, F., Wang, X., Xing, Z., et al. (2021). Effects and Mechanisms of Basic Fibroblast Growth Factor on the Proliferation and Regenerative Profiles of Cryopreserved Dental Pulp Stem Cells. *Cell Prolif* 54, 1–12. doi:10.1111/cpr.12969

Maddaluno, L., Urwyler, C., and Werner, S. (2017). Fibroblast Growth Factors: Key Players in Regeneration and Tissue Repair. *Dev.* 144, 4047–4060. doi:10.1242/dev.152587

Marler, J. J., Guha, A., Rowley, J., Koka, R., Mooney, D., Upton, J., et al. (20002049–2058). Soft-Tissue Augmentation with Injectable Alginate and Syngeneic Fibroblasts. *Plast. Reconstr. Surg.* 105, 2049–2058. doi:10.1097/00006534-200005000-00020

Matsumine, H., Sasaki, R., Tabata, Y., Matsui, M., Yamato, M., Okano, T., et al. (2016). Facial Nerve Regeneration Using Basic Fibroblast Growth Factor-Impregnated Gelatin Microspheres in a Rat Model. *J. Tissue Eng. Regen. Med.* 10, E559–E567. doi:10.1002/term.1884

Melissa, J. M., and Kristi, S. A. (2006). Contrasting Effects of Collagen and bFGF-2 on Neural Cell Function in Degradable Synthetic PEG Hydrogels. *Wiley Intersci.* 81, 269–278. doi:10.1002/jbm.a.30970

Min, J.-H., Ko, S.-Y., Cho, Y.-B., Ryu, C.-J., and Jang, Y.-J. (2011). Dentinogenic Potential of Human Adult Dental Pulp Cells during the Extended Primary Culture. *Hum. Cel* 24, 43–50. doi:10.1007/s13577-011-0010-7

Morito, A., Kida, Y., Suzuki, K., Inoue, K., Kuroda, N., Gomi, K., et al. (2009). Effects of Basic Fibroblast Growth Factor on the Development of the Stem Cell Properties of Human Dental Pulp Cells. *Arch. Histology Cytol.* 72, 51–64. doi:10.1679/aohc.72.51

Mullane, E. M., Dong, Z., Sedgley, C. M., Hu, J. C. C., Botero, T. M., Holland, G. R., and et al (2008). Effects of VEGF and FGF2 on the Revascularization of Severed Human Dental Pulps. *J. Dent. Res.* 87, 1144–1148. doi:10.1177/154405910808701204

Müller, A.-K., Meyer, M., and Werner, S. (2012). The Roles of Receptor Tyrosine Kinases and Their Ligands in the Wound Repair Process. *Semin. Cel Dev. Biol.* 23, 963–970. doi:10.1016/j.semcdb.2012.09.015

Murray, P. E., Garcia-Godoy, F., and Hargreaves, K. M. (2007). Regenerative Endodontics: A Review of Current Status and a Call for Action. *J. Endodontics* 33, 377–390. doi:10.1016/j.joen.2006.09.013

Nagashima, K., Miwa, T., Soumiya, H., Ushiro, D., Takeda-Kawaguchi, T., Tamaoki, N., et al. (2017). Priming with FGF2 Stimulates Human Dental Pulp Cells to Promote Axonal Regeneration and Locomotor Function Recovery after Spinal Cord Injury. *Sci. Rep.* 7, 1–12. doi:10.1038/s41598-017-13373-5

Nam, H., Kim, G.-H., Bae, Y.-K., Jeong, D.-E., Joo, K.-M., Lee, K., et al. (2017). Angiogenic Capacity of Dental Pulp Stem Cell Regulated by SDF-1α-CXCR4 Axis. *Stem Cell Int.* 2017, 1–10. doi:10.1155/2017/8085462

Nawrocka, D., Kornicka, K., Szydlarska, J., and Marycz, K. (2017). Basic Fibroblast Growth Factor Inhibits Apoptosis and Promotes Proliferation of Adipose-Derived Mesenchymal Stromal Cells Isolated from Patients with Type 2 Diabetes by Reducing Cellular Oxidative Stress. *Oxidative Med. Cell Longevity* 2017, 1–22. doi:10.1155/2017/3027109

Novais, A., Lesieur, J., Sadoine, J., Slimani, L., Baroukh, B., Saubaméa, B., et al. (2019). Priming Dental Pulp Stem Cells from Human Exfoliated Deciduous Teeth with Fibroblast Growth Factor-2 Enhances Mineralization within Tissue-Engineered Constructs Implanted in Craniofacial Bone Defects. *STEM CELLS Translational Med.* 8, 844–857. doi:10.1002/sctm.18-0182

Nowwarote, N., Manokawinchoke, J., Kanjana, K., Fournier, B. P. J., Sukarawan, W., and Osathanon, T. (2020). Transcriptome Analysis of Basic Fibroblast Growth Factor Treated Stem Cells Isolated from Human Exfoliated Deciduous Teeth. *Heliyon* 6, e04246. doi:10.1016/j.heliyon.2020.e04246

Nowwarote, N., Sukarawan, W., Pavasant, P., Foster, B. L., and Osathanon, T. (2018). Basic Fibroblast Growth Factor Regulates Phosphate/pyrophosphate Regulatory Genes in Stem Cells Isolated from Human Exfoliated Deciduous Teeth. *Stem Cel Res Ther* 9, 1–14. doi:10.1186/s13287-018-1093-9

Nowwarote, N., Sukarawan, W., Pavasant, P., and Osathanon, T. (2017). Basic Fibroblast Growth Factor Regulates REX1 Expression via IL-6 in Stem Cells Isolated from Human Exfoliated Deciduous Teeth. *J. Cel. Biochem.* 118, 1480–1488. doi:10.1002/jcb.25807

Nunes, Q. M., Li, Y., Sun, C., Kinnunen, T. K., and Fernig, D. G. (2016). Fibroblast Growth Factors as Tissue Repair and Regeneration Therapeutics. *PeerJ.* 4, e1535. doi:10.7717/peerj.1535

Ornitz, D. M., and Itoh, N. (2001). Fibroblast Growth Factors. *Genome Biol.* 2. doi:10.1186/gb-2001-2-3-reviews3005REVIEWS3005

Orti, V., Collart-Dutilleul, P.-Y., Piglionico, S., Pall, O., Cuisinier, F., and Panayotov, I. (2018). Pulp Regeneration Concepts for Nonvital Teeth: From Tissue Engineering to Clinical Approaches. *Tissue Eng. B: Rev.* 24, 419–442. doi:10.1089/ten.teb.2018.0073

Osathanon, T., Nowwarote, N., and Pavasant, P. (2011). Basic Fibroblast Growth Factor Inhibits Mineralization but Induces Neuronal Differentiation by Human Dental Pulp Stem Cells through a FGFR and PLCγ Signaling Pathway. *J. Cel. Biochem.* 112, 1807–1816. doi:10.1002/jcb.23097

Peng, L., Ye, L., and Zhou, X. D. (2009). *Mesenchymal Stem Cell Tooth Eng. Int J Oral Sci.* 1, 6–12. doi:10.4248/ijos.08032

Qian, J., Jiayuan, W., Wenkai, J., Peina, W., Ansheng, Z., Shukai, S., et al. (2015). Basic Fibroblastic Growth Factor Affects the Osteogenic Differentiation of Dental Pulp Stem Cells in a Treatment-dependent Manner. *Int. Endod. J.* 48, 690–700. doi:10.1111/iej.12368

Sagomonyants, K., Kalajzic, I., Maye, P., and Mina, M. (2015). Enhanced Dentinogenesis of Pulp Progenitors by Early Exposure to FGF2. *J. Dent Res.* 94, 1582–1590. doi:10.1177/0022034515599768

Sagomonyants, K., Kalajzic, I., Maye, P., and Mina, M. (2017). FGF Signaling Prevents the Terminal Differentiation of Odontoblasts. *J. Dent Res.* 96, 663–670. doi:10.1177/0022034517691732

Sagomonyants, K., and Mina, M. (2014b). Biphasic Effects of FGF2 on Odontoblast Differentiation Involve Changes in the BMP and Wnt Signaling Pathways. *Connect. Tissue Res.* 55, 53–56. doi:10.3109/03008207.2014.923867

Sagomonyants, K., and Mina, M. (2014a). Stage-Specific Effects of Fibroblast Growth Factor 2 on the Differentiation of Dental Pulp Cells. *Cells Tissues Organs* 199, 311–328. doi:10.1159/000371343

Sasaki, R., Aoki, S., Yamato, M., Uchiyama, H., Wada, K., Okano, T., et al. (2008). Neurosphere Generation from Dental Pulp of Adult Rat Incisor. *Eur. J. Neurosci.* 27, 538–548. doi:10.1111/j.1460-9568.2008.06026.x

Schmalz, G., Widbiller, M., and Galler, K. M. (2017). Signaling Molecules and Pulp Regeneration Gottfried. *J. Endod.* 43, s7–s11. doi:10.1016/j.joen.2017.06.003

Schmidt, A., Ladage, D., Schinköthe, T., Klausmann, U., Ulrichs, C., Klinz, F.-J., et al. (2006). Basic Fibroblast Growth Factor Controls Migration in Human Mesenchymal Stem Cells. *Stem Cells* 24, 1750–1758. doi:10.1634/stemcells.2005-0191

Simon, S. R. J., Berdal, A., Cooper, P. R., Lumley, P. J., Tomson, P. L., and Smith, A. J. (2011). Dentin-Pulp Complex Regeneration. *Adv. Dent Res.* 23, 340–345. doi:10.1177/0022034511405327

Sjögren, U., Hägglund, B., Sundqvist, G., and Wing, K. (1990). Factors Affecting the Long-Term Results of Endodontic Treatment. *J. Endod.* 16, 498–504. doi:10.1016/S0099-2399(07)80180-4

Solchaga, L. A., Penick, K., Porter, J. D., Goldberg, V. M., Caplan, A. I., and Welter, J. F. (2005). FGF-2 Enhances the Mitotic and Chondrogenic Potentials of Human Adult Bone Marrow-Derived Mesenchymal Stem Cells. *J. Cel. Physiol.* 203, 398–409. doi:10.1002/jcp.20238

Srisuwan, T., Tilkorn, D. J., Al-Benna, S., Vashi, A., Penington, A., Messer, H. H., et al. (2012). Survival of Rat Functional Dental Pulp Cells in Vascularized Tissue Engineering chambers. *Tissue Cel Survival rat Funct. dental pulp Cell vascularized Tissue Eng. chambers.* Tissue Cel. 44, 111–121. doi:10.1016/j.tice.2011.12.003

Sukarawan, W., Nowwarote, N., Kerdpon, P., Pavasant, P., and Osathanon, T. (2014). Effect of Basic Fibroblast Growth Factor on Pluripotent Marker Expression and colony Forming Unit Capacity of Stem Cells Isolated from Human Exfoliated Deciduous Teeth. *Odontology* 102, 160–166. doi:10.1007/s10266-013-0124-3

Suzuki, T., Lee, C. H., Chen, M., Zhao, W., Fu, S. Y., Qi, J. J., et al. (2011). Induced Migration of Dental Pulp Stem Cells for *In Vivo* Pulp Regeneration. *J. Dent Res.* 90, 1013–1018. doi:10.1177/0022034511408426

Takedachi, M., Yanagita, M., and Ito, M. (2009). *Fibroblast Growth Factor Regulates Cel Funct. Hum. Dental Pulp Cell* J. Endod. 35, 1529–1535. doi:10.1016/j.joen.2009.08.010

Takeuchi, N., Hayashi, Y., Murakami, M., Alvarez, F., Horibe, H., Iohara, K., et al. (2015). Similar *In Vitro* Effects and Pulp Regeneration in Ectopic Tooth Transplantation by Basic Fibroblast Growth Factor and Granulocyte-colony Stimulating Factor. *Oral Dis.* 21, 113–122. doi:10.1111/odi.12227

Tassi, E., Al-Attar, A., Aigner, A., Swift, M. R., McDonnell, K., Karavanov, A., et al. (2001). Enhancement of Fibroblast Growth Factor (FGF) Activity by an FGF-Binding Protein. *J. Biol. Chem.* 276, 40247–40253. doi:10.1074/jbc.M104933200

Tomson, P. L., Lumley, P. J., Smith, A. J., and Cooper, P. R. (2017). Growth Factor Release from Dentine Matrix by Pulp-Capping Agents Promotes Pulp Tissue Repair-Associated Events. *Int. Endod. J.* 50, 281–292. doi:10.1111/iej.12624

Torabinejad, M., Parirokh, M., and Dummer, P. M. H. (2018). Mineral Trioxide Aggregate and Other Bioactive Endodontic Cements: an Updated Overview - Part II: Other Clinical Applications and Complications. *Int. Endod. J.* 51, 284–317. doi:10.1111/iej.12843

Trubiani, O., Orsini, G., Zini, N., Di Iorio, D., Piccirilli, M., Piattelli, A., et al. (2008). Regenerative Potential of Human Periodontal Ligament Derived Stem Cells on Three-Dimensional Biomaterials: A Morphological Report. *J. Biomed. Mater. Res.* 87A, 986–993. doi:10.1002/jbm.a.31837

Tsikandelova, R., Mladenov, P., Planchon, S., Kalenderova, S., Praskova, M., Mihaylova, Z., et al. (2018). Proteome Response of Dental Pulp Cells to Exogenous FGF8. *J. Proteomics* 183, 14–24. doi:10.1016/j.jprot.2018.05.004

Tsuboi, T., Mizutani, S., Nakano, M., Hirukawa, K., and Togari, A. (2003). FGF-2 Regulates Enamel and Dentine Formation in Mouse Tooth Germ. *Calcified Tissue Int.* 73, 496–501. doi:10.1007/s00223-002-4070-2

Tsutsumi, S., Shimazu, A., Miyazaki, K., Pan, H., Koike, C., Yoshida, E., et al. (2001). Retention of Multilineage Differentiation Potential of Mesenchymal Cells during Proliferation in Response to FGF. *Biochem. Biophysical Res. Commun.* 288, 413–419. doi:10.1006/bbrc.2001.5777

Vaseenon, S., Chattipakorn, N., and Chattipakorn, S. C. (2020). The Possible Role of Basic Fibroblast Growth Factor in Dental Pulp. *Arch. Oral Biol.* 109, 104574. doi:10.1016/j.archoralbio.2019.104574

Vining, K. H., Mooney, D. J., Mina, M., Vijaykumar, A., and Kalajzic, I. (2018). FGF2 Enhances Odontoblast Differentiation by αSMA $^{+}$ Progenitors *In Vivo*. J. Dent Res. 97, 1170–1177. doi:10.1177/0022034518769827

Wang, D.-R., Wang, Y.-H., Pan, J., Tian, W.-D., Key, S., and Disease, O. (2020). Neurotrophic Effects of Dental Pulp Stem Cells in Repair of Peripheral Nerve after Crush Injury. *Wjsc* 12, 1196–1213. doi:10.4252/wjsc.v12.i10.1196

Wang, D., Wang, Y., Tian, W., and Pan, J. (2019a). Advances of Tooth - Derived Stem Cells in Neural Diseases Treatments and Nerve Tissue Regeneration. *Cel Prolif* 52, e12572. doi:10.1111/cpr.12572

Wang, J., Liu, S., Li, J., and Yi, Z. (2019b). The Role of the Fibroblast Growth Factor Family in Bone-related Diseases. *Chem. Biol. Drug Des.* 94, 1740–1749. doi:10.1111/cbdd.13588

Wigler, R., Kaufman, A. Y., Lin, S., Steinbock, N., Hazan-Molina, H., and Torneck, C. D. (2013). Revascularization: A Treatment for Permanent Teeth with Necrotic Pulp and Incomplete Root Development. *J. Endodontics* 39, 319–326. doi:10.1016/j.joen.2012.11.014

Wu, J., Huang, G. T.-J., He, W., Wang, P., Tong, Z., Jia, Q., et al. (2012). Basic Fibroblast Growth Factor Enhances Stemness of Human Stem Cells from the Apical Papilla. *J. Endodontics* 38, 614–622. doi:10.1016/j.joen.2012.01.014

Yamamura, T. (1985). Differentiation of Pulpal Cells and Inductive Influences of Various Matrices with Reference to Pulpal Wound Healing. *J. Dent Res.* 64, 530–540. doi:10.1177/002203458506400406

Yang, J.-w., Zhang, Y.-f., Sun, Z.-y., Song, G.-t., and Chen, Z. (2015). Dental Pulp Tissue Engineering with bFGF-Incorporated Silk Fibroin Scaffolds. *J. Biomater. Appl.* 30, 221–229. doi:10.1177/0885328215577296

Yang, J., Yuan, G., and Chen, Z. (2016). Pulp Regeneration: Current Approaches and Future Challenges. *Front. Physiol.* 7, 1–8. doi:10.3389/fphys.2016.00058

Ye, Q., Wu, Y., Wu, J., Zou, S., Al-Zaazaai, A. A., Zhang, H., et al. (2018). Neural Stem Cells Expressing bFGF Reduce Brain Damage and Restore Sensorimotor Function after Neonatal Hypoxia-Ischemia. *Cell Physiol Biochem* 45, 108–118. doi:10.1159/000486226

Yeoh, J. S. G., and de Haan, G. (2007). Fibroblast Growth Factors as Regulators of Stem Cell Self-Renewal and Aging. *Mech. Ageing Dev.* 128, 17–24. doi:10.1016/j.mad.2006.11.005

Yuan, X., Cao, X., and Yang, S. (2019b). IFT80 Is Required for Stem Cell Proliferation, Differentiation, and Odontoblast Polarization during Tooth Development. *Cell Death Dis.* 10, 63. doi:10.1038/s41419-018-0951-9

Yuan, X., Liu, M., Cao, X., and Yang, S. (2019a). Ciliary IFT80 Regulates Dental Pulp Stem Cells Differentiation by FGF/FGFR1 and Hh/BMP2 Signaling. *Int. J. Biol. Sci.* 15, 2087–2099. doi:10.7150/ijbs.27231

Zbinden, A., Browne, S., Altiok, E. I., Svedlund, F. L., Jackson, W. M., and Healy, K. E. (2018). Multivalent Conjugates of Basic Fibroblast Growth Factor Enhance *In Vitro* Proliferation and Migration of Endothelial Cells. *Biomater. Sci.* 6, 1076–1083. doi:10.1039/c7bm01052d

Zhang, C., Chen, J., Feng, C., Shao, X., Liu, Q., Zhang, Q., et al. (2014). Intranasal Nanoparticles of Basic Fibroblast Growth Factor for Brain Delivery to Treat Alzheimer's Disease. *Int. J. Pharmaceutics* 461, 192–202. doi:10.1016/j.ijpharm.2013.11.049

Zhang, J., Lian, M., Cao, P., Bao, G., Xu, G., Sun, Y., et al. (2017). Effects of Nerve Growth Factor and Basic Fibroblast Growth Factor Promote Human Dental Pulp Stem Cells to Neural Differentiation. *Neurochem. Res.* 42, 1015–1025. doi:10.1007/s11064-016-2134-3

Zhang, R., Xie, L., Wu, H., Yang, T., Zhang, Q., Tian, Y., et al. (2020). Alginate/laponite Hydrogel Microspheres Co-encapsulating Dental Pulp Stem Cells and VEGF for Endodontic Regeneration. *Acta Biomater.* 113, 305–316. doi:10.1016/j.actbio.2020.07.012

Zhang, R., Zhang, M., Li, C., Wang, P., Chen, F., and Wang, Q. (2013). Effects of Basic Fibroblast Growth Factor and Vascular Endothelial Growth Factor on Proliferation,migration and Adhension of Human Periodontal Ligament Stem Cells *In Vitro*. *Chinise* 48, 278–284. doi:10.3760/cma.j.issn.1002-0098.2013.05.006

Zheng, K., Feng, G., Zhang, J., Xing, J., Huang, D., Lian, M., et al. (2020). Basic Fibroblast Growth Factor Promotes Human Dental Pulp Stem Cells Cultured in 3D Porous Chitosan Scaffolds to Neural Differentiation. *Int. J. Neurosci.* 131, 625–633. doi:10.1080/00207454.2020.1744592

Zhou, Y., Wang, Z., Li, J., Li, X., and Xiao, J. (2018). Fibroblast Growth Factors in the Management of Spinal Cord Injury. *J. Cel. Mol. Med.* 22, 25–37. doi:10.1111/jcmm.13353

Conflict of Interest: The authors declare that the research was conducted in the absence of any commercial or financial relationships that could be construed as a potential conflict of interest.

frontiers in Genetics

ORIGINAL RESEARCH
published: 18 August 2021
doi: 10.3389/fgene.2021.695835

The Interaction of Single Nucleotide Polymorphisms on Fibroblast Growth Factor 19 Superfamily Genes Is Associated With Alcohol Dependence-Related Aggression

Jinzhong Xu[1†], Fenzan Wu[2†], Fan Wang[3,4†], Fan Yang[5], Meng Liu[5], Mengbei Lou[5], Linman Wu[5], Hui Li[4], Wenhui Lin[6], Yunchao Fan[6], Li Chen[5,7], Yanlong Liu[5,7], Haiyun Xu[5,7] and Jue He[7,8,9,10]**

[1] Department of Clinical Pharmacy, Affiliated Wenling Hospital, Wenzhou Medical University, Wenling, China, [2] Laboratory of Translational Medicine, Affiliated Cixi Hospital, Wenzhou Medical University, Ningbo, China, [3] Psychiatry Research Center, Beijing Hui-Long-Guan Hospital, Peking University, Beijing, China, [4] Xinjiang Key Laboratory of Neurological Disorder Research, The Second Affiliated Hospital of Xinjiang Medical University, Ürümqi, China, [5] School of Mental Health, Wenzhou Medical University, Wenzhou, China, [6] Department of Cardiovascular Medicine, Affiliated Wenling Hospital, Wenzhou Medical University, Wenling, China, [7] The Affiliated Kangning Hospital, Wenzhou Medical University, Wenzhou, China, [8] Xiamen Xian Yue Hospital, Xiamen, China, [9] First Affiliated Hospital, Institute of Neurological Disease, Henan University, Kaifeng, China, [10] Institute of Aging, Key Laboratory of Alzheimer's Disease of Zhejiang Province, Wenzhou Medical University, Wenzhou, China

OPEN ACCESS

Edited by:
Yidong Wang,
Xi'an Jiaotong University, China

Reviewed by:
Xingguang Luo,
Yale University, United States
Lijing Wang,
University of Michigan, United States

***Correspondence:**
Jue He
heje2002@hotmail.com
Haiyun Xu
hyxu@stu.edu.cn

† These authors have contributed equally to this work

Specialty section:
This article was submitted to Stem Cell Research, a section of the journal Frontiers in Genetics

Received: *15 April 2021*
Accepted: *22 June 2021*
Published: *18 August 2021*

Citation:
Xu J, Wu F, Wang F, Yang F, Liu M, Lou M, Wu L, Li H, Lin W, Fan Y, Chen L, Liu Y, Xu H and He J (2021) The Interaction of Single Nucleotide Polymorphisms on Fibroblast Growth Factor 19 Superfamily Genes Is Associated With Alcohol Dependence-Related Aggression. Front. Genet. 12:695835. doi: 10.3389/fgene.2021.695835

Alcohol dependence (AD) is characterized by compulsive alcohol consumption, which involves behavioral impairments such as aggression. Members of fibroblast growth factor (FGF) 19 superfamily, including FGF19, FGF21, and FGF23, are major endocrine mediators that play an important role in alcohol metabolism and alcohol related disorders. The objective of the present study is to explore the possible associations among the interaction of single nucleotide polymorphisms (SNPs) of the FGF 19 superfamily, AD occurrence, and aggression in patients with AD. A total of 956 subjects were enrolled in this study, including 482 AD patients and 474 healthy controls (HCs). Michigan alcoholism screening test (MAST) was used to measure the level of AD, a Chinese version of the Buss–Perry Aggression Questionnaire was used to evaluate the aggressive behavior of subjects, and MassARRAY@ system was used to genotype rs948992 of FGF19, rs11665841 and rs11665896 of FGF21, rs7955866 and rs11063118 of FGF23. The results showed that AD patients presented a significantly higher level of aggression compared to HCs, and MAST scores were significantly positively associated Buss–Perry aggression scores ($r = 0.402$, $p < 0.001$) in AD patients. The interaction of FGF19 rs948992 TC × FGF21 rs11665896 GG presented the high-risk genotype combination predicting the high level of AD. In addition, the interaction of FGF19 rs948992 TC × FGF21 rs11665896 TG × FGF23 rs11063118 TT presented the high-risk genotype combination predicting the high level of aggression in AD patients. Our results added evidence linking the combination of rs948992 TC × rs11665896 TG × rs11063118 TT to aggressive behavior in AD patients and pointed out the potential usefulness of the SNPs of FGF19 superfamily as a predictor for the aggression in AD patients.

Keywords: FGF21, FGF19, FGF23, alcohol dependence, aggression, single nucleotide polymorphism

INTRODUCTION

Alcohol dependence (AD) is a common psychiatric disorder and is characterized by loss of control over alcohol drinking, which is associated with impaired decision-making, seeking alcohol regardless of health status and behavioral impairments such as aggression and impulsivity, even suicide attempts (Tobore, 2019; Witkiewitz et al., 2019). Pieces of evidence suggested that AD was a multifactorial and genetic disease, and the pathogenesis of AD included neurobiological, genetic and epigenetic, psychological, social, and environmental factors (Kiive et al., 2017; Newman et al., 2018; Malamut et al., 2021). Some patients with AD recover after lifestyle modifications in the absence of medical treatment, while many of them relapse and display damaged brain structure and function (Grant et al., 2015; Abrahao et al., 2017; Erickson et al., 2019). AD is usually reported to combine with behavioral impairments or mental disorders such as aggression, suicide, major depression, anxiety, insomnia, and drug addiction (Dick and Agrawal, 2008; Schuckit, 2009).

As a harmful behavior induced by AD, aggression is an important alcohol-related phenotype and could endanger other individuals and society in general through violence and even crime (Heinz et al., 2011; Chester et al., 2020). Increasing evidence suggested that neurobiological, genetic and epigenetic mechanisms such as the involvement of dopamine, serotonin, gamma-aminobutyric acid (GABA), and neuroendocrine systems may be related to AD and AD-related aggression (Heinz et al., 2011; Nedic Erjavec et al., 2014; Gan et al., 2015; Plemenitas et al., 2015; Waltes et al., 2016). The environmental factors and specific genes may be the important causes for AD and alcohol-use disorders including aggression (Schuckit, 2009; Plemenitas et al., 2015). The interaction among the single nucleotide polymorphisms (SNPs) of genes of oxytocin and its receptor was reported to be related to alcohol disorder and aggressive behavior (Yang et al., 2017). The GABA type A receptor subunit alpha (GABRA) 2 rs279826/rs279858 A-allele interacts with stress, contributing to the development of alcohol use and aggressive behavior (Kiive et al., 2017).

Fibroblast growth factor (FGF) 19, FGF21, and FGF23 belong to FGF19 superfamily. The members of this subfamily are characterized by their reduced binding affinity for heparin that enables them to be transported in the circulation and function in an endocrine manner (Kharitonenkov and DiMarchi, 2017). The proteins of FGF19 subfamily influence the enterohepatic circulation of bile, participate in glucose and lipid metabolism regulation, and maintenance of phosphorus and vitamin D3 homeostasis (Dolegowska et al., 2019). Recent studies suggest that FGF19, FGF21, and FGF23 are associated with alcohol and alcohol-related disorders (Schumann et al., 2016; Quintero-Platt et al., 2017; Brandl et al., 2018; Gonzalez-Reimers et al., 2018; Epperlein et al., 2021). Serum FGF19 level and FGF19 mRNA expression both increase strongly in patients with alcohol use disorder (Brandl et al., 2018). The circulating FGF 21 level also increased significantly after binge alcohol consumption (Desai et al., 2017). Studies suggested heavy alcohol intake could induce FGF 21 high expression, however, overexpressing FGF 21 may decrease alcohol preference by regulating the drinking behavior in part through SIM1-positive neurons of the hypothalamus (Desai et al., 2017; Soberg et al., 2018; Song et al., 2018). In alcoholic patients, the levels of FGF 23 also increased significantly (Quintero-Platt et al., 2017). The evidence about FGF19 superfamily members associated with alcohol consumption is relatively abundant, but the reports about FGF19 superfamily members' polymorphisms with AD are still rare. A study found that the A allele of rs838133 on the FGF21 gene is significantly associated with increased alcohol intake (Soberg et al., 2017). Another study demonstrated that the FGF19/21-β-Klotho signaling pathway is associated with alcohol consumption and the substream essential receptor protein β-Klotho gene SNP rs11940694 is significantly related to alcohol intake (Schumann et al., 2016).

As an important member of the FGF19 superfamily, FGF21 has an extensive biologic effect on mediating the central nervous system. FGF21 might be involved in mood disorders through stimulating dopamine signaling in the prefrontal cortex (Chiavaroli et al., 2017). A recent study has indicated that FGF21 was significantly associated with alcohol craving (Epperlein et al., 2021), which is associated with aggression in patients with alcohol use disorder (Roozen et al., 2013; Park et al., 2019). FGF21 genetic or near the FGF21 locus variants are associated with carbohydrate preference and consumption of addictive substances (Heianza et al., 2016; Frayling et al., 2018). Furthermore, physiological effects of FGF21 were tightly correlated with the dopamine and serotonin system (Han et al., 2016; Recinella et al., 2017; Gibson, 2018), which both play an important role in mediating aggressive behavior (Brodie et al., 2016). All the above studies indicate a potential association between FGF19 superfamily and aggressive behavior.

The rs948992 of FGF19 SNP and rs11665841 and rs11665896 of FGF21 SNPs are located on 3′ untranslated region (3′UTR; Zhang et al., 2012),[1] where miRNAs could bind and further impact target gene protein translation (Chen and Rajewsky, 2006; Landi et al., 2008). The genetic variants of miRNA target sites may induce phenotypic changes and increase the risk of developing diseases (Sethupathy and Collins, 2008; Zhang et al., 2012). The sequence variation C716T (rs7955866) is located in exon 3 of FGF23 gene, which could affect the FGF23 activity by the missense variation designated T239M and the exchange of T239M (Nguyen et al., 2010). In addition, rs11063118 of FGF23 was selected based on the tagging SNP approach, optimal sets of SNPs were derived from genetic databases in order to tag haplotypes across genes (Rothe et al., 2017). Thus, in order to explore the possible associations of FGFs 19, 21, and 23 polymorphisms with AD and AD-related aggression, rs948992 of FGF19, rs11665841, and rs11665896 of FGF21, and rs7955866 and rs11063118 of FGF23 were chosen to evaluate genotypes by using MassARRAY@ system, Michigan alcoholism screening test (MAST) was used to measure the level of AD, and a Chinese version of the Buss–Perry Aggression Questionnaire was used to evaluate the aggressive behavior of subjects in the present study.

[1] https://www.ncbi.nlm.nih.gov/snp/rs948992

MATERIALS AND METHODS

Subjects

A total of 956 unrelated Han population males aged above 18 years in northern China were recruited in this cross-section study, including 482 patients in AD-group and 474 healthy control subjects in HC-group. Because there were too few female patients with AD in this study, they were excluded. All alcoholism patients were diagnosed according to the Diagnostic and Statistical Manual of the American Psychiatric Association, fourth edition (DSM-IV). Participants with the following conditions were excluded: had a family history of psychosis and neurological diseases, severe systemic diseases, central nervous system diseases, cancer, and cognitive impairment. According to self-reporting and confirmation by the next of kin and family members, subjects with a history of drug abuse or dependence were also excluded, except for alcohol and nicotine abuse. The clinical characteristics data were collected after enrollment including age, years of education, marital status, and living conditions.

The Assessment of Aggression Associated With Alcohol Dependence

The Chinese version (Yang et al., 2017) revised from Buss–Perry Aggression Questionnaire (Buss and Perry, 1992) was used to measure five aspects of human aggression. The original 29-item scale with 4 subscales became a 30-item scale with 5 subscales: physical aggression (7 items), verbal aggression (5 items), anger (6 items), hostility (7 items), and aggression toward self (5 items). All items are 5-point Likert scales (none, seldom, sometimes, often, and always) scored 0–4, so the total score ranges from 0 to 120 with higher scores representing greater aggression. In addition, the MAST was performed to evaluate the influence of alcohol on individuals with AD (Selzer, 1971). The MAST is a 25-item, self-report questionnaire on which respondents rate the severity of a range of AD using a 4-point scale ranging from 1 (not at all) to 4 (extremely). The scale has high internal-consistency reliability, with alpha values of 0.90 (Skinner, 1982). Higher scores indicate greater AD. This study was approved by the Peking University Institutional Review Board. For each participant, written informed consent was obtained directly from the subjects or their responsible guardians. All procedures performed in this study involving human participants were following the 1964 Helsinki declaration and its later amendments or comparable ethical standards.

Selection and Genotyping of Single Nucleotide Polymorphism

Genomic DNA was extracted from 5 ml peripheral blood using the salting-out method from all the subjects (Tian et al., 2008). Buffy coats of nucleated cells obtained from anticoagulated blood (ACD or EDTA) were resuspended in 15 ml polypropylene centrifugation tubes with 3 ml of nuclei lysis buffer (10 mM Tris–HCl, 400 mM NaCl, and 2 mM Na_2EDTA, pH 8.2). The cell lysates were digested overnight at 37°C with 0.2 ml of 10% SDS and 0.5 ml of a protease K solution (1 mg protease K in 1% SDS and 2 mM Na_2EDTA). After digestion was complete, 1 ml of saturated NaCl (approximately 6M) was added to each tube and shaken vigorously for 15 s, followed by centrifugation at 2,500 rpm for 15 min. The precipitated protein pellet was left at the bottom of the tube and the supernatant containing the DNA was transferred to another 15 ml polypropylene tube. Exactly 2 volumes of room temperature absolute ethanol was added and the tubes inverted several times until the DNA precipitated. The precipitated DNA strands were removed with a plastic spatula or pipette and transferred to a 1.5 ml microcentrifuge tube containing 100–200 μl TE buffer (10 mM Tris–HCl, 0.2 mM Na_2EDTA, pH 7.5). The DNA was allowed to dissolve 2 h at 37°C before quantitating (Miller et al., 1988). Three SNPs of the gene including rs948992, rs11665841, rs11665896, rs7955866, and rs11063118 were genotyped using MALDI-TOF based scalable MassARRAY@ System (Agena Bioscience, Inc., San Diego, CA, United States). The protocol was performed according to the manufacturer's instructions. The primers are shown in **Table 1**. All the laboratory procedures were carried out in a blind manner to case/control status. The conditions of PCR were as follows: 94°C for 30 s [40 cycles × (94°C for 5 s), 5 cycles × (52°C for 5 s 80°C for 5 s, and 72°C for 3 min)]. Ten percent of the DNA samples were duplicated randomly and tested, and no-fault genotyping was found.

Statistical Analysis

Continuous variables were expressed as the mean ± standard and categorical variables were expressed as the absolute value. χ^2 test was performed to evaluate the difference of the categorical variables between the groups. Analysis of variance (ANOVA) for age and education years was performed to assess the differences of groups. Analysis of covariance (ANCOVA) for other continuous variables was performed with age and years of education as

TABLE 1 | Polymerase chain reaction (PCR) primers used for single nucleotide polymorphism (SNP) analysis of FGF19, FGF21, and FGF23 genes.

Polymorphism	Primer	Sequence (5′–3′)
rs948992	R-primer	ACGTTGGATGTAACTTGCTGTCCCGGTGTC
	F-primer	ACGTTGGATGAATCCATGGGGAGGCATGTG
	Single base extension	CAGAGGGCTGGTGGGCTGGG
rs11665841	R-primer	ACGTTGGATGAGAGCGAGACTCCGTCTCAA
	F-primer	ACGTTGGATGTACACCTCCCCTCACGTGG
	Single base extension	AAAAAGTGAGGCCCA
rs11665896	R-primer	ACGTTGGATGCAGCTGTTTTGTCTCCCTTG
	F-primer	ACGTTGGATGGAAAAAAGTGAGGCCCAGTG
	Single base extension	CCCATCCCCTCACGTGGTCC
rs11063118	R-primer	ACGTTGGATGGCTCACGTTTAATAGCTGGG
	F-primer	ACGTTGGATGAATGGGCAGTGCAGACTAGG
	Single base extension	TGGGGTTTGAACTCAGGCA
rs7955866	R-primer	ACGTTGGATGTCGAGTGAACACGCACGCTG
	F-primer	ACGTTGGATGAGCGACCCTAGATGAACTTG
	Single base extension	GGGCACACGCACGCTGGGGGAA

covariates using SPSS 20.0 (Statistical Package for Social Studies, Version 20.0, SPSS Inc., Chicago, IL, United States). Hardy–Weinberg equilibrium (HWE) test, linkage disequilibrium (LD) and the frequencies of the distribution of genotypes and alleles in both AD-group and HC-group were analyzed using SHEsis and SHEsis-Plus platform[2] (Shi and He, 2005). Generalized multifactor dimensionality reduction (GMDR), a genetic model-free alternative to logistic regression, is used to detect the interaction of gene and environment, which was performed to calculate the interaction of five loci (Lou et al., 2007). All tests were two-tailed, the *p*-value less than 0.05 was considered statistically significant.

RESULTS

The General Characteristics of the Study Population

In the present study as shown in **Table 2**, all the participants ranged from 20 to 67 years old (40.63 ± 11.68 years) with the education years from 5 to 18 years (10.78 ± 3.48 years). The age of subjects in the AD-group was 44.08 ± 11.96 years and significantly higher than that of the HC-group ($p < 0.001$), but the education years of subjects of the former were 9.88 ± 3.68 years and significantly lower than that of the latter ($p < 0.001$). In the AD-group, the proportion of patients with never married was 9.3% and was significantly lower compared with the HC-group ($p < 0.001$). The rate of patients with divorce/widowed history was significantly higher than that of the HC-group after multiple comparisons ($p < 0.001$). The MAST (Chinese version) 19 was performed to evaluate the severity of AD and it is a 22-item self-scoring test.

The Difference in Aggression Between the Two Groups

Because the age and years of education were different between the two groups, ANCOVA was used to calculate the difference of aggression with the year of education as covariables, respectively. The Aggression Scale total score was 34.83 ± 17.63 in the AD-group and higher than that of the HC-group (21.71 ± 15.04; $p < 0.001$). Physical aggression of the AD-group was higher compared with the HC-group (37.13 ± 21.01 vs. 26.15 ± 18.81; $p < 0.001$). Verbal aggression also significantly increased in the AD-group (41.41 ± 23.40 vs. 22.68 ± 18.94; $p < 0.001$). The level of anger in the AD-group was 41.41 ± 23.40 and significantly higher than that of the HC-group ($p < 0.001$). The subjects in the AD-group have stronger hostility than the HC-group (30.579 ± 19.18 vs. 18.12 ± 15.90; $p < 0.001$). The levels of self-aggression also elevated in subjects with AD than that of the HC-group (33.10 ± 20.05 vs. 15.01 ± 16.72; $p < 0.001$; **Table 3**).

The Association Between Aggression and MAST Scores

The association between MAST scores and aggression related to AD were investigated with age and years of education

[2]http://analysis.bio-x.cn/myAnalysis.php

TABLE 2 | Clinical characteristics of all participants.

Characteristics	AD (*n* = 482)	HC (*n* = 474)	*p*
Age	44.08 ± 11.96	37.07 ± 10.24	< 0.001
Years of education	9.88 ± 3.68	11.70 ± 2.99	< 0.001
Marital status *n*, (%)			
Never married	45 (9.3%)	105 (22.2%)	< 0.001
Married	362 (75.1%)	352 (74.3%)	0.765
Divorced/widowed	75 (15.6%)	17 (3.6%)	< 0.001
Living conditions			
Live alone	65 (13.5%)	87 (18.4%)	0.040
Living ingroup quarters	55 (11.4%)	58 (12.2%)	0.693
Livingwith family	362 (75.1%)	329 (69.4%)	0.049

AD, alcohol dependences; HC, healthy controls.
Analysis of variance was performed to analyze the difference of age and years of education between the groups. χ^2 test was performed to evaluate the difference of the categorical variables between the groups.

TABLE 3 | The difference in aggression related to AD compared with the HC-group.

Aggression and MAST scores	AD-group (*n* = 482)	HC-group (*n* = 474)	*p*
Aggression Scale total score	34.83 ± 17.63	21.71 ± 15.04	<0.001
Physical aggression	37.13 ± 21.01	26.15 ± 18.81	<0.001
Verbal aggression	37.72 ± 19.87	26.29 ± 18.15	<0.001
Anger	41.41 ± 23.40	22.68 ± 18.94	<0.001
Hostility	30.579 ± 19.18	18.12 ± 15.90	<0.001
Self-aggression	33.10 ± 20.05	15.01 ± 16.72	<0.001
MAST scores	10.09 ± 5.07	/	

AD, alcohol dependences; HC, healthy controls.
Analysis of covariance was performed to analyze the difference between the two groups with years of education as covariates.

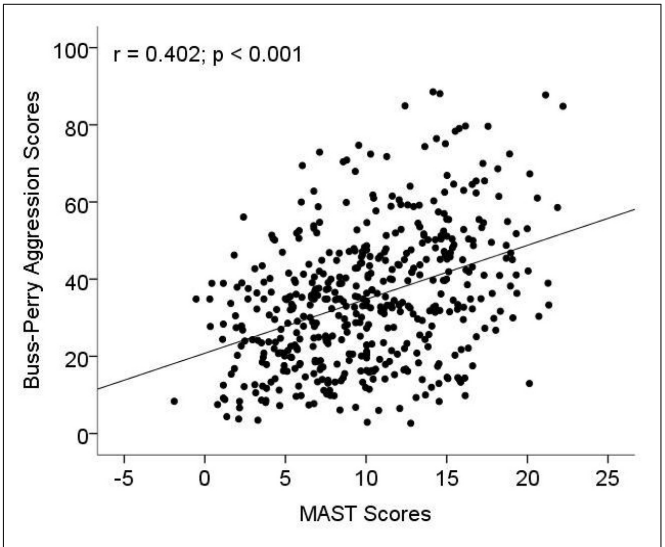

FIGURE 1 | The association between aggression and Michigan alcoholism screening test (MAST) scores. MAST was used to measure the level of alcohol dependence (AD), and a Chinese version of the Buss–Perry Aggression Questionnaire was used to evaluate the aggressive behavior of subjects.

as covariables. The result showed that MAST scores were significantly positively associated Buss–Perry aggression scores (r = 0.402, $p < 0.001$; **Figure 1**). In multiple linear regression model, increased MAST scores contributed to Buss–Perry aggression scores (OR: 1.44, 95%CI: 1.1–1.75) after being adjusted for age, education years and marital status (**Table 4**).

Genetic Polymorphisms Analysis

Genotype distributions of rs948992, rs11665841, rs11665896, rs7955866, and rs11063118 loci were consistent with Hardy–Weinberg proportions (AUD: $\chi^2 = 0.043$, $p = 0.98$; $\chi^2 = 1.81$, $p = 0.40$; $\chi^2 = 1.95$, $p = 0.38$; $\chi^2 = 1.47$, $p = 0.48$; $\chi^2 = 7.40$, $p = 0.024$; HC: $\chi^2 = 0.13$, $p = 0.94$; $\chi^2 = 3.12$, $p = 0.21$; $\chi^2 = 2.33$, $p = 0.31$; $\chi^2 = 0.46$, $p = 0.79$; and $\chi^2 = 2.17$, $p = 0.34$, respectively). As shown in **Table 5**, the distributions of genotypes and alleles of the five loci were not significantly different between the two groups, respectively (all $p > 0.05$).

Generalized Multifactor Dimensionality Reduction Analysis of Gene–Gene of FGF 19 and 21 Interaction for AD

Generalized multifactor dimensionality reduction analysis was performed to evaluate the cross-validation consistency and the prediction error for each number of loci. The model of FGF21 rs11665896 – FGF19 rs948992 combination was significant (p = 0.010) with a training accuracy of 55.68% and testing accuracy of 53.97%, and with a maximum cross-validation consistency (10/10) after permutation testing (**Table 6**). The two-locus genotype combinations related to different risk for each multilocus-genotype combination was analyzed and showed in **Figure 2**. The model of FGF21 rs11665896 (GG) – FGF19 rs948992 (TC) presented the high-risk genotype combination, and FGF21 rs11665896 (TT) – FGF19 rs948992 (TT) presented the low-risk genotype combinations (**Figure 2**).

TABLE 4 | The multiple linear regression analysis of the association between MAST scores and Buss–Perry aggression scores.

Buss–Perry aggression scores	Model 1		Model 2	
	β, 95% CI	*p*	β, 95% CI	*p*
MAST scores	1.41 (1.11–1.70)	<0.001	1.44 (1.14–1.75)	<0.001

Model 1: unadjusted.
Model 2: adjusted for age, education years and marital status.

Generalized Multifactor Dimensionality Reduction Analysis of Gene–Gene Interaction for Aggression Associated With AD

The model of FGF 19rs948992 – FGF21 rs11665896 – FGF23 rs11063118 combination was significant (p = 0.0017) with a training accuracy of 56.85% and testing accuracy of 50.32%, and with a close to maximum cross-validation consistency (9/10) after permutation testing (**Table 7**). The two-locus genotype combinations related to a different risk for each multilocus-genotype combination is shown in **Figure 3**. In the model of FGF19 rs948992 – FGF21 rs11665896 – FGF23 rs11063118, (TC) – (TG) – (TT) presented the high-risk genotype combination, (CC) – (TT) – (CC) and (TT) – (TT) – (CC) presented the low-risk genotype combinations (**Figure 3**).

DISCUSSION

In the present study, we attempted to evaluate the association between AD-related aggression and genetic variants of the FGF19 subfamily members including FGF19, FGF21, and FGF23 genes in a Chinese population. No significant differences were found of frequencies of allelic distribution of 5 SNPs in three loci of FGFs between AD and HC. We found that the aggression level of the AD subjects was higher than that of the HC group. Our results had also shown that the interaction of FGF21 rs11665896 GG × FGF19 rs948992 TC presented the high-risk genotype combination associated with AD, and FGF21 rs11665896 TT × FGF19 rs948992 TT presented the low-risk genotype combinations of AD. In addition, FGF19 rs948992 TC × FGF21 rs11665896 TG × FGF23 rs11063118 TT presented the high-risk genotype combination of aggression associated with AD.

The behavioral impairments related to alcohol have been reported in numerous studies about impulsivity, aggression, depression, suicidal behavior, and other mental disorders (Tobore, 2019). Alcohol-related aggression was a common violent behavior in individuals with AD, it was considered a brain disfunction with cognitive disruption (Heinz et al., 2011). It has been suggested that alcohol could disrupt the crucial contents of

TABLE 5 | The frequencies of genotypic and allelic distributions of five loci.

SNP		Major/minor allele	Major allele frequency		*p*	Major allele frequency		*p*
			HC	AD		HC (AA/Aa/aa)	AD (AA/Aa/aa)	
FGF19	rs948992	C/T	0.51	0.54	0.27	121/225/112	121/213/90	0.49
FGF21	rs11665841	C/T	0.68	0.69	0.76	230/187/55	219/177/48	0.93
	rs11665896	G/T	0.68	0.69	0.84	230/190/54	219/178/49	0.92
FGF23	rs7955866	G/A	0.84	0.85	0.52	337/123/14	327/106/13	0.76
	rs11063118	T/C	0.80	0.81	0.68	308/141/24	298/119/25	0.61

AA = major allele homozygous; Aa = heterozygous; aa = minor allele.

TABLE 6 | The best model for predicting the occurrence of AD.

Best model[a]	Training accuracy (%)	Testing accuracy (%)	CVC	χ^2	*p*	95% CI
1	52.71	37.80	6/10	1.07	0.302	1.24 (0.82, 1.88)
1, 2	55.68	53.97	10/10	6.51	0.010	1.74 (1.13, 2.66)
1, 2, 3	57.26	51.21	5/10	0.0064	0.936	1.05 (0.29, 3.71)
1, 2, 3, 4	58.66	51.82	8/10	0.715	0.398	1.72 (0.48, 6.08)
1, 2, 3, 4, 5	59.37	50.71	10/10	1.004	0.316	1.97 (0.52, 7.50)

[a]*Number 1–5 represented FGF19 rs948992, FGF21 rs11665896, FGF23 rs11063118, FGF23 rs7955866, and FGF21 rs11665841, respectively.*

social information and further engendered aggressive behavior under mis-interpretation (Beck and Heinz, 2013; Parrott and Eckhardt, 2018). But this association showed a controversial result with the development of alcohol exposure. Some studies suggested that increasing alcohol consumption was associated with violent behaviors including aggression (Stappenbeck and Fromme, 2010; Sacco et al., 2015). In an animal model, alcohol-related aggression increased with elevated doses of alcohol, but the dose-dependent association might be disrupted by higher doses (Weerts et al., 1993). Other studies reported that alcohol-related aggression did not happen much in individuals with AD (Murphy et al., 2005; Beck and Heinz, 2013). Thus, acute and excessive alcohol consumption seemed to more likely engender aggressive behavior (Fals-Stewart, 2003). In our study, higher MAST scores presented a higher risk of aggression in individuals with AD.

The studies about the genetic link between the FGF21 gene and alcohol intake increased gradually. It has been demonstrated that rs838133 and rs838145 were associated with higher carbohydrate intake, which also may affect alcohol intake (von Holstein-Rathlou and Gillum, 2019). The two SNPs in this present study, including rs11665896 and rs11665841, only rs11665896 was confirmed to influence carbohydrate metabolic (Ruiz-Padilla et al., 2019). Another study attempted to assess the association between rs11665841 and carbohydrate metabolism, but no significant association was found (Zhang et al., 2012). Although FGF19 mRNA overexpression was associated with alcohol-related decreases (Zhang et al., 2013), whether the SNPs of FGF19 including rs948992 were related to alcohol intake remains not clear. In this study, we found the interaction of FGF19 rs948992 TC × FGF21 rs11665896 GG presented the high-risk genotype combination associated with AD.

MicroRNAs constitute a growing class of non-coding RNAs that suppress target gene protein translation by combining with 3′ UTR (Bartel, 2004). Rs948992 is located on 3′ UTR of FGF19 gene, and rs1166584 and rs11665896 are both located about 500 bp downstream at 3′ end of the FGF21 gene, based on dbSNP database. The T allele of rs11665896 carriers consumed higher amounts of carbohydrates compared to carrying the GG or GT genotypes (Ruiz-Padilla et al., 2019), and alcohol in circulation was delayed in the G allele carriers compared to the T carriers, which means that the metabolic capability of GG genotype for alcohol may be weaker than the TT genotype. In addition, the two SNPs are located at the 3′UTR region, in which target sites for miRNAs are located and their genetic variants were associated with genotype alteration (Zhang et al., 2012). Speculatively, the change of allele exchange resulting from these loci could affect miRNA binding, perhaps reducing FGF19 and FGF21 transcription, as it has been shown for other genes (Sethupathy and Collins, 2008; Moszynska et al., 2017). In the present study, the interaction combination of FGF19 rs948992 TC × FGF21 rs11665896 TG × FGF23 rs11063118 TT showed a significant correlation with aggression associated with AD.

Some limitations of the present study should be noted. Firstly, the age and the years of education were not well-matched between the HC and AD subjects. The age and education years may have effects on aggression, although the conclusions about the effects of age and education years on aggression are inconsistent in previous studies. A recent study suggested that physical aggression declined with age in boys instead of girls, but indirect aggression increased with age in girls, such as anger and hostility (Tsorbatzoudis et al., 2013). Another study suggested that age had bi-directional moderating effects

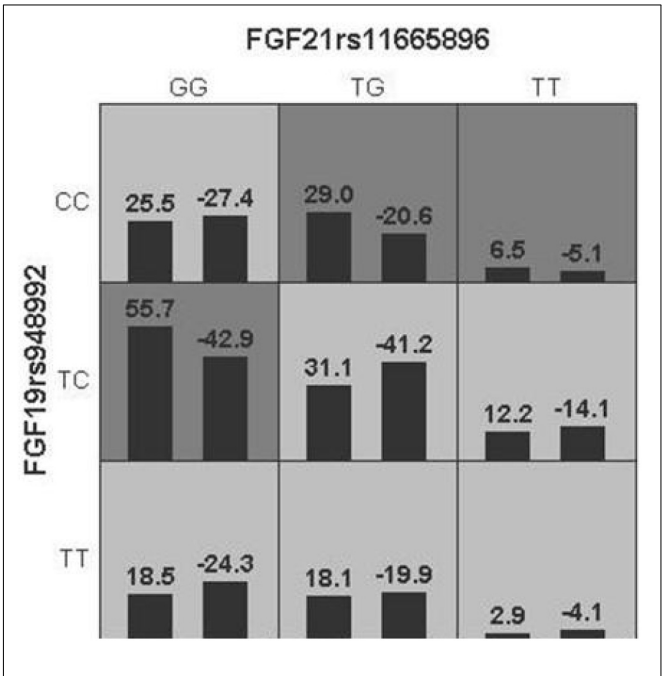

FIGURE 2 | The best model based on generalized multifactor dimensionality reduction (GMDR) analyses showed the interaction effect of FGF19 rs948992 TC × FGF21 rs11665896 GG on AD. The shaded dark gray cell presented a high-risk combination and shaded light gray presented a low-risk combination.

TABLE 7 | The best model for predicting the aggression in AD.

Best model[a]	Training accuracy (%)	Testing accuracy (%)	CVC	χ^2	*p*	95% CI
1	53.32	50.78	9/10	0.23	0.629	0.94 (0.76, 1.18)
1, 2	54.09	50.32	8/10	1.39	0.237	0.87 (0.70, 1.09)
1, 2, 3	56.85	52.66	9/10	9.89	0.0017	1.44 (1.15, 1.80)
1, 2, 3, 4	58.19	51.43	6/10	0.568	0.451	1.08 (0.88, 1.33)
1, 2, 3, 4, 5	59.33	53.88	10/10	0.213	0.644	0.95 (0.75, 1.19)

[a]*Number 1–5 represented FGF19 rs948992, FGF21 rs11665896, FGF23 rs11063118, FGF23 rs7955866, and FGF21 rs11665841, respectively.*

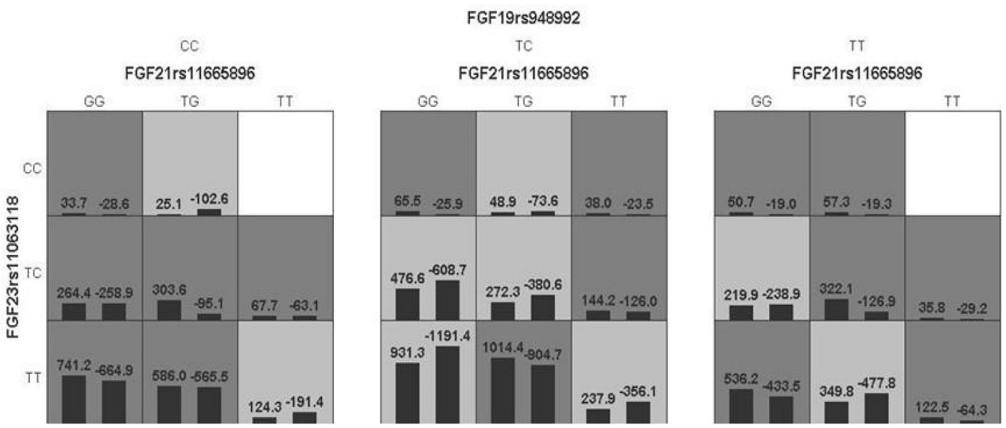

FIGURE 3 | The best model based on GMDR analyses showed the interaction effect of FGF19 rs948992 TC × FGF21 rs11665896 TG × FGF23 rs11063118 TT on AD related aggression. The shaded dark gray cell presented a high-risk combination and shaded light gray presented a low-risk combination.

on aggression based on the levels of reactive aggression (Smeets et al., 2017). Generally for male drinkers, daily alcohol intake increases with age but declines in those with more education (Li et al., 2014). Perpetrators of peer aggression were reported to be associated with non-completion of secondary school (Moore et al., 2015) and aggression negatively predicted higher education (Rabinowitz et al., 2020). Although the statistical analysis of ANCOVA was performed with age and education years as covariates to weaken the influence of age and education year differences on aggression between the HC and AD groups, age and education year differences might still possibly cause the observed difference in the aggression of HC and AD groups in the present study. Secondly, more variations of these three genes, including tags and functional variations should be genotyped to obtain more information. Finally, the information of SNPs on FGF 23 in AD and aggression is rare, and needs to be further investigated.

CONCLUSION

The aggression increases significantly associated with the level of AD in the AD subjects. The interaction of FGF19 rs948992 TC × FGF21 rs11665896 GG presented the high-risk genotype combination predicting the high level of AD. In addition, the interaction of FGF19 rs948992 TC × FGF21 rs11665896 TG × FGF23 rs11063118 TT presented the high-risk genotype combination predicting the high level of aggression in AD patients.

DATA AVAILABILITY STATEMENT

The raw data supporting the conclusions of this article will be made available by the authors, without undue reservation.

AUTHOR CONTRIBUTIONS

JH and HX conceived and designed the research. JX, FeW, FaW, FY, MLi, MLo, LW, and JH performed the experiments and wrote the manuscript together. HL and YF supplied the important and thoughtful advice and performed the experiments. LC, YL, and WL performed the statistical analysis and supplied much technology and fund assistant. FeW performed the experiments and wrote the manuscript, and made an important contribution to the work. All authors discussed the drafting of the manuscript. HX edited the last version of the manuscript.

FUNDING

This work was supported by the Basic and public research project of Zhejiang province (LGF18H020001), the Open Project Program of Key Laboratory of Drug Prevention and Control Technology of Zhejiang Province (2020012), the Natural Science Foundation of Xinjiang Uyghur Autonomous Region (2018D01C228), the Health Technology Program in Zhejiang Province (2017KY720), the Fujian Provincial Health Commission (2017-CXB-17), and the National Nature Science Foundation of China (81671266).

REFERENCES

Abrahao, K. P., Salinas, A. G., and Lovinger, D. M. (2017). Alcohol and the brain: neuronal molecular targets, synapses, and circuits. *Neuron* 96, 1223–1238. doi: 10.1016/j.neuron.2017.10.032

Bartel, D. P. (2004). MicroRNAs: genomics, biogenesis, mechanism, and function. *Cell* 116, 281–297. doi: 10.1016/s0092-8674(04)00045-5

Beck, A., and Heinz, A. (2013). Alcohol-related aggression-social and neurobiological factors. *Dtsch. Arztebl. Int.* 110, 711–715. doi: 10.3238/arztebl.2013.0711

Brandl, K., Hartmann, P., Jih, L. J., Pizzo, D. P., Argemi, J., Ventura-Cots, M., et al. (2018). Dysregulation of serum bile acids and FGF19 in alcoholic hepatitis. *J. Hepatol.* 69, 396–405. doi: 10.1016/j.jhep.2018.03.031

Brodie, M. J., Besag, F., Ettinger, A. B., Mula, M., Gobbi, G., Comai, S., et al. (2016). Epilepsy, antiepileptic drugs, and aggression: an evidence-based review. *Pharmacol. Rev.* 68, 563–602. doi: 10.1124/pr.115.012021

Buss, A. H., and Perry, M. (1992). The aggression questionnaire. *J. Pers. Soc. Psychol.* 63, 452–459. doi: 10.1037//0022-3514.63.3.452

Chen, K., and Rajewsky, N. (2006). Natural selection on human microRNA binding sites inferred from SNP data. *Nat. Genet.* 38, 1452–1456. doi: 10.1038/ng1910

Chester, D. S., Bucholz, K. K., Chan, G., Kamarajan, C., Pandey, A. K., Wetherill, L., et al. (2020). Alcohol-related, drug-related, and non-substance-related aggression: 3 facets of a single construct or 3 distinct constructs? *Alcohol. Clin. Exp. Res.* 44, 1852–1861. doi: 10.1111/acer.14412

Chiavaroli, A., Recinella, L., Ferrante, C., Martinotti, S., Vacca, M., Brunetti, L., et al. (2017). Effects of central fibroblast growth factor 21 and irisin in anxiety-like behavior. *J. Biol. Regul. Homeost. Agents* 31, 797–802.

Desai, B. N., Singhal, G., Watanabe, M., Stevanovic, D., Lundasen, T., Fisher, F. M., et al. (2017). Fibroblast growth factor 21 (FGF21) is robustly induced by ethanol and has a protective role in ethanol associated liver injury. *Mol. Metab.* 6, 1395–1406. doi: 10.1016/j.molmet.2017.08.004

Dick, D. M., and Agrawal, A. (2008). The genetics of alcohol and other drug dependence. *Alcohol Res. Health* 31, 111–118.

Dolegowska, K., Marchelek-Mysliwiec, M., Nowosiad-Magda, M., Slawinski, M., and Dolegowska, B. (2019). FGF19 subfamily members: FGF19 and FGF21. *J. Physiol. Biochem.* 75, 229–240. doi: 10.1007/s13105-019-00675-7

Epperlein, S., Gebhardt, C., Rohde, K., Chakaroun, R., Patt, M., Schamarek, I., et al. (2021). The effect of FGF21 and its genetic variants on food and drug cravings, adipokines and metabolic traits. *Biomedicines* 9:345. doi: 10.3390/biomedicines9040345

Erickson, E. K., Blednov, Y. A., Harris, R. A., and Mayfield, R. D. (2019). Glial gene networks associated with alcohol dependence. *Sci. Rep.* 9:10949. doi: 10.1038/s41598-019-47454-4

Fals-Stewart, W. (2003). The occurrence of partner physical aggression on days of alcohol consumption: a longitudinal diary study. *J. Consult. Clin. Psychol.* 71, 41–52. doi: 10.1037//0022-006x.71.1.41

Frayling, T. M., Beaumont, R. N., Jones, S. E., Yaghootkar, H., Tuke, M. A., Ruth, K. S., et al. (2018). A common allele in FGF21 associated with sugar intake is associated with body shape, lower total body-fat percentage, and higher blood pressure. *Cell Rep.* 23, 327–336. doi: 10.1016/j.celrep.2018.03.070

Gan, G., Sterzer, P., Marxen, M., Zimmermann, U. S., and Smolka, M. N. (2015). Neural and behavioral correlates of alcohol-induced aggression under provocation. *Neuropsychopharmacology* 40, 2886–2896. doi: 10.1038/npp.2015.141

Gibson, E. L. (2018). Tryptophan supplementation and serotonin function: genetic variations in behavioural effects. *Proc. Nutr. Soc.* 77, 174–188. doi: 10.1017/S0029665117004451

Gonzalez-Reimers, E., Romero-Acevedo, L., Espelosin-Ortega, E., Martin-Gonzalez, M. C., Quintero-Platt, G., Abreu-Gonzalez, P., et al. (2018). Soluble klotho and brain atrophy in alcoholism. *Alcohol Alcohol.* 53, 503–510. doi: 10.1093/alcalc/agy037

Grant, B. F., Goldstein, R. B., Saha, T. D., Chou, S. P., Jung, J., Zhang, H., et al. (2015). Epidemiology of DSM-5 alcohol use disorder: results from the national epidemiologic survey on alcohol and related conditions III. *JAMA Psychiatry* 72, 757–766. doi: 10.1001/jamapsychiatry.2015.0584

Han, W., Tellez, L. A., Niu, J., Medina, S., Ferreira, T. L., Zhang, X., et al. (2016). Striatal dopamine links gastrointestinal rerouting to altered sweet appetite. *Cell Metab.* 23, 103–112. doi: 10.1016/j.cmet.2015.10.009

Heianza, Y., Ma, W., Huang, T., Wang, T., Zheng, Y., Smith, S. R., et al. (2016). Macronutrient intake-associated FGF21 genotype modifies effects of weight-loss diets on 2-year changes of central adiposity and body composition: The POUNDS lost trial. *Diabetes Care* 39, 1909–1914. doi: 10.2337/dc16-1111

Heinz, A. J., Beck, A., Meyer-Lindenberg, A., Sterzer, P., and Heinz, A. (2011). Cognitive and neurobiological mechanisms of alcohol-related aggression. *Nat. Rev. Neurosci.* 12, 400–413. doi: 10.1038/nrn3042

Kharitonenkov, A., and DiMarchi, R. (2017). Fibroblast growth factor 21 night watch: advances and uncertainties in the field. *J. Intern. Med.* 281, 233–246. doi: 10.1111/joim.12580

Kiive, E., Laas, K., Vaht, M., Veidebaum, T., and Harro, J. (2017). Stressful life events increase aggression and alcohol use in young carriers of the GABRA2 rs279826/rs279858 A-allele. *Eur. Neuropsychopharmacol.* 27, 816–827. doi: 10.1016/j.euroneuro.2017.02.003

Landi, D., Gemignani, F., Barale, R., and Landi, S. (2008). A catalog of polymorphisms falling in microRNA-binding regions of cancer genes. *DNA Cell Biol.* 27, 35–43. doi: 10.1089/dna.2007.0650

Li, Y., Zhang, M., Jiang, Y., Deng, Q., Zhao, Y., Huang, Z., et al. (2014). [Drinking behaviors and patterns among floating population aged 18-59 years old in China, 2012]. *Zhonghua Liu Xing Bing Xue Za Zhi* 35, 1186–1191.

Lou, X. Y., Chen, G. B., Yan, L., Ma, J. Z., Zhu, J., Elston, R. C., et al. (2007). A generalized combinatorial approach for detecting gene-by-gene and gene-by-environment interactions with application to nicotine dependence. *Am. J. Hum. Genet.* 80, 1125–1137. doi: 10.1086/518312

Malamut, S. T., van den Berg, Y. H. M., Lansu, T. A. M., and Cillessen, A. H. N. (2021). Bidirectional associations between popularity, popularity goal, and aggression, alcohol use and prosocial behaviors in adolescence: a 3-year prospective longitudinal study. *J. Youth Adolesc.* 50, 298–313. doi: 10.1007/s10964-020-01308-9

Miller, S. A., Dykes, D. D., and Polesky, H. F. (1988). A simple salting out procedure for extracting DNA from human nucleated cells. *Nucleic Acids Res.* 16:1215. doi: 10.1093/nar/16.3.1215

Moore, S. E., Scott, J. G., Thomas, H. J., Sly, P. D., Whitehouse, A. J., Zubrick, S. R., et al. (2015). Impact of adolescent peer aggression on later educational and employment outcomes in an Australian cohort. *J. Adolesc.* 43, 39–49. doi: 10.1016/j.adolescence.2015.05.007

Moszynska, A., Gebert, M., Collawn, J. F., and Bartoszewski, R. (2017). SNPs in microRNA target sites and their potential role in human disease. *Open Biol.* 7:170019. doi: 10.1098/rsob.170019

Murphy, C. M., Winters, J., O'Farrell, T. J., Fals-Stewart, W., and Murphy, M. (2005). Alcohol consumption and intimate partner violence by alcoholic men: comparing violent and nonviolent conflicts. *Psychol. Addict. Behav.* 19, 35–42. doi: 10.1037/0893-164x.19.1.35

Nedic Erjavec, G., Nenadic Sviglin, K., Nikolac Perkovic, M., Muck-Seler, D., Jovanovic, T., and Pivac, N. (2014). Association of gene polymorphisms encoding dopaminergic system components and platelet MAO-B activity with alcohol dependence and alcohol dependence-related phenotypes. *Prog. Neuropsychopharmacol. Biol. Psychiatry* 54, 321–327. doi: 10.1016/j.pnpbp.2014.07.002

Newman, E. L., Terunuma, M., Wang, T. L., Hewage, N., Bicakci, M. B., Moss, S. J., et al. (2018). A role for prefrontal cortical NMDA receptors in murine alcohol-heightened aggression. *Neuropsychopharmacology* 43, 1224–1234. doi: 10.1038/npp.2017.253

Nguyen, M., Boutignon, H., Mallet, E., Linglart, A., Guillozo, H., Jehan, F., et al. (2010). Infantile hypercalcemia and hypercalciuria: new insights into a vitamin D-dependent mechanism and response to ketoconazole treatment. *J. Pediatr.* 157, 296–302. doi: 10.1016/j.jpeds.2010.02.025

Park, C. I., Kim, H. W., Hwang, S. S., Kang, J. I., and Kim, S. J. (2019). Influence of dopamine-related genes on craving, impulsivity, and aggressiveness in Korean males with alcohol use disorder. *Eur. Arch. Psychiatry Clin. Neurosci.* 271, 865–872. doi: 10.1007/s00406-019-01072-3

Parrott, D. J., and Eckhardt, C. I. (2018). Effects of alcohol on human aggression. *Curr. Opin. Psychol.* 19, 1–5. doi: 10.1016/j.copsyc.2017.03.023

Plemenitas, A., Kores Plesnicar, B., Kastelic, M., Porcelli, S., Serretti, A., and Dolzan, V. (2015). Genetic variability in tryptophan hydroxylase 2 gene in alcohol dependence and alcohol-related psychopathological symptoms. *Neurosci. Lett.* 604, 86–90. doi: 10.1016/j.neulet.2015.07.037

Quintero-Platt, G., Gonzalez-Reimers, E., Rodriguez-Gaspar, M., Martin-Gonzalez, C., Perez-Hernandez, O., Romero-Acevedo, L., et al. (2017). Alpha klotho and fibroblast growth factor-23 among alcoholics. *Alcohol Alcohol.* 52, 542–549. doi: 10.1093/alcalc/agx041

Rabinowitz, J. A., Kuo, S. I., Domingue, B., Smart, M., Felder, W., Benke, K., et al. (2020). Pathways between a polygenic score for educational attainment and higher educational attainment in an African American sample. *Behav. Genet.* 50, 14–25. doi: 10.1007/s10519-019-09982-7

Recinella, L., Leone, S., Ferrante, C., Chiavaroli, A., Di Nisio, C., Martinotti, S., et al. (2017). Effects of central fibroblast growth factor 21 (FGF21) in energy balance. *J. Biol. Regul. Homeost. Agents* 31, 603–613.

Roozen, H. G., Wetering, B. J., and Franken, I. H. (2013). Does alcohol craving mediate the impulsivity-aggression relationship in recently detoxified alcohol-dependent patients? *Am. J. Drug Alcohol Abuse* 39, 57–60. doi: 10.3109/00952990.2012.677888

Rothe, H., Brandenburg, V., Haun, M., Kollerits, B., Kronenberg, F., Ketteler, M., et al. (2017). Ecto-5' -Nucleotidase CD73 (NT5E), vitamin D receptor and FGF23 gene polymorphisms may play a role in the development of calcific uremic arteriolopathy in dialysis patients – Data from the German Calciphylaxis registry. *PLoS One* 12:e0172407. doi: 10.1371/journal.pone.0172407

Ruiz-Padilla, A. J., Morales-Hernandez, G., Ruiz-Noa, Y., Alonso-Castro, A. J., Lazo-de-la-Vega-Monroy, M. L., Preciado-Puga, M. D. C., et al. (2019). Association of the 3′UTR polymorphism (rs11665896) in the FGF21 gene with metabolic status and nutrient intake in children with obesity. *J. Pediatr. Endocrinol. Metab.* 32, 921–928. doi: 10.1515/jpem-2018-0546

Sacco, P., Bright, C. L., Jun, H. J., and Stapleton, L. M. (2015). Developmental relations between alcohol and aggressive behavior among adolescents: neighborhood and sociodemographic correlates. *Int. J. Ment. Health Addict.* 13, 603–617. doi: 10.1007/s11469-015-9546-1

Schuckit, M. A. (2009). Alcohol-use disorders. *Lancet* 373, 492–501. doi: 10.1016/S0140-6736(09)60009-X

Schumann, G., Liu, C., O'Reilly, P., Gao, H., Song, P., Xu, B., et al. (2016). KLB is associated with alcohol drinking, and its gene product β-Klotho is necessary for FGF21 regulation of alcohol preference. *Proc. Natl. Acad. Sci. U.S.A.* 113, 14372–14377. doi: 10.1073/pnas.1611243113

Selzer, M. L. (1971). The Michigan alcoholism screening test: the quest for a new diagnostic instrument. *Am. J. Psychiatry* 127, 1653–1658. doi: 10.1176/ajp.127.12.1653

Sethupathy, P., and Collins, F. S. (2008). MicroRNA target site polymorphisms and human disease. *Trends Genet.* 24, 489–497. doi: 10.1016/j.tig.2008.07.004

Shi, Y. Y., and He, L. (2005). SHEsis, a powerful software platform for analyses of linkage disequilibrium, haplotype construction, and genetic association at polymorphism loci. *Cell Res.* 15, 97–98. doi: 10.1038/sj.cr.7290272

Skinner, H. A. (1982). The drug abuse screening test. *Addict. Behav.* 7, 363–371. doi: 10.1016/0306-4603(82)90005-3

Smeets, K. C., Oostermeijer, S., Lappenschaar, M., Cohn, M., van der Meer, J. M., Popma, A., et al. (2017). Are proactive and reactive aggression meaningful distinctions in adolescents? A variable- and person-based approach. *J. Abnorm. Child Psychol.* 45, 1–14. doi: 10.1007/s10802-016-0149-5

Soberg, S., Andersen, E. S., Dalsgaard, N. B., Jarlhelt, I., Hansen, N. L., Hoffmann, N., et al. (2018). FGF21, a liver hormone that inhibits alcohol intake in mice, increases in human circulation after acute alcohol ingestion and sustained binge drinking at Oktoberfest. *Mol. Metab.* 11, 96–103. doi: 10.1016/j.molmet.2018.03.010

Soberg, S., Sandholt, C. H., Jespersen, N. Z., Toft, U., Madsen, A. L., von Holstein-Rathlou, S., et al. (2017). FGF21 is a sugar-induced hormone associated with sweet intake and preference in humans. *Cell Metab.* 25, 1045–1053.e6. doi: 10.1016/j.cmet.2017.04.009

Song, P., Zechner, C., Hernandez, G., Cánovas, J., Xie, Y., Sondhi, V., et al. (2018). The hormone FGF21 stimulates water drinking in response to ketogenic diet and alcohol. *Cell Metab.* 27, 1338–1347.e4. doi: 10.1016/j.cmet.2018.04.001

Stappenbeck, C. A., and Fromme, K. (2010). A longitudinal investigation of heavy drinking and physical dating violence in men and women. *Addict.Behav.* 35, 479–485. doi: 10.1016/j.addbeh.2009.12.027

Tian, W., Wang, F., Cai, J. H., and Li, L. X. (2008). Polymorphic insertions in 5 Alu loci within the major histocompatibility complex class I region and their linkage disequilibria with HLA alleles in four distinct populations in mainland China. *Tissue Antigens* 72, 559–567. doi: 10.1111/j.1399-0039.2008.01152.x

Tobore, T. O. (2019). On the neurobiological role of oxidative stress in alcohol-induced impulsive, aggressive and suicidal behavior. *Subst. Use Misuse* 54, 2290–2303. doi: 10.1080/10826084.2019.1645179

Tsorbatzoudis, H., Travlos, A. K., and Rodafinos, A. (2013). Gender and age differences in self-reported aggression of high school students. *J. Interpers. Violence* 28, 1709–1725. doi: 10.1177/0886260512468323

von Holstein-Rathlou, S., and Gillum, M. P. (2019). Fibroblast growth factor 21: an endocrine inhibitor of sugar and alcohol appetite. *J. Physiol.* 597, 3539–3548. doi: 10.1113/jp277117

Waltes, R., Chiocchetti, A. G., and Freitag, C. M. (2016). The neurobiological basis of human aggression: a review on genetic and epigenetic mechanisms. *Am. J. Med. Genet. B Neuropsychiatr. Genet.* 171, 650–675. doi: 10.1002/ajmg.b.32388

Weerts, E. M., Tornatzky, W., and Miczek, K. A. (1993). Prevention of the pro-aggressive effects of alcohol in rats and squirrel monkeys by benzodiazepine receptor antagonists. *Psychopharmacology (Berl.)* 111, 144–152. doi: 10.1007/bf02245516

Witkiewitz, K., Litten, R. Z., and Leggio, L. (2019). Advances in the science and treatment of alcohol use disorder. *Sci. Adv.* 5:eaax4043. doi: 10.1126/sciadv.aax4043

Yang, L., Wang, F., Wang, M., Han, M., Hu, L., Zheng, M., et al. (2017). Association between oxytocin and receptor genetic polymorphisms and aggression in a northern Chinese Han population with alcohol dependence. *Neurosci. Lett.* 636, 140–144. doi: 10.1016/j.neulet.2016.10.066

Zhang, C., Ojiaku, P., and Cole, G. J. (2013). Forebrain and hindbrain development in zebrafish is sensitive to ethanol exposure involving agrin, Fgf, and sonic hedgehog function. *Birth Defects Res. A Clin. Mol. Teratol.* 97, 8–27. doi: 10.1002/bdra.23099

Zhang, M., Zeng, L., Wang, Y. J., An, Z. M., and Ying, B. W. (2012). Associations of fibroblast growth factor 21 gene 3' untranslated region single-nucleotide polymorphisms with metabolic syndrome, obesity, and diabetes in a Han Chinese population. *DNA Cell Biol.* 31, 547–552. doi: 10.1089/dna.2011.1302

Conflict of Interest: The authors declare that the research was conducted in the absence of any commercial or financial relationships that could be construed as a potential conflict of interest.

Advantages of publishing in Frontiers

OPEN ACCESS
Articles are free to read for greatest visibility and readership

FAST PUBLICATION
Around 90 days from submission to decision

HIGH QUALITY PEER-REVIEW
Rigorous, collaborative, and constructive peer-review

TRANSPARENT PEER-REVIEW
Editors and reviewers acknowledged by name on published articles

Frontiers
Avenue du Tribunal-Fédéral 34
1005 Lausanne | Switzerland

Visit us: www.frontiersin.org
Contact us: frontiersin.org/about/contact

REPRODUCIBILITY OF RESEARCH
Support open data and methods to enhance research reproducibility

DIGITAL PUBLISHING
Articles designed for optimal readership across devices

FOLLOW US
@frontiersin

IMPACT METRICS
Advanced article metrics track visibility across digital media

EXTENSIVE PROMOTION
Marketing and promotion of impactful research

LOOP RESEARCH NETWORK
Our network increases your article's readership